AES 2026 Catania – Italy

The 12th International Conference on Antennas and Electromagnetic Systems

3–6 June 2026
Catania, Italy

Proceedings
aesconference.org
ISSN 2491-2417

AES 2026

The 12th International Conference on Antennas and Electromagnetic Systems

Catania, Italy · 3–6 June 2026

Dates	3–6 June 2026
Venue	Monastero dei Benedettini di San Nicolò l'Arena, University of Catania, Piazza Dante 32, 95124 Catania, Italy
Website	aesconference.org
Contact	contact@aesconference.org
Indexing	SCOPUS indexed
Partners	Paris-Saclay University, France
ISSN	2491-2417

PERMANENT PROCEEDINGS REPOSITORY

The official permanent repository of the AES Conference Proceedings is available at:

https://aesconference.org/proceedings/

This repository provides long-term public access to the proceedings volumes of all editions of the International Conference on Antennas and Electromagnetic Systems (AES).

EDITED BY

Santi Concetto Pavone	University of Catania, Italy
Gino Sorbello	University of Catania, Italy
Loreto Di Donato	University of Catania, Italy
Said Zouhdi	Paris-Saclay University, France

© 2008–2026 AES Conference · ISSN 2491-2417 · All rights reserved

Preface

AES 2026

This volume constitutes the official proceedings of **AES 2026**, the 12th International Conference on Antennas and Electromagnetic Systems, held on 3–6 June 2026 at the Monastero dei Benedettini di San Nicolò l'Arena, University of Catania, Italy.

Since its first edition, the AES conference series has offered a forum where the antennas, microwave and electromagnetic-systems community meets the rapidly evolving fields of metamaterials, plasmonics, nanophotonics and quantum technologies. This cross-fertilisation is the hallmark of AES: the present volume spans subjects from antenna theory, computational electromagnetics and inverse problems to nonlinear flat optics, phase-change photonics and quantum light control.

AES 2026 gathered authors from **36 countries** across five continents. Following evaluation by the Scientific Advisory Committee and the Technical Program Committee, **231 contributions** were accepted for presentation and are collected here: 5 plenary lectures, 12 keynote lectures, 161 invited talks, 30 contributed oral presentations and 23 poster presentations, organised in 2 symposia, 13 special sessions and 6 general sessions.

Every contribution in this volume was reviewed for originality, technical soundness and relevance to the conference scope, and is published in the form provided by its authors. The peer-review and publication policy is detailed on the following page.

We warmly thank the members of all committees and the session organisers for the quality of the scientific selection, the University of Catania for hosting the conference in an exceptional setting, our partner institutions, and above all the authors and participants who make AES what it is. We hope this volume will serve as a lasting record of the conference and a useful reference for the community.

Catania, June 2026 *The Editors*

Santi Concetto Pavone	University of Catania, Italy
Gino Sorbello	University of Catania, Italy
Loreto Di Donato	University of Catania, Italy
Said Zouhdi	Paris-Saclay University, France

Peer Review & Publication Policy

AES 2026

Peer Review

All contributions submitted to AES 2026 were evaluated by members of the Scientific Advisory Committee and of the Technical Program Committee, with the support of the symposium and special-session organisers. Submissions were assessed on the basis of extended abstracts or full papers; acceptance was notified together with the presentation category (plenary, keynote, invited, oral or poster).

Selection Criteria

Reviewers were asked to assess each submission against the following criteria:

- originality and novelty of the work;
- technical soundness and scientific rigour;
- relevance to the scope of the conference;
- clarity of the presentation.

Publication Ethics

Authors certify that their contribution is original, that it does not infringe any third-party rights, and that all sources are duly acknowledged. Each paper is published as supplied by its authors, who bear full responsibility for its content. At least one author of each contribution registered for and presented the work at the conference.

Indexing & Archiving

The AES proceedings are published under **ISSN 2491-2417** and are **indexed in SCOPUS**. The present volume is archived and available at aesconference.org.

SUGGESTED CITATION OF THIS VOLUME

Proceedings of the 12th International Conference on Antennas and Electromagnetic Systems (AES 2026), S.C. Pavone, G. Sorbello, L. Di Donato and S. Zouhdi, Eds., Catania, Italy, 3–6 June 2026. ISSN 2491-2417.

Copyright

© 2026 the respective authors. All rights reserved. Reproduction of any part of this volume requires the permission of the authors concerned.

Contents

§ **Preface** 3

A word from the editors · review process · acknowledgements

§ **Peer Review & Publication Policy** 4

Selection criteria · publication ethics · indexing & archiving

§ **Organization & Committees** 6

General Co-Chairs · Scientific Advisory Committee · Technical Program Committee

§ **Plenary Talks** 8

5 plenary lectures: Z.N. Chen · G. Leo · E. Martini · E. Rajo-Iglesias · V.M. Shalaev

§ **Keynote Talks** 13

12 keynotes: A. Alù · A. Boltasseva · L. Crocco · A. Di Falco · M. Ettorre · A. Grbic· O. Hess · T.F. Krauss · S. Maci · M. Soljačić · F. Vipiana · D.-X. Xu

§ **Conference Papers** 19

Plenary · Keynote · Symposia · Special & General Sessions · Posters · Indexes

Talk type colour code used throughout this booklet:

PLENARY 35 min · KEYNOTE 30 min · INVITED 20 min

ORAL 15 min · POSTER Session

Organization & Committees

AES 2026

AES 2026 General Co-Chairs

Santi Concetto Pavone
AES 2026 General Co-Chair
University of Catania
Italy

Gino Sorbello
AES 2026 General Co-Chair
University of Catania
Italy

Loreto Di Donato
AES 2026 General Co-Chair
University of Catania
Italy

Said Zouhdi
AES General Chair
Paris-Saclay University
France

Scientific Advisory Committee

Matteo Albani	IT	Kotaro Kajikawa	JP	Luca Pierantoni	IT
Andrea Alù	US	Tommaso Isernia	IT	Francesco Prudenzano	IT
Francesco Andriulli	IT	Koichi Ito	JP	O. Quevedo-Teruel	SE
Christos Christopoulos	UK	Ahmed Kishk	CA	Eva Rajo-Iglesias	ES
Tie Jun Cui	CN	Giuseppe Leo	FR	Paul Smith	AU
Costantino De Angelis	IT	Joe Lo Vetri	CA	Raffaele Solimene	IT
Giuseppe Della Valle	IT	Kwai Man Luk	HK	Stefano Trillo	IT
Peter de Maagt	NL	Stefano Maci	IT	Luca Vincetti	IT
Mauro Ettorre	US	Enrica Martini	IT		
D. González-Ovejero	FR	Andrea Massa	IT		

Technical Program Committee

C. Argyropoulos	US	Yangjian Cai	CN	Paolo Franceschini	IT
Rita Asquini	IT	Pai-Yen Chen	US	Walter Fuscaldo	IT
Mirko Barbuto	IT	Christophe Craeye	BE	Marco Gandolfi	IT
Martina Bevacqua	IT	Alessandro Fanti	IT	T.S.J. Horng	TW
Xavier Begaud	FR	Alessandro Fedeli	IT	Zhirun Hu	UK

Ruey-Bing Hwang	TW	Andrea Michel	IT	Stefano Vellucci	IT
Sungtek Kahng	KR	Alessio Monti	IT	Enrico M. Vitucci	IT
Allen M. Larar	US	Roberta Palmeri	IT	Kaikai Xu	CN
Howard Lee	US	Cristina Ponti	IT	Kuang Zhang	CN
Jensen Li	HK	Blaise Ravelo	CN	Qi-Jun Zhang	CA
A.M. Loconsole	IT	Junsuk Rho	KR	Linjie Zhou	CN
Jean-Marc Lopez	FR	J.T. Sri Sumantyo	JP		
M.J. Mencagli	US	Andrea Tognazzi	IT		

Symposia Organizers

Andrea Di Falco
UK

Kotaro Kajikawa
Japan

Junichi Takahara
Japan

Special Session Organizers

Francesco Anelli	IT	José L. Gómez Tornero	ES	Emilija Petronijević	IT
Giada M. Battaglia	IT	Maria Josè Lo Faro	IT	Piotr Piotrowski	PL
Martina Bevacqua	IT	Antonella M. Loconsole	IT	Julien Sarrazin	FR
Mirko Barbuto	IT	Stefano Maci	IT	Rosa Scapaticci	IT
Francesco Chietera	IT	Maria Antonia Maisto	IT	Olga Sergaeva	IT
Costantino De Angelis	IT	Mario J. Mencagli	US	Dimitrios Sounas	US
Paolo Franceschini	IT	Alessio Monti	IT	Andrea Tognazzi	IT
Marco Gandolfi	IT	Alessio Mostaccio	IT	Stefano Vellucci	IT
Andrea Gerini	FR	Giacomo Muntoni	IT		
Maria Caterina Giordano	IT	Edoardo Negri	IT		
Federico Giusti	IT	Roberta Palmeri	IT		

Plenary Talks

AES 2026

PLENARY 5 plenary lectures · 35 minutes each including Q&A

PLENARY LECTURE 1

PLENARY · 35 min

Zhi Ning Chen

National University of Singapore, Singapore

Provost's Chair and Professor of Electrical and Computer Engineering and founder & Director of the Advanced Research and Technology Innovation Centre (ARTIC), NUS. He received two PhD degrees in Electrical Engineering, from the Institute of Communications Engineering, China (1993) and the University of Tsukuba, Japan (2003). He has published over 730 academic papers and six books (citations >34 000, h-index 100), holds 35 patents and 43 licensed deals. Pioneer in small and ultra-wideband antennas, wearable and implanted antennas, lens antennas, microwave metamaterial-metasurface antennas, and AI-guided generative antenna design. **IEEE Fellow** (2007), Fellow of the Academy of Engineering Singapore (2019). Recipient of the **IEEE AP-S John Kraus Antenna Award** (2021) and the **EurAAP Antenna Award** (2025).

TALK TITLE

Advancements in Deep Learning-enabled Generative Design of Metalens Antenna and Frequency-Selective Surface

ABSTRACT

The recent progress in developing prior-knowledge-guided DL-enabled generative designs of metalens antennas and FSSs in our group is updated. The generative metalens antenna achieves a dual-polarized low-scanning-loss across a wide-angle scanning range, and FSS demonstrates a low in-band loss, high lower-band suppression and sharp selection under dual-polarized wide-angle incident waves.

PLENARY LECTURE 2

PLENARY · 35 min

Giuseppe Leo

Université Paris Cité, France

Received a Laurea degree (cum laude) in Electrical Engineering from La Sapienza, Rome (1990) and a PhD in Physics from Paris-Saclay University (2001). Was at Roma Tre University as assistant (1992–2002) and associate professor (2002–04). Full Professor at Université Paris Cité since 2004, founder and former director of the Denis Diderot School of Engineering (2010–2022), and leader of the Nonlinear Optical Devices group of MPQ since 2007. Research in nonlinear integrated optics, nanophotonics and metasurfaces. **Optica Fellow**; Member of Institut Universitaire de France. Coordinator of national and EU research programs. 148 articles, 7 patents, 120 invited presentations (h-index 43, >6 000 citations).

TALK TITLE

Dielectric Metasurfaces: a New Platform for Nonlinear Optics

ABSTRACT

Flat optics revolutionized light propagation, and today dielectric metasurfaces enable to structure light in all its degrees of freedom, beyond the limits of the superposition principle. The irruption of nonlinear wavefront shaping, chirality, and analog processing on the scene makes nonlinear meta-optics an ever more exciting theater to perform forefront research.

PLENARY LECTURE 3

PLENARY · 35 min

Enrica Martini

University of Siena, Italy

Received the Laurea degree (cum laude) in telecommunication engineering from the University of Florence (1998) and dual PhDs from the University of Florence and the University of Nice-Sophia Antipolis (2002). Hans Christian Ørsted Postdoctoral Fellow at the Technical University of Denmark (2005–2007). Currently Associate Professor, Department of Information Engineering and Mathematics, University of Siena. Co-founder of Wave Up Srl, Siena (2012). Research: metasurfaces and metamaterial characterisation, metasurface-based antennas and microwave devices, electromagnetic scattering, antenna measurements and tropospheric propagation. Co-recipient of the **2016 Schelkunoff Transactions Prize Paper Award**; Best Paper Award at EuCAP 2017 and EuCAP 2021.

TALK TITLE

Intelligent Surface Wave Metasurfaces for Future Wireless Systems

ABSTRACT

This talk presents a surface-wave-based metasurface architecture for future high-frequency wireless systems that receives, guides, and re-radiates signals. A systematic design methodology enables flexible beam control, shaping, lateral shifts, obstacle bypassing around corners, and physical-layer frequency multiplexing by routing different frequencies along distinct paths.

PLENARY LECTURE 4

PLENARY · 35 min

Eva Rajo-Iglesias

University Carlos III of Madrid, Spain

Born in Monforte de Lemos, Spain, in 1972. Received the MSc in telecommunication engineering from the University of Vigo (1996) and the PhD from the University Carlos III of Madrid (2002). Full Professor in the Department of Signal Theory and Communications since 2018. Affiliated Professor with the Antenna Group, Chalmers University of Technology (2009–2016). Research: microstrip patch antennas, metamaterials, artificial surfaces and periodic structures, gap waveguide technology and MIMO systems. 75+ JCR journal papers; 120+ conference papers. Recipient of the **Loughborough AP Conference Best Paper Award** (2007), Bell Labs Prize Third Place (2014). Associate Editor, IEEE Antennas and Propagation Magazine.

TALK TITLE

Overview of Gap Waveguide Technology for Satellite Antenna Systems

ABSTRACT

An overview of Gap Waveguide technology for satellite communications will be presented, highlighting innovative scanning and multibeam antenna designs. The presentation will also include an analysis of the multipactor effect in high-frequency environments. Particular emphasis will be placed on cost-effective solutions that achieve sufficient gain and high-purity circular polarization.

PLENARY LECTURE 5

PLENARY · 35 min

Vladimir M. Shalaev

Purdue University, USA

Scientific Director for Nanophotonics at Birck Nanotechnology Center and Distinguished Professor of Electrical and Computer Engineering at Purdue University. Specialises in nanophotonics, plasmonics, optical metamaterials and quantum photonics. **Fellow of IEEE, APS, SPIE, MRS and Optica**. Highly Cited Researcher (Web of Science) for 7 consecutive years (2017–2023). Recipient of the **APS Frank Isakson Prize** for Optical Effects in Solids, **Optica Max Born Award** for pioneering contributions to optical metamaterials, Willis E. Lamb Award for Laser Science and Quantum Optics, **IEEE Photonics Society William Streifer Scientific Achievement Award**, Rolf Landauer Medal (ETOPIM), and the **UNESCO Medal** for the development of nanosciences and nanotechnologies.

TALK TITLE

Quantum Photonics and Space-Time Metamaterials

ABSTRACT

In this talk we first discuss quantum photonic integrated circuitry (qPIC) based on the recently discovered single-photon emitters in silicon nitride and the avalanche-enhanced optical modulation in silicon at single-photon intensities.

Keynote Talks

AES 2026

KEYNOTE 12 keynote lectures · 30 minutes each including Q&A

KEYNOTE 1

KEYNOTE · 30 min

Andrea Alù

City University of New York (CUNY), USA

Distinguished Professor and Founding Director of the Photonics Initiative at CUNY ASRC. Fellow of NAI, AAAS, IEEE, MRS, Optica, SPIE and APS. Highly Cited Researcher since 2017. Recipient of the **NSF Alan T. Waterman Award**, Blavatnik National Award for Physical Sciences, **IEEE Kiyo Tomiyasu Award**, and **URSI Issac Koga Gold Medal**.

TALK TITLE

Extreme Wave Control with Space-Time Metamaterials

ABSTRACT

In my talk, I will discuss the underlying physical principles that span over a wide range of frequencies in the design of metamaterials, and focus on the relevance of the temporal dimension as a knob for wave control. I will also discuss the impact of space-time metamaterials on practical technologies.

KEYNOTE 2

KEYNOTE · 30 min

Alexandra Boltasseva

Purdue University, USA

Ron and Dotty Garvin Tonjes Distinguished Professor of ECE at Purdue University. PhD from DTU (2004). Fellow of NAI, MRS, IEEE, Optica and SPIE. Former Editor-in-Chief of *Optical Materials Express*. Recipient of the **2023 R.W. Wood Prize** (Optica) and 2022 Guggenheim Fellowship.

TALK TITLE

Tailorable Quasi-2D Materials for Photonics

ABSTRACT

In this talk, we discuss the designer-like characteristics of MXenes, achievable with the choice of transition metal and control of stoichiometry and outstanding tailorability of properties of TD materials. We also analyze physical effects in atomically thin TD plasmonic films enabling metal-to-insulator transitions.

KEYNOTE 3

KEYNOTE · 30 min

Lorenzo Crocco

IREA-CNR, Italy

Research Director at the Institute for the Electromagnetic Sensing of the Environment, CNR. Activities: diagnostic and therapeutic uses of EM fields, ground-penetrating radars. **World's Top 2% Scientists** (since 2021). EurAAP Delegate for Italy, San Marino and Vatican City (since 2024). IEEE Senior Member, URSI Senior Member.

TALK TITLE

A New Two-Step Framework for Effective Electromagnetic Inverse Scattering

ABSTRACT

We introduce a unified perspective on a new class of methods for electromagnetic inverse scattering based on a two-step decomposition. The first step focuses on the joint retrieval of the contrast source and total field, while the second step consists of the linear inversion of their relationship.

KEYNOTE 4

KEYNOTE · 30 min

Andrea Di Falco

University of St Andrews, UK

Leader of the Synthetic Optics group, School of Physics and Astronomy, University of St Andrews. Research on multi-material platforms for nanoscale light control, with applications in biophotonics, imaging, augmented reality, and optical neural networks.

TALK TITLE

Optical Neural Networks Based on Photovoltaic Elements

ABSTRACT

Photovoltaic neural networks provide a powerful route to scalable optical computing by directly converting optical signals into electrical outputs. This enables efficient, large-area signal acquisition while simplifying system architectures and reducing energy consumption, opening pathways toward compact, self-powered optical neural networks for next-generation AI and edge computing.

KEYNOTE 5

KEYNOTE · 30 min

Mauro Ettorre

Michigan State University, USA

Professor at MSU (since 2023). Research: quasi-optical systems, wideband arrays, mm-wave antennas, non-diffractive radiation. 90+ journal papers, 14 patents. **IEEE Fellow**. **IEEE MTT-S and AP-S Inter-Society Distinguished Lecturer** (2024). Best Paper Awards at EuCAP 2018 and EuCAP 2021.

TALK TITLE

Long Slot Arrays: Advancing Next-Generation Communications Networks and Beyond

ABSTRACT

During this presentation, I will discuss the modeling of long slot arrays and highlight their advantages in terms of bandwidth and scanning capabilities, as well as their physical implementation. I will demonstrate the capability of these arrays to radiate short, high-power pulses, thereby extending their applications to high-power scenarios.

KEYNOTE 6

KEYNOTE · 30 min

Anthony Grbic

University of Michigan, Ann Arbor, USA

John L. Tishman Professor of Engineering, EECS, University of Michigan. Research: metamaterials, metasurfaces, wireless power transmission, space-time varying EM systems. **IEEE Fellow**. **IEEE MTT-S Distinguished Microwave Lecturer** (2022–2025). NSF CAREER Award; Presidential Early Career Award for Scientists and Engineers.

TALK TITLE

Beamforming with Metasurfaces Connected to Reactive Loads or Networks

ABSTRACT

The talk will describe how a metasurface connected to reactive loads or networks can serve as a low-cost beamforming technology. Strong coupling between the unit cells, tailored by these reactive loads, allows energy to be shuttled across the aperture to enable beam steering, beam shaping, and multiple simultaneous beams.

KEYNOTE 7

KEYNOTE · 30 min

Ortwin Hess

Trinity College Dublin, Ireland

Chair Professor of Quantum Nanophotonics, Trinity College Dublin. Editor-in-Chief of *APL Quantum*. Fellow of the Institute of Physics and Optica. Discoverer of the 'trapped-rainbow' principle; pioneered active nanoplasmonics with quantum gain. Recipient of the **Royal Society Rumford Medal**.

TALK TITLE

Nanoplasmonic Cavities for Electromagnetic Wave Control: Quantum Dynamics in Open Resonators

ABSTRACT

Nanoplasmonic cavities enable extreme subwavelength electromagnetic control with strong light-matter coupling in open, lossy resonators. Combining waveguide-integrated architectures and quantum quasinormal-mode theory, this work shows how dissipation can be engineered for coherent control, state preparation, and stabilization, establishing nanoplasmonic systems as versatile platforms for room-temperature quantum electromagnetic functionality.

KEYNOTE 8

KEYNOTE · 30 min

Thomas F. Krauss

University of York, UK

Chair of Photonics, University of York (since 2012). Pioneered photonic crystals in semiconductor waveguides. Research on guided mode resonance for biosensing and healthcare applications. ≈400 publications; **h-index 98**, cited 35 000+ times.

TALK TITLE

Metasurfaces for Biomedical Sensing

ABSTRACT

Metasurfaces hold much promise for novel sensing systems, but their operation needs to be properly understood; simply maximising Q-factor is insufficient. We present a comprehensive framework for assessing their performance and apply it to the difficult problems of measuring small peptides as well as drug concentrations in the mid-IR.

KEYNOTE 9

KEYNOTE · 30 min

Stefano Maci

University of Siena, Italy

Professor at the University of Siena (since 1997). Founder and Director of the **European School of Antennas (ESoA)**: 34 courses, 150 teachers from 15 countries. Research: high-frequency methods, phased arrays, metamaterials and metasurfaces. **IEEE Fellow** (2004). EurAAP Award (2014), Shelkunoff Prize (2015), Chen-To Tai Award (2016). h-index 41, >6800 citations.

TALK TITLE

Multibeam Antennas without Beam Forming Networks

ABSTRACT

Gradient-index (GRIN) lenses and metasurface antennas enable compact, low-cost multibeam systems without beam forming networks. Designed using advanced synthesis and fast geometrical optics solvers, GRIN lenses achieve wideband and precise beam shaping. Metasurfaces convert guided or space waves into directive beams via engineered impedance which operate as a continuous BFN.

KEYNOTE 10

KEYNOTE · 30 min

Marin Soljačić

MIT, USA

Professor of Physics, MIT. Founder of WiTricity (2007) and Lightelligence (2017). Research: AI, nanophotonics, non-linear optics, wireless power transfer. 300+ articles, 100+ US patents. **MacArthur Fellowship** (2008), **Max Born Award** (Optica, 2023). Highly Cited Researcher for 7 consecutive years (2019–2025).

TALK TITLE

Certain Recent Developments in Photonics

ABSTRACT

I will present some of our recent results in the field of photonics, including novel phenomena in scintillators, X-ray imaging, and AI and robotics for photonic-science automation.

KEYNOTE 11

KEYNOTE · 30 min

Francesca Vipiana

Politecnico di Torino, Italy

Full Professor, Department of Electronics and Telecommunications, Politecnico di Torino (since 2021). Research: integral equation methods, multiresolution schemes, domain decomposition, microwave imaging for medical and industrial applications. **IEEE AP-S Lot Shafai Mid-Career Distinguished Award** (2017). Member of the EurAAP Board of Directors.

TALK TITLE

Integral Equations Advanced Techniques for the EM Analysis of Real-Life Multi-Scale Antenna Problems

ABSTRACT

This talk addresses the efficient and accurate analysis of real-life multi-scale antenna problems via the moment method (MoM) solutions of surface integral equations (SIEs). SIEs have emerged as the dominant technology for the EM modeling of antenna placement on large and complex platforms such as aircrafts, ships, satellite, and vehicles.

KEYNOTE 12

KEYNOTE · 30 min

Dan-Xia Xu

NRC Canada

Principal Research Officer, Quantum and Nanotechnologies Research Center, NRC Canada. **Fellow of the Royal Society of Canada** and Fellow of Optica. Research: AI-enabled photonic chip design, silicon photonics, machine-learning-assisted inverse design and fabrication optimisation. 400+ publications, 7 patents.

TALK TITLE

Machine Learning-Enabled Design and Metrology of Integrated Optical Antennas

ABSTRACT

We demonstrate how machine learning advances integrated optical antenna design and application by enabling structured exploration of high-dimensional parameter spaces, capturing environment-dependent effective-medium behavior, and converting radiative responses into fabrication diagnostics. Together, these capabilities establish a unified, closed-loop framework for scalable, physically informed photonic antenna engineering.

AES 2026 · CATANIA, ITALY · 3–6 JUNE 2026

Conference Papers

Full texts of the plenary, keynote, invited, oral and poster contributions presented at AES 2026

231
Papers
all accepted contributions

17
Lectures
5 plenary · 12 keynote

21
Sessions
2 symposia · 13 special · 6 general

23
Posters
3 thematic groups

Monastero dei Benedettini di San Nicolò l'Arena · University of Catania

aesconference.org · ISSN 2491-2417

Proceedings Contents

Plenary Presentations 35

Intelligent Surface Wave Metasurfaces for Future Wireless Systems 36
Enrica Martini

Advancements in Deep Learning-enabled Generative Design of Metalens Antenna and Frequency-selective-surface 37
Zhi Ning Chen, Yanhe Lyu

Dielectric metasurfaces: a new platform for nonlinear optics 39
Giuseppe Leo

Overview of Gap Waveguide Technology for Satellite Antenna Systems 40
Eva Rajo-Iglesias

Quantum Photonics and Space-Time Metamaterials 41
Vladimir M. Shalaev

Keynote Presentations 42

Optical Neural Networks based on photovoltaic elements 43
Andrea Di Falco

Multibeam Antennas without Beam Forming Networks 44
Stefano Maci

Long Slot Arrays: Advancing Next-Generation Communications Networks and Beyond 45
Mauro Ettorre

Nanoplasmonic Cavities for Electromagnetic WaveControl: Quantum Dynamics in Open Resonators 46
Ortwin Hess

Metasurfaces for biomedical sensing 47
Thomas Krauss

Machine Learning-Enabled Design and Metrology of Integrated Optical Antennas 48
Dan-Xia Xu

Integral Equations Advanced Techniques for the Electromagnetic Analysis of Real-Life Multi-Scale Antenna Problems 50
Francesca Vipiana

A New Two-Step Framework for Effective Electromagnetic Inverse Scattering: From Contrast Source Retrieval to Linear Contrast Reconstruction 51
Lorenzo Crocco

Extreme Wave Control with Space-Time Metamaterials 52
Andrea Alu

Beamforming with Metasurfaces Connected to Reactive Loads or Networks 53
Anthony Grbic, Malik Almunif

Tailorable Quasi-2D Materials for Photonics 54
Alexandra Boltasseva

Certain recent developments in photonics 55
Marin Soljacic

Recent Advances in Nanophotonics and Metamaterials 56

Hybrid 2D-plasmonic nanoantennas for photon emission and sensing 57
Maria Caterina Giordano, Giorgio Zambito, Giulio Ferrando, Matteo Barelli, Francesco Buatier de Mongeot, Antonino Foti, Pietro Gucciardi, Simone Sotgiu, Tommaso Venanzi, Erica Fragomeni, Leonetta Baldassarre

Field-enhancement in plasmonic tagged nanoplastics 59
Maria Antonia Iatì, Shadi Rezaei, Alessandro Veltri, Pietro G. Gucciardi, Onofrio M. Maragò, Rosalba Saija

Textile-Embedded Metasurfaces for Enhancing Smart Devices Connectivity 60
Francisco Cuesta, Xianghui Qiu, Mohammad Asgari, Shuai Yuan, Sergei Tretyakov, Xuchen Wang, Viktar Asadchy

Constructing High-order Exceptional Points and Perfect Absorber Based loss engineering 63
Changzhi Gu, Peng Fu

Near-field polarization photonics: controlling polarization of localized waves with metasurfaces 64
Oleh Yermakov

The role of resonances at dangling ligaments in the absorption of nanoporous gold 65
Muhammad Salman Wahidi, Maurice Pfeiffer, Xinyan Wu, Parastoo Ebrahimi, Manfred Eich, Alexander Yu. Petrov

Near-Infrared Spectroscopy Using Plasmonic Si MEMS 66
Tetsuo Kan, Teruya Noguchi, Eslam Abubakr, Shiro Saito, Hironori Suzuki

Fluorescence-based chiral sensing with silicon metasurfaces 68
Tom T. C. Sistermans, Artemijs Krimovs, Robert Pal, Alberto G. Curto

Non-dichroic Chiral Photoelectron Spectroscopy 70
Letizia Fede, Debobrata Rajak, Chris Sparling, David Ayuso, Sylvain Betoule, Valérie Blanchet, Piero Decleva, Dominique Descamps, Stéphane Petit, Bernard Pons, Yann Mairesse, Andrés Ordóñez

Photoacoustic spectroscopy on plasmonic materials 71
Claudia Skubisz, E. Petronijevic, N. Borriello, G. Leahu, R. Li Voti, C. Sibilia, A. Belardini

Solar-thermal conversion with titanium nitride metamaterials 73
Luca Mascaretti, Morteza Afshar, Andrea Schirato, Alessandro Alabastri, Paolo Fornasiero, Ladislav Kalvoda, Stepan Kment, Alberto Naldoni, Ivan Richter

Toward Robust SE-FSRS: Managing Nanoantenna-Induced Spectral Distortions via Excitation-Wavelength and Pulse-Energy Tuning 75
Patryk Pyrcz, Sylwester Gawinkowski

Tip-Enhanced Nanocavities: Advances for Linear and Nonlinear Vibrational Spectroscopy 76
Philippe Roelli, Isabel Pascual Robledo, Iker Herrero Leon, Javier Aizpurua, Rainer Hillenbrand

Inverse Electromagnetic Design for THz Antennas, Resonators and Wave-Based Analog Computing 77
Nikolas Hadjiantoni, Heedong Goh, Dou Feng, Andrea Alù, Miguel Navarro-Cía, Stephen Hanham

Plasmonic Metasurface Arrays for Universal Liquid Sensing 79
Justin Sperling, Finlay Walton, Daniel Osborne, Badri Aekbote, Anthony Perri, Rebecca Setford, Hanyu Gao, Liam Wilson, Chad Siperley, Rudolf Schick, Baptiste Poursat, Caroline Gauchotte-Lindsay, William Peveler, Alasdair Clark

Chiral Nonlinear Polaritonics and Quantum Metaphotonics with Bound States in the Continuum 80
Maxim Gorkunov, Alena Mamonova

Efficient Lasing Metasurfaces Enabled by Quasi-Dark Resonances: A Temporal Coupled Mode Theory Approach 81
Georgios Nousios, Thomas Christopoulos, Dimitrios Zografopoulos, Emmanouil Kriezis, Odysseas Tsilipakos

Microbridge-Array Based Reconfigurable Intelligent Surfaces 85
Steffen Klingel, Lars Franke, Marco Rahm

Microcomb-Enabled Low-Phase-Noise Terahertz Wireless Links for High-Order Modulation 87
Takasumi Tanabe

Polymeric dynamic nanoantennas and metasurfaces **88**
Magnus Jonsson

Controlling Fisher Information Flow in Optical Metrology **89**
Kevin MacDonald, Maximilian Weimar, Huanli Zhou, Luca Neubacher, Thomas Grant, Jakob Hüpfl, Stefan Rotter, Nikolay Zheludev

Fluctuation-induced Hall-like forces in a chiral-gain environment **90**
Daigo Oue, Mário Silveirinha

Atomistic Electromagnetic Model for Realistic Nanoplasmonics **91**
Tommaso Giovannini

Time-Domain Modeling of Pulsed Dielectric Laser Accelerators **92**
Davide Guarnera, Hatou Yvelin Donkeng, Roberta Palmeri, Giorgio Sebastiano Mauro, Nunzio Salerno, Alberto Bacci, Santi Concetto Pavone, Giuseppe Torrisi, Andrea Locatelli, Gino Sorbello

Enhanced Light Absorption and Photoluminescence in monolayer WS2 on Si Huygens Metasurface **93**
Junichi Takahara

Controlling Light confinement in metasurfaces: Gold Temporal Chirality and hBN Mie Resonators **94**
Oscar Avalos-Ovando, Wei Wang, Ruggero Emmanuele, Gary Wiederrecht, Lucas Besteiro, Alexander Govorov, Sergio Ulloa, Xuedan Ma

Quantum Corrections in Nanoplasmonics and Thermoelectric Phenomena with Graphene Plasmons **96**
P. André Gonçalves

Electrical Control of Light–Matter Interactions and Nonlinear Optics in Plasmonic Tunnel Junctions **97**
Hayk Harutyunyan

Engineering Plasmonic Nanoantennas to Boost Quantum Emitter Performance in the Visible and NIR **98**
Nerea Zabala, Luis Montano-Priede, Mario Zapata-Herrera, Ruben Esteban, Javier Aizpurua

Free Space Whispering Gallery Microlaser for Biosensing **99**
Stefano Ferretti, Angela Capocefalo, Neda Ghofraniha

Vibrations of single metal nanoparticles: morphology and environment effects **101**
Noelle Lascoux, Clément Panais, Sylvie Marguet, Natalia Del Fatti, Sylvie Marguet, Aurélien Crut

Single-molecule Nanospectroscopy and Beyond with Scanning Tunneling Microscopy **102**
Hiroshi Imada

Frustrated Non-Hermitian Skin Effect and gauge-invariant ladder operators in a Floquet Photonic System **103**
Li Ge

Topological metasurface based on exceptional points **105**
Qinghua Song

Metasurfaces-Enabled Cold Atoms Array Generation **107**
Hac Huong Thu Le, Ryohei Takei, Akifumi Takamizawa, Sota Kagami, Yuiichi Kurashima, Taisei Motomura

Ultra-confined plasmonics for control of light-matter interactions at nanoscale **108**
Alexey Krasavin, Junsheng Zheng, Chenxinyu Pan, Limin Tong, Pan Wang, Anatoly Zayats

Quantum Non-Reciprocity in Photon-Pair Generation from Nonlinear Metasurfaces **110**
Jinyong Ma, Xiwen Qiu, Tongmiao Fan, Tuomas Haggren, Hark Hoe Tan, Chennupati Jagadish, Andrey Sukhorukov

Aluminum optical nanoantennas **111**
Davy Gerard

A nuclear clock accelerated by collective coherence **112**
Karen Mamian, Georgy A. Kazakov, Jan de Haan, Kasper van Gasse, Thorsten Schumm, Charles Roques-Carmes

Ultralow-power-operable monopixel reflective displays with thin-film photonics **114**
Song Young Min

Thermoplasmonic Coupler for On-Chip Spatial Control of Heat Delivery **115**
Giovanni Piscopo, Francesca Filograno, Marius Crouzier, Béatrice Dagens, Giovanna Calò, Antonella D'Orazio, Giovanni Magno

Laser photo-acoustic spectroscopy with microscope for hyperspectral imaging of absorption and chirality in nanomaterials **116**
Emilija Petronijevic, Grigore Leahu, Claudia Skubisz, Imene Kouicem, Concita Sibilia, Roberto Li Voti, Alessandro Belardini

Transition metal nitrides as potential alternative for noble metals for SERS sensing **117**
Jan Krajczewski, Aleksandra Michałowska, Aleksandra Szymańska, Libor Nozka

Plasmonic Metasurfaces for Enhanced Chiral Sensing **119**
Alexa Guglielmelli, Giovanna Palermo, Giuseppe Strangi

Complex on-fiber micro-optical systems with high-resolution 3D-printing **121**
Carlo Liberale

Rice-Mele nanolaser **122**
Kaiwen Ji, Melissa Hedir, Qi Zhong, Ramy ElGanainy, Alejandro Yacomotti, Li Ge

Manipulating evanescent waves with non-Hermitian spectral singularities **123**
Huanan Li

Enabling Materials – Optical and Functional Composites **125**
Dorota Pawlak, Piotr Piotrowski, Monika Tomczyk, Katarzyna Sadecka, Nada Aghad, Kingshuk Bandopadhyay, Ali Abbas, Krzysztof Markus, Andrzej Materna, Hamid Reza-Darabian

Metasurfaces for Millimeter-Wave Wireless Systems **127**
Miguel Beruete, Alicia E. Torres-García, Jorge Teniente, Damián E. Rodríguez-Trujillo

GEGD: Efficient Quasi-Global Search Algorithm for Strictly Fabrication-Feasible Design of Freeform Devices **129**
Seokhwan Min, Junhyung Park, Jonghwa Shin

Terahertz Quantum Communication with Chip-integrated Superconducting Circuits **131**
Kaveh Delfanazari

Graphene Nanosheet Gold Nanopatch Metasurfaces for Nonlinear Terahertz Response **132**
A. Theodosi, I. Appiah Oto, A. D. Koulouklidis, N. Matthaiakakis, G. Kakarantzas, P. Mustonen, H. Lipsanen, G. Fedorov, I. Liontos, P. Kuzhir, M. Kafesaki, Odysseas Tsilipakos, Stelios Tzortzakis

Microwave stress monitoring using amorphous microwire assessed by free space measurements **133**
Valentina Zhukova, Mihail Ipatov, Arcady Zhukov

Surface-protected electromagnetic nanoresonators for Raman analysis of surfaces **135**
Andrzej Kudelski

Bound States in the Continuum for Biosensing and Selective Raman Enhancement **136**
Silvia Romano

Time-synthetic optical neural networks with stable programmable gain **138**
Bei Wu, Yudong Ren, Rui Zhao, Haiyao Luo, Fujia Chen, Li Zhang, Lu Zhang, Hongsheng Chen, Yihao Yang

Collision-driven out-of-equilibrium nonlinear optics in ultraviolet epsilon-near-zero materials **140**
Matteo Silvestri, Luca Assogna, Davide Tedeschi, Carino Ferrante, Andrea Marini

Active Control of Optical Diffraction Using Excitonic Gratings **142**
Ershad Mohammadi, Mehmet Atif Durmus, Jorik van de Groep

Tautochrone and Squeezing in Nonuniform Lattices 145
Ioannis Kiorpelidis, Matthias Heinrich, Alexander Szameit, Georgios A. Siviloglou, Konstantinos G. Makris

Applications of single photons for quantum technologies 147
Christophe Couteau

Broadband EM wave analysis and manipulation based on time-frequency structured light processing 148
Jose Azana, Xinyi Zhu, Benjamin Crockett, Lim Geunweon, Majid Goodarzi, Connor Rowe, Hao Sun

Electromagnetic Wave Localisation in Hyperuniform Disordered Photonic Structures 149
Marian Florescu, Alexander Meek

Brillouin scattering in integrated photonic circuits 150
Moritz Merklein

Advanced photonics with liquid crystals in microcavities 151
Dmitry Solnyshkov, M. Muszynski, P. Kokhanchik, I. Septembre, D. Bobylev, R. Mirek, D. Urbonas, P. Tassan, P. Kapuscinski, P. Oliwa, I. Georgakilas, T. Stoferle, R. F. Mahrt, M. Forster, U. Scherf, D. Dovzhenko, E. Oton, R. Mazur, P. Morawiak, W. Piecek, P. Kula, W. Bardyszewski, M. Krol, M. Kedziora, K. Łempicka-Mirek, P. G. Lagoudakis, B. Pietka, G. Malpuech, J. Szczytko

Breakdown of Harmonic Conversion Scaling Laws in Nonlinear Nanocavities 153
Marco Gandolfi, Michael Scalora, Costantino De Angelis, Maria Antonietta Vincenti

Computational Electromagnetics for Radiating Structures and Complex Media 155

Reduced-Order Framework for Layered Photonic Cavities 156
Przemysław Oliwa, Helgi Sigurdsson, Witold Bardyszewski, Jacek Szczytko

Leakage from Uniform and Periodically Loaded Line Waveguides 158
Mikhail Madji, Paolo Baccarelli, Alessio Monti, Alessandro Toscano, Filiberto Bilotti, Paolo Burghignoli

Infrared Cavity Enhanced Vibrational Relaxation in Layered MoS2 159
Kosei Ueno

Broadband Low-Reflectivity Design of Moth-Eye Structures Using RCWA and Bayesian Optimization 161
Yutaro Sato, Maria Vanessa Balois-Oguchi, Kotaro Kajikawa

Advanced computational design of nonlinear and functional nanophotonics 163
Catarina Ferreira, Joel D. Cox, Line Jelver

Nanoparticles of nitride-based materials for plasmonics and lattice-mode resonances 165
Ermelinda Salvaggio, Jérémie Béal, Gregory Abadias, Sophie Camelio, David Babonneau, Davy Gérard, Christophe Couteau, Jérôme Plain

Retrieving Electric and Magnetic Conductivities of Anisotropic Metasurfaces under Oblique Incidence 167
Dimitrios Chatzidimitriou, Alexandros Pitilakis, Odysseas Tsilipakos

Plasmonic lightning-rod effect and nanofocusing: Revisiting traditional design concepts for plasmonic antennas 170
Rostislav Řepa, Michal Horák, Pavel Gajdoš, Tomáš Šikola, Vlastimil Křápek

Advancements in Electromagnetic FEM forParametric Studies, Frequency Sweeps and ShapeOptimization 172
Michal Baronowski, Adam Lamecki, Michal Mrozowski

Hybrid AI design of reconfigurable and compact plasmonic Arithmetic and Logic Units 173
Amine Khitous, Nicolas Gros, Léo Martin, Florian Dell'Ova, Aurélie Bertaux, Ouassila Narsis-Labbani, Gérard Colas des Francs, Christophe Nicolle, Alexandre Bouhelier, Erik Dujardin

Leaf-based Ground Planes for Sustainable Wireless Communication 176

Jaume Anguera

Fully Programmable Reflect/Transmit sub-THz Surfaces with CMOS Ics 177
Kaushik Sengupta

Formation of Electromagnetic Spin Skyrmionsby Sparse Antenna Arrays 178
Andrei Afanasev

The Quasi-Normal Mode Method Applied to the Study of the Radiating Properties of Quasi-Bound States in the Continuum 179
Emmanuel Centeno, Victor Kalt, Rafik Smaali, Antoine Moreau

Opto-thermal tunability in phase-change metasurfaces 180
Marco Gandolfi, Jesse Frantz, Natalia M. Litchinitser, Costantino De Angelis, Maria Antonietta Vincenti

Theoretical Modeling of Surface Electromagnetic Wave-Based Underwater Radio Communication 182
Igor Smolyaninov

Multi-order exceptional points and structured perturbations 183
Konstantinos Makris

Multipolar THz field generation using spintronic elements 185
Jamal Berakdar

Ultraviolet to Near Infrared Spectroscopic Emitters Based on Broadband Rare Earth-free Phosphors 186
Tadaaki Nagao, B. K. Barman, D. Hernandez-Pinilla, K. Watanabe, D. Thien Ngo

Numerical Investigation of Hyperbolic Metamaterial Probes for Broadband Near-field Enhancement in Tip-Enhanced Raman Spectroscopy 187
Maria Vanessa Oguchi

The Leaky-Wave Paradigm for Nondiffractive Beams 189
Edoardo Negri, Stella Ventucci, Walter Fuscaldo, Paolo Burghignoli, Alessandro Galli

Ultrafast Electron and Phonon Dynamics in Metasurface-Driven Photocatalysis 190
Alessandro Alabastri

In-Situ Physical Adjoint Computing 192
Tsampikos Kottos, John Guillamon, Cheng-Zhen Wang, Zin Lin

Artificial fractal network of silicon nanowires for imaging and sensing 193
Maria Josè Lo Faro, Antonio Leonardi, Maurilio Galletta, Francesco Priolo, Barbara Fazio, Alessia Irrera

Atomic-scale Investigation of Energy Conversion in a Single Molecule 195
Miyabi Imai-Imada

Electromagnetic Inverse Scattering Problems for Imaging, Sensing and Communications 196

Handheld millimeter-wave scanner enabled by freehand imaging: acquisition design 197
Guillermo Alvarez-Narciandi, Maria Garcia-Fernandez, Jaime Laviada, Fernando Las-Heras

On the usage of 1D Dynamic Metasurface Antennas for 3D Computational Radar Imaging 199
Maria Garcia-Fernandez, Guillermo Alvarez-Narciandi, Okan Yurduseven

Assessment of Anatomical Prior Information in the Inversion Kernel for Microwave Brain Imaging 201
Alex Ramiro Masaquiza-Caiza, David Orlando Rodriguez-Duarte, Francesca Vipiana

Indirect Holography MIMO Imaging Exploiting Antenna Coupling 203
Alejandro del Hoyo Vijande, Yuri Álvarez-López, Fernando Las-Heras, Jaime Laviada

Point-Like Target Detection and Localization via Phase-Space Back-Projection 205
Davide Santagata, Gabriele Gradoni, Raffaele Solimene

Fast imaging methods for real-time electromagnetic tomography 210
Antonello Tamburrino, Vincenzo Mottola, Gianpaolo Piscitelli

Averaged Steklov eigenvalues and applications toelectromagnetic imaging problems 212
Mayeul Chavanne, Lorenzo Audibert, Houssem Haddar

A Three-Phase Quantitative Data-Assisted Microwave Imaging Method 214
Mohammad Omki, Alessandro Fedeli, Andrea Randazzo

Light Engineering at the Nano-Scale: Insights from Plasmonics and Metamaterials 215

Real-Space Plasmon Imaging Reveals Modified Charge Dynamics of Gold at the Monolayer Limit 216
Andrei Bylinkin, Philippe Roelli, Naveen Shetty, Rositsa Yakimova, Ulrich Starke, Camilla Coletti, Stiven Forti, A. Zakharov, Vyacheslav M. Silkin, Samuel Lara-Avila, Rainer Hillenbrand

Whispering-Gallery Mode Microcavities & Microlasers: From Advanced Single Molecule Measurements to Applications in Biology 217
Frank Vollmer

Polaritonic metasurfaces: extended hybridization and energy transfer 218
Clementine Symonds, Jean-Michel Benoit, François Bessueille, Joel Bellessa

Recursive analog computing with light 219
Andrea Cordaro

Liquid-Crystalline Chiral Nanophotonics: From Plasmonic Circular Dichroism to Circularly Polarized Luminescence 220
Wiktor Lewandowski

DNA-Origami-Assembled Rhodium Nanoantennasfor Deep-UV Label-Free Single-Protein Detection 221
Karol Kolataj

Deterministic Strain Engineered Quantum Emitters in Two Dimensional Semiconductors 223
Snezana Lazic Knezevic, Sanja Đurđić Mijina

Metasurface modeling from Microwave to Optics 225

Solving the Helmholtz equation with waveguide-based metatronic circuits 226
Ross Glyn MacDonald, Alex Yakovlev, Victor Pacheco-Peña

Local-Based Synthesis of Reconfigurable Huygens' Metasurfaces for Beam Steering 229
Stefano Vellucci, Alessio Monti, Mirko Barbuto, Alessandro Toscano, Filiberto Bilotti

Nonlinear Coupling between Nonlocal Resonances in a High-Contrast Grating Metasurface 232
Paolo Franceschini, Andrea Tognazzi, Evgenii Menshikov, Leonid Y. Beliaev, Radu Malureanu, Osamu Takayama, Ivano Alessandri, Alfonso C. Cino, Domenico de Ceglia, Andrei V. Lavrinenko, Costantino De Angelis

Controlling Quantum Dot Emission and Enhancing Second Harmonic Generation with Dielectric Nanocylinders 234
Andrea Tognazzi

Metasurfaces for Extreme Wave Control 235
Andrea Alu

Advanced Techniques for Antennas, RF, and MW Components Fabrication 236

Investigation on Powder-Bed Fusion Laser-Based Process for the Manufacturing of D-band Feed Horns 237
Giuseppe Addamo, Flaviana Calignano, Mario Zannoni, Lorenzo Scalcinati, Oscar Antonio Peverini, Fabio Paonessa

Additive Manufacturing Techniques for Post-Fabrication Frequency Tuning of Printed Planar Antennas 238
Rubén Pedreño Martínez, David Cañete Rebenaque, José Luis Gómez Tornero

A 3D-printed Convex Antenna for ARBW and Gain Enhancement 242
Giacomo Muntoni

Nonlinear metasurface and flat-optics 245

Hot-carrier Mediated Modulation of Linear and Nonlinear Photonic Metastructures 246
Andrea Schirato, Giulia Crotti, Giuseppe Della Valle

Peculiarities of the nonlinear optical effects in ultrathin dielectric membranes 247
Maxim Nikitin, Olav Thorbjørn Sandberg Schiess, Andrea Tognazzi, Paolo Franceschini, Osamu Takayama, Radu Malureanu, Ole Bang, Costantino De Angelis, Andrei Laurynenka

High-Harmonic Generation from Resonant Dielectric Metasurfaces 248
Ivan Sinev, Pavel Tonkaev, Felix Brikh, Ivan Toftul, Maria Antonietta Vincenti, Michael Scalora, Hatice Altug, Yuri Kivshar

Nonlinear metasurfaces for Advanced Terahertz Generation 250
Davide Rocco, Luca Carletti, Paolo Franceschini, Andrea Tognazzi, Olga Sergaeva, Unai Arregui Leon, Giuseppe Della Valle, Costantino De Angelis

Linear-Nonlinear: Polarization- and Orientation-Dependent Harmonic Response 253
Kristina Frizyuk

Nanoimprinted barium titanate sol-gel for electro-optic modulation 254
Virginia Falcone, Eleni Prountzou, Rachel Grange

Recent Advancements in Metamaterials and Metasurfaces for Scattering and Wave Engineering 255

Analytical Modeling of Anomalous Reflection viaPiecewise-Uniform Boundary Conditions 256
Federico Giusti, Enrica Martini, Stefano Maci, Matteo Albani

Scattering properties of a cylindrical scatterer with time-modulated permittivity 259
Jiaruo Yan, Ioannis Katsantonis, Mohamed Mostafa, Viktar Asadchy, Maria Kafesaki

Efficient Optimization of Metasurface for Near-fieldmmWave Communications 262
Alvaro F. Vaquero, Manuel Arrebola, Marcos R. Pino

Spatially-fed Metasurface Antenna with Active Feeder for Reconfigurable Beam Coverage 263
Daniel Martinez-de-Rioja, Yolanda Rodriguez-Vaqueiro, Antonio Pino, Eduardo Martinez-de-Rioja, Jose A. Encinar, Manuel Arrebola

Polarization-Decoupled Programmable Metasurface for Integrated Beam Steering and Electromagnetic Illusion 265
Yitian Huang, Min Huang, Ruichen Li, Haoran Han, Bin Zheng, Jiwei Zhao

Physically Consistent Modeling of RIS Scattering under Multipath Incidence 267
Gang Yu, Gabriele Gradoni

Gain-Enabled Spectral Singularities in Metasurface Cavities 268
Rasmus E. Jacobsen, Pietro Brugnolo, Samel Arslanagić

Time-modulated Electromagnetic Systems 270

Multimodal Space-Time Electromagnetic Structures 271
Anthony Grbic, Amirhossein Babaee

Sculpting waves in four dimensions: emulating time refraction and steering waves 272
Victor Pacheco-Peña

Wave Control at Space-Time Interface in Dispersive Media 274
Carlo Rizza, Alessandra Contestabile, Maria Antonietta Vincenti, Giuseppe Castaldi, Michael Scalora, Marcello Ferrera, Vincenzo Galdi

Temporal Modulation for Dispersion-Free Impedance Matching 275
Mario Junior Mencagli, Dimitrios Sounas

Nano-objects and metasurfaces for opto-thermo-mechanical management 276

Modeling Terahertz Scattering from Plastic Contaminants for Inspection Applications 277
Rizwan Asif, Marco Gandolfi, Alfonso Tanga, Matteo Gabardi, Silvia Liprandi, Bruno Garavelli, Mark Justine Zapanta, Wouter Saeys, Claudio Giannetti

Wiener--Hopf Modeling of a Parity Time Duality Waveguide Based on a Bed of Nails Metasurface 280
Xenofon Mitsalas, Nelson Castro, Eva Rajo Iglesias, Stefano Maci

Quantization Pressure and Commensurability in Morphogenetic Metasurface Design 282
Thomas Fromentèze, Chidinma Uche, Emebet Hadgu, Cyril Decroze, Raphaël Pestourie

Ultrafast thermal exchanges around nano-objects probed by time-resolved optical spectroscopy 283
Margherita Vittucci, Alessandro Casto, Fabiano Tarulli, Matteo Fasano, Aurélien Crut, Francesco Banfi, Natalia Del Fatti, Paolo Maioli

Controlling nonlinear THz generation via two-beam excitation of all-dielectric nanostructures 285
Unai Arregui Leon, Luca Carletti, Davide Rocco, Costantino De Angelis, Giuseppe Della Valle

Supermode Theory for Broadband All-Dielectric Metasurfaces 287
Pooja Uday Naik, Massimiliano Guasoni

Ultrafast modulation of semiconductor metasurfaces with photo-induced spatial inhomogeneities 288
Giulia Crotti, Pietro Baldin, Andrea Schirato, Olesiya Pashina, Olga Sergaeva, Mihail Petrov, Costantino De Angelis, Margherita Maiuri, Giuseppe Della Valle

Mid-infrared Light Modulation with Silicon Membrane Metasurfaces 290
Ivan Sinev, Felix Brikh, Aleksei Ezerskii, Olesia Pashina, Nikita Glebov, Mihail Petrov, Sergey Makarov, Hatice Altug

Young Researchers in Antennas and Metasurfaces 292

In-Phase TE/TM Surface Wave Excitation on Self-Complementary Metasurfaces 293
Bouchez Marceau, David Gonzalez-Ovejero, Stefano Maci

Multifunctional Metasurfaces with Mutual Coupling Mitigation for Advanced Wireless Systems at Millimeter-Waves and Terahertz 294
Damián Ernesto Rodríguez Trujillo, Alicia Elena Torres García, Mikel Aldea Esnaola, Jorge Teniente Vallinas, Asier Marzo Pérez, Miguel Beruete Diaz

Low-Cost 3-D Printable Modulated Dielectric Leaky-Wave Antenna 297
Ravel Carlos de Miranda Pimenta, Massimiliano Casaletti

Low-Loss CLAF Waveguides and Slot Arrays for 77 GHz Automotive Radar Using 300

Mirror-Stacked Glide-Symmetric Mushroom EBGs
Ashray Ugle, Massimiliano Casaletti, Marta Arias Campo, Simona Bruni, Guido Valerio

Magnetically Tunable Graphene PlasmonicEmission for THz Amplification **302**
Michela Longhi, Davide Mencarelli, Alessandro Toscano, Luca Pierantoni

Advanced Near-Field Beam Synthesis via Spatially Distributed Ray-Caustics **303**
Federica Anfuso, Ahsan Ullah Khan, Gino Sorbello, Santi Concetto Pavone

Interpolation of Periodic Method-of-Moments Impedance Matrices with a Physically Motivated Regularisation **304**
Martin Petek, Denis Tihon, Jorge Alberto Tobon Vasquez, Cristophe Craeye, Francesca Vipiana

Generalized Rigorous Coupled Wave Analysis for Higher-Symmetric Dielectric Media **306**
Dubravko Tomić, Zvonimir Šipuš

Analysis of polarization purity in dual-polarized phased array antennas **308**
Pilar Castillo Tapia, Gabriele Federico, Bart Smolders

Advanced antenna designs for Joint Communication and Sensing, Localization and Radiative Wireless Power Transfer **309**

Monopulse-Based Blind-Spot Correction using a Full-Azimuthal Leaky-Wave Antenna Array **310**
Alejandro Gil-Martínez, Jesus Perez-Valero, Julien Sarrazin, Guido Valerio, Antonio Skarmeta

Phase-Based Ranging and Direction-of-Arrival Localization with a single-port Frequency-Scanned Antenna **313**
Antonio David Hernández Mateos, José Antonio López Pastor, José Luis Gómez Tornero

Acoustic leaky-wave antennas for localization of IoT devices **316**
Pablo Antonio Martínez Vicente, Astrid Algaba-Brazalez, Jens Forssén, Jose Luis Gomez-Tornero

Inverse problems for synthesis, design and characterization of electromagnetic devices **318**

MIMO Array Design for Near-Field Radar Imaging by a Warping Strategy **319**
Mario Del Prete, Raffaele Solimene, Maria Antonia Maisto

Numerical investigation of the internal scattering operator in a 2D geometry **320**
Giovanni Leone, Giovanni Volpicelli, Rocco Pierri

Ruling (e.m.) Wavefields through Primary Sources and Inverse Designed Scatterers: A Mediterranean Route **321**
Tommaso Isernia, Renat Abdullin, Giada Maria Battaglia, Andrea Francesco Morabito, Roberta Palmeri

Robust phase retrieval using learned phase diversity **323**
Kedar Khare

Intensity-Only Linear Inverse Scattering via Phase-Space Formulation **324**
Davide Santagata, Maria Antonia Maisto, Raffaele Solimene

Inverse Profiling of Plasma in Compact Reactor:Actual Challenges and Opportunities **329**
Shaimaa Elseddiq Abuelsaud Ali Elghetany, Maria A. Maisto, Raffaele Solimene, Gino Sorbello, Luigi Celona, Loreto Di Donato

Fault Detection in Antenna Arrays Through Inverse Approaches **331**
Alessandro Fedeli, Maryam Iftikhar, Andrea Randazzo

From UV to Mid-IR: A Broad Spectrum for Innovative Applications 332

Er3+ ions luminescence in nanoparticles-doped optical fibers 333
Nadia Giovanna Boetti, Zhuorui Lu, Joris Lousteau, Maria Rita Cicconi, Franck Pigeonneau, Wilfried Blanc

Development and Integration of Fluoride-Based Fiber Gratings for Mid-IR Photonics 334
Antreas Theodosiou

Mid-IR Dispersion Spectroscopy for Liquid Sensing 335
Bernhard Lendl, Leopold Lindenbauer, Mauro David, Georg Ramer, Alicja Dabrowska

Hybrid laser integration for sensing application 337
Nicola Maraviglia, Davide Monopoli, Artem Vorobev, Fatih Bilge Atar, Natale Pruiti, Giovanna Calò, Simone Iadanza, Marc Sorel, Brian Corbett, Liam O'Faolain

Development of Mid-Infrared Lasers in Fluoride Glasses with Positive Index Waveguides 338
Ori Henderson-Sapir, David Lancaster, David Ottaway, Heike Ebendorff-Heidepriem, Toney Fernandez

Fluoride all-Fibre Lasers: Opportunities and Challenges 341
Maria Chernysheva, Kirill Grebnev

Hollow-Core Optical Fibers: Guiding Light from UV to Mid-IR and Beyond 342
Luca Vincetti

Germanate Glass as a Versatile Platform for Efficient 2 µm Laser Sources 344
Nadia Giovanna Boetti, Guy Shafriri, Amiel Ishaaya, Martha Segura, Davide Janner, Simone Normani, Pavel Loiko, Venkatesan Jambunathan, Alain Alain Braud, Patrice Camy, Joris Lousteau

Nanomaterials and Complex Media for Sensing and Optoelectronic Devices 346

Nanoscale terahertz dynamics in materials 347
Frank Hegmann

Spacetime Imaging and Ultrafast Control of THz Surface Plasmon Polaritons of Graphene 348
Simon Anglhuber, Martin Zizlsperger, Eva A. A. Pogna, Yaroslav A. Gerasimenko, Anastasios D. Koulouklidis, Imke Gronwald, Svenja Nerreter, Leonardo Viti, Miriam S. Vitiello, Rupert Huber, Markus A. Huber

Compact High-Q Photonic Crystal Cavities with Improved Robustness to Disorder 350
Nicoletta Granchi, Camilla Gonzini, Matteo Lodde, Gabriele Calusi, René P. J. van Veldhoven, Andrea Fiore, Guillermo Arregui, Francesca Intonti

All-fibre-based MoS2 photodetector for wearable applications 352
Felice Torrisi, Tong Wang, Longren Li, Shuwei Wu, Ao Yan, Artem Bakulin

Resonance Raman spectroscopy as a tool to assess the scattering channels in van der Waals materials for near-IR applications 355
Leonetta Baldassarre

Antenna Theory and Design 357

Design and Optimization of a Multilayer Dielectric Radome for Ka-, Q-, and V-Band Applications 358
Olga Basile, Marco Simone, Santi Concetto Pavone, Gino Sorbello

868 MHz Yagi-Uda Antenna for Educational Purposes: Design and Measurement 361
Mauro da Silva Leme, João Alexandre Batista Coelho, João Paulo Coelho

Electromagnetic Theory: Analytical, Computational and Numerical Methods 365

Leaky-Wave Analysis of Circularly Polarized Bessel-Beam Launchers based on Anisotropic Modulated Metasurfaces 366
Edoardo Negri, Federico Giusti, David Gonzalez-Ovejero, Enrica Martini, Walter Fuscaldo

Improving the performance of Iterative Physical Optics algorithm with Div/Curl-conforming basicfunctions 368
Michael Katsav

Method of Moments for the Analysis of Arbitrarily Shaped Metasurfaces 370
Federico Giusti, Stefano Maci, Enrica Martini

Inverse Design by Alternating Projections of Physically Realizable Modulated Metasurface Antennas 372
Marco Faenzi, David Gonzalez Ovejero, Enrica Martini, Stefano Maci

Novel Materials, Metamaterials, Metasurfaces, FSS and EBG 376

A Wide-Angle Reconfigurable Metasurface Retroreflector with Enhanced Angular Stability 377
Xin Wei, Wei Zhou, Bin Zheng

Performance Analysis of RIS-Assisted Secrecy Key Generation in Indoor Environments 379
Alessandro Santorsola, Giovanni Magno, Vincenzo Petruzzelli, Sabino Roberto Caporusso, Giovanna Calo

An Investigation of Aperiodic Array Design via Particle Swarm Optimization and Möbius-Transformed N × N Uniform Arrays 381
Waroth Kuhirun

Advancements in Meta-Mirrors for High-Precision Optical Metrology 385
Stefanie Kroker

Terahertz, Nanophotonics and Quantum Optics 388

Tunable Subterahertz Reflectarrays based on Novel Highly Anisotropic Liquid Crystals 389
Sergei Kuznetsov, Valeri Lapanik, Uładzimir Kislyi

Temporal Dispersion Effects in Optical Spectra of Exciton-Plasmon Systems at Strong Coupling 391
Gabriele Williams, Sancenia Johnson, Tigran Shahbazyan

Ultra-small and ultra-efficient source of photon pairs 393
Stanislas Pasternak, Alfredo De Rossi, Sylvain Combrie

Optics, Photonics and Nanophotonics 394

Bridging Simulation and Measurement: Complex Permittivity Estimate with Neural Network Based on Calibrated Data 395
Francesco Ferretti, Emidio DiGiampaolo, Alessandro Di Carlofelice

Investigation of Co-Directional Coupling in Mid-Infrared Fiber Gratings Fabricated by the Pull-and-Heat Technique 397
Francesco Anelli, Antonella Maria Loconsole, Federico Moscatelli, Francesco Prudenzano

Convex Optimization for Deep-Null Synthesis inSKA-Low Station Beamforming 400
Giuseppe Caruso, Giada Maria Battaglia, Pietro Bolli, Maria Grazia Labate, Andrea Francesco Morabito

Scalar Potentials of Solutions to the Vibrotransport Maxwell's Equations 404
Lyudmila Alexeyeva, Ilmira Kanymgaziyeva

Antennas, Metasurfaces and Electromagnetic Devices 406

Photonic space-time metamaterials: mimicking isotropic-to-anisotropic time interfaces 407
Andrew Naylor, Victor Pacheco-Peña

Calculating the solution of partial differential equations using photonics analog processors 410
Ross Glyn MacDonald, Victor Pacheco-Peña

Plasmonic Nanoantenna Architectures for Solar-Driven Hydrogen Production and Biomass Upgrading 413
Thanh-Lam Bui, Luca Mascaretti, Rambabu Yalavarthi, Hana kmentova, Alberto Naldoni, Stepan Kment

Phase-Transparent Frequency Selective Metasurface Design via Kolmogorov-Arnold Network Based Generative Modeling 415
Wei Du, Jiwei Zhao, Bin Zheng

Antennas, Microwave Systems and Electromagnetic Structures 417

Probabilistic Risk Mapping for Low-Altitude UAV Communications: An Empirical Tail Approach to Multipath and Interference Modeling 418
Hang Zhou, Zeyu Long, Yalong Qin

Ni-Co-Zn Composite Loaded Patch Antenna for MICS Band Biomedical Communications 420
Poonam Lathiya

Flexible metasurface integrated planar rigid antenna for circular polarization in K band 423
Garima Joshi, R. Vijaya

Advanced Dielectric Transmit-array Antennas for RF and Microwave Applications 426
Alvaro F. Vaquero, Marcos R. Pino

A Comparison of Dirichlet-Impulse Frequency Diverse Array and Phased Array Radars 427
Altunkan Hizal, Ramazan Cetiner, Hayrullah Yildiz

A 2-D Leaky-Wave Antenna Array for joint sensing, communication and wireless power transfer 433
Alejandro Gil-Martínez, Antonio Skarmeta, José Luis Gómez Tornero

Wideband Design of a Breakdown-Safe WR-15 Multilayer Vacuum Window 436
Olga Basile, Marco Simone, Santi Concetto Pavone, Gino Sorbello

Control of Mode Propagation and End-Fire Radiation in Rectangular Waveguides with Metasurface Boundaries 440
Zisis Foufas, Thomas Koschny, Odysseas Tsilipakos

A Preliminary Study on Multipath-Based Techniques for Radar Imaging 443
Raffaele Solimene, Antonio Cuccaro, Angela Dell'Aversano, Loreto Di Donato

Time-Modulated Metasurface-Based Corner Reflector for Radar Target Feature Manipulation 445
Haoran Han, Jiwei Zhao, Huan Lu, Peixuan Zhu, Rongrong Zhu, Bin Zheng

A Wideband Fast-response Energy Selective Surface 447
Jinghao Lv, Jiwei Zhao, Haoran Han, Huan Lu, Bin Zheng

Diffraction Contribution by a Junction of Chiral Layers with PEC Backing 449
Giovanni Riccio, Flaminio Ferrara, Gianluca Gennarelli, Rocco Guerriero, Francesco Chiadini

Photonics, Plasmonics and Optical Devices 452

Effect of asymmetry and disorder on spontaneous emission in resonant gratings supporting quasi-bound states in the continuum 453
Victor Kalt, Emmanuel Centeno, Rafik Smaali, Antoine Moreau

Defect-Engineered ZnO/Ag Nano-heterostructures for Energy-Related Applications 456
Roman Redko, Grigorii Milenin, Vitaliy Shvalagin, Svitlana Redko, Yelizaveta Savchuk

Metasurfaces for Light Harvesting in Perovskite Solar Cells 458
Sergii Mamykin, Iryna Mamontova, Roman Redko, Olena Shtykalo, Tetiana Lunko, Igor Dmytruk, Oleg Yeshchenko, Olexander Fedotov, Nataliya Berezovska, Anatoliy Pinchuk

Numerical Design of Field-of-View-Efficient Silicon Optical Phased Arrays 460
Henna Farheen, Andreas Strauch, J. Christoph Scheytt, Viktor Myroshnychenko, Jens Förstner

Investigation on Q-switching pulsed lasing in Mid-IR via Semiconductor Saturable-Absorber Mirrors 462
Antonella Maria Loconsole, Francesco Anelli, Federico Moscatelli, Francesco Prudenzano

Plasmonic switches based on the composite gold-vanadium dioxide material platform 465
Rostislav Řepa, Jiří Kabát, Jiří Liška, Tomáš Šikola, Vlastimil Křápek

Lithium-Niobate-Enabled Tuning of Optical Absorbance in Single- and Double-Layer Metallic Circular-Hole Arrays 468
Hanan Alhesseny, Christian Johnson-Richards, Ross Glyn MacDonald, Noel Healy, Toby Hallam, Victor Pacheco-Peña

Triple-doping in optical plasmonic glass nanocomposites 470

Electromagnetic Sensing and Materials Characterization 472

Giant Magnetoimpedance effect at GHz frequencies in amorphous microwires 473
Arcady Zhukov, Mihail Ipatov, Paula Corte-Leon, Juan Maria Blanco, Valentina Zhukova

Numerical Simulation of a Low-Frequency Electromagnetic Induction Sensor for Non-Contact Soil Electrical Conductivity Measurement 475
Nahal Akbari, Mohammad Asefi, Greg Bridges, Behzad Kordi

Contactless Determination of Martensitic Phase in Austenitic Steels 478
Tatiana Damatopoulou, Athanasios Markoulis, Nikolaos Tsouvalis, Evangelos Hristoforou

Author Index 479
Session Index 488
Country Index 489

Plenary Presentations

Intelligent Surface Wave Metasurfaces for Future Wireless Systems

T. Arshed, S. Maci, E. Martini*

Department of Information Engineering and Mathematical Science, University of Siena, Siena, Italy
*Corresponding author: enrica.martini@unisi.it

***Abstract*— This talk presents a surface-wave-based metasurface architecture for future high-frequency wireless systems that receives, guides, and re-radiates signals. A systematic design methodology enables flexible beam control, shaping, lateral shifts, obstacle bypassing around corners, and physical-layer frequency multiplexing by routing different frequencies along distinct paths.**

***Keywords*— metasurfaces, smart radio environment, surface wave, reflective intelligent surface.**

Advancements in Deep Learning-enabled Generative Design of Metalens Antenna and Frequency-selective-surface

Zhi Ning Chen[1] and Yanhe Lyu[1]

[1]Department of Electrical and Computer Engineering, National University of Singapore, Singapore

*Corresponding author: eleczn@nus.edu.sg

***Abstract*— The recent progress in developing prior-knowledge-guided DL-enabled generative designs of metalens antennas and FSSs in our group is updated. The generative metalens antenna achieves a dual-polarized low-scanning-loss across a wide-angle scanning range, and FSS demonstrates a low in-band loss, high lower-band suppression and sharp selection under dual-polarized wide-angle incident waves.**

***Keywords*— metasurfaces, deep learning, metalens, antennas, frequency-selective-surfaces.**

I. Introduction

Deep learning (DL) has emerged as a transformative paradigm for the synthesis of electromagnetic (EM) devices, offering a robust alternative to conventional optimization. By leveraging generative models, researchers can navigate high-dimensional design spaces to realize complex topologies that exceed the limitations of standard geometric shapes. These DL-based approaches are particularly vital as the demand for increased degrees of freedom (DoF) in next-generation antennas and metasurfaces grows.

Despite this potential, significant challenges remain in achieving angular stability and polarization consistency. In metalens antennas, beamscanning performance is often hindered by scan losses arising from the angular instability of transmission coefficients. This issue is exacerbated in dual-polarized applications, where a profound imbalance between TE and TM modes occurs at low elevation angles. Because TM-polarized oblique incidence possesses a significant normal component, traditional two-dimensional (2D) metacells often fail to resonate effectively, limiting the aperture efficiency and coverage of the lens.

Similarly, Frequency Selective Surfaces (FSSs) suffer from performance fluctuations as the incident wave deflects. Changes in effective aperture and inter-element mutual coupling lead to frequency shifts and insertion loss discrepancies. For FSSs, the challenge lies in maintaining a stable frequency response across wide-angle, dual-polarized incidence, where TM waves again introduce more significant discrepancies than TE waves.

To address these multi-objective mapping issues, current research shifts toward generative DL methods, such as conditional Generative Adversarial Networks (cGANs). These frameworks facilitate the synthesis of miniaturized, high-DoF topologies—ranging from cage-like metacells to non-standard FSS patterns—enabling the wide-angle stability and polarization balance required for advanced satellite and wireless communication links.

II. Generative Metalens Antenna

First, a miniaturized, cage-like metacell is designed for balanced TE and TM wide-angle transmission. The design leverages a Prior Knowledge (PK)-guided generative deep learning approach to overcome traditional limitations in metalens antenna scan-loss. By incorporating physical constraints and engineering expertise into the initial topology and pattern generation rules, we successfully constructed a high-DoF dataset to train a conditional deep convolutional generative adversarial network (cDCGAN).

The resulting DL-enabled metacells demonstrate exceptional performance at 10 GHz, maintaining a transmittance above 0.75 and a phase shift range of 295° under both TE and TM polarized waves at incident angles ranging from 0° to 45°. To validate this generative framework, a metalens antenna prototype was developed and tested. Experimental results, illustrated in Figs. 1 and 2, confirm a realized gain of 26.2 dBi and an aperture efficiency of 36.3%. Notably, the antenna achieves highly stable beam scanning from −40° to 40°, with measured scan

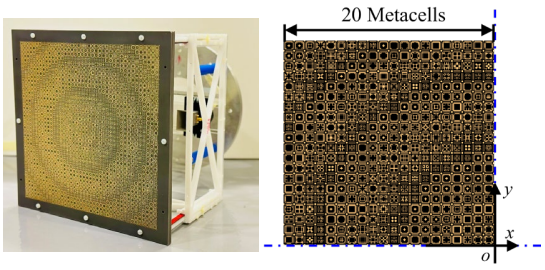

(a) (b)

Fig. 1 (a) The prototype and (b) the top-left one-quarter aperture of the proposed metalens antenna.

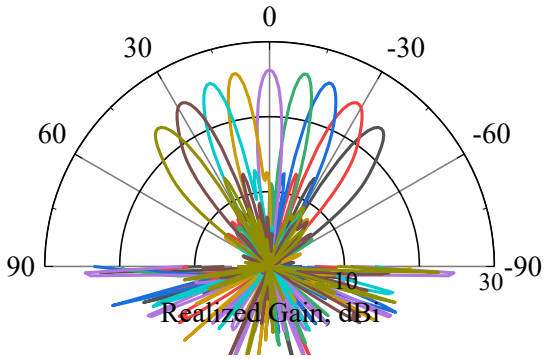

Fig. 2 Simulated patterns for TE beamscanning from −40° to 40° at 10 GHz, compared to the Jerusalem Cross (JC) metalens antenna.

losses kept below 2.6 dB and 2.4 dB for TE and TM polarizations, respectively.

III. Generative FSS

This research develops a generative deep learning (GDL)-enabled approach for the multi-objective synthesis of dual-polarized, wide-angle frequency selective surfaces (FSSs). Central to this method is a novel multichannel conditional generative adversarial network (MC-cGAN). To maximize the design potential, the team established specific FSS topologies and pattern generation rules, enabling high-DoF pixelated elements to meet complex performance goals. The resulting FSS structure is highly compact—with a period of just 0.22 wavelengths—comprising five layers of resonant and non-resonant loop-family slots and four substrates.

The MC-cGAN architecture utilizes dual channels to effectively learn multi-layer patterns while accounting for sensitive inter-layer mutual coupling. It also integrates a weighted updating strategy guided by physical generation rules. Once trained, the generator can synthesize a variety of high-performance designs based on specific condition vectors. Both simulation and experimental validation, as shown in Fig. 3, confirms that the GDL-enabled FSS realizes a stable passband from 2.5 to 3 GHz with an insertion loss below 2.6 dB. It simultaneously achieves a pre-band suppression greater than 31 dB and a sharp roll-off within a narrow 0.08 GHz band. These metrics are maintained under both dual-polarized waves and wide incident angles ranging from 0° to 60°.

IV. Conclusion

A prior-knowledge-guided deep learning-enabled generative design framework has been developed and experimentally validated in a dual-polarized low-scan-loss metalens antenna and a dual-polarized wide-angle multi-task frequency-selective surface. Both generative designs are constructed on establishing initial topologies and pattern generation rules, and driven by conditional generative models, where the prior knowledge guidance is derived from physical insights, design experience, and fabrication limitations. The proposed methodology and beyond-logic meta-devices pave a unique path towards

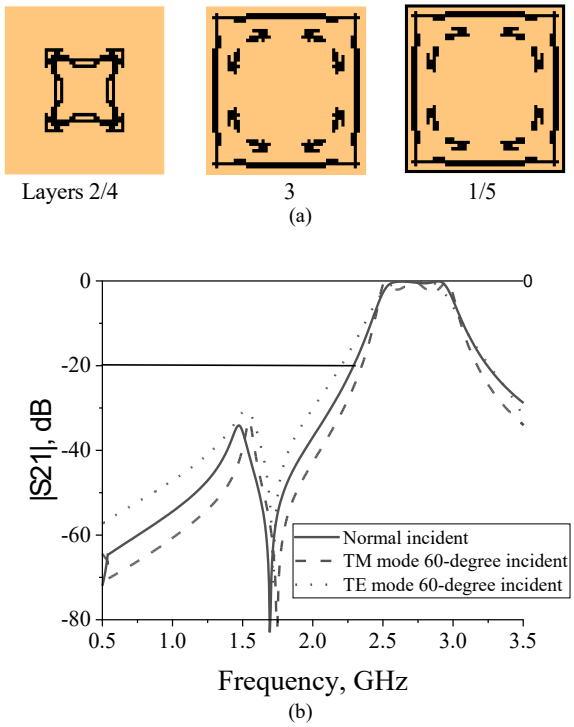

Fig. 3. (a) The photo of the FSS prototype. (b) Simulated $|S_{21}|$ of generative FSS designs under TE and TM incident waves at 0° and 60°.

upcoming wireless communication and sensing applications.

Acknowledgments

This work was partially supported by Project of MOET2EP5-01-2024.

References

[1] C. G. M. Ryan, M. R. Chaharmir, J. Shaker, J. R. Bray, Y. M. M. Antar, and A. Ittipiboon, "A wideband transmitarray using dual-resonant double square rings," *IEEE Trans. Antennas Propag.*, vol. 58, no. 5, pp. 1486–1493, May 2010.

[2] Z. N. Chen et al., "Microwave Metalens Antennas," *Proceedings of the IEEE*, vol. 111, no. 8, pp. 978-1010, Aug. 2023.

[3] T. Li and Z. N. Chen, "Compact wideband wide-angle polarization-free metasurface lens antenna array for multibeam base stations," *IEEE Trans. Antennas Propag.*, vol. 68, no. 3, pp. 1378–1388, Mar. 2020.

[4] P. Liu, L. Chen, and Z. N. Chen, "Prior-knowledge-guided deep-learning-enabled synthesis for broadband and large phase-shift range metacells in metalens antenna," *IEEE Trans. Antennas Propag.*, vol. 70, no. 7, pp. 5024-5034, Jul. 2022.

[5] P. Liu and Z. N. Chen, "Full-range amplitude-phase metacells for sidelobe suppression of metalens antenna using prior-knowledge-guided deep-learning-enabled synthesis," *IEEE Trans. Antennas Propag.*, vol. 71, no. 6, pp. 5036-5045, Jun. 2023.

[6] Y. Lyu, T. H. Gan, and Z. N. Chen, "TE-TM balanced wide-angle metacells for low scan-loss metalens antenna using prior knowledge-guided generative deep learning-enabled method," *IEEE Trans. Antennas Propag.*, vol. 73, no. 5, pp. 2940 – 2949, May 2025

[7] Z. Gu et al., "A solution to the dilemma for FSS inverse design using generative models," *IEEE Trans. Antennas Propag.*, vol. 71, no. 6, pp. 5100-5109, Jun. 2023.

[8] Y. Lyu, Y. Hong, and Z. N. Chen, "Generative Deep Learning-Enabled Multiobjective Synthesis of Dual-Polarized Wide-Angle Loop-Family Frequency-Selective Surfaces," *IEEE Trans. Antennas Propag.*, vol.74, no.1, pp. 456-466, Jan. 2026.

Dielectric metasurfaces: a new platform for nonlinear optics

Giuseppe Leo[1,2,*]

[1]Materiaux et Phénomènes Quantiques, Université Paris Cité & CNRS, Paris, France
[2]Institut Universitaire de France
*giuseppe.leo@u-paris.fr

***Abstract*—Flat optics revolutionized light propagation, and today dielectric metasurfaces enable to structure light in all its degrees of freedom, beyond the limits or superposition principle. The irruption of nonlinear wavefront shaping, chirality, and analog processing on the scene makes nonlinear meta-optics an ever more exciting theater to perform forefront research.**

***Keywords*— metasurfaces, nonlinear optics.**

Overview of Gap Waveguide Technology for Satellite Antenna Systems

Eva Rajo-Iglesias

University Carlos III of Madrid, Spain
Corresponding author: eva@tsc.uc3m.es

***Abstract*— During this talk, an overview of Gap Waveguide technology for satellite communications will be presented, highlighting innovative scanning and multibeam antenna designs. The presentation will also include an analysis of the multipactor effect in high-frequency environments. Particular emphasis will be placed on cost-effective solutions that achieve sufficient gain and high-purity circular polarization. In addition, recent developments in this technology and their application to advanced antenna design will be discussed.**

Quantum Photonics and Space-Time Metamaterials

Vladimir M. Shalaev

School of Electrical and Computer Engineering, Purdue University
West Lafayette, IN, USA
Corresponding author: shalaev@purdue.edu

***Abstract*— In this talk we first discuss quantum photonic integrated circuitry (qPIC) based on the recently discovered single-photon emitters in silicon nitride and the avalanche-enhanced optical modulation in silicon at single-photon intensities. Then, we show that transparent conducting oxides (TCOs) operating in the near-zero index (NZI) regime can provide strong ultrafast modulation, enabling novel optical phenomena in such extreme time-varying media, including photonic time crystals and 4D space-time metamaterials**

***Keywords*— metamaterials, space-time metamaterials, quantum photonics, photonic time crystals.**

Keynote Presentations

Optical Neural Networks based on photovoltaic elements

Andrea Di Falco[1,*]

[1]School of Physics and Astronomy, University of St Andrews, United Kingdom
*Corresponding author: adf10@st-andrews.ac.uk

***Abstract*— Photovoltaic neural networks provide a powerful route to scalable optical computing by directly converting optical signals into electrical outputs. This enables efficient, large-area signal acquisition while simplifying system architectures and reducing energy consumption. Such materials-driven approaches open pathways toward compact, potentially self-powered optical neural networks for next-generation artificial intelligence and edge computing.**

***Keywords*—machine learning, optical neural networks, metamaterials.**

Multibeam Antennas without Beam Forming Networks

Stefano Maci*,

[1]Department of Information Engineering and Matematics, University of Siena, Italy
*Corresponding Advancements author: macis@dii.unisi.it

Abstract— **Gradient-index (GRIN) lenses and metasurface antennas enable compact, low-cost multibeam systems without beam forming networks. Designed using advanced synthesis and fast geometrical optics solvers, GRIN lenses achieve wideband and precise beam shaping. Metasurfaces convert guided or space waves into directive beams via engineered impedance which operate as a continuous BFN, offering thin, efficient, and easily integrated antenna solutions for multibeams.**

***Keywords*—Multibeam Antennas, GRIN Lenses, metasurfaces.**

Long Slot Arrays: Advancing Next-Generation Communications Networks and Beyond

Mauro Ettorre

Department of Electrical and Computer Engineering, Michigan State University,
East Lansing, MI 48824, USA
*Corresponding author: ettorre@msu.edu

***Abstract*— High-speed wireless networks will leverage the abundant bandwidth available in the sub- and millimeter frequency ranges, mainly through XG systems and New Space technologies. Wideband arrays are key technologies for fully leveraging these wide bandwidths and establishing efficient data links for mobile users. In this context, long slot arrays and, in general, connected arrays, are very attractive solutions, offering decade-wide bandwidths, a large field of view, and a low-profile design. During this presentation, I will discuss the modeling of long slot arrays and highlight their advantages in terms of bandwidth and scanning capabilities, as well as their physical implementation. We will also discuss how thinned connected array solutions may be implemented without affecting the radiation properties of such antennas. We will also cover the implementation of long slot arrays across various technologies, particularly in millimeter and sub-millimeter frequency bands, aimed at next communications networks. Finally, I will demonstrate the capability of these arrays to radiate short, high-power pulses, thereby extending their applications to high-power scenarios.**

***Keywords*— wideband arrays, long slot arrays, connected arrays, non-dispersive radiation.**

Nanoplasmonic Cavities for Electromagnetic Wave Control: Quantum Dynamics in Open Resonators

Ortwin Hess[1,*]

[1]School of Physics, Trinity College Dublin, The University of Dublin, Dublin, Ireland
*Corresponding author: ortwin.hess@tcd.ie

***Abstract*— Nanoplasmonic cavities enable extreme subwavelength electromagnetic control with strong light-matter coupling in open, lossy resonators. Combining waveguide-integrated architectures and quantum quasinormal-mode theory, this work shows how dissipation can be engineered for coherent control, state preparation, and stabilization, establishing nanoplasmonic systems as versatile platforms for room-temperature quantum electromagnetic functionality.**

***Keywords*— nanoplasmonic cavities, strong light-matter coupling, quantum quasinormal modes, coherent perfect absorption.**

Nanoplasmonic cavities constitute an extreme nanophotonic limit of electromagnetic wave control, enabling strong light–matter coupling under ambient conditions [1]. These structures are highly open, dispersive, and non-Hermitian resonators in which geometry, radiation leakage, and material response jointly determine modal confinement, field enhancement, and coupling on the few-nanometre, few-femtosecond scale. They thereby connect open-resonator electrodynamics, waveguide coupling, loss engineering, and nanoscale light control with quantum photonics..

In this contribution, a unified perspective on nanoplasmonic cavities that links device-level electromagnetic architectures [2,3] with rigorous open-system quantization is presented. On the architectural side, waveguide-addressable nanoplasmonic platforms enable efficient in- and out-coupling while preserving extreme local confinement. In particular, quantum nanoplasmonic coherent perfect absorption (qnCPA) [4]exploits impedance matching between a plasmonic waveguide and a strongly coupled cavity–emitter system to selectively initialize and stabilize individual dressed states. In this regime, dissipation is elevated from a limitation to a control parameter: coherent, unidirectional feeding compensates loss and locks the system into a chosen polaritonic state, providing a route to functional electromagnetic wave control at the quantum level.

On the theoretical side, we will discuss a quantum quasinormal-mode (QNM) framework [5]based on macroscopic QED and complex coordinate transformations. Radiative leakage is regularized using perfectly matched layers, converting open-boundary loss into effective material dissipation and enabling a consistent definition of modal creation and annihilation operators for lossy resonators. This leads to a modal Fock-space description and a systematically derived Lindblad master equation that captures both coherent and dissipative inter-mode coupling intrinsic to non-Hermitian nanocavities. Benchmark studies show quantitative agreement with exact macroscopic-QED treatments of spontaneous emission and strong-coupling dynamics.

Taken together, these results establish nanoplasmonic cavities as more than extreme cQED platforms: they are engineered electromagnetic systems in which confinement, radiation, material dispersion, and dissipation can be co-designed for ultrafast light–matter functionality. By combining nanoscale plasmonic confinement with rigorous open-system quantization, such cavities offer a route toward room-temperature devices where loss, modal hybridization, and waveguide coupling are deliberately shaped for quantum state preparation, stabilization, and on-chip electromagnetic wave control.

[1] X. Xiong, N. Kongsuwan, Y. Lai, C. E. Png, L. Wu, and O. Hess, Room-temperature plexcitonic strong coupling: Ultrafast dynamics for quantum applications, Appl. Phys. Lett. **118**, 130501 (2021).
[2] D. D. A. Clarke and O. Hess, Near-field strong coupling and entanglement of quantum emitters for room-temperature quantum technologies, PhotoniX **5**, 33 (2024).
[3] O. Hess, Nanoplasmonic cavity quantum electrodynamic architectures for room-temperature quantum technologies, Eur. Phys. J. Spec. Top. (2025).
[4] Y. Lai et al., Room-temperature quantum nanoplasmonic coherent perfect absorption, Nat. Commun. **15**, 6324 (2024).
[5] L. Meschede, D. D. A. Clarke, and O. Hess, Quantum quasinormal mode theory for dissipative nano-optics and magnetodielectric cavity quantum electrodynamics, APL Quantum **3**, 016103 (2026).

Metasurfaces for biomedical sensing

Thomas F Krauss

School of Physics, Engineering and Technology, University of York, UK
thomas.krauss@york.ac.uk

***Abstract*— Metasurfaces hold much promise for novel sensing systems, but their operation needs to be properly understood; simply maximising the Q-factor is insufficient. We present a comprehensive framework for assessing their performance and apply it to the difficult problems of measuring small peptides as well as drug concentrations in the mid-IR.**

***Keywords*— metasurface, resonance amplitude, biomedical sensing.**

I. Introduction

Resonant photonic sensors are enjoying much attention based on the worldwide drive toward personalized healthcare diagnostics and the need to better monitor the environment. Recent developments exploiting novel concepts such as metasurfaces, bound states in the continuum, and topological sensing have added to the interest in this topic. There is a trend of exploiting novel phenomena towards increasing the quality (Q)-factors of such structures, which makes it critical to understand the impact of realistic limitations such as losses. We highlight that Q-factor alone is not sufficient, however, to describe a high performance sensor and note that the effect of the resonance amplitude has been largely ignored in the literature; resonance amplitude can be understood as a proxy for the signal to noise ratio (SNR) of the system, and it is widely accepted that SNR is the most important parameter of any test&measurement system.

II. Results and Discussion

Surprisingly, there is no physical model clearly describing the relationship between the limit of detection (LOD), Q-factor, and resonance amplitude available in the literature. We have therefore developed a novel ab initio analytical model, where we derive the complete figure of merit for resonant photonic sensors and determine their LOD [1]. We show that, counter-intuitively, optimization of the LOD is not achieved by maximization of the Q-factor but by counterbalancing the Q-factor and amplitude. We have validated the model experimentally and show that it is essential for applying novel sensing concepts in realistic scenarios.

As an example for the successful application of this strategy, we have developed a novel dielectric nanopillar photonic crystal structure in a dimer configuration [2]. Using a dimer configuration increases the degrees of freedom available for tuning the performance of the structure and we have been able to combine high resonance Q-factor, amplitude, and sensitivity in the same structure. In addition, we have used gold nanoparticles as an amplification mechanism and note that these nanoparticles do not compromise the high Q-factor and amplitude available with our structure. As a result, we have been able to detect small (3-4 kDa) molecules such as amyloid-β (Aβ) peptides that are indicators for Alzheimer's disease. Detecting these molecules at clinically relevant concentrations is extremely challenging, but we have manged to detect 0.2 pg/ml of Aβ42 and Aβ40 in 1% human blood serum, equivalent to 20 pg/ml in undiluted serum, which is the clinically required level.

We also show the detection of Aβ42 and Aβ40 peptides in the same channel, which is highly relevant for assessing disease progress and opens a route toward multiplexing. Together with the hand-held operation we have demonstrated previously, these photonic innovations make a major contribution to the ability to detect and monitor the progression of neurodegenerative diseases such as Alzheimer's.

We have applied similar principles in the mid-IR, where we have designed a metasurface resonance that hybridises with the vibrational resonance of the target drug molecule, thereby increasing the effective absorbance significantly [3]. The metasurface topology also promotes ordered drug crystallisation in regions with the strongest field enhancement, further contributing to the absorption enhancement. Using this design, we are able to repeatedly detect phenytoin (an anti-epilleptic drug) in the therapeutic range at concentrations below 10 µg/ml, which is the first demonstration, to the best of our knowledge, that achieves the detection limit clinically required for monitoring drug molecules with a resonant photonic structure.

References

[1] D Conteduca, GS Arruda, I Barth, Y Wang, TF Krauss and ER Martins, "Beyond Q: The Importance of the Resonance Amplitude for Photonic Sensors", ACS Photonics 9, 1757-1763 (2022).

[2] X GS Arruda, K Morris, A Martins, Y Wang, S Sloan-Dennison, D Graham, SD Quinn, ER Martins and Thomas F Krauss, "Ultrasensitive Alzheimer's disease biomarker detection with nanopillar photonic crystal biosensors", Optica 12, 1587-1596 (2025).

[3] K Li, P Dong, AV Veluthandath, S Kharratian, A Martins, GS Murugan, Y Wang and TF Krauss, "Metasurface-Enhanced Molecular Absorption at Mid-Infrared wavelengths for Therapeutic Drug Monitoring" (submitted)

Machine Learning-Enabled Design and Metrology of Integrated Optical Antennas

Dan-Xia Xu

Quantum and Nanotechnologies Research Center
National Research Council Canada, Ottawa, ON K1A0R6, Canada
*Corresponding author: Danxia.Xu@nrc-cnrc.gc.ca

***Abstract*— We demonstrate how machine learning advances integrated optical antenna design and application by enabling structured exploration of high-dimensional parameter spaces, capturing environment-dependent effective-medium behavior, and converting radiative responses into fabrication diagnostics. Together, these capabilities establish a unified, closed-loop framework for scalable, physically informed photonic antenna engineering.**

***Keywords*— integrated antenna, machine learning, metamaterials, optical metrology.**

I. Introduction

Optical antennas underpin a broad range of electromagnetic systems spanning free-space beam shaping, optical interconnects, sensing, and emerging quantum and terahertz platforms. Despite their diversity, most implementations fall into two architectural classes. The first comprises metasurfaces, where arrays of subwavelength scatterers are illuminated by an external beam, typically from the surface-normal direction, to synthesize desired wavefronts. The second consists of integrated waveguide-excited antennas, in which guided modes are gradually radiated into free space through engineered scattering elements such as gratings or leaky-wave structures.

Although both classes share common electromagnetic foundations, their design approaches diverge significantly. Metasurface design can benefit from the local periodicity approximation, where each unit cell is treated as an independent scatterer embedded in a periodic environment. This approximation enables tractable phase-gradient synthesis but begins to break down when strong inter-cell coupling or large angular deflection is required. In contrast, integrated waveguide-fed antennas operate in a fundamentally nonlocal regime. Radiation results from the cumulative evolution of guided power along the propagation direction, governed by longitudinal near-field coupling, distributed scattering, and modal phase matching. In these structures, strong near-field interaction is not incidental. Rather, it forms the basis for generating the desired optical response. These features introduce distinct and often more stringent design challenges for integrated antennas [1].

This keynote reviews our work on design methodologies and applications for integrated optical antennas and grating couplers, with emphasis on how machine learning is reshaping the design process. We focus on antennas designed on the silicon-on-insulator platform for perfectly vertical emission, where second-order Bragg resonances naturally arise. These resonances introduce destabilizing back-reflections into the feeding waveguide, degrading system performance and laser stability. Achieving high-efficiency, low-reflection emission therefore requires more sophisticated unit cells and careful co-optimization of radiation strength, phase synchronism, and fabrication constraints. At the same time, the spectral features associated with vertical emission can be intentionally made highly sensitive to unit-cell geometry. This sensitivity enables grating antennas to function as metrology tools, allowing retrieval of fabricated device parameters from optical responses in dimensional regimes where conventional optical metrology solutions are unavailable.

II. Discussion

The high dimensionality of complex unit-cell parameter spaces complicates antenna design. The resulting landscape is nonlinear and often non-intuitive. Conventional optimization approaches, such as parameter sweeps, adjoint-based gradients, or evolutionary searches, typically converge to isolated optima, offering limited visibility into the broader design space. The challenge becomes even more pronounced when multiple performance objectives must be considered simultaneously. To overcome this limitation, we developed a machine-learning-assisted framework that reframes antenna design as a global design-space mapping problem. Starting from a sparse set of high-performance devices, unsupervised learning techniques, such as principal component analysis (PCA), identify lower-dimensional manifolds in which optimal radiating structures reside [2, 3]. Within these reduced spaces, key performance metrics, including radiation efficiency, back-reflection, bandwidth, and fabrication tolerance, can be systematically mapped. Rather than yielding a single optimal solution, this approach reveals continuous families of viable designs and provides an intuitive performance landscape that enables designers to select geometries tailored to specific application requirements.

While global mapping enhances physical insight, computational cost remains a major barrier, particularly for

antenna designs that incorporate subwavelength metamaterials to tailor scattering strength and expand design freedom [4]. In most integrated antennas, such metamaterials are realized as periodically segmented subwavelength gratings (SWGs), where segmentation occurs in the transverse direction with a period below the diffraction limit. These structured regions are embedded within the antenna unit cell to engineer its effective scattering strength and phase response. To enable efficient design, the segmented region is represented as an effective medium characterized by an index n_{SWG}. This abstraction permits 2D simulation of the grating antenna, significantly reducing computational complexity while preserving the dominant modal behavior.

Traditionally, the relationship between n_{SWG} and geometric parameters is derived using the slab model, which determines n_{SWG} by matching the modal index of a uniform slab waveguide to that of a periodically segmented layer. This approach implicitly assumes that the transverse periodic structure extends infinitely along the longitudinal propagation direction and relates the equivalent index solely to the pitch and duty cycle [4]. However, when these transversely segmented SWGs are embedded within a finite, radiating antenna unit cell, the slab model breaks down [5]. The electromagnetic response is influenced not only by local transverse segmentation but also by longitudinal power evolution, radiation leakage, and the surrounding antenna environment. Under these conditions, the conventional slab model becomes inaccurate, even when the segmentation period is significantly subwavelength, necessitating full 3D simulation for reliable antenna design.

We show, however, that the effective-medium concept itself remains valid. What fails is the assumption that the effective index depends only on local geometry. Instead, it becomes an environment-dependent parameter n'_{SWG}. To capture this behavior, we develop a deep-learning surrogate model trained on paired two- and three-dimensional simulations for a variety of unit cells. The model learns the modified mapping between geometry and effective index under realistic antenna operating conditions. The resulting framework, termed *Metastrip Net*, restores pseudo-3D optimization within a two-dimensional simulation environment while maintaining physical fidelity [6, 7]. It reduces computational cost by orders of magnitude and enables broadband multi-objective optimization of radiation efficiency and back-reflection.

Beyond forward design, machine learning enables a largely untapped opportunity: the use of optical antennas as fabrication metrology probes. Because antenna radiation characteristics can be intentionally engineered to be exquisitely sensitive to nanoscale geometry, their measured optical responses inherently encode detailed structural information about the fabricated device. By leveraging this sensitivity, we developed inverse neural-network frameworks capable of retrieving antenna geometry directly from spectral responses [8]. These models establish a bidirectional mapping between structure and electromagnetic performance, enabling nanometer-scale reconstruction of geometric parameters and quantitative assessment of fabrication variability.

This capability opens regimes inaccessible to conventional physical metrology tools. Rather than relying solely on electron microscopy or destructive cross-sectioning, antenna responses themselves become diagnostic signals. Moreover, this approach enables evaluation of significantly smaller feature sizes than previous optical metrology techniques based on ring resonators or Mach-Zehnder interferometers, and evaluate wire waveguide width in the range of several hundred nanometers. Such methods enable wafer-scale process monitoring, rapid yield analysis, and feedback loops between fabrication and design, effectively creating digital electromagnetic twins of integrated photonic systems.

Taken together, these developments define a machine-learning-enabled development cycle for integrated antenna engineering: global design-space discovery, accelerated surrogate optimization, and inverse-response metrology. As integrated photonic systems grow in structural complexity and functional integration, machine learning will serve not only as a computational accelerator but as a framework for extracting physical insight from high-dimensional electromagnetic data. In this emerging paradigm, Maxwell's equations and machine learning operate in concert—transforming antenna design from isolated optimization to structured exploration, and fabrication characterization into closed-loop intelligence across scales and frequencies.

ACKNOWLEDGMENTS

This work was partially funded by the National Research Council (NRC) Canada, the AI for Design Challenge Program of NRC, and by the European Union through the European Research Council (ERC) project BEAMS (Grant agreement No. 101041131).

REFERENCES

[1] D. Melati, D.-X. Xu, Y. Grinberg, M. Al-Digeil, "Inverse design of photonic integrated devices: Optimization and machine learning". *APL Photonics* 1 October 2025.

[2] D. Melati, Y. Grinberg, M. K. Dezfouli, S. Janz, P. Cheben, J. H. Schmid, A. Sánchez-Postigo, and D.-X. Xu, "Mapping the global design space of nanophotonic components using machine learning pattern recognition," Nature Communications, vol. 10, no. 1, pp. 1-9 (2019).

[3] M. K. Dezfouli, Y. Grinberg, D. Melati, P. Cheben, J. H. Schmid, A. Sánchez-Postigo, A. Ortega-Moñux, et al., "Perfectly vertical surface grating couplers using subwavelength engineering for increased feature sizes," Optics Letters, vol. 45, no. 13, pp. 3701-3704 (2020).

[4] J. M. Luque-González, A. Sánchez-Postigo, A. Hadij-ElHouati, A. Ortega-Moñux, J. G. Wangüemert-Pérez, J. H. Schmid, P. Cheben, Í. Molina-Fernández, and R. Halir, "A review of silicon subwavelength gratings: building break-through devices with anisotropic metamaterials," Nanophotonics 10, 2765–2797 (2021).

[5] J. Zhang, D. Melati, Y. Grinberg, M. Vachon, S. Wang, M. Al-Digeil, S. Janz, J. H. Schmid, P. Cheben, and D.-X. Xu, "Perfectly vertical silicon metamaterial grating couplers with large segmentation periods up to 650 nm," arxiv.org/pdf/2311.12057 (2023).

[6] Q. Wang, N. Israel, D. Xu, Y. Grinberg, and L. Ramunno, "A Machine Learning-Based Framework for Pseudo-3D Optimization of Metamaterial Grating Couplers," in *Advanced Photonics Congress*, paper ITu2B.2, Marseille, July 2025

[7] N. S. Israel, D. Blankespoor, D.-X. Xu, Y. Grinberg and L. Ramunno, "Machine Learning-Enabled Inverse Design of Subwavelength Waveguide Gratings using Environment-Aware Effective Medium Approximations," Photonics North, Montreal, Canada, pp. 1-2, 2023.

[8] A. Masominia, D. Melati, D.-X. Xu, Y. Grinberg, M. Al-Digeil, "Retrieving the Design Parameters of Silicon Photonic Devices from Optical Responses Using an Inverse Neural Network Model". Silicon Photonics Conference, Ottawa, April 2026.

Integral Equations Advanced Techniques for the Electromagnetic Analysis of Real-Life Multi-Scale Antenna Problems

Francesca Vipiana

Department of Electronics and Telecommunications, Politecnico di Torino, Torino, Italy
*Corresponding author: francesca.vipiana@polito.it

***Abstract*— In the last years, the electromagnetic (EM) problems have scaled up in complexity and size: the EM simulations are attempted of the entire system, and the use of simulation tools has been explored as a way to reduce the cost of certifying complex platforms. This talk will address the efficient and accurate analysis of real-life multi-scale antenna problems via the moment method (MoM) solutions of surface integral equations (SIEs). SIEs have emerged as the dominant technology for the EM modeling of antenna placement on large and complex platforms such as aircrafts, ships, satellite, and vehicles.**

***Keywords*— integral equations, method of moments, multi-scale, antennas, computational EM**

A New Two-Step Framework for Effective Electromagnetic Inverse Scattering: From Contrast Source Retrieval to Linear Contrast Reconstruction

Lorenzo Crocco

Institute for electromagnetic Sensing of the Environment (IREA)
Consiglio Nazionale delle Ricerche (CNR), Napoli, Italy
lorenzo.crocco@cnr.it

***Abstract*— This talk introduces a unified perspective on a new class of methods for electromagnetic inverse scattering based on a two-step decomposition. The first step focuses on the joint retrieval of the contrast source and total field, while the second step consists of the linear inversion of their relationship to directly estimate the contrast. Within this framework, two novel approaches are presented. The first, named LUCIE, leverages a reformulation of the governing equations in which a carefully selected hyperparameter mitigates intrinsic nonlinearity, enabling stable and accurate recovery of the contrast source. The second approach revisits the classical Contrast Source Inversion (CSI) method by replacing the traditional state equation term with an alternative formulation that explicitly depends on the unknown contrast source, total field, and known incident field. This modification enhances robustness and proves particularly effective in MRI-based electric property tomography, while remaining applicable to microwave imaging scenarios. The proposed framework highlights common structural features of these methods and provides insight into their theoretical and practical advantages for solving nonlinear inverse scattering problems.**

***Keywords*— electromagnetic scattering inverse problems, inverse problems, microwave imaging, electric property tomography, magnetic resonance imaging, contrast source inversion, contraction integral equation.**

Space-Time Metamaterials

Andrea Alù[1,2]

[1]Photonics Initiative, Advanced Science Research Center, City University of New York, New York, NY 10031, USA
[2]Physics Program, Graduate Center, City University of New York, New York, NY 10016, USA
*Corresponding author: aalu@gc.cuny.edu

***Abstract*— Metamaterials offer a powerful platform to manipulate wave propagation and gain control over waves, from radio-frequencies to light and sound. In this talk, I will discuss our recent progress in developing new metamaterial technologies, introducing time as an additional dimension for wave control.**

***Keywords*— metamaterials, space and time modulation.**

I. Introduction

The field of metamaterials, artificial engineered materials, has been rapidly evolving in the past two decades, demonstrating extreme optical phenomena and unprecedented control over wave propagation. In this talk, I discuss recent developments in this field of research, with an emphasis on the role of symmetries in establishing emerging electromagnetic responses for metamaterials based on otherwise simple constituents. Geometrical rotations, suitably tailored perturbations, and broken time reversal symmetry can be carefully engaged to tailor waves in robust and efficient ways, control their propagation, break Lorentz reciprocity and enable topological order and phase transitions. In my talk, I will discuss the underlying physical principles that span over a wide range of frequencies in the design of metamaterials, and focus on the relevance of the temporal dimension as an additional knob for wave control. I will also discuss the impact of metamaterials on practical technologies, from imaging, energy and sensing to computing and wireless communications.

Beamforming with Metasurfaces Connected to Reactive Loads or Networks

Anthony Grbic* and Malik Almunif

Department of Electrical Engineering and Computer Science, University of Michigan, USA
*Corresponding author: agrbic@umich.edu

***Abstract*— The talk will describe how a metasurface connected to reactive loads or networks can serve as a low-cost beamforming technology. The reactively-loaded metasurfaces consists of a grid of subwavelength unit cells that are connected to individual ports. Some ports are directly excited while the remaining ports are terminated in reactive loads/networks and function as parasitic radiators. After an initial full-wave characterization of the metasurface in terms of an impedance matrix and its active element patterns, the loads/network required to achieve a targeted radiation pattern are found through microwave network theory. Strong coupling between the unit cells, tailored by these reactive loads, allows energy to be shuttled across the aperture to enable beam steering, beam shaping, and multiple simultaneous beams driven by separate feeds. Prototypes consisting of metasurfaces with aperture-coupled unit cells will be reported at the conference.**

***Keywords*— metasurface, antenna beamforming, microwave network theory.**

Tailorable Quasi-2D Materials for Photonics

Alexandra Boltasseva

Elmore Family School of Electrical and Computer Engineering, Purdue University
West Lafayette, IN 47907, USA
Corresponding author: aeb@purdue.edu

***Abstract*— The recent advent of tailorable, two-dimensional (2D) and quasi-2D materials such as trans-dimensional (TD) plasmonic semi-metals, including several atomic layers thin titanium-, zirconium-, and hafnium nitrides, and 2D transition-metal carbides and nitrides (MXenes) is currently driving the development of new concepts for metasurfaces and on-chip devices for communication, sustainable energy and quantum technologies. These materials exhibit great tailorability of their optical properties, remarkable dynamic tunability under external electric, optical, mechanical and other stimuli, strong plasmonic behavior, and high optical nonlinearities. These platforms also offer pathways to uncovering new phenomena ranging from epsilon-near-zero (ENZ) behavior to strongly correlated electronic systems. In this talk, we discuss the designer-like characteristics of MXenes, achievable with the choice of transition metal and control of stoichiometry and outstanding tailorability of properties of TD materials. We also analyze physical effects in atomically thin TD plasmonic films enabling metal-to-insulator transitions.**

***Keywords*— 2D materials, MXenes, photonic materials.**

Certain recent developments in photonics

Marin Soljacic[1,*]

[1]Department of Physics, MIT, USA
*Corresponding author: soljacic@mit.edu

***Abstract*— I will present some of our recent results in the field of photonics, including novel phenomena in scintillators, X-ray imaging, and AI and robotics for photonic-science automation.**

***Keywords*— AI, robotics, photonics.**

Recent Advances in Nanophotonics and Metamaterials

Hybrid 2D-plasmonic nanoantennas for photon emission and sensing

Maria Caterina Giordano[1,*], Giorgio Zambito[1], Giulio Ferrando[1], Matteo Barelli[1], Francesco Buatier de Mongeot[1], Antonino Foti[2], Pietro Gucciardi[2], Simone Sotgiu[3], Tommaso Venanzi[3], Erica Fragomeni[3], Leonetta Baldassarre[3]

[1] Dipartimento di Fisica, Università di Genova, Via Dodecaneso 33, 16146 Genova, Italy
[2]CNR-IPCF, Viale F. Stagno D'Alcontres 37, 98158, Messina, Italy
[3]Dipartimento di Fisica, Sapienza Università di Roma, Roma, Italy
*Corresponding author: maria.caterina.giordano@unige.it

Abstract

Hybrid 2D-plasmonic nanoantennas are engineered via thermal nanolithography to tailor the photon emission properties of 2D semiconductor layers. The plasmonic response of these nanosystems is tuned over a broadband spectrum showing plasmon enhanced photon emission in the Visible spectrum and resonant enhancement of the weak Raman signal in the Infrared.

***Keywords*— plasmonic nanoantennas, 2D semiconductors, photon emission, Infrared Raman signal.**

I. Introduction

Two-dimensional (2D) Transition Metal Dichalcogenides (TMD) layers, featuring strong light-matter interaction effects, recently emerged due to their exceptional optoelectronic properties as both absorbers and quantum emitters, and to the possibility to tailor their photonic response via strain engineering. However, key issues such as the relatively low optical absorption of atomic layers and their poor quantum efficiency still limit their integration in competitive photonic devices[1].

To overcome these limitations the ability to reshape 2D TMDs at the nanoscale represents a crucial step toward the fabrication of TMD-based flat-optics metasurfaces featuring enhanced photon harvesting and/or photon emission[2,3].

II. Results and Discussion

In this work, we demonstrate the engineering of 2D nanostructures and/or hybrid 2D-plasmonic nanoantennas based on 2D TMDs semiconductor layers via non-invasive thermal Scanning Probe Lithography (t-SPL) approaches[4]. The optical response of these nanosystems have been tuned to amplify the photon emission properties of the 2D layers in the Visible and Infrared spectral range.

We develop high-resolution 3D nanopatterns characterized by out-of-plane tilted nanofacets via grayscale t-SPL and exploit such templates for the conformal transfer of 2D MoS_2 layers tailoring their optoelectronic response at the local scale via strain engineering[5]. Alternatively, grayscale t-SPL templates have been exploited for the maskless confinement of tilted noble metal nanoantenna arrays supporting Localized Surface Plasmon (LSP) resonances that can be tuned over a broadband Visible and Near-Infrared spectrum. The following conformal transfer of 2D MoS_2 monolayers onto the nanoantennas allow to achieve hybrid 2D-plasmonic nanoemitter arrays characterized by deterministic morphology and out-of-plane tilt. Under this condition the photoluminescence emission of the hybrid nanosystems has been investigated, observing a polarization-sensitive enhancement of the signal when the LSP is tuned in resonance with the 2D TMD exciton polaritons.

In parallel the possibility to enhance the weak Raman emission of non-resonant $MoTe_2$ layers have been investigated[6] tuning the plasmon resonance of the nanoantennas in the Near-Infrared. Under this condition we showed polarization-sensitive enhancement of the weak Raman emission in the Infrared opening new possibilities for the investigation of 2D layers.

III. Conclusion

We have developed hybrid 2D-plasmonic nanosystems with tunable optical properties over a broadband spectral range, demonstrating plasmon enhanced photon emission in the Visible spectrum and amplified Raman signal in the Infrared. These results select these hybrid 2D-plasmonic nanoemitter arrays as promising platforms for applications in many fields ranging from photonics and energy conversion, to Infrared sensing and quantum technologies.

Acknowledgments

The authors are grateful to Daniele Marrè, Michele Ceccardi, Dipartimento di Fisica, Università di Genova, and to Federico Caglieris and Francesco Bisio, CNR-SPIN for experimental support. This work was supported by the National Recovery and Resilience Plan (NRRP), Call for tender no. 1409 PRIN 2022 PNRR by Ministero dell'Università e della Ricerca (MUR), funded by the European Union – NextGenerationEU, project title "2D-PLANET" (code P2022JWKAC), and Call for tender no. 104 PRIN 2022, project title "design" (code 2022EE8KH9), and project title FLASH-2D, code

“2022FWB2HE”.

REFERENCES

[1] D. Jariwala, et al. ACS Photonics 4, 2962 (2017).
[2] M. Bhatnagar et al. Nanoscale 12, 24385 (2020).
[3] M. Gardella et al. Small Small 21 (15), 2400943 (2025).
[4] M. C. Giordano et al. Advanced Materials Interfaces 10, 2201408 (2023).
[5] G. Zambito et al. Small Science (2025) https://doi.org/10.1002/smsc.202500404
[6] S. Sotgiu et al. Physical Review B 113, 085201 (2026) https://doi.org/10.1103/ty8m-mgml

Field-enhancement in plasmonic tagged nanoplastics

Maria Antonia Iatì[1,*], Shadi Rezaei[1,2], Alessandro Veltri[3], Pietro G. Gucciardi[1], Onofrio M. Maragò[1], and Rosalba Saija[1,2]

[1]CNR-IPCF, Istituto per i Processi Chimico-Fisici, Messina, Italy
[2]Dip. di Scienze Matematiche e Informatiche, Scienze Fisiche e Scienze della Terra, Università di Messina, Italy
[3]Dip. di Fisica, Università della Calabria, Rende (Cosenza), Italy
*Corresponding author: mariaantonia.iati@cnr.it

***Abstract*— Nano-plastics represent a topic of growing interest due to their widespread presence in the environment. However, their identification is still quite challenging. Plasmon field enhancement has the potential to be used for developing sensitive detection methods. Here, we present a computational approach, based on the Transition matrix method, capable of modelling the optical response in plasmonic tagged nanoplastics.**

***Keywords*— light scattering, plasmonics, nano-plastics**

Textile-Embedded Metasurfaces for Enhancing Smart Devices Connectivity

Francisco S. Cuesta[1,*], Xianghui Qiu[2], Mohammad M. Asgari[1], Shuai S. A. Yuan[1], Sergei Tretyakov[1], Xuchen Wang[2], Viktar Asadchy[1]

[1] Department of Electronics and Nanoengineering, Aalto University, Finland
[2]College of Physics and Optoelectronic Engineering, Harbin Engineering University, China
*Corresponding author: francisco.cuestasoto@aalto.fi

***Abstract*—In this talk, we present a textile-based metasurface to improve connectivity between a smart device, located at the edge of the metasurface, and the network. The metasurface, performing propagating to surface wave conversion, was designed based on the impedance density matrix approach, with induced currents' Green function estimated using simulation data.**

***Keywords*— Metasurfaces, smart textiles, impedance matrix, Green's function, wireless communications.**

I. Introduction

Current and future wireless technologies have entered into a paradox. On one side, the constantly growing demand for faster data-transfer rates and broader bandwidths require a shift towards higher frequency bands. On the other hand, smart devices are required to become more energy efficient and more compact as the technology evolves. At this point, it becomes counter-intuitive that the combination of higher frequency bands with smaller devices will affect the performance of the wireless link. After all, if the carrier frequency increases, its corresponding wavelength decreases, becoming comparable to the size of the smart device's antenna. However, due to the increase in the electric path that the signals have to travel at higher frequencies, the link between the smart device and the base station degrades more than the gain increase coming from having an antenna comparable to the wavelength.

Unfortunately, a smart device has limited options to improve the link, as its design limits how much power it can consume (due to battery size and time between charges) and the physical size of the antenna (as large as the device itself). A possibility is to use a high-gain external antenna, which can provide a larger geometric aperture without compromising power consumption [1], [2]. However, having to carry an external antenna connected physically to a mobile device is not an appealing concept from an end-user perspective. A better approach could be to integrate a passive reflector into the user's clothing, allowing us to collect the incident signal using a much wider effective area.

In this talk, we present a flexible textile metasurface, which can be embedded on the front and back of conventional clothing, to enhance the connectivity of smart devices. The textile metasurface can collect the incident signal from a large surface and send them to the edge of the structure as a surface wave [3]. At the edge of the metasurface, the surface wave will reradiate towards the smart device located at its vicinity. The metasurface pattern is optimized numerically, taking into account the mutual coupling between strips using the impedance density matrix approach [4], to maximize the power delivered to the device's antenna. The metasurface is designed as an array of surface impedance strips. Unlike previous approaches [5]–[9], this metasurface architecture can be implemented using screen-printing technologies [10], [11], which can provide enough accuracy and can be integrated into large-scale fabrication chains.

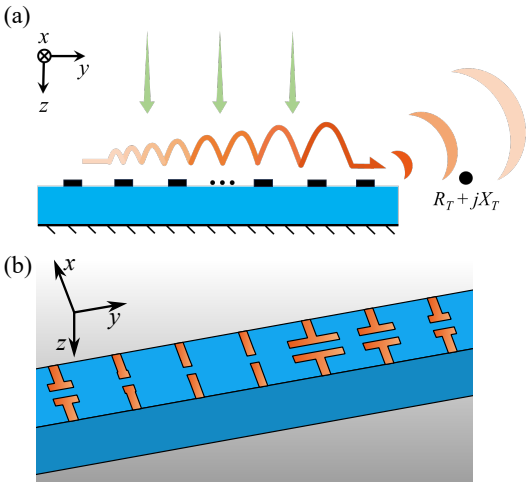

Fig. 1. (a) A textile metasurface designed to transfer an incident traveling wave towards a reference antenna located at the edge of the metasurface. (b) The metasurface can be implemented as an array of strips made of conductive ink, with a dog-bone pattern to tune the surface impedance.

II. Methods

For the design, we consider a metasurface illuminated by a Transverse Electric (TE) incident wave propagating in the yz plane. The metasurface itself is modeled as an array of N reactive-loaded conductive strips over a substrate (the garment's textiles), and a flexible ground plane below the cloth, as shown in Fig. 1(a). This metasurface model is a fair approximation for the front and back sides of smart clothes, which provides a nearly flat surface with smooth curvature.

The objective of the textile-embedded metasurface is to maximize the power delivered in a given point in space. For such a purpose, a Figure of Merit (FoM) can be established by placing a reference antenna at one of the metasurface edge, as described in Fig. 1(a). The antenna has an input impedance per length $Z_T = R_T + jX_T$. The delivered power $P_{\text{del}} = \frac{1}{2}|I_T|^2 R_T$ depends on the induced currents on the antenna, which is a linear function of the received scattered field at that point. Therefore, the Figure of Merit is expressed as $\text{FoM} = P_{\text{del}}/P_{\text{inc}}$, where $P_{\text{inc}} = \frac{E_{\text{in}}^2}{2\eta} L \cos\theta_i$ (with E_{in} and θ_i are the electric field amplitude and angle of the incident wave, respectively, η as the free-space characteristic impedance and L is the metasurface length) is the power collected by the metasurface geometric cross section.

The scattered electric field at the reference point can be calculated from the induced currents at the metasurface strips. Using Ohm's law, we can determine the relation between the external electric field E^{ext} (combination of the incident wave with the reflected wave coming from the ground plane) and the induced currents for each strip. The external field can be written as

$$E_x^{\text{ext}}(y,z) = E_{\text{in}} \left[e^{-jk_1 \cos\theta_i z} + R_0 e^{+jk_1 \cos\theta_i (z+2h)} \right] e^{-jk_1 \sin\theta_i y}, \quad (1)$$

where R_0 is the reflection coefficient of the substrate (with thickness h) and ground plane combined below the strips, and k_1 is the wavenumber of the incident wave in free-space. Therefore, the relation between the external electric field and the induced currents at the strips is given by the expression

$$[\mathbf{Z}] \cdot [\mathbf{I}] = [\mathbf{E}], \quad (2)$$

where $[\mathbf{I}] = [I_1, I_2, \ldots, I_N]^T$ and $[\mathbf{E}] = [E_x^{\text{ext}}(y_1, -h), \ldots, E_x^{\text{ext}}(y_N, -h)]^T$ describe the electric field and induced currents at each strip location, respectively. The impedance density matrix describes the intrinsic self- and mutual-coupling of the strips in the array and the effect of the added load impedance. Therefore, the matrix is written as $[\mathbf{Z}] = [\mathbf{Z}_s] + [\mathbf{Z}_m] + [\mathbf{Z}_{\text{L}}]$, where the mutual impedance density matrix has the form

$$[\mathbf{Z}_m] = \begin{pmatrix} 0 & Z_{1,2} & Z_{1,3} & \cdots & Z_{1,N} \\ Z_{2,1} & 0 & Z_{2,3} & \cdots & Z_{2,N} \\ Z_{3,1} & Z_{3,2} & 0 & \cdots & Z_{3,N} \\ \vdots & \vdots & \vdots & \ddots & \vdots \\ Z_{N,1} & Z_{N,2} & Z_{N,3} & \cdots & 0 \end{pmatrix} \quad (3)$$

while the self-impedance $[\mathbf{Z}_s] = \text{diag}(Z_1, Z_2, \ldots, Z_N)$ and load impedance density matrices $[\mathbf{Z}_{\text{L}}] = \text{diag}(Z_{\text{L},1}, Z_{\text{L},2}, \ldots, Z_{\text{L},N})$ have a diagonal form.

Due to the architecture used in the proposed design of Fig. 1(a), it is not possible to find an analytical form that describes the self- and mutual-coupling between strips. Instead, the values for $[\mathbf{Z}_s]$ and $[\mathbf{Z}_m]$ were estimated using a numerical simulations in COMSOL, where a reference 1 [A] current source was placed at each strip's location to find the resulting scattering field where the other strips are located. The ratio between the scattered electric field and the reference current is equal to the Green's function for the given strip. Likewise, the equivalent Green function for each strip that computes its contribution to the scattered field at the reference point can be estimated using a similar COMSOL simulation.

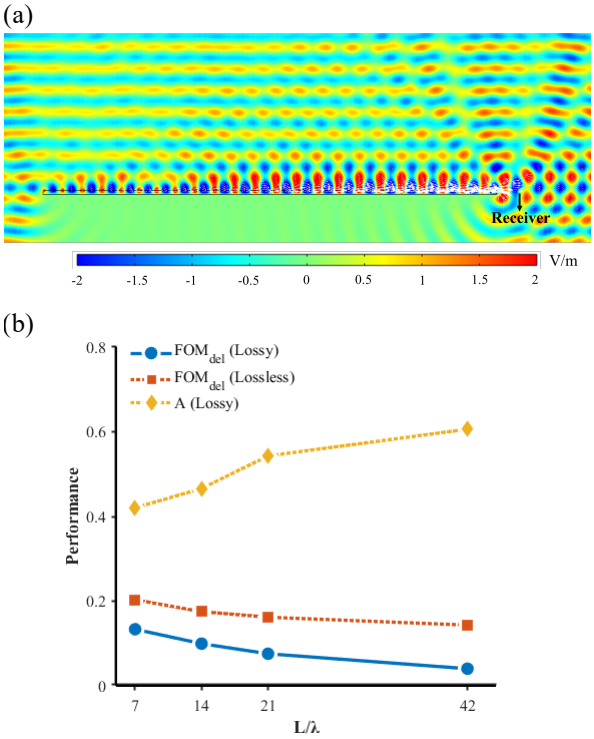

Fig. 2. (a) Total electric field produced by the textile metasurface under normal illumination. (a) Performance comparison as a function of the metasurface length L in terms of FoM and absorption A.

At this point, the missing link to this metasurface design is to find the set of load impedances $[\mathbf{Z}_{\text{L}}]$ which will produce the right combination of induced currents that maximizes the delivered power at the reference point P_{del}. This set of optimized load impedances is determined using an implementation of the Multi-Population Genetic Algorithm (MPGA) in MATLAB with the objective of maximizing the FoM. The algorithm is tuned to determine the best combination of capacitive loads, which can be implemented using a flat dog-bone topology, as shown in Fig. 1(b).

III. Results and Discussion

For this proof-of-concept, we used a normal incident wave with a reference frequency of 26 GHz (wavelength $\lambda = 11.54$ mm). The metasurface was designed assuming a cotton-polyester textile substrate ($\varepsilon_2 = 1.81$, $\tan\delta = 0.015$ and thickness $h = 2.2$ mm), with dog-bone patterns made of conductive ink ($\rho = 0.0716\ \Omega \cdot \mu\text{m}$) and strips width $w = \lambda/43$, a period in y direction of $d = \lambda/6$ and in x direction of $b = \lambda/5.5$; and a gap between same-strip dog-bones of $b = \lambda/5.5$

Figure 2(a) show that the ideal surface impedance strips, simulated in COMSOL, is capable to redirect the normal

incident wave towards the antenna at the right side of the metasurface, with weak leakage at the left side. Moreover, in Fig. 2(b), we can observe the effects of the metasurface length L over its performance in terms of FoM and losses absorption A. While the FoM remains quite stable (about 20% in the lossless case) for any length, the performance degrades as the metasurface length increases due to internal absorption.

IV. Conclusion

In this work, we presented a novel approach to improve smart devices' connectivity by embedding a flexible metasurface into the user's clothing. The integrated metasurface provides a larger surface to collect the power coming from the transmitter, redirects such power towards the device near the garment, and couples it with the device's antenna for maximizing power transfer. The textile-embedded metasurface is designed to convert the incident wave into surface waves, which are re-radiated at the edge of the smart textile. The design itself is based on an impedance-matrix approach, where the meta-atom's reactances are tuned to control the induced currents over the textile and maximize the power conversion. Due to the reciprocal nature of the textile metasurface, it improves both reception and transmission capabilities of the smart device that takes advantage of this external aperture. The design effectiveness in power conversion has been tested and demonstrated using full-wave simulations. The proposed design can be implemented using easy-scalable low-cost screen printing technology, allowing the implementation of such smart textiles in clothes, canvas, and any other textile-based surface.

Acknowledgments

This work was supported by the Research Council of Finland within the RCF-DoD Future Information Architecture for IoT initiative grant no. 365679, Research Council of Finland grant no. 371367, and the Finnish Foundation for Technology Promotion.

References

[1] N. H. M. Rais, P. J. Soh, F. Malek, S. Ahmad, N. B. M. Hashim, and P. S. Hall, "A review of wearable antenna," in *Proc. Loughborough Antennas & Propagation Conf. (LAPC)*, pp. 225–228, 2009.

[2] K. N. Paracha, S. K. A. Rahim, P. J. Soh, and M. Khalily, "Wearable antennas: A review of materials, structures, and innovative features for autonomous communication and sensing," *IEEE Access*, vol. 7, pp. 56694–56712, 2019.

[3] S. N. Tcvetkova, D.-H. Kwon, A. Díaz-Rubio, and S. A. Tretyakov, "Near-perfect conversion of a propagating plane wave into a surface wave using metasurfaces," *Physical Review B*, vol. 97, no. 11, Art. no. 115447, 2018.

[4] Y. Li, X. Ma, V. Asadchy, and S. A. Tretyakov, "All-angle scanning leaky-wave antennas and surface-wave routing by reconfigurable metasurfaces," *arXiv preprint* arXiv:2506.14954, 2025. [Online]. Available: https://arxiv.org/abs/2506.14954

[5] L. Burgnies, C. Cochrane, F. Rault, V. Sadaune, É. Lheurette, V. Koncar, and D. Lippens, "Experimental phase-advance in woven textile metasurface," *Applied Physics Letters*, vol. 107, no. 20, 2015.

[6] L. Alonso-González, S. Ver-Hoeye, M. Fernández-García, and F. Las-Heras Andrés, "Broadband flexible fully textile-integrated bandstop frequency selective surface," *IEEE Transactions on Antennas and Propagation*, vol. 66, no. 10, pp. 5291–5299, Oct. 2018.

[7] M. M. Tahseen and A. A. Kishk, "Flexible and portable textile-reflectarray backed by frequency selective surface," *IEEE Antennas and Wireless Propagation Letters*, vol. 17, no. 1, pp. 46–49, 2017.

[8] X. Tian, Q. Zeng, S. A. Kurt, R. R. Li, D. T. Nguyen, Z. Xiong, Z. Li, *et al.*, "Implant-to-implant wireless networking with metamaterial textiles," *Nature Communications*, vol. 14, no. 1, Art. no. 4335, 2023.

[9] M. J. Carter, L. Resneck, Y. Ra'di, and N. Yu, "Flat-knit, flexible, textile metasurfaces," *Advanced Materials*, vol. 36, no. 32, Art. no. 2312087, 2024.

[10] J. Suikkola, T. Björninen, M. Mosallaei, T. Kankkunen, P. Iso-Ketola, L. Ukkonen, J. Vanhala, and M. Mäntysalo, "Screen-Printing Fabrication and Characterization of Stretchable Electronics," *Scientific Reports*, 6, 25784, 2016.

[11] D. Di Vito, T. Salo, J. Vanhala and M. Mäntysalo, "Stretchable electronic devices for wearable and on-skin applications: effects of material anisotropy and extensibility in simple stretchable systems," *2021 XXXIVth General Assembly and Scientific Symposium of the International Union of Radio Science (URSI GASS)*, Rome, Italy, pp. 1-4, 2021.

Constructing High-order Exceptional Points and Perfect Absorber Based loss engineering

Changzhi Gu*, Peng Fu

Institute of Physics, Chinese Academy of Science, Beijing 100190, China
*Corresponding author: czgu@iphy.ac.cn

***Abstract*— We center on the concepts of "loss engineering" and systematically investigates the modeling, optimization, and application of non-Hermitian metasurfaces. Based on the machine learning, the third-order exceptional points (EP3) in terahertz non-Hermitian metasurfaces were designed; and a Polarization- and Angle-Insensitive Ultrawideband Perfect Absorber Metasurface was fabricated.**

***Keywords*— metasurface, machine learning, exceptional points, perfect absorber.**

I. Introduction

Metasurfaces are artificially engineered subwavelength electromagnetic structures arrays capable of precisely manipulating multiple optical parameters of electromagnetic waves, and they exhibit tremendous potential in cutting-edge applications. However, practical metasurface applications inevitably suffer from material and radiation losses. While traditionally considered detrimental to system performance, the development of non-Hermitian physics has reshaped this perspective. By incorporating loss into the design space, a series of novel physical mechanisms have emerged, including exceptional points (EPs) induced unidirectional transmission, topological phases, loss-induced transparency, revival of lasing, and perfect absorption. In this work, we center on the concepts of "loss engineering" and systematically investigates the modeling, optimization, and application of non-Hermitian metasurfaces.

II. Methods

The rapid evolution of machine learning, particularly deep learning, provides powerful modeling and optimization capabilities in high-dimensional parameter spaces. This opens a new paradigm for the intelligent design of non-Hermitian metasurfaces. Integrating non-Hermitian physics with machine learning holds the potential to shift metasurface design from empirical to data-driven strategies, and from single-functionality to multifunctional intelligent optimization.

III. Results and Discussion

1.Design and Experimental Realization of Third-Order Exceptional Points (EP3) in Terahertz Non-Hermitian Metasurfaces: A strategy to construct EP3 by introducing weak coupling perturbations into a metasurface system supporting second-order EPs (EP2) is proposed. A hybrid-coupled dual-layer terahertz metasurface composed of three split resonant rings (SRRs) is designed and fabricated. By precisely controlling the coupling among the SRRs and utilizing a neural network–assisted global optimization algorithm, the optimal EP3 position is intelligently located in the high-dimensional parameter space, where three eigenvalues and their corresponding eigenvectors coalesce. The feasibility of EP3 formation is experimentally validated via terahertz time-domain spectroscopy and quasi-mode coupled theory.

2.Inverse Optimization of a Polarization- and Angle-Insensitive Ultrawideband Perfect Absorber Metasurface: An ultra-broadband metasurface absorber insensitive to polarization and incidence angle is designed. The structure consists of five layers: a top C4-symmetric $Ge_2Sb_2Te_5$ (GST) layer, intermediate SiO_2, ultrathin Cr and GST spacer layers, and a bottom Cr reflector. Using a genetic algorithm, global optimization is performed over structural parameters including periodicity, thickness, and shape to achieve four design objectives: broadband operation, high efficiency, polarization insensitivity, and angle tolerance. The device exhibits an average absorption rate of 92.17% for unpolarized light in the 200–2500 nm range, and maintains 87.68% absorption under oblique incidence up to 85°.

IV. Conclusion

We have constructing high-order EPs and Perfect Absorber Based loss engineering. This work lays both theoretical and experimental foundations for EP3-based devices such as ultrasensitive biosensors, with potential applications in noninvasive cellular diagnostics. The proposed design of perfect absorber holds broad application potential in solar photovoltaics, infrared detection, and photothermal conversion.

Acknowledgments

This work was supported by the National Key Research and Development Program of China under Grant Nos. 2024YFA1207700.

Near-field polarization photonics: controlling polarization of localized waves with metasurfaces

Oleh Yermakov[1,*]

[1]Department of Fiber Photonics, Leibniz Institute of Photonic Technology, Germany
*Corresponding author: oleh.yermakov@leibniz-ipht.de

***Abstract*—We demonstrate near-field polarization control of localized electromagnetic waves using dielectric and self-complementary metasurfaces. The approach relies on TE–TM polarization degeneracy of guided and surface waves, enabling their on-demand polarization transformation and generation. The results experimentally verified in the microwaves opening a direction of near-field polarization photonics.**

***Keywords*— metasurfaces, polarization, near-field.**

I. Introduction

The eigenmodes of a bulk isotropic medium are double-degenerate with respect to polarization. It means that the dispersions of the orthogonally polarized transverse-electric (TE) and transverse-magnetic (TM) modes are the same, i.e. their group velocities (wave numbers) completely coincide at any frequency and in any direction. The coherent superposition of TE and TM modes enables arbitrary polarization states. To modify the polarization state of propagating plane waves, anisotropic slabs (waveplates, retarders, etc.) are used to break the TE-TM degeneracy and adjust the required phase and amplitude difference between the TE and TM modes leading to the necessary polarization state. However, in the near-field spectrum, the dispersion relations of the localized (guided or surface) modes differ, preventing the broadband TE-TM degeneracy. This limitation is inherent to conventional dielectric waveguides and surface-wave platforms, which makes stable polarization control impossible during wave propagation.

In this work, we aim to restore TE–TM degeneracy for localized waves, opening a near-field polarization degree of freedom. Two distinct physical mechanisms enable this effect: dispersion engineering of dielectric metasurfaces and fundamental symmetry-protected Babinet's principle in self-complementary metasurfaces.

II. Planar guided-wave polarizer

All-dielectric metasurfaces composed of subwavelength cylindrical resonators can support polarization TE-TM degenerate guided modes. The degeneracy is achieved by overlapping electric and magnetic collective dipole-like resonances. By tailoring the resonator geometry and lattice period, one can minimize the difference between the wavevectors of TE and TM eigenmodes, and achieve nearly identical dispersions. This condition restores polarization freedom for guided waves.

This design strategy is broadband and scalable across different materials from visible to microwave frequency regimes [1]. Experimental demonstrations in the microwave domain confirm the existence of polarization-degenerate guided modes [1]. In particular, we implement the planar near-field linear-to-circular polarizer transforming the polarization of the propagating guided waves at the operating frequency [2].

III. Generating surface waves with pre-selected polarization state

An alternative route to TE–TM degeneracy relies on Babinet's principle applied to self-complementary metasurfaces. Such structures consist of mutually inverted metallic and aperture patterns within each unit cell. Surface waves supported by these metasurfaces exhibit fundamentally symmetry-protected TE–TM degeneracy along specific propagation directions [3].

As a result, any polarization state can be generated by exciting the two degenerate modes separately with controlled mutual amplitude and phase [4]. Microwave experiments demonstrate a generation of surface waves with on-demand polarization states covering the whole Poincaré sphere in both far- and near-field regimes.

IV. Conclusion

Metasurfaces enable a new paradigm of near-field polarization photonics by restoring TE-TM degeneracy for localized waves. We demonstrate two approaches supporting the near-field polarization control over guided and surface waves based on dielectric and self-complementary metasurfaces. The theoretical results are supported by microwave experiments. These results introduce a new degree of freedom for planar photonic systems and open opportunities for in-plane polarization converters, sensors, and integrated photonic components.

References

[1] R. Li, S. Polevoy, V. R. Tuz, and O. Yermakov, "Merging high localization and TE-TM polarization degeneracy of guided waves in dielectric metasurfaces," *Physical Review Applied*, vol. 23, p. 014084, 2025.

[2] S. Asadulina, A. Bogdanov, and O. Yermakov, "All-dielectric metawaveguides for flexible polarization control of guided light," *Laser and Photonics Reviews*, vol. 18(12), p. 2300544, 2024.

[3] O. Yermakov, V. Lenets, A. Sayanskiy, J. Baena, E. Martini, S. Glybovski, and S. Maci, "Surface waves on self-complementary metasurfaces: all-frequency hyperbolicity, extreme canalization, and TE-TM polarization degeneracy," *Physical Review X*, vol. 11(3), p. 031038, 2021.

[4] S. Polevoy, and O. Yermakov, "Excitation of surface waves with on-demand polarization at self-complementary metasurface," *IEEE Antennas and Wireless Propagation Letters*, vol. 22(8), pp. 1962–1966, 2023.

The role of resonances at dangling ligaments in the absorption of nanoporous gold

Muhammad Salman Wahidi[1], Maurice Pfeiffer[1], Xinyan Wu[1], Parastoo Ebrahimi[1], Manfred Eich[1], Alexander Yu. Petrov[1,*]

[1]Institute of Optical and Electronic Materials, Hamburg University of Technology (TUHH), Germany

*Corresponding author: a.petrov@tuhh.de

***Abstract*— Nanoporous gold (npAu) exhibits strong broadband absorption that cannot be explained by the bulk response alone. We show that plasmon resonances at gaps between dangling ligaments at the surface of npAu films dominate absorption and introduce ligament-size dependence. The decrease in the surface density of such resonances explains reduced absorption upon coarsening.**

***Keywords*— nanoporous gold, metamaterial, plasmonics, absorption, gap resonances.**

Nanoporous gold (npAu) exhibits remarkable broadband absorption across the visible and near-infrared spectral range, which can be utilized for applications in sensing, photocatalysis, and energy conversion. However, conventional descriptions based on effective medium theories of bulk npAu fail to explain both the magnitude of absorption and its dependence on structural parameters such as ligament size. We present a unified physical picture that attributes the enhanced and size-dependent absorption of npAu to gap plasmon resonances arising from dangling ligaments at the npAu film surfaces.

Using realistic three-dimensional leveled-wave approximants, we numerically reproduce experimental absorption spectra and identify that dominant resonances originate from nanoscale gaps between opposing ligament ends at the top and bottom surfaces of npAu films. These surface-localized resonances are not considered in standard bulk effective medium models, which therefore underestimate absorption or wrongly attribute it to unphysical resonances inside npAu. Quantitative analysis of simulations reveals that such surface resonances can contribute up to ~80% of the total absorption. Additionally, controlled numerical "short-circuiting" of individual ligament gaps suppresses specific resonances and reduces the optical absorption toward the effective-medium baseline of the bulk npAu, confirming the role of these surface features.

Building on this mechanism, we further demonstrate that the optical response of npAu exhibits a clear dependence on ligament size, L. By systematically varying the mean ligament diameter in npAu approximants, we show that absorption decreases upon coarsening, consistent with experimental observations. This behavior is explained by a scaling law: while the number of surface resonances scales with the surface density of dangling ligaments ($\sim 1/L^2$), their oscillator strength increases approximately proportional to the ligament size ($\sim L$), resulting in an overall absorption contribution that scales inversely with ligament size ($\sim 1/L$).

Overall, these results establish that npAu cannot be described as a purely homogeneous effective medium. Instead, its optical properties arise from a hybrid response combining bulk-like behavior with a distribution of plasmonic resonances at the surface. This framework provides a predictive link between morphology and optical properties, offering new strategies for application of npAu for light-matter interactions.

References:

M. S. Wahidi, M. Pfeiffer, X. Wu, F. Ebrahimi, M. Eich, and A. Yu. Petrov, "Exceptional broadband absorption of nanoporous gold explained by plasmonic resonances at dangling ligaments," accepted in *Optics Express* (2026).

Near-Infrared Spectroscopy Using Plasmonic Si MEMS

Tetsuo Kan[1,*], Teruya Noguchi[1], Eslam Abubakr[1,3], Saito Shiro[2], Hironori Suzuki[2]

[1]Department of Mechanical Engineering and Intelligent Systems, The University of Electro-Communications, Japan
[2]IMRA JAPAN CO., LTD., Japan
[3]Department of Electrical Engineering, Aswan University, Egypt
*Corresponding author: tetsuokan@uec.ac.jp

***Abstract*— Silicon has no intrinsic sensitivity to infrared light; however, by utilizing the Schottky barrier formed at a metal/Si interface, infrared detection becomes possible. Furthermore, by introducing periodic structures into the metal layer, surface plasmon resonance can be excited under optical illumination. Such plasmonic structures enable not only the measurement of incident light intensity but also the detection of wavelength spectra, incident angles, and polarization states. In this paper, we report on our ongoing research into plasmonic Si-based MEMS technologies for infrared detection and spectroscopic measurement.**

***Keywords*— Surface Plasmon Resonance, Schottky Barrier, Infrared Photodetection, Near-Infrared Polarization Spectroscopy**

I. Introduction

Metal plasmonic structures can absorb light of specific wavelengths and polarization states with high efficiency, depending on their geometry and orientation. When such structures are fabricated on a semiconductor, a Schottky barrier, an energy barrier formed at the metal–semiconductor interface, is created. As a result, free electrons in the metal excited by the absorbed light can be injected into the semiconductor and read out as an electrical current[1]. In particular, the Schottky barrier formed at a metal/Si interface has a lower energy barrier than the Si bandgap, enabling the development of Si-based infrared detectors. In this case, by exploiting the wavelength- and polarization-selective absorption characteristics of the plasmonic structures, infrared spectroscopic functionality can be realized, and spectroscopy with polarization-state discrimination also becomes possible.

II. Methods

A typical device configuration, as shown in Fig. 1 (top), consists of a gold diffraction grating fabricated on an n-type Si (n-Si) substrate. Because a Schottky barrier is formed at the Au–n-Si interface, when the incident light is absorbed by the gold grating as a surface plasmon resonance, a photocurrent is generated. The excitation condition for surface plasmon resonance can be described by the following relationship[2].

$$k_0\sqrt{\varepsilon_{\mathrm{Air}}}\sin\theta+\frac{2m\pi}{a}=\frac{\omega}{c}\sqrt{\frac{\varepsilon_{\mathrm{Air}}\varepsilon_{\mathrm{Au}}}{\varepsilon_{\mathrm{Air}}+\varepsilon_{\mathrm{Au}}}}$$

According to this relation, the absorption angle is determined almost uniquely as the incident wavelength changes. By exploiting this phenomenon, one can tilt the device relative to the incident light and measure the photocurrent while varying the angle θ, thereby enabling reconstructive spectroscopy of the incident light from the acquired angle–current data[3], [4], [5].

III. Results and Discussion

Using a plasmonic device in which gold nanostructures are fabricated on a silicon substrate, we demonstrated reconstructive spectroscopy in the 1300–1500 nm wavelength band with a wavelength resolution of 20 nm[6]. The demonstrated spectral performance is comparable to that of commercially available spectrometers. In addition, extending the detectable wavelength range toward longer wavelengths is feasible by inserting an intermediate metal between gold and silicon to reduce the barrier height. For example, when Ti is

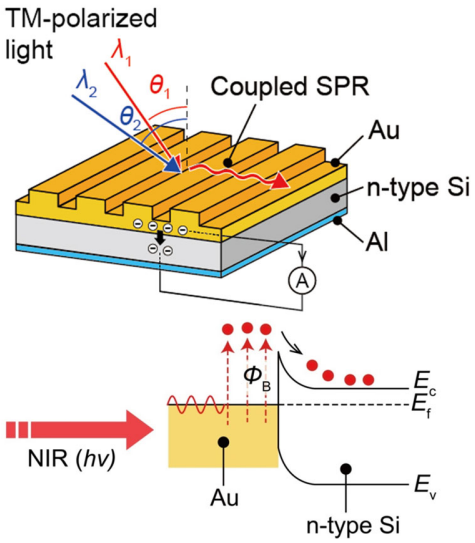

Fig. 1 Plasmonic Si MEMS Photodetector.

inserted, the Schottky barrier height becomes approximately 0.5 eV, and the detection cutoff exceeds a wavelength of 2 μm; accordingly, spectroscopic operation up to 1.8 μm was experimentally demonstrated[7]. This enables spectroscopy covering the entire near-infrared wavelength range. Furthermore, by exploiting the fact that a one-dimensional diffraction grating responds only to TM polarization, we also confirmed that, with appropriate device layout, TM- and TE-polarized components can also be spectrally resolved independently. Moreover, by implementing the tilt mechanism using MEMS technology, the actuator can be integrated with the device element, making it possible to realize a one-chip system[8], [9].

IV. Conclusion

By fabricating plasmonic structures on Si and combining them with photocurrent readout via a Schottky barrier, the excellent optical resonance properties provided by the plasmonic structures can be leveraged for photodetection. This enables applications in sensing, such as spectrometers and chemical sensors. If infrared detection can be achieved using Si, infrared sensor devices can be realized with low cost and high integrability without relying on compound semiconductors. In the future, in addition to improving sensitivity and other performance metrics, we will further advance MEMS integration, such as incorporating a tilt actuator for angular scanning, to realize a more practical infrared photodetection technology.

Acknowledgments

This work was supported by the Ministry of Education, Culture, Sports, Science and Technology (MEXT) “Advanced Research Infrastructure for Materials and Nanotechnology” program (Project No. JPMXP1225UT1123). Microfabrication was carried out using the cleanroom facilities of the Advanced Facilities Division (Darf) at the Research Equipment Center, the University of Electro-Communications, and the facilities of the University of Tokyo d.lab.

References

[1] C. Scales and P. Berini, “Thin-film Schottky barrier photodetector models,” *IEEE J. Quantum Electron.*, vol. 46, no. 5, pp. 633–643, 2010, doi: 10.1109/JQE.2010.2046720.

[2] H. Raether, *Surface Plasmons on Smooth and Rough Surfaces and on Gratings*, vol. 111. Berlin, Heidelberg: Springer, 1988. doi: 10.1007/BFb0048317.

[3] W. Chen, T. Kan, Y. Ajiki, K. Matsumoto, and I. Shimoyama, “NIR spectrometer using a Schottky photodetector enhanced by grating-based SPR,” *Opt. Express*, vol. 24, no. 22, p. 25797, 2016, doi: 10.1364/OE.24.025797.

[4] Y. Suido, Y. Yamamoto, G. Thomas, Y. Ajiki, and T. Kan, “Extension of the Measurable Wavelength Range for a Near-Infrared Spectrometer Using a Plasmonic Au Grating on a Si Substrate,” *Micromachines*, vol. 10, no. 6, p. 403, 2019, doi: 10.3390/mi10060403.

[5] Y. Kaneda *et al.*, “Plasmonic photodetector with submicron grating for reconstructive spectroscopy of low-intensity broadband light,” *Opt. Lasers Eng.*, vol. 183, Dec. 2024, doi: 10.1016/j.optlaseng.2024.108501.

[6] Y. Yamamoto, M. Oshita, S. Saito, and T. Kan, “Near-Infrared Spectroscopic Gas Detection Using a Surface Plasmon Resonance Photodetector with 20 nm Resolution,” *ACS Appl. Nano Mater.*, vol. 4, no. 12, pp. 13405–13412, Dec. 2021, doi: 10.1021/acsanm.1c02925.

[7] E. Abubakr, A. Abadi, M. Oshita, S. Saito, H. Suzuki, and T. Kan, “Advanced Room-Temperature NIR Plasmonic Photodetection and Reconstructive Spectroscopy,” *IEEE Trans. Electron Devices*, vol. 72, no. 1, pp. 301–305, Jan. 2025, doi: 10.1109/TED.2024.3509385.

[8] M. Oshita, H. Takahashi, Y. Ajiki, and T. Kan, “Reconfigurable Surface Plasmon Resonance Photodetector with a MEMS Deformable Cantilever,” *ACS Photonics*, vol. 7, no. 3, pp. 673–679, 2020, doi: 10.1021/acsphotonics.9b01510.

[9] M. Oshita, S. Saito, and T. Kan, “Electromechanically reconfigurable plasmonic photodetector with a distinct shift in resonant wavelength,” *Microsyst. Nanoeng.*, vol. 9, no. 1, p. 26, Dec. 2023, doi: 10.1038/s41378-023-00504-4.

Fluorescence-based chiral sensing with silicon metasurfaces

Tom T.C. Sistermans[1], Artemijs Krimovs[2], Robert Pal[2], Alberto G. Curto[1*]

[1]Photonics Research Group, Ghent University-imec, Ghent, Belgium
[2]Department of Chemistry, Durham University, Durham, UK
*Corresponding author: Alberto.Curto@UGent.be

***Abstract*— Chiral molecules with opposite handedness can have strongly differing biological properties. Identifying chirality is, however, limited by low sensitivity, restricting detection to high concentrations and large sample volumes. To overcome this, we propose a silicon nanophotonics-based sensing technique to enhance the sensitivity of chiral molecular detection.**

***Keywords*— metasurface, chirality, sensing, nanophotonics.**

Detecting the handedness of chiral molecules is essential in biochemistry, as the biological behavior of proteins, amino acids, and carbohydrates can differ dramatically between enantiomers. Circularly polarized light is commonly used to distinguish enantiomers by their differential absorption of left- and right-handed circularly polarized light, a technique known as circular dichroism (CD). However, this transmission-based technique relies on detecting small absorption differences, which becomes challenging at low concentrations where the overall absorption is negligible. Consequently, the weak signal becomes buried in background noise, severely limiting sensitivity and requiring high molecular concentrations and long measurement times. These limitations make conventional CD unsuitable for critical applications such as the early detection of protein aggregates associated with various diseases.

Using circularly polarized luminescence (CPL), some of the limitations of CD can be bypassed. The luminescence is shifted in wavelength, allowing separation from the excitation beam and strongly reducing background noise. The chirality is now detected by analyzing the circular polarization of the luminescence. Nonetheless, CPL contrasts are typically small because fluorescence is weak and the polarization asymmetry is low. To address this, we employ a metasurface composed of an array of silicon nanodisks, which act as optical resonators to enhance light–matter interaction [1-3]. The periodic arrangement introduces collective resonances that further enhance fields and scattering [4]. In addition, the resonators can increase the radiative decay rate via the Purcell effect and improve emission directionality, enabling more efficient detection. Together, these mechanisms can substantially boost the detected fluorescence intensity.

For chiral discrimination, the emission polarization properties are equally critical. High-index dielectric nanodisks allow tuning of electric and magnetic resonances to control the local optical chirality density, potentially enabling super-chiral near fields to enhance the CPL.

The metasurface is fabricated by electron-beam lithography from crystalline silicon, providing high refractive-index contrast and low optical losses in the visible range. Deposited on a glass substrate, the structures are compatible with transmission-mode measurements in our custom-built polarization microscope. The setup integrates dual single-photon counting detectors and dual photoelastic modulators to enable full Stokes polarimetry of the photoluminescence, allowing reliable CPL quantification with a spatial resolution of a few micrometers.
To evaluate performance, we deposit a chiral lanthanide complex embedded in a PMMA layer on the metasurface. Depending on the nanodisk radius, the fluorescence intensity increases by up to 2.5 times compared to the bare thin film. Importantly, by carefully tuning the electric and magnetic resonances of the silicon disks, this enhancement is achieved while largely preserving the emitters' intrinsic circular polarization. This combination of simultaneous enhancement of fluorescence while preserving circular polarization is a key advantage over other enhancement approaches and highlights the strength of high-index dielectric metasurfaces for chiral sensing.Overall, the metasurface more than doubles the total CPL sensitivity, demonstrating that silicon nanophotonics can substantially boost fluorescence-based chiral readout.

Acknowledgements. This work was financially supported by the European Research Council (ERC) under the European Union's Horizon 2020 research and innovation program (grant agreement 948804, CHANSON).

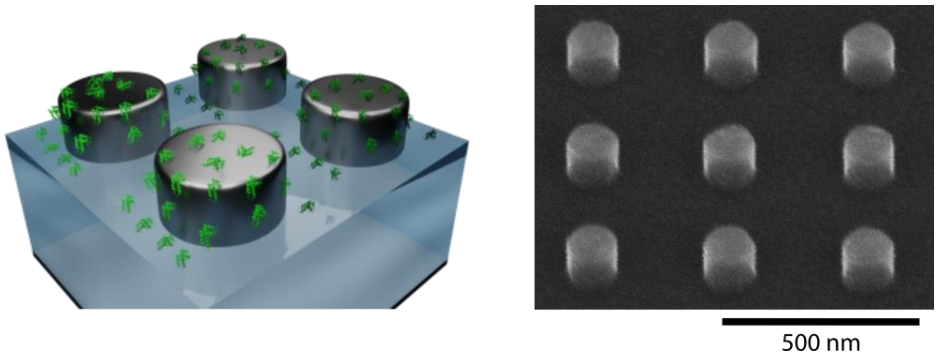

Figure 1: (left) Chiral molecules on a silicon metasurface. (right) SEM micrograph of a silicon metasurface

REFERENCES

[1] E. Mohammadi, A. Tittl, K. L. Tsakmakidis, T. V. Raziman, and A. G. Curto, "Dual Nanoresonators for Ultrasensitive Chiral Detection," ACS Photonics, vol. 8, no. 6, 2021, doi: 10.1021/acsphotonics.1c00311.

[2] T. V. Raziman, R. H. Godiksen, M. A. Müller, and A. G. Curto, "Conditions for Enhancing Chiral Nanophotonics near Achiral Nanoparticles," ACS Photonics, vol. 6, no. 10, 2019, doi: 10.1021/acsphotonics.9b01200.

[3] E. Mohammadi, T. V. Raziman, and A. G. Curto, "Nanophotonic Chirality Transfer to Dielectric Mie Resonators," Nano Lett, vol. 23, no. 9, 2023, doi: 10.1021/acs.nanolett.3c00739.

[4] S. Murai, G. W. Castellanos, T. V. Raziman, A. G. Curto, and J. G. Rivas, "Enhanced Light Emission by Magnetic and Electric Resonances in Dielectric Metasurfaces," Adv Opt Mater, vol. 8, no. 16, 2020, doi: 10.1002/adom.201902024.

Non-dichroic Chiral Photoelectron Spectroscopy

Letizia Fede[1], Debobrata Rajak[2], Chris Sparling[3], David Ayuso[4], Sylvain Betoule[5], Valérie Blanchet[1], Piero Decleva[6], Dominique Descamps[1], Stéphane Petit[1], Bernard Pons[1], Yann Mairesse[1], Andrés Ordóñez[7]

[1]Université de Bordeaux – CNRS – CEA, CELIA, Talence, France
[2]ELI ALPS, The Extreme Light Infrastructure ERIC, Szeged, Hungary
[3]Institute of Photonics and Quantum Sciences, Heriot-Watt University, Edinburgh, UK
[4]Department of Chemistry, Imperial College London, London, UK
[5]Sorbonne Université, CNRS, LCPMR, Paris, France
[6]Università degli Studi di Trieste, Trieste, Italy
[7]Department of Physics, Freie Universität, Berlin, Germany

*Corresponding authors: yann.mairesse@u-bordeaux.fr, andres.ordonez@fu-berlin.de

***Abstract*— We find enantiosensitive but non-dichroic signals in the 3D photoelectron angular distribution of chiral molecules upon multiphoton ionization with elliptically polarized light. The robustness of enantiosensitivity against ellipticity is an example of symmetry protection, opening unexplored opportunities for imaging ultrafast dynamics in chiral molecules with polarization-structured light.**

***Keywords*— chirality, multiphoton, symmetry, ellipticity, laser, photoelectron.**

The interaction of randomly oriented chiral molecules with circularly polarized light leads to effects that change sign upon reversal of either molecular chirality (enantiosensitivity) or light's polarization (circular dichroism). Among these effects, multiphoton ionization has provided privileged access to ultrafast electron dynamics in randomly oriented chiral molecules through the forward-backward asymmetry of photoelectron angular distributions (PADs) [1].

Here, we found that the combination of elliptical polarization, multiphoton ionization, and 3D detection reveals the presence of Non-Dichroic EnantioSensitive (NoDES) tensor observables in the PAD [2,3]. That is, upon expansion of the PAD into spherical harmonics, we found that certain expansion coefficients have opposite sign for opposite enantiomers but do not change sign upon reversal of the ellipticity, confirming recent theoretical suggestions [4]. Our experiments on camphor, fenchone, and alpha-pinene demonstrate that these NoDES contributions reach about 1% of the total ionization yield.

We found that NoDES contributions originate from the combination of two effects: (i) dichroic and enantiosensitive forward-backward asymmetry and (ii) dichroic and non-enantiosensitive angular streaking. The product of these two effects leads to a cancellation of dichroism without a cancellation of enantiosensitivity.

Our symmetry analysis reveals that the NoDES observables belong to the A_u irreducible representation of the PAD, which is antisymmetric with respect space inversion and hence enantiosensitive, but symmetric with respect to π rotations that reverse the ellipticity and hence non-dichroic. That is, the behavior of NoDES observables stems from the symmetry of a subset of (rank ≥ 3) tensors in the PAD.

Besides elliptical polarization, A_u also emerges, e.g., in bichromatic ω-2ω fields with linear polarizations perpendicular to each other. Indeed, our numerical simulations for the latter field also show NoDES contributions of the order of 1% in the two-photon, multiphoton, and strong-field regimes.

NoDES observables open new opportunities for imaging chirality when polarization is not constant throughout the interaction region, e.g., when using structured light.

Acknowledgments

Royal Society URF\R\251036. Heriot-Watt University EPSRC Doctoral Prize Fellowship. DFG-543760364. ULTRAFAST TORNADO PEPR LUMA. ANR-21-CE30-038-01, ANR-23-EXLU-0002, ANR-23-EXLU-0004, IdEx University of Bordeaux GPR LIGHT, EU Horizon 2020 871124, ELI-ALPS GINOP-2.3.6-15-2015-00001.

References

[1] C. Sparling and D. Townsend, "Two decades of imaging photoelectron circular dichroism: from first principles to future perspectives" Physical Chemistry Chemical Physics, vol. 27, pp. 2888-2907, 2025.
[2] L. Fede et al., "Non-Dichroic Enantio-Sensitive Chiroptical Spectroscopy" arXiv:2512.19062, 2025.
[3] A. Ordóñez et al., "Theory of Non-Dichroic Enantio-Sensitive Chiroptical Spectroscopy" arXiv:2512.17840, 2025.
[4] A. Ordóñez and O. Smirnova, "Disentangling enantiosensitivity from dichroism using bichromatic fields" Physical Chemistry Chemical Physics, vol. 24, pp. 7264-7273, 2022

Photoacoustic spectroscopy on plasmonic materials

C. Skubisz[1,*], E. Petronijevic[1], N. Borriello[1] G. Leahu[1],R. Li Voti[1], C. Sibilia[1] and A. Belardini[1]

[1]Sapienza Università di Roma, SBAI Department, Italy
*Corresponding author:claudia.skubisz@uniroma1.it

***Abstract*—The Photoacoustic spectroscopy (PAS) is a technique that allow to study the local absorption of the sample by monitoring the heat produced and transferred to the surrounding air, regardless the transmitted, reflected, and scattered light that ows away from the sample without damaging the sample. In this work, we present a new PAS set-up that enables variation of the chopper frequency, laser wavelength, polarization, beam diameter, and spatial positioning via translational and rotational stages. This technique allows for precise spatial and spectral mapping of absorption enabling the study of extrinsic chirality in nanostructured metasurfaces, potentially addressing also important issues on homogeneity of the nanostructures.**

***Keywords*—Photo-acoustic spectroscopy, Circular dichroism, Plasmonic-materials**

I. Introduction

Metamaterials have revolutionized electromagnetic wave control. The growing demand for advanced terahertz technologies necessitates innovative material design approaches. Circularly polarized light is conventionally used to probe the chirality of the sample , left and right circular polarization are absorbed differently, and this difference is defined as Circular Dichroism (CD). The chirality can be induced by combining the asymmetry of the sample and the optical set-up. This property is called extrinsic chirality and it is obtained by breaking the symmetry of the light-sample interaction by forming a non-planar triad of vectors between the light wave-vector, the normal of the sample's surface, and the vector of the sample's asymmetry. Previously, the chirality was studied by conventional techniques only for a single laser [1] wavelengths, however to measure the directly absorption response we can use unconventional photo-thermal techniques. Photo-acoustic spectroscopy (PAS) is a photothermal technique that exploits the interaction between an incident light beam and matter, inducing a non-radiative de-excitation process that generates heat. The fluctuations produce an acoustic signal, converted into an electrical signal and this approach enables direct measurement of local absorption, thereby detecting effects that might otherwise be obscured by other scattering-dependent techniques.

II. Methods

The PAS set-up Figure 1, used for the measurement consists of a widely tunable near-infrared laser, covering a wavelength range from 680 nm to 1080 nm[2]. The light is modulated by a mechanical chopper at different frequencies. Before reaching the sample housed within the photoacoustic cell, the light beam, passes through a polarizer, a quarter-wave plate and the light can be focused on the sample in a closed PAS cell. This therefore allows for the characterization of chirality. The photoacoustic cell is equipped with a rotating stage ,that allows examination of the sample at different angles of incidence relative to the surface normal, a translation stage that allows the scanning of the sample in different areas and a microscope. It is possible to create a spatial maps in a specific area of the sample for a specific wavelength and frequency.

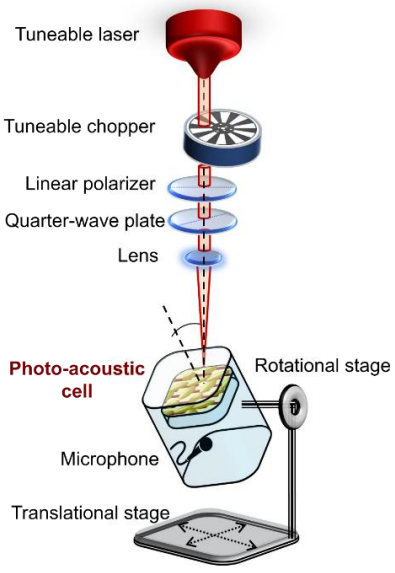

Figure 1. PAS set-up

III. Conclusion

Through the use of current technique, we are now able to significantly extend the potential of photo-acoustic, allowing the analysis and study the homogeneity of the sample even on very small areas.

Acknowledgments

C. Skubisz ackowledges PNRR MUR project PE0000023-NQSTI.

References

[1] Leahu, G., Petronijevic, E., Belardini, A., Centini, M., Sibilia, C., Hakkarainen, T., Koivusalo, E., Piton, M.R., Suomalainen, S., and Guina, M. (2017). Evidence of Optical Circular Dichroism in GaAs-Based Nanowires Partially Covered with Gold. Advanced Optical Materials, 5(16), 1601063.

[2] Skubisz, C., Petronijevic, E., Leahu, G., Cesca, T., Scian, C., Mattei, G., Concita, S., Belardini, A., (2024). Tecnica fotoacustica con laser ampiamente sintonizzabile: risposta al dicroismo circolare della metasuperficie. *Journal of the European Optical Society-Rapid Publications* , *20* (1), 20.

Solar-thermal conversion with titanium nitride metamaterials

Luca Mascaretti[1,2,*], Morteza Afshar[1], Andrea Schirato[3,4,5], Alessandro Alabastri[5], Paolo Fornasiero[6], Ladislav Kalvoda[2], Štěpan Kment[1,7], Alberto Naldoni[8], Ivan Richter[2]

[1]Czech Advanced Technology and Research Institute, Regional Centre of Advanced Technologies and Materials, Palacký University Olomouc, Czech Republic
[2]Faculty of Nuclear Sciences and Physical Engineering, Czech Technical University in Prague, Czech Republic
[3]Department of Physics, Politecnico di Milano, Italy
[4]Istituto Italiano di Tecnologia, Genova, Italy
[5]Department of Electrical and Computer Engineering, Rice University, Houston, TX, United States
[6]Department of Chemical and Pharmaceutical Sciences, Center for Energy, Environment and Transport Giacomo Ciamciam, INSTM Trieste Research Unit and ICCOM-CNR Trieste Research Unit, University of Trieste, Italy
[7]CEET, Nanotechnology Centre, VŠB-Technical University of Ostrava, Czech Republic
[8]Department of Chemistry and NIS Centre, University of Turin, Italy
*Corresponding author: luca.mascaretti@upol.cz

***Abstract*— Solar-thermal conversion requires solar absorbers with engineered optical properties. We discuss two different strategies based on titanium nitride (TiN) metamaterials: separated nanotube arrays and planar ultrathin metal/insulator/metal multilayers.**

***Keywords*— solar-thermal conversion; titanium nitride; metamaterials; nanotubes; multilayers.**

Solar-thermal conversion is a promising strategy to collect light energy from the Sun and transform it into heat for a variety of applications. This can be achieved by engineering the optical properties of solar absorber materials to achieve nearly unitary absorption from the ultraviolet to the near-infrared regions of the electromagnetic spectrum (250–2500 nm).[1]

Two main alternative strategies to realize solar absorbers consist in either utilizing nanostructured surfaces, such as metasurfaces,[2] or stacking more materials together into planar multilayers, such as metal-insulator-metal (MIM) structures or metamaterials.[3] The former typically feature limited thickness but relatively complex fabrication processes, while the latter are conceptually simpler but require stacking several layers to achieve a broadband absorption spectrum.

The shortcomings of both these strategies may be partially overcome by employing titanium nitride (TiN) as a material for solar absorbers. This is related to its refractory character and, especially, high optical tunability by adjusting its stoichiometry or morphology at the nanoscale.[4] In this regard, two examples involving TiN are presented. The first one consists of a metamaterial-like nanostructured absorber based on spaced titanium oxynitride (TiO_xN_y) nanotubes exhibiting ~ 99% optical absorption from the ultraviolet to the near-infrared wavelength range. This behavior was numerically reproduced by taking into account the nano-porosity in the tube walls through a "nanoporous permittivity model" and the spaced TiO_xN_y nanotubes exhibited excellent photothermal efficiency.[5] The simple and scalable synthetic approach, which is based on electrochemical anodization of Ti and subsequent nitridation, opens the way for various solar-thermal applications, including the recently emerging photothermal catalysis.[6]

The second strategy consists of MIM absorbers where the substrate is once again Ti metal and the top layer is an ultrathin film of TiN. The latter was synthesized by atomic layer deposition (ALD) using a standard plasma process with $TiCl_4$ precursor and NH_3 plasma. The optical properties of ultrathin TiN films in the 5–40 nm range were investigated by spectroscopic ellipsometry to extract the complex permittivity and highlight its dependence on thickness. An insulator TiO_2 spacer was then considered and its thickness was optimized by numerical simulations. As a result, a TiN (10 nm)/TiO_2 (45 nm)/Ti MIM structure achieved ~ 73% absorption of the solar spectrum, which is remarkable for an ultrathin absorber.

In conclusion, TiN showed a promising performance in terms of solar absorption in nanoporous as well as planar structures,

which both displayed scalability potential. The broadband optical tuning of TiN-based metamaterials may lead to further applications beyond solar-thermal devices, such as in solar cells and terahertz detectors.

ACKNOWLEDGMENTS

The authors acknowledge support from: the Ministry of Education, Youth and Sports of the Czech Republic (MEYS-CR), grant numbers CZ.02.1.01/0.0/0.0/16_019/0000778 and CZ.02.01.01/00/22_008/0004587 (“TECHSCALE”) of the European Structural and Investments Funds; European Union’s Horizon 2020 project “METAFAST” (Grant Agreement No. 899673); the Project CH4.0 under the MIUR program “Dipartimenti di Eccellenza 2023-2027” (CUP: D13C2200352001). The authors also acknowledge CzechNanoLab Research Infrastructure supported by MEYS CR (LM2023051). This work reflects only the author’s view, and the European Commission is not responsible for any use that may be made of the information it contains.

REFERENCES

[1] L. A. Weinstein *et al.*, “Concentrating solar power,” Chemical Reviews, vol. 115, pp. 12797–12838, 2015.
[2] C.-C. Chang *et al.*, “High-temperature refractory metasurfaces for solar thermophotovoltaic energy harvesting,” Nano Letters, vol. 18, pp. 7665–7663, 2018.
[3] D. Zhao *et al.*, “Ultra-narrow-band light dissipation by a stack of lamellar silver and alumina”, Applied Physics Letters, vol. 104, pp. 221107, 2014.
[4] L. Mascaretti *et al.*, “Plasmonic titanium nitride nanomaterials prepared by physical vapor deposition methods”, Nanotechnology, vol. 34, pp. 502003, 2023.
[5] M. Afshar *et al.*, “Nanoporous titanium oxynitride nanotube mematamerials with deep subwavelength heat dissipation for perfect solar absorption”, ACS Photonics, vol. 10, pp. 3291–3301, 2023.
[6] A. Naldoni *et al.*, “Solar thermoplasmonic nanofurnace for high-temperature heterogeneous catalysis”, Nano Letters, vol. 20, pp. 3663–3672, 2020.

Toward Robust SE-FSRS: Managing Nanoantenna-Induced Spectral Distortions via Excitation-Wavelength and Pulse-Energy Tuning

Patryk Pyrcz, Sylwester Gawinkowski*

Institute of Physical Chemistry, Polish Academy of Sciences, Poland

*Corresponding author: sgawinkowski@ichf.edu.pl

***Abstract*— We investigate how pulse energy and excitation wavelength govern spectral fidelity in suface-enhanced femtosecond stimulated Raman scattering (SE-FSRS). Distortions correlate with strong broadband backgrounds and are wavelength-dependent. By optimizing energies and wavelength choices, we suppress artifacts, recover reliable vibrational line shapes, and provide practical guidelines for robust quantitative SE-FSRS measurements.**

***Keywords*— FSRS, nanoparicles, plasmonics, optical antennas.**

Optical antennas composed of metallic nanoparticles find extensive use across numerous scientific and industrial domains, primarily because they can concentrate and manipulate optical fields on subwavelength length scales. In particular, plasmonic nanoantennas enable strong near-field enhancement and nanoscale confinement of electromagnetic energy, which has positioned them as key building blocks for ultrasensitive spectroscopy, sensing, and nonlinear optics.

Beyond their role in linear optics and sensing, optical antennas also provide a powerful platform for ultrafast spectroscopy by localizing intense electromagnetic fields into nanoscale volumes. In parallel, ultrashort laser pulses have become indispensable in advanced spectroscopic techniques, offering high temporal resolution and enabling diverse nonlinear phenomena in nanoscale systems. In this context, Femtosecond Stimulated Raman Scattering (FSRS) is particularly attractive, as it combines ultrafast time resolution with the chemical specificity of vibrational fingerprints. By positioning target molecules close to these nanoantennas, one can probe ultrafast molecular events with remarkable spatial and temporal precision.

Surface-Enhanced Femtosecond Stimulated Raman Scattering (SE-FSRS) was proposed by merging FSRS with Surface-Enhanced Raman Scattering (SERS). This hybrid technique aims to harness both the temporal resolution of FSRS and the sensitivity gains from SERS, pushing the boundaries of molecular dynamics analysis. Although initial demonstrations were promising, they revealed unexpected spectral distortions that complicated data interpretation [1]. Identifying the origins of these artifacts therefore became crucial for establishing SE-FSRS as a reliable analytical method.

Our investigations show that these distortions mainly stem from photothermal effects induced by intense plasmonic excitations within the nanoantennas. Rapid heating, localized refractive-index changes, and possible alterations in chemical bonding can markedly reshape the observed spectral features. By carefully selecting pulse energies and excitation wavelengths, we have minimized these adverse effects and optimized the SE-FSRS output [2]. Moreover, we have demonstrated how to deliberately adjust the spectral profile of SE-FSRS signals, offering greater flexibility in designing experiments for specific molecular targets.

Taken together, these results underline the intricate relationship between nonlinear optical mechanisms and photothermal dynamics in ultrafast spectroscopy. By elucidating how to harness and control these effects, we provide a roadmap for more robust and versatile SE-FSRS experiments. Our work not only highlights strategies to mitigate unwanted heating and spectral distortions but also points to improved methods for detecting subtle molecular signatures. This deeper understanding represents an essential step forward in expanding SE-FSRS for applications in ultrafast chemical analysis, sensing, and other advanced areas where precise molecular insight is of paramount importance.

ACKNOWLEDGMENTS

This work was supported by the Polish National Science Center, Grant No. 2020/39/B/ST4/01523.

REFERENCES

[1] Frontiera, RR., Henry, A-I., Gruenke, NL. and Van Duyne, RP. “Surface-Enhanced Femtosecond Stimulated Raman Spectroscopy,” J. Phys. Chem. Lett., Vol. 2, No. 10, 1199–1203, 2011.

[2] Pyrcz, P. and Gawinkowski, S. “Advancements in surface-enhanced femtosecond stimulated Raman spectroscopy: exploring factors influencing detectability and shapes of spectra,” Nanophotonics, Vol. 14, No. 1, 1-12, 2025.

Tip-Enhanced Nanocavities: Advances for Linear and Nonlinear Vibrational Spectroscopy

P. Roelli[1*], I. Pascual[1,2], I. Herrero[1], J. Aizpurua[3,4], and R. Hillenbrand[1]

[1]CIC nanoGUNE BRTA, Tolosa Hiribidea 76, 20018 Donostia-San Sebastián, Spain
[2]Materials Physics Center, CSIC-UPV/EHU, 20018 Donostia-San Sebastián, Spain
[3]Donostia International Physics Center (DIPC), 20018 Donostia-San Sebastián, Spain
[4]IKERBASQUE, Basque Foundation for Science, 48013 Bilbao, Spain
*Corresponding author: p.roelli@nanogune.eu

***Abstract*— Tip-enhanced nanocavities enable efficient light coupling into subwavelength gaps while minimally perturbing cavity modes, opening new opportunities for nanoscale vibrational spectroscopy spanning the infrared and visible spectral ranges.**

***Keywords*— vibrational spectroscopy; IR–VIS upconversion; phonon-polaritons nanocavities; scanning near-field optical microscopy.**

Subwavelength nanocavities have emerged as powerful platforms for probing light–matter interactions at the nanoscale, enabling spectroscopic access to localized molecular ensembles and even single molecules. Despite their strong field confinement, efficiently coupling external illumination into such deeply subwavelength cavities—and dynamically controlling the interaction with embedded molecules—remains a key challenge. In this talk, I introduce a tip-enhanced nanocavity approach that combines a scanning metallic tip with nanoparticle-on-mirror (NPoM) cavity to control electromagnetic field enhancements across the visible (VIS) and infrared (IR) spectral ranges. The tip acts as a secondary dipolar illumination source, concentrating incident radiation into the nanocavity gap while only weakly perturbing the axially symmetric cavity resonances. This approach enables two complementary spectroscopic modalities: (i) linear infrared absorption measurements of individual phonon-polariton NPoM cavity resonances using nano-FTIR spectroscopy, and (ii) nonlinear vibrational spectroscopy via continuous-wave IR-to-VIS upconversion for molecular monolayers confined in NPoM gaps.

Inverse Electromagnetic Design for THz Antennas, Resonators and Wave-Based Analog Computing

Nikolas Hadjiantoni[1], Heedong Goh[2,3], Dou Feng[4], Andrea Alù[3], Miguel Navarro-Cía[1,4], S. M. Hanham[1,5*]

[1]School of Engineering, University of Birmingham, Birmingham, U.K.
[2]Seoul National University, Seoul, South Korea
[3]Physics Program, Graduate Center, The City University of New York, New York, U.S.A.
[4]School of Physics and Astronomy, University of Birmingham, Birmingham, U.K.
[5]Department of Materials, Imperial College London, U.K.
*Corresponding author: stephen.hanham@imperial.ac.uk

***Abstract*— Inverse electromagnetic design provides a systematic framework for engineering wave–matter interactions beyond intuition-driven approaches. We present our recent progress combining topology optimization and gradient-based methods for designing terahertz lens antennas, high-Q/V dielectric resonators, and global–local optimization approaches for analog computing platforms based on gyrotropic electromagnetic scattering.**

***Keywords*— topology optimization, terahertz, resonators, antennas, analog computing.**

I. Introduction

Computational inverse design has emerged as a powerful paradigm for engineering electromagnetic systems beyond intuition-driven approaches. By formulating device synthesis as an optimization problem constrained by Maxwell's equations and fabrication restrictions, inverse methods enable the systematic discovery of high-performance and non-intuitive fabricable geometries across a wide range of problem classes [1], [2].

In this work, we present recent advances in the application of computational inverse electromagnetic design. We demonstrate gradient-based topology optimization (TO), in which the spatial material distribution within a prescribed domain is treated as a continuous design variable and iteratively updated using adjoint sensitivity analysis. Using this framework, we demonstrate the automated synthesis of compact terahertz lens antennas with tailored radiation characteristics, as well as dielectric resonators exhibiting enhanced quality-factor-to-mode-volume (Q/V_m) ratios through engineered modal confinement. Additionally, we describe how a combination of global and local optimizers can design a system of gyrotropic and dielectric scatterers whose electromagnetic scattering characteristics can be used to implement an analog computing device capable of solving ODEs.

II. THz Leaky-wave Fed Lens Antenna

In this work, a multi-physics TO framework is developed for the design of a low-profile polymer leaky-wave fed lens antenna operating in the G-band (140–220 GHz) for future 6G applications and compatible with stereolithography (SLA) 3D printing [3].

The problem is formulated as a dielectric lens region with a permittivity distribution to be determined above a $\lambda/2$ thick air cavity formed between the bottom of the lens and a ground plane. The cavity supports a leaky wave which feeds the lens and is excited by a rectangular waveguide. The permittivity distribution of the dielectric lens region is treated as a continuous design domain and optimized using topology optimization (TO). Manufacturability constraints are incorporated directly into the optimization by application of spatial filters: a conic density filter enforces a minimum feature size consistent with SLA printing resolution, while a hyperbolic tangent projection promotes a binary material distribution. Connectivity constraints are enforced using simple isotropic material with penalization (SIMP). The optimised objective function is a combination of an electromagnetic objective maximising broadside gain and a structural objective penalising any lack of connectivity within the lens structure. The adjoint method is used for the efficient evaluation of the gradients of the optimization objective function with respect to the parameters defining the lens permittivity distribution. Gradient-based optimization is performed using the Method of Moving Asymptotes (MMA) [4], and the FDTD and FEM techniques are used to evaluate the antennas electromagnetic and structural performance, respectively, at each iteration.

As an example, it is shown that after ~350 iterations, a leaky lens antenna with radius $5\lambda_0$ and thickness $2\lambda_0$ can realize a gain of 23 dBi at 0.2 THz with a low side-lobe level of −20 dB.

III. THz Dielectric Resonators

Achieving simultaneous high quality (Q-) factor and deep subwavelength modal confinement is a central objective in resonant cavity design with photonic crystal resonators (PCRs) offering a promising platform for terahertz sensing [5] and oscillator applications [6] amongst others.

The problem of systematically designing PCRs that maximize the quality factor to modal volume ratio remains challenging. Resonator designs for the optical region of the spectrum featuring dielectric bowties to "squeeze" the electric field maxima have demonstrated modal volumes of $5 \times 10^{-4} \left(\frac{\lambda}{n}\right)^3$ [7]. Recent approaches using TO techniques have yielded optical cavities with quality factor and modal volumes of $V_m \sim 3 \times 10^{-4} \lambda^3$ and 1100, respectively [8].

In this work, we apply TO to the problem of 2D slab PCR design for the terahertz frequency domain. The permittivity distribution of a 2λ by 2λ design area defining the PCR is optimized. A dielectric slab waveguide is defined for exciting the resonator from one edge. Irradiated high-resistivity silicon is used for the resonator which has been shown to have one of the lowest loss tangents in the THz band (see [9]).

A similar TO approach is used as that described in Section II but in the present case the objective function is defined to maximize the field amplitude squared in the center of the cavity. Results will be presented for cavity designs optimized for either electric or magnetic field enhancement, with discussion of their relevance to sensing and oscillator applications.

IV. Analog Computing using EM Scattering from Gyroscopic Media

Wave-based analog computation enables the implementation of complex mathematical operations by engineering the scattering response of tailored electromagnetic structures [10]. In recent work [11], we show how the electromagnetic scattering characteristics of a system of gyrotropic and dielectric scatterers is capable of solving ODEs with up to seven inputs. Here, the computational input is defined by the spherical harmonics of an incident electromagnetic wave and the computational solution is encoded in the spherical harmonics of the scattered field.

To define the ODE to be solved, both global and local optimizers are used to determine the position of the gyrotropic and dielectric cylinder scatterers. We will show that through the adoption of gyrotropic scatterer arrays, a more general class of differential equations can be solved compared to previous works.

V. Conclusion

The three works demonstrate the versatility of computational electromagnetic inverse design. Gradient-based TO was used to design a high-performance THz leaky wave fed lens antenna and high-Q/V 2D slab PCR for the THz band. Additionally, it was used to engineer a system of dielectric and gyrotropic scatterers capable of solving ODEs based on their electromagnetic scattering characteristics.

References

[1] S. Molesky, Z. Lin, A. Y. Piggott, W. Jin, J. Vucković, and A. W. Rodriguez, "Inverse design in nanophotonics," *Nat. Photonics*, vol. 12, no. 11, pp. 659–670, Nov. 2018, doi: 10.1038/s41566-018-0246-9.

[2] R. E. Christiansen and O. Sigmund, "Inverse design in photonics by topology optimization: tutorial," *Journal of the Optical Society of America B*, vol. 38, no. 2, 2021, doi: 10.1364/josab.406048.

[3] N. Hadjiantoni, D. Feng, M. Navarro-Cia, and S. M. Hanham, "Topological Optimization Framework for the Automated Design of 3D Printable THz Lens Antennas," *IEEE J. Multiscale Multiphys. Comput. Tech.*, vol. 10, 2025, doi: 10.1109/JMMCT.2025.3558662.

[4] K. Svanberg, "The method of moving asymptotes—a new method for structural optimization," *Int. J. Numer. Methods Eng.*, vol. 24, no. 2, 1987, doi: 10.1002/nme.1620240207.

[5] S. M. Hanham, C. Watts, W. J. Otter, S. Lucyszyn, and N. Klein, "Dielectric measurements of nanoliter liquids with a photonic crystal resonator at terahertz frequencies," *Appl. Phys. Lett.*, vol. 107, no. 3, p. 032903, Jul. 2015, doi: 10.1063/1.4927242.

[6] E. Lia *et al.*, "Novel mm-wave oscillator based on an electromagnetic bandgap resonator," *IEEE Microw. Wirel. Technol. Lett.*, vol. 33, no. 6, pp. 863–866, Jun. 2023, doi: 10.1109/LMWT.2023.3268090.

[7] S. Hu and S. M. Weiss, "Design of Photonic Crystal Cavities for Extreme Light Concentration," *ACS Photonics*, p. acsphotonics.6b00219, Aug. 2016, doi: 10.1021/acsphotonics.6b00219.

[8] M. Albrechtsen *et al.*, "Nanometer-scale photon confinement in topology-optimized dielectric cavities," *Nat. Commun.*, vol. 13, no. 1, 2022, doi: 10.1038/s41467-022-33874-w.

[9] S. M. Hanham *et al.*, "Low Dielectric Filling Factor Millimeter-Wave Photonic Crystal Resonator Micromachined from NTD High-Resistivity Silicon," *IEEE Trans. Microw. Theory Tech.*, vol. 72, no. 11, pp. 6601–6612, 2024, doi: 10.1109/TMTT.2024.3396631.

[10] H. Goh and A. Alù, "Nonlocal Scatterer for Compact Wave-Based Analog Computing," *Phys. Rev. Lett.*, vol. 128, no. 7, 2022, doi: 10.1103/PhysRevLett.128.073201.

[11] N. Hadjiantoni, H. Goh, S. M. Hanham, M. Navarro-Cía, and A. Alù, "Inverse-designed gyrotropic scatterers for non-reciprocal analog computing," *Nanophotonics*, vol. 14, no. 27, 2025, doi: 10.1515/nanoph-2025-0247.

Plasmonic Metasurface Arrays for Universal Liquid Sensing

Justin R Sperling[1], Finlay Walton[1], Daniel D Osborne[3], Badri Aekbote[1], Anthony E Perri[2], Rebecca A Setford[1], Hanyu Gao[1], Liam T Wilson[3], Chad M Sipperley[2], Rudolf J Schick[2], Baptiste Poursat[1], Caroline Gauchotte-Lindsay[1], William J. Peveler[3], Alasdair W. Clark[1]

[1]James Watt School of Engineering, University of Glasgow, Glasgow, United Kingdom
[2] Spraying Systems Co., Glendale Heights, IL 60139, United States
[3] School of Chemistry, University of Glasgow, Glasgow, United Kingdom

*Corresponding author: Alasdair.clark@glasgow.ac.uk

***Abstract*— We present a reusable, cross-reactive plasmonic metasurface sensor for liquid-phase chemical analysis. A 24-element metasurface, read by hyperspectral imaging, generates high-dimensional optical patterns reflecting overall sample composition. Lightweight machine learning enables both holistic quality monitoring and targeted event detection, supporting universal, point-of-need chemical sensing across beverage and drinking-water systems.**

***Keywords*— Plasmonics; sensor array; chemical sensor; nanophotonics; metasurface; taste; cross reactive sensing; food; beverage; environmental sensing.**

Industries whose primary commercial products are liquids, including beverage manufacturing and drinking-water treatment, operate within chemically complex and continuously evolving environments. Monitoring these systems remains challenging, as conventional approaches rely heavily on centralised laboratory analysis or sensory evaluation, limiting the ability to detect quality drift, emerging faults, or contamination events in real time. This talk will describe recent progress toward nanophotonic metasurface sensors designed to provide rapid, point-of-need chemical insight in such settings.

We have developed a reusable, cross-reactive plasmonic metasurface sensing platform that captures chemical information from liquids through differential optical responses rather than target-specific recognition. A single 24-element metasurface chip, patterned with distinct non-binding surface chemistries, is interrogated using hyperspectral imaging to generate high-dimensional optical patterns upon exposure to a liquid sample. Each metasurface element acts as a differential sensing region, collectively producing a characteristic spectral signature that reflects overall chemical composition and subtle environmental changes.

Rather than isolating individual analytes, this architecture enables holistic chemical sensing. The resulting optical patterns can be interpreted using lightweight machine-learning models to support multiple analytical modes, ranging from continuous quality monitoring and process stability assessment to targeted detection of specific events or threshold exceedances. Crucially, the same metasurface chip can be applied across diverse sensing tasks without redesign or refunctionalisation, underscoring its generality as a chemical sensing platform.

This presentation will concentrate on our work across beverage analysis and drinking-water treatment, highlighting examples including product classification, quality assurance, process monitoring, and detection of low-level contaminants. Together, these studies demonstrate how plasmonic metasurfaces can function as universal chemical sensors for real-world liquid monitoring. More broadly, this work illustrates how metasurface-enabled sensing can shift chemical analysis from retrospective laboratory testing toward real-time, field-deployable measurement.

Chiral Nonlinear Polaritonics and Quantum Metaphotonics with Bound States in the Continuum

Maxim V. Gorkunov* and Alena V. Mamonova

National University of Science and Technology "MISiS", Moscow, Russia

*Corresponding author: gorkunov@crys.ras.ru

***Abstract*—High quality factor photonic eigenstates stemming from bound states in the continuum drastically enhance nonlinearity of dielectric metasurfaces. We discuss chiral harmonic generation underpinned by single and multiple states and demonstrate that spontaneous parametric down conversion by a state with controlled extrinsic chirality yields photon pairs with variable entanglement degree.**

***Keywords*— chiral metasurfaces, nonlinear optics, harmonics generation, entangled photon pairs.**

Optical properties of metasurfaces can be efficiently tailored and optimized by engineering their photonic eigenstates. High quality factor states are especially advantageous for nonlinear metaphotonics as they amplify near-field light intensities by orders of magnitude thus dramatically enhancing the strength of nonlinear light-matter interactions. In this context, quasi-bound states in the continuum (qBICs) are especially valuable. On the one hand, their coupling to free-space light, the related radiative quality factor and the near-field enhancement are precisely controlled by small variations of the metastructure shape [1]. On the other hand, the state symmetry and far-field polarization determine all important characteristics of a nonlinear-optical process including its chirality.

For chiral optics, chiral qBICs isolated from electromagnetic waves of certain helicity are especially valuable [2]. Recently, their very different examples have been demonstrated in metasurfaces with meta-atoms of variable tilt [3] and height [4]. For more convenient for nanolithography planar structures, the mirror symmetry can be efficiently broken by substrates [5], [6]. While linear-optical chiral transmission and reflection resonances are convenient fingerprints of chiral qBICs, their true practical impact is much broader and includes numerous nonlinear-optical processes.

Even weak chirality of eigenstate excitation results in strong circular dichroism of third harmonic generation (THG) which becomes very selective with respect to the pump wave helicity [5]. When a state is a chiral qBIC, it effectively serves as a chiral junction between free-space light and various phenomena in metasurface material. In particular, a chiral qBIC metasurface made of excitonic van der Waals material realizes chiral strong coupling of photons with excitons and paves the way for chiral polaritonics. In the nonlinear-optical regime, chiral polaritons empower THG with remarkable chiral selectivity [7].

Tunable nonlinear chirality occurs when several quasi-degenerate states of different parity contribute to THG by an achiral metasurface. Their peculiar interplay allows controlling the harmonics helicity by the pump wave polarization enabling ultrafast all-optically controlled chiral THG [8].

Another remarkable extension of nonlinear metasurface functionality is achieved by employing chiral qBICs in the nonlinear process reciprocal to harmonic generation – the spontaneous parametric down conversion (SPDC). By engineering a flatband qBIC with extrinsic-chiral sides for certain angles of incidence, one can establish photon pair generation with continuously variable degree of polarization entanglement. Such metasurface, arranged from dimers of rods made of nonlinear semiconductor with Zinkblende crystal structure, generates ideal Bell's states or pure product states or their intermediates depending on fine tuning of the pumping radiation wavelength.

We analyze all these chiral nonlinear phenomena in terms of the eigenstate excitation and emission, elucidating the role of their degeneracy and quasi-degeneracy, flatbands and angular dispersion, as well as of their near- and far-field coupling.

Support from the Russian Science Foundation (project 25-22-00837, https://rscf.ru/project/22-00837/) is gratefully acknowledged.

References

[1] K. Koshelev, A. Bogdanov, and Y. Kivshar, "Engineering with Bound States in the Continuum," *Optics & Photonics News*, vol. 31, no. 1, p. 38, 2020.

[2] M. V. Gorkunov, A. A. Antonov, and Y. S. Kivshar, "Metasurfaces with Maximum Chirality Empowered by Bound States in the Continuum," *Phys. Rev. Lett.*, vol. 125, no. 9, p. 093903, 2020.

[3] X. Zhang, Y. Liu, J. Han, Y. Kivshar, and Q. Song, "Chiral emission from resonant metasurfaces," *Science*, vol. 377, no. 6611, pp. 1215–1218, 2022.

[4] L. Kühner, F.J. Wendisch, A. A. Antonov, J. Bürger, L. Hüttenhofer, L. De S. Menezes, S.A. Maier, M.V. Gorkunov, Y. Kivshar, A. Tittl, "Unlocking the out-of-plane dimension for photonic bound states in the continuum to achieve maximum optical chirality," *Light: Sci. & Appl.*, vol. 12, no. 1, p. 250, 2023.

[5] I. Toftul, P. Tonkaev, K. Koshelev, F. Lai, Q. Song, Q., M. Gorkunov, Y. Kivshar, "Chiral Dichroism in Resonant Metasurfaces with Monoclinic Lattices," *Phys. Rev. Lett.*, vol. 133, p. 216901, 2024

[6] M. V. Gorkunov, A. A. Antonov, A. V. Mamonova, E. A. Muljarov, and Y. Kivshar, "Substrate-Induced Maximum Optical Chirality of Planar Dielectric Structures," *Adv. Opt. Mater.*, vol. 13, no. 3, p. 2402133, 2025.

[7] C. Heimig, A.A. Antonov, D. Gryb, T. Possmayer, T. Weber, M. Hirler, J. Biechteler, L. Sortino, L. de S. Menezes, S.A. Maier, M.V. Gorkunov, Y. Kivshar, A. Tittl, "Chiral Nonlinear Polaritonics with van der Waals Metasurfaces," *Sci. Adv.*, in press 2026, arXiv:2410.18760.

[8] F. Lai, J. Yin, I. Toftul, H. Barkaoui, H. Deng, X. Sha, M. V. Gorkunov, Y. S. Kivshar, Q. Song, "Nonlinear chiral light generation from resonant metasurfaces," *Nat. Commun.*, vol. 16, no. 1, p. 10686, 2025.

Efficient Lasing Metasurfaces Enabled by Quasi-Dark Resonances: A Temporal Coupled Mode Theory Approach

Georgios Nousios[1,2], Thomas Christopoulos[3], Dimitrios C. Zografopoulos[1,2], Emmanouil E. Kriezis[1], Odysseas Tsilipakos[4,*]

[1]School of Electrical and Computer Engineering, Aristotle University of Thessaloniki (AUTh), Thessaloniki GR-54124, Greece

[2]Consiglio Nazionale delle Ricerche, Istituto per la Microelettronica e Microsistemi (CNR-IMM), Rome, 00133, Italy

[3]Laboratoire Photonique, Numérique et Nanosciences (LP2N), IOGS-Université de Bordeaux-CNRS, 33400 Talence, France

[4]Theoretical and Physical Chemistry Institute, National Hellenic Research Foundation (NHRF), Athens GR-11635, Greece

*Corresponding author: otsilipakos@eie.gr

***Abstract*—We develop a rigorous temporal coupled-mode-theory framework to accurately model light emission from metasurfaces incorporating conventional bulk or sheet (2D) gain media. The framework is validated via time-domain finite-element simulations and then used to design light-emitting metasurfaces that support sharply-resonant (high-Q) quasi-bound states in the continuum. We showcase examples of lasing in the near infrared with a transition metal dichalcogenide hetero-bilayer as the gain medium and lasing in the visible using organic dyes.**

***Keywords*— Optical metasurfaces, dielectric metasurfaces, light emission, bound states in the continuum, broken symmetry, transition metal dichalcogenides, organic dyes, near infrared, visible.**

I. Introduction

During the last decade, metasurfaces (MSs) have gathered significant interest for light emission [1]. A resonant MS can act as a compact optical cavity and provide the necessary feedback mechanism for enabling ultrathin lasing elements. In particular, MSs supporting quasi bound states in the continuum (qBICs) offer an attractive route to achieving efficient lasing, since they are in principle characterized by particularly high radiation quality factors [1], [2]. Thus, a number of MS lasers based on symmetry-protected resonances have been recently proposed [3], [4], [5].

Here, we use temporal coupled-mode theory (CMT) [6] in order to thoroughly design metasurface-based lasers by engineering the underlying resonances and their overlap with the gain medium. This approach allows to propose efficient laser designs as well as obtain physical insight into the light-matter interactions. We showcase two examples: lasing in the near infrared with a transition metal dichalcogenide heterobilayer as the gain medium [7] and lasing in the visible using organic dyes [8], [9].

II. Coupled-mode theory framework for metasurface lasers

To assess the lasing response of sharply-resonant metasurfaces comprising bulk or sheet gain media, we have developed a highly-efficient temporal coupled-mode theory (CMT) framework, rigorously implementing a semiclassical description of the light-matter interactions at the nanoscale through the Maxwell-Bloch equations and first-order perturbation theory. The framework boils down to a system of nonlinear coupled ODEs, which involve the lasing mode amplitude, the carrier densities, and the lasing/pump polarization fields. It was developed for integrated nanophotonic [10] and metasurface lasers [11], extended to describe Q-switching when a saturable absorber is present [12], and adapted to organic dye gain media which are characterized by significant overlap between their emission and absorption spectra, giving rise to reabsorption of the emitted light [9]. The CMT results are systematically verified against full-wave nonlinear time-domain FEM (TD-FEM) simulations, showing excellent agreement [11], [9]. Note that compared to other models [13], our CMT framework is cast in terms of the mode amplitude and retains both amplitude and phase information. It does not require for the cavity and atomic transition frequencies to coincide and can be used to estimate the resulting lasing frequency [10]. It rigorously assesses the interaction between the gain medium and the lasing/pump modes through overlap integrals taking into account the exact physical system and the vectorial nature of the fields. Moreover, it allows to easily incorporate other nonlinear phenomena such as saturable absorption (important for Q-switching) or Kerr nonlinearity [12]. On the whole, the proposed framework constitutes an advantageous approach (efficient and accurate) for designing a broad range of nanophotonic lasing elements.

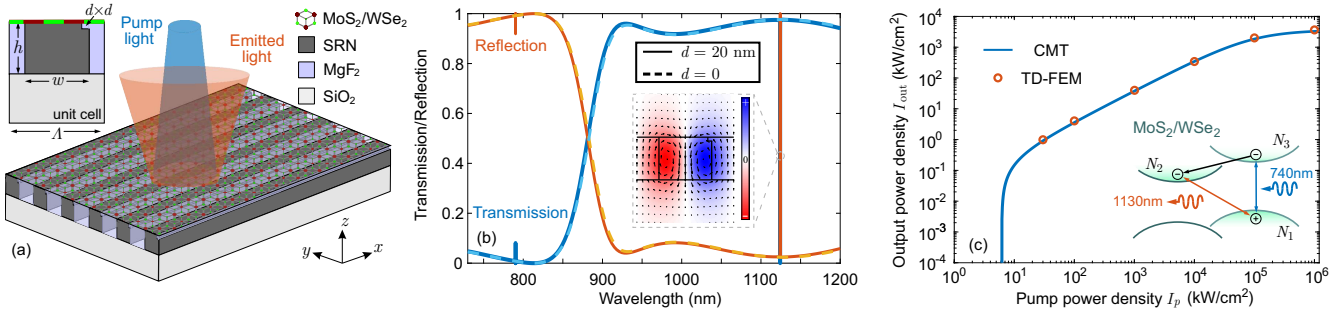

Fig. 1. (a) Metasurface laser for near infrared frequencies consisting of broken-symmetry SRN stripes (cut-out $d \times d$) periodically arrayed on a SiO_2 substrate [11]. The structure is overlaid with the MoS_2/WSe_2 hetero-bilayer; it is optically pumped by a normally-incident plane wave at λ_p and emits vertically in both $\pm\hat{\mathbf{z}}$ directions at λ_L due to the radiative recombination of interlayer excitons (see inset in panel c). (b) Transmission and reflection spectra under vertical plane-wave illumination when $d = 20$ nm (solid lines) and $d = 0$ (dashed lines). In the $d = 20$ nm case, a qBIC mode is excited near ~ 1128 nm, with the field profile shown in the inset (color: $\mathrm{Re}\{E_x\}$, arrows: magnetic field). (c) CW light-light curve obtained by both CMT (solid lines) and TD-FEM (circular markers) showing excellent agreement. The lasing threshold is ~ 6 kW/cm^2.

III. MoS_2/WSe_2-Based Metasurface for Lasing in the Near Infrared

The first example concerns lasing in the near infrared by exploiting a transition metal dichalcogenide (TMD) hetero-bilayer [11]. More specifically, MoS_2/WSe_2 hosts bright interlayer excitons [14] characterized by long metastable lifetimes exceeding 1 ns. We combine MoS_2/WSe_2 with a strongly-resonant qBIC metasurface composed of silicon-rich nitride ($n_{\mathrm{SRN}} \approx 3.15$) meta-atoms arrayed in a subdiffractive lattice and residing on a SiO_2 substrate, Fig. 1(a). The periodic configuration is planarized with a MgF_2 cladding so that a flat surface is available for the hetero-bilayer to reside on. MgF_2 is a favorable cladding material characterized by both low refractive index $n_{\mathrm{MgF_2}} = 1.37$ and high thermal conductivity helping with thermal management [11]. The MoS_2/WSe_2 hetero-bilayer is overlaid and provides gain around 1130 nm after being optically pumped at 740 nm, see inset in Fig. 1(c).

The height of the SRN stripes is set to the typical value of $h = 220$ nm. By adjusting the width to $w = 272$ nm, an out-of-plane magnetic dipole resonance (MD_z) falls near the maximum of the MoS_2/WSe_2 emission spectrum, i.e., 1128 nm (1.1 eV) [15]. The MD_z mode is completely decoupled from the radiation channel in the normal direction (dark), as can be deduced by the antisymmetry of the mode profile with respect to xz plane [see inset of Fig. 1(b)]. Breaking the symmetry with a $d \times d$ square cut-out for instance [Fig. 1(a)], the mode becomes controllably quasi-dark by acquiring a residual horizontal magnetic dipole moment and can couple with free space [11]. This can be seen in Fig. 1(b), where the transmission and reflection spectra under vertical plane-wave illumination (E_x polarization) are presented for $d = 0$ and $d = 20$ nm. Values of the defect size d between 15 and 40 nm (corresponding to Q_{rad} values between $\sim 60\,000$ and $1\,000$) attract the main interest as they can strike a compromise between achieving a high Q for low lasing threshold while permitting a sufficient amount of optical power to be emitted.

To assess the metasurface laser performance under CW conditions we calculate the light-light curve (I_{out} versus I_p). The result by both CMT (solid line) and TD-FEM (circular markers) is depicted in Figure 1(c); see [11] for a description of the methods. A broad range of pump power density levels is covered and the agreement between the two methods is excellent. The examined metasurface laser exhibits a very low lasing threshold of $I_{p,\mathrm{th}} = 6.16\,\mathrm{kW/cm^2}$ and a total efficiency (I_{out}/I_p) of $\sim 3.7\%$. Although the incident pump wave is not coupled to a high quality-factor mode of the MS, the absorption efficiency, η_p, is still significant with $\eta_p = 9.56\%$. In addition, CMT and TD-FEM agree in the prediction of the lasing frequency, for which it holds $\lambda_L \sim \lambda_{21}$ since we had initially aligned the cavity resonance with the peak of the gain spectrum, i.e., $\lambda_{c,0} \approx \lambda_{21}$. The excellent agreement extends to the spatially-averaged surface carrier densities and, importantly, to transient phenomena and pulsed pumping scenarios [11]. The importance of these results should not be overlooked: using only first order simplifications and spatial averaging, we are able to reproduce the temporal response of a highly inhomogeneous metasurface accurately predicting not only the emitted power but also the carrier densities in the gain medium.

IV. Slot TiO_2 Metasurface with Organic Dyes for Lasing in the Visible

We next focus on the visible region and utilize highly fluorescent rhodamine 6G (R6G) molecules dissolved in methanol as the gain medium, with a gain spectrum centered at 555 nm [top inset in Fig. 2(a)]. Note, that the emission and absorption spectra overlap, giving rise to considerable reabsorption of the emitted light. The rigorous incorporation of the reabsorption effect in the CMT framework is essential in order to accurately assess the lasing response [9]. The MS hosting the organic dye medium comprises square slots etched in a thin TiO_2 layer of thickness $h = 250$ nm and arrayed periodically in a subdiffractive lattice of pitch Λ. Owing to the high-index contrast between TiO_2 and methanol, the investigated metasurface supports a symmetry-protected BIC [16], [7], which is predominantly confined inside the slot [bottom inset in Fig. 2(a)]. The slot width is $s = 40$ nm while the distance

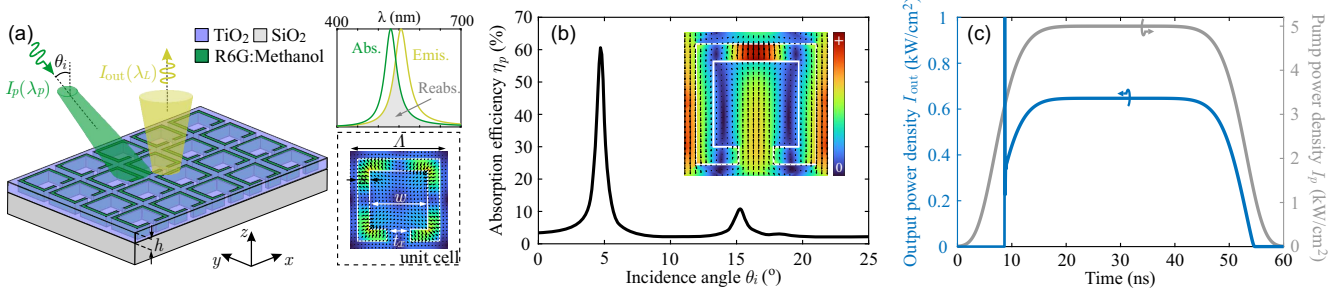

Fig. 2. (a) Metasurface laser for visible frequencies consisting of periodically arrayed split-square slots etched in a thin TiO_2 layer and filled with R6G molecules dissolved in methanol. The MS is optically pumped by a plane wave with wavelength λ_p and emits in both $\pm\hat{\mathbf{z}}$ directions at wavelength λ_L. Bottom inset: Unit cell of the MS with field profile at $z = 0$ (middle of the TiO_2 layer) of the qBIC lasing mode when $w = 195$ nm (color: $|\mathbf{E}|$, arrows: $\mathbf{E}_{\parallel}$). Top inset: Normalized absorption/emission spectra of R6G; the spectral overlap gives rise to reabsorption of the emitted light by the gain medium. (b) Pump absorption efficiency at $\lambda_p = 532$ nm as a function of θ_i (s polarization in the xz plane of incidence). The absorption efficiency is maximized ($\eta_p \approx 60\%$) at $\theta_i = 4.7^{\circ}$ due to the excitation of a bright mode (see inset for corresponding mode profile at $z = h/4$). (c) Temporal evolution of the output power density I_{out} when the structure is pumped with $I_p = 5$ kW/cm^2 with a fourth-order super-Gaussian pulse with FWHM $= 45$ nm.

between adjacent squares is set to 50 nm and w is left as a design parameter to tune the lasing mode resonance wavelength. The bridge of width t_x transforms the lasing mode from BIC to qBIC [16], [7]. For $t_x = 80$ nm, Q_{rad} lies in the range between 10 000 and 20 000, allowing a sufficient fraction of the emitted power to radiate in the far-field.

Importantly, to maximize pump absorption we utilize resonant pumping through a bright resonance of the metasurface. We find a bright mode at 524.73 nm and exploit its angular dispersion to shift the resonant wavelength (and, thus, maximize absorption) at 532 nm [Fig. 2(b)]. The absorption efficiency reaches ∼60% for $\theta_i = 4.7^{\circ}$. It is also important to reduce the reabsoprtion losses suffered by the lasing mode [9]. This is achieved by tuning the resonance wavelength of the lasing mode to 570 nm, i.e., away from the emission peak at 555 nm. Addressing these two design considerations, the MS laser is made to exhibit a very low lasing threshold of $I_{p,\text{th}} = 1.3$ kW/cm^2 with an overall efficiency reaching 15%.

Finally, in Fig. 2(c) we plot the temporal evolution of the output power density I_{out} (blue line) when the metasurface is pumped with a fourth-order super-Gaussian pulse with peak power density equal to $I_p = 5$ kW/cm^2 (gray line). Pulsed pumping is typical for dye lasers to avoid molecular crossing into the triplet states and the associated deleterious photobleaching effect occurring in millisecond timescales [17]. After a brief transient effect with a single abrupt peak, the output pulse closely follows the shape of the pump pulse.

V. Conclusion

We have demonstrated efficient metasurface lasers enabled by quasi-dark resonances. We have exploited the MoS_2/WSe_2 hetero-bilayer for lasing at near infrared frequencies and rhodamine 6G molecules for lasing at visible frequencies. In both examples, the underlying metasurface is meticulously designed to allow for strong resonant interaction between the optical and matter states resulting in high pump absorption and low lasing threshold. The design process has been greatly facilitated by a temporal coupled-mode-theory framework, which allows to perform efficient and accurate simulations (as verified by comparing against time-domain finite-element simulations) and obtain considerable physical insight into the light-matter interaction processes.

References

[1] A. Vaskin, R. Kolkowski, A. F. Koenderink, and I. Staude, "Light-emitting metasurfaces," *Nanophotonics*, vol. 8, no. 7, pp. 1151–1198, 2019.

[2] D. C. Zografopoulos and O. Tsilipakos, "Recent advances in strongly resonant and gradient all-dielectric metasurfaces," *Materials Advances*, vol. 4, no. 1, pp. 11–34, 2023.

[3] M. Wu, S. T. Ha, S. Shendre, E. G. Durmusoglu, W. K. Koh, D. R. Abujetas, J. A. Sánchez-Gil, R. Paniagua-Domínguez, H. V. Demir, and A. I. Kuznetsov, "Room-Temperature Lasing in Colloidal Nanoplatelets via Mie-Resonant Bound States in the Continuum," *Nano Letters*, vol. 20, no. 8, pp. 6005–6011, 2020.

[4] J.-H. Yang, Z.-T. Huang, D. N. Maksimov, P. S. Pankin, I. V. Timofeev, K.-B. Hong, H. Li, J.-W. Chen, C.-Y. Hsu, Y.-Y. Liu, T.-C. Lu, T.-R. Lin, C.-S. Yang, and K.-P. Chen, "Low-Threshold Bound State in the Continuum Lasers in Hybrid Lattice Resonance Metasurfaces," *Laser & Photonics Reviews*, vol. 15, no. 10, p. 2100118, 2021.

[5] A. V. Prokhorov, M. Y. Gubin, A. V. Shesterikov, A. V. Arsenin, V. S. Volkov, and A. B. Evlyukhin, "Lasing Effect in Symmetrical van der Waals Heterostructured Metasurfaces Due to Lattice-Induced Multipole Coupling," *Nano Letters*, vol. 23, no. 23, pp. 11 105–11 111, 2023.

[6] T. Christopoulos, O. Tsilipakos, and E. E. Kriezis, "Temporal coupled-mode theory in nonlinear resonant photonics: From basic principles to contemporary systems with 2D materials, dispersion, loss, and gain," *Journal of Applied Physics*, vol. 136, no. 1, p. 011101, 07 2024.

[7] G. Nousios, J. Algorri, W. Fuscaldo, F. Dell'Olio, S. Romano, G. Zito, B. Miranda, Y. Ding, V. Dmitriev, L. Andreani, M. Galli, O. Tsilipakos, E. Kriezis, and D. Zografopoulos, "Silicon slot metasurface supporting a multitude of bound states in the continuum: theoretical and experimental studies," *Optics & Laser Technology*, vol. 192, p. 113398, Dec. 2025.

[8] G. Nousios, F. Dell'Olio, J. Algorri, W. Fuscaldo, O. Tsilipakos, E. Kriezis, and D. Zografopoulos, "Dielectric metasurfaces enabling lasing in the visible via a slot-type bound state in the continuum and fluorescent dye molecules," in *SPIE Photonics West 2026*, no. 13879-33, 2026.

[9] G. Nousios, O. Tsilipakos, T. Christopoulos, J. F. Algorri, W. Fuscaldo, F. Dell'Olio, E. E. Kriezis, and D. C. Zografopoulos, "Lasing in strongly resonant metasurfaces with fluorescent dyes: quasi-dark and bright optical states and the reabsorption effect," *submitted*.

[10] G. Nousios, T. Christopoulos, O. Tsilipakos, and E. E. Kriezis, "Integrated Lasers with Transition-Metal-Dichalcogenide Heterostructures: Analysis and Design Utilizing Coupled-Mode Theory for Two-Dimensional Materials," *Phys. Rev. Appl.*, vol. 19, p. 064027, Jun 2023.

[11] G. Nousios, T. Christopoulos, E. E. Kriezis, and O. Tsilipakos, "Efficient lasing in MoS_2/WSe_2-based metasurfaces enabled by quasi-dark magnetic dipole resonance," *ACS Applied Nano Materials*, vol. 9, pp. 2301–2308, Jan. 2026.
[12] G. Nousios, T. Christopoulos, O. Tsilipakos, and E. E. Kriezis, "Theoretical Analysis of Integrated Nanophotonic Q-Switched Laser Based on Gain and Saturable Absorption by Two-Dimensional Materials," *Advanced Photonics Research*, vol. 5, no. 6, p. 2300249, 2024.
[13] A. E. Siegman, *Lasers*. University Science Books, 1986.
[14] Y. Jiang, S. Chen, W. Zheng, B. Zheng, and A. Pan, "Interlayer exciton formation, relaxation, and transport in TMD van der Waals heterostructures," *Light: Science & Applications*, vol. 10, no. 1, p. 72, Apr. 2021.
[15] Y. Liu, H. Fang, A. Rasmita, Y. Zhou, J. Li, T. Yu, Q. Xiong, N. Zheludev, J. Liu, and W. Gao, "Room temperature nanocavity laser with interlayer excitons in 2D heterostructures," *Science Advances*, vol. 5, no. 4, p. eaav4506, 2019.
[16] J. F. Algorri, F. Dell'Olio, P. Roldán-Varona, L. Rodríguez-Cobo, J. M. López-Higuera, J. M. Sánchez-Pena, V. Dmitriev, and D. C. Zografopoulos, "Analogue of electromagnetically induced transparency in square slotted silicon metasurfaces supporting bound states in the continuum," *Opt. Express*, vol. 30, no. 3, pp. 4615–4630, Jan 2022.
[17] S.-L. Chua, B. Zhen, J. Lee, J. Bravo-Abad, O. Shapira, and M. Soljačić, "Modeling of threshold and dynamics behavior of organic nanostructured lasers," *Journal of Materials Chemistry C*, vol. 2, no. 8, p. 1463, 2014.

Microbridge-Array Based Reconfigurable Intelligent Surfaces

Steffen Klingel[1,*], Lars Franke[1], and Marco Rahm[1]

[1]Department of Electrical and Computer Engineering and Research Center OPTIMAS, RPTU Kaiserslautern-Landau, Germany

*Corresponding author: steffen.klingel@rptu.de

***Abstract*—We report a MEMS-switchable reconfigurable intelligent surface (RIS) for beam control in the sub-terahertz frequency band. Simulation results promise a phase tuning range of 300° at 100 GHz with a reflection magnitude above 0.9. The operation bandwidth exceeds 4 GHz. A fabricated 10x10 unit cell prototype evidences the manufacturability of our design.**

***Keywords*— beam steering, wireless communication, MEMS, RIS.**

I. Introduction

As wireless communication systems move into the sub-THz and THz frequency ranges, they enable higher data rates but face challenges such as high propagation losses, short transmission distances, and frequent signal blockage. These limitations make reliable communication difficult, particularly in dense urban environments. Reconfigurable intelligent surfaces (RIS), composed of many controllable unit cells, offer a solution by dynamically manipulating electromagnetic waves for beamforming, beam steering, and signal redirection. Traditional RIS designs rely on semiconductor components such as varactor diodes and PIN diodes, which provide continuous and discrete phase tuning, respectively [1], [2], [3], [4]. However, at sub-THz frequencies, these approaches struggle to achieve a wide phase tuning range over a sufficient bandwidth. They also suffer from reduced reflection amplitude, which limits efficiency and the overall beamforming performance.

To overcome these limitations, the presented work introduces a novel RIS design based on microelectromechanical systems (MEMS). Instead of relying on electronic tuning elements, this approach uses mechanically actuated microbridges to control the electromagnetic response of each unit cell. The microbridges are fabricated from silicon dioxide (SiO_2) and copper on a silicon substrate with a metallized backside. By applying a DC voltage between the bridges and the ground plane, electrostatic forces induce a controllable mechanical deflection of the bridges. This deflection effectively alters the electromagnetic properties of the unit cell, enabling quasi-continuous phase tuning similar to varactor-based systems but potentially more suitable for high-frequency operation.

II. Results and Discussion

Simulation studies of the proposed unit cell design demonstrate promising performance. At an operation frequency of 100 GHz, the system achieves a phase tuning range of approximately 300°, with the reflection magnitude remaining above 0.9 across a bandwidth of more than 4 GHz (98–102 GHz). This represents a substantial improvement over traditional diode-based RIS at similar frequencies. The results indicate that mechanical tuning via MEMS structures can provide both a wide phase range and high reflection efficiency, which are critical for effective beamforming and beam steering.

Following the simulation phase, a prototype RIS consisting of a 10×10 array of unit cells was fabricated using standard microfabrication techniques on a silicon wafer. The process involved multiple lithography steps, oxide etching, metal deposition, and silicon underetching using a TMAH solution to release the microbridges. Special design adaptations, such as introducing small holes along the bridges, were implemented to ensure proper underetching despite geometric constraints.

Although the fabrication process was largely successful, experimental observations revealed a key challenge: the microbridges exhibited unintended initial bending toward the substrate. This deformation is likely caused by surface tension effects during drying, particularly from isopropyl alcohol. Since the device's sensitivity is highest at small deflections, excessive bending significantly reduces the achievable phase shift, limiting the prototype's effectiveness for beam steering applications.

To address this issue, future work will focus on improving the fabrication process, specifically by using a critical point drying technique to eliminate surface tension effects during drying. This adjustment is expected to preserve the intended mechanical structure of the microbridges and restore their full tuning capability.

III. Conclusion

In summary, the MEMS-based RIS concept presents a promising alternative to conventional diode-based designs for sub-THz and THz applications. By leveraging mechanical actuation, it enables large, continuous phase tuning with high reflection efficiency, potentially overcoming key limitations of existing technologies. Further optimization of the fabrication process will be essential to fully realize its potential in next-generation wireless communication systems.

REFERENCES

[1] X. Wan et al., "Reconfigurable Sum and Difference Beams Based on a Binary Programmable Metasurface," in *IEEE Antennas and Wireless Propagation Letters*, vol. 20, no. 3, pp. 381-385, March 2021.

[2] J. -B. Gros, V. Popov, M. A. Odit, V. Lenets and G. Lerosey, "A Reconfigurable Intelligent Surface at mmWave Based on a Binary Phase Tunable Metasurface," in *IEEE Open Journal of the Communications Society*, vol. 2, pp. 1055-1064, 2021.

[3] Alexander Wolff, Lars Franke, Steffen Klingel, Janis Krieger, Lukas Mueller, Ralf Stemler, and Marco Rahm, Continuous beam steering with a varactor-based reconfigurable intelligent surface in the Ka-band at 31 GHz. *J. Appl. Phys*. 21 September 2023; 134 (11): 114502.

[4] da Silva LG, Chu Z, Xiao P and Cerqueira S Jr. A (2023) A varactor-based 1024-element RIS design for mm-waves. *Front. Comms. Net*, 4:1086011.

Microcomb-Enabled Low-Phase-Noise Terahertz Wireless Links for High-Order Modulation

Takasumi Tanabe* and Liu Bowen

[1]Department of Electronics and Electrical Engineering, Faculty of Science and Technology, Keio University, Japan

*Corresponding author: takasumi@elec.keio.ac.jp

***Abstract*— Terahertz wireless links promise fiber-like capacity but are limited by oscillator phase noise. We present a photonic approach using microcombs to suppress phase noise and enable high-order QAM transmission and reveal a phase-noise tolerance boundary for robust operation**

***Keywords*— microcomb, THz communications, phase noise.**

I. Introduction

Terahertz (THz) wireless communication is emerging as a key technology for B5G and 6G systems due to its vast available bandwidth. However, the performance of THz links is limited by oscillator phase noise, which becomes particularly severe for high-order modulation formats such as M-QAM.

Photonic approaches, especially microresonator-based optical frequency combs (microcombs), offer a promising alternative. Owing to their intrinsic phase coherence and low phase noise, microcombs can generate THz carriers via photomixing without the noise amplification inherent to electronic frequency multiplication, enabling more robust, high-capacity wireless links.

II. Results and Discussion

We analyze the impact of phase noise by reconstructing time-domain fluctuations from measured spectra and embedding them into a single-carrier THz communication model. This provides a direct mapping from oscillator noise to symbol distortion. Two dominant mechanisms are identified: a slow common phase error that can be compensated by carrier recovery, and a fast instantaneous phase jitter that remains as residual noise and limits performance. To quantify this, we introduce a 3×EVM margin framework linking phase noise magnitude to constellation distortion.

The results reveal a clear phase-noise tolerance boundary for high-order QAM transmission (Fig. 1). After phase recovery, residual white phase noise dominates system performance, defining a transition between noise-limited and SNR-limited regimes. Microcomb-based photonic oscillators exhibit significantly lower instantaneous phase noise, enabling higher-order modulation with reduced SNR penalty. As a result, modest phase-noise improvement yields orders-of-magnitude BER improvement, highlighting microcombs as a key enabler for THz wireless links.

III. Extension to Photonic Systems

Beyond THz wireless links, these insights extend to photonic systems where phase noise is critical. Phase stability limits performance similarly to high-order QAM distortion, and effects such as EEPN show that residual phase noise persists after compensation.

Thus, phase-noise tolerance provides a useful framework beyond wireless links, highlighting the importance of low-phase-noise sources such as microcombs.

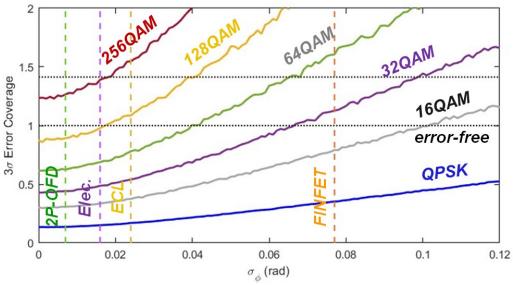

Fig. 1: 3×EVM margin versus phase noise. Microcomb (2P-OFD) can achieve 128QAM (30 dB SNR with 2048 OFDM)

IV. Conclusion

We show that oscillator phase noise fundamentally limits high-order QAM THz links, and introduce a phase-noise tolerance framework based on a 3×EVM margin. Residual phase noise after compensation dominates system performance, while microcomb-based photonic oscillators enable higher-order modulation with reduced SNR penalty.

These insights also extend to optical communication and photonic computing, highlighting low-phase-noise photonic sources as a key technology for scalable and reliable systems.

Acknowledgments

This work was supported by JST-CREST (#JPMJCR24R4) and JST-CRONOS (#JPMJCS24N7).

References

[1] B. Liu and T. Tanabe, "Quantifying Phase Noise Tolerance for Single-Carrier M-QAM Terahertz Wireless Communications with Advantages of Photonic Approaches," J. Lightwave Technol. early access (2026).

Polymeric dynamic nanoantennas and metasurfaces

Magnus P. Jonsson[1,*]

Laboratory of Organic Electronics, Linköping University, Norrköping, SE-60174, Sweden
*Corresponding author: magnus.jonsson@liu.se

***Abstract*— Conducting polymers can be switched between plasmonic and dielectric properties through their redox state. We will here present our latest advances in utilizing this capability for active nanoantennas and metasurfaces.**

***Keywords*— metasurfaces, nanoantennas, conducting polymers, gate, plasmonics, redox-tuning.**

In 2020, we demonstrated for the first time that conducting polymers can act as redox-switchable plasmonic materials, enabling chemically or electrically controlled nanoantennas and metasurfaces.[1-3] Here, I will present recent advances in this emerging area of plasmonics and metasurfaces. These advances include extension from PEDOT to other polymer systems including n-type PBFDO,[4,5] narrowing of resonances through nonlocal coupling,[6] unique possibilities through aligned hyperbolic polymers[7,8], nearfield coupling to epsilon-near-zero materials,[9] and exploration of different spectral ranges, including the mid-IR[10] and the visible, with the latter through the concept of conducting polymer-gated optical confinement.[11]

Acknowledgments

We acknowledge support from the European Research Council (Consolidator Grant, 101086683), the Knut and Alice Wallenberg Foundation (Wallenberg Academy Fellow, KAW 2019.0163, 2020.0301), the Swedish Research Council (VR, Consolidator Grant, 2020-00287), and the Swedish Government Strategic Research Area in Materials Science on Functional Materials at Linköping University (Faculty Grant SFO-Mat-LiU No. 2009 00971).

References

[1] S. Chen *et al.* "Conductive polymer nanoantennas for dynamic organic plasmonics", *Nature Nanotech.* 15, 35-40 (2020)
[2] Karki *et al.* "Electrical Tuning of Plasmonic Conducting Polymer Nanoantennas", *Adv. Mater.* 34, 2107172, (2022)
[3] Chen et al. "Dynamic conducting polymer plasmonics and metasurfaces", *ACS Phot.* 10, 3, 571–581, (2023)
[4] Karki et al. "Doped Semiconducting Polymer Nanoantennas for Tunable Organic Plasmonics", *Comm. Mat.* 3, 48 (2022)
[5] Kazi et al. "n-Type redox-tuneable conducting polymer optical nanoantennas", *JMCC* 12, 17469–17474 (2024)
[6] Lin et al. "Switchable Narrow Nonlocal Conducting Polymer Plasmonics", *Nature Communications*, 16, 4484 (2025)
[7] Duan et al. "Tuneable anisotropic plasmonics with shape-symmetric conducting polymer nanoantennas", *Advanced Materials* 35, 51, 2303949 (2023)
[8] Duan et al. "Broadband chiroptics with twist-stacked hyperbolic conducting polymer thin films", *Advanced Materials, 37, 16, 2417024* (2025)
[9] Duan et al. "Electrotunable coupling between epsilon-near-zero thin film and conducting polymer nanoantennas", *PNAS* , in press (2026)
[10] Bandaru et al. "Switchable thermal mid-IR conducting polymer antenna arrays", *Advanced Functional Materials*, early view, e25508 (2025)
[11] Lin et al. "Dynamic Optical Lattices through Conducting Polymer-Gated Confinement", *Advanced Materials*, e20674, early view (2025)

Controlling Fisher Information Flow in Optical Metrology

Kevin F. MacDonald[1,*], Maximilian Weimar[2], Huanli Zhou[1], Luca Neubacher[2], Thomas A. Grant[1], Jakob Hüpfl[2], Stefan Rotter[2], and Nikolay I. Zheludev[1]

[1]Optoelectronics Research Centre, University of Southampton, UK
[2] Institute for Theoretical Physics, Vienna University of Technology (TU Wien), Austria
*Corresponding author: kfm@orc.soton.ac.uk

***Abstract*— Fisher information defines the limit of measurement precision. We show it can be viewed as a propagating physical entity, which can resonate, diffract, and interfere. We illustrate how material composition, geometry, and environmental design can control generation and flow of information, just as antennas and metasurfaces can sculpt electromagnetic energy.**

***Keywords*— Fisher information, optical metrology, plasmonics, nanophotonics.**

Optical metrology has a broad scope of applications in smart manufacturing, precise instrumentation, nanotechnology, bioimaging and materials research. While sophisticated interferometry is used for positional and dimensional metrology of macroscopic objects, different approaches are required for nanoscale objects, and a variety of approaches leveraging nonlinear phenomena, statistical accumulation, structured illumination, and machine learning-based estimators (trained on measurand variations) can deliver deeply sub-wavelength, even atomic scale, precision. We argue that further improvements in many forms of optical scattering metrology can be achieved by better understanding of the information aspect.

The central concept here is Fisher information (FI), which sets the so-called Cramér-Rao lower bound on the precision with which a parameter, such as the position or size of a scatterer, can be estimated from a given measurement. It has recently been shown that FI does more than merely quantify measurement precision – it can be understood as a quantity carried by electromagnetic waves as they propagate [1]: FI is generated when a light field interacts with an object of interest and is carried by the scattered field through the surrounding medium (towards a detector); it obeys a continuity equation akin to those found in classical field theories, and is conserved in dissipation-free regions, much like energy.

On this basis, we demonstrate that FI flow inherits the wave-like character of light itself: it can resonate, diffract, and, perhaps most surprisingly, interfere [2]. This has profound implications for optical design: Plasmonic and dielectric resonances can enhance information generation, and FI flow can be guided (analogously to beam steering), through appropriate design of a measurement target's environment.

This perspective reframes metrology as a discipline in which resolution can be purposely engineered by tailoring the sources and flow of information to serve applications in atomic-scale diagnostics and fabrication.

Acknowledgments

This work was funded in parts by the UK Engineering and Physical Sciences Research Council (EPSRC) [EP/T02643X/1, EP/Z53285X/1] and the Austrian Science Fund (FWF) [10.55776/PIN7240924].

References

[1] J. Hüpfl, F. Russo, L. M. Rachbauer, D. Bouchet, J. Lu, U. Kuhl and S. Rotter, "Continuity equation for the flow of Fisher information in wave scattering," Nature Physics, vol. 20, pp. 1294-1299, 2024.

[2] M. Weimar, H. Zhou, L. Neubacher, T. A. Grant, J. Hüpfl, K. F. MacDonald, S. Rotter, and N. I. Zheludev, "Controlling the flow of information in optical metrology," arxiv.org/abs/2508.13640, 2025.

Fluctuation-induced Hall-like forces in a chiral-gain environment

Daigo Oue[1,2,3,*], Mário G. Silveirinha[1]

[1]Instituto Superior Técnico–University of Lisbon and Instituto de Telecomunicações, Lisbon, Portugal
[2]The Blackett Laboratory, Imperial College London, United Kingdom
[3]RIKEN Centre for Advanced Photonics, Saitama, Japan
*Corresponding author: daigo.oue@gmail.com

***Abstract*—We show that a particle near a substrate under electrostatic bias experiences a Hall-like force parallel to the surface. This force arises from polarisation-selective amplification and dissipation. The effect is governed by the Berry-curvature dipole of the substrate's response. Our results open new routes for vacuum-mediated control at the nanoscale.**

Non-Hermitian electromagnetic media, characterised by loss and/or gain, support wave phenomena without counterparts in passive systems. In current-biased conductors, an electrostatic field drives carrier drift that modifies the optical response and can induce polarisation-dependent gain. In low-symmetry materials possessing a finite Berry-curvature dipole, an electrostatic bias produces chiral gain, where one circular polarisation is amplified while the opposite is dissipated. Consequently, both inversion and time-reversal symmetries are effectively broken, leading to nonreciprocal electromagnetic behaviour rooted in the quantum geometry of the electronic bands.

We investigate fluctuation-induced forces in such a chiral-gain electromagnetic environment. A small polarisable particle is placed near a biased substrate (Fig. 1). In contrast to

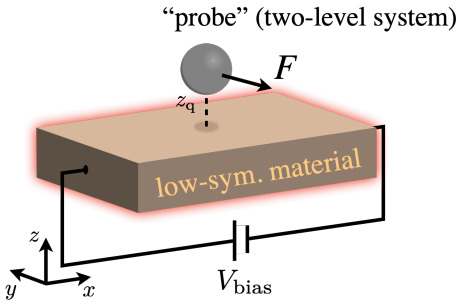

Fig. 1. A polarisable particle modelled by a two-level system placed above a low-symmetry material under an electrostatic bias.

conventional Casimir–Polder or van der Waals forces, which act normal to a surface in passive media, we show that vacuum electromagnetic fluctuations generate a steady Hall-like lateral force parallel to the interface. The effect originates from the imbalance of circularly polarised electromagnetic modes and the resulting directional momentum exchange enabled by the non-Hermitian response of the substrate.

The analysis is based on Green-function field quantisation in dispersive and active media combined with the Lindblad formalism to derive a reduced master equation for the particle. The steady-state momentum transfer between the particle and the surrounding field yields the lateral force. We demonstrate that the magnitude of the force is governed by the Berry-curvature dipole of the substrate response, establishing a direct link between electromagnetic quantum geometry and fluctuation-induced forces. The force exhibits a $1/z_q$ distance dependence in the near-field regime (Fig. 2).

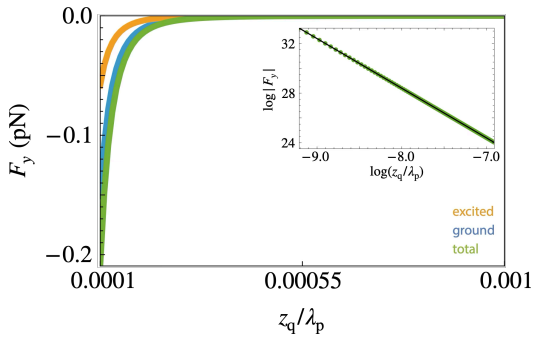

Fig. 2. Fluctuation-induced Hall-like force as a function of the distance z_q between the surface and the particle. The inset is the logarithmic plot, implying the force is proportional to $1/z_q^4$.

These results reveal a previously unexplored mechanism for directional vacuum forces arising purely from non-Hermitian electromagnetic response, highlighting the role of active, nonreciprocal media in fluctuation electrodynamics.

Acknowledgments

D.O. is supported by JSPS Overseas Research Fellowship and by the RIKEN special postdoctoral researcher program. M.S. is partially supported by the Simons Foundation (award SFI-MPS-EWP-00008530-10) and by national funds through FCT – Fundação para a Ciência e a Tecnologia, I.P., and, when eligible, co-funded by EU funds under project/support UID/50008/2025 – Instituto de Telecomunicações, with DOI identifier https://doi.org/10.54499/UID/50008/2025.

References

[1] T. A. Morgado et al., *Phys. Rev. B* **109**, 245126, 2024.
[2] D. Oue and M. G. Silveirinha, *Phys. Rev. Research* **8**, 013158, 2026.

Atomistic Electromagnetic Model for Realistic Nanoplasmonics

Tommaso Giovannini[1,*]

[1]Department of Physics, University of Rome Tor Vergata, Via della Ricerca Scientifica 1, Rome, Italy
*Corresponding author: tommaso.giovannini@uniroma2.it

***Abstract*—We present an atomistic classical electromagnetic model that enables the simulation of the plasmonic response of realistic nanostructures. Our framework captures intraband and interband response, quantum tunneling in subnanometer gaps, and atomistic effects of defects, porosity, and chemical composition, including alloys and graphene.**

***Keywords*— nanoplasmonics, atomistic, quantum tunneling, interband transitions, sensing, field enhancement.**

I. Introduction

Nanoplasmonics exploits the collective excitations of conductive electrons, known as localized surface plasmons, to confine and enhance electromagnetic fields at the nanoscale, enabling applications in optical sensing, field enhancement, photocatalysis, and light-matter manipulation [1]. Predictive modeling becomes challenging when atomistic morphology, defects, and subnanometer gaps play a crucial role in determining the plasmonic response.

II. Methods

We develop a fully atomistic, classical electrodynamics framework based on frequency-dependent response charges and dipoles assigned to each atom, modeling Drude-like intraband conduction, and interband transitions, respectively [4]. The method also incorporates a phenomenological description of quantum tunneling, enabling the treatment of subnanometer junctions [3]. We here discuss an open-source implementation which enables large-scale simulations and post-processing of field-related observables [5].

III. Results and Discussion

The atomistic description captures key nanoplasmonic trends, including tunneling-mediated behavior in subnanometer gaps [3] and the role of interband effects in realistic metals [4]. In particular, we show that the method can accurately describe the optical response of bimetallic systems [6], graphene substrates [7], nanoparticles in solution [8], polycrystalline substrates [9], ultrafast plasmonics [10], atomically defined structures such as picocavities [11], and porous materials [12].

IV. Conclusion

Our atomistic classical electromagnetic model provides a scalable and physically grounded route to model nanoplasmonic response across materials, morphologies, and gap regimes relevant to sensing, enhanced spectroscopies, and ultrafast nanophotonic design.

Acknowledgments

This work has received funding from the ERC under the European Union's Horizon Europe research and innovation programme (grant no. 101219149, project CHOPIN). Views and opinions expressed are however those of the author only and do not necessarily reflect those of the European Union or ERC Executive Agency. Neither the European Union nor the granting authority can be held responsible for them.

References

[1] K. L. Kelly, E. Coronado, L. L. Zhao, and G. C. Schatz, "The optical properties of metal nanoparticles: The influence of size, shape, and dielectric environment," *J. Phys. Chem. B*, vol. 107, pp. 668–677, 2003.

[2] J. Langer *et al.*, "Present and future of surface enhanced Raman scattering," *ACS Nano*, vol. 14, pp. 28–117, 2020.

[3] T. Giovannini, M. Rosa, S. Corni, C. Cappelli, "A classical picture of subnanometer junctions: an atomistic Drude approach to nanoplasmonics," *Nanoscale*, vol. 11, pp. 6004-6015, 2019.

[4] T. Giovannini, L. Bonatti, P. Lafiosca, L. Nicoli, M. Castagnola, P. G. Illobre, S. Corni, and C. Cappelli, "Do we really need quantum mechanics to describe plasmonic properties of metal nanostructures?," *ACS Photonics*, vol. 9, pp. 3025–3034, 2022.

[5] T. Giovannini, P. Grobas Illobre, P. Lafiosca, L. Nicoli, L. Bonatti, S. Corni, C. Cappelli. "plasmonX: an Open-Source Code for Nanoplasmonics," *Comput. Phys. Commun.*, vol. 322, p. 110035, 2026.

[6] L. Nicoli, P. Lafiosca, P. Grobas Illobre, L. Bonatti, T. Giovannini, and C. Cappelli, "Fully atomistic modeling of plasmonic bimetallic nanoparticles: nanoalloys and core-shell systems," *Front. Photon.*, vol. 4, p. 1199598, 2023.

[7] T. Giovannini, L. Bonatti, M. Polini, and C. Cappelli, "Graphene plasmonics: Fully atomistic approach for realistic structures," *J. Phys. Chem. Lett.*, vol. 11, pp. 7595–7602, 2020.

[8] L. Nicoli, S. Sodomaco, P. Lafiosca, T. Giovannini, and C. Cappelli, "Atomistic Multiscale Modeling of Colloidal Plasmonic Nanoparticles," *ACS Phys. Chem. Au*, vol. 4, pp. 669–678, 2024.

[9] S. Zanotto, L. Bonatti, M. F. Pantano, V. Miseikis, G. Speranza, T. Giovannini, C. Coletti, C. Cappelli, A. Tredicucci, and A. Toncelli, "Strain-induced plasmon confinement in polycrystalline graphene," *ACS Photonics*, vol. 10, pp. 394–400, 2023.

[10] P. Lafiosca, L. Nicoli, S. Pipolo, S. Corni, T. Giovannini, and C. Cappelli, "Real-time formulation of atomistic electromagnetic models for plasmonics," *J. Phys. Chem. C*, vol. 128, pp. 17513–17525, 2024.

[11] T. Giovannini, L. Nicoli, S. Corni, and C. Cappelli, "The Electric Field Morphology of Plasmonic Picocavities," *Nano Lett.*, vol. 25, pp. 10802–10808, 2025.

[12] T. Tapani, J. M. Pettersson, N. Henriksson, C. M. Brunner, A. C. Zimmermann, E. Zäll, N. V. Hauff, L. Das, A. Sapunova, A. Balestra, G. Cuscunà, A. De Andrés, T. Giovannini, D. Garoli, N. Maccaferri, "Morphology-modified contributions of electronic transitions to the optical response of plasmonic nanoporous gold metamaterial," *Nat. Commun.*, vol. 17, p. 829, 2026.

Time-Domain Modeling of Pulsed Dielectric Laser Accelerators

D. Guarnera[1], H. Y. Donkeng[2], R. Palmeri[3], G. S. Mauro[4], N. Salerno[1], A. Bacci[5], S. C. Pavone[1], G. Torrisi[4], A Locatelli[2,*], G. Sorbello[1]

[1]University of Catania, DIEEI, Italy
[2]University of Brescia, DII, Italy
[3]University Mediterranea of Reggio Calabria, DIIES, Italy
[4]National Institute for Nuclear Physics, LNS, Italy
[5]National Institute for Nuclear Physics, INFN-Milano, Italy
*Corresponding author: andrea.locatelli@unibs.it

***Abstract*— Dielectric laser accelerators based on waveguiding structures have recently emerged as a promising platform for compact, high-gradient particle acceleration. In this work, a general time-domain modeling for waveguide dielectric accelerators operating in the pulsed regime is presented. Accounting for the pulse propagation within the tapered structure, the developed approach ensures continuous synchronization between the accelerating field and particle motion by co-determining the waveguide taper and particle dynamics along the accelerating path. This is achieved using a beam propagation method, and the taper is accurately modeled by considering its impact both on higher-order dispersion coefficients and on the guided field amplitude. The approach demonstrates high versatility and accuracy and provides a robust framework for the development of next-generation compact dielectric laser accelerators for advanced scientific and medical applications.**

***Keywords*— Dielectric laser accelerators, guided-wave structures, time-domain electromagnetic modeling, optical pulse propagation, dispersion engineering, tapered waveguides.**

I. Introduction

The concept of laser light for particle acceleration was first proposed in 1962. However, it was only after approximately five decades, with the development of suitable laser sources and advanced lithographic nanofabrication techniques, that the first experimental demonstration was achieved.

In this framework, an efficient approach is provided by guided-wave, laser-driven accelerators, where a well-confined laser mode copropagates with the particle beam. These co-propagating schemes facilitate the design of extended interaction lengths, as the laser power distribution network scales linearly with the structure length L. In contrast, side-pumped configurations require a more complex two-dimensional feeding network, whose footprint scales as L^2.

However, guided-wave structures require precise synchronization of both phase and group velocities of the accelerating wave. The phase velocity of the accelerating wave must be progressively matched to the instantaneous electron velocity, with proposed approaches including tapered slot waveguides and tapered dielectric-lined waveguides.

Phase slippage, caused by a mismatch between phase velocity and beam velocity, typically absent in relativistic designs, can be effectively mitigated by tapering the accelerating structure enforcing continuous synchronous acceleration. However, unless continuous-wave (CW) operation is employed, the particle–laser interaction is often limited by walk-off effects arising from group velocity mismatch.

II. Methods and Results

To properly consider temporal effects, a time-domain modeling framework for dielectric laser accelerators (DLAs) operating in the pulsed regime is proposed. The method incorporates pulse propagation using a Beam Propagation Method (BPM) that solves the Schrodinger equation, allowing us to self-consistently describe dispersion and field evolution within the structure. Following the design principle which enforces particle synchrony through the modal characterization of the waveguide under analysis, the taper of the dielectric structure is co-determined with the particle dynamics at each point along the accelerating path, based on the pulse propagation within the taper itself.

The BPM algorithm proper operation is cross validated by exploiting the solution of an analytically derived ODE for particle dynamics and a pulse envelope obtained from a simplified slot waveguide model, in which some taper induced effects on the propagation are neglected. The proposed method is quite general, and it is discussed with respect to silicon slot waveguides as the accelerating structures.

Acknowledgments

This work was supported in part by the Italian Ministry for University and Research and the European Union – Next Generation EU Mission 4 Component 1, as part of PRIN 2022 project DOSE (CUP D53D23001350006) and PRIN 2022 PNRR project IDEAS (CUP E53D23014520001) and from the INFN V National Committee through the CoDLAS grant.

Enhanced Light Absorption and Photoluminescence in monolayer WS_2 on Si Huygens Metasurface

Junichi Takahara[1,2*]

[1]Dept. of Applied Physics, Graduate School of Eng., The University of Osaka, Japan
[2]Photonics Center, Graduate School of Eng., The University of Osaka, Japan
*Corresponding author: takahara@ap.eng.osaka-u.ac.jp

***Abstract*— We demonstrate enhanced light absorption and photoluminescence from two-dimensional exciton in monolayer WS_2 placed on Silicon Huygens Metasurface. We attribute such phenomena to the formation of Miexciton, which is a coupled mode of Huygens dipoles in Mie resonator and A-exciton in monolayer WS_2.**

***Keywords*— metasurface, Huygens metasurface, CMDC, WS_2**

I. Introduction

Two-dimensional (2D) nanomaterials hold promise for many photonics applications [1]. Thanks to strong 2D exciton confinement, monolayer transition metal dichalcogenides (TMDCs) are expected to be applied in nanophotonic devices as semiconductor at room temperature. However, light-matter interaction is weak due to the monolayer thickness; absorptivity of exciton in monolayer TMDCs is 2-12% [2].

To further enhance absorptivity of 2D exciton, plasmonic nanocavity utilizing a metal mirror has been proposed so far [2,3]. Recently, we theoretically proposed an absorption enhancement method based on the degenerate critical coupling (DCC) in Silicon (Si) Huygens metasurface coupled with TMDC as shown in Fig. 1. Numerical simulations show that absorption of Miexciton reaches ~0.9, with WS_2 contributing an absorption fraction of 0.7, corresponding to an enhancement factor of about 12 compared with WS_2 on a bare quartz substrate [4].

In this study, we report the recent progress of our experimental results of absorption and photoluminescence (PL) in monolayer WS_2 hybridized with Si Huygens metasurface.

II. FABRICATION AND MEASUREMENT

We used Si metasurface consisting of cylindrical crystalline Si (c-Si) nanocavity with the radius of 114nm, the height of 86nm and the period of 334nm, placed on a quartz substrate. It was fabricated by conventional nanofabrication process using electron beam lithography and dry etching system. After fabrication, we transferred commercially available monolayer WS_2 onto it by surface-energy-assisted transferring process.

Measurements of optical reflection and transmission spectra were performed using an optical microscope with a focal spot diameter of 2μm with 20x objective lens and a supercontinuum white-light source.

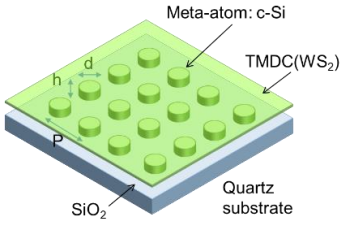

Fig. 1 Schematic view of Si Huygens metasurface coupled with TMDC (WS_2 etc.).

III. RESULTS AND DISCUSSION

In experiments, we observed the total absorptivity of the Miexciton reaches ~0.84. In addition, the PL measurements reveal an emission intensity increase exceeding 18-fold [5]. These results suggest the cooperative excitation of electric and magnetic dipole modes under DCC enables substantial enhancement of optical absorption and emission processes, providing a powerful strategy for boosting light–matter interactions in 2D nanomaterials.

Acknowledgments

This work was supported in part by Japan Society for the Promotion of Science (KAKENHI 23H00274).

References

[1] F. J.G. de Abajo *et al.*, "Roadmap for Photonics with 2D Materials," ACS Photonics, 12, pp. 3961–4095, 2025.
[2] I. Epstein *et al.*, "Near-Unity Light Absorption in a Monolayer WS_2 Van der Waals Heterostructure Cavity," Nano Lett., 20, pp. 3545–3552, 2020.
[3] N. Ansari *et al.*, "Enhancement of light absorption in a WS_2 monolayer using spacer and Au layers," J. Appl. Phys., 127, 063101, 2020.
[4] D. Chen, and J. Takahara, "Enhancement of excitonic absorption in WS_2 mediated by Huygens Si metasurfaces," Opt. Lett., 50(13), pp. 4246 – 4249, 2025.
[5] D. Chen, and J. Takahara, "Demonstration of Miexciton: enhancement of light–matter interaction in monolayer WS_2 on a Si metasurface," Opt. Lett., 50(24), pp. 7508 – 7511, 2025.

Controlling Light confinement in metasurfaces: Gold Temporal Chirality and hBN Mie Resonators

Oscar R. Avalos-Ovando[1,*], Wei Wang[2], Ruggero Emmanuele[3], Gary Wiederrecht[2], Lucas V. Besteiro[4], Alexander Govorov[5], Sergio E. Ulloa[5], Xuedan Ma[2,3]

[1]Dept. of Nanoscience, Joint School of Nanoscience and Nanoengineering, University of North Carolina at Greensboro, Greensboro, NC, USA
[2]Center for Nanoscale Materials, Argonne National Laboratory, Lemont, Illinois, USA
[3]Dept. of Materials Science and NanoEngineering, Rice University, Houston, Texas, USA
[4]CINBIO, Universidade de Vigo, 36310 Vigo, Spain
[5]Dept. of Physics and Astronomy and Nanoscale and Quantum Phenomena Institute, Ohio University, Athens, Ohio, USA
*Corresponding author: oravalosova@uncg.edu

***Abstract*—We study two types of metasurfaces platforms for controlling light confinement. First, we show temporal chirality imprinting in several gold metastructures, both chiral and achiral. Second, we demonstrate high Q-factors in a square array of tapered cylindrical resonators of hexagonal boron nitride, which can even increase upon coating.**

***Keywords*— metamaterials, plasmonics, chirality, Mie, gold, hexagonal boron nitride.**

I. Introduction

Metastructures, which are repeated patterns of some material/shape supported by a substrate that collectively create a new resonant structure upon illumination, have allowed engineering new ultrafast light manipulation devices. In plasmonic materials, such as Au, a new knob in plasmonics has emerged over the past decade, chiral plasmonics.[1] Whereas chiral metastructures have been previously studied in the CW regime, there are a few reports on how chiral photothermal responses behave at ultrafast time scales. Here, we computationally study both chiral and achiral metastructures, and how they respond to ultrashort illumination pulses.[2] On the other hand, in all-dielectric (Mie) materials, research is mainly driven by their low material losses and support of both electric and magnetic Mie modes.[3] There is, however, an important caveat in coupling quantum emitters to dielectric Mie modes: shielding decreases Q-factors. Here we study the effects of shielding hBN resonators with PMMA, and show they are efficient in sustaining large Q-factors and even hosting qBICs.[4]

II. Methods

To computationally model the optical properties of the metastructures, we used COMSOL Multiphysics® commercial software, with the RF module. The system is built with a typical absorption/scattering far-field setup, as a periodic array of resonators on a substrate, where a plane polarized electromagnetic wave is incident on the resonators with normal incidence. We first compute a background field from the plane wave incident on the substrate and then use that to calculate the total field with the resonators present. The absorption is calculated by integrating the total power dissipation density over the resonator's volume. The transmittance T and reflectance R are finally calculated by integrating the time-averaged Poynting vector over set planes below and above the resonators array.

III. Results and Discussion

For the plasmonic gold's metastructure, we consider the interaction of the gold structures with their environment media set as glass. We irradiate the gold nanostructures with circularly polarized light (CPL) in two regimes, either the static CW (linear response) or the temporal pulsed excitation, and then for the latter we study the photothermal induced heat propagation due to photoinjected carriers with two models: a 1T model which solves the lattice temperature Tl, and a 2T model which solves both the electronic temperature Te and the lattice temperature Tl simultaneously.

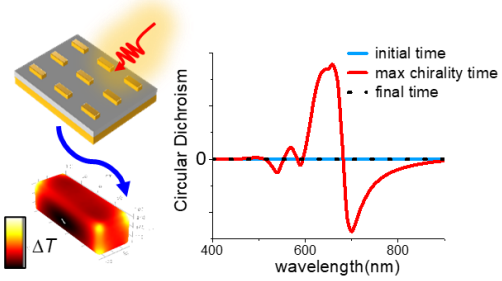

Fig. 1 - Schematics of photothermal heating concept, for a nanorods metastructure (left). Three circular dichroism (CD) traces for different times, showing a regime in where CD is finite (red).

We find that CPL pulses induced new near-field chiral patterns in different plasmonics hotspots of each structure (Fig. 1, left), at different time scales, which we identify and classify. These near-field patterns translate into a finite circular dichroism spectrum at specific time scales, even for geometrically achiral resonators (Fig. 1, right). We find that this effect is rather universal at every structure we studied, which is why we termed the effect "chirality imprinting." We also discuss why the mostly used thermal 1T model cannot fully describe the photothermal effects associated with chirality imprinting, such that the 2T model becomes necessary. Our findings agree very well with recent reported experiments.[5]

For the Mie resonators here studied, specifically hBN truncated-cones, we consider an infinite array of resonators on a quartz substrate, and we illuminate the metastructure or various resonator heights and light wavelengths (schematics in Fig. 2, right). First, we study the case when the resonators are without shielding, just with surrounding air (Fig. 2, blue curve). As the height of the resonators increases, the electric dipole (ED) and magnetic dipole (MD) modes decouple, with the ED remaining mostly in the visible region (610-640 nm) and the MD extending to the NIR. In particular, the Q-factor typically defined as the frequency-to-bandwidth ratio of the resonator, shows to be high (~50), as one can measure from the blue spectrum in Fig. 2.

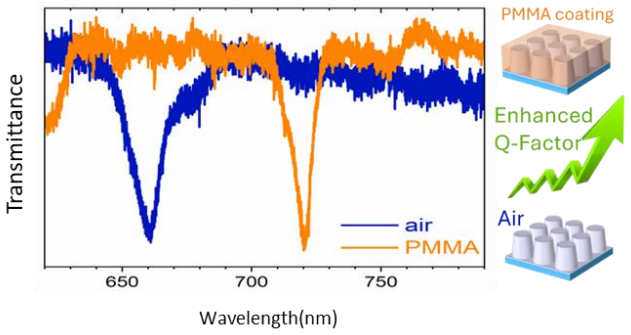

Fig. 2 Measured transmittance spectra of 420 nm high resonators array, before and after being coated with PMMA. Schematics shown on the right.

After PMMA coating, the MD resonance, which occurs ~620-700 nm in the height range investigated before coating PMMA, redshifts by nearly 40 nm (Fig. 2, orange curve). Also, the Q-factor now reaches values of ~100. The clear improvement in Q-factor by designing vertically symmetric structures signals the potential for improving light confinement in properly designed resonator arrays.

IV. Conclusion

Using realistic models of gold achiral and chiral metastructures, we demonstrate the chirality imprinting in several anisotropic metastructures. The mechanism of chiral imprinting is owing to an interplay between the external CPL and the strong local fields in a metastructure. We have also demonstrated qBIC based on a low refractive index material, hBN. We find that the quality factor of its tapered cylindrical resonator arrays increases when approaching the qBIC condition. Moreover, quality factors of the resonator arrays can be further improved by PMMA coating to symmetrize their dielectric environment. These finds suggest qBIC as an effective approach for concentrating light in low-index dielectric materials.

Acknowledgments

O.A.-O. and A.O.G acknowledge the generous support from the United States-Israel Binational Science Foundation (BSF), Grant No. 2018050. L.V.B acknowledges the support from the Spanish Ministerio de Ciencia e Innovacion through a Ramon y Cajal fellowship (RYC2021-033818-I) and under projects Grant Nos. PID2020–118282RA-I00 and TED2021–130038A-I00. W.W., G.W., and X.M. acknowledge support from the U.S. Department of Energy, Office of Science, Basic Energy Sciences, Materials Science and Engineering Division, and BES Microelectronics, under Contract No. DE-AC02-06CH11357. R.E. acknowledges support from the National Science Foundation under award no. DMR-2421596.

References

[1] Y. Yao, O. Avalos-Ovando, T. Ding, R. A. Alvarez-Puebla, P. Yu, E. Ashalley, L. Ma, Z. Wang, G. Markovich, and A. O. Govorov, "From chiral biomolecules to chiral nanocrystals: A review of the latest developments and emerging concepts," Chem Cell, vol. 11, pp. 102544, 2025.

[2] O. Ávalos-Ovando, V. A. Bahamondes Lorca, L. V. Besteiro, A. Movsesyan, Z. Wang, G. Markovich, A. O. Govorov, "Universal imprinting of chirality with chiral light by employing plasmonic metastructures," Applied Physics Reviews, vol. 10, pp. 031412, 2023.

[3] K. Koshelev, and Y. Kivshar, "Dielectric Resonant Metaphotonics," ACS Photonics, vol. 8, pp. 102-112, 2021.

[4] W. Wang, R. Emmanuele, G. Wiederrecht, O. Avalos-Ovando, S. E. Ulloa, and X. Ma, "Confining Light in Hexagonal Boron Nitride Photonic Resonators," submitted, 2026.

[5] A. S. Kim, A. Goswami, M. Taghinejad, and W. Cai, "Phototransformation of achiral metasurfaces into handedness-selectable transient chiral media," PNAS, vol. 121, pp. e2318713121, 2024.

Quantum Corrections in Nanoplasmonics and Thermoelectric Phenomena with Graphene Plasmons

P. André D. Gonçalves[1,*]

[1]POLIMA – Center for Polariton-driven Light-Matter Interactions, University of Southern Denmark, Denmark
*Corresponding author: padgo@mci.sdu.dk

***Abstract* — We present analytical expressions for quantum-corrected scattering coefficients of metallic cylinders, discussing how quantum effects influence plasmon resonances and light–matter interactions in single cylinders and in dimers. We then show that graphene plasmons can be leveraged to probe ultrafast thermoelectric phenomena and manipulate donor–acceptor energy-transfer rates in nanoribbons.**

***Keywords* — quantum plasmonics, graphene plasmonics, thermoplasmonics, light–matter interactions.**

Metallic nanostructures at the nanometer scale ($\lesssim$10 nm) exhibit optical responses that deviate from classical predictions due to quantum nonlocal effects. Additionally, such nonclassical effects also arise in larger systems when plasmon-mediated interactions involve near fields with large wavevector components [1–3]. The surface-response formalism based on Feibelman's *d*-parameters provides a general and practical framework for incorporating quantum nonlocal effects in nanoplasmonic systems [1–3]. After reviewing recent progress in this area, we present closed-form, analytical expressions for the *d*-parameter-corrected scattering coefficients of metallic cylinders (including both quantum effects as well as retardation), thereby completing the set of highly symmetric canonical geometries—the planar interface and the sphere having been derived previously in Refs. [3] and [1], respectively. We further analyze the impact of quantum surface response on plasmon resonances, plasmon-mediated Purcell enhancement, and electron energy-loss spectra for both single metallic cylinders and dimers.

In the second part, we present a novel scheme for probing ultrafast thermoelectric effects in graphene following plasmon-enhanced light absorption in nanostructured graphene. In particular, we theoretically show how graphene nanostructures can be designed in such a way that the absorbed power density has an inhomogeneous distribution and thus generates a transient (~ps regime) non-uniform temperature distribution, which, in turn, leads to finite electromotive force, due to the so-called Seebeck effect, and whose signature is the presence of an ultrafast electric field. We further show that this ultrafast, transient field can be sizable and propose approaches to measure it experimentally, namely, by monitoring the Stark shifts of a nearby molecule or quantum dot/well or by employing ultrafast electron microscopy techniques

REFERENCES

[1] P. A. D. Gonçalves, et al., "Plasmon–Emitter Interactions at the Nanoscale", Nat. Commun. **11**, 366 (2020).
[2] P. A. D. Gonçalves, *Plasmonics and Light–Matter Interactions in Two-Dimensional Materials and in Metal Nanostructures: Classical and Quantum Considerations* (Springer Nature, 2020).
[3] P. J. Feibelman, "Surface electromagnetic fields", Prog. Surf. Sci. **12**, 287–407 (1982).

Electrical Control of Light–Matter Interactions and Nonlinear Optics in Plasmonic Tunnel Junctions

Hayk Harutyunyan[1,*]

[1]Department of Physics, Emory University, Atlanta, GA, USA
*Corresponding author: hharuty@emory.edu

***Abstract*— Ultrastable epitaxial plasmonic tunnel junctions combine extreme optical confinement with direct electrical control. I will present clear identification of photon-assisted transport mechanisms including optical rectification and hot-electron currents, and demonstrate electrically tunable second-harmonic generation with large modulation depths, establishing this platform for active nonlinear nanophotonics.**

***Keywords*— metamaterials, plasmonics, tunnel juntions, nonlinear optics, second harmonic generation, optical rectification.**

REFERENCES

[1] Y. Tang, S. Prakash, M. S. Allen, J. W. Allen, A. Ariando, A. Agrawal, H. Harutyunyan, "Electrically tunable nonlinear light generation in plasmonic tunnel junctions" Optica, 13, 476–484, (2026)

[2] Y. Tang, S. Prakash, P. Nandi, A. Ariando, A. Agrawal, H. Harutyunyan, "Light-Matter Interaction in Ultrastable Tunneling Nanogaps" ACS Nano, 19, 27204–27214, (2025)

Engineering Plasmonic Nanoantennas to Boost Quantum Emitter Performance in the Visible and NIR

Nerea Zabala[1,2,3,*], Luis Montaño-Priede[2], Mario Zapata-Herrera[3], Ruben Esteban[2,3], Javier Aizpurua[1,3,4]

[1]Department of Electricity and Electronics, University of the Basque Country (EHU), Bilbao, Spain
[2]Materials Physics Center CSIC-EHU, Donostia-San Sebastian, Spain
[3]Donostia International Physics Center, Donostia-San Sebastian, Spain
[4]Ikerbasque, Basque Foundation for Science, Bilbao, Spain
*Corresponding author: nerea.zabala@ehu.eus

***Abstract*—We present a theoretical investigation of light emission enhancement of quantum emitters placed in plasmonic nanoantenna configurations. Numerical simulations are illustrated with experimental studies of photoluminescence enhancement of quantum dots in gold nanoantenna metasurfaces. The work provides design guidelines for efficient visible and near-infrared light emission engineering in nanophotonic platforms.**

***Keywords*— plasmonic nanoantenna, quantum emitter, photoluminescence enhancement, FDTD.**

Plasmonic nanostructures offer powerful tools to tailor and enhance light emission properties of quantum emitters, enabling performance improvements across a wide range of photonic technologies. This work presents a unified overview of recent advances in the design, modeling, fabrication, and optical characterization of hybrid systems combining colloidal quantum dots with engineered plasmonic nanoantennas operating from the visible to the near-infrared (NIR) spectral ranges. We first establish a theoretical framework by systematically analyzing four canonical nanoantennas—spheres, rods, disks, and crescents—configured in single, gap, and nanoparticle on mirror geometries [1]. Electromagnetic finite difference time domain (FDTD) simulations reveal that rod-based gap nanoantennas provide the strongest photoluminescence enhancement, reaching up to three orders of magnitude through combined increases in excitation rate, quantum yield, radiative efficiency, and emission directivity. These insights guided the experimental realization of an accessible plasmonic nanocavity formed by double gold discs separated by a silica spacer. A controlled wet etching step selectively opens the cavity gap, enabling deterministic quantum dot placement and yielding photoluminescence enhancements up to tenfold over a gold film and 3.5-fold relative to closed gap antennas [2].
Extending these concepts to technological NIR wavelengths, we demonstrate selective excitation and photoluminescence enhancement of PbS/CdS quantum dots coupled to gold crescent metasurfaces designed for telecommunication 1.55 μm wavelength operation. The anisotropic plasmonic response enables polarization dependent enhancement factors up to 1.6, consistent with 3D FDTD simulations [3].
Altogether, these studies provide design guidelines and experimental validation for plasmon enhanced quantum emitter architectures, paving the way toward high performance light sources for quantum technologies, imaging, sensing, and telecommunications.

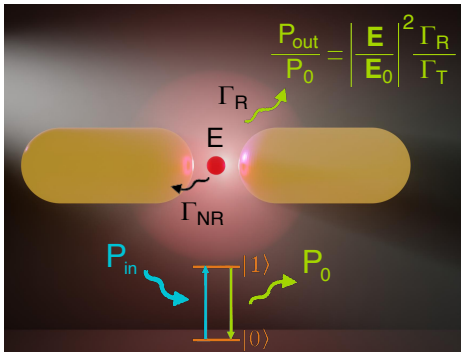

Fig. 1. Schematic of photoluminescence enhancement of a quantum emitter (red dot) in a plasmonic cavity formed by two metallic nanoantennas.

We acknowledge financial support by MICIU/AEI/10.13039/501100011033 and ERDF/EU through Project Ref. No. PID2022-139579NB-I00, and by the Department of Science, Universities and Innovation of the Basque Government through Project Ref. No. IT1526-22.

References

[1] J. L. Montaño-Priede, M. Zapata-Herrera, R. Esteban, N. Zabala, and J. Aizpurua, "An Overview on Plasmon-enhanced Photoluminescence via Metallic Nanoantennas," *Nanophotonics*, vol. 13(26), pp. 4771–4794, 2024.

[2] V. Gupta, J. L. Montaño-Priede, S. Hu, E. S. A. Goerlitzer, M. Zapata-Herrera, R. Esteban, N. Zabala, J. J. Baumberg, J. Aizpurua, and N. Vogel , "Emission Enhancement of Colloidal Quantum Dots Confined in Double Disc Nano-antennas with Controlled Opening," *Nanoscale*, vol. 18, pp. 1576–1588, 2026.

[3] A. Al-Hamadani, V. Gupta, J. L. Montaño-Priede, R. Thomas, A. Muravitskaya, L. Markey, C. Roux-Byl, T. Pons, M. Zapata-Herrera, N. Zabala, J-C. Weeber, S. Suckow, N. Vogel, J-S. G.Bouillard, and A. M. Adawi, "Photoluminescence Enhancement at Telecom Wavelengths from PbS/CdS Quantum Dots coupled to a Plasmonic Crescent Metasurface," *ACS Appl. Nano Mater.*, vol. 8, pp. 19474–19482, 2025.

Free Space Whispering Gallery Microlaser for Biosensing

Stefano Ferretti, Angela Capocefalo and Neda Ghofraniha*
Institute of Complex Systems-National Council of Reseatch (ISC-CNR)
* neda.ghofraniha@cnr.it

***Abstract*—We report a free-space Whispering Gallery Mode (WGM) microlaser designed for highly sensitive, specific, label-free biosensing. By monitoring shifts in the lasing emission induced by minute enviromental changes, the device enables robust detection of biomolecular interactions without the need for fiber or waveguide coupling. Deep learning autoencoder is also used for automated spectral feature extraction.**

***Keywords*— microlaser, whispering gallery, deep learning, photonic biosensor.**

I. Introduction

Free-space Whispering Gallery Mode (WGM) microlasers provide an ultra-sensitive and compact photonic platform for biosensing applications. In these devices, light is confined along the perimeter of high-Q microresonators, where minute changes in refractive index or absorption—caused by interactions with biomolecules, cells, or nanoparticles—induce measurable shifts in the lasing emission[1], [2]. The free-space configuration removes the need for fiber or waveguide coupling, simplifying the experimental architecture and enabling more robust and efficient detection in open or microfluidic environments. Owing to their high sensitivity, rapid response, and potential for miniaturization, free-space WGM microlasers offer a promising label-free biosensing approach with potential applications in early diagnostics, environmental monitoring, and high-precision biomolecular analysis.

To date, sensing with WGM microlasers has predominantly relied on detecting fine spectral line shifts [3], [4], [5]. Despite the excellent sensitivities achieved through this approach, its dependence on manual or semi-automated spectral fitting remains a significant bottleneck. Incorporating artificial intelligence for automated analysis could dramatically improve the speed, robustness, and accuracy of next-generation photonic sensors. Moreover, in many practical situations the spectral resolution of spectrographs is not sufficiently high to reliably resolve the minute wavelength shifts in the emission spectra that need to be detected. A tool capable of exploiting the full spectral information—rather than relying solely on peak positions—and reducing it to a small set of robust parameters suitable for sensing would therefore represent a major advancement in the field.

In this work, we design, fabricate, and validate a highly sensitive free-space microlaser biosensor for accurate and specific detection of label-free antigens. We demonstrate that the proposed photonic immunosorbent microsensor PHISA is capable of revealing 10 pg mL^{-1} of IFN-γ protein concentration in a small sample volume of 2 μL.

Moreover, we investigate the use of autoencoder-based deep learning for the analysis of WGM microlaser spectra. We use the experimental spectra as input and from the latent representation, we extract two or three parameters that are show to be directly linked to physical quantities of interest. We demonstrate their evolution and their sensitivity to subtle environmental changes experienced by the microsensors.

II. Results and Discussion

For specific sensing, we develop a protocol to functionalize the surface of our dyed microspheres. Using a commercial ELISA kit for human IFN-γ, we functionalize the sphere surfaces with the capture antibody and with the reagents designed in the ELISA procedure to coat the bottom of multiwell plates. The final product is a suspension of polymeric microspheres coated with a specific antibody that enables the attachment of IFN-γ proteins. Our procedure monitors the gradual attachment dynamics of the antigens to the microsphere surface by recording time-resolved emission spectra. We apply 2 μL of IFN-γ–buffer dispersion onto the antibody-coated spheres and acquire emission spectra over time. Gradual wavelength shifts occur as a direct consequence of protein attachment. To exclude non-specific effects, we also monitor a control sample containing only buffer; as expected, its spectral position remains unchanged throughout the entire measurement window.

We validate the response of the proposed photonic biosensor by comparing PHISA measurements with a standard ELISA test performed using the same human IFN-γ kit. The optimized immuno-functionalization protocol, together with high-quality spectral acquisition and analysis, provides—for the first time—two measurable parameters, namely the laser resonance shift and its temporal growth rate, that reproduce the standard calibration curve obtained from ELISA assays. These results, fully validated through biochemical controls, open the way to next-generation biosensors powered by photonic devices and immuno-based microlaser technology.

Using the same dataset, we also employ deep-learning autoencoders and extract two reduced parameters from the bottleneck layer. These encoded parameters successfully follow the wavelength-shift and modal-intensity trends observed during the spectral time evolution.

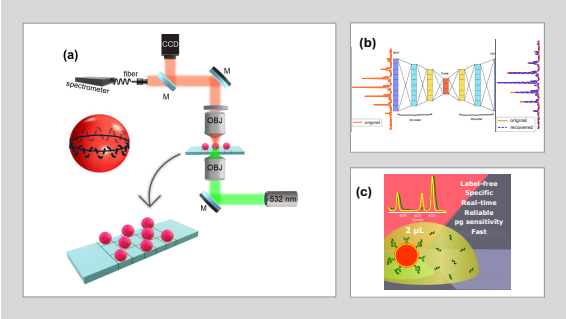

Fig. 1. a) Experimental setup for microlaser excitation and emission. b) Autoencoder that takes the WGM spectra as input and reproduces them as output. From the bottleneck hidden layer, two parameters are extracted that automatically characterize the spectral evolution. c) PHISA cartoon for specific detection.

III. Conclusion

We propose a proof-of-concept photonic microsensor for specific label-free antigen detection, which is easily deployable on any surface and within diverse fluid environments, ideal for cellular and in-vivo applications, without any tagging procedure. The device is cost-effective and does not rely on sophisticated fabrication techniques such as clean room facilities, making it a practical and efficient tool for selective detection. In addition, we show the prototype of an AI assited microsensor which can reveal with accuracy small enviromental variations by using an optimized autoencoder algorithm.

Acknowledgments

We acknowledge Project ECS 0000024 Rome Technopole - CUP B83C22002890005, NRP Mission 4 Component 2 Investment 1.5, Funded by the European Union - NextGenerationEU.

References

[1] N. Toropov, G. Cabello, MP Serrano, R. Gutha, M. Rafti, and F. Vollmer, "Review of Biosensing with Whispering-Gallery Mode Lasers," *Light: Science & Applications*, vol. 10, pp. 1–19, 2021.

[2] A, Capocefalo, E. Quintiero , C. Conti, N. Ghofraniha and I. Viola"Droplet Lasers for Smart Photonic Labels," *ACS Applied Materials & Interfaces*, vol. 13, pp. 51485-51494, 2021.

[3] A, Capocefalo, S. Gentilini, L. Barolo, P. Baiocco, C. Conti, and N. Ghofraniha, "Biosensing with free space whispering gallery mode microlasers," *Photonics Research*, vol. 11, pp. 732–741, 2023.

[4] M. Ceraolo, S. Ferretti, S. Gentilini, A. Capocefalo. C.Bearzi, C. Conti, B. Cortese, R. Rizzi and N. Ghofraniha "Photonic Immunosorbent Assay PHISA for specific detection of label-free biomolecules," *Photonics Research*, Accepted, To be published, 2026.

[5] G. Pirnat, M. Marinčič, M. Ravnik and M. Humar "Quantifying local stiffness and forces in soft biological tissues using droplet optical microcavities," *Proceedings of the National Academy of Sciences*, vol. 121, pp. e2314884121, 2024.

Vibrations of single metal nanoparticles: morphology and environment effects

Nathan Berrit[1], Noelle Lascoux[1], Clément Panais[1], Sylvie Marguet[2], Natalia Del Fatti[1,3], Aurélien Crut[1,*]

[1] Université de Lyon, CNRS-UCBL, Institut Lumière Matière, 69622 Villeurbanne, France
[2] Université Paris-Saclay, CEA, CNRS, NIMBE, 91191 Gif-sur-Yvette, France
[3] Institut Universitaire de France (IUF), France
*Corresponding author: aurelien.crut@univ-lyon1.fr

Abstract— **The vibrational dynamics of gold nanodisks deposited on various solid substrates were investigated using single-particle time-resolved optical spectroscopy combined with finite-element numerical simulations. These studies clarify how the vibrational quality factors depend on both the nanodisk properties and their surrounding environment.**

***Keywords*— Ultrafast dynamics, metal nanoparticles, single-particle spectroscopy, mechanical nanoresonators.**

I. Introduction

Mechanical micro- and nanoresonators play an important role in modern technology. In this context, metal nanoparticles offer several advantages, including high vibrational frequencies in the GHz-THz range, low mass and well-established chemical synthesis and optical probing methods. However, their typically low vibrational quality factors (often only a few tens at room temperature and ambient pressure) constitute a major limitation for practical applications. Improving their performance as mechanical nanoresonators therefore requires a detailed understanding and minimization of vibrational damping mechanisms, namely intrinsic dissipation and acoustic radiation into the surrounding medium. Here, we discuss insights gained from recent systematic studies on the dependence of vibrational quality factors on nano-object morphology and substrate properties.

II. Methods

Gold nanodisks with various diameters were synthesized using colloidal chemistry and deposited on several solid substrates differing in composition and thickness. Optical experiments were performed at the single-particle level, thereby avoiding inhomogeneous broadening effects inherent to ensemble measurements. Spatial modulation spectroscopy was employed to locate individual nanodisks on the substrates and to record their extinction spectra. Single-particle time-resolved optical spectroscopy was then used to probe their transient optical response following impulsive optical excitation. The measured signals exhibit oscillations associated with the acoustic vibrations of the nanodisks, from which vibrational frequencies and quality factors were extracted. These optical experiments were complemented by detailed numerical modeling of the vibrational dynamics, explicitly accounting for radiative damping through the emission of acoustic waves into the surrounding medium.

III. Results and Discussion

Our results elucidate how nanodisk morphology—including diameter, thickness, and deviations from an ideal cylindrical shape—as well as substrate properties influence the vibrational dynamics of the nanodisks. Vibrational frequencies are primarily governed by the nanodisk dimensions and exhibit only a weak dependence on substrate properties. In contrast, vibrational quality factors depend strongly on the substrate, indicating that radiative losses play a dominant role in the damping observed in our experiments. We further discuss, from both theoretical and experimental perspectives, the possibility of a near suppression of radiative damping for specific nanoresonator morphologies [1,2].

IV. Conclusion

This work clarifies the respective roles of intrinsic and extrinsic properties in shaping the vibrational dynamics of metal-based mechanical nanoresonators. Future studies may focus on the experimental observation of vibrational modes with enhanced quality factors, as well as on the analysis of the transient optical response associated with acoustic vibrations.

Acknowledgments

This work was supported by the French National Research Agency (ANR) under the reference ANR-20-CE30-0016 (ULTRASINGLE project).

References

[1] F. Medeghini et al., “Controlling the Quality Factor of a Single Acoustic Nanoresonator by Tuning its Morphology” Nano Lett., vol. 18, 5159-5166, 2018.
[2] A. Crut, “Substrate-supported nano-objects with high vibrational quality factors” J. Appl. Phys., vol. 131, 244301, 2022.

Single-molecule Nanospectroscopy and Beyond with Scanning Tunneling Microscopy

Hiroshi Imada[1,2,3*]

[1] Surface and Interface Science Laboratory, RIKEN, Japan.
[2] Department of Chemistry, Gwangju Institute of Science and Technology, Republic of Korea.
[3] Center for Mesoscopic Sciences, Institute for Molecular Science, Japan.
*Corresponding author: himada@riken.jp

***Abstract*— We developed single-molecule nanospectroscopy combining scanning tunneling microscopy (STM) and near-field optics, enabling submolecular resolution of electronic, optical, and vibrational properties. This photon-STM approach overcomes limitations of conventional spectroscopy, visualizes frontier orbitals, and controls competing processes, offering new insights into excited states and energy conversion at the molecular scale.**

***Keywords*— Single molecule, STM, Near-field optics, Plasmon-enhanced light-matter interaction.**

Frustrated Non-Hermitian Skin Effect and gauge-invariant ladder operators in a Floquet Photonic System

Li Ge[1,2,*]

[1]Department of Physics and Astronomy, College of Staten Island, CUNY, Staten Island, NY, USA
[2]The Graduate Center, CUNY, New York, NY, USA
*Corresponding author: li.ge@csi.cuny.edu

***Abstract*—The non-Hermitian skin effect (NHSE) is conventionally understood as boundary accumulation induced by nonreciprocal couplings. Here we demonstrate the failure of this picture by a geometric scaling of the lattice couplings. We also reveal gauge-invariant ladder operators for the equally spaced Dirac-cone states when the Floquet bandgap closes. *Keywords*—non-Hermitian photonics, skin effect, non-reciprocity, floquet bandgap, ladder operators.**

Non-Hermitian physics [1] is a rapidly developing frontier field that explores intriguing phenomena arising from the openness of physical systems. In contrast to conventional Hermitian systems, non-Hermitian systems display distinctive dynamical behavior arising from complex eigenvalues, leading to the breakdown of energy conservation and adiabaticity. This field encompasses many fascinating symmetries and phenomena, such as parity-time (PT) symmetry, anti-PT symmetry, non-Hermitian particle-hole symmetry, exceptional points, and the NHSE. Their studies not only expand the classification of topological phases in theoretical physics but also provide critical insights into the design of new materials and devices.

The explorations of such non-Hermitian phenomena are carried out on many experimental platforms, such as photonics, electronic circuits, and so on. Among them, optical waveguides provide an excellent opportunity to investigate non-Hermitian physics within the framework of the Schrödinger equation: The propagation of light in such parallel and coupled waveguide systems is governed by the paraxial Helmholtz equation, which is mathematically equivalent to the Schrödinger equation. Distributed optical gain and loss and versatile coupling schemes can be conveniently introduced in the transverse plane, which are crucial to achieve various non-Hermitian symmetry paradigms. In addition, by modifying these waveguides along the propagation axis, a temporally modulated Hamiltonian can be effectively introduced, and this Floquet (i.e., periodic) driving protocol has played a key role in the observation of topological edge states and solitons in the optical domain.

Combining the spatial complexity of non-Hermitian symmetries and the temporal flexibility of Floquet driving further enriches the range of physical effects that can be explored in optical systems. On the one hand, their interplay enables a powerful scheme to exploit coupled spatial and temporal dynamics. On the other hand, Floquet driving enables the realization of effective non-Hermitian Hamiltonians difficult to realize otherwise, such as non-reciprocal couplings in waveguide systems that are fundamental to the observation of the aforementioned NHSE. NHSE is a significant discovery marked by the localization of most (if not all) energy eigenstates at one boundary of the system. On an intuitive level, it is typically attributed to non-reciprocal couplings: The stronger couplings in one direction result in the accumulation of probability amplitudes at the end of that direction.

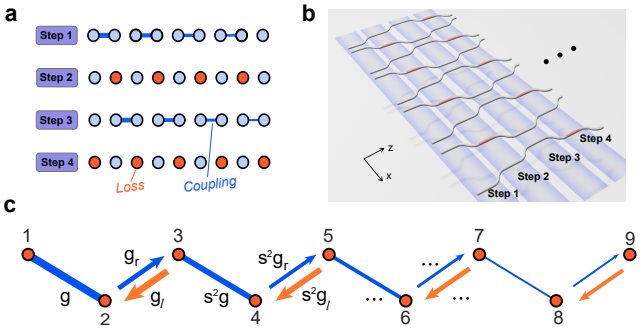

Fig. 1. **Floquet photonic system for FNHSE and NHSE**. **a,b** Schematics of the system and its experimental realization using waveguides. In panel **a**, scaled coupling along the lattice is illustrated using blue lines with different thickness. The identical loss γ is represented by red dots. **c** Simplified Floquet Hamiltonian of our system. Thinning lines and arrows show the scaling of both reciprocal and non-reciprocal couplings towards the right by s^2 $(s < 1)$, starting with $g = sC/4$ and $g_{l,r} = s^2C(1 \mp \tilde{\gamma})/4$ on the left. Red dots show uniform loss $\gamma/4$.

Here, we report the discovery of a "frustrated" non-Hermitian skin effect (FNHSE), where the hallmark boundary accumulation of the NHSE is suppressed by a monotonic geometric scaling of the lattice. We reveal that by varying the lattice spacing and creating a geometric series of couplings (see Fig. 1), a competing localization mechanism—which we term geometric localization—is established. It directly competes with and can cancel out the non-reciprocal skin localization. Consequently, the system undergoes a transition from skin modes back to extended bulk modes. In experiments, we start from a Floquet photonic lattice consisting of optical waveguides fabricated through the femtosecond laser-writing method. A

distinct feature of our system is the generation of effective non-reciprocal couplings from purely reciprocal physical interactions and loss, achieved via a precise spatiotemporal modulation protocol.

By introducing geometric scaling to this Floquet lattice, we observe the breakdown of NHSE: The same excitation that populates an edge state in the uniform lattice now propagates into the bulk in the scaled lattice. These findings demonstrate that lattice geometry can serve as a powerful degree of freedom to impact the manifestations of non-Hermitian topology, expanding the horizon of light modulation and control.

Next, we turn our attention to non-Hermitian operators in a Hermitian Floquet system, similar to that shown in Fig. 1 but without the loss. When its Floquent bandgap closes, a Dirac cone is formed in the continuous limit, and correspondingly, we find equally spaced Floquet quasi-energies in the finite lattice.

To understand their origin, we turn to the ladder operators, with examples such as the creation and annihilation operators used in quantum harmonic oscillators. They are non-Hermitian by nature and provide an elegant approach to solve or understand otherwise intricate physics problems. Here, we discuss ladder operators for a discrete energy spectrum bounded both from below and above. They still lead to equally spaced energy levels, but importantly, the repeated applications of the raising or lowering operator cycle through all these energy levels periodically, with the highest (lowest) level directly descending (asending) to the lowest (highest) level via a single raising (lowering) operation. Different from their non-cyclic counterparts, these cyclic ladder operators, while still non-Hermitian, have a complete eigenbasis and can be diagonalized, which makes them gauge-invariant.

REFERENCES

[1] L. Feng, R. El-Ganainy, and L. Ge, “Non-Hermitian photonics based on parity–time symmetry,” Nature Photonics, vol. 11, pp. 752, 2017.

Topological metasurface based on exceptional points

Qinghua Song[1,*]

[1]Tsinghua Shenzhen International Graduate School, Tsinghua University, Shenzhen, China
*Corresponding author: song.qinghua@sz.tsinghua.edu.cn

***Abstract*— In this talk, we will present topological metasurface based on exceptional points and their applications in wavefront manipulation. Unconventional arbitrary polarized exceptional point and zero-eigenvalue exceptional point are demonstrated.**

***Keywords*— metasurface, exceptional point, non-Hermitian, topological photonics.**

I. Introduction

Exceptional points (EPs) are spectral singularities of non-Hermitian systems that occur whenever complex eigenvalues and eigenstates coalesce, leading to a reduction of the Hilbert space dimension. Traditional photonic systems typically exhibit coalesced eigenstates that correspond to circularly polarized light of a specific handedness, thereby restricting their applicability to only two antipodal points located on top or bottom of the Poincaré sphere. Here, we introduce a continuum of EPs for which the corresponding coalesced eigenstates can access any point on the Poincaré sphere (**Fig. 1**). Our theoretical proposal and experimental implementation overcome the main practical limitation of EPs, extending the applicability of the topological phase to any arbitrarily-polarized light state. In addition, we theoretically and experimentally demonstrate a counterintuitive topological strategy based on zero-eigenvalue EP (**Fig. 2**), in which the complete suppression of the system scattering enables an effective expansion of accessible topological degrees of freedom. The emergence of these non-conventional EPs not only introduces a realm of disruptive applications in wavefront engineering and optical multiplexing, but also brings in new fundamental properties of topological systems in general.

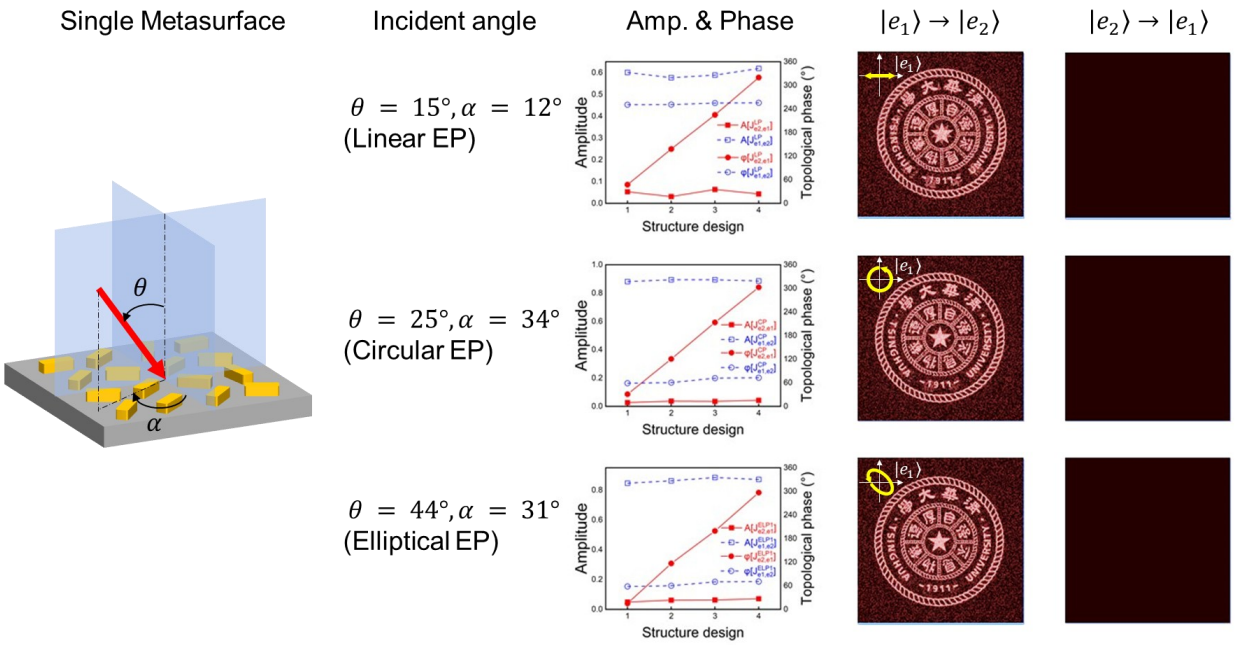

Fig. 1 Single metasurface for arbitrary polarized exceptional points.

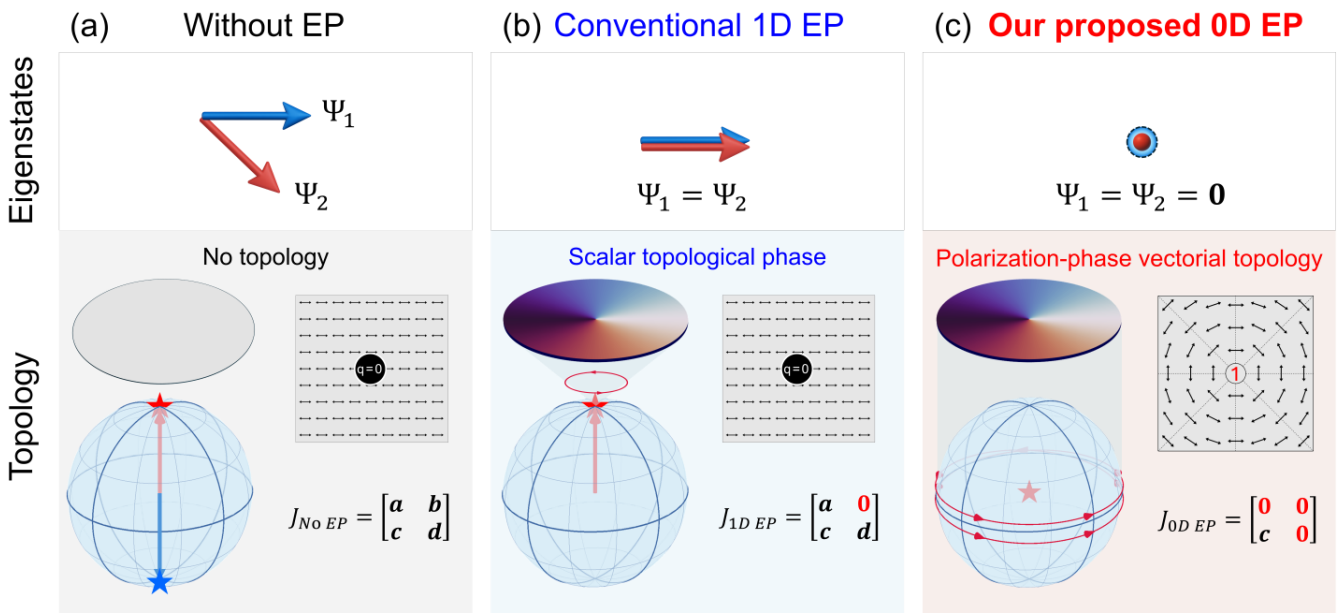

Fig. 2 Zero-eigenvalue exceptional point with vectorial topology

REFERENCES

[1] Q. Song, M. Odeh, J. Zúñiga-Pérez, B. Kanté, P. Genevet, "Plasmonic topological metasurface by encircling an exceptional point," Science, vol. 373, pp. 1133-1137, 2021.

[2] Z. Yang, P.-S. Huang, Y.-T. Lin, H. Qin, J. Zúñiga-Pérez, Y. Shi, Z. Wang, X. Cheng, M.-C. Tang, S. Han, B. Kanté, B. Li, P. C. Wu, P. Genevet, Q. Song, "Creating pairs of exceptional points for arbitrary polarization control: asymmetric vectorial wavefront modulation," Nature Communications, vol. 15, pp. 232, 2024.

[3] Z. Yang, P.-S. Huang, Y.-T. Lin, H. Qin, J. Chen, S. Han, W. Huang, Z.-L. Deng, B. Li, J Zúñiga-Pérez, P. Genevet, P. C. Wu, Q. Song, "Asymmetric Full-Color Vectorial Meta-holograms Empowered by Pairs of Exceptional Points," Nano Letters, vol. 24, pp. 844–851, 2024.

[4] H. Qin, Z. Yang, P.-S. Huang, X. Mu, S.-H. Huang, Y. Shi, W. Zhao, B. Li, J. Zhou, J. Zúñiga-Pérez, P. Genevet, P. C. Wu, Q. Song, "Sphere of arbitrarily polarized exceptional points with a single planar metasurface," Nature Communications, vol. 16, pp. 2656, 2025.

Metasurfaces-Enabled Cold Atoms Array Generation

Thu H. H. Le,[1] R. Takei, A. Takamizawa,[1] S. Kagami,[2] Y. Kurashima,[1] T. Motomura[1]*

[1] National Institute of Advanced Industrial Science and Technology (AIST), Japan
[2] NEC-AIST Quantum Technology Cooperative Research Laboratory, Japan
*Corresponding author: thu.le@aist.go.jp

***Abstract*—This study reports a novel scheme of using flat optics composed of dielectric metasurfaces to prepare arrays of individual cold atoms. Our method exploits the capabilities of metastructures in controlling the phase, amplitude and polarization states of light at the sub-wavelength resolution to generate specific wavefronts necessary for magneto-optical trapping and optical dipole trapping of neutral atoms.**

***Keywords*—cold atoms array, dielectric metasurfaces, magneto-optical trapping (MOT), optical dipole trapping (ODT).**

I. Introduction

Cold-atom arrays prepared by laser cooling and trapping are central to precision measurements and quantum technologies, underpinning advances in quantum metrology, sensing, quantum computing, and quantum simulation. In typical experiments, alkali or alkaline-earth atoms confined in an ultrahigh-vacuum chamber are first cooled near the Doppler limit using a magneto-optical trap (MOT) and subsequently trapped and arranged into lattice configurations using optical dipole traps (ODTs). However, conventional MOT and ODT implementations rely on complex and bulky optical systems, resulting in large experimental footprints and high sensitivity to optical misalignment. Here, we propose and experimentally demonstrate a metasurface-based platform that integrates laser cooling and optical trapping within a compact and planar architecture. By exploiting dielectric metastructures capable of controlling the phase, amplitude, and polarization of light at sub-wavelength scale, our approach enables both cooling and the assembly of cold atoms into arrays using planar optics.

II. Methods

For magneto-optical trapping, we design and demonstrate a metasurface-based MOT configuration that employs Pancharatnam–Berry (PB) phase metastructures to simultaneously engineer transmitted and diffracted wavefronts with the circular polarizations required for MOT operation. This scheme enables stable cooling and trapping under axial illumination using a single planar element, significantly reducing system complexity compared with the conventional six-beam MOT configuration.

Atoms cooled by the metasurface MOT are subsequently arranged into prescribed arrays using ODTs based on the optical tweezer principle. We demonstrate a metasurface hologram that simultaneously generates and focuses light into arrays of focal spots, forming optical tweezer arrays under the irradiation with a collimated beam, as described in Fig. 1(a).

III. Results and Discussion

Operating at the 940-nm ODT wavelength, the metasurface functions as a phase-only hologram, in which the phase profile is implemented through the in-plane rotation of PB-phase metastructures. Owing to its subwavelength-scale phase modulation—approximately 20 times finer than that achievable with conventional spatial light modulators—the fabricated meta-hologram produces trapping potentials equivalent to those of a high-numerical-aperture lens with *NA* up to 0.9, corresponding to a beam waist of 635 nm, shown in Fig. 1(b)). Furthermore, it enables the formation of dual-spot arrays with inter-spot separations approaching the diffraction limit of light.

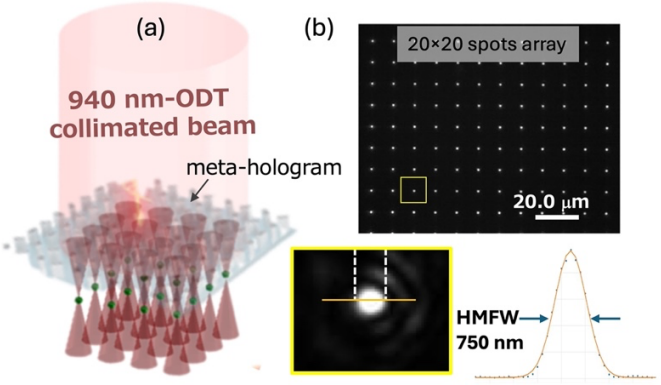

Fig. 1. (a) Schematic and (b) demonstration of optical tweezer arrays with beam waist of 635 nm generated by meta-hologram.

IV. Conclusion

These results demonstrate the feasibility of metasurface-enabled cooling and trapping of neutral atoms without the need for additional bulk optical components. The high optical efficiency, scalability, and planar integration offered by metasurfaces highlight their potential for realizing compact cold-atom platforms with broad applications in quantum metrology, quantum information processing, and atomic physics.

Acknowledgments

This study was supported by PRESTO (JPMJPR235C) from The Japan Science and Technology Agency.

Ultra-confined plasmonics for control of light-matter interactions at nanoscale

Alexey V. Krasavin[1,*], Junsheng Zheng[2], Chenxinyu Pan[2], Limin Tong[2], Pan Wang[2], Anatoly V. Zayats[1]

[1] Department of Physics and London Centre for Nanotechnology, King's College London, Strand, London WC2R 2LS, UK

[2] Interdisciplinary Center for Quantum Information, New Cornerstone Science Laboratory, State Key Laboratory of Extreme Photonics and Instrumentation, College of Optical Science and Engineering, Zhejiang University, Hangzhou 310027, China

*Corresponding author: alexey.krasavin@kcl.ac.uk

***Abstract*— Ultra-confined plasmonics provides a unique opportunity to localize and enhance light at the subwavelength dimensions, offering a wide playground for manipulation of light-matter interactions. In this talk we will overview our recent results on plasmonically-assisted control of strong coupling, electroluminescence and nonlinear harmonic generation at the nanoscale.**

***Keywords*— plasmonics, single nanocavity, ultrathin, strong coupling, electroluminescence, nonlinear harmonic generation.**

I. Introduction

Enhancement of optical fields with photonic nanostructures strongly intensifies optical phenomena at the nanoscale. Furthermore, when the size of the nanostructures themselves approaches few nanometers, quantum effects, such as quantum confinement and electron tunnelling come into consideration. These two classes of phenomena, especially through their interplay, provide ample abilities to enhance and control light-matter interactions at the length scales down to atomic dimensions.

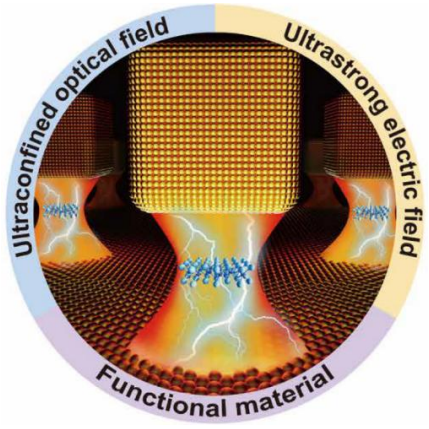

Fig. 1 Concept of electrically-driven active control of light-matter interactions in plasmonic nanocavities, encompassing enhanced optical field, ultrastrong electric field and functional materials.

II. Results and Discussion

In this talk we will overview our recent results on plasmonically-assisted manipulation and enhancement of light-matter interactions at the nanoscale. Combining intensified optical fields, ultrastrong control electrical fields and functional materials (Fig. 1), we demonstrate highly-efficient electrical control of excitonic strong coupling and tunnelling-driven electroluminescence in plasmonic nanocavities, formed by single crystal gold nanocubes and microflakes, and functionalized with semiconductor monolayers [1]. For strong coupling, the application of a moderate bias of just 2.5 V created an ultrastrong electric field across the functionalized nanocavity gap and led to the realization of reversible modulation of the Rabi splitting between 108 and 102 meV. With the decrease of the nanocavity gap down to 2.5 nm, electron tunnelling regime has been initiated, leading to the onset of excitonic electroluminescence, which spectral position can be controlled by voltage polarity. Furthermore, the developed approach of atomic-level precision chemical etching allowed us to fabricate microflakes of a truly nanometer thickness [2,3], which led to the observation of resonant nonlinear harmonic generation enabled by quantization of the electronic levels across the flake.

III. Conclusion

The overviewed novel approaches for electrically- and optically-driven control of light at the nanoscale, open new opportunities in both fundamental research and development of new generation of active photonic devices.

Acknowledgments

This work was supported by National Key Research and Development Project of China (grant 2023YFB2806701 to P.W.), National Natural Science Foundation of China (grants

62075195, 92250305, and 92150302 to P.W.), UK EPSRC CPLAS project EP/W017075/1 (to A.V.Z.), New Cornerstone Science Foundation (nci202216 to L.To.), and Zhejiang Provincial Natural Science Foundation of China (grant LDT23F04015F05 to P.W.).

REFERENCES

[1] J. Zheng, A. V. Krasavin, R. Yang, Z. Wang, Y. Feng, L. Tang, L. Li, X. Guo, D. Dai, A. V. Zayats, L. Tong, and P. Wang, "Active control of excitonic strong coupling and electroluminescence in electrically driven plasmonic nanocavities," *Science Advances*, vol. 11, article eadt9808, 2025.

[2] C. Pan, Y. Tong, H. Qian, A. V. Krasavin, J. Li, J. Zhu, Y. Zhang, B. Cui, Z. Li, C. Wu, L. Liu, L. Li, X. Guo, A. V. Zayats, L. Tong, and P. Wang, "Large area single crystal gold of single nanometer thickness for nanophotonics," Nature Communications, vol. 15, article 2840, 2024.

[3] L. Liu, A. V. Krasavin, J. Zheng, Y. Tong, P. Wang, X. Wu, B. Hecht, C. Pan, J. Li, L. Li, X. Guo, A. V. Zayats, and L. Tong, "Atomically smooth single-crystalline platform for low-loss plasmonic nanocavities," Nano Letters, vol. 22, pp. 1786–1794, 2022.

Quantum Non-Reciprocity in Photon-Pair Generation from Nonlinear Metasurfaces

Jinyong Ma[1,2,*], Xiwen Qiu[1], Tongmiao Fan[1], Tuomas Haggren[1], Hark Hoe Tan[1], Chennupati Jagadish[1], Andrey A. Sukhorukov[1]

[1]ARC Centre of Excellence for Transformative Meta-Optical Systems (TMOS), Department of Electronic Materials Engineering, Research School of Physics, The Australian National University, Canberra ACT 2601, Australia

[2]Institute of Quantum Precision Measurement, State Key Laboratory of Radio Frequency Heterogeneous Integration, College of Physics and Optoelectronic Engineering, Shenzhen University, Shenzhen 518060, P. R. China

*Corresponding authors: jinyong.ma@szu.edu.cn, andrey.sukhorukov@anu.edu.au

***Abstract*—Photon-pair generation from ultra-thin nonlinear metasurfaces opens new frontiers in quantum technologies. We reveal that the quantum photon states can exhibit a strongly non-reciprocal behaviour, where the generation rate and quantum entanglement can dramatically vary when the optical pump is incident on either side of the metasurface.**

***Keywords*— non-reciprocity; metasurface; biphoton entanglement**

I. Introduction

Optical metasurfaces incorporating nonlinear materials are emerging as new platforms for generating photon pairs through spontaneous parametric down-conversion (SPDC) at the nanoscale with tunable frequency [1] and polarization [2], [3], [4] entanglement. However, the directional control of quantum states was limited to nonreciprocal structures with thickness of multiple wavelengths [5]. We reveal, for the first time to our knowledge, that photon generation from metasurfaces with sub-wavelength-thin nonlinear nanostructures can exhibit strong non-reciprocity. Specifically, we predict theoretically and establish experimentally that the rate and quantum state of the signal and idler photons can dramatically depend on their emission and the pump incidence directions, as schematically illustrated in Fig. 1.

II. Results and Discussion

We demonstrate nonreciprocity for a semiconductor metasurface incorporating [110] InGaP nano-resonators with approximately cylindrical shapes [4]. Whereas the presence of the substrate makes the whole metasurface asymmetric, the linear transmission and reflection remains independent of the pump direction.

Most remarkably, we find that the nonlinear process of SPDC can feature strong differences in the generation of entanglement between various polarization components depending on the incidence direction, as sketched in Fig. 1. Our numerical simulations identify optimal metasurface designs that resonantly enhance nonreciprocity, enabling a generation rate contrast up to 20 dB and a creation of totally distinct quantum states. We further confirm these principles experimentally by fully characterizing the quantum states.

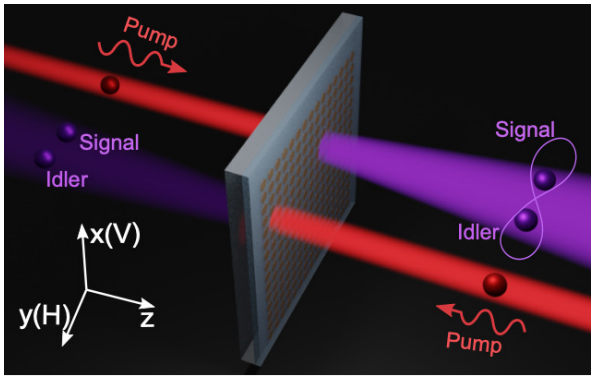

Figure 1. Concept of non-reciprocal generation of quantum-entangled pairs of signal and idler photons from a nonlinear metasurface. The process efficiency and emerging quantum state can dramatically depend on the pump incidence and the corresponding photon emission directions.

III. Conclusion

In conclusion, we report the first prediction and experimental observation of quantum nonreciprocity in the generation of entangled photons from ultra-thin nonlinear metasurfaces, revealing new possibilities for multi-functional and reconfigurable operation of quantum nanophotonic devices.

References

[1] T. Santiago-Cruz *et al.*, "Resonant metasurfaces for generating complex quantum states," *Science*, vol. 377, pp. 991–995, 2022.

[2] J. Noh *et al.*, "Quantum pair generation in nonlinear metasurfaces with mixed and pure photon polarizations," *Nano Lett.*, vol. 24, pp. 15 356–15 362, 2024.

[3] W. H. Jia *et al.*, "Polarization-entangled Bell state generation from an epsilon-near-zero metasurface," *Sci. Adv.*, vol. 11, p. eads3576, 2025.

[4] J. Y. Ma *et al.*, "Nonlinearity symmetry breaking for generating tunable quantum entanglement in semiconductor metasurfaces," *Sci. Adv.*, vol. 11, p. eadu4133, 2025.

[5] J.-T. Pan *et al.*, "Nonreciprocal quantum photon-pair source with chiral ferroelectric nematics," *arXiv*, p. 2503.11399, 2025.

Aluminum optical nanoantennas

Davy Gérard[1,*]

[1]Light, nanomaterials, nanotechnologies (L2n), Université de Technologie de Troyes & CNRS, Troyes, France
*Corresponding author: davy.gerard@utt.fr

***Abstract*— Aluminum supports broadband plasmonic resonances from the UV to the IR and offers a low-cost platform for optical nanoantennas. This contribution reviews single aluminum antenna characterization by EELS, from nanorods to fractal geometries, notably highlighting plasmon–interband hybridization effects.**

***Keywords*— optical nanoantennas, aluminum, electron energy-loss spectroscopy.**

I. Introduction

Aluminum exhibits a broadband plasmonic response spanning from the ultraviolet (UV) to the infrared (IR) spectral range. In addition to this wide spectral coverage, it is an abundant, low-cost, and non-critical material that is fully compatible with CMOS technology [1]. Despite exhibiting higher losses than noble metals, aluminum therefore represents an attractive platform for the realization of optical nanoantennas operating over a broad wavelength range.

II. Results and discussion

This contribution provides an overview of aluminum-based optical nanoantennas, with a particular emphasis on single-antenna characterization. Electron energy-loss spectroscopy (EELS) is employed to investigate the localized surface plasmon resonances supported by these structures, ranging from simple nanorod antennas [2] to more complex fractal-like geometries (Fig. 1). [3]

The influence of bulk aluminum interband transitions and their hybridization with surface plasmon modes is then discussed, as this interplay can critically shape the optical response of these nanoantennas. [4] Finally, selected applications of these structures are presented, notably their use for luminescence enhancement. [5]

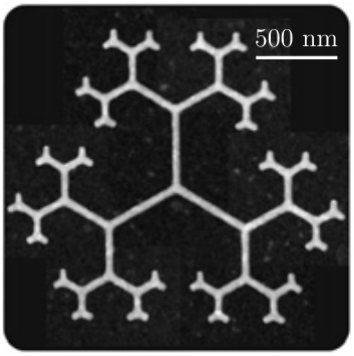

Fig. 1 Example of fractal-like aluminum nanoantenna

Acknowledgments

This work received support from National Agency for Research under Grant QUENOT (ANR-20-CE30-0033). We acknowledge financial support from CNRS-CEA "METSA" French Network (Grant FR CNRS 3507) on the platform LPS-STEM. Samples were realized on the Nanomat platform (https://www.nanomat.eu/).

References

[1] Gérard, D., & Gray, S. K. "Aluminium plasmonics," *Journal of Physics D: Applied Physics* 48(18), 184001, 2015.

[2] Martin, J., Kociak, M., Mahfoud, Z., Proust, J., Gérard, D., & Plain, J. "High-resolution imaging and spectroscopy of multipolar plasmonic resonances in aluminum nanoantennas," *Nano Letters* 14(10), 5517-5523, 2014.

[3] Simon, T., Li, X., Martin, J., Khlopin, D., Stéphan, O., Kociak, M., & Gérard, D. "Aluminum Cayley trees as scalable, broadband, multiresonant optical antennas," *Proceedings of the National Academy of Sciences* 119(4), e2116833119, 2022.

[4] Martin, J., Avalos-Ovando, O., Simon, T., Arditi, G., Lamaze, F., Proust, J., ... & Gérard, D. "Plasmon-Interband Hybridization and Anomalous Production of Hot Electrons in Aluminum Nanoantennas," *ACS Nano* 19, 22343-22356, 2025.

[5] Simon, T., Kostcheev, S., Rumyantseva, A., Béal, J., Gérard, D., & Martin, J. "Band-edge emission enhancement in sputtered ZnO thin films with ultraviolet surface lattice resonances," *Journal of Applied Physics* 130(22), 2021.

A nuclear clock accelerated by collective coherence

Karen Mamian[1,*], Georgy A. Kazakov[2,3], Jan de Haan[4],
Kasper van Gasse[4], Thorsten Schumm[2], and Charles Roques-Carmes[1]

[1]Institute of Science and Technology Austria (ISTA), Klosterneuburg, Austria
[2] Atominstitut TU Wien, Vienna, Austria
[3] Wolfgang Pauli Institute (WPI), Vienna, Austria
[4] Photonics Research Group, INTEC, Ghent University–imec, Ghent, Belgium
*Corresponding author: karen.mamian@ist.ac.at

***Abstract*—We propose and analyze a method to accelerate the operation of a nuclear clock based on collective nuclear coherence build-up in a doubly resonant cavity doped with thorium-229.**

***Keywords*— nuclear clock, thorium-229, cavity QED.**

I. Introduction

Passive optical atomic clocks, based on electronic transitions in atoms, provide an unmatched precision and stability [1]. A clock based on a nuclear transition instead would naturally offer even greater robustness to external perturbations [2]. The uniquely low-lying ^{229}Th isomer at $\hbar\omega_{\rm iso} = 8.4$ eV (148 nm), recently excited by a vacuum ultraviolet (VUV) laser in breakthrough experiments with Th:CaF_2 crystals [3], is a strong candidate for the clock transition, although standard Ramsey/Rabi interrogation protocols are not directly applicable. Therefore, the leading proposal for a nuclear frequency standard relies on a fluorescence-based nuclear clock scheme [4], requiring long interrogation and detection cycles due to the isomer's long lifetime, as well as a technically demanding 148 nm light source.

Recently, the optonuclear quadrupolar (ONQ) two-photon pumping mechanism [5] was proposed, which enables the use of a commercially available 296 nm laser operating in air, instead of a 148 nm VUV laser necessary for single-photon excitation of the isomer transition. Here, we propose to leverage and analyze the coherent collective dynamics of an ensemble of ^{229}Th nuclei in a doubly resonant cavity, pumped by a laser at $\omega_{\rm iso}/2$ via the ONQ, to accelerate the clock operation and open a path toward on-chip integration.

II. Methods

The interaction between N identical coherently driven ^{229}Th nuclei (whose ground $\leftrightarrow$ isomeric transitions are described by effective spin operators $\sigma^i_{+,-}$) and a photonic 148 nm ($\omega_2 = \omega_{\rm iso}$) cavity mode (annihilation operator a_2) is modeled by the Hamiltonian:

$$\frac{H}{\hbar} = \Delta a_2^\dagger a_2 + \sum_i^N \Delta\frac{\sigma_z^i}{2} + DE_1^2\left(\sum_i^N \sigma_+^i + \sum_i^N \sigma_-^i\right) + G\left(a_2\sum_i^N \sigma_+^i + a_2^\dagger\sum_i^N \sigma_-^i\right), \quad (1)$$

where $\Delta = \omega_2 - 2\omega_{\rm pump}$ is the pump detuning, $G = \frac{\langle\mu\rangle}{\hbar}\sqrt{\frac{\mu_0\hbar\omega_2}{2V_2}}$ is the magnetic dipole coupling constant, depending on the 148 nm mode magnetic field volume V_2; $E_1^2 \propto P_{\rm in}Q_1V_1^{-1}$ is pump intracavity electric field, D describes the ONQ matrix element of the 2$^{\rm nd}$ order electric-field gradient response at the site of nuclei. Lindbladian losses include nuclear spontaneous decay γ and decoherence γ_z (fundamentally limited by the interaction with surrounding fluorine spins in the crystal assuming other noise sources are suppressed), and the 148 nm cavity photon lifetime κ_2. For numerical simulations, we consider ^{229}Th embedded (doped or implanted) in a CaF_2 whispering gallery (WGM) mode resonator, a well-established high-Q fluoride platform, and take $\gamma = 1.59\times10^{-3}$ s^{-1} $\ll \gamma_z = 2\pi\times300$ Hz [3], [4]; still, due to the weak coupling of the nucleus to the field we operate in the "bad-cavity" regime: $\kappa_2 \gg 4G^2N/\kappa_2$. Crucially, a spatial homogeneity of G, E_1^2 is assumed, which in the case of WGM could be ensured by phase-matching between the pump 296 nm and transition 148 nm modes so that nuclei emit constructively. Such phase-matching was demonstrated, for example, in lithium niobate WGM resonators [6]; with fluorides, potential ways may include the use of birefringence or geometrical dispersion engineering, as well as deterministic implantation of ^{229}Th into the resonator. However, the described clock photon detection scheme below is general regardless of the specific cavity type. Mean-field equations of motion correctly describe the system dynamics in the considered parameter range (verified by higher-order cumulant expansion simulations [7]).

III. Results and Discussion

The simulated output 148 nm photon flux dynamics $\Phi_2^{\rm out}(t) = \kappa_2^{\rm ext}|a_2|^2$ is shown on Fig. 1. As the cavity loss is the dominant rate in the system, a_2 adiabatically follows the collective nuclear dipole: $\langle a_2\rangle = \frac{-2iGN\langle\sigma_-\rangle}{\kappa_2+2i\Delta}$. $\Phi_2^{\rm out}(t,\Delta)$ reaches an intermediary plateau on the timescale of dephasing $t_1 = 1/\gamma_z$, where nuclei are not significantly excited up to $\sim t_2$. Using the approach based on two subsequent measurements with red- and blue-shifted pumping laser frequency from [4] to determine and correct the interrogating frequency offset, we propose to collect the coherent photons over a shorter

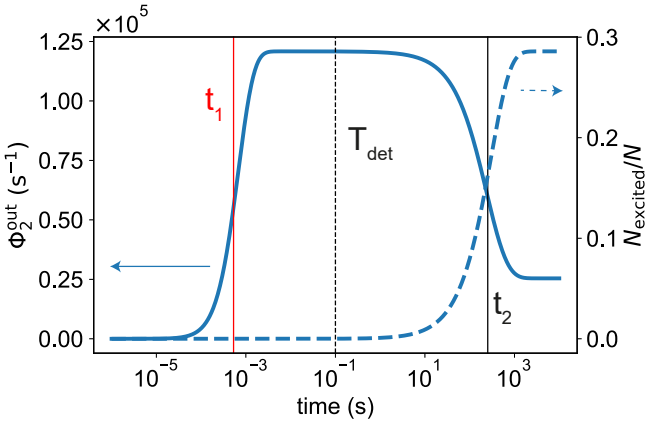

Fig. 1. Mean-field dynamics of the system with a constant input power of $P_{\text{in}} = 5$ mW, where $t_1 = 1/\gamma_z, t_2 = \gamma + 4\Omega^2/\gamma_z$.

time, until $T_{\text{det}} \ll t_2$. With a peak $\Phi_2^{\text{out}}(\Delta) \approx 10^5$ s^{-1} and $T_{\text{det}} \approx 0.1$ s one can measure a total of $\Phi_2^{\text{out}}(\Delta) \times T_{\text{det}} = 10^4$ photons. Then, as the pump is turned off at T_{det}, the photon number (adiabatically following $|\langle\sigma_-\rangle|^2$) decays on the millisecond timescale of coherence (γ_z), not the 100-1000 s of the nuclear decay (γ) as it would be with incoherent photons generated by nuclear fluorescence. Thus, as photon detection does not require waiting for nuclear deexcitation, the next cycle with an opposite interrogation laser detuning may commence immediately.

IV. Conclusion

We have proposed a nuclear clock scheme which leverages the collective dipole created by the coherent interaction of cavity modes with the nuclear ensemble in the bad-cavity regime, with relaxed requirements on the interrogating system. The described method reduces 1) the detection time itself and 2) the time between the cycles, also featuring no dead-time. Future work is dedicated to quantifying the frequency instability of the proposed scheme.

Acknowledgments

KM and CRC are supported by the Institute of Science and Technology, Austria. The study is supported by ERC Synergy grant no. 856415 “Thorium nuclear clock” and by ERC Starting grant no. 101078281 “LASIQ”.

References

[1] S. M. Brewer *et al.*, “$^{27}Al^+$ Quantum-Logic Clock with a Systematic Uncertainty below 10^{-18},” *Phys. Rev. Lett.*, vol. 123, no. 3, p. 033201, 2019.

[2] E. Peik and Chr. Tamm, “Nuclear laser spectroscopy of the 3.5 eV transition in ^{229}Th,” *EPL (Europhys. Lett.)*, vol. 61, no. 2, p. 181, 2003.

[3] J. Tiedau *et al.*, “Laser Excitation of the Th-229 Nucleus,” *Phys. Rev. Lett.*, vol. 132, no. 18, p. 182501, 2024.

[4] G. A. Kazakov, A. N. Litvinov, V. I. Romanenko, L. P. Yatsenko, A. V. Romanenko, M. Schreitl, G. Winkler, and T. Schumm, “Performance of a ^{229}Thorium solid-state nuclear clock,” *New J. Phys.*, vol. 14, no. 8, p. 083019, 2012.

[5] H. Xu, C. Li, G. Wang, H. Wang, H. Tang, A. R. Barr, P. Cappellaro, and J. Li, “Two-Photon Interface of Nuclear Spins Based on the Optonuclear Quadrupolar Effect,” *Phys. Rev. X*, vol. 13, no. 1, p. 011017, 2023.

[6] J. U. Fürst, D. V. Strekalov, D. Elser, M. Lassen, U. L. Andersen, C. Marquardt, and G. Leuchs, “Naturally Phase-Matched Second-Harmonic Generation in a Whispering-Gallery-Mode Resonator,” *Phys. Rev. Lett.*, vol. 104, p. 153901, 2010.

[7] D. Plankensteiner, C. Hotter, and H. Ritsch, “QuantumCumulants.jl: A Julia framework for generalized mean-field equations in open quantum systems,” *Quantum*, vol. 6, p. 617, 2022.

Ultralow-power-operable monopixel reflective displays with thin-film photonics

Young Min Song[1,*]

[1]School of Electrical Engineering, KAIST, Korea
*Corresponding author: ymsong@kaist.ac.kr

Abstract—We introduce a sub-1-volt, ultralow-power monopixel reflective display utilizing a reconfigurable Gires-Tournois resonator integrated with polyaniline. It achieves dynamic full-color tuning and ultrahigh 16,900 PPI scalability. By incorporating an active-matrix architecture, we resolve high-density array power dissipation, enabling highly efficient next-generation displays.

***Keywords*— Gires-Tournois resonator, reflective display, electrochemistry, thin-film stacks**

The growing demand for advanced terahertz technologies necessitates innovative material design approaches. Achieving vibrant, energy-efficient color modulation across micrometer-scale pixels remains a critical challenge for modern reflective and near-eye displays. Conventional approaches often suffer from scalability limits, high operating voltages, and significant optical losses, hindering their application in ultrahigh-density devices. To overcome these barriers, we present a full-color, electrically reconfigurable Gires-Tournois (r-GT) resonator integrated with a conductive polymer, polyaniline (PANI).

The proposed r-GT architecture utilizes a tailored trilayer design—incorporating a porous Germanium (Pr-Ge) lossy interlayer—that achieves near-perfect optical impedance matching. By driving the PANI layer through distinct redox states within a CMOS-compatible sub-1-volt range (-0.2 V to 0.8 V), the device modulates complex refractive indices to produce sharp resonance shifts. This mechanism yields a vibrant chromatic variation exceeding a complementary hue range (ΔHue ~ 220.6°) while consuming an ultra-low power density of just 90 μW cm^{-2}. Furthermore, the thin-film photonics approach guarantees exceptional scalability, enabling downscaling to a pixel pitch of 1.5 μm (approximately 16,900 pixels per inch) without structural or optical degradation.

In addition to excellent static performance, the r-GT monopixels demonstrate robust electrochemical stability facilitated by an in-situ formed GeO_2 self-passivation layer, which protects the porous structure from acidic electrolytes during rapid redox cycling. The metastable nature of PANI further enables a "Memory-in-Pixel" functionality, retaining optical states without continuous power input and dramatically improving energy efficiency compared to traditional emissive displays. Finally, to extend this technology toward commercial, high-density applications, we demonstrate the integration of these r-GT resonators into an active-matrix architecture. This active-matrix driving addresses the power dissipation and selectivity challenges of passive arrays, establishing a highly reliable and scalable platform for next-generation, ultralow-power reflective displays.

Acknowledgments

This work was supported by National Research Foundation of Korea (NRF) funded by the Ministry of Science and ICT (2023R1A2C3004531, 2021M3H4A1A04086357).

References

[1] J. H. Ko et al., Nanophotonics 13, 749 (2024)
[2] J. H. Ko et al., Light: Sci. & Appl 15, 134 (2026)
[3] J. H. Ko et al., Adv. Mater. 36, 2310556 (2024)

Thermoplasmonic Coupler for On-Chip Spatial Control of Heat Delivery

Giovanni Piscopo[1,*], Francesca Filograno[1,*], Marius Crouzier[2], Béatrice Dagens[2], Giovanna Calò[1], Antonella D'Orazio[1], and Giovanni Magno[1]

[1]Department of Electrical and Information Engineering, Polytechnic University of Bari, Bari, Italy
[2]Centre for Nanosciences and Nanotechnologies, CNRS, Université Paris-Saclay, Palaiseau, France
*Corresponding author: antonella.dorazio@poliba.it

***Abstract*— We introduce a novel thermoplasmonic architecture based on a tapered gold nanoparticle chain coupled to a silicon-on-insulator (SOI) waveguide. Wavelength-dependent plasmonic coupling enables localized heating and reversible vanadium dioxide (VO_2) phase switching with milliwatt-level optical power. This architecture is suitable for integration in photonics devices and may support applications in adaptive optics, optical switching, and programmable photonic systems.**

***Keywords*— integrated plasmonics, phase change materials, silicon photonics, thermoplasmonics, plasmonic chains, VO_2**

I. Introduction

Plasmonic nanostructures enable subwavelength electromagnetic field confinement and efficient light-to-heat conversion, which has motivated extensive research into reconfigurable integrated photonic devices [1]. Their ability to localize optical absorption at the nanoscale has been exploited for a range of photonic functionalities, including modulation, switching, optical trapping [2], and plasmon-assisted interconnects [3]. Thermally mediated effects are particularly relevant when combined with phase-change materials, such as vanadium dioxide (VO_2), which exhibits a reversible insulator-to-metal transition triggered by temperature [4]. The associated variation of its optical properties enables plasmon-assisted architectures based on localized thermal control. Integrating plasmonic structures with silicon waveguides allows localized thermal control through an all-optical, electrical-contact-free approach compatible with silicon photonic platforms.

II. Methods, Results and Discussion

We propose a device comprising a tapered chain of elliptical gold nanoparticles evanescently coupled to a silicon-on-insulator (SOI) waveguide and embedded in a silicon dioxide cladding (Fig. 1). A VO_2 layer is positioned near the plasmonic chain. Near-infrared excitation of the fundamental transverse-electric waveguide mode couples to localized surface plasmon resonances (LSPR) supported by the nanoparticle chain. The tapering introduces a spatially varying plasmonic response that allows phase matching to occur locally at specific sections of the nanoparticle chain; by varying the excitation wavelength, the phase-matched region shifts along the propagation direction. This mechanism results in wavelength-dependent, spatially localized electromagnetic hotspots. Optical–thermal multiphysics simulations are employed to evaluate hotspot localization, absorption, and the associated temperature rise. The extent of the VO_2 area that undergoes metallic phase transitions increases with illumination time and injected power, consistent with a cumulative thermal activation of the insulator-to-metal transition.

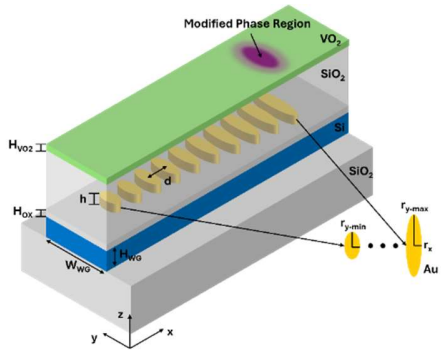

Fig. 1 Sketch of the proposed thermoplasmonic coupler: gold plasmonic chain of ellipsoidal nanocylinders on a SOI waveguide cladded by silicon dioxide.

III. Conclusion

This contribution outlines a thermoplasmonic coupler enabling wavelength-controlled localized heating and reversible phase switching of VO_2. The underlying physical mechanisms, numerical modeling approach, and potential implications for reconfigurable integrated photonics will be discussed in detail during the presentation.

References

[1] M. C. Nevárez Martínez, D. Kreft, M. Grzegorczyk, S. Mahlik, M. Narajczyk, A. Zaleska-Medynska, D. P. Morales, J. A. Hollingsworth, and J. H. Werner, "Numerical simulation of light to heat conversion by plasmonic nanoheaters," Nano Lett., vol. 25, no. 1, pp. 230–235, 2025.

[2] G. Magno, A. Ecarnot, C. Pin, V. Yam, P. Gogol, R. Mégy, B. Cluzel, and B. Dagens, "Integrated plasmonic nanotweezers for nanoparticle manipulation," Opt. Lett. 41, pp. 3679-3682, 2016.

[3] S. Abadian, G. Magno, V. Yam, and B. Dagens, "Broad-band plasmonic isolator compatible with low-gyrotropy magneto-optical material," Opt. Express 29, 4091-4104 (2021)

[4] T. Guo, et al., "Durable and programmable ultrafast nanophotonic matrix of spectral pixels," Nat. Nanotechnol., vol. 19, pp. 1635–1643, 2024.

Laser photo-acoustic spectroscopy with microscope for hyperspectral imaging of absorption and chirality in nanomaterials

Emilija Petronijevic[1,*], Grigore Leahu[1], Claudia Skubisz[1], Imene Kouicem[2], Concita Sibilia[1], Roberto Li Voti[1], Alessandro Belardini[1]

[1]Sapienza University, Department SBAI, Italy
[2]University of Eloued, Physics Department, Algeria
*Corresponding author: emilija.petronijevic@uniroma1.it

***Abstract*— We present a microscope-boosted photo-acoustic spectroscopy set-up which uses a scattering-free photo-acoustic signal to precisely monitor absorption in nanostructures. Multiple degrees of freedom (light polarization, modulation frequency, angle of incidence, positioning, beam diameter, variable power) show great potential in direct characterization of absorption and chirality at the nanoscale.**

***Keywords*— metamaterials, photo-acoustic spectroscopy, microscopy, nanostructures, chirality.**

Transition metal nitrides as potential alternative for noble metals for SERS sensing

Jan Krajczewski[1,*], Aleksandra Michałowska[1], A. Szymańska[1,2], L. Nozka[3,4]

[1]Faculty of Chemistry, University of Warsaw,1 Pasutera Str., 02-093 Warsaw, Poland
[2]Faculty of Physics, University of Warsaw, 5 Pasteura Str., 02-093 Warsaw, Poland
[3]Institute of Physics of the Czech Academy of Sciences, Joint Laboratory of Optics of Palacky University and Institute of Physics AS CR, 17. Listopadu 50a, 772 07 Olomouc, Czech Republic
[4]Palacký University in Olomouc, Faculty of Science, Joint Laboratory of Optics of Palacký University and Institute of Physics AS CR, 17. listopadu 12, 771 46 Olomouc, Czech Republic
*Corresponding author: jkrajczewski@chem.uw.edu.pl

***Abstract*— In this study, we demonstrate a SERS platform based on titanium nitride thin films. The sputtering conditions are shown to strongly influence the resulting film morphology and optical response. Furthermore, the SERS performance of TiN can be improved by decoration with gold nanoparticles.**

***Keywords*— SERS, TiN, titanium nitride, plasmonics, sensors**

I. Introduction

Surface-enhanced Raman spectroscopy (SERS) is one of the most sensitive analytical techniques for the detection of trace amounts of organic molecules. Most SERS platforms rely on plasmonic noble metals such as gold and silver; however, their performance is approaching practical limitations. Therefore, transition metal nitrides, owing to their favorable optical properties, high stability, and good biocompatibility have emerged as promising alternatives to noble-metal-based SERS substrates.

II. Methods

TiN thin films were deposited using magnetron sputtering. Structural characterization was performed using scanning electron microscopy (SEM), while optical properties were investigated by diffuse reflectance spectroscopy (DRS) and spectroscopic ellipsometry. Raman measurements were carried out using a Horiba Jobin–Yvon LabRAM HR800 spectrometer equipped with a 600 grooves/mm holographic grating and a Peltier-cooled CCD detector, under various excitation wavelengths.

III. Results and Discussion

In the research we used oblique angle deposition method to study the morphology of deposited films. SEM analysis showed change in the morphology with the angle deposition. However, the deposited TiN thin films on flat surface did not exhibit high SERS performance, the estimated EF was in the range of 10^3, much lower than typical value for noble metals. Therefore, we have used a new method of RF sputtering that led to formation of films with better optical properties.

In order to increase SERS performance we investigate the Si pyramids samples coated with TiN and Au layers of thicknesses. The SEM analysis showed that deposited TiN and Au layers were continuous and did not cover the morphology of Si micropyramids. The optical studies were done by ellipsometry. SERS results showed that deposition of TiN thin films with nano- or microstructure led to significantly higher SERS performance than in case of deposition on flat surfaces as Si wafers.

We have also further tune the SERS activity of TiN based samples by deposition of gold nanoparticles. In an effect we were able to detect the vitamin B12 even at low concentrations levels as 10^{-9} M.

IV. Conclusion

We have demonstrated that TiN microstructures can be used as SERS-active platforms. Although the achieved enhancement factors are lower than those obtained for noble-metal-based substrates, metal nitrides offer exceptional chemical and thermal stability. Therefore, the further development of TiN-based SERS substrates remains a promising and actively pursued research direction.

Acknowledgments

J. K. thanks the University of Warsaw, Faculty of Chemistry for its financial support, L. N. thanks MSMT of the Czech

Republic (OP JAK CZ.02.01.01/00/22_008/0004596) for its financial support.

References

[1] Ma, J., Wu, M., Du, Y., Chen, S., Li, G. and Hu J. “Synthesis of nanocrystalline titanium nitride at low temperature and its thermal stability”, J. Alloys Compd., Vol. 1-2, 603-605, 2009.

[2] Krajczewski J., Michałowska A., Ctvrtlik R., Nozka L., Tomastik J., Vaclavek L., Turczyniak-Surdacka S., Bieńkowski K., Solarska R. “The battle for the future of SERS – TiN vs Au thin films with the same morphology“,Appl. Surf. Sci., Vol. 618, 156703, 2023.

[3] Michałowska, A., Szymańska, A., Ambroziak, R., Nozka L., Vaclavek, J., Tomastik J., Turczyniak-Surdacka S., J. Krajczewski. “Improved SERS activity of TiN microstructures by surface modification with Au“, J Mater Sci 59, Vol. 59, 16918–16931, 2024.

[4] Nožka, L., Hrabovský, M., Hubička, Z., Písařík̆ová, A., J. Krajczewski, Schovánek, P., Tomáštík, J., Václavek, L. “Plasmonic Characteristics of TiN Layers Deposited by ECWR Assisted MF Magnetron Sputtering”, Advanced Physics Research, Vol. 5, e00166, 2025

Plasmonic Metasurfaces for Enhanced Chiral Sensing

Alexa Guglielmelli[1,2*], Giovanna Palermo[1,2], Giuseppe Strangi[1,2,3]

[1] Department of Physics, NLHT Lab - University of Calabria 87036 - Rende, Italy
[2]CNR-NANOTEC Istituto di Nanotecnologia, 87036 - Rende, Italy
[3]Department of Physics, Case Western Reserve University, 2076 Adelbert Rd, Cleveland, Ohio 44106, USA
*Corresponding author: alexa.guglielmelli@unical.it

***Abstract*—Chirality plays a crucial role in biology and pharmacology, as enantiomers of the same molecule may induce distinct physiological effects. Here we propose plasmonic metasurfaces for enhanced circular dichroism sensing, enabling sensitive and selective enantio-discrimination for biomedical diagnostics and bioanalytical applications.**

***Keywords*— plasmonics, metasurface, biosensing, chirality.**

I. Introduction

Chirality describes the property of an object that cannot be superimposed onto its mirror image. In stereochemistry, such mirror-related structures are referred to as enantiomers. Although enantiomers share the same chemical formula, they can exhibit profoundly different biological activities.

In biological systems, chirality is ubiquitous. Amino acids, proteins, and many metabolites exist in specific handed forms, and deviations from physiological enantiomeric ratios have been correlated with severe pathologies, including neurodegenerative and metabolic diseases. Therefore, accurate enantioselective detection is essential in pharmacology, toxicology, and clinical diagnostics.

Conventional chiral discrimination techniques include liquid chromatography, gas chromatography, capillary electrophoresis, and circular dichroism spectroscopy. Circular dichroism (CD), is defined as:

$$\Delta A(\lambda) = A_L(\lambda) - A_R(\lambda) \tag{1}$$

where A_L and A_R represent the absorbance under left- and right-circularly polarized light, respectively. The CD signal is directly proportional to ΔA. However, natural CD signals of molecules are intrinsically weak, requiring high concentrations and sophisticated instrumentation.

Plasmonic metasurfaces offer a promising alternative. By tailoring subwavelength metallic nanoantennas, it is possible to engineer enhanced electromagnetic near-fields and increase the local optical chirality density. This enables surface-enhanced chiral sensing, overcoming the limitations of traditional CD spectroscopy.

II. Methods

We design, fabricate and characterize two-dimensional plasmonic metasurfaces composed of periodic arrays of metallic nanoresonators supporting localized surface plasmon resonances (LSPR). The metasurfaces are engineered to maximize the local optical chirality density

$$C = -\frac{\omega}{2c^2}\,\mathrm{Im}\left(\tilde{\mathbf{E}}^* \cdot \tilde{\mathbf{H}}\right) \tag{2}$$

in the vicinity of the nanostructures under circularly polarized illumination. In this expression, ω and c are the angular frequency and speed of light in vacuum, and $\tilde{E}$ and $\tilde{H}$ are the complex electric and magnetic field intensities.

Numerical simulations are performed to evaluate the electric and magnetic field distributions and to optimize geometrical parameters for maximum near-field enhancement. Experimental characterization is carried out via reflectance spectroscopy and CD measurements in different refractive index environments and upon biomolecular functionalization.

III. Results and Discussion

- Planar plasmonic metasurfaces provide a scalable and fabrication-friendly platform for chiral sensing.
- The presence of chiral analytes modulates both reflectance and CD responses, enabling enantioselective detection through near-field–mediated light–matter interaction.
- Strong electromagnetic field confinement enhances local optical chirality density, leading to amplified molecular and induced CD signals.
- Refractive index sensitivities reaching several hundred nm/RIU demonstrate competitive performance for label-free biosensing.
- These results validate plasmonic metasurfaces as compact and highly sensitive platforms for enantioselective detection and chiral bioanalysis.

IV. Conclusion

We have presented plasmonic metasurfaces as efficient platforms for enhanced chiral sensing. By engineering near-field distributions and optical chirality density, it is possible to significantly amplify weak molecular CD signals. This approach paves the way toward miniaturized, high-sensitivity devices for pharmaceutical analysis and biomedical diagnostics.

ACKNOWLEDGMENTS

This work was supported by the "NLHT- Nanoscience Laboratory for Human Technologies" - (POR Calabria FESR-FSE 14/20 – CUP: J22C14000230007) and POS RADIOAM-ICA project funded by the Italian Minister of Health (CUP: H53C22000650006). The authors thank the Institute of Applied Sciences and Intelligent Systems "E. Caianiello" CNR, for fabrication support.

REFERENCES

[1] Lininger, A., Palermo, G., Guglielmelli, A., Nicoletta, G., Goel, M., Hinczewski, M., & Strangi, G., "Chirality in Light–Matter Interaction", *Advanced Materials*, vol. 35 (34), pp. 2107325, 2023.

[2] Guglielmelli, A., Palermo, G., & Strangi, G., "Unveiling chirality: Exploring nature's blueprint for engineering plasmonic materials", *Mrs Communications*, vol. 13 (5), pp. 704-713, 2023.

[3] Palermo, G., Guilcapi, B., Kolkowski, R., Guglielmelli, A., Aceti, D. M., Valente, L., ... & Strangi, G., "Plasmonic Metasurfaces with Structural Chirality and Pseudo-Chirality for Enhanced Circular Dichroism and Enantiomeric Recognition", *Advanced Optical Materials*, vol. 14 (1), pp. e02488, 2026.

Complex on-fiber micro-optical systems with high-resolution 3D-printing

Carlo Liberale

Biological and Environmental Science and Engineering Division, KAUST, Thuwal, Saudi Arabia
carlo.liberale@kaust.edu.sa

***Abstract*— Two-photon lithography-based micro-3D printing is a cutting-edge technique for fabricating intricate miniaturized optical systems in situ. Here I present its use in developing innovative fiber-integrated optical devices, with applications including structured light generation and polarization control.**

***Keywords*— 3D printing, optical fibers, microfabrication, structured light.**

I. Introduction

Micro-3D printing based on two-photon lithography is a powerful technology for developing advanced miniaturized optical systems. It provides exceptional design flexibility, high resolution, and the ability to fabricate intricate optical structures in situ with remarkable precision. The process relies on a near-infrared femtosecond laser, tightly focused through a high-numerical-aperture (NA) objective, triggering two-photon absorption and initiating photopolymerization within a confined focal volume. In our research, we utilize a commercial TPL-based micro-3D printing system (Photonic Professional GT, Nanoscribe GmbH) and proprietary acrylate photoresins (Nanoscribe GmbH), selected based on the required resolution and surface smoothness of the fabricated optical components. Notably, this fabrication technique enables the direct in-situ manufacturing of compact hybrid optical systems in a single step [1]. These systems can integrate various photonic components, such as micro-lenses, micro-reflectors, and photonic crystal fiber (PCF)-based waveguides. The ability to integrate these components into a single, compact system highlights the versatility and potential of micro-3D printing in advancing optical technologies.

II. Results and Discussion

A remarkable achievement of this research is the development of an all-fiber polarization beam splitter (PBS) device using photonic crystal fibers (PCFs) [2]. We first demonstrated the drawing-less fabrication of PCF segments by high-resolution 3D printing. Then, the unprecedented precision and flexibility of this method allowed the creation of the first-ever all-fiber polarization beam splitter based on PCFs. The resulting device is ultra-compact, with a total length of just 210μm, and is seamlessly integrated onto a commercial single-mode optical fiber.

In another application, we focused on the on-fiber generation of Bessel beams (BB), which are of great interest in the scientific community due to their diffraction-free propagation and self-healing properties. Generating BB from optical fibers has garnered further interest because of its potential to create compact, robust, and alignment-free devices.

Traditional methods for generating BB from fibers have various limitations and typically only produce zeroth-order BB. To overcome these challenges, we introduced a novel stacked hybrid photonic structure that transforms the output beam from single-mode fibers into both zeroth- and vortex BB [3]. Our approach offers a unified solution to the generation of zeroth- and vortex BB from fibers.

Acknowledgments

The author thanks all the group members and collaborators for their contributions.

References

[1] Gonzalez-Hernandez D., Varapnickas S., Bertoncini A., Liberale C., Malinauskas M., "Micro-Optics 3D Printed via Multi-Photon Laser Lithography," Adv. Optical Mater., Vol. 11, 2201701, 2023.

[2] Bertoncini A., Liberale C., "3D printed waveguides based on photonic crystal fiber designs for complex fiber-end photonic devices," Optica, Vol. 7, 1487-1494, 2020.

[3] Reddy I. V. A. K., Bertoncini A., Liberale C., "3D-printed fiber-based zeroth- and high-order Bessel beam generator," Optica, Vol. 9, 645-651, 2022.

Rice-Mele nanolaser

Kaiwen Ji[1], Melissa Hedir[2], Qi Zhong[3], Ramy El-Ganainy[3], Alejandro M. Yacomotti[1], Li Ge[4]

[1]Laboratoire Photonique Numérique et Nanosciences,
Institut d'Optique d'Aquitaine, Université Bordeaux, CNRS, Rue François Mitterrand, Talence, 33400, France
[2]Laboratoire des technologies de la microelectronique, CNRS, Grenoble, 38054, France
[3]Department of Electrical and Computer Engineering, Saint Louis University, Saint Louis, MO 63103, USA
[4]Department of Engineering Science and Physics, College of Staten Island, CUNY, Staten Island, NY 10314, USA

***Abstract*—We experimentally demonstrate an orbital angular momentum (OAM) nanolaser ring array on an InP photonic crystal membrane implementing a non-Hermitian Rice–Mele model with alternating couplings and imaginary detunings.**

***Keywords*— nanolasers, non-Hermitian photonics, exceptional points, photonic crystals.**

I. Introduction

Structured light sources with controllable orbital angular momentum (OAM) are central to integrated photonics and on-chip beam engineering, yet scalable phase locking of nanolaser arrays remains challenging. Non-Hermitian photonic systems offer new opportunities for enforcing collective phase structure and directional energy transfer through symmetry and exceptional-point physics. Here, we harness a non-Hermitian extension of the Rice–Mele model in a nanolaser ring array to realize robust phase winding and controllable OAM emission.

II. Results and Discussion

The periodic Rice–Mele lattice can host an exceptional point featuring unidirectional power propagation (Figs. 1 (a) and (b)). When two unit cells of this lattice are isolated and arranged into a ring, the unidirectional flow is converted into near-field power circulation, producing orbital angular momentum emission whose origin can be traced to the geometric chirality of the structure (Fig. 1 (c)).

Here, we experimentally implement this concept in an OAM nanolaser array formed in a compact ring on an InP-based photonic crystal membrane, where lasing occurs in a symmetry-protected non-Hermitian zero mode. In this regime, light propagates unidirectionally between nanocavities despite reciprocal coupling, resulting in far-field emission with nonzero OAM. The mechanism is a sequential $\pi/2$ phase shift across the array arising from the interplay between non-Hermitian particle–hole symmetry and broken geometric chirality; as the zero mode approaches a chiral exceptional point, the field amplitudes across the nanolasers become equalized.

This concept motivates an element-wise design strategy, in which the array is constructed from an optimized repeating unit cell. The resulting structure features modulated gain/loss and alternating coupling strengths, effectively realizing a non-Hermitian Rice–Mele model with complex on-site detunings.

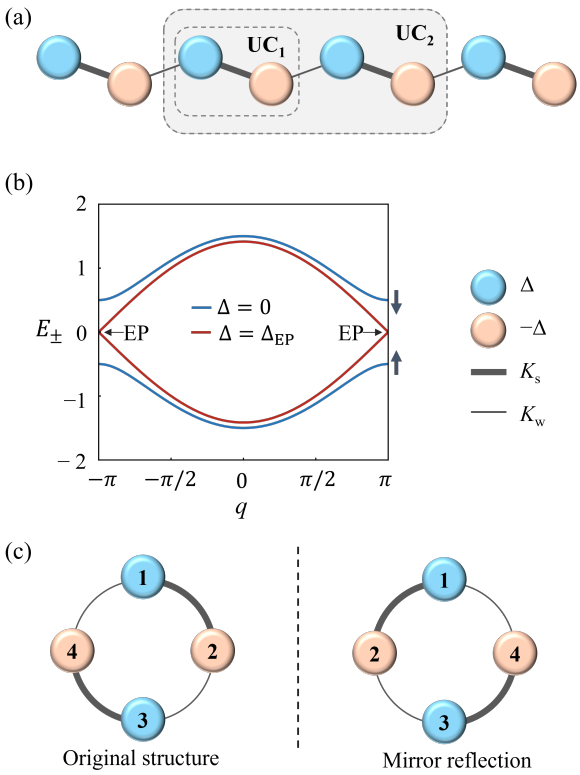

Fig. 1. Conceptual illustration of the operating principle of the non-Hermitian Rice–Mele laser demonstrated in this work.

III. Conclusion

In summary, we realize a non-Hermitian nanolaser ring array that enforces robust phase winding through symmetry-protected zero-mode physics. By tuning gain and loss to a chiral exceptional point, we achieve directional energy flow and far-field emission carrying orbital angular momentum. This work establishes a compact and scalable route to phase-locked laser arrays with controllable structured-light output.

Manipulating evanescent waves with non-Hermitian spectral singularities

Huanan Li*

MOE Key Laboratory of Weak-Light Nonlinear Photonics, School of Physics, Nankai University, Tianjin 300071, China
*corresponding author: hli01@nankai.edu.cn

Abstract: We study evanescent-wave manipulation enabled by spectral singularities in non-Hermitian systems, focusing on their synergy with effective parity-time (PT) symmetry and saturable nonlinearity. The results reveal non-Hermitian mechanisms for controlling evanescent-wave responses and achieving extreme light-matter interactions, with potential applications in functional devices for communications and signal processing.

Research on wave scattering in non-Hermitian photonics has thus far focused almost exclusively on propagating waves. However, evanescent waves—characterized by exponential decay arising from an imaginary wave-vector component—are ubiquitous in photonics and underpin intriguing phenomena such as subdiffraction imaging and super-Planckian thermal emission. It is therefore highly desirable to integrate evanescent waves into non-Hermitian systems, as this not only deepens our understanding of non-Hermitian systems but also provides new strategies for the manipulation of evanescent waves. In this context, anti-PT-symmetric systems provide a revealing example: they can exhibit effective PT symmetry under evanescent-wave scattering, thereby opening avenues for manipulating evanescent waves in non-Hermitian photonics [1-2].

In this talk, we show that arbitrary anti-PT-symmetric photonic heterostructures, characterized by complex permittivity and permeability profiles satisfying $\varepsilon(-z) = -\varepsilon^*(z)$ and $\mu(-z) = -\mu^*(z)$, can exhibit effective PT symmetry under evanescent-wave excitation [3]. At an appropriate level of gain, the most unstable pole of the generalized scattering matrix—governing evanescent-wave scattering—reaches the real-frequency axis, giving rise to a spectral singularity (SS) for evanescent waves [4]. Owing to the effective PT symmetry, the pole necessarily coincides with a zero on the same axis, resulting in a PT-symmetric laser-absorber mode for evanescent-wave scattering in the anti-PT-symmetric heterostructure. Building on this mode, we demonstrate that such anti-PT-symmetric systems can strongly amplify evanescent waves incident from either side, while completely absorbing coherently incident evanescent waves with appropriate amplitudes and phases. Furthermore, together with excitation-frequency tuning, this functionality enables extreme tunability of energy transport mediated by interfering evanescent waves between the excitation source and the anti-PT-symmetric structure in the presence of realistic material dispersion. We further extend this mode to realize a unidirectional SS, producing infinite reflection of evanescent waves from one side and vanishing reflection from the other, while maintaining a reciprocal finite transmission.

On the other hand, the reciprocity principle constrains both propagating and evanescent wave regimes, yet magnet-free approaches to nonreciprocal transmission have so far been explored only for propagating waves. Here, we also explore large nonreciprocal transmission of evanescent waves enabled by the synergy between nonlinearity and an SS [5]—extending nonlinear SSs from propagating to evanescent waves. In our system, an asymmetric nonlinear defect embedded in an otherwise uniform waveguide produces strongly direction-dependent scattering of evanescent waves within a bandgap. Evanescent-wave excitation from one port induces loss saturation and triggers the SS, whereas excitation from the opposite port does not, yielding a large transmission contrast over a broad range of incident

intensities. Compared with the propagating-wave scenario, the requirements for SS-assisted nonreciprocal transmission are reduced.

References

1. H. Li, A. Mekawy, and A. Alù, "Gain-free parity-time symmetry for evanescent fields," Phys. Rev. Lett. 127, 014301 (2021).
2. Z. Chen, H. He, H. Li, M. Li, J.-L. Kou, Y.-Q. Lu, J. Xu, and A. Alù, "Observation of parity-time symmetry for evanescent waves," Commun. Phys. 7, 339 (2024).
3. M. Li, C. Tao, H. He, S. Zhang, H. Li, and J. Xu, "PT-symmetric laser absorber modes for evanescent waves in anti-PT-symmetric photonic heterostructures," Phys. Rev. B 113, 045412 (2026).
4. H. He, Z. Chen, H. Li, C.-H. Tu, J. Xu, and A. Alù, "Evanescent wave spectral singularities in non-Hermitian photonics," Phys. Rev. B 109, L041405 (2024).
5. H. He, Z. Chen, H. Li, Z. Xiao, Y. Lu, J. Xu and A. Alù, "Evanescent-wave nonreciprocity via nonlinear spectral singularities," under review (2026).

Enabling Materials – Optical and Functional Composites

Dorota Anna Pawlak[1*], Piotr Piotrowski[1], Monika Tomczyk[1], Katarzyna Sadecka[1], Nada Aghad[1], Kingshuk Bandopadhay[1], Ali Abbas[1], Krzysztof Markus[1], Andrzej Materna[1], Hamid Reza-Darabian[1]

[1]Centre of Excellence ENSEMBLE3 sp. z o. o.

Wólczynska 133, 01-919 Warsaw, Poland
*Corresponding author: dorota.anna.pawlak@ensemble3.eu

***Abstract*— Directional solidification provides a powerful platform for fabrication of bulk metamaterials and plasmonic composites. Using eutectic self-organization and nanoparticle direct doping methods, a broad range of functional photonic materials has been demonstrated, including plasmonic, luminescent, magneto-optical, and energy-related systems. Recent work also explores topological heterostructures generating THz radiation.**

***Keywords*— directional solidification, metamaterials, plasmonics, eutectic structures, nanoparticle-doped composites, photonic materials.**

Recently, we proposed the concept of utilizing directional solidification as a versatile method for manufacturing metamaterials and plasmonic materials [1–2]. Directional solidification provides a unique pathway to fabricate volumetric structures with controlled micro- and nanostructures, enabling the development of materials with engineered electromagnetic responses. Within this approach we have developed two complementary fabrication strategies: (i) a method based on directionally grown self-organized eutectic structures [3–5]; and (ii) the NanoParticles Direct Doping (NPDD) method, which relies on directional solidification of dielectric matrices doped with various nanoparticles [6–9]. Both approaches allow relatively simple fabrication of bulk composite materials in which resonant optical phenomena can be exploited to tailor unusual electromagnetic properties.

The self-organized eutectic structures formed during directional solidification create periodic or quasi-periodic arrangements of phases with characteristic dimensions on the micro- and nanoscale. Such architectures enable strong light–matter interactions and support plasmonic resonances or other resonant effects. The NPDD approach, in turn, enables incorporation of metallic or conductive nanoparticles into transparent dielectric matrices, providing additional degrees of freedom for tuning optical properties through particle composition, concentration, and distribution.

Using these approaches, we have demonstrated a variety of functional materials with unique electromagnetic and optical properties. These include: (i) volumetric eutectic-based materials exhibiting localized surface plasmon resonance (LSPR) at visible wavelengths [10–11]; (ii) enhanced luminescence and up-conversion processes in eutectic materials displaying LSPR and co-doped with erbium ions [6]; (iii) matrix–nanoparticle composites with plasmonic resonances in both visible and infrared spectral regions, based on silver (Ag), antimony-tin-oxide (ATO), and titanium nitride (TiN) nanoparticles [6,12]; and (iv) composites exhibiting enhanced photoluminescence at the telecommunication wavelength of 1.5 μm. Additional demonstrated functionalities include materials showing subwavelength transmission at infrared frequencies [13], narrow-band optical filters and polarizers [14–15], and bulk eutectic materials capable of surface-enhanced Raman scattering (SERS) with selective enhancement of Raman modes [16].

Beyond photonic and plasmonic applications, the developed materials have also shown potential for magneto-optical systems with enhanced Faraday effect, as well as for energy-related applications such as photoanodes in photoelectrochemical cells for hydrogen generation [17–18]. More recently, the methodology has been extended toward advanced heterostructures, including topological insulator systems capable of generating polarized terahertz radiation [19–20]. The latest experimental and conceptual developments in these areas will be discussed.

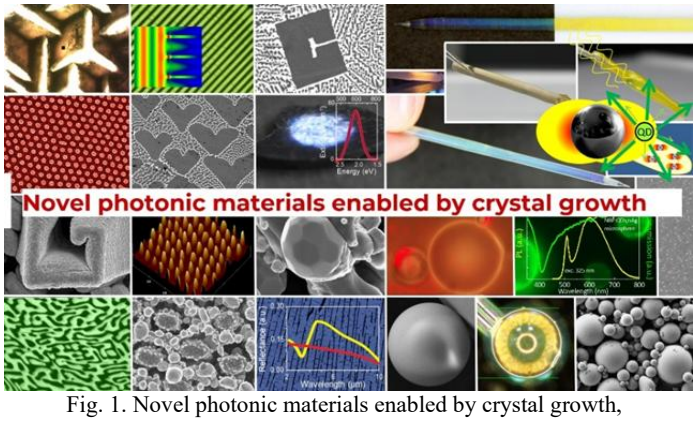

Fig. 1. Novel photonic materials enabled by crystal growth, manufactured in Ensemble3.

ACKNOWLEDGMENTS

The authors thank the ENSEMBLE3 Project carried within the International Research Agendas Programme of the Foundation for Polish Science co-financed by the European Union under the European Funds for Smart Economy and the Teaming Horizon 2020 programme of the European Commission (GA No. 857543) for supporting this work.

REFERENCES

[1] D. R. Smith, et al. Science, vol. 305, p. 788, 2004; A. M. Urbas, et al., J. Optics, vol. 18, p. 093005, 2016.
[2] L. Barnes, et al., Nature, vol. 424, p.824, 2003.
[3] D. A. Pawlak, et al. Chem. Mater. vol. 18, p. 2450, 2006.
[4] D. A. Pawlak, et al. Crystal Growth & Design, vol. 8, p. 1243, 2008.
[5] D. A. Pawlak, et al. Adv. Funct. Mat. vol. 20, p. 1116, 2010.
[6] M. Gajc, et al. Adv. Funct. Mat. vol. 23, p. 3443, 2013.
[7] R. Nowaczynski, et al. PPSC vol. 36, p. 1800124, 2019.
[8] M. Gajc, et al. Sci. Rep. vol. 8, p. 13425, 2018.
[9] P. Piotrowski, Nature Comm. vol. 15, p. 3309, 2024.
[10] K. Sadecka, et al. Adv. Opt. Mat. vol. 3, p. 381, 2015.
[11] K. Sadecka, et al. Opt. Express vol. 23, p. 19098, 2015.
[12] https://www.facebook.com/fmlaboratory/videos/608375495898423/ - demonstration of the plasmonic resonance in materials obtained by NanoParticle Direct Doping method.
[13] V. Myroshnychenko, Opt. Express vol. 20, p. 10879, 2012.
[14] P. Osewski, et al. Adv. Opt. Mater. vol. 8, p. 1901617, 2020.
[15] E. Petronijevic, et al. Adv. Mater. vol. p. 2206005, 2023.
[16] K. Szlachetko, et al. Nanophotonics vol. 9, p. 4307, 2020.
[17] K. Wysmulek, et al. Appl. Catalysis B: Environ. vol. 206, p. 538, 2017.
[18] K. Kolodziejak, et al. J. Catalysis, vol. 352, p. 93, 2017.
[19] K. Bandopadhyay, Next Materials vol. 5, p. 100252, 2024.
[20] F. Murakami, APL Materials vol. 11, p. 031102, 2023.

Metasurfaces for Millimeter-Wave Wireless Systems

Miguel Beruete[1,2*], Alicia E. Torres-García[1,2], J. Teniente[1,2], Damián E. Rodríguez-Trujillo[1,2]

[1]Department of Electrical and Electronic Engineering, Antennas Group–TERALAB, Public University of Navarre (UPNA), Pamplona, Spain
[2]Institute of Smart Cities (ISC), Public University of Navarre (UPNA), Pamplona, Spain
*Corresponding author: miguel.beruete@unavarra.es

***Abstract*— This talk presents advanced metasurface concepts for millimeter-wave wireless devices, with emphasis on phase engineering, holography, and multifunctionality. Using representative implementations from the last decade, it discusses how metasurface design evolves from ideal phase masks to realistic radiating devices for next-generation wireless systems.**

***Keywords*— metasurfaces, millimeter waves, holography, metalenses, radiating structures.**

I. Introduction

Metasurfaces have established themselves as a versatile platform for electromagnetic wave manipulation, enabling compact implementations of functionalities traditionally associated with bulky optical or antenna systems. At millimeter-wave and terahertz frequencies, this paradigm has opened new possibilities for wireless communications, imaging, and sensing, where integration, weight, and form factor are critical constraints

Early metasurface implementations demonstrated that planar phase discontinuities could be exploited to control wavefronts with subwavelength resolution. Over the years, these concepts have evolved toward increasingly complex devices operating as integral parts of radiating systems, rather than as isolated components.

The rapid evolution of wireless systems toward higher carrier frequencies, wider bandwidths, and increased functional density has further shifted the role of metasurfaces toward elements embedded within complete electromagnetic environments. Concepts such as smart walls, wireless-on-wall platforms, and environment-assisted communications illustrate this transition, where metasurfaces interact directly with antennas, propagation channels, and the surrounding radio ecosystem [1].

II. Phase Engineering in Metasurface-Based Devices

Phase engineering constitutes the common theoretical framework behind a wide range of metasurface functionalities. By prescribing a spatial phase distribution, metasurfaces can implement holographic wavefront shaping, focusing, beam steering, and cloaking within ultrathin platforms.

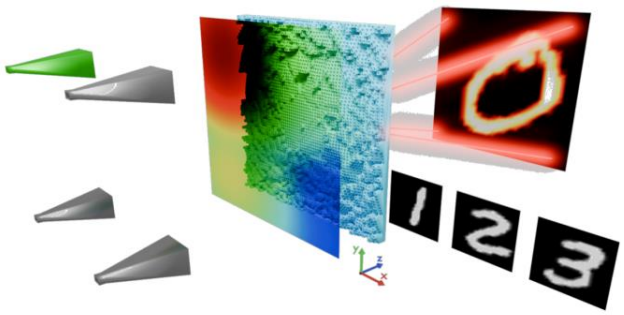

Fig. 1 Schematic illustration of a multifunctional holographic metasurface operating under complex illumination conditions.

Representative examples include planar holographic metasurfaces for terahertz focusing [2], ultrathin carpet cloaks based on metasurface concepts [3], [4], and Pancharatnam–Berry phase metalenses operating at millimeter-wave frequencies [5]. These works illustrate how both resonant and geometric-phase mechanisms can be exploited to achieve efficient phase control across electrically thin structures.

III. Multifunctional Metasurfacess

Beyond single-function devices, metasurfaces have progressively evolved toward multifunctional architectures capable of performing several electromagnetic operations within a single structure. This includes devices operating in transmission and reflection, at multiple frequencies, or under different polarization and illumination conditions (Fig. 1).

Full-space metasurfaces represent a particularly illustrative example, where independent phase responses are engineered for transmission and reflection channels. Such architectures extend the design space of conventional metasurfaces and enable compact implementations of multifunctional radiating devices without duplicating hardware.

As metasurfaces evolve toward electrically large, strongly aperiodic, and multifunctional architectures, electromagnetic interactions between neighboring elements become increasingly relevant. In particular, mutual coupling effects and near-field interactions progressively undermine the validity of design approaches based on local periodicity and isolated unit-cell responses, leading to deviations between prescribed phase profiles and actual radiated fields.

This effect is especially pronounced when a multifunctional

response is desired, as abrupt spatial phase variations are required to encode complex functionalities. In these scenarios, discrepancies between the target phase distribution and the effective phase response of the structure arise from mutual interaction between adjacent elements that are not captured by local or weak-coupling assumptions.

Recent work has demonstrated that neural-network-based approaches can be effectively used to model and mitigate coupling-induced distortions by adjusting the target phase profile in the presence of mutual coupling [6]. In particular, a phase-smoothing strategy is employed to obtain a better approximation to the local periodicity assumption. By combining physical insight with data-driven modeling, this approach improves the agreement between intended and realized metasurface behavior, especially in complex millimeter-wave radiating structures.

IV. Conclusions

This contribution has presented a consolidated perspective on metasurfaces for millimeter-wave wireless devices, emphasizing phase engineering as a unifying design principle across holographic, metalens-based, and multifunctional architectures. The examples discussed illustrate how metasurfaces have evolved from isolated phase-manipulating elements into key components of realistic radiating systems, where system-level considerations become increasingly relevant.

As metasurface functionalities grow in complexity, traditional physics-driven design approaches face inherent limitations when addressing strongly aperiodic and multifunctional configurations. In this context, hybrid design strategies that combine electromagnetic modeling with artificial intelligence and neural-network-assisted optimization are emerging as a powerful complement to conventional methodologies. These approaches enable the exploration of complex design spaces while preserving physical insight and practical feasibility.

Overall, the fusion of metasurface physics with advanced computational and data-driven tools opens new opportunities for the realization of high-performance, multifunctional radiating structures. This synergy is expected to play a central role in the development of future millimeter-wave and beyond-5G wireless systems, as well as in the broader vision of smart and adaptive electromagnetic environments.

Acknowledgments

This work was supported by Project No. PID2022-137845NB-C21, funded by MCIN/AEI/10.13039/501100011033 and by ERDF “A way of making Europe.” The author acknowledges the contributions of the Antennas Group–TERALAB team and collaborators in the works cited.

References

[1] Y. Liu et al., “Reconfigurable Intelligent Surfaces: Principles and Opportunities,” IEEE Communications Surveys & Tutorials, vol. 23, no. 3, pp. 1546–1577, 2021, doi: 10.1109/COMST.2021.3077737.

[2] S. A. Kuznetsov, M. A. Astafev, M. Beruete, and M. Navarro-Cía, “Planar Holographic Metasurfaces for Terahertz Focusing,” Scientific Reports, vol. 5, p. 7738, Jan. 2015, doi: 10.1038/srep07738.

[3] B. Orazbayev, N. M. Estakhri, M. Beruete, and A. Alù, “Terahertz carpet cloak based on a ring resonator metasurface,” Physical Review B, vol. 195444, pp. 1–5, 2015, doi: 10.1103/PhysRevB.91.195444.

[4] B. Orazbayev, N. Mohammadi Estakhri, A. Alù, and M. Beruete, “Experimental Demonstration of Metasurface-Based Ultrathin Carpet Cloaks for Millimeter Waves,” Advanced Optical Materials, vol. 5, no. 1, p. 1600606, Jan. 2017, doi: 10.1002/adom.201600606.

[5] A. Moreno-Peñarrubia, J. Teniente, S. Kuznetsov, B. Orazbayev, and M. Beruete, “Ultrathin and high-efficiency Pancharatnam – Berry phase metalens for millimeter waves,” Applied Physics Letters, vol. 118, no. 22, p. 221105, 2021, doi: 10.1063/5.0048907.

[6] D. Rodríguez-Trujillo, A. E. Torres-García, M. Aldea, J. Teniente, A. Marzo-Pérez, and M. Beruete, “Phase Smoothing for Mutual Coupling Mitigation in Multifunctional Metasurfaces Designed with Diffractive Neural Networks,” Advanced Optical Materials, vol. 14, no. 1, p. e02746, 2026, doi: 10.1002/adom.202502746.

GEGD: Efficient Quasi-Global Search Algorithm for Strictly Fabrication-Feasible Design of Freeform Devices

Seokhwan Min[1], Junhyung Park[1], Jonghwa Shin[1,*]

[1]Department of Material Science and Engineering,
Korea Advanced Institute of Science and Technology, Republic of Korea
*Corresponding author: qubit@kaist.ac.kr

***Abstract*—We present an optimization algorithm which minimizes the ensemble cost of fabrication-feasible designs sampled under a Gaussian distribution by optimizing the distribution mean. It seamlessly transitions between exploration and exploitation while maintaining strict fabrication feasibility.**

***Keywords*— topology optimization, freeform design, global search, inverse design.**

I. Introduction

Freeform designs have revolutionized nanophotonics in the past decade for a variety of applications such as integrated photonic devices [1]. However, the efficient and effective design of density-parameterized freeform devices is hampered by the enforcement of fabrication feasibility.

Fabrication feasibility imposes stringent constraints on design parameters that hinder effective gradient-based optimization. Many fabrication methods (e.g., photolithography) can only fabricate devices consisting of two discrete materials, which introduces difficulties in gradient computation. In addition, fabrication resolutions impose highly non-linear minimum feature size constraints on the fabricated device. Current methods use continuous latent parameters that map to (near-)feasible designs to handle fabrication constraints. However, they suffer from weak feasibility enforcement, the use of inaccurate substitute gradient estimators, or high memory and computation overhead.

The non-differentiability of fabrication constraints is easily handled by many types of population-based heuristic global search methods such as particle swarm optimization (PSO), which has the added benefit of being able to locate superior local optima. However, they suffer from the curse of dimensionality that greatly reduces their efficiency in high-dimensional freeform parameter spaces.

In this work, we propose the Gaussian ensemble gradient descent (GEGD) framework to address these issues. The enforcement of feasibility leads to a piecewise-constant cost function (f) in the latent density space, where multiple latent densities map to the same feasible design (Fig. 1a). GEGD eliminates the discontinuities by convolving the function with a Gaussian kernel (Fig. 1b), after which the function becomes differentiable everywhere. GEGD then optimizes the mean ($\vec{\mu}_\mathrm{R}$) of the Gaussian distribution to minimize the convolved f. The convolved function is equivalent to the expectation of f under a Gaussian distribution, which can be estimated by Monte Carlo sampling. GEGD is strictly feasible because all cost evaluations are done with respect to feasible designs and differentiable because the gradients are defined with respect to $\vec{\mu}_\mathrm{R}$. Furthermore, the non-local cost function information gathered by ensemble sampling allows GEGD to effectively perform a global search of the feasible design space while still benefiting from the fast convergence of gradient descent.

II. Results

In each iteration, the algorithm begins with a mean latent density ($\vec{\mu}_\mathrm{L}$) that is filtered and projected ($\vec{\mu}_\mathrm{R}$) (Fig. 1c). An ensemble of filtered and projected densities are generated as $\vec{\rho}_\mathrm{R} \sim N\left(\vec{\mu}_\mathrm{R}, \sigma_\mathrm{R}^2 \mathbf{\Sigma}_\mathrm{RBF}\right)$ where σ_R^2 is a scalar variance. The covariance is defined using radial basis functions as $\mathbf{\Sigma}_{\mathrm{RBF},ij} = \exp\left(-8\left\|\vec{x}_i - \vec{x}_j\right\|^2 / L_\mathrm{min}^2\right)$ where $\vec{x}_i$ denotes the position of pixel i. The sampled $\vec{\rho}_\mathrm{R}$ are then used to generate feasible designs ($\vec{\rho}_\mathrm{F}$) using the algorithm by Schubert *et al.* [2]. $\mathbf{\Sigma}_\mathrm{RBF}$ ensures that the randomly sampled perturbations to the mean have a certain length-scale associated with the minimum feature size (L_min), leading to significant variations in $\vec{\rho}_\mathrm{F}$ and preventing samples from being wasted on similar designs.

As discussed previously, the Gaussian convolution of the cost function is equivalent to its expectation. Differentiating the convolution integral expression with respect to $\vec{\mu}_\mathrm{R}$ leads to:

$$\frac{\mathrm{d}}{\mathrm{d}\vec{\mu}_\mathrm{R}}\mathrm{E}\left[f\right] = \int p\left(\vec{\rho}_\mathrm{R}; \vec{\mu}_\mathrm{R}, \sigma_\mathrm{R}^2 \mathbf{\Sigma}_\mathrm{RBF}\right) \cdot \vec{q}\left(\vec{\rho}_\mathrm{R}\right) \cdot f\left(\vec{\rho}_\mathrm{R}\right) \mathrm{d}\vec{\rho}_\mathrm{R} \approx \langle \vec{q} \cdot f \rangle \tag{1}$$

where p is a Gaussian probability density function and $\vec{q} = \sigma_\mathrm{R}^{-2} \mathbf{\Sigma}_\mathrm{RBF}^{-1}\left(\vec{\rho}_\mathrm{R} - \vec{\mu}_\mathrm{R}\right)$. The integral in Eq. (1) can be interpreted as the expectation of the vector function $\vec{q}f$ under the same Gaussian distribution, and can thus be estimated through Monte Carlo sampling as $\langle \vec{q}f \rangle$. Note that the same forward-simulated Monte Carlo samples can be used to estimate both the ensemble cost $\langle f \rangle$ and the ensemble gradient; adjoint simulations or autodifferentiation are not necessary. The ensemble gradient is then backpropagated and used to update $\vec{\mu}_\mathrm{L}$.

We benchmarked GEGD against the three-field method (TF) [3] and always-feasible parameterization with gradient

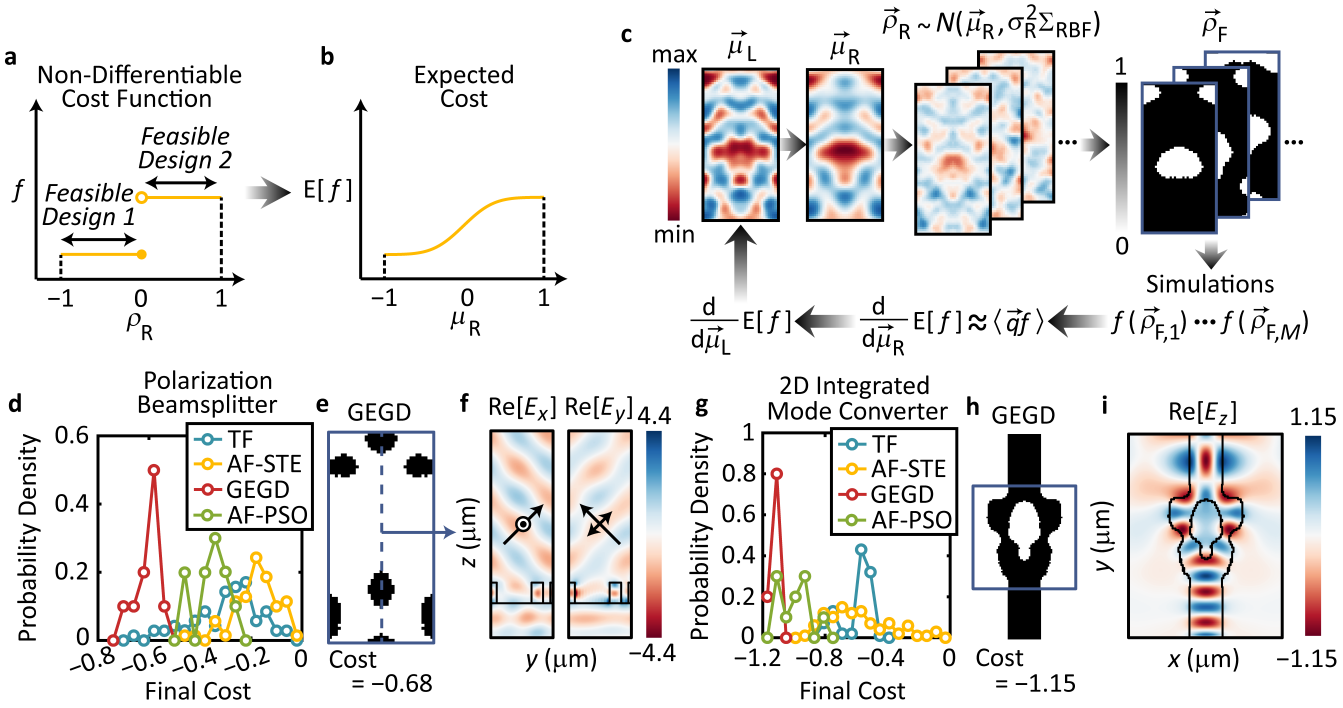

Fig. 1. **a–b**, Working principle of GEGD. **a**, A typical piecewise-constant cost function based on always-feasible parameterization. **b**, Gaussian-convolved cost function. **c**, Schematic of the feasible design sampling, ensemble gradient estimation, and gradient backpropagation procedures. **d–f**, Optimization results for the polarization beamsplitter. **g–i**, Optimization results for the 2D integrated mode converter. **d, g**, Histograms (normalized into probability densities) of benchmark results for different algorithms. **e, h**, Best GEGD-optimized designs. **f**, Re $[E_x]$ (left) and Re $[E_y]$ (right) for x and y-polarized incidence, respectively. The fields are plotted across the yz-plane at the center of the unit cell denoted by the dotted line in **e**. **i**, Re $[E_z]$ for TE_0 mode input from the bottom waveguide.

descent (AF-STE) [2] and PSO (AF-PSO) on the design of polarization beamsplitters (2D integrated mode converters) with 1260 (2450) independent density parameters. The computational load per iteration for GEGD and AF-PSO was set as close as possible to 10 (20) forward simulations for the polarization beamsplitter (mode converter). A total of 10 runs with different random seeds were performed for GEGD and AF-PSO. A total of 70 (100) runs were performed for TF and AF-STE to ensure that the total computation budgets of all algorithms were as close as possible. Normalized histograms of the final costs demonstrate the superiority of GEGD over other algorithms (Figs. 1d,g). In particular, GEGD is also much more consistent (smaller variance in the final cost), demonstrating its effective global search capabilities. The best GEGD-optimized designs and the corresponding field plots are shown in Figs. 1e,h and Figs. 1f,i, respectively.

III. Conclusion

In conclusion, we have proposed GEGD, which simultaneously provides an efficient global search algorithm and a fully differentiable parameterization method for strictly feasible freeform designs. Through benchmark tests, we have demonstrated its superior performance against conventional gradient- and population-based methods.

Acknowledgments

This work is supported by the National Research Foundation of the Republic of Korea (RS-2024-00414119, RS-2023-00283667).

References

[1] A. Y. Piggot, J. Lu, K. G. Lagoudakis, J. Petykiewicz, T. M. Bibinec, and J. Vučković, "Inverse design and demonstration of a compact and broadband on-chip wavelength demultiplexer," *Nat. Photon.*, vol. 9, pp. 374–377, 2015.

[2] M. F. Schubert, A. K. C. Cheung, I. A. D. Williamson, A. Spyra, and D. H. Alexander, "Inverse Design of Photonic Devices with Strict Foundry Fabrication Constraints," *ACS Photonics*, vol. 9, pp. 2327–2336, 2022.

[3] F. Wang, B. S. Lazarov, and O. Sigmund, "On projection methods, convergence and robust formulations in topology optimization," *Struct. Multidiscip. Optim.*, vol. 43, pp. 767–784, 2011.

Terahertz Quantum Communication with Chip-integrated Superconducting Circuits

Kaveh Delfanazari
James Watt School of Engineering, University of Glasgow, UK
*Corresponding author: Kaveh.Delfanazari@glasgow.ac.uk

***Abstract*— In this talk, we present our recent progress in terahertz quantum communication, covering both quantum key distribution protocols and chip-scale superconducting hardware. By integrating coherent THz emitters, detectors, and tunable quantum circuits, we show the potential of superconducting coherent THz devices for secure, high-bandwidth, and energy-efficient communication, advancing scalable quantum networks.**

***Keywords*— Quantum communication, terahertz, quantum key distribution, superconducting coherent light sources and sensors.**

Graphene Nanosheet Gold Nanopatch Metasurfaces for Nonlinear Terahertz Response

A. Theodosi[1,2], I. Appiah Otoo[3], A. D. Koulouklidis[1], N. Matthaiakakis[4], G. Kakarantzas[5], P. Mustonen[6], H. Lipsanen[6], G. Fedorov[3], I. Liontos[1], P. Kuzhir[3], M. Kafesaki[1,2], Odysseas Tsilipakos[5], and S. Tzortzakis[1,2*]

[1]Institute of Electronic Structure and Laser, FORTH, 70013 Heraklion, Greece
[2]Materials Science & Engineering Department, University of Crete, 70013 Heraklion, Greece
[3]Department of Physics & Math., University of Eastern Finland, 80101 Joensuu, Finland
[4]Institute of Nanoscience and Nanotechnology, NCSR "Demokritos", 15341 Athens, Greece
[5]Theoretical and Physical Chemistry Institute, NHRF, 11635 Athens, Greece
[6]Department of Electronics and Nanoengineering, Aalto University, 02150 Espoo, Finland
*Corresponding author: stzortz@iesl.forth.gr

***Abstract*— We demonstrate a fabrication friendly graphene gold metasurface engineered for strong nonlinear terahertz response. Doubly resonant enhancement enables predicted third harmonic efficiencies of 3.2% under continuous wave excitation at modest intensities. Experiments reveal intensity driven resonance shifts ~0.5 THz, confirming pronounced nonlinear modulation.**

***Keywords*— Graphene, metasurfaces, terahertz, nonlinear optics, third harmonic generation.**

I. Introduction

Graphene exhibits strong third-order nonlinear conductivity at terahertz frequencies, enabling compact nonlinear photonic devices. Patterning graphene increases fabrication complexity and may degrade material quality. Here, we transfer the patterning to a metallic layer, combining a uniform graphene nanosheet with resonant gold nanopatches to achieve enhanced nonlinear response while preserving fabrication simplicity.

II. Methods

The metasurface consists of rectangular gold patches arranged periodically on a graphene-coated polymer spacer, which is backed by a gold reflector. Geometrical tuning aligns two resonances at a 1:3 frequency ratio, enabling doubly resonant enhancement of third-harmonic generation.

Frequency-domain simulations predict conversion efficiencies of up to -15 dB (3.2%) at an input intensity of 0.1 MW/cm^2. Samples were fabricated via electron-beam lithography and characterized using terahertz time-domain spectroscopy, with peak electric fields up to 450 kV/cm.

III. Results and Discussion

Linear measurements confirm resonances near 4 and 12 THz with strong field confinement at the graphene layer. Under intense pulsed excitation, both resonances exhibit nonlinear redshifts up to 0.5 THz, corresponding to a 12.5% fractional shift attributed to self-phase modulation.

Although third harmonic radiation could not be isolated experimentally due to broadband excitation, time domain simulations verify harmonic generation and confirm cubic power scaling. These results demonstrate efficient nonlinear modulation enabled by resonance engineered graphene metasurfaces.

IV. Conclusion

We present a hybrid graphene gold metasurface combining fabrication simplicity with strong nonlinear terahertz response. Doubly resonant design enables high predicted harmonic efficiency, while experiments demonstrate substantial intensity driven spectral tuning. The platform provides a scalable route toward compact nonlinear terahertz photonic components.

Acknowledgments

This work was supported by EU Horizon 2020 CHARTIST, Research Council of Finland PREIN (368653, 368652, 343393, 358812), and the Hellenic Foundation for Research and Innovation (916-PHOTOSURF and 4542-ENTERS).

References

[1] A. Theodosi *et al*., ACS Appl. Nano Mater. **8**, 51, 24473–24479 (2025)

Microwave stress monitoring using amorphous microwire assessed by free space measurements

Valentina Zhukova[1,2,3], Mihail Ipatov[4] and Arcady Zhukov[2,3,5,*]

[1]Department of Polymers and Advanced Materials, University of the Basque Country, UPV/EHU, 20018 Donostia-San Sebastian, Spain
[2]Department Applied Physics, Faculty of Engineering, Gipuzkoa EIG, University of the Basque Country, UPV/EHU, 20018 Donostia-San Sebastian, Spain.
[3]EHU Quantum Center, University of the Basque Country, UPV/EHU, 20018 Donostia-San Sebastian, Spain.
[4]General Magnetic Measurement Service of Advanced Research Facilities (SGIker), University of the Basque Country, UPV/EHU, Donostia-San Sebastián, Spain.
[5]IKERBASQUE, Basque Foundation for Science, 48011 Bilbao, Spain.
*Corresponding author: arkadi.joukov@ehu.es

***Abstract*—We provide new experimental results on studies on effect of applied stress on Reflection coefficient (S_{22} parameter) of Co-rich glass-coated ferromagnetic microwire measured using free space microwave spectroscopy at 2.45 GHz. The experimentally discovered stress dependence of the reflection coefficient allows for contactless stresses and damage monitoring of composites with microwire inclusions.**

***Keywords*—microwave stress monitoring, Giant magnetoimpedance, sensing composites, magnetic microwire inclusions.**

I. Introduction

The magnetic wires with a Giant magnetoimpedance, GMI, effect at GHz frequencies have been proposed for development of Free Space microwave sensing technique based on tunable effective permittivity at the GHz range in composites with magnetic wire inclusions [1-3]. The starting point for the concept of such smart composites is the tunability of the effective permittivity at the GHz range due to magnetic wire inclusions [2,3]. Finally, experimentally was demonstrated that the composite media with ferromagnetic wires exhibit a frequency region at the microwave regime with scattering spectra strongly dependent on external stimuli (applied magnetic field and applied stress) [2,4].

Remarkable dependences of the effective permittivity, transmission or reflection parameters of such smart composites on external stimuli in the GHz range indicate that such composite with magnetic microwire inclusions can be useful for structural health monitoring and self-sensing applications [3-5]. One of the advantages of this technology is that proposed free space microwave spectroscopy allows remote monitoring of external stimuli, like stress or temperature [4].

Although there are several reports on tunability of the effective permittivity, transmission or reflection parameters of such composites with magnetic wires inclusion at the GHz range on applied magnetic field, stress or heating [2,4], the influence of applied stress on microwave response of single microwire at GHz frequencies has not been experimentally studied.

Accordingly, we present our recent experimental results on in-situ studies of applied stress in microwave response of single Co-rich microwire using free space technique

II. Methods

We studied $Co_{72}Fe_4B_{13}Si11$ glass-coated amorphous microwires with metallic nucleus diameters, d, of about 40 μm and a total diameter, D, of about 45 μm manufactured by the aforementioned Taylor-Ulitovsky method [6]. For wireless measurements of microwire response under stress at 2.45 GHz, we used the free space measurement system, consisting of two broadband horn antennas fixed to the anechoic chamber and a vector network analyzer, previously used for the composites characterization at free space [2]. We measured the scattering S_{22}, parameter. As recently proposed [7], the AC modulating magnetic field (frequency 80 Hz) was applied parallel to the ferromagnetic microwires to modulate the impedance in the microwire. During the free space measurements, a tensile stress was applied to the sample by means of a mechanical load hanged to one end of studied microwire. The applied stresses value, σ, acting on the metallic nucleus has been evaluated considering different Young's moduli of the metallic alloy and the glass, as was described earlier [6].

III. Results and Discussion

In Fig. 1a the dependence of S_{22} parameters measured at 2.45 GHz on frequency, f, is shown. In the case of using one single microwire, the reflected by a single microwire signal is very low, it is below the noise level in time domain. To detect such a low signal, we acquired the reflection waveform at fixed frequency (2.45 GHz) and applied Fast Fourier Transform (FFT) to obtained the frequency spectrum.). As observed, the S_{22} parameters present a maximums at f=80n (n=1,2,3…), reflecting effect of modulating low frequency field at f=80 Hz and 1,2,3, n harmonics. Upon application of stress a substantial decay of the S_{22} parameter measured at 2,45 GHZ is observed (see Fig.1a,b). The dependence of S_{22} on σ, evaluated from Fig.1b is shown in Fig. 1c. From Figs.1b,c is evident that upon the applied stress from 0 to 225 MPa, S_{22} changes on 40 dB (100 times) from -50 to -90 dB.

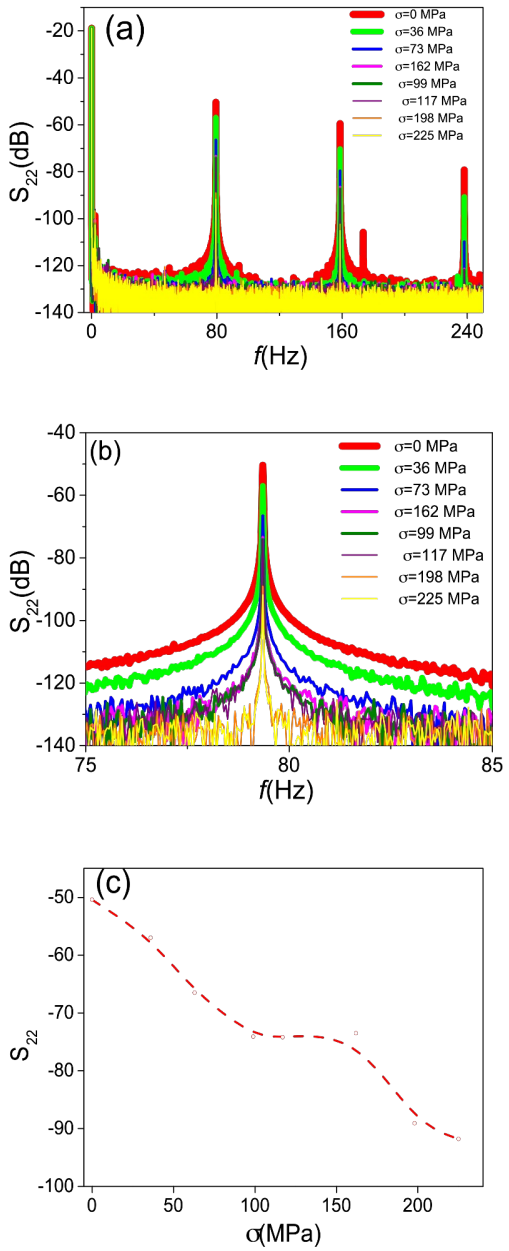

Fig.4. Frequency Spectrum of S_{22} module (a), zoom (b) and effect of applied stress on amplitude of the 1st harmonic (fundamental, 80 Hz) of S_{22} at different σ-values (c)

The observed substantial S_{22} σ) dependence can be explained considering the change in magnetic permeability upon applied stress.

The observed $S_{22}(\sigma)$ dependence at microwave frequencies is potentially suitable for exciting applications in structural integrity and health monitoring related to wireless stresses monitoring and integrity in civil engineering, aircraft, automobile and construction industries.

IV. Conclusion

We have demonstrated the influence of applied stress on Reflection coefficient (S_{22} parameter) of Co-rich glass-coated ferromagnetic microwire measured using free space microwave spectroscopy. The experimentally discovered remarkable dependence of the reflection coefficient on applied stress opens up possibilities for contactless monitoring of stresses and damages in smart composites through magnetic microwires inclusions.

Acknowledgments

This work was supported by the Spanish MICIN under PID2022-141373NB-I00, by the Government of the Basque Country under Elkartek (ATLANTIS and MOSINCO) projects and under the scheme of “Ayuda a Grupos Consolidados” (ref. IT1670-22). The authors thank for the technical and human support provided by SGIker (Medidas Magnéticas Gipuzkoa) (UPV/EHU, ERDF, EU).

References

[1] A.N. Lagarkov, A. K. Sarychev, “Electromagnetic properties of composites containing elongated conducting inclusions,” Phys. Rev. B, vol. 53(10), pp.6318-6336, 1996.

[2] . D. Makhnovskiy, A. Zhukov, V. Zhukova, J. Gonzalez, “Tunable and self-sensing microwave composite materials incorporating ferromagnetic microwires”, Advances in Science and Technology, vol. 54, pp. 201-210, 2008.

[3] L. V. Panina, M. Ipatov, V. Zhukova, A. Zhukov, and J. Gonzalez, “Magnetic field effects in artificial dielectrics with arrays of magnetic wires at microwaves”, J. Appl. Phys. vol. 109, p.053901, 2011.

[4] A. Allue, P. Corte-León, K. Gondra, V. Zhukova, M. Ipatov, J. M. Blanco, J. Gonzalez, M. Churyukanova, S. Taskaev, A. Zhukov, “Smart composites with embedded magnetic microwire inclusions allowing non-contact stresses and temperature monitoring, “ Compos. Part A Appl. Sci. Manuf., vol. 120, pp.12-20, 2019.

[5] A. Uddin, D. Estevez, F.X. Qin F X “From functional units to material design: A review on recent advancement of program-mable microwire metacomposites”, Compos. Part A Appl. Sci. Manuf., vol. 153, p. 106734, 2022.

[6] A. Zhukov, P. Corte-Leon, L. Gonzalez-Legarreta, M. Ipatov, J.M. Blanco, A. Gonzalez, V. Zhukova, “Advanced functional magnetic microwires for technological applications, “J. Phys. D: Appl. Phys. 55 (2022) 253003, doi: 10.1088/1361-6463/ac4fd7

[7] V. Zhukova, M. Ipatov, P. Corte-Leon, A. Gonzalez, A.García- Gómez, F. J. Vallejo, P. Olaskoaga, R. Garcia-Etxabe6, J.Malm, C. Johansson and A. Zhukov, “Free Space Microwave Sensing of Carbon Fiber Composites With Ferromagnetic Microwire Inclusions,” IEEE Sensors Letters, 1. vo8(1) (2024) 2500104, doi: 10.1109/LSENS.2023.3337071

Surface-protected electromagnetic nanoresonators for Raman analysis of surfaces

Andrzej Kudelski*

Faculty of Chemistry, University of Warsaw, Poland
*Corresponding author: akudel@chem.uw.edu.pl

***Abstract*— Example applications of surface-protected nanoresonators for Raman analysis of various surfaces and example methods of synthesis of such nanomaterials will be presented. It will be demonstrated that Raman scattering from surfaces covered with surface-protected nanoresonators is a sensitive method useful for surface chemical analysis of various objects, including biological ones.**

***Keywords*— surface analysis, shell-isolated nanoparticle-enhanced Raman spectroscopy, SHINERS.**

I. Introduction

Analyzing surfaces of various materials is crucial from both a scientific and economic perspective. Surface analysis is particularly challenging in the case of so-called buried interfaces (e.g., the surface of a solid sample immersed in a liquid or in a gas at high pressure).

II. Methods

One of the tools that can be used for investigations of buried interfaces is shell-isolated nanoparticle-enhanced Raman spectroscopy – SHINERS [1]. In this method, the surface under study is covered with a layer of surface-protected plasmonic P@D nanoparticles (where P denotes a plasmonic metal as Ag or Au, and D denotes a transparent dielectric, e.g., SiO_2, Al_2O_3, MnO_2, TiO_2 or ZrO_2), and then the Raman spectrum is recorded (see Figure 1 [2]).

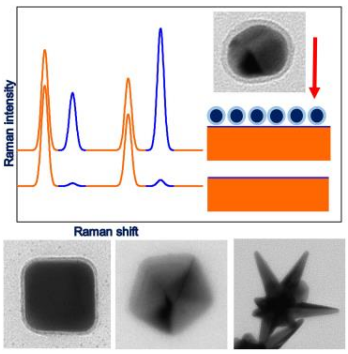

Fig. 1 Illustration of the principles of SHINERS measurements and TEM images of example anisotropic SHINERS nanoresonators (cubic-Ag@MnO_2, decahedral-Ag@SiO_2, star-Au@SiO_2). Reprinted from ref. [2]. CC BY-NC-ND license.

The plasmonic cores of the deposited nanoparticles act as electromagnetic resonators, significantly enhancing the electric field of the incident electromagnetic radiation, which leads to a very large increase in the intensity of the generated Raman signal. The ultrathin protecting coating does not significantly damp the enhancement of the electric field generated by the plasmonic cores, but it does separate the metallic plasmonic cores from direct contact with the analyzed material (the analyzed sample can significantly change its structure during direct interaction with metals, therefore, covering the plasmonic cores with a protective layer allows for obtaining information about a much less disturbed sample) and prevents agglomeration of nanoparticles.

III. Results and Discussion

Synthesis of various SHINERS nanoresonators (differences in: plasmonic materials, shapes of plasmonic cores, and materials used to protect the plasmonic cores) and their example applications will be presented. The synthesis and applications of SHINERS nanoresonators with magnetic properties will be also discussed.

IV. Conclusion

SHINERS spectroscopy is a very sensitive tool useful in the chemical analysis of various surfaces, including surfaces of biological objects in *in situ* conditions.

Acknowledgments

The author thanks: J. Krajczewski, A. Michałowska, K. Kołątaj, H. B. Abdulrahman, M. Żygieło, and S. Wojtysiak for their participation in this research.

References

[1] J. F. Li, Y. F. Huang, Y. Ding, Z. L. Yang, S. B. Li, X. S. Zhou, F. R. Fan, W. Zhang, Z. Y. Zhou, D. Y. Wu, B. Ren, Z. L. Wang, and Z. Q. Tian, "Shell-isolated nanoparticle-enhanced Raman spectroscopy," Nature, vol. 464, pp. 392–395, 2010.

[2] J. Krajczewski and A. Kudelski, "Shell-isolated nanoparticle-enhanced Raman spectroscopy," Frontiers in Chemistry, vol. 7, article 410, 2019.

[3] A. Michałowska, M. Żygieło, and A. Kudelski, "Fe_3O_4-protected gold nanoparticles: New plasmonic-magnetic nanomaterial for Raman analysis of surfaces," Applied Surface Science, vol. 562, article 150220, 2021.

Bound States in the Continuum for Biosensing and Selective Raman Enhancement

Silvia Romano

Institute of Applied Sciences and Intelligent Systems, National Research Council, Naples, 80131, Italy
*Corresponding author: silvia.romano@cnr.it

***Abstract*— Bound states in the continuum (BICs) sustained by photonic crystal slabs (PhCS) support ultrahigh-Q resonances and intense electromagnetic-field localization, making them highly attractive for applications in label-free biosensing and surface-enhanced Raman spectroscopy (SERS). Herein, we report our recent progress on PhCS-based platforms exploiting BIC resonances for the real-time investigation of biomolecular interaction dynamics.**

Keywords— bound states in the continuum, sensing, photonic crystals.

Photonic bound states in the continuum (BICs) supported by photonic crystal slabs and metasurfaces represent a remarkable class of electromagnetic modes that, although embedded in the radiation continuum, remain effectively decoupled from radiative losses [1-3]. Owing to their intrinsically non-radiative nature, these modes exhibit ultrahigh quality factors and strong electromagnetic-field confinement, enabling extreme sensitivity to refractive-index variations and enhanced light–matter interaction. These features make BICs particularly attractive for advanced biosensing, molecular analysis, and surface-enhanced spectroscopies. In this invited contribution, we present our recent advances in BIC-enabled nanophotonic platforms for integrated biosensing, with particular emphasis on label-free detection, real-time monitoring of biomolecular interactions, and selective Raman enhancement [5-11]. Our work exploits all-dielectric photonic crystal slabs and metasurfaces engineered to sustain high-Q resonances compatible with microfluidic integration and scalable fabrication. By functionalizing large-area transparent devices with biomolecular recognition elements, including proteins, aptamers, and molecularly imprinted polymers, we demonstrate highly selective sensing of biological and chemical analytes at extremely low concentrations, down to the femtomolar range. These platforms are capable of monitoring protein interaction dynamics in real time, thus providing direct access to interfacial binding kinetics and molecular recognition processes.

A major focus of our recent research is the development of hybrid dielectric–plasmonic architectures that combine the sharp spectral response of BIC-assisted dielectric resonances with the strong near-field localization provided by metallic nanostructures such as gold nanoparticles. By engineering the coupling between photonic and plasmonic modes, we achieve selective enhancement of Raman signals while preserving high sensitivity to biomolecular binding events. This approach enables the simultaneous acquisition of label-free sensing information and spectroscopic molecular fingerprints, offering a powerful route toward multifunctional platforms for dynamic biochemical analysis. In this framework, BIC-assisted hybrid nanostructures provide an effective strategy for reconciling high sensitivity, high figure of merit, and selective spectroscopic readout within a single integrated device.

Finally, we discuss recent developments on hollow bound states in the continuum for enhanced sensing. In particular, we investigate silicon slotted metasurfaces with circular and rectangular slot geometries designed to confine optical fields within low-index air voids through Mie-type mechanisms. Unlike conventional dielectric nanostructures, where the field is mainly localized inside the high-index material, these hollow configurations maximize the overlap between the optical mode and the surrounding analyte, thereby improving sensitivity and opening new opportunities for highly responsive photonic sensing platforms. Overall, our results highlight the versatility and potential of BIC-enabled photonic architectures for next-generation biosensing technologies. By combining ultrahigh-Q resonances, strong field confinement, selective biofunctionalization, microfluidic compatibility, and hybrid dielectric–plasmonic design, these platforms offer promising solutions for healthcare diagnostics, personalized medicine, environmental monitoring, and high-throughput bioanalytics.

References

[1] C. Hsu et al., *Nat. Rev. Mater.* **1,** (2016)
[2] J. Lee et al., *Phys. Rev. Lett.* **109,** 67401 (2012)
[3] V. Mocella and S. Romano, *Phys. Rev. B - Condens. Matter Mater. Phys.* **92,** 1–5 (2015)
[4] S. Romano et al., Photon. Res. 6, 726 (2018)
[5] G. Zito *et al.*, Nanophotonics-Berlin 10, 4279, (2021)
[6] S. Romano et al., ACS Nano 14, 15417, (2020)
[7] C Schiattarella et al., Biosensors and Bioelectronics: X 12, 100262 (2022)

[8] S. Romano et al., *J. Phys. Chem.* **122,** 19738–19745 (2018)
[9] C. Schiattarella et al., Nature (2024)
[10] G. Zito et al., Advanced Science 11.41, 2401843 (2024)
[11] B. Miranda et al., Biosensors and Bioelectronics, 117754 (2025)

Time-synthetic optical neural networks with stable programmable gain

Bei Wu, Yudong Ren, Rui Zhao, Haiyao Luo, Fujia Chen, Li Zhang, Lu Zhang, Hongsheng Chen and Yihao Yang*

[1] State Key Laboratory of Extreme Photonics and Instrumentation, ZJU-Hangzhou Global Scientific and Technological Innovation Center, Zhejiang University, Hangzhou 310027, China

[2] International Joint Innovation Center, The Electromagnetics Academy at Zhejiang University, Zhejiang University, Haining 314400, China

[3] Key Lab. of Advanced Micro/Nano Electronic Devices & Smart Systems of Zhejiang, Jinhua Institute of Zhejiang University, Zhejiang University, Jinhua 321099, China

[4] Shaoxing Institute of Zhejiang University, Zhejiang University, Shaoxing 312000, China

*Corresponding author: yangyihao@zju.edu.cn

***Abstract*— Optical neural networks suffer from limited depth due to signal decay in passive systems. This work integrates programmable gain into a time-synthetic ONN. Its forward-only evolution suppresses instability, enabling stable loss compensation and deeper networks. Experiments demonstrate robust image classification, offering a scalable path for photonic AI.**

***Keywords*— optical neural networks, time synthetic dimension, non-Hermitian photonics.**

I. Introduction

Optical neural networks (ONNs) have attracted growing interest as a promising platform for accelerating artificial intelligence (AI), owing to the massive parallelism, broad bandwidth, and negligible Joule heating offered by photons. Over the past decade, interferometric photonic processors[1-4], diffractive optical networks[5,6], and metasurface-based architectures[7-9] have shown great performance in low-power inference and optical matrix multiplication. Nevertheless, despite active elements are sometimes used, like in optical-electrical-optical conversion stages or nonlinear activation modules, the computational cores of current ONNs are predominantly passive[10]. Since these passive transformations are either energy-conserving or dissipative, they can only achieve unitary or contraction matrices[11]. As optical signals propagate through such networks, losses caused by beam splitters, modulators, waveguides, and coupling interfaces unavoidably accumulate[12]. In deep circuits, the cumulative losses quickly lower the signal-to-noise ratio (SNR), making outputs dominated by thermal and detector noise and preventing current ONNs from reaching the depths required for modern AI workloads.

Incorporating optical gain offers a natural route to overcoming these limitations. In principle, controlled amplification could counteract propagation losses, preserve signal strength across long optical paths, and expand the transformation space from unitary operations to any complex-valued matrices[13]. Yet integrating gain directly into the computational pathways of an ONN is far from straightforward. Even small amplification imbalances can cause runaway power growth, chaotic oscillations, or mode-selective instabilities—phenomena that are greatly amplified in spatial photonic meshes dense with unavoidable feedback loops and unwanted parasitic reflections[14]. Consequently, the majority of ONN architectures choose to avoid inline gain, accepting the resulting performance degradation as an inevitable compromise. This tension has caused a long-standing dilemma in this field: while gain is essential for maintaining computational fidelity in deep optical networks, its direct incorporation tends to destabilize the very systems it is meant to enhance.

In this work, we address this contradiction by developing a fully programmable ONN that integrates gain within a time-synthetic dimension instead of a spatial photonic mesh[15-18]. A pair of coupled optical loops with slightly different lengths creates a temporal lattice in which optical pulses evolve through discrete time steps while experiencing dynamically programmed gain, loss, and phase shifts. Because computation only happens in the forward direction of time[19], the architecture is inherently causal: pulses never retrace their paths, and energy flow does not go backwards. This temporal causality stops the feedback pathways that usually cause gain-induced instabilities in spatial systems. As a result, the network can reliably harness amplification to counteract losses and sustain deep computation, as long as the programmed gain stays below the point where instability would happen.

The time-synthetic dimension also provides a powerful

scalability advantage. Network depth is based on the number of round trips, not the number of physical components, enabling one compact unit to emulate tens of thousands of effective optical gates[20,21]. This reduces the $O(N^2)$ scaling of spatial photonic processors into an O(1) footprint and makes the network more robust. To enable the network learning in realistic hardware, we further develop an in-situ optical training scheme that gets gradients directly from measured intensities, allowing the system to adapt to hardware imperfections, thermal drift, and accumulated noise[22-24]. Numerical studies indicate that gain maintains signal strength and stabilizes gradient propagation in deep temporal networks, while experiments on a coupled-loop platform with more than 30,000 effective time gates exhibit robust inference on datasets such as MNIST and CIFAR-10. These results collectively demonstrate that the incorporation of gain into a time-synthetic dimension offers a stable, scalable, and programmable pathway to deep optical neural networks, effectively addressing the depth and fidelity constraints associated with passive photonic processors.

REFERENCES

[1] Shen, Y., et al. “Deep learning with coherent nanophotonic circuits, ” Nat. Photon. vol. 11, pp. 441-446 (2017).

[2] Deng, H., & Khajavikhan, M. “Parity-time symmetric optical neural networks, ” Optica vol. 8, pp. 1328-1333 (2021).

[3] Liu, C., et al. “A programmable diffractive deep neural network based on a digital-coding metasurface array, ” Nat. Electron. vol. 5, pp. 113-122 (2022).

[4] Dong, B., et al. “Partial coherence enhances parallelized photonic computing, ” Nature vol. 632, pp. 55-62 (2024).

[5] Psaltis, D., Brady, D., Gu, X. G., & Lin, S. “Holography in artificial neural networks, ” Nature vol. 343, pp. 325-330 (1990).

[6] Wang, C., Cheng, Y., Xu, Z., Dai, Q., & Fang, L. “Diffractive tensorized unit for million-TOPS general-purpose computing, ” Nat. Photon. vol. 19, pp. 1078-1087 (2025).

[7] Lin, X., et al. “All-optical machine learning using diffractive deep neural networks, ” Science vol. 361, pp. 1004-1008 (2018).

[8] Xia, F., et al. Nonlinear optical encoding enabled by recurrent linear scattering, ” Nat. Photon. vol. 18, pp. 1067-1075 (2024).

[9] Yildirim, M., Dinc, N. U., Oguz, I., Psaltis, D., & Moser, C. “Nonlinear processing with linear optics, ” Nat. Photon. vol. 18, pp. 1076-1082 (2024).

[10] Xu, Z., et al. Large-scale photonic chiplet Taichi empowers 160-TOPS/W artificial general intelligence, ” Science vol. 384, pp. 202-209 (2024).

[11] Yu, S., & Park, N. “Heavy tails and pruning in programmable photonic circuits for universal unitaries, ” Nat. Commun. vol. 14, pp. 1853 (2023).

[12] Xie, Y., et al. “Complex-valued matrix-vector multiplication using a scalable coherent photonic processor, ” Sci. Adv. vol. 11, pp. eads7475 (2025).

[13] Singh, N., et al. “Watt-class silicon photonics-based optical high-power amplifier, ” Nat. Photon. vol. 19, pp. 307-314 (2025).

[14] Song, A., Murty Kottapalli, S. N., Goyal, R., Schölkopf, B., & Fischer, P. “Low-power scalable multilayer optoelectronic neural networks enabled with incoherent light, ” Nat. Commun. vol. 15, pp. 10692 (2024).

[15] Buddhiraju S., Dutt A., Minkov M., Williamson I. A., & Fan S. “Arbitrary linear transformations for photons in the frequency synthetic dimension, ” Nat. Commun. vol. 12, pp. 2401 (2021).

[16] Zhao, H., Li, B., Li, H., & Li, M. “Enabling scalable optical computing in synthetic frequency dimension using integrated cavity acousto-optics, ” Nat. Commun. vol. 13, pp. 5426 (2022).

[17] Ozawa, T., & Price, H. M. “Topological quantum matter in synthetic dimensions, ” Nat. Rev. Phys. vol. 1, pp. 349-357 (2019).

[18] Dutt, A., et al. “A single photonic cavity with two independent physical synthetic dimensions, ” Science vol. 367, pp. 59-64 (2020).

[19] Dong, Z., et al. “Quantum time reflection and refraction of ultracold atoms, ” Nat. Photon. vol. 18, pp. 68-73 (2024).

[20] Weidemann, S., et al. “Topological funneling of light. Science vol. 368, pp. 311-314 (2020).

[21] Ren, Y., et al. “Observation of momentum-gap topology of light at temporal interfaces in a time-synthetic lattice, ” Nat. Commun. vol. 16, pp. 707 (2025).

[22] Hughes, T. W., “Minkov, M., Shi, Y., & Fan, S. Training of photonic neural networks through in situ backpropagation and gradient measurement, ” Optica vol. 5, pp. 864-871 (2018).

[23] Pai, S., et al. “Experimentally realized in situ backpropagation for deep learning in photonic neural networks, ” Science vol. 380, pp. 398-404 (2023).

[24] Xue, Z., et al. “Fully forward mode training for optical neural networks, ” Nature, vol. 632, pp. 280-286 (2024).

Collision-driven out-of-equilibrium nonlinear optics in ultraviolet epsilon-near-zero materials

M. Silvestri[1], L. Assogna[1], D. Tedeschi[1,2], C. Ferrante[2], and A. Marini[1,2,*]

[1] Department of Physical and Chemical Sciences, University of L'Aquila, Via Vetoio, 61700 L'Aquila, Italy

[2] Consiglio Nazionale delle Ricerche, CNR-SPIN, Via Vetoio 10, 67100 L'Aquila, Italy

*Corresponding author: andrea.marini@univaq.it

***Abstract*— We theoretically model collision-driven out-of-equilibrium nonlinear optics in ultraviolet epsilon-near-zero materials, particularly sodium and aluminum, exploring their potential for the development of table-top extreme ultraviolet radiation sources and integrated spectroscopy schemes.**

***Keywords*—Epsilon-near-zero media, nonlinear optics, nanophotonics.**

I. Introduction

Nonlinear (NL) radiation-matter interactions give rise to many physical phenomena particularly relevant to quantum mechanical processes, and offer a promising platform to devise compact ultraviolet (UV) radiation sources. Harmonic generation (HG) is one of the main nonlinear effects amplified by photonic materials with low dielectric permittivity, known as epsilon near zero (ENZ) materials.

ENZ materials, thanks to their natural ability to bypass phase-matching, enhance NL radiation-matter interactions and play a crucial role for advanced NL phenomena, e.g., optical switching. Currently, ENZ media are adopted to enhance NL optical effects, particularly in the near-infrared part of the spectrum, where doped semiconductors, oxides, and nitrides display ENZ behavior. Poor materials show marked ENZ features in the UV that are promising for resonant third-harmonic generation (THG) in heterogeneous nanostructures, and for manipulation and guidance of UV radiation.

II. Methods

Here, we investigate the potential of nanostructures based on sodium (Na), aluminum (Al), and sodium-aluminum (Na-Al) heterostructures for NL applications [1-4]. We study the THG due to the out-of-equilibrium (OOE) electron dynamics. In turn, to model NL electron dynamics in the heterogeneous nanostructures we consider the Fokker-Planck-Landau (FPL) theoretical framework. We analytically calculate the Landau collisional integral in the weak coupling limit [5], obtaining a set of hydrodynamical equations (HDEs). By solving perturbatively HDEs, we derive an analytical expression for the dependence of the collision-driven THG NL-susceptibility over the pump field angular frequency. Moreover, to obtain the pump field distribution within the heterogeneous nanostructures, we use the undepleted pump approximation, modeling the THG radiation process accounting for multiple reflections of forward (FW) and backward (BW) waves.

III. Results and Discussion

Due to the coupling of the pump field enhancement and the radiation of the microscopic dipoles, the THG process exhibits a double resonance for transverse magnetic (TM) pump excitation at due to dipolar emission in an ENZ environment. Conversely, for transverse electric (TE) pump excitation we observe THG enhancement due to the excitation of Fabry-Perot resonances of the considered nanostructures. Finally, we find that for specifically incidence angle conditions it is possible to excite surface plasmon polaritons (SPPs) at the Na-Al interface thanks to attenuated total internal reflection (ATIR). This enables to attain a THG enhancement factor of 7 orders to magnitude as compared to non-resonant conditions, thus suggesting that ENZ heterogeneous nanostructures offer a promising platform for the development of integrated XUV sources.

IV. Conclusion

In conclusion, we observe that ENZ nanostructures constitute a promising platform to attain efficient THG in the UV spectral domain. Both Na and Al are promising ENZ media undergoing mitigated absorption. In addition, thanks to the broadband ENZ behavior of Na, we observe that SPPs can get excited at Na-Al interfaces, contributing to the maximization of THG efficiency. Our results indicate that Al/Na ENZ nanostructures are promising for integrated nonlinear conversion platforms.

Acknowledgments

This work has been partially funded by the European Union, NextGenerationEU, under the Italian Ministry of University and Research (MUR) National Innovation Ecosystem Grant No. ECS00000041-VITALITY-CUP E13C22001060006. This work has been partially supported by the Progetti di ricerca di

Rilevante Interesse Nazionale (PRIN) of the Italian Ministry of University and Research PHOTO (PHOtonics Terahertz devices based on tOpological materials) 2020RPEPNH and TransientMeta (Light-programmed two-dimensional meta-holograms for integrated neuromorphic computing) 2022N738SA-CUP E53D23001780006.

REFERENCES

[1] M. Silvestri, A. Sahoo, L. Assogna, P. Benassi, C. Ferrante, A. Ciattoni, and A. Marini, "Resonant third-harmonic generation driven by out-of-equilibrium electron dynamics in sodium-based near-zero index thin films," Nanophotonics vol. 13, pp. 2003-2013 (2024).

[2] M. Silvestri, M. Venturi, M. Di Muzio, R. Adhikary, C. Ferrante, P. Benassi, and A. Marini, "Harnessing collisional nonlinearity for enhanced harmonic generation by ultraviolet plasmonic nanoparticles," J. Chem. Phys. vol. 161, 054111 (2024).

[3] M. Silvestri, A. Sahoo, C. Ferrante, P. Benassi, A. Ciattoni, and A. Marini, "Doubly resonant third-harmonic generation in near-zero-index heterogeneous nanostructures," Phys. Rev. A 110, 023524 (2024).

[4] C. Ferrante, E. Principi, L. Assogna, A. Sahoo, G. Batignani, G. Fumero, L. Foglia, R. Mincigrucci, L. Giannessi, T. Scopigno, C. Masciovecchio, and A. Marini, "Epsilon-near-zero nonlinearity enhancement in the extreme ultraviolet," Light Sci Appl vol. 14, 374 (2025).

[5] A. Marini, A. Ciattoni, and C. Conti, "Out-of-equilibrium electron dynamics of silver driven by ultrafast electromagnetic fields – a novel hydrodynamical approach," Faraday Discuss. vol. 214, pp. 235-243 (2019).

Active Control of Optical Diffraction Using Excitonic Gratings

Ershad Mohammadi[1], **Mehmet Atıf Durmuş**[1], **Jorik van de Groep**[1]

[1] *Van der Waals-Zeeman Institute, Institute of Physics, University of Amsterdam, Amsterdam, the Netherlands*

e.mohammadi@uva.nl

Abstract:
We propose excitonic diffractive gratings with tunable diffraction efficiency. We develop an analytical framework that reveals how material properties and grating parameters determine device performance. We find the fundamental limits of diffraction modulation and provide physical insight into the design of ultrathin, actively tunable diffractive elements.
© 2026 The Author(s)

1. Introduction

Two-dimensional semiconductors, such as WS_2, exhibit exceptionally strong light–matter interactions that are pushing photonic devices toward the ultimate limits of miniaturization [1]. These phenomena are driven by excitons—bound electron–hole pairs—which dominate the optical response due to reduced screening and enhanced quantum confinement. The ability to dynamically modulate excitonic resonances via external stimuli, such as electrical gating [2], offers a route toward reconfigurable nanophotonics. Such active control can enable dynamic beam steering [3], typically achieved via a linear phase gradient across the unit cell that directs most of the power into a single diffraction order. However, an alternative functionality is the dynamic control of optical power in symmetric diffraction channels, a regime that conventional phase-engineering strategies cannot readily address.

Here, we introduce tunable gratings based on excitonic modulation at room temperature. This allows the grating strength to be dynamically controlled while preserving the symmetry of the diffracted orders, enabling potential applications including optical attenuators, diffractive switches, and high-speed imaging systems [4].

To realize a grating switch, one approach is to use an excitonic grating, such as WS_2, on a simple substrate like glass. The diffraction modulation in reflection and transmission is defined as $\Delta R^{\pm1} = R^{\pm1}_{\mathrm{ON}} - R^{\pm1}_{\mathrm{OFF}}$ and $\Delta T^{\pm1} = T^{\pm1}_{\mathrm{ON}} - T^{\pm1}_{\mathrm{OFF}}$, where $R^{\pm1}$ and $T^{\pm1}$ denote the reflectance and transmittance into the ±1 diffracted orders, respectively. The ON and OFF subscripts refer to excitons being present or suppressed in the monolayer via electrical gating.

For a WS_2 grating with a period of $2\,\mu$m and a line width of $1\,\mu$m on a glass substrate, the diffraction efficiency is extremely low with $\Delta R^{\pm1} \approx 0.05\%$ and $\Delta T^{\pm1} \approx 0.075\%$. Our analytical framework elucidates that the low efficiency arises from destructive interference between the field scattered by the excitonic layer and the background reflection or transmission from the substrate.

We demonstrate that placing the excitonic grating on top of a secondary grating can significantly enhance performance (Figure 1a) by introducing constructive interference between the two structures. In the ideal case, this substrate grating diffracts 50% of the incident power into each of the ±1 orders in the OFF state, while turning the excitons ON completely suppresses the diffraction. However, a WS_2 grating made from a single monolayer cannot fully achieve this desired operation, raising the question of how much diffraction modulation can realistically be obtained. To answer this, we derive closed-form expressions for diffraction modulation in reflection and transmission as:

$$\Delta R^{\pm1} = \frac{4k_0\delta}{\pi^2}\frac{(n_s-1)}{(n_s+1)^3}\,\mathrm{Im}\left\{\Delta\varepsilon_{\mathrm{ex}}\left[\exp(i2k_0h)-1\right]\right\} \tag{1}$$

and,

$$\Delta T^{\pm1} = \frac{8k_0\delta}{\pi^2}\frac{n_s}{(n_s+1)^3}\,\mathrm{Im}\left\{\Delta\varepsilon_{\mathrm{ex}}\left(1-\exp\left[-ik_0(n_s-1)h\right]\right)\right\} \tag{2}$$

where k_0 is the wave number in free space, and $\delta = 0.62$ nm is the thickness of the monolayer. n_s and h are the refractive index and the height of the substrate grating, respectively. $\Delta\varepsilon_{\mathrm{ex}} = \varepsilon_{\mathrm{ex,ON}} - \varepsilon_{\mathrm{ex,OFF}}$ is the change in excitonic permittivity for the ON and OFF states (inset in Figure 1c). In deriving these equations, we use the small-phase approximation within the monolayer ($k_0 n_{\mathrm{ex}}\delta \ll 1$, where $n_{\mathrm{ex}} = \sqrt{\varepsilon_{\mathrm{ex}}}$), as well as the local approximation commonly used for designing local metasurfaces [5].

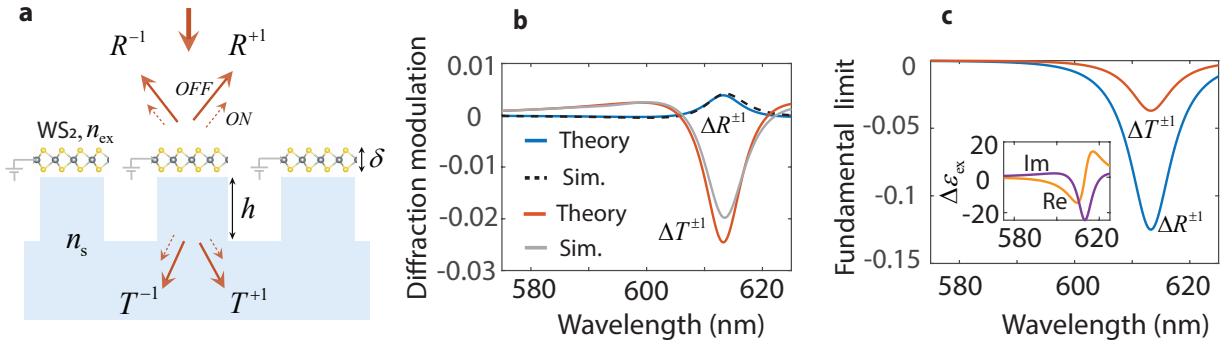

Fig. 1. **The diffraction modulation for an excitonic grating formed by an electrically tunable monolayer of WS_2 placed on top of another grating**. (a) The excitonic response for WS_2 can be electrically switched ON and OFF, which in turn modulates the diffraction efficiency of the system. The underlying grating introduces a controlled phase shift that interferes with the scattering phase of the excitons in the monolayer, enhancing the overall diffraction efficiency. (b) Modulation of the $+1$ or -1 diffracted orders in reflection ($\Delta R^{\pm1}$) and transmission ($\Delta T^{\pm1}$) for binary phase gratings made of glass ($n_s = 1.457$). The blue and orange curves represent the theoretical reflectance and transmittance modulation calculated from Eqs. (1) and (2), respectively. The dark and gray curves correspond to the results from RCWA simulations. (c) Fundamental limits of diffraction modulation in reflection and transmission, given by Eqs. (3) and (4).

To validate these derivations, we consider glass-based binary phase gratings in reflection and transmission, for which the required grating heights are $h = \lambda_0/4$ and $h = \lambda_0/2(n_s - 1)$, respectively. $\lambda_0 = 613.5$ nm is the excitonic resonance wavelength at room temperature and $n_s = 1.457$ is the refractive index of glass. The period and the line width for these gratings are $2\,\mu$m and $1\,\mu$m, respectively. Such gratings alone (without excitonic grating on top) achieve diffraction efficiencies of approximately 40.5% in reflection and 38% in transmission. After placing the WS_2 grating on top, we calculate the diffraction modulations $\Delta R^{\pm1}$ and $\Delta T^{\pm1}$ using Eqs. (1) and (2) (blue and orange curves in Figure 1b) and compare them with RCWA simulations (dashed black and gray curves in Figure 1b). Theory and simulation show good agreement, highlighting the applicability of the model and corroborating the physical insights provided by it. The maximum modulation reaches 0.4% in reflection and 2% in transmission, corresponding to increases of 8× and 27× compared to the excitonic grating on a glass substrate.

Interestingly, the interference condition is maximized for substrates with unconventional refractive indices. For example, for $n_s = 0$ and $h = [\tan^{-1}(\Delta\varepsilon_{\mathrm{ex,Re}}/\Delta\varepsilon_{\mathrm{ex,Im}}) + \pi]/2k_0$ we obtain the upper limit of Eq. (1) as:

$$\Delta R^{\pm1}_{ul} = \frac{4k_0\delta}{\pi^2}\left(\sqrt{\Delta\varepsilon^2_{\mathrm{ex,Re}} + \Delta\varepsilon^2_{\mathrm{ex,Im}}} - \Delta\varepsilon_{\mathrm{ex,Im}}\right) \tag{3}$$

This corresponds to a substrate with unity reflection coefficient and zero reflection phase. Similarly, for $n_s = 0.5$, and $h = 2[\tan^{-1}(\Delta\varepsilon_{\mathrm{ex,Re}}/\Delta\varepsilon_{\mathrm{ex,Im}}) + \pi]/k_0$ we find the upper limit of Eq. (2) as:

$$\Delta T^{\pm1}_{ul} = \frac{32k_0\delta}{27\pi^2}\left(\sqrt{\Delta\varepsilon^2_{\mathrm{ex,Re}} + \Delta\varepsilon^2_{\mathrm{ex,Im}}} - \Delta\varepsilon_{\mathrm{ex,Im}}\right) \tag{4}$$

These fundamental limits are shown in Figure 1c (blue and orange curves), corresponding to 12.5% for $\Delta R^{\pm1}$ and 3.7% for $\Delta T^{\pm1}$, respectively. Although the substrate grating can be engineered to approach these bounds through optimal interference, it does not increase the intrinsic light–matter interaction of the monolayer. The modulation is therefore fundamentally limited by the small optical thickness ($k_0\delta$) and the achievable change in excitonic permittivity, $\Delta\varepsilon_{\mathrm{ex}}$. Surpassing these limits requires enhancing the local field at the monolayer, for instance, via resonant structures, strong confinement, or multilayer designs [6].

References

1. F Javier García de Abajo, Dmitri N Basov, Frank HL Koppens, Lorenzo Orsini, Matteo Ceccanti, Sebastián Castilla, Lorenzo Cavicchi, Marco Polini, Paulo André D Gonçalves, Antonio T Costa, et al. Roadmap for photonics with 2d materials. *ACS photonics*, 12(8):3961–4095, 2025.
2. Jorik Van de Groep, Jung-Hwan Song, Umberto Celano, Qitong Li, Pieter G Kik, and Mark L Brongersma. Exciton resonance tuning of an atomically thin lens. *Nature Photonics*, 14(7):426–430, 2020.

3. Melissa Li, Claudio U Hail, Souvik Biswas, and Harry A Atwater. Excitonic beam steering in an active van der waals metasurface. *Nano Letters*, 23(7):2771–2777, 2023.
4. Jahja I Trisnadi, Clinton B Carlisle, and Robert Monteverde. Overview and applications of grating-light-valve-based optical write engines for high-speed digital imaging. In *MOEMS Display and Imaging Systems II*, volume 5348, pages 52–64. SPIE, 2004.
5. Nanfang Yu, Patrice Genevet, Mikhail A Kats, Francesco Aieta, Jean-Philippe Tetienne, Federico Capasso, and Zeno Gaburro. Light propagation with phase discontinuities: generalized laws of reflection and refraction. *science*, 334(6054):333–337, 2011.
6. Tom Hoekstra and Jorik van de Groep. Electrically tunable strong coupling in a hybrid-2d excitonic metasurface for optical modulation. *Light: Science & Applications*, 15(1):28, 2026.

Tautochrone and Squeezing in Nonuniform Lattices

I. Kiorpelidis[1,2], M. Heinrich[3], A. Szameit[3], G. A. Siviloglou[1,2,4], and K. G. Makris[1,2]

[1]Department of Physics, University of Crete, 70013 Heraklion, Greece
[2]Institute of Electronic Structure and Laser (IESL), FORTH, 71110 Heraklion, Greece
[3]Institute for Physics, University of Rostock, Rostock, Germany
[4]Department of Physics, Southern University of Science and Technology, Shenzhen 518055, China
*Corresponding author: gkiorpelidis@iesl.forth.gr

***Abstract*—We introduce photonic lattices with nonuniform couplings that manifest the classical tautochrone phenomenon and mimic quantum squeezed state dynamics. We also demonstrate that Kerr nonlinearity provides a mechanism to control the evolution between coherent-state-like and squeezed regimes.**

***Keywords*— Quantum-Classical Analogies, Waveguide Arrays, Beam Engineering.**

I. Introduction

The tautochrone problem, solved by Christiaan Huygens in the 17th century [1], demonstrates that a particle sliding without friction along a cycloid reaches the lowest point in the same time regardless of its initial position. In this work, we translate this classical principle into the realm of discrete optics by utilizing photonic lattices [2] —arrays of evanescently coupled waveguides— with nonuniform coupling between neighbouring waveguides [3]. Furthermore, we demonstrate that the evolution of Gaussian beams in these lattices mirrors the dynamics of squeezed states [4]. Depending on the initial parameters, the beam either maintains its shape (coherent-state-like propagation) or undergoes periodic width oscillations characteristic of squeezed evolution. Finally, we show that Kerr nonlinearity [5] serves as a critical control parameter, enabling the transition between the coherent-state-like and squeezed regimes.

II. Results

A. Nonuniform Coupling Profile

We consider a one-dimensional array of N evanescently coupled waveguides where the light evolution is described by the paraxial coupled mode equations. Namely, the evolution of the electric field envelope ψ_i in the i^{th} waveguide is given by

$$i\frac{d\psi_1}{dz} = -J_1\psi_2, \tag{1}$$
$$i\frac{d\psi_n}{dz} = -J_{n-1}\psi_{n-1} - J_n\psi_{n+1}, \quad n = 2,\dots,N-1, \tag{2}$$
$$i\frac{d\psi_N}{dz} = -J_{N-1}\psi_{N-1}, \tag{3}$$

with J_n being the hopping amplitude between waveguides n and $n+1$ [inset of Fig. 1(a)]. To achieve the tautochrone effect, we introduce a square-root coupling profile for the coupling:

$$J_n = \omega\sqrt{C^2 - \left(n - \frac{N}{2}\right)^2}. \tag{4}$$

Here, ω defines the oscillation frequency, and the parameter $C \geq N/2$ governs the degree of lattice inhomogeneity. It is noted here that for $C = N/2$, the coupling profile given in Eq. (4) reduces to that of the J_x-lattice [6]. This specific profile ensures that a Gaussian beam

$$\psi_n = \frac{1}{\sqrt{2\pi w_0^2}}\exp\left[-\frac{(n-n_0)^2}{2w_0^2}\right], \tag{5}$$

launched into the lattice, undergoes oscillatory motion with a period that is independent of its initial position n_0.

B. Optical Tautochrone and Squeezing Dynamics

The hallmarks of this system are illustrated in Fig. 1. We observe the following key phenomena:

- Tautochrone Focusing: As shown in Fig. 1(a), Gaussian beams launched from different initial locations focus simultaneously at the lattice midpoint ($n = 150$) after a fixed propagation distance $z = \pi/(4\omega)$. This confirms that the oscillation frequency is independent of the starting position, mimicking the classical tautochrone property.
- Coherent-State-like Propagation: The widths of the beams in Fig. 1(a) were specifically chosen to balance the lattice inhomogeneity. This ensures that each wavepacket preserves its shape throughout the entire evolution, a behavior analogous to quantum coherent states.
- Squeezing Evolution: The lattice dynamics fundamentally mirror those of a quantum harmonic oscillator. For a Gaussian beam where the initial width w_0 does not satisfy the "coherent-state-like condition", the width $w(z)$ undergoes periodic oscillations. This results in phase or amplitude squeezing, as illustrated in the dynamics of Figs. 1(b) and 1(c).

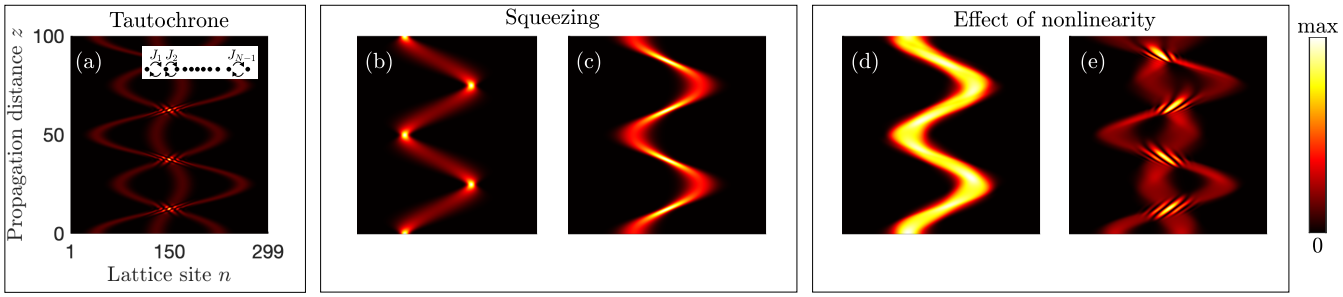

Fig. 1. Intensity evolution of three Gaussian wavepackets in a lattice of $N = 299$ sites, launched from $n_0 = 40$, 130, and 225 with widths $w_0 \approx 11.4$, 13, and 12.4 respectively. All beams focus simultaneously at the lattice midpoint ($n = 150$) with parameters $C = 3N/2$ and $\omega = 2\pi/100$. Inset: Cross-section schematic of the waveguide array. (b)-(c) Propagation of a Gaussian input centered at $n_0 = 100$ and initial widths $w_0 \approx 4.8$ and $w_0 \approx 20.8$, demonstrating phase and amplitude squeezing respectively. (d) Near-coherent propagation for a broad beam (the same beam used in panel c) achieved at a nonlinearity strength of $\gamma = 0.4$. (e) Intensity evolution for two beams launched from $n_0 = 70$ with $w_0 = 19.5$ and $n_0 = 170$ with $w_0 = 21$ in the nonlinear regime ($\gamma = 0.4$), confirming the persistence of the tautochrone effect.

C. Nonlinear Control

The introduction of Kerr nonlinearity provides a mechanism to manipulate the coherent-state-like and squeezed regimes. By adding a nonlinear term $-\gamma|\psi_i|^2\psi_i$ to the system equations, we demonstrate the following:

- Width Tuning: Increasing the nonlinearity parameter γ can reduce the amplitude of width oscillations for a broad beam, leading to near coherent-state-like propagation as shown in Fig. 1(d).
- Nonlinear Tautochrone: Despite the nonlinear interactions, the simultaneous focusing of beams (the tautochrone effect) persists, as confirmed in Fig. 1(e).

III. Conclusion

In this work, we have demonstrated a class of nonuniform photonic lattices that serve as a platform for exploring analogies between classical mechanics, quantum optics, and photonics. By engineering a specific square-root coupling profile, we manifested the optical analogue of the classical tautochrone problem, where optical beams launched from arbitrary positions focus at the same lattice site after a fixed propagation distance. We also showed that these lattices support quantum-inspired dynamics, including coherent-state-like propagation and periodic squeezing. Furthermore, we established that Kerr nonlinearity provides a degree of freedom for beam engineering, allowing for the control of a beam's diffraction; Specifically, nonlinearity can be utilized to tune width oscillations or to enable a transition between the squeezed and coherent regimes. These results open new avenues for light control in complex media through geometric engineering of the coupling coefficients.

Acknowledgments

I. K., G. A. S., and K. G. M. acknowledge support from the ERC (Grant 101045135, Beyond Anderson) and the SNF/H.F.R.I. (Project 11496, PSEUDOTOPPOS). G. S. further acknowledges NSFC Grant 12474262. M. H. and A. S. acknowledge the DFG (GRK 2676/1-2023, project 437567992; and SFB 1477, project 441234705).

References

[1] C. Huygens (Hugenii), Horologium Oscillatorium (Apud F. Muguet, Paris, France (1673). English translation: The Pendulum Clock (Iowa State University Press, Ames, 1986).
[2] D. N. Christodoulides, F. Lederer, and Y. Silberberg. Nature **424**, 817 (2003).
[3] I. Kiorpelidis, M. Heinrich, A. Szameit, G. A. Siviloglou, and K. G. Makris. arXiv:2512.05811 (2025).
[4] G. Breitenbach, S. Schiller, and J. Mlynek. Nature (London) **387**, 471 (1997).
[5] D. N. Christodoulides and R. I. Joseph. Opt. Lett. **13**, 794 (1988).
[6] R. Gordon. Opt. Lett. **29**, 2752 (2004).

Applications of single photons for quantum technologies

Christophe Couteau[1,2*]

[1] Laboratory Light, nanomaterials & nanotechnologies (L2n)
University of Technology of Troyes (UTT) & CNRS UMR 7076, Troyes, France
[2] EUT+ Institute of Nanomaterials & Nanotechnologies-EUTINN,
European University of Technology, European Union
*Corresponding author: christophe.couteau@utt.fr

***Abstract*— We will describe how single photon emission coming from single colour centres in diamond can be used for applications in quantum technologies such as quantum key distribution and quantum memristors. We will describe the optical properties of nanodiamonds and how they can be integrated into photonic platforms.**

***Keywords*— quantum optics, single photons, quantum technologies, quantum photonics.**

Broadband EM wave analysis and manipulation based on time-frequency structured light processing

José Azaña[1,*], Xinyi Zhu[1], Benjamin Crockett[1,2], Lim Geunweon[1], Majid Goodarzi[1], Connor Rowe[1], and Hao Sun[1]

[1]Institut National de la Recherche Scientifique – Energie, Matériaux, Télécommunications (INRS-EMT), Montreal/Varennes, QC, Canada
[2]Dept. of Electrical and Computer Engineering, University of British Columbia, Vancouver, BC, Canada
*Corresponding author: Jose.azana@inrs.ca

***Abstract*— This talk will review recent progress on photonic-enhanced real-time analysis and processing of broadband EM waves, including denoising and joint time-frequency analysis and filtering, over THz instantaneous bandwidths. The focus will be on a general, efficient methodology combining highly structured phase-only wave manipulations along time and frequency with solid potential for on-chip integration.**

***Keywords*— photonic signal processing, broadband EM waves, structured temporal modulation, phase filtering, time-frequency analysis and filtering.**

Electromagnetic Wave Localisation in Hyperuniform Disordered Photonic Structures

Marian Florescu, Alex Meek

Optoelectronics Research Centre, University of Southampton, United Kingdom
*Corresponding author: m.florescu@soton.ac.uk

***Abstract*— We study electromagnetic wave transport and localisation in one dimensional stealthy hyperuniform disordered photonic structures. Ensemble simulations show that correlated disorder tunes transparency, localisation, and band gap formation. A minimum spacing constraint stabilises short range structure and enables controlled localisation.**

***Keywords*— hyperuniform disorder, correlated disorder, photonic structures, wave localisation.**

I. Introduction

Hyperuniform disordered photonic structures suppress large scale density fluctuations while retaining tunable short and intermediate range correlations [1]. The one- and two-dimensional cases exhibit distinct structural behaviour compared with higher dimensions, with unusually persistent short-range correlations that strongly influence wave transport and localisation. In this context, correlated disorder provides a powerful route to control light localisation, bridging regimes of extended transport and Anderson localised states without relying on perturbed periodic order or complete randomness [2-6].

II. Methods

We generate one dimensional stealthy hyperuniform point patterns with controlled disorder strength, optionally enforcing a minimum spacing between neighbouring points. Photonic microstructures are constructed by arranging high index scatterers along the unit cell. We compute eigenmodes and localisation metrics using band structure simulations and validate transport trends using a scattering matrix approach across ensembles and system sizes. Statistical averaging over large ensembles is used to suppress sample-specific fluctuations and isolate the role of structural correlations in governing localisation and transport behaviour.

III. Results and Discussion

Results and Discussion

• The results reveal a clear separation between distinct transport regimes governed by the degree of hyperuniformity. At low frequencies, correlated disorder gives rise to extended transparency regimes in which wave propagation is robust despite the absence of periodic order. As frequency increases, modes progressively localise, with localisation strength and spectral extent strongly modulated by the underlying structural correlations.

• Analysis of inverse participation ratios, density of states, and level spacing statistics shows that one dimensional hyperuniform systems support both single parameter scaling and non scaling transport regimes. The boundaries between these regimes shift systematically with disorder strength, reflecting the competition between long range hyperuniform correlations and short-range structural fluctuations.

• Introducing a minimum spacing between scattering elements suppresses pathological short-range clustering while preserving hyperuniformity. This modification enables the emergence of photonic band gap behaviour and produces a more controlled localisation landscape. Disorder resolved analysis demonstrates that the observed transport properties remain stable under additional non hyperuniform perturbations, highlighting the resilience of correlated disorder engineered photonic media.

IV. Conclusion

One dimensional hyperuniform disorder provides a compact route to engineer transparency and localisation through structural correlations rather than periodicity alone. These findings establish correlated disorder as a practical and robust design parameter for photonic and metamaterial systems.

Acknowledgments

This work was supported by EPSRC DTP awards EP/W524463/1 and EP/R513350/1. M. Florescu acknowledges EPSRC support under Grant EP/Y016440/

References

[1] M. Florescu, S. Torquato, and P. J. Steinhardt, Proceedings of the National Academy of Sciences, vol. 106, pp. 20658 to 20663, 2009.
[2] P. W. Anderson, Physical Review, vol. 109, pp. 1492 to 1505, 1958.
[3] S. John, Physical Review Letters, vol. 58, pp. 2486 to 2489, 1987.
[4] E. Abrahams, P. W. Anderson, D. C. Licciardello, and T. V. Ramakrishnan, Physical Review Letters, vol. 42, pp. 673 to 676, 1979.
[5] C. M. Soukoulis and E. N. Economou, Waves in Random Media, vol. 9, pp. 255 to 272, 1999.
[6] L. S. Froufe-Perez, M. Engel, J. J. Saenz, and F. Scheffold, Proceedings of the National Academy of Sciences, vol. 114, pp. 9570 to 9574, 2017.

Brillouin scattering in integrated photonic circuits

Moritz Merklein

The University of Sydney, Australia

*Corresponding author: moritz.merklein@sydney.edu.au

***Abstract*— This talk will explore stimulated Brillouin scattering (SBS) in photonic integrated circuits as a versatile mechanism for strong light–sound interactions on chip. I will compare different waveguide platforms that enable strong SBS, focusing on implementations based on both bulk acoustic waves and more recent breakthroughs that harness surface acoustic waves. I will further discuss how engineering the optical density of states provides powerful ways to tailor and manipulate Brillouin interactions, enabling new opportunities for signal processing.**

Advanced photonics with liquid crystals in microcavities

D. Solnyshkov[1,9,*], M. Muszyński[2], P. Kokhanchik[1], I. Septembre[1], D. Bobylev[1], R. Mirek[3], D. Urbonas[3], P. Tassan[3], P. Kapuściński[2], P. Oliwa[2], I. Georgakilas[3], T. Stöferle[3], R. F. Mahrt[3], M. Forster[4], U. Scherf[4], D. Dovzhenko[5], E. Oton[6], R. Mazur[6], P. Morawiak[6], W. Piecek[6], P. Kula[7], W. Bardyszewski[2], M. Król[2], M. Kedziora[2], K. Łempicka-Mirek[2], P. G. Lagoudakis[5], B. Pietka[2], G. Malpuech[1], J. Szczytko[2]

[1]Université Clermont Auvergne, Clermont Auvergne INP, CNRS, Institut Pascal, Clermont-Ferrand, France
[2]University of Warsaw, Poland
[3]IBM Research Europe – Zurich, Säumerstrasse, Rüschlikon, Switzerland
[4]Bergische Universität Wuppertal, Gauss Strasse, Wuppertal, Germany
[5]School of Physics and Astronomy, University of Southampton, Southampton, United Kingdom
[6]Institute of Applied Physics, Military University of Technology, Warsaw, Poland
[7]Institute of Chemistry, Military University of Technology, Warsaw, Poland
[8]Institut Universitaire de France (IUF), 75231 Paris, France
*Corresponding author: dmitry.solnyshkov@uca.fr

***Abstract*—We provide an overview of recent results for microcavities with liquid crystals in the fields of topological and non-Hermitian photonics. We demonstrate synthetic gauge fields, spin-orbit coupling, control and annihilation of exceptional points, strong coupling and polariton condensation into a supersolid state, as well as OAM lasing from topological defects.**

***Keywords*— liquid crystals, spin-orbit coupling, topological photonics.**

Liquid crystals are well-known for their optical properties, which are extensively studied fundamentally and at the same time used for applications in everyday life, such as flat screens. Among these optical properties one can name the strong birefringence due to the asymmetry of the molecules composing the liquid crystals. The molecule orientation can be controlled by anchoring and by applying an electric field, which gives the access to tunable birefringence.

A system composed of two textbook ingredients: a planar resonator and a liquid crystal with controllable birefringence, was recently shown to exhibit a very non-trivial and useful behavior [1]. When the birefringence is sufficiently large so that two orthogonally-polarized modes with mode numbers of opposite parity come into resonance, the system as a whole starts to exhibit emergent optical activity: the eigenstates in the direction perpendicular to the plane of the tilt of the optical axis become circular-polarized, with opposite circular polarization for opposite wave vectors.

This can be described as an emergent Rashba-Dresselhaus spin-orbit coupling [1], which can be represented as a synthetic gauge field (non-Abelian in the general case). Similar effects have been observed in other materials with large birefringence, such as organic crystal cavities and perovskites.

In liquid crystal cavities, this original spin-orbit coupling can be combined with other ingredients, such as photonic potentials (localized or periodic), allowing the study of localized photonic states, their coupling, as well as the formation of periodic bands.

In particular, we have studied individual and coupled photonic traps in presence of spin-orbit coupling, demonstrating the possibility of a topological transition related to the inversion of the sign of the effective tunneling coefficient [2] in addition to the possibility of the modulation of its phase [3].

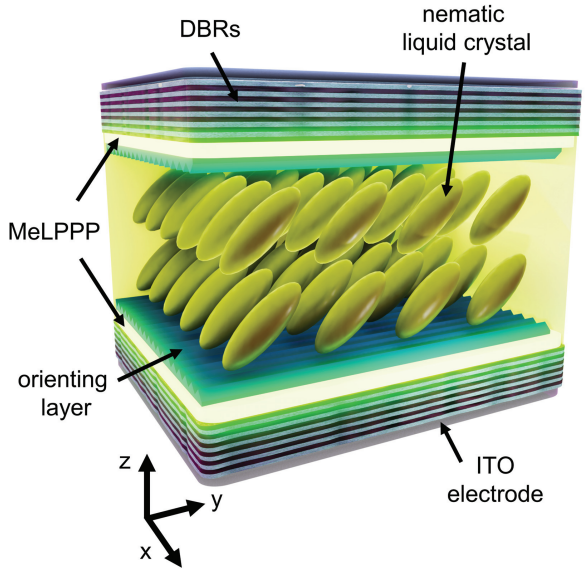

Fig. 1. A liquid crystal microcavity with an organic polymer.

Adding layers of materials with strong excitonic resonances into the cavity allows obtaining the regime of strong light-

matter coupling (Fig. 1). We have demonstrated the condensation of resulting exciton-polaritons in presence of spin-orbit coupling in different configurations. In particular, condensation in the two minima of the Rashba-Dresselhaus dispersion leads to the formation of a polariton supersolid [4], [5], combining superfluidity with periodic density modulation. The polarization texture of the condensate represents a persistent spin helix.

The liquid crystals in the microcavities can also form a uniform lying helix, providing both a spin-orbit coupling and a periodic potential. This has allowed us to study photonic bands in presence of spin-orbit coupling and polariton condensation and lasing in these bands [6].

In addition, the above ingredients can be combined with strong non-Hermiticity arising from the birefringence of liquid crystals, allowing the observation and study of exceptional points, their motion and annihilation [7].

To conclude, liquid crystals in microcavities represent an extremely rich systems with interesting optical properties.

Acknowledgments

This work was supported by the European Union's Horizon 2020 program, through a FET Open research and innovation action under the grant agreements No. 964770 (TopoLight) and EU H2020 MSCA-ITN project under grant agreement No. 956071 (AppQInfo). Additional support was provided by the ANR Labex GaNext (ANR-11-LABX-0014), the ANR program "Investissements d'Avenir" through the IDEX-ISITE initiative 16-IDEX-0001 (CAP 20-25), the ANR project MoirePlusPlus (ANR-23-CE09-0033), and the ANR project "NEWAVE" (ANR-21-CE24-0019). We are grateful to the Mésocentre Clermont-Auvergne of the Université Clermont Auvergne for providing help, computing and storage resources.

References

[1] K. Rechcińska, M. Król, R. Mazur, P. Morawiak, R. Mirek, K. Łempicka, W. Bardyszewski, M. Matuszewski, P. Kula, W. Piecek *et al.*, "Engineering spin-orbit synthetic Hamiltonians in liquid-crystal optical cavities," *Science*, vol. 366, no. 6466, pp. 727–730, 2019.

[2] R. Mirek, P. Kokhanchik, D. Urbonas, I. Georgakilas, M. Muszyński, P. Kapuściński, P. Oliwa, B. Pietka, J. Szczytko, M. Forster *et al.*, "In situ tunneling control in photonic potentials by rashba–dresselhaus spin–orbit coupling," *Optica*, vol. 12, no. 9, pp. 1548–1552, 2025.

[3] P. Kokhanchik, D. Solnyshkov, T. Stöferle, B. Pietka, J. Szczytko, and G. Malpuech, "Modulated rashba-dresselhaus spin-orbit coupling for topology control and analog simulations," *Physical Review Letters*, vol. 129, no. 24, p. 246801, 2022.

[4] M. Muszyński, P. Kokhanchik, D. Urbonas, P. Kapusciński, P. Oliwa, R. Mirek, I. Georgakilas, T. Stoferle, R. F. Mahrt, M. Forster, U. Scherf, D. Dovzhenko, R. Mazur, P. Morawiak, W. Piecek, P. Kula, B. Pietka, D. Solnyshkov, G. Malpuech, and J. Szczytko, "Observation of a supersolid phase in a spin-orbit coupled exciton-polariton Bose-Einstein condensate at room temperature," *arXiv:2407.02406*, 2024.

[5] D. Solnyshkov, R. Mirek, D. Urbonas, E. Kobiyama, P. Tassan, I. Georgakilas, R. F. Mahrt, M. Forster, U. Scherf, M. Muszynski *et al.*, "Kibble-zurek mechanism in a polariton supersolid," *arXiv preprint arXiv:2512.17362*, 2025.

[6] M. Muszyński, P. Oliwa, P. Kokhanchik, P. Kapuściński, E. Oton, R. Mazur, P. Morawiak, W. Piecek, P. Kula, W. Bardyszewski *et al.*, "Electrically tunable spin-orbit coupled photonic lattice in a liquid crystal microcavity," *Laser & Photonics Reviews*, vol. 19, no. 7, p. 2400794, 2025.

[7] M. Król, I. Septembre, P. Oliwa, M. Kedziora, K. Łempicka-Mirek, M. Muszyński, R. Mazur, P. Morawiak, W. Piecek, P. Kula *et al.*, "Annihilation of exceptional points from different dirac valleys in a 2d photonic system," *Nature Communications*, vol. 13, no. 1, p. 5340, 2022.

Breakdown of Harmonic Conversion Scaling Laws in Nonlinear Nanocavities

Marco Gandolfi[1,2,3,*], Michael Scalora[1], Costantino De Angelis[1,2,3], and Maria Antonietta Vincenti[1,2,3]

[1]Dipartimento di Ingegneria dell'Informazione Università degli Studi di Brescia, Via Branze 38, Brescia 25123, Italy
[2]Consiglio Nazionale delle Rircerche, Istituto Nazionale di Ottica, Via Branze 45, Brescia 25123, Italy
[3]Consorzio Nazionale Interuniversitario per le Telecomunicazioni (CNIT), Viale G.P. Usberti 181/A Sede Scientifica di Ingegneria-Palazzina 3, Parma 43124, Italy

*Corresponding author: marco.gandolfi1@unibs.it

***Abstract*— We derive a relation that predicts the pump-intensity threshold at which deviations from the conventional n-1 power-law scaling of the nth-harmonic conversion efficiency emerge. This relation is validated through full-wave nonlinear simulations.**

***Keywords*— higher harmonic generation, nonlinear optical processes, coupled mode theory, unconventional power law scaling.**

I. Introduction

Nonlinear optics emerged in the 1960s with the development of the laser, which provided the coherent and intense light necessary to access nonlinear optical phenomena. Since then, the field has advanced dramatically. The advent of metasurfaces (MSs) marked a significant step forward, enabling unprecedented control over light and allowing efficient generation of new wavelengths with remarkable design flexibility [1-3].

Despite the maturity of this technology and its extensive exploration, some puzzling questions still remain not answered. In particular, an unconventional trend in the power-law scaling has been observed in some metasurface platforms with particularly high quality-factor resonances or for elevated pump power (P_{pump}) values. For example, in Ref. [4] the output power of the n-th harmonic was found to scale as P_{pump}^{β}, with $\beta < n$, for n=3,5,7,and 9 in a symmetry-broken silicon membrane supporting quasi–bound states in the continuum. An analogous trend was reported also in Refs. [5, 6]. Strikingly, this unconventional scaling was not clearly observed in other studies [7]. This discrepancy may be attributed to differences in the quality factors of the investigated structures at the pump wavelength, which shift the intensity range where the unconventional scaling emerges. As a result, this effect may become inaccessible in certain MSs when excited with the power levels available from standard lasers.

To clarify this intricate scenario, we develop a model based on the coupled-mode theory to study the resonant high-harmonic (HH) generation. We derive a simple expression relating the Q-factor of the involved modes to the threshold pump intensity I_{th} at which the conversion efficiency (defined as $\eta^{(n)} = I^{(n)}/I_{pump}$, where $I^{(n)}$ and I_{pump} denote the intensity at the n-th harmonic frequency and at the pump) starts deviating from the conventional I_{pump}^{n-1} scaling.

II. Results and Discussion

We develop a model based on the coupled mode theory [8,9] and we predict the following scaling law:

$$I_{th} \propto Q_{FF}^{-\frac{n}{n-1}} Q_n^{-\frac{1}{n-1}}, \qquad (1)$$

Where Q_{FF} and Q_n are the Q-factor of the involved modes at the fundamental frequency (FF) and the n-th harmonics frequency.

To test the validity of this law, we develop a numerical model to calculate the higher harmonic generation, solved with Finite Elements Method (FEM). As a simple, but instructive, case study we consider a Distributed Bragg Reflector (DBR) with N barriers. As schematized in Fig. 1a, in the middle of the DBR, a defect is placed, leading to a confined cavity mode that creates a transmission peak inside the high reflectance band typical of the DBR. The Q-factor of this mode increases with the number of barriers. The barriers are achieved by alternating slabs of SiO_2 and TiO_2, of thickness $\lambda_0/4n_{SiO2}$ and $\lambda_0/4n_{TiO2}$ respectively, where λ_0 is the wavelength of the high transmittance mode. The cavity is made of TiO_2, and its thickness is $\lambda_0/2n_{TiO2}$. All the structure is sandwiched between a semi-infinite substrate and a superstrate, both made of SiO_2. For the sake of simplicity, here we neglect the materials dispersion, and we use $n_{SiO2} = 1.45$ and $n_{TiO2} = 2.45$. Furthermore, we suppose that the optical nonlinearity is active only in the cavity, a good approximation since the fields are very intense only in that spatial region. We illuminate with a plane wave at normal incidence, with wavelength λ_0 =1.55 μm.

For a fixed number of barriers, we calculate with FEM the conversion efficiency as a function of the incident power, and we select the pump intensity for which the conversion efficiency $\eta^{(n)}$ deviates of more than 1% with respect to the n-1 power scaling law. We repeat this analysis by changing N and both for second harmonic generation (SHG) and third harmonic generation (THG) processes.

In Fig. 1b we report I_{th} for SHG calculated for N running from 1 to 10, and as a function of the Q factor of the FF mode for the same number of barriers. This graph shows a quadratic scaling, as demonstrated by the good fit with Q^{-2} function. This result matches very well Eq. 1, considering that the system does not support a high Q mode at the SH frequency related to the DBR, thus $Q_2 \approx 1$.

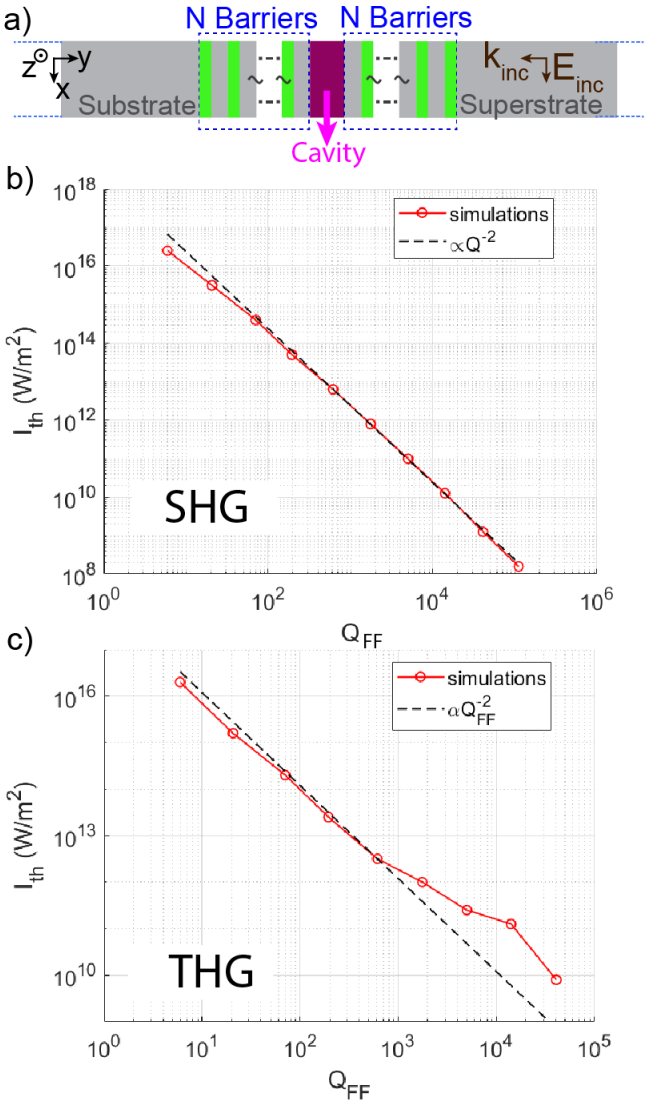

Fig. 1 a) Geometry of the DBR with a defect playing as cavity. b) and c): Threshold intensity as a function of the Q-factor of the mode at the FF, for SHG and THG, respectively.

In Fig. 1c), instead, we analyze the THG. In the modeling we have included also self-phase and cross-phase modulation terms. Surprisingly, also in this case the computed threshold intensity scales as Q_{FF}^{-2}. This result can be easily justified by means of Eq. (1), if we consider that the Q-factor of the mode at the TH frequency scales as $Q_3 \propto Q_1$.

III. Conclusion

We have exploited the coupled mode theory to derive a general equation ruling the threshold intensity (where the unconventional lower power scaling of the conversion efficiency starts to play) in terms of the Q-factors of the involved modes. We have benchmarked this trend against the SHG and THG in a DBR system with a cavity, solved with FEM. However, the derived equation is very general and can be applied for a wide range of experimental situations.

These findings shed light on the intricate dynamics of HH generation at moderate to high pump powers and offer critical guidance for tailoring metasurface design to either amplify or mitigate the emergence of unconventional scaling behaviour.

References

[1] S. Keren-Zur, O. Avayu, L. Michaeli, and Tal Ellenbogen., "Nonlinear Beam Shaping with Plasmonic Metasurfaces," ACS Photonics, 3, 1, 2015.

[2] Y. Xu, J. Sun, J. Frantz, M. I. Shalaev, W. Walasik, A. Pandey, J. D. Myers, R. Y. Bekele, A. Tsukernik, J. S. Sanghera, and N. M. Litchinitser "Reconfiguring structured light beams using nonlinear metasurfaces," Optics Express 26, 23, 2018.

[3] L. Qu, Wei Wu, D. Zhang, C. Wang, L. Bai, C. Li, W. Cai, M. Ren, A. Alù, J. Xu, "Beam Shaping by Stacked Nonlinear Moiré Metasurfaces," Nano Letters 25, 12, 2025.

[4] P. Tonkaev, F. Richter, I. Toftul, P. Tonkaev, F. Richter, I. Toftul, M. A. Vincenti, I. Sinev, M. Scalora, H. Altug, Y. Kivshar, "Unconventional high-harmonic generation in resonant membrane metasurfaces," arXiv:2506.20873, (2025).

[5] V. Korolev, A. D. Sinelnik, M. V. Rybin, P. Lazarenko, O. M. Kushchenko, V. Glukhenkaya , S. Kozyukhin, M. Zuerch , C. Spielmann, T. Pertsch, I. Staude and D. Kartashov, "Tunable high-order harmonic generation in GeSbTe nano-films," a Nanophotonics, 13, 18, 2024.

[6] Y. Yang, J. Lu, A. Manjavacas, T. S. Luk, H. Liu, K. Kelley, J.-P. Maria, E. L. Runnerstrom, M. B. Sinclair, S. Ghimire, I. Brener "High-harmonic generation from an epsilon-near-zero material," Nature Physics 15, 1022–1026, 2019.

[7] G. Zograf, K. Koshelev, A. Zalogina, V. Korolev, R. Hollinger, D.-Y. Choi, M. Zuerch, C. Spielmann, B. Luther-Davies, D. Kartashov, S. V. Makarov, S. S. Kruk, Y. Kivshar, "High-Harmonic Generation from Resonant Dielectric Metasurfaces Empowered by Bound States in the Continuum," ACS Photonics, 9, 567−574, 2022.

[8] Alejandro Rodriguez, Marin Soljačić, J. D. Joannopoulos, and Steven G. Johnson, "$\chi^{(2)}$ and $\chi^{(3)}$ harmonic generation at a critical power in inhomogeneous doubly resonant cavities", Optics Express, 15, 12, 2007.

[9] Hila Hashemi, Alejandro W. Rodriguez, J. D. Joannopoulos, Marin Soljačić, and Steven G. Johnson, "Nonlinear harmonic generation and devices in doubly resonant Kerr cavities", Physical Review A, 79, 013812, 2009,

Computational Electromagnetics for Radiating Structures and Complex Media

Reduced-Order Framework for Layered Photonic Cavities

Przemysław Oliwa[1], Helgi Sigurdsson[1], Witold Bardyszewski[2], Jacek Szczytko[1,*]
[1]Institute of Experimental Physics, Faculty of Physics, University of Warsaw, Poland
[2] Institute of Theoretical Physics, Faculty of Physics, University of Warsaw, Poland
*Corresponding author: Jacek.Szczytko@fuw.edu.pl

***Abstract* — We introduce a symmetry-guided optimization framework that reconstructs effective photonic 2-mode Hamiltonians directly from measured or transfer-matrix-derived Stokes fields and energy for bands. The effective Hamiltonian provides rapid and predictive access to the polarization-resolved band structure across momentum or real space.**

***Keywords* — liquid-crystal microcavities, optical Rashba-Dresselhaus spin-orbit coupling**

I. Introduction

Accurate modeling of layered photonic cavities relies on Maxwell-based formalisms such as the transfer matrix method (TMM), which require repeated calculations over many in-plane wavevectors and polarization states, making the exploration of complex dispersion landscapes computationally demanding. While transfer matrix approach provides rigorous optical solutions, extracting physical insight and efficiently scanning parameter spaces remain significant challenges, particularly in cavities exhibiting strong birefringence, optical activity, and non-Hermitian behavior [1].

II. Methods

We introduce a symmetry-guided optimization framework that reconstructs effective photonic 2-mode Hamiltonians directly from measured or transfer-matrix-derived Stokes fields and energy for bands (Fig. 1). Fitting complex 2D polynomial with arbitrary order to Hamiltonian's coefficients allows for reproducing numerical data with high precision and dramatically reduces number of TMM simulation. Once obtained, the effective Hamiltonian provides rapid and predictive access to the polarization-resolved band structure across momentum or real space.

This reduced-order description enables efficient investigation of higher-order photonic spin-orbit coupling, exceptional points, Fermi arcs, and polarization singularities without exhaustive numerical sampling. Applicable to a wide class of layered systems – including cavities with quantum wells, perovskites, organic materials, and liquid crystals [2] – the approach establishes a practical bridge between rigorous Maxwell solvers and compact analytical models. More broadly, the framework is applicable to band-structured systems in which polarization – or other internal degrees of freedom like electron spin – are intrinsically linked to the dispersion. It therefore offers a powerful computational tool for studying complex photonic and topological phenomena [3] and for steering the design of next-generation anisotropic cavity platforms.

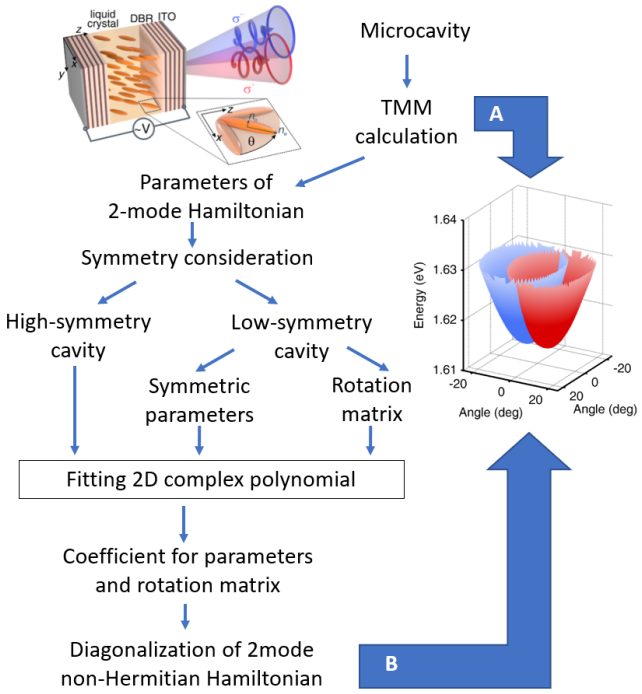

Fig. 1. Schematic illustration of the method. The images show a sketch of a liquid-crystal microcavity and the dispersion relation $E(\vec{k})$ for circularly polarized emission in the Rashba-Dresselhaus spin-orbit coupling regime [2]. Numerical **method A** (Transfer Matrix Method) is exact but computationally demanding. **Method B** requires the calculation of only a few points in parameter space while providing accurate estimates of $E(k)$,optical losses and distribution of Stokes polarization parameters.

III. Results and Discussion

In the first approximation, the (micro)cavity mode exhibits a parabolic dispersion $E(\vec{k})$ as a function of the wavevector $\vec{k} = (\vec{k}_\parallel, k_z)$, described by the following equation:

$$E(\vec{k}) = \frac{\hbar c}{n}\sqrt{k_z^2 + \vec{k}_\parallel^2} \approx E_N + \frac{\hbar^2 \vec{k}_\parallel^2}{2m^*}$$

where quantized momentum perpendicular to the cavity plane is $k_z = N\pi/nL$, N is the mode index and n is a refractive index of media inside cavity, $E_N = \hbar c N\pi/nL$ and the effective mass of the cavity photon $m^* = N\hbar\pi n/cL$ for a cavity of length L.

In addition, this mode exhibits a characteristic distribution of electric field vector as a function of the wavevector. This distribution can be conveniently described using the Stokes polarization parameters as functions of $\vec{k}_\parallel = (k_x, k_y)$. In systems with multiple modes, where only two are relevant, the interaction between them can be effectively captured using a two-mode Hamiltonian [1].

In our approach, using TMM calculation for microcavities belonging to different point group, we generate the distributions of complex energy $E(\vec{k}_\parallel)$ and Stokes polarization parameters $s_i(\vec{k}_\parallel), i = \{0,1,2,3\}$. Based on these distributions, we construct an effective 2-mode Hamiltonian that reproduces both the dispersion and polarization structure.

Importantly, the general method presented here is not limited to photonic systems. It can be applied to any scenario in which one can define the dispersion $E_\pm(\vec{r})$ (generally representing two eigenvalues marked as $\pm$) and Stokes polarization parameters $s_{i\pm}(\vec{r})$ (generally representing two eigenvectors) for a pair of states varying in a parameter space $\vec{r}$. For example, this framework can be extended to describe band structures of electrons, holes, phonons, magnons, or excitons in a wide range of physical systems.

The general form of the 2-mode non-Hermitian Hamiltonian in the linear basis is given by:

$$\mathcal{H}(\vec{k}_\parallel) = h_0\sigma_0 + h^T(\vec{k}_\parallel)\cdot\vec{\sigma}$$

where $h(\vec{k}_\parallel) = [h_z(k_\parallel), h_x(k_\parallel), h_y(k_\parallel)]$ and $\vec{\sigma} = [\sigma_z, \sigma_x, \sigma_y]^T$ where σ_i are Pauli matrices. The Hamiltonian $\mathcal{H}(\vec{k}_\parallel)$ has the following complex eigenvalues $E_\pm(\vec{k}_\parallel)$ and eigenvectors $\vec{v}_\pm(\vec{k}_\parallel)$:

$$E_\pm(\vec{k}_\parallel) = h_0(\vec{k}_\parallel) \pm \sqrt{h^T(\vec{k}_\parallel)\cdot h(\vec{k}_\parallel)}$$

$$\mathcal{H}(\vec{k}_\parallel)\,\vec{v}_\pm(\vec{k}_\parallel) = E_\pm(\vec{k}_\parallel)\vec{v}_\pm(\vec{k}_\parallel)$$

Using eigenvectors or density matrices, one can define the normalized Stokes polarization parameters. Therefore, apart from the positions of exceptional points [4], the distributions of the $h_i(\vec{k}_\parallel)$ parameters in the 2-mode non-Hermitian Hamiltonian $\mathcal{H}(\vec{k}_\parallel)$ can be uniquely determined for any given dispersion and Stokes polarization structure of both branches in a planar cavity. The $h_i(\vec{k}_\parallel)$ parameters may exhibit lower symmetry than the symmetry of considered cavity (low-symmetry cavity). Nevertheless, we proposed symmetrization procedure that restores the symmetry of the $h_i(\vec{k}_\parallel)$ parameters to match the symmetry of the point group. Therefore they can be approximated with a general 2D complex polynomial function. In addition, we introduce the correction matrix to properly reproduce distribution of Stokes polarization parameters.

It should be emphasized that this method is not limited to the analysis of numerical data, but can also be applied to experimental measurements, for example those obtained using polarization- and angle-resolved tomography spectroscopy.

IV. Conclusion

We present a symmetry-guided optimization framework that extracts the effective photonic Hamiltonian from measured or transfer-matrix-derived Stokes fields and energy of bands. By determining the complex coefficients of the parameters of 2-mode non-Hermitian Hamiltonian, the method provides an accurate and compact description of cavity photon states. It is broadly applicable to layered planar systems, including structures with quantum wells, perovskites, organic materials, birefringent liquid crystals and rapidly developed structures with gratings.

Acknowledgments

The authors acknowledge the support of the project No 2023/51/B/ST3/03025 by the Polish National Science Centre.

References

[1] P. Oliwa, W. Bardyszewski, and J. Szczytko, "Quantum mechanical-like approach with non-Hermitian effective Hamiltonians in spin-orbit coupled optical cavities", Phys. Rev. Research **6**, 013324 (2024)

[2] K. Rechcińska, et al., "Engineering spin-orbit synthetic Hamiltonians in liquid-crystal optical cavities", Science 366, 727-730 (2019)

[3] P. Oliwa, et al. "Electrically Tunable Momentum Space Polarization Singularities in Liquid Crystal Microcavities", Advanced Science **12**, 2500060 (2025)

[4] M. Król et al. "Annihilation of exceptional points from different Dirac valleys in a 2D photonic system" Nature Communications **13**, 5340 (2022)

Leakage from Uniform and Periodically Loaded Line Waveguides

Mikhail Madji[1], Paolo Baccarelli[2], Alessio Monti[2], Alessandro Toscano[2], Filiberto Bilotti[2], Paolo Burghignoli[1,*]

[1]Department of Information Engineering, Electronics and Telecommunications, Sapienza University of Rome, Italy
[2]Department of Industrial, Electronic, and Mechanical Engineering, Roma Tre University of Rome, Italy
*Corresponding author: paolo.burghignoli@uniroma1.it

***Abstract*—This contribution presents recent results on dispersion and radiation properties of leaky edge modes (or line waves) supported by a linear discontinuity between inductive and capacitive metasurfaces.**

***Keywords*— line waves, leaky waves, leaky-wave antennas, metasurfaces, periodic structures.**

I. Introduction

Line waves are edge modes supported by linear discontinuities in the surface impedance of planar or even curved metasurfaces. They have received considerable attention in the last decade, in view of their intriguing properties including extreme transverse subwavelength field confinement, wide propagation bandwidth in bound regimes, resilience to backscattering, spin-momentum locking, and radiative effects in leaky regimes [1].

II. Leaky Line Waves: two Scenarios

We consider here single-layer, double face line waveguides with transverse cross section exhibiting central symmetry, designed according to the workflow presented in [2]. In particular, two configurations are studied, in which two different mechanisms provide power leakage: *i*) a uniform waveguide, constituted by two pairs of complementary inductive and capacitive metasurfaces sharing the same substrate, realized through metal grid and patch arrays, respectively [cf. Fig. 1(a)]; *ii*) the same structure, periodically loaded with metal patches [cf. Fig. 1(b)].

In the former case, a wideband modal analysis allows for following the line-wave dispersion curve inside the entire bound-mode triangle in a Brillouin diagram and eventually outside it, at frequencies beyond the homogenization regime for the constituent metasurfaces. In such regime, the line wave becomes leaky and both surface and volume leaky regimes are observed [3].

In the latter case, the structure possesses a double periodicity, i.e., a micro-period pertaining to the constituent metasurfaces, much smaller than the free-space wavelength in the considered frequency range, and a macro-period comparable to free-space wavelength, introduced with the aim of achieving leaky regimes with controlled backward and forward radiative features.

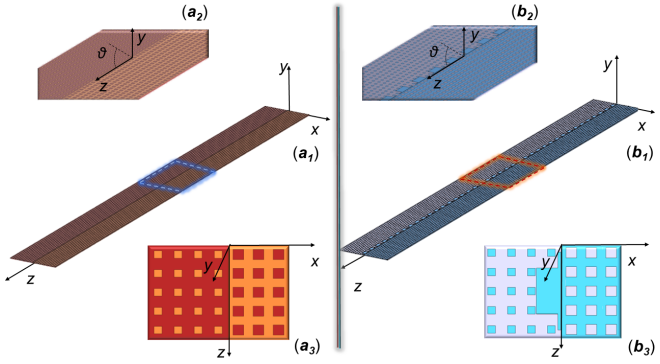

Fig. 1. The two line waveguides supporting leaky line waves considered here, without a periodic load $(a_1) - (a_3)$ and with a periodic load $(b_1) - (b_3)$.

III. Conclusion

Additional information on the analysis methods and numerical results on dispersive features of the considered leaky line waves as well as input scattering parameters and radiation patterns of the considered uniform and periodic structures will be presented at the conference.

Acknowledgments

This work was supported in part by the European Union - Next Generation EU under the Italian National Recovery and Resilience Plan, Mission 4, Component 2, Investment 1.3, CUP B53C22004050001, partnership on "Telecommunications of the Future" under Grant PE00000001 - program "RESTART" and in part by the Italian Ministry of University and Research under the research contract "MEETAPP" PRIN 2022 under Grant 2022ZZ8APA.

References

[1] S. Singh et al., "Advances in metasurfaces: Topology, chirality, patterning, and time modulation," *IEEE Antennas Propag. Mag.*, vol. 64, no. 4, pp. 51–62, Aug. 2022,

[2] A. Monti et al., "Design and characterization of line-waves waveguides for microwave applications," *IEEE Open J. Antennas Propag.*, vol. 6, no. 1, pp. 293—303, Feb. 2025.

[3] M. Madji, P. Baccarelli, A. Monti, A. Toscano, F. Bilotti and P. Burghignoli, "Wideband modal analysis of a double-layer line-wave waveguide: Dispersive properties and radiative effects," *IEEE Open J. Antennas Propag.*, vol. 6, no. 6, pp. 1957–1971, Dec. 2025.

Infrared Cavity Enhanced Vibrational Relaxation in Layered MoS_2

Kosei Ueno*

Department of Chemistry, Faculty of Science, Hokkaido University, Japan

*Corresponding author: ueno@sci.hokudai.ac.jp

***Abstract*— We demonstrate acceleration of excited state relaxation in multilayer MoS_2 by engineering infrared cavity resonances. Spectral matching between cavity modes and intermolecular vibrations enhances vibrational relaxation via the infrared Purcell effect, leading to reduced carrier lifetime and suppressed emission. This work highlights cavity-controlled energy dissipation in solid state systems.**

***Keywords*— infrared cavity, Purcell effect, vibrational relaxation, molybdenum disulfide, photonic environment.**

I. Introduction

Strong light–matter interactions in the infrared regime provide a powerful platform for controlling energy dissipation processes in condensed matter systems. While recent studies in polaritonic chemistry have demonstrated that coupling molecular vibrational modes to optical cavities can modify chemical reactivity, much less attention has been paid to how cavity induced modifications of vibrational relaxation affect excited state dynamics in solids [1-3].

From an electromagnetic perspective, the infrared Purcell effect offers a route to engineer vibrational energy relaxation by tailoring the photonic density of states [4,5]. Enhancement of vibrational emission into cavity modes is expected to accelerate phonon mediated energy dissipation, which can in turn influence electronic relaxation pathways [4,5]. However, experimental verification of this mechanism remains limited, particularly for intermolecular or interlayer vibrational modes in layered materials.

In this work, we focus on multilayer MoS_2 as a model system, where low frequency interlayer breathing modes provide a well-defined vibrational degree of freedom [6,7]. By spectrally matching these vibrational modes with infrared cavity resonances formed by silicon based thin film structures, we investigate how cavity enhanced vibrational relaxation modifies carrier dynamics and emission properties [4,8]. Our aim is to clarify the role of the infrared Purcell effect in accelerating nonradiative excited state relaxation through engineered vibrational dissipation.

II. Methods

Multilayer MoS_2 films were synthesized on silicon substrates using chemical vapor deposition [6]. The number of layers was controlled by growth conditions, enabling systematic investigation of thickness dependent vibrational properties.

Intermolecular vibrational dynamics were probed using a pump–probe setup based on a mode locked Ti:sapphire laser with a center wavelength of 800 nm, pulse duration of 17 fs, and repetition rate of 80 MHz. The second harmonic at 400 nm was used as the pump to excite carriers, while the fundamental wavelength served as the probe. Coherent vibrational oscillations were extracted from transient reflectance signals to analyze vibrational dephasing dynamics associated with the interlayer breathing mode.

To characterize infrared cavity resonances originating from thin film interference in silicon substrates, a terahertz time domain spectroscopy system was constructed using a separate mode locked Ti:sapphire laser with a pulse duration of 30 fs [8,9]. A photoconductive antenna was employed for terahertz generation and detection, allowing precise determination of cavity resonance frequencies. MoS_2 samples on resonant and non-resonant substrates were directly compared under identical optical excitation conditions.

III. Results and Discussion

Transient reflectance measurements of bilayer MoS_2 revealed coherent oscillations superimposed on the carrier decay signal. After subtracting the non-oscillatory carrier component, periodic oscillations with a period of approximately 830 fs were clearly observed, as shown in Fig. 1. The extracted oscillatory component is well reproduced by a damped harmonic oscillation model, enabling quantitative evaluation of the vibrational phase relaxation dynamics.

Systematic measurements on samples with different layer numbers showed a clear thickness dependent frequency shift of the oscillation, confirming that the observed coherent modulation originates from the interlayer out-of-plane breathing mode of MoS_2 [6,7]. These results establish the interlayer vibration as a well-defined probe for investigating vibrational relaxation under different photonic environments.

Terahertz time domain spectroscopy indicated that the cavity resonance frequency of the silicon substrate spectrally overlaps with the breathing mode frequency. When MoS_2 was placed on the resonant cavity substrate, the vibrational dephasing time of

the breathing mode was significantly reduced compared to that on a non-resonant substrate, indicating enhanced vibrational energy dissipation under resonant conditions.

In addition to vibrational dynamics, carrier relaxation was also strongly affected by the cavity environment. Transient reflectance measurements showed shorter carrier lifetimes under resonant conditions, indicating accelerated nonradiative relaxation. Photoluminescence measurements further revealed suppressed emission intensity on the cavity substrate. These observations collectively suggest that cavity enhanced vibrational relaxation increases phonon mediated energy dissipation, thereby accelerating nonradiative decay from the excited electronic state.

From an electromagnetic viewpoint, these results provide direct experimental evidence that the infrared Purcell effect enhances vibrational energy relaxation, linking photonic density of states engineering to electronic relaxation dynamics in layered materials [10].

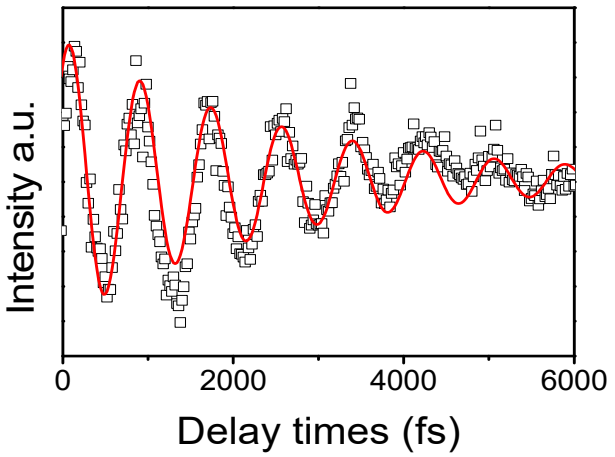

Figure 1. Coherent interlayer out-of-plane breathing mode oscillations and phase relaxation dynamics observed in bilayer MoS_2. The oscillatory component extracted from the transient reflectance signal exhibits a period of approximately 830 fs. Solid lines represent fits using a damped harmonic oscillation model.

IV. Conclusion

We have demonstrated that infrared cavity resonances can accelerate excited state relaxation in multilayer MoS_2 by enhancing vibrational energy dissipation. Spectral matching between interlayer vibrational modes and cavity resonances shortens vibrational dephasing times, leading to faster carrier relaxation and suppressed emission. This work establishes infrared photonic environment engineering as an effective strategy for controlling energy relaxation pathways in solid state systems.

Acknowledgments

This work was supported by JSPS KAKENHI Grant Numbers JP21H05232, JP21H05237, JP23K26675, JP23K26487, JP25K08568, JP25K08449, the Photoexcitonix Project in Hokkaido University, TokyoOhka Foundation, and ARIM Japan No. JPMXP1225HK0070 (Hokkaido University).

References

[1] J. A. Hutchison, T. Schwartz, C. Genet, E. Devaux, and T. W. Ebbesen, "Modifying chemical landscapes by coupling to vacuum fields," Angewandte Chemie International Edition, vol. 51, pp. 1592–1596, 2012.

[2] A. Thomas, J. George, A. Shalabney, et al., "Ground-state chemical reactivity under vibrational coupling to the vacuum electromagnetic field," Angewandte Chemie International Edition, vol. 55, pp. 11462–11466, 2016.

[3] M. Delor, P. A. Scattergood, I. V. Sazanovich, A. W. Parker, G. M. Greetham, A. J. H. M. Meijer, M. Towrie, and J. A. Weinstein, "Toward control of electron transfer in donor-acceptor molecules by bond-specific infrared excitation," Science, vol. 346, pp. 1492–1495, 2014.

[4] E. M. Purcell, "Spontaneous emission probabilities at radio frequencies," Physical Review, vol. 69, p. 681, 1946.

[5] P. Törmä and W. L. Barnes, "Strong coupling between surface plasmon polaritons and emitters: a review," Reports on Progress in Physics, vol. 78, p. 013901, 2015.

[6] C. Lee, H. Yan, L. E. Brus, T. F. Heinz, J. Hone, and S. Ryu, "Anomalous lattice vibrations of single- and few-layer MoS_2," ACS Nano, vol. 4, pp. 2695–2700, 2010.

[7] X. Zhang, W. P. Han, J. B. Wu, et al., "Raman spectroscopy of shear and layer breathing modes in multilayer MoS_2," Physical Review B, vol. 87, p. 115413, 2013.

[8] H. A. Macleod, Thin-Film Optical Filters, 4th ed., CRC Press, Boca Raton, 2010.

[9] D. M. Mittleman, Sensing with Terahertz Radiation, Springer, Berlin, 2003.

[10] S. Mukamel, Principles of Nonlinear Optical Spectroscopy, Oxford University Press, Oxford, 1995.

Broadband Low-Reflectivity Design of Moth-Eye Structures Using RCWA and Bayesian Optimization

Yutaro Sato[1], Maria Vanessa Balois-Oguchi[1], Kotaro Kajikawa[1,*]

[1]Department of Electrical and Electronic Engineering, Institute of Science Tokyo, Japan
*Corresponding author: kajikawa@ee.e.titech.ac.jp

***Abstract*— To maximize anti-reflection performance in the visible light region, we developed a shape optimization method for moth-eye structures using Differentiable Rigid Coupled Wave Analysis (RCWA). As a result, we successfully designed a moth-eye structure capable of reducing the reflectance to 0.004% for PMMA film.**

***Keywords*— metamaterials, Rigid Coupled Wave Analysis.**

I. Introduction

Moth-eye structures exhibit high anti-reflection across a wide range of wavelengths and, for this reason, has been of great interest to scientists and engineers alike. One particular area focuses on optimizing the shape of the moth-eye structures depending on the target application. Conventional shape optimization often employs parameter sweeps assuming simple tapered shapes (cones or parabolas) or particle swarm optimization algorithms [1][2]. However, these methods suffer from limitations in the search space or require enormous computational time to converge. Therefore, in this study, we adopted the differentiable RCWA method (TORCWA [3]), which makes the electromagnetic field simulation itself differentiable. By calculating the gradient of reflectance with respect to the structural parameters (radii of each layer), we achieved an efficient and highly flexible search. Our design is also aimed for the structure to be fabricated using nanoimprint lithography.

II. Methods

The design target is a square array of cylindrical structures, modeled as discrete layers stacked vertically (15 layers in this study) (Fig. 1). The optimization process consists of two stages. First, an inner loop uses the Adam optimizer to directly refine the radius of each layer, using the average reflectance in the visible band (400-700 nm) as the loss function. Second, as an outer loop, Bayesian optimization (Optuna [4]) was introduced to globally search hyperparameters such as the initial structure and learning rate, thereby avoiding local optima. The material used in the simulations was poly(methyl methacrylate) (PMMA).

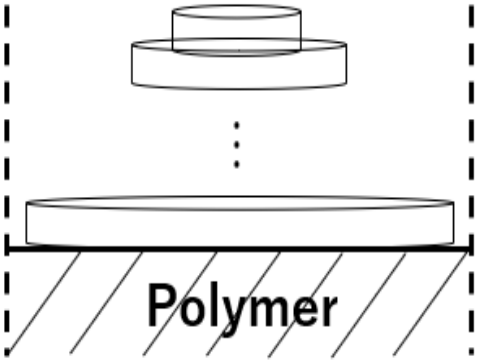

Fig. 1 Unit cell geometry of the proposed metamaterial.

III. Results and Discussion

Simulations using our proposed method yielded nonlinear side profiles optimal for broadband impedance matching, differing from simple linear tapers. As verification, high-precision simulations considering higher-order modes confirmed that the designed structure exhibits remarkably low reflectivity of 0.004% across the entire visible spectrum for vertically incident light.

This method is applicable to materials with arbitrary thicknesses and dispersion characteristics, and is expected to become a powerful tool for next-generation optical element design.

IV. Conclusion

We developed a novel design methodology utilizing automatic differentiation to maximize the anti-reflection performance of moth-eye structures manufacturable via nanoimprint lithography.

Acknowledgments

This work was supported by the Technology Agency (JST) CREST (JPMJCR22B4, JPMJCR24R1).

REFERENCES

[1] Z. Khezripour, F. F. Mahani, and A. Mokhtari, “Optimized design of silicon-based moth eye nanostructures for thin film solar cells,” in Proc. 3rd Conference on Swarm Intelligence and Evolutionary Computation (CSIEC), Bam, Iran, Mar. 2018.

[2] C. Zhang, P. Yi, L. Peng, and J. Ni, "Optimization and continuous fabrication of moth-eye nanostructure array on flexible polyethylene terephthalate substrate towards broadband antireflection," Appl. Opt., vol. 56, no. 10, pp. 2901–2907, Apr. 2017.

[3] C. Kim and B. Lee, “TORCWA: GPU-accelerated Fourier modal method and gradient-based optimization for metasurface design,” Computer Physics Communications, vol. 282, p. 108552, 2023.

[4] T. Akiba, S. Sano, T. Yanase, T. Ohta, and M. Koyama, “Optuna: A next-generation hyperparameter optimization framework,” in Proc. of the 25th ACM SIGKDD International Conference on Knowledge Discovery & Data Mining (KDD), Anchorage, AK, USA, Aug. 2019, pp. 2623–2631.

Advanced computational design of nonlinear and functional nanophotonics

Catarina Ferreira[1,2,3], Joel D. Cox[1,4], Line Jelver[1,*]

[1] POLIMA Center for Polariton-driven Light-Matter Interactions, University of Southern Denmark, DK-5230 Odense M, Denmark.

[2] SDU Climate Cluster, University of Southern Denmark, DK-5230 Odense, Denmark.

[3] CAPE Centre for Advanced Photovoltaics and Thin-film Energy Devices, Mads Clausen Institute, University of Southern Denmark, DK-6400 Sønderborg, Denmark.

[4] Danish Institute for Advanced Study, University of Southern Denmark, DK-5230 Odense M, Denmark.

*Corresponding author: lije@mci.sdu.dk

***Abstract*—The evolution of integrated photonics demands materials and design frameworks that offer both extreme optical control and scalable manufacturability. Here we present two complementary computational advances that span from fundamental quantum dynamics in 2D nanostructures to neural networks for optimization of multilayer photonic devices.**

***Keywords*— Nonlinear nanophotonics, plasmonic heterostructures, structural colors, first-principles modelling, neural networks**

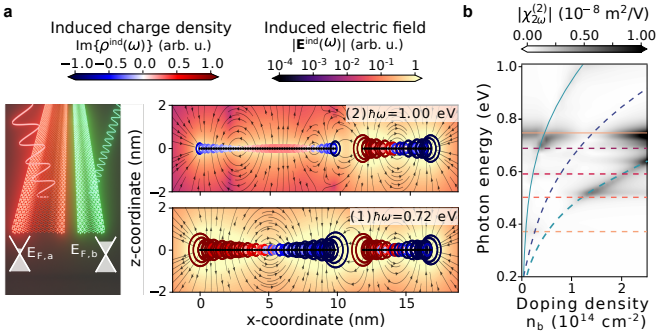

Fig. 1. **Active tuning of linear and second-order optical processes in co-planar graphene nanoribbon (GNR) dimers. a** Schematic of second-harmonic generation in a co-planar GNR dimer with unequal ribbon widths and independent doping (Fermi energies $E_{\mathrm{F,a}}$ and $E_{\mathrm{F,b}}$). **b** Linear near-fields $\mathbf{E}^{(1)}$ of selected hybridized plasmon modes (parameters in inset), computed from the induced charge density $\rho^{\mathrm{ind}}_{i,l}$: $\mathrm{Im}[\rho^{\mathrm{ind}}_{i,l}]$ shown as color-coded markers at atomic positions, and $\mathrm{Im}[\mathbf{E}^{(1)}]$ shown as field vectors over the total field magnitude. **c** Second-harmonic susceptibility of the same dimer; dashed (solid) curves mark conditions where 2ω (ω) is resonant with the plasmon modes of the individual ribbons.

Nonlinear and interference-based nanophotonic platforms offer powerful routes to manipulate light in space and time, but their practical deployment hinges on simultaneously understanding extreme light–matter interactions and navigating vast, fabrication-constrained, design spaces [1], [2].

First, we address extreme nonlinear light–matter interactions in low-dimensional materials. Using an *ab initio* framework based on maximally localized Wannier functions and self-consistent perturbation theory, which captures quantum finite-size effects and nonlocal electrodynamics in nanostructured 2D materials [3], [4], we characterize the nonlinear response of phosphorene and graphene nanoribbon heterostructures [5]. As illustrated in Fig. 1, inter-ribbon coupling together with independent electrostatic control of the carrier densities activates strong even-order nonlinearities (e.g., second-harmonic generation) and extends into the extreme regime to yield efficient high-harmonic generation (HHG) via active or passive inversion-symmetry breaking. More broadly, these results show how tuning each constituent ribbon provides practical design knobs to selectively enhance targeted harmonic orders, establishing 2D nanoribbon heterostructures as versatile platforms for nonlinear nanophotonics.

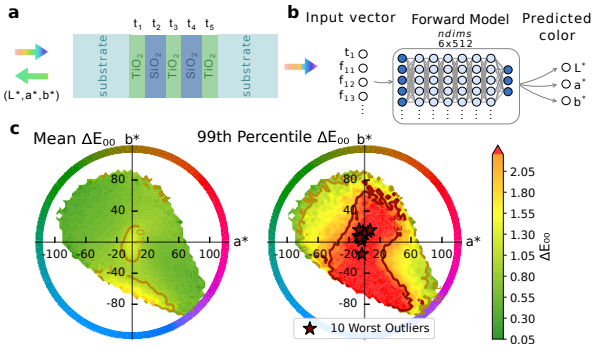

Fig. 2. **Design of structural colors. a** Thin-film elements considered here: dielectric multilayer stacks made of two alternating materials (TiO_2/SiO_2, TiO_2/Si_3N_4, or Si_3N_4/SiO_2) with variable layer thicknesses t_i, on optically thick substrates, illuminated at normal incidence. Reflected color is obtained from the visible reflectance $R(\lambda)$ converted to CIE $L^*a^*b^*$ coordinates to quantify perceived color. **b** Neural network forward model mapping a stack configuration to predicted $L^*a^*b^*$ coordinates. **c** Forward-model color error in CIELAB space: mean ΔE_{00} versus color coordinates in the a^*–b^* color diagram (left), with the 99th percentile and the ten largest outliers of the test set (right). $\Delta E_{00} < 1$ is considered as perceptually indistinguishable, while $\Delta E_{00} > 2.3$ indicates a noticeable color mismatch; errors are largest for low-chroma colors near the origin.

Second, we present an integrated deep-learning pipeline for thin-film structural-color design that combines perceptual objectives, physical constraints, and the inherently one-to-many nature of inverse mapping. Trained on transfer-matrix

spectra for $TiO_2/Si_3N_4/SiO_2$ multilayers (3–7 layers) mapped to CIE Lab* color coordinates [6], [7], our neural network enables rapid forward prediction of reflected color and, when coupled with population-based optimization, produces diverse, fabrication-feasible, thin-film designs. As shown in Fig. 2, the forward model attains near-indistinguishable perceptual accuracy (characterized by a difference in color perception $\Delta E_{00} < 1$) over most of the color space. Our framework unifies perceptual accuracy and fabrication robustness and provides a major speed-up compared to traditional transfer-matrix based methods.

Together, these results illustrate the power of computational design for modern nanophotonics: utilizing *ab initio* modelling to uncover novel nonlinear phenomena in 2D heterostructures, while employing machine learning to navigate the vast design spaces required for real-world applications.

ACKNOWLEDGMENTS

L.J. is supported by a career grant from the Novo Nordisk Foundation (grant no. NNF25OC0105410). J.D.C. is a Sapere Aude research leader supported by Independent Research Fund Denmark (grant no. 0165-00051B). The Center for Polariton-driven Light-Matter Interactions (POLIMA) is funded by the Danish National Research Foundation (Project No. DNRF165). Part of the computation in this project was performed on the DeiC Large Memory HPC system managed by the eScience Center at the University of Southern Denmark.

REFERENCES

[1] D. E. Chang, V. Vuletić, and M. D. Lukin, "Quantum nonlinear optics — photon by photon," *Nature Photonics*, vol. 8, pp. 685–694, 2014.

[2] A. Dutt, A. Mohanty, A. L. Gaeta, and M. Lipson, "Nonlinear and quantum photonics using integrated optical materials," *Nature Reviews Materials*, vol. 9, pp. 321–346, 2024.

[3] J. D. Cox, I. Silveiro, and F. J. G. de Abajo, "Quantum effects in the nonlinear response of graphene plasmons," *ACS Nano*, vol. 10, pp. 1995–2003, 2016.

[4] L. Jelver and J. D. Cox, "Nonlinear plasmonics in nanostructured phosphorene," *ACS Nano*, vol. 17, pp. 20 043–20 052, 10 2023.

[5] ——, "Nonlocal and nonlinear plasmonics in atomically thin heterostructures," *arXiv:2512.18339*, 2025.

[6] C. G. Ferreira, J. Lamminaho, A. Paul, M. Babin, N. L. Andersen, S. Thorsteinsson, P. B. Poulsen, K. Petersons, L. Yde, J. F. Stensborg *et al.*, "Optical design of structural colored photovoltaics for building integration: From periodic configurations to optimization algorithms," *Nano Energy*, p. 111659, 2025.

[7] C. G. Ferreira, A. Paul, M. Babin, J. Lamminaho, N. L. Andersen, S. Thorsteinsson, P. B. Poulsen, K. Petersons, L. Yde, J. F. Stensborg *et al.*, "Structural colored planar multilayers with minimal angular color dependence for building integrated photovoltaics," *Solar RRL*, vol. 9, no. 23, p. e202500674, 2025.

Nanoparticles of nitride-based materials for plasmonics and lattice-mode resonances

E. Salvaggio[1,2], J. Béal[1,2], G. Abadias[3], S. Camelio[3], D. Babonneau[3], D. Gérard[1,2], C. Couteau[1,2] and J. Plain[1,2,*]
[1]L2n, University of technology of Troyes and CNRS, Troyes, France
2 EUTINN, European University of Technology Eut+, EU
[3] Institut Pprime, Département Physique et Mécanique des Matériaux, CNRS and Université de Poitiers, SP2MI, Poitiers, France
*Corresponding author: jerome.plain@utt.fr

Abstract— **This work characterizes TiN/ZrN nanoparticle films and networks and shows that stoichiometry can be used to adjust their plasmonic and photothermal responses. Measurements and simulations reveal narrow, tunable, and robust plasmonic network resonances that show promise for nitride-based devices and metasurfaces.**

***Keywords*— metamaterials, nitrides, TiN, ZrN, plasmonics.**

I. Introduction

Transition metal nitrides, and in particular titanium nitride (TiN) and zirconium nitride (ZrN), are emerging as robust alternatives to noble metals for plasmonics owing to their high thermal stability, CMOS compatibility, and tuneable optical response. In this work, we provide a combined experimental and numerical study of nitride thin films and lithographically defined nitride nanoparticle arrays, and we assess their potential for near-field enhancement, photothermal conversion, and surface lattice resonance engineering from the visible to the near-infrared.

II. Methods

TiN and ZrN films are grown by DC magnetron sputtering under mixed Ar/N_2 atmospheres, with the nitrogen flow systematically varied to tune stoichiometry. We correlate deposition conditions with crystalline structure (XRD), morphology (AFM/SEM), thickness and density (X-ray reflectivity), DC resistivity (Van der Pauw), and complex permittivity extracted from spectroscopic ellipsometry using a Drude + multi-oscillator (Tauc–Lorentz) model. The films are cubic, with nitrogen content controlling lattice constant, grain size (≈9–29 nm), density, and resistivity, and leading to sub- or over-stoichiometric compositions depending on the material. From UV–visible transmission we determine indirect optical bandgaps in the 1.2–2.4 eV range, with values and trends that differ from many literature reports due to the nature of the electronic transitions and stoichiometry.

III. Results and Discussion

Using the measured optical constants, we quantify for each film the Faraday and Joule figures of merit, which separate near-field enhancement from heat generation [1]. ZrN exhibits a pronounced plasmonic resonance around 500–600 nm with strong near-field enhancement but limited broadband photothermal response, whereas TiN shows a broader response extending into the near-IR, with a Joule number that remains significant at long wavelengths, making it attractive for broadband heat generation.

We then fabricate square arrays of nitride nanoparticles (cones and truncated cones) on fused silica by electron-beam lithography and reactive ion etching, covering diameters from 120 to 200 nm, heights from 40 to 80 nm, and periods from 200 to 700 nm. Extinction spectra are measured in a quasi-symmetric dielectric environment by index-matching glycerol, and are compared to 3D FDTD simulations using the experimentally retrieved n and k. We observe good agreement between experiment and theory, including the emergence of narrow, Fano-like lattice resonances when the localized surface plasmon of individual particles hybridizes with Rayleigh anomalies of the array. Increasing the period produces red-shifts and linewidth narrowing consistent with plasmonic surface lattice resonances, while increasing particle size induces a strong red-shift and broadening in line with Mie-type behaviour.

IV. Conclusion

Our results demonstrate that both TiN and ZrN support strong, tuneable plasmonic and lattice-mode responses, with the nitride stoichiometry offering an additional handle to engineer linewidth, resonance position, and the balance between field enhancement and photothermal conversion. These properties make nitride nanoparticle arrays promising platforms for robust, high-temperature plasmonic devices, meta surfaces, and

thermoplasmonic applications where conventional noble metals are limited.

Acknowledgments

This work was supported by the French National Agency for Research ANR under contracts NATO (ANR-13-BS10-0013) and NOSE (ANR-21-CE39-0014).

References

[1] A. Lalisse, G.Tessier, J. Plain and G. Baffou, "Quantifying the efficiency of plasmonic materials for near-field enhancement and photothermal conversion," The Journal of Physical Chemistry C 119 (45), 25518-25528, 2025.

Retrieving Electric and Magnetic Conductivities of Anisotropic Metasurfaces under Oblique Incidence

Dimitrios Chatzidimitriou[1,*], Alexandros Pitilakis[1], Odysseas Tsilipakos[1]

[1]Theoretical and Physical Chemistry Institute, National Hellenic Research Foundation Athens, Greece
*Corresponding author: chatzid@eie.gr

***Abstract*—Analytical parameter-retrieval formulas are developed for anisotropic, electromagnetically thin metasurfaces with electric and magnetic surface currents. Valid for arbitrary polarizations and incidence angles, the approach avoids bidirectional scattering data. Examples of microwave and THz meta-atoms illustrate efficient polarization conversion and practical and experimental relevance.**

***Keywords*— metasurfaces, anisotropic meta-atoms, polarization conversion, parameter retrieval, photonics, microwaves.**

I. Introduction

Effective-parameter retrieval for metasurfaces (MSs) has received attention over the past decade [1], [2], [3], [4], motivated by the need for models that accurately describe their electromagnetic response. A comprehensive framework was introduced in Ref. [4], addressing fully anisotropic metasurfaces and explicitly accounting for magnetoelectric coupling. While rigorous, that formulation yields relatively involved retrieval expressions, as it requires reflection and transmission coefficients obtained under illumination from both sides of the metasurface.

In practice, acquiring bidirectional scattering data can be inconvenient, particularly in experimental implementations. At the same time, reciprocity ensures that forward and backward scattering responses are not independent, indicating that such measurements are not fundamentally required.

Here, we derive analytical retrieval formulas for anisotropic metasurfaces that are electromagnetically thin, such that magnetoelectric coupling and normal surface current components are absent. The resulting expressions determine the equivalent electric and magnetic surface conductivities using scattering data from a single incidence direction. The formulation remains valid for arbitrary polarization states and oblique plane-wave incidence, providing a streamlined and experimentally accessible characterization method.

II. Methods

An anisotropic metasurface (MS) is modeled as an electromagnetically thin sheet located at $z = 0$, separating two homogeneous half-spaces with permittivities ε_1 and ε_2. The structure is assumed laterally uniform, so that reflection and refraction occur in the specular direction. The excitation is a linearly polarized plane wave incident at an arbitrary oblique angle θ_i, with the corresponding transmission angle θ_t determined by Snell's law.

The electromagnetic response of the metasurface is described using generalized boundary conditions that relate discontinuities of the tangential field components to induced surface currents [5]. These boundary conditions introduce electric and magnetic surface conductivity tensors, $\overline{\overline{\sigma}}_e$ and $\overline{\overline{\sigma}}_m$, which fully characterize the in-plane anisotropic response of the metasurface and allow for four independent tensor components each. They are given by

$$\hat{\mathbf{z}} \times (\mathbf{E}_1 - \mathbf{E}_2) = -\tfrac{1}{2}\overline{\overline{\sigma}}_m(\mathbf{H}_1 + \mathbf{H}_2)_{\parallel}, \tag{1a}$$

$$\hat{\mathbf{z}} \times (\mathbf{H}_1 - \mathbf{H}_2) = \tfrac{1}{2}\overline{\overline{\sigma}}_e(\mathbf{E}_1 + \mathbf{E}_2)_{\parallel}, \tag{1b}$$

where the subscript "$\parallel$" denotes components tangential to the metasurface plane. The total fields are $\mathbf{E}_1 = \mathbf{E}_i + \mathbf{E}_r$ and $\mathbf{E}_2 = \mathbf{E}_t$, with analogous expressions for the magnetic fields.

Substituting the total fields into (1) yields closed-form analytical expressions for the electric and magnetic surface conductivities, reported in (2) and (3). While the conductivity tensors are expressed in Cartesian coordinates (e.g., σ_e^{xx}, σ_e^{xy}), the scattering response is naturally described in the s (TE) and p (TM) polarization basis, including cross-polarized coefficients arising from anisotropy.

$$\overline{\overline{\sigma}}_e = 2\begin{bmatrix} \dfrac{1+r_{pp}}{\zeta_1^p} - \dfrac{1}{\zeta_2^p}\dfrac{\cos\theta_t}{\cos\theta_i}t_{pp} & \dfrac{\cos\theta_i}{\zeta_1^p}r_{ps} - \dfrac{\cos\theta_t}{\zeta_2^p}t_{ps} \\ -\dfrac{1}{\zeta_1^s}\dfrac{r_{sp}}{\cos\theta_i} - \dfrac{1}{\zeta_2^s}\dfrac{t_{sp}}{\cos\theta_i} & \dfrac{1-r_{ss}}{\zeta_1^s} - \dfrac{t_{ss}}{\zeta_2^s} \end{bmatrix} \begin{bmatrix} 1 - r_{pp} + \dfrac{\cos\theta_t}{\cos\theta_i}t_{pp} & -r_{ps}\cos\theta_i + \cos\theta_t t_{ps} \\ \dfrac{r_{sp}+t_{sp}}{\cos\theta_i} & 1 + r_{ss} + t_{ss} \end{bmatrix}^{-1}, \tag{2}$$

$$\overline{\overline{\sigma}}_m = 2\begin{bmatrix} \dfrac{t_{sp}-r_{sp}}{\cos\theta_i} & -1 - r_{ss} + t_{ss} \\ 1 - r_{pp} - t_{pp}\dfrac{\cos\theta_t}{\cos\theta_i} & -r_{ps}\cos\theta_i - t_{ps}\cos\theta_t \end{bmatrix} \begin{bmatrix} \dfrac{1}{\zeta_1^s}\dfrac{r_{sp}}{\cos\theta_i} - \dfrac{1}{\zeta_2^s}\dfrac{t_{sp}}{\cos\theta_i} & -\dfrac{1-r_{ss}}{\zeta_1^s} - \dfrac{1}{\zeta_2^s}t_{ss} \\ \dfrac{1+r_{pp}}{\zeta_1^p} + \dfrac{1}{\zeta_2^p}t_{pp}\dfrac{\cos\theta_t}{\cos\theta_i} & \dfrac{1}{\zeta_1^p}r_{ps}\cos\theta_i + \dfrac{1}{\zeta_2^p}t_{ps}\cos\theta_t \end{bmatrix}^{-1}. \tag{3}$$

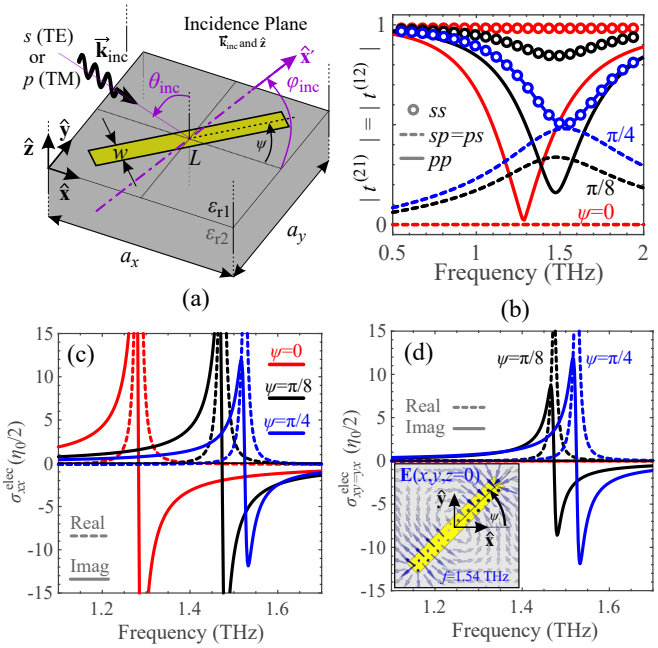

Fig. 1. Electrically resonant cut-wire metasurface operating in the THz regime. (a) Unit-cell geometry and orientation of the metallic wire, rotated by an azimuth angle ψ in the xy plane. (b) Transmission coefficients as a function of frequency for selected rotation angles, showing the emergence of cross-polarized components. (c),(d) Retrieved components of the electric surface conductivity tensor. The inset in (d) shows the electric-field distribution at resonance, highlighting the predominantly electric nature of the response.

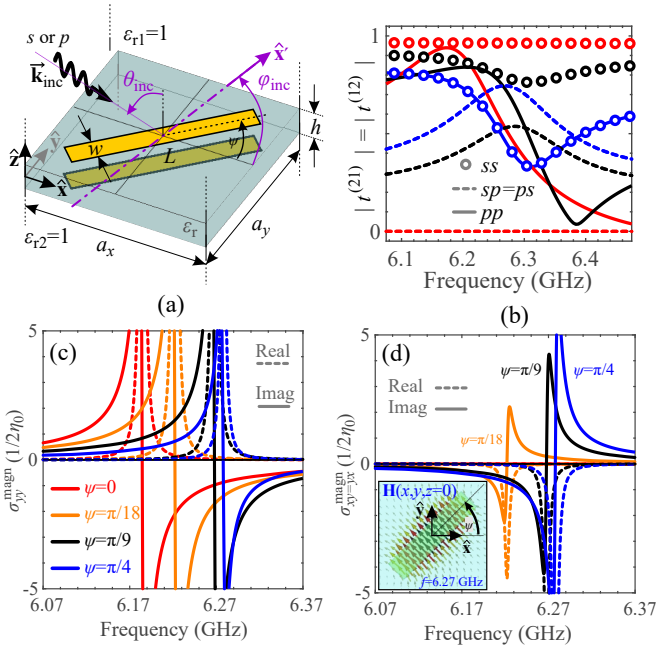

Fig. 2. Magnetically resonant cut-wire-pair metasurface. (a) Geometry of the paired-wire unit cell, including substrate separation and in-plane rotation. (b) Transmission spectra for different azimuth angles, revealing magnetic and electric resonances. (c),(d) Retrieved magnetic surface conductivity tensor components at normal incidence. The inset in (d) displays the magnetic-field distribution at the dominant resonance, confirming its magnetic character.

The wave impedances for obliquely incident TE and TM plane waves are defined as $\zeta_1^s = \eta_1/\cos\theta_i$, $\zeta_2^s = \eta_2/\cos\theta_t$, $\zeta_1^p = \eta_1\cos\theta_i$, and $\zeta_2^p = \eta_2\cos\theta_t$, where η_1 and η_2 denote the intrinsic impedances of the two surrounding media.

III. Results and Discussion

We first examine a metasurface composed of electrically resonant cut-wire elements operating in the THz regime. The geometry, shown in Fig. 1(a), consists of a gold wire with dimensions $w \times L = 10\ \mu\text{m} \times 82\ \mu\text{m}$ arranged in a square lattice with period $a_x = a_y = 85\ \mu\text{m}$ and placed at the interface between air and a dielectric substrate with relative permittivity $\varepsilon_r = 2.1$. The wire is rotatable in the xy plane by an azimuth angle ψ about the z axis.

For plane-wave excitation in a principal plane ($\varphi_{\text{inc}} = m\pi/2$, m integer), rotation of the wire introduces anisotropy and enables polarization conversion. In particular, cross-polarized scattering is expected to be strongest near $\psi = \pi/4$, which is confirmed by the transmission spectra shown in Fig. 1(b). The corresponding reflection coefficients (not shown) exhibit consistent behavior.

The electric surface conductivity tensor is retrieved from the numerically obtained RT coefficients using (2), and the resulting components are shown in Fig. 1(c,d). As expected for a single metallization layer, no magnetic surface conductivity is retrieved. The co-polarized electric conductivity exhibits a Lorentzian resonance whose spectral position shifts toward higher frequencies as ψ increases, while the off-diagonal component vanishes for $\psi = 0$ and reaches its maximum near $\psi = \pi/4$. This behavior is consistent with the observed polarization conversion. The electric-field distribution at resonance, shown in the inset of Fig. 1(d), further confirms the electric nature of the response.

To demonstrate the applicability of the retrieval approach to magnetic responses, we next consider a metasurface composed of paired cut wires implemented on a printed circuit board, as illustrated in Fig. 2(a). The lattice is square with period $a_x = a_y = 15$ mm, and each unit cell contains two copper wires of dimensions $w \times L = 3$ mm $\times$ 14 mm and conductivity $\sigma = 5.8 \cdot 10^7$ S/m. The two metallization layers are separated by a dielectric substrate of thickness $h = 1.5$ mm, relative permittivity $\varepsilon_r = 3$, and loss tangent $\tan\delta = 0.001$.

In this configuration, antiparallel surface currents supported by the two wires give rise to a magnetic resonance near 6 GHz, while an additional electric resonance associated with parallel currents appears at higher frequencies (8–10 GHz). The transmission spectra for different rotation angles are shown in Fig. 2(b).

The retrieved magnetic surface conductivity at normal incidence is plotted in Fig. 2(c,d). In contrast to the single-layer metasurface, a clear Lorentzian resonance is observed in the magnetic conductivity, in correspondence with extrema in the transmission coefficients. The retrieved electric conductivity remains nonzero, reflecting the hybrid nature of the response. As the rotation angle approaches $\psi = \pi/4$,

the off-diagonal magnetic conductivity component increases, leading to enhanced polarization conversion. The magnetic-field distribution shown in the inset of Fig. 2(d) confirms the magnetic character of the dominant resonance.

IV. Conclusion

We have presented analytical parameter-retrieval formulas for anisotropic, electromagnetically thin metasurfaces based on generalized boundary conditions and single-sided scattering data. The formulation applies to arbitrary incidence angles and polarization states, enabling the extraction of both electric and magnetic surface conductivities. Numerical examples at THz and GHz frequencies demonstrate the accuracy of the approach and its ability to capture polarization-conversion effects in electrically and magnetically resonant metasurfaces.

Acknowledgments

Support by the European Union under Grant Agreement 101168152. Views and opinions expressed are however those of the author(s) only. Neither the European Union nor the granting authority can be held responsible for them.

References

[1] D. C. Zografopoulos and O. Tsilipakos, "Recent advances in strongly resonant and gradient all-dielectric metasurfaces," *Materials Advances*, vol. 4, no. 1, p. 11–34, 2023.

[2] C. L. Holloway, E. F. Kuester, and A. Dienstfrey, "Characterizing metasurfaces/metafilms: The connection between surface susceptibilities and effective material properties," *IEEE Antennas and Wireless Propagation Letters*, vol. 10, p. 1507–1511, 2011.

[3] P. Tassin, T. Koschny, and C. M. Soukoulis, "Effective material parameter retrieval for thin sheets: Theory and application to graphene, thin silver films, and single-layer metamaterials," *Physica B: Condensed Matter*, vol. 407, no. 20, p. 4062–4065, Oct. 2012.

[4] C. Pfeiffer and A. Grbic, "Emulating nonreciprocity with spatially dispersive metasurfaces excited at oblique incidence," *Physical Review Letters*, vol. 117, no. 7, Aug. 2016.

[5] O. Tsilipakos, T. Koschny, and C. M. Soukoulis, "Antimatched electromagnetic metasurfaces for broadband arbitrary phase manipulation in reflection," *ACS Photonics*, vol. 5, no. 3, p. 1101–1107, Jan. 2018.

Plasmonic lightning-rod effect and nanofocusing: Revisiting traditional design concepts for plasmonic antennas

Rostislav Řepa[1], Michal Horák[1], Pavel Gajdoš[1], Tomáš Šikola[1], and Vlastimil Křápek[1,*],

[1]Brno University of Technology, Brno, Czechia
*Corresponding author: krapek@vutbr.cz

***Abstract*—We analyze the plasmonic lightning-rod effect and the nanofocusing of localized surface plasmons and discuss their consequences for the design of plasmonic antennas.**

***Keywords*— plasmonic antenna, field enhancement, lightning-rod effect, nanofocusing.**

I. Introduction

Plasmonic antennas (PAs) are praised for their ability to confine and enhance electric and magnetic fields at optical frequencies. Field enhancement is one of the key parameters of PAs, relevant for applications e.g. in enhanced photoluminescence [1] or strong light-matter coupling [2]. Various concepts are exploited to design PAs with desired properties, such as the strong field enhancement. In our communication, we revisit two of the concepts that are seemingly intuitive, but exhibit non-trivial features upon a closer examination.

Lightning-rod effect refers to the formation of strong electric field near sharp features of charged metal. We focus on a detailed analysis of similarities and differences between the electrostatic and plasmonic lighning-rod effects, and isolate the lightning-rod effect from other concurrent effects to retrieve a rigorous relation between the local curvature and electric field.

Nanofocusing traditionally refers to a concentration of electromagnetic energy of surface plasmon polaritons (SPP) as they propagate in the plasmonic structure with a decreasing cross-section (e.g., a tapered waveguide). We discuss whether this effect can be translated to localized surface plasmons (LSP) supported by PAs. We introduce a concept of the charge reservoir represented by the broader part of the PA, and evaluate its significance for relevant figures of merit.

II. Methods

The methodology combines experimental electron energy loss spectroscopy (EELS) with numerical electromagnetic simulations. EELS provides qualitative insight into the near field of PAs and verifies the simulations, which provide additional quantities such as a full quantitative characterization of the electric field.

III. Results and Discussion

The plasmonic lightning-rod effect is isolated using a series of plasmonic beetroots [Fig. 1(a)] and dumbbells – rod-like PAs of identical length with two cylindrical terminations,

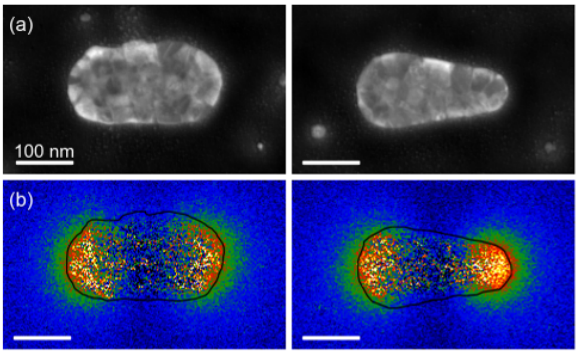

Fig. 1. Experimental manifestation of the plasmonic lightning-rod effect. Two plasmonic beetroots from a series with the fixed radius r_{fix} of 70 nm at the left side and a variable radius r_{var} of either 70 nm or 40 nm) at the right side imaged by transmission electron microscope (a) together with experimental EELS map of their dipole localized surface plasmon resonance (b). The plasmonic lightning-rod effect is manifested as the intense loss signal at the sharp side of the PAs at the bottom panel ($r_{\mathrm{var}} = 40$ nm).

one with a fixed radius r_{fix} and one with a variable radius r_{var} (individual PAs within the series have a common value of r_{fix} but differ in r_{var}). The field enhancement and the loss probability are evaluated at both termination, with the fixed-radius termination serving as a reference. At the fixed-radius termination, we observe the identical loss probability [Fig. 1(b)] and field enhancement for all the PAs within the series. This ensures that the variations in the response at the variable-radius termination can be attributed purely to the local curvature. The values of the electric field shown in Fig. 2 represent quantification of the plasmonic lightning-rod effect. Finally, we present an intuitive phenomenological model for the induced electric field based on an effective induced point charge. Within this model, we demonstrate that the effective radius of the PAs (defined by the position of the effective charge) is considerably lower than the geometrical radius, making PAs effectively sharper. Further details are provided in Ref. [3].

Further, we explore the possibility to exploit nanofocusing in the design of PAs. Nanofocusing shall occur in tapered PAs, where a broad part is continuously transformed to a narrow part. We propose a hypothesis that the broad part can act as a

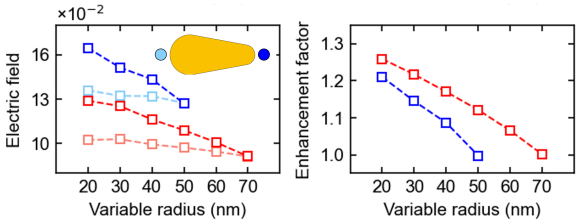

Fig. 2. Theoretical quantification of the plasmonic lightning-rod effect. (left) The relative magnitude field of the electric field evaluated at the distance of 20 nm from a fixed-radius side (light colors) or a variable-radius side (dark colors) of the PA. (right) The magnitude of the electric field evaluated at the distance of 20 nm from a variable-radius side divided by the same quantity for a symmetric PA ($r_{\mathrm{var}} = r_{\mathrm{fix}}$) is displayed as a function of the local variable radius. Stronger fields obtained from sharper features of PAs represent the quantified manifestation of PLRE. Blue and red color corresponds to the series of PAs with r_{fix} of 50 nm and 70 nm, respectively.

reservoir of the charge for plasmonic oscillations; when driven by an external excitation, the broad part provides electrons that can be concentrated at the narrow part, forming a large induced charge accompanied by a large electric near field. In our communication, we will show that this hypothesis only partially correct. The broader part can be indeed related to a large charge participating in plasmon oscillations. However, the most prominent manifestation of this large charge is in increased radiative losses, which in turn result in a broadening of plasmon resonances and a decrease of the field induced by PAs. The details of this analysis are published in Ref. [4].

IV. Conclusion

We have rigorously demonstrated and quantified the plasmonic lightning-rod effect. Next, we discussed the possibility to extend the concept of nanofocusing from propagating plasmons to localized plasmons. We analyzed the consequences of both concepts for the design of plasmonic antennas, showing that the field enhancement is positively correlated with the large geometrical curvature and negatively correlated with the charge reservoir due to enhanced radiative losses.

Acknowledgments

We acknowledge support from the Ministry of Education, Youth, and Sports of the Czech Republic, projects No. CZ.02.01.01/00/22008/0004572 (QM4ST) and LM2023051 (CzechNanoLab).

References

[1] A. Kinkhabwala, Z. Yu, S. Fan, Y. Avlasevich, K. Müllen, and W. E. Moerner, “Large single-molecule fluorescence enhancements produced by a bowtie nanoantenna,” *Nature Photonics*, vol. 3, pp. 654–657, 2009.

[2] O. Bitton, S.N. Gupta, L. Houben, M. Kvapil, V. Krapek, T. Sikola, and G. Haran, “Vacuum Rabi splitting of a dark plasmonic cavity mode revealed by fast electrons,” *Nature Commununication*, vol. 11, p. 487, 2020.

[3] V. Krapek, R. Repa, M. Foltyn, T. Sikola, and M. Horak, “Plasmonic lightning-rod effect,” *arXiv*:2407.09454, 2024.

[4] R. Repa, M. Horak, T. Sikola, and V. Krapek,“Charge reservoir as a design concept for plasmonic antennas,” *Nanophotonics*, vol. 14, pp. 4637–4645, 2025.

Advancements in Electromagnetic FEM for Parametric Studies, Frequency Sweeps and Shape Optimization

Michal Baranowski[1], Adam Lamecki[1], Michal Mrozowski[1,*]

[1]Faculty of Electronics, Telecommunications and Informatics,
Gdańsk University of Technology, Poland
*Corresponding author: m.mrozowski@ieee.org

***Abstract*—We present recent advancements in a high-order finite element solver for electromagnetic analysis of microwave components and antennas. The solver uses curvilinear tetrahedral elements with Ingelström basis functions up to order $p = 2$ and supports broadband characterization via model-order reduction and interpolatory frequency-sweep techniques, fully accounting for dispersive ports and frequency-dependent materials. Large-scale problems are addressed using a p-multilevel V-cycle preconditioner. Parametric studies employ mesh morphing, while shape optimization combines mesh morphing with free-form deformation based on radial basis functions, enabling geometric variations beyond conventional constructive solid geometry (CSG)-based parameterization.**

***Keywords*— finite element method, frequency sweep, free-form deformation.**

I. Introduction

The Finite Element Method (FEM) remains a versatile tool for the analysis of electromagnetic structures, including antennas, arrays, waveguide components, and scattering scenarios in heterogeneous media. However, broadband analysis, dispersive materials, electrically large models, and the growing need for parametric studies and optimization significantly increase computational cost. This work presents recent developments in our high-order FEM solver aimed at addressing these challenges and enabling efficient frequency sweeps, parametric exploration, and shape optimization within a unified simulation framework.

II. Efficient Broadband FEM Solutions for Parametric Studies and Shape Deformation

We developed the solver to enable efficient computation of broadband frequency responses without performing full-wave solutions at every frequency. To this end, two complementary methods are implemented. The first is a model-order reduction (MOR) approach that builds a reduced basis from either a single matrix factorization at one frequency or solutions computed at a few selected frequency snapshots, allowing rapid evaluation across wide bands. The second is an interpolatory sweep technique based on rational approximation, reconstructing the multi-frequency response from a small number of frequency points. Both methods offer substantial savings in computational effort while maintaining accuracy. They naturally support dispersive ports, and dispersive material including frequency-dependent metal loss, and Debye, Drude, and Lorentz media models.

The spatial discretization employs curvilinear tetrahedral elements with higher-order hierarchical Ingelström basis functions up to $p = 2$, ensuring accurate representation of curved geometries and reducing numerical dispersion compared to low-order methods. These basis functions also capture field singularities near edges and tips, making them suitable for broadband antenna simulations.

To handle large-scale problems, the solver incorporates a p-multilevel preconditioned iterative method based on a V-cycle multilevel scheme. By building a hierarchy of approximation spaces with decreasing polynomial order, the preconditioner maintains stable convergence. Results for large antenna arrays demonstrate the scalability of this approach for systems with hundreds of thousands to millions of unknowns.

In addition to broadband analysis, the solver enables systematic design exploration. One feature is interactive design tuning, which uses design sensitivities to allow manual, real-time adjustment of scattering parameters. A second capability is intended for larger geometric variations. Instead of generating a new mesh for each geometry update, parametric studies are performed using mesh morphing, which smoothly deforms an existing high-quality curvilinear mesh. This approach eliminates the need for remeshing and preserves mesh topology—an important advantage in optimization workflows. For shape optimization, a free-form deformation framework based on radial basis functions (RBF-FFD) is used. In contrast to CSG-based parameterizations used in most commercial EM tools, RBF-FFD supports smooth, unconstrained geometric variations driven by the motion of a set of control points, allowing exploration of novel shapes not representable with standard geometric primitives.

III. Conclusion

The presented framework integrates high-order discretization, efficient broadband frequency-sweep techniques, support for dispersive media, scalable p-multilevel preconditioning, mesh morphing, and RBF-based free-form deformation within a single FEM platform.

Hybrid AI design of reconfigurable and compact plasmonic Arithmetic and Logic Units

Amine Khitous,[1] Nicolas Gros,[2] Léo Martin,[1] Florian Dell'Ova,[1] Aurélie Bertaux,[2] Ouassila Narsis Labbani,[2] Gérard Colas des Francs,[2] Christophe Nicolle,[3] Alexandre Bouhelier,[1] Erik Dujardin[1] *

[1] Laboratoire Interdisciplinaire Carnot de Bourgogne (ICB), Université Bourgogne Europe CNRS UMR 6303, 21000 Dijon, France.
[2] Connaissances et Intelligence Artificielle Distribuée (CIAD), Université Bourgogne Europe ER 7533, 21000 Dijon, France.

* Corresponding author: Erik.Dujardin@cnrs.fr

***Abstract*— We recently introduced the concept of all-optical arithmetic and logic units (ALU) in single plasmonic cavities. The first prototype showed the addition of two 1-bit numbers and all 2-input logic gates In the absence of an established design theory for such holistic devices, we have developed a new hybrid AI approach that optimizes the design beyond the performances of the initial intuitive demonstrator and paves the way to more complex optical Boolean computing. We will present here the experimental testing of the AI-designed ALU structures and operation conditions and benchmark our design approach for future optical processors of higher complexity.**

***Keywords*— optical computing, plasmonics, hybrid AI, non-linear optics.**

I. Introduction

Photonics has revolutionized information transfer, but processing and computing remain provided by microelectronic solutions that face fundamental limitations, including the interconnect bottleneck: circuits of smaller switching devices need longer and narrower interconnects, where most energy is dissipated.

We recently proposed a new concept of micrometric, all-optical and interconnect-free, reconfigurable Arithmetic and Logic Units (ALU) of increasing computing capacity. The shape of a 2D single crystalline gold microcavity defines a set of plasmon modes to be used as reconfigurable computation channels.[1,2] The plasmonic landscape, optically excited by N Boolean inputs encoded into two polarization states of focused fs-pulsed laser spots, generates a remote optical Boolean calculus at the ALU output ports. The arithmetic or logic function is directly realized by the relationship between the inputs and outputs. Unlike all information paradigms that rely on concatenated switching devices to realize logic gates, Shannon's theory of switching circuits does not apply to our holistic devices and we need to uncover the specific rules governing our ALU design and operation for given Boolean functions. The first prototype to demonstrate experimentally this concept, though sub-optimally, was a cavity with a double hexagon (DH) shape.[1,2] To improve the device performance, we have created a hybrid AI (HAI) tool able to propose candidate cavity shapes as well as optimal excitation/detection condition and successfully shown that they outperform the DH prototype in realizing the 1-bit Full-Adder function. We experimentally benchmark the performances of the HAI proposals by nanofabricating the HAI-inverse-designed cavities, explore the determinant coherent conditions to generate a contrasted output and establish the performance roadmap of this new series of optical computing devices. By jointly optimizing the cavity geometry and the excitation conditions, we realize reconfigurable all-optical plasmonic arithmetic and logic units, culminating in the experimental demonstration of a cascade-free 1-bit optical full adder within a single plasmonic cavity with a 200% output contrast improvement.

II. Methods

A robust Boolean function is achieved in plasmonic modal ALU devices when the transmittance, probed here as the non-linear photoluminescence (NPL) transmittance, between the input and output ports obeys the truth table with a high Boolean contrast (i.e. a large difference between '0' and '1' output values). This condition can be expressed for any Boolean function and used to identify where and when an output signal fulfils it.[2] We have created a purpose-conceived Hybrid AI framework that comprises two genetic algorithms to tests millions of cavity shapes and excitation/detection schemes, check the viability of the proposal based on a specific set of ontologies [3] and assesses the optical response of the cavity with a 30 000x acceleration factor compared to standard simulation tools to finally provide most promising solutions.[4]

This HAI approach was employed to optimize both the excitation conditions and the geometries of the plasmonic cavities. In our setup, two laser beams coherently illuminate each cavity at distinct positions, and the logical information is encoded in the polarization of each beam (810 nm, 140 fs, 80

MHz), representing “0” or “1,” as illustrated in **Fig.1**, which shows both the experimental instrument and the cavity irradiation scheme. With two beams and two polarization states, four input configurations are possible (00, 01, 10, 11).

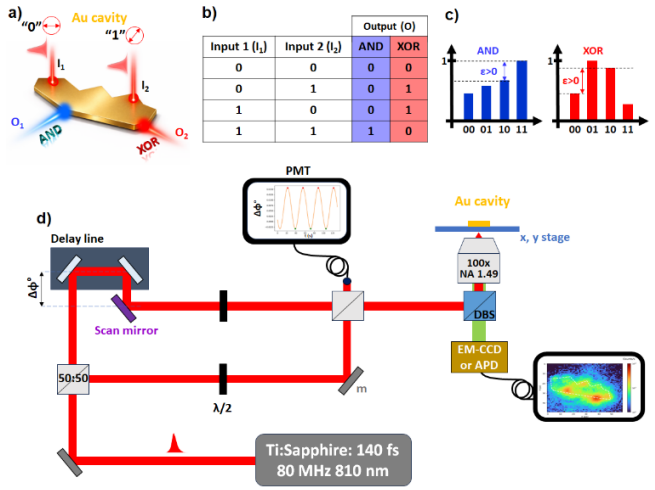

Fig.1: (**a**) Conceptual schematic of the plasmonic cavity. (**b**) Combined truth tables of the output positions simultaneously implementing AND and XOR logic (full-adder operation) within a single plasmonic cavity. (**c**) Bar-plot representation of the AND and XOR logic gates, highlighting a positive Boolean contrast (ε). (**d**) Schematic of the experimental setup used for optical characterization of the full-adder.

In this work, we focus on a 2×1-bit full adder, which requires a XOR gate to perform the sum and an AND gate to generate the carry. To perform an addition correctly, both the XOR and AND gates must operate simultaneously for the same input configuration. The Boolean contrast (ε), defined as the measure of distinguishability between the logical states “0” and “1” based on their output intensities, was enhanced through HAI-guided optimization (**Fig.1.b-c**).

The 2D plasmonic cavities were fabricated by focused ion beam milling chemically synthesized single-crystal gold microflakes deposited on a transparent glass substrate with a 10-nm nominal conductive indium tin oxide layer. [**1,2**] The milling of the polygonal shapes of the cavities was directly implemented from the Hybrid AI output files by simply adjusting the ion dose to the microflake thickness.

III. Results and Discussion

Within a few computation days, this HAI tool has identified optimal coherent drive conditions for the DH cavity and a set of 5 cavities with increasing overall Boolean contrast for the joint (AND, XOR) Boolean function that implements the 1-bit Full-Adder function. As Fig. 2 shows, the performance is increased by a factor of 200% compared to the optimized DH case.

Experimental realization and testing of such plasmonic ALUs and the effective assessment of the computation quality was carried out and will be introduced but detailed in a separate contribution. In particular, the cavity shapes are realized, from the geometrical description by the HAI, by focused ion beam (FIB) milling of single crystalline gold microflakes. The optical Boolean computation is obtained by implementing the coherent 2-beam excitation of the cavity [5] and controlling the excitation parameters (beam positions, linear polarization set encoding the Boolean inputs and relative phase-shift between the two incident fs-pulsed beams).

We will also discuss the extension and generalization of our approach towards more complex Boolean functions taking the 2xN-bit Full-Adder as a user case requiring 2N inputs and N+1 outputs.

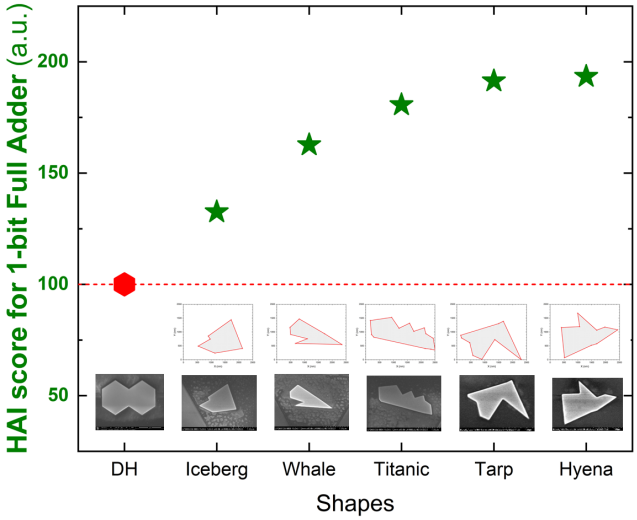

Fig. 1: Optimal 1-bit Full-Adder Boolean contrast (normalized to the one of the DH cavity) for the series of HAI-design plasmonic cavities. Each simulated score corresponds to a specific set of excitation conditions (input locations, linear polarization set, phase shift between exciting pulses). In inset: geometric shape provided by the HAI (top row) and SEM images of the nanofabricated cavities from single crystalline flakes (bottom row). [6].

IV. Conclusion

In conclusion, HAI-driven optimization enables the design of plasmonic cavities with high performance and reconfigurability. NPL generation is governed by confined cavity transport modes and strongly depends on beam polarization and position, with sharp corners serving as efficient output points. The optimized geometries outperform the reference double-hexagon design, achieving up to twofold improvement in Boolean contrast. Phase-dependent control allows dynamic switching between AND and XOR gates without changing the cavity, while long-range plasmon propagation and local hot-electron transport explain the observed NPL patterns. These results confirm the accuracy of AI predictions and highlight a physical performance plateau set by intrinsic plasmonic constraints, demonstrating that AI-assisted inverse design is a powerful strategy for creating robust, high-performance, and reconfigurable plasmonic logic devices

Acknowledgments

This work has been partially funded by the French Agence Nationale de la Recherche (ANR-20-CE24−0001 DALHAI, ANR-25-TSIA-0001 CAIPOP, ANR-25-CE24-7238

POMMARD, ISITE-BFC ANR-15-IDEX-0003), the REMONTADA project of the EIPHI Graduate School (ANR-17-EURE-0002). The authors also acknowledge the support of CNRS MITI (Project BOTAI 2023-24). Device nanofabrication and characterization was performed at the technological platforms SMARTLIGHT, ARCEN Carnot at ICB and MIMENTO at FEMTO-ST under program Investment for the Future (ANR-21-ESRE- 0040), the Région de Bourgogne Franche-Comté, the CNRS, and the French Renatech+ network..

REFERENCES

[1] Kumar, U *et al*., "Interconnect-Free Multibit Arithmetic and Logic Unit in a Single Reconfigurable 3 μm2 Plasmonic Cavity", ACS Nano 2021, 15, 13351−13359

[2] Dell'Ova, F., Brûlé, Y., Gros, N., Bizouard, J., Shakirova, D., Bertaux, A., ... & Dujardin, E. (**2024**). Compact implementation of a 1-bit adder by coherent 2-beam excitation of a single plasmonic cavity. ACS photonics, 11(2), 752-761.

[3] Labbani Narsis, O., Dujardin, E., Nicolle, C., Gros, N. "From Human Cognitive Expertise to Ontological Formalization: Bridging the Knowledge Gap for Nanophotonic Calculator Design and Simulation." Joint Ontology Workshops (JOWO) - 14th International Conference on Formal Ontology in Information Systems (FOIS 2024), Jul 2024, Enschede, Netherlands. (hal-05411152)

[4] Manvendra Janmaijaya, et al., "ESPLANADE: Efficient Simulation of Plasmonic Logic and Arithmetic NAnoDEvice", Submitted for publication, hal-05411342

[5] F. Dell'Ova, et al., " Coherent two-beam steering of delocalized nonlinear photoluminescence in a plasmon cavity", Opt Express 2022 30, 10, 17517-17528

[6] A. Khitous, N. Gros, L. Martin, F. Dell'Ova, A. Bertaux, O. Labbani Narsis, G. Colas des Francs, C. Nicolle, A. Bouhelier, E. Dujardin, 2026, in preparation..

Leaf-based Ground Planes for Sustainable Wireless Communication

Jaume Anguera[1,2*]

[1]Department of Technology, Ignion, Barcelona, Spain
[2]Engineering Department, La Salle Engineering, Universitat Ramon Llull, Barcelona, Spain
*Corresponding author: jaume.anguera@salle.url.edu

***Abstract*— Monitoring soil and wilderness is vital for environmental sustainability, biodiversity, and climate resilience. Traditional methods rely on manual observation, which is limited by human resources and area size. Existing automated solutions, such as satellites and sensor networks, face challenges in power, data transmission, durability, scalability, and ecosystem integration. This invited talk proposes a techno-natural IoT system that transforms living plants into self-sustained digital nodes. By integrating plant microbial fuel cells with leaf-based antenna systems embedding antenna boosters, plants become self-powered sensing and communication nodes, enabling autonomous data transmission and defining a new paradigm of plant-based cybernetic interaction for large-scale, sustainable ecosystem monitoring.**

***Keywords*—Internet of Things (IoT), antenna booster technology, organic ground plane, sustainable wireless communications, antenna miniaturization.**

I. Introduction

The rapid expansion of the Internet of Things (IoT) has increased the need for energy-efficient and environmentally sustainable wireless technologies. Since antennas strongly influence both power consumption and communication quality in IoT devices, their design plays a central role in reducing environmental impact. This work presents an alternative antenna approach that employs Aloe Vera as an organic ground plane material to enhance antenna efficiency while contributing to more sustainable device design.

The proposed concept is based on Antenna Booster Technology [1], which enables compact wireless devices without sacrificing performance. In this study, an Aloe Vera layer is introduced as a ground plane extension and its influence on antenna behaviour is analysed at 900 MHz, a frequency band commonly used by IoT standards such as LoRaWAN, Zigbee and cellular IoT [2], [3].

In conventional antenna designs, ground plane dimensions are a key factor in achieving high efficiency. At 900 MHz, optimal performance typically requires a metallic ground plane of about 0.4λ, corresponding to a size of approximately 130 mm. Such dimensions hinder device miniaturisation and rely heavily on materials like FR4, which contribute to a non-negligible carbon footprint. To address these limitations, this work investigates the possibility of reducing the effective ground plane size to below 0.1λ by using Aloe Vera as a ground plane enlarger mechanism to improve efficiency.

Both numerical simulations and experimental measurements confirm that Aloe Vera can effectively act as a ground plane extension. The antenna booster, which is electrically small and non-resonant (approximately λ/30), is combined with a matching network to achieve proper impedance matching to 50 Ω. When Aloe Vera is used as part of the ground plane, the antenna exhibits a significant improvement in performance, with a measured increase of 3.1 dB in total efficiency compared to a compact conventional ground plane implemented with copper and FR4.

While further optimisation and long-term studies are required, the results demonstrate that natural materials can be successfully incorporated into antenna systems.

Overall, this work highlights the potential of organic ground planes as a viable solution for future IoT devices. The use of materials such as Aloe Vera offers a promising path towards greener wireless technologies, enabling compact designs, improved efficiency and reduced environmental impact in next-generation IoT applications.

Acknowledgments

This work has been partially supported by the European Innovation Council under grant agreement No 101186925.

References

[1] J. Anguera and A. Andújar, “Antenna Booster Technology for Wireless Communications,” Institute of Engineering and Technology, July 2024, ISBN-13: 978-1-83953-300-6.

[2] L. A. M. Geubbels, G. Federico, V. Vidojkovic, J. Anguera and L. A. Bronckers, “Plantenna: Using Plant Leaves to Increase Antenna Performance,” 2022 16th *European Conference on Antennas and Propagation* (EuCAP), Madrid, Spain, 2022, pp. 1-5, doi: 10.23919/EuCAP53622.2022.9769173.

[3] J. Anguera, I. Ripoll, G. Massana and A. Andújar, "Organic Ground Planes for Wireless Devices Embedding Antenna Boosters," *2025 19th European Conference on Antennas and Propagation (EuCAP)*, Stockholm, Sweden, 2025, pp. 1-3, doi: 10.23919/EuCAP63536.2025.10999582.

Fully Programmable Reflect/Transmit sub-THz Surfaces with CMOS ICs

Kaushik Sengupta

[1]Department of Electrical and Computer Engineering,
Princeton University,
*Corresponding author: kaushiks@princeton.edu

***Abstract*— Large-scale metasurfaces can allow new applications in reconfigurable intelligent surfaces, and lead to new phased array architectures for extremely large apertures that can be scaled as tiles. We will demonstrate how silicon ICs can enable a new class of programmable metasurfaces at THz and scalable RIS at mm-wave frequencies for resilient communication links.**

***Keywords*— metamaterials, terahertz, machine learning, reflect arrays. Transmit arrays, 6G**

Formation of Electromagnetic Spin Skyrmions by Sparse Antenna Arrays

Andrei Afanasev[1,*]

[1]Department of Physics, The George Washington University, USA
*Corresponding author: afanas@gwu.edu

***Abstract*— We theoretically investigate properties of topological spin structures of electromagnetic waves formed by sparse phased antenna arrays. Formation of isolated electromagnetic spin skyrmions, their lattices and their propagation in space are described.**

***Keywords*—phased arrays, topological photonics, electromagnetic spin, electromagnetic skyrmions.**

Recently, novel three-dimensional (3D) spin skyrmions were observed experimentally near phase singularities of both optical and acoustic vortex beams [1-3]. They are robust against propagation of expanding wave fronts, maintaining constant transverse dimensions.

Here we provide a comparative analysis of skyrmionic spin textures that can be formed with antenna arrays across multiple scales, from RF phased arrays to atomic antennas. Theoretical foundations of our approach may be found in Ref.[3,4]. We consider, in particular, the arrays with a limited number of elements, or sparse arrays, as shown in Fig.1. Interference patterns of the antenna's radiation are characterized by lattices of phase singularities that have topological charges of ± 1 and 2, depending on the number of antenna elements, as shown in Fig.2. If radiation from individual antenna elements is circularly polarized, then skyrmionic spin textures are formed near the lattice sites that have opposite signs of the singularity's topological charge and spin helicity. Therefore, these electromagnetic spin skyrmions can be turned on or off, or moved to a neighboring lattice site by flipping a sign of circular polarization of the electromagnetic radiation. A detailed analysis reveals that these spin textures can be associated with Bloch-type merons (N_{sk}=1/2) and skyrmions (N_{sk}=1), where N_{sk} is Skyrme number.

Propagating of the photonic lattice into the far field, we observe that while the size of the lattice cells expands due to diffraction, the skyrmion textures maintain a constant transverse size.

We further present a theory of spin transfer of electromagnetic 3D spin skyrmions to matter.

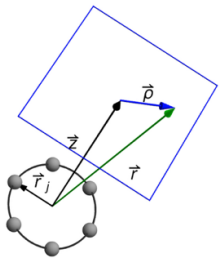

Figure 1. Sparse phased array geometry.

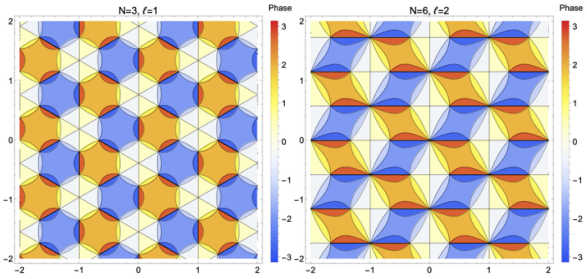

Fig. 2. Lattices of phase singularities formed by a phased array with N elements and a phase number l: (a) N=3, l=1; (b) N=6, l=2.

ACKNOWLEDGMENTS

This work was supported by the US Army Research Office Award W911NF-23-1-0085.

REFERENCES

[1]. N. Mata-Cervera, D. K. Sharma, Y. Shen, R. Paniagua- Dominguez, and M. A. Porras, Phys. Rev. Lett. **135**, 033805 (2025).
[2]. N. Mata-Cervera, et al. arXiv preprint arXiv:2509.06555 (2025).
[3]. E. Annenkova, A. Afanasev, and E. Brasselet, arXiv preprint arXiv:2512.02964.
[4]. H. Wang and A. Afanasev, Appl. Sci. **13**, 5672 (2023); https://doi.org/10.3390/app13095672

The Quasi-Normal Mode Method Applied to the Study of the Radiating Properties of Quasi-Bound States in the Continuum

Emmanuel Centeno[1,*], Victor Kalt[2], Rafik Smaali[1] Antoine Moreau[1]

[1]Université Clermont Auvergne, Clermont Auvergne INP, CNRS, Clermont-Ferrand, France
[2]Université de Lyon, Laboratoire Hubert Curien, UMR 5516, Université Jean Monnet, Saint-Etienne, France
*Corresponding author: emmanuel.centeno@uca.fr

***Abstract*— We study the radiating properties of dimer grating supporting quasi-bound states in the continuum (QBICs) with a novel approach based on the quasi-normal mode method. This work clarifies the interplay between structural symmetry, disorder, and light–matter interaction in photonic structures supporting BICs and QBICs.**

***Keywords*— Bound states in the continuum, grating, spontaneous emission,**

I. Introduction

Increasing the light matter interaction in photonic nanostructures is fundamental for lighting, communication, imaging, and medicine applications. Optical bound states in the continuum (BICs) constitute an elegant solution to boost the photoluminescence quantum yield [1]. In this work, we develop a QNM theory to calculate the radiative properties of a dimer grating which supports BICs and Quasi-BICs (QBICs) [2].

II. Methods

We use the QMN expansion to calculate the RE in the normal direction and for the target wavelength for the QBICs [2]. We consider a unique dipole into a dimmer grating. In the following analysis, the radiative enhancement and decay rate are averaged over the horizontal and vertical orientations of the emitter.

III. Results and Discussion

The dimmer grating consists of a supercell period 2D, made of TiO_2 ribbons of width $w\pm\Delta w$ with $w=D/2$ above a quartz substrate. We denote the gap distance $L\pm\Delta L$. We introduce the coefficients $\alpha=\Delta w/2w$ and $\beta=\Delta L/2L$. For the regular grating with $\alpha=0$ and $\beta=0$ presents a BIC at the Γ-point. To assess the influence of structural disorder on the radiative properties, we consider a supercell consisting in six TiO_2 ribbons, whose widths and lateral positions are individually randomly distributed. δ is quantified the disorder strength. The normalized radiated power P_r is averaged over 30 realizations for increasing the disorder strength, Fig. 1.

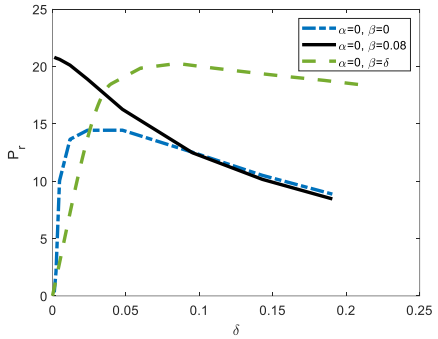

Fig. 1 Normalized radiated power in normal direction for the regular ($\alpha = 0$, $\beta = 0$) and dimer gratings ($\alpha = 0$, $\beta = 0.08$). The green curve is P_r for the dimer grating free of disorder for an increasing β.

IV. Conclusion

The dimer grating free of disorder (green curve) is clearly identified as the optimal structure when the asymmetry attains 8%. In this configuration, structural disorder is shown to degrade the normalized power (black curve). The regular grating ($\alpha = 0$, $\beta = 0$) starts to emit when the structural disorder is increased. In that case, the BIC transforms into a QBIC because of the symmetry breaking induced by disorder. However, when the strength of disorder attains 10 % both dimer and regular gratings presents the same efficiency.

Acknowledgments

The authors thank the French “Agence Nationale de la Recherche” in the framework of the COULEURS project (ANR-22-CE39-0013).

References

[1] S. I. Azzam and A. V. Kildishev, “Photonic bound states in the continuum: from basics to applications”, Advanced Optical Materials Vol.9, 2001469 (2021).
[2] E. Centeno, V. Kalt, R. Smaali, A. Moreau,” Disorder-induced effects on spontaneous emission from quasi-bound states in the continuum in regular and dimer gratings”, Physical Review B, 112(13), 134202, (2025).

Opto-thermal tunability in phase-change metasurfaces

Marco Gandolfi[1,2,3,*], Jesse Frantz[4], Natalia M. Litchinitser[5], Costantino De Angelis[1,2,3], and Maria Antonietta Vincenti[1,2,3]

[1]Dipartimento di Ingegneria dell'Informazione Università degli Studi di Brescia, Via Branze 38, Brescia 25123, Italy
[2]Consiglio Nazionale delle Rircerche, Istituto Nazionale di Ottica, Via Branze 45, Brescia 25123, Italy
[3]Consorzio Nazionale Interuniversitario per le Telecomunicazioni (CNIT), Viale G.P. Usberti 181/A Sede Scientifica di Ingegneria-Palazzina 3, Parma 43124, Italy
[4]US Naval Research Laboratory, 4555 Overlook Ave., SW, Washington, DC 20375, USA
[5]Department of Electrical and Computer Engineering, Duke University, Durham, NC 27708, USA

*Corresponding author: marco.gandolfi1@unibs.it

***Abstract*— We study the opto-thermal reconfiguration of nanostructures and metasurfaces composed of phase-changing materials. We propose a GST ($Ge_2Sb_2Te_5$)-based metasurface enabling partial crystallization of the structure through all-optical ultrafast excitation. We prove that partial crystallization can be induced using an infrared laser pulse with an intensity as low as 35 MW/cm².**

***Keywords* — phase-change materials, GST, light induced phase-transition, metasurfaces, bound stated in the continuum.**

I. Introduction

Metasurfaces are useful for manipulating light at the nanoscale [1]. One strategy for tuning their optical response dynamically is the introduction of phase-change materials, that can dramatically change their properties when an external stimulus is applied [2]. Depending if the phase transition in the component materials is volatile or permanent – as in VO_2 or $Ge_2Sb_2Te_5$ (GST from now on), respectively – the metasurface reconfiguration may be temporary or durable [3-5].

In this work we investigate the mechanisms leading to a phase transition in a metasurface due to due to the heating after absorption of a powerful short laser pulse [6]. In particular, we consider the paradigmatic case of permanent phase transition in a GST metasurface. By illuminating with a near infrared light pulse (duration 1 ns, intensity 35 MW/cm^2), we demonstrate partial crystallization of the structure [7].

II. Results and Discussion

The investigated geometry is a metasurface made of GST nanoblocks placed over a silica substrate and embedded in air, as shown in Fig. 1. The unit cell of this geometry is composed of two identical nanoblocks. By properly tuning the geometrical parameters, this metasurface can show a bound state in the continuum (BIC) optical mode in the near infrared range. By slightly perturbing the width of one block, the BIC evolves into a quasi-BIC, with a very high electric field enhancement within the blocks, a favorable situation to have a strong light-to-heat conversion upon illumination with a moderate light intensity pulse.

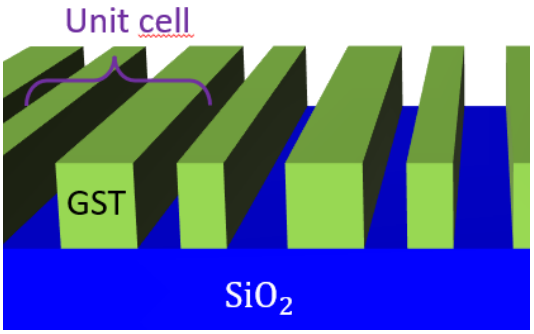

Fig. 1 Unit cell geometry of the metasurface.

We introduce a self-consistent opto-thermal model that quantifies the temperature increase induced by the laser. We show that upon illumination with a moderate peak intensity (35 MW/cm^2, the temperature can easily exceed 600° C, the value required to induce crystallization in the GST. However, the asymmetric distribution of the electric field imply a high temperature increase only in the smaller nanoblock, thus limiting the crystallization to that part of the geometry.

III. Conclusion

We developed a complete and self-consistent opto-thermal model to describe ultrafast phase-change transitions. This model can be utilized to characterize both the volatile and permanent phase transitions in phase-change materials metasurfaces. In particular, we demonstrated that a 1 ns infrared pulse with a moderate pump intensity on the order of 35 MW/cm² can induce partial crystallization in selected regions of the metasurface featuring GST. We show that full crystallization of a small portion of the proposed geometry

leads to a controlled resonance shift exceeding 350 nm.

ACKNOWLEDGMENTS

M.G. acknowledges the European Union for the financial support through “FESR o FSE, PON Ricerca e Innovazione 2014-2020 - DM 1062/2021”. J.F., acknowledges NRL Base Program 6.1 funding. N.M.L. and M.A.V. acknowledge partial funding from NATO SPS Grant No. G5984. M.A.V. also thanks MUR as part of the PRIN 2022 project PILLARS (2022YJ5AZH).

REFERENCES

[1] N. Yu and F. Capasso, “Flat optics with designer metasurfaces” Nature Matererials, 13, 139, 2014.

[2] S. V. Makarov, A. S. Zalogina, M. Tajik, D. A. Zuev, M. V. Rybin, A. A. Kuchmizhak, S. Juodkazis, and Y. Kivshar, “Light-induced tuning and reconfiguration of nanophotonic structures,” Laser Photonics Reviews, 11, 5, 1700108, 2017.

[3] C.Wan, E. H. Horak, J. King, J. Salman, Z. Zhang, Y. Zhou, P. Roney, B. Gundlach, S. Ramanathan, R. H. Goldsmith, and M. A. Kats, “Limiting optical diodes enabled by the phase transition of vanadium dioxide,” ACS Photonics 5, 7, 2018.

[4] C Baratto, M Gandolfi, A Tognazzi, P Franceschini, G Ambrosio, B Li, R Camacho Morales, D De Ceglia, AC Cino, DN Neshev, C De Angelis, “Optical Limiting Sensor Based on Multilayer Optimization of Ag/VO2 Phase Change Material”, IEEE Sensors Letters, 7, 9, 2023.

[5] A. Karvounis, B. Gholipour, K. F. MacDonald, and N. I. Zheludev, “All-dielectric phase-change reconfigurable metasurface”, Applied Physical Letters 109, 051103, 2016.

[6] A. Tognazzi, M. Gandolfi, B. Li, G. Ambrosio, P. Franceschini, R. Camacho-Morales, A. C. Cino, C. Baratto, D. de Ceglia, D. Neshev et al., “Opto-thermal dynamics of thin-film optical limiters based on the VO_2 phase transition”, Opt. Mater. Express 13, 41 (2023).

[7] M. Gandolfi, M. E. Serrano Flores, J. Frantz, J. Myers, R. Bekele, J. Sanghera, A. Clabeau, N. M. Litchinitser, and M. A. Vincenti, “Dynamic light-driven metasurface: Harnessing quasibound states in the continuum for laser-induced selective crystallization”, Physical Review A, 110, 013510 (2024).

Theoretical Modeling of Surface Electromagnetic Wave-Based Underwater Radio Communication

Igor I. Smolyaninov[1,*]

[1]Saltenna Inc., 1751 Pinnacle Dr. Ste. 600, McLean, VA 22102-4007, USA
*Corresponding author: igor.smolyaninov@saltenna.com

***Abstract*— Surface electromagnetic waves propagating along the water-air interface may exhibit a "plasmonic gradient resonance", which leads to highly unusual propagation properties of radio fields, resulting in extremely large penetration depth and very large communication distances of radio fields underwater, reaching hundreds and in some cases thousands of skin depths.**

***Keywords*— underwater radio communication, surface electromagnetic waves, plasmonic gradient resonance.**

I. Introduction

While water is fundamental to life and technology, many of its properties are not well understood. Even such seemingly simple processes like electromagnetic field propagation through water are still being actively researched [1]. Our study is motivated by an analogy between electromagnetic properties of water in the radio frequency range and the properties of some recently discovered electromagnetic metamaterials, which until now avoided scrutiny. These are natural and artificial materials having the real part of ε^2 approximately equal to zero. We will call this novel class of metamaterials "epsilon-squared near zero" (ESNZ) materials. Note that ESNZ conditions are not equivalent to ENZ conditions since $\mathrm{Re}(\varepsilon^2)=\varepsilon'^2-\varepsilon''^2$, where ε' and ε'' are the real and imaginary parts of ε, respectively, which may not be small.

II. Methods

Our methodology is based on the recently introduced description of the surface electromagnetic waves in gradient media in terms of an effective Schrödinger equation as

$$-\frac{\partial^2\psi}{\partial z^2}+\left(-\frac{\varepsilon(z)\omega^2}{c^2}-\frac{1}{2}\frac{\partial^2\varepsilon}{\varepsilon\partial z^2}+\frac{3}{4}\frac{\left(\partial\varepsilon/\partial z\right)^2}{\varepsilon^2}\right)\psi=-\frac{\partial^2\psi}{\partial z^2}+V(z)\psi=-k^2\psi$$

where the wave function ψ is introduced via the z-component of electric field as $E_z=\psi/\varepsilon^{1/2}$, $V(z)$ is an effective potential, and the term $-k^2$ behaves as an effective energy [1]. The resonant conditions are observed if $\varepsilon^2\approx 0$.

Fig. 1 Example of an underwater radio operating at 30 MHz.

III. Results and Discussion

Our detailed theoretical analysis and the proof of principle experiments (see Fig.1 as an example) demonstrate extremely large penetration depth and very large communication distances of radio fields underwater, reaching hundreds and in some cases thousands of skin depths. The discovered phenomenology may also have very interesting applications in silicon UV nanophotonics, since ESNZ conditions may also be expected in typical semiconducting materials.

IV. Conclusion

We have demonstrated a practical underwater radio communication scheme capable of operating in the HF and VHF bands. The described phenomenology should also have numerous applications in nanophotonics.

Acknowledgments

This work was completed as an internal research and development project by Saltenna Inc..

References

[1] I. I. Smolyaninov, Q. Balzano, N. Dale, V. I. Smolyaninova, D. Young, "Experimental observation of a radio frequency plasmonic gradient resonance in water", Scientific Reports vol. 15, p. 31513, 2025.

Multi-order exceptional points and structured perturbations

Konstantinos G. Makris [1,2*]
[1]Department of Physics, University of Crete, 70013, Heraklion, Greece
[2]Institute of Electronic Structure and Laser (IESL),FORTH, 71110, Heraklion, Greece
*Corresponding author: makris@physics.uoc.gr

***Abstract*—The unique spectral singularities known as exceptional points (EPs) are typical in non-Hermitian photonics. Here we present a new class of EPs, the multi-order exceptional points (MoEPs) in composite 2D-waveguide lattices with distributed gain and loss. We systematically investigate the role of perturbation symmetries on their ultrasensitive-behavior.**

***Keywords* nonlinear optics, non-Hermitian optics, multimode waveguides, photonic lattices.**

I. Introduction

Non-Hermitian (NH) Hamiltonians are widely used in many areas of physics, since they effectively model actual physical systems that are coupled to their environment. Recently guided optics and coupled resonators have provided a test ground for experimental realizations of such concepts, leading thus to the area of non-Hermitian photonics [1], [2], [3]. Quite intriguing characteristics of such Hamiltonians are the so-called exceptional points (EPNs) of N^{th}-order, that been recently experimentally demonstrated in coupled optical microcavities [4]. In fact, near these singularities the system's sensitivity is enhanced, and more specifically exhibits a nonlinear dependence on the imposed perturbation strength.

In our work, we introduce the new concept of multi-order exceptional points (MoEPs) [5]. Multi-order exceptional points arise when a system hosts multiple exceptional points of different orders simultaneously. More specifically, we present a direct computational method to generate MoEPs in two- and three-dimensions, based on corresponding one-dimensional lattices, that already exhibit EPNs.

II. Methods

Regarding our methodology, is threefold: (a) The spectral calculation is based on exact diagonalization of the associated non-Hermitian matrices, (b) the construction of MoEPs is performed by tensor products, and (c) the sensitivity of the physical system is characterized by the complex and structured pseudospectra of the non-Hermitian Hamiltonians [6], [7], [8], [9], [10], [11].

III. Results and Discussion

Our results are shown in Fig.1 and Fig.2. In particular, a schematic illustration of one representative lattice that exhibits a MoEP is shown in Fig.1(a). The circles represent the lattice sites, which couple only to the nearest-neighbors, resulting in orthogonal coupling directions along x and y directions. The color indicates the gain and loss strength at each lattice site, with red (green) corresponding to gain (loss). Note that the real part of the onsite potential is the same for all waveguides, here taken to be zero. The indices of $\text{MoEP}_{2,4}$ indicate the number and order of the underlying exceptional points. For example, $\text{MoEP}_{2,4}$ indicates that there are two exceptional points of orders 2 and 4, simultaneously. Similarly, $\text{MoEP}_{2,4,6}$ indicates there are three exceptional points of orders 2, 4 and 6.

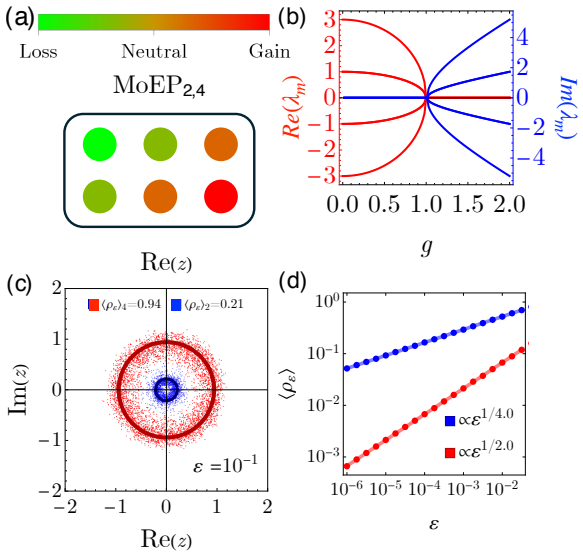

Fig. 1. (a) Schematic illustration of a lattice that exhibits a MoEP of orders 2 and 4. A dual color scheme is used to indicate the relative gain-loss strength. (b) Real (red curves) and imaginary (blue curves) parts of the eigenvalue spectrum as a function of the gain/loss parameter g. (c) Pseudospectra of the lattice in panel on the complex plane (a). Red (blue) pseudoeigenvalue clouds correspond to the $EP4$ ($EP2$) respectively, while the red (blue) continuous circle marks the average eigenvalue norm of the $EP4$ ($EP2$) eigenvalues for perturbation strength $\varepsilon = 10^{-1}$. (d) Pseudospectral radii (dots) and their corresponding power-law scalings (lines) for different values of the perturbation strengths ε, that correspond to the underlying EPs.

To quantify the sensitivity of the MoEPs to perturbations, we compute the corresponding pseudospectra [6], [7]. The general theory of pseudospectra is well developed and has been applied in diverse areas of physics, including non-modal stability in fluid mechanics, nonlinear dynamics, and complex networks [6], [7]. We focus on a random matrix perturbation approach, here we perturb the Hamiltonian as $\mathcal{H} \rightarrow \mathcal{H} +$

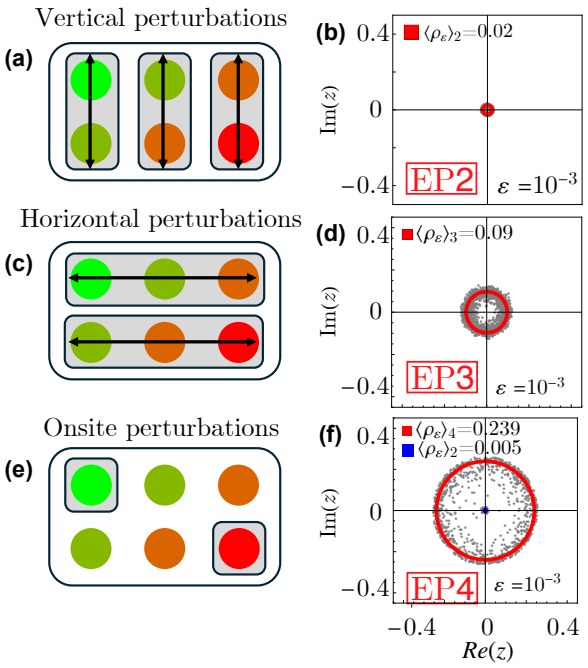

Fig. 2. Role of structured perturbations on the sensitivity of the lattice. (a),(c),(e) Schematic depictions of three type of structured perturbations, that applied along the direction of the arrows. (b), (d), (f) the corresponding structured pseudospectra on the complex plane that reveal the sensitivity related to an EP2, EP3, and EP4, respectively. For panels (b), (d), and (f), the perturbation strength is set to $\varepsilon = 10^{-3}$,

εE. Here, ε sets the overall perturbation strength, and E is a random matrix strictly normalized to unity. Specifically, $E = \frac{\hat{E}}{\|\hat{E}\|}$, where $\|\cdot\|$ denotes the matrix norm defined as $\|\Gamma\| = \sup_{x\neq 0} \frac{\|\Gamma x\|}{\|x\|}$. The impact of these globally applied complex perturbations is illustrated in Fig.1(c), where the pseudoeigenvalues disperse to form distinct clouds in the complex plane around the unperturbed eigenvalue spectrum. Specifically, the red and blue clouds correspond to the EP_4 and EP_2, respectively. To quantify this spectral sensitivity, we introduce the pseudospectral radius, $\langle\rho_\varepsilon\rangle_N$, defined as the mean distance of the perturbed eigenvalues from their original degenerate positions. Fig.1(d) displays how these radii evolve as a function of the perturbation strength ε. For both the $N = 4$ and $N = 2$ cases, the calculated scaling strictly follows the fractional power law $\langle\rho_\varepsilon\rangle_N \propto \varepsilon^{1/N}$, a typical signature of higher order exceptional points [5].

The role of structured perturbations is now clearly demonstrated in Fig.2. We note that the two-dimensional lattices that are constructed with our method, can exhibit different responses depending the form of the perturbations. More specifically, the one-dimensional component lattices that are used to define the two-dimensional systems with MoEPs, do critically determine the sensitive of the structure. In fact, perturbations applied symmetrically along the x- or y-directions activate the response of one of the one-dimensional component lattice. A perturbation along the x-direction probes the exceptional-point (EP) sensitivity of the second component, while one along the y-direction reveals the corresponding sensitivity of the first component. In other words, different structured perturbations trigger sensitivity that corresponds to EPs of different order.

IV. Conclusion

In conclusion, we have presented a new class of non-Hermitian singularities, the multi-order exceptional points and present a method to construct them in two- and three- dimensional lattices. The proposed geometries are experimentally relevant and are derived based on one-dimensional system that exhibit EPs. Remarkably, the MoEPs are characterized by extreme sensitivity that corresponds to EPs of different orders. The symmetry of the imposed structured perturbations determines which order is relevant every time, thus highlighting their potential use for novel sensing applications.

Acknowledgments

This work was supported by by the European Research Council (ERC-Consolidator) under the grant agreement No. 101045135 (Beyond_Anderson) and the Hellenic Foundation for Research and Innovation (H.F.R.I.) through the 5th Call of the "Science and Society" Action, titled "Always strive for excellence-Theodoros Papazoglou" (Project Number: 11496, "PSEUDOTOPPOS").

References

[1] D.F. Pile, and D. N. Christodoulides, Nat. Phot. **11**, 742 (2017).
[2] R. El-Ganainy, K.G. Makris, M. Khajavikhan, Z.H. Musslimani, S. Rotter, and D. N. Christodoulides, Nat. Phys. **14**, 11 (2018).
[3] M. H. Teimourpour, R. El-Ganainy, A. Eisfeld, A. Szameit, and D. N. Christodoulides, Phys. Rev. A **90**, 053817 (2014).
[4] H. Hodaei, et al., Nature **548**, 187 (2017).
[5] A. Athanasopoulos, D. Kaltsas, and K.G.Makris, under submission (2026).
[6] K. G. Makris, L. Ge, and H. E. Türeci, Phys Rev. X **4**, 041044 (2014).
[7] K. G. Makris, Phys. Rev. E **104**, 054218 (2021).
[8] D. Kaltsas, I. Komis, and K. G. Makris, Opt. Lett. **47**, 4447 (2022).
[9] I. Komis, D. Kaltsas, S. Xia, H. Buljan, Z. Chen, and K. G. Makris, Phys. Rev. Res. **4**, 043219 (2022).
[10] K. G. Makris, Appl. Phys. Lett. **125**, 011102 (2024).
[11] I. Kiorpelidis, and K.G. Makris Phys. Rev. Res. **7**, L032043 (2025).

Multipolar THz field generation using spintronic elements

Christian Bohley[1], Vakhtang Jandieri[2], Ramaz Khomeriki[3], Benjamin Schwager[1], Douglas H. Werner[4] , and Jamal Berakdar[1,*]

[1]Martin-Luther University, Halle-Wittenberg, 06099 Halle, Germany
[2]Nagoya Institute of Technology, Nagoya, Aichi 466-8555, Japan
[3]Physics Department, Tbilisi State University, 3 Chavchavadze, 0128 Tbilisi, Georgia
[4]Department of Electrical Engineering, The Pennsylvania State University, University Park, PA 16802, USA
[*]corresponding author: jamal.berakdar@physik.uni-halle.de

Abstract: Engineered spintronic THz emitters are shown to be capable of producing focused, broadband THz fields with multipolar character and also fields which embody spin, and orbital angular momentum densities as well as optical chirality density.

The spin current buildup and decay in materials with large spin-orbit coupling (as realized in spintronic emitters [1]) are accompanied with a charge current pulse that leads to coherent broadband radiation in the THz range. In this presentation we discuss how engineering the spintronic elements [2] results in an effective engineering of the emitted THz fields in the near and far field limit. In particular, we show how multipolar fields can controllably be generated as well as fields embodying well-defined spin and orbital angular momentum as well as optical chirality density. Some applications of the generated fields in connection with light-matter interaction will be discussed.

Acknowledgements: This work is funded by the DFG.

References

1. Th. E. Papaioannou, and R. Beigang, Nanophotonics, 10, 1243-1257, 2021
2. D. Schulz, B. Schwager, and J. Berakdar, ACS Photonics, 4, 1248–1255, 2022

Ultraviolet to Near Infrared Spectroscopic Emitters Based on Broadband Rare Earth-free Phosphors

T. Nagao[*,1,2], B. K. Barman[1,3], D. Hernandez-Pinilla[1,4], K. Watanabe[1], D. Thien Ngo[1],
[1]Research Center for Materials Nanoarchitectonics, National Institute for Materials Science 305-0044, Tsukuba-city, Japan.
[2]Department of Condensed Matter Physics, Hokkaido University, Sapporo, Hokkaido, Japan.
[3]Centre for Interdisciplinary Research (CIDR) SRM University - AP, Amaravati Andhra Pradesh 522240, India
[4]Dept. of Physics of Materials, Universidad Autónoma de Madrid (UAM), Madrid 28049, Spain
[*]Corresponding author: NAGAO.Tadaaki@nims.go.jp

***Abstract*— We introduce our recently developed light-emitting devices combining rare-earth free carbon-dot phosphors and distributed Bragg reflector (DBR)-based microcavity as well as microbead whispering gallery mode resonator. We successfully demonstrated to spectroscopically engineer the sharp resonant emission and chromaticity via wavelength-tunable photoluminescence, lasing, and infrared emission.**

***Keywords*— carbon-dot phosphor, distributed Bragg reflector, whispering gallery mode, wavelength-tunable photoluminescence.**

Numerical Investigation of Hyperbolic Metamaterial Probes for Broadband Near-field Enhancement in Tip-Enhanced Raman Spectroscopy

Maria Vanessa Balois-Oguchi[1,*]

[1]Department of Electrical and Electronic Engineering, Institute of Science Tokyo, Japan
*Corresponding author: balois@ee.e.titech.ac.jp

***Abstract*— We numerically investigate the use of hyperbolic metamaterials to design probes with broadband near-field enhancement for tip-enhanced Raman spectroscopy. Using Au/Al_2O_3 multilayers, we examine how layer number and thickness influence the spectral response of a SiO_2 TERS probe, targeting robust enhancement across the 600 nm - 1100 nm wavelength range.**

***Keywords*— hyperbolic metamaterials, near-field enhancement, tip-enhanced Raman spectroscopy.**

I. Introduction

Tip-enhanced Raman spectroscopy (TERS) is a powerful technique for highly sensitive chemical identification with nanometer-scale spatial resolution. The near-field enhancement in TERS is largely determined by the electromagnetic properties of the probe. However, the operational bandwidth of conventional TERS probes is typically narrow, with specific materials often selected for particular excitation wavelengths, such as Ag tips for 532 nm excitation and Au tips for 633 nm excitation. It has been shown that hyperbolic metamaterials can strongly modify the optical response of materials [1,2], and have been explored in surface-enhanced Raman spectroscopy (SERS) as a means of increasing electromagnetic field enhancement [3]. Here, we investigate a hyperbolic metamaterial (HMM)-based tip design as a possible route toward broadband near-field enhancement, with the goal of allowing a single TERS probe to operate over a wider spectral range.

II. Methods

Figure 1a shows the simulation model of our TERS tip. A two-dimensional (2D) model was used to capture the essential electromagnetic coupling while avoiding the excessive computational cost of a full three-dimensional model. The model consists of three parts: (1) the probe shaft, (2) the probe apex, and (3) the substrate. These are represented as cylinders in the 2D system. The probe shaft is modeled as a SiO_2 core with a radius r_0 = 25 nm, which is typically used for atomic force microscope-based TERS systems [4]. The SiO_2 core is surrounded by a cylindrical hyperbolic metamaterial (CHMM) consisting of Au/Al_2O_3 multilayers, with individual layer thicknesses denoted by r_1 to r_N, where N is the total number of layers. At the bottom of the shaft is a Au nanosphere that represents the metal coated apex of the TERS probe. Below the probe apex is another Au nanosphere representing the substrate, separated by a gap distance d_{gap} = 2 nm. In the 2D model, the nanospheres are modeled as cylinders with equivalent radii (r_{sph} = 30 nm). A gap-mode configuration was chosen since it is commonly used in TERS to increase field enhancement. The effective-medium approximation for CHMMs was used as a guideline to determine the number of layers and layer thicknesses [5]. The incident light propagates along the ***x***-direction, with the electric field polarized along the transverse direction of the cylindrical axis, as shown in Fig. 1a.

Finite-difference time-domain (FDTD) simulations were performed to visualize the electric field distribution and determine the electric field enhancement from visible to near-infrared wavelengths. The electric field was monitored at the center of the gap between the Au spheres.

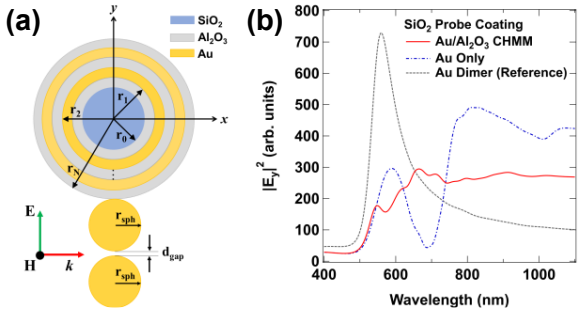

Fig. 1(a) Schematic of the TERS probe geometry and substrate used in the simulations. (b) Near-field enhancement at the center of the gap between the Au nanospheres shown in (a).

III. Results and Discussion

From the numerical calculations, we found:

- A configuration consisting of 5 Au/Al_2O_3 pairs, with individual metal and dielectric layer thicknesses of 9 nm,

was suitable for the target wavelength range

- With the Au/Al_2O_3 CHMM coating, the near-field enhancement is relatively uniform at longer wavelengths (600 nm – 1100 nm) (Fig. 1b), compared to a typical dimer configuration or a uniformly Au-coated probe with the same total thickness.

The overall enhancement of the CHMM-coated SiO_2 probe is weaker than the Au-coated probe with same total thickness. However, the Au-coated probe exhibits a pronounced drop in enhancement at around 700 nm, whereas the CHMM-coated probe maintains a more stable response across the spectrum, which is desirable for broadband operation. This decrease in the Au-coated case is likely related to coupling between the apex gap mode and the extended metallic coating.

IV. Conclusion

We showed that introducing a Au/Al_2O_3 CHMM coating onto a SiO_2 TERS probe can lead to broadband near-field enhancement particularly at the 600 nm – 1100 nm wavelength region. Effects of increasing the number of Au spheres and using a Au slab as the substrate are currently being investigated.

Acknowledgments

This work was supported by the Japan Society for the Promotion of Science (23K13640, 25K08558).

References

[1] A. Poddubny, I. Iorsh, P. Belov, and Y. Kivshar, “Hyperbolic metamaterials,” Nature Photonics, vol. 7, pp. 948–957, 2013.

[2] R. Kumar and K. Kajikawa, “Superscattering from cylindrical hyperbolic metamaterials in the visible region,” Optics Express, vol. 28, pp. 1507–1517, 2020.

[3] R. Liu, Z. Zha, M. Shafi, C. Li, W. Yang, S. Xu, M. Liu, and S. Jiang, “Bulk plasmon polariton in hyperbolic metamaterials excited by multilayer nanoparticles for surface-enhanced Raman scattering (SERS) sensing,” Nanophotonics, vol. 10, pp. 2949–2958, 2021.

[4] N. Hayazawa, T. Yano, and S. Kawata, “Highly reproducible tip-enhanced Raman scattering using an oxidized and metallized silicon cantilever tip as a tool for everyone,” Journal of Raman Spectroscopy, vol. 43, pp. 1177–1182, 2012.

[5] R. Kumar and K. Kajikawa, “Comparison of cylinder- and planar-effective medium approximations on calculation of scattering properties of cylindrical hyperbolic metamaterials,” vol. 36, pp. 559–564, 2019.

The Leaky-Wave Paradigm for Nondiffractive Beams

Edoardo Negri[1], Stella Ventucci[2], Walter Fuscaldo[1], Paolo Burghignoli[2], Alessandro Galli[2,*]

[1]Istituto per la Microelettronica e i Microsistemi, Consiglio Nazionale delle Ricerche, Rome, Italy
[2]Department of Information Engineering, Electronics and Telecommunications, Sapienza University of Rome, Rome, Italy
*Corresponding author: alessandro.galli@uniroma1.it

***Abstract*—This contribution presents a comprehensive review of devices radiating nondiffractive beams, ranging from microwaves to THz, designed according to a leaky-wave paradigm.**

***Keywords*—Nondiffractive beams, near-field focusing, Bessel beams, leaky waves.**

I. Introduction

Nondiffractive beams in the microwave, millimeter- and submillimeter-wave frequency ranges have recently attracted much interest in different application contexts, spanning from wireless power transfer and near-field information links to imaging and security screening [1]. Referring to the important class of devices able to generate a Bessel-beam (BB) distribution (i.e., a solution of the Helmholtz equation with remarkable nondiffractive, focusing, and self-healing properties), this paper deals with a comprehensive review of leaky-wave radiators, commonly referred to as *Bessel-beam launchers* [1]. With respect to other solutions, the latter stand out for their compact, single-feeder, planar, and cost-effective architecture.

II. Leaky-Wave Bessel-Beam Launchers

Leaky-wave BB launchers are constituted by partially opened waveguides engineered to operate in a regime where the aperture-field distribution is dominated by the leaky-wave contribution [1]. Consequently, the near-field behavior is governed by the spectral features of the leaky mode, and a *leaky-wave paradigm* provides an adequate description of these devices. Specifically, the generation of a BB-field distribution in these launchers relies on the constructive interference between outward- and inward-propagating cylindrical leaky waves. Depending on how these contributions are excited, leaky-wave nondiffractive devices are commonly classified into two main families: *resonant* and *wideband* BB launchers.

The former are constituted by a grounded dielectric slab with a homogenized metasurface (i.e., an arrangement of 2D, subwavelength metallic elements) on top and encircled by a metallic rim (see Fig. 1(a)). In this case, the inward cylindrical leaky wave is generated by the reflection of the outward contribution—launched by a simple dipole-like central source—on the circular metallic rim. To achieve a constructive interference among these waves, the device has to satisfy both an amplitude and a phase resonant condition, which inherently requires a compact radiating aperture at the expense of a narrowband behavior [1]. In these conditions, a BB is generated over a conical-shaped region whose apex is determined by the so-called *nondiffractive range* [1].

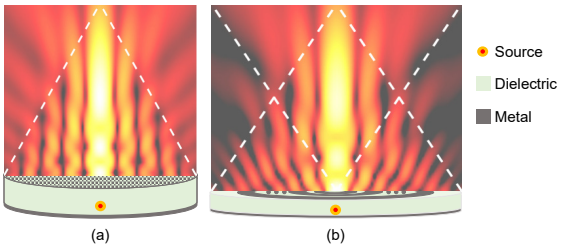

Fig. 1. Representation of a (a) resonant and of a (b) wideband BB launcher with their near-field distribution in a dB colormap. A (a) triangular- and a (b) diamond-shaped nondiffractive region is highlighted with dashed white lines.

As the name suggests, a larger frequency range can be achieved with *wideband* BB launchers at the expense of an electrically large aperture [2]. In these devices, the inward character of the cylindrical leaky wave is achieved through a radially periodic, annular, metal strip grating on top of a wider and thin grounded dielectric slab (see Fig. 1(b)). In this manner, the nondiffractive region has a diamond shape [2].

In both cases, the capability of expressing the aperture fields in terms of leaky waves allows us to reach an effective computational strategy to accurately analyze and design such type of BB radiating devices.

III. Conclusion

We have considered the radiation properties of nondiffractive devices, such as Bessel-beam launchers, that can accurately be described through the leaky-wave paradigm. Additional information on their working principles, design, and applications will be presented at the conference.

References

[1] E. Negri, W. Fuscaldo, P. Burghignoli, and A. Galli, "A leaky-wave analysis of resonant Bessel-beam launchers: Design criteria, practical examples, and potential applications at microwave and millimeter-wave frequencies," *Micromachines*, vol. 13, no. 12, p. 2230, Dec. 2022.

[2] D. Comite, W. Fuscaldo, S. K. Podilchak, P. D. Hílario-Re, V. Gómez-Guillamón Buendía, P. Burghignoli, P. Baccarelli, and A. Galli, "Radially periodic leaky-wave antenna for Bessel beam generation over a wide-frequency range," *IEEE Trans. Antennas Propag.*, vol. 66, no. 6, pp. 2828–2843, Jun. 2018.

Ultrafast Electron and Phonon Dynamics in Metasurface-Driven Photocatalysis

Alessandro Alabastri[1,2]

[1]Department of Electrical and Computer Engineering, Rice University, USA
[2]Smalley-Curl Institute, Rice University, USA
*corresponding author: alabastri@rice.edu

Abstract: We discuss recent advances in ultrafast electron and phonon dynamics modeling in nanophotonic systems. In particular, we describe the spatio-temporal evolution of plasmon-induced hot-carrier dynamics, demonstrate efficient energy funneling with dielectric metasurfaces, and uncover fundamental phenomena such as electron-phonon temperature inversion under pulsed illumination.

Predictive modeling of ultrafast dynamics in plasmonic nanostructures is critical for enhancing photocatalytic efficiency. We recently developed the Generalized Extended Two-Temperature Model (GE2TM), a comprehensive framework capable of describing energy transfer from plasmonically excited hot carriers to molecular adsorbates at short timescales. The GE2TM provides quantitative insights into how electron excitation dynamics and thermal effects interplay, enabling systematic optimization of reaction rates under pulsed illumination conditions [1].

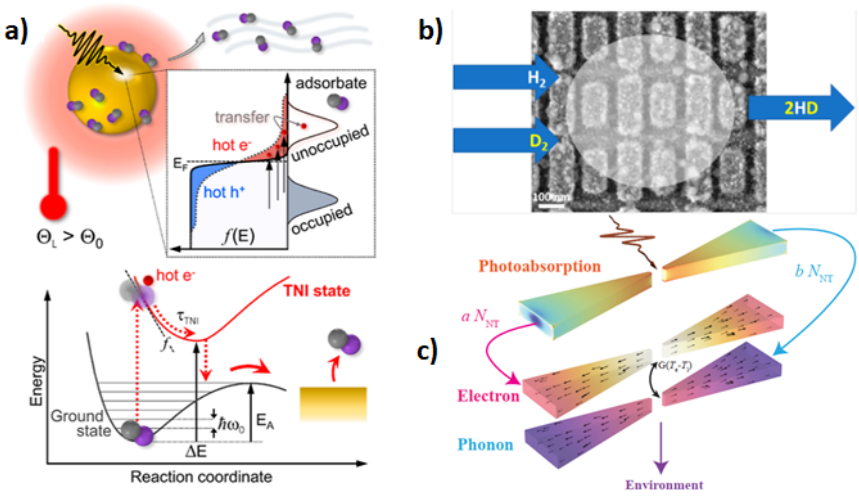

Fig. 1. **a)** Modeling approach for the ultrafast dynamics of plasmonic HCs in the presence of an adsorbate [1]. *Adapted with permission from ACS Nano 2024, 18, 29, 18933–18947. Copyright 2024 American Chemical Society* **b)** Hybrid metallo-dielectric metasurface for photocatalysis [2]. *Adapted from Nano Letters, 24, 1, 172-179. Copyright 2024 American Chemical Society* **c)** Electron-phonon coupling mechanisms in extended nanostructures [3].

However, beyond modeling electronic processes, optimizing overall photocatalytic efficiency critically depends on the effectiveness of funneling photons into active sites. In our recent work, we employed quasi-Bound States in the Continuum (quasi-BIC) dielectric metasurfaces to overcome these challenges, creating highly efficient antenna-reactor systems. These metasurfaces, composed of lossless Si3N4 structures decorated with Ni nanoparticles, concentrate electromagnetic fields and thus enhance photocatalytic reactions significantly. By

precisely engineering photon capture and concentration, these metasurface-based systems complement our hot-carrier injection model by maximizing photon utilization and catalytic efficiency [2].

Finally, by utilizing our modeling scheme, we show intriguing phenomena in ultrafast photothermal dynamics. Our recent predictive simulations reveal the unexpected possibility of sizable electron-phonon temperature inversion—where phonon temperatures transiently exceed electron temperatures—in spatially extended nanostructures under pulsed excitation. This counterintuitive mechanism emerges from complex interactions between electron-phonon coupling and spatial thermal diffusion. Such phenomena, so far explored in thin films, open new pathways to engineer nanostructured systems for controlled energy transfer mechanisms, leveraging this inverted thermal gradient to potentially enhance catalytic processes [3].

This integrated research approach—spanning predictive hot-carrier modeling, photon funneling optimization, and fundamental energy-transfer phenomena—offers new opportunities to advance the efficiency and selectivity of ultrafast nanophotonic devices.

References:

[1] A. Schirato et al., "Quantifying Ultrafast Energy Transfer from Plasmonic Hot Carriers for Pulsed Photocatalysis on Nanostructures "ACS Nano, 2024.

[2] L. Yuan et al., "A Quasi-Bound States in the Continuum Dielectric Metasurface-Based Antenna−Reactor Photocatalyst" Nano Lett., 2023.

[3] Q. Ye et al., "Electron-Phonon Temperature Inversion in Nanostructures under Pulsed Photoexcitation" J. Phys. Chem., 2024.

In-Situ Physical Adjoint Computing

Tsampikos Kottos[1,*], John Guillamon[1], Cheng-Zhen Wang[1], Zin Lin[2]

[1]Wave Transport in Complex Systems Lab, Department of Physics, Wesleyan University, Middletown, CT-06459, USA

[2]Bradley Department of Electrical and Computer Engineering, Virginia Tech, Blacksburg, VA-24060, USA

*Corresponding author: tkottos@wesleyan.edu

***Abstract*—We show real-time wave control in complex multi-resonant environments using time- and energy- efficient adjoint optimization. By exploiting multipath scattering, small in-situ perturbations are amplified, enabling targeted channel emission, coherent perfect absorption and camouflage. Our approach is applicable to in-door wireless technologies, imaging, power electronic and optical neural networks.**

***Keywords*— Adjoint Optimization, in-situ computation, wave control.**

I. Introduction

We experimentally demonstrate an in-situ Physical Adjoint Computing (i-PAC) for a variety of optimization modalities that leverages adjoint sensitivity analysis to control and harness complex wave dynamics. The computing protocol is built around three components: in-situ measurements, targeted perturbations, and an external control mechanism, which collectively enable the real-time optimization of wave networks through two sequential field propagations -- forward and adjoint. First, local probes are employed to measure both the forward and adjoint wave fields at specific elements within the system. Forward propagation is utilized to compute a desired merit (or cost) function and to determine the excitation profile required for the subsequent adjoint propagation. The adjoint field, in turn, provides a comprehensive and simultaneous measurement of all targeted sensitivities. An external control mechanism evaluates these sensitivities to identify the potential perturbations which could enhance (or diminish) the merit (cost) function. These adjustments are then delivered by local actuators to the targeted components (i.e., the tunable degrees of freedom of the system). The cycle is repeated as many times as necessary to maximize (minimize) the merit (cost) function. To demonstrate the versatility of our protocol we showcase three different modalities, namely, targeted channel emission, coherent perfect absorption, and camouflaging, using a microwave experimental platform. The latter consists of a network of coupled coaxial microwave cables whose wave transport demonstrates features characterizing wave chaotic systems. These networks are frequently used as models for mesoscopic quantum transport, sound propagation, and electromagnetic wave behavior in complex interconnected structures such as buildings, ships, and aircrafts and therefore constitute a simple and versatile platform for experimentally implementing our in-situ optimization protocol.

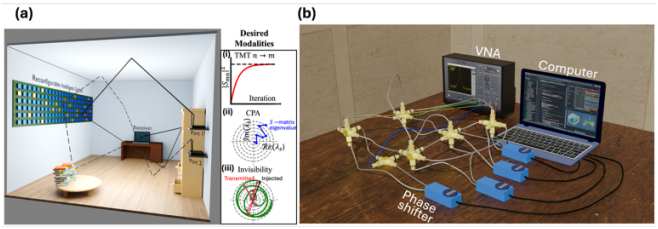

Figure 1: (a) An example of wireless communications in an in-doors complex electromagnetic environment which utilizes an in-situ Physical Adjoint Computing (i-PAC) based on RIS for a variety of modalities: (i)Targeted Mode Transport; (ii)Coherent Perfect Absorption; (iii) Invisibility. (b)The experimental proof-of-principle platform that we have used to demonstrate the i-PAC. It consists of a complex network of coaxial cables. The protocol used as control parameters, the relative amplitudes and phases of injected waves (which were controlled by a VNA), and a targeted set of coaxial cables of the network whose electrical lengths were digitally controlled using phase-shifters

Acknowledgments

This work was partially supported by DOE DE-SC0024223, Simons Foundation (SFI-MPS-EWP-00008530-08) and MURI ONR-N00014241254.

References

[1] J. Guillamon, C-Z Wang, Z. Lin, T. Kottos, "In-situ physical adjoint computing in multiple-scattering electromagnetic environments for wave control," Nature Communications, vol. 16, pp. 11466, 2025.

Artificial fractal network of silicon nanowires for imaging and sensing

Maria Josè Lo Faro[1,*], Antonio Alessio Leonardi[2], Maurilio Galletta[3], Barbara Fazio[3], Francesco Priolo[1], Alessia Irrera[3]

[1] Department of Physics and Astronomy, University of Catania, Via Santa Sofia 64, 95123 Catania, Italy
[2] Department of Chemical, Biological, Pharmaceutical and Environmental Sciences, University of Messina, Viale F. Stagno D'Alcontres 31, 98158 Messina, Italy
[3] CNR IMM Institute for Microelectronics and Microsystems National Research Council, Viale F. Stagno D'Alcontres 31, 98158 Messina, Italy
*Corresponding author: mariajose.lofaro@dfa.unict.it

Abstract **Artificial fractal silicon nanowire networks enable strong light scattering, photoluminescence, and coherent Raman beaming for imaging and sensing. Fourier imaging reveals diffusion and localization lengths. Complementary fractal silver dendrites provide efficient surface enhanced Raman sensing of biomolecules in compact silicon compatible photonic platforms.**
Keywords**— silicon nanowires, fractals, light scattering, Raman spectroscopy, sensing.**

I. Introduction

Disorder in photonic materials is no longer regarded as a detrimental condition for light propagation, but as a powerful design parameter enabling unconventional optical functionalities [1]. Between perfect periodicity and uncorrelated randomness lies a class of engineered disordered systems where structural correlations govern light transport, localization, and emission. Two-dimensional disordered platforms are particularly effective because in-plane multiple scattering combined with out-of-plane leakage enables efficient coupling between free space radiation and quasi-guided optical modes [2,3]. In this framework, fractal disorder represents an extreme case of correlated randomness, where refractive index fluctuations occur on all length scales, promoting broadband light trapping, localization effects, and enhanced light–matter interaction. Fractal arrays of silicon nanowires fabricated by metal-assisted chemical etching represent an ideal realization of this concept, combining industrial compatibility, extreme surface-to-volume ratio, and tunable morphology with remarkable optical properties.

II. Methods

Two-dimensional random fractal arrays of vertically aligned silicon nanowires are fabricated starting from commercial silicon wafers by thin-film metal-assisted chemical etching [4] as shown in Fig. 1.

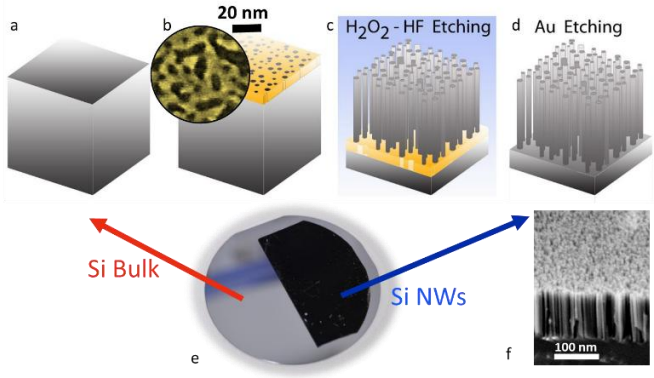

Fig. 1 Scheme of the thin-film metal-assisted chemical etching of Si NWs (a-d). Photo of a Si wafer before and after the Si NWs synthesis (e). Scanning electron microscopy of vertically aligned fractal Si NWs array.

A discontinuous gold layer of about 2 nm acts as catalyst in an HF and hydrogen peroxide solution, enabling a maskless and low-cost process compatible with silicon technology (Fig.1 b). This approach produces ultrathin quantum confined nanowires (NWs) with an average diameter of about 7 nm, lengths tunable from hundreds of nanometers up to several micrometers, and densities reaching 10^{11}–10^{12} nanowires/cm^2 [5]. Optical investigation combines real-space microscopy, Fourier imaging, Raman and photoluminescence spectroscopy, and coherent backscattering measurements to probe light transport within the fractal network [6,7].

III. Results and Discussion

The fractal morphology of silicon nanowire arrays induces strong in-plane multiple scattering correlated with refractive index fluctuations on all length scales. These structures exhibit extremely low reflectance, reaching values as low as 0.1% when the wavelength matches the heterogeneity scale (lacunarity) of the network (Fig. 2 a-c). This behavior is

accompanied by enhanced Raman scattering and bright room-temperature photoluminescence.

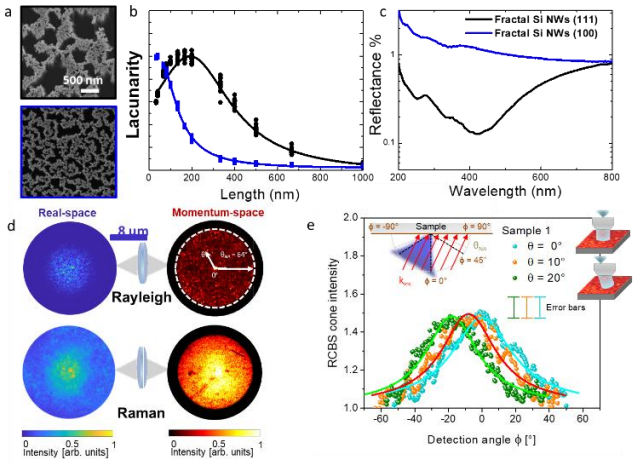

Fig. 2 a SEM images of two fractal morphologies. Lacunarity (b) and reflectance (c) dependence showing strong light trapping for both sample over and extended range. Real-space and momentum-space visualization of light transport in fractal silicon nanowire networks and corresponding Fourier-space distributions revealing isotropic Rayleigh scattering and directional Raman beaming (d). Raman coherent backscattering cone for different incidence angles, demonstrating weak localization and phase-coherent multiple scattering in the disordered fractal network [5–7].

Within these media, coherent backscattering of inelastic Raman radiation has been experimentally observed (Fig. 2). Real-space and Fourier imaging enable the direct visualization of Rayleigh scattering, photoluminescence, and weakly localized Raman light. From the spatial profiles of these signals, diffusion and localization lengths are extracted, and a clear out-of-plane directional beaming of Raman light is observed [7].
The control of optical response through fractal morphology is further demonstrated by decorating the Si NWs arrays with erbium-doped yttrium oxide, tuning the fractal coverage and morphology and enhancing the erbium emission at 560 nm of 2 orders of magnitude for telecom applications [8]. The same ultrathin fractal silicon nanowire arrays have demonstrated a maximum specific capacitance of 274.2 µF cm^{-2} at 50 mV s^{-1} and a stable value of about 180 µF cm^{-2} for scan rates above 200 mV s^{-1} when used as lithium battery anodes, confirming the role of fractal morphology and extreme nanowire density in maximizing the electrochemically active surface area [9].

Silicon nanowire fractal platform also enables optical biosensing based on its room-temperature light emission due to quantum confinement and strong light–matter interaction, allowing detection of SARS-CoV-2 and its Omicron variant with a limit of detection of 4 copies without genome amplification [10].

A complementary fractal platform is provided by silver dendrites that spontaneously form during the metal-assisted chemical etching process. These dendritic structures enable highly efficient surface-enhanced Raman scattering with enhancement factors on the order of 10^6 for biomolecule detection in hydration conditions [11].

IV. Conclusion

Engineered fractal disorder in silicon nanowire networks enables strong light trapping, coherent Raman phenomena, controllable optical emission, and highly sensitive optical sensing in silicon-compatible platforms, bridging fundamental light transport physics with practical imaging and biosensing technologies.

Acknowledgment

UNCT acknowledges BraIn aNd GuT: from olivE mill waste water to the delivery of natuRal substAnCes targeting metabolic syndrome related to cogniTIVE impairment (INTERACTIVE)'—Linea di Intervento 1-Progetti di Ricerca Collaborativa del 'PIAno di inCEntivi per la RIcerca di Ateneo' 2024/2026 Università di Catania and by Linea Open Access. CNR-IMM of Messina acknowledges the Italian Project PNNR "I-PHOQS─Integrated Infrastructure Initiative in Photonic and Quantum Science CUP B53C22001750006." The Prin 2022X29985─FAN-SECARS, FrActal Nanostructures Surface-Enhanced Coherent Anti-Stokes Raman Scattering at ultimate sensitivity for next-generation biochemical sensing CUP B53D23005320006 project, is acknowledged.

References

[1] D. S. Wiersma, "Disordered photonics," Nature Photonics, vol. 7, pp. 188–196, 2013.
[2] K. Vynck, M. Burresi, F. Riboli, and D. S. Wiersma, "Photon management in two-dimensional disordered media," Nature Materials, vol. 11, pp. 1017–1022, 2012.
[3] M. D. Kelzenberg et al., "Enhanced absorption and carrier collection in Si wire arrays for photovoltaic applications," Nature Materials, vol. 9, pp. 239–244, 2010.
[4] S. Yu et al., "Engineered disorder in photonics", Nature Reviews Materials, vol. 6, pp. 226–243, 2020.
[5] B. Fazio et al., "Strongly enhanced light trapping in a two-dimensional silicon nanowire random fractal array," Light: Science & Applications, vol. 5, e16062, 2016.
[6] B. Fazio et al., "Coherent backscattering of Raman light," Nature Photonics, 2017, doi:10.1038/nphoton.2016.278.
[7] M. J. Lo Faro et al., "Visualization of directional beaming of weakly localized Raman from a random network of silicon nanowires," Advanced Science, vol. 8, 2100139, 2021.
[8] M. J. Lo Faro et al., "Erbium emission in Er:Y2O3 decorated fractal arrays of silicon nanowires," Scientific Reports, vol. 10, 12854, 2020.
[9] A. A. Leonardi et al., "SARS-CoV-2 and Omicron variant detection with a high selectivity, sensitivity, and low-cost silicon bio-nanosensor," Nano Select, vol. 4, pp. 160–169, 2023.
[10] A. A. Leonardi et al., "2D fractal arrays of ultrathin silicon nanowires as cost-effective and high-performance substrate for supercapacitors," Advanced Energy and Sustainability Research, vol. 5, 2400080, 2024.
[11] M. J. Lo Faro et al., "Fractal silver dendrites as 3D SERS platform for highly sensitive detection of biomolecules in hydration conditions," Nanomaterials, vol. 9, 1630, 2019.

Atomic-scale Investigation of Energy Conversion in a Single Molecule

Miyabi Imai-Imada[1,2*]

[1]Department of Physics, Institute of Science Tokyo, Japan
[2] RIKEN, Cluster for Pioneering Research (CPR), Japan
*Corresponding author: miyabi@riken.jp

***Abstract*— In this study, we use scanning tunnelling microscopy with plasmonic excitation to image photocurrent through molecular orbitals of a single free-base phthalocyanine. Bias-dependent, counter-flowing channels and competition with photoluminescence are observed, demonstrating controllable relaxation pathways and tunable energy-conversion efficiency via atomic-scale coupling engineering strategies.**

***Keywords*— single molecule, scanning tunneling microscope, energy conversion, photocurrent.**

I. Introduction

Photoinduced electron transfer (PET) plays a decisive role in various energy conversion processes, including photocurrent generation photocatalysis and photosynthesis. To deepen understanding of PET by correlating its efficiency with the local morphology of molecules, much effort has been devoted to developing microscopic techniques for photocurrent measurements. However, the spatial resolution in the previous studies has been still not enough to resolve individual molecules, and the fundamentals of the PET have remained elusive.

II. Methods

In this presentation, we report atomic-scale visualization of photocurrent channels through the molecular orbitals of a single free-base phthalocyanine (FBPc) molecule using a scanning tunnelling microscope (STM) combined with a tuneable laser[1,2]. The experimental setup was carefully designed to optimize the efficiency of molecular excitation. The excitation laser energy is tuneable to the single-molecule absorption resonance with μeV precision. Moreover, the field of the laser light is strongly enhanced in the plasmonic nanogap that consists of a noble-metal tip and a substrate. As a sample we used isolated FBPc molecules adsorbed on a 4-monolayer (ML) NaCl(100) film grown on the Ag(111) substrate. The NaCl film was used to decouple the molecule from the metal substrate and to maintain the intrinsic optical properties of the molecule.

III. Results and Discussion

PET from a single FBPc molecule in the first excited state was distinctly detected as the photoinduced tunnelling current through the STM tip. Depending on the applied bias voltage, not only the direction but also the spatial distribution of the photocurrent drastically changes. The atomically resolved photocurrent maps allowed us to discover counterflowing multiple photocurrent channels, existing even at the voltage where the averaged photocurrent is almost zero. Moreover, we found a direct evidence of competition between PET and photoluminescence (PL) and demonstrated the controllability of their branching ratio during energy relaxation by three-dimensional positioning of the STM tip with atomic precision.

IV. Conclusion

Our findings present that selective promotion and suppression of a specific photocurrent channel is possible by tuning the coupling between the molecular orbitals and wavefunction of metals, which provides a new perspective for improving the energy conversion efficiency by atomic-scale electronic and geometric engineering of molecular interfaces.

Acknowledgments

This work was financially supported in part by JST PRESTO and by Japan Society for the Promotion of Science (JSPS) KAKENHI.

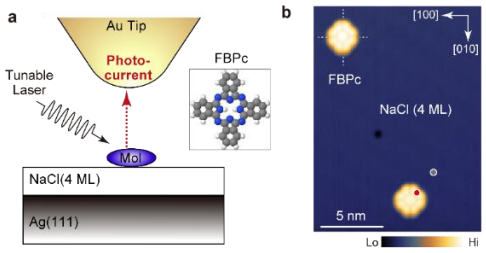

Fig. 1 a. Schematic illustration of Photon-STM.
b. An STM image of the FBPc/NaCl(4-ML)/Ag(111).

References

[1] H. Imada, M. Imai-Imada et al.," Single-molecule laser nanospectroscopy with micro–electron volt energy resolution," Science **373**, 95-98 (2021).
[2] M. Imai-Imada, H. Imada, et al., "Orbital-resolved visualization of single-molecule photocurrent channels," Nature **603**, 829-834 (2022).

Electromagnetic Inverse Scattering Problems for Imaging, Sensing and Communications

AES 2026 · Catania, Italy · ISSN 2491-2417

Handheld millimeter-wave scanner enabled by freehand imaging: acquisition design

Guillermo Alvarez-Narciandi[1,*], Maria Garcia-Fernandez[1], Jaime Laviada[1], Fernando Las-Heras[1]

[1]Group of Signal Theory and Communications, University of Oviedo, Spain
*Corresponding author: alvareznguillermo@uniovi.es

***Abstract*—Freehand radar systems offer fast high-resolution imaging capabilities by moving a compact radar-on-chip module by hand over the area under inspection. In particular, this work focuses on assessing the impact of positioning errors, irregular trajectories and limited survey speed on the imaging quality.**

***Keywords*— radar, freehand imaging, handheld scanner, millimeter-wave imaging.**

I. Introduction

Millimeter-wave (mmWave) imaging enables the retrieval of images from targets covered and also embedded within certain optically-opaque materials. Thus, mmWave imaging systems are of great interest in different fields such as personnel screening and defense [1], [2], medical imaging [3], or non-destructive evaluation [4] to name a few. To obtain high-resolution capabilities, a large physical aperture comprising many transmitting (TX) and receiving (RX) elements can be used or, alternatively, a reduced number of them can be moved across the inspected scene, artificially synthesizing a large aperture. The latter approach, which relies on synthetic aperture radar (SAR) techniques, can be leveraged to build portable mmWave scanners, which are compact by design. In particular, freehand imaging systems, which are based on moving a compact radar module by hand acquiring measurements while its position is tracked, have been recently proposed to enable handheld high-resolution mmWave scanners [5].

Compared to fixed or mechanically moved imaging systems, freehand imaging requires simpler infrastructure and lower hardware complexity, and offers great flexibility to scan the regions of interest. On the other hand, portable mmWave imaging systems face several challenges that must be overcome to enable the retrieval of fast, high-resolution images, namely positioning errors, nonuniform acquisition distributions, and limited survey speed to acquire enough measurements to reconstruct the scene under inspection. This work analyses the impact of these factors on the performance of a freehand imaging system.

II. System description

This study considers the specifications of the compact radar module used in [6], which is shown in Fig. 1(b). It comprises 20 TXs and 20 RXs arranged in an *L*-configuration, which yield a total of 400 independent radiofrequency channels. The time required to perform a full acquisition is 200 ms, and the bandwidth from the radar ranges from 62 GHz to 69 GHz.

The considered scanning procedure resembles a freehand acquisition. Thus, it consists of moving the radar module describing a zig-zag pattern over the scene under inspection. Ideally, the radar module would describe a regular grid. Although in practice this is not the case, as the radar is moved by hand by an operator, the ideal trajectory will by used as reference. In the following section, the aforementioned parameters are used to synthesize radar data considering various survey speeds, positioning errors and for different degrees of nonuniformity of the acquisitions to study their impact on the image reconstruction performance. Measurement results supporting this analysis will be provided at the conference.

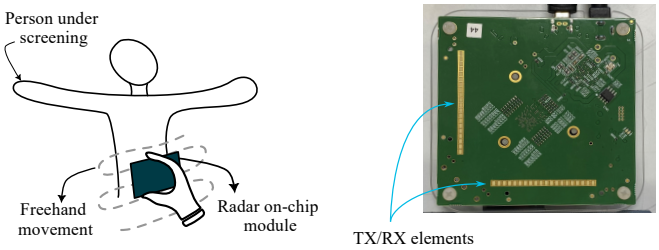

Fig. 1. (a) Scheme of a freehand imaging system and (b) picture of the considered mmWave radar module.

III. Imaging results

A test target consisting of two metallic stripes of 1 cm × 6 cm with a 3 cm spacing between their centers, and placed at 7 cm from the scanning plane is used. In addition, to obtain a reference result, a positioning accuracy of 0.2 mm, i.e., approximately $\lambda/20$ is considered. This accuracy is in agreement with that achieved with motion capture systems employed in some freehand imaging systems.

Positioning errors have been generated as independent Gaussian distributions for each movement axis. Furthermore, the deviation from the ideal trajectory (due to the movement by hand) has been stochastically modelled as a random walk (with a mean deviation from the ideal grid of μ_{dev}). The ideal regular trajectory consisting of an acquisition grid of 16 cm × 16 cm, and the actual scanning path of the reference result are depicted in Fig. 2(a). The image obtained with this configuration, which assumed $\mu_{dev} = 1$ cm, a movement speed

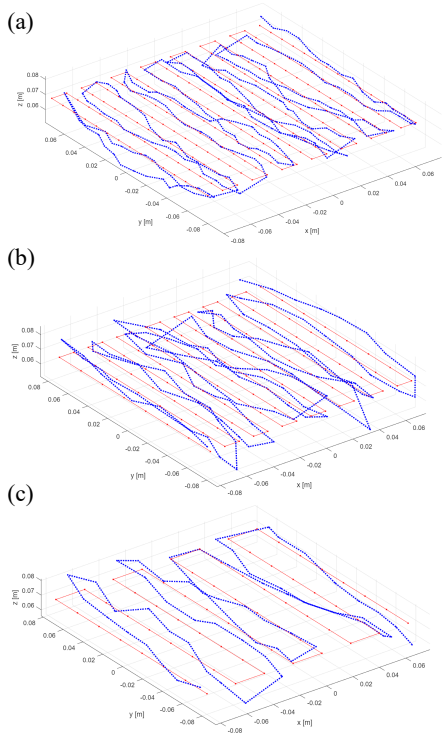

Fig. 2. Actual paths of the handheld scanner (blue line) and ideal regular grid of measurement positions (red) for (a) $v_{sc} = 5.5\,\text{cm/s}$, $d_x = 1\,\text{cm}$ and $\mu_{dev} = 1\,\text{cm}$, (b) $v_{sc} = 12.5\,\text{cm/s}$, $d_x = 1\,\text{cm}$ and $\mu_{dev} = 2\,\text{cm}$, and (c) $v_{sc} = 12.5\,\text{cm/s}$, $d_x = 2\,\text{cm}$ and $\mu_{dev} = 2\,\text{cm}$.

of the radar of $v_{sc} = 5.5\,\text{cm/s}$, and a spacing between along-track lines of $d_x = 1\,\text{cm}$, is depicted in Fig. 3(a). As can be observed, both targets are accurately reconstructed. If the movement speed is increased to $v_{sc} = 12.5\,\text{cm/s}$, reducing by more than half the acquisition time, the quality of the obtained image is still high (Fig. 3(b)). Towards decreasing the acquisition time, the spacing between along-track lines was increased to $d_x = 2\,\text{cm}$, i.e., $\sim 5\lambda$ (Fig. 3(c)). In this case, the clutter level of the image grows significantly, but the targets can still be detected.

The same experiments were conducted for a larger mean deviation from the ideal grid: $\mu_{dev} = 2\,\text{cm}$. The radar paths with larger deviations from the ideal path are depicted in Fig. 2(b) and 2(c), for $v_{sc} = 12.5\,\text{cm/s}$ and $d_x = 1\,\text{cm}$ and for $v_{sc} = 12.5\,\text{cm/s}$ and $d_x = 2\,\text{cm}$, respectively. The results are depicted in Figs. 3(d)-(f). As can be observed, for $v_{sc} = 12.5\,\text{cm/s}$ and $d_x = 1\,\text{cm}$, the targets can still be reconstructed. However, if the spacing between along-track sweeps is further increased the scene cannot be accurately imaged.

IV. Conclusion

We have studied the impact of increasing the movement speed of a freehand scanner on its imaging capabilities, as well as the spacing between along-track sweeps in the presence of tracking errors and position deviations from an ideal scanning

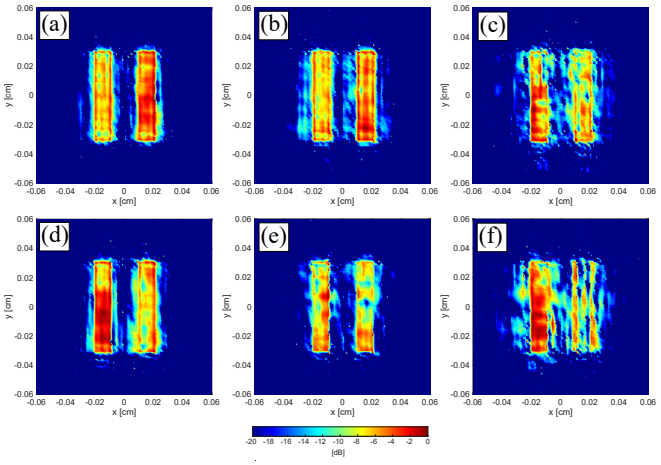

Fig. 3. Imaging results for $\mu_{dev} = 1\,\text{cm}$ and (a) $v_{sc} = 5.5\,\text{cm/s}$ and $d_x = 1\,\text{cm}$, (b) $v_{sc} = 12.5\,\text{cm/s}$ and $d_x = 1\,\text{cm}$ and (c) $v_{sc} = 12.5\,\text{cm/s}$ and $d_x = 2\,\text{cm}$. Imaging results for $\mu_{dev} = 2\,\text{cm}$ and (d) $v_{sc} = 5.5\,\text{cm/s}$ and $d_x = 1\,\text{cm}$, (e) $v_{sc} = 12.5\,\text{cm/s}$ and $d_x = 1\,\text{cm}$ and (f) $v_{sc} = 12.5\,\text{cm/s}$ and $d_x = 2\,\text{cm}$.

trajectory. Results show that the movement speed and spacing between sweeps that provide good imaging capabilities are limited by the extent of the deviations from the ideal scanning path. In particular, for a mean deviation of 1 cm, the survey speed of the freehand system can be twice as high when the mean deviation is 2 cm.

Acknowledgments

This work has been supported by MICIU/AEI/10.13039/501100011033, ESF+ and ERDF/EU, under grants PID2024-160008OA-I00, RYC2023-043020-I, and RYC2023-045010-I, and by Government of Asturias-Sekuens/FEDER under grant IDE-2024-000693.

References

[1] S. S. Ahmed, A. Schiessl, and L. P. Schmidt, "A novel fully electronic active real-time imager based on a planar multistatic sparse array," *IEEE Trans. Microw. Theory Techn.*, vol. 59, no. 12, pp. 3567–3576, Dec 2011.

[2] M. García-Fernádez, G. Álvarez Narciandi, J. Laviada, Y. Álvarez López, and F. Las-Heras, "Towards real-time processing for UAVmounted GPR-SAR imaging systems," *ISPRS Journal of Photogrammetry and Remote Sensing*, vol. 212, pp. 1–12, 2024.

[3] M. Ambrosanio, M. T. Bevacqua, J. LoVetri, V. Pascazio and T. Isernia, "In-Vivo Electrical Properties Estimation of Biological Tissues by Means of a Multi-Step Microwave Tomography Approach," *IEEE Transactions on Medical Imaging*, vol. 43, no. 5, pp. 1983-1994, May 2024.

[4] W. Cheng, H.-H. Sun, K. H. Tan, and Z. Fan, "Early Detection of Corrosion Damage in Reinforced Concrete Using GPR Array Imaging Method," *IEEE Transactions on Instrumentation and Measurement*, vol. 73, pp. 1–9, 2024.

[5] G. Álvarez Narciandi, M. López-Portugués, F. Las-Heras, and J. Laviada, "Freehand, agile, and high-resolution imaging with compact mmwave radar," *IEEE Access*, vol. 7, pp. 95 516–95 526, 2019.

[6] G. Álvarez Narciandi, J. Laviada, and F. Las-Heras, "Short-time coherent–incoherent synthetic aperture radar processing for a handheld imaging system," *IEEE Transactions on Instrumentation and Measurement*, vol. 73, pp. 1–9, 2024.

On the usage of 1D Dynamic Metasurface Antennas for 3D Computational Radar Imaging

Maria Garcia-Fernandez[1,*], Guillermo Alvarez-Narciandi[1], Okan Yurduseven[2]

[1]Group of Signal Theory and Communications, University of Oviedo, Spain
[2]Centre for Wireless Innovation, Queen's University Belfast, United Kingdom
*Corresponding author: garciafmaria@uniovi.es

***Abstract*—This contribution explores the usage of 1D single-fed Dynamic Metasurface Antennas (DMAs) for 3D Computational Microwave Imaging (CMI). Whilst recent works have focused on the Mills-Cross arrangement, in this case the linear motion of the antennas is exploited to generate a 2D aperture.**

***Keywords*— radar, computational imaging, reconfigurable metasurfaces, dynamic metasurface antennas.**

I. Introduction

Synthetic Aperture Radar (SAR) systems have been widely used to generate 2D and 3D high-resolution radar images across various application fields [1]. Such high-resolution is usually achieved by mechanically moving a set of transmitting and receiving antennas in order to synthesize a large aperture. To overcome the need of acquiring a large number of measurements as well as increasing the acquisition speed, Computational Microwave Imaging (CMI) offers a relevant alternative [2].

CMI systems illuminate the scene under inspection with a set of spatially diverse patterns, hence encoding the scene information into a reduced number of measurements. For this purpose, metasurface-based antennas are usually employed. Furthermore, two main working principles are considered to generate such spatially diverse patterns: frequency diversity [3] and dynamic reconfiguration [4], [5]. Whereas frequency-diverse antennas radiate distinct patterns as a function of frequency, Dynamic Metasurface Antennas (DMAs) can generate diverse patterns by reconfiguring the states of the tuning elements (e.g., PIN diodes) that drive the unit cells populating the metasurface aperture.

DMAs offer greater flexibility, at the expense of more complicated designs (due to the need of biasing and control circuits). In the majority of designs each tuning element is independently controlled, which helps to increase the diversity of the radiation patterns. Hence, the complexity markedly grows when 2D DMAs are considered, as they involve a large number of tuning elements.

In order to retrieve 3D radar images, a 2D aperture is required. To alleviate the hardware complexity, this 2D aperture can be generated with 1D DMAs. In particular, the use of a Mills-Cross arrangement (with two 1D DMAs perpendicular to each other) has gained significant interest as it directly creates a 2D aperture [5], [6]. In this work, an alternative approach relying on parallel-aligned 1D DMAs, which are mechanically moved to synthesize a 2D aperture, is explored. This arrangement ensures a co-polarized operation among the transmitting and receiving DMAs, further facilitating the design.

II. System Description

The reconfigurable CMI system explored in this work, which is depicted in Fig. 1, comprises two single-fed 1D DMAs placed parallel to each other and separated by 3.7 cm. Each DMA is populated with 32 irregularly located unit cells, which are independently tuned with PIN diodes [5]. The operating frequency ranges from 18 to 20 GHz. For each DMA $N_{\text{masks}} = 15$ sets of tuning states of the PIN diodes have been considered, and the electric near-field (NF) has been measured at $N_f = 51$ points. Thus, the number of measurements modes to probe the scene under inspection is $M = N_{\text{masks}}^2 N_f$.

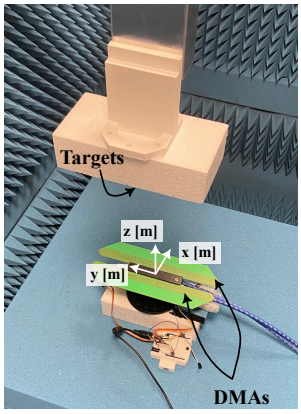

Fig. 1. Reconfigurable CMI system with 1D DMAs in a parallel configuration.

III. Results and Discussion

As the DMAs are placed along the $y-$axis, the proposed arrangement can provide 2D images in the YZ plane and, by moving the DMAs along the $x-$axis, 3D reconstructions are also enabled. To initially assess the imaging capabilities, as well as establishing the appropriate along-track spacing Δx, different scenarios have been simulated (considering the sensing matrix computed from the NF measurements [7], [8]) and the corresponding 3D images are retrieved using a least-squares algorithm.

A scenario with 4 point scatterers located at $x = \pm 2\,\text{cm}$, $y = \pm 2\,\text{cm}$ and $z = 31\,\text{cm}$ has been selected to illustrate the performance of this arrangement. The reconstructed images in the XY plane (at $z = 31\,\text{cm}$) and in the YZ plane (at $x = 0$) are shown in Fig. 2 when only one measurement position is considered (i.e., when the DMAs are static). As expected, the reconstructed image exhibits good resolution in the $y-$ and $z-$axis, whereas the targets appear elongated in the $x-$axis (due to the severely limited resolution across this axis).

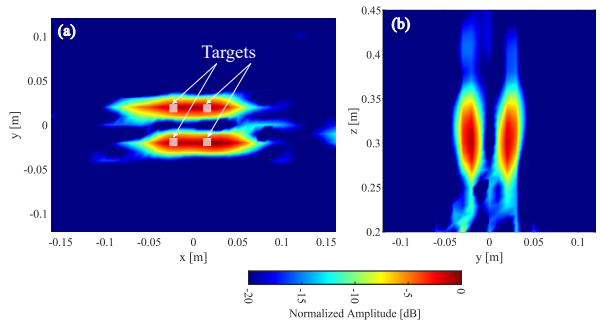

Fig. 2. Reconstructed images at $z = 31\,\text{cm}$ (a) and $x = 0$ (b). The position of the targets in the XY plane is depicted in white in (a).

To achieve good resolution in all imaging axes, the DMAs are moved along the $x-$axis, thus synthesizing a 2D aperture. The reconstructed images in the XY plane (at $z = 31\,\text{cm}$) for different values of the along-track spacing is shown in Fig. 3. As can be observed, with $\Delta x \leq 2\lambda$ (where λ is the wavelength at the maximum frequency, i.e., at 20 GHz) the four targets can be clearly distinguished and the clutter level remains low. For greater values of the along-track spacing, artifacts that can be misidentified as targets start to appear in the reconstructed images.

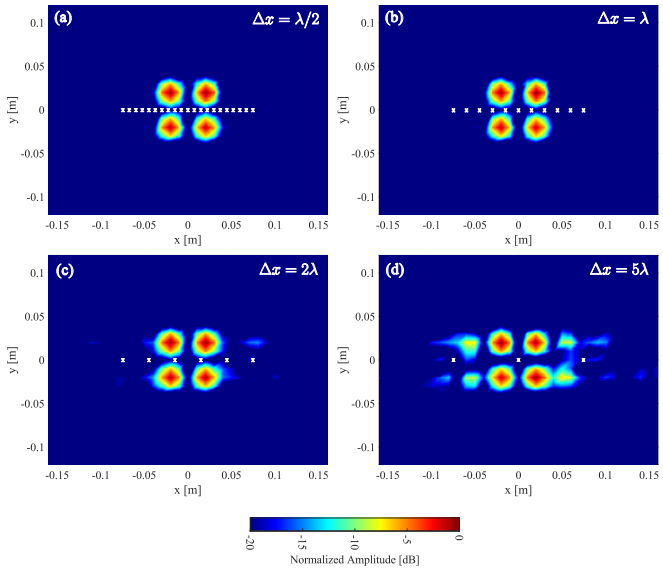

Fig. 3. Reconstructed images at $z = 31\,\text{cm}$ for different values of the along-tracking spacing Δx. The measurement positions are depicted with white $\times$.

IV. Conclusion

This contribution has explored the usage of parallel-aligned 1D DMAs for CMI. This arrangement helps to reduce the design complexity associated to 2D DMAs, at the expense of a severely limited resolution in the horizontal axis perpendicular to the DMAs. Results show that this limitation can be overcome by moving the DMAs along this axis and, furthermore, the along-track spacing required to achieve high resolution is significantly greater (up to 2λ) than that usually considered in SAR imaging systems ($\lambda/2$). Experimental results of this arrangement will be presented at the conference.

Acknowledgments

This work has been supported by MICIU/AEI/10.13039/501100011033, ESF+ and ERDF/EU, under grants PID2024-160008OA-I00, RYC2023-043020-I, and RYC2023-045010-I, and by Government of Asturias-Sekuens/ERDF/EU under grant IDE-2024-000693.

References

[1] D. M. Sheen, D. L. McMakin, and T. E. Hall, "Three-dimensional millimeter-wave imaging for concealed weapon detection," *IEEE Trans. Microw. Theory Techn.*, vol. 49, no. 9, pp. 1581–1592, Sep 2001.

[2] J. Gollub et al., "Large metasurface aperture for millimeter wave computational imaging at the human-scale," *Sci Rep*, vol. 7, no. 42650, 2017.

[3] M. Garcia-Fernandez, G. Alvarez Narciandi, and O. Yurduseven, "Single channel frequency-diverse computational imaging system for through-the-wall sensing," *IEEE Transactions on Geoscience and Remote Sensing*, vol. 62, pp. 1–10, 2024.

[4] A. Diebold, M. Boyarsky, and D. Smith, "A K-band, varactor-tuned dynamic metasurface aperture for microwave computational imaging," in *2023 IEEE Conference on Antenna Measurements and Applications (CAMA)*, 2023, pp. 474–478.

[5] G. Alvarez Narciandi, M. Garcia-Fernandez, V. Skouroliakou, and O. Yurduseven, "Dynamic Metasurface Antenna-based Mills-Cross Aperture for 3D Computational Microwave Imaging," *IEEE Antennas and Wireless Propagation Letters*, pp. 1–5, 2024.

[6] G. Alvarez-Narciandi, M. Garcia-Fernandez, M. Khalily, and O. Yurduseven, "Reconfigurable metasurface antenna-based Mills-Cross compressive aperture for computational microwave imaging," *in 19th European Conference on Antennas and Propagation (EuCAP)*, Stockholm (Sweden), April 2025.

[7] G. Lipworth et al., "Comprehensive simulation platform for a metamaterial imaging system," *Applied Optics*, vol. 54, no. 31, pp. 9343–9353, Nov 2015.

[8] M. Garcia-Fernandez, G. Alvarez-Narciandi, O. Yurduseven, "Efficient PWS-Based Computation of the Sensing Matrix for Computational Radar Imaging Systems," *IEEE Antennas Wireless Propag. Lett.*, 2024.

Assessment of Anatomical Prior Information in the Inversion Kernel for Microwave Brain Imaging

Alex. R. Masaquiza-Caiza, David O. Rodriguez-Duarte, Francesca Vipiana*

Dept. Electronics and Telecommunications, Politecnico di Torino, Torino, Italy
*Corresponding author: francesca.vipiana@polito.it

***Abstract*—This work studies the impact of head anatomy-derived prior information on the imaging kernel of a Truncated Singular Value Decomposition-Based algorithm. Numerical results show that even anatomy-simplified imaging kernels, when no prior information is available, can provide valuable information about the morphological progression of an intracranial hemorrhage.**

***Keywords*— brain stroke monitoring, inverse scattering, microwave imaging, prior information, real-time monitoring.**

I. Introduction

Medical microwave imaging (MMWI) is a diagnostic modality that exploits frequency-dependent dielectric contrast between biological tissues to detect pathophysiological alterations in the internal anatomical structures [1]. One of the applications of MMWI technology is the monitoring of cerebrovascular accidents; whether ischemic, arising from vascular occlusion, or intracranial hemorrhage (ICH), consequent to vessel rupture and extravasation [2]. At microwave frequencies, these alterations create dielectric contrasts that allow the reconstruction of internal tissue profiles. However, independently of the microwave imaging (MWI) inversion algorithm, any mismatch between patient-specific head anatomy and the one assumed in the inversion kernel can introduce modeling errors into the inverse problem formulation, resulting in artifacts and inaccuracies in the reconstructed dielectric profiles. In clinical scenarios, such as post-acute stroke monitoring, scans of head tissues from magnetic resonance imaging (MRI) or computer tomography (CT) are frequently available [3], [4]. These modalities can provide anatomical information about the head tissues to be integrated into the imaging kernel.

In order to study the impact of prior anatomical information on the quality of MWI reconstructions, we conduct a numerical experiment mimicking the temporal progression of an ICH stroke. For the imaging retrieval, we use different inversion kernels with different amounts of anatomical information, from a multi-tissue to a simplified single-tissue head model.

II. Numerical Assessment

A. Simulation Setup

We perform 3-D electromagnetic full-wave simulations to assess how anatomical prior information affects imaging retrieval. The computational model of the head has five tissues: skin, fat, bone, cerebrospinal fluid (CSF), and brain parenchyma (gray and white combined as a single tissue). The MWI system consists of a 24-antenna array, evenly distributed around the upper cranial region, operating at around 1.1 GHz. This system has been previously proposed and validated in [5], [6]. The dielectric properties of each tissue are fixed according to [7], and the ICH stroke is located in the left posterior lobe of the brain. It is modeled as a homogeneous ellipsoidal-like mass of blood that evolves temporally in the transversal body plane from an initial volume of 10 mL to a volume of 30 mL.

B. Differential Microwave Imaging Approach

The employed MWI algorithm maps the differential scattering data ΔS between two consecutive monitoring instants to a dielectric contrast map $\Delta\chi$ using the Born approximation to linearize the scattering problem, and the truncated singular value decomposition (TSVD) to regularize and stabilize the ill-conditioned inversion as:

$$\Delta\chi = \sum_{n=1}^{T} \frac{1}{\sigma_n} \langle \Delta S, u_n \rangle \, v_n, \tag{1}$$

where σ_n, u_n, and v_n are the n-th singular value, right, and left singular vectors, respectively, obtained via the singular value decomposition (SVD) of the discretized kernel. The last is computed using 3-D EM full-wave simulations of the domain of imaging (DoI), i.e., the head tissues. Accordingly, five kernel operators (reference scenarios) are defined to represent realistic clinical cases with limited or absent prior information. These operators are summarized in Table I, the vertical bar symbol (|) denotes the boundaries between different tissues, while the plus sign (+) denotes that multiple tissues are combined into a single tissue whose dielectric properties are taken as the average of the constituent tissues. The kernels are chosen according to the information typically available from CT and MRI. CT scans provide high contrast for bone but poor soft-tissue discrimination, whereas MRI provides strong soft-tissue contrast but less precise bone delineation. This

TABLE I
Inversion kernel operators for the assessment.

Kernel	Reference head model	Prior Information
K1	Skin | Fat | Bone | CSF | Brain	Full prior information
K2	Skin + Fat | Bone | CSF + Brain	Partial prior information
K3	Skin + Fat + Bone | CSF + Brain	Partial prior information
K4	Skin + Fat + Bone + CSF + Brain	No prior information

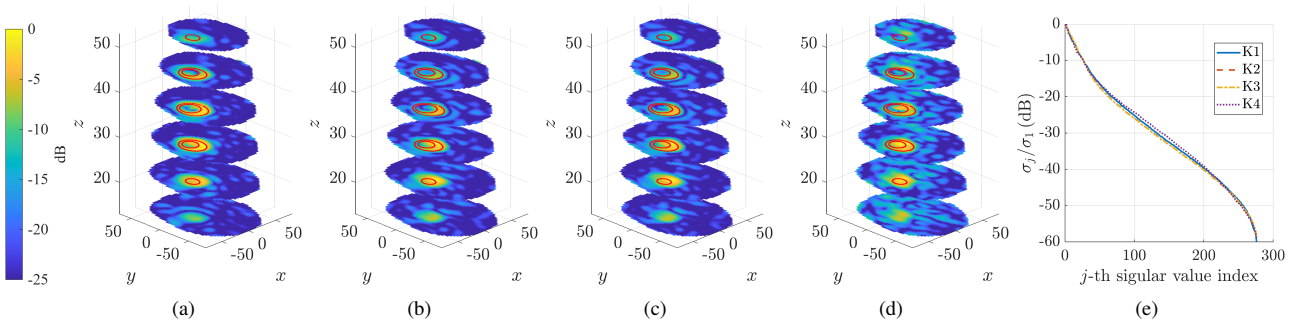

Fig. 1. Normalized transversal slices along the z-axis of the reconstructed ICH evolution using the kernels: (a) K1, (b) K2, (c) K3, and (d) K4, with singular value truncation at –35 dB. Panel (e) shows the singular values of the inversion kernel operators. The red contours in (a)–(d) delineate the ICH boundaries. Dimensions are in mm.

complementary information is then used to model head tissues and construct the inversion kernel operator.

III. Numerical Results

The results of the imaging retrieval are shown in Fig. 1. The red contour lines indicate the stroke boundaries (the inner is the initial 10 mL volume, and the outer is the evolved 30 mL volume). To evaluate the reconstructions performance, we use four metrics: structural similarity index (SSIM) [8], dice similarity coefficient (DSC) [9], a size-based metric (S-BM) and a boundary-based metric (B-BM), both proposed in [10]. To compute these metrics, we compare a binary ground-truth volume with a binarized version of the reconstructed map where all values above -5 dB are set to 1 and 0 otherwise. Fig. 2 presents the performance metrics for the different inversion kernels. It is worth noticing that the simplified kernels (K2, K3, K4) achieve comparable performance with respect to the baseline case. It confirms that even approximate models can provide valuable information on stroke monitoring.

IV. Conclusion

This work investigates the impact of anatomical prior information on the imaging retrieval for brain stroke monitoring. Four inversion kernel operators are quantitatively evaluated using multiple performance metrics. The results demonstrate that both a highly simplified head model (homogeneous head) and a simplified model that maintains bone boundaries have good performance for brain stroke monitoring. These findings are clinically significant, considering that the patient-specific information in clinical scenarios is often limited or unavailable.

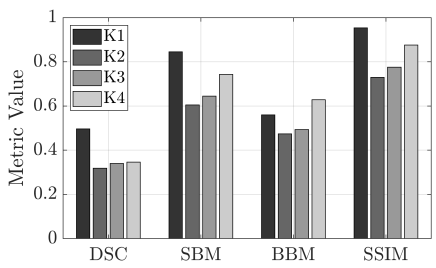

Fig. 2. Imaging performance metrics using the different inversion kernels. All metrics are bounded from 0 (no correspondence) to 1 (perfect correspondence) with the ground truth.

Acknowledgments

This work was supported in part by the EU project "3BAtwin" (GA: 101159623) and by the project "MedWaveImage", funded by Interreg Central Europe (CE0200670).

References

[1] C. Origlia, D. O. Rodriguez-Duarte, J. A. Tobon Vasquez, J.-C. Bolomey, and F. Vipiana, "Review of microwave near-field sensing and imaging devices in medical applications," *Sensors*, vol. 24, no. 14, 2024.

[2] D. Kuriakose and Z. Xiao, "Pathophysiology and treatment of stroke: present status and future perspectives," *International journal of molecular sciences*, vol. 21, no. 20, p. 7609, 2020.

[3] J. J. Nukovic, V. Opancina, E. Ciceri, M. Muto, N. Zdravkovic, A. Altin, P. Altaysoy, R. Kastelic, D. M. Velazquez Mendivil, J. A. Nukovic, N. V. Markovic, M. Opancina, T. Prodanovic, M. Nukovic, J. Kostic, and N. Prodanovic, "Neuroimaging modalities used for ischemic stroke diagnosis and monitoring," *Medicina*, vol. 59, no. 11, 2023.

[4] K. B. Walsh, "Non-invasive sensor technology for prehospital stroke diagnosis: Current status and future directions," *International Journal of Stroke*, vol. 14, no. 6, pp. 592–602, 2019.

[5] D. O. Rodriguez-Duarte, J. A. T. Vasquez, R. Scapaticci, L. Crocco, and F. Vipiana, "Assessing a microwave imaging system for brain stroke monitoring via high fidelity numerical modelling," *IEEE Journal of Electromagnetics, RF and Microwaves in Medicine and Biology*, vol. 5, no. 3, pp. 238–245, 2021.

[6] D. O. Rodriguez-Duarte, C. Origlia, J. A. T. Vasquez, R. Scapaticci, L. Crocco, and F. Vipiana, "Experimental assessment of real-time brain stroke monitoring via a microwave imaging scanner," *IEEE Open Journal of Antennas and Propagation*, vol. 3, pp. 824–835, 2022.

[7] IFAC-CNR, "Dielectric properties of body tissues," Available at: https://niremf.ifac.cnr.it/tissprop/, 2023, accessed: February 2026.

[8] Z. Wang, A. Bovik, H. Sheikh, and E. Simoncelli, "Image quality assessment: from error visibility to structural similarity," *IEEE Transactions on Image Processing*, vol. 13, no. 4, pp. 600–612, 2004.

[9] K. H. Zou, S. K. Warfield, A. Bharatha, C. M. Tempany, M. R. Kaus, S. J. Haker, W. M. Wells III, F. A. Jolesz, and R. Kikinis, "Statistical validation of image segmentation quality based on a spatial overlap index1: scientific reports," *Academic radiology*, vol. 11, no. 2, pp. 178–189, 2004.

[10] F. Xue, L. Guo, A. Bialkowski, and A. M. Abbosh, "Integrated boundary-overlap-size metric for local assessment of deep learning methods in medical microwave imaging," *IEEE Journal of Electromagnetics, RF and Microwaves in Medicine and Biology*, vol. 9, no. 2, pp. 229–239, 2025.

Indirect Holography MIMO Imaging Exploiting Antenna Coupling

Alejandro del Hoyo Vijande[1,*], Yuri Álvarez-López[1], Fernando Las-Heras[1], Jaime Laviada[1]

[1]TSC-Uniovi Research Group, Universidad de Oviedo, Gijón, Spain

*Corresponding author: hoyoalejandro@uniovi.es

***Abstract*—This work proposes a novel holographic multiple-input multiple-output (MIMO) imaging system that exploits antenna coupling to retrieve complex scattered fields from amplitude-only measurements by means of indirect holography techniques. Simulation results show that the quality of the reconstructed images is comparable to that obtained when processing vector field measurements.**

***Keywords*— millimeter-wave imaging, MIMO radar, antenna coupling, phase retrieval, indirect holography.**

I. Introduction

Microwave and millimeter-wave imaging systems can be used in a wide variety of non-destructive inspection applications. Personnel security screening [1], through-the-wall imaging [2], landmine detection systems [3] and medical diagnostics [4] are just a few examples where this type of technology can be applied.

Phaseless imaging techniques [5] allow to retrieve images from intensity-only measurements. This scalar acquisition approach presents several advantages over traditional vector-based methods, such as reduced hardware complexity, lower costs and simplified calibration procedures. Indirect holography [6] comprehends a particular set of iteration-free methods that exploit the interference between a known reference wave and the unknown scattered field to reconstruct the complex electromagnetic field from intensity-only measurements.

This work presents a novel multiple-input multiple-output (MIMO) imaging system that exploits indirect holography techniques using an L-shaped array. The proposed method leverages mutual coupling between the transmitting and receiving antennas to generate the reference wave. By processing the power measurements of the interference pattern, high-resolution images can be generated without the need for direct phase measurements.

II. Method

In indirect holography, the scalar measurements, $I(x,y)$, that are processed to generate the electromagnetic images correspond to power samples of an interference pattern between the scattered field, $E_s(x,y)$, produced by the targets within the region of interest (ROI), and a well-known reference wave, $E_r(x,y)$. Expanding the squared magnitude of the sum of both terms, the following relationship can be reached:

$$\begin{aligned} I(x,y) &= |E_s(x,y)+E_r(x,y)|^2 \\ &= \Big(E_s(x,y)+E_r(x,y)\Big)\Big(E_s^*(x,y)+E_r^*(x,y)\Big) \\ &= |E_s(x,y)|^2+|E_r(x,y)|^2+E_s(x,y)E_r^*(x,y) \\ &\quad + E_s^*(x,y)E_r(x,y)\ . \end{aligned} \tag{1}$$

In the proposed MIMO acquisition approach, the transmitters (Tx) are moved along the y-axis whereas the receivers (Rx) are moved along the x-axis, yielding an L-shaped array whose effective phase centers [7] are equally spaced. All samples are acquired at a fixed distance from the targets, z_0.

By arranging the MIMO measurements into a matrix where index m identifies the Tx antenna and index n corresponds to the Rx antenna, and leveraging the linear properties of the Fourier transform (FT), (1) can be rewritten as follows:

$$\begin{aligned} FT\left\{I[m,n]\right\} &= FT\left\{|E_s[m,n]|^2\right\}+FT\left\{|E_r[m,n]|^2\right\} \\ &\quad + FT\left\{E_s[m,n]\right\}\circledast FT\left\{E_r^*[m,n]\right\} \\ &\quad + FT\left\{E_s^*[m,n]\right\}\circledast FT\left\{E_r[m,n]\right\}\ . \end{aligned} \tag{2}$$

In the proposed approach, we will use an analytical model of the field coupled between the Tx and the Rx at each position as the reference field E_r. In this case, the complex-valued mutual coupling between antennas is exploited as a reference wave, whose expression can be derived analytically provided that the antenna positions are known with sufficient accuracy. It can be verified that the first two terms of (2) are centered at the origin of the plane-wave-like spectrum, while the last two terms are shifted in this transformed domain [6]. As long as the different spectal components do not overlap and the reference wave is well characterized, the complex scattered field can be retieved from amplitude-only measurements through filtering and deconvolution.

III. Simulated Setup

Fig. 1 shows the L-shaped MIMO configuration used in the simulation. A working frequency of 60 GHz was considered, since vector field measurements in this band often require expensive hardware. However, the method can be applied to any other frequency. The distance between the imaging plane and the MIMO array was set to $z_0 = 70\lambda$, where λ is the free-space wavelength at the working frequency.

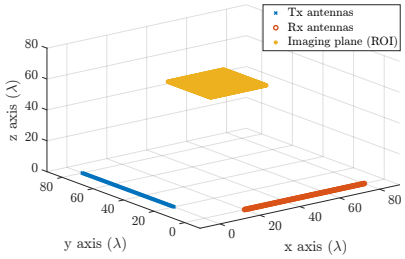

Fig. 1: Imaging setup used in the simulation.

In the simulation, the scattered field was generated by solving the direct propagation problem taking into account the geometry of the MIMO arrray and the reflectivity values of the targets within the ROI. Mutual coupling between the antennas was simulated by means of free-space Green's functions. In this way, every MIMO channel measurement contains both scattered field and reference wave information.

IV. Results and Discussion

The phaseless measurements acquired with the MIMO array are shown in Fig. 2a. The corresponding hologram, obtained by applying a 2D Fourier transform to the measurements, is shown in Fig. 2b. The red circle drawn in this plane-wave-like spectrum indicates the spectral component that was selected to retrieve the scattered field by means of deconvolution with the complex conjugate of the reference wave.

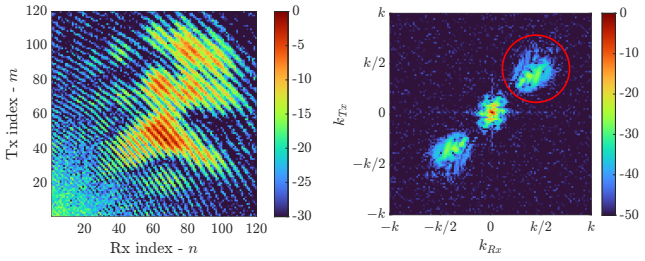

(a) (b)

Fig. 2: Set of scalar measurements acquired by the different channels of the MIMO array (a) and its corresponding phaseless hologram (b).

Fig. 3a shows the geometry of the targets placed within the imaging plane for the simulation (ground truth image). The field scattered by those metallic silhouettes was combined with the antenna coupling to create the interference pattern. Noise was also added to the field measurements to yield a signal-to-noise ratio (SNR) of 10 dB. The reconstructed phaseless image, obtained using backprojection algorithm after the explained holographic method, is shown in Fig. 3b. It represents a complex-valued reflectivity map whose amplitude resembles the shape of the targets. The root mean square error (RMSE) between the reconstructed image and the ground truth is 0.163, which is nearly as low as the RMSE of 0.158 obtained when generating a synthetic aperture radar (SAR) image by processing simulated vector fields.

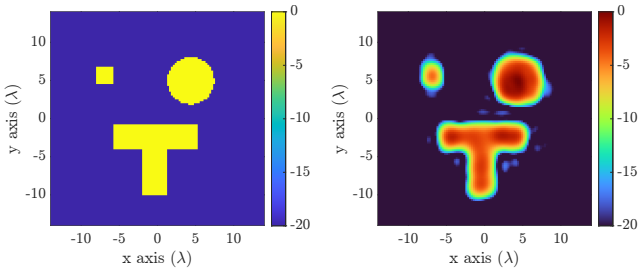

(a) (b)

Fig. 3: 2D metallic targets used for the simulation (a) and phaseless image of the ROI obtained with the proposed method (b). Amplitude values of both reflectivity maps are represented in dB.

V. Conclusion

This work shows how mutual antenna coupling in a MIMO configuration can be exploited to generate electromagnetic images from amplitude-only measurements by means of indirect holography. The antenna coupling in the L-shaped array can be used as a reference wave to retrieve the complex scattered field and generate a SAR image of the ROI. The results show that the quality of the reconstructed image is comparable to that obtained when processing vector fields.

Acknowledgments

This work has been funded by Ministerio de Ciencia e Innovación of the Spanish Government and the Spanish Research Agency under projects "META-IMAGER" PID2021-122697OB-I00 and "EMPOWERED" PID2024-160008OA-I00, and by the Government of Asturias-Sekuens/FEDER under grant GRU-GIC-24-008.

References

[1] D. M. Sheen, D. L. McMakin, and T. E. Hall, "Three-Dimensional Millimeter-Wave Imaging for Concealed Weapon Detection," *IEEE Transactions on Microwave Theory and Techniques*, vol. 49, no. 9, pp. 1581–1592, 2002.

[2] J. Laviada, A. Arboleya, F. López-Gayarre, and F. Las-Heras, "Broadband Synthetic Aperture Scanning System for Three-Dimensional Through-the-Wall Inspection," *IEEE Geoscience and Remote Sensing Letters*, vol. 13, no. 1, pp. 97–101, 2015.

[3] M. G. Fernández, Y. Á. López, A. A. Arboleya, B. G. Valdés, Y. R. Vaqueiro, F. L.-H. Andrés, and A. P. García, "Synthetic Aperture Radar Imaging System for Landmine Detection Using a Ground Penetrating Radar on Board a Unmanned Aerial Vehicle," *IEEE Access*, vol. 6, pp. 45 100–45 112, 2018.

[4] E. J. Bond, X. Li, S. C. Hagness, and B. D. Van Veen, "Microwave Imaging via Space-Time Beamforming for Early Detection of Breast Cancer," *IEEE Transactions on Antennas and Propagation*, vol. 51, no. 8, pp. 1690–1705, 2003.

[5] J. Dong, L. Valzania, A. Maillard, T.-a. Pham, S. Gigan, and M. Unser, "Phase Retrieval: From Computational Imaging to Machine Learning," *IEEE Signal Processing Magazine*, vol. 40, no. 1, pp. 45–57, 2023.

[6] D. Smith, O. Yurduseven, B. Livingstone, and V. Schejbal, "Microwave Imaging Using Indirect Holographic Techniques," *IEEE Antennas and Propagation Magazine*, vol. 56, no. 1, pp. 104–117, 2014.

[7] Z. Wang, Q. Guo, X. Tian, T. Chang, and H.-L. Cui, "Near-Field 3-D Millimeter-Wave Imaging Using MIMO RMA With Range Compensation," *IEEE Transactions on Microwave Theory and Techniques*, vol. 67, no. 3, pp. 1157–1166, 2018.

Point-Like Target Detection and Localization via Phase-Space Back-Projection

Davide Santagata[1,*], Gabriele Gradoni[2] and Raffaele Solimene[1]

[1]Department of Engineering, University of Campania "Luigi Vanvitelli", Aversa, Italy
[2]6G Innovation Centre, Institute for Communication Systems, University of Surrey, Guildford, U.K.
[*]Corresponding author: davide.santagata@unicampania.it

***Abstract*—We introduce a phase-space approach for localization of point-like scatterers using intensity-only, single-frequency measurements. By interpreting intensity along aspect-limited lines as a smoothed Wigner distribution, we obtain tomographic projections that enable linear imaging via inverse Radon transform. Simulations demonstrate accurate and robust reconstruction.**

***Keywords*— phase-space, imaging, inverse scattering, intensity-only measurements, back-projection, Wigner distribution, interference terms, Radon transform, deconvolution, Wiener filter.**

I. Introduction

Electromagnetic scattering phenomena represent a valuable resource, as they can be exploited in non-destructive imaging strategies for target characterization, including detection, localization, and extraction of shape-related information [1, 2].

In a wide range of applications, from defense and remote sensing to subsurface inspection and biomedical imaging [3–6], a critical system-design factor for electromagnetic measurements is the choice of the operating frequency, which directly determines penetration depth, achievable resolution, and hardware feasibility.

In this context, millimeter- and sub-millimeter-wave regimes have attracted increasing interest due to their non-ionizing nature, enabling biologically safe, high-resolution imaging [7–12].

Nonetheless, coherent (amplitude and phase) measurements become increasingly difficult and costly at higher frequencies. While amplitude-and-phase acquisition is feasible in microwave and millimeter-wave systems, obtaining reliable phase data at superior frequencies can be extremely challenging or even impractical. Moreover, even when phase information is available, amplitude measurements generally remain more accurate and robust [13].

These considerations motivate the development of imaging strategies via intensity-only field acquisitions. Such an approach entails an architectural advantage, as it simplifies the measurement setup and improves robustness. However, the inversion procedure from intensity-only data is inherently nonlinear and is typically tackled through iterative algorithms, which aim to minimize non-quadratic cost functions [13, 14]. These algorithms can be computationally intensive and sensitive to initialization, convergence, and modeling errors, especially in the presence of noise [13, 15, 16].

In this context, we propose an alternative framework based on a *phase-space analysis* [17], where representations such as Mark's Physical Spectrum and the Wigner distribution rigorously link far-field intensity measurements (spectrograms) to bilinear space–spatial-frequency descriptions [18, 19].

In our framework, point-like targets embedded in a two-dimensional scenario are illuminated with a single-frequency incident wave. Thus, the objects are modelled as secondary sources.

The scattered field's squared magnitude is recorded over a collection of far-field aspect-limited straight lines. These intensity-only measurements correspond to field spectrogram (i.e., Mark's Physical Spectrum), which represents a smoothed version of the Wigner distribution linked to the scattered field, with a smoothing kernel determined by the intensity-sensor aperture [20].

This interpretation enables a linear inversion strategy based on regularized phase-space deconvolutions, where the Wigner distribution is recovered.

Due to its quadratic nature, the Wigner distribution [19] offers a phase-space description of the scattered field with superior resolution. However, it suffers from interference terms [23–25], which affect the representation. Such a problem is addressed via the implementation of a filter that mitigates such artifacts while maintaining resolution enhancement.

Thus, a cross-term-free Wigner distribution produces a collection of tomographic projections, from which the reconstruction of the scenario is achieved via inverse Radon transform.

In conclusion, this framework enables a linear formulation of the inverse problem from intensity-only data without requiring iterative phase-retrieval procedures, thus overcoming the limitations of standard phase-retrieval approaches. It provides a robust and computationally efficient alternative for high-frequency electromagnetic imaging, promoting the development of new competitive imaging strategies in scenarios where phase information is inaccessible.

To illustrate the main concepts in a simple yet informative setting, we focus on a two-dimensional scalar configuration at a single frequency, involving point objects on a plane and intensity-only scattered-field data collected along aspect limited lines.

The remainder of the paper is organized as follows. Section II introduces the scattering scenario, including the illumination and acquisition strategy, the forward model, and the adopted mathematical conventions. Section III presents the method, describing the deconvolution step, which is inherently ill-posed and regularized using a Wiener filter [6, 13] together with the proposed cross-term suppression filter. Section IV presents numerical results demonstrating the effectiveness of the proposed approach, and conclusions follow.

II. System Model and Preliminaries

We consider the scattering scenario illustrated in Fig. 1, where M point-like objects are embedded in a homogeneous medium within a circular domain

$$D = \left\{ \mathbf{r} \in \mathbb{R}^2 : |\mathbf{r}| \leq d \right\}. \tag{1}$$

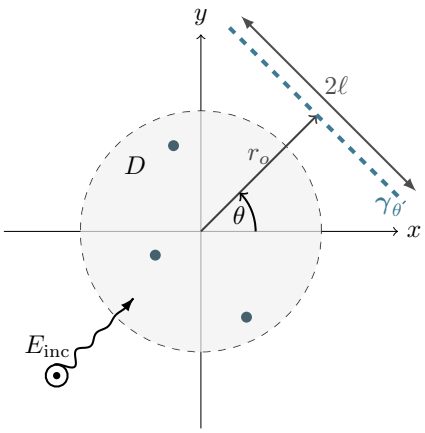

Fig. 1. Scattering scenario considered in this work.

A single-frequency field with wavelength λ ($k = 2\pi/\lambda$) illuminates the targets, producing secondary sources described by the object function

$$\rho(\mathbf{r}) = \sum_{m=0}^{M-1} \tau_m \delta(\mathbf{r} - \mathbf{r}_m), \tag{2}$$

where $\mathbf{r}_m = (x_m, y_m)$ denote the target positions and τ_m their complex scattering coefficients.

Mutual interactions between scatterers are neglected (Born approximation). Under this assumption, the scattered field is given by

$$E_s(\mathbf{r}) = \int_D \mathcal{G}(\mathbf{r} - \mathbf{r}')\, \rho(\mathbf{r}')\, d\mathbf{r}', \tag{3}$$

with the 2D Green's function

$$\mathcal{G}(\mathbf{r} - \mathbf{r}') = \frac{j}{4} H_0^{(2)}\left(k|\mathbf{r} - \mathbf{r}'|\right). \tag{4}$$

The scattered field is observed along segments $\boldsymbol{\gamma}_\theta(\eta)$ at angle θ, with minimum distance r_o from the origin:

$$\boldsymbol{\gamma}_\theta(\eta) = r_o \begin{pmatrix} \cos\theta \\ \sin\theta \end{pmatrix} + \eta \begin{pmatrix} -\sin\theta \\ \cos\theta \end{pmatrix}, \quad -\ell \leq \eta \leq \ell. \tag{5}$$

A sensor [20] moving along γ_θ measures the spectrogram of the local field, namely $\mu_\theta(\eta, k_\eta)$

$$\mu_\theta(\eta, k_\eta) = \left|\mathcal{S}_{E_s}(\eta, k_\eta)\right|^2, \tag{6}$$

where

$$\mathcal{S}_{E_s}(\eta, k_\eta) = \int_{\gamma_\theta} a(\eta' - \eta) E_s(\boldsymbol{\gamma}_\theta(\eta')) e^{jk_\eta \eta'} d\eta' \tag{7}$$

with $a(\eta)$ being the sensor aperture [20].

For further analysis, a rotated Cartesian system (ξ, η) is introduced, with ξ_m and η_m representing the target coordinates in this reference frame.

It is useful to consider the Fourier transform of the field $E_s(\eta, r_o)$ at depth $\xi = r_o$, with respect to the variable η:

$$\hat{E}_s(k_\eta, r_o) = \int_{-\infty}^{+\infty} E_s(\eta, r_o)\, e^{jk_\eta \eta}\, d\eta \tag{8}$$

$$\triangleq \underset{\eta \to k_\eta}{\mathscr{F}} \left\{ E_s(\eta, r_o) \right\}. \tag{9}$$

Here, k_η represents the spatial frequency along η, directly related to the propagation constant.

The field at any depth ξ can be propagated using

$$\hat{E}_s(k_\eta, \xi) = e^{jT(k_\eta)(\xi - r_o)} \hat{E}_s(k_\eta, r_o), \tag{10}$$

where the function $T(k_\eta)$ accounts for propagation along ξ, with real values for propagating components ($|k_\eta| < k$) and purely imaginary values for evanescent components ($|k_\eta| > k$):

$$T(k_\eta) = \begin{cases} \sqrt{k^2 - k_\eta^2}, & |k_\eta| < k, \\ j\sqrt{k_\eta^2 - k^2}, & |k_\eta| > k. \end{cases} \tag{11}$$

A. The Wigner Distribution

For the field $E_s(\eta, r_o)$ at depth $\xi = r_o$, its Wigner distribution $W_{E_s}(\eta, k_\eta)$ is defined as

$$W_{E_s}(\eta, k_\eta) = \int_{-\infty}^{+\infty} E_s\left(\eta + \tfrac{\zeta}{2}\right) E_s^*\left(\eta - \tfrac{\zeta}{2}\right) e^{jk_\eta \zeta}\, d\zeta. \tag{12}$$

Using the Moyal formula [22], the Wigner distribution at depth ξ can be computed via the propagation operator $\mathcal{P}_\xi$:

$$\mathcal{P}_\xi \left\{ W_{E_s}(\eta, k_\eta) \right\} = W_{\mathscr{G}}(\eta, k_\eta) \underset{\eta}{*} W_{E_s}(\eta, k_\eta), \tag{13}$$

where

$$W_{\mathscr{G}} = \frac{1}{2\pi} \int_{-\infty}^{+\infty} e^{j\left[T\left(k_\eta + \frac{q}{2}\right) - T^*\left(k_\eta - \frac{q}{2}\right)\right]\xi} e^{-j\eta q} dq \tag{14}$$

represents the Wigner transform of the Field Propagator $e^{jT(k_\eta)\xi}$ in (10).

III. Phase-Space Method

Equation (15) shows that the Mark's spectrum μ_θ can be expressed in terms of 2D convolution involving the Wigner distribution of the sensor aperture W_a and of the scattered field W_{E_s} (12).

$$\mu_\theta(\eta, k_\eta) = W_a(-\eta, k_\eta) \underset{\eta,k_\eta}{*} W_{E_s}(\eta, k_\eta; \theta). \tag{15}$$

Once sensor aperture $a(\eta)$ is specified, $W_a(\eta, k_\eta)$ can be computed. $W_{E_s}(\eta, k_\eta; \theta)$ is then obtained by deconvolving (15), which is ill-posed and requires regularization [6, 13]. To this aim, we adopt the Wiener filter [13]

$$W_{E_s}(\eta, k_\eta; \theta) = \mathscr{F}^{-1}\left\{ \frac{\mathscr{F}\{\mu_\theta(\eta, k_\eta)\}\, \mathscr{F}^*\{W_a(-\eta, k_\eta)\}}{|\mathscr{F}\{W_a(-\eta, k_\eta)\}|^2 + \epsilon} \right\}, \tag{16}$$

where $\mathscr{F}$ denotes the 2D Fourier transform, $\mathscr{F}^{-1}$ its inverse, $*$ complex conjugation, and ϵ a small regularization constant.

Due to its quadratic nature, the Wigner distribution $W_{E_s}(\eta, k_\eta; \theta)$ contains interference terms that degrade its interpretation. However, the oscillatory behavior of cross-terms enables their discrimination and suppression. Accordingly, the following filtering strategy is employed to obtain a cross-term-free representation while preserving higher resolution than Mark's Physical Spectrum μ_θ.

$$\tilde{W}_{E_s}(\eta, k_\eta) = \max_{\xi} \left| \mathcal{P}_{-\xi}\Big\{ \mathcal{F}_{\mathrm{LP}}\big\{ \mathcal{P}_{\xi}\{W_{E_s}(\eta, k_\eta)\} \big\} \Big\} \right|. \tag{17}$$

For each depth ξ, the Wigner distribution is back-propagated via $\mathcal{P}_\xi$ (13), a low-pass filter is applied, then forward-propagated $\mathcal{P}_{-\xi}$. The maximum over all depths gives the cross-term-free representation $\tilde{W}_{E_s}$.

After cross-term suppression, note that evaluating $\tilde{W}_{E_s}$ at $k_\eta = 0$ produces

$$\tilde{W}_{E_s}(\eta, 0) \approx \sum_{m=0}^{M-1} |\tau_m|^2 h(\eta - \eta_m, \xi_m), \tag{18}$$

with

$$h(\eta, \xi) = 4(\ell - |\eta|)\, \mathrm{sinc}\left[2\,(\ell - |\eta|) \left(k \frac{\eta}{|r_o - \xi|} \right) \right], \tag{19}$$

and

$$\mathrm{sinc}(\eta) \triangleq \frac{\sin(\eta)}{\eta}. \tag{20}$$

The function $s_\theta(\eta) = \tilde{W}_{E_s}(\eta, 0)$ exhibits peaks at target positions along η. The width of each sinc pattern depends on the depth $d_m = |r_o - \xi_m|$. Hence, $s_\theta(\eta)$ can be interpreted as tomographic projections of the object function ρ for different angles θ.

Finally, backprojection via the inverse Radon transform [2, 13] reconstructs the object function $o(x, y)$

$$o(x, y) = \mathscr{F}^{-1}\Big\{ \underset{\eta \to k_\eta}{\mathscr{F}} \big\{ s_\theta(\eta) \big\}(k_\eta, \theta) \Big\}, \tag{21}$$

where $\mathscr{F}_{\eta \to k_\eta}$ is the 1D Fourier transform along η, yielding the frequency domain k_η, and $\mathscr{F}^{-1}$ is the 2D inverse Fourier transform along (k_η, θ) to reconstruct $o(x, y)$.

IV. Simulations and Discussion

To validate the proposed procedure, several numerical simulations were carried out in noisy environments containing point scatterers, each characterized by the same unitary scattering coefficient τ_m. Additive white Gaussian noise (AWGN) $n(\eta, k_\eta)$ with zero mean was modeled so as to affect the measurements as follows

$$\mu_\theta(\eta, k_\eta) = |\mathcal{S}_{E_s}(\eta, k_\eta) + n(\eta, k_\eta)|^2 \tag{22}$$

where the Signal-to-Noise Ratio (SNR) between $\mathcal{S}_{E_s}(\eta, k_\eta)$ and $n(\eta, k_\eta)$ was set to 20 dB, if not differently stated. The scene was illuminated with a monochromatic wave at $f_0 = c_0/\lambda = 300$ GHz. The distance r_o was set to 20λ, and the observation curve γ_θ was defined such that its half-length is $\ell = 20\lambda$. The sensor aperture $a(\eta)$ was modeled as a rectangular window with semi-extension $\ell_a = 3\lambda$, namely

$$a(\eta) = \Pi\left(\frac{\eta}{2\ell_a} \right). \tag{23}$$

Inversion to recover $W_{E_s}(\eta, k_\eta; \theta)$ was performed using the Wiener filter in (16). The regularization parameter ϵ was empirically selected to ensure numerical stability of the inversion while preserving the relevant spectral content, and the same value was used consistently across all the simulations presented. The low-pass filter $\mathcal{F}_{\mathrm{LP}}$ was designed with a Gaussian transfer function, characterized by a standard deviation

$$\sigma_f = \frac{1}{5} \frac{\pi}{k_{\max}} = 1 \times 10^{-4}, \tag{24}$$

where $k_{\max}$ is the maximum k_η-component, set equal to k in our simulations. This choice is motivated by two considerations: (i) for a Gaussian of this width, approximately 99% of the energy is contained within $\pm 5\sigma_f$, ensuring that most of the auto-term spectral content is preserved; (ii) analytical considerations indicate that the auto-term spectrum has significant values roughly from $-\pi/k$ to π/k, which aligns well with the $\pm 5\sigma_f$ interval. Together, these arguments justify the selection of σ_f to achieve effective cross-term suppression while preserving the energy of the auto-terms.

Figs. 2–5 show the normalized reconstructed magnitudes $o(x, y)$ for different target scenarios. Figures 2 and 3 illustrate a scenario with three targets located at $(-5\lambda, 2\lambda)$, $(0, -4\lambda)$, and $(3\lambda, 2.5\lambda)$ and SNR = 20 dB. Figures 4 and 5 depict a configuration involving four objects located at $(-4\lambda, 0)$, $(\lambda, -5\lambda)$, $(2\lambda, 4\lambda)$, and $(3\lambda, 0)$, with a signal-to-noise ratio (SNR) of 10 dB.

The simulation results confirm the analytical findings, demonstrating that the proposed phase-space approach provides superior spatial resolution when compared to backprojection directly obtained from the measurements μ_η. All the presented reconstructions successfully produce object functions exhibiting local maxima at the true target locations, thereby enabling accurate target detection and localization. Furthermore, the results validate that the proposed filter (17) effectively suppresses cross-term artifacts, leading to a novel imaging strategy based on phase-space backprojection, which

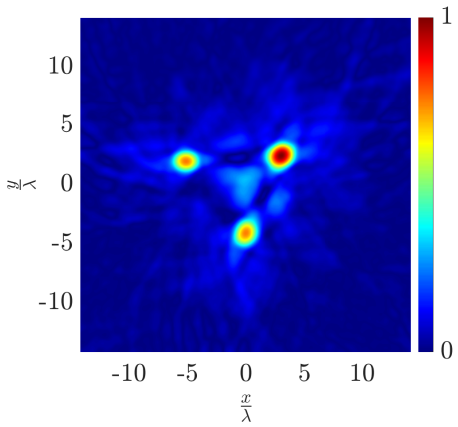

Fig. 2. Three targets located at $(-5\lambda, 2\lambda)$, $(0, -4\lambda)$, and $(3\lambda, 2.5\lambda)$, with a signal-to-noise ratio (SNR) of 20 dB.

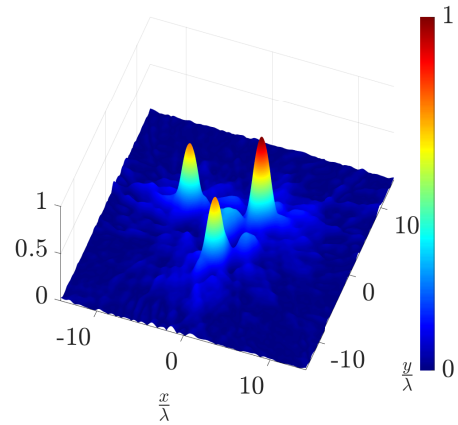

Fig. 3. 3D representation of reconstruction in Fig. 2.

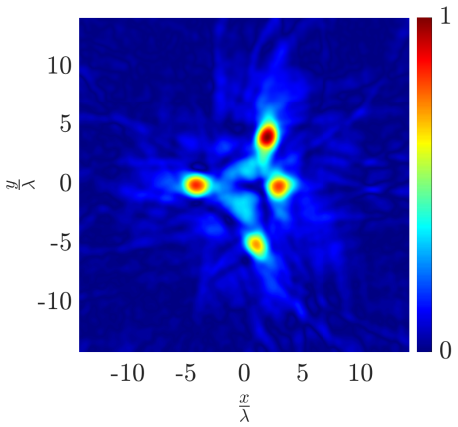

Fig. 4. Four objects located at $(-4\lambda, 0)$, $(\lambda, -5\lambda)$, $(2\lambda, 4\lambda)$, and $(3\lambda, 0)$, with a signal-to-noise ratio (SNR) of 10 dB.

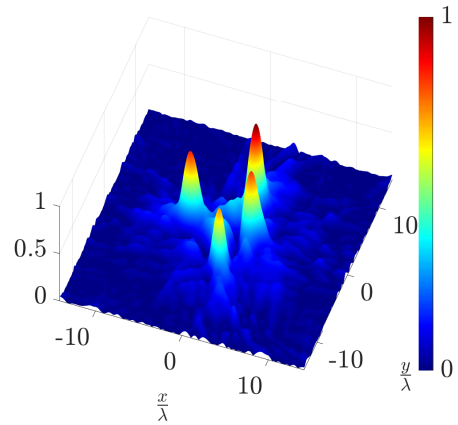

Fig. 5. 3D representation of reconstruction in Fig. 4.

emerges as a viable alternative to conventional tomographic approaches.

V. Conclusions

This work introduces a phase-space imaging framework for target localization based on backprojection via amplitude-only measurements. The proposed method operates directly in phase-space, providing a set of tomographic projections of the target scene.

Unlike conventional amplitude-only imaging strategies, the presented method does not require iterative algorithms, thus significantly reducing computational burden and overcoming the the problem of reliability.

Theoretical analysis and numerical results demonstrate that the proposed phase-space approach enables effective target detection and localization using the Wigner distribution, while mitigating cross-term interference through appropriate filtering strategies. These findings suggest that the proposed approach constitutes a valid alternative to standard imaging techniques.

Future work will focus on extending the approach to more general target scenarios, including extended objects and multi-frequency illumination.

References

[1] M. Soumekh, *Fourier Array Imaging*. Englewood Cliffs, NJ: Prentice Hall, 1994, ISBN: 978-0130660001.

[2] A. J. Devaney, *Mathematical Foundations of Imaging, Tomography and Wavefield Inversion*. Cambridge, UK: Cambridge University Press, 2012, ISBN: 978-0-521-11974-0.

[3] F. Soldovieri and R. Solimene, "Ground penetrating radar subsurface imaging of buried objects," in *Radar Technology*, G. Kouemou, Ed., Rijeka: IntechOpen, 2010, ch. 6. DOI: 10.5772/7176. [Online]. Available: https://doi.org/10.5772/7176.

[4] Y. Wang, W. Wang, M. Zhou, A. Ren, and Z. Tian, "Remote monitoring of human vital signs based on 77-ghz mm-wave fmcw radar," *Sensors*, vol. 20, no. 10, p. 2999, 2020. DOI: 10.3390/s20102999. [Online]. Available: https://doi.org/10.3390/s20102999.

[5] J. W. Goodman, *Introduction to Fourier Optics*, 4th. McMillan Learning, 2017, p. 564, ISBN: 9781319119164.

[6] M. Bertero and P. Boccacci, *Introduction to Inverse Problems in Imaging*, 1st. New York: Springer, 2010.

[7] D. Grischkowsky, S. Keiding, M. van Exter, and C. Fattinger, "Far-infrared time-domain spectroscopy with terahertz beams of dielectrics and semiconductors," *Journal of the Optical Society of America B*, vol. 7, pp. 2006–2015, 1990. DOI: 10.1364/JOSAB.7.002006.

[8] J. E. Pedersen and S. R. Keiding, "Thz time-domain spectroscopy of nonpolar liquids," *IEEE Journal of Quantum Electronics*, vol. 28, no. 10, pp. 2518–2522, Oct. 1992. DOI: 10.1109/3.159511.

[9] M. C. Nuss, P. M. Mankiewich, M. L. O'Malley, E. H. Westerwick, and P. B. Littlewood, "Dynamic conductivity and coherence peak in $YBa_2Cu_3O_7$ superconductors," *Physical Review Letters*, vol. 66, no. 25, pp. 3305–3308, Jun. 1991. DOI: 10.1103/PhysRevLett.66.3305. [Online]. Available: https://link.aps.org/doi/10.1103/PhysRevLett.66.3305.

[10] H. Harde and D. Grischkowsky, "Coherent transients excited by subpicosecond pulses of terahertz radiation," *Journal of the Optical Society of America B*, vol. 8, no. 8, pp. 1642–1651, Aug. 1991. DOI: 10.1364/JOSAB.8.001642. [Online]. Available: https://opg.optica.org/josab/abstract.cfm?URI=josab-8-8-1642.

[11] R. Fukasawa, "Terahertz imaging: Widespread industrial application in non-destructive inspection and chemical analysis," *IEEE Transactions on Terahertz Science and Technology*, vol. 5, no. 6, pp. 1121–1127, 2015.

[12] J. True, C. Xi, N. Jessurun, K. Ahi, and N. Asadizanjani, "Review of thz-based semiconductor assurance," *Optical Engineering*, vol. 60, no. 6, p. 060 901, Jun. 2021. DOI: 10.1117/1.OE.60.6.060901. [Online]. Available: https://doi.org/10.1117/1.OE.60.6.060901.

[13] R. H. T. Bates and M. J. McDonnell, *Image Restoration and Reconstruction*. Oxford: Clarendon Press, 1986.

[14] C. Vogel, *Computational Methods for Inverse Problems*, 1st. Philadelphia: SIAM, 2002.

[15] T. Isernia, F. Soldovieri, G. Leone, and R. Pierri, "On the local minima in phase reconstruction algorithms," *Radio Science*, vol. 31, no. 6, pp. 1887–1899, 1996. DOI: 10.1029/96RS02154.

[16] R. Pierri and R. Moretta, "On data increasing in phase retrieval via quadratic inversion: Flattening manifold and local minima," *IEEE Transactions on Antennas and Propagation*, vol. 68, no. 12, pp. 8104–8113, 2020. DOI: 10.1109/TAP.2020.2998923.

[17] A. Torre, *Linear Ray and Wave Optics in Phase Space*, 2nd. Elsevier, 2019.

[18] M. J. Bastiaans, "Application of the wigner distribution function in optics," W. Mecklenbräuker and F. Hlawatsch, Eds., pp. 375–426, 1997.

[19] B. Boashash, *Time Frequency Signal Analysis and Processing - A Comprehensive Reference*. Elsevier, 2003.

[20] H.-Y. Liu, E. Jonas, L. Tian, J. Zhong, B. Recht, and L. Waller, "3d imaging in volumetric scattering media using phase-space measurements," *Optics Express*, vol. 23, no. 11, pp. 14 461–14 471, 2015. DOI: 10.1364/OE.23.014461. [Online]. Available: https://www.osapublishing.org/oe/abstract.cfm?uri=oe-23-11-14461.

[21] W. C. Chew, *Waves and Fields in Inhomogeneous Media*. New York: IEEE Press, 1995.

[22] J. E. Moyal and M. S. Bartlett, "Quantum mechanics as a statistical theory," *Mathematical Proceedings of the Cambridge Philosophical Society*, vol. 45, no. 01, p. 99, 1949. DOI: 10.1017/s0305004100000487.

[23] T. A. C. M. Claasen and W. F. G. Mecklenbräuker, "The wigner distribution - a tool for time-frequency signal analysis - part 1: Continuous-time signals," *Philips J. Res.*, vol. 35, pp. 217–250, 1980.

[24] T. A. C. M. Claasen and W. F. G. Mecklenbräuker, "The wigner distribution - a tool for time-frequency signal analysis - part 2: Discrete-time signals," *Philips J. Res.*, vol. 35, pp. 276–300, 1980.

[25] T. A. C. M. Claasen and W. F. G. Mecklenbräuker, "The wigner distribution - a tool for time-frequency signal analysis - part 3: Relations with other time-frequency signal transformations," *Philips J. Res.*, vol. 35:6, pp. 372–389, 1980.

Fast imaging methods for real-time electromagnetic tomography

Antonello Tamburrino[1,*], Vincenzo Mottola[1], Gianpaolo Piscitelli[2]

[1] Department of Electrical and Information Engineering, University of Cassino and Southern Lazio, 03043 Cassino (FR), Italy

[2]Dipartimento di Scienze Economiche Giuridiche Informatiche e Motorie, Università degli Studi di Napoli Parthenope, 80035 Nola (NA), Italy.

*Corresponding author: antonello.tamburrino@unicas.it

***Abstract*—Industry 4.0 demands fast, low-cost techniques for real-time material health monitoring. Soft-field electromagnetic tomography is particularly attractive due to its contactless nature and inexpensive hardware. This talk presents the latest advances in real-time imaging methods for soft-field tomography, addressing both linear and nonlinear material responses.**

***Keywords*— soft-field tomography, monotonicity principle, kernel method, real-time imaging.**

I. Introduction

Electromagnetic tomography is a non-destructive imaging technique widely used for material inspection. In soft-field configurations, low-frequency electromagnetic fields provide non-ionizing radiation, low-cost hardware, and robustness in industrial environments. However, fast imaging remains challenging, since the reconstruction of electromagnetic properties from field measurements leads to a severely ill-posed and nonlinear inverse problem, even for linear materials.

Existing approaches can be broadly classified into iterative and non-iterative methods. Iterative schemes formulate the problem as a nonlinear optimization, requiring repeated forward simulations and thus preventing real-time applications while suffering from local minima. Non-iterative methods, instead, exploit structural properties of the physical model to derive an indicator function a priori. This function is then applied to the measured data to directly obtain the reconstruction, enabling real-time imaging and avoiding local minima. Only a few such methods are currently available, including the Linear Sampling Method, the Factorization Method [1], the Enclosure Method [2], and the Monotonicity Principle [3].

This work extends the class of non-iterative imaging techniques. A new method for linear materials, called the Kernel Method, is introduced, exhibiting a reduced computational complexity. Moreover, a novel framework for non-iterative imaging of materials with nonlinear constitutive laws is proposed, providing the first real-time inversion methods for general nonlinear media.

II. Statement of the problem

The targeted problem is Electrical Resistance Tomography. The specimen is a conductive body excited by DC voltages applied at the boundary through electrodes, while its response is measured in terms of the resulting currents on the same electrodes (see Figure 1). The aim is to reconstruct the shape, position, and size of an unknown inclusion V embedded in a known background (see Figure 1), from boundary measurements only (inverse obstacle problem).

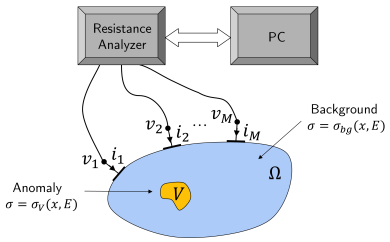

Fig. 1. Targeted problem in Electrical Resistance Tomography

In this contribution, both the background and inclusion conductivities are allowed to be nonlinear, namely depending on the spatial variable and on the magnitude of the electric field. Boundary measurements are described through the Dirichlet-to-Neumann (DtN) map Λ_V, which associates prescribed boundary voltages to the resulting boundary currents. This operator can be interpreted as the continuum limit of the voltage-to-current matrix as the number of electrodes $M \to \infty$ and their size tends to zero.

III. The Kernel Method

The Kernel Method addresses the inverse obstacle problem for linear background and inclusion conductivities. It exploits a key property of the steady-state current problem. Specifically, it is possible to prescribe a boundary voltage v_0 to the reference configuration, that is a defect-free configuration ($V = \emptyset$), such that the resulting electric current density vanishes in a prescribed region of the domain, while remaining nonzero elsewhere [4]. A second key result is that a boundary voltage v_0 able to make vanishing the current density in the anomalous region V can be computed from boundary measurements only, by solving an eigenvalue problem for the operator $\Lambda_V - \Lambda_\emptyset$, where $\Lambda_\emptyset$ is the DtN map for the reference configuration.

Based on these properties, an imaging method is obtained by: (i) computing the boundary voltage v_0 from measured

data; (ii) simulating the response of the reference configuration under the excitation v_0; and (iii) identifying the inclusion as the region where the resulting electric current density is negligible. Representative reconstructions obtained with the Kernel Method are shown in Figure 2.

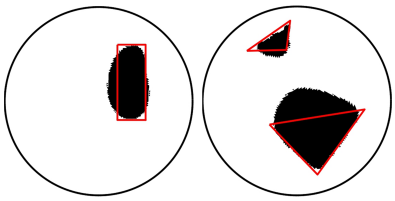

Fig. 2. Reconstructions by the Kernel Method on synthetic data corrupted by numerical noise. The level affects the third significant digit of the measurements. In red the boundary of the actual anomaly and in black the reconstructed region.

IV. Imaging of nonlinear materials

Real-time imaging methods can be extended to general nonlinear electrical conductivities of the form $\sigma(x, E)$, where E denotes the magnitude of the electric field. As discussed in detail in [8], the proposed framework encompasses a broad class of nonlinear constitutive laws comprising almost all constitutive relationship that can be found in a practice.

A key ingredient in the development of this framework is the recognition that boundary measurements must be modeled through a new nonlinear operator. To this end, the average Dirichlet-to-Neumann operator (aDtn) $\overline{\Lambda}$ is introduced [5], [6], mapping prescribed boundary voltages to an appropriate average of the measured boundary currents. This operator plays a central role, as it is the only boundary operator known to satisfy a Monotonicity Principle in a general nonlinear setting.

This principle provides the foundation for the proposed non-iterative imaging method, as it establishes a direct link between boundary measurements and the internal conductive properties of the specimen. In particular, it enables a simple monotonicity test to determine whether a given test region T is contained within the actual anomaly V. Specifically, denoting by $\overline{\Lambda}_V$ the aDtN operator associated with the inspected specimen and by $\overline{\Lambda}_T$ the corresponding operator for a configuration in which the anomaly occupies the test region T, the following characterization holds [5], [6], [8]

$$T \subseteq V \Longleftrightarrow \overline{\Lambda}_T \leqslant \overline{\Lambda}_V,$$

for a connected anomaly V. In other words, if $T \subseteq V$, boundary measurements associated with the test configuration are always smaller than those corresponding to the actual anomaly. Conversely, if there exists a boundary voltage such that the corresponding measurements on the test anomaly are greater than the one in the presence of V, one can conclude that $T \not\subseteq V$. In [7], this characterization is translated into a real-time imaging method by devising a strategy to identify suitable boundary voltages for testing the condition $T \not\subseteq V$. Representative reconstructions are shown in Figure 3. Notably, each reconstruction requires only a few milliseconds on a standard laptop.

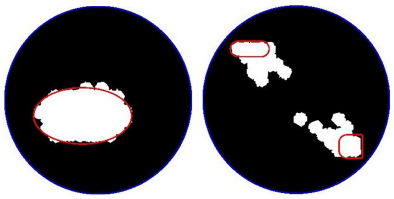

Fig. 3. Reconstructions by the Monotonicity Principle Method on synthetic data corrupted by numerical noise. The background material is common steel, while the anomaly is filled by a nonlinear composite. In red the boundary of the actual anomaly and in white the reconstructed region.

Apart from its real-time capability, the method exhibits additional relevant features: (i) a rigorous theoretical performance limit, ensuring exact reconstruction of the anomaly shape in the absence of noise, except for some of its cavities not electrically connected to the boundary; and (ii) intrinsic stability with respect to measurement noise.

As a final remark, [9] proposes an alternative strategy for handling nonlinearities, tailored to materials exhibiting extremely high electrical conductivity compared to the surrounding background, such as superconductors. In this regime, it is rigorously shown that the original nonlinear conductivity problem can be recast as an equivalent linear one, thus allowing the direct application of well-established tomographic methods for linear media.

Acknowledgment

The authors would like to thank Antonio Corbo Esposito, Luisa Faella, and Ravi Prakash for their valuable contributions to the imaging of nonlinear materials.

References

[1] Kirsch, A. (1998). Characterization of the shape of a scattering obstacle using the spectral data of the far field operator. Inverse Problems, 14(6), 1489.
[2] Ikehata, Masaru. (1999). How to draw a picture of an unknown inclusion from boundary measurements. Two mathematical inversion algorithms. Journal of Inverse and Ill-Posed Problems. 7. 255-271.
[3] Tamburrino, A., & Rubinacci, G. (2002). A new non-iterative inversion method for electrical resistance tomography. Inverse Problems, 18(6), 1809.
[4] Tamburrino, A., & Mottola, V. (2024) Imaging of conducting materials via the Kernel Method. International Journal of Applied Electromagnetics and Mechanics, 74(4), 441-446.
[5] Corbo Esposito, A., Faella, L., Piscitelli, G., Prakash, R., & Tamburrino, A. (2021). Monotonicity Principle in tomography of nonlinear conducting materials*. Inverse Problems, 37(4), 045012.
[6] Corbo Esposito, A., Faella, L., Mottola, V., Piscitelli, G., Prakash, R., & Tamburrino, A. (2024). Piecewise nonlinear materials and Monotonicity Principle. Inverse Problems, 40(8), 085001.
[7] Mottola, V., Corbo Esposito, A., Piscitelli, G., & Tamburrino, A. (2024). Imaging of nonlinear materials via the Monotonicity Principle. Inverse Problems, 40(3), 035007.
[8] Mottola, V., Corbo Esposito, A., Faella, L., Piscitelli, G., Prakash, R., & Tamburrino, A. (2025). The inverse obstacle problem for nonlinear inclusions. Inverse Problems, 41(5), 055002.
[9] Corbo Esposito, A., Faella, L., Piscitelli, G., Mottola, V., Prakash, R., & Tamburrino, A. (2024). The p_0-Laplace "Signature" for Quasilinear Inverse Problems. SIAM Journal on Imaging Sciences, 17(1), 351-388.

Averaged Steklov eigenvalues and applications to electromagnetic imaging problems

Mayeul Chavanne [1,*], Lorenzo Audibert [2], Houssem Haddar [1]

[1] IDEFIX team, INRIA Saclay, France
[2] EDF R&D and IDEFIX team INRIA Saclay, France
*Corresponding author: mayeul.chavanne@inria.fr

***Abstract*—We study electromagnetic inverse scattering problems at fixed frequency using multi-static data. Classical imaging methods typically fail when the background medium is highly oscillatory. To overcome this limitation, we propose a new method based on the introduction of artificial resonators.**

***Keywords*— Quantitative inversion methods, Linear Sampling Method, Steklov eigenvalues.**

I. Introduction

Classical "solver-free" inversion methods fail to accurately and efficiently account for the physical properties of materials in the presence of densely distributed small-scale heterogeneities. This limitation arises either because such methods only reconstruct the shape of diffracting objects, or because they rely on structural assumptions that fit the data but do not correspond to the actual physical quantities of interest. Alternative approaches, known as full-wave inversion methods, rely on computationally expensive optimization procedures, which may fail to converge and often struggle to determine whether certain physical parameters lie above or below critical thresholds. In this work, we develop a new inversion method that is computationally efficient, since it does not require repeatedly solving forward problems, and capable of quantitatively characterizing relevant physical properties at a mesoscopic scale.

II. Sketch of the inversion algorithm

The inverse problem considered here takes as input measurements of scattered waves recorded at large distances from an object, known as the far-field pattern, at a fixed frequency. The goal is to recover information about the internal composition of the probed domain. The general structure of the proposed algorithm is as follows:

Algorithm 1

- At a point z in the investigated domain Ω, we numerically introduce an artificial resonator D_z (see Fig. 2).
- We define in D_z an artificial spectral problem with a unique resonance eigenvalue λ, and relate this resonance to a quantitative indicator function $I(z)$ (see Formulae (1) (2))
- The resonance parameter is identified from the far field data using the Inside-Outside Duality, or the Linear Sampling Method (see [4], [5])
- The indicator function $I(z)$ is computed by sweeping z over the inspected area.

In this short abstract, we do not detail the third step of the algorithm, although it is essential, as it has already been thoroughly addressed in the cited references. Instead, we focus on the structure of the resonator that can be used numerically, relate its spectrum to the material properties, and describe its behavior with respect to frequency for both acoustic and electromagnetic problems.

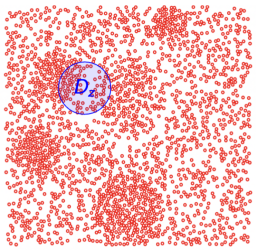

Fig. 1. Heterogeneous material probed by a resonator

III. Structure of the Spectral Problems

The artificial spectral problem in the resonator D_z reads as follows for the acoustic case:

Find λ_φ such that there exists $u \in H^1(D_z) \setminus \{0\}$ that satisfies:

$$\begin{aligned} \Delta u + k^2 n^2 u = 0 \quad &\text{in } D_z, \\ \lambda_\varphi u_{|\partial D_z} + \left(\int_{\partial D_z} \partial_\nu u \bar{\varphi} \mathrm{d}s \right) \varphi = 0 \quad &\text{on } \partial D_z. \end{aligned}$$

where ν denotes the outward normal field on ∂D_z, n is the refraction index of the medium, $k > 0$ is the wavenumber, and $\varphi \in H^{1/2}(\partial D_z)$ with $\|\varphi\|_{L^2(\partial D_z)} = 1$.

In the electromagnetic case, with constant magnetic permeability, the problem can be formulated for the electric field as:

Find λ_ϕ such that there exist $u \in H(\mathrm{curl}, D_z) \setminus \{0\}$ that satisfies:

$$\begin{aligned} \mathrm{curl}\,\mathrm{curl}\, u - k^2 \epsilon u = 0 \quad &\text{in } D_z, \\ \lambda_\phi \nu \times (u \times \nu) - \left(\int_{\partial D_z} \nu \times \mathrm{curl}\, u \cdot \bar{\phi} \mathrm{d}s \right) \phi = 0 \quad &\text{on } \partial D_z, \end{aligned}$$

where ϵ is the electric permittivity tensor field, and $\phi \in H_t^{-1/2}(\mathrm{Curl}, \partial D_z)$ with $\|\phi\|_{L_t^2(\partial D_z)} = 1$.

IV. Results on the Spectral Problems

The main theoretical result we obtain for these problems is that, except for a discrete set of wavenumber, corresponding to the eigenvalues of the associated Dirichlet problem, there exists a unique eigenvalue λ, which we refer to as the *averaged Steklov eigenvalue*. This uniqueness property is crucial for retrieving the eigenvalue from the far-field data, as it ensures improved stability and accuracy of the reconstruction method [4], [5]. The respective Dirichlet problems involve finding k^2 such that there exists a non-trivial field u satisfying:

$$\begin{aligned} \Delta u + k^2 n^2 u = 0 \quad &\text{in } D_z, \\ u_{|\partial D_z} = 0 \quad &\text{on } \partial D_z. \end{aligned}$$

in the acoustic case, and:

$$\begin{aligned} \operatorname{curl}\operatorname{curl} u - k^2 \epsilon u = 0 \quad &\text{in } D_z, \\ \operatorname{div}(\epsilon u) = 0 \quad &\text{in } D_z, \\ \nu \times (u \times \nu) = 0 \quad &\text{on } \partial D_z, \end{aligned}$$

in the electromagnetic case. If one denotes $\sigma = \{\kappa_m\}_{m\in\mathbb{N}^*}$ the increasing sequence of positive numbers that constitute this spectrum, and if $\{u_m\}_{m\in\mathbb{N}^*}$ is an associated orthonormal eigenbasis, then in the acoustic case one has the following expansion of the eigenvalue:

$$\lambda_\varphi = \int_{D_z} \left(k^2 n^2 |u_\varphi^0|^2 - |\nabla u_\varphi^0|^2\right) - \sum_{m\geq 1} \frac{k^4 \kappa_m^{-2}}{k^2 - \kappa_m} \left| \int_{\partial D_z} \partial_\nu u_m \bar{\varphi} \right|^2$$

where u_φ^0 the unique solution of:

$$\begin{aligned} \Delta u_\varphi^0 = 0 \quad &\text{in } D_z, \\ u_{\varphi|\partial D_z}^0 = \varphi \quad &\text{on } \partial D_z. \end{aligned}$$

In the electromagnetic case, with the same notations for the Dirichlet eigenvalues and eigenvectors, the expression of λ is similar:

$$\begin{aligned} \lambda_\phi = &\int_{D_z} \left(k^2 \epsilon u_\phi^0 \cdot \bar{u}_\phi^0 - |\operatorname{curl} u_\phi^0|^2\right) \\ &- \sum_{m\geq 1} \frac{k^4 \kappa_m^{-2}}{k^2 - \kappa_m} \left| \int_{\partial D_z} \nu \times \operatorname{curl} u_m \cdot \bar{\phi} \right|^2 \end{aligned}$$

where u_ϕ^0 is the unique solution of:

$$\begin{aligned} \operatorname{curl}\operatorname{curl} u_\phi^0 = 0 \quad &\text{in } D_z, \\ \operatorname{div}(\epsilon u_\phi^0) = 0 \quad &\text{in } D_z, \\ \nu \times (u_\phi^0 \times \nu) = \phi \quad &\text{on } \partial D_z. \end{aligned}$$

In the acoustic case, if one could access the averaged Steklov eigenvalue λ_φ for small wavenumbers, such that one can reconstruct from data the slope of the function $k^2 \mapsto \lambda_\varphi$ at the origine, defining:

$$I(z) = \sqrt{|\partial D_z|} \frac{\mathrm{d}\lambda_\varphi}{\mathrm{d}k^2}(k^2 = 0) \tag{1}$$

with $\varphi = 1/\sqrt{|\partial D_z|}$, then one has:

$$I(z) = \int_{D_z} n^2(x) \mathrm{d}x$$

which means that this indicator function can be used to give a quantification of the local average of the refraction index. In

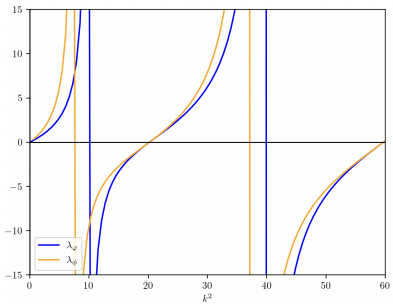

Fig. 2. Averaged Steklov eigenvalue as functions of k^2, in the Helmholtz (λ_φ) and Maxwell (λ_ϕ) cases for specific φ and ϕ

the electromagnetic case, with the assumption that ϵ is locally uniform in the resonator D_z if one can reconstruct from the data the slope of the function $k^2 \mapsto \lambda_\phi$ at the origine, defining the hermitian matrix $I(z)$ such that for all $\hat{e} \in \mathbb{C}^3$, $\|\hat{e}\| = 1$:

$$I(z)\hat{e} \cdot \bar{\hat{e}} = \frac{\|\nu \times (\hat{e} \times \nu)\|^2_{L_t^2(\partial D_z)}}{|D_z|} \frac{\mathrm{d}\lambda_\phi}{\mathrm{d}k^2}(k^2 = 0) \tag{2}$$

with $\phi = \nu \times (\hat{e} \times \nu)/\|\nu \times (\hat{e} \times \nu)\|_{L_t^2(\partial D_z)}$, then one has:

$$I(z) = \epsilon$$

This means that one can reconstruct from the data the local structure of the anisotropic electric permittivity ϵ over the domain. Similar considerations can be applied for the magnetic permeability.

V. Conclusion

We proposed an artificial spectral problem for the Helmholtz and Maxwell equations that singularly have a unique eigenvalue, which can be computed from the far field data. Our analysis had lead us to find an explicit formula of this eigenvalue, which could be used in the acoustic case to quantify the average value of the refraction index on a mesoscopic scale. In the electromagnetic case, it could allow us to reconstruct anisotropic behaviors in the electric permittivity of a media. Those ideas are currently being tested numerically.

References

[1] Cakoni, F., Colton, D., & Haddar, H. (2022). *Inverse scattering theory and transmission eigenvalues*. Society for Industrial and Applied Mathematics.

[2] Colton, D. L., Kress, R., & Kress, R. (1998). *Inverse acoustic and electromagnetic scattering theory* (Vol. 93, pp. 21-28). Berlin: Springer.

[3] Monk, P. (2003). *Finite element methods for Maxwell's equations*. Oxford university press.

[4] Audibert, L., Haddar, H., & Pourre, F. (2025). Averaged Steklov Eigenvalues, Inside Outside Duality and Application to Inverse Scattering. *SIAM Journal on Applied Mathematics*.

[5] Audibert, L., Haddar, H., & Pourre, F. (2024). Reconstruction of averaging indicators for highly heterogeneous media. *Inverse Problems*, 40(4), 045028.

A Three-Phase Quantitative Data-Assisted Microwave Imaging Method

Mohammad Omki[1], Alessandro Fedeli[1], Andrea Randazzo[1, *]

[1]Department Department of Electrical, Electronic, Telecommunication Engineering, and Naval Architecture (DITEN), University of Genoa, Italy
*Corresponding author: andrea.randazzo@unige.it

***Abstract*—A three-phase approach is presented in this paper for quantitative microwave imaging. It combines a fully connected neural network with a mild data-driven inexact-Newton approach, to solve the nonlinear inverse scattering problem and retrieve the dielectric properties of objects, allowing their reconstruction.**

***Keywords*—microwave imaging, inexact-Newton, neural networks.**

I. Introduction

In many applications, non-invasive and non-destructive techniques are highly recommended for a safe retrieval of some physical parameters and to derive information about the structural condition of targets [1].

In microwave imaging, to achieve this goal, a nonlinear and ill-posed inverse problem is required to be solved. Several approaches have been developed to address the problem solution. In particular, quantitative methods aim at a full reconstruction of the dielectric properties' distributions. However, the high complexity and long computing time make the problem more challenging [2].

In practice, to lower the required computational resources, simplified assumptions are often considered, where two-dimensional (2-D) canonical settings are assumed. However, this creates a model error, which needs to be properly corrected in order to process experimental data. Moreover, it has been proven that the introduction of prior information is useful to avoid the cost function trap in local minima [3].

In this contribution, to address the points above, the combination of a neural network with a mild data-driven inexact Newton approach (MDD-IN) is proposed.

II. Overview of the Approach

The proposed scheme is presented in Fig. 1. It can be divided into three sequential phases.

The first phase consists in modelling the scenario in a realistic 3D configuration on Ansys HFSS software (version 2025 R1), in a set of randomly generated cases. In this phase, the S-parameters are obtained from the 3D simulations, whereas the corresponding z-components of the total and incident electric fields around the investigation domain in a canonical 2D settings with idealized field probes and line/current sources are computed by a method of moments code.

In the second phase, a fully connected neural network (FCNN) is employed to compensate the modelling error by learning the connection between the measured S-parameters elements and the corresponding z-component of the total electric fields.

The final step is the solution of the inverse scattering problem by the proposed MDD-IN approach, which involves two nested iterative loops. The outer loop linearizes the inverse scattering problem, whereas the inner loop handles the resulting linearized problem by means of the truncated Landweber method [1]. In addition, prior information is introduced minimizing a term based on a surrogate model of the scattering problem, which is constructed by using a set of numerical simulations with random properties of the objects [3].

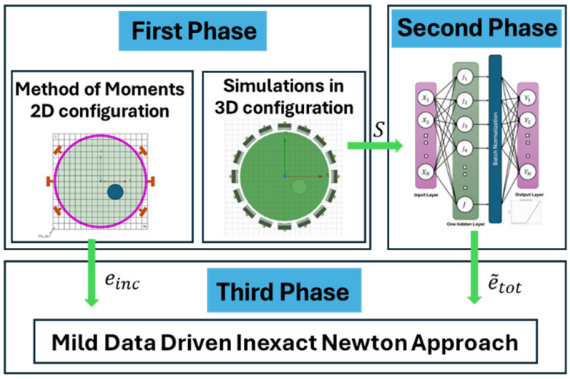

Fig. 1 An overview of the data-assisted MDD-IN inversion pipeline.

Acknowledgment

This work was supported by the Italian Ministry of University and Research, project PRIN 2022 "NEar-FiEld micRowave imaging for unconvenTionAl scenaRIos (NEFERTARI)" 20225KYR9F.

References

[1] M. Pastorino and A. Randazzo, *Microwave Imaging Methods and Applications*. Boston, MA: Artech House, 2018.

[2] M. T. Bevacqua and T. Isernia, 'Quantitative non-linear inverse scattering: A wealth of possibilities through smart rewritings of the basic equations', *IEEE Open Journal of Antennas and Propagation*, vol. 2, pp. 335–348, 2021, doi: 10.1109/OJAP.2021.3063248.

[3] C. Estatico, V. Schenone, A. Fedeli, and A. Randazzo, 'Application of a mild data-driven technique to Lippmann–Schwinger inverse scattering in variable-exponent Lebesgue spaces for microwave imaging', *Inverse Problems*, vol. 40, no. 6, p. 065007, May 2024, doi: 10.1088/1361-6420/ad3ea9.

Light Engineering at the Nano-Scale: Insights from Plasmonics and Metamaterials

AES 2026 · Catania, Italy · ISSN 2491-2417

Real-Space Plasmon Imaging Reveals Modified Charge Dynamics of Gold at the Monolayer Limit

A. Bylinkin[1,*], P. Roelli[1], N. Shetty[2], R. Yakimova[3], U. Starke[4], C. Coletti[5], S. Forti[5], A. Zakharov[6], V. M. Silkin[7,8,9], S. Lara-Avila[2], R. Hillenbrand[1,8,10]

[1]CIC nanoGUNE BRTA, 20018 Donostia-San Sebastián, Spain
[2]Department of Microtechnology and Nanoscience, Chalmers University of Technology, Gothenburg, Sweden
[3]Department of Physics, Chemistry and Biology (IFM), Linköping University, Linköping, Sweden
[4]Max Planck Institute for Solid State Research, Stuttgart, Germany
[5]Center for Nanotechnology Innovation@NEST, Istituto Italiano di Tecnologia, Pisa, Italy
[6]MAX IV Laboratory, Lund University, Lund, Sweden
[7]Donostia International Physics Center, Donostia-San Sebastián, Spain
[8]IKERBASQUE, Basque Foundation for Science, Bilbao, Spain
[9]Universidad del País Vasco UPV/EHU, Donostia-San Sebastián, Spain
[10]Department of Electricity and Electronics, University of the Basque Country (UPV/EHU), Leioa, Spain
*Corresponding author: a.bylinkin@nanogune.eu

***Abstract*—We present the first optical study of a quasi-freestanding gold monolayer formed between graphene and silicon carbide. Near-field microscopy reveals propagating plasmon polaritons and their dispersion. Analysis shows bulk-like scattering time but enhanced Drude weight, indicating modified collective charge dynamics and electronic response in atomically thin gold.**

***Keywords*— 2D metal, near-field microscopy, gold, plasmon, polariton interferometry.**

I. Summary

Gold is a remarkable material with exceptional optical, electronic, and chemical properties. When thinned down to the nanometre scale, gold exhibits properties that differ from those of its bulk form [1–4]. However, its optical properties in the monolayer limit remain largely experimentally unexplored, mainly due to long-standing challenges in fabrication and characterisation. Here, we present the first optical study of a stable, quasi-freestanding gold monolayer (ML-Au) [5]. The ML-Au is formed by intercalating gold atoms between graphene and silicon carbide substrate [6]. Using scattering-type scanning near-field optical microscopy (s-SNOM), we observe plasmon polaritons in ML-Au and extract their dispersion relation through polariton interferometry. Modelling the plasmon-polariton dispersion with a Drude-type two-dimensional optical conductivity allows us to determine the conductivity of ML-Au and extract key transport parameters: the Drude weight $D \propto n/m_{\text{eff}}$ (where n is the 2D carrier concentration and m_{eff} is the effective mass of carriers), representing the electron stiffness, and the carrier scattering time τ. We find that τ is comparable to that of bulk gold, while D is nearly twice the value expected from bulk properties, indicating a significant modification of the electronic response in the monolayer. Density functional theory (DFT) calculations of the electronic band structure in freestanding monolayer gold support the observed enhancement of the Drude weight. These results provide direct insights into the transport and optical properties of monolayer gold and establish ML-Au as a promising platform for fundamental studies and for future optoelectronic applications.

References

[1] H. Qian, Y. Xiao, and Z. Liu, "Giant Kerr response of ultrathin gold films from quantum size effect," *Nature Communications*, vol. 7, pp. 13153, 2016.
[2] C. Pan, et al., "Large area single crystal gold of single nanometer thickness for nanophotonics," *Nature Communications*, vol. 15, pp. 2840, 2024.
[3] C. O. Karaman, et al., "Ultrafast hot-carrier dynamics in ultrathin monocrystalline gold," *Nature Communications*, vol. 15, pp. 703, 2024.
[4] S. Zhao, et al., "Electrical conductivity of goldene," *Physical Review B*, vol. 110, pp. 085111, 2024.
[5] A. Bylinkin, P. Roelli, N. Shetty, R. Yakimova, U. Starke, C. Coletti, S. Forti et al., "Real-Space Plasmon Imaging Reveals Modified Electronic Structure of Gold at the Monolayer Limit," *arXiv preprint*, arXiv:2603.05030, 2026.
[6] S. Forti, et al., "Semiconductor to metal transition in two-dimensional gold and its van der Waals heterostack with graphene," *Nature Communications*, vol. 11, pp. 2236, 2020.

Whispering-Gallery Mode Microcavities & Microlasers: From Advanced Single Molecule Measurements to Applications in Biology

Frank Vollmer[1]

[1]Department of Physics & Living Systems Institute, University of Exeter, EX44QD, UK: f.vollmer@exeter.ac.uk

***Abstract*— Whispering-gallery-mode (WGM) optical microcavities enable ultrasensitive, label-free biosensing via evanescent fields. Plasmonic nanorods enhance light–matter interactions, achieving single-molecule detection of proteins and neurotransmitters. Recently developed WGM microlasers lasers capable of detecting individual molecules and even single atomic ions enable real-time, and enable future lab-on-a-chip biosensing for single-molecule biophysics and ultrasensitive in vivo biosensing applications.**

***Keywords*— metamaterials, terahertz, machine learning, photonic crystals.**

I. Introduction

This talk will focus on optical microcavities[1-3] and fundamental physics enabling single-molecule sensing, with particular emphasis on plasmonics and microlaser-based cascaded signal enhancement mechanisms. Optical whispering-gallery mode (WGM) microcavities provide high Q-factors and small effective mode volumes, allowing minute perturbations in refractive index or molecular polarizability to be transduced into measurable spectral shifts. When combined with plasmonic nanostructures such as gold nanorods, the evanescent cavity field is compressed into nanoscale hot spots, enabling detection at the single-molecule level.

The presentation will outline the sensing mechanism underlying optoplasmonic WGM devices and explain how localized near-field enhancements allow observation of biomolecular binding, conformational transitions, and protein dynamics within strongly inhomogeneous plasmonic fields. Particular attention will be given to recent demonstrations of microcavity-based detection of protein conformational changes occurring in the near-field of nanorods, where spatial field gradients provide sensitivity to subnanometer structural rearrangements.

A central theme of the talk is cascaded signal enhancement through active cavities. In microlaser-based WGM systems, rare-earth-ion-doped silica microspheres operated above threshold exhibit Purcell-induced linewidth narrowing, enabling spectral resolution that may enable sensitive detection beyond what is possible with passive resonators. Plasmon-induced mode splitting generates a self-heterodyne beatnote whose frequency shifts report single binding events while suppressing thermal noise.

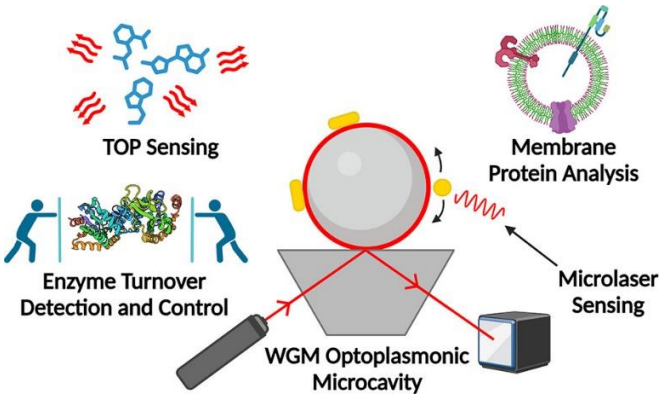

Figure: WGM Microcavities and their Applications. From ACS Photonics 2024, 11, 3, 892-903

Most recent advances include microlaser sensing of neurotransmitters and active optoplasmonic detection of protein dynamics within nanorod-enhanced fields. I will also discuss the use of WGM microcavities as single-molecule absorption spectrometers, enabling the detection of molecular transitions, for example, into radical states, that exhibit strong optical absorption.

References

[1] Samir Vartabi Kashanian & Frank Vollmer, “Single Atomic Ion Detection with Plasmon-Enhanced Whispering Gallery Mode Microlasers” Nature Photonics in press

[2] TL Derrien, AK Arunkumar, R Cross, E Sunnucks, F Vollmer “Uncovering the Lipid Interface in Neurotransmission: Single Molecule Measurements of Neurotransmitters Interacting with Membranes Reveal Species Dependent Membrane Binding” Adv. Sci. 2026, 13, e15727

[3] MC Houghton, SV Kashanian, TL Derrien, K Masuda, F Vollmer “Whispering-gallery mode optoplasmonic microcavities: from advanced single-molecule sensors and microlasers to applications in synthetic biology” ACS Nano 2024, 18, 17534−17546

Polaritonic metasurfaces: extended hybridization and energy transfer

C. Symonds[1*], J.M. Benoit[1], F. Bessueille[2], J. Bellessa[1]

[1]Université de Lyon, Université Claude Bernard Lyon 1, CNRS, Institut Lumière Matière, F-69622, Villeurbanne, France

[2]Université de Lyon, CNRS, Université Claude Bernard Lyon 1, Institut des Sciences Analytiques, UMR 5280, 5 rue de la Doua, F-69100 Villeurbanne, France.

*Corresponding author: clementine.symonds@univ-lyon1.fr

***Abstract*— Extended plasmon–exciton polaritonic states enable long-range energy transfer between spatially separated donor and acceptor dye arrays on a metal film. Moiré-patterned multimaterial systems exhibit hybrid polaritonic modes that mediate energy transport beyond near-field interactions through collective strong coupling.**

***Keywords*— strong light-matter coupling, organic materials, surface plasmon, energy transfer.**

I. Introduction

Strong light-matter coupling profoundly modifies the optical properties of materials by giving rise to hybrid excitations with collective and coherent character [1]. In metal-organic systems, the resulting plasmon-excitons polaritons can extend over micrometer scale distances [2]. Exploiting this extended polaritonic coherence offers new opportunities to design metasurfaces [3] and multimaterial systems where hybridization and energy transfer can be engineered at the microscale.

II. Methods

Multimaterial samples were fabricated by depositing two spatially separated organic emitters on a silver film using micro-contact printing. Periodic arrays of donor and acceptor J-aggregate dyes were patterned in complementary geometries with a micrometer scale lattice constant.

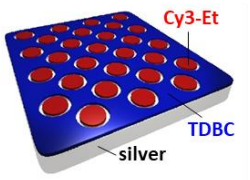

Fig. 1 Sketch of a multimaterial array deposited on silver.

III. Results and Discussion

Angle-resolved spectroscopy reveals that both excitonic transitions strongly couple to the same propagating surface plasmon, giving rise to three polaritonic branches. The observed anti-crossings demonstrate that the hybrid modes persist independently of whether the emitters are spatially separated or stacked, highlighting the key role of the extended polaritonic coherence length rather than local overlap. Photoluminescence measurements further show that this hybridization enables long-range energy transfer between the emitters. Upon selective excitation of the donor dye, emission from the acceptor is observed several micrometers away when the structure is deposited on a metal film, while no such transfer occurs on a dielectric substrate.

IV. Conclusion

These results demonstrate that polaritonic metasurfaces enable efficient energy transfer between spatially separated donor and acceptor arrays through collective strong coupling. This approach offers a robust and scalable route to engineered energy transfer in organic photonic systems.

Acknowledgments

The authors acknowledge financial support from French Agence Nationale de la Recherche on AAPG project 18-CE30-0014 PlasHybrid.

References

[1] V. M. Agranovich, M. Litinskaia, D. G. Lidzey, Phys. Rev. B 2003, 67, 085311.
[2] S. Aberra Guebrou, C. Symonds, E. Homeyer, J. C. Plenet, Yu. N. Gartstein, V. M. Agranovich, J. Bellessa, PRL 2012, 108, 066401.
[3] K. Chevrier, J. M. Benoit, C. Symonds, S. K. Saikin, J. Yuen-Zhou, J. Bellessa, Phys. Rev. Lett. 2019, 122, 173902.

Recursive analog computing with light

Andrea Cordaro[1]*, Xudong Li[1], Yaowen Hu[2], Tong Ge[1], Brian Edwards[3], Vahid Nikkhah[3], Yunxiang Song[1], Xinrui Zhu[1], Shengyuan Lu[1], Keith Powell[1], Letícia Magalhães[1], Urban Senica[1], Neil Sinclair[1], Andrea Alù[4,5], Nader Engheta[3], Albert Polman[2], Marko Lončar[1]

[1] John A. Paulson School of Engineering and Applied Sciences, Harvard University, USA
[2]State Key Laboratory for Mesoscopic Physics, Peking University, China[3]
Department of Electrical and Systems Engineering, University of Pennsylvania, USA
[4]Photonics Initiative, Advanced Science Research Center, City University of New York, USA
[5] Physics Program, Graduate Center, City University of New York, USA
[6] Center for Nanophotonics, AMOLF, Netherlands.
*Corresponding author: acordaro@g.harvard.edu

Abstract **- We report optical analog computing platforms based on metasurfaces and integrated photonics. Inverse-designed metagratings implement free-space integral equation solvers, while recursive electro-optic circuits enable programmable spectral and temporal operations. These results highlight new routes toward scalable high-speed optical computation.**

Keywords **- lithium niobate, photonic integrated circuit, metasurfaces.**

Liquid-Crystalline Chiral Nanophotonics: From Plasmonic Circular Dichroism to Circularly Polarized Luminescence

Wiktor Lewandowski[1,*]

[1]NanoOrgMat Group, Faculty of Chemistry, University of Warsaw, Warsaw, Poland
*Corresponding author: wiktor.lewandowski@uw.edu.pl

***Abstract*— We present a scalable route to chiral photonic thin films in which nanoparticles are helically organized within a liquid-crystalline matrix. For gold nanobipyramids, we achieve tunable plasmonic circular dichroism, while perovskite nanocrystals exhibit strong circularly polarized luminescence (g_{lum} ~0.24). Laser-writing enables microscale programming of handedness and chiroptical sign.**

***Keywords*— chiral nanophotonics, plasmonic circular dichroism, circularly polarized luminescence.**

I. Introduction

Chiroptical thin films that selectively absorb or emit circularly polarized light are attractive for applications ranging from sensing and optical data storage to circularly polarized light sources. However, methods for the scalable fabrication of chiral photonic films that enable spectral tunability and post-fabrication active control remain challenging. We address this problem using liquid-crystalline films that form helical supramolecular architectures and organize nanoparticles into chiral three-dimensional assemblies.

II. Methods

Our approach is based on chiral liquid crystals, which exhibit spontaneous symmetry breaking in thin films, forming helical channels. We use these channels to organize nanodopants.

Au NBPs with variable aspect ratios were synthesized using literature procedures and functionalized with binary ligand shells comprising alkyl and liquid-crystal-like thiols. This enables incorporation into helical channels of HNF.

$CsPbX_3$ perovskite nanocrystals were embedded using their native ligands.

Chiroptical properties were characterized by circular dichroism (CD) and circularly polarized luminescence (CPL) spectroscopies, as well as full Mueller-matrix polarimetry.

Local handedness was programmed by laser-directed recrystallization of the HNF-based composite film.

III. Results and Discussion

Films based on Au NBPs, organized within HNF channels, form helical assemblies, which induce plasmonic CD response with dissymmetry factors (g_{ext}) on the order of 10^{-2}. The response is spectrally tunable across the visible range by varying particle aspect ratio [1]. Electromagnetic simulations rationalize the observed CD sign and magnitude as a consequence of the plasmonic coupling within the three-dimensional helical arrangement of the nanoparticles [1].

Films based on $CsPbX_3$ halide perovskite nanocrystals emit circularly polarized luminescence across the visible spectrum with dissymmetry factors (g_{lum}) up to 0.24 [2]. This emission can be deconvoluted into two additive contributions: (i) intrinsic term arising from near-field chiral organization of the nanocrystals, and (ii) host-filtering term. Red-emitting perovskites reach the highest intrinsic dissymmetry [2].

Composite films can be locally recrystallized using laser writing, enabling the programming of pixels with opposite handedness (and chiroptical sign) [3].

IV. Conclusion

With this research, we establish a scalable route to chiral photonic films based on the organization of nanoparticles within liquid-crystalline helical scaffolds. Their chiroptical response can be tuned through nanoparticle choice, supramolecular organization, film processing, and laser-directed chirality writing.

Acknowledgments

This work was supported by the Foundation for Polish Science (FNP) within the project “BCP-LED: Bi-chiral sources of circularly polarized light” under the First Team programme, co-financed by the European Union under the European Funds for a Modern Economy 2021–2027 (FENG).

References

[1] Wasiluk et al., Adv. Funct. Mater., 2025, 35, 2500933.
[2] M. Pawlak et al., Angew. Chem. Int. Ed., 2026, 65, e07812.
[3] P. Szustakiewicz et al., Adv. Mater., 2024, 36, 2310197.

DNA-Origami-Assembled Rhodium Nanoantennas for Deep-UV Label-Free Single-Protein Detection

Nicco Corduri[1], Malavika Kayyil Veedu[2],Yifan Yu[3], Yanqiu Zou[4], Jie Liu[3], Denis Garoli[4,5,6], Guillermo P. Acuna[1,7], Jérôme Wenger[2], Karol Kołątaj[1,*]

[1] Department of Physics, University of Fribourg, Switzerland
[2] Aix Marseille Univ, CNRS, Centrale Méditerranée, Institut Fresnel, AMUTech, France
[3] Department of Chemistry, Duke University, North Carolina, USA
[4] College of Optical and Electronic Technology, China Jiliang University, China
[5] Optoelectronics, Istituto Italiano di Tecnologia, Genova, Italy
[6] Dipartimento di Scienze e Metodi dell'Ingegneria, Università di Modena e Reggio Emilia, Via Amendola 2 Padiglione Tamburini, Italy
[7] Swiss National Center for Competence in Research (NCCR) Bio-Inspired Materials, University of Fribourg, Switzerland
Corresponding author: karol.kolataj@unifr.ch

***Abstract*— In this work, we demonstrate the fabrication of plasmonic nanoantennas operating in the deep ultraviolet. A ligand exchange protocol enables DNA functionalization of rhodium nanoparticles and their precise positioning on DNA origami, yielding reproducible structures that enable label-free and highly specific fluorescence detection of single proteins.**

***Keywords*— UV-plasmonics, single-molecule detection, DNA origami, rhodium nanocubes**

I. Introduction

Plasmonic nanostructures enhance light–matter interactions by localizing electric field at the nanoscale, enabling highly sensitive spectroscopic techniques. DNA origami provides a powerful bottom-up approach for constructing such systems, allowing programmable and precise positioning of nanoparticles and biomolecules with nanometer accuracy, and enabling reproducible plasmonic architectures.[1]

While most plasmonic systems rely on gold and silver and operate in the visible range, extending plasmonics into the ultraviolet (UV) is highly desirable, as many biomolecules exhibit strong intrinsic absorption and autofluorescence in this spectral range, enabling label-free detection.[2] Rhodium is an especially promising material in this regard due to its plasmonic response in the UV and high colloidal stability;[3] however, its integration into well-defined nanoarchitectures remains limited. Here, we address this challenge by combining rhodium nanoparticles with DNA origami to realize precisely engineered UV plasmonic nanoantennas for single-protein fluorescence detection.

II. Results and Discussion

First, we developed a ligand exchange protocol enabling DNA functionalization of rhodium nanocubes through removal of the native PVP ligand, followed by attachment of thiolated DNA strands. This approach yields functional nanoparticles with a surface DNA density of ~0.05 molecules nm^{-2}, enabling reliable integration into DNA origami structures.

Second, DNA origami scaffolds were used to assemble rhodium nanocubes into dimer nanoantennas with a high yield of 69% and an average interparticle gap of 10.7 ± 3.2 nm, ensuring reproducible hotspot formation and controlled plasmonic coupling (see Fig. 1a, b).

The functionality of the nanoantennas was demonstrated through single-molecule autofluorescence measurements of native streptavidin selectively positioned in the nanogap. The nanoantennas exhibit fluorescence enhancement of up to 22× (see Fig. 1c), accompanied by a reduction of the fluorescence lifetime and 10× increase in the total photon budget, enabling robust label-free detection of single proteins.

Finally, numerical simulations reproduce the experimental observations, confirming strong field confinement within the dimer nanogap with fluorescence enhancement of up to ~24× under optimal polarization. Beyond the experimentally realized face-to-face configuration, additional simulations of edge-to-edge and tip-to-tip geometries predict even stronger near-field enhancements, highlighting the potential for further performance optimization through geometry control.

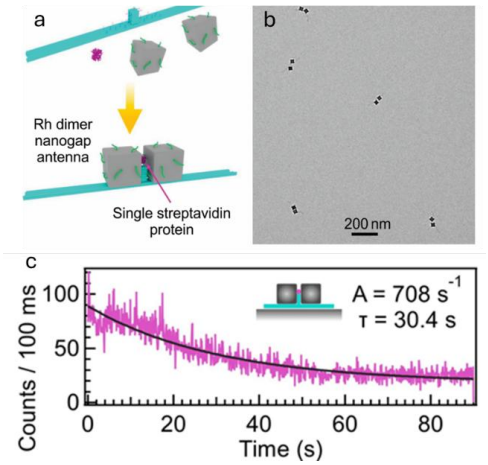

Fig. 1 a) Schematic representation of the Rh nanocube dimer synthesis b) TEM of the obtained structures, and c) representative fluorescence spectra of a single streptavidin in the dimer.

III. Conclusion

In summary, we demonstrate a DNA origami–based strategy for assembling rhodium nanocube dimers as plasmonic nanoantennas operating in the deep UV. A tailored ligand exchange protocol enables efficient DNA functionalization and reproducible assembly with yields up to 69%. The nanoantennas enable deterministic single-protein positioning and label-free detection via enhanced UV autofluorescence, with brightness enhancements of up to 22×.

Overall, this work extends DNA-origami plasmonics into the ultraviolet regime and provides a platform for label-free single-molecule spectroscopy.

Acknowledgments

G. P. A. and D. G. acknowledge funding from the European Union Program HORIZON-Pathfinder-Open: 3D-BRICKS, grant Agreement 101099125 and from the Swiss State Secretariat for Education, Research and Innovation (SERI) contract number 23.00075. M.K.V., J.W. and D.G. acknowledge funding from the European Research Executive Agency (REA) under the Marie Skłodowska-Curie Actions doctoral network program (Grant Agreement No. 101072818). Y.Y. and Y.Z. acknowledge funding from the U.S. National Science Foundation (Grant No. CHE-1954838).

References

[1] Kuzyk, A.; Jungmann, R.; Acuna, G. P.; Liu, N. DNA Origami Route for Nanophotonics. *ACS Photonics* **2018**, *5* (4), 1151–1163. https://doi.org/10.1021/acsphotonics.7b01580.

[2] Zhao, D.; Lin, Z.; Zhu, W.; Lezec, H. J.; Xu, T.; Agrawal, A.; Zhang, C.; Huang, K. Recent Advances in Ultraviolet Nanophotonics: From Plasmonics and Metamaterials to Metasurfaces. Nanophotonics 2021, 10 (9), 2283–2308. https://doi.org/10.1515/nanoph-2021-0083.

[3] Xu, L.; Liu, D.; Chen, D.; Liu, H.; Yang, J. Size and Shape Controlled Synthesis of Rhodium Nanoparticles. Heliyon 2019, 5 (1), e01165. https://doi.org/10.1016/j.heliyon.2019.e01165

Deterministic Strain Engineered Quantum Emitters in Two Dimensional Semiconductors

Snežana Lazića[1,*], Sanja Đurđić Mijina[1,2]

[1] Departamento de Física de Materiales, Instituto 'Nicolás Cabrera' and Instituto de Física de Materia Condensada (IFIMAC), Universidad Autónoma de Madrid (UAM), 28049 Madrid, Spain

[2] Institute of Physics Belgrade, University of Belgrade, Pregrevica 118, 11080 Belgrade, Serbia USA

*Corresponding author: lazic.snezana@uam.es

***Abstract*— We present a cost-efficient method to create deterministic quantum emitters in two-dimensional semiconductors using localized strain induced by dielectric microparticles. The approach enables spatial control of nanoscale light sources with single photon emission and exciton biexciton cascades for quantum photonic applications.**

***Keywords*— quantum emitters, two-dimensional semiconductors, strain engineering, excitons, quantum photonics.**

I. Introduction

Two-dimensional semiconductors are emerging as a powerful platform for nanoscale light sources due to their strong excitonic response and mechanical flexibility. However, scalable and deterministic positioning of quantum emitters remains a major challenge for their use in photonic and optoelectronic systems.

II. Methods

Few layer GaSe and WSe_2 flakes were mechanically exfoliated from bulk crystals and transferred using an all-dry viscoelastic stamping method onto Si substrates coated with a 300 nm thick SiO_2 layer. The substrates were pre-decorated with optically active $LiYF_4:Nd^{3+}$ microparticles that were randomly dispersed on the surface. These microparticles have a square based bipyramidal geometry with sharp edges and corners and typical lateral dimensions of about 2 to 3 µm.

The bipyramidal geometry of the microparticles is critical, since the sharp corners induce strong localized bending of the two-dimensional flakes when the flakes conform to the particle surface. This produces highly localized strain gradients that locally modify the GaSe bandgap and create deep exciton trapping potentials. In addition, the optical activity of the Nd^{3+} doped microparticles provides a built-in reference signal at around 1.436 eV, which allows to determine the exact position of each microparticle and thus of the strain field to be identified using standard micro photoluminescence spectroscopy without the need for scanning electron or atomic force microscopy.

Low temperature optical characterization was performed at 10 K using a continuous wave 532 nm laser line focused to a spot of about 1.5 µm. The emitted photoluminescence was collected by the same microscope objective and analyzed using a grating spectrometer and a cooled CCD detector. Polarization-resolved measurements were performed using a half-wave plate and a beam displacing prism. Photon correlation measurements were carried out using a Hanbury Brown and Twiss interferometer with two single photon avalanche detectors and time correlated single photon counting electronics.

The sample fabrication, microparticle geometry, and optical identification of the strain sites are illustrated in Fig. 1 and described in detail in Ref. [1].

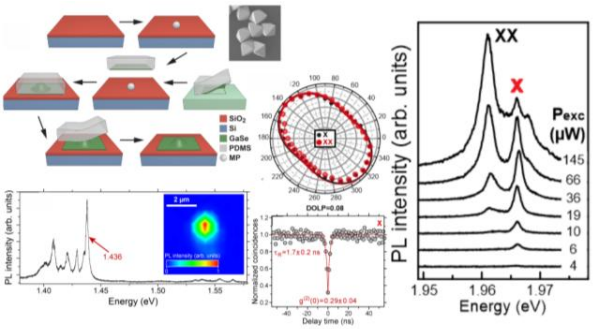

Fig. 1: Fabrication and optical characterization of strain induced quantum emitters in GaSe using bipyramidal dielectric $LiYF_4:Nd^{3+}$ microparticles, showing localized emission, polarization, photon antibunching and exciton (X) and biexciton (XX) features.

III. Results and Discussion

When GaSe flakes are transferred onto the $LiYF_4:Nd^{3+}$ microparticles, they conform to the particle surface and bend strongly at the sharp corners. Optical microscopy reveals clear color and contrast changes in these regions, indicating

significant local deformation. Micro-photoluminescence spectra measured on strained regions differ strongly from those recorded on unstrained parts of the same flake, which show only broad emission characteristic of multilayer GaSe.

At the strain maxima, narrow emission lines appear on top of the broad background. Spatial mapping of the photoluminescence integrated over these narrow lines shows that the emission is confined to regions smaller than 1 μm and centered on the microparticle corners, demonstrating that the excitons are funneled toward the maximum strain regions where they become trapped in a localized potential well.

Power dependent measurements reveal that the dominant emission line labeled X grows approximately linearly or sub-linearly with excitation power, while a second line labeled XX appears at higher power and increases quadratically. This behavior identifies the two lines as exciton (X) and biexciton (XX) recombination, respectively, from the same localized emitter. Polarization-resolved measurements show that both X and XX lines are elliptically polarized with the same polarization axis and degree, further confirming that they originate from a single quantum confined state.

The energy separation between the X and XX lines corresponds to a biexciton binding energy of approximately 5 meV. Using a standard quantum confinement model, this value corresponds to an effective trap radius of about 13 nm, indicating that the strain induced potential created by the microparticle corners acts as a true nanoscale quantum dot within the two-dimensional crystal.

Photon correlation measurements performed on the isolated emission lines show strong antibunching with $g^{(2)}(0)<0.3$, which approaches zero after background correction. This demonstrates that each strain induced site acts as a single photon emitter. The measured decay times of 1 to 3 ns are consistent with excitonic recombination in GaSe quantum emitters.

Representative optical spectra, polarization and photon correlation data of the strain induced emitters are shown in Fig. 1 and discussed in Ref. [1].

Importantly, measurements on multiple microparticles and different flakes yield consistent results, and the brightest emitters are always found at the positions of maximum strain created by the microparticle corners. This shows that the emitter formation is governed by particle geometry and provides a pathway toward controlling emitter position and density by engineering the shape and placement of the microparticles.

IV. Conclusion

We demonstrate a scalable and lithography free method to engineer quantum light sources in two-dimensional materials using strain fields. This platform provides cost-efficient deterministic optical emitters for nanophotonic and optoelectronic systems based on layered semiconductors.

Acknowledgments

This work was supported by the Spanish MCIU through the projects PID2020 113415RB C21 and TED2021 129666B C21. The authors thank Patricia Haro Gonzalez (UAM) for assistance with microparticles.

References

[1] S. Djurdjić Mijin, I. dePedro-Embid, N. Panov, E. Hemmer and S. Lazić, Cost-Efficient Deterministic Engineering of Single Photon Emitters in Two-Dimensional Materials. ACS Appl. Mater. Interfaces 17, 31306 (2025).

Metasurface modeling from Microwave to Optics

Solving the Helmholtz equation with waveguide-based metatronic circuits.

Ross G. MacDonald[1], Alex Yakovlev[2] and Victor Pacheco-Peña[1,*]

[1]School of Mathematics, Statistics and Physics, Newcastle University, Newcastle Upon Tyne, NE1 7RU, United Kingdom

[1]School of Engineering, Newcastle University, Newcastle Upon Tyne, NE1 7RU, United Kingdom

*Corresponding author: victor.pachecopena@gmail.com

***Abstract*— Arrays of waveguide-based metatronic circuits are used to solve the Helmholtz equation. The analogy between the behavior of the network and a finite difference mesh is established and implemented to produce solutions to Dirichlet boundary value problems. It may also be applied to solve open boundary value problems such as the scattering or focusing of waves.**

***Keywords*— Analog computing, wave-based computing, metamaterials, metatronic circuits.**

I. Introduction

Electromagnetic (EM) wave-based structures have opened alternative directions for computing as they enable high speed [1] and parallelization of calculations [2, 3]. Examples of operations using EM wave-based analog processors include differentiation [4-6], convolution [7], vector-matrix multiplication [8], integral equation solving [9, 10] and partial differential equation (PDE) solving [11-14], to name a few [15, 16].

Historically, analog PDE solvers have been implemented by exploiting networks of lumped circuit elements [17, 18]. In such networks, the solution of a PDE is carried out by emulating the performance of a typical finite difference mesh used by numerical solvers. Similar approaches have also been exploited to produce PDE solutions at higher frequencies by exploiting photonic integrated circuits [12] and epsilon-near-zero media [13]. Recently, metatronic circuits [19], nanoscale structures which emulate the behavior of lumped elements, have made possible the translation of well-known circuit theory concepts to the EM/photonics realm [13, 20-22]

Inspired by the potential of metatronic circuits, in this work we demonstrate the possibility to solve PDEs in the form of the Helmholtz equation. This is done by using a grid-like network of metatronic filters emulating the behavior of T-circuits [14]. As will be discussed in the conference, by tailoring the effective impedance values of the metatronic filters, accurate solutions to a range of PDE problems may be calculated. The possibility to solve Dirichlet boundary value problems and "open" boundary problems will also be presented.

II. Methods

A schematic depicting the operating principle of the PDE solving network is presented in Fig. 1a. The network consists of an array of metatronic T-circuits connected in series to form a regular grid. Each metatronic T-circuit (Fig. 1b, left panel) is composed of three dielectric (or metallic) slabs embedded into a parallel plate waveguide at $\lambda/4$ intervals (λ being the wavelength of the operating signal within the waveguide). In this way, the whole waveguide structure acts as a metatronic filter emulating the behavior of a T-circuit with series and parallel impedances Z_s and Z_p (Fig. 1b, right panel) [18, 21, 22]. A schematic showing the electrical network being emulated by the proposed network is presented in the middle panel of Fig. 1a.

But how can this network be used to solve PDEs? As it can be seen, the T-circuits are connected in series at junctions [23-25]. Considering the division of current through each connecting T-circuit and applying Kirchoff's voltage law at each junction, the following equation can be obtained:

$$|Z_p|^2\left(-4I_{i,j}+\sum\nolimits_{x\in A} I_x\right)=4Z_p^*Z_sI_{i,j} \qquad (1)$$

where $I_{i,j}$ is the current rotating around the junction at position i,j, and $A\in\{(i,j+1),(i,j-1),(i+1,j),(i-1,j)\}$ is the set containing junctions adjacent to i,j. Now consider the following substitution into Eq. 1: $|Z_p|=1/h$ and $4Z_p^*Z_s=-k^2$. From this, Eq. 1 yields the standard five-point, second-order central-difference [26] form of the Helmholtz equation, with h as the grid spacing and k the wavenumber. This means that the rotating current distribution (and magnetic field distribution) of the network will thus conform to and solve a discretized form of the Helmholtz equation with parameters determined by the impedances of the metatronic circuit elements.

Dirichlet boundary conditions may be enforced by applying external signals to the outermost junctions of the network (called *boundary junctions*) and PDE solutions may be

extracted by measuring the out-of-plane magnetic field at the center of each junction.

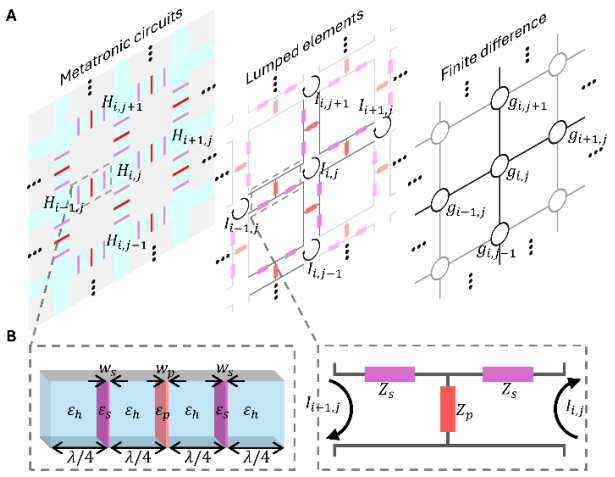

Fig. 1 **a**. Operating principle of the PDE solving network. (Left) Schematic representation. (Middle) Equivalent circuit model. (Right) Schematic of the equivalent Finite difference mesh. **b**. Metatronic circuit (left) that emulates a T-circuit (right)

III. Results and Discussion

As an example, we provide the results shown in Fig. 2 for a Dirichlet boundary value problem. A 25×25 network is used with metatronic elements designed to emulate the impedances $Z_s = 0.225i$ and $Z_p = -10i$ (corresponding to $h = 0.1$, $k = 3$), is used. The external signals are applied such that the signal at each *boundary junction* has the same magnetic field value ($H = 1$, arb. units). A scattering obstacle (a metallic cube) is inserted into the PDE problem as an example. It is placed at the center of the simulation region. This is implemented in the PDE network by removing connections between junctions at the center of the waveguide network. With this configuration, the theoretical results of the PDE solution produced by the waveguide network are presented in Fig. 2a. For comparison, the analytical solution to this problem [produced using a finite element method (FEM) simulation tool (MATLABs® Partial Differential Equation Toolbox™)], is also provided (Fig. 2a, right panel). As can be seen, there is a clear agreement between the theoretical and analytical results, indicating that the PDE solving network is indeed producing an accurate solution. This agreement is also evidenced in Fig. 2b where a comparison between the results is presented by extracting the magnetic field along a diagonal line from the results in Fig. 2a. These results demonstrate the potential of this approach to solve Dirichlet boundary value problems. Further analysis and examples will be provided during the conference including the possibility tosolve open boundary value problems.

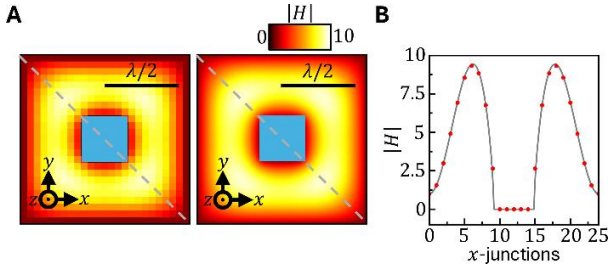

Fig. 2 **a**. Example solution of a Dirichlet boundary value problem. (Left) Theoretical and (right) analytical results showing the absolute value of magnetic field using a 25×25 network. **b.** 2D plot showing the extracted $|H|$ from panel **a** along a diagonal line for both numerical and analytical results.

IV. Conclusion

In this work, solutions to PDEs in the form of the Helmholtz equation have been calculated using networks of metatronic circuits. An example included the calculation of a Dirichlet boundary value problem with an obstacle. We envision this technique may open opportunities for analog PDE solving at different wavelengths as the approach may be transferable across different frequency regimes.

Acknowledgments

This work was supported by the Leverhulme Trust under the Leverhulme Trust Research Project Grant scheme (RPG-2023-024).

References

[1] F. Zangeneh-Nejad, D. L. Sounas, A. Alù, and R. Fleury, "Analogue computing with metamaterials," *Nat. Rev. Mater.*, vol. 6, no. 3, pp. 207–225, Oct. 2020.

[2] A. Momeni, K. Rouhi, and R. Fleury, "Switchable and simultaneous spatiotemporal analog computing with computational graphene-based multilayers," *Carbon N. Y.*, vol. 186, pp. 599–611, Jan. 2022.

[3] H. Rajabalipanah, A. Momeni, M. Rahmanzadeh, A. Abdolali, and R. Fleury, "Parallel wave-based analog computing using metagratings," *Nanophotonics*, vol. 11, no. 8, pp. 1561–1571, May 2022.

[4] R. G. MacDonald, A. Yakovlev, and V. Pacheco-Peña, "Time derivatives via interconnected waveguides," *Sci. Rep.*, vol. 13, no. 1, p. 13126, Aug. 2023.

[5] T. Knightley, A. Yakovlev, and V. Pacheco-Peña, "Neural Network Design of Multilayer Metamaterial for Temporal Differentiation," *Adv. Opt. Mater.*, vol. 11, no. 5, p. 2202351, Mar. 2023.

[6] T. Zhu *et al.*, "Plasmonic computing of spatial differentiation," *Nat. Commun.*, vol. 8, no. 1, p. 15391, Aug. 2017.

[7] M. Park and Y. Park, "Metasurface-Based Imagers Enabled Arbitrary Optical Convolution Processing," *Light Sci. Appl.*, vol. 11, no. 1, p. 98, Apr. 2022.

[8] V. Nikkhah, A. Pirmoradi, F. Ashtiani, B. Edwards, F. Aflatouni, and N. Engheta, "Inverse-designed low-index-contrast structures on a silicon photonics platform for vector–matrix multiplication," *Nat. Photonics*, vol. 18, no. 5, pp. 501–508, May 2024.

[9] D. C. Tzarouchis, M. J. Mencagli, B. Edwards, and N. Engheta, "Mathematical operations and equation solving with reconfigurable metadevices," *Light Sci. Appl.*, vol. 11, no. 1, p. 263, Sep. 2022.

[10] N. Mohammadi Estakhri, B. Edwards, and N. Engheta, "Inverse-designed metastructures that solve equations," *Science (1979).*, vol. 363, no. 6433, pp. 1333–1338, Mar. 2019.

[11] J. Anderson *et al.*, "Virtualizing a Post-Moore's Law Analog Mesh Processor: The Case of a Photonic PDE Accelerator," *ACM Transactions on Embedded Computing Systems*, vol. 22, no. 2, pp. 1–26, Mar. 2023.

[12] S. Sun *et al.*, "Induced homomorphism: Kirchhoff's law in photonics," *Nanophotonics*, vol. 10, no. 6, pp. 1711–1721, Apr. 2021.
[13] M. Miscuglio *et al.*, "Approximate analog computing with metatronic circuits," *Commun. Phys.*, vol. 4, no. 1, p. 196, Aug. 2021.
[14] R. G. MacDonald, A. Yakovlev, and V. Pacheco-Peña, "Solving partial differential equations with waveguide-based metatronic networks," *Advanced Photonics Nexus*, vol. 3, no. 05, p. 056007, Oct. 2024.
[15] W. Rogers, C. Johnson-Richards, A. Yakovlev, and V. Pacheco-Peña, "Perfect splitting in rectangular-waveguide junctions for analog computing," *Phys. Rev. Appl.*, vol. 21, no. 5, p. 054054, May 2024.
[16] C. Johnson-Richards, A. Yakovlev, and V. Pacheco-Peña, "Topological Valley Photonic Waveguides: Scattering Matrix Evaluation for Linear Computing," *Adv. Photonics Res.*, vol. 6, no. 11, Nov. 2025.
[17] G. Kron, "Electric circuit models of partial differential equations," *Electrical Engineering*, vol. 67, no. 7, pp. 672–684, Jul. 1948.
[18] Y. D. Save, H. Narayanan, and S. B. Patkar, "Solution of Partial Differential Equations by electrical analogy," *J. Comput. Sci.*, vol. 2, no. 1, pp. 18–30, Mar. 2011.
[19] N. Engheta, "Circuits with Light at Nanoscales: Optical Nanocircuits Inspired by Metamaterials," *Science (1979).*, vol. 317, no. 5845, pp. 1698–1702, Sep. 2007.
[20] A. Alù and N. Engheta, "Tuning the scattering response of optical nanoantennas with nanocircuit loads," *Nat. Photonics*, vol. 2, no. 5, pp. 307–310, May 2008.
[21] Y. Li, I. Liberal, C. Della Giovampaola, and N. Engheta, "Waveguide metatronics: Lumped circuitry based on structural dispersion," *Sci. Adv.*, vol. 2, no. 6, pp. 1–8, Jun. 2016.
[22] W. Sun, X. Qin, H. Li, Z. Zhou, and Y. Li, "Impedance matching via ultrathin metatronic layer assisted by Smith Chart.," *Opt. Express*, vol. 30, no. 14, pp. 25567–25580, Jul. 2022.
[23] A. Yakovlev and V. Pacheco-Peña, "Enabling High-Speed Computing with Electromagnetic Pulse Switching," *Adv. Mater. Technol.*, vol. 5, no. 12, p. 2000796, Dec. 2020.
[24] V. Pacheco-Peña and A. Yakovlev, "Computing with Square Electromagnetic Pulses," in *Handbook of Unconventional Computing,* 1st ed., A. Adamatzky, Ed., London: World Scientific, 2021, pp. 465–492.
[25] R. G. MacDonald, A. Yakovlev, and V. Pacheco-Peña, "Amplitude-Controlled Electromagnetic Pulse Switching Using Waveguide Junctions for High-Speed Computing Processes," *Advanced Intelligent Systems*, vol. 4, no. 12, p. 2200137, Dec. 2022.
[26] S. Mazumder, "The Finite Difference Method," in *Numerical Methods for Partial Differential Equations*, vol. M, Elsevier, 2016, pp. 51–101.

Local-Based Synthesis of Reconfigurable Huygens' Metasurfaces for Beam Steering

Stefano Vellucci*[1], Alessio Monti[2], Mirko Barbuto[2], Alessandro Toscano[2], Filiberto Bilotti[2]

[1]Department of Engineering, Niccolò Cusano University, 00166, Rome, Italy
[2]Department of Industrial, Electronic and Mechanical Engineering, ROMA TRE University, 00146 Rome, Italy
*Corresponding author: stefano.vellucci@unicusano.it

***Abstract*—This work presents a dual-state multi-objective optimization framework for the local impedance synthesis of reconfigurable transmissive Huygens' metasurfaces. The approach enforces distinct transmission phase transformations while preserving high efficiency within a fixed multilayer architecture. Two array-based examples validate the proposed modeling-driven design strategy.**

***Keywords*— Huygens' metasurface, beam-steering, reconfigurable metasurface.**

I. Introduction

Reconfigurable Huygens' metasurfaces (HMSs) have attracted significant attention as compact platforms for adaptive wavefront manipulation from microwave to optical frequencies [1]-[3]. In most reported implementations, reconfigurability is achieved through full-wave optimization of tunable unit cells integrated with active components, biasing networks, and vertical interconnections (vias) to independently control electric and magnetic responses [4]-[6]. Such approaches typically require multilayer architectures and geometry-specific co-design, increasing structural complexity and reducing physical transparency of the synthesis process.

In this contribution, we focus instead on a modeling-oriented perspective and present a local synthesis framework for reconfigurable transmissive Huygens' metasurfaces based on an analytical matrix formulation and dual-state multi-objective optimization framework. The approach directly links the desired macroscopic wave transformation to the required surface impedance profiles. Reconfigurability is introduced at the modeling level through discrete impedance states, emulating ideal PIN-diode switching.

Two representative numerical examples are presented. The first demonstrates ON/OFF beam steering enabled by switching between uniform and phase-gradient transmission profiles. The second shows how a reconfigurable metasurface can be employed to extend the scan range of sparse antenna arrays beyond the conventional grating-lobe limit. In both cases, the metasurface is treated as an ideal multilayer Huygens structure synthesized through a matrix-based local design procedure.

II. Local Modeling and Synthesis

The proposed approach models the reconfigurable Huygens' metasurface at the impedance level using a multilayer transmission-matrix formulation. Each unit cell is described as a cascade of reactive impedance sheets separated by identical dielectric spacers. In the case of a three-layered configuration, under normal plane-wave illumination, the overall unit-cell transmission matrix is expressed as [7],[8]:

$$\mathbf{T}_{\mathrm{UC}} = \mathbf{T}_{Z_{s,3}}\mathbf{T}_{d}\mathbf{T}_{Z_{s,2}}\mathbf{T}_{d}\mathbf{T}_{Z_{s,1}},$$

from which the transmission coefficient is obtained as [9]:

$$S_{21} = \frac{2}{A + B/\eta_0 + \eta_0 C + D},$$

where A, B, C, D are the entries of $\mathbf{T}_{\mathrm{UC}}$ and η_0 is the free-space impedance. This compact relation directly links the surface impedances $Z_{s,n}$ to the transmission phase ϕ and magnitude, enabling local synthesis without specifying the physical geometry of the unit cell.

A prescribed wave transformation is achieved by assigning distinct impedance triplets $\left\{Z_{s,1}^{(m)}, Z_{s,2}^{(m)}, Z_{s,3}^{(m)}\right\}$ to the unit cells forming one supercell of spatial period Λ. For anomalous refraction toward angle θ_t, the discrete phase distribution is chosen consistently with the grating condition [10]:

$$\sin\,\theta_p = \frac{p\lambda_0}{\Lambda},$$

so that the desired transmitted beam corresponds to a selected Floquet order [11]. Reconfigurability is introduced by constraining the multilayer architecture to remain unchanged while allowing only the first reactive sheet to switch between two impedance values:

$$Z_{s,1}^{(ON)} \text{and } Z_{s,1}^{(OFF)},$$

emulating ideal PIN-diode control. The remaining sheets $Z_{s,2}$ and $Z_{s,3}$ are invariant across states. This constraint enforces structural invariance while enabling two distinct transmission

responses. The synthesis problem is formulated as a multi-objective optimization directly in the impedance domain. For each unit cell m, two transmission states are simultaneously enforced: (i) a refracting state (OFF) with transmission phase $\phi_{OFF}^{(m)} = \phi_{\text{target}}^{(m)}$, ($ii$) a transparent state (ON) with uniform transmission phase $\phi_{ON}^{(m)} = \phi_{\text{ref}}$. The cost function is defined as:

$$F^{(m)} = w_1 \mid \phi_{OFF}^{(m)} - \phi_{\text{target}}^{(m)} \mid + w_2 \mid \phi_{ON}^{(m)} - \phi_{\text{ref}} \mid$$

$$+ w_3 P(\mid S_{21,ON}^{(m)} \mid) + w_4 P(\mid S_{21,OFF}^{(m)} \mid),$$

where $P(\cdot)$ penalizes transmission magnitudes below a prescribed threshold and w_i are weighting coefficients.

This formulation enforces that the same multilayer unit cell satisfies two independent electromagnetic transformations through impedance switching of a single layer. Such a local multi-objective synthesis provides physically interpretable solutions while avoiding full-wave supercell optimization. The resulting impedance sets can then be directly implemented as ideal boundary conditions for system-level simulations.

III. Numerical Examples

The impedance sets obtained through the above dual-state synthesis are next employed as ideal boundary conditions in full-wave simulations to assess the macroscopic response of metasurface for beam-steering applications. In the following section, two representative numerical scenarios are presented to validate the modeling framework.

As a first example, we consider a transmissive Huygens' metasurface designed to operate at a fixed frequency under normal plane-wave illumination. Using the matrix synthesis procedure, two impedance configurations are derived for the same multilayer structure. In the OFF state, the synthesized impedances produce a spatially uniform transmission phase, resulting in broadside radiation. In the ON state, the impedance of a single reactive layer is modified, leading to a linear phase gradient across the aperture corresponding to a steering angle of 30°.

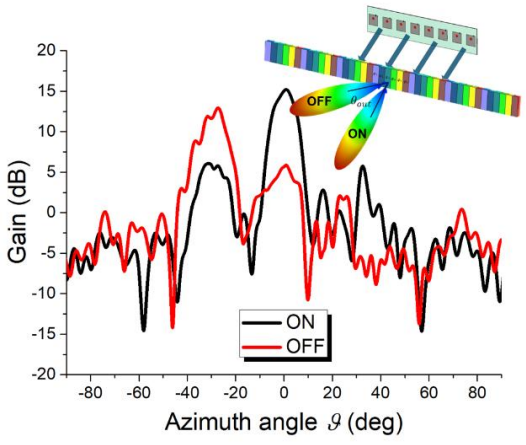

Fig. 1 Reconfigurable metasurface for beam-steering in broadside-arrays.

The metasurface is modeled in full-wave simulations using impedance boundary conditions derived from the matrix synthesis. The results show that the OFF state preserves the incident beam direction with negligible reflection, while the ON state produces a single transmitted Floquet mode at the prescribed angle. Since the electric and magnetic responses remain balanced in both states, good transmission efficiency is maintained and backscattering is suppressed.

In the second example, the matrix-synthesized metasurface is employed in conjunction with a sparse linear antenna array whose element spacing exceeds half a wavelength. In such arrays, grating lobes limit the maximum achievable scan angle.

The metasurface is designed to exhibit two states. In the first state, it provides nearly uniform transmission and therefore does not alter the array radiation when scanning near broadside. In the second state, the synthesized impedance profile introduces an additional phase gradient, effectively adding a fixed angular tilt to the transmitted field.

When the array is electronically steered toward large angles, activating the phase-gradient state results in a total beam direction approximately equal to the sum of the array scan angle and the metasurface-induced deflection. Full-wave simulations of the array combined with the impedance-sheet model demonstrate that the effective scan range can be extended beyond the nominal grating-lobe limit of the bare array. At broadside, the metasurface can be switched to the uniform state, ensuring that the radiation pattern remains unperturbed.

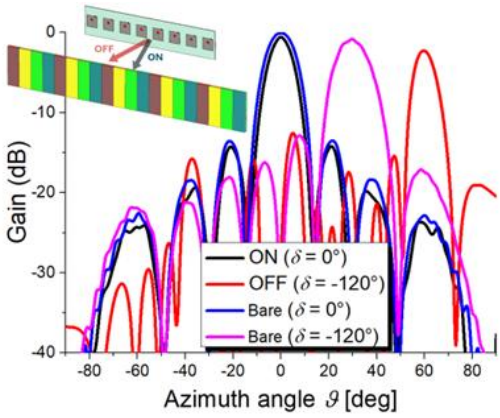

Fig. 2 Reconfigurable metasurface for extending the scanning range of sparse arrays.

IV. Conclusion

A local matrix-based modeling and synthesis framework for reconfigurable transmissive Huygens' metasurfaces has been presented. By exploiting a multilayer transmission-matrix formulation, the required impedance states corresponding to different wave transformations can be derived analytically and implemented as discrete switching configurations. Two numerical examples have been reported and the preliminary numerical results show that this approach enables both ON/OFF

beam steering and scan-range extension of sparse arrays. The methodology is general and applicable across frequency regimes, providing a unified modeling tool for reconfigurable metasurface design from microwave to optics.

ACKNOWLEDGMENTS

This work has been developed in the frame of the research contracts: "MEETAPP" PRIN 2022 (protocol number 2022ZZ8APA) funded by the Italian Ministry of University and Research.

REFERENCES

[1] F. Bilotti et al., "Reconfigurable intelligent surfaces as the keyenabling technology for smart electromagnetic environments", Adv. Phys. X, vol. 9, no. 1, pp. 1-47, 2024.
[2] Z. Pourgholamhossein and T. A. Denidni, "Reconfigurable Huygens' Metasurface-Based Unit-Cell and Electronically Steerable Active Flat-Lens Antenna at the Ka-Band," IEEE Trans. Antennas Propag., vol. 73, no. 5, pp. 2791-2803, 2025.
[3] Chen K, Feng Y, Monticone F, Zhao J, Zhu B, Jiang T, Zhang L, Kim Y, Ding X, Zhang S, Alù A, Qiu CW. "A Reconfigurable Active Huygens' Metalens". Adv Mater., 29, 17, 2017.
[4] X. Wang, P. -Y. Qin, A. Tuyen Le, H. Zhang, R. Jin and Y. J. Guo, "Beam Scanning Transmitarray Employing Reconfigurable Dual-Layer Huygens Element," IEEE Trans. Antennas Propag., vol. 70, no. 9, pp. 7491-7500, Sept. 2022.
[5] S. Vellucci et al., "Phase-Gradient Huygens Metasurface Coatings for Dynamic Beamforming in Linear Antennas," IEEE Trans. Antennas Propag, vol. 71, no. 10, pp. 7752-7765, Oct. 2023.
[6] V. G. Ataloglou et al., "Static and Reconfigurable Huygens' Metasurfaces: Use in Antenna Beamforming and Beam Steering," IEEE Antennas Propag. Mag., vol. 64, no. 4, pp. 73-84, Aug. 2022.
[7] D.M. Pozar, Microwave Engineering. John Wiley & Sons Inc, 2011.
[8] C. Pfeiffer and A. Grbic, "Cascaded metasurfaces for complete phase and polarization control," Appl. Phys. Lett. 102, 231116 (2013).
[9] A. Monti et al., "Quadratic-Gradient Metasurface-Dome for Wide-Angle Beam-Steering Phased Array With Reduced Gain Loss at Broadside" IEEE Trans. Antennas Propag., vol. 71, no. 2, pp. 2022-2027, Feb. 2023.
[10] N. Yu et al., "Light propagation with phase discontinuities: Generalized laws of reflection and refraction," Science, vol. 334, no. 6054, pp. 333–337, 2011.
[11] S. Larouche and D. R. Smith, "Reconciliation of generalized refraction with diffraction theory," Opt. letters, 37, 436 2391–2393, 2012.

Nonlinear Coupling between Nonlocal Resonances in a High-Contrast Grating Metasurface

Paolo Franceschini[1,2,*], Andrea Tognazzi[2,3], Evgenii Menshikov[1,4], Leonid Y. Beliaev[5], Radu Malureanu[5,6], Osamu Takayama[5], Ivano Alessandri[1,2], Alfonso C. Cino[3], Domenico de Ceglia[1,2] Andrei V. Lavrinenko[5], Costantino De Angelis[1,2]

[1]Department of Information Engineering, University of Brescia, Brescia, Italy
[2]National Institute of Optics-National Research Council, Brescia, Italy
[3]Department of Engineering, University of Palermo, Palermo, Italy
[4]School of Physics and Engineering, ITMO University, St. Petersburg, Russia
[5]Department of Electrical and Photonics Engineering, Technical University of Denmark, Kongens Lyngby, Denmark
[6]DTU Nanolab, National Centre for Nano Fabrication and Characterization, Kongens Lyngby, Denmark
*Corresponding author: paolo.franceschini@unibs.it

***Abstract*—Here we report on the nonlinear coupling between two nonlocal resonances with different nature (*i.e.*, a guided mode resonance and a quasi bound state in the continuum) via third-order nonlinear generation of radiation in a silicon-based high-index contrast metasurface.**

***Keywords* nonlocal metasurface, guided mode resonance, bound state in the continuum, four-wave mixing.**

I. Introduction

Metasurfaces, *i.e.*, spatially engineered distributions of nanoscatterers with sub-wavelength size, represent a powerful platform for the manipulation of phase, amplitude, and polarization state of the incident light and they find applications in various fields ranging from telecommunications, nonlinear optics, to biophotonics [1], [2], [3].

The foundation of their performances rely on their capability of confining the electric field within the nanoscatterer, thus giving rise to a resonant mode, which can be spatially extended or localized, over the metasurface itself. In the former case, which corresponds to the so-called nonlocal metasurfaces (*i.e.*, spatially extended modes) [4], one of the most important realization schemes is the high-contrast grating structure, which consists in the infinitely periodic structures composed by a high-valued refractive index material, thus ensuring large field enhancement. Moreover, this platform is of particular interest since it can host resonant nonlocal modes with different nature [5], whose spectral position can be selected by tuning the geometrical parameters of the constituent meta-atoms.

Here, we report on the nonlinear coupling between two nonlocal resonant modes, *i.e.*, a guided mode resonance (GMR) and a quasi bound-state in the continuum (qBIC), located in the near-infrared (NIR) spectral range. Upon illumination from a fundamental frequency (FF) broadband input radiation, the generated third-order nonlinear signal in the visible (VIS) comprises contributions due to sum four-wave mixing processes involving photons at GMR and qBIC.

II. Methods

The one-dimensional periodic high-contrast grating (period Λ) under analysis consists in the repetition of the unit cell sketched in Fig. 1a (top), which includes an amorphous-silicon (a-Si) bar (width w and heigth h) placed on top of an intermediate silicon dioxide (SiO_2) buffer layer (thickness t), supported by a cristalline silicon (Si) substrate. In addition, a thin cladding layer of poly(methyl methacrylate) (PMMA) has been employed as surrounding medium. The geometry of the unit cell has been tuned to obtain two nonlocal resonances, a GMR and a qBIC, in the spectral range corresponding to the third operating window of telecommunications. A metasurface with $\Lambda = 840$ nm, $w = 225$ nm, $h = 489$ nm, and $t = 1140$ nm has been fabricated [6].

III. Results and Discussion

The occurrence of the designed modes in the fabricated metasurface has been verified by linear spectroscopy by using a linearly polarized probe radiation, whose direction is parallel to the grating bars. The two peaks in the measured reflectance spectrum (Fig. 1b) at 1470 nm (LE, leaky) and at 1590 nm (BE, bounded) are ascribed to the GMR and qBIC modes, respectively, as confirmed by the field distribution maps (Fig. 1a, bottom). The third-order nonlinear coupling between the two resonant modes has been investigated by a nonlinear microscopy experiment in which the metasurface has been excited by a FF radiation (yellow solid line in Fig. 1b), whose broadband spectrum (~ 100 nm bandwidth) comprises both LE and BE. The spectrally-resolved third-order nonlinear radiation emitted in the VIS exhibits four peaks (Fig. 1c, right), which are ascribed to the four possible contributions resulting from sum four-wave mixing processes involving photons at LE and BE, as described by the diagrams in Fig. 1c (left) [6].

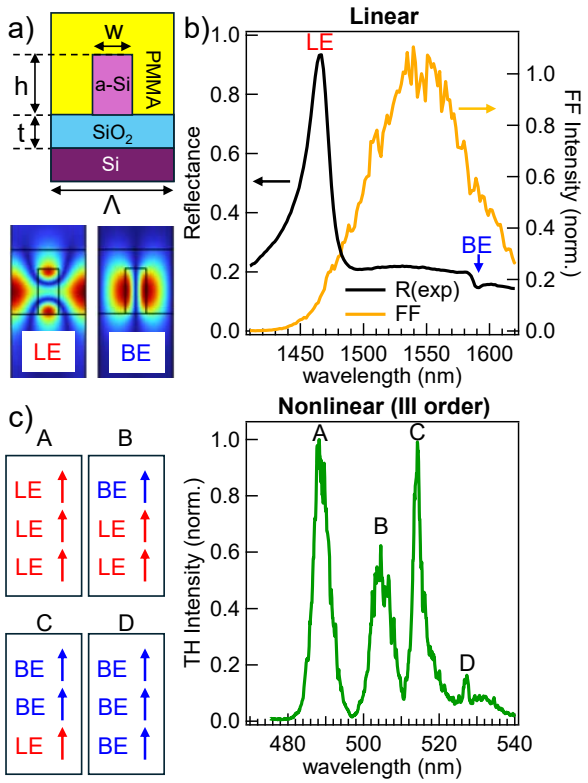

Fig. 1. (a) Top: sketch of the metasurface unit cell. Bottom: field distribution maps. (b) Linear reflectance spectrum (black solid line, left axis) of the fabricated metasurface together with the spectrum of the broadband FF beam (yellow solid line, right axis) employed for nonlinear generation. (c) Left: energy level diagrams of the four-wave mixing process terms. Right: spectrum of the third-order generated output radiation after illumination by the FF broadband beam in panel b.

IV. Conclusion

Our results demonstrate intrapulse four-wave sum mixing in a nonlocal metasurface by exploiting a GMR and a qBIC, thus supporting the application of high-contrast grating for the realization of compact nonlinear devices.

Acknowledgments

A. V. L. acknowledges the Independent Research Fund Denmark, DFF Research Project 2, ADaptive optics for ELEctron beams (ADELE) 2035-00126B. This work was partially supported by the European Union under the Italian National Recovery and Resilience Plan (NRRP) of NextGenerationEU, of partnership on Telecommunications of the Future (PE00000001 - program RESTART), S2 SUPER Programmable Networks, Cascade project PRISM - CUP: C79J24000190004. This work was partially supported by the project Smart Metasurfaces Advancing Radio Technology (SMART), CUP E63C22002040007.

References

[1] S. M. Kamali, E. Arbabi, A. Arbabi, and A. Faraon, "A review of dielectric optical metasurfaces for wavefront control", *Nanophotonics*, vol. 7, pp. 1041–1068, 2018.

[2] A. V. Kildishev, A. Boltasseva, and V. M. Shalaev, "Planar photonics with metasurfaces", *Science*, vol. 339, 1232009, 2013.

[3] G. Grinblat, Y. Li, M. P. Nielsen, R. F. Oulton, and S. A. Maier, "Degenerate Four-wave mixing in a multiresonant germanium nanodisk", *ACS Photonics*, vol. 4, pp. 21442149, 2017.

[4] A. Overvig and A. Alu', "Diffractive Nonlocal Metasurfaces", *Laser Photonics Rev.*, vol. 16, 2100633, 2022.

[5] P. Franceschini, A. Tognazzi, G. Finco, L. Carletti, I. Alessandri, A. C. Cino, C. De Angelis, O. Takayama, R. Malureanu, A. V. Lavrinenko, and D. de Ceglia, "Nonlocal resonances in pedestal high-index-contrast metasurfaces based on a silicon-on-insulator platform", *Appl. Phys. Lett.*, vol. 123, 071701, 2025.

[6] P. Franceschini, A. Tognazzi, E. Menshikov, L. Y. Beliaev, R. Malureanu, Os. Takayama, I. Alessandri, A. C. Cino, D. de Ceglia, A. V. Lavrinenko, and C. De Angelis, "Intrapulse multimodal four-wave sum mixing in the visible range from high contrast index grating with PMMA layer", *Light Sci Appl*, vol. 15, pp. 51, 2026.

Controlling Quantum Dot Emission and Enhancing Second Harmonic Generation with Dielectric Nanocylinders

Andrea Tognazzi[1,*]

[1]Department of Engineering, Unviersity of Palermo, Palermo, Italy
*andrea.tognazzi@unipa.it

***Abstract*—Dielectric nanocylinders provide a versatile platform for engineering light–matter interactions at the nanoscale, enabling simultaneous control of quantum emitter radiation and nonlinear optical processes. We demonstrate several use cases of dielectric nanocylinders to tailor quantum dot emission directivity or to enhance second harmonic generation through resonant field confinement.**

***Keywords*— second harmonic generation, quantum dot, emission control.**

I. Introduction

At the fundamental frequency, nanocylinders support Mie-type resonances—including electric and magnetic dipoles and higher-order multipoles—that strongly localize electromagnetic fields. By exploiting interference between these modes, such as under Kerker-type conditions, the angular emission of embedded or coupled QDs can be reshaped, yielding pronounced forward scattering and enhanced extraction efficiency[1]. The spectral and spatial overlap between QD emission and resonant modes enables up to order-of-magnitude increases in collected photoluminescence, with emission patterns governed by the relative excitation of electric and magnetic multipoles.

Simultaneously, resonant dielectric nanocylinders dramatically enhance SHG by concentrating the pump field inside the nonlinear material. In high-index semiconductors and ferroelectric platforms, magnetic dipole and quadrupole resonances at the fundamental wavelength boost nonlinear conversion even in regimes where material absorption is non-negligible. In polycrystalline $BaTiO_3$ nanocylinders, we show that crystalline domain orientation and spatial distribution critically determine the polarization-dependent SHG response[2]. A simplified domain-based model captures the impact of local symmetry breaking and field "hot spots," revealing that SH efficiency is maximized when nonlinear domains overlap with resonant field maxima.

We further discuss interface-driven nonlinear enhancement in layered van der Waals nanoantennas, where inversion symmetry breaking at hetero-bilayer interfaces produces strong SHG despite centrosymmetric bulk constituents[3]. When excitonic resonances and anapole-mediated field confinement coincide, SHG enhancement exceeding two orders of magnitude is observed, highlighting the importance of engineering both material symmetry and photonic resonance.

II. Methods

Finite element simulations were performed to design dielectric nanocylinders supporting multipolar resonances and to evaluate electric field confinement and nonlinear enhancement. Nanostructures were fabricated using electron beam lithography and dry etching. Quantum dot emission and second harmonic generation were characterized through polarization resolved micro spectroscopy under resonant excitation conditions.

III. Conclusion

Together, these results establish dielectric nanocylinders as multifunctional building blocks for integrated nanophotonics. By co-designing geometry, material anisotropy, and crystalline or interfacial symmetry, one can directly control single-photon emission or boost nonlinear frequency conversion. This approach opens pathways toward compact quantum light sources, on-chip frequency converters, and hybrid photonic platforms that unify quantum emission control with nonlinear optical functionality.

References

[1] C. Cruciano et al., "Shaping the emission directivity of single quantum dots in dielectric nanodisks exploiting Mie resonances," *ACS Nano*, vol. 19, pp. 3500–3509, 2025.

[2] A. Tognazzi et al., "A Simplified Model for Polycrystalline $BaTiO_3$ Nanoresonator for Second Harmonic Generation," *Advanced Optical Materials*, vol. 13, pp. 2402484, 2025.

[3] A. Tognazzi et al., "Interface second harmonic generation enhancement in bulk WS_2/MoS_2 hetero-bilayer van der Waals nanoantennas," *Light: Science & Applications*, vol. 14, pp. 346, 2025.

Metasurfaces for Extreme Wave Control

Andrea Alù[1,2]

[1]Photonics Initiative, Advanced Science Research Center, City University of New York, New York, NY 10031, USA
[2]Physics Program, Graduate Center, City University of New York, New York, NY 10016, USA
*Corresponding author: aalu@gc.cuny.edu

***Abstract*— Metasurfaces offer a powerful platform to address the challenges of modern technologies, from imaging to wireless communications, especially when considering the opportunity to integrate conventional metasurface elements with nonlocal phenomena, nonlinearities and time-varying elements. Here we discuss the opportunities of metasurfaces for extreme wave control, with an emphasis on their applications in various fields of technology.**

***Keywords*— metamaterials, space and time modulation.**

I. Introduction

Metasurfaces are formed by planarized two-dimensional arrays of subwavelength tailored constituent elements, which control locally the amplitude, phase and polarization features of the outgoing electromagnetic wave and enable extreme wavefront engineering. The conventional technologies underlying these engineered surfaces is passive, static, linear and time-invariant, hence it has limited opportunities for wireless communication systems, and it suffers from inherent challenges, including limited efficiency, loss and bandwidth constraints. At microwave and mm-wave frequencies, however, the metasurface elements can be quite straightforwardly integrated with tailored circuits, enabling real-time reconfigurability, feedback, amplification, nonlinear responses, parametric phenomena and temporal modulations.

These functionalities can largely enhance the degrees of freedom available to manipulate the overall scattering response of metasurfaces, and they are instrumental in enhancing spectrum efficiency of wireless networks towards enabling a better use of frequency channels. As an additional opportunity, metasurfaces may offer an agile platform for analog signal processing, leveraging advanced dispersion engineering through their nonlocal response to impart on the impinging signals mathematical operations of choice, hence enabling the processing of signals and images at low energy and fast speeds.

In this talk, we discuss the opportunities of metasurfaces for extreme wave control, spanning from radio-frequencies to optics, for a range of applied technologies.

Advanced Techniques for Antennas, RF, and MW Components Fabrication

Investigation on Powder-Bed Fusion Laser-Based Process for the Manufacturing of D-band Feed Horns

Giuseppe Addamo[1*], Flaviana Calignano[2], Mario Zannoni[3], Lorenzo Scalcinati[3], Oscar A. Peverini[1] and F. Paonessa[1]

[1] Consiglio Nazionale delle Ricerche, IEIIT, Corso Duca degli Abruzzi 24, Torino, Italy
[2] Politecnico di Torino, DIGEP, Corso Duca degli Abruzzi 24, 10129, Torino, Italy
[3]Physics Department, University of Milano Bicocca, Piazza della Scienza 3, Milano, Italy
*Corresponding author: giuseppe.addamo@cnr.it

***Abstract*—Millimeter wave and sub-THz components represent the future of satellite communications and astrophysical research. Their realization through classical manufacturing processes, such as CNC or multi-layer platelet solutions, can exhibit some limitations related to high costs, stringent assembly tolerances, RF leakage, and losses. The latter are particularly critical in those science experiments where the control of instrumental systematic effects is fundamental. In this work, we present the outcomes of an ongoing research activity devoted to understand the limits of the Low Power Bed Fusion on metal process in the manufacturing of D-band horn antennas.**

***Keywords*— PBF-LB/M; additive manufacturing; smooth wall horn; D-band.**

I. Introduction

Systems operating in millimeter wave and sub-THz regime find different application domains spanning from future broadband satellites communications to Earth observation and astrophysical experiments. This reason has pushed the interest of the scientific and industrial communities in their design, manufacturing and characterization. The realization of RF devices operating in W (89-110 GHz) and higher frequency band is particularly challenge due the very small dimensions. Subtractive methods, such as CNC or electroforming, face, indeed, problems in terms of mass, volume, and costs. Solutions based on a multi-layer platelet approach exhibit, instead, practical problems not only related to their assembly, *i.e.* RF leakage at the interfaces, but also in terms of thermal performances. While the former can be mitigated using for instance EBG structures [1], the latter can represent a strong limitation in those applications where the front-end are usually cooled at cryogenic temperature and the control of systematic errors is fundamental for an accurate detection. QUBIC (Q&U Bolometric Interferometer for Cosmology) experiment is an interesting example in this context [2]. It consists in a ground-based observation of the sky in two main spectral bands centered at 150 and 220 GHz for the measurement of the B-mode polarization anisotropies of the Cosmic Microwave Background (CMB).

II. Study on Additive Manufacturing Solution

In the case of all-metal components, an interesting option for the problems described in the previous section is represented by the laser powder-bed fusion on metal (PBF-LB/M) process that enables direct fabrication of complex RF components as monolithic lightweight parts leaving, moreover, high flexibility to the designer in exploring new architectures. Unfortunately, the process presents some limitations in terms of achievable accuracy and surface roughness of the internal channels. Both these aspects can be partially mitigated by adopting a multi-disciplinary design approach that considers both electromagnetic, mechanical, and thermal aspects, leading to the PBF-LB/M application to components up to Q/V bands or higher. Following the approach described in [3], here we present the outcomes of an on-going feasibility study on Al-alloy additive-manufacturing of horn antennas operating in D-band. A smooth-wall horn architecture has been selected as a suitable benchmark since its geometry can be naturally realized through PBF-LB/M avoiding both use of supports and inclination of the part in the building machine. As a reference scenario, we have considered requirements compatible to the QUBIC experiment. Different horn prototypes have been built to improve, gradually, electromagnetic performance. While nice outcomes have been achieved in terms of return loss, insertion loss, and co-polar radiated radiation pattern, still some issues are present in terms of high XPD on axis. A mechanical analysis has shown that the problem is related to a runout along the horn structure whose mitigation is under study. The detailed outcomes of this study will be presented at the conference.

References

[1] A. Vosoogh et al., "An E-band Compact Frequency Division Duplex Radio Front-end Based on Gap Waveguide Technology," 2019 13th EuCAP, Krakow, Poland, 2019.
[2] J.-C Hamilton, J.-C et al QUBIC I: Overview and science program. J. Cosmol. Astropart. Phys. 2022, 2022, 34.
[3] G. Addamo et al. "3-D Printing of High-Performance Feed Horns From Ku- to V-Bands". IEEE Antennas Wirel. Propag. Lett. 2018, 17.
[4] G. Addamo et al. "Feasibility Study on Additive Manufacturing of Feed Horn Operating in D-Band. Sensors 2025, 25, 523A.

Additive Manufacturing Techniques for Post-Fabrication Frequency Tuning of Printed Planar Antennas

Rubén Pedreño-Martínez[1*], David Cañete-Rebenaque[1], José Luis Gómez-Tornero[1]

[1]Department of Information and Communications Technologies, Technical University of Cartagena, 30202, Cartagena, Spain

*Corresponding author: ruben.pedreno@edu.upct.es

***Abstract*—Manufacturing tolerances in printed RF antennas often lead to undesired frequency shifts, increasing development time and cost due to iterative redesign, especially for dispersive structures. This work presents two additive-only post-fabrication techniques to address these issues, based on the controlled addition of conductive or dielectric elements. A microstrip leaky-wave antenna is proposed to demonstrate the suitability of this approach.**

***Keywords*— printed antennas, microstrip leaky-wave antenna, frequency detuning, post-fabrication tuning, additive manufacturing, manufacturing tolerances**

I. Introduction

Prototype fabrication constitutes a critical stage in the validation of novel RF and microwave engineering concepts with practical and societal impact. In both academic and industrial environments, this process is commonly outsourced to specialized manufacturing facilities, which provide higher precision and repeatability than manual fabrication. Nevertheless, deviations between the nominal design and the manufactured prototype remain unavoidable due to material tolerances, process inaccuracies, and variability in substrate parameters.

While such deviations are generally acceptable in low-frequency systems, they become a major limitation in radiofrequency and microwave applications, where electrically small variations in geometry or dielectric properties can significantly perturb the electromagnetic response. As a result, the measured frequency response of printed antennas often differs from the simulated design, leading to undesired frequency shifts that may compromise compliance with standardized frequency bands or system-level requirements. Consequently, multiple redesign and refabrication cycles are required, increasing both development time and cost.

This issue is particularly critical in dispersive planar antenna structures, such as microstrip leaky-wave antennas (MLWAs), where the radiation characteristics are inherently linked to the frequency-dependent phase constant of the guided mode. MLWAs have attracted considerable interest due to their low profile, simple feeding, and suitability for printed-circuit fabrication. In recent years, microstrip LWAs have been successfully employed in a wide range of applications, including UHF RFID systems [1], [2], WiFi-based localization [3]–[5], Bluetooth Low Energy (BLE) indoor positioning [6]–[8], RADAR systems operating at ultra-wideband [9] and mmWave frequencies [10], as well as LEO satellites [11]. Many of these applications operate under stringent performance constraints, such as narrow standardized frequency channels, high operating frequencies, or phase- and time-based signal processing schemes, making them especially sensitive to fabrication-induced detuning.

To mitigate these limitations, additive manufacturing and post-fabrication correction techniques have emerged as an effective alternative to conventional redesign approaches. Instead of modifying or re-fabricating the original structure, these methods rely on the controlled addition of conductive or dielectric elements to compensate for frequency-response deviations introduced during fabrication. This strategy enables the electromagnetic response of the prototype to be realigned with the nominal design specifications in a simple and cost-effective manner.

In this work, two additive-only post-fabrication techniques for frequency-response correction in printed planar antennas are presented. The proposed methods are illustrated through a half-width microstrip leaky-wave antenna example, as shown in Fig.1, and demonstrate the feasibility of readjusting the operational frequency band without altering the original antenna structure. The proposed approach is particularly well-suited for rapid prototyping and experimental validation of printed antenna systems affected by manufacturing tolerances.

II. Additive Post-Fabrication Technique

In [1], a half-width microstrip leaky-wave antenna (HWM-LWA) was fabricated for operation in the UHF band, targeting IoT-oriented applications such as RFID systems. The antenna design follows the principles described in [12], where accurate frequency scanning is required.

The antenna comprises a top conductive strip of width W and length L, printed on a grounded substrate characterized by width W_{SUBS}, length L_{SUBS}, thickness H_{SUBS}, and relative permittivity ϵ_{SUBS}. Radiation is produced through a longitudinal aperture of width W_R, whose dimensions directly affect the leakage rate and dispersion characteristics of the antenna. In order to compensate for the observed frequency deviation without modifying the original structure, two additive-only

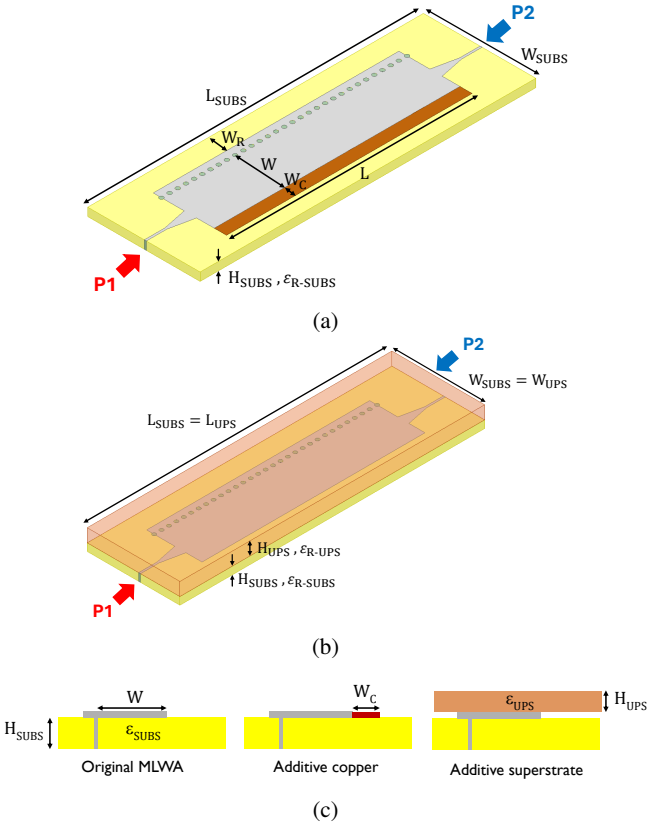

Fig. 1: Proposed additive techniques for a HWM-LWA. a) Additive copper technique, b) Additive superstrate technique, c) Lateral scheme of the proposed structures

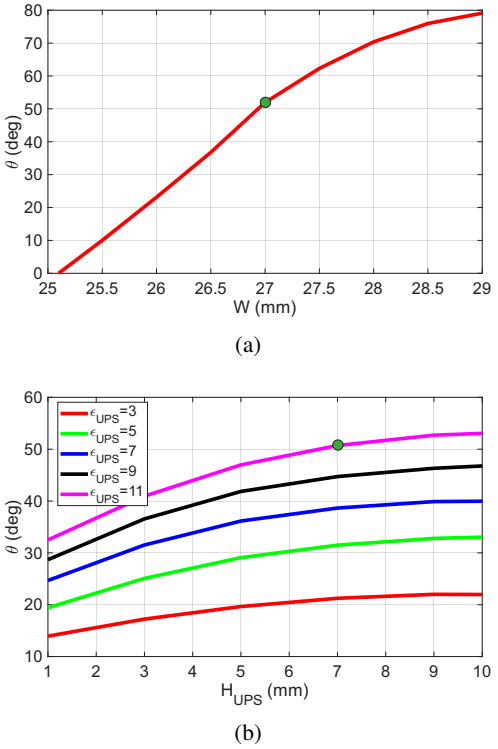

Fig. 2: Evaluation of the dispersive response of the proposed techniques. a) Additive copper technique, b) Additive superstrate technique

post-fabrication techniques are proposed and schematically illustrated in Fig.1a and Fig.1b.

The first approach consists of increasing the effective width of the top conductor by adding a narrow conductive strip of width W_C along the radiating aperture region, as shown in Fig.1a. This technique modifies the main conductive strip width and alters the leaky-wave mode dispersion characteristics. As a result, the phase constant is shifted, leading to a controlled displacement of the frequency–angle response of the antenna and enabling realignment of the operational band with the nominal design.

This technique is compact and cost-effective, only requiring the addition of a conductive element with a prescribed geometry. However, fine frequency adjustments demand high dimensional accuracy, which may require specialized fabrication equipment. This concern is illustrated in Fig.2a for a HWM-LWA, where the relation between width of the top conductive strip and the resulting beam steering is evaluated for a specific frequency. Increments of 0.5 mm, due to copper additive technique, produces angular displacements of up to 15 degrees, indicating a high sensitivity for detuning applications.

In addition, increasing the conductor width reduces the aperture width W_R, which must be considered at the initial design stage to avoid degradation of the radiation characteristics.

The second approach relies on a dielectric superstrate placed above the fabricated antenna, characterized by width W_{UPS}, length L_{UPS}, thickness H_{UPS}, and relative permittivity ϵ_{UPS}, as depicted in Fig.1b. The presence of this superstrate modifies the effective permittivity seen by the guided mode, thereby shifting the dispersion curve and enabling frequency tuning of the antenna response.

A graphical representation of the dispersion characteristics of the HWM-LWA, as a function of the superstrate permittivity and thickness, is shown in Fig.2b. Thicker substrates produce proportional increases in the beam pointing angle at a given frequency. Similarly, an increase in the superstrate permittivity results in higher system sensitivity, as well as a shift in the dispersion curve.

Beyond frequency correction, dielectric superstrates are known to enhance antenna gain and directivity through wavefront shaping effects, while also providing mechanical protection to the radiating structure [13]. Compared to the conductive loading technique, this approach is less invasive and easier to implement, offering a wider tuning range at the expense of increased volume and material cost.

Finally, a lateral scheme of the proposed structures is depicted in Fig.1c.

TABLE I: Antennas Main Dimensions in mm

L	W	L_{SUBS}	W_{SUBS}	W_R
506	25.8	550	51	10
H_{SUBS}	ε_{SUBS}	H_{UPS}	ε_{UPS}	W_C
1.27	10.2	7	11	1.13

III. Simulation Results

The proposed additive post-fabrication techniques presented in Section II, are now evaluated through full-wave simulations using the MLWA previously presented. Dimensions of the systems proposed in Fig.1 are summarized in Table.I, along with the green points in Fig.2.

The antenna pointing angle as a function of frequency has been selected as the main figure of merit, since it directly reflects the dispersive behavior of the leaky-wave mode and is highly sensitive to fabrication-induced detuning. Fig.3a shows the measured frequency–angle response of the fabricated antenna [1], before applying the proposed additive correction techniques. Results show that the antenna exhibits a noticeable shift of the operational frequency band with respect to the nominal design, resulting in a displacement of the expected radiation angles of 15, 50 and 65 degrees.

Alternatively, Fig.3b shows the resulting pointing angle as a function of frequency, after applying the corresponding additive techniques.

When the additive conductive strip technique is applied, a clear shift of the frequency–angle response is observed. The increase in the effective width of the radiating conductor modifies the dispersion characteristics of the guided mode, producing a controlled realignment of the phase constant. As a result, the radiation angles are displaced, effectively compensating for the fabrication-induced frequency deviation.

Similarly, the dielectric superstrate technique also produces a significant correction of the frequency response. By increasing the effective permittivity seen by the guided mode, the dispersion curve is shifted in a comparable manner, leading again to a recovery of the intended operational frequency band. The measured radiation angles obtained with the superstrate closely follow those achieved with the conductive loading approach.

A comparison between both techniques reveals that they provide very similar frequency–angle correction trends, demonstrating that both methods are effective for post-fabrication frequency tuning of dispersive planar antennas. No significant degradation of the angular scanning behavior is observed, and the overall shape of the frequency–angle response is preserved after correction. This confirms that the proposed techniques enable frequency realignment without fundamentally altering the radiation mechanism of the leaky-wave antenna.

From a practical perspective, the conductive loading approach offers a more compact solution suitable for fine frequency adjustments, whereas the dielectric superstrate provides a wider tuning range with relaxed fabrication tolerances and implementation simplicity. The choice between both techniques can therefore be made depending on the specific application requirements and implementation constraints.

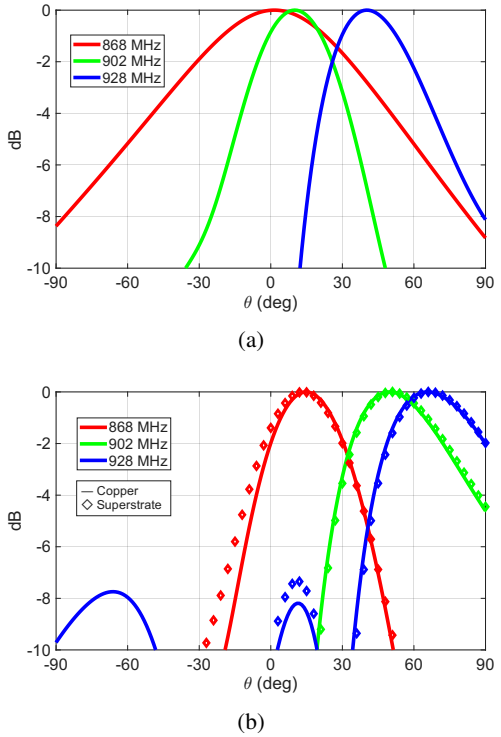

Fig. 3: HWM-LWA radiation patterns. a) Original structure, b) Additive copper and superstrate techniques

IV. Conclusions

This work has presented two additive post-fabrication techniques for compensating frequency detuning in printed planar antennas caused by manufacturing tolerances. The proposed approaches rely on the controlled addition of either a conductive element or a dielectric superstrate, avoiding redesign or refabrication of the original antenna.

The techniques have been evaluated through full-wave electromagnetic simulations using a half-width microstrip leaky-wave antenna as a representative dispersive structure. The simulated frequency–angle responses show that both methods effectively correct the frequency shift of the fabricated antenna, while preserving the characteristic angular scanning behavior. Both approaches exhibit similar tuning trends, confirming their suitability for post-fabrication frequency realignment. The conductive loading technique is more compact and well suited for fine tuning, whereas the dielectric superstrate provides greater tuning flexibility with relaxed fabrication constraints. Overall, the proposed methods offer a practical solution for rapid prototyping and simulation-driven validation of printed dispersive antenna designs.

ACKNOWLEDGMENTS

This work was supported by Spanish National Project PID2022-136590OB-C42.

REFERENCES

[1] A. Gil-Martinez, M. Poveda-Garcia, D. Canete-Rebenaque, and J. L. Gomez-Tornero, "Frequency-Scanned Monopulse Antenna for RSSI-Based Direction Finding of UHF RFID Tags," *IEEE Antennas and Wireless Propagation Letters*, vol. 21, no. 1, pp. 158–162, 2022.

[2] A. Gil-Martinez, M. Poveda-Garcia, J. Garcia-Fernandez, M. M. Campo-Valera, D. Canete-Rebenaque, and J. L. Gomez-Tornero, "Direction Finding of RFID Tags in UHF Band Using a Passive Beam-Scanning Leaky-Wave Antenna," *IEEE Journal of Radio Frequency Identification*, vol. 6, no. 21, pp. 552–563, 2022.

[3] A. Gil-Martinez, D. Cañete-Rebenaque, M. Poveda-Garcia, A. Algaba-Brazalez, and J. L. Gómez-Tornero, "Multibeam Microstrip Leaky-Wave Antenna Array for Passive 2-D Scanning in the 5 GHz Wi-Fi Band," *IEEE Open Journal of Antennas and Propagation*, 2023.

[4] J. A. López-Pastor, M. Poveda-García, A. Gil-Martínez, D. Cañete-Rebenaque, and J. L. Gómez-Tornero, "2-D Localization System for Mobile IoT Devices Using a Single Wi-Fi Access Point With a Passive Frequency-Scanned Antenna," *IEEE Internet of Things Journal*, vol. 10, no. 17, pp. 14995–15011, 2023.

[5] R. Pedreño-Martinez, A. Gil-Martinez, A. Algaba-Brazalez, and J. L. Gomez-Tornero, "Microstrip Leaky-Wave Antennas with Parasitic Matching Strips for Enhanced Radiation Efficiency," in *2025 IEEE International Symposium on Antennas and Propagation and North American Radio Science Meeting (AP-S/CNC-USNC-URSI)*, Ottawa, Canada, 2025, pp. 2272–2275.

[6] J. A. López-Pastor, A. Gil-Martínez, A. Hernández Mateos, A. Algaba-Brazález, and J. L. Gómez Tornero, "Bluetooth Low Energy separate-channel fingerprinting with frequency-scanned antennas," *Internet of Things*, vol. 33, 101732, 2025.

[7] J. L. Gómez-Tornero, J. A. López-Pastor, A. Gil-Martinez, M. Poveda-García, and A. Algaba-Brazalez, "GHz Prism: Frequency-Scanned Antennas to Improve Localization with Separate-Channel Fingerprinting," in *18th European Conference on Antennas and Propagation (EuCAP)*, Glasgow, UK, 2024, pp. 1–5.

[8] R. Faragher and R. Harle, "Location Fingerprinting With Bluetooth Low Energy Beacons," *IEEE Journal on Selected Areas in Communications*, vol. 33, no. 11, pp. 2418–2428, Nov. 2015.

[9] J. L. Gomez-Tornero, M. Poveda-Garcia, R. Romero-Justiniano, A. Gil-Martínez, and D. Cañete-Rebenaque, "Design of Frequency-Beam Scanning Antennas for Ultra Wide Band Impulse RADAR Applications," in *17th European Conference on Antennas and Propagation (EuCAP)*, Florence, Italy, 2023, pp. 1–4.

[10] M. Poveda-García, A. Gil-Martínez, F. Salmerón, and J. L. Gómez-Tornero, "Frequency-Beam-Scanning mm-Wave Antennas for Direction Finding RADAR," in *19th European Radar Conference (EuRAD)*, Milan, Italy, 2022, pp. 293–296.

[11] J. L. Gómez-Tornero, A. Gil Martínez, M. Poveda-García and D. Cañete-Rebenaque, "ARIEL: Passive Beam-Scanning Antenna terminal for Iridescent and Efficient LEO Satellite Connectivity," in IEEE Antennas and Wireless Propagation Letters, vol. 21, no. 11, pp. 2268-2272, Nov. 2022.

[12] A. G. Martinez, M. P. Garcia, and J. L. Gómez-Tornero, "Direct synthesis of frequency-scanned monopulse half-width microstrip leaky-wave antennas," in *Proc. 14th Eur. Conf. on Antennas and Propagation (EuCAP)*, Copenhagen, Denmark, 2020, pp. 1–4.

[13] N. Alexopoulos and D. Jackson, "Fundamental superstrate (cover) effects on printed circuit antennas," *IEEE Trans. Antennas Propag.*, vol. 32, no. 8, pp. 807–816, Aug. 1984.

A 3D-printed Convex Antenna for ARBW and Gain Enhancement

Giacomo Muntoni[1,*], Alessandro Fanti[1], Giuseppe Mazzarella[1]

[1] Department of Electrical and Electronic Engineering (DIEE), University of Cagliari, 09123 Cagliari, Italy

*Corresponding author: giacomo.muntoni@unica.it

***Abstract*— A convex microstrip patch antenna, obtained taking advantage of the 3D printing procedures, is proposed in this work, demonstrating the ability of the curved substrate to enhance the axial ration bandwidth of a circularly polarized antenna, as well as its efficiency and its realized gain.**

***Keywords*— 3D Printing, ARBW, Gain Enhancement, Curved Antenna.**

I. Introduction

With the advent of additive manufacturing techniques, the fabrication and prototyping of antenna substrates have gained a degree of freedom never seen before [1]. Three-dimensional printing enables low-cost, lightweight, and innovative layouts to support antennas and other radio-frequency and microwave components. In recent years, several studies have addressed the effects of curved substrate geometries [2], [3], obtained by means of 3D printing, highlighting benefits in terms of impedance bandwidth (IBW) and efficiency enhancement [2]. These improvements are achieved thanks to the average substrate thickness increment provided by the curved substrate, without running into common drawbacks typical of thicker substrates (such as inductive contribution of a longer coaxial pin, spurious feed radiation, surface wave propagation) [4]. However, all works published to date have investigated the use of such unconventional substrates only for linearly polarized antennas. In this work, we show that the advantages provided by curved substrates can also be extended to circularly polarized antennas. The proposed antenna is based on a convex substrate, rather than on the concave substrates reported so far [2], [3], [5], [6]. Nevertheless, these two layouts share some similarities, most notably the fact that the curved geometry involves only the area directly beneath the patch. To demonstrate the benefits introduced by the convex antenna, a comparison with a benchmark antenna, i.e. a simple circular patch in circular polarization (CP), is drawn, highlighting the increased axial ratio bandwidth (ARBW) and efficiency (and consequently gain) of the proposed antenna. The presented curved antenna has been designed to be fabricated using a poly-lactic acid (PLA) thermoplastic filament and copper for the conductive parts. A parametric investigation on the role of the curvature radius of the convex antenna is also presented.

II. Antenna Design and Simulations

The layout of the proposed antenna is shown in Fig. 1. From the image it can be seen that the convex patch antenna lies on a convex profile, obtained by carving a spherical recess within an inverted truncated cone. This structure itself sits on an additional squared substrate with side $W = 80$ mm and thickness $H_S = 2$ mm. The radius of the spherical recess is equal to $R_{sph} = 26.5$ mm. To achieve CP, a slot rotated by 45° has been cut from the center of the metal patch. All the remaining key dimensions of the layout are reported in the caption of Fig. 1. The height of the truncated section has been chosen to center the resonance frequency of the convex antenna to 2.5 GHz.

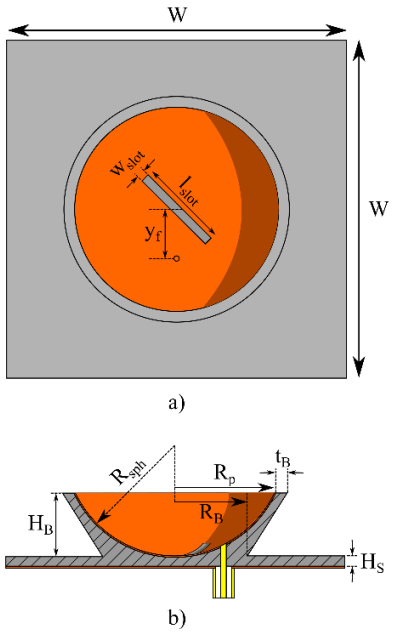

Fig. 1 Layout of the proposed antenna: a) top view; b) cross-sectional view. Parameters: $W = 80$ mm, $y_f = 11.5$ mm, $l_{slot} = 21$ mm, $w_{slot} = 2$ mm, $H_B = 15$ mm, $H_S = 2$ mm, $R_{sph} = 26.5$ mm, $R_p = 23.9$ mm, $R_B = 17$ mm, $t_B = 2.6$ mm.

For comparison, a benchmark antenna, consisting of a planar circular patch in CP, has been also been designed and the layout is reported in Fig. 2.

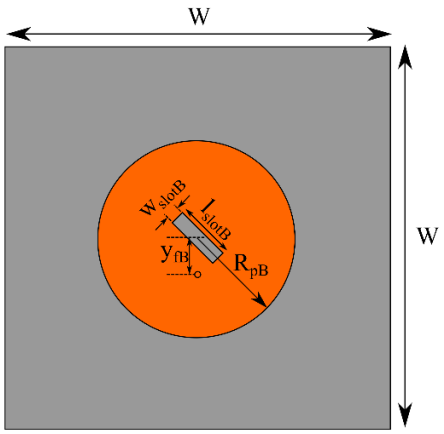

Fig. 2 Layout of the flat circular CP antenna used as a benchmark. Parameters: W = 80 mm, y_{fB} = 8 mm, l_{slotB} = 12 mm, w_{slotB} = 2.5 mm.

The numerical simulations have been carried out using CST Studio Suite 2022 software, comparing the performance of the proposed antenna with varying curvature radius. It can be seen that the antenna curvature affects the IBW, the ARBW, and the efficiency, also influencing the realized gain of the antenna. The results of the parametric variation of the curvature radius R_{sph} are reported in Figs. 3, 4, and 5, including the performance of the benchmark antenna, which is depicted as having virtually an infinite curvature radius.

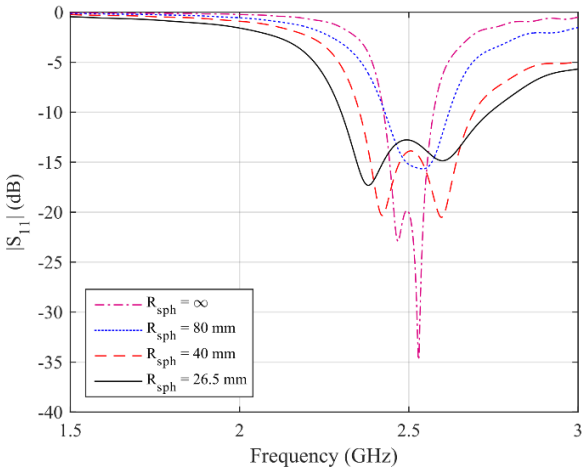

Fig. 3 Simulated $|S_{11}|$ of the convex patch antenna for R_{sph} varying between 26.5 mm (proposed layout) and infinity (benchmark planar antenna).

From these results, it can be inferred that there is a sensible increase in the IBW, from 6% (2.42–2.57 GHz) for the benchmark antenna to 17.7% (2.30–2.74 GHz) for the proposed convex antenna (nearly three times), but more importantly in the ARBW, from 1.4% (2.472–2.507 GHz), to 4.1% (2.443–2.545 GHz) for the proposed layout. Improvements can also be appreciated for the efficiency and realized gain, as shown in Fig. 5: the efficiency rises from 60% to about 90%, whereas the realized gain rises from 4.46–5.34 dBi, to 7.37–7.42 dBi.

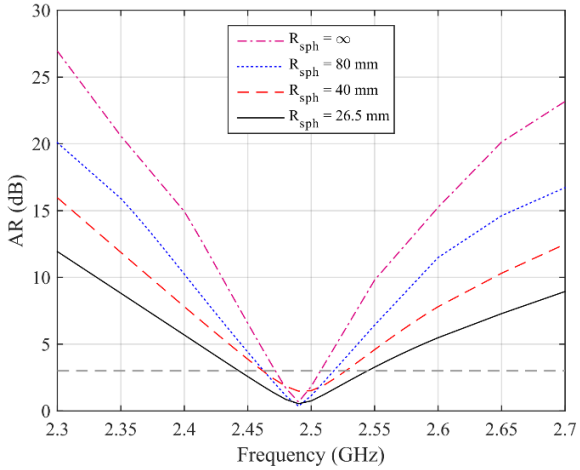

Fig. 4 Simulated AR of the convex patch antenna for R_{sph} varying between 26.5 mm (proposed layout) and infinity (benchmark planar antenna).

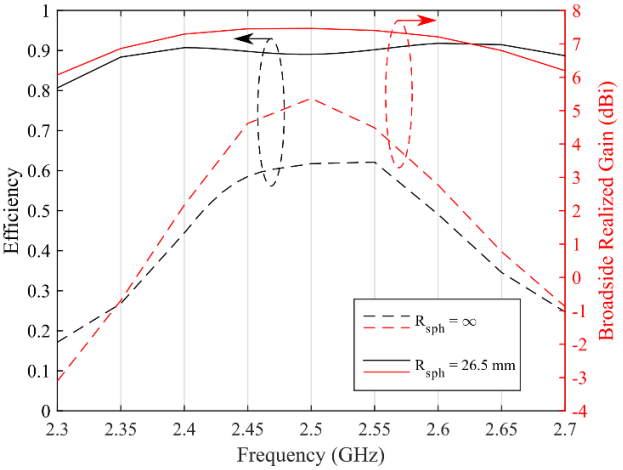

Fig. 5 Comparison between the simulated efficiency and realized gain for the benchmark and proposed convex antenna.

Finally, the simulated radiation patterns for LHCP and RHCP at the central frequency of 2.5 GHz are reported in Fig. 6.

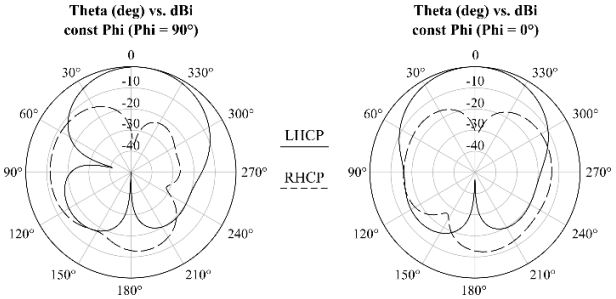

Fig. 6 Simulated radiation patterns for the proposed convex antenna at 2.5 GHz.

III. Conclusion

Through the usage of the 3D printing manufacturing, a curved microstrip patch antenna with a rather peculiar convex profile has been presented, in this study. The adoption of the curved profile provides improvements also to circularly polarized antennas, and not only to linearly polarized ones, as extensively demonstrated in the scientific literature on the same topic. The curved antenna show enhancements in IBW and ARBW (almost tripling both bandwidths), as well as in efficiency and realized gain.

Acknowledgements

This work has been developed within the framework of the project eINS- Ecosystem of Innovation for Next Generation Sardinia (cod. ECS 00000038) funded by the Italian Ministry for Research and Education (MUR) under the National Recovery and Resilience Plan (PNRR) - MISSION 4 COMPONENT 2, "From research to business" INVESTMENT 1.5, "Creation and strengthening of Ecosystems of innovation" and construction of "Territorial R&D Leaders".

References

[1] S. S. Carvalho, J. R. V. Reis, A. Mateus and R. F. S. Caldeirinha, "Exploring Design Approaches for 3D Printed Antennas," in IEEE Access, vol. 12, pp. 10718–10735, 2024, doi: 10.1109/ACCESS.2024.3354372.

[2] G. Muntoni et al., "A Curved 3-D Printed Microstrip Patch Antenna Layout for Bandwidth Enhancement and Size Reduction," in IEEE Antennas and Wireless Propagation Letters, vol. 19, no. 7, pp. 1118–1122, July 2020, doi: 10.1109/LAWP.2020.2990944.

[3] G. Muntoni et al., "A Curved 3D-Printed S-Band Patch Antenna for Plastic CubeSat," in IEEE Open Journal of Antennas and Propagation, vol. 3, pp. 1351–1363, 2022, doi: 10.1109/OJAP.2022.3222454.

[4] J. M. Kovitz and Y. Rahmat-Samii, "Using thick substrates and capacitive probe compensation to enhance the bandwidth of traditional CP patch antennas," IEEE Transactions on Antennas and Propagation, vol. 62, no. 10, pp. 4970–4979, Oct. 2014.

[5] G. Muntoni, G. A. Casula and G. Montisci, "The 3D-Printed Non-Radiating Edge Gap-Coupled Curved Patch Antenna," in IEEE Open Journal of Antennas and Propagation, vol. 4, pp. 229–236, 2023, doi: 10.1109/OJAP.2023.3247173.

[6] G. Montisci, G. Mura, G. Muntoni, G. A. Casula, F. P. Chietera and M. Aburish-Hmidat, "A Curved Microstrip Patch Antenna Designed From Transparent Conductive Films," in IEEE Access, vol. 11, pp. 839–848, 2023, doi: 10.1109/ACCESS.2022.3233471.

Nonlinear metasurface and flat-optics

Hot-carrier Mediated Modulation of Linear and Nonlinear Photonic Metastructures

A. Schirato[1,2], G. Crotti[1], and G. Della Valle[1,*]

[1]Dipartimento di Fisica, Politecnico di Milano, Italy
[2]Department of Physics and Astronomy, Rice University, Houston (TX), USA
*Corresponding author: giuseppe.dellavalle@polimi.it

***Abstract*— Hot carriers photogenerated at the nanoscale by femtosecond laser pulses enable efficient modulation of linear and nonlinear photonic metastructures. Here, we review our recent results in the field, where a versatile multi-temperature semiclassical approach is exploited to model a variety of systems, ranging from semiconductor metasurfaces to plasmonic pico-cavities.**

***Keywords*— metasurfaces, plasmonics, hot carriers, ultrafast photonics.**

I. Introduction

It is since a long time ago that hot carriers photogenerated by intense femtosecond laser pulses are known to preside over the giant nonlinear optical response of a variety of solid-state media, including metallic and semiconductor materials. A consistent quantitative model of the phenomenon has been originally introduced for gold only in 2012 as a delayed cubic nonlinearity, derived by combining a semiclassical description of material band structure and an improved version of the classic two-temperature model for electron-electron and electron-phonon thermalization processes [1]. Hot carriers are now considered as an unparalleled channel for manipulating photoinduced phenomena on picosecond timescales [2,3].

II. Results and Discussion

Here, we review our recent results in the field. We show how multi-temperature modeling of the hot carrier dynamics combined with a semiclassical description of light-matter interactions at the nanoscale offers a versatile tool for the modeling and design of reconfigurable/switchable photonic metastructures based on noble metals, degenerate semiconductors and even all-dielectric media. Our modeling, based on a rate-equation approach, is validated by quantitative comparison with ultrafast spectroscopy measurements in a variety of configurations and for different functionalities, including ultrafast giant light amplitude modulation, dichroism and birefringence modulation [4], ultrafast diffraction management, and the tailoring of the modulation dynamics [5]. Moreover, shaping at the deep sub-wavelength scale the spatio-temporal evolution of nonequilibrium carriers can be crucial to disclose unprecedented possibilities for ultrafast all-optical control of light from semiconductor metasurfaces [6]. Finally, our hot-carrier based modeling is also capable to simulate sub-picosecond timescale modulation of electronic resonance Raman scattering from a plasmonic picocavity [7].

III. Conclusion

Multi-temperature modeling of hot-carrier dynamics ar exploited to design active metastructures of metallic or dielectric media for a variety of applications. Thanks to their spatial confinement, inherited by localization of the resonant excitation fields, hot carriers enable all-optical reconfiguration at deep sub-wavelength scales and at unprecedented speed, with renewed degrees of freedom for ultrafast nanophotonics.

Acknowledgments

This work is funded by the European Union− Next Generation EU PNRR − M4C2 I1.1 - PRIN 2022 - Progetto HOTMETA, ID 2022LENW33, CUP:D53D2300229 0006. We also acknowledge the EU's Horizon 2020 METAFAST project under grant agreement no. 899673, and EU's Horizon Europe research and innovation programme under the MSCA PATHWAYS HORIZON-MSCA-2023-PF-GF no. 101153856.

References

[1] M. Conforti and G. Della Valle, "Derivation of third-order nonlinear susceptibility of thin metal films as a delayed optical response", Phys. Rev. B, vol. 85, 245423, 2012.
[2] M. Brongersma, N. J. Halas, P. Nordlander, "Plasmon-induced hot carrier science and technology," Nat. Nanotech., vol. 10, pp. 25-34, 2015.
[3] M. Maiuri, A. Schirato, G. Cerullo and G. Della Valle, "Ultrafast All-Optical Metasurfaces: Challenges and New Frontiers," ACS Photonics, vol. 11, pp. 2888-2905, 2024.
[4] G. Crotti, M. Akturk, A. Schirato, V. Vinel, A.A. Trifonov, et al. "Giant ultrafast dichroism and birefringence with active nonlocal metasurfaces," Light: Science & Applications, vol. 13, 204, 2024.
[5] A. Schirato, M. Maiuri, G. Cerullo, and G. Della Valle, "Ultrafast hot electron dynamics in plasmonic nanostructures: experiments, modelling, design," Nanophotonics, Vol. 12, No. 1, 1-28, 2023.
[6] G. Crotti, A. Schirato, O. Pashina, O. Sergaeva, M. Petrov, C. De Angelis, and G. Della Valle, "Ultrafast switching of a metasurface quasi-bound state in the continuum via transient optical symmetry breaking," Light: Science & Applications, vol. 14, 240, 2025.
[7] Y. Luo, S. Sheng, A. Schirato, A. Martin-Jimenez, G. Della Valle, G. Cerullo, K. Kern, M. Garg, "Visualizing hot carrier dynamics by nonlinear optical spectroscopy at the atomic length scale", Nat. Commun., vol. 15, 4999, 2024.

Peculiarities of the nonlinear optical effects in ultrathin dielectric membranes

Maxim Nikitin[1], Olav Thorbjørn Sandberg Schiess[1], Andrea Tognazzi,[2,3], Paolo Franceschini,[3,4] Osamu Takayama[1], Radu Malureanu[1], Ole Bang[1], Costantino De Angelis[3,4], Andrei V. Lavrinenko[1*]

[1]Department of Electric and Photonics Engineering, Technical University of Denmark, Kongens Lyngby, Denmark

[2]Department of Engineering, University of Palermo, Palermo, Italy

[3]National University of Brescia, Department of Information Engineering, Brescia, Italy

[4]National Institute of Optics – National Research Council (INO-CNR), Brescia, Italy

*Corresponding author: alav@dtu.dk

***Abstract*— We investigated nonlinear properties of ultrathin dielectric free-standing membranes. In particular, we studied the generation of the third harmonic in the membrane and analyzed possible enhancement of the effect by the film patterning. Such patterning generates resonances. Their scaling, enhancement factors and potential constraints limiting these factors will be reported.**

***Keywords*— metasurfaces, third harmonic generation, guided mode resonances.**

I. Introduction

Metasurfaces have established the realm of flat optics. While their imaging properties and possible constraints are well understood, the nonlinear effects brought by various metasurfaces designs are still considered as quite novel phenomena. We provide some analysis, how geometrical and temporal characteristics can be tuned to deliver optimal performance.

II. Methods

We consider the third harmonic generation in a silicon nitride membrane. This material is chosen as from one side, the fabrication flow of producing ultrathin structured membranes is well established. On the other hand, this material plays an important role in photonic circuitry possessing nice combination of mechanical and optical properties. The latter are also extended over a pronounced range of wavelengths from UV to mid-IR.

III. Results and Discussion

The explicit FDTD simulations predicted that third-order nonlinearities in thin SiN membranes can be enhanced by patterning by a few tens of thousands of times [1]. However, in the Z-scan experiments, the observed enhancement factors of the nonlinear refractive index and nonlinear absorption coefficient were below five times. We found the explanation of this effect [2]. The two crucial factors limiting the nonlinearity enhancement factor are: the duration of the pump pulse and the spot size of the active metasurface area. The pulse duration should be sufficiently long such that its bandwidth is comparable to or smaller than the bandwidth of resonances. The finite size of the number of illuminated unit cells by the laser beam also decreases the effective Q-factor. By modeling, we found that the experimentally observed enhancement factors are fully explained by accounting for these two reasons.

As we aim to utilize such membranes for the generation of UVC radiation, thorough experimental validation of the nonlinear effects is required. Thus, the accurate tuning of the most effective resonances in the membranes to the pump laser wavelength becomes an important issue. We show in which limits the variation of the lattice constant of the patterning can tune the position of the resonances.

Acknowledgments

A. T. acknowledges financial support from the University of Palermo. C.D.A. acknowledges financial support from the European Union under the Italian National Recovery and Resilience Plan (NRRP). C.D.A. acknowledges financial support from NATO project. A.L. acknowledges financial support from Villum Fonden. O.T. acknowledges financial support from Novo Nordisk Fonden.

References

[1] M. Nikitin, K. Nijsen, A. Moltke, O. Takayama, R. Malureanu, O. Bang, and A. V. Lavrinenko, "Third-harmonic generation of ultraviolet light in silicon nitride metasurface: a numerical study of pulse duration dependence," Opt. Express, vol. 33, pp. 17693–17704, 2025.

[2] P. Franceschini, M. Nikitin, A. Tognazzi, K. Brańko, O. Takayama, R. Malureanu, A. C. Cino, C. De Angelis, and A. Lavrinenko, "Enhanced Effective Nonlinearities in Silicon Nitride Free-standing Nanopatterned Membranes", APL Photonics, accepted.

High-Harmonic Generation from Resonant Dielectric Metasurfaces

Ivan Sinev[1,*], Pavel Tonkaev[2], Felix Brikh[1], Ivan Toftul[2], Maria Antonietta Vincenti[3], Michael Scalora[4], Hatice Altug[1], Yuri Kivshar[2]

[1]Institute of Bioengineering, EPFL, Switzerland
[2]Nonlinear Physics Center , Australian National University, Australia
[3]Department of Information Engineering, University of Brescia, Italy
[4]Aviation and Missile Center, U.S. Army CCDC, USA
*Corresponding author: ivan.sinev@epfl.ch

***Abstract*— We discover that highly resonant metasurfaces driven by quasi-bound states in the continuum manifest non-integer intensity dependencies of the generated powers of higher harmonics. We demonstrate that these unconventional nonlinearities are enabled by strong local fields arising from the high-Q resonances that substantially alter the effective nonlinearities of the system.**

***Keywords*— metasurface, nonlinear optics, high harmonic generation.**

I. Introduction

High-harmonic generation (HHG) is a fundamental phenomenon at the intersection strong-field physics, ultrafast science, and nonlinear optics [1]. Recently, metasurfaces enabled advanced engineering of local electromagnetic fields and resonances to amplify nonlinear interactions well beyond what is achievable in unstructured media [2]. Particularly, metasurfaces based on bound states in the continuum (BICs) offer ultrahigh-Q resonances that can significantly alter the conventional nonlinear regimes [3]. Here, we investigate HHG from free-standing metasurface membranes that support high-Q resonances, revealing a regime of *unconventional, non-integer power dependence* of harmonic intensities driven by resonant local field enhancement.

II. Methods

We designed free-standing crystalline silicon membrane metasurfaces perforated with a hexagonal array of elliptical holes, engineered to support high quality factor resonances in the mid-infrared spectral range. The metasurfaces were fabricated using standard silicon-on-insulator processing followed by removal of supporting substrates to minimize extrinsic symmetry breaking and optical losses. Nonlinear HHG experiments were performed by pumping the metasurfaces with a tunable femtosecond laser in the 3.85–4.05 μm window. Harmonic signals up to the ninth order were recorded as functions of pump wavelength and power. Numerical simulations solving the nonlinear wave equation with higher-order nonlinear susceptibilities supplemented the experimental findings and provided insight into the modified effective nonlinear response under resonant excitation.

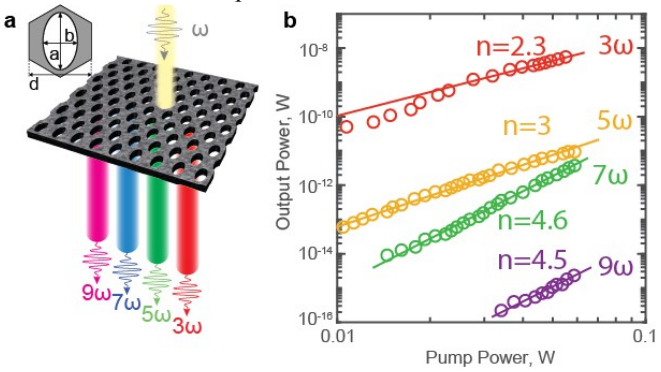

Fig. 1 a, Concept of high-harmonic generation from resonant membrane metasurfaces. The inset shows the unit cell of the structure. b, Comparison of power dependencies of HHG from the membrane metasurface, illustrating the non-integer power scaling.

III. Results and Discussion

Resonant excitation of the q-BIC mode induced strong local field enhancement, yielding HHG efficiencies that exceed those of unpatterned membranes by more than three orders of magnitude. Third, fifth, seventh, and ninth harmonics were observed with conversion efficiencies that peaked near the q-BIC resonance. Notably, the power scaling of harmonic intensities deviated from conventional integer laws: while unpatterned silicon membranes exhibited slopes perfectly matching the order of the nonlinear process, resonant metasurfaces displayed non-integer effective slopes (e.g., ~2.3 for third harmonic and ~4.6 for seventh harmonic) [4]. Numerical modelling showed that this non-integer scaling arises from a complex interplay of local field enhancement and contributions from higher-order nonlinear susceptibilities that are amplified in highly resonant conditions. Our simulations reproduced both the resonance-enhanced efficiency and the altered scaling behavior, confirming that the modified effective nonlinearity stems from resonant field dynamics.

IV. Conclusion

Our results demonstrate that high-Q resonant metasurfaces can fundamentally alter the scaling behavior of HHG, transitioning from classical perturbative power laws to unconventional non-integer dependencies. This regime originates from resonant amplification of local fields and the effective mixing of higher-order nonlinear polarization terms that are available even under moderate pump intensities, underscoring the transformative role of metasurface design in nonlinear optics.

Acknowledgments

Y.K. acknowledges support from the Australian Research Council (Grant No. DP210101292) and the International Technology Center Indo-Pacific (ITC IPAC) via Army Research Office (contract FA520923C0023). F.R., I.S., and H.A. thank the Swiss State Secretariat for Education, Research and Innovation (SERI) for financial support under the contract numbers 22.00018 and 22.00081 in connection with the projects from the European Union's Horizon Europe Research and Innovation Programme under agreements 101046424 (TwistedNano) and 101070700 (MIRAQLS). M.A.V. acknowledges financial support from NATO Science for Peace and Security program (Grant no. 5984).

References

[1] S. Ghimire, A. D. DiChiara, E. Sistrunk, P. Agostini, L. F. DiMauro, and D. A. Reis, "Observation of high-order harmonic generation in a bulk crystal," *Nature Physics*, vol. 7, pp. 138–141, 2011.

[2] M. R. Shcherbakov, D. N. Neshev, B. Hopkins, A. S. Shorokhov, I. Staude, E. V. Kivshar, and A. A. Fedyanin, "Generation of even and odd high harmonics in resonant metasurfaces using single and multiple ultra-intense laser pulses," *Nature Communications*, vol. 12, pp. 1–6, 2021.

[3] G. Zograf, F. B. Arango, M. Rybin, I. Toftul, M. Petrov, and Y. Kivshar, "High-harmonic generation from resonant dielectric metasurfaces empowered by bound states in the continuum," *ACS Photonics*, vol. 9, pp. 567–574, 2022.

[4] P. Tonkaev, F. Richter, I. Toftul, et al., "Unconventional high-harmonic generation in resonant membrane metasurfaces," *Nature Communications*, vol. 16, p. 11571, 2025

Nonlinear metasurfaces for Advanced Terahertz Generation

Davide Rocco[1,2*], Luca Carletti[1,2], Paolo Franceschini[1,2], Andrea Tognazzi[3], Olga Sergaeva[1], Unai Arregui Leon[4], Giuseppe Della Valle[4], Costantino De Angelis[1,2]

[1]Department of Information Engineering, University of Brescia, Italy
[2]National Institute of Optics, Consiglio Nazionale delle Ricerche, Brescia, Italy
[3]Department of Engineering, University of Palermo, Italy
[4]Department of Physics, Politecnico di Milano, Italy
*Corresponding author: davide.rocco@unibs.it

***Abstract*—The terahertz spectral region offers unique opportunities for imaging, communications, and material characterization. This work reports terahertz generation in resonant AlGaAs dielectric metasurfaces via second-order nonlinearity. Specifically, difference-frequency generation enables compact THz emission and analog processing, yielding an output proportional to the temporal derivative of the optical inputs.**

***Keywords*— metamaterials, terahertz, nonlinear optics, difference frequency generation.**

I. Introduction

The terahertz (THz) spectral region remains one of the most challenging frontiers in photonics, largely due to the difficulty of realizing compact, efficient, and robust radiation sources. This long-standing limitation, commonly referred to as the THz gap, originates from material constraints and technological bottlenecks that hinder broadband, high-repetition-rate THz generation. Established approaches such as THz quantum cascade lasers, photoconductive antennas, and optical rectification in bulk nonlinear crystals have enabled significant progress, particularly in spectroscopy and imaging. However, these solutions are often constrained by factors including cryogenic operation, limited bandwidth or efficiency, and the need for relatively large interaction volumes or high pump energies. These limitations have motivated a search for innovative approaches that can bridge the gap between laboratory-scale demonstrations and practical, deployable THz technologies, capable of addressing applications ranging from wireless communications to biomedical sensing.

Recent advances in nanophotonics have introduced resonant sub-wavelength platforms as a pathway toward more compact and controllable THz emitters [1-3]. In particular, plasmonic metastructures have demonstrated THz generation through enhanced nonlinear interactions, allowing emission from deeply sub-wavelength volumes and even enabling complex spatiotemporal field shaping. Beyond mere size reduction, these structures offer the possibility of integrating multiple functionalities on a single chip, potentially transforming how THz systems are designed and implemented. Despite these achievements, metallic losses fundamentally limit the efficiency of plasmonic schemes. Furthermore, the sensitivity of plasmonic resonances to fabrication imperfections and environmental factors presents an additional challenge for scalable applications.

All-dielectric metasurfaces have therefore emerged as a compelling alternative [4]. Owing to their low optical losses and strong bulk nonlinear response, dielectric resonators can support efficient nonlinear frequency conversion without relying on conventional phase-matching conditions. Instead, nanoscale mode confinement and resonance engineering govern the conversion process, enabling flexible control over the emitted THz radiation. By exploiting high-Q resonances and tailored unit-cell geometries, dielectric metasurfaces offer additional functionalities such as polarization control, wavefront shaping, and enhanced conversion efficiency. These advantages position dielectric metasurfaces as versatile platforms not only for THz generation but also for multifunctional photonic devices that can manipulate light at multiple frequencies simultaneously.

This work reports recent developments in THz generation via nonlinear optical processes in resonant dielectric metasurfaces, with a focus on high-index semiconductor platforms such as AlGaAs. It also highlights the potential for analog signal processing, as difference-frequency generation enables compact THz emission proportional to the temporal derivative of the optical inputs.

II. Results and Discussion

The nonlinear response of AlGaAs has been extensively investigated in the context of frequency conversion and THz generation. In particular, previous studies have shown that the second-order nonlinear susceptibility ($\chi^{(2)}$) exhibits a quasi-

linear frequency dependence in the THz range [4-6], with a distinct zero crossing of its real part occurring around 5.6 THz, as highlighted in the inset of Fig. 1. This dispersive feature plays a key role in shaping the nonlinear response of AlGaAs-based flat-optics platforms.

In the following, this material property is exploited to demonstrate a nonlinear analog signal-processing functionality enabled by an AlGaAs metasurface. The metasurface consists of a square lattice of AlGaAs nanopillars with radius 160 nm, height 400 nm, and period 400 nm, layered on a sapphire substrate. Specifically, we show that, when the structure is excited by two optical input fields under suitable spectral and temporal conditions, the resulting difference-frequency generation process leads to the emission of a THz field that is proportional to the first temporal derivative of the product of the input signals. This behavior forms the basis for temporal edge detection within a compact, planar nonlinear platform.

An idealized reference model is first introduced, as schematically illustrated in Fig. 1(a), aimed at capturing the essential physics of the nonlinear process under investigation. Two independent time-varying optical signals, denoted as $I_a(t)$ and $I_b(t)$, characterized by carrier frequencies f_a and f_b, respectively, are assumed to impinge on a thin nonlinear structure. For clarity, the second-order nonlinear susceptibility is treated as real-valued and assumed to vary linearly with frequency within the THz range. In this initial framework, the finite thickness of the device is neglected.

The quantity of interest is the THz-frequency electric field generated at the output of the AlGaAs metasurface through a difference-frequency generation (DFG) process, which is proportional to the second-order nonlinear polarization. Each incident electric field associated with the input signals can be expressed as:

$$E_{in}(k)=p_k(t)e^{j2\pi f_k t}+c.c. \quad \text{with} \quad k=a,b \tag{1}$$

where $p_k(t)$ represents the slowly varying temporal envelope of the optical pulse and *c.c.* denotes the complex conjugate.

The second-order surface polarization generated within the flat-optics element is therefore proportional to the temporal convolution of the total incident field and $\chi^{(2)}(t)$ which accounts for the dispersive nature of the second-order nonlinear response of the metasurface.

Under the assumption that the bandwidth of the pulse envelopes is much smaller than the generated THz carrier frequency $f_{THz}=f_a-f_b$, the nonlinear polarization can be simplified to:

$$P_s^{(2)}(t) \propto \frac{-i}{\pi}\left[\frac{\partial}{\partial t}\left(p_a(t)p_b^*(t)\right)\cdot e^{j2\pi f_{THz}t}-c.c.\right] \tag{2}$$

For real-valued temporal envelopes $p_a(t)$ and $p_b(t)$, this expression further reduces to:

$$P_s^{(2)}(t) \propto \frac{1}{\pi}\sin\left(2\pi f_{THz}t\right)\frac{\partial}{\partial t}\left[p_a(t)p_b(t)\right] \tag{3}$$

clearly indicating that the THz field produced by the DFG process oscillates at the difference frequency (f_{THz}) and is proportional to the temporal derivative of the product of the input signal envelopes. This result highlights the intrinsic capability of the metasurface to perform a first-order temporal differentiation of the incident optical signals.

To validate this analytical description, full-wave numerical simulations are performed using COMSOL Multiphysics, considering a metasurface with finite thickness and geometry. In the simulated configuration, one optical pump is modeled as a continuous-wave (CW) excitation, while the second pump carries the information signal and is temporally modulated within a given bandwidth. By selecting the frequency separation between the CW and the center frequency of the modulated signal to match the AlGaAs zero-crossing frequency (approximately 5.6 THz), the emitted THz field becomes proportional to the temporal derivative of the information-bearing signal alone.

The structure is illuminated at an incidence angle of 45° by a CW beam at λ_{CW} equal to 1030 nm and by a second optical beam modulated by a rectangular temporal pulse. Frequency-domain simulation results are converted into the time domain via inverse Fourier transformation.

For these design parameters, the nanopillars support a magnetic dipole resonance at the CW wavelength, resulting in approximately a twofold enhancement of the generated THz signal compared to an unpatterned AlGaAs slab. Figure 1(b) reports the *x*-component of the emitted THz electric field, normalized to the CW pump amplitude. Notably, the temporal profile of the THz output exhibits two pronounced peaks corresponding to the rising and falling edges of the information signal, in agreement with the predicted differentiation behavior. These results confirm the validity of the theoretical framework developed under the simplifying assumptions of negligible device thickness and idealized nonlinear response. More broadly, they demonstrate that engineered dielectric metasurfaces constitute an effective nanoscale platform not only for THz generation, but also for the simultaneous implementation of analog signal-processing operations such as temporal edge detection.

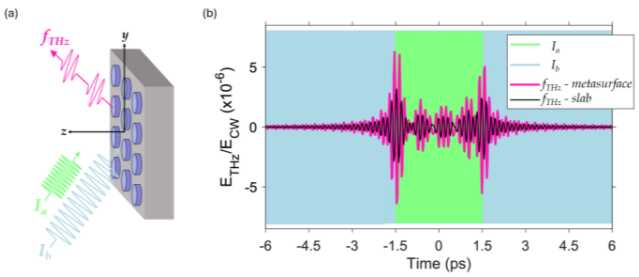

Fig. 1 (a) Schematic of the proposed temporal edge detection mechanism: two input signals, I_a and I_b, impinge on a metasurface made of $\chi^{(2)}$ dielectric material. The output signal oscillates at f_{THz}, corresponding to the difference between the incident pump frequencies. (b) THz emission from the AlGaAs metasurface compared to an unpatterned AlGaAs thin film, with the inputs being a CW pump (light-blue background) and an information signal represented by the green rectangular pulse.

III. Conclusion

This study demonstrates that dielectric metasurfaces constitute a viable flat-optics platform for the effective generation of terahertz radiation. Beyond serving as compact THz emitters, these structures are shown to support analog signal processing functionalities. Specifically, we show that terahertz difference-frequency generation in AlGaAs metasurfaces can be exploited to identify the temporal edges of optical pump pulses. This capability highlights the potential of such metasurface-based devices for applications in event detection and motion sensing.

Acknowledgments

This work was financially supported by the European Union–Next Generation EU, Mission 4 Component 1–PRIN 2022 project GRACE6G (2022H7RR4F) CUP D53D23001250001.

References

[1] Tal M., Keren-Zur S., and Ellenbogen T. "Nonlinear plasmonic metasurface terahertz emitters for compact terahertz spectroscopy systems," ACS photonics, vol. 7, pp. 3286-3290, 2020.

[2] Fang M., Niu K., Huang Z., Sha W.E., Wu X., Koschny T., and Soukoulis M. "Investigation of broadband terahertz generation from metasurface," Optics Express, vol. 27, pp. 14241-14250, 2018.

[3] Sideris S., Zixian H., McDonnell C., Li G., and Ellenbogen T. "Holographic THz beam generation by nonlinear plasmonic metasurface emitters," ACS photonics, vol. 10, pp. 2972-2979, 2023.

[4] Leon U.A., Rocco D., Carletti L., Peccianti M., Maci S., Della Valle G., and De Angelis, C. "THz-photonics transceivers by all-dielectric phonon-polariton nonlinear nanoantennas," Scientific Reports, vol. 12, p. 4590, 2022.

[5] Leon U.A., Carletti L., Rocco D., De Angelis C., and Della Valle G. "THz Generation via Optical Rectification in Nanomaterials: Universal Modeling Approach and Effective $\chi^{(2)}$ Description," Laser & Photonics Reviews, vol. 18, p. 2300669, 2024.

[6] Leon U.A., Franceschini P., Sergaeva O., Tognazzi A., Rocco D., Carletti L., de Ceglia D., Della Valle G., and De Angelis C. "Event detection via THz generation with flat nonlinear optics," Optical Materials Express, vol. 15, pp. 307-318, 2025.

Linear-Nonlinear: Polarization- and Orientation-Dependent Harmonic Response

Kristina Frizyuk[1,*]
[1]Karlsruhe Institute of Technology, Kaiserstrasse, 12, Karlsruhe, 76131, Germany
*Corresponding author: kristina.friziuk@kit.edu

***Abstract*—We discuss two recent results showing that seemingly distinct polarization- and rotation-dependent phenomena in second-harmonic generation (SHG) admit compact "linearized" descriptions with predictive power.**

First case is nonlinear polarimetric analysis based on SH emission from AlGaAs dielectric gratings [1]. SHG is bilinear in the pump field, $\mathbf{P}_{2\omega} = \chi^{(2)} : \mathbf{E}^{\text{int}}_{\omega} \otimes \mathbf{E}^{\text{int}}_{\omega}$, where $\mathbf{E}^{\text{int}}_{\omega}$ is an internal field inside the nonlinear material. It turns out [1], [2], SHG can be viewed as the action of an effective linear operator on the tensor product $\mathbf{E}_{\omega} \otimes \mathbf{E}_{\omega}$, where $\mathbf{E}_{\omega}$ is the incident field. In simple terms, once the response of the structure is known for a small set of basis tensor products of the form $\mathbf{E}^1_{\omega} \otimes \mathbf{E}^2_{\omega}$, the response to an arbitrary polarization follows automatically. Any input polarization can be decomposed into these basis components, and since SHG acts linearly in the tensor-product space, the corresponding SH field and intensity are obtained by superposition. In this sense, the nonlinear polarimetric response of the system is completely determined by its action on a finite set of elementary tensor product states. In the proposed platform, a twist between the nanostructure orientation and the crystalline lattice produces strong polarization selectivity, including near-unity nonlinear circular dichroism around 1550 nm and an approximately polarizer-like dependence on the linear polarisation angle. A four-element "super-pixel" consisting of four rotated but geometrically identical units enables single-shot Stokes retrieval from SH intensity only.

Second, we consider tensor-driven geometric phase in AlGaAs nanoresonators and metasurfaces [3]. The nanostructure here is rotated, while the lattice orientation is fixed. Here the key step is that a rotation of the nonlinear susceptibility tensor around the optical axis can be written as a linear combination of two fixed tensor components,

$$\chi^{(2)\prime} = \cos(2\beta)\chi^{(2)}_1 + \sin(2\beta)\chi^{(2)}_2,$$

which implies an analogous superposition for the particular TAM component of the generated SH field,

$$\mathbf{E}_{2\omega} = \cos(2\beta)\mathbf{E}_1 + \sin(2\beta)\mathbf{E}_2.$$

This decomposition makes the orientation dependence fully predictable. Even though the SH intensity and phase as functions of the relative rotation angle may appear nontrivial, for a given TAM component they are entirely determined by the interference of two fixed complex responses associated with the two basis components. Once the SH response is known for these two reference tensor contributions, the SH amplitude and phase for an arbitrary relative orientation between the nanoresonator (or metasurface) and the crystal axes follow directly by superposition, including both the intensity and the phase.

The theoretical framework is confirmed experimentally using two AlGaAs devices. In a nonlinear beam-steering metasurface, opposite circular polarization components of the SH are deflected into opposite diffraction orders, producing angular separation of $\pm 12^{\circ}$. In a second device, the same mechanism is used to generate a structured SH beam with topological charge $\ell = 1$.

Together, these works show how operator-level reformulations, *i.e.* linear action on the tensor product, provide predictive, design-oriented models for polarization and orientation functionalities in SHG from nanostructures.

Acknowledgments

I gratefully thank all the co-authors of the presented works, namely, E. Menshikov, M. A. L'opez S'anchez, P. Franceschini, A. Tognazzi, D. de Ceglia, C. De Angelis, G. Guercio, A. Gerini, M. Morassi, A. Lemaitre, L. Carletti, and G. Leo. I gratefully acknowledge support from the Alexander von Humboldt Foundation.

References

[1] E. Menshikov, M. A. L'opez S'anchez, P. Franceschini, A. Tognazzi, D. de Ceglia, K. Frizyuk, and C. De Angelis, "Near-infrared polarimetric imaging with nonlinear flat-optics," *arXiv preprint arXiv:2512.01525*, 2025.

[2] L. Freter, B. Zerulla, M. Krsti'c, C. Holzer, C. Rockstuhl, and I. Fernandez-Corbaton, "Tensor product space for studying the interaction of bipartite states of light with nanostructures," *Phys. Rev. A*, vol. 110, p. 043516, 2024.

[3] G. Guercio, A. Gerini, K. Frizyuk, C. De Angelis, M. Morassi, A. Lemaitre, L. Carletti, and G. Leo, "Tensor-driven geometric phase in nonlinear AlGaAs metasurfaces," *arXiv preprint arXiv:2601.18246*, 2026.

Nanoimprinted barium titanate sol-gel for electro-optic modulation

Virginia Falcone[1,*], Eleni Prountzou[1] and Rachel Grange[1]

[1]Department of Physics, Institut für Quantenelektronik, ETH Zürich, Switzerland

*Corresponding author: vfalcone@phys.ethz.ch

***Abstract*—Solution-processed $BaTiO_3$ patterned by soft nanoimprint lithography enables scalable electro-optic devices in both metasurface and integrated platforms. Resonant field confinement and ferroelectric domain alignment enhance modulation efficiency. These results demonstrate a versatile, low-cost route toward oxide-based active photonic devices across free-space and integrated photonics.**

***Keywords*— Barium titanate, nanoimprinting, electro-optic modulation.**

I. Introduction

Efficient electro-optic modulation is a key requirement for active photonic and flat-optics devices. Among metal oxides, barium titanate ($BaTiO_3$, BTO) is particularly attractive due to its strong Pockels effect and wide transparency window, making it promising for both free-space and integrated platforms. However, conventional growth techniques such as MBE, CVD, and PLD [1] rely on costly equipment, restrict substrate choice, and make nanopatterning challenging due to the chemical inertness of the material.

Chemical solution deposition provides a low-cost and versatile alternative, enabling polycrystalline $BaTiO_3$ films with electro-optic coefficients comparable to bulk lithium niobate and compatibility with a wide range of substrates [2]. When combined with soft nanoimprint lithography (SNIL), this bottom-up approach enables direct nanopatterning of the material into functional nanostructures for electro-optic devices.

II. Results and Discussion

$BaTiO_3$ films deposited by chemical solution processing are directly patterned by soft nanoimprint lithography, enabling etch-free nanostructuring with tunable optical properties through process optimization. Imprinted metasurfaces composed of subwavelength BTO pillars exhibit a strongly enhanced electro-optic response compared to unstructured films, arising from resonant optical confinement and improved electric field distribution within the active material. Two optimized fabrication configurations further increase the modulation efficiency, while the application of a static bias partially aligns the ferroelectric domains, enhancing the effective electro-optic coefficient and the achievable transmission modulation [3], [4].

The versatility of this approach is further demonstrated in integrated devices, where nanoimprinted sol-gel BTO waveguides enable electro-optic phase modulation at 1550 nm on SiO_2 substrates. By tuning the sol-gel process parameters, optical losses are reduced by 50% and modulation efficiency is improved through grain size control. Partial domain poling, as in the metasurfaces, further enhances the modulation, confirming the versatility of this approach across both free-space and guided photonic architectures [3].

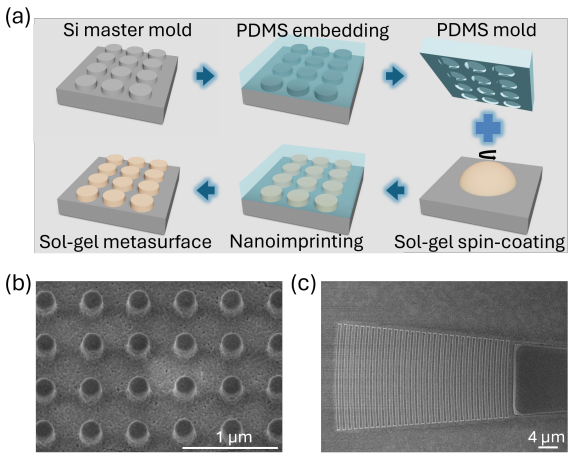

Fig. 1. (a) Schematic of the soft nanoimprint lithography process for patterning BTO sol-gel metasurfaces. (b) SEM image (tilted 30°) of an imprinted BTO metasurface. (c) Imprinted grating coupler and taper of a BTO sol-gel waveguide for integrated electro-optic devices.

III. Conclusion

In conclusion, solution-processed BTO combined with soft nanoimprint lithography enables scalable electro-optic devices spanning both metasurface and integrated photonic platforms. Resonant field engineering and ferroelectric domain alignment jointly enhance the effective electro-optic response in polycrystalline films. This approach opens a new route toward efficient flat-optics and integrated oxide photonic modulators.

References

[1] K. J. Kormondy, et al.," *Nanotechnology*, vol. 28, pp. 075706, 2017.
[2] B. I. Edmondson, et.al.," *J. Am. Ceram. Soc.*, vol. 103, pp. 1209, 2020.
[3] E. Prountzou, H. C. Weigand, V. Falcone, Ü.-L. Talts, and R. Grange," *arXiv:2601.20434*, 2026.
[4] H. C. Weigand, Ü.-L. Talts, A.-L. Vieli, V. V. Vogler-Neuling, A. Nardi, and R. Grange," *Nano Lett.*, vol. 24, no. 18, pp. 5536–5542, 2024.
[5] V. Falcone, E. Prountzou, J. Kellner, Ü.-L. Talts, and R. Grange," *arXiv:2601.14938*, 2026.

Recent Advancements in Metamaterials and Metasurfaces for Scattering and Wave Engineering

AES 2026 · Catania, Italy · ISSN 2491-2417

Analytical Modeling of Anomalous Reflection via Piecewise-Uniform Boundary Conditions

Federico Giusti, Enrica Martini, Stefano Maci, Matteo Albani

Department of Information Engineering and Mathematics, University of Siena, 53100 Siena

*Corresponding author: federico.giusti2@unisi.it

***Abstract*—Recent advances in anomalous reflectors design have led to a variety of synthesis techniques, ranging from analytical formulations to optimization-driven methods. In this work, we present an analytical solution for the canonical problem of anomalous reflection over a homogenized impenetrable impedance with a tangent profile. The proposed theoretical framework is validated through full-wave simulations of a -20° to +60° anomalous reflection under transverse-electric polarization, demonstrating excellent agreement in both amplitude and phase for all reflected Floquet harmonics.**

***Keywords*— Metasurfaces, anomalous reflection, Floquet harmonics, reflecting intelligent susrfaces.**

I. Introduction

Metasurfaces (MTSs) are ultrathin, engineered structures that provide an efficient, low-profile platform for controlling electromagnetic wavefronts, enabling a wide range of applications [1]. Among these, MTSs are particularly notable for facilitating anomalous reflection and transmission [2]–[6]. Early developments in this field mainly relied on phase-gradient MTSs [2], [3], which impose linearly varying phase delays to steer electromagnetic waves along non-specular directions. These devices are typically modeled using idealized, passive, lossless, and dispersionless impedance profiles.

Although more advanced synthesis methods have been developed to enhance control over anomalous scattering across wide angles [5]–[9], the conventional design of anomalous reflectors, particularly in the context of reconfigurable intelligent surfaces, still largely relies on prescribing a constant phase gradient for the reflection coefficient. Consequently, an analytical treatment of the canonical phase-gradient metasurface problem remains essential, as it provides fundamental physical insight along with a quantitative assessment of non-idealities. A significant step in this direction was presented in [10], which analyzed the Floquet-Bloch response of passive Huygens metasurfaces for anomalous transmission. More recently, preliminary investigations in [11] identified and numerically verified an intrinsic ambiguity in the phase of the specular (zero-th order) Floquet harmonic when the anomalous reflector is modeled as an impenetrable continuous reactance boundary with a tangential profile. Since higher-order harmonics with negative index are found to be proportional to the zero-th order term, this ambiguity propagates, rendering all negatively indexed harmonics indeterminate. This ambiguity can be solved by explicitly accounting for the MTS discretization in unit cells through a piecewise-uniform impedance profile.

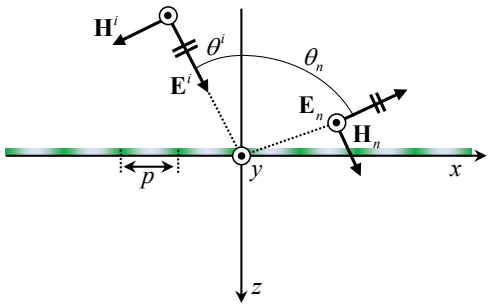

Fig. 1: Geometry for the TE-polarized anomalous reflection over a homogenized, impenetrable MTS periodically modulated with period p along the x-axis. The configuration is uniform and invariant along the y-axis. The incident (θ^i) and reflected (θ_n) angles, corresponding to the n-th Floquet harmonic, are measured from the negative z-axis illustrated with the vertical black line.

In this work, we present an analytical solution for the canonical problem of anomalous reflection based on a piecewise-uniform boundary condition (PUBC), providing a well-posed and physically consistent formulation that resolves the indeterminacy of the zero-th order Floquet harmonic. The validity of the solution is assessed through full-wave simulations of a $-20°$ to $+60°$ anomalous reflection under transverse-electric (TE) polarization, showing excellent agreement in both amplitude and phase for all reflected Floquet harmonics.

II. Theoretical Framework and Numerical Results

This section presents a theoretical framework providing an analytical solution to the canonical problem of TE-polarized anomalous reflection of a plane wave incident on a homogenized, periodic, impenetrable MTS located at $z = 0$, as illustrated in Fig. 1. Due to the periodic nature of the MTS, the incident fields ($\mathbf{E}^i$, $\mathbf{H}^i$) are scattered into an infinite set of propagating and evanescent Floquet harmonics, denoted as ($\mathbf{E}_n$, $\mathbf{H}_n$), with n indicating the harmonic index. The reflection coefficients are defined as $\Gamma_n = E_n/E_0^i$, with E_0^i and E_n being the amplitudes of the incident and scattered fields. The MTS is described through the following Leontovich boundary condition

$$E_y(x, z = 0) = -Z^{\mathrm{TE}}(x)\frac{\partial E_y(x, z = 0)}{\partial z} \qquad (1)$$

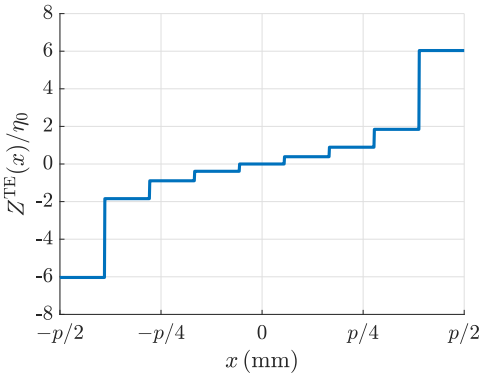

Fig. 2: Piecewise-uniform impedance profile over the macroperiod p for a $-20°$ to $+60°$ anomalous reflection.

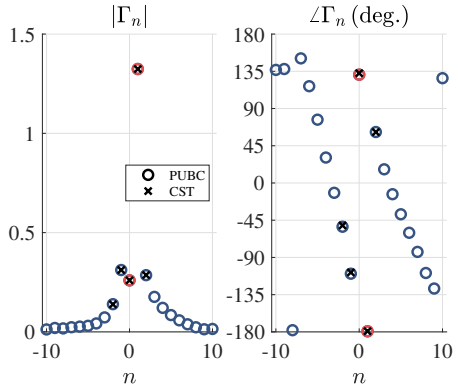

Fig. 3: Amplitude and phase of the reflection coefficients Γ_n for the propagating (orange markers) and evanescent (black markers) Floquet harmonics with orders ranging from -10 to $+10$ obtained imposing a piecewise-uniform boundary condition (PUBC). Black crossed markers denote the corresponding full-wave simulation results obtained using CST Microwave Studio.

where, to resolve the indeterminacy of the continuous tangent profile reported in [11], we consider a piecewise-uniform profile obtained by discretizing the tangent profile into M uniform segments of width $w = \frac{p}{M}$ (see Fig. 2). With the m-th segment centered at $x_m = \frac{p}{M}m$, the piecewise-uniform impedance is given by

$$Z^{\mathrm{TE}}(x_m) = j\frac{\eta_0}{\cos\theta^i}\tan\left(\frac{\pi}{p}x_m\right) = \frac{\eta_0}{\cos\theta^i}\frac{e^{j\frac{2\pi}{M}m}-1}{e^{j\frac{2\pi}{M}m}+1}\,. \quad (2)$$

Considering the piecewise-uniform boundary condition (PUBC) defined by inserting (2) into (1), one can derive the following linear system of equations whose solution provides all the complex reflection coefficients Γ_n:

$$\sum_{q=-\infty}^{\infty}\left(1+\frac{\cos\theta_{n+1+qM}}{\cos\theta^i}\right)\mathrm{sinc}\left(\frac{1+qM}{M}\right)\Gamma_{n+1+qM} \quad (3)$$
$$+\left(1-\frac{\cos\theta_n}{\cos\theta^i}\right)\Gamma_n = -2\delta_{n0}\,, \quad \forall q\in\mathcal{Z}\,.$$

To validate the proposed theoretical framework, we examine the case of a $-20°$ to $+60°$ anomalous plane-wave reflection at 27 GHz. For this case, the period of the MTS is set to $p = 9.19$ mm and the $n = 0, +1$ are the only propagating Floquet harmonics. As shown in Fig. 2, the continuous tangential profile is discretized into $M = 9$ elements, corresponding to a step of $w = 1.02$ mm. Reflection coefficients Γ_n are computed by truncating (3) at $N = 1000$ harmonics, ensuring convergence [12], and the amplitude and phase of all harmonics are reported in Fig. 3. Full-wave simulations in CST Studio Suite model the MTS with ideal impenetrable impedance strips, periodic boundary conditions in the xy-plane, and a Floquet port along z at distance w. The results in Fig. 3 show excellent agreement between the PUBC predictions (circular markers) and CST simulations (black crosses), confirming the accuracy of the PUBC.

III. Conclusion

In this work, we present an analytical formulation for the canonical problem of anomalous reflection, based on a piecewise-uniform impenetrable continuous boundary condition with a tangential profile. The theoretical framework is validated via full-wave simulations of TE-polarized anomalous reflection from $-20°$ to $+60°$, demonstrating excellent agreement in both amplitude and phase across all reflected Floquet harmonics. A physical implementation using real elements, as well as results for a TM-polarized case, will be presented at the conference.

References

[1] S. B. Glybovski, S. A. Tretyakov, P. A. Belov, Y. S. Kivshar, and C. R. Simovski, "Metasurfaces: from microwaves to visible," *Physics Reports*, vol. 634, pp. 1–72, 2016.

[2] N. Yu and F. Capasso, "Flat optics with designer metasurfaces," *Nature Mater.*, vol. 13, no. 2, pp. 139–150, 2014.

[3] N. Mohammadi Estakhri and A. Alù, "Wave-front transformation with gradient metasurfaces," *Phys. Rev. X*, vol. 6, p. 041008, Oct 2016.

[4] V. S. Asadchy, M. Albooyeh, S. N. Tcvetkova, A. Díaz-Rubio, Y. Ra'di, and S. A. Tretyakov, "Perfect control of reflection and refraction using spatially dispersive metasurfaces," *Physical Review B*, vol. 94, p. 075142, Aug 2016.

[5] M. Movahediqomi, G. Ptitcyn, and S. Tretyakov, "Comparison between different designs and realizations of anomalous reflectors for extreme deflections," *IEEE Transactions on Antennas and Propagation*, vol. 71, no. 10, pp. 8007–8017, 2023.

[6] F. Giusti, E. Martini, S. Maci, and M. Albani, "Comparison between different approaches for the design of anomalous refractors," *IEEE Transactions on Antennas and Propagation*, vol. 72, no. 4, pp. 3495–3506, 2024.

[7] A. Epstein and G. V. Eleftheriades, "Arbitrary power-conserving field transformations with passive lossless omega-type bianisotropic metasurfaces," *IEEE Transactions on Antennas and Propagation*, vol. 64, no. 9, pp. 3880–3895, 2016.

[8] D.-H. Kwon, "Planar metasurface design for wide-angle refraction using interface field optimization," *IEEE Antennas Wireless Propag. Lett.*, vol. 20, no. 4, pp. 428–432, 2021.

[9] F. Giusti, E. Martini, S. Maci, and M. Albani, "Lossless planar metasurface for wide-angle anomalous refraction based on an efficient surface field optimization," in *2022 IEEE International Symposium on Antennas and Propagation and USNC-URSI Radio Science Meeting (AP-S/URSI)*, 2022, pp. 561–562.

[10] A. Epstein and G. V. Eleftheriades, "Floquet-Bloch analysis of refracting Huygens metasurfaces," *Phys. Rev. B*, vol. 90, p. 235127, Dec 2014.

[11] F. Giusti, P. Terekhina, E. Martini, S. Maci, and M. Albani, "Closed-form solution for the scattering coefficients in the canonical problem of anomalous reflection," in *2025 19th European Conference on Antennas and Propagation (EuCAP)*, 2025, pp. 1–5.

[12] F. Giusti, E. Martini, S. Maci, and M. Albani, "A rigorous model for anomalous reflection using piecewise-uniform boundary conditions," in *2026 20th European Conference on Antennas and Propagation (EuCAP)*, 2026, pp. 1–4.

Scattering properties of a cylindrical scatterer with time-modulated permittivity

J. Yan[1,*], I. Katsantonis[1], M. Mostafa[2], V. Asadchy[2] and M. Kafesaki[1]

[1]Institute of Electronic Structure and Laser, Foundation for Research and Technology-Hellas, Crete, Greece
[2]Department of Electronics and Nanoengineering, School of Electrical Engineering, Aalto University, Finland
*jiaruo.yan@iesl.forth.gr

***Abstract*—Employing Floquet-Mie theory, we study the scattering properties of an infinitely-long cylinder with permittivity that is modulated periodically in time. The interference between scattering coefficients of different harmonics, as well as of different multipolar orders, allows for the design of radiation direction via tuning the modulation parameters.**

***Keywords*— metamaterials, time-varying medium.**

I. Introduction

Time variation in the material properties of a medium introduces more freedom to the control of wave-medium interactions [1]. The time modulation can be of various forms, be it discontinuous, aperiodic or periodic[2], [3]. Floquet theory is applicable if temporal periodicity is assumed. It has been shown that momentum bandgap is formed if a homogeneous medium undergoes periodic time modulation in its electromagnetic properties[4], [5]. Scatterers of different shapes with time-varying material properties, have also been studied in literature[6], [7], [8].

In this work, we present our results on cylindrical scatterers of infinite length and time-modulated relative permittivity. Analytical results on the parametric Mie resonances and the required modulation parameters are discussed, as well as the possibility to engineer the far-field distribution from such scatterers via controlling the interference between the scattered harmonics.

II. Methods

We assume a sinusoidal variation in ε_r of a dielectric cylinder of infinite length as follows

$$\varepsilon(t) = \varepsilon_{r0} + \Delta\varepsilon\cos(\omega_{\mathrm{m}}t) = \sum_{n=-N}^{N} \varepsilon(n)\exp(in\omega_{\mathrm{m}}t) \quad (1)$$

where ε_{r0} is the reference permittivity in the absence of modulation, $\Delta\varepsilon$ is the modulation strength. $\varepsilon(n)$ are the Fourier coefficients, with the Fourier series truncated to a highest order N. $\omega_{\mathrm{m}} = 2\pi/T_{\mathrm{m}}$ is the modulation frequency in rad/s. The scattered harmonics then have frequencies of $f - nf_m$, where f is the incident frequency, n is the order of the scattered harmonic.

The E and H fields can be expanded into Fourier series, based on the Floquet theorem. Substituting the expanded fields and ε_r into the Maxwell's equations, we arrive at an eigenvalue problem describing the periodically time-modulated homogeneous medium as below:

$$\mu_c(2\pi\frac{f-nf_m}{c})^2 \sum_{\nu=-N}^{N} \varepsilon(n-\nu)\mathbf{E}^{(\nu)} = q^2\mathbf{E}^{(n)}. \quad (2)$$

where μ_c is the permeability of the medium, assumed to be $\mu_c = 1$ from now on. q and is the square root of the eigenvalue solutions, representing the allowed wavenumbers in the modulated medium. The eigenvectors $\mathbf{v}_\nu$ contains $2N+1$ elements that represent the field amplitudes of the scattered harmonic.

Considering a cylindrical scatterer of time-modulated permittivity, we express the total electric or magnetic fields in the host medium and within the cylinder both based on cylindrical expansions. Take the TE polarization as an example, where the electric field is perpendicular to the cylinder axis, the expressions for the electric fields are as below,

$$\mathbf{E}_{\mathrm{h}}^{(n)}(\mathbf{r}) = i\sum_{l}\left[a_l^0\mathbf{m}_l(k_0,\mathbf{r})\delta_{n0} + a_{l+}^{(n)'}\mathbf{m}_l'(q_{\mathrm{h}n},\mathbf{r})\right] \ , \quad (3)$$

$$\mathbf{E}_{c}^{(n)}(\mathbf{r}) = i\sum_{\nu=-N}^{N} v_\nu(n)\sum_{l} a'_{l;\nu}\mathbf{m}_l(q_\nu,\mathbf{r}) \ , \quad (4)$$

where $\mathbf{m}_l$ is the vector cylindrical harmonic of order l, $a_{l+}^{(n)'}$ is the scattering coefficient of the n-th harmonic arising from the time modulation, and if normalized to the incident coefficient a_l^0, gives $a_{l+}^{(n)} = a_{l+}^{(n)'}/a_l^0$. $q_{hn} = \frac{\omega - n\omega_m}{c}$ is the wavenumber of the n-th harmonic in the host medium (assumed to be free space from now on), and k_0 is the wave number of the incident wave in the host medium. The expressions for the magnetic fields are written analogously using the vector cylindrical harmonics (also functions of the Bessel functions, and will be omitted here.

Applying the spatial boundary conditions based on the tangential components of the electric fields $\mathbf{E}$ and magnetic fields $\mathbf{H}$, one can obtain, for each n and l,

$$\sum_{\nu=-N}^{N} a_{l;\nu}\, v_\nu(n)\frac{\partial J_l(q_\nu R)}{\partial(q_\nu R)} = \frac{\partial J_l(k_0R)}{\partial(k_0R)}\delta_{n0} + a_{l+}^{(n)}\frac{\partial H_l(q_{\mathrm{h}n}R)}{\partial(q_{\mathrm{h}n}R)} \ , \quad (5)$$

$$\sum_{\nu=-N}^{N} b_{l;\nu}\, v_\nu(n) J_l(q_\nu R) = J_l(k_0 R)\delta_{n0} + b_{l+}^{(n)} H_l(q_{\mathrm{h}n} R)\ , \tag{6}$$

where R is the radius of the cylinder, J_l, H_l are the l-th order Bessel function and Hankel function respectively. $a_{l+}^{(n)} = \sqrt{\mu_h/\varepsilon_h}\, b_{l+}^{(n)}$. Therefore, there are essentially $2(2N+1)$ parameters, numerically solvable based on the above set of simultaneous equations.

We define the total scattering efficiency, the summation of the contributions from all the harmonics taken into account in the calculations as,

$$Q_{\mathrm{sc}} = \sum_{n=-N}^{N} Q^{(n)} = \sum_{n=-N}^{N} \frac{2}{|q_{\mathrm{h}n}|R} \sum_{l} \frac{2}{1+\delta_{l0}} |a_{l+}^{(n)}|^2\ . \tag{7}$$

If $N = 0$, the above formalism reduces to the problem of scattering from a time-invariant infinite cylinder [9].

III. Results and Discussion

Based on the method in Section II, and taking the modulation frequency $f_m = 2f$, we observed that the dominant harmonics are $n = 0, 1$ if parametric resonances are reached, under the assumption that the modulation strength $\Delta\varepsilon$ is small. These two harmonics correspond to frequencies $f_{n=0,1} = \pm f$. The simultaneous equations as in Eq. (5) then reduce to a set of four equations, along with the eigen-problem condition where there is no incident waves. For non-zero solutions to the scattering coefficients to exist, we can solve this truncated eigen-problem to obtain the required modulation strengths at each modulation frequency (recall that we always have $f_m = 2f$). Choosing parameters $\varepsilon_{r0} = 12$, $R = 5\,\mathrm{mm}$, the semi-analytical results are plotted in Fig. 1 for both TE (upper) and TM (lower) polarizations as the colored solid curves. The different colors of the solid curves represent results of different multipolar orders l. These results correspond to the left y-axis in both subplots. The scattering efficiency over incident frequency is also plotted in black dashed curves for a reference static system with $\varepsilon_r = 12$, with the y-axes being on the right. Mie resonances of different orders are clearly seen with the chosen frequency range.

The minimum required $\Delta\varepsilon_{th}$ (upper curves) for each order l occurs at frequency f that correspond to the Mie resonant frequency of the static reference system ($\varepsilon_r = \varepsilon_{r0} = 12$), and the minimum value decreases as l increases. This can be explained by the reduced losses in the higher-order Mie resonances of the static cylinder, as shown by the sharper peaks of the dashed curves as frequency increases.

For the TE polarization, a different approach to calculate the required $\Delta\varepsilon_{th}$ for parametric resonance, based on the simultaneous equations in Eq. (5) and (6), and taking into account higher-order scattered harmonics up to $N = 3$, was adopted. The corresponding results for different order l are plotted as the colored dots in Fig. 1, to compare with the results from the truncated eigen-problem. Larger deviations are observed as $\Delta\varepsilon_{th}$ increases, due to the presence of higher-order scattered harmonics when stronger modulation is applied, reducing the accuracy of the truncated eigen-problem approximation. The overlap between the dots of different colors shows the modulation conditions where multipoles of different orders can be excited simultaneously. For example at around 12 GHz and modulation strength $\Delta\varepsilon \approx 5.5$, TE polarized case, electric dipole and quadrupole can be excited at the same time, and backward radiation is shown with certain modulation parameters as in the field distribution plotted in Fig. 2. The interactions between different modes, as well as the scattered harmonics arising from time modulation (with phase differences between them), result in various far-field distributions that can be tailored.

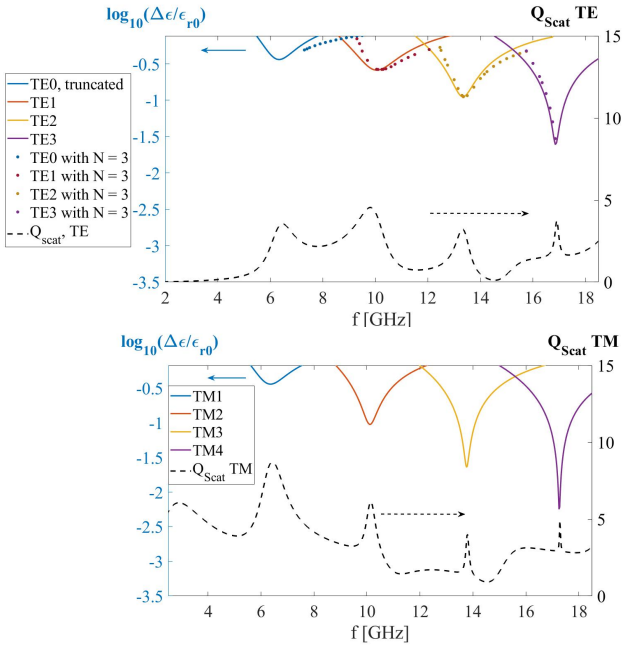

Fig. 1. Left axes in both figures: Log-scale of the ratio between threshold modulation strength $\Delta\varepsilon_{th}$ for parametric resonance under $f_m = 2f$, and the static relative permittivity ε_{r0}, results over incident frequency f in colored solid curves. Right axes: scattering efficiencies over frequency f, linear scales, plotted in black dashed curves. Upper plot: TE mode, also plotted in dots are the results from Eqns (5) and (6) from Section II, taking into account up to third-order harmonics. Lower: TM mode.

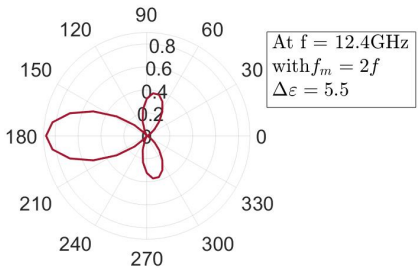

Fig. 2. Field distribution in the farfield, $|E|^2$, for a time-modulated cylinder of $\varepsilon_{r0} = 12$, $R = 5\,\mathrm{mm}$, $f = f_m/2 = 12.4\,\mathrm{GHz}$, $\Delta\varepsilon = 5.5$.

IV. Conclusion

We have investigated a cylindrical scatterer of infinite length and of periodically time-modulated relative permittivity. The semi-analytical results on calculating the scattering properties of the time-varying scatterer, based on Floquet-Mie theory and the spatial boundary conditions, indicate that the modulation parameters for achieving parametric Mie resonances are related to the resonant properties of the static system. Parametric resonances can be obtained for different multipolar modes at the same time, allowing for different far-field distributions to be designed and achieved. Further analysis will be extended to plasma cylinders of time-varying plasma properties, which may be realized in practice through controlling the plasma ignition or sustain sources. Such time modulated scatterers can be formed into time-varying metamaterial structures, with applications in, for instance, wavefront engineering.

Acknowledgments

This work was supported by the European Union under the call "EIC Pathfinder Open 2022" (Project PULSE, project no. 101099313).

References

[1] C. Caloz and Z.-L. Deck-Leger, "Spacetime metamaterials—part ii: Theory and applications," *IEEE Trans- actions on Antennas and Propagation*, vol. 68, no. 3, pp. 1583–1598, 2019.

[2] F. R. Morgenthaler, "Velocity modulation of electromagnetic waves," *IRE Transactions on microwave theory and techniques*, vol. 6, no. 2, pp. 167–172, 2003.

[3] E. Galiffi, R. Tirole, S. Yin, et al., "Photonics of time-varying media," *Advanced Photonics*, vol. 4, no. 1, pp. 014 002–014 002, 2022.

[4] M. M. Asgari, P. Garg, X. Wang, M. S. Mirmoosa, C. Rockstuhl, and V. Asadchy, "Theory and applications of photonic time crystals: A tutorial," *Advances in Optics and Photonics*, vol. 16, no. 4, pp. 958–1063, 2024.

[5] X. Wang, P. Garg, M. Mirmoosa, A. Lamprianidis, C. Rockstuhl, and V. Asadchy, "Expanding momentum bandgaps in photonic time crystals through resonances," *Nature Photonics*, vol. 19, no. 2, pp. 149–155, 2025.

[6] I. Stefanou, P. A. Pantazopoulos, and N. Stefanou, "Light scattering by a spherical particle with a time-periodic refractive index," *Journal of the Optical Society of America B*, vol. 38, no. 2, pp. 407–414, 2021.

[7] G. Ptitcyn, A. Lamprianidis, T. Karamanos, et al., "Floquet–mie theory for time-varying dispersive spheres," *Laser & Photonics Reviews*, vol. 17, no. 3, p. 2 100 683, 2023.

[8] V. Asadchy, A. Lamprianidis, G. Ptitcyn, et al., "Parametric mie resonances and directional amplification in time-modulated scatterers," *Physical Review Applied*, vol. 18, no. 5, p. 054 065, 2022.

[9] C. P. Mavidis, A. C. Tasolamprou, E. N. Economou, C. M. Soukoulis, and M. Kafesaki, "Polaritonic cylin- ders as multifunctional metamaterials: Single scattering and effective medium description," *Physical Review B*, vol. 102, no. 15, p. 155 310, 2020.

Efficient Optimization of Metasurface for Near-field mmWave Communications

Álvaro F. Vaquero[1,*], Manuel Arrebola[2], Marcos R. Pino[1]

[1]Department of Electrical Engineering, University of Oviedo, Spain
[2]Information Processing and Telecommunications Center, Universidad Politécnica de Madrid, Spain
*Corresponding author: fernandezvalvaro@uniovi.es

***Abstract*—This work presents a computationally efficient framework for near-field optimization of electrically large metasurfaces. By combining the Plane Wave Spectrum method with Differential Contributions, the proposed approach accelerates the field computation on gradient based optimization by reducing field evaluations. The method scales efficiently with metasurface size, enabling practical metasurface synthesis.**

***Keywords*— Electrically Large Antenna, Metasurface, mmWave band, Near-field Synthesis.**

I. Introduction

Reflective metarsurfaces (MS) have emerged as a key enabling technology for millimeter-wave (mmWave) communication system, supporting applications such as point-to-point links, coverage enhacement, and advanced beamforming capabilities. Their design is commonly addressed through phase-only synthesis or direct optimization techniques. While direct optimization offers higher accuracy by accounting for the full electromagnetic response of the unit cell, it entails a significant computational burden, particularly when near-field constraints and large apertures are considerd.

Gradient-based optimization frameworks, such as the generalized Intersection Approach, are especially attractive for near-field synthesis. However, their practical application is limited by the high computational cost associated with evaluating the Jacobian matrix, which requires repeated volumetric near-field calculations over electrically large domains. Although the Differential Contributions (DFC) technique [1] alleviates the issue by exploiting the linear relationship between the tangential field at the aperture and the radiated field, as Maxwell's Equation state, the overall cost remain prohibitive when conventional field computation strategies are used.

To address this limitation, this work proposes a computationally efficient framework that combines the Plane Wave Spectrum (PWS) method [2] with the DFC technique. By leveraging spectral propagation, the proposed approach significantly accelerates the evaluation of near-field distributions and gradient computation, enabling the practical optimization of large optimization problems.

II. Results

The proposed method discretizes the volumetric observation domain into a finite set of parallel planes and employs PWS formulation to propagate the aperture field to all observation planes through spectral phase shifting. This allows the near-field distribution over the entire volume to be obtained efficiently from a single spectral representation of the aperture field.

The computational complexity of this approach shows a significant reduction compared to conventional methods, such as Principle of Superposition, or other plane-wise FFT-based propagation. The proposed PWS-DFC approach virtually removes the multiplicative dependence on the number of observation planes. Specifically, the dominant computational cost scales linearly with the numer of MS elements, making it particularly suitable for electrically large MS with thousands of elements.

III. Conclusion

An efficient framework for near-field optimization of MS has been presented, combining the PWS method with DFC techniques. The proposed approach significantly reduces the computational burden associated with gradient-based optimization by decoupling the cost from the number of observation planes in the volumetric domain.

This method enables the practical synthesis of large MS under near-field constraints and represents a powerful alternative to classical near-field optimization strategies, particularly for mmWave communication systems requiring complex field control.

Acknowledgments

This work was supported in part by Grant PID2023-146246OB-C32 (ANT4IT) funded by Spanish Government through MCIU /AEI /10.13039/501100011033 / FEDER, UE (Ministerio de Ciencia, Innovación y Universidades, Agencia Estatal de Investigación y Fondo Europeo de Desarrollo Regional de la Unión Europea); and in part by the Government of Asturias-Sekuens/FEDER under grant IDE-2024-000693.

References

[1] D. R. Prado, Á. F. Vaquero, M. Arrebola, M. R. Pino, and F. Las-Heras, "Acceleration of gradient-based algorithms for array antenna synthesis with far-field or near-field constraints," *IEEE Trans. Antennas Propag.*, vol. 66, no. 10, pp. 5239–5248, Oct. 2018.

[2] R. H. Clarke and J. Brown, *Diffraction Theory and Antennas*. Chichester, UK / New York, NY, USA: Ellis Horwood Ltd. / Halsted Press, 1980.

Spatially-fed Metasurface Antenna with Active Feeder for Reconfigurable Beam Coverage

Daniel Martinez-de-Rioja[1*], Yolanda Rodriguez-Vaqueiro[2], Antonio Pino[2], Eduardo Martinez-de-Rioja[3], Jose A. Encinar[1], Manuel Arrebola[1]

[1]Information Processing and Telecommunications Center, Universidad Politécnica de Madrid, Spain
[2]AtlanTTic Research Center for Telecommunication Technologies, Universidade de Vigo, Spain
[3]AtlanTTic Dept. of Signal Theory and Communications and Telematic Systems and Computing, Universidad Rey Juan Carlos, Spain

*Corresponding author: jd.martinezderioja@upm.es

ABSTRACT

Recent advances in metamaterials and metasurfaces have enabled unprecedented capabilities for controlling electromagnetic scattering and wave propagation through engineered artificial media. Within this context, metasurface based on reflectarrays concepts have been proposed for high-gain applications [1], polarization control [2], and beam shaping [3] in far-field and near-field applications. This contribution focuses on a hybrid antenna architecture in Ka-band, in which a metasurface-based reflectarray is illuminated by an active phased array, enabling dynamic and flexible control of the reflected radiation characteristics through electronic beam steering at the feed level, following a defocused fed array reflector architecture [4] (see Fig. 1).

The proposed approach allows for dynamic beam pointing and beam shaping, controlled by the phased-array, while the reflectarray is engineered to provide additional electromagnetic functionalities in terms of beam shaping corrections and polarization conversion. The proposed metasurface makes it possible to reduce the complexity of the phased-array with respect to conventional fed array reflector antennas while preserving high reconfigurability. The work addresses the modeling, analysis, and synthesis of such phased-array–illuminated metasurfaces, emphasizing the interaction between the incident field distribution generated by the phased array and the final radiation pattern of the metasurface. Analytical models allow to characterize the main design parameters of the metasurface and phased-array in an efficient way under different antenna scenarios and objective beam coverages.

The proposed architecture is particularly attractive for next-generation communication and sensing systems, where dynamic beam steering and beam shaping can be simultaneously required. The use of hybrid antenna solutions that combine electrically large passive metasurfaces and reconfigurable feed networks reduces the associated costs and provides a practical implementation, demonstrating how hybrid solutions can overcome traditional trade-offs between performance, complexity, and reconfigurability.

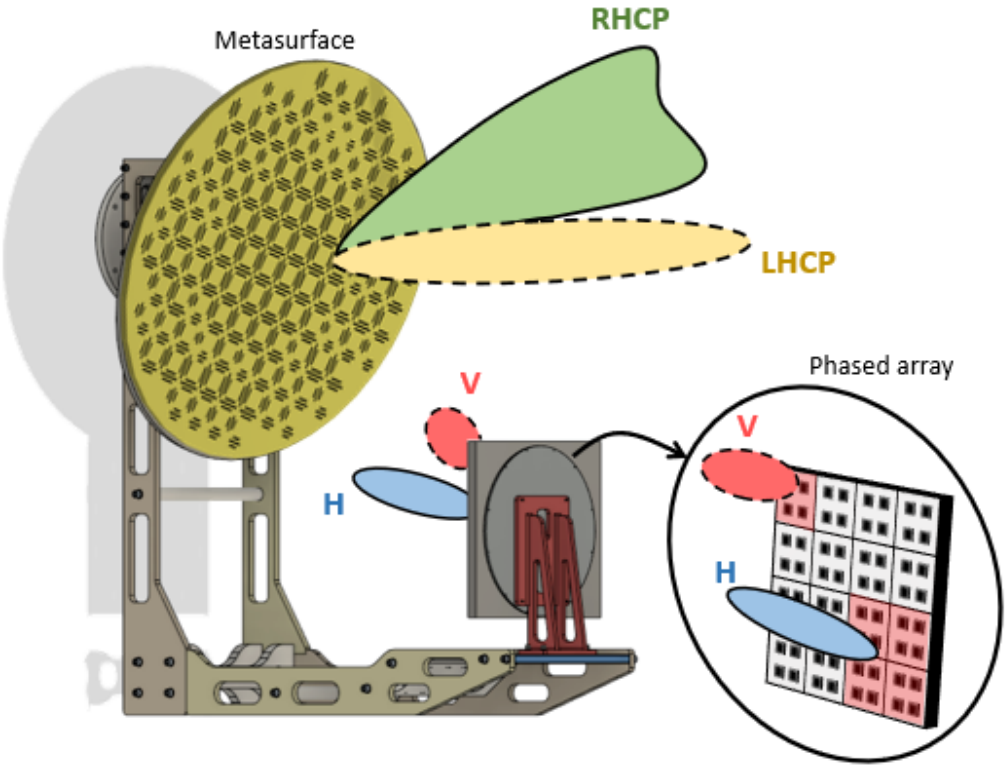

Fig. 1 Proposed antenna configuration with a reconfigurable phased array and passive metasurface as main reflector.

ACKNOWLEDGMENTS

This research has been supported by the Madrid Government (Comunidad de Madrid, Spain) under the Multiannual Agreement 2023-2026 with Universidad Politécnica de Madrid in Line A, Emerging PhD researchers (project STARS); by the Spanish Government through MCIU / AEI / 10.13039 / 501100011033 / FEDER, UE within the projects PID2023-146246OB-C31-2 (ANT4IT), PID2024-161515OAI00 (brAIn-5G) and RYC2021-033593-I; and by the Regional Government of Galicia under project GRC-ED431C-2023/26 and agreement for funding AtlantTIC.

REFERENCES

[1] E. Martinez-de-Rioja et al., "Advanced Multibeam Antenna Configurations Based on Reflectarrays: Providing multispot coverage with a smaller number of apertures for satellite communications in the K and Ka bands," in IEEE Antennas and Propagation Magazine, vol. 61, no. 5, pp. 77-86, Oct. 2019, doi: 10.1109/MAP.2019.2932311.

[2] D. Martinez-de-Rioja, B. Imaz-Lueje, E. Martinez-de-Rioja, M. R. Pino, J. A. Encinar and M. Arrebola, "Broadband Polarizer Reflectarray Antenna in Dual-Circular Polarization for Satellite Applications in Ka-Band," in IEEE Transactions on Antennas and Propagation, vol. 73, no. 10, pp. 7122-7133, Oct. 2025.

[3] Á. F. Vaquero, D. Martinez-de-Rioja, E. Martinez-de-Rioja, M. Arrebola, J. A. Encinar and M. R. Pino, "Near-Field Model for the Computation of Coverage Generated by an IRS: Formulation and Validation," 2022 IEEE MTT-S International Conference on Numerical Electromagnetic and Multiphysics Modeling and Optimization (NEMO), Limoges, France, 2022, pp. 1-4, doi: 10.1109/NEMO51452.2022.10038955.

[4] N. J. G. Fonseca, E. Girard and H. Legay, "Doubly Curved Reflector Design for Hybrid Array Fed Reflector Antennas," in IEEE Transactions on Antennas and Propagation, vol. 66, no. 4, pp. 2079-2083, April 2018, doi: 10.1109/TAP.2018.2800800.

Polarization-Decoupled Programmable Metasurface for Integrated Beam Steering and Electromagnetic Illusion

Yitian Huang[1,2,3], Min Huang[4], Ruichen Li[1,2,5], Haoran Han[1,2,3], Bin Zheng[1,2,3], Jiwei Zhao[1,2,3*]

[1]State Key Laboratory of Extreme Photonics and Instrumentation, ZJU-Hangzhou Global Scientific and Technological Innovation Center, Zhejiang University, Hangzhou 310027, China.
[2]International Joint Innovation Center, The Electromagnetics Academy at Zhejiang University, Zhejiang University, Haining 314400, China
[3]Zhejiang Key Laboratory of Intelligent Electromagnetic Control and Advanced Electronic Integration, Jinhua Institute of Zhejiang University, Zhejiang University, Jinhua 321099, China
[4]College of Electronic Science and Technology, National University of Defense Technology, Changsha 410073, China
[5]AVIC Chengdu Aircraft Design & Research Institute, National Key Laboratory of Electromagnetic Information Control and Effects, Chengdu, China.
*Corresponding author: jackokie@zju.edu.cn

***Abstract*— A polarization-decoupled programmable metasurface is presented for multifunctional electromagnetic control. Independent phase manipulation of two linear polarizations enables broadband wide-angle beam steering and target-driven scattering synthesis on a shared aperture. Experiments verify broadband wide-angle steering performance and high-fidelity electromagnetic illusion under normal and oblique incidences.**

***Keywords*— Polarization Decoupling, Programmable Metasurface, Multifunctional Integration**

I. Introduction

Programmable metasurfaces provide a powerful platform for dynamic electromagnetic wave manipulation [1-10]. However, most existing designs support single-polarization or homogeneous functions [11-15], limiting system flexibility. This work addresses these limitations by exploiting polarization decoupling to integrate heterogeneous electromagnetic functionalities within a single reconfigurable aperture.

II. Methods

A one-bit reflective programmable metasurface is designed using PIN-diode-integrated meta-elements with orthogonal bias networks. Each element supports independent phase control for two linear polarizations. For complex scattering synthesis, a differential-evolution-based phase programming framework is developed to directly generate deployable digital phase codes from desired far-field targets under discrete phase constraints.

III. Results and Discussion

The proposed metasurface demonstrates:

- Broadband wide-angle beam steering in one polarization channel
- High-fidelity reproduction of prescribed scattering patterns in the orthogonal channel
- Stable performance under both normal and oblique incidences

Full-wave simulations and microwave anechoic-chamber measurements show good agreement, validating polarization-decoupled operation and multifunctional integration on a single aperture.

IV. Conclusion

A polarization-decoupled programmable metasurface enabling heterogeneous electromagnetic functions is demonstrated. By combining low-bit hardware with target-driven phase optimization, the proposed approach offers a practical solution for multifunctional antenna systems and adaptive electromagnetic platforms.

REFERENCES

[1] R.A. Shelby, D.R. Smith, S. Schultz, Experimental verification of a negative index of refraction, Science 292(5514) (2001) 77–79.

[2] J.B. Pendry, D. Schurig, D.R. Smith, Controlling electromagnetic fields, Science 312(5781) (2006) 1780–1782.

[3] D. Schurig, J.J. Mock, B.J. Justice, et al., Metamaterial electromagnetic cloak at microwave frequencies, Science 314(5801) (2006) 977–980.

[4] F. Aieta, A. Kabiri, P. Genevet, et al., Reflection and refraction of light from metasurfaces with phase discontinuities, J. Nanophotonics 6(1) (2012) 063532.

[5] J. Zhang, W.C. Li, Y. Kang, et al., Design of absorption-scattering integrated multi-layer metasurfaces for large-angle anomalous reflection, Prog. Electromagn. Res. 183 (2025).

[6] R.E. Jacobsen, S. Arslanagic, All-dielectric cylindrical metasurfaces for enhanced directional scattering, Prog. Electromagn. Res. 183 (2025) 1–8.

[7] H. Lu, J.W. Zhao, P.X. Zhu, et al., Neural network-assisted metasurface design for broadband remote invisibility, Adv. Funct. Mater. (2025) 2506085.

[8] Y.H. Yang, H.P. Wang, F. Yu, et al., A metasurface carpet cloak for electromagnetic, acoustic and water waves, Sci. Rep. 6 (2016) 20219.

[9] Y.H. Yang, L.Q. Jing, B. Zheng, et al., Full-polarization 3D metasurface cloak with preserved amplitude and phase, Adv. Mater. 28(32) (2016) 6866–6871.

[10] M. Huang, B. Zheng, R.C. Li, et al., Evolutionary games-assisted synchronization metasurface for simultaneous multisource invisibility cloaking, Adv. Funct. Mater. 34(36) (2024) 2401909.

[11] L.H. Zhu, J.Q. Han, G.X. Li, et al., Dual linearly polarized 2-bit programmable metasurface with high cross-polarization discrimination, IEEE Trans. Antennas Propag. 72(2) (2023) 1510–1520.

[12] M.T. Wang, D.S. Liao, J.Y. Dai, et al., Dual-polarized reconfigurable metasurface for multifunctional control of electromagnetic waves, IEEE Trans. Antennas Propag. 70(6) (2022) 4539–4548.

[13] C. Huang, J.N. Yang, X.Y. Wu, et al., Reconfigurable metasurface cloak for dynamical electromagnetic illusions, ACS Photonics 5(5) (2017) 1718–1725.

[14] X.Y. Cheng, Y.X. Jin, Y. Tang, et al., Image wireless transmission based on microwave digital coding metasurfaces, J. Opt. Soc. Am. B 41(11) (2024) D31–D39.

[15] J.C. Liang, Y. Gao, Z.W. Cheng, et al., An optically transparent reconfigurable intelligent surface with low angular sensitivity, Adv. Opt. Mater. 12(6) (2024) 2202081.

Physically Consistent Modeling of RIS Scattering under Multipath Incidence

Gang Yu[1], Gabriele Gradoni[1,*]

[1]6G Innovation Centre (6GIC), Institute for Communication Systems (ICS), University of Surrey, UK
*Corresponding author: g.gradoni@surrey.ac.uk

***Abstract*—This paper presents a physically consistent macroscopic model for finite size RISs under multipath incidence. By combining physical optics and diffraction grating theory, phase nonuniformity is mitigated via a dominant path reference, enabling efficient far field scattering prediction and seamless integration into ray tracing frameworks for smart radio environment optimization.**

***Keywords*— reconfigurable intelligent surfaces (RISs), electromagnetic modeling, far field scattering.**

I. Introduction

Reconfigurable intelligent surfaces (RISs) are expected to play a key role in dynamically tailoring wireless propagation environments for future 6G networks [1], [2]. Evaluating their performance requires realistic models that accurately capture electromagnetic behaviors, as idealized theoretical models based on the generalized Snell law of refraction often neglect local impedance mismatches and parasitic scattering [2]. Under realistic conditions, finite size panels generate multimode scattering that distributes power into unwanted directions. Full wave electromagnetic simulations can capture these effects but are too computationally demanding for large scale system level simulations [2]. To bridge this gap, macroscopic models based on surface impedance and equivalent currents have been developed [1]. However, practical indoor environments excite these surfaces with multiple incident waves simultaneously, introducing severe phase distortions across the aperture. To address these limitations, this paper proposes a computationally efficient macroscopic framework that captures realistic multimode reradiation and diffuse scattering under arbitrary multipath incidence, providing a robust and practical solution.

II. Methods

To ensure physical consistency, the proposed macroscopic modeling approach maps ray clusters onto an angular plane wave spectrum, enabling a wave domain representation of the composite multipath field. Based on the induction theorem and generalized Huygens principle [3], the reradiated field from the illuminated surface is characterized by equivalent electric and magnetic surface currents [2]. Because multiple reflected harmonics coexist, the total reflection is modeled as the superposition of all propagating Floquet Bloch modes. Within this framework, a global optimization is performed to coherently combine multiple incident components into desired single or multiple beams while suppressing undesired specular reflections under power conservation constraints [4].

III. Results and Discussion

Simulation results demonstrate the clear advantage of the multipath aware design over conventional single path approaches. Under identical multipath illumination, the proposed optimized configuration mitigates phase mismatch and suppresses partial destructive interference. As a result, an 88% improvement in electric field intensity along the desired direction is achieved compared to unoptimized designs, which is consistent with a 48.9% enhancement validated by full wave simulations. In terms of computational efficiency, the proposed framework synthesizes far field radiation patterns in only 8.368 seconds, whereas conventional full wave simulations require 788 minutes [2].

IV. Conclusion

This paper proposes a physically consistent framework combining physical optics and diffraction grating theory to model finite size scattering under multipath illumination. By aligning the global phase reference, the design ensures highly coherent reradiation and avoids phase mismatches. Reducing computational time to seconds compared to full wave simulations, this highly efficient method can seamlessly integrate into ray tracing engines for practical indoor network optimization.

References

[1] G. Yu, W. Xi, A. T. Joy, J. Chen, A. Tishchenko, D. Sergiou, H. Taghvaee, M. Khalily, J. Zhang, G. Gradoni, and R. Tafazolli, "Self-consistent modeling of RIS operating in real-life propagation environments via ray-tracing simulations," in *Proc. IEEE INFOCOM Workshops (INFOCOM WKSHPS)*, May. 2025, pp. 1–6.

[2] G. Yu, A. T. Joy, W. Xi, J. Zhang, M. Khalily, G. Gradoni, and R. Tafazolli, "Physically consistent modelling and analysis of RIS under multipath incidence," in *Proc. 20th Eur. Conf. Antennas Propag. (EuCAP)*, Dublin, Ireland, Apr. 2026, accepted.

[3] V. Degli-Esposti, E. M. Vitucci, M. D. Renzo, and S. A. Tretyakov, "Reradiation and scattering from a reconfigurable intelligent surface: A general macroscopic model," *IEEE Trans. Antennas Propag.*, vol. 70, no. 10, pp. 8691–8706, Oct. 2022.

[4] M. Di Renzo, F. H. Danufane, and S. Tretyakov, "Communication models for reconfigurable intelligent surfaces: From surface electromagnetics to wireless networks optimization," *Proceedings of the IEEE*, vol. 110, no. 9, pp. 1164–1209, Aug. 2022.

Gain-Enabled Spectral Singularities in Metasurface Cavities

Rasmus E. Jacobsen[1,*], Pietro Brugnolo[1,2], Samel Arslanagić[1]

[1] Department of Space Research and Space Technology, Technical University of Denmark, Denmark

[2] Department of Electrical and Information Technology, Lund University, Sweden

*Corresponding author: rajac@dtu.dk

***Abstract*—We present a theoretical framework for spectral singularities in metasurface cavities, characterized by effective electric and magnetic surface impedances, considering planar and curved metasurfaces in passive and active regimes. Divergent scattered fields with simultaneously vanishing internal fields of the respective cavities are demonstrated. The work includes analytical and numerical results.**

***Keywords*— metasurfaces, bound states in the continuum, impedance surface.**

I. Introduction

Metasurface (MS) cavities have recently emerged as a versatile class of open resonant systems that enable extreme control over wave scattering and confinement [1]-[4]. By tailoring subwavelength electric and magnetic surface responses, these cavities allow the realization of bound states in the continuum (BICs), i.e., nonradiating modes embedded within the radiation spectrum [5]-[6]. Such states arise from engineered interference mechanisms and are associated with extreme field localization and diverging quality factors, making them attractive for many applications including sensing, photonics and lasing.

Recent theoretical work has demonstrated that MS cavities characterized by effective electric and magnetic surface impedances can support BICs in both planar and curved configurations, including cylindrical and spherical geometries. This unified impedance-based description provides a powerful analytical framework that extends the BICs physics beyond conventional photonic crystal and waveguide platforms, while remaining applicable across a broad frequency range. In this contribution, we investigate BICs formation in MS cavities with particular emphasis on active, gain-assisted regimes, where additional spectral singularities emerge.

II. Results and Discussion

Using an analytical scattering-matrix formalism, we show that the coexistence of electric and magnetic MS responses gives rise to two distinct singular states of the system. In the absence of loss and gain, BICs originate from the formation of zero–pole pairs of the internal field response, resulting in complete suppression of radiation despite the openness of the cavity.

When gain is introduced, an additional regime becomes accessible. In this case, a spectral singularity appears as a scattering pole associated with a lasing mode that coalesces with a BIC. At this singular point, the cavity exhibits a striking and counterintuitive decoupling between internal and external fields: under ideal tuning, the internal field vanishes while the scattered field diverges. Slight detuning from this condition leads to quasi-BICs characterized by strong field confinement combined with strongly enhanced scattering due to the nearby lasing pole. This is illustrated in Figure 1, which shows the local electric field for the excitation of a higher-order mode quasi-BIC in a cylindrical MS cavity. This behavior represents an unusual coexistence of nonradiating confinement and amplified radiation within a single-mode system.

Closed-form analytical conditions for the emergence of both BICs and spectral singularities are derived for planar, cylindrical, and spherical MS cavities, providing a unified and practical design framework. The theoretical predictions are validated using full-wave simulations of homogenized all-dielectric cylindrical MS implementations embedded in a gain medium. These results, that will be presented at the conference, highlight the potential of active MS cavities as a new platform for controlling wave–matter interactions and for enabling compact, highly tunable devices for lasing, sensing, radiation control, and integrated photonic systems.

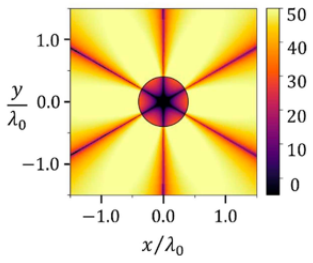

Fig. 1 Normalized total electric field (logarithmic scale) of a MS cavity exciting a high-order mode.

III. Conclusion

In conclusion, active metasurface cavities provide a unified platform for realizing bound states in the continuum and spectral singularities across multiple geometries. The derived analytical conditions enable systematic design of open resonators with tailored confinement and scattering properties.

References

[1] F. S. Cuesta, V. S. Asadchy, A. D. Sayanskiy, V. A. Lenets, M. S. Mirmoosa, X. Ma, S. B. Glybovski, and S. A. Tretyakov, "Nonscattering metasurface-bound cavities for field localization, enhancement, and suppression," IEEE Transactions on Antennas and Propagation, vol. 68, no. 1689, pp. 1689-1703, 2020.

[2] R. E. Jacobsen and S. Arslanagić, "Extreme localization of fields in open cylindrical impedance surface cavities," IEEE Transactions on Antennas and Propagation, vol. 72, no. 2, pp. 1686-1693, 2024.

[3] P. Brugnolo, S. Arslanagić, and R. E. Jacobsen, "Bound states in the continuum in cylindrical all-dielectric metasurface cavities," Physical Review Letters, vol. 134, 096902, 2025.

[4] P. Brugnolo, S. Arslanagić, and R. E. Jacobsen, "Conditions for enhanced scattering and field confinement in single-mode metasurface cavities," Physical Review B, vol. 112, L241112, 2025.

[5] C. W. Hsu, B. Zhen, A. D. Stone, J. D. Joannopoulos, and M. Soljačić, "Bound states in the continuum," Nature Reviews Materials, vol. 1, 16048, 2016.

[6] A. Krasnok, D. Baranov, H. Li, M.-A. Miri, F. Monticone, and A. Alú, "Anomalies in light scattering," Advances in Optics and Photonics, vol. 11, no. 4, pp. 892-951, 2019.

Time-modulated Electromagnetic Systems

Multimodal Space-Time Electromagnetic Structures

Anthony Grbic* and Amirhossein Babaee

Department of Electrical Engineering and Computer Science, University of Michigan, USA
*Corresponding author: agrbic@umich.edu

***Abstract*— This presentation will describe semi-analytical methods to model and design multimodal, time-varying electromagnetic structures. These are structures that, in the absence of time modulation, can support multiple modes at the frequencies of operation such as multiconductor transmission lines.**

***Keywords*— metamaterials, multiconductor systems, time-varying electromagnetic structures.**

I. Summary

The presentation will describe semi-analytical methods to model and design multimodal, time-varying electromagnetic structures. These are structures that, in the absence of time modulation, can support multiple modes at their frequencies of operation. With time/space-time modulation, these modes can be coupled to create spatiotemporal modes of operation. In linear, periodically time-varying systems, the electromagnetic fields are distributed over modes and frequency harmonics of the modulation and therefore can be indexed over mode number and harmonic number.

Multimodal time-varying systems can be analyzed by adding time variation to the multimodal transfer matrix method [1] typically used to analyze spatially periodic structures. It is an extension of the single-mode, time-varying microwave network theory that has been developed by our research group in recent years for 2-port time or space-time modulated lumped as well as distributed circuit networks [2-3].

In this presentation, a form of space-time modulation, referred to a spatially discrete traveling wave modulation (SDTWM), will be considered. In this spatially discretized version of traveling-wave modulation, a modulation period in space consists of N unit cells, referred to as stixels (space-time pixels). The modulation of each stixel is staggered in time by a time interval equal to 1/N of the temporal modulation period (T). Such a modulation scheme establishes a space-time periodic boundary condition, referred to as the Interpath Relation, across each stixel.

One of the most basic forms of multimodal systems that can be varied in time are multiconductor electromagnetic structures that support guided waves (see Fig. 1). Time invariant multiconductor structures consist of more than one signal line and a ground plane, and as a result can support multiple simultaneous modes. For example, a time-invariant, 3-conductor system with 2 signal lines and a ground plane can support even and odd modes simultaneously. Examples will be shown of how these modes can be coupled through time and space-time variation and exploited in design.

This work is relevant to numerous multiconductor time- and space-time-modulated systems. Examples include space-time-modulated electrically small antennas and frequency-converting coupled-line couplers. It is also relevant to N-path non-reciprocal networks, parametric structures with separate modulation and signal lines, Floquet topological structures, and those exhibiting exceptional points of degeneracy.

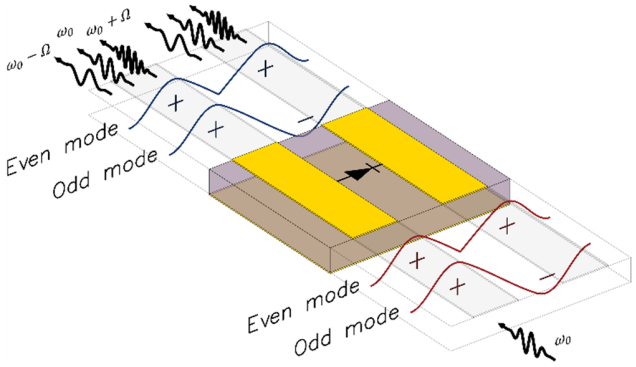

Fig. 1 A space-time varying coupled-line coupler as a multiconductor (multimodal) space-time electromagnetic structure.

Acknowledgments

This work has been supported by US Air Force grant FA8650-22-D-5406 through a subcontract with Azimuth Corporation.

References

[1] F. Mesa, G. Valerio, R. Rodríguez-Berral and O. Quevedo-Teruel, "Simulation-Assisted Efficient Computation of the Dispersion Diagram of Periodic Structures: A comprehensive overview with applications to filters, leaky-wave antennas and metasurfaces," IEEE Antennas and Propagation Magazine, vol. 63, no. 5, pp. 33-45, Oct. 2021.

[2] C. Scarborough and A. Grbic, "Generalized Eigenvalue Problem for Spatially Discrete Traveling-Wave-Modulated Circuit Networks," IEEE Transactions on Microwave Theory and Techniques, vol. 71, no. 2, pp. 511-521, Feb. 2023.

[3] A. Babaee, Z. Fritts, S. Young, A. Grbic, "Modal and Driven Solutions to Spatially-Discrete Traveling-Wave Modulated Networks," TechRxiv, March 19, 2025.

Sculpting waves in four dimensions: emulating time refraction and steering waves

Victor Pacheco-Peña[1,*]

[1]School of Mathematics, Statistics and Physics, Newcastle University, Newcastle Upon Tyne, NE1 7RU, United Kingdom

*Corresponding author: victor.pachecopena@gmail.com

***Abstract*— We will present our latest efforts in the field of temporal/spatiotemporal metamaterial. We will show how time refraction by a time interface can be emulated using smooth changes of the optical properties of materials. The combination of spatial and temporal boundaries to emulate temporal aiming will also be discussed.**

***Keywords*— metamaterials, 4D metamaterials, time interfaces, Time-Varying media.**

I. Discussion

Metamaterials working in the time-harmonic scenario (frequency domain) have been key to manipulate wave propagation in three dimensions (3D) [1–3], with time t, also being introduced as an extra dimension. This has given rise to four-dimensional manipulation of waves (x,y,z,t) [4–6].

In this realm, time interfaces have been of interest to the scientific community as they can be considered as the time equivalent of spatial interfaces [7]. A time interface consists of a rapid change (with time variations smaller than the period of the wave within the medium) of the optical properties of the material where the wave propagates (for instance permittivity, ε and/or permeability, μ). They were first proposed in the last century, but it has not been until recently that they have been studied in detail, giving rise to exotic physical phenomena including temporal anisotropy [8–12], antireflection coatings and filters in the time domain [13–16], static-to-dynamic field conversion [17], effective medium theory [18,19] as well as their combination with spatial boundaries [20,21], as examples [22]. Importantly, experimental works have started to be reported [23,24], demonstrating the importance of this research topic.

In this work, we will discuss some of our recent efforts in the field of 4D metamaterials by studying temporal modulations as well as spacetime functions of the materials where the wave propagates. In the former scenario, we develop a detailed theory of wave propagation within a medium with optical properties (permittivity and permeability) that change smoothly in time following a sigmoid function [25]. The aim here is to demonstrate how it is indeed possible to mimic the time refracted wave (forward wave) produced by a time interface but now with slow modulations instead. Given that the time reflected wave can be eventually neglected for long sigmoid [26], we consider a medium with a time-independent impedance.

The second application involves the emulation of *temporal aiming* [9] using a combination of spatial and temporal boundaries to mimic an effective medium in space and time via isotropic media[27,28]. All the results will be supported by numerical simulations.

Acknowledgments

This work was supported by the Leverhulme Trust under the Leverhulme Trust Research Project Grant scheme (RPG-2023-024). The authors have applied a CC BY public copyright license to any Author Accepted Manuscript (AAM) version arising from this submission.

References

[1] V. Pacheco-Peña, B. Orazbayev, V. Torres, M. Beruete, and M. Navarro-Cía, Ultra-compact planoconcave zoned metallic lens based on the fishnet metamaterial, Appl. Phys. Lett. 103, 183507 (2013).

[2] A. Alù, S. Maci, and N. Engheta, Metasurfaces and Metamaterials for Electromagnetics, IEEE Transactions on Antennas and Propagation DOI 10.1109/TAP.2025.3588766 1 (2025).

[3] T. Knightley, A. Yakovlev, and V. Pacheco-Peña, Neural Network Design of Multilayer Metamaterial for Temporal Differentiation, Adv. Opt. Mater. 11, 2202351 (2023).

[4] E. Galiffi, R. Tirole, S. Yin, H. Li, S. Vezzoli, P. A. Huidobro, M. G. Silveirinha, R. Sapienza, A. Alù, and J. B. Pendry, Photonics of time-varying media, Advanced Photonics 4, 1 (2022).

[5] Y. Hadad and D. Sounas, Space-time modulated loaded-wire metagratings for magnetless nonreciprocity and near-complete frequency conversion, Opt. Mater. Express 14, 1295 (2024).

[6] N. Engheta, Four-dimensional optics using time-varying metamaterials, Science (1979). 379, 1190 (2023).

[7] F. Morgenthaler, Velocity Modulation of Electromagnetic Waves, IEEE Trans. Microw. Theory Tech. 6, 167 (1958).

[8] A. Akbarzadeh, N. Chamanara, and C. Caloz, Inverse Prism based on Temporal Discontinuity and Spatial Dispersion, Opt. Lett. 43, 3297 (2018).

[9] V. Pacheco-Peña and N. Engheta, Temporal aiming, Light Sci. Appl. 9, 1 (2020).

[10] V. Pacheco-Peña and N. Engheta, Temporal equivalent of the Brewster angle, Phys. Rev. B 104, 214308 (2021).

[11] V. Pacheco-Peña and N. Engheta, Spatiotemporal isotropic-to-anisotropic meta-atoms, New J. Phys. 23, 095006 (2021).

[12] G. Ptitcyn and N. Engheta, Temporal Twistronics, ArXiv:2403.10477 (2024).
[13] V. Pacheco-Peña and N. Engheta, Antireflection temporal coatings, Optica 7, 323 (2020).
[14] I. Liberal, J. E. Vázquez-Lozano, and V. Pacheco-Peña, Quantum Antireflection Temporal Coatings: Quantum State Frequency Shifting and Inhibited Thermal Noise Amplification, Laser Photon. Rev. 17, 1 (2023).
[15] D. Ramaccia, A. Alù, A. Toscano, and F. Bilotti, Temporal multilayer structures for designing higher-order transfer functions using time-varying metamaterials, Appl. Phys. Lett. 118, 101901 (2021).
[16] G. Castaldi, V. Pacheco-Peña, M. Moccia, N. Engheta, and V. Galdi, Exploiting space-time duality in the synthesis of impedance transformers via temporal metamaterials, Nanophotonics 10, 3687 (2021).
[17] M. J. Mencagli, D. L. Sounas, M. Fink, and N. Engheta, Static-to-dynamic field conversion with time-varying media, Phys. Rev. B 105, (2022).
[18] V. Pacheco-Peña and N. Engheta, Effective medium concept in temporal metamaterials, Nanophotonics 9, 379 (2020).
[19] P. A. Huidobro, M. G. Silveirinha, E. Galiffi, and J. B. Pendry, Homogenization Theory of Space-Time Metamaterials, Phys. Rev. Appl. 16, 014044 (2021).
[20] V. Pacheco-Peña, M. Fink, and N. Engheta, Temporal chirp, temporal lensing, and temporal routing via space-time interfaces, Phys. Rev. B 111, L100306 (2025).
[21] L. Stefanini, E. Galiffi, S. Yin, S. Singh, D. M. Solís, N. Engheta, A. Toscano, D. Ramaccia, F. Bilotti, and A. Alù, Theory and Experimental Observation of Scattering by a Space-Time Corner, Phys. Rev. Lett. 135, (2025).
[22] Y. Sharabi, E. Lustig, and M. Segev, Disordered Photonic Time Crystals, Phys. Rev. Lett. 126, 163902 (2021).
[23] H. Moussa, G. Xu, S. Yin, E. Galiffi, Y. Ra'di, and A. Alù, Observation of temporal reflection and broadband frequency translation at photonic time interfaces, Nat. Phys. 19, 863 (2023).
[24] R. Tirole, S. Vezzoli, E. Galiffi, I. Robertson, D. Maurice, B. Tilmann, S. A. Maier, J. B. Pendry, and R. Sapienza, Double-slit time diffraction at optical frequencies, Nat. Phys. 19, 999 (2023).
[25] M. Antyufeyeva and V. Pacheco-Peña, Emulating time refraction at photonic time interfaces via smooth temporal transitions, Phys. Rev. Appl. 24, 034004 (2025).
[26] E. Galiffi, S. Yin, and A. Alú, Tapered photonic switching, Nanophotonics 11, 3575 (2022).
[27] V. Pacheco-Peña and N. Engheta, Merging Effective Medium Concepts of Spatial and Temporal Media: Opening new avenues for manipulating wave-matter interaction in 4D, IEEE Antennas Propag. Mag. 65, 39 (2023).
[28] A. M. Naylor and V. Pacheco-Peña, " Anisotropic photonic time interfaces via isotropic spacetime modulations", in preparation, 2026.

Wave Control at Space-Time Interface in Dispersive Media

C. Rizza[1,*], A. Contestabile[1], M.A. Vincenti[2], G. Castaldi[3], M. Scalora[2], M. Ferrera[4], V. Galdi[3]

[1]*Department of Physics and Chemical Science, University of L'Aquila, I-67100, Italy*
[2] *Department of Information Electrical Engineering, University of Brescia, I-25123, Italy*
[3] *Fields & Waves Lab, Department of Engineering, University of Sannio, I-82100, Italy*
[4] *Istitute of Photonics and Quantum Sciences, Heriot-Watt University SUPA Edinburgh, EH14 4AS United Kingdom*

*Corresponding author: carlo.rizza@univaq.it

Abstract— **We investigate wave scattering at a space–time interface. Specifically, we focus on a time-varying dispersive boundary characterized by Lorentz-type dispersion whose plasma frequency undergoes an abrupt temporal change. Our analysis reveals several unconventional photonic phenomena arising from such spatiotemporal discontinuities.**

First, we demonstrate that a space–time interface enables linear frequency generation at all wave modes supported by the medium [1]. As an example, it can excite waves at the system's intrinsic resonance frequencies and at the epsilon-near-zero (ENZ) crossing points (ENZ and Berreman modes).

Second, unlike conventional approaches that rely on spatial structuring (such as gratings or prisms) our method shows that incident propagating waves can directly excite evanescent modes triggered by a sudden temporal boundary.

Third, we explore the spin-dependent effects occurring at a space–time interface [2]. A purely temporal interface induces phase-conjugated backward waves and leads to anomalous spin conversion. When both spatial and temporal boundaries are present, the scattered field results from their combined action, forming a superposition of the incident wave's polarization and its phase-conjugated counterpart. Remarkably, this mechanism enables polarization conversion without the need for bi-anisotropy, chirality, or nonlinear effects.

Finally, we discuss potential implementations in realistic material systems, emphasizing that the investigated parameters are compatible with semiconductor platforms operating at terahertz frequencies. We also review and analyze the opportunities offered by ENZ materials (such as ITO, AZO) which exhibit unconventional nonlinear response and time-varying electromagnetic properties [3-5]. These materials provide a promising platform for achieving time-varying anisotropy and chirality [6].

***Keywords*— metamaterials, time-varying media, epsilon-near-zero**

REFERENCES

[1] C. Rizza, M. A. Vincenti, G. Castaldi, A. Contestabile, V. Galdi, M. Scalora, "Harnessing the natural resonances of time-varying dispersive interfaces", Phys. Rev. Lett. 2024, 133 186902.
[2] C.Rizza , A.Contestabile , A.M.Vincenti , G.Castaldi, M.Ferrera, A .Stroppa, M. Scalora , V.Galdi, Small.Struct., 000:e20250039 (2025).
[3] W. Jaffray, F. Belli, E. G. Carnemolla, C. Dobas, M. Mackenzie, J. Travers, A. K. Kar, M. Clerici, C. DeVault, V. M. Shalaev, A. Boltasseva, and M. Ferrera, Nat. Commun. **13**, 3536 (2022).
[4] W. Jaffray, S. Stengel, F. Biancalana, C. B. Frühling, M. G. Özlü, M. Scalora, A. Boltasseva, V. M. Shalaev, and M. Ferrera, *Nat. Photonics* **19**, 558 (2025).
[5] M. Scalora, M. A. Vincenti, D. de Ceglia, N. Akozbek, M. Ferrera, C. Rizza, A. Alù, N. Litchinitser, C. Cojocaru, and J. Trull, Phys. Rev. A 112, 013502 (2025).
[6] W. Jaffray, S. Stengel, A. Boltasseva, V. M. Shalaev, M. A. Vincenti, D. de Ceglia, M. Scalora, C. Rizza, and M. Ferrera, "All-optical polarization control in time-varying low-index films via plasma symmetry breaking," arXiv:2510.06985 (2025).

Temporal Modulation for Dispersion-Free Impedance Matching

Mario Junior Mencagli[1,*], Dimitrios L. Sounas[2]

[1]Department of Electrical and Computer Engineering, University of Delaware, Newark, DE 19716, USA
[2]Department of Electrical and Computer Engineering, Wayne State University, Detroit, MI 48202, USA
*Corresponding author: mencagli@udel.edu

***Abstract*—Impedance matching is fundamentally limited by the Bode–Fano bound for passive, linear, time-invariant networks. By relaxing time invariance, we show that a realistically aperiodically modulated capacitor surpasses this bound while preserving pulse shape, enabling dispersionless broadband matching for electrically small antennas, resonators, and absorbers.**

***Keywords*— time-varying networks, broadband matching, dispersionless, electrically small antennas.**

I. Summary

Over the past decade, electromagnetic systems incorporating time-modulated elements and time-varying media have attracted significant research interest (see, e.g., Refs. [1], [2]). This body of work has uncovered a range of novel wave phenomena, including static-to-dynamic field conversion [3], temporal aiming [4], time-domain analog signal processing [5], and temporal Wood anomalies [6]. Beyond revealing new physical effects, time-varying electromagnetic platforms offer a powerful means to mitigate, or even circumvent, fundamental limitations inherent to time-invariant systems [7]. A prominent example is the extensive development of time-modulated nonreciprocal devices [8], [9]. In addition to enabling nonreciprocity, temporal modulation offers a pathway to surpass the Bode–Fano bound [10], [11], a fundamental limitation governing all linear, time-invariant matching networks. Overcoming this bound is particularly impactful for electrically small antennas, absorbers, and resonators. Previous approaches [12], [13], [14] have achieved broadband matching through switching techniques; however, these methods typically introduce waveform distortion, resulting in transmitted or radiated signals that deviate from the input.

In this presentation, building upon our earlier work [15], we will introduce a time-modulated impedance-matching strategy that surpasses conventional time-invariant approaches by enabling complete reflection cancellation over a broad bandwidth beyond the Bode–Fano limit, while preserving the temporal profile of the signal, namely, without inducing dispersion, pulse compression, or temporal broadening. The proposed scheme is based on a capacitor with a time-varying capacitance $C(t)$ which, when appropriately pre-charged by a DC bias, enables dispersionless broadband matching with a positive, finite, and physically realizable capacitance trajectory. Alongside a practical implementation, we will discuss general theoretical bounds on the minimum required biasing and modulation requirements necessary to achieve distortionless broadband matching, as well as present a comprehensive efficiency analysis accounting for the incident pulse energy, the energy dissipated in the load, and the energy expended in driving the temporal modulation. These results highlight the potential of the proposed approach to significantly extend the operational bandwidth of electrically small antennas and other inherently narrowband electromagnetic devices.

References

[1] C. Caloz and Z.-L. Deck-Léger, "Spacetime metamaterials—part I: General concepts," *IEEE Trans. Antennas Propag.*, vol. 68, no. 3, pp. 1569–1582, 2020.
[2] S. Yin, E. Galiffi, and A. Alù, "Floquet metamaterials," *eLight*, vol. 2, 2022.
[3] M. J. Mencagli, D. L. Sounas, M. Fink, and N. Engheta, "Static-to-dynamic field conversion with time-varying media," *Phys. Rev. B*, vol. 105, p. 144301, 2022.
[4] V. Pacheco-Pena and N. Engheta, "Temporal aiming," *Light Sci Appl*, vol. 9, p. 129, 2020.
[5] G. Castaldi, C. Rizza, N. Engheta, and V. Galdi, "Multiple actions of time-resolved short-pulsed metamaterials," *Applied Physics Letters*, vol. 122, no. 2, p. 021701, 01 2023.
[6] E. Galiffi, Y.-T. Wang, Z. Lim, J. B. Pendry, A. Alù, and P. A. Huidobro, "Wood anomalies and surface-wave excitation with a time grating," *Phys. Rev. Lett.*, vol. 125, p. 127403, Sep 2020.
[7] G. Ptitcyn, M. S. Mirmoosa, A. Sotoodehfar, and S. A. Tretyakov, "A tutorial on the basics of time-varying electromagnetic systems and circuits: Historic overview and basic concepts of time-modulation," *IEEE Antennas Propag. Mag.*, vol. 65, no. 4, pp. 10–20, 2023.
[8] A. Kord, D. L. Sounas, and A. Alù, "Microwave nonreciprocity," *Proceedings of the IEEE*, vol. 108, no. 10, pp. 1728–1758, 2020.
[9] V. S. Asadchy, M. S. Mirmoosa, A. Díaz-Rubio, S. Fan, and S. A. Tretyakov, "Tutorial on electromagnetic nonreciprocity and its origins," *Proceedings of the IEEE*, vol. 108, no. 10, pp. 1684–1727, 2020.
[10] H. W. Bode, *Network Analysis and Feedback Amplifier Design*. Van Nostrand, New York, 1945.
[11] R. M. Fano, "Theoretical limitations on the broadband matching of arbitrary impedances," technical Report No. 41, Research Laboratory of Electronics, MIT, 1948.
[12] A. Shlivinski and Y. Hadad, "Beyond the bode-fano bound: Wideband impedance matching for short pulses using temporal switching of transmission-line parameters," *Phys. Rev. Lett.*, vol. 121, p. 204301, Nov 2018.
[13] H. Li, A. Mekawy, and A. Alù, "Beyond chu's limit with floquet impedance matching," *Phys. Rev. Lett.*, vol. 123, p. 164102, Oct 2019.
[14] X. Yang, E. Wen, and D. F. Sievenpiper, "Broadband time-modulated absorber beyond the bode-fano limit for short pulses by energy trapping," *Phys. Rev. Appl.*, vol. 17, p. 044003, Apr 2022.
[15] K. Hecht, D. González-Ovejero, D. L. Sounas, and M. J. Mencagli, "First-principles analysis of energy exchange in time-varying capacitors for energy trapping applications," *IEEE Access*, vol. 11, pp. 71 494–71 502, 2023.

Nano-objects and metasurfaces for opto-thermo-mechanical management

Modeling Terahertz Scattering from Plastic Contaminants for Inspection Applications

Rizwan Asif[1,2,3], Marco Gandolfi[4,5,6], Alfonso Tanga[7], Matteo Gabardi[7], Silvia Liprandi[7], Bruno Garavelli[7], M. J. Zapanta[3], Wouter Saeys[3], Claudio Giannetti[1,2,6,*]

[1]Department of Mathematics and Physics, Università Cattolica del Sacro Cuore, Brescia, Italy

[2]ILAMP, Università Cattolica del Sacro Cuore, Brescia, Italy

[3]Department of Biosystems, KU Leuven, Leuven, Belgium

[4]Dipartimento di Ingegneria dell'Informazione, Università degli Studi di Brescia, Brescia, Italy
Via Branze 38, 25123 Brescia, Italy

[5]Consorzio Nazionale Interuniversitario per le Telecomunicazioni (CNIT),
Viale G.P. Usberti 181/A, Sede Scientifica di Ingegneria – Palazzina 3,
43124 Parma, Italy

[6]Consiglio Nazionale delle Ricerche, Istituto Nazionale di Ottica,
Via Branze 45, 25123 Brescia, Italy

[7]Xnext S.p.A, Via Valtorta 48, 20127 Milano, Italy

[*]Corresponding author: claudio.giannetti@unicatt.it

***Abstract*—Plastic contaminants can be weakly absorbing, so detectability is often limited by scattering and collection optics rather than transmission contrast. We present a simulation-to-measurement workflow: COMSOL scattered-field modeling, near-to-far-field transformation, and finite-aperture integration for detector-collected signal. Lorenz–Mie benchmarking validates accuracy; extensions target nonspherical fragments and realistic inspection geometries.**

***Index Terms*—terahertz, food inspection, scattering, COMSOL, Mie theory.**

I. Introduction

Plastic foreign bodies are difficult to detect because they can be weakly absorbing and exhibit low contrast in many standard inspection modalities [1]. Terahertz (THz) imaging can exploit dielectric contrast and scattering signatures, but detectability depends heavily on particle size, refractive-index contrast, and measurement geometry [2]. Consequently, a physics-driven modeling workflow is valuable for guiding inspection configurations and identifying detection features beyond intensity-only contrast.

Most THz foreign-body studies report detectability using intensity/contrast in transmission or reflection, implicitly assuming that the measured signal scales with material absorption or simple Fresnel effects. The gap in current literature is the missing link between (i) full-wave scattering physics and (ii) the *detector-collected observable* that ultimately sets the signal-to-noise ratio (SNR) in an inspection head. In practice, detectability is governed by the *collected* scattered signal—i.e., the scattered field that falls within the finite acceptance cone of the collection optics and couples into the detector—rather than by the total scattered power integrated over all angles.

We address this by computing the far-field angular scattering and integrating it over the receiver acceptance cone to obtain the detector-collected power. This approach enables geometry-aware detectability metrics beyond intensity-only contrast.

II. Methods

Frequency-domain simulations are performed in COMSOL Multiphysics (Wave Optics module) over the 0.43–0.5 THz range. A scattered-field decomposition is used:

$$\mathbf{E}_{\mathrm{tot}} = \mathbf{E}_{\mathrm{inc}} + \mathbf{E}_{\mathrm{sc}}. \tag{1}$$

where $\mathbf{E}_{\mathrm{tot}}$ is the total electric field, $\mathbf{E}_{\mathrm{inc}}$ is the prescribed background (incident) field that would exist in the absence of the object, and $\mathbf{E}_{\mathrm{sc}}$ is the field scattered by the object. In the COMSOL Wave Optics interface, scattering quantities are computed exclusively from $\mathbf{E}_{\mathrm{sc}}$. Perfectly matched layers (PMLs) truncate the computational domain to emulate radiation into free space.

To ensure numerical accuracy, the mesh resolution is constrained by the local wavelength within the media. The maximum element size, h_{max}, is determined by:

$$h_{\mathrm{max}} = \frac{\lambda_0}{n \cdot N} \tag{2}$$

where λ_0 is the free-space wavelength, n is the refractive index of the medium, and N is the mesh parameter defining the number of elements per effective wavelength. In this work, convergence is evaluated at distinct mesh densities, denoted $\lambda/5$ ($N = 5$), $\lambda/7$ ($N = 7$), and $\lambda/10$ ($N = 10$).

A. Mesh convergence and cost metrics

To select a practical mesh density, we quantify accuracy of scattering cross section using the Relative Root Mean Square Error (RRMSE) on a consistent set of wavelengths. We also report mesh-driven cost indicators—degrees of freedom (DoF)

TABLE I
MESH-DEPENDENT ACCURACY AND COST INDICATORS. RRMSE IS COMPUTED WITH RESPECT TO THE LORENZ–MIE REFERENCE ON A CONSISTENT 12-WAVELENGTH SUBSET (THE SAME 12 WAVELENGTHS USED FOR THE $\lambda/10$ RUN).

Mesh Density	DoF	Peak Mem. (GB)	RRMSE (%)
$\lambda/5$ ($N = 5$)	2,760,630	16.46	2.0583
$\lambda/7$ ($N = 7$)	6,821,946	38.21	1.5349
$\lambda/10$ ($N = 10$)	18,640,926	50.81	1.3117

and solver-reported peak physical memory (GB)—which are less sensitive to workstation variations than runtime. RRMSE is computed as:

$$\mathrm{RRMSE}(\%) = 100\sqrt{\frac{1}{M}\sum_{i=1}^{M}\left(\frac{C_{\mathrm{sim}}(\lambda_i) - C_{\mathrm{ref}}(\lambda_i)}{C_{\mathrm{ref}}(\lambda_i)}\right)^2}, \quad (3)$$

where M is the number of wavelength points ($M = 12$), C_{sim} is the simulated scattering cross section, and C_{ref} is the analytical Lorenz–Mie reference [3]. We compute the scattering cross section C_{sca} by integrating the scattered Poynting flux over a closed surface surrounding the particle and normalizing by the incident intensity I_0.

As shown in Table I, refining from $\lambda/5$ to $\lambda/7$ reduces RRMSE from 2.06% to 1.53% (0.52 percentage points; 25.4% relative reduction), whereas $\lambda/10$ reduces it further to 1.31% (additional 0.22 percentage points; 14.5% relative reduction), at a significantly higher computational cost. Consequently, we select $\lambda/7$ as a practical trade-off for subsequent 3D simulations.

B. Far-field transformation

Far-field angular scattering $\mathbf{E}_{\mathrm{far}}(\theta, \phi)$ is obtained via a near-to-far-field transformation based on the Stratton-Chu surface equivalence principle [4]. This step is essential because the experiment is *optics-limited*: the receiver captures only the fraction of the scattered field within an acceptance cone defined by the collection lens (Fig. 1).

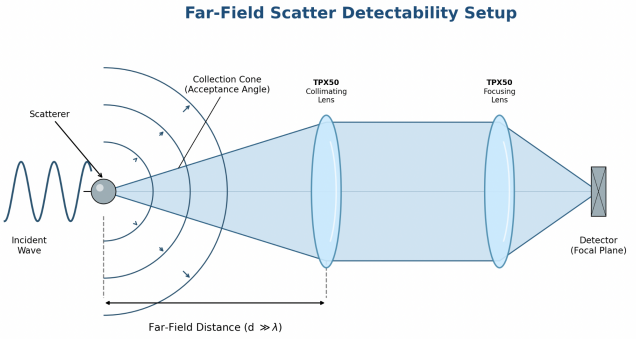

Fig. 1. Far-field scatter detectability setup. An incident THz wave illuminates a contaminant; the scattered field is transformed to the far field, and the detector-collected signal is determined by integrating intensity within the receiver acceptance cone defined by the TPX50 collection optics.

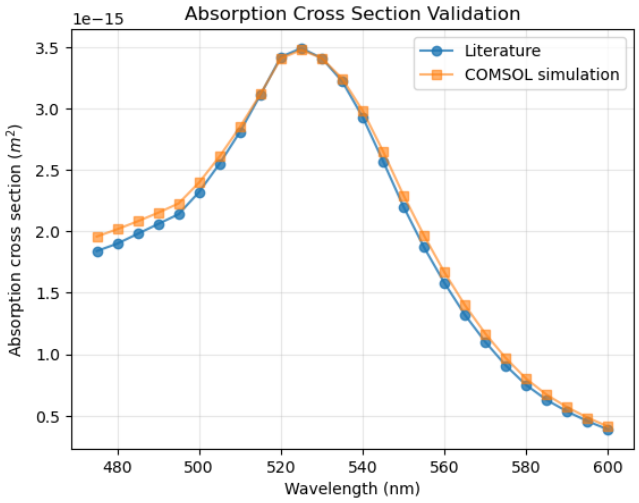

Fig. 2. Optical consistency check: absorption of a 20 nm-radius gold nanosphere (475–600 nm) compared to [6].

The *collected scattered power* is computed by integrating the far-field intensity $I(\theta, \phi)$ over the solid angle Ω_{NA} subtended by the optical system:

$$P_{\mathrm{col}} \propto \int_{\Omega_{\mathrm{NA}}} I(\theta, \phi)\, \mathrm{d}\Omega. \quad (4)$$

$I(\theta, \phi)$ denotes the scattered far-field intensity normalized to the incident intensity I_0, and the integral assumes polarization-aligned collection so that collected power scales with angular intensity within the lens acceptance cone. For a rotationally symmetric collection system, Ω_{NA} corresponds to $0 \le \theta \le \theta_{\max}$ with $\theta_{\max} = \arcsin(\mathrm{NA})$.

Optical consistency check: As a secondary verification in a strongly dispersive, lossy regime, we simulated a 20 nm-radius gold nanosphere using Johnson–Christy optical constants [5]. The wavelength-dependent absorption cross section $C_{\mathrm{abs}}(\lambda)$ computed by COMSOL matches literature references as shown in Fig.2, with an RRMSE below 5% [6]. This confirms the solver's validity for material systems with strong dispersion and loss, which is a prerequisite for simulating complex food matrices in future work.

III. RESULTS AND DISCUSSION

This study investigates 1 mm-radius particles within the 0.43–0.5 THz range. The wavelengths involved ($\lambda \approx 0.6$–0.7 mm) are comparable to the contaminant size, placing the interaction in the Mie scattering regime. Here, scattering is dominated by resonances occurring when particle size matches the incident wavelength.

The interaction regime can be expressed using the size parameter

$$x = k_m r = \frac{2\pi n_m r}{\lambda_0}, \quad (5)$$

where r is the particle radius, λ_0 is the free-space wavelength, and n_m is the refractive index of the surrounding medium.

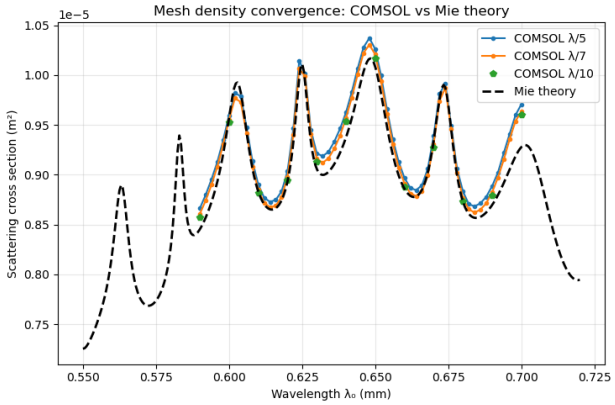

(a) Scattering cross section for two different mesh densities compared to Mie prediction.

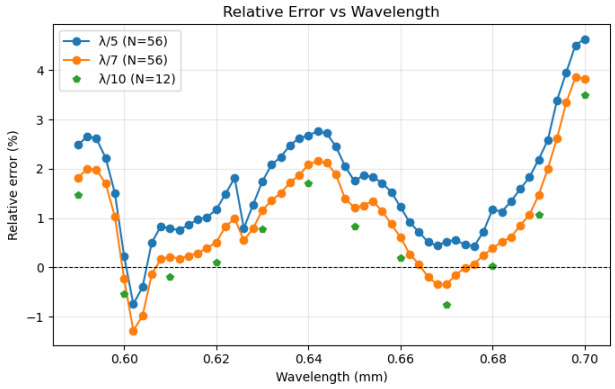

(b) Relative error versus wavelength showing reduced error for finer mesh.

Fig. 3. COMSOL validation against Lorenz–Mie theory. Also shown are $\lambda/10$ results at 12 representative wavelengths (markers)

For an air host ($n_m \approx 1$) with $r = 1$ mm and $\lambda_0 \in [0.592, 0.700]$ mm,

$$x = \frac{2\pi r}{\lambda_0} \approx 9.0\text{–}10.6, \tag{6}$$

placing the interaction firmly in the resonant Mie regime [3], where multiple multipole orders contribute and the scattering cross section exhibits pronounced oscillations which can be noted from Fig.3(a). This "spectral fingerprint" is vital for enhancing detectability, enabling physics-driven features that distinguish subtle plastic fragments from the food matrix.

Figure 3(a) benchmarks the COMSOL Wave Optics workflow against analytical Lorenz-Mie theory for a 1 mm-radius dielectric sphere ($n = 1.55$) in air. The simulated results closely track the theoretical prediction, capturing the oscillatory peaks and valleys. Figure 3(b) quantifies the error reduction as the mesh is refined from $\lambda/5$ to $\lambda/7$ and when further refined to $\lambda/10$, confirming the convergence behavior analyzed in Section II.

IV. Conclusion

We presented a verified full-wave simulation workflow for terahertz scattering from plastic contaminants. A 1 mm sphere benchmark shows excellent agreement with Lorenz–Mie theory, with accuracy improving significantly (RRMSE dropping from 2.06% to 1.53%) upon mesh refinement. Future work will extend the host medium to lossy, heterogeneous dielectrics and incorporate realistic collection optics to model non-spherical contaminant detectability.

Acknowledgments

R. A. and C. G. acknowledge financial support from MIUR through the PNRR-DM352 2022 and Xnext S.p.A for its valuable insights and support.

References

[1] M. Edwards, *Detecting Foreign Bodies in Food*. Woodhead, 2004.
[2] F. Tebbenjohanns, M. Frimmer, and L. Novotny, "Optimal position detection of a dipolar scatterer in a focused field," *Phys. Rev. A*, vol. 100, no. 4, p. 043821, 2019.
[3] C. F. Bohren and D. R. Huffman, *Absorption and Scattering of Light by Small Particles*. New York: Wiley-VCH, 1998.
[4] J. A. Stratton and L. J. Chu, "Diffraction theory of electromagnetic waves," *Phys. Rev.*, vol. 56, no. 1, pp. 99–107, 1939.
[5] P. B. Johnson and R. W. Christy, "Optical constants of the noble metals," *Phys. Rev. B*, vol. 6, no. 12, pp. 4370–4379, 1972.
[6] M. Gandolfi, F. Banfi, and C. Glorieux, "Optical wavelength dependence of photoacoustic signal of gold nanofluid," *Photoacoustics*, vol. 20, p. 100199, 2020.

Wiener–Hopf Modeling of a Parity Time Duality Waveguide Based on a Bed of Nails Metasurface

Xenofon M. Mitsalas*, Nelson Castro†, Eva Rajo-Iglesias† and Stefano Maci*
* Department of Information Engineering and Mathematics, Universita di Siena, Italy
xenofon.mitsalas@unisi.it, macis@dii.unisi.it
† Department of Signal Theory and Communications, University Carlos III of Madrid, Spain
ncastro@pa.uc3m.es, erajo@tsc.uc3m.es

***Abstract*—A compact analytical model is presented for a parity time duality waveguide based on a bed of nails metasurface. The approach combines surface impedance and Wiener–Hopf methods to describe polarization selective dispersion, spectral confinement, and energy localization relevant to opto–thermo–mechanical metasurface platforms and applications.**

***Index Terms*—parity time duality, metasurfaces, bed of nails, surface impedance, Wiener-Hopf**

I. Introduction

Parity time duality symmetry enables reciprocal edge guided transport enforced by an antisymmetric scattering response [1]. While exact formulations exist for ideal impedance boundaries, practical metasurface realizations introduce dispersive and polarization dependent responses that require revised analytical descriptions. In emerging opto–thermo–mechanical systems, engineered metasurfaces are increasingly exploited to control electromagnetic confinement, losses, and local heating, motivating compact analytical tools able to connect dispersion properties with energy management. This work provides a compact one page model, aligned with surface impedance and spectral viewpoints, for a bed of nails implementation relevant to realistic PTD waveguides and multifunctional nano-enabled platforms.

II. Spectral framework

Guided fields propagate along the longitudinal direction and decay away from the interface. The spectral wavenumbers satisfy

$$k_x^2 + k_y^2 + k_z^2 = k_0^2, \tag{1}$$

where k_0 is the free space wavenumber. The transverse behavior is governed by boundary induced resonance conditions rather than bulk propagation. These resonances determine the spatial localization of electromagnetic energy and, consequently, the regions of enhanced thermal and mechanical interaction in integrated platforms.

III. Effective surface impedance viewpoint

The bed of nails metasurface is modeled through an effective normalized surface reactance X_s, acting at the lower wall of a parallel plate configuration, consistently with established BoN-based waveguide models [2]. This allows the boundary condition to be written in compact form as

$$\hat{n} \times \mathbf{E}_t = Z_s \mathbf{H}_t, \tag{2}$$

where $\mathbf{E}_t$ and $\mathbf{H}_t$ are the tangential fields at the metasurface plane.

The dispersive nature of $Z_s = iX_s$, normalized with respect to the free-space impedance $120\pi\,[\Omega]$, enables frequency-selective field confinement and controlled surface currents, which are key mechanisms for regulating local absorption and thermo–mechanical actuation in functional metasurfaces.

For transverse magnetic polarization with respect to the plates, the surface reactance modifies the transverse resonance condition,

$$\frac{k_y}{k_0}\tan(k_y d) + X_s(k_y, \omega) = 0, \tag{3}$$

where d is the plate separation. This relation admits both evanescent and propagating solutions for k_y, depending on frequency and metasurface parameters.

IV. Wiener–Hopf interpretation

The edge guided mode supported at the PTD junction is determined within a Wiener–Hopf (WH) spectral framework by enforcing impedance boundary conditions at the two parallel plate half regions through auxiliary spectral functions. Unlike ideal PTD impedance junctions, the present metasurface implementation does not satisfy the canonical PTD orthogonality condition and the TM and TE contributions must therefore be retained in their general form.

The auxiliary functions $\Phi^{\pm}_{A,\mathrm{TM}}$ and $\Phi^{\pm}_{A,\mathrm{TE}}$ represent half range Fourier transforms of the tangential fields evaluated at the metasurface boundary and embed the corresponding impedance boundary conditions, as established in [3]. They constitute the basic unknowns of the WH system and encode the polarization dependent boundary response, which directly impacts energy concentration and dissipation mechanisms.

After kernel factorization, the spectral solution exhibits nonphysical poles at

$$k_x = \pm i\alpha_0, \qquad \alpha_0 = \frac{k_y k_z}{k_0}, \tag{4}$$

which do not correspond to admissible eigenmodes and must be canceled, as discussed in [3]. The dispersion relation follows from pole cancellation and yields the global characteristic condition

$$\frac{1}{X_2}\frac{\Phi^{-}_{A,\mathrm{TM}}(i\alpha_0)\,\Phi^{+}_{A,\mathrm{TE}}(i\alpha_0)}{\Phi^{+}_{A,\mathrm{TM}}(i\alpha_0)\,\Phi^{-}_{A,\mathrm{TE}}(i\alpha_0)} = \frac{1}{X_1}, \tag{5}$$

where X_1 denotes the normalized surface reactance of the metasurface boundary and X_2 denotes the PEC reactance, equal to zero. A complicated and lengthy algebraic procedure follows to alleviate the undesired zero in the denominator caused by X_2, which for the sake of brevity is not presented herein. Together with (1), (5) determines the longitudinal wavenumber k_z and the dispersion of the edge guided mode.

V. Discussion

Equation (3) clarifies the polarization selective nature of the bed of nails implementation. TM polarized modes depend explicitly on the dispersive surface reactance and may undergo a frequency controlled transition from vertically evanescent to propagating behavior. This property enables selective electromagnetic energy trapping and release, which is of interest for thermally assisted switching and mechanically reconfigurable devices. TE polarized modes, instead, remain governed by geometry and do not exhibit an analogous transition. This separation is directly reflected in the structure of the Wiener–Hopf condition (5).

VI. Conclusion

A compact analytical description has been presented for a realistic parity time duality waveguide implemented with a bed of nails metasurface. By combining a surface impedance viewpoint with a spectral Wiener–Hopf interpretation, the model captures polarization selective dispersion and provides a direct analytical bridge between metasurface physics and opto–thermo–mechanical energy management in advanced nano-enabled systems.

References

[1] M. G. Silveirinha, “Parity time duality symmetry in electromagnetics,” *Phys. Rev. B*, 2017.

[2] A. Polemi, S. Maci, and P.-S. Kildal, “Dispersion characteristics of bed of nails waveguides,” *IEEE Trans. Antennas Propag.*, 2011.

[3] X. M. Mitsalas, C. De Angelis, and S. Maci, “Exact Solution of a PTD-Symmetric Bifilar-Line Waveguide Formed by Parallel-Plate Impedance Junctions,” *IEEE Trans. Antennas Propag.*, vol. 72, no. 10, pp. 7830–7840, Oct. 2024.

Quantization Pressure and Commensurability in Morphogenetic Metasurface Design

Thomas Fromentèze[1,2,*], Chidinma Uche[1], Emebet Woldu Hadgu[1], Cyril Decroze[1], Raphaël Pestourie[3]

[1]XLIM, University of Limoges, CNRS, Limoges, France
[2]Institut Universitaire de France, France
[3]Georgia Institute of Technology, Atlanta, USA
*Corresponding author: thomas.fromenteze@unilim.fr

***Abstract*—This study addresses domain size effects in the characterization of self-organizing metasurfaces. It is demonstrated that periodic boundaries induce a commensurability pressure, causing effective tensors to oscillate. This quantization phenomenon is analyzed, and a methodology is proposed to select optimal unit cells for accurate impedance synthesis.**

***Keywords*— Morphogenesis, Homogenization, Metasurfaces, Commensurability.**

I. Introduction

Morphogenetic metasurfaces [1], inspired by Turing's work [2], leverage decentralized reaction-diffusion rules to generate spatial patterns and synthesize electromagnetic tensors. The dynamics are governed by the anisotropic Gray-Scott model:

$$\begin{aligned}\frac{\partial u}{\partial t} &= \nabla \cdot (\mathbf{D}_u \nabla u) - uv^2 + F(1-u) \\ \frac{\partial v}{\partial t} &= \nabla \cdot (\mathbf{D}_v \nabla v) + uv^2 - (F+k)v\end{aligned} \tag{1}$$

where u, v are species concentrations and F, k are reaction rates. Anisotropy is introduced via $\mathbf{D}_{u,v} = d_{u,v}\mathbf{T}$, with $\mathbf{T} = \mathbf{R}_\theta \,\mathrm{diag}(a, 1-a)\, \mathbf{R}_\theta^T$ defined by orientation θ and anisotropy factor a. Enabling decentralized metasurface synthesis requires a database linking local generative parameters to the emergent geometries and effective electromagnetic tensors. Building such a database demands accurate homogenization from finite simulation domains, raising a fundamental problem of commensurability between the intrinsic pattern wavelength and domain size.

II. Quantization Pressure

Self-organization drives the system towards compact arrangements. In finite periodic domains, a *quantization pressure* arises when the domain size is not commensurate with the motif period. Topological constraints force pattern adjustments, distort local geometry, and finally bias effective properties. Crucially, morphogenetic synthesis enables rotation-invariant electromagnetic properties, requiring characterization across varying motif orientations θ [3]. As illustrated in Fig. 1, when the principal axes of the pattern are aligned with those of the simulation domain ($\theta = 0°$), the effective tensor converges smoothly. When they are misaligned ($\theta = 45°$ in the depicted case), geometric frustration is amplified, leading to stronger oscillations and larger distortions in the extracted parameters.

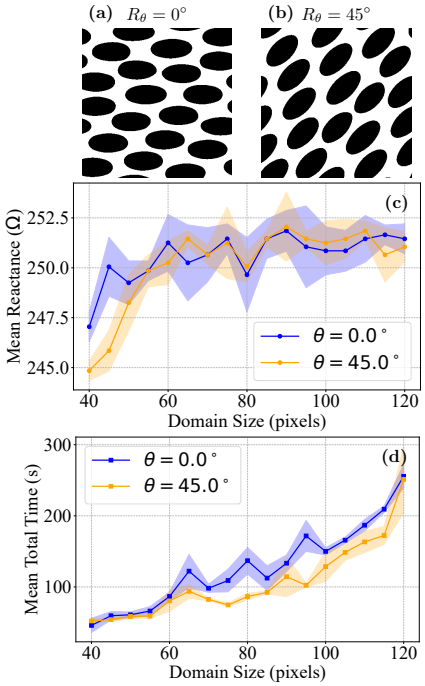

Fig. 1. Commensurability effects. (a-b) Self-organized patterns: aligned (0°) vs. frustrated (45°). (c) Reactance convergence: smooth vs. oscillatory. (d) Computational cost vs. domain size. Values are estimated over 5 random seeds (1σ).

III. Conclusion

Commensurability artifacts in morphogenetic metasurfaces mirror condensed matter phenomena. Quantifying this pressure is the first step towards defining predictive models for extracting infinite-domain parameters from small representative volume elements.

References

[1] T. Fromenteze, O. Yurduseven, C. Uche, E. Arnaud, D. R. Smith, and C. Decroze, "Morphogenetic metasurfaces: Unlocking the potential of Turing patterns," *Nat. Commun.*, vol. 14, no. 1, p. 6249, 2023.
[2] A. M. Turing, "The chemical basis of morphogenesis," *Philos. Trans. R. Soc. Lond. B*, vol. 237, no. 641, pp. 37–72, 1952.
[3] C. N. Uche, N. Parsaei, C. Decroze, and T. Fromentèze, "Breaking periodicity with morphogenetic metasurfaces," *IEEE Trans. Antennas Propag.*, 2025.

Ultrafast thermal exchanges around nano-objects probed by time-resolved optical spectroscopy

Margherita Vittucci[1], Alessandro Casto[1], Fabiano Tarulli[2], Matteo Fasano[2], Aurélien Crut[1], Francesco Banfi[1], Natalia Del Fatti[1,3], Paolo Maioli[1,*]

[1]Université Claude Bernard Lyon 1, CNRS, Institut Lumière Matière, Villeurbanne, France
[2]Politecnico di Torino, Department of Energy, Torino, Italy
[3]Institut Universitaire de France (IUF), France
*Corresponding author: paolo.maioli@univ-lyon1.fr

***Abstract*—Ultrafast thermal energy exchange between absorbing nano-objects and surrounding liquid or solid environments is investigated by time-resolved optical spectroscopy. Cooling dynamics are monitored from picoseconds to nanoseconds after excitation. An opto-thermal model extracts thermal boundary resistance and environmental thermal conductivity, enabling quantitative characterization of nanoscale heat transfer.**

***Keywords*— ultrafast optics, thermo-optical coupling, plasmonic nano-objects, carbon nanotubes.**

Recent advances in nanotechnology have intensified the need to investigate the thermal properties of materials at the nanoscale. In this context, we focus on thermal energy exchange between nano-objects and their liquid or solid environments, which is primarily governed by the thermal boundary resistance (TBR), also known as Kapitza resistance, at the interface. From a fundamental perspective, this phenomenon is particularly compelling, as the dependence of TBR on the physical properties of the interfacing materials and on interfacial conditions remains incompletely understood.

Time-resolved optical spectroscopy provides a non-contact and non-destructive means to monitor nanoparticle cooling dynamics on picosecond to nanosecond timescales, enabling a detailed analysis of nanoscale heat transfer. In a pump–probe experiment, an ultrafast laser pulse rapidly heats the sample, while a time-delayed probe pulse measures the induced changes in optical absorption (see Figure 1, top). A higher TBR leads to slower nanoparticle cooling, as energy transfer from the nano-objects to the surrounding medium is impeded, resulting in longer decay times in the transient optical response (Figure 1, bottom). The TBR values quantitatively extracted at nanometric interfaces can then be directly compared with theoretical models [1].

To interpret the experimental data, we developed a comprehensive opto-thermal model [2] that accounts for the coupled thermal dynamics of both the nano-objects and their environment, as well as their influence on the transient optical absorption. The thermal boundary resistance values quantitatively extracted from the experiments are then compared with numerical models based on molecular dynamics simulations [3]. This combined experimental–theoretical approach enables refinement of the models and advances our understanding of thermal transport across nanoscale interfaces.

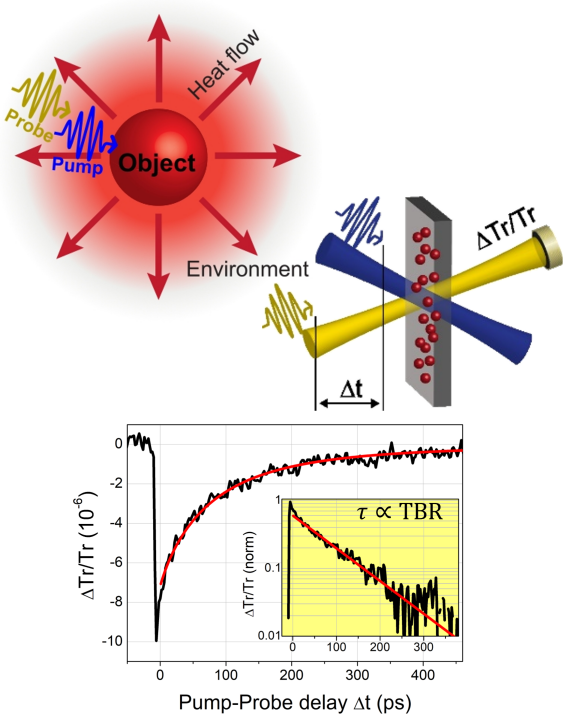

Fig. 1. Principle of time-resolved optical spectroscopy applied to the characterization of ultrafast cooling dynamics at the nanoscale.

We will review experiments on noble metal nanoparticles dispersed in solid and liquid environments, together with more recent studies on multi-wall and single-wall carbon nanotubes dispersed in solvents and epoxy matrices.

References

[1] A. Casto, M. Vittucci, F. Vialla, A. Crut, F. M. Bellussi, M. Fasano, F. Vallée, N. Del Fatti, F. Banfi, and P. Maioli, "Experimental optical retrieval of the Thermal Boundary Resistance of carbon nanotubes in water," *Carbon*, vol. 229, p. 119445, Oct. 2024, doi:10.1016/j.carbon.2024.119445.

[2] M. Gandolfi, A. Crut, F. Medeghini, T. Stoll, P. Maioli, F. Vallée, F. Banfi, and N. Del Fatti, "Ultrafast thermo-optical dynamics of plasmonic nanoparticles," *J. Phys. Chem. C*, vol. 122, no. 15, pp. 8655–8666, 2018, doi:10.1021/acs.jpcc.8b01875.

[3] F. Tarulli, F. M. Bellussi, M. Provenzano, P. De Angelis, A. Casto, M. Vittucci, N. Del Fatti, F. Banfi, P. Maioli, and M. Fasano, "Role of surface oxidation in enhancing heat transfer across graphene–water interface via thermal boundary resistance modulation," *Int. Commun. Heat Mass Transf.*, vol. 172, p. 110364, 2026, doi:10.1016/j.icheatmasstransfer.2025.110364.

Controlling nonlinear THz generation via two-beam excitation of all-dielectric nanostructures

Unai Arregui Leon[1,*], Luca Carletti[2], Davide Rocco[2], Costantino De Angelis[2], Giuseppe Della Valle[1]

[1]Department of Physics, Politecnico di Milano, Italy
[2]Department of Information Engineering, University of Brescia, Italy
*Corresponding author: unai.arregui@polimi.it

***Abstract*— All-dielectric nanoresonators exhibiting high second-order nonlinearity are a widely adopted platform for nanoscale frequency conversion. The all-optical management of terahertz radiation emitted nonlinearly from Mie-resonant nanoantennas is reported here. The method relies on the interaction among the multipolar moments induced at the difference-frequency window of two individual infrared excitation beams.**

***Keywords*— terahertz, difference-frequency generation, metasurfaces, all-dielectric**

I. Introduction

The development of efficient, compact, and tunable terahertz (THz) sources in the spectral region ranging from 1 THz to 15 THz is crucial for applications not only in basic science (spectroscopy, near-field optics, microscopy...) but also in advanced technology for imaging, telecommunications or biomedicine [1]. The use of the difference-frequency generation (DFG) downconversion process mediated by the bulk second-order nonlinear susceptibility ($\chi^{(2)}$) of non-centrosymmetric crystals is on the grounds of the laser-driven methods for THz generation. Due to the advances on nanofabrication techniques, such an approach can nowadays be exploited in a phase-matching-free regime by resorting to all-dielectric $\chi^{(2)}$-metasurfaces, i.e. quasi-2D arrays of sub-wavelength resonant nanoantennas which emit THz radiation through the current density induced therein by the DFG between two near-infrared (NIR) mode profiles. In fact, such a three-wave mixing approach naturally allows to conceive two different excitation mechanisms: (i) a single inicident optical pump beam where two intrapulse components are mixed (intrapulse-DFG or optical rectification); and (ii) the input spectrum is constituted by two individual optical beams (interpulse-DFG). Both illumination schemes can be advantageous depending on the functionality to be addressed and, in particular, the two-beam excitation has already been adopted in the framework of nonlinear nanophotonics for the control of the on-axis sum-frequency generation polarization state [2], third-harmonic generation enhancement [3] or temporal edge detection [4].

In this spirit, the potential of all-dielectric nanopillars to efficiently tailor nonlinear THz far-field emission is proposed in this work, through an analytical and numerical investigation of the intrapulse- and interpulse-DFG processes. AlGaAs and $LiNbO_3$ are tested as candidates for the generation medium, owing to their high-index transparency windows in the NIR, strong $\chi^{(2)}$ components for optical-to-THz conversion and several commercially available cleavage planes. Extending the two-beam illumination strategy to periodic nanoantenna arrays paves the way toward the realization of all-optically reconfigurable metasurfaces for THz photonics.

II. Methods

The THz radiation intensity, i.e. the time-averaged power radiated per unit solid angle, from a free-standing nonlinear nanoantenna is determined by the coherent interference between the electric (a_E) and magnetic (a_M) multipoles of the emitted THz far-field as follows:

$$\frac{dP}{d\Omega}(\theta,\varphi) \propto \left| \sum_{l,m} (-i)^{l+1}(2l+1) \begin{bmatrix} i^l a_M(l,m)\, \vec{X}_{lm}(\theta,\varphi) + \\ + i^{l+1} a_E(l,m)\, \hat{r} \wedge \vec{X}_{lm}(\theta,\varphi) \end{bmatrix} \right|^2 \quad (1)$$

where $l \in \mathbb{N}$ and $m = -l, \dots, l$ are, respectively, the quantum numbers specifying the total and the z-component of orbital angular momentum of the THz photons, and $\vec{X}_{lm}$ are the normalized vector spherical harmonics [5]. The multipolar coefficients $a_{E,M}$ are ultimately specified by the THz polarization current density induced by the internal NIR fields and the material's $\chi^{(2)}$. As such, the effective nonlinear THz generation response of the nanoantenna in the spatial domain can be engineered at will by controlling the illumination conditions and the relative orientation of its geometry with respect to the crystal lattice.

III. Results and Discussion

The lower level of crystallographic, and thereby, optical symmetry of $LiNbO_3$ in comparison to AlGaAs makes the former an ideal platform for the exploration of advanced THz routing strategies. It is found that, in the transition from two co-polarized incident NIR fields to a cross-polarized interpulse-DFG scenario, the far-field pattern of a Z-cut $LiNbO_3$ nanocylinder can evolve from that of a vertical electric dipole

toward that of a purely horizontal one, at almost no cost in terms of conversion efficiency. In the case of AlGaAs nanopillars, the NIR-to-THz efficiency shows a detrimental dependence on the angle between both incoming optical beams in the interpulse-DFG scheme. Interestingly, though, the multipolar analysis elucidates that the <111>-oriented nanopillar allows for the efficient control of the THz radiation pattern through the polarization state of the single pump in the intrapulse-DFG. Finally, the level of management of nonlinear THz emission is further lifted by resorting to a metasurface configuration, where the full platform response is dictated by the combination of the single meta-atom response with Bloch-Floquet theory in the nonlinear optical regime.

IV. Conclusion

An analytical and numerical study is reported in order to design and model all-dielectric nonlinear nanopillars for the efficient control of THz emission via DFG. Following a multipolar theory approach, it is found that the strong influence of the illumination scheme on the generation process can be exploited as a way to unlock advanced THz functionalities, such as wide-angle beam steering or nonlinear routing.

Acknowledgments

This work was supported by the HOTMETA project under the PRIN 2022 MUR program funded by the European Union – Next Generation EU – PNRR – M4C2, investimento 1.1 – “Fondo PRIN 2022” – HOT-carrier METasurfaces for Advanced photonics (HOTMETA), contract no. 2022LENW33 – CUP: D53D2300229 0006.

References

[1] A. Leitenstorfer, et al., “The 2023 terahertz science and technology roadmap”, Journal of Physics D: Applied Physics, vol. 56, no. 22, p. 223001, 2023.

[2] M. A. Weissflog, et al., “Far-field polarization engineering from nonlinear nanoresonators”, Laser & Photonics Reviews, vol. 16, no. 12, p. 2200183, 2022.

[3] A. Zilli, et al., “Frequency tripling via sum-frequency generation at the nanoscale”, ACS Photonics, vol. 8, no. 4, pp. 1175-1182, 2021.

[4] U. Arregui Leon, et al., “Event detection via THz generation with flat nonlinear optics”, Optical Materials Express, vol. 15, no. 2, pp. 307-318, 2025.

[5] J. D. Jackson, “Classical electrodynamics”, John Wiley & Sons, 3rd ed., 1999.

Supermode Theory for Broadband All-Dielectric Metasurfaces

Pooja Uday Naik[1,*], Massimiliano Guasoni[1]

[1]Optoelectronics Research Centre, University of Southampton, Southampton, SO17 1BJ, UK
*Corresponding author: P.U.Naik@soton.ac.uk

***Abstract*— Broadband metasurfaces are often chosen for robustness, yet their collective electromagnetic behavior remains underexplored. We present a supermode framework for metasurfaces that unifies linear and non-linear response. The approach reveals how broadband polarization functionality and stability arise from the collective response, informing the design of scalable metasurface systems.**

***Keywords*— all-dielectrics, multilayer metasurface, supermodes**

I. Introduction

Non-resonant metasurfaces offer broadband, power-scalable optical functionality with superior robustness compared to high-Q resonant structures [1, 2]. However, these structures are fundamentally collective electromagnetic systems governed by coupling across neighbouring meta-atoms rather than by isolated responses [3]. Understanding this collective behaviour requires a physically transparent theoretical framework. We introduce a supermode-based description that unifies the linear and non-linear electromagnetic response of non-resonant, multilayer metasurfaces.

II. Methods

The metasurface is modeled using a supermode formulation in which the structured layer is treated as a finite guiding region supporting a single supermode. The electromagnetic field inside the metasurface of thickness L is expanded in forward- and backward-propagating guided supermodes,

$$E = \sum_m (B_{f,m} e^{i\beta_m L} + B_{b,m} e^{-i\beta_m L}) \quad (1)$$

where, $B_{f,m}$ and $B_{b,m}$ are complex amplitudes of forward (+) and backward (-) propagating components of the supermode m with a propagation constant β_m, respectively.

This supermode-based description enables a physically transparent treatment of collective electromagnetic response in metasurfaces and provides a compact representation of phase accumulation and interference within the structured layer. The framework is further extended to nonlinear optical processes, including third-harmonic generation (THG). The analytical predictions for THG power in a periodic cylindrical silicon (Si) metasurface embedded in silica are validated against full-wave numerical simulations as shown in Fig.1.

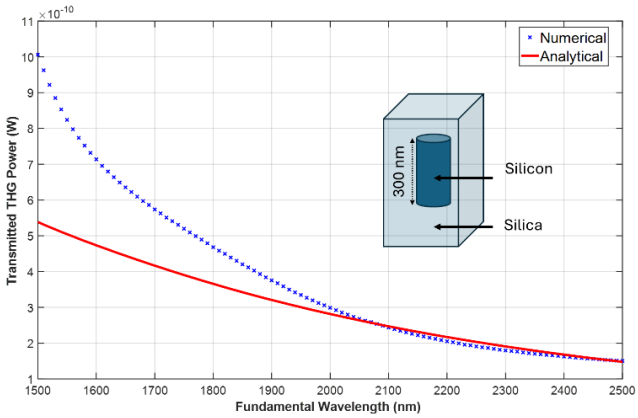

Fig. 1 THG power as a function of fundamental wavelength, comparing numerical simulations with the analytical supermode-based model. The inset illustrates the simulated unit cell, consisting of a cylindrical Si meta-atom embedded in silica.

III. Results and Discussion

The results demonstrate:

- Angle-robust characterization that is compatible with arbitrary unit cell geometries.
- 1000X faster high resolution reverse engineering model for multilayer metasurface devices.

IV. Conclusion

A supermode framework is established for strongly coupled meta-atoms, a regime that has received limited attention despite its rich physics. By unifying linear and nonlinear optical response, the approach provides physical insights into collective behavior while creating an electromagnetic foundation for engineering multilayer metasurface devices.

References

[1] M. Khorasaninejad and F. Capasso, "Metalenses: Versatile multifunctional photonic components," *Science,* vol. 358, no. 6367, p. eaam8100, 2017.

[2] A. Arbabi, Y. Horie, M. Bagheri, and A. Faraon, "Dielectric metasurfaces for complete control of phase and polarization with subwavelength spatial resolution and high transmission," *Nature nanotechnology,* vol. 10, no. 11, pp. 937–943, 2015.

[3] P. Lalanne and P. Chavel, "Metalenses at visible wavelengths: past, present, perspectives," *Laser & Photonics Reviews,* vol. 11, no. 3, p. 1600295, 2017.

Ultrafast modulation of semiconductor metasurfaces with photo-induced spatial inhomogeneities

Giulia Crotti[1,*], Pietro Baldin[1,], Andrea Schirato[1,2], Olesiya Pashina[3,4], Olga Sergaeva[4], Mihail Petrov[3], Costantino De Angelis[4], Margherita Maiuri[1], Giuseppe Della Valle[1,*]

[1]Department of Physics, Politecnico di Milano, Milan, Italy
[2]Department of Physics and Astronomy, Rice University, Houston, TX, USA
[3]School of Physics and Engineering, ITMO University, Saint Petersburg, Russia
[4]Department of Information Engineering, University of Brescia, Brescia, Italy

*Corresponding author: giulia1.crotti@polimi.it, giuseppe.dellavalle@polimi.it

***Abstract*—**
Semiconductor metasurfaces can be reconfigured in an ultrafast and efficient way, exploiting photogenerated hot carriers for transient permittivity modulations. Here, we present our theoretical work on spatially inhomogeneous permittivity perturbations and demonstrate how to leverage them for novel reconfiguration strategies and faster modulation performances.

***Keywords*— Ultrafast control, metasurfaces, hot carriers, spatial inhomogeneities.**

I. Introduction

Metasurfaces have granted the capability of implementing optical functionalities within thicknesses of a few hundreds of nanometers [1-2]. The possibility of reconfiguring such architectures in an ultrafast and fully reversible way is crucial for several applications. To this end, the all-optical paradigm applied to semiconductor metasurfaces has yielded important results in terms of both efficiency and speed [3-4]. The rationale is to modulate the material properties using an external optical stimulus (pump pulse). Its absorption entails the photogeneration of hot carriers, which in turn are responsible for a permittivity perturbation that evolves in time, following the energy relaxation of the carriers towards the lattice. In this transient regime, the metasurface is interrogated with a second pulse (probe) to reveal the photoinduced changes to its optical response.

Here, we report our theoretical work on the role of spatial inhomogeneities in the carrier population distribution and perturbed permittivity, presenting the design of semiconductor metasurfaces in which spatial transients are leveraged to obtain innovative modulation strategies. This ultimately allows to overcome the recovery speed bottleneck of hot-carrier relaxation. In particular, the idea is to treat spatial inhomogeneities as knobs to modify and tune the optical symmetry properties dynamically.

II. Methods

We relied on a multi-step, segregated modelling approach. We developed a spatially dependent version (I2TM) of the well-known Two Temperature Model. Its driving term is proportional to the (inhomogeneous) pump absorption, that is extracted from full-wave electromagnetic simulations. After solving I2TM for the local expressions of carrier density and lattice temperature, we employed an analytic, semiclassical description of optical transitions to obtain the permittivity perturbations. Finally, we performed full-wave electromagnetic simulations for the perturbed optical response.

III. Results and Discussion

Our first design of an AlGaAs nanowires metasurface allows to switch a quasi-Bound state In the Continuum (qBIC) resonance by breaking in-plane C_2 symmetry using a tilted pump beam [5]. The sub-picosecond alteration makes the qBIC mode transiently accessible to the probe beam, so that an ultra-narrow resonance appears almost instantaneously in transmission. It disappears again on the timescale of symmetry restoration, i.e., of carrier diffusion (~2 ps), thus overcoming the speed limit set by carrier recombination (tens of ps).

A second design of a semiconductor metasurface is proposed where the meta-atom includes two nanowires made of AlGaAs, geometrically identical but with different stoichiometric compositions. We demonstrate that it is possible to induce a transient (< 1 ps) degeneracy of the refractive indexes, by pumping in a spectral region where only one of the two nanowires efficiently absorbs. We thus modify the discrete translational symmetry of the system, by effectively halving the metasurface periodicity. We exploit this strategy to transiently suppress the first diffracted order over a relatively broad spectral range and efficiently redistribute power among the other diffraction channels.

IV. Conclusion

We have demonstrated that modulation of symmetry properties by inhomogeneous distributions of hot carriers at the nanoscale can be an innovative and effective tool for ultrafast all-optical control of semiconductor metasurfaces.

ACKNOWLEDGMENTS

We acknowledge the EU's Horizon 2020 METAFAST project under grant agreement no. 899673 and the ERC-StG ULYSSES grant agreement no. 101077181 funded by the European Union. We also acknowledge the European Union− Next Generation EU PNRR − M4C2 I1.1 - PRIN 2022 - Progetto HOTMETA, ID 2022LENW33, CUP:D53D2300229 0006..

REFERENCES

[1] N. Yu, F. Capasso, "Flat Optics with Designer Metasurfaces," Nature Materials, vol.13, pp. 139−150, 2014.

[2] A. I. Kuznetsov*, M. L. Brongersma*, J. Yao, *et al*., "Roadmap for Optical Metasurfaces," ACS Photonics, vol. 11, pp. 816−865, 2024.

[3] M. R. Shcherbakov, S. Liu, V.V. Zubyuk, A. Vaskin, *et al.* "Ultrafast all-optical tuning of direct-gap semiconductor metasurfaces," Nature Communications, vol. 8, 17, 2017.

[4] G. Della Valle, B. Hopkins, L. Ganzer, T. Stoll, *et al.* "Nonlinear Anisotropic Dielectric Metasurfaces for Ultrafast Nanophotonics," ACS Photonics, vol. 4, 2129, 2017.

[5] G. Crotti, A. Schirato, O. Pashina, O. Sergaeva, M. Petrov, C. De Angelis and G. Della Valle, "Ultrafast switching of a metasurface quasi-bound state in the continuum via transient optical symmetry breaking," Light: Science & Applications, vol. 14, 240, 2025.

Mid-infrared Light Modulation with Silicon Membrane Metasurfaces

Ivan Sinev[1,*], Felix U. Brikh[1], Aleksei Ezerskii[2,3], Olesia Pashina[2], Nikita Glebov[1], Mihail Petrov[2], Sergey Makarov[2,3], Hatice Altug[1]

[1]Institute of Bioengineering, EPFL, Switzerland
[2]School of Physics and Engineering, ITMO University, Russia
[3]Qingdao Innovation and Development Center, Harbin Engineering University, China
*Corresponding author: ivan.sinev@epfl.ch

***Abstract*— Actively tunable single-crystalline silicon membrane metasurfaces overcome low-Q and static limitations in mid-IR photonics. Achieving record resonance Q-factors up to 3000, they enable efficient electro-thermal modulation at kHz speeds and low-power all-optical tuning with nanosecond-scale response times.**

***Keywords*— metasurfaces, electro-thermal modulation, all-optical modulation.**

I. Introduction

Metasurfaces offer universal control over phase, amplitude, and polarization of light, enabling compact optical components for sensing, imaging, and communication. Recently, realization of ultra-high-quality-factor (high-Q) resonances became one of the main goals in the field, as they allow to dramatically enhance light–matter interactions, improve sensing performance and emission control, and enable extreme nonlinear effects[1]. Narrow linewidth resonances also facilitate active tuning of metasurfaces, as even small perturbations can lead to significant modulation of their optical response. However, achieving high-Q resonances typically compromises amplitude contrast, which is a major limiting factor for efficient modulation schemes.

Mid-infrared (mid-IR) photonics have the potential to greatly benefit from both the high Q-factor modes and active tuning, which can be utilized for enhanced detection of chemical and biological compounds, spectroscopy, and efficient high harmonic generation. However, as compared to their visible/near-IR analogues, experimentally reported Q-factors of mid-IR metasurfaces are still moderate and do not reach above a few hundred for neither passive nor active solutions [2]. This is mostly related to the fact that standard fabrication bases, such as silicon-on-insulator and silicon-on-sapphire, that allow to attain Q-factors as high as 10^5 in the telecom spectral range[3], cannot be scaled towards the mid-IR due to the onset of absorption in the low-index substrate material.

In this work [4], using the principles of quasi-bound states in the continuum (q-BIC) in silicon membrane metasurface platform, we experimentally achieve record-high quality factors wtih strong amplitude contrast that was so far elusive for the mid-IR range. Building on this foundation, we demonstrate two complementary active tuning schemes within the same platform to realize free-space Mid-IR modulators extending beyond commonly available solutions in the telecom range [5].

II. Methods

At the core of our approach are single-crystalline silicon membrane metasurfaces that can be fabricated via high-throughput, wafer-scale processes. Metasurfaces are based on a 1 μm thick silicon membrane perforated with a hexagonal lattice of holes optimized to support symmetry-protected bound states in the continuum (BICs) in the mid-IR range. We reduce the symmetry of the lattice by introducing controlled ellipticity of the holes, thus realizing quasi-BIC resonances with finite but ultra-high quality factors. This suspended membrane design enables record-high Q values up to ≈3000 at mid-IR wavelengths.

We then implement active light modulation via two distinct tuning schemes:

- Electro-thermal tuning, realized by Joule heating of the membrane through integrated electrodes. Here, amplitude modulation is achieved at CMOS-compatible drive voltages and kilohertz-range speeds.
- Ultrafast all-optical tuning by generation of free carriers in the membrane, supporting nanosecond-scale modulation responses.

We characterize our mid-IR modulators using customized mid-IR spectroscopy, back-focal-plane imaging, and time-resolved measurements to reveal both their static and dynamic responses.

III. Results and Discussion

Our membrane metasurfaces exhibit extremely sharp mid-IR resonances with measured Q-factors reaching ≈3000, among the highest reported for free-space metasurfaces in this spectral regime. we experimentally achieve record-high quality factors approaching 3000 together with strong amplitude contrast that was so far elusive for the mid-IR range. Building on this

foundation, we demonstrate two complementary active tuning schemes within the same platform to realize free-space Mid-IR modulators extending beyond commonly available solutions in the telecom range [5]. Electro-thermal modulation driven by integrated Joule heating at CMOS-compatible voltages (5 V), sustains >50% modulation depths with speeds up to 14.5 kHz. In the second approach, we realize all-optical modulation is via ultrafast carrier generation in silicon, achieving nanosecond-scale response times and enabling estimated modulation rates in the sub-GHz regime. Importantly, this modulation is achieved at pump fluences as low as 5 uJ/cm^2, almost two orders of magnitude smaller than for visible and near-infrared modulators [6].

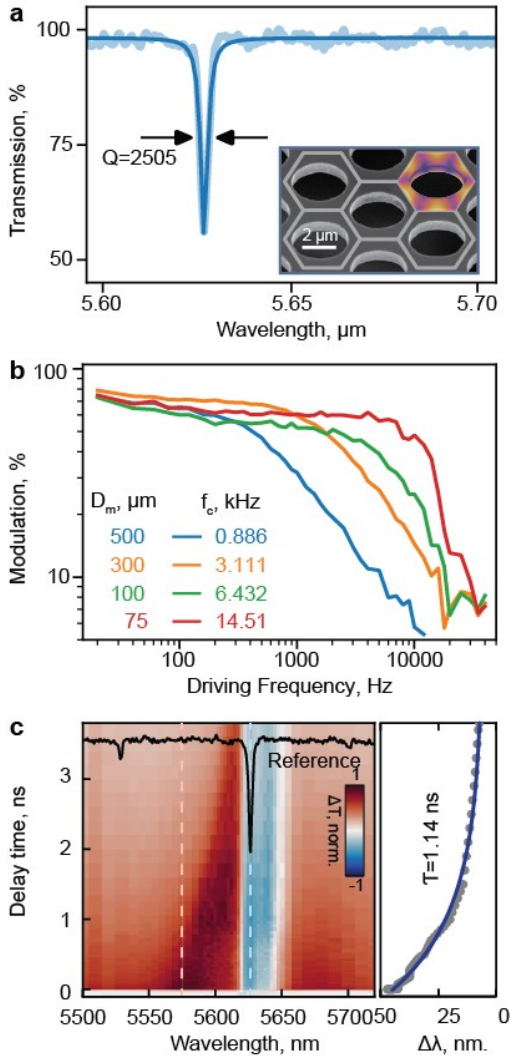

Fig. 1 a, Transmission spectrum of a high-Q silicon membrane metasurface. Inset: SEM image of the metasurface. b, Electro-optical modulation response of the metasurfaces of different sizes. c, Time-resolved reflectivity spectra of the metasurface pumped with femtosecond laser pulses at 430 nm wavelength (average power 1.2 mW). Curve on the right shows the recovery of the resonance after the pump pulse with a characteristic time of 1.14 ns.

IV. Conclusion

Together, these results advance the mid-IR photonics by providing dynamic tunability through engineered high-Q resonances. Furthermore, we demonstrate full compatibility of our design with wafer-scale fabrication, which opens up new opportunities for mid-IR metasurfaces to make impact in a wide range of applications including chemical and biological sensing, free-space optical communication, and thermal emission management.

Acknowledgments

We acknowledge the European Union's Horizon Europe Research and Innovation Programme under agreements 101046424 (TwistedNano) and 101070700 (MIRAQLS). This work was supported by the Swiss State Secretariat for Education, Research and Innovation (SERI) under contract numbers 22.00018 and 22.00081.

References

[1] K. Koshelev, A. Bogdanov, and Y. Kivshar, “Meta-optics and bound states in the continuum,” *Science Bulletin*, vol. 64, no. 12, p. 836, 2019.

[2] A. Aigner, T. Weber, A. Wester, S. A. Maier, and A. Tittl, “Continuous spectral and coupling-strength encoding with dual-gradient metasurfaces,” *Nature Nanotechnology*, vol. 19, p. 1804, 2024.

[3] J. Jin, X. Yin, L. Ni, M. Soljačić, B. Zhen, and C. Peng, “Topologically enabled ultrahigh-Q guided resonances robust to out-of-plane scattering,” Nature, vol. 574, no. 7779, p. 12, 2019.

[4] F. U. Brikh, A. Ezerskii, O. Pashina, N. Glebov, W. Yin, M. Petrov, S. Makarov, I. Sinev, and H. Altug, “Mid-IR light modulators enabled by dynamically tunable ultra high-Q silicon membrane metasurfaces,” arXiv preprint, arXiv:2509.23167, 2025

[5] G. Soma, K. Ariu, S. Karakida, Y. Tsubai, and T. Tanemura, “Subvolt high-speed free-space modulator with electro-optic metasurface,” *Nature Nanotechnology*, 2025.

[6] Tognazzi, A., Franceschini, P., Sergaeva, O., Carletti, L., Alessandri, I., Finco, G., Takayama, O., Malureanu, R., Lavrinenko, A. V., Cino, A. C., de Ceglia, D., & De Angelis, C., “Giant photoinduced reflectivity modulation of nonlocal resonances in silicon metasurfaces,” Advanced Photonics, vol. 5, no. 6, Article 066006, 2023

Young Researchers in Antennas and Metasurfaces

In-Phase TE/TM Surface Wave Excitation on Self-Complementary Metasurfaces

Marceau Bouchez[1,*], David González-Ovejero[1], Stefano Maci[2]

[1]Univ Rennes, CNRS, IETR (Institut d'Électronique et des Technologies du numéRique) – UMR 6164, F-35000, Rennes, France

[2]University of Siena, Siena, Italy

*Corresponding author: marceau.bouchez@univ-rennes.fr

***Abstract*—We propose a simplified dual-polarized excitation strategy for self-complementary metasurfaces. By exploiting intrinsic self-dual symmetry, our theoretical framework demonstrates the equalization of TE and TM surface waves using a dual-feed configuration, overcoming standard network complexity.**

***Keywords*— metasurfaces, dual-polarization, self-complementary structures, surface waves.**

I. Introduction

Modulated Metasurface (MTS) antennas have established themselves as a powerful technology for high-gain aperture antennas. However, efficient strategies for achieving dual-polarization remain an open challenge. Existing solutions often rely on complex feeding networks and intricate unit cell geometries to control cross-polarization levels. [1], [2]

The goal of this research is to simplify this architecture by leveraging the properties of anisotropic self-complementary surfaces. These surfaces possess a unique property where the inductive and capacitive entries in the impedance tensor are mathematically linked, potentially allowing for the simultaneous, balanced support of both TE and TM modes.

This paper outlines the proposed methodology to exploit this phenomenon for a new class of "Bull's-Eye" antennas capable of radiating two orthogonal polarizations with identical radiation patterns.

II. Theoretical Framework

The core of our proposal relies on the spectral domain analysis of impedance surfaces.

A. The self-complementary condition

We model the metasurface using a tensor impedance boundary condition (IBC). Our approach consists in enforcing the self-complementary condition on the surface reactance tensor $\underline{\underline{X}}$:

$$\underline{\underline{X}} = X_L \hat{\rho}\hat{\rho} + X_C \hat{\varphi}\hat{\varphi}, \qquad X_L X_C = -\zeta^2, \tag{1}$$

where X_L and X_C are the inductive and capacitive surface reactances, and ζ is the free-space impedance.

It can be shown that, under this condition, the surface supports TE and TM surface waves (SWs) with identical wavenumbers (k_{sw}). This symmetry provides a mathematical guarantee that a vertical electric dipole (VED) and a vertical magnetic dipole (VMD) interact with the surface in an equivalent manner.

B. Green's function formulation

To validate this, we are developing a full spectral dyadic Green's function formulation. The objective is to derive the electric field spectra generated by elementary sources:

- Vertical electric dipole (VED): Exciting TM modes.
- Vertical magnetic dipole (VMD): Exciting TE modes.

By analyzing the residues of the Green's function at the SW pole, we aim to derive the exact ratio of source amplitudes required to equalize the power launched into both modes.

C. The generalized Huygens condition

A critical aspect of our theoretical work is the derivation of a "Generalized Huygens Condition" for surface waves. We anticipate that by combining horizontal electric and magnetic currents in a specific ratio derived from the spectral analysis, we can achieve unidirectional SW propagation. This condition is fundamental for maximizing the aperture efficiency of the final antenna.

III. Conclusion

This work outlines a pathway toward simplified dual-polarized metasurface antennas. By rigorously applying the self-complementary impedance condition, we demonstrate that phase-balanced TE and TM modes can be excited efficiently.

Acknowledgments

This work has been supported by the outgoing mobility program of the Collège doctoral de Bretagne, Brittany Region and Rennes Métropole. This work has also received support from the French National Research Agency (ANR) through through the AROMA (reference ANR-22-CE24-0013) and SAGACITY (reference ANR-22-CE25-0020) projects. Finally, this work has also been supported by the École Normale Supérieur Paris-Saclay through a Contrat Doctoral Spécifique Normalien.

References

[1] A. Tellechea Pereda, F. Caminita, E. Martini, I. Ederra, J. C. Iriarte, R. Gonzalo, and S. Maci, "Dual circularly polarized broadside beam metasurface antenna," *IEEE Trans. Antennas Propagat.*, vol. 64, no. 7, pp. 2944–2953, Jul. 2016.

[2] R. Thanikonda, M. Faenzi, D. González-Ovejero, E. Martini, and S. Maci, "Multi-beam dual polarised metasurface antenna in Ka-band," in *2024 18th Eur. Conf. Antennas Propag. EuCAP*. Glasgow, United Kingdom: IEEE, Mar. 2024, pp. 1–4.

Multifunctional Metasurfaces with Mutual Coupling Mitigation for Advanced Wireless Systems at Millimeter-Waves and Terahertz

Damián Rodríguez-Trujillo[1,2,*], Alicia E. Torres-García[1,2], Mikel Aldea[3], Jorge Teniente[1,2], Asier Marzo-Pérez[3], Miguel Beruete[1,2]

[1]Department of Electrical and Electronic Engineering, Public University of Navarre (UPNA), Spain
[2]Institute of Smart Cities (ISC), Public University of Navarre (UPNA), Spain
[3]Department of Mathematics and Computer Engineering, Public University of Navarre (UPNA), Spain
*Corresponding author: damianernesto.rodriguez@unavarra.es

***Abstract*—This work presents a single-layer transmission-mode multifunctional metasurface optimized using a neural-network-assisted model. By varying the illumination conditions, the metasurface projects different holographic patterns within a single passive structure. The proposed method combines theoretical electromagnetic formulations with mutual coupling regularization scheme for advanced wireless communication systems.**

***Keywords*— metasurfaces, neural networks, holography, multifunctional devices, mutual coupling, mmWaves**

I. Introduction

The evolution of wireless systems toward increasingly dense and heterogeneous communication scenarios is imposing new requirements on spectral efficiency, adaptability, and hardware scalability. As conventional microwave solutions approach their practical limits, higher-frequency bands, particularly millimeter-wave (mmWave) and terahertz (THz), are being actively explored, offering significantly larger bandwidths to support emerging functionalities in advanced communication systems. However, these frequency ranges also amplify challenges related to wave propagation and system integration [1], [2].

In this context, metasurfaces have emerged as planar, highly efficient and ultracompact structures, designed at subwavelength scales, capable of precisely manipulating the amplitude, phase, and polarization of electromagnetic wavefronts [3], to address the challenges associated with future communication systems [4], [5], [6], [7], [8].

Considerable research is currently focused on implementing Reconfigurable Intelligent Surfaces (RIS) with dynamic responses using tunable elements [9]. However, recent studies have shown that their implementation at mmWave and THz bands is limited by additional losses, reduced efficiency, and increased complexity [10]. As an alternative, passive multifunctional metasurfaces exploit variations in illumination conditions—such as polarization, incidence angle, or spatial excitation—to generate multiple responses from a single static design, reducing system complexity and improving robustness [11], [12].

In this work, we present a design methodology for transmission-mode multifunctional metasurface that combines analytical wave propagation models, based on the Huygens–Fresnel (HF) principle [13], with diffractive neural networks (DNN) assisted by artificial intelligence (AI) [14], [15], [16]. This approach enables the synthesis of phase profiles capable of supporting multiple responses while mitigating undesired effects such as mutual coupling between elements. Although the methodology is demonstrated for holographic field generation, it is general and extendable to other scenarios.

II. Methods

The structure design methodology can be modeled as a diffractive neural network (Fig. 1), where the operational principle of the multifunctional metasurface relies on illumination-dependent responses without active components.

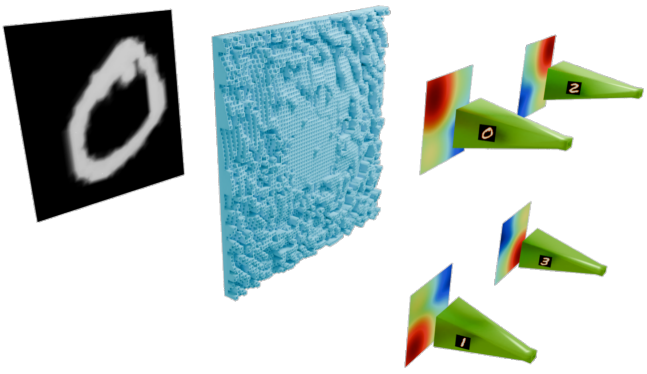

Fig. 1. Schematic of our Diffractive Neural Network (DNN), showing the antenna field sources (input layer), the metasurface (hidden layer), and the target holographic patterns (output layer). Each antenna illuminates the metasurface to generate the associated digit patterns 0, 1, 2, or 3.

In the proposed neural network architecture for metasurface design, the input layer corresponds to the incident field from an antenna, while the metasurface acts as the hidden layer. The output layer represents the target amplitude pattern in the

observation plane, with the phase shift introduced by each unit cell acting as the neuron bias.

An antenna sequentially illuminates different regions of the metasurface, generating distinct holographic patterns, through a varying unit cell phase profile. To optimize the phase distribution (Fig. 2a), we employed gradient-based backpropagation with the Adam optimizer, minimizing the mean squared error (MSE) between target (taken from MNIST dataset) and predicted fields (Fig. 2c). A custom loss function incorporating a gradient-based regularization term was introduced to enforce smooth phase transitions (Fig. 2b), mitigating mutual coupling effects between neighboring elements that would otherwise degrade hologram quality. As a result, the predicted field distributions obtained with phase smoothing exhibit good agreement (Fig. 2d).

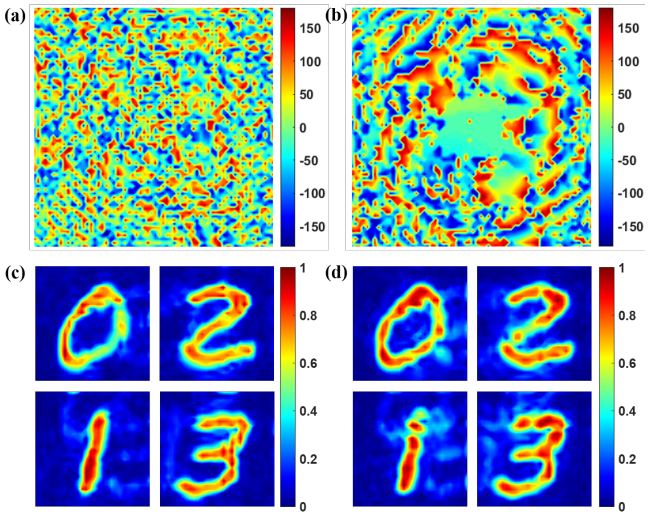

Fig. 2. Comparison of phase profiles and pattern amplitudes. (a) Optimized phase profile (no smoothing), (b) Optimized phase profile (smoothing). (c) Analytically predicted pattern amplitudes (no smoothing), and (d) Predicted pattern amplitudes (smoothing).

III. Results and Discussion

Full-wave simulations confirmed that unsmoothed designs suffer from significant mutual coupling (Fig. 3a), while optimized smoothed profiles reproduced the intended holographic patterns with high accuracy (Fig. 3b).

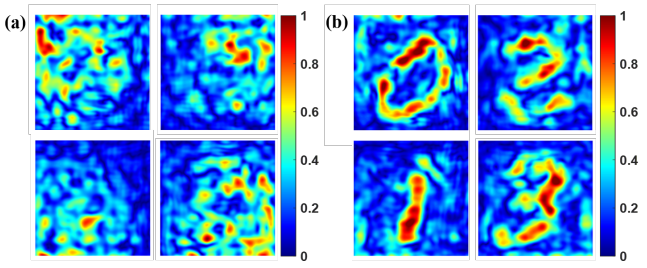

Fig. 3. Comparison of pattern amplitudes. (a) Simulated patterns (no smoothing), and (b) Simulated patterns (smoothing).

Experimental validation further confirmed that the generated holograms (Fig. 4a) closely matched the target patterns for multiple input positions, demonstrating robust multifunctionality in a fully passive metasurface (Fig. 4b).

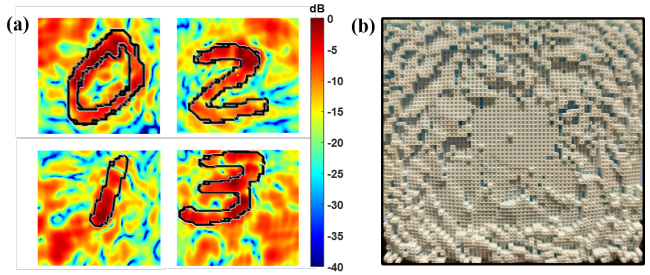

Fig. 4. (a) Measured holographic patterns at the output plane for the four illumination configurations. (b) Image of the fabricated dielectric metasurface.

These results highlight the effectiveness of combining DNN-assisted phase optimization with phase-smoothing strategies to produce high-fidelity, multifunctional metasurfaces capable of generating multiple outputs under different illumination conditions, providing a scalable approach for high-frequency electromagnetic systems.

Finally, the proposed optimization framework can be directly applied to antenna design, enabling the synthesis of radiation patterns with beams steered toward multiple directions and reduced sidelobe levels, which is particularly relevant for compact antenna architectures operating in millimeter-wave bands.

IV. Conclusion

This work introduces a multifunctional metasurface optimized via neural networks for advanced wireless communication systems. The passive nature of the design eliminates the need for active tuning, providing a scalable and cost-effective solution. The demonstrated functionalities, including holographic imaging and beam steering, pave the way for practical implementations in next-generation networks and beyond.

Acknowledgments

This work was supported by Project No. PID2022-137845NB-C21, funded by MCIN/AEI/10.13039/501100011033 and by ERDF "A way of making Europe."

References

[1] C. D'Andrea, J. M. Jornet, A. Singh *et al.*, "6G wireless technologies," in *The Road towards 6G: Opportunities, Challenges, and Applications*. Springer, 2024, pp. 51–114.

[2] A. Alhammadi, I. Shayea, A. A. El-Saleh *et al.*, "Artificial intelligence in 6G wireless networks: Opportunities, applications, and challenges," *International Journal of Intelligent Systems*, vol. 2024, p. 8845070, 2024.

[3] J. Hu, S. Bandyopadhyay, Y.-H. Liu, and L.-Y. Shao, "A review on metasurface: From principle to smart metadevices," *Frontiers in Physics*, vol. 8, 2021.

[4] Y. Monnai, X. Lu, and K. Sengupta, "Terahertz beam steering: From fundamentals to applications," *Journal of Infrared, Millimeter, and Terahertz Waves*, vol. 44, no. 3, pp. 169–211, 2023.
[5] L. Zhu, Y. Wang, L. Dong, G. Shang, S. N. Burokur, and X. Ding, "High-efficiency and full-space indoor holographic communication system assisted by complex-amplitude metasurface," *Advanced Optical Materials*, vol. 13, no. 16, p. 2500070, 2025.
[6] L. Huang, S. Zhang, and T. Zentgraf, "Metasurface holography: from fundamentals to applications," *Nanophotonics*, vol. 7, no. 6, pp. 1169–1190, 2018.
[7] K. Zhang, Y. Wang, Y. Yuan, and S. N. Burokur, "A review of orbital angular momentum vortex beams generation: From traditional methods to metasurfaces," *Applied Sciences*, vol. 10, no. 3, 2020.
[8] S. Legaria, J. Teniente, S. Kuznetsov, V. Pacheco-Peña, and M. Beruete, "Highly efficient focusing of terahertz waves with an ultrathin super-oscillatory metalens: Experimental demonstration," *Advanced Photonics Research*, vol. 2, no. 9, p. 2000165, 2021.
[9] B. Rana, S.-S. Cho, and I.-P. Hong, "Review paper on hardware of reconfigurable intelligent surfaces," *IEEE Access*, vol. 11, pp. 29 614–29 634, 2023.
[10] M. Pérez-Escribano, Ángel Palomares-Caballero, P. Padilla, J. F. Valenzuela-Valdés, and E. Márquez-Segura, "Broadband parasitic modeling of diodes in the millimeter-wave band," *AEU - International Journal of Electronics and Communications*, vol. 177, p. 155216, 2024.
[11] H. Li, G. Li, Z.-L. Deng, W. Xu, H. Xu, J. Li, C. Song, F. Qiu, Y. Zhang, Y. Ren, and J. Yao, "Multifunctional all-silicon terahertz chiral metasurfaces via integrated moiré and spin-decoupled phase engineering," *Laser & Photonics Reviews*, p. e03260, 2026.
[12] F. Zhao, P. Dong, K. Li, M. Zhang, W. Hou, and V. Melikyan, "Inverse design of terahertz metasurfaces for multi-channel holographic imaging based on the modified gradient descent method," *Optics Express*, vol. 33, no. 8, pp. 18 005–18 016, Apr 2025.
[13] B. Orazbayev, V. P.-P. na, M. Beruete, and M. Navarro-Cía, "Exploiting the dispersion of the double-negative-index fishnet metamaterial to create a broadband low-profile metallic lens," *Optics Express*, vol. 23, no. 7, pp. 8555–8564, 2015.
[14] G. Wang, X. Zang, Z. Tan, T. Zhang, Z. Gao, Y. Wang, D. Zhang, A. P. Shkurinov, Y. Zhu, and S. Zhuang, "Modular diffractive neural networks using cascaded metasurfaces," *Laser & Photonics Reviews*, vol. 19, no. 22, p. e00923, 2025.
[15] D. Liao, M. Wang, K. F. Chan, C. H. Chan, and H. Wang, "A deep-learning enabled discrete dielectric lens antenna for terahertz reconfigurable holographic imaging," *IEEE Antennas and Wireless Propagation Letters*, vol. 21, no. 4, pp. 823–827, 2022.
[16] Y. Ma, Q. Luo, C. Zhang, and G. Yang, "Deep learning enables multifunctional metasurfaces design with mutual coupling estimation," *IEEE Transactions on Antennas and Propagation*, vol. 72, no. 11, pp. 8443–8451, 2024.

Low-Cost 3-D Printable Modulated Dielectric Leaky-Wave Antenna

Ravel C. M. Pimenta[1,2,*], Massimiliano Casaletti[1,2]

[1]Sorbonne Université, CNRS, Laboratoire GeePs, 75252 Paris, France
[2]Université Paris-Saclay, CentraleSupélec, CNRS, Laboratoire GeePs, 91192 Gif-sur-Yvette, France
*Corresponding author: ravel.de_miranda_pimenta@sorbonne-universite.fr

***Abstract*—A low-cost 3-D-printable dielectric leaky-wave antenna operating at 20 GHz is presented, where substrate-height modulation synthesizes a scalar surface impedance for holographic beam control. Full-wave simulations demonstrate broadside linearly polarized radiation, 22.8 dBi directivity, 20.1 dBi gain, and a 9.1% 3-dB gain bandwidth.**

***Keywords*— 3D printing, leaky waves, linear polarization, metasurface, impedance modulation**

I. Introduction

Recent advances in additive manufacturing and three-dimensional (3-D) printing technologies are transforming the realization of electromagnetic devices [1], [2], [3], enabling complex dielectric profiles with submillimeter resolution, low cost, and rapid prototyping that are difficult to achieve using conventional printed-circuit techniques [4]. In parallel, modulated impedance surfaces and holographic leaky-wave antennas have emerged as powerful solutions for beam shaping and wavefront control, combining low-profile geometries with electrically large apertures and high directivity [5].

Within this framework, scalar-impedance metasurfaces have attracted growing interest due to their simplicity and fabrication tolerance [6], [7]. Conventional implementations rely on metallic patches or resonant inclusions [8], [9]. However, the prospect of realizing impedance modulation through purely dielectric means is particularly attractive, especially in view of modern 3-D printing platforms capable of producing refined substrate geometries with relatively low cost.

In this paper, a leaky-wave antenna is proposed in which the scalar surface impedance is synthesized by locally modulating the thickness of a grounded dielectric slab. The height modulation controls the propagation constant of the supported transverse-magnetic (TM) surface wave and enables its conversion into a radiating spatial harmonic without metallic elements. A holographic synthesis procedure is employed to generate a directive broadside beam with linear polarization, and full-wave simulations demonstrate good impedance matching and high directivity.

II. Theoretical Background

A. Scalar Metasurface Antenna Model

The considered antenna geometry consists of a grounded dielectric slab whose thickness $h(\rho, \phi)$ is locally modulated, as illustrated in Fig. 1. A feeder positioned at the center excites a cylindrical TM mode that travels radially along the surface. The effective surface impedance distribution (Z_s) across the antenna is achieved exclusively through the controlled modulation of the substrate height, which modifies the boundary condition experienced by the supported surface wave. The structure is engineered so that only the dominant TM surface-wave mode propagates over the aperture [10].

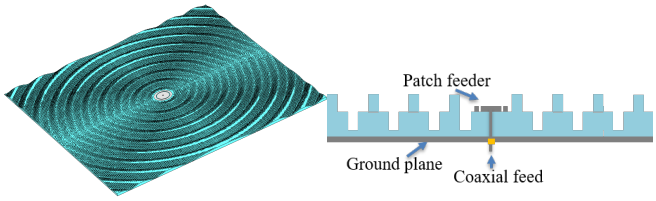

(a) (b)

Fig. 1: (a) (a) Simulated perspective view of the height-modulated dielectric leaky-wave antenna. (b) Cross-sectional schematic illustrating the grounded substrate, coaxial feed, and circular patch exciter..

The electromagnetic boundary condition at the interface $z = 0$ is expressed through the scalar surface impedance relation [5]

$$\mathbf{E}_t = Z_s(\rho, \phi)\hat{\mathbf{n}} \times \mathbf{H}_t = Z_s(\rho, \phi)\,\mathbf{J}, \tag{1}$$

where $\hat{\mathbf{n}}$ is the outward unit normal vector, $\mathbf{E}_t(\mathbf{H}_t)$ is the tangential electric (magnetic) field, and $\mathbf{J}$ is the equivalent surface electric current density. By introducing a slow spatial variation of h, a weak modulation of the surface reactance is produced while preserving single-mode TM propagation.

The feeder excites a TM surface wave characterized by the propagation constant

$$k_{sw}^{t} = k_0\sqrt{1 - \left(\frac{\bar{X}_s(\hat{\mathbf{k}}_{sw}^{t})}{\zeta_0}\right)^2}, \tag{2}$$

where k_0 is the free-space wavenumber, ζ_0 is the free-space impedance, and $\bar{X}_s$ is the surface reactance associated with that position hereafter referred to as the average impedance.

Following the holographic leaky-wave approach, the surface reactance is weakly modulated according to [5], [8]

$$Z_s(\rho') = j\bar{X}_s\left[1 + M(\rho')\cos\left(\frac{2\pi}{p(\rho')}\hat{\mathbf{k}}_{sw}^t(\rho')\cdot\boldsymbol{\rho'}\right)\right], \quad (3)$$

where $M < 1$ is the modulation index. If the following condition is respected [8]

$$k_{sw}^t - \frac{2\pi}{p} < k_0, \quad (4)$$

the -1 spatial harmonic (Floquet-Bloch mode expansion [7]) becomes radiative, generating a leaky wave in free space. The resulting equivalent magnetic surface current density, $\mathbf{J}_m$, associated with this radiating harmonic is expressed as:

$$\mathbf{J}_m(\rho') = \bar{X}_s M(\rho') e^{-j\left(k_{sw}^t - \frac{2\pi}{p(\rho')}\right)\hat{\mathbf{k}}_{sw}^t)(\rho')\cdot\boldsymbol{\rho'}}\hat{\boldsymbol{\phi}}. \quad (5)$$

B. Incident Surface Wave

A cylindrical TM surface wave launched by a central feeder is assumed:

$$H_\phi^{inc}(\rho) = A\, H_1^{(2)}(k_t\rho), \quad (6)$$

where A is a complex amplitude and $H_1^{(2)}(\cdot)$ is the Hankel function of second kind and first order. Using the far-field asymptotic form of the Hankel function, the magnetic current associated with the radiating harmonic can be extracted from (5):

$$\mathbf{J}_m(\rho') = jA\bar{X}_s M(\rho') e^{-j\frac{\pi}{4}} C(\rho') e^{-j\left(k_{sw}^t - \frac{2\pi}{p(\rho')}\right)\hat{\mathbf{k}}_{sw}^t)(\rho')\cdot\boldsymbol{\rho'}}\hat{\boldsymbol{\phi}} \quad (7)$$

where $C(\rho') = \sqrt{2/(\pi k_t \rho')}$. Aperture field theory is then applied to synthesize the desired radiation pattern and polarization.

The metasurface design is performed by imposing the following condition [8]:

$$\mathbf{J}_m(\rho') = B(\rho')\|\mathbf{G_m}(\rho')\| e^{jArg\{\mathbf{G_m}(\rho')\}}\hat{\boldsymbol{\phi}} \quad (8)$$

where $\mathbf{G_m}(\rho')$ is the surface current distribution that gives us the desired radiated field and $B(\rho')$ is an arbitrary amplitude distribution. The required impedance distribution is then obtained by applying the boundary conditions over the radiating plane. The scalar metasurface is conceived by locally building up this impedance tensor in terms of amplitude and the phase for the required polarization.

III. Results and Discussion

A metasurface antenna was designed and numerically characterized for operation at 20 GHz. The structure employs a grounded dielectric substrate with relative permittivity $\epsilon_r = 4.3$, loss tangent $\tan\delta = 0.025$, and a square radiating aperture of side length $L = 6\lambda_0$. The holographic modulation is synthesized to radiate a linearly polarized beam at broadside ($\theta_0 = 0°, \phi_0 = 0°$).

The relation between the scalar surface impedance and the substrate thickness is obtained through a transmission-line model [10] of the grounded dielectric slab supporting the dominant TM surface-wave mode. This model provides the mapping between local slab height, propagation constant, and average surface reactance required by the holographic synthesis. The dielectric thickness is modulated from 0.05 mm to 2.06 mm across the aperture, around an average height of 1.64 mm corresponding to $\bar{X}_s = 250$. This range ensures weak modulation while preserving single-mode surface-wave propagation.

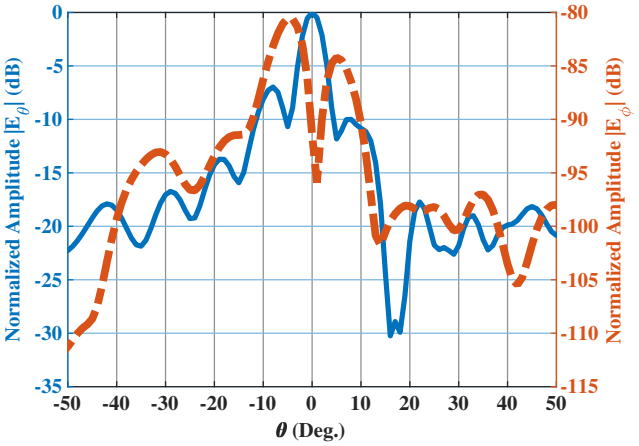

Fig. 2: Simulated co-polarized and cross-polarized electric-field radiation patterns at 20 GHz in the $\phi = 0°$ cut plane.

The incident surface wave is generated by a coaxially fed circular patch located at the center of the structure. The patch has a radius of 4.9 mm and is surrounded by an external ring of radius 6.57 mm separated by a 0.46 mm gap. This feeding configuration was optimized to maximize the launched surface-wave power and minimize the input reflection coefficient [8], [9]. Full-wave simulations were carried out using CST Studio Suite 2023. A spatial discretization corresponding to a mesh resolution of approximately $\lambda/20$ was adopted after convergence testing.

Fig. 2 depicts the electric-field radiation pattern in the $\phi = 0°$ plane, where the copolarized and cross-polarized components are shown in blue and red, respectively. A broadside ($\theta = 0°$) θ-polarized beam is successfully obtained, with maximum sidelobe level around -7 dB. The cross-polarized component remains extremely low over the entire angular range.

A maximum directivity of 22.8 dBi and a peak gain of 20.1 dBi are achieved at 20 GHz, with a half-power beamwidth (HPBW) of 2.7° and a 3-dB gain bandwidth of 9.1%, as shown in Fig. 3. Because the holographic synthesis is implemented using a purely scalar impedance modulation, the leakage rate and polarization purity cannot be independently optimized across the aperture, which leads to a non-uniform surface-wave power extraction and hence to a reduced effective radiating area. This intrinsic limitation of scalar metasurfaces results in an aperture efficiency of 7.2%.

The antenna remains well matched across a large frequency

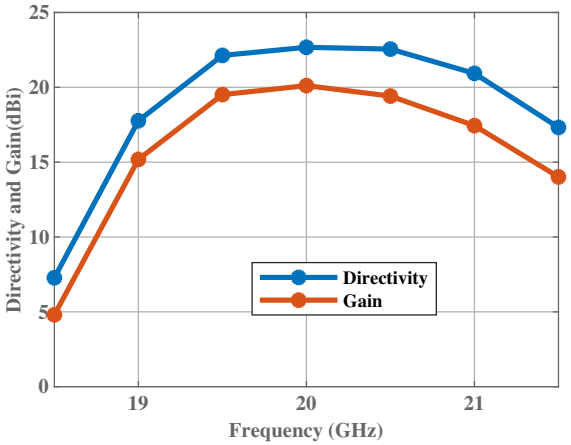

Fig. 3: Simulated directivity and Gain at broadside ($\theta_0 = 0°, \phi_0 = 0°$) along frequency.

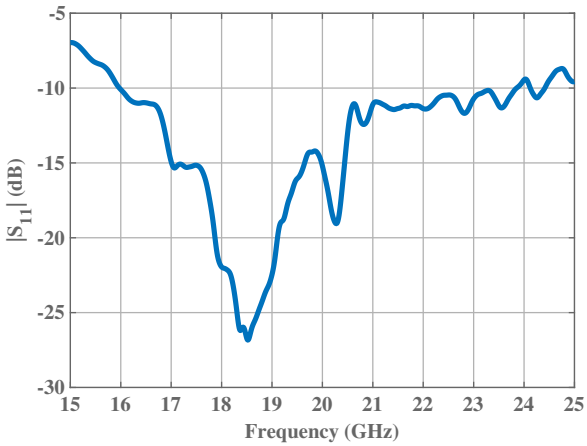

Fig. 4: Simulated return loss.

band, with $|S_{11}| < -10$ dB from 16 to 23.8 GHz, as shown in Fig. 4. This good impedance matching is achieved through the use of a circular patch located above the coaxial feed pin.

Since this investigation focuses on structures compatible with 3D-printing additive manufacturing, the dielectric characterization of available materials, such as Polylactic Acid (PLA) [11], becomes critical. The effective relative permittivity (ϵ_r) of these materials is known to fluctuate based on printer settings, most notably the infill rate, which introduces air into the structure and alters the overall dielectric profile [12]. As the next stage of this research involves the physical prototyping of the antenna, the substrate will be precisely characterized using a resonant circuit method. This characterization is essential to ensure an accurate design and mitigate discrepancies between numerical simulations and experimental measurements prior to final fabrication.

IV. Conclusion

A height-modulated dielectric leaky-wave antenna capable of radiating a directive linearly polarized beam has been presented. By exploiting the local variation of the substrate thickness, the required scalar surface impedance distribution is synthesized without resorting to metallic metasurface elements, making the proposed approach particularly well suited to modern additive-manufacturing processes. A holographic design methodology has been employed to control the phase of the radiating spatial harmonic and to achieve efficient beam formation at broadside.

Numerical results confirm that the antenna exhibits good impedance matching over a large frequency range, achieves peak directivity and gain of 22.8 dBi and 20.1 dBi, respectively, at 20 GHz, and provides a 3-dB gain bandwidth of 9.1%, together with an aperture efficiency of 7.2%. Ongoing work focuses on the dielectric characterization of printable materials and on prototype fabrication for experimental validation.

References

[1] B. Zhang, Y. -X. Guo, H. Zirath and Y. P. Zhang, "Investigation on 3-D-Printing Technologies for Millimeter- Wave and Terahertz Applications," in *Proceedings of the IEEE*, vol. 105, no. 4, pp. 723-736, April 2017

[2] J. Sorocki, I. Piekarz, I. Slomian, S. Gruszczynski and K. Wincza, "Realization of Compact Patch Antennas on Magneto-Dielectric Substrate Using 3D Printing Technology with Iron-Enhanced PLA Filament," *2018 International Conference on Electromagnetics in Advanced Applications (ICEAA)*, Cartagena, Colombia, 2011

[3] E. Wojtczak, W. Kalista, L. Leszkowska, M. Rzymowski, K. Nyka and Ł. Kulas, "Directional Antennas Using Ecofriendly Materials and 3D Printing," 2025 19th European Conference on Antennas and Propagation (EuCAP), Stockholm, Sweden, 2025

[4] S. Wang et al., "Compact Circularly Polarized Patch Antennas Using 3-D Printed Non-Uniform Metal/Dielectric Structure," in *IEEE Antennas and Wireless Propagation Letters*, 2026

[5] G. Minatti, F. Caminita, M. Casaletti and S. Maci, "Spiral Leaky-Wave Antennas Based on Modulated Surface Impedance," in *IEEE Transactions on Antennas and Propagation*, vol. 59, 2011

[6] S. Pandi, C. A. Balanis and C. R. Birtcher, "Design of Scalar Impedance Holographic Metasurfaces for Antenna Beam Formation With Desired Polarization," in *IEEE Transactions on Antennas and Propagation*, vol. 63, 2015

[7] M. Casaletti, M. Śmierzchalski, M. Ettorre, R. Sauleau and N. Capet, "Polarized Beams Using Scalar Metasurfaces," in *IEEE Transactions on Antennas and Propagation*, vol. 64, no. 8, 2016

[8] A. Arroyo, R. Contreres, A. Piche, H. Roussel and M. Casaletti, "Linear Polarization from Scalar Modulated Metasurfaces," *2022 16th European Conference on Antennas and Propagation (EuCAP)*, Madrid, Spain, 2022

[9] Mounia Djoudi, Mohamed Lamine Tounsi, Julien Sarrazin, and Massimiliano Casaletti, "Efficient Design of a Novel Multibeam Antenna Using Scalar Metasurfaces," *Progress In Electromagnetics Research*, vol. 183, 2025

[10] D. M. Pozar, Microwave Engineering, 4th ed. New York, NY, USA: Wiley, 2011

[11] A. K. Bhattacharyya, D. R. Jackson, J. T. Williams and R. Smith, "Microstrip patch designs which do not excite surface waves," *Antennas and Propagation Society Symposium 1991 Digest*, vol. 1, London, ON, Canada, 1991,

[12] Mirzaee, M. and Noghanian, S., "High frequency characterisation of wood-fill PLA for antenna additive manufacturing application," *Electronics Letters*, vol. 52, 2016

[13] Y. S. Tanaydin and M. Duman, "Design and Frequency Characterization of a Rose Antenna Produced with 3D Printing," *2023 7th International Symposium on Innovative Approaches in Smart Technologies (ISAS)*, Istanbul, Turkiye, 2023

Low-Loss CLAF Waveguides and Slot Arrays for 77 GHz Automotive Radar Using Mirror-Stacked Glide-Symmetric Mushroom EBGs

Ashray Ugle[1,2,3,*], Massimiliano Casaletti[1,2], Marta Arias Campo[3], Simona Bruni[3], Guido Valerio[1,2]

[1]Sorbonne Université, Laboratoire de Génie Électrique et Électronique de Paris (GeePs), 75005, Paris, France
[2]Université Paris-Saclay, CentraleSupélec, CNRS, GeePs, 91192, Gif-sur-Yvette, France
[3]IMST GmbH, Sub-THz Antenna Systems, 7475, Kamp-Lintfort, Germany
*Corresponding author: ashray.ugle@sorbonne-universite.fr

***Abstract*—This work presents cost-effective CLAF waveguides using mirror-stacked glide-symmetric mushroom EBGs at 76-81 GHz. Building on prior dispersion analysis, prototypes are designed, fabricated and characterised, including straight and bent waveguides, power dividers and slot arrays. Measurements confirm low-loss, cost-efficient mmWave automotive radar components.**

***Keywords*— multimodal bloch analysis, electromagnetic bandgap materials, glide symmetry, automotive radars.**

I. Introduction

The mass-production requirements for automotive radars at 77 GHz demand cost-effective solutions for millimetre wave (mmWave) antenna and beamforming technologies. Although standard printed circuit board (PCB) fabrication is well suited to mass production, transmission lines and antennas on PCBs suffer from high dielectric losses and low efficiencies unless expensive RF substrates are used.

Nevertheless, cost-effective PCB substrates can guide propagation in air by using contactless air-filled (CLAF) waveguides, thereby achieving higher efficiencies. PCB-based periodic structures with electromagnetic bandgap (EBG) characteristics, such as mushrooms, suppress the lateral leakage of parallel-plate waveguide (PPW), enabling guided propagation in air, [1], [2] as shown in Fig. 1a.

This work builds upon our previous study on the dispersion analysis of mirror-stacked glide-symmetric (GS) mushrooms, which exhibit a wider bandgap than stacked conventional mushrooms [3]. This wide bandgap is essential for the design of CLAF waveguides and slot arrays, as it mitigates the stopband shifts arising from fabrication tolerances associated with standard PCB manufacturing. Here, we apply this concept to practical CLAF waveguide components across the automotive radar band of 76–81 GHz, including fabrication and measurement.

II. Unit-Cell Bloch Analysis Results

For CLAF waveguides employing conventional mushrooms, design flexibility in the waveguide height is limited due to the frequency-scaling of their bandgap properties. Consequently, increasing the height requires vertical stacking of EBG cells; however, conventional mushrooms suffer a reduction in stopband bandwidth when stacked [4].

The dispersion analysis presented here is taken from our prior work [3] and is included for completeness to illustrate the wide bandgap that motivates the CLAF waveguide designs discussed later. Using the multimodal transfer matrix method [5], the complex wavenumber $k = \beta - \mathrm{j}\alpha$ (β is the phase constant and α is the attenuation constant) is calculated for the two unit cells shown in Fig. 1a. The normalised phase and attenuation constants for the two unit cells are presented in Figs. 1b and 1c, respectively, with the former compared against commercial CST Eigenmode Solver (ES) [6] results, showing good agreement. The mirror-stacked GS mushroom exhibits a wider bandgap than the conventional stacked mushroom, as indicated by the shaded regions in Fig. 1b.

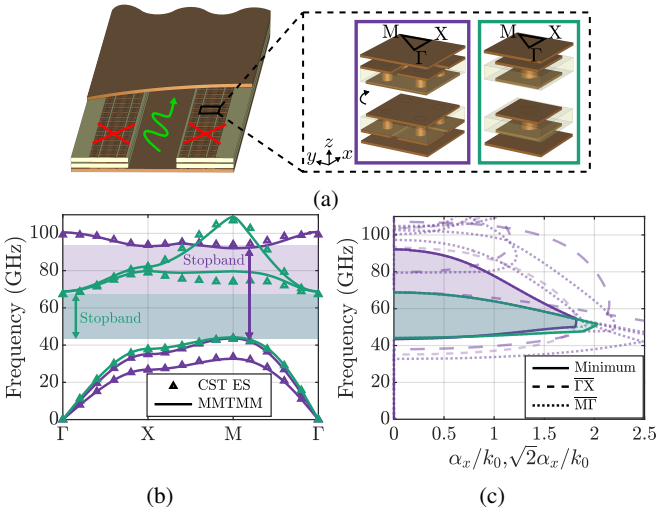

Fig. 1: (a) Stacked PCB CLAF waveguide showing propagation in air using unit cells of mirror-stacked GS mushroom and conventional mushroom structures. (b) Normalised phase constant in the irreducible Brillouin zone, and (c) normalised attenuation constant for the two unit cells.

III. Prototypes, Measurement and Results

Building on the dispersion characteristics from our previous study, prototypes of CLAF waveguide components were designed, fabricated and characterised at 76-81 GHz. As an illustrative example, the S-parameters of a double-bend CLAF waveguide with a electrical an length of 10λ at 78 GHz, simulated using Empire XPU [7], are presented in Fig. 2. The simulated results show good reflection and transmission performance, with stable behaviour across the 76–81 GHz band.

Measurement results for various components, including straight sections, bends, power dividers, slot-coupled multi-level lines, and slot arrays based on CLAF waveguides utilizing mirror-stacked GS mushrooms, will be presented at the conference. These measurements demonstrate low-loss propagation, confirm the wide stopband predicted by the prior dispersion analysis and highlight the practical feasibility of the proposed approach for mmWave automotive radar systems at 77 GHz.

IV. Conclusion

We demonstrate the advantage of using GS mushrooms for low-loss, cost-effective CLAF waveguide components with stacked PCB technology for 76–81 GHz automotive radars. The mirror-stacked configuration provides a wide, fabrication-tolerant bandgap, enabling robust design of straight and bent waveguides, power dividers, slot-coupled multi-level lines, and slot arrays. Measurement results for these prototypes, which will be presented at the conference, confirm the low-loss performance and practical feasibility of the proposed approach for mmWave automotive radar components.

Acknowledgments

This publication is based upon work supported by the Horizon Europe Research and Innovation Program and UKRI under the GENIUS Project, Marie Skłodowska-Curie Grant under Agreement 101072560.

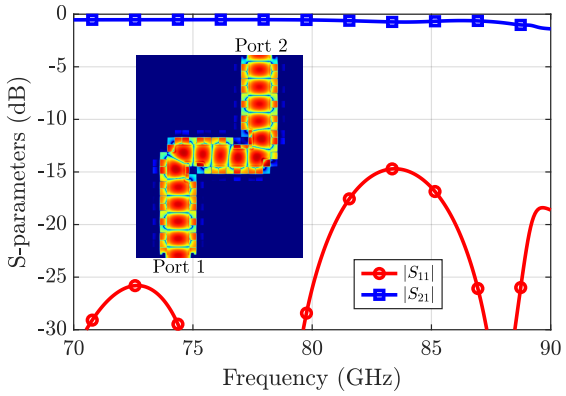

Fig. 2: Simulated S-parameters of a double-bend CLAF waveguide. The inset shows the electric-field distribution at 78 GHz, illustrating transmission from Port 1 to Port 2.

References

[1] P.-S. Kildal, E. Alfonso, A. Valero-Nogueira, and E. Rajo-Iglesias, "Local metamaterial-based waveguides in gaps between parallel metal plates," *IEEE Antennas and Wireless Propagation Letters*, vol. 8, pp. 84–87, 2009.

[2] N. Bayat-Makou and A. A. Kishk, "Contactless air-filled substrate integrated waveguide," *IEEE Transactions on Microwave Theory and Techniques*, vol. 66, no. 6, pp. 2928–2935, 2018.

[3] A. Ugle, M. Casaletti, M. A. Campo, S. Bruni, and G. Valerio, "Stacked multi-via mushroom-type EBG structures with glide symmetry," in *2025 19th European Conference on Antennas and Propagation (EuCAP)*, pp. 1–5, 2025.

[4] X.-F. Zhao, J.-Y. Deng, J.-Y. Yin, D. Sun, L.-X. Guo, X.-H. Ma, and Y. Hao, "Novel suspended-line gap waveguide packaged with stacked-mushroom EBG structures," *IEEE Transactions on Microwave Theory and Techniques*, vol. 69, no. 5, pp. 2447–2457, 2021.

[5] F. Mesa, G. Valerio, R. Rodríguez-Berral, and O. Quevedo-Teruel, "Simulation-assisted efficient computation of the dispersion diagram of periodic structures: A comprehensive overview with applications to filters, leaky-wave antennas and metasurfaces," *IEEE Antennas and Propagation Magazine*, vol. 63, no. 5, pp. 33–45, 2021.

[6] "CST Studio Suite 3D Electromagnetic Analysis Software Package." https://www.3ds.com/products/simulia/cst-studio-suite.

[7] "Empire XPU: Extremely fast 3D simulator for electromagnetic fields." https://empire.de/.

Magnetically Tunable Graphene Plasmonic Emission for THz Amplification

Michela Longhi[1,*], Davide Mencarelli[2], Alessandro Toscano[3], Luca Pierantoni[2]

[1]Niccolò Cusano University, Rome, 00166, Italy
[2]Marche Polytechnic University, Ancona, 60131, Italy
[3]Roma Tre University, Rome, 00144, Italy
[*]Corresponding author: michela.longhi@unicusano.it

***Abstract*—Graphene monolayers confined between metallic electrodes enable low-THz amplification via the quantum Čerenkov effect, yielding plasmonic emission rates up to an order of magnitude higher. Introducing a transverse static magnetic field induces Landau quantization and magnetoplasmons, allowing directional, nonreciprocal, and frequency-tunable emission through resonant inter-Landau transitions.**

***Keywords*— Graphene, Čerenkov Effect, THz Amplification.**

I. Introduction

Quantum Čerenkov emission in confined graphene is used as a mechanism to generate and control THz plasmons in engineered electromagnetic structures [1]. Metallic confinement enhances emission and tailors dispersion, while electrostatic bias tunes surface impedance. A transverse magnetic field induces magnetoplasmons, enabling directional, broadband, and nonreciprocal radiation [2]. So, the system behaves as a tunable THz amplificator linking graphene emitters to next-generation antennas and wave-control devices.

II. Quantum Čerenkov Emission

In confined graphene, high-velocity Dirac carriers strongly couple to confined plasmons, whose dispersion is shaped by metallic boundaries. Moving carriers emit plasmons via the quantum Čerenkov effect since their velocity exceeds the plasmon phase velocity. A transverse magnetic field converts these modes into chiral magnetoplasmons with phase velocities $v_p^{\pm}$, lifting degeneracy and splitting the emission into two magnetically controlled angular branches. This magnetic bias introduces an additional degree of freedom for steering the radiation process, linking carrier dynamics to macroscopic angular redistribution of the emitted energy and allowing the emission direction and symmetry properties to be tuned through the external field. Including quantum energy corrections, the generalized Čerenkov condition becomes:

$$\cos\theta_C^{\pm} = \frac{v_p^{\pm}}{v_F}\left[1 - \frac{\hbar\omega}{2E_i}\left(1 - \left(\frac{v_F}{v_p^{\pm}}\right)^2\right)\right], \qquad (1)$$

showing that the radiation direction depends on the magnetically tunable phase velocities $v_p^{\pm}(B)$. The magnetic field therefore enables beam steering through control of magnetoplasmon dispersion and the symmetry breaking between chiral modes.

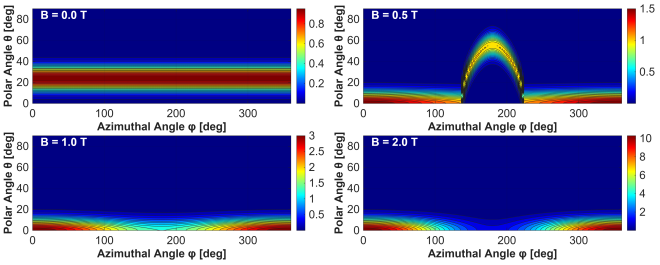

Fig. 1. Angular radiation intensity at $f = 1$ THz versus θ and φ for increasing transverse magnetic field.

Fig. 1 visualizes this effect: without magnetic bias, radiation is nearly azimuthally symmetric around the nominal Čerenkov angle, while increasing magnetic field produces angular modulation and highly directional lobes. The patterns reflect magnetoplasmon dispersion and chiral symmetry breaking, showing that the magnetic field enables beam steering.

III. Conclusion

Beyond the specific physical mechanism, the combined electrical and magnetic control introduces a new approach to actively manipulate surface-wave radiation at THz frequencies. This approach enables compact platforms capable of integrated beam shaping, wavefront control, and polarization engineering, addressing key challenges in scalable THz systems for advanced wireless communication and power transfer.

Acknowledgments

This work has been supported by the European Union - Next Generation EU under the Italian National Recovery and Resilience Plan (NRRP), Mission 4, Component 2, Investment 1.3, CUP B53C22003970001, partnership on "Telecommunications of the Future" (PE00000001 - program "RESTART").

References

[1] L. A. Samoska, "An overview of solid-state integrated circuit amplifiers in the submillimeter-wave and thz regime," *IEEE Transactions on Terahertz Science and Technology*, vol. 1, no. 1, pp. 9–24, 2011.

[2] L. Pierantoni, T. Rozzi, D. Mencarelli, G. M. Zampa, A. Toscano, and M. Longhi, "Graphene plasmonic emission by quantum Čerenkov effect in confined structures: Magnetic field control and tunability," 2024, sSRN Preprint. [Online]. Available: https://doi.org/10.2139/ssrn.6139861

Advanced Near-Field Beam Synthesis via Spatially Distributed Ray-Caustics

Federica Anfuso[1,*], Ahsan Ullah Khan[1], Gino Sorbello[1], and Santi C. Pavone[1]

[1] Department of Electrical, Electronics, and Computer Engineering,
University of Catania, Via S. Sofia 64, 95123 Catania, Italy
*Corresponding author: federica.anfuso@phd.unict.it

***Abstract*—This work presents a method based on spatially distributed ray-caustics for synthesizing curved and focused electromagnetic beams in the near field. By defining the beam trajectory through a target caustic curve, the method enables precise control of field distribution. Simulations demonstrate accurate beam shaping along the prescribed trajectories.**

***Keywords*— Caustics, Curved Beams, Focused Beams, Geometrical Optics, Near-field beam synthesis, NLOS.**

I. Introduction

The synthesis of electromagnetic beams along curved and focused trajectories in the near field is challenging due to complex wave interactions and propagation constraints. Analytical non-diffracting solutions, such as Bessel and Airy beams, have been widely investigated for structured wave propagation. While these beams exhibit remarkable self-healing and diffraction-resistant properties, their practical applicability is constrained by limited trajectory flexibility, as they naturally follow straight or parabolic trajectories [1]–[8].

The distributed ray-caustic (DRC) method [9] overcomes these limitations by exploiting caustics. In geometrical optics [10]–[12], a caustic can be defined as the envelope of tangents to rays radiated by some source distribution. By properly designing the phase distribution on a radiating aperture, the DRC method enables beams to follow prescribed trajectories while preserving field localization and focus. Within this approach, the synthesized field naturally follows the designed path, even in the presence of obstacles and non-line-of-sight conditions.

II. Outline of the Proposed Method

The proposed method enables the synthesis of near-field electromagnetic beams along arbitrarily curved trajectories by leveraging the DRC approach [9]. The target beam path is defined through a continuous and differentiable caustic curve in the near field. A ray-retrieval procedure determines the local ray tilt angles along the caustic, from which the spatial phase profile on the radiating aperture is derived. This phase distribution governs the field synthesis, producing beams that closely follow the prescribed caustic trajectory.

The method is illustrated through a set of numerical examples that aim to clarify the synthesis procedure. These cases are validated through full-wave simulations in COMSOL Multiphysics, where the robustness of the synthesized beams is assessed by introducing obstacles along the intended propagation path, demonstrating robust field distributions under scattering and non-line-of-sight conditions.

Practical implementation aspects are further investigated in CST Microwave Studio using a slotted parallel-plate waveguide. In this framework, a physics-based optimization algorithm is used to adjust the slit configurations to reproduce the target caustic [13]. These results confirm the effectiveness of the proposed approach for accurately synthesizing near-field beams along prescribed curved trajectories.

Acknowledgments

The work was partially supported by the EU under the NRRP of NextGenerationEU, partnership on “Telecommunications of the Future” (program RESTART). Santi C. Pavone would like to thank also the project PIA.CE.RI. “ROSALIND”, granted by the University of Catania.

References

[1] J. Durnin, “Exact solutions for nondiffracting beams. I. The scalar theory,” *JOSA A*, vol. 4, no. 4, pp. 651–654, 1987.
[2] J. Durnin, J. Miceli Jr, and J. Eberly, “Diffraction-free beams,” *Phys. Rev. Lett.*, vol. 58, no. 15, p. 1499, 1987.
[3] M. Lapointe, “Review of non-diffracting Bessel beam experiments,” *Optics & Laser Tech.*, vol. 24, no. 6, pp. 315–321, 1992.
[4] H. E. Hernández-Figueroa, M. Zamboni-Rached, and E. Recami, *Localized waves*. John Wiley & Sons, 2008, vol. 194.
[5] ——, *Non-diffracting waves*. John Wiley & Sons, 2013.
[6] S. C. Pavone, M. Casaletti, and M. Albani, “Automatic design of a CP fan-beam linear slotted array in SIW technology,” *IEEE Access*, vol. 7, pp. 155 977–155 985, 2019.
[7] Y. Kaganovsky and E. Heyman, “Wave analysis of Airy beams,” *Opt. Express*, vol. 18, no. 8, pp. 8440–8452, Apr 2010.
[8] ——, “Airy pulsed beams,” *J. Opt. Soc. Am. A*, vol. 28, no. 6, pp. 1243–1255, Jun 2011.
[9] F. Anfuso, A. U. Khan, G. Sorbello, and S. C. Pavone, “On the Radiation of Curved Beams in the Near-Field by Distributed Caustics for NLOS Applications,” *IEEE Open Journ. Antennas Propag.*, Early Access, 2025.
[10] M. Born and E. Wolf, *Principles of optics: electromagnetic theory of propagation, interference and diffraction of light*. Elsevier, 2013.
[11] L. Zhu, A. Wang, and J. Wang, “Free-space data-carrying bendable light communications,” *Sci. Rep.*, vol. 9, no. 1, p. 14969, 2019.
[12] X. Zhou, H. Wang, S. Liu, H. Wang, J. Y. E. Chan, C.-F. Pan, D. Zhao, J. K. Yang, and C.-W. Qiu, “Arbitrary engineering of spatial caustics with 3d-printed metasurfaces,” *Nature Comm.*, vol. 15, no. 1, p. 3719, 2024.
[13] D. Guarnera, S. C. Pavone, A. Morabito, L. D. Donato, T. Isernia, and G. Sorbello, “A two-steps optimal full-wave design of slotted arrays for arbitrarily constrained pencil beams,” *IEEE Antennas Wireless Propag. Lett.*, vol. 24, no. 9, pp. 2999–3003, 2025.

Interpolation of Periodic Method-of-Moments Impedance Matrices with a Physically Motivated Regularisation

Martin Petek[1,*], Denis Tihon[2], Jorge A. T. Vásquez[1], Cristophe Craeye[2], Francesca Vipiana[1]

[1]Dept. of Electronics and Telecommunications, Politecnico di Torino, 10129, Torino, Italy
[2]ICTEAM Institute, Université catholique de Louvain (UCLouvain), Louvain-la-Neuve, Belgium
*Corresponding author: martin.petek@polito.it

***Abstract*—This work presents preliminary efforts for development of a combined frequency and wave vector interpolation approach for periodic method of moments problems. The interpolation method extracts the difficult-to-interpolate term, interpolates the remainder, and re-adds the extracted terms. We demonstrate the applicability of the approach to frequency interpolation.**

***Keywords*— Method of Moments (MoM), periodic structures, frequency interpolation, metamaterials.**

I. Introduction

Many different applications can be found for periodic structures in electromagnetics, for example arrays, metamaterials, and electromagnetic bandgap structures. Such structures are characterized by a repetition of a single element, the unit cell. In practice, many properties of finite (truncated) periodic structure may be understood from an idealized model which assumes an infinite repetition of the unit cell.

To analyse such structures, various modelling techniques have been developed. For example, in time domain with finite differences [1] to, or in frequency domain with finite elements [2] and the Method of Moments (MoM) [3]. With the latter, the periodic nature and possible symmetries of the structure can be efficiently captured in the periodic Green's function [4].

In this work, we provide results of our preliminary efforts to accelerate the computation of impedance matrices, found in MoM problems. Previously, various interpolation approaches have been introduced to improve the speed of evaluation of periodic MoM problems [5], [6], [7]. Our work is based on a recent work [8], which extracts the first few spectral terms of the impedance matrix, interpolates the remainder and then re-adds the extracted terms. However, the method in [8] is limited to planar geometries. We build on our findings regarding accurate evaluation of spectral MoM terms in [9] to generalize the approach to three-dimensional structures and demonstrate the applicability of the method for interpolation in frequency.

II. Interpolation approach and results

An element of the periodic MoM impedance matrix, Z, may be computed in either spatial form, as in [3], or in spectral form as a double infinite sum

$$Z(f) = \sum_{p=-\infty}^{\infty} \sum_{q=-\infty}^{\infty} Z_{pq} \,, \tag{1}$$

where f is the frequency and the Z_{pq} is given in [9].

Here, we combine the two approaches to devise an efficient interpolation scheme. First, we compute a few samples of Z with a full method. Then, we regularize their behaviour by subtracting first few terms from (1), which contain the difficult-to-interpolate terms [8]:

$$Z_{\mathrm{reg}}(f) = Z(f) - \sum_{p=-P}^{P} \sum_{q=-Q}^{Q} Z_{pq} \,, \tag{2}$$

which removes the aforementioned discontinuities. Then, we further extract the average phase behaviour and remove the $1/f$ dependence

$$Z_{\mathrm{reg},2}(f) = Z_{\mathrm{reg}}(f) \frac{f}{\exp\left(-\mathrm{j}\mathbf{k}_{\mathrm{t}} \cdot (\mathbf{r}_{\mathrm{bt}} - \mathbf{r}_{\mathrm{bs}})\right)} \,, \tag{3}$$

where $\mathbf{k}_{\mathrm{t}}$ is the transverse phasing wave vector and $\mathbf{r}_{\mathrm{bt/bs}}$ are the barycenters of the test/source basis functions. Then, a polynomial model of $Z_{\mathrm{reg},2}(f)$ is obtained, after which we may obtain a finer sampling by readding the extracted terms with (2).

The results of the approach for the interaction between the two coloured basis is presented in Fig. 1 for $\mathbf{k}_{\mathrm{t}} = \{2\pi/(3a), \pi/(3a)\}$ and the geometry in [3] with the period $a = 3.2$ mm. We additionally compare the proposed approach with a "direct" interpolation, where (2) is omitted and only phase and $1/f$ is extracted [as in (3)]. Note that the proposed interpolation performs well, obtaining 3 or more significant digits over the entire frequency range from 5 to 50 GHz using only three sample points, extracting 9 terms of the spectral series ($P = Q = 1$), and a second-order polynomial for interpolation of $Z_{\mathrm{reg},2}$. Conversely, the direct interpolation of the same order fails to achieve a good result, and is especially inaccurate in the vicinity of the discontinuity (marked with D in the horizontal axis). Hence, the proposed interpolation approach shows great promise for a fast evaluation of periodic MoM problems.

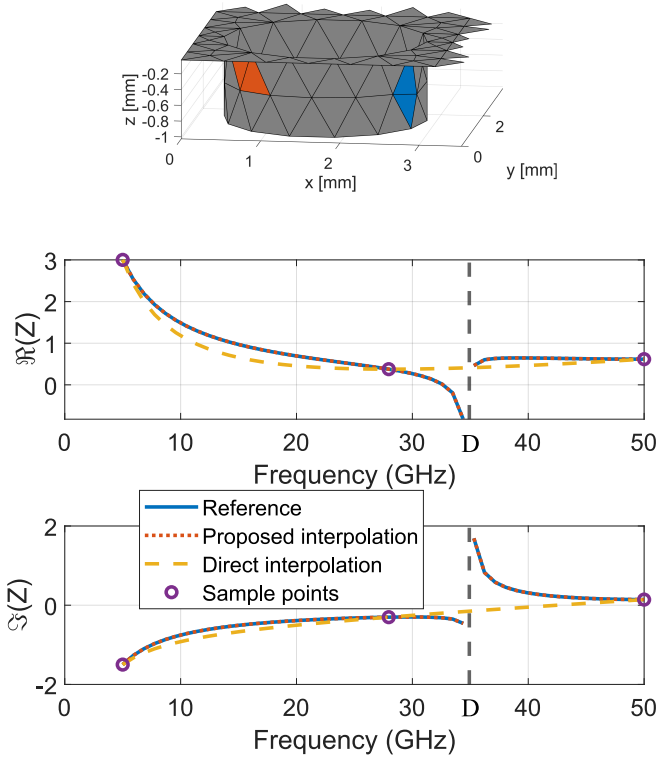

Fig. 1. Results of the interpolation approach for the case of vertically overlapping coloured basis functions (top) for both real and imaginary component of Z (bottom).

III. Conclusion

In this work, we presented our initial experiments to generalize the method proposed in [8] to fully three-dimensional geometries. We demonstrate the applicability to the method for frequency interpolation. Future work consists of developing joint frequency-wave vector interpolation and implementing the method in an efficient way.

Acknowledgments

This work is supported in part by the Horizon Europe Research and Innovation Program under the GENIUS project (GA101072560), and in part by Interreg Central Europe under the MedWaveImage project (CE0200670). It is also partially supported by a 2025 EurAAP ECAP-TICRA Grant and a 2025 IEEE APS Fellowship.

References

[1] A. J. Kogon and C. D. Sarris, "Finite-Difference Time-Domain Modeling of Periodic Structures: A review of constant wave vector techniques," *IEEE Antennas and Propagation Magazine*, vol. 64, no. 3, pp. 59–70, 2022.

[2] J.-M. Jin, *The finite element method in electromagnetics*. John Wiley & Sons, 2015.

[3] M. Petek, J. Rivero, J. A. T. Vásquez, G. Valerio, O. Quevedo-Teruel, and F. Vipiana, "Method of Moments for the Dispersion Modeling of Glide-Symmetric Periodic Structures," *IEEE Trans. Antennas Propag.*, vol. 72, no. 1, pp. 756–766, 2024.

[4] F. T. Celepcikay, D. R. Wilton, D. R. Jackson, and F. Capolino, "Choosing splitting parameters and summation limits in the numerical evaluation of 1-D and 2-D periodic Green's functions using the Ewald method," *Radio Science*, vol. 43, no. 06, pp. 1–11, 2008.

[5] A. Barlevy and Y. Rahmat-Samii, "Characterization of electromagnetic band-gaps composed of multiple periodic tripods with interconnecting vias: concept, analysis, and design," *IEEE Trans. Antennas Propag.*, vol. 49, no. 3, pp. 343–353, 2001.

[6] L. Li, D. Werner, J. Bossard, and T. Mayer, "A model-based parameter estimation technique for wide-band interpolation of periodic moment method impedance matrices with application to genetic algorithm optimization of frequency selective surfaces," *IEEE Trans. Antennas Propag.*, vol. 54, no. 3, pp. 908–924, 2006.

[7] Z. Wang and S. V. Hum, "A Broadband Model-Based Parameter Estimation Method for Analyzing Multilayer Periodic Structures," *IEEE Trans. Antennas Propag.*, vol. 69, no. 9, pp. 5771–5780, 2021.

[8] D. Tihon, S. N. Jha, M. Bodehou, and C. Craeye, "Efficient Tracking of Dispersion Surfaces for Printed Structures Using the Method of Moments," *IEEE Trans. Antennas Propag.*, vol. 72, no. 1, pp. 61–74, 2024.

[9] M. Petek, D. Tihon, J. A. T. Vásquez, C. Craeye, and F. Vipiana, "A Numerical Verification of Analytical Solution for the Mixed Fourier Transform Equation," in *2025 19th European Conference on Antennas and Propagation (EuCAP)*, 2025, pp. 1–5.

Generalized Rigorous Coupled Wave Analysis for Higher-Symmetric Dielectric Media

Dubravko Tomić* and Zvonimir Šipuš

University of Zagreb Faculty of Electrical Engineering and Computing, Unska 3, 10000 Zagreb, Croatia
*Corresponding author: dubravko.tomic@fer.unizg.hr

***Abstract*—This research extends Rigorous Coupled Wave Analysis to incorporate glide symmetry in multilayer periodic structures. Symmetry-specific matrices reduce computational complexity and enable semi-analytical calculation of dispersion diagrams. The method facilitates the optimization of leaky-wave antennas and microwave sensors by engineering unique electromagnetic responses through structural symmetry manipulation.**

***Keywords*— Rigorous Coupled Wave Analysis, glide symmetry, periodic structures, leaky-wave antennas.**

I. Summary

Current progress in wireless communication and sensor technologies is linked to the use of periodic electromagnetic media, often categorized as metamaterials, which provide unique capabilities to engineer the wave propagation. The performance of these systems is typically determined by the arrangement and geometric modification of unit cells. With the emergence of additive manufacturing, it has become possible to realize sophisticated dielectric topologies that were once considered practically impossible to manufacture. Using higher symmetries, most notably glide symmetry, it is possible to achieve interesting dispersion properties, such as the elimination of traditional stopbands and more stable dispersion profiles. Although conventional full-wave numerical solvers are robust, they often function as "black boxes" that obscure the underlying physics of mode coupling and radiation phenomena. Consequently, there is a need for computationally efficient analytical frameworks capable of evaluating complex permittivity distributions to facilitate the development of next-generation devices such as leaky-wave antennas.

We propose an extension to the Rigorous Coupled Wave Analysis (RCWA) framework [1], [2] with the aim of including higher symmetries, specifically, glide-symmetry. This frequency domain semi-analytical technique represents electromagnetic fields as a superposition of spatial harmonics, or Bloch-Floquet modes, within each periodic layer. By matching the tangential field components at the boundaries between stacked regions, the algorithm relates the wave amplitudes to extract the fundamental guiding and leakage properties of the unit cell. The core of the proposed extension lies in the direct integration of glide-shift between the layers into the mathematical formulation. Rather than treating shifted layers as independent entities, the physical displacement is characterized by a symmetry-specific constant matrix that maps the fields of a reference layer to its shifted counterpart. This mathematical "shortcut" reduces the computational complexity, and the dispersion characteristics can be calculated by analyzing only a portion of the unit cell, with the matrix accounting for the remaining symmetric features. Furthermore, this approach yields a versatile dispersion equation that remains valid for both ideal glide symmetric configurations [3], [4] and more complex states where symmetry is intentionally broken [4], [5], [6], [7], [8].

Systems based on two dielectric layers provide a mechanism for controlling the propagation constant β_x and the leakage rate α_x, i.e., they can be used to construct leaky wave antennas. The application of the extended RCWA method has enabled the design of dielectric LWAs with more complex unit cells. By precisely calculating dispersion diagrams through the proposed RCWA formulation, it is possible to analyze and design dielectric diffraction grating that incorporate glide-shifted layers suitable for LWAs. The reason for including the glide-shift is to have additional degrees of freedom in the design, without having to use two different dielectric materials, thus simplifying the manufacturing process. By changing the ratio of the two identical glide-shifted periodic dielectric layers, the leakage rate α_x of the grating can be modified without affecting the propagation constant β_x, thus providing a mechanism to tailor the illumination of the aperture of the LWAs [6]. On the other hand, by misaligning the two layers so that they are neither mirror-symmetric nor glide-symmetric, it is possible to change the propagation constant β_x, thus changing the direction of the main beam of the LWAs. Such asymmetric shifts also make it possible to radiate through the broadside, overcoming a common challenge in periodic LWA designs, where reflections typically degrade performance at the broadside frequency [7].

Beyond antenna applications, the developed framework is utilized for the dielectric characterization of materials at microwave frequencies [5]. The sensing setup exploits glide-symmetry and the fact that glide-symmetry closes the first stopband. Breaking the symmetry by the presence of a different dielectric slab on one side of the structure opens a stopband in the dispersion characteristic. RCWA allows for rapid inverse extraction of material parameters from stopband frequencies determined from S_{11} measurements, making these structures ideal for industrial and laboratory sensing applications.

Lastly, a certain algebraical similarity exists between proper and broken glide-symmetric structures. Using the Frobenius

norm to quantify the mathematical similarity between certain elements of the final dispersion equation, it was demonstrated that specific parameter choices allow broken-symmetric structures to achieve ”glide-like” propagation properties [8].

ACKNOWLEDGMENTS

This work was supported by the Croatian Science Foundation under the project number HRZZ-IP-2022-10-3029.

REFERENCES

[1] M. G. Moharam and T. K. Gaylord, “Rigorous coupled-wave analysis of planar-grating diffraction,” *J. Opt. Soc. Am.*, vol. 71, no. 7, pp. 811–818, Jul 1981.

[2] S. T. Peng, “Rigorous formulation of scattering and guidance by dielectric grating waveguides: general case of oblique incidence,” *J. Opt. Soc. Am. A*, vol. 6, no. 12, pp. 1869–1883, Dec 1989.

[3] D. Tomić and Z. Šipuš, “Rigorous coupled wave analysis of parallel-plate waveguides loaded with glide-symmetric dielectric structures,” *IEEE Transactions on Microwave Theory and Techniques*, vol. 72, no. 8, pp. 4542–4554, 2024.

[4] D. Tomić, F. Mesa, and Z. Šipuš, “Modeling of open dielectric structures with glide and broken mirror symmetries,” in *2025 19th European Conference on Antennas and Propagation (EuCAP)*, 2025, pp. 1–5.

[5] D. Tomić and Z. Šipuš, “Symmetry breaking as a basis for characterization of dielectric materials,” *Sensors*, vol. 25, no. 2, 2025.

[6] D. Tomić, F. Mesa, and Z. Šipuš, “Glide-shifted dielectric gratings for independent leakage and phase tuning in leaky-wave antennas,” *IEEE Open Journal of Antennas and Propagation*, vol. 6, no. 5, pp. 1471–1481, 2025.

[7] D. Tomić and Z. Šipuš, “Rigorous coupled wave analysis: Paving the way for innovative leaky-wave antennas,” in *2026 20th European Conference on Antennas and Propagation (EuCAP)*, 2025, pp. 1–5.

[8] ——, “Achieving glide-like dispersion properties in broken-glide symmetric structures,” in *2025 Nineteenth International Congress on Artificial Materials for Novel Wave Phenomena (Metamaterials)*, 2025, pp. X–333–X–335.

Analysis of polarization purity in dual-polarized phased array antennas

Pilar Castillo-Tapia[1,*], Gabriele Federico[1], Bart Smolders[1]

[1]Department of Electrical Engineering, Eindhoven University of Technology, The Netherlands
*Corresponding author: p.castillo.tapia@tue.nl

***Abstract*—In weather radars, phased array antennas are required to maintain high polarization purity over wide scanning angles to provide information about constitution of water drops. Here, we analyze the cross-polarization level of a patch antenna embedded in an infinite array at different scanning angles and in two different lattice configurations.**

***Keywords*— patch antenna, phased array antenna, polarization purity, weather radar.**

I. Introduction

Weather radars aim to study cloud formation and distinguish among rain drops, snow and/or ice. To achieve this, phased array antennas must support dual polarization with very high polarization purity. Two main strategies have been proposed to reduce cross-pol levels at the antenna-element level: sequential rotation [1], [2] and differential feeding [3]. However, most analyses of antenna cross-pol levels are based on broadside radiation, and limited information is available for other scanning angles, especially in the diagonal plane. In this work, we analyze the cross-pol levels of different antenna elements in under various scanning conditions.

II. Analysis of polarization purity in phased array antennas

A dual-polarized circular patch antenna working in the band of 15.4-15.7 GHz is used in this study. A model of the antenna is shown in Fig. 1a. Full-wave simulations are performed in CST using periodic boundary conditions to account for mutual coupling between elements. In Fig. 1b we compare the cross-pol levels when the antenna is set in a square and triangular lattice for four different scan angles, namely $\theta_0 = 0°, \phi_0 = 0°$ (broad side), $\theta_0 = 45°, \phi_0 = 0°$ (horizontal plane), $\theta_0 = 45°, \phi_0 = 90°$ (vertical plane) and $\theta_0 = 45°, \phi_0 = 45°$ (diagonal plane). For broadside radiation, the antenna exhibits cross-pol levels below -38 dB across the frequency band for both configurations. When a square lattice is employed the cross-pol level increases to -26.2 dB in the horizontal plane, ranges between -18 and -23 dB in the vertical plane, and lies between -21 and -24 dB in the diagonal plane. In contrast, in the triangular lattice configuration, the cross-pol level in the horizontal (vertical) plane is reduced to -28.4 dB, and the vertical (horizontal) plane goes from -26 to -20 dB for the x (y) polarization. Finally, in the diagonal plane, both polarizations have cross-pol levels between -29 and -25 dB.

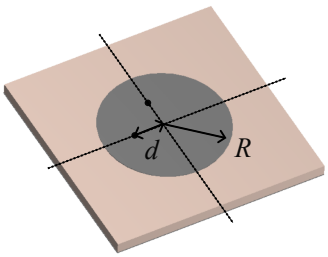

(a)

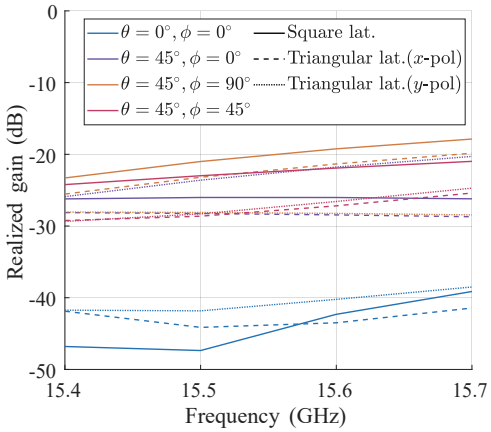

(b)

Fig. 1: (a) Circularly-polarized patch antenna. (b) Cross-pol levels for different lattices and scanning angles. The antenna parameters are $R = 2.785$ mm, $d = 0.9$ mm, with substrate RO4003C of thickness 0.51 mm.

Acknowledgments

This document is a result of the PHARA project, which is funded by the Dutch Research Council within the research program Research Infrastructure (RI): national consortia.

References

[1] K. Woelders and J. Granholm, "Cross-polarization and sidelobe suppression in dual linear polarization antenna arrays," *IEEE Trans. Antennas Propag.*, vol. 45, no. 12, pp. 1727–1740, Dec. 1997.

[2] H. Saeidi-Manesh and G. a. Zhang, "Challenges and limitations of the cross-polarization suppression in dual-polarization antenna arrays using identical subarrays," *IEEE Transactions on Antennas and Propagation*, vol. 68, no. 4, pp. 2853–2866, 2020.

[3] M. Mirmozafari, G. Zhang, C. Fulton, and R. J. Doviak, "Dual-polarization antennas with high isolation and polarization purity: A review and comparison of cross-coupling mechanisms," *IEEE Antennas Propag. Mag.*, vol. 61, no. 1, pp. 50–63, 2019.

Advanced antenna designs for Joint Communication and Sensing, Localization and Radiative Wireless Power Transfer

AES 2026 · Catania, Italy · ISSN 2491-2417

Monopulse-Based Blind-Spot Correction using a Full-Azimuthal Leaky-Wave Antenna Array

Alejandro Gil-Martínez*, Jesús Perez-Valero[1], Julien Sarrazin[2], Guido Valerio[2], Antonio Skarmeta[1]

[1]Departmento de Ingeniería de la Información y las Comunicaciones, Universidad de Murcia, 30100, Murcia, Spain.

[2]CNRS Laboratoire de Gènie Electrique et Electronique de Paris, Sorbonne University, 75252, Paris, France.

*Corresponding author: alejandrorafael.gil@um.es

***Abstract*— This paper presents a theoretical full-azimuthal angle estimation algorithm for ISAC systems based on a triangular array of bi-directional leaky-wave antennas. The impact of angular blind spots on amplitude-monopulse estimation is analyzed, and a lightweight deep-learning correction is introduced to improve angular robustness without increasing system complexity.**

***Keywords*— Localization, Leaky-Wave Antennas, Integrated Sensing and Communication, Deep-Learning.**

I. Introduction

Integrated sensing and communication (ISAC) has emerged as a key paradigm for future wireless systems by combining localization and communication functionalities within a unified framework, where accurate direction finding is essential for reliable positioning and beamforming [1]. In this context, leaky-wave antennas (LWAs) offer compact implementations and inherent beam-scanning capabilities, enabling wide angular coverage with reduced hardware complexity [2]. However, single-element and multi-element LWA-based configurations often exhibit limited or non-uniform azimuthal responses, especially in full-azimuth architectures, leading to angular blind spots where directive radiation is weak or absent [3]. These blind-spot regions introduce systematic degradation in classical angle estimation techniques using antenna arrays [4], such as amplitude monopulse, due to reduced signal observability. Moreover, it is not a case that can be only applied to power information algorithms, but it can be observed in phased arrays and complex amplitude and phase localization algorithms. Recent data-driven methods have shown potential to complement model-based processing by learning correction patterns associated with such systematic distortions. Motivated by this, this work provides a simplified theoretical framework that analyzes blind-spot effects in full-azimuth LWA-based ISAC systems and introduces a lightweight learning-assisted correction to improve angular robustness without increasing antenna or system complexity. A schematic of the blind spot problem can be observed in Fig. 1.

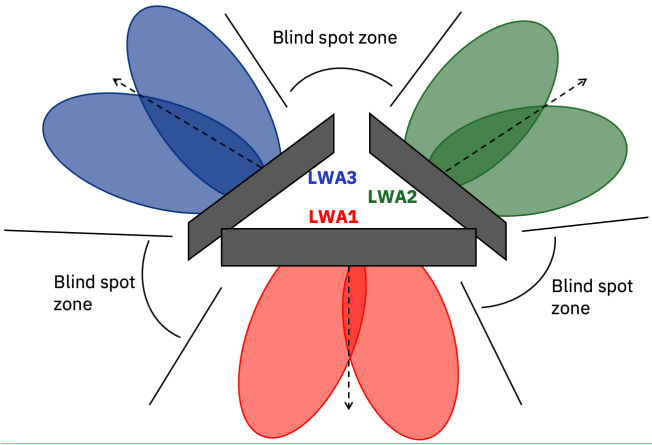

Fig. 1 Proposed leaky-wave antenna array geometry for full-azimuthal coverage.

II. Methods

The proposed full-azimuth direction-finding architecture is based on three identical bidirectional leaky-wave antennas arranged in an equilateral triangular configuration to enable 360° azimuthal coverage. Each antenna generates two directive beams when excited from opposite ports, providing wide angular coverage with a compact and low-complexity structure. By properly orienting the three elements, the array covers the full azimuth through the superposition of their radiation patterns. However, due to the finite beamwidth and non-overlapping regions between adjacent beams, certain angular sectors exhibit reduced radiation levels, referred to as angular blind spots. In these regions, the signal amplitude is significantly attenuated, which inherently limits the accuracy of classical amplitude-monopulse direction-of-arrival estimation. This work adopts a simplified theoretical radiation model of the array to analyze the impact of blind spots on angle estimation performance and to serve as a reference framework for the comparison between monopulse-based and learning-based estimation strategies.

The direction-of-arrival (DoA) estimation problem can be addressed using classical amplitude monopulse processing, which exploits the relative power differences between pairs of directive beams. Let us consider a multi-port antenna system characterized by its angular power response.

For a signal arriving from an unknown direction θ_0, the received power at the m-th port can be expressed as:

$$P_m[k] = P_s \cdot g_m(\theta_0) + w_m[k]$$

where P_s denotes the transmitted signal power, $g_m(\theta)$ is the radiation pattern associated with the m-th port, and $w_m[k]$ represents additive noise, typically modeled as a zero-mean Gaussian random variable.

By combining multiple ports, a vector observation can be defined as:

$$p[k] = P_s \cdot g(\theta_0) + w[k]$$

where $g(\theta)$ contains the angular responses of all ports.

For each pair of beams (i, j), a monopulse ratio is constructed using the sum and difference of received powers:

$$\Sigma_{ij}=P_i+P_j \; ; \; \Delta_{ij} = P_i - P_j$$

The corresponding monopulse observable is defined as:

$$MV_{ij} = (P_i - P_j) / (P_i + P_j)$$

This ratio provides an estimate of the angular deviation relative to the boresight (or symmetry axis) between the two beams.

In the vicinity of the beam crossover region, the monopulse function exhibits an approximately linear behavior:

$$MV(\theta) \approx K \cdot (\theta - \theta_ref)$$

where K is the monopulse slope and θ_ref is the reference direction (typically the midpoint between the two beams). This linearity enables a direct inversion to estimate the angle.

To improve robustness, the monopulse value is compared against its theoretical angular response. For each beam pair, a pseudospectrum is defined as:

$$APS_n(\theta) = -10 \log_{10} (1 / | MF_n(\theta) - MV_n |)$$

where $MF_n(\theta)$ denotes the theoretical monopulse function associated with the n-th beam pair.

The different pseudospectra are then combined to form a global angular response:

$$APS(\theta) = F \{ APS_1(\theta), APS_2(\theta), ..., APS_N(\theta) \}$$

where $F\{\cdot\}$ represents a fusion operator (e.g., averaging or maximum selection).

Finally, the DoA estimate is obtained as the peak with the maximum amplitude.

From a theoretical standpoint, monopulse technique provides low-complexity and physically interpretable DoA estimation. Its accuracy is maximized in regions where the radiation patterns overlap significantly and the monopulse slope remains linear. However, when the received power is weak or the beam overlap is limited, the monopulse ratio becomes highly nonlinear, leading to large estimation errors. These regions can be interpreted as low-observability zones in the angular domain, where classical estimators lose reliability.

To overcome the intrinsic nonlinearities of the antenna response and the limitations of analytical inversion, the DoA estimation problem can be reformulated as a supervised learning task.

Let $x \in \mathbb{R}^{(M\times K)}$ denote the input data matrix, containing K temporal snapshots of the received power across M antenna ports. The goal is to learn a nonlinear mapping:

$$\hat{\theta} = f(x)$$

where $f(\cdot)$ is a parametric function implemented by a neural network.

A lightweight convolutional neural network (CNN) can be employed to extract relevant features from the input data. The processing pipeline consists of:

1. A one-dimensional convolution layer applied along the snapshot dimension.
2. A nonlinear activation function (e.g., ReLU).
3. A global pooling stage to aggregate temporal information.

The convolution operation can be expressed as:

$$h = \sigma(W * x + b)$$

where W represents the convolution kernels, b is the bias term, and $\sigma(\cdot)$ denotes the nonlinear activation.

Instead of directly estimating θ, the model predicts a continuous angular embedding:

$$\hat{y} = [\hat{y}_1, \hat{y}_2] = [\sin(\hat{\theta}), \cos(\hat{\theta})]$$

This representation avoids discontinuities at the angular boundaries (±180°) and ensures smooth learning behavior.

The final DoA estimate is recovered as:

$$\hat{\theta} = \text{atan2}(\hat{y}_1, \hat{y}_2)$$

The network is trained using a mean squared error loss between predicted and true angular embeddings:

$$L = (1/N) \sum ||\hat{y}_i - y_i||^2$$

where:

$$y_i = [\sin(\theta_i), \cos(\theta_i)]$$

and N is the number of training samples.

From a theoretical viewpoint, deep learning enables the approximation of highly nonlinear mappings between electromagnetic observations and angular parameters. This is particularly advantageous in scenarios where the antenna response is irregular or where classical assumptions (e.g., linear

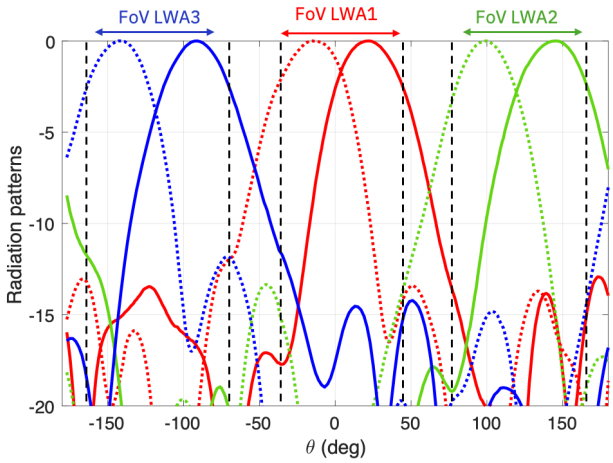

Fig. 2. Simulated normalized full azimuthal leaky wave antenna array radiation patterns. Solid line: port 1 of each individual LWA. Dotted line: port 2 o

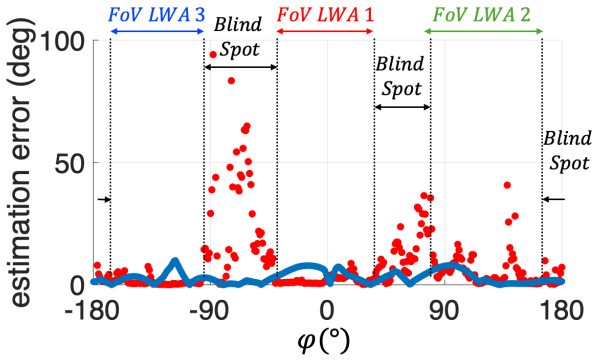

Fig. 3. Absolute angular error of the proposed algorithms over the full range. Red dots, monpulse algorithm. Blue dots, monopulse deep-learning reinforced algorithm.

monopulse behavior) do not hold.

Unlike analytical methods, the deep-learning algorithm implicitly learns the inverse mapping without requiring explicit knowledge of the radiation patterns. However, its performance depends on the representativeness of the training dataset and the generalization capability of the model.

III. Results and Discussion

The performance of the proposed direction-of-arrival estimation approaches is evaluated over the full azimuth range from −180° to 180° using simulated snapshots at a fixed signal-to-noise ratio of 10 dB. The radiation patterns of the leaky-wave antenna array are plotted in Fig. 2. The angular estimation error across the complete field of view is illustrated in Fig. 3, while the overall trends are discussed in terms of robustness and accuracy. As observed, the classical amplitude-monopulse method provides accurate angle estimates in regions where the antenna radiation exhibits sufficient directive gain. However, its performance degrades significantly in angular blind-spot sectors, where reduced signal amplitude leads to nonlinear monopulse ratios and large estimation errors.

In contrast, the deep-learning-based approach maintains a more uniform estimation accuracy across the full azimuth. By learning the underlying relationship between the received signal amplitudes and the angle of arrival, the model is able to compensate for the systematic distortions introduced by blind-spot regions, effectively reducing large angular outliers.

Overall, these results highlight the limitations of purely model-based monopulse estimation in full-azimuth LWA systems and demonstrate that even a simple data-driven approach can significantly enhance angular robustness in blind-spot regions without increasing system or antenna complexity.

IV. Conclusion

This paper has compared classical amplitude-monopulse estimation with a deep-learning-based approach for full-azimuth direction-of-arrival estimation using LWA arrays. While monopulse provides a simple and physically interpretable solution, its performance degrades in angular blind-spot regions. The learning-based method improves angular accuracy across the azimuth by compensating for systematic distortions, demonstrating its potential as a low-complexity enhancement for blind-spot mitigation in ISAC systems.

Acknowledgments

A. Gil-Martıinez, Jesús Perez-Valero and A. Skarmeta are with the Department of Information and Communication Engineering, Universidad de Murcia, 30100, Spain. Their work is supported by Grant PID2023-148104OB-C43 funded by MICIU/AEI/ 10.13039/ 501100011033 and by ERDF/EU.
Julien Sarrazin and Guido Valerio are with the Laboratoire de Genie Electrique et Electronique de Paris, CNRS, Sorbonne Universite, 75252, France. Their work is supported by the ANR BeSensiCom project, grant ANR-22-CE25-0002 of the French Agence Nationale de la Recherche.

References

[1] W. Chen et al., ”5G-Advanced Toward 6G: Past, Present, and Future,” in *IEEE Journal on Selected Areas in Communications*, vol. 41, no. 6, pp. 1592-1619, June 2023.

[2] A. Gil-Martinez et al., “Monopulse leaky wave antennas for RSSI based direction finding in wireless local area networks”, in IEEE Trans. Antennas Propag., vol. 71, no. 11, pp. 8602-8615, 2023.

[3] M. Temiz et al., “Deep-learning based techniques for integrated sensing and communication systems: state of the art, challenges and opportunities,” in *IEEE Open Journal of the Communication Society*, vol. 6, pp. 5940-5968, 2025.

[4] T. Crépin *et al.*, "Blind spot mitigation in phased array antenna using metamaterials," *2014 International Radar Conference*, Lille, France, 2014, pp. 1-4.

Phase-Based Ranging and Direction-of-Arrival Localization with a single-port Frequency-Scanned Antenna

Antonio Hernández Mateos[1,*], José A.López Pastor[2], José Luis Gómez Tornero[1]

[1]Department of Information and Communication Technologies, Technical University of Cartagena, Cartagena, Campus Muralla del Mar, 30202 Cartagena, Spain
[2]Department of Electonic, Computer Technology, and Projects, Technical University of Cartagena, Cartagena, Campus Muralla del Mar, 30202 Cartagena, Spain
*Corresponding author: adavid.hernandez@edu.upct.es

***Abstract*— A two-dimensional location system is proposed and simulated in this work thanks to the combination of a Direction of Arrival (DoA) and Phase-Based Ranging (PBR) technique implemented with a single-port frequency-dispersive leaky-wave antenna in the 2.4 GHz ISM band.**

***Keywords*— Direction of Arrival (DoA), Phase-based ranging (PBR), Leaky-Wave Antenna.**

I. Introduction

The phase-based ranging (PBR) technique has been widely employed to measure distances in several active sensing systems, such as industrial ultrasonic sensors, frequency-modulated continuous wave (FMCW) radars, and amplitude-modulated continuous wave (AMCW) LiDAR. A similar mechanism has been integrated into communication RF systems for WLAN-like WiFi and WPANs such as Bluetooth or UWB. In WiFi, the PBR is computed employing the channel state information (CSI). Regarding Bluetooth, the BLE 6.1 standard introduced the PBR. It is called Channel Sounding (CS) and measures the magnitude and phase of every channel available for this purpose, allowing ranging estimation [1,2]. Therefore, several technologies can implement the PBR mechanism natively.

However, to obtain a precise location system, the ranging procedure must be combined with a direction-finding (DF) technique, such as Direction-of-arrival (DoA). The combination of a ranging system and an DoA system allows precise two-dimensional {x,y} positioning. In every RF technology, angular determination typically requires combining multiple antennas with known separations to estimate the DoA.

In this work, we propose a precise two-dimensional location system that employs a single-port frequency-scanning antenna (FSA) based on the leaky-wave radiation principle extensively studied in planar microstrip structures [3-5]. This is possible because the direction and the amplitude of the directive beams of the FSA change with the frequency. With this amplitude and angular variations, the DoA is computed as explained later. The ranging procedure, in this case a PBR mechanism, is implemented through phase-shift changes induced also by the changing directive property of the antenna, depending on the frequencies. Fig. 1 illustrates the FSA employed; in this case, a single-port half-microstrip leaky-wave antenna (LWA) fed by Port 1 that irradiates the beam into the positive quadrant. In this antenna type, the beam points more perpendicularly when lower frequencies are employed (red beam), and it points in higher angular directions when higher frequencies are employed (blue beam).

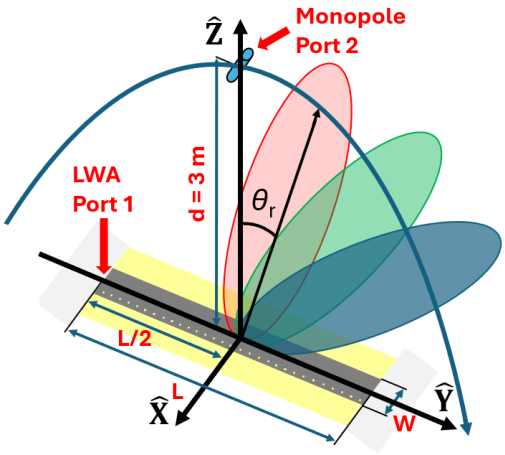

Fig. 1.Ansys HFSS simulated scenario

II. Angle of Arrival with Amplitude

The proposed approach computes the DoA using the amplitudes of an RF transmitted signal. To achieve this aim, the DoA is determined by performing a frequency-beam scan to identify the angle with the maximum gain at each frequency and measuring the power of the transmitted signal. Because the direction and amplitude of the directive beam generated by the LWA employed change with frequency, both parameters must be characterized. Therefore, the angle with the maximum transmitted power at different frequencies, as well as the S21

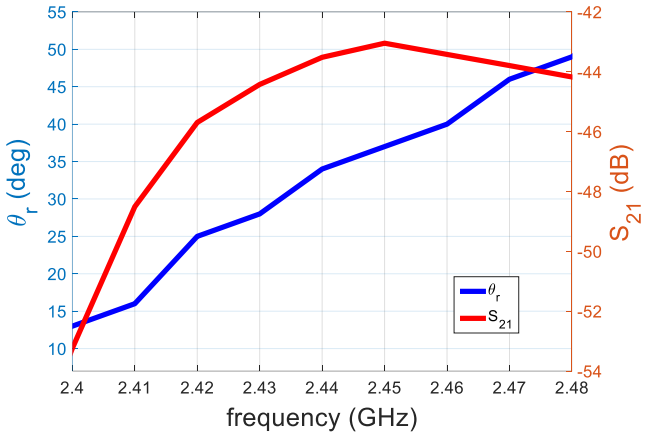

Fig. 2. Maximum value of S_{21} parameter depending on the frequency (red line) and angle where the values were measured (blue line).

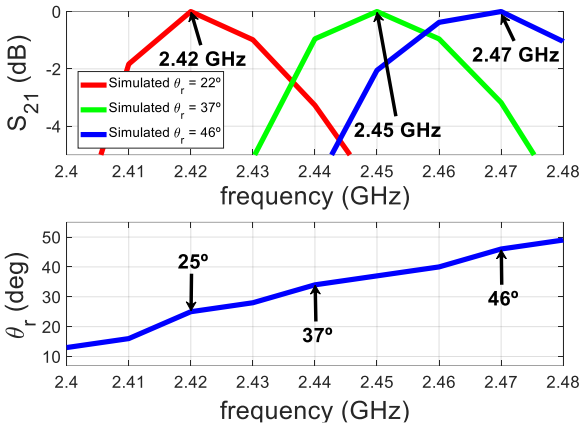

Fig. 3. Different S21 measurements and the estimated angle obtained.

parameter relative to a reference transmitter, must be characterized. Fig. 2 illustrates these two values for the proposed LWA operating in the 2.4-2.48 GHz band with a directivity from 5º to 55º and simulated in ANSYS HFSS software. The red line in Fig. 2 represents the maximum gain of each one of the frequencies, and the blue trace represents the angle (Θ_r) where the maximum gain with the S21 was measured.

Fig.3(a) illustrates the variation of the direction of the pointing beam depending on the frequency for three different frequencies, 2.42 GHz, 2.45 GHz, and 2.47 GHz. Once the values are normalized, it can be observed that the different frequencies generate beams pointing at 25º, 37º, and 46º, respectively. With the pointing angles obtained with the normalized amplitude because of the frequency beam scanning, the Θ_r values of Fig. 3(b).

After characterizing the Θ_r, to estimate an angular Θ_{DOA} from an incoming signal at a test point Θ_t, a frequency beam scan has to be performed, and with the frequency where the maximum gain is obtained, a look-up has to be performed in the Θ_r vector values. The main problem is that for a single maximum frequency value, some Θ_{DOA} can be obtained because the relationship between frequencies and Θ_r is not exactly linear. If

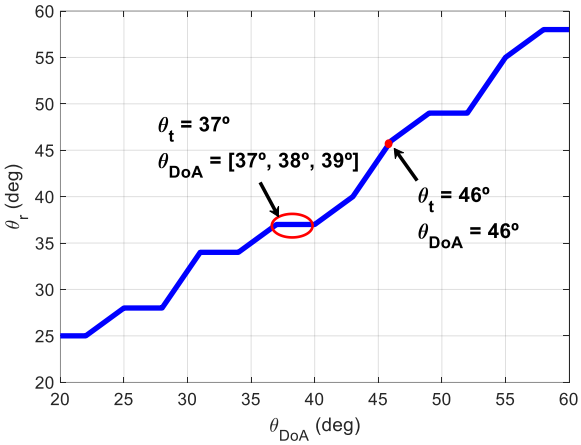

Fig. 4. Estimated Θ_{DoA} w.r.t of Θ_r for two different Θ_t

the angular determination depending on the frequency of the vector Θr is represented against a linearly sorted vector of angles, no linear relationship can be observed. This phenomenon is illustrated in Fig. 4 with some numerical values. If the frequency scan is performed from a device placed at Θ_t = 37º, the estimated Θ_{DOA} is not a single value but rather a set of multiple Θ_{DOA} values. In this case Θ_{DOA} = [37º, 38º, 39º].

III. Calibrated Phase-Based Ranging

This section describes the measurement of distance using phase-based ranging (PBR) procedure. This method estimates the distance between two devices by exploiting the phase variation of the received signal across multiple frequencies. The method employed to measure the distance with PBR is the linear adjustment of the unwrapped phase of the frequency-scan measurement to a polyonomy of grade one. This adjustment is performed using the least-squares method and yields the slope factor (a). The formula employed is:

$$a = \frac{\sum_k (f_k - \bar{f})(\phi_k - \bar{\phi})}{\sum_k (f_k - \bar{f})^2} \quad (1)$$

where k represents the number of frequencies used in the frequency scan measurement, $\bar{f}$ is the central frequency to center the data, and finally, $\bar{\phi}$ is the mean unwrapped phase. This slope is directly related to the distance (d) following the one-way ranging formula:

$$d = \frac{c}{2\pi}|a| \quad (2)$$

It is important to bear in mind that the frequency-dispersive nature of the LWA affects the slope measured depending on the DoA. Fig.5 represents the unwrapped phases simulated at three different angles, 22º, 37º, and 46º (red, green, and blue lines, respectively), employing Ansys HFSS. Finally, they are centered at 2.44 GHz with a magenta line representing a theoretical 3m unwrapped phase. In this way, the different slopes can be appreciated.

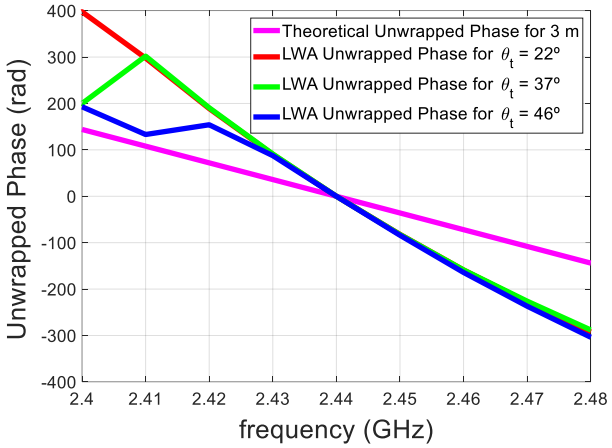

Fig. 5. Unwrapped phases centered to visualize the different slopes

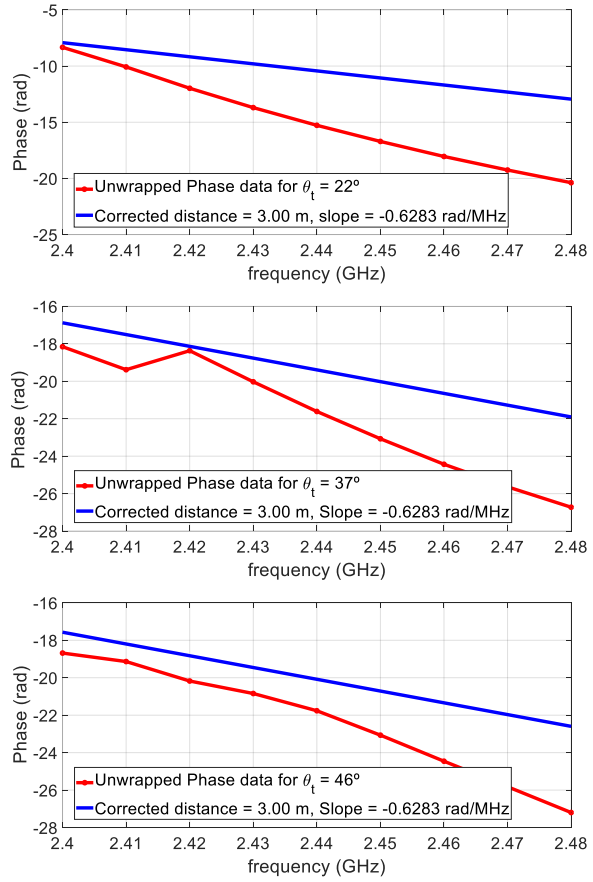

Fig. 6. Corrected distance measurement for different angles of the LWA

It can be observed that each simulation has a different slope, which slightly modifies the PBR measurement of the distance. To eliminate this effect, it is important to characterize the LWA in the simulation at a precisely known distance. In this case, it was characterized at 3 m. Once characterized, the slope obtained for each frequency is subtracted from the theoretical 3 m phase following this equation:

$$\Delta a(\theta_{DoA}) = a_{3m} - a(\theta_{DoA}) \qquad (3)$$

And once the real DoA is obtained with AODF, the increase of slope (Δa) can be used to correct the PBR measurement obtained with a precise 3m distance. This can be seen in Fig.6, where for every real DoA, the distance measurement is calibrated with Δa and obtained the corrected 3 m distance.

IV. Conclusion

This paper presents a system that combines an amplitude-based Direction of Arrival (DoA) method with a phase-based ranging (PBR) procedure to generate a precise two-dimensional location system. The system is implemented and simulated employing only one port of a frequency-scanned leaky-wave antenna (LWA). To our knowledge, this is the first approach to estimating the angular longitudinal DoA and the distance using a single port of an LWA antenna, reducing the hardware complexity and the signal processing of the location system based on PBR. Future work will focus on extending the method to more challenging propagation environments, such as multipath scenarios, and on integrating the proposed approach with several antennas to generate a 3D location system.

Acknowledgments

This work was supported by the Agencia Estatal de Investigación (AEI) through the project PID2022-136590OB-42 and the Grant TED2021-129196BC42.

References

[1] A. Santra, I. Kravets, N. Kotliar, A. Pandey, Enhancing bluetooth channel sounding performance in complex indoor environments, IEEE Sens. Lett. 8 (10) (2024) 1–4. Art no. 7005104.

[2] M. Nikodem, G. Trajnowicz, G.Salvatore de Blasio, F.Alexis Quesada-Arencibia, Experimental evaluation of multicarrier phase difference localization in bluetooth low energy, IEEE Sens J 25 (1) (2025) 1548–1560, 1 Jan.1.

[3] A. J. Martinez-Ros, J. L. Gómez-Tornero, F. Quesada-Pereira and A. Alvarez-Melcon, "Transverse resonance analysis of a planar leaky wave antenna with flexible control of the complex propagation constant," 2011 IEEE International Symposium on Antennas and Propagation (APSURSI), Spokane, WA, USA, 2011, pp. 1289-1292.

[4] J. L. Gomez-Tornero, A. T. Martinez, D. C. Rebenaque, M. Gugliemi and A. Alvarez-Melcon, "Design of tapered leaky-wave antennas in hybrid waveguide-planar technology for millimeter waveband applications," in IEEE Transactions on Antennas and Propagation, vol. 53, no. 8, pp. 2563-2577, Aug. 2005.

[5] J. L. Gómez-Tornero *et al.*, "Analysis and design principles of leaky-wave antennas," in *Antenna Theory and Design*, Wiley-IEEE Press, 2018, ch. 4. Available: https://onlinelibrary.wiley.com/doi/abs/10.1002/9781119813910.ch4

Acoustic leaky-wave antennas for localization of IoT devices

Pablo Antonio Martínez-Vicente[1], Astrid Algaba-Brazalez[1], Jens Forssén[2], Jose Luis Gómez-Tornero[1,*]

[1]Department of Communication and Information Technologies, Technical University of Cartagena, Spain
[2]Department of Architecture and Civil Engineering, Chalmers University of Technology, Sweden
*Corresponding author: joseL.Gomez@upct.es

***Abstract*—This work presents an analytical design approach for acoustic leaky-wave antennas (ALWAs) using the Transverse Resonance Equation and Transverse Equivalent Network modeling. The method enables efficient leaky-mode analysis for synthesizing ALWAs with controlled leakage and beam scanning, with potential for IoT device localization in GNSS-denied, multipath environments.**

***Keywords*— Acoustic leaky-wave antenna, direction finding, IoT localization, transverse equivalent network, transverse resonance equation.**

I. Introduction

The Internet of Things (IoT) has driven the need for reliable localization and tracking of large numbers of low-cost devices. In dense urban, industrial, and indoor scenarios, radio-based positioning often degrades due to multipath propagation and attenuation, while satellite navigation can become unreliable, resulting in environments with limited Global Navigation Satellite System (GNSS) availability. These limitations motivate alternative sensing modalities capable of robust direction finding and localization. Acoustic Leaky-Wave Antennas (ALWAs) represent a promising solution, translating leaky-wave radiation concepts into the acoustic domain to achieve frequency-controlled beam steering and direction finding [1], [2], [3], [4].

In such scenarios, an ALWA offers a simpler, more cost-effective alternative to complex and hardware-intensive microphone or loudspeaker arrays by producing a steerable directive beam from a single waveguide source. Their ability to estimate source direction using compact and low-cost transducers makes them ideal for sustainable and energy-efficient terrestrial localization systems. To avoid computationally expensive full-wave 3D sweeps, we adapt a TEN/TRE-based model to rapidly tune ALWA scanning and leakage to IoT localization.

II. Methods

The ALWA is driven by two acoustic transducers (Port A and B) placed at opposite ends of the waveguide (Fig. 1), enabling bidirectional illumination, making positive and negative scanning angles (see Fig.2). The main geometric parameters of the antenna are: waveguide width W, height H, wall thickness W_s, total length L, hole radius r, and hole spacing (period) P. The values used in the simulations are listed in Table I.

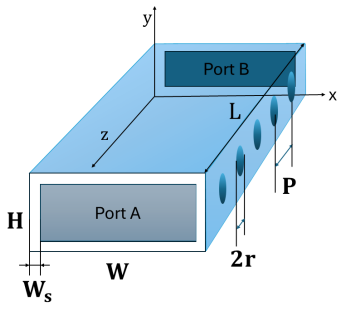

Fig. 1. Perforated-waveguide ALWA with dual-end transducers for bidirectional scanning.

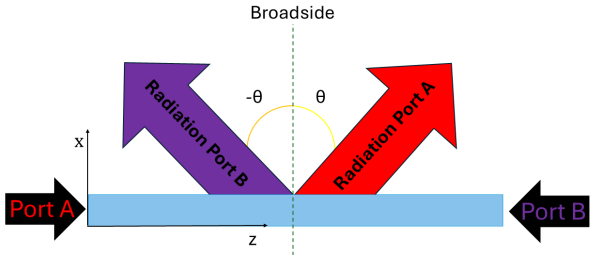

Fig. 2. Dual-port ALWA enabling beam scanning toward positive and negative angles with respect to broadside.

To obtain the dispersion curves that characterize the leaky-mode behavior, we apply a TRE/TEN modal formulation well established in electromagnetic LWA theory. The TEN [5], [6] provides a circuit model of the acoustic waveguide's cross-section, treating the aperture as an impedance load. By applying the transverse resonance condition to this network, we derive a Transverse Resonance Equation (TRE) whose solutions yield the leaky-wave's modal propagation constants [7].

TABLE I
Acoustic Waveguide main dimensions in mm.

W	H	W_s	L	P	r
95	35	2.5	1500	4.5	9

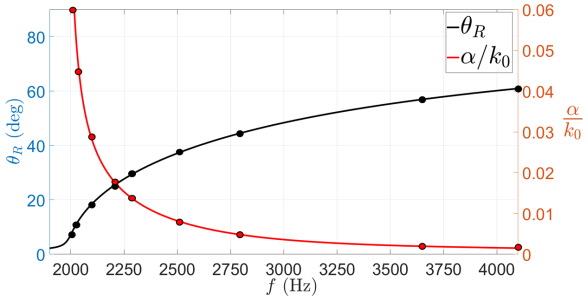

Fig. 3. Leaky-mode dispersion: scanned angle θ_R and normalized leakage α/k_0 versus frequency.

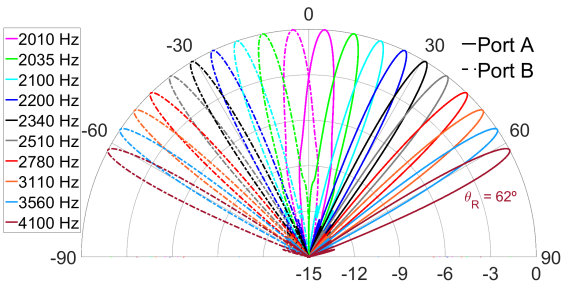

Fig. 4. Frequency-scanned radiation patterns (2–4.0 kHz), showing $\approx 120°$ field of view.

III. Results and Discussion

The leaky-mode dispersion and the resulting frequency-scanned radiation patterns are reported in Figs. 3 and 4, respectively. The radiation patterns in Fig. 4 are computed at the frequencies marked in Fig. 3, using the corresponding θ_R values extracted from the dispersion curves.

As frequency increases, the main beam steers over a wide angular sector, providing an effective field of view of approximately 120° within the 2000–4000 Hz band using both ports. This controlled scanning enables direction finding with a compact single-aperture structure. In addition, the obtained patterns in Fig. 4 are used to compute a monopulse response (Fig. 5). A monopulse function is an angular discriminator obtained from the difference-to-sum ratio Δ/Σ of two beams; it varies monotonically with angle over a field of view, enabling the estimation of the direction of arrival (DoA) [8], [9].

IV. Conclusion

This paper proposes a practical ALWA concept as a compact and low-complexity acoustic solution enabling frequency-controlled beam scanning for direction finding. A TEN/TRE model is considered to guide geometry tuning and reduce reliance on full-wave 3D sweeps. The approach is promising for scalable IoT localization nodes operating in GNSS-denied environments.

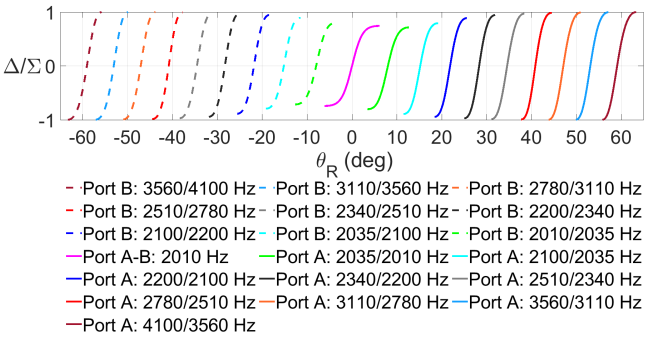

Fig. 5. Monopulse discriminator curves built from the frequency-scanned beampatterns in Fig. 4. The central curve is obtained by applying the monopulse operation Δ/Σ to the two-port patterns at the same frequency (Port A(f) and Port B(f), e.g., $f = 2010$ Hz). All remaining curves are computed from adjacent-frequency pairs within a single port: Port A uses (f_i, f_{i-1}) on the positive-angle side, while Port B uses the symmetric construction on the negative-angle side (listed in reverse order to follow the scan progression).

Acknowledgments

This work was supported in part by the Spanish Projects under Grant PID2022-136590OB-C42, and in part by Regional Fundacion Seneca Project 22076/PI/22. The work of A. Algaba-Brazález is supported by the Grant RYC2022-037385-I funded by MCIN/AEI/10.13039/501 and by ESF+.

References

[1] C. J. Naify, M. Haberman, M. D. Guild, and C. F. Sieck, "Acoustic leaky-wave antennas direction-finding via dispersion," *Acoust. Today*, 2018.

[2] H. Esfahlani, S. Karkar, H. Lissek, and J. R. Mosig, "Exploiting the leaky-wave properties of transmission-line metamaterials for single microphone direction finding," *J. Acoust. Soc. Am.*, vol. 139, no. 6, pp. 3258–3265, 2016.

[3] I. Felis-Enguix *et al.*, "Practical aspects of acoustic leaky-wave antennas applied to underwater direction finding," *Eng. Proc.*, vol. 2, no. 1, art. no. 93, 2020.

[4] Q. Wang *et al.*, "Acoustic source localization based on acoustic leaky-wave antenna with heterogeneous structure," *J. Acoust. Soc. Am.*, vol. 153, no. 1, pp. 487–495, 2023.

[5] A. A. Oliner and D. R. Jackson, "Leaky-wave antennas," in *Antenna Engineering Handbook*, New York, NY, USA: McGraw-Hill, 2007.

[6] T. Tamir and A. A. Oliner, "Guided complex waves—Part I: Fields at an interface," *Proc. Inst. Electr. Eng.*, vol. 110, pp. 310–324, Feb. 1963.

[7] R. Sorrentino and M. Mongiardo, "Transverse resonance techniques," in *Encyclopedia of RF and Microwave Engineering*, Apr. 2005.

[8] M. Poveda-García, D. Cañete-Rebenaque, and J. L. Gómez-Tornero, "Frequency-Scanned Monopulse Pattern Synthesis Using Leaky-Wave Antennas for Enhanced Power-Based Direction-of-Arrival Estimation," *IEEE Trans. Antennas Propag.*, vol. 67, no. 11, pp. 7071–7086, 2019, doi: 10.1109/TAP.2019.2925970.

[9] A. G. Martinez, M. P. Garcia, and J. L. Gómez-Tornero, "Direct Synthesis of Frequency-Scanned Monopulse Half-Width Microstrip Leaky-Wave Antennas," in *Proc. 14th Eur. Conf. Antennas Propag. (EuCAP)*, 2020, pp. 1–4, doi: 10.23919/EuCAP48036.2020.9135317.

Inverse problems for synthesis, design and characterization of electromagnetic devices

MIMO Array Design for Near-Field Radar Imaging by a Warping Strategy

Mario Del Prete [1,*], Raffaele Solimene[1], Maria Antonia Maisto[1]

[1]University of Campania "Luigi Vanvitelli"

*Corresponding author: mario.delprete@unicampania.it

***Abstract*—In this contribution, we extend the warping approach to design MIMO arrays for near-field radar imaging purposes. It is shown that, although transmitting and receiving elements must be arranged non-uniformly, the number of sensors is dramatically reduced compared to other approaches, without any degradation in achievable imaging performance.**

I. Summary

Near-field millimeter-wave (mm-Wave) radar imaging has emerged as a fundamental technology for high-resolution sensing in critical sectors, including concealed weapon detection (CWD) [1], through-the-wall radar imaging (TWRI) [2], and non-destructive testing [3]. To achieve the angular resolution and target separability required for these applications, large scan apertures are required. However, conventional monostatic configurations typically required uniform sampling according to the Nyquist criterion, leading to an overwhelmingly large number of sensors as operating frequencies scale into the Ka or W bands. This hardware density imposes significant challenges regarding system cost, data acquisition speed, and computational overhead. To address these limitations, the state-of-the-art has shifted toward Multiple-Input Multiple-Output (MIMO) array architectures. MIMO systems exploit spatial diversity to synthesize an equivalent "virtual array" or "effective aperture," which mimics the performance of a densely sampled monostatic array using only a fraction of the physical elements [4], [5]. Standard design methodologies revolve around the factorization of a desired effective aperture into optimized transmit (Tx) and receive (Rx) sub-arrays[6]. This paradigm is fundamentally rooted in far-field assumptions, where the propagator can be accurately modeled as a plane wave. In near-field scenarios, the kernel of the radiation operator does not satisfy the far-field approximation resulting in overpopulated arrays that fail to fully exploit the underlying physics of near-field propagation.

Accordingly, there is still room for further optimization of MIMO arrays in near-field applications.

In this work, we introduce a paradigm shift in array design through the extension of the Warping strategy [7] to MIMO array configurations. The warping strategy employs a non-linear transformation of the observation coordinates to restore a Fourier-like relationship between the target contrast and the scattered field (in a linear framework). By recasting the phase terms of the near-field Green's function, the radiation kernel became approximately band-limited in the transformed ("warped") domain [7]. This allows for the rigorous application of the Shannon sampling theorem, yielding sensor distributions that are inherently non-uniform but mathematically optimized for the specific geometry of the near-field imaging scenario. Numerical validations and comparative analyses demonstrate that MIMO warping can achieve a dramatic reduction in the number of sensors compared to other approaches in literature. This facilitates the implementation of high-performance, real-time mm-Wave imaging systems with significantly reduced hardware complexity.

References

[1] Sheen, D. M., McMakin, D. L., and Hall, T. E. Three-dimensional millimeter-wave imaging for concealed weapon detection IEEE Transactions on Microwave Theory and Techniques, vol. 49, pp. 1581-1592, 2001.

[2] M. A. Maisto, M. Masoodi, R. Pierri and R. Solimene, "Sensor Arrangement in Through-the Wall Radar Imaging," in IEEE Open Journal of Antennas and Propagation, vol. 3, pp. 333-341, 2022, doi: 10.1109/OJAP.2022.3159279.

[3] H. Cetinkaya, S. Nowok and R. Herschel, "MIMO-ISAR-Based UWB Imaging System for Non-Destructive Testing," 2020 17th European Radar Conference (EuRAD), Utrecht, Netherlands, 2021, pp. 334-337, doi: 10.1109/EuRAD48048.2021.00092.

[4] A. M. Haimovich, R. S. Blum, and L. J. Cimini, "MIMO radar with widely separated antennas," IEEE Signal Processing Magazine, vol. 25, no. 1, pp. 116–129, Jan. 2008

[5] J. Li and P. Stoica, "MIMO radar with colocated antennas," IEEE Signal Processing Magazine, vol. 24,no. 5, pp. 106–114, Sep. 2007

[6] C. Dahl, I. Rolfes and M. Vogt, "Comparison of virtual arrays for MIMO radar applications based on hexagonal configurations," 2015 European Microwave Conference (EuMC), Paris, France, 2015, pp. 1439-1442, doi: 10.1109/EuMC.2015.7346044.

[7] M. A. Maisto, R. Pierri and R. Solimene, "Near-Field Warping Sampling Scheme for Broad-Side Antenna Characterization". Electronics 9, no. 6: 1047.

Numerical investigation of the internal scattering operator in a 2D geometry

Giovanni Leone[1,*], Giovanni Volpicelli[1], Rocco Pierri[1]

[1]Department of Engineering, University of Campania, Italy
*Corresponding author: giovanni.leone@unicampania.it

***Abstract*— A spectral analysis of the internal scattered field operator in the data equation arising in the inverse scattering problem is performed numerically for an homogeneous dielectric strip. The comparison with the 1D reveals analogies and differences.**

***Keywords*— forward scattering, spectral decomposition, optimal discretization**

I. Introduction

The Lippman-Schwinger formulation of the inverse electromagnetic scattering problem consists in the solution of two coupled integral equations. One of them, the "state equation", provides the connection between the dielectric properties of the object, the total internal field and the incident, known, exciting field. It involves two terms, i.e. the total internal field and the internal scattered field, which, in turn, is related to the total internal field by a linear operator (once the dielectric properties of the object are fixed). Hereafter we are interested in the solution of this equation of the forward scattering model. To this end suitable finite sets of orthogonal basis functions must be devised so that the corresponding linear inversion problem is recast as a matrix inversion. However, one of the crucial point, both from the theoretical and from the numerical points of view, is the appropriate discretization of all involved functions. In particular, we choose to investigate this point by the numerical computation of the spectral decomposition of the pertinent integral operator. Here we consider a thin uniform dielectric strip in a 2D geometry. In this way a direct comparison with the 1D case [1-2] can be established.

II. The Integral Equation

In the 2D geometry for a homogenous dielectric D thin strip, $2a$ long, the pertinent integral equation for the internal scattered field is:

$$E_s(x,y) = -j\frac{\beta^2}{4}\chi \int_D E(x',y')H_0^{(2)}(\beta\rho)dx'dy' \quad (1)$$

for both (x,y) and $(x',y')\epsilon D$, where E_s denotes the internal scattered field, E the internal field, χ the contrast of the dielectric object. By a standard discretization of the integral equation [3] (1) is recast a matrix operator. As a first step towards its spectral decomposition its eigenvalues and its eigenfunctions are depicted in fig. 1 for $a=2\lambda$.

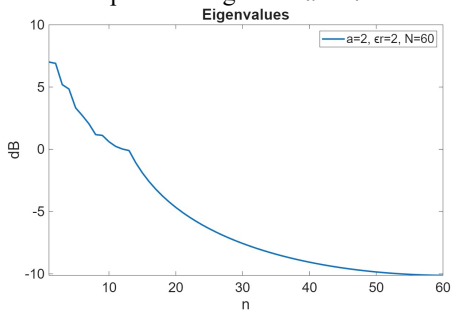

Fig. 1 Eigenvalues of (1)

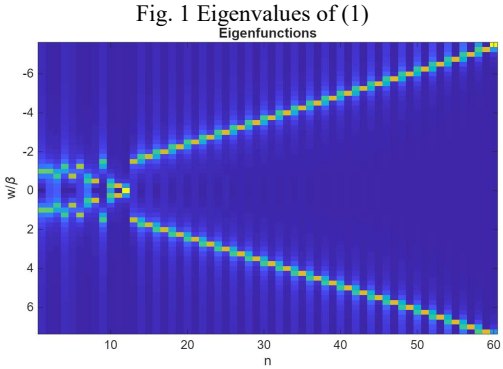

Fig. 2 Fourier transforms of the eigenfunctions of (1)

Similar behaviors as the simpler 1D geometry result [1-2]. However, the dynamic of the eigenvalues is lower, as it can be expected according to the different Fourier transform of the kernel functions. On the other hand, the harmonic content of the eigenfunctions is very similar to 1D geometry.

This means that a similar analysis can be developed in order to define the correct number of eigenfunctions, and then, of the Fourier harmonic required to solve numerically the integral equation (1).

References

[1] G. Leone, G. Volpicelli and R. Pierri, "Numerical results in a convolution approach in scattering theory: the 1D case," 2025 URSI Asia-Pacific Radio Science Meeting (AP-RASC), Sydney, Australia, 2025.

[2] G. Leone, G. Volpicelli and R. Pierri, "Eigenvalue analysis of the 1D internal scattering operator," submitted.

[3] J. Richmond, "Scattering by a dielectric cylinder of arbitrary cross section shape," in IEEE Transactions on Antennas and Propagation, vol. 13, no. 3, pp. 334-341,

Ruling (e.m.) Wavefields through Primary Sources and Inverse Designed Scatterers: A Mediterranean Route

T. Isernia, R. Abdullin, G. M. Battaglia, A. F. Morabito, R. Palmeri

[1]DIIES, Univ. Mediterranea di Reggio Calabria, Italy

***Abstract*— We review recent results obtained at Università Mediterranea of Reggio Calabria on the optimal mask-constrained power-pattern synthesis of far and near fields. The problem is addressed as a minimal-size synthesis of an aperture field, which can be either the primary source of interest or realized through inverse-designed scatterers.**

***Keywords*—minimal size synthesis, antenna design, inverse design, metasurfaces.**

I. Introduction

The optimal synthesis of far and near fields is a canonical problem in electromagnetics, and its specification in terms of a power mask for the field components provides the designer with the maximum possible number of degrees of freedom in all the very many applications (e.g., telecommunications, wireless power transfer) where phase distributions are not of interest.

II. An Effective Approach to the Minimal-Size Synthesis of Mask-Constrained Power Patterns

Leveraging the band-limited nature of electromagnetic fields, the squared-amplitude distributions of far-field components are also band-limited in space, so that they admit an effective and minimally redundant sampling representation in both 1-D and 2-D problems. This representation can also be reformulated in terms of a Fourier series, whose coefficients serve as the initial auxiliary unknowns of our problem. Notably, the number of these coefficients is directly related to the dimensions of the planar source at hand.

Then, the problem is conveniently split into two steps.

In the first step, the repeated solution of a Linear Programming (LP) problem (in terms of the auxiliary functions) allows the determination of the minimal dimensions capable of fulfilling the specifications, as given in terms of a 'mask' on the power pattern (see figure 1) [1]. Notably, once the problem becomes feasible in terms of compatibility between dimensions and specifications, the determined auxiliary unknowns also define a nominal power pattern to be pursued.

The second step therefore amounts to solve a problem analogous to the phase-retrieval problem [2]-[5]. This problem, whose solution was well-known in the 1-D case, has been recently and satisfactorily solved in the 2-D case by ourselves in [6], where a deterministic, non-iterative procedure is proposed and validated. Subject to the subtleties and modifications thoroughly discussed in [7], the approach is also highly effective for the second step of the synthesis problem considered here. Notably, the solution of this step implicitly provides the aperture field required to realize the specified field.

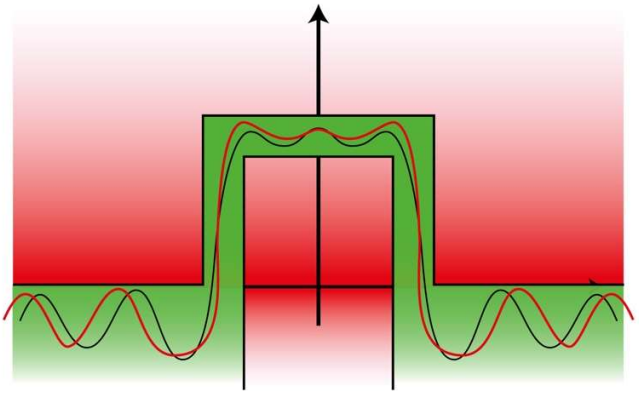

Figure 1: Power-pattern mask.

Very interestingly, the exploitation of warping transformations, as discussed in Solimene et al. [8],[9], allows us to state that near fields on a line (or on a plane) also admit non redundant, array-like (Fourier) representation. As a consequence, all results developed for the far-field case can be effectively widened to consider the near-field case, which has already been demonstrated for 1-D problems [10].

In both near-field and far-field cases, the determination of the aperture field (or radiated field) concludes the synthesis problems when designing an array. In fact, any field synthesis procedure (which is a linear problem if excitations of the array are the degrees of freedom) can be successfully used.

In other cases, one aims to realize such an aperture field by means of a simple primary source and suitably designed scatterers. This second case includes reflectarrays, transmitarrays, metagratings, Reconfigurable Intelligent Surfaces (RIS), and much more. In these scenarios, the goal is typically to redirect incident fields in order to achieve a 'Smart

Radio Environment'. Some contributions to the design of this kind of devices are recalled in the following section.

III. REALIZING APERTURE FIELDS VIA INVERSE DESIGN: A NEW COMBINED IMAGE THEORY-SCATTERING MATRIX METHOD

Inverse scattering problems are another classical topic in electromagnetics. In such problems, one typically wants to quantitatively retrieve the characteristic of some scatterer from the knowledge of the incident field and the corresponding scattered fields. As observed in [11], once the measured scattered fields are replaced by specifications, the theoretical framework developed for inverse-scattering retrieval problem becomes immediately suitable for the design of (innovative) devices. This approach has been pursued in many works by the authors and by other research groups.

In this context, decisive advances in computational efficiency and in the ability to control the desired phenomena have been achieved by leveraging the so-called 'Scattering Matrix Method (SMM) [12]. In fact, this 'mesoscale' tool avoids homogenization approximations or brute-force numerical approaches, while requiring only a reduced number of parameters.

Along the overall journey, our more recent efforts have focused on the case in which the scatterers to be designed (and positioned) are located in the presence of a planar Perfect Electric Conductor (PEC), as is typical in RIS configurations.

For the z-invariant case, at least three novel results have recently been achieved.

First, the original SMM method has been widened to account for the presence of a planar PEC. Notably, a simple trial-and-error exploitation of the 'forward-problem' procedure already allows the effective synthesis of anomalous reflection and other interesting non-standard behaviors [13].

Second, we introduced a very effective framework (together with dedicated codes) for cases in which the scatterers are enclosed in PEC dihedra with apex angles of the form π/N [14]. Once again, a simple trial-and-error procedure allows to design of novel and interesting antenna configurations.

Last for the time being (but not surely least), an effective framework (together with a semi-analytical synthesis procedure) has been introduced for scatterers constituted by loaded wires [16] and promising design solutions for innovative devices are currently emerging.

IV. CONCLUSION

A route conceived and developed at Università Mediterranea di Reggio Calabria for achieving designed far- and near-field distributions, together with the associated innovative theoretical and computational tools, has been briefly reviewed. The achieved theoretical and applicative results encourage us to further progress along this journey.

ACKNOWLEDGMENTS

This work was partially supported by the Italian National Recovery and Resilience Plan (NRRP) of NextGenerationEU, partnership on "Telecommunications of the Future" (PE00000001 - program RESTART"), by the Italian Ministry of University and Research with projects "IDEAS – Inverse Design of terahertz interAction Structures" (PRIN2022 PNRR P202293B5X), and "MEETAPP – MEtasurface-based tEchnology Towards industrial APPlications" (PRIN2022 P2022ZZ8APA).

REFERENCES

[1] T. Isernia, O. M. Bucci, and N. Fiorentino, "Shaped beam antenna synthesis problems: feasibility criteria and new strategies," *Journal of Electromagnetic Waves and Applications*, vol.12, n. 1, pp.103-137, 1998, DOI: 10.1163/156939398X00098.

[2] L. Taylor, "The phase retrieval problem," *IEEE Transactions on Antennas and Propagation*, vol. 29, n. 2, pp. 386-391, 1981, DOI: 10.1109/TAP.1981.1142559.

[3] J. R. Fienup, "Phase retrieval algorithms: a comparison," Applied Optics, vol. 21, pp. 2758-2769, 1982, DOI: https://doi.org/10.1364/AO.21.002758.

[4] G. Leone and R. Pierri, "Reflector antenna diagnosis from phaseless data," *IEEE Transactions on Antennas and Propagation*, vol. 45, no. 8, pp. 1236-1244, 1997, DOI: 10.1109/8.611242.

[5] G. M. Battaglia, T. Isernia, A. F. Morabito, R. Palmeri, R. Solimene and M. A. Maisto, "Single Measurement Surface 2-D Near-Field Phase Recovery via Smart Warping Sampling and Factorization of 1-D Polynomials," *IEEE Transactions on Antennas and Propagation*, vol. 73, n. 9, pp. 6228-6240, 2025, DOI: 10.1109/TAP.2025.3573178.

[6] G. M. Battaglia, A. F. Morabito, R. Palmeri and T. Isernia, "Effective Non-Iterative Phase Retrieval of 2-D Bandlimited Signals With Applications to Antenna Characterization and Diagnostics," *IEEE Transactions on Antennas and Propagation*, vol. 71, n. 8, pp. 6444-6453, 2023, DOI: 10.1109/TAP.2023.3283044.

[7] G. M. Battaglia, A. F. Morabito, R. Palmeri and T. Isernia, "Minimal-Size 2-D Sources for Mask-Constrained Synthesis of Shaped Patterns," *IEEE Open Journal of Antennas and Propagation*, vol. 7, n. 1, pp. 128-139, 2026, DOI: 10.1109/OJAP.2025.3637546.

[8] M. A. Maisto, G. Leone, A. Brancaccio, and R. Solimene, "Efficient Planar Near-Field Measurements for Radiation Pattern Evaluation by a Warping Strategy," *IEEE Access*, vol. 9, pp. 62255-62265, 2021, DOI: 10.1109/ACCESS.2021.3074786.

[9] R. Solimene, M. A. Maisto, and R. Pierri, "Sampling approach for singular system computation of a radiation operator," *Journal of the Optical Society of America A*, vol. 36, n. 3, pp. 353-361, 2019, DOI: 10.1364/JOSAA.36.000353.

[10] G. M. Battaglia, T. Isernia, R. Palmeri, M. Antonia Maisto, R. Solimene and A. Francesco Morabito, "Near-Field Synthesis of 1-D Shaped Patterns Through Spectral Factorization and Minimally-Redundant Array-Like Representations," *IEEE Transactions on Antennas and Propagation*, vol. 73, n. 5, pp. 2713-2724, 2025, DOI: 10.1109/TAP.2024.3525137.

[11] R. Palmeri, M. T. Bevacqua, A. F. Morabito and T. Isernia, "Design of Artificial-Material-Based Antennas Using Inverse Scattering Techniques," *IEEE Transactions on Antennas and Propagation*, vol. 66, n. 12, pp. 7076-7090, 2018, DOI: 10.1109/TAP.2018.2871707.

[12] D. Felbacq, G. Tayeb, and D. Maystre, "Scattering by a random set of parallel cylinders," *Journal of the Optical Society of America A*, vol. 11, pp. 2526-2538, 1994, DOI: https://doi.org/10.1364/JOSAA.11.002526.

[13] R. Abdullin, G. M. Battaglia, A. F. Morabito, L. Crocco, T. Isernia and R. Palmeri, "An Effective Approach to Scattering From Parallel Cylinders Above a Planar Conducting Surface," *IEEE Open Journal of Antennas and Propagation*, vol. 6, n. 5, pp. 1423-1434, 2025, DOI: 10.1109/OJAP.2025.3584242.

[14] R. Abdullin, T. Isernia, G. M. Battaglia, L. Crocco, A. F. Morabito and R. Palmeri, "A Combined Image Theory-Scattering Matrix Method for PEC Dihedral Geometries," *IEEE Open Journal of Antennas and Propagation*, DOI: 10.1109/OJAP.2026.3655137.

[15] R. Abdullin "Extended Scattering Matrix Method for Inverse Design of Reflective Metasurfaces" PhD Thesis @Università Mediterranea, submitted for defense, February 2026

Robust phase retrieval using learned phase diversity

Kedar Khare[1,*]

[1]Optics and Photonics Centre, Indian Institute of Technology Delhi, New Delhi, India
*Corresponding author: kedark@opc.iitd.ac.in

***Abstract*— When a test object is illuminated by two phase-coded illuminations, the corresponding diffraction intensity patterns have implicit local correlations that may be learnt using image-to-image networks. The pseudo-diffraction data thus generated in this manner is shown to resolve the well-known stagnation problems in phase retrieval with simple Error-Reduction type algorithm.**

***Keywords*— phase retrieval, phase diversity, image-to-image translation networks, stagnation problems in phase retrieval**

I. Introduction

Phase retrieval from single Fourier magnitude data frame has been an important inverse problem of interest in optics, coherent X-ray, electron microscopy and antenna research. Phase-less measurements usually require simpler detection hardware, however, the stagnation problems [1] in phase retrieval continue to pose challenges for realizing complete systems. On the other hand, it is known that multiple intensity measurements with phase diversity can lead to robust phase retrieval. Various forms of diversity mechanisms, e.g. defocus diversity, vortex phase diversity, ptychography, etc. have been explored in literature. The vortex phase diversity is a special case since the two diffraction patterns with and without charge-1 phase vortex coding are on a similar footing and are known to show local negative intensity correlations. It has also been shown that iterative phase retrieval algorithms with vortex coded diffraction data avoids stagnation problems [2]. Here we present initial results that suggest that the image-to-image translation networks (e.g. UNet) can learn to predict vortex coded diffraction intensity data from the usually available diffraction data with plane wave illumination with good accuracy. Availability of this pseudo generated data then helps resolve stagnation problems in phase retrieval [3].

II. Methods

Our methodology aims to learn the relation between two diffraction intensity patterns described by:

$$I_1(f_x, f_y) = |\mathcal{F}\{g(x,y)\, C(x,y)\}|^2, \quad (1)$$

$$I_2(f_x, f_y) = |\mathcal{F}\{\exp(i\theta)\, g(x,y)\, C(x,y)\}|^2. \quad (2)$$

Here $g(x,y)$ is the unknown object to be determined, $C(x,y)$is the support and $\theta(x,y) = \arctan(y/x)$ is the polar angle in the test object plane. Figure 1 (a), (b) show typical diffraction pattern associated with a phase object in the form of an image from the fashion MNIST dataset obtained corresponding to Eq.s (1) and (2). The negative correlation between the two patterns may be noted. A UNet is trained with 2000 pairs of plane wave and vortex coded diffraction patterns and achieves > 90% training accuracy in 50 iterations (or epochs) of training with batch size of 4.

III. Results and Discussion

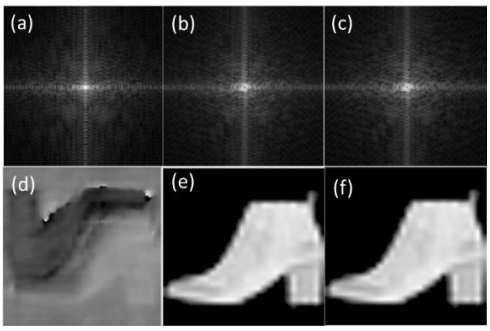

Fig.1 Illustration of phase retrieval using pseudo-data

The vortex coded diffraction pattern predicted by a trained network using the plane wave diffraction pattern is shown in Fig. 1 (c). Figure 1 (d), (e), (f) show phase reconstructions obtained using plane wave data alone, using the plane wave and vortex wave ground truth data and using the plane wave and pseudo-generated vortex coded data. The reconstruction in Fig. 1(d) shows severe twin stagnation, whereas results in Fig. 1(e), (f) are highly similar and do not show any stagnation problems.

IV. Conclusion

We introduced the idea of using image-to-image translation networks for generating physics-inspired diverse data using training examples. The trained network can then generate pseudo-data that makes the reconstruction problem well-posed.

Acknowledgments

National Quantum Mission of DST, India; University of Campania Visiting Professorship.

References

[1] J. R. Fienup, C. C. Wackerman, "Phase-retrieval stagnation problems and solutions", JOSA A 3, pp. 1897, 1986.
[2] M. Kularia, M. Banerjee, K. Khare, "Twin-stagnation-free phase retrieval with vortex phase illumination", JOSA A 41, pp. 1166, 2024.
[3] J. Birdi, T. Majumder, D. Halder, M. Kularia, K. Khare, "Learning phase diversity for solving ill-posed inverse problems in imaging", arXiv:2511.09952, 2025.

Intensity-Only Linear Inverse Scattering via Phase-Space Formulation

Davide Santagata[1,*], Maria Antonia Maisto[1] and Raffaele Solimene[1]

[1]Department of Engineering, University of Campania "Luigi Vanvitelli", Aversa, Italy
[*]Corresponding author: davide.santagata@unicampania.it

***Abstract*—We present a phase-space framework for tomographic reconstruction from intensity-only, single-frequency measurements. Structured illumination models far-field intensities as a filtered Wigner distribution of the contrast function, with a smoothing kernel governed by the incident field. This formulation enables linear inversion via deconvolution, overcoming limitations of phaseless approaches.**

***Keywords*— phase-space, imaging, inverse scattering, intensity-only measurements, phaseless inverse approach, Wigner distribution, deconvolution, Wiener filter.**

I. Introduction

Electromagnetic waves are widely employed in non-destructive imaging and target characterization, enabling detection, localization, and the extraction of both morphological and material properties [1, 2]. Across domains such as defense, remote sensing, subsurface inspection, and biomedical imaging, electromagnetic measurements underpin a variety of reconstruction methods and imaging techniques [3–6]. A critical system-design factor in these applications is the operating frequency band, as it directly impacts penetration depth, achievable resolution, and hardware feasibility.

In particular, millimeter- and sub-millimeter-wave regimes have received increasing attention for their non-ionizing effect while allowing high-resolution imaging [7–12].

However, accurate phase measurements become increasingly difficult and costly at higher frequencies. Although amplitude-and-phase acquisition is feasible in some microwave and millimeter-wave systems, reliable phase information at higher frequencies is often difficult or impractical to obtain. Moreover, even when phase data are available, amplitude measurements generally remain more accurate and robust [13].

These considerations motivate intensity-only acquisition, where only the squared magnitude of the field is recorded and subsequently processed. Even though this approach simplifies the measurement setup and improves robustness, it transfers computational complexity to the reconstruction stage. Indeed, the inversion procedure from intensity-only data is inherently nonlinear and is typically addressed through iterative mini mization of non-quadratic cost functions [13, 14], which can be computationally intensive and sensitive to initialization, convergence, and modeling errors, especially in the presence of noise [13, 15, 16].

In this context, we propose an alternative framework based on a *phase-space formulation* [17] of far-field intensities.

To this end, representations such as Mark's Physical Spectrum [18] and the Wigner distribution [18, 19] are involved, thus rigorously linking windowed Fourier intensity measurements (spectrograms) to bilinear space–spatial-frequency descriptions.

In our framework, the target cross-section is illuminated with a series of focused spatial-support patterns, shifted and modulated using a properly excited uniform circular array. Due to practical limitations, the desired incident field can only be approximated, and a condition necessary for an optimal implementation is addressed.

For each illumination, the scattered field's squared magnitude is recorded over a full-view far-field circumference. Under the Born approximation [20], these intensity-only measurements correspond to Mark's Physical Spectrum [18], which represents a smoothed version of the contrast's Wigner distribution with a smoothing kernel determined by the incident field. This interpretation enables a *linear* inversion strategy based on regularized phase-space deconvolution, producing a tomographic intensity map without requiring iterative phase-retrieval procedures.

To illustrate the main concepts in a simple yet informative setting, we focus on a two-dimensional scalar configuration at a single frequency, involving extended objects of varying morphologies on a plane and intensity-only scattered-field data collected along a surrounding circumference.

The remainder of the paper is organized as follows. Section II introduces the mathematical tools and conventions adopted throughout the paper. Section III describes the scattering scenario, including the illumination and acquisition strategy. Section IV presents the proposed inversion procedure, and Section V reports numerical results demonstrating the effectiveness of the approach. Finally, conclusions are drawn.

II. Definitions and Formulations

Throughout the paper, the Fourier transform conventions

$$\mathscr{F}\{g(\mathbf{r})\}(\mathbf{k}) = \iint_{-\infty}^{+\infty} g(\mathbf{r})\, e^{j\mathbf{k}\cdot\mathbf{r}}\, d\mathbf{r}, \tag{1}$$

and

$$\mathscr{F}^{-1}\{G(\mathbf{k})\}(\mathbf{r}) = \frac{1}{4\pi^2} \iint_{-\infty}^{+\infty} G(\mathbf{k})\, e^{-j\mathbf{k}\cdot\mathbf{r}}\, d\mathbf{k}, \tag{2}$$

are adopted.

For a function f, the associated Wigner distribution W_f is defined as [19]

$$W_f(\mathbf{r},\mathbf{k}) = \mathscr{F}\left\{f\left(\mathbf{r}+\tfrac{\mathbf{s}}{2}\right) f^*\left(\mathbf{r}-\tfrac{\mathbf{s}}{2}\right)\right\} = \iint_{-\infty}^{+\infty} f\left(\mathbf{r}+\tfrac{\mathbf{s}}{2}\right) f^*\left(\mathbf{r}-\tfrac{\mathbf{s}}{2}\right) e^{j\mathbf{k}\cdot\mathbf{s}}\, d\mathbf{s}, \quad (3)$$

where $\mathbf{r}$ and $\mathbf{k}$ denote the spatial and spatial-frequency variables, respectively.

III. Problem Description

We consider the scattering configuration illustrated in Fig. 1. The scattering object is assumed to be invariant along the z-axis and is described by the object function $o(\mathbf{r})$, with $\mathbf{r} = (x, y)$, supported over the 2D spatial region (i.e., the investigation domain)

$$D = \{(x,y) : |x| < \ell,\ |y| < \ell\}. \quad (4)$$

The scene is illuminated by a monochromatic incident field with wavelength λ and wavenumber $k = 2\pi/\lambda$, polarized along z. Accordingly, the scattered field is also z-polarized, allowing the problem to be formulated within a two-dimensional scalar framework.

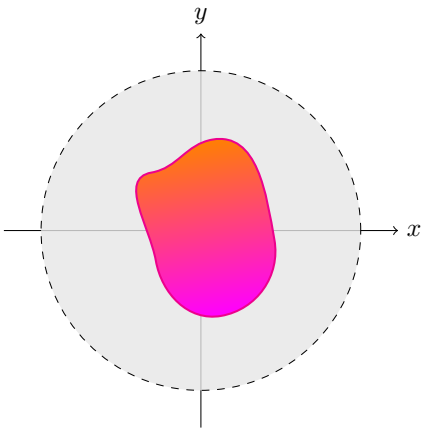

Fig. 1. Illustration of the considered scenario.

Under Born approximation [20], the scattering phenomenon is described by the following expression

$$E_{\text{scat}}(\mathbf{r}) \approx k^2 \int_D \mathcal{G}(\mathbf{r}-\mathbf{r}')\, o(\mathbf{r}')\, E_{\text{inc}}(\mathbf{r}')\, d\mathbf{r}'. \quad (5)$$

with $\mathbf{r}' = (x', y')$, and $\mathcal{G}(\mathbf{r})$ is the Green function, which is, for 2D geometries

$$\mathcal{G}(\mathbf{r}) = \frac{j}{4}\mathcal{H}_0^{(2)}(kr). \quad (6)$$

Evaluating (5) over a far-field circumference of radius $r = r_0$ yields

$$E_{\text{scat}}(\hat{\mathbf{s}}) = \mathcal{C}_0 \int_D e^{jk\hat{\mathbf{s}}\cdot\mathbf{r}'}\, o(\mathbf{r}')\, f(\mathbf{r}')\, d\mathbf{r}', \quad (7)$$

$$\mathcal{C}_0 = -k^2 \frac{e^{-jkr_0}}{\sqrt{8\pi k r_0}} e^{-j\pi/4}, \quad (8)$$

and $\hat{\mathbf{s}} = (\cos\theta, \sin\theta)$ denotes the direction of observation, where θ is the azimuthal angle measured from the x-axis. The incident field is modeled as a spatially shifted modulated Gaussian function,

$$E_{\text{inc}}(\mathbf{r}_s, \mathbf{r}) = a(\mathbf{r}-\mathbf{r}_s)\exp\left[-jk\hat{\mathbf{s}}_\alpha\cdot\mathbf{r}\right], \quad (9)$$

where $\mathbf{r}_s = (x_s, y_s)$ denotes the displacement, $\hat{\mathbf{s}}_\alpha = (\cos\alpha, \sin\alpha)$ with α being a polar angle with is pole parallel to x-axis, and $a(\mathbf{r})$ indicates the Gaussian envelope

$$a(\mathbf{r}) = \exp\left(-\frac{|\mathbf{r}|^2}{2\sigma^2}\right). \quad (10)$$

From a practical perspective, the aim is to obtain a local plane-wave propagating along a certain direction $\hat{\mathbf{s}}_\alpha$. Such an incident field (9) can be synthesized using a properly designed antenna array. Due to physical constraints, only an approximate realization of (9) is achievable. It can be shown that for $\sigma = \lambda/\pi$, the best approximation of the desired incident field is obtained.

For each illumination position $\mathbf{r}_s$, the corresponding far-field scattered response is therefore

$$E_{\text{scat}}(\mathbf{r}_s, \hat{\mathbf{s}}-\hat{\mathbf{s}}_\alpha) \simeq \mathcal{C}_0 \int_D e^{jk(\hat{\mathbf{s}}-\hat{\mathbf{s}}_\alpha)\cdot\mathbf{r}'}\, o(\mathbf{r}')\, a(\mathbf{r}'-\mathbf{r}_s)\, d\mathbf{r}'. \quad (11)$$

Introducing the spatial-frequency variable

$$\mathbf{k} = k(\hat{\mathbf{s}}-\hat{\mathbf{s}}_\alpha) \quad (12)$$

equation (11) can be rewritten as

$$E_{\text{scat}}(\mathbf{r}_s, \mathbf{k}) \simeq \mathcal{C}_0 \int_D e^{j\mathbf{k}\cdot\mathbf{r}'}\, o(\mathbf{r}')\, a(\mathbf{r}'-\mathbf{r}_s)\, d\mathbf{r}'. \quad (13)$$

The measured data consist of the squared magnitude of (13), namely Mark's Physical Spectrum [18],

$$\mu(\mathbf{r}_s, \mathbf{k}) = |E_{\text{scat}}(\mathbf{r}_s, \mathbf{k})|^2. \quad (14)$$

The objective of this work is to recover, from the intensity-only measurements $\mu(\mathbf{r}_s, \mathbf{k})$, the squared magnitude of the object function $|o(\mathbf{r})|^2$, which provides a *tomographic reflectivity map* of the investigated sceario. The corresponding inversion strategy is developed in the following section.

IV. Phase-Space Inversion

The proposed inversion strategy aims at constructing a *tomographic map* of the investigated scenario from intensity-only measurements. The inversion framework is most conveniently derived in the phase-space domain, via the Moyal identity [21], reported below

$$\mu(\mathbf{r}_s, \mathbf{k}) = W_a(-\mathbf{r}_s, \mathbf{k}) \underset{\mathbf{r}_s,\mathbf{k}}{*} W_o(\mathbf{r}_s, \mathbf{k}). \quad (15)$$

As a consequence, a *phase-space reformulation* of the scattered field intensity leads to a *convolutive* relationship between the unknown function $W_o(\mathbf{r}_s, \mathbf{k})$ and the measured intensity data $\mu(\mathbf{r}_s, \mathbf{k})$, governed by W_a, i.e., the Wigner distribution of the Gaussian envelope $a(\mathbf{r})$ associated with the incident field function E_{inc} (9).

Once an estimate of W_o is obtained through a deconvolution step, the desired metric $|o(\mathbf{r})|^2$ recovered by exploiting the marginal property of the Wigner distribution [22–24], reported below

$$|o(\mathbf{r})|^2 = \frac{1}{4\pi^2} \iint_{-\infty}^{+\infty} W_o(\mathbf{r}, \mathbf{k})\, d\mathbf{k}. \tag{16}$$

Eventually, by combining (15) and (16) one obtains

$$|o(\mathbf{r})|^2 = \frac{1}{16\pi^4} \mathscr{F}^{-1} \left\{ \frac{\mathscr{F}\{m(\mathbf{r})\}}{\mathscr{F}\{|a(\mathbf{r})|^2\}} \right\}. \tag{17}$$

where

$$m(\mathbf{r}) = \iint_{-\infty}^{+\infty} \mu(\mathbf{r}, \mathbf{k})\, d\mathbf{k}. \tag{18}$$

The reconstruction of $|o(\mathbf{r})|^2$ from (17) involves a deconvolution, which is inherently ill–posed. In particular, the division in (17) is numerically unstable, especially in the presence of noise and when the denominator assumes small values. Therefore, step (17) is tackled by leveraging the Wiener filter [13]. Accordingly, the deconvolution (17) is regularized as follows

$$|o(\mathbf{r})|^2 = \frac{1}{16\pi^4} \mathscr{F}^{-1} \left\{ \mathscr{F}\{m(\mathbf{r})\} \frac{\mathscr{F}^*\{|a(\mathbf{r})|^2\}}{|\mathscr{F}\{|a(\mathbf{r})|^2\}|^2 + \epsilon} \right\}, \tag{19}$$

where ϵ is a small positive constant introduced to ensure numerical stability and robustness of the inversion [6].

Moreover, the finite support of the measured spatial frequencies $\mathbf{k}$, imposed by the limited angular range $\alpha, \theta \in [0, 2\pi]$, together with the regularization required by the inversion procedure, jointly act as a smoothing operator on the reconstruction.

Therefore, the recovered tomographic reflectivity map should be interpreted as a smoothed estimate of $|o(\mathbf{r})|^2$.

V. Numerical Simulations

To validate the proposed framework, numerical experiments were carried out on noisy scenarios containing extended objects described by the contrast function $o(\mathbf{r})$, considering different Signal-to-Noise ratios.

A. Simulation setup

The investigation domain D is defined as in Section III, with $\ell = 30\,\mathrm{mm}$, in which are located several extended targets: square-shaped and circular-shaped with different size, position and orientation.

The incident field is synthesized by a uniform circular array with $N = 150$ elementary antennas placed on a circumference of radius $\rho = 60\,\mathrm{mm}$. Denoting by $\mathcal{A}\{\cdot\}$ the array radiation operator, the coefficients are computed through the corresponding adjoint operator $\mathcal{A}^\dagger\{\cdot\}$ as

$$I_n = \mathcal{A}^\dagger\{E_{\mathrm{inc}}(\mathbf{r}_s, \mathbf{r})\}, \;\; |\mathbf{r}| \leq 0.9 \cdot \rho \tag{20}$$

where, for a discrete sequence f_n, $\mathcal{A}$ is defined as

$$\mathcal{A}\{f_n\} \coloneqq \sum_{n=0}^{N-1} f_n\, H_0^{(2)}(k\,|\mathbf{r} - \mathbf{r}_n|)\,, \;\; |\mathbf{r}| \leq 0.9 \cdot \rho. \tag{21}$$

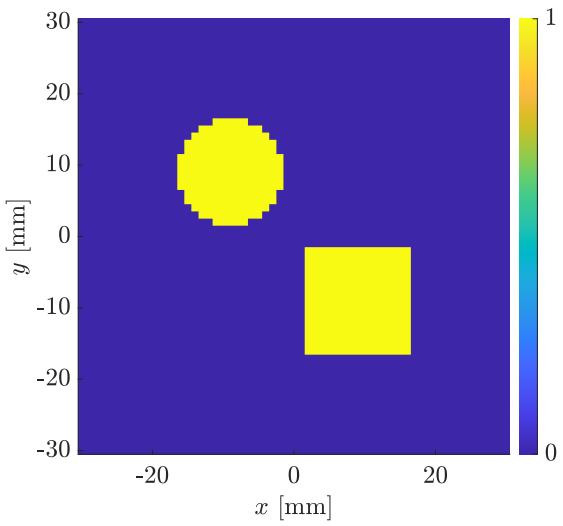

Fig. 2. Picture showing the normalized constrast function $o(\mathbf{r})$ representing the target under investigation.

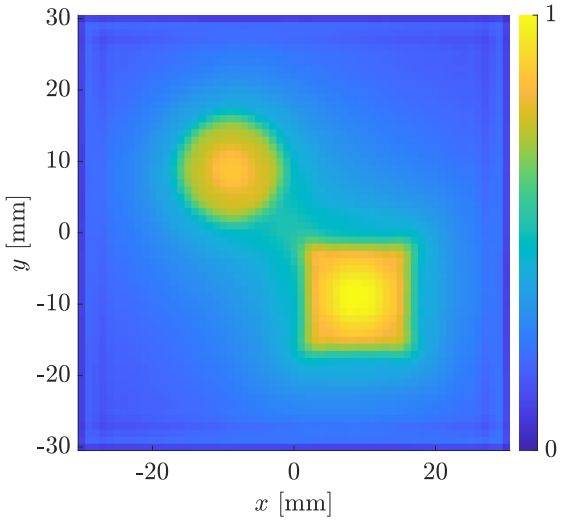

Fig. 3. Picture showing the reconstruction via the proposed phase-space method.

Due to physical constraints, only an approximate realization of (9) can be achieved. For $\sigma = \lambda/\pi$, we obtain the best approximation of the desired incident field. In addition, the selected operating frequency is $f = 50$ GHz.

Concerning the sampling of the intensity data $\mu(\mathbf{r}_s, \mathbf{k})$, it is collected adopting a uniform sampling along observation angle θ and synthesis parameter α, which governs the local plane-wave direction.

Specifically, the sampling steps for θ and α, denoted as δ_θ and δ_α, are both set to $2\pi/120 \approx 0.0524$ rad. The sampling

steps for x_s and y_s, namely δ_x and δ_y, are both set to $2\ell/180 \approx 3 \times 10^{-4}$ m.

Measurement noise is modeled at the *field* level: the scattered field is corrupted by complex additive white Gaussian noise (AWGN) $n(\mathbf{r}_s, \mathbf{k})$ and the intensity-only data are formed as

$$\mu(\mathbf{r}_s, \mathbf{k}) = \left| E_{\text{scat}}(\mathbf{r}_s, \mathbf{k}) + n(\mathbf{r}_s, \mathbf{k}) \right|^2, \tag{22}$$

so that the noise affecting μ is signal-dependent after the magnitude-square operation. In simulations, several signal-to-noise ratio (SNR) between $E_{\text{scat}}(\mathbf{r}_s, \mathbf{k})$ and $n(\mathbf{r}_s, \mathbf{k})$ are considered to assess the proposed strategy.

Reconstructions are performed using the proposed inversion procedure in (19), where ϵ is chosen as a fixed regularization parameter and maintained constant across all simulations.

The normalized scenario under test is reported in Fig. 2. It is assumed that Born approximation is validated. Fig. 3 depicts the reconstruction the constrast, obtained through the proposed stragety (19), with a Signal-to-Noise ration of 20 dB.

VI. Discussion and Conclusions

This paper presented a linear, intensity-only imaging strategy for tomographic reconstruction, based on a phase-space formulation of the inverse scattering problem. By exploiting the relationship between Mark's Physical Spectrum and the Wigner distribution, single-frequency far-field magnitude-squared data are recast into a phase-space inversion problem. The measurements provide a smoothed phase-space representation of the object, which can be inverted via regularized deconvolution to yield tomographic intensity maps, bypassing the nonlinear phase-retrieval procedures typically required in intensity-only imaging.

Numerical simulations under additive noise confirmed that the proposed approach provides meaningful qualitative information on target morphology and relative reflectivity.

Future work includes testing the proposed methods under more challenging scenarios, as well as extending the single-frequency setting to incorporate frequency diversity and structured illuminations, with the goal of further improving reconstruction quality and recovering both the real and imaginary parts of the contrast.

References

[1] M. Soumekh, *Fourier Array Imaging*. Englewood Cliffs, NJ: Prentice Hall, 1994, ISBN: 978-0130660001.

[2] A. J. Devaney, *Mathematical Foundations of Imaging, Tomography and Wavefield Inversion*. Cambridge, UK: Cambridge University Press, 2012, ISBN: 978-0-521-11974-0.

[3] F. Soldovieri and R. Solimene, "Ground penetrating radar subsurface imaging of buried objects," in *Radar Technology*, G. Kouemou, Ed., Rijeka: IntechOpen, 2010, ch. 6. DOI: 10.5772/7176. [Online]. Available: https://doi.org/10.5772/7176.

[4] Y. Wang, W. Wang, M. Zhou, A. Ren, and Z. Tian, "Remote monitoring of human vital signs based on 77-ghz mm-wave fmcw radar," *Sensors*, vol. 20, no. 10, p. 2999, 2020. DOI: 10.3390/s20102999. [Online]. Available: https://doi.org/10.3390/s20102999.

[5] J. W. Goodman, *Introduction to Fourier Optics*, 4th. McMillan Learning, 2017, p. 564, ISBN: 9781319119164.

[6] M. Bertero and P. Boccacci, *Introduction to Inverse Problems in Imaging*, 1st. New York: Springer, 2010.

[7] D. Grischkowsky, S. Keiding, M. van Exter, and C. Fattinger, "Far-infrared time-domain spectroscopy with terahertz beams of dielectrics and semiconductors," *Journal of the Optical Society of America B*, vol. 7, pp. 2006–2015, 1990. DOI: 10.1364/JOSAB.7.002006.

[8] J. E. Pedersen and S. R. Keiding, "Thz time-domain spectroscopy of nonpolar liquids," *IEEE Journal of Quantum Electronics*, vol. 28, no. 10, pp. 2518–2522, Oct. 1992. DOI: 10.1109/3.159511.

[9] M. C. Nuss, P. M. Mankiewich, M. L. O'Malley, E. H. Westerwick, and P. B. Littlewood, "Dynamic conductivity and coherence peak in $YBa_2Cu_3O_7$ superconductors," *Physical Review Letters*, vol. 66, no. 25, pp. 3305–3308, Jun. 1991. DOI: 10.1103/PhysRevLett.66.3305. [Online]. Available: https://link.aps.org/doi/10.1103/PhysRevLett.66.3305.

[10] H. Harde and D. Grischkowsky, "Coherent transients excited by subpicosecond pulses of terahertz radiation," *Journal of the Optical Society of America B*, vol. 8, no. 8, pp. 1642–1651, Aug. 1991. DOI: 10.1364/JOSAB.8.001642. [Online]. Available: https://opg.optica.org/josab/abstract.cfm?URI=josab-8-8-1642.

[11] R. Fukasawa, "Terahertz imaging: Widespread industrial application in non-destructive inspection and chemical analysis," *IEEE Transactions on Terahertz Science and Technology*, vol. 5, no. 6, pp. 1121–1127, 2015.

[12] J. True, C. Xi, N. Jessurun, K. Ahi, and N. Asadizanjani, "Review of thz-based semiconductor assurance," *Optical Engineering*, vol. 60, no. 6, p. 060 901, Jun. 2021. DOI: 10.1117/1.OE.60.6.060901. [Online]. Available: https://doi.org/10.1117/1.OE.60.6.060901.

[13] R. H. T. Bates and M. J. McDonnell, *Image Restoration and Reconstruction*. Oxford: Clarendon Press, 1986.

[14] C. Vogel, *Computational Methods for Inverse Problems*, 1st. Philadelphia: SIAM, 2002.

[15] T. Isernia, F. Soldovieri, G. Leone, and R. Pierri, "On the local minima in phase reconstruction algorithms," *Radio Science*, vol. 31, no. 6, pp. 1887–1899, 1996. DOI: 10.1029/96RS02154.

[16] R. Pierri and R. Moretta, "On data increasing in phase retrieval via quadratic inversion: Flattening manifold and local minima," *IEEE Transactions on Antennas and Propagation*, vol. 68, no. 12, pp. 8104–8113, 2020. DOI: 10.1109/TAP.2020.2998923.

[17] A. Torre, *Linear Ray and Wave Optics in Phase Space*, 2nd. Elsevier, 2019.

[18] M. J. Bastiaans, "Application of the wigner distribution function in optics," W. Mecklenbräuker and F. Hlawatsch, Eds., pp. 375–426, 1997.

[19] B. Boashash, *Time Frequency Signal Analysis and Processing - A Comprehensive Reference*. Elsevier, 2003.

[20] W. C. Chew, *Waves and Fields in Inhomogeneous Media*. New York: IEEE Press, 1995, ISBN: 978-0780310287.

[21] J. E. Moyal and M. S. Bartlett, "Quantum mechanics as a statistical theory," *Mathematical Proceedings of the Cambridge Philosophical Society*, vol. 45, no. 01, p. 99, 1949. DOI: 10.1017/s0305004100000487.

[22] T. A. C. M. Claasen and W. F. G. Mecklenbräuker, "The wigner distribution - a tool for time-frequency signal analysis - part 1: Continuous-time signals," *Philips J. Res.*, vol. 35, pp. 217–250, 1980.

[23] T. A. C. M. Claasen and W. F. G. Mecklenbräuker, "The wigner distribution - a tool for time-frequency signal analysis - part 2: Discrete-time signals," *Philips J. Res.*, vol. 35, pp. 276–300, 1980.

[24] T. A. C. M. Claasen and W. F. G. Mecklenbräuker, "The wigner distribution - a tool for time-frequency signal analysis - part 3: Relations with other time-frequency signal transformations," *Philips J. Res.*, vol. 35:6, pp. 372–389, 1980.

Inverse Profiling of Plasma in Compact Reactor: Actual Challenges and Opportunities

Shaimaa E. Elghetany[1,3,4], M. A. Maisto[2], R. Solimene[2], G. Sorbello[1,5], L. Celona[5], L. Di Donato[1,5]

[1]Department of Electrical, Electronics and Computer Engineering, University of Catania, 95123 Catania, Italy
[2] Department of Engineering of the University della Campania "L. Vanvitelli", 81031, Aversa, Italy
[3] Università degli Studi Mediterranea di Reggio Calabria, DIIES, Reggio di Calabria, 89122, Italy
[4] Faculty of Engineering, Port Said University, Port Said, 42524, Egypt
[5] Laboratori Nazionali del Sud - Istituto Nazionale di Fisica Nucleare, 95123 Catania
*Corresponding author: shaimaa.elghetany@unict.it

***Abstract*—This paper provides a methodical investigation of the main challenges inherent to the one-dimensional inverse scattering problem as applied to plasma profiling, particularly ill-posedness, nonlinearity, and limited data diversity. It explains how these factors impact reconstruction accuracy and presents and compares linearized, iterative, and data-driven strategies to overcome these issues.**

***Keywords*— Inverse Scattering Problem, Microwave and mm-wave Imaging Profiling, Plasma Diagnostics, Machine Learning.**

I. Introduction

The inverse scattering problem (ISP) pertains to identifying the characteristics of an object through the processing of the measured scattered field. Significant applications that can gain efficient electromagnetic imaging techniques based on solving the inverse scattering problem include remote sensing, non-destructive evaluation, geophysics, biological imaging and diagnostics. In this context, non-invasive plasma diagnostics represents an exciting domain where the classical inverse profiling problem can be examined and employed to acquire critical information about the electron density distribution along a designated propagation axis within a plasma region. Both small and large reactors, such as electron cyclotron ion sources (ECRIS) [1] and fusion reactors [2] can take potentially advantages of this approach. The most daunting challenge of an ISP lies in its inherent ill-posedness and non-linearity, which complicates the problem significantly. Although regularization techniques serve as useful solutions for managing ill-posedness, the non-linearity between the data and the unknowns greatly restricts the feasible solutions due to the emergence of false solutions linked to the local minima of the cost function that needs to be minimized. In the case of 1D inverse scattering, this challenge is exacerbated as the non-linearity associated with multiple scattering phenomena within the slab arises as the refractive index of the slab increases relative to the refractive index of the background medium. For this reason, linearized models have been proposed and analyzed. Nevertheless, the primary findings indicate that the challenge of reconstructing an embedded slab (by processing single-view multi-frequency data) is significantly constrained both in terms of the information available (degree of freedom of the scattered field) and the spatial frequency content of the slabs, which can be conveyed back by single-view multi-frequency measured scattered field data [3], [4]. This work provides a comparative review of the key computational strategies utilized for 1D inverse profiling, which include linearized solving methods, iterative field-type algorithmic approaches, and recent data-driven techniques based on ML/DL approaches.

II. Mathematical Formulationethods

Considering the setup of 1D ISP, the unknown slab is characterized by a complex permittivity $\varepsilon(\omega, z)$ and the background medium by a complex dielectric permittivity, ε_b. Plane waves of unitary amplitude illuminate the slab propagating in the positive z-direction at different frequencies, wherein $k_z = \omega_0\sqrt{\mu_0\varepsilon_0\varepsilon_b}$ is the propagation constant. The scattered field data is assumed to be measured at $z^m = z^- \leq 0$ and $z^m = z^+ \geq L$.

The state and data equations, respectively, for the ISP are [5]:

$$E_t(z,\omega) = E_i(z,\omega) + k_z^2 \int_0^L g_i(z,z',\omega)E_t(z',\omega)\chi(z',\omega)dz' \qquad \omega \in \Omega, z \in [0,L] \tag{1}$$

$$E_s(z^m,\omega) = k_z^2 \int_0^L g_e(z^m,z',\omega)E_i(z',\omega)\chi(z',\omega)dz' \qquad \omega \in \Omega, z^m \in [z^- \leq 0 \cup z^+ \geq L] \tag{2}$$

where $\chi(z,\omega) = \frac{\varepsilon(\omega,z)}{\varepsilon_b} - 1$ is the contrast function, the actual unknown and $\Omega = [\omega_1, \omega_2, \omega_3, \cdots, \omega_M]$ is the discrete set of the probing angular frequencies that used to gather field data. For a vacuum homogeneous background medium, $\chi(z,\omega)$ can be written as:

$$\chi(z,\omega) = -\frac{\omega_p^2(z)}{\omega^2 + \nu^2(z)} - j\frac{\omega_p^2(z)\nu(z)}{\omega[\omega^2 + \nu^2(z)]}, \tag{3}$$

In case of high frequency probing regime which can be always satisfied due to the choice of the probing frequency bandwidth with respected to the expected electron density range and losses in the plasma ($\omega >> \nu$), $\chi(z,\omega)$ can be reduced to:

$$\chi(z,\omega) = -\frac{\omega_p^2(z)}{\omega^2} \tag{4}$$

It is worth underlining that the lossless cold plasma permittivity assumption allows one to deal with almost linear model (under BA), otherwise due to the contrast plasma permittivity expression, the data-to-unknowns relationship becomes highly non-linear.

III. Historical Perspectives on Challenges and Solution Strategies in 1D ISP

The development of inverse scattering methodologies has progressed through several phases. Linearized approximations such as the Born and Rytov models were introduced to simplify the nonlinear data–contrast relationship, through their validity was restricted to weak scattering regimes [5]. To address stronger contrasts, iterative nonlinear schemes, including the Born iterative method (BIM) and the distorted Born iterative method (DBIM) [6], were developed, enabling improved accuracy at the cost of increased computational complexity[5]. Also, the sparse approaches based on compressive sensing (CS) involves handling reflected fields across a broad frequency range to improve the reconstruction accuracy [7] also in presence of a reflecting backed plane [8], [9]. However, it reduces actual possibilities for slowly varying profiles. More recently, data-driven techniques, including deep neural networks [10] and physics-informed models [11], have emerged, aiming to enhance reconstruction performance. This evolution reflects a continuous effort to balance physical rigor, numerical stability, and computational efficiency in solving the inverse scattering problem.

IV. Numerical Examples

Resampling expected plasma profiles in a compact-sized ECRIS plasma reactor will be presented at the conference. By underlying the actual possibilities with the available methods.

Acknowledgments

We acknowledge financial support under the National Recovery and Resilience Plan (NRRP), Mission 4, Component 2, Investment 1.1, Call for tender No. 104 published on 2.2.2022 by the Italian Ministry of University and Research (MUR), funded by the European Union – NextGenerationEU– Project Title PLasma Advanced Sensing Methodologies And Reconstructions in Ecr ion sources (PLASMARE) – CUP E53D23001060006 - Grant Assignment Decree No. 960 adopted on 30/06/2023 by the Italian Ministry of Ministry of University and Research (MUR).

References

[1] R. Geller, *Electron cyclotron resonance ion sources and ECR plasmas*. Routledge, 2018.
[2] H.-J. Hartfuss and T. Geist, *Fusion Plasma Diagnostics with mm-waves: an introduction*. John Wiley & Sons, 2013.
[3] R. Pierri, R. Persico, and R. Bernini, "Information content of the born field scattered by an embedded slab: multifrequency, multiview, and multifrequency–multiview cases," *Journal of the Optical Society of America A*, vol. 16, no. 10, pp. 2392–2399, 1999.
[4] A. G. Tijhuis, "Born-type reconstruction of material parameters of an inhomogeneous, lossy dielectric slab from reflected-field data," 12 1987.
[5] M. Pastorino, *Microwave imaging*. John Wiley & Sons, 2010.
[6] S. E. Elghetany, R. Dima, M. A. Maisto, G. Sorbello, and L. D. Donato, "An effective distorted iterative method for inverse profiling of plasma," in *2025 IEEE Conference on Antenna Measurements and Applications (CAMA)*, 2025, pp. 1–3.
[7] L. Di Donato, A. F. Morabito, G. Torrisi, T. Isernia, and G. Sorbello, "Electromagnetic inverse profiling for plasma diagnostics via sparse recovery approaches," *IEEE Transactions on Plasma Science*, vol. 47, no. 4, pp. 1781–1787, 2019.
[8] M. A. Maisto, R. Dima, L. Di Donato, A. Dell'Aversano, R. Solimene, and A. Cuccaro, "Linear one-dimensional inverse profiling: the role of a perfect reflecting plane in the background," *Journal of the Optical Society of America A*, vol. 42, no. 8, pp. 1191–1205, 2025.
[9] L. Di Donato, D. Mascali, A. F. Morabito, and G. Sorbello, "A finite-difference approach for plasma microwave imaging profilometry," *Journal of imaging*, vol. 5, no. 8, p. 70, 2019.
[10] R. Guo, T. Huang, M. Li, H. Zhang, and Y. C. Eldar, "Physics-embedded machine learning for electromagnetic data imaging: Examining three types of data-driven imaging methods," *IEEE Signal Processing Magazine*, vol. 40, pp. 18–31, 3 2023.
[11] A. D. Magdum, H. Shimoga Beerappa, and M. Erramshetty, "Deep learning based distorted born iterative method for improving microwave imaging," *Frequenz*, vol. 78, no. 1-2, pp. 1–8, 2024.

Fault Detection in Antenna Arrays Through Inverse Approaches

Alessandro Fedeli[1], Maryam Iftikhar[1], Andrea Randazzo[1,*]

[1]Department of Electrical, Electronic, Telecommunications Engineering, and Naval Architecture, University of Genoa, Genoa, Italy
*Corresponding author: andrea.randazzo@unige.it

***Abstract*—Fault diagnosis plays a fundamental role in modern antenna array systems. This task can be regarded as an inverse problem, in which, starting from radiated field measurements, the aim is the retrieval of the antenna excitations. In this contribution, recent inversion approaches for addressing such an inverse problem are discussed.**

***Keywords*—Antenna arrays, inverse problems, fault detection.**

I. Introduction

Antenna arrays, thanks to their flexibility and reconfigurability, are important parts of sensing and communication systems [1]. In several applications, the number of elements may be very large, posing the problem of identifying eventually faulty elements, which may degrade radiation properties and negatively affect reconfigurability. Consequently, in the last years, there has been a growing research activity in the development of effective fault detection schemes. In most cases, this operation involves the solution of an inverse problem, in which starting from measurements of the field radiated by the antenna the aim is to reconstruct the antenna current distribution (or some related parameters). However, such an inverse problem is usually strongly ill posed, thus requiring proper regularization approaches.

II. Overview of the Problem

The scenario considered in this paper is schematically shown in Fig. 1. The array under test is composed by N elements with feed coefficients $a_n, n = 1, \dots, N$. The field $\underline{e}_{rad}$ radiated by the array is collected on a measurement plane $\mathcal{M}$. The fault detection problem can be formulated as an inverse problem where, starting from the available measurements, the aim is the reconstruction of the feed coefficients (or aperture field distribution). From such information, and knowing the characteristics of the reference (fully working) array, it is possible to identify the defective elements, adopting proper detection schemes [2]. When full complex data are available, the measured field samples are related to the feed coefficients (or, equivalently, to the tangential field distribution $\underline{e}_{ap}$ over the array aperture) through a linear relationship. However, in several cases, phase information cannot be reliably obtained, especially when high-frequency antennas are concerned. Consequently, the radiation model at hand needs to be modified in order to relate the amplitude-only data to the feed coefficients (or aperture-field distribution), resulting in a non-linear relationship [3]. In both situations, the resulting inverse problems are strongly ill-posed, and, consequently, proper regularizing techniques are needed. In this contribution, fault detection schemes based on regularization schemes in Lebesgue spaces [4] and artificial intelligence paradigms [2] are presented for addressing the previous issues and validation results concerning realistic planar arrays are discussed.

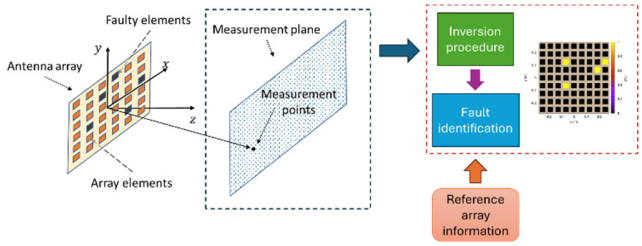

Fig. 1. Array diagnostic configuration.

Acknowledgments

This work was partly supported by the European Union - Next Generation EU under the Italian National Recovery and Resilience Plan (NRRP), Mission 4, Component 2, Investment 1.3, CUP D43C22003080001, partnership on "Telecommunications of the Future" (PE00000001 - program "RESTART").

References

[1] R. Palmeri, G. M. Battaglia, A. F. Morabito, S. Costanzo, F. Venneri, and T. Isernia, "Fault diagnosis of realistic arrays from a reduced number of phaseless near-field measurements," *IEEE Trans. Antennas Propag.*, vol. 71, no. 9, pp. 7206–7219, Sept. 2023.

[2] V. Schenone, A. Fedeli, and A. Randazzo, "An antenna array diagnosis approach based on CNN inversion and CFAR detection," *IEEE Trans. Antennas Propag.*, vol. 73, no. 9, pp. 6252–6262, Sept. 2025.

[3] R. Palmeri, T. Isernia, and A. F. Morabito, "Diagnosis of planar arrays through phaseless measurements and sparsity promotion," *IEEE Antennas Wirel. Propag. Lett.*, vol. 18, no. 6, pp. 1273–1277, June 2019.

[4] V. Schenone, A. Fedeli, C. Estatico, M. Pastorino, and A. Randazzo, "Detection of failures in antenna arrays through a Lebesgue-space approach," *IEEE Open J. Antennas Propag.*, vol. 3, pp. 652–662, 2022.

From UV to Mid-IR: A Broad Spectrum for Innovative Applications

AES 2026 · Catania, Italy · ISSN 2491-2417

Er^{3+} ions luminescence in nanoparticles-doped optical fibers

Nadia G. Boetti[1,*], Zhuorui Lu[2,3], Joris Lousteau[4], Maria Rita Cicconi [5], Franck Pigeonneau [3], Wilfried Blanc[2]

[1]LINKS Foundation, Via Pier Carlo Boggio 61, 10138, Turin, Italy, [2]Université Côte d'Azur, CNRS, INPHYNI, France, [3] MINES Paris, PSL University, CEMEF - Centre for material forming, CNRS UMR 7635, CS 10207, rue Claude Daunesse 06904 Sophia Antipolis Cedex, France [4]DCMC, Politecnico di Milano, Via Edoardo Bassini,6, I-20133 Milano, Italy, [5]Friedrich-Alexander-Universität Erlangen-Nürnberg, Department of Materials Science and Engineering, Institute of Glass and Ceramics, Erlangen, Germany

*Corresponding author: nadia.boetti@linksfoundation.com

***Abstract*—Rare-earth-doped oxide nanoparticles optical fibers offer new opportunities for fiber lasers and amplifiers. Here, we focus on the effects of optical fiber manufacturing conditions on variations in the luminescence properties of Er^{3+} ions.**

***Keywords*— optical fibers, nanoparticles, erbium, luminescence.**

I. Introduction

Since the development of nanoparticles in optical fibers, a major objective has been to modify the luminescence properties of active ions, such as rare earth ions, and transition metals[1]. Indeed, incorporating these ions into nanoparticles with a different composition than the host glass matrix provides a new chemical and structural environment (either amorphous or crystalline). Engineering luminescence properties with this approach would offer new opportunities for fiber optic lasers and amplifiers, such as widening the emission bandwidth or promoting energy transfer processes between luminescent ions, potentially enabling efficient visible light emission.

Among the various existing manufacturing methods, the MCVD (Modified Chemical Vapor Deposition) industrial process has proven particularly interesting for growing nanoparticles in situ in optical fiber preforms through phase separation mechanisms [2]. During this presentation, we will focus in particular on the effects of phase separator concentration (lanthanum ions) and drawing temperature on the emission properties of Er^{3+} ions.

II. Methods

Preforms were prepared using the MCVD process, as previously reported [2]. Lanthanum and erbium chloride salts were dissolved in the doping solution. The doping concentration varied between 0.7 and 0.175 mol/L for $LaCl_3$ and 0.01 mol/l for $ErCl_3$. The draw temperature varied from 1850 to 2050 °C.

III. Results and Discussion

The emission spectra of Er^{3+} ions measured in fibers containing three different concentrations of La are reported in Fig. 1. Reducing the La concentration from 0.7 to 0.35 mol/L only has a minor effect on the shape of the Er^{3+} luminescence spectrum. However, reducing the highest concentration (0.7 mol/L) by a factor of four to 0.175 mol/L alters the shape of the luminescence spectrum. In this presentation, we will discuss these changes in relation to the modification of the environment of the Er^{3+} ions for the different La concentrations and draw temperatures. These results will be compared to those obtained in the preforms.

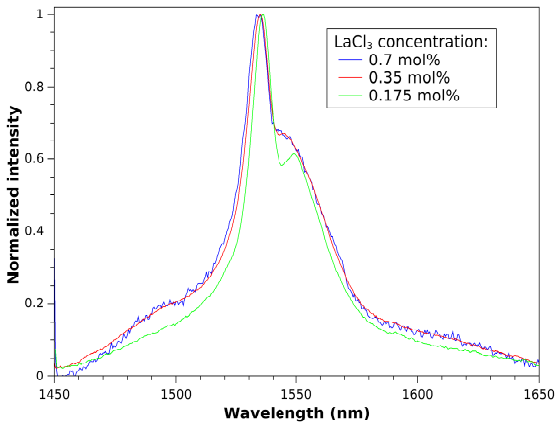

Fig. 1. Er^{3+} emission spectra of nanoparticles-doped optical fibers doped with three different concentrations of $LaCl_3$.

IV. Conclusion

Controlling the concentration of phase-separating elements (here, La) and the draw temperature provides a valuable means of fine-tuning the luminescence properties of rare-earth ions in optical fibres.

References

[1] W. Blanc, D. Tosi, A. Leal-Junior, M. Ferrari, and J. Ballato, "Are low-and high-loss glass–ceramic optical fibers possible game changers?,"*Optics Communications*, vol. 575, pp. 131300, 2025.

[2] W Blanc, V Mauroy, L Nguyen, BN Shivakiran Bhaktha, P Sebbah, BP Pal, B. Dussardier, "Fabrication of rare earth-doped transparent glass ceramic optical fibers by modified chemical vapor deposition," *Journal of the American Ceramic Society*, vol. 94, pp. 2315–2318, 2011.

Development and Integration of Fluoride-Based Fiber Gratings for Mid-IR Photonics

Antreas Theodosiou[1, *]

[1]Photonics Research Center (PRC), Lumoscribe, Paphos, Cyprus
*Corresponding author: theodosiou.antreas@lumoscribe.com

***Abstract*— This work reports on recent advances in the inscription, characterization, and integration of gratings within fluoride and silica fibers. Key developments in inscription techniques, enhanced sensing performance for chemical detection, and splicing methodologies are discussed. The results demonstrate a pathway toward compact, monolithic mid-infrared sensing platforms and fiber laser systems.**

***Keywords*— midIR lasers, fiber lasers, fiber Bragg gratings, long period gratings.**

I. Introduction

Fluoride glass fibers, particularly ZBLAN-(ZrF_4-BaF_2-LaF_3-AlF_3-NaF) and InF_3-based platforms, have emerged as key enabling technologies for exciting applications reaching well beyond the operational transmission window of standard silica fibers. While silica is limited by multi-phonon absorption beyond 2.2 µm, fluoride glasses offer high transparency stretching deep into the mid-infrared (mid-IR) region. Recently, the manufacturing quality of fluoride-based fibers has reached a high level of maturity, enabling unprecedented technological achievements in mid-IR fiber lasers, supercontinuum sources, and chemical sensors.

Despite the excellent passive properties of these fibers, the development of integrated all-fiber components, remains significantly more challenging than in silica. In Near-Infrared (NIR) silica systems, gratings are essential for defining laser cavities and creating high-sensitivity sensors. However, fluoride glasses possess lower glass transition temperatures, different photosensitivity mechanisms, and unique mechanical properties that complicate traditional ultraviolet or femtosecond laser inscription processes. Bridging this gap is critical for transitioning from bulky, free-space mid-IR setups to robust, integrated fiber systems.

II. Methods

This work, summarized recent advances in the inscription, characterization, and integration of various grating structures within both fluoride and silica platforms to push the boundaries of mid-IR photonics. Our research focuses on three primary architectures, *i) Fiber Bragg Gratings (FBGs), ii) Tilted Fiber Bragg Gratings (TFBGs), and iii) Long-Period Gratings (LPGs).*

III. Results

Beyond the inscription process, we address the practical "bottlenecks" of fluoride fiber technology such as strategies for splicing between dissimilar fibers (e.g., fluoride-to-silica), which is vital for protecting the moisture-sensitive fluoride facets and integrating them into existing fiber infrastructures.

Furthermore, system-level implementations are discussed, showcasing how these gratings perform in real-world laser configurations and sensing environments. The results demonstrate that optimized gratings provide enhanced sensitivity for chemical sensing purposes such as liquid sensing and temperature, and tuning mechanism required for the next generation of mid-IR applications, ranging from environmental gas monitoring to surgical laser systems.

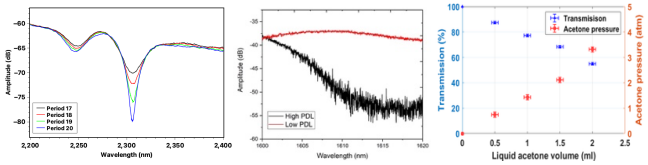

Fig 1: a) transmission spectrum of a fluoride LPG; b) fluoride TFBG PDL; c) acetone absorption using monolithic 3.46 µm fiber laser.

Acknowledgments

This work was co-funded by the European Union and the Research and Innovation Foundation in Cyprus under the grant: SMALL SCALE INFRASTRUCTURES/1222/0234 (WAGES). Support was also provided by the Ministry of Education, Youth and Sports under the Marie Skłodowska-Curie Cz grant agreement No CZ.02.01.01/00/22_010/0001912.

References

[1] A. Theodosiou, Y. Baravets, P. Peterka, "Long period grating in ZBLAN fiber using the *pull-and-heat* method," Opt. Lett. 50, 5678-5681 (2025).

[2] A. Theodosiou, et al., "Understanding the Temperature Conditions for Controlled Splicing Between Silica and Fluoride Fibers. Adv. Photonics Res., 6: 2400150, 2025

[3] A. Theodosiou, O. Henderson-Sapir, Kyriacos Kalli, "Femtosecond laser written ZBLAN tilted fibre Bragg grating for mode-locked mid-infrared laser applications," Proc. SPIE 12573, Specialty Optical Fibres, 1257303 (30 May 2023).

[4] A. Theodosiou, K. Kalli O. Sapir-Henderson, "Acetone Gas Sensing Using a Hybrid Mid-Infrared Fluoride Fiber Laser," in *IEEE Sensors Journal*, vol. 24, no. 13, pp. 20669-20673, 2024

Mid-IR Dispersion Spectroscopy for Liquid Sensing

Bernhard Lendl[1*], Leopold Lindenbauer[1], Mauro David[1], Georg Ramer[1,2], Alicja Dabrowska[1]

[1]Department of Chemical Technologies and Analytics Physics, TU Wien, Vienna, Austria

[2] Christian Doppler Laboratory for Advanced Mid-Infrared Laser Spectroscopy in (Bio-)process Analytics, TU Wien, Vienna, Austria

*Corresponding author: bernhard.lendl@tuwien.ac.at

***Abstract*— A mid-IR laser spectrometer for recording refractive index and absorbance spectra of liquids is presented. It is based on a tunable External Cavity Quantum Cascade Laser and a Mach-Zehnder Interferometer. Results will be shown on the analysis of phosphate and sugars in aqueous solution and compared to established FTIR spectrometry.**

***Keywords*— Quantum Cascade Lasers, Mach Zehnder interferometer, liquid sensing.**

I. Introduction

Mid-IR quantum cascade lasers (QCLs) are increasingly used as light sources in mid-IR spectroscopy. QCLs offer high spectral power densities, fast amplitude and frequency modulation possibilities, polarized and coherent radiation. Based on these properties new sensing schemes can be developed. In our work we exploit the coherence of EC-QCLs to measure refractive index as well as absorbance spectra of liquids using a Mach Zehnder Interferometer (MZI). This presentation will show results on the analysis of phosphate, ethanol and sugars in aqueous solution and compare the obtained figures of merit to those obtained using established FTIR spectroscopy.

II. Methods

A schematic layout of the spectrometer is shown in Fig.1. The liquid cells for the reference and the sample are made of 1mm CaF_2 windows and have an optical pathlength of 120 µm.

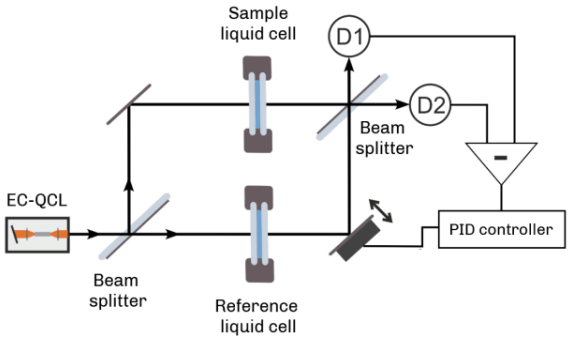

Fig. 1 Layout of the Mach Zehnder Interferometer for liquid sensing.

As the pulsed operated laser (Hedgehog from DRS Daylight Solutions, San Diego, CA) is tuned the two beams encounter different refractive indexes in the two liquids (reference and sample) leading to a phase shift between the two arms. This occurs due to anomalous dispersion in the sample. The introduced phase shift is constantly compensated by moving a mirror in one arm of the MZI, which is mounted on a piezo-element. The MZI is locked to its quadrature point by using a PID controller, and the intensities at both TE-cooled MCT detectors (VIGO, Warsaw, Poland) are recorded and registered as a function of mirror displacement at every laser wavelength. From these data the refractive index as well as absorbance spectra can be calculated.

III. Results and Discussion

As an example, the obtained refractive index as well as absorbance spectra of phosphate in aqueous solution are shown in Fig.2.

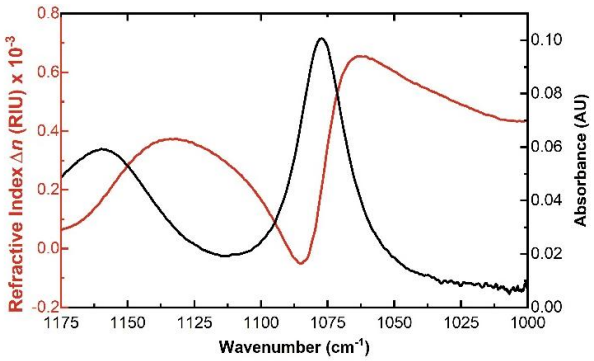

Fig. 2 IR spectra of phosphate (1g/L, pH=5).

The advantages of dispersion spectroscopy compared to established absorption spectroscopy based on Beer´s law are: i) immunity to intensity noise of the laser source, ii) background free measurements, iii) constant sensitivity over a large concentration range and iv) increased pathlength. These fundamental properties will be explained using data from the measurement of aqueous ethanol solutions of different concentrations [1,2]. Furthermore, results will be shown on the investigation of the invertase catalyzed hydrolysis of sucrose

into α-D glucose and fructose. In addition to the split of the disaccharide into the two monosaccharides also the ensuing mutarotation reactions of the two monosaccharides are clearly visible in the recorded time resolved dispersion spectra. A detailed analysis of the recorded time resolved spectra using two dimensional correlation analysis (2DCoS) will be shown by presenting synchronous as well as asynchronous correlation maps [3].

IV. Conclusion

We introduce a new sensing modality for liquids that exploits the coherent nature of mid-IR laser sources. This new sensing scheme is based on phase resolved instead of intensity resolved spectroscopy and as such will allow for different optimization strategies to be implemented than established absorption spectroscopy based on Beer´s law.

Acknowledgments

This work was supported by the European Union within the projects M3NIR, dAIry4.0 (no. 101093008 and 101119714). The financial support by the Austrian Federal Ministry of Labour and Economy, the National Foundation for Research, Technology and Development and the Christian Doppler Research Association is gratefully acknowledged.

References

[1] A. Dabrowska, S. Lindner, A. Schwaighofer, B. Lendl, „Mid-IR Dispersion Spectroscopy – A New Avenue for Liquid Phase Analysis" Spectrochimica Acta Part A: Molecular and Biomolecular Spectroscopy, vol 286, pp. 122014, 2023.

[2] T. G. Mayerhoefer, A. Dabrowska, A. Schwaighofer, B. Lendl, J. Popp "Beyond Beer's Law: Why the Index of Refraction Depends (Almost) Linearly on Concentration" ChemPhysChem vol 21, pp. 707 –711, 2020.

[3] A. Dabrowska, A. Schwaighofer, B. Lendl, "Mid-Infrared dispersion spectroscopy as a tool for monitoring time-resolved chemical reactions on the examples of enzyme kinetics and mutarotation of sugars" Applied Spectroscopy vol 78(9), 982-992, 2024.

Hybrid laser integration for sensing application

Nicola Maraviglia[1,2 *], Davide Monopoli[1,2,3], Artem S. Vorobev[1,2], Fatih B. Atar[1], Natale G. Pruiti[4], Giovanna Calò[3], Simone Iadanza[5,6], Marc Sorel[4,7], Brian Corbett[1], Liam O'Faolain[1,2*].

[1]Center for Advanced Photonics and Process Analysis, Munster Technological University, Ireland
[2] Tyndall National Institute, Ireland
[3]Department of Electrical and Information Engineering, Polytechnic University of Bari, Italy
[4]School of Engineering, University of Glasgow, UK
[5]Laboratory of Nano and Quantum Technologies, Paul Scherrer Institut, Switzerland
[6]Laboratory of Integrated Nanoscale Photonics and Optoelectronics, École Polytechnique Fédérale de Lausanne, Switzerland
[7]Institute of Technologies for Communication, Information and Perception (TeCIP), Sant'Anna School of Advanced Studies, Italy
*Corresponding author: nicola.maraviglia@mtu.ie ; William.Whelan-Curtin@mtu.ie

***Abstract*— We present a selection of lasing systems obtained by hybrid integration of silicon nitride photonic chips with III-V semiconductor optical amplifiers. On-chip side-coupled Fabry Perot cavities are used to control the wavelength of the laser emission and narrow its linewidth. The adoption of micro transfer-printing further improves the mechanical stability of the whole system, making it suitable for thermal and chemical sensing applications.**

***Keywords*— hybrid integration, photonics, sensing, external cavity laser.**

I. Introduction

Photonic integrated circuits (PICs) are bringing the high accuracy of optical sensing into handheld and portable devices. Recently, the hybrid integration of silicon-based PICs with direct band gap III-V semiconductor components allowed the realization of compact external cavity lasers that provide improved linewidth performance [1], together with added functionalities such as microwave generation [2]. Here we present recent advances in hybrid external cavity lasers realized with integrated side-coupled Fabry-Perot and micro transfer-printed (µTPed) reflective semiconductor optical amplifier (rSOA) coupons acting as gain medium. The lasing devices are tested as sensor for refractive index changes induced by variations of the environment.

II. Methods

Side-coupled Fabry-Pérot (SCFP) cavities are defined in a 300 nm thick silicon nitride layer on top of 1.5 µm bottom oxide cladding over a silicon substrate. Distributed Bragg gratings are used as cavity reflectors and the resonant modes evanescently couple to a laterally adjacent waveguide that is then connected to the gain section heterogeneously integrated on the PIC via µTP. This integration technique allows the fabrication of the desired rSOA coupons with angled facets on a separate epitaxially grown multi-quantum-well wafer. These are then transferred on the desired PIC with a pick and place technique based on elastomeric stamps [2]. To favor efficient heat dissipation and a better alignment between the butt coupled rSOA and the SiN waveguide, the bottom oxide is selectively removed in the region of the PIC where the gain section will be transferred. The mode coupling between the rSOA and the SiN waveguide is mediated by an SU8 waveguide. The extended cavity originated by the reflection form the SCFP and the back mirror of the rSOA induces laser emission restricted at the wavelengths resonant with the SCFP.

III. Results and Discussion

The hybrid laser obtained via µTP showed narrower linewidth a greater stability than equivalent lasers obtained with same PIC designs and butt-coupled to commercial rSOA dies, while also reducing the setup complexity. We monitored the heterodyne interference of the integrated laser against an external bench-top reference laser to monitor changes in the local environment.

Acknowledgments

This work has received funding in part by the Science Foundation Ireland under Grant SFI 2/RC/2276_P2 IPIC and the European Innovation Council under grant agreement No. 101214114.

References

[1] F. B. Atar *et al*., "On-Chip Microwave Photonic System Through Multi-Component Micro-Transfer Print Integration," *2024 International Topical Meeting on Microwave Photonics (MWP)*, 2024, pp. 1-4,
[2] C. Chen *et al.*, "Hybrid integrated Si3N4 external cavity laser with high power and narrow linewidth," Opt. Express 31, 26078-26091 (2023).

Development of Mid-Infrared Lasers in Fluoride Glasses with Positive Index Waveguides

O. Henderson-Sapir[1,2,3,4,*], D. G. Lancaster[1,3], D.J. Ottaway[1,2], H Ebendorff-Heidepriem[1,3] T. T, Fernandez[1,3]

[1] Institute for Photonics and Advanced Sensing, School of Physics, Chemistry and Earth Sciences, The Adelaide University, Australia
[2] Australian Research Council, Centre of Excellence for Gravitational Wave (OzGrav), Australia
[3] Australian Research Council COMBS Centre of Excellence, Australia
[4] Mirage Photonics, Australia

*Corresponding author: ori.henderson-sapir@adelaide.edu.au

***Abstract*— Preliminary results in mid-infrared Er:ZBAN glass waveguide lasers using positive index modifications are presented. Single and dual-wavelength pumping are resulting with mid-IR fluorescence. Combined with numerical modelling, we demonstrate the first steps towards compact, mid-IR, integrated glass waveguide laser sources at 2.8 µm and 3.5 µm.**

***Keywords*— Mid-IR, Waveguide lasers, fs-writing, Er:ZBLAN**

I. Introduction

Mid-infrared (mid-IR) fibre lasers have gained increasing prominence in areas such as molecular spectroscopy, environmental monitoring, and materials processing, largely due to their alignment with fundamental vibrational absorption bands. Although glass-based waveguide laser cavities offer strong promise in this wavelength range, experimental demonstrations have so far been limited to wavelengths below 2.9 µm [1]. This limitation is primarily attributed to the low numerical aperture (NA) achievable in depressed-cladding architectures fabricated from conventional ZBLAN glass, which constrains the minimum attainable core dimensions [2]. Recently, Fernandez et al. [3] reported localized positive refractive index modifications in ZBAN fluoride glass with substantially higher NA, enabling the first demonstration of stable type I waveguides and marking a significant step towards integrated mid-IR photonic devices.

II. Methods

A numerical modelling framework developed at the University of Adelaide [4], previously applied to 2.8 µm fibre lasers and dual-wavelength-pumped systems operating at 3.5 µm [5], was employed to assess the feasibility of a waveguide laser based on a positive refractive index modification (Fig. 1). The simulations assumed a 28 mm long waveguide written in 6 mol % erbium-doped ZBAN glass, with core diameters spanning 5–60 µm and a numerical aperture of 0.2. Pumping

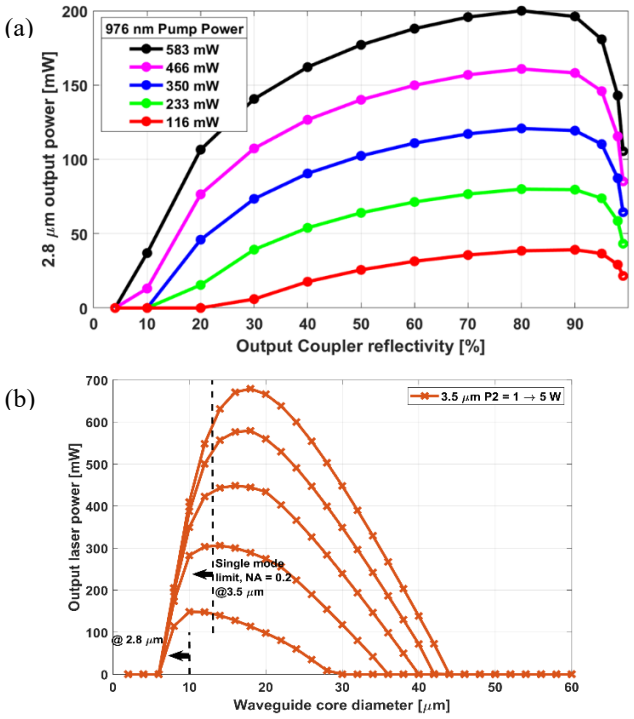

Fig. 1 (a) Simulated 2.8 µm and (b) 3.5 µm laser output power as a function of 976nm (for 2.8 µm) and both 976 nm and 1973 nm (P2) pumps for 3.5 µm. Simulation uses currently available pump powers in our setup of 0.58 W at 976 nm and 5W of 1973 pump incident. NA=0.2 and 90% reflective output coupler. 15 µm core diameters were assumed for the 2.8 µm waveguide laser operation.

conditions were selected to reflect practical availability, comprising up to 583 mW at 976 nm and 5 W at 1973 nm, together with an output coupler reflectivity of 90 %. The modelling predicted maximum performance for a 15 µm diameter waveguides with output powers approaching 200 mW at 2.8 µm and exceeding 600 mW at 3.5 µm, indicating strong performance potential for this waveguide architecture.

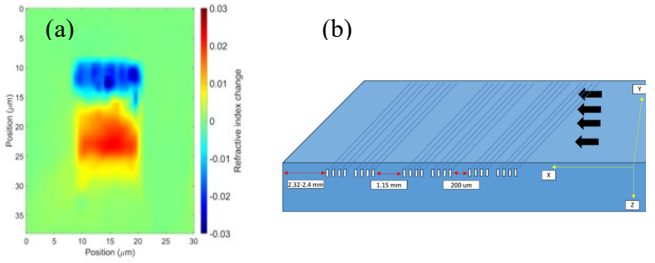

Fig. 2 (a) Positive (red) waveguide written into ZBAN glass. (b) Full waveguide configuration in glass slab.

Building on our previous demonstrations of depressed-cladding waveguides in ZBLAN glass [2], this work transitioned to femtosecond-laser-written positive refractive index modifications in ZBAN glass, as shown in Fig. 2, with the aim of achieving laser emission at 2.8 µm and 3.5 µm.

Bulk Er:ZBAN glass (note the removal of Lanthanum from standard ZBLAN composition), doped with 6 mol % Er3+ and having a nominal composition of 48 ZrF4 – 20 BaF2 – 4 AlF3 – 20 NaF – 6 ErF (mol %), was fabricated in-house. The samples were subsequently polished and laser processed to form waveguides approximately 28 mm in length, with guiding core dimensions in the range 9–15 µm.

Waveguides were fabricated using a line-by-line inscription technique, in which refractive index modification was achieved by stacking multiple 1 µm-wide tracks written side-by-side, Fig 2(a). Both positive (blue) and negative (red) refractive index changes were produced, as characterised using a Rinck refracted near-field profilometer, with effective mode confinement arising from the positive index modification.

The waveguide laser systems shown schematically in Fig. 3,

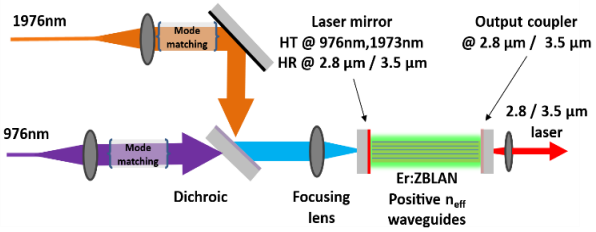

Fig. 3 Waveguide laser experimental setup layout.

employed similar linear resonator configurations for operation at 2.8 µm and 3.5 µm. For 2.8 µm operation, pumping was provided by a single-mode, fibre-coupled 976 nm diode laser. In the dual-wavelength-pumped configuration for 3.5 µm emission [5], an additional 1973 nm pump source was introduced concurrently. Distinct sets of resonator mirrors were used for the two wavelength regimes to enable appropriate transmission of the pump wavelengths and to provide suitable output coupler reflectivities at 2.8 µm and 3.5 µm [2,5]. Waveguide emission output characteristics were evaluated using a monochromator, thermal camera, and a power meter.

III. Results and Discussion

As illustrated in Fig. 4(a,b), strong green and red fluorescence are observed from the waveguide when pumped at 976 nm and

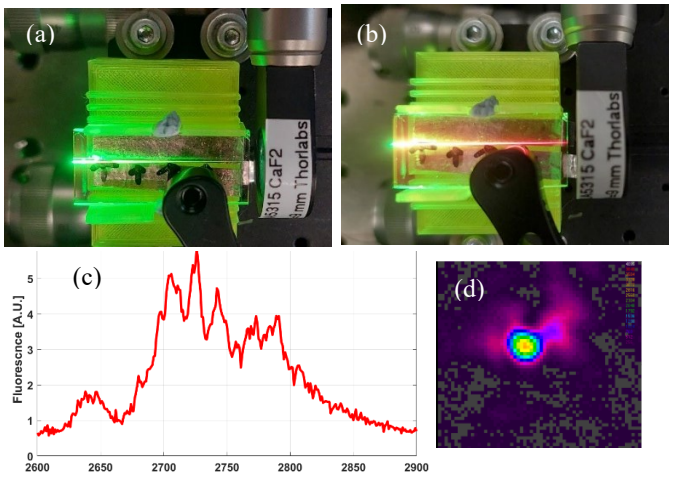

Fig. 4 (a) Green fluorescence under 976 nm pumping (b) Red fluorescence under 976 nm + 1973 nm pumping. (c) 2.8 µm fluorescence from the waveguide under 976nm pumping. (d) 3.5 µm confined mode in the waveguide.

976 nm + 1973 nm, respectively, indicating effective absorption of the 976 nm pump leading to 2.8 µm fluorescence seen in Fig 4(c), and excited-state absorption and excitation to the $^4S_{3/2}$ level causing the green fluorescence. When both pumps operate concurrently, we observe efficient population of the $^4F_{9/2}$ energy level required for 3.5 µm emission, as well as effective optical transmission through the written waveguides. A clear, confined and guided mode is observed when a 2 µm, or 3.5 µm laser beams from a Mirage Photonics laser are launched into the waveguide, Fig 4(d).

IV. Conclusion

We report the initial demonstration of positive refractive index waveguides in Er:ZBLAN glass, exhibiting both visible and mid-infrared fluorescence. Detailed waveguide characterisation will be presented, along with results obtained on the path towards achieving lasing from these structures.

Acknowledgments

This work was performed in part at the Opto-Fab node of the Australian National Fabrication Facility supported by the Commonwealth and SA State Government. The authors acknowledge the support from the Commonwealth of Australia through an Australian Research Council (ARC) Discovery Grant No. DP220102516 and Centre of Excellence Grant Nos. CE230100016, CE230100006. TTF, DL acknowledge support received from Electro Optic Systems Pty. Limited.

References

[1] Lancaster, D. G. et al., An Ultra-Stable 2.9 µm Guided-Wave Chip Laser and Application to Nano-Spectroscopy. APL Photonics 2019, 4 (11), 110802.

[2] Henderson-Sapir, O., et al. Mid-Infrared Er3+:ZBLAN Waveguide Using ZBLAN Glass Extrusion, Femto-Second Inscription and Dual-Wavelength Pumping for the Generation of 3.5 µm Lasing. in 2020 22nd International Conference on Transparent Optical Networks (ICTON). 2020.

[3] Fernandez, T.T., et al., Ultrafast Laser-Fabricated Fluoride Glass Waveguides with Exceptionally High Refractive Index Change for Mid-Infrared Integrated Opt.. Exp., 2024, 32(24): p. 42938-42950.
[4] Henderson-Sapir, O., D. Beniwal, and D.J. Ottaway. Numerical optimization of high power 3.5 μm erbium-doped mid-infrared fiber laser and amplifiers. in Proceedings of SPIE - The International Society for Optical Engineering. 2022.
[5] Henderson-Sapir, O., J. Munch, and D.J. Ottaway, Mid-infrared fiber lasers at and beyond 3.5um using dual-wavelength pumping. Opt. Lett., 2014. 39(3): p. 493-496

Fluoride all-Fibre Lasers: Opportunities and Challenges

Kirill Grebnev, Maria Chernysheva*

Leibniz Institute of Photonic Technologies, Germany
*Corresponding author: chernyshevamaria@ipht-jena.de

***Abstract*— While only a few laser technologies have matured beyond the near-IR window, fluoride fibres enable broadband operation from visible to mid-IR. Along with new design opportunities, they also introduce distinct material and engineering challenges. This talk analyses the physical constraints and cavity design strategies toward spectrally versatile, fully fibre-integrated systems. .**

***Keywords*— optical fibers, fiber lasers**

Harnessing a mid-IR wavelength range has become an urgent challenge as it can enable the accurate detection of molecular vibrational modes in biological tissues, lying, for example, at around 3 μm (C-H, N-H, O-H stretches). Thus, since the 2000s, Mid-IR light sources and sensors have become an object for extensive research and industrial interest, also triggered by high demand for greenhouse gases and pollutants monitoring, optical frequency standards for global positioning systems and optical clocks, free space and fibre optic communications, LIDAR systems, medical diagnostics and surgery. A few mid-IR laser technologies have reached maturity, such as optical parametric oscillators, bulk Cr/Fe-doped solid-state lasers, sources employing nonlinear effects, such as supercontinuum generation or soliton-self-frequency shift, and quantum cascade lasers (QCLs). Fibre-based laser systems present a more promising platform compared to QCLs due to their high stability, cost-effectiveness, and flexibility in output parameters. Unfortunately, the silica fibre technology is not a remedy for all photonics applications and demonstrates strong attenuation beyond 2.5 μm.

Similarly, the development of visible fibre lasers is strategically important, as it extends the robustness and integration advantages of fibre technology into a spectral region traditionally dominated by bulk solid-state systems in applications ranging from bioimaging and precision spectroscopy to quantum optics and nonlinear frequency conversion.

Unique soft-glass materials have to replace silica fibres to expand beneficial fibre optics platforms towards the visible and Mid-IR wavelength range [1,2]. Recent works of the research community have demonstrated great success in the first fluoride and chalcogenide fibre-based ultrafast laser systems operating beyond 2.8 μm[3] and a range of visible transitions [4]. Still, currently deployed systems rely on free-space coupling from bulk laser components into an active fibre [5,6]. This approach drastically limits the possibilities of manipulating the dynamics of ultrashort pulses. The translation to soft glass materials does not call for a straightforward engineering solution, yet brings forth immersing fundamental and methodological gaps due to drastically different material, thermal and chemical properties.

The talk will discuss the choice of gain media with an operational wavelength range across 2.8 – 5 μm of rare earth elements, chemical, optical and mechanical properties of soft glass fibres, followed by the development of efficient novel fibre arrangements and laser components for Mid-IR and Vis wavelength ranges. Overall, the talk will provide a promising outlook for the exploration of laser generation regimes and flexible fibre laser designs, significantly surpassing the performance of semiconductor laser systems.

References

[1] G. Tao, et al. “Infrared fibres,” Advances in Optics and Photonics 7(2) 379-458 (2015)
[2] A. B. Seddon, et al. “Short review and perspective: Chalcogenide glass mid-infrared fibre lasers,” European Physical Journal Plus 139, 1–10 (2024)
[3] F. Jobin, et al, “Recent developments in lanthanide-doped mid-infrared fluoride fiber lasers (invited),” Optics Express 30, 8615–8640 (2022)
[4] E. Kifle, et al. “Recent progress in visible fluoride fiber lasers,” in Proc. Fiber Lasers and Glass Photonics: Materials through Applications IV, 13003, 55-65 (2024).
[5] S. D. Jackson “Mid-infrared fiber laser research: Tasks completed and the tasks ahead,” APL Photonics 9, 070904 (2024)
[6] K. Grebnev, et al. “Fluoride and chalcogenide glass fiber components for mid-infrared lasers and amplifiers: Breakthroughs, challenges, and future perspective,” APL Photonics 9, 110901 (2024)

Hollow-Core Optical Fibers: Guiding Light from UV to Mid-IR and Beyond

Luca Vincetti

Department of Engineering "Enzo Ferrari", University of Modena and Reggio Emilia, Italy
luca.vincetti@unimore.it

***Abstract*— Hollow-core fibers offer unprecedented broadband light guidance from UV to mid-IR. By minimizing material interaction and enabling tunable light–matter interaction, they overcome conventional fiber limitations. This talk highlights design principles, loss-engineering strategies, and transformative applications in high-power delivery, gas photonics, classical and quantum optical communications.**

***Keywords*— hollow-core fibers, UV, mid-IR, terahertz.**

I. CONTENT

It is increasingly recognized within the optical fiber community that Hollow-Core Fibers (HCFs) represent one of the most significant innovations in photonics over the past decades. Although the pursuit of hollow-core guidance dates back to the early days following the advent of the laser [1], and was revitalized at the beginning of this century with the introduction of photonic crystal fibers [2], it is only since the 2010s that these fibers have begun to gain practical relevance thanks to the introduction of a novel confinement mechanism known as inhibited coupling [3]. Hollow-core fibers exploiting Inhibited Coupling (IC-HCFs), also referred to as Anti-Resonant fibers (AR-HCFs), are now emerging as a transformative technology across multiple areas of photonics, including laser manufacturing [4], gas lasers [5] gas-based photonics [6], optical communications [7], and quantum photonics [8]. By virtue of their hollow core, these fibers enable, on one hand, the minimization of light–material interaction with the solid microstructured cladding, thereby decoupling the transmission properties from those of the host material. On the other hand, filling the core with appropriate gases or liquids can significantly enhance light–matter interactions compared to free-space propagation. This dual capability makes IC-HCFs highly versatile and competitive relative to conventional solid-core technologies.

This work analyzes the various mechanisms that make these fibers particularly attractive [9]. Special emphasis is placed on confinement loss, which constitutes the ultimate limitation in terms of attenuation for these fiber types. The most recent theoretical and semi-analytical models applied to different IC-HCF architectures are presented, including tube lattice fibers (TLFs) [10], nested anti-resonant nodeless fibers (NANFs) [11], and Hybrid lattice Fibers (HFs) [12]. The discussion highlights how the engineering of key geometric parameters—such as core diameter, capillary wall thickness, and the presence of nested elements—directly affects confinement losses, bending sensitivity, dispersion, and the spectral transmission window [13-15]. These models provide design-relevant scaling laws, reducing reliance on computationally intensive finite-element method (FEM) simulations and enabling a more physically intuitive design approach. This methodology has proven particularly effective in optimizing transmission performance over spectral ranges extending from the ultraviolet (UV) to the visible, near-infrared (NIR), and mid-infrared (Mid-IR), up to Terahertz (THz) regions. In addition, various loss-engineering strategies aimed at minimizing the principal sources of attenuation—including cladding leakage, surface scattering, and bending-induced losses—are discussed. Finally, the presentation addresses several key applications enabled by hollow-core anti-resonant fibers, demonstrating their transformative potential across modern photonics.

REFERENCES

[1] E. A. J. Marcatili and R. A. Schmeltzer, "Hollow metallic and dielectric waveguides for long distance optical transmission and lasers," Bell Syst. Tech. J., vol. 43, pp. 1783–1809, 1964.

[2] R.F. Cregan, B.J. Mangan, J.C. Knight, T.A. Birks, P.S.J. Russell, P.J. Roberts, D.C. Allan, "Single-Mode Photonic Band Gap Guidance of Light in Air," Science vol. 285, pp. 1537–1539, 1999.

[3] Y.Y. Wang, N.V. Wheeler, F. Couny, P.J. Roberts, F. Benabid, "Low loss broadband transmission in hypocycloid-core Kagome hollow-core photonic crystal fiber," Opt. Lett. Vol. 36, pp. 669–671, 2011.

[4] B. Debord, A. Amsanpally, M. Alharbi, L. Vincetti, J. Blondy, F. Gerome, and F. Benabid, "Ultra-large core size hypocycloid-shape inhibited coupling kagome fibers for high-energy laser beam handling," J. Lightwave Technol., vol. 33, pp. 3630–3634, 2015.

[5] A. V. V. Nampoothiri, A. M. Jones, C. Fourcade-Dutin, C. Mao, N. Dadashzadeh, B. Baumgart, Y. Wang, M. Alharbi, T. Bradley, N. Campbell, F. Benabid, B. R. Washburn, K. L. Corwin, and W. Rudolph, "Hollow-core optical fiber gas lasers (hofglas): a review," Opt. Mater. Express, vol. 2, pp. 948–961, 2012.

[6] B. Debord, F. Amrani, L. Vincetti, F. Gérome, and F. Benabid, "Hollow-core fiber technology: The rising of "gas photonics"," Fibers, vol. 7, 2019.

[7] M. Petrovich, E.. Fokoua, Y. Chen, et al. Broadband optical fibre with an attenuation lower than 0.1 decibel per kilometre. Nat. Photon. 19, 1203–1208 (2025).

[8] M. Antesberger, C. M. D. Richter, F. Poletti, R. Slavık, P. Petropoulos, H. Hubel, A. Trenti, P. Walther, and L. A. Rozema, "Distribution of telecom entangled photons through a 7.7 km antiresonant hollow-core fiber," Optica Quantum, vol. 2, no. 3, pp. 173–180, Jun 2024.

[9] L. Vincetti, "Empirical formulas for calculating loss in hollow core tube lattice fibers," Opt. Express, vol. 24, no. 10, pp. 10 313–10 325, 2016.

[10] L. Vincetti, V. Setti, and M. Zoboli, “Terahertz tube lattice fibers with octagonal symmetry,” IEEE Photonics Technology Letters, vol. 22, no. 13, pp. 972–974, 2010.
[11] F. Poletti, “Nested antiresonant nodeless hollow core fiber,” Opt. Exp., vol. 22, pp. 23807–23828, 2014.
[12] F. Amrani et al., “Low-loss single-mode hybrid-lattice hollow-core photonic-crystal fibre,” Light Sci. Appl., vol. 10, 2021.
[13] L. Vincetti and L. Rosa, “A simple analytical model for confinement loss estimation in hollow-core tube lattice fibers,” Opt. Exp., vol. 27, pp. 5230–5237, 2019.
[14] L. Rosa, F.Melli, and L. Vincetti, “Analytical formulas for dispersion and effective area in hollow-core tube lattice fibers,” Fibers, vol. 9, 2021.
[15] F. Melli, L. Rosa and L. Vincetti, "Analytical Formulas for Micro-Bending and Surface Scattering Loss Estimation in Tube Lattice Fibers," J. Lightwave Technol., vol. 41, pp. 5714-5721, 2023.

Germanate Glass as a Versatile Platform for Efficient 2 µm Laser Sources

Nadia G. Boetti[1], Guy Shafriri[2], Amiel Ishaaya[2], Martha Segura[3], Davide Janner[4], Simone Normani[5], Pavel Loiko[5], Venkatesan Jambunathan[5], Alain Braud[5], Patrice Camy[5], Joris Lousteau[6]

[1]Fondazione LINKS, Via Pier Carlo Boggio 61, 10138, Torino, Italy
[2] School of Electrical and Computer Engineering, Ben-Gurion University of Negev, Beer-Sheva 8410501, Israel
[3] Universitat Rovira i Virgili (URV), E-43007 Tarragona, Spain
[4] DISAT-Politecnico di Torino, C.so Duca degli Abruzzi 24, 10129 Torino, Italy
[5] CIMAP, UMR 6252 CEA-CNRS-ENSICAEN, Université de Caen Normandie, 6 Boulevard Maréchal Juin, 14050 Caen, France
[6]DCMC, Politecnico Di Milano, Via Edoardo Bassini, 6, Milano, I-20133, Italy

*Corresponding author: nadia.boetti@linksfoundation.com

***Abstract*— Germanate glass is investigated as a host material for laser sources operating near 2 micrometers. Its infrared transparency, high rare earth solubility, and good thermal stability enable efficient emission. Bulk and fiber laser demonstrations with thulium and holmium doping confirm the suitability of this glass system for eye-safe laser applications.**

***Keywords*— germanate glass, rare earth doped glass, holmium, thulium, fiber laser, 2 µm lasers, eye safe lasers**

I. Introduction

Laser sources operating in the 2 µm spectral region are attracting increasing attention for applications in medicine, environmental sensing, spectroscopy, and defense, where eye-safe operation and favorable atmospheric transmission are key requirements [1]. Among the available host materials, oxide glasses offer broad emission bandwidths, flexible geometries, and cost-effective processing compared to crystalline systems. In this context, germanate glass represents a particularly promising platform due to its relatively low phonon energy, wide infrared transparency window (0.4 to 4.5 µm), and high rare earth (RE) ion solubility (up to 10^{21} ions/cm^3) [2]. These features support efficient emission from thulium (Tm^{3+}) and holmium (Ho^{3+}) ions in the 2 µm region, while enabling both bulk and fiber laser configurations. Moreover, germanate glass exhibits exceptional resistance to laser-induced damage, ensuring robustness for high-power operation.

In this work, a custom GeO_2-based germanate glass system designed for RE doping is investigated. The material was synthesized, thermally characterized, and processed into both bulk samples and optical fibers. Laser experiments with Tm^{3+} and Ho^{3+} doping are presented to validate the suitability of this glass composition for efficient 2 µm laser sources.

II. Methods

Two germanate glasses (GeO_2–PbO–ZnO–Nb_2O_5–Na_2O–Gd_2O_3) were synthesized by the standard melt-quenching technique using high-purity (99+%) chemicals, one doped with Tm^{3+} and one with Ho^{3+} ions, both at a concentration of 2.6×10^{20} ions/cm^3. The chemicals were weighed and mixed in a dry box to minimize hydroxyl ion (OH^-) content. Melting was carried out at 1200 °C for 2 h in a chamber furnace under controlled dry atmosphere (water content <3 ppm), followed by casting into a preheated brass mold and annealing near the glass transition temperature for 5 h. Flat specimens were cut and optically polished for characterization.

Density was measured by the Archimedes method. Thermal properties, including glass transition temperature (T_g) and crystallization onset temperature (T_x), were determined by differential thermal analysis (DTA). The refractive index was measured by prism-coupling technique. Continuous-wave photoluminescence spectra were acquired using a Jobin Yvon iHR320 spectrometer equipped with a Hamamatsu P4631-02 detector, exciting the samples at 794 nm for Tm^{3+} and 450 nm for Ho^{3+}. Fluorescence lifetimes were obtained by exciting with light pulses and fitting the decay traces with a single exponential function.

For fiber fabrication, a preform was prepared using the rod-in-tube method (see Fig. 1) and drawn on an in-house induction-heated drawing tower, yielding a 45/125 µm core/cladding Ho:Germanate fiber.

Laser experiments were carried out in two configurations: a 3 mm Tm^{3+}-doped bulk sample end-pumped by a Ti:Sapphire laser at 792 nm, and the Ho:Germanate fiber integrated into a linear cavity and in-band pumped by an all-fiber Tm-doped fiber laser operating at 1931 nm with up to 15 W output power.

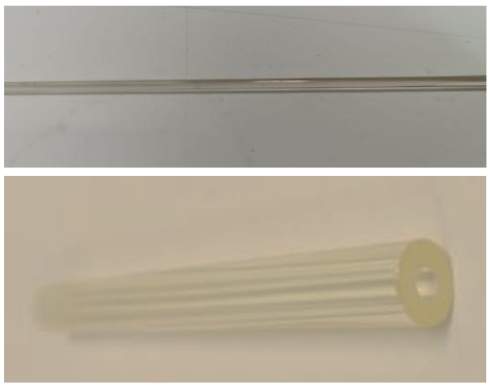

Fig. 1 Components of the fiber preform: Ho^{3+}-doped germanate core rod and passive cladding tube.

III. Results and Discussion

The fabricated germanate glasses were first evaluated in terms of physical and thermal properties. The measured parameters are summarized in Table 1.

Typical physical and thermal properties:	
Density	4.69 ± 0.05 g/cm^3
Glass transition temperature (T_g)	456 ± 3 °C
Crystallization temperature (T_x)	753 ± 3 °C
Glass stability parameter ($\Delta T = T_x - T_g$)	297 ± 6 °C
Core refractive index @ 1533 nm	1.813 ± 0.001

Table 1. Typical physical and thermal properties of the fabricated germanate glasses.

The glass transition temperature was 456 °C and the crystallization onset occurred at 753 °C, resulting in a stability parameter ΔT of 297 °C. This wide processing window ensures reliable fiber drawing and confirms the good thermo-mechanical stability of the material. The refractive index at 1533 nm was 1.813, suitable for high numerical aperture core designs.

Spectroscopic measurements showed broad emission bands in the 2 µm region for both dopants (Fig. 2). The Tm-doped bulk sample exhibited emission associated with the $^3F_4 \rightarrow {}^3H_6$ transition and a measured lifetime of 1.45 ms, enabling continuous wave laser generation at 1948 nm under 792 nm pumping [3]. The Ho-doped glass displayed emission from the $^5I_7 \rightarrow {}^5I_8$ transition extending beyond 2.1 µm [4], with a measured lifetime of 3.0 ms.

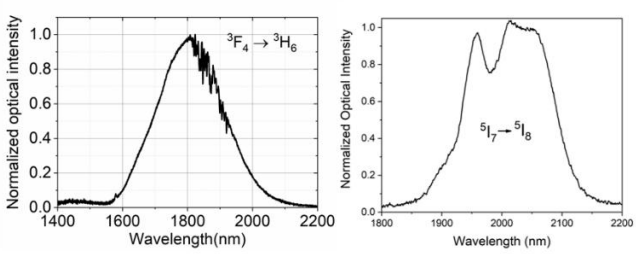

Fig. 2 Fluorescence spectra of the Tm^{3+}-doped (left) and Ho^{3+}-doped (right) germanate glass.

The fabricated Ho:Germanate fiber of 45/125 µm core/cladding geometry exhibited a well-defined core–cladding interface without visible crystallization or structural defects (see Fig. 3). Optical guiding was verified by near-infrared light injection, confirming proper confinement within the core.

In-band pumping of the Ho:Germanate fiber at 1931 nm resulted in stable continuous wave laser emission at 2.1 µm with output power exceeding 1 W.

These results confirm that the investigated germanate composition provides efficient RE emission together with adequate thermal stability for both bulk and fiber laser configurations.

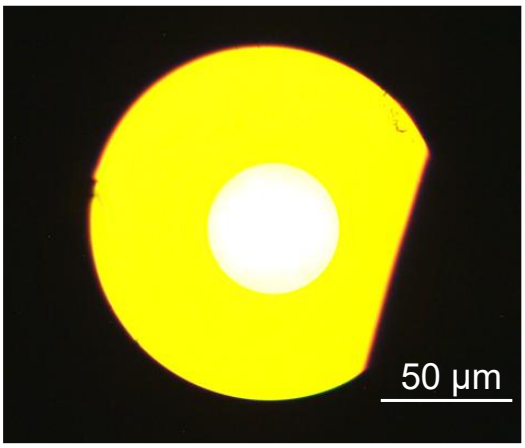

Fig. 3 Ho^{3+}-doped germanate glass fiber cross section.

IV. Conclusion

This work demonstrates germanate glass as a versatile and high-performance host for 2 µm laser sources. Tm^{3+}-doped bulk glass yielded CW laser emission at 1948 nm, while Ho^{3+}-doped fibers demonstrated in-band pumped CW emission at 2.1 µm with output power above 1 W. The excellent thermal stability (ΔT = 297 °C), broad emission bandwidths, and long upper-state lifetimes confirm the potential of this glass system for compact, efficient, and eye-safe mid-infrared laser sources.

References

[1] K. Scholle, S. Lamrini, P. Koopmann, and P. Fuhrberg, "2 µm laser sources and their possible applications," in Frontiers in Guided Wave Optics and Optoelectronics, IntechOpen, 2010.

[2] F. Ben Slimen, S. Chen, J. Lousteau, Y. Jung, N. White, S. Alam, D. J. Richardson, and F. Poletti, "Highly efficient Tm^{3+} doped germanate large mode area single mode fiber laser," Optical Materials Express, vol. 9, pp. 4115–4125, 2019.

[3] M. Segura, D. Pugliese, M. Ceballos, F. Diaz, M. Aguiló, X. Mateos, N. Boetti, and J. Lousteau, "Fabrication and spectroscopy of high-quality Tm^{3+}-doped germanate glass for 2 µm laser emission," in Conference on Lasers and Electro-Optics Europe and European Quantum Electronics Conference, Technical Digest Series, Optica Publishing Group, 2023, paper ca_p_20.

[4] X. Fan, P. Kuan, K. Li, L. Zhang, D. Li, and L. Hu, "Spectroscopic properties and quenching mechanism of 2 µm emission in Ho^{3+} doped germanate glasses and fibers," Optical Materials Express, vol. 5, pp. 1356–1365, 2015.

Nanomaterials and Complex Media for Sensing and Optoelectronic Devices

Nanoscale terahertz dynamics in materials

Frank A. Hegmann*

Department of Physics, University of Alberta, Edmonton, Alberta, T6G 2E1, Canada
*hegmann@ualberta.ca

***Abstract*— Time-resolved terahertz spectroscopy (TRTS) and ultrafast terahertz scanning tunneling microscopy (THz-STM) are excellent probes of ultrafast nanoscale dynamics in nanomaterials and on surfaces. The application of these techniques to the study of carrier dynamics in silicon nanomaterials and on silicon surfaces down to the atomic scale is discussed.**

***Keywords*— ultrafast time-resolved terahertz spectroscopy, terahertz scanning tunneling microscopy, nanomaterials, silicon.**

I. Introduction

The ability to probe ultrafast phenomena on the nanoscale is essential to our understanding of excitation dynamics in materials and in the development of new device technologies. The nature of charge transport in nanomaterials can also be affected by nanoscale morphology. Advances in terahertz (THz) pulse technology have enabled studies of nanoscale ultrafast charge transport in nanomaterials by spectroscopic techniques and more recently by spatially-resolved techniques down to the nanoscale.

II. Methods

Time-resolved THz spectroscopy (TRTS) is a well-established non-contact technique for probing the real and imaginary components of the ultrafast photoconductivity dynamics of a material with picosecond time resolution and over a wide range of temperatures, revealing early-time hot carrier dynamics and longer time recombination dynamics [1,2]. Fitting the measured complex terahertz conductivity spectra to various models provides insight into the nature of charge carrier transport, such as the transition from free-to-localized transport in silicon nanomaterials [3]. However, the precise interpretation of nanoscale dynamics from model fits to observed spectra has some limitations.

Spatially-resolved probes that can directly observe ultrafast dynamics on the nanoscale are therefore very desirable. However, achieving this capability has been challenging and is the focus of research in many labs around the world. Terahertz scanning tunneling microscopy, or THz-STM, is a powerful new technique that enables direct imaging of sub-picosecond dynamics in materials down to the atomic scale [4]. In this technique, ps-duration THz pulses are antenna-coupled to an STM tip, and the resulting field enhancement at the junction produces sub-picosecond transient tunnel currents that can be used to probe ultrafast dynamics on the nanoscale [5].

III. Results and Discussion

Time-resolved terahertz spectroscopy measurements of silicon nanocrystal films reveal localized behavior in photocarrier transport, with significant interface scattering as well as percolative transport between nanocrystals [3]. Other nanomaterial systems have been explored, such as photoexcitation and charge transport dynamics in films of CdS semiconductor nanowires [6]. THz-STM of silicon surfaces have shown extreme tunnel currents exceeding 10^{11} A/cm^2 through single silicon atoms [5]. More recently, THz-STM has been used to study tunneling dynamics in single dangling bonds on silicon surfaces as well as single silicon nanocrystals. Efforts are currently underway to establish multi-probe THz-STM that will allow unprecedented imaging of ultrafast nanoscale dynamics in quantum materials.

IV. Conclusion

Time-resolved terahertz spectroscopy and terahertz scanning tunneling microscopy are ideal tools for probing ultrafast nanoscale carrier dynamics in nanomaterials and on surfaces.

Acknowledgments

This work was supported by the Natural Sciences and Engineering Council of Canada (NSERC), the Canada Foundation for Innovation (CFI), and Alberta Innovates.

References

[1] P. U. Jepsen, D. G. Cooke, and M. Koch, "Terahertz spectroscopy and imaging—Modern techniques and applications", Laser Photonics Rev. 5, 124 (2011).

[2] N. B. Refvik, *et al.*, "Ultrafast photoconductivity dynamics in narrow-gap HgCdTe films", APL Mater. 12, 121116 (2024).

[3] L. V. Titova, *et al.*, "Ultrafast percolative transport dynamics in silicon nanocrystal films", Phys. Rev. B 83, 085403 (2011).

[4] T. L. Cocker, V. Jelic, R. Hillenbrand, and F. A. Hegmann, "Nanoscale terahertz scanning probe microscopy", Nat. Photon. 15, 558 (2021).

[5] V. Jelic, *et al.*, "Ultrafast terahertz control of extreme tunnel currents through single atoms on a silicon surface", Nat. Phys. 13, 591 (2017).

[6] C. E. Jensen, *et al.*, "Ultrafast charge-carrier localization and separation dynamics in CdS nanowires wrapped in C_3N_5 nanosheets", J. Chem. Phys. 163, 234711 (2025).

Spacetime Imaging and Ultrafast Control of THz Surface Plasmon Polaritons of Graphene

Simon Anglhuber[1], Martin Zizlsperger[1], Eva A. A. Pogna[2], Yaroslav A. Gerasimenko[1], Anastasios D. Koulouklidis[1], Imke Gronwald[1], Svenja Nerreter[1], Leonardo Viti[3], Miriam S. Vitiello[3], Rupert Huber[1], and Markus A. Huber[1]

[1]Department of Physics and Regensburg Center for Ultrafast Nanoscopy (RUN), University of Regensburg, Regensburg, Germany
[2]Istituto di Fotonica e Nanotecnologie, Consiglio Nazionale delle Ricerche (CNR-IFN), Milano, Italy
[3]NEST, CNR – Istituto Nanoscienze and Scuola Normale Superiore, Pisa, Italy

*Presenting author: eva.pogna@cnr.it

***Abstract* — Field-resolved terahertz near-field microscopy directly maps graphene plasmon polariton dynamics in both space and time, revealing key characteristics of their propagation such as group and phase velocities and damping. Interband photoexcitation with femtosecond pulses, provides sub-cycle control over non-equilibrium polariton properties.**

***Keywords* — terahertz near-field imaging, ultrafast sub-cycle control, plasmon polaritons, graphene.**

I. Introduction

Engineering surface polaritons — hybrid light–matter excitations confined to material interfaces — has remained a major focus of nano -photonics and -optoelectronics research for decades [1]. Owing to their strong field confinement and rapid propagation, these modes are attractive for applications including polaritonic logic architectures, sensing platforms, photodetectors, and nanoscale waveguiding components [2]. Scattering-type near-field microscopy has proven to be a powerful technique to investigate polaritons properties by imaging their propagation in real space, using sharp metallic probes. To date, most investigations have concentrated either on single-frequency imaging or on analyzing broadband responses in the spectral domain. More recently, field-resolved experiments employing ultrashort broadband pulses have enabled direct visualization of polariton dynamics in both space and time [3,4], opening new opportunities for ultrafast tracking and active control.

II. Methods

Terahertz (THz) spacetime nanoimaging exploits a broadband THz pulse, which illuminates the sharp metallic probe of a scattering-type near-field microscope [5–7], thereby launching polaritons in the sample, placed beneath the probe at near-field distances (Fig. 1a). The excited polariton modes propagate from the tip, eventually reflect at dielectric discontinuities, e.g. sample edges, and return to the tip position.

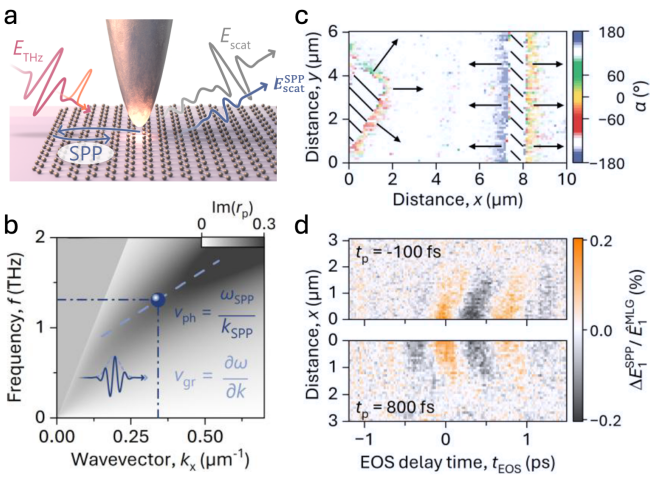

Fig. 1 Spacetime imaging and ultrafast control of graphene SPPs. a, A THz field excites SPPs beneath a sharp metallic tip; the modes reflect at the sample edge and are detected via electro-optic sampling (EOS). Referencing the scattered signal to a region without significant SPP contribution isolates the propagating component. b, SPP dispersion simulation compared with experimental phase and group velocities. c, 2D maps visualizing SPP propagation across larger areas and complex geometries. d, Pump-induced field changes demonstrate femtosecond, sub-cycle control of the SPP amplitude via adjustment of the pump delay t_p.

Upon recoupling at the tip, the polariton electric field is scattered into the far field, yielding a temporally delayed contribution associated with the reflected surface polariton, $E^{\mathrm{SPP}}_{\mathrm{scat}}$. This scattered component is overlapped to a quasi-instantaneous background term, E_{scat}, which originates from

the direct dielectric interaction between tip and sample.

By electro-optic sampling (EOS) the scattered waveforms at varying distances from a sample edge and subtracting the instantaneous component, we can directly reconstruct the spatiotemporal evolution of the polariton wave packet.

III. Results and Discussion

Here, we explore surface plasmon polaritons (SPPs) of graphene at THz frequencies, using a spacetime imaging approach and, demonstrate sub-cycle control of propagating polaritons via ultrafast photoexcitation [8].

We characterize multiple graphene samples produced by dry exfoliation and chemical vapor deposition, spanning different Fermi levels and carrier scattering times.

As the tip is moved away from the graphene edges at which the SPP wave is reflected, we observe that the polariton field amplitude decreases and its temporal maximum shifts to longer EOS delay times, reflecting propagation and damping.

We model the signal as a carrier oscillation modulated by a Gaussian envelope - describing the THz pulse duration - and an exponential decay term, describing the polariton damping. From fitting all transients to one global set of parameters, we obtain direct access to the spatial damping of the wave packet, yielding a 1/e decay length of δx, as well as to the propagation velocities of both the carrier and envelope. From the spacetime maps we extract a phase velocity v_{ph} and a group velocity v_g at the THz pulse central frequency $f_{SPP} \approx 1.31$ THz. In frequency-momentum (f,k)-space (Fig. 1b), the phase velocity determines the dispersion point via $v_{ph}=2\pi f_{SPP}/k_{SPP}$ (blue sphere), while the group velocity corresponds to the local slope of the dispersion curve $v_g=2\pi\partial f/\partial k$ (dashed line) within the experimentally accessed bandwidth.

The values measured in dry-exfoliated and CVD graphene are quantitatively supported by calculations of the imaginary part of the Fresnel reflection coefficient, Im(r_p), incorporating the full multilayer sample geometry (background in Fig. 1b), showing excellent agreement.

Notably, this analysis remains robust even for strongly damped SPP modes at room temperature, without relying on cryogenic operation, elaborate spectral post-processing, or tailored nanostructuring.

By acquiring referenced two-dimensional image sequences at varying electro-optic delays, the spacetime analysis can be extended to full 2D visualization of SPP propagation. These datasets can be transformed into maps resolving distinct propagation directions (Fig. 1c) and, analogously, local phase and group velocities across extended sample regions. This makes the method particularly powerful for anisotropic materials supporting nonspherical polariton wavefronts.

Furthermore, direct time-domain access enables the investigation of nonequilibrium polariton dynamics with femtosecond resolution. Using ultrashort optical pump pulses, we induce interband excitation in graphene, transiently reducing its THz conductivity and thereby modifying the polariton response. Analysis of the SPP field reveals a polarity reversal, indicating a pump-induced decrease in polariton amplitude (Fig. 1d). By tuning the delay between THz excitation and optical pumping, selected segments of the propagating wave packet can be addressed with sub-cycle accuracy. This capability allows deterministic reshaping of SPP waveforms on ultrafast timescales—orders of magnitude faster than electrostatic gating—highlighting the potential for high-speed plasmonic logic architectures.

IV. Conclusion

We introduce an advanced near-field imaging scheme that permits direct visualization and dynamic manipulation of polariton propagation in space and time, employing graphene SPPs as a model platform. The technique enables direct determination of phase and group velocities, as well as propagation losses, from a single spatiotemporal dataset, eliminating the need for frequency-domain analysis. These observables provide detailed access to the underlying dispersion relation, even for strongly damped modes at ambient conditions. The framework can be extended to two spatial dimensions, allowing real-time imaging of polariton dynamics in anisotropic media. Moreover, resolving the temporal evolution of the fields offers a direct means to study non-equilibrium polariton transport. By means of ultrafast photoexcitation, the THz conductivity of graphene can be transiently suppressed, enabling sub-cycle control of the SPP amplitude. Beyond graphene, the method is readily transferable to a broad class of materials, including anisotropic platforms.

References

[1] D. N. Basov et al., “Polariton Panorama,” Nanophotonics, vol. 10, pp. 549-577 (2020).

[2] A. L. Pyayt et al., “Integration of photonic and silver nanowire plasmonic waveguides,” Nature Nanotechnology, vol. 3, pp. 660-665 (2008).

[3] O. Mitrofanov et al., “Probing terahertz surface plasmon waves in graphene structures,” Applied Physics Letters, vol. 103, 111105 (2013).

[4] S. Xu et al., “Electronic interactions in Dirac fluids visualized by nano-terahertz spacetime interference of electron-photon quasiparticles,” Science Advances, vol. 10, eado5553 (2024).

[5] M. Plankl et al., “Subcycle contact-free nanoscopy of ultrafast interlayer transport in atomically thin heterostructures,” Nature Photonics, vol. 15, pp. 594-600 (2021).

[6] T. Siday et al., “Ultrafast Nanoscopy of High-Density Exciton Phases in WSe_2,” Nano Letters, vol. 22, pp. 2561-2568 (2022).

[7] M. Zizlsperger et al., “In situ nanoscopy of single-grain nanomorphology and ultrafast carrier dynamics in metal halide perovskites,” Nature Photonics, vol. 18, pp. 975-981 (2024).

[8] S. Anglhuber et al., “Spacetime Imaging of Group and Phase Velocities of Terahertz Surface Plasmon Polaritons in Graphene,” Nano Letters, vol. 25, pp. 2125-2132 (2025).

Compact High-Q Photonic Crystal Cavities with Improved Robustness to Disorder

Nicoletta Granchi[1,2,*], Camilla Gonzini[2], Matteo Lodde[3], Gabriele Calusi[1], René P. J. van Veldhoven[3], Andrea Fiore[3], Guillermo Arregui[4,5] and Francesca Intonti[1,2]

[1]Department of Physics and Astronomy, University of Florence, Italy
[2]European Laboratory for Non-Linear Spectroscopy (LENS), Italy
[3]Department of Applied Physics, Eindhoven University of Technology, The Netherlands
[4] Swiss Federal Institute of Technology Lausanne (EPFL), Switzerland
[5]Center for Quantum Science and Engineering, EPFL, Switzerland
*Corresponding author: nicoletta.granchi@unifi.it

***Abstract*— Compact photonic crystal cavities enable dense integration but typically require large footprints to achieve high Q-factors, increasing sensitivity to fabrication disorder. We present high-Q, small-footprint cavities optimized through a non-Hermitian perturbation theory framework, where periodicity breaking enhances resilience to fabrication-induced disorder as demonstrated by the near-field scanning optical microscopy experiment.**

***Keywords*— photonic-crystals, optical nanocavities, near-field scanning optical microscopy, non-Hermitian photonics.**

I. Introduction

Periodic nanostructures are widely used in photonics to engineer light–matter interaction [1-4]; however, their optical response is often strongly affected by fabrication imperfections, motivating increasing interest in design strategies that enhance robustness and reproducibility in real nanofabricated systems. Among those, photonic crystal (PhC) slab cavities [1] enabling strong light confinement within ultra small volumes, are widely used in integrated photonics and quantum optical platforms. Achieving high quality (Q) factors in these systems typically requires extended periodic mirrors surrounding the cavity defect, leading to large device footprints and enhanced sensitivity to fabrication induced disorder. Nanofabrication imperfections such as hole size variations, sidewall roughness, and positional errors introduce scattering losses and resonance detuning, limiting device reproducibility. This issue is particularly critical for applications requiring spectral alignment across multiple devices.

In this work, PhC slab cavities as small as 4 × 4 μm^2, achieving relatively high Q comparable to conventional large L3 cavities, despite occupying only a fraction of their footprint, are numerically and experimentally demonstrated. These structures are obtained through an optimization process that introduces an aperiodic, yet highly controlled, pattern of holes surrounding the cavity [4,5].

II. Methods

The investigated structures are based on L3 PhC slab cavities defined within a footprint of approximately 4 × 4 μm^2 (corresponding to 6 lattice periods). Starting from the unoptimized periodic design (R6), a gradient-based optimization framework based on non-Hermitian perturbation theory for quasinormal modes [4,6] is employed to maximize the cavity Q-factor of the fundamental L3 mode (Fig. 1a) by

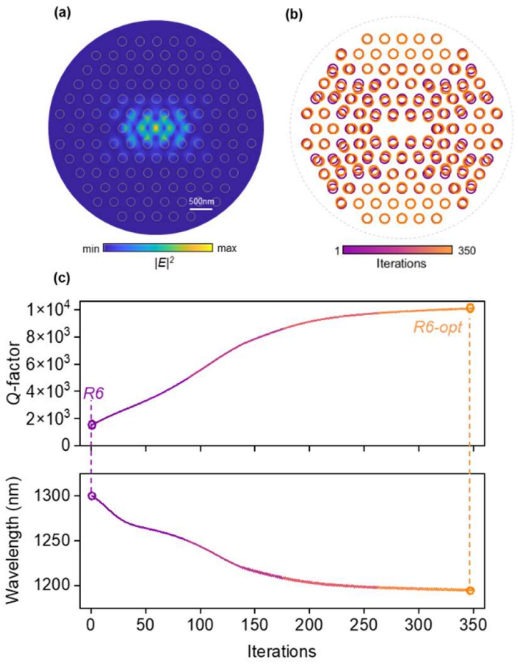

Fig. 1 (a) Simulated near-field electric field intensity maps for the fundamental mode of the original L3 cavity (R6). (b) Evolution of hole positions during the optimization process from the unperturbed reference cavity (R6, purple) to the fully optimized configuration (R6--opt, orange). (c) Simulated Q-factor (top panel) and resonant wavelength (bottom panel) as a function of optimization iteration for an L3 with lattice constant a=330nm and holes radius = 0.79a.

iteratively displacing the air holes surrounding the defect region. The optimization introduces in the final optimized design (labelled as R6-opt) correlated hole displacements that progressively break the original lattice periodicity while preserving the overall cavity symmetry [5]. Fig. 1(b) illustrates the displacement pattern of the air holes introduced during the optimization, while Fig. 1(c) summarizes the evolution of the cavity Q-factor (top panel) and resonant wavelength (bottom panel) along the optimization trajectory from R6 to R6-opt. The fabricated samples are based on GaAs heterostructures incorporating a dense layer of InAs quantum dots (QDs) emitting at 1300 nm. Optical characterization is achieved at room temperature using scanning near-field optical microscopy (SNOM).

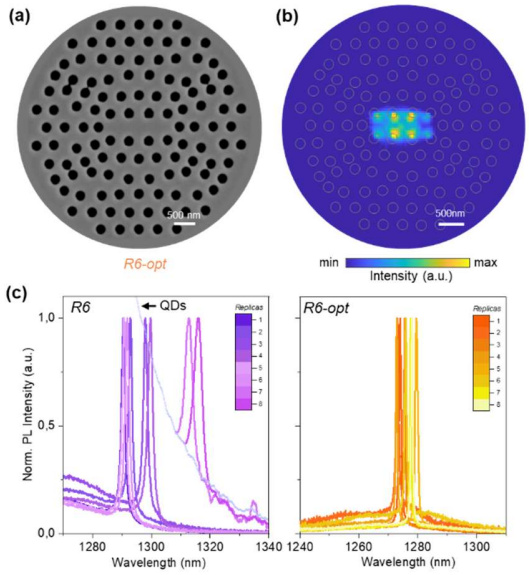

Fig. 2 (a) SEM image of the fabricated optimized R6-II cavity. (b) SNOM map of the optimized fundamental mode in the R6-II cavity. (c) Normalized SNOM PL spectra acquired at the location of maximum emission of eight nominally identical replica of R6 with a=320nm (left) and R6 II with a=350nm (right) and nominal radii. In the left graph the QD PL emission (light blue) is overlapped to the spectra.

III. Results and Discussion

In Fig. 2a we report the Scanning Electron Microscopy (SEM) image of the fabricated L3 cavity with optimized design (R6-opt), characterized by a final Q of $\sim 10^4$, that is comparable to the Q of a standard L3 cavity with 12 lattice periods (therefore extending up to 8×8 μm^2 for the same lattice constant). A rigorous experimental characterization performed on R6-opt cavities with different lattice constants confirm that Q-factors follow the trend predicted by simulations, with a systematic increase from the unoptimized R6 design to the fully optimized design [4,5]. Moreover, the SNOM map acquired on the R6-opt cavity, shown in Fig. 1 (b), further demonstrates that the cavity mode remains well confined and spatially stable despite the periodicity breaking.

Beyond quality factor optimization, spectral reproducibility represents a critical and often overlooked limitation, largely arising from fabrication-induced disorder. Quantifying spectral stability provides a stringent metric to evaluate the applicability of the proposed cavities. In particular, for cavity–emitter coupling, performance is governed by the spectral alignment between the cavity mode and the emitter ensemble. Imperfections inherent to electron-beam lithography and etching processes are known to induce substantial device-to-device variations in photonic crystal cavity resonances. Here, we approach this issue by systematically investigating the spectral stability of optimized small-footprint cavities through a statistical analysis performed on multiple nominally identical replicas, directly linking engineered periodicity breaking to enhanced robustness against fabrication-induced disorder. Figure 2 (c) compares the SNOM photoluminescence (PL) spectra measured on multiple nominally identical replicas, revealing a significantly reduced spread of resonance wavelengths for the optimized cavities (right panel) with respect to the standard L3 R6 (left panel). This behavior indicates a reduced sensitivity to fabrication-induced imperfections, attributed to the correlated nature of the periodicity breaking introduced by the optimization [5].

IV. Conclusion

We have demonstrated that controlled periodicity breaking enables compact photonic crystal slab cavities combining high Q-factors with enhanced robustness to fabrication-induced disorder. By applying mode-driven optimization to small-footprint L3 cavities, we achieve improved optical performance together with significantly enhanced spectral reproducibility. In contrast to strictly periodic or fully disordered designs, PhC cavities based on engineered aperiodicity simultaneously achieve compact footprints, high optical performance, and improved reproducibility, making them suitable for dense on-chip integration.

References

[1] Y. Akahane, T. Asano, B. S. Song, S. Noda, “High-Q photonic nanocavity in a two-dimensional photonic crystal,” *Nature*, vol. 425, pp. 6961, 2003.

[2] M. Modaresialam, N. Granchi, M. Stehlik, C. Petite, S. Delegeanu, A. Gourdin, M. Bouabdellaoui, F. Intonti, B. Kerzabi, D. Grosso, L.t Gallais, and M. Abbarchi, "Nano-imprint lithography of broad-band and wide-angle antireflective structures for high-power lasers," *Optics Express*, vol. 32, pp. 12967-12981, 2024.

[3] L. Fagiani, N. Granchi, A. Zilli, C. Barri, F. Rusconi, M. Montanari, E. Mafakheri, M. Celebrano, M. Bouabdellaoui, M. Abbarchi, F. Intonti, A. Khursheed, P. Biagioni, M. Finazzi, M. A. Vincenti, M. Bollani, “Linear and nonlinear optical properties of dewetted SiGe islands”. *Optical Materials: X*, vol. 13, pp. 100116, 2022.

[4] N. Granchi, F. Intonti, M. Florescu, P. D. García, M. Gurioli, and G. Arregui, “Q-Factor Optimization of Modes in Ordered and Disordered Photonic Systems Using Non-Hermitian Perturbation Theor,” *ACS Photonics*, vol. 10 (8), pp. 2808-2815, 2023.

[5] N. Granchi, C. Gonzini, M. Lodde, G. Calusi, René P. J. Van Veldhovem, A. Fiore, G. Arregui and F. Intonti, “Improved Disorder Resilience in Small-Footprint Photonic Cavities with Periodicity Breaking”, *Advanced Optical Materials*, doi.org/10.1002/adom.202502531, 2026.

[6] P. Lalanne, W. Yan, K. Vynck, C. Sauvan, J. P. Hugonin, “Light Interaction with Photonic and Plasmonic Resonances”, *Laser & Photonics Review*, vol. 12, pp.17000113, 2018.

All-fibre-based MoS_2 photodetector for wearable applications

Felice Torrisi[1,2,3*], Tong Wang[3], Longren Li[3], Shuwei Wu[3], Ao Yan[3], Artem Bakulin[3]

[1] Dipartimento di Fisica e Astronomia, Università di Catania, Via S. Sofia 64, Catania, 95123, Italy

[2] CNR-IMM (Catania Universita'), Via S. Sofia 64, Catania, 95123, Italy

[3] Molecular Sciences Research Hub, Department of Chemistry & Centre for Processable Electronics, Imperial College London, White City Campus, 82 Wood lane, London, W12 0BZ, United Kingdom

*Corresponding author: f.torrisi@imperial.ac.uk

***Abstract*— Fibre photodetectors struggle with conformal 2D coverage on cylindrical substrates, while molybdenum disulfide (MoS_2) devices face persistent photoconductivity limiting performance. This work demonstrated an all-fibre-based devices integrating wet-spun rGO fibre electrodes and inkjet-printed silver fibres, demonstrating: complete cylindrical coverage (Raman/SEM), broadband response (470-680 nm), rapid switching (2.39 s rise/1.99 s fall), with high on/off ratio (4.62). The rGO fibre configuration proves critical for dark current suppression via work function modulation ($\Delta\phi$), enabling scalable wearable optoelectronics.**

***Keywords*— 2D materials, optoelectronics, e-textiles, wearable electronics.**

I. Introduction

Photodetectors are devices that convert the incident photons into electrical signals, which are widely used in imaging, communications, environmental monitoring, biosensing, automotive, space, astronomical exploration, and human-machine interaction. Recently, development of textile/fibre-based photodetectors has emerged as a significant trends driven by factors including: garment-level distributed light sensing (e.g., UV dosage monitoring, ambient light mapping, posture/occlusion feedback); conformability to the curved surfaces of the human body (small bending radius, sewable/weavable integration); lightweight and low-power operation; washability and high-cycle mechanical durability; and the need for seamless integration with wearable systems such as energy harvesters and wireless readout modules [1,2]. By integrating photoactive materials onto fibres, photodetectors with a fibre form factor can be created and woven into clothing as regular fibres, establishing truly wearable electronic textile (e-textile) applications [3]. Their cylindrical geometry naturally couples incident and scattered light, making them suitable for ambient-light and direction-sensitive tasks [4]. They are also compatible with conventional textile processes, including winding, stitching, and weaving. Representative advances include fibre devices based on ZnO/GaN nanowires for UV/solar blind operation; carbon core–sheath fibres (CNT/graphene) with inorganic/organic/perovskite sensitisers enabling conformability and on/off ratios ; and perovskite-coated fibres offering broadband response despite stability/encapsulation trade-offs.

In this study, we demonstrate a novel coating process, the capillary effect coating (CEC) process, to achieve scalable and cost-effective deposition of MoS_2 on fibre substrates. An all-in-one fibre-based MoS_2 photodetector was then demonstrated by our CEC approach. Two distinct types of electrodes were employed in this study to contact the MoS_2 coated fibre: inkjet-printed silver electrodes (resulting in a MoS_2-silver fibre Photodetector) and winded reduced graphene oxide (rGO) fibre electrodes (resulting in a MoS_2-rGO fibre Photodetector). The photodetectors with inkjet-printed silver electrodes demonstrated broadband response(470 nm – 680 nm) under visible light irradiation, with a high responsivity of 14.6 $mA \cdot W^{-1}$. Remarkably, by replacing the silver electrodes with entangled rGO fibres, the response time of the device is significantly shortened. Our work demonstrated a new coating methodology for 2D materials' functionalisation on fibre to build core-shell e-textiles and highlights the potential of fibre-based MoS_2 photodetector for integration into smart textiles and wearable applications.

II. Methods

Preparation of the MoS_2 dispersion

An MoS_2 crystal was cut into a 0.8×0.4×1 mm piece. The crystal was electrochemically exfoliated for 2h with graphite as anode, at 8V in 5 mg/mL THAB in MeCN electrolyte. Then the expanded MoS_2 crystal was washed with EtOH and subsequently sonicated in PVP/DMF (0.8892 g PVP in 40 mL DMF) for 30 min. The as-produced dispersion was centrifuged at 400 G for 5 min. The top 80\ % of the dispersion is then extracted for further characterisation.

Preparation of graphene oxide

Graphite (0.5 g) and sulfuric acid (100 mL) were mixed and stirred in a flask for 24 hours. Then, ground $KMnO_4$ (5 g) was added to the mixture dropwise and stirred for another 24 hours. This mixture was then transferred into an ice bath, with deionised water added dropwise (100 mL) for 1 hour. During this process, the temperature was kept under 25 ℃ . The dispersion is allowed to settle down for 30 minutes, after which H_2O_2 (25 ml) was added to the mixture dropwise. The

colour of the GO solution changed from atrovirens to dark brown. The solution was then washed with HCl and deionised water and purified by centrifugation (5500 – 10,000 rpm, 30 min) to remove the impurity until the pH was close to 7.

Preparation of the rGO fibre

The GO dispersion was transferred into a syringe and injected into a rotating acetic acid coagulation bath at a rate of 10 mg h^{-1}. The fibre was then collected from the coagulation bath and dried in airfor . The GO fibre was chemically reduced to rGO fibre by immersing the GO fibre in hydroiodic acid (HI) for 4 hours, followed by rinsing with ethanol and water to remove residual HI and then air-dried.

III. Results and Discussion

During the capillary effect coating (CEC) process applied to a fibre bundle (Figure 1 a), the MoS_2 dispersion is confined within the inter-fibre capillaries and around the polyamide (PA) filaments. Upon solvent evaporation, the MoS_2 retained within the capillary network contributes directly to the final coating, in contrast to conventional dip-coating where excess dispersion drains off the bundle, leading to substantial material loss and thickness gradients along the fibre length and circumference. As a result, CEC enables more efficient material utilisation and intrinsically favours conformal coverage on cylindrical substrates. The morphology and continuity of the MoS_2 coating on PA

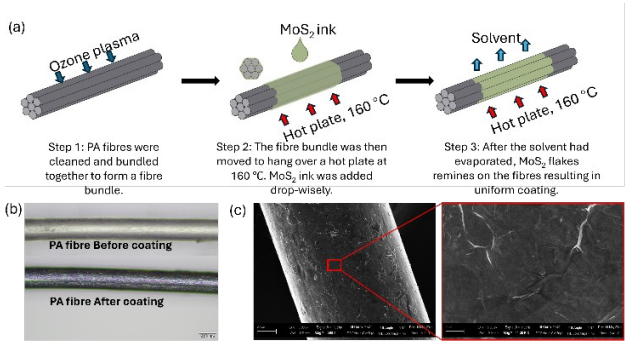

Figure 1

fibres were first evaluated by optical and electron microscopy. After coating, the fibre surface is completely and uniformly covered by a continuous dark green layer, corresponding to the MoS_2 coating (Figure 1 b). SEM images of the coated fibres (Figure 1 c) reveal a continuous MoS_2 shell surrounding individual PA filaments, with no visible bare PA regions or large-scale delamination over the inspected length scale (tens of micrometres). Compared to uncoated PA fibres, which exhibit pronounced surface texture and inter-fibre gaps, the coated surface appears significantly smoother, with the MoS_2 layer filling surface asperities and partially bridging inter-fibre voids. This continuous and smoothed coating is essential for subsequent electrode integration: for inkjet-printed Ag electrodes, it minimises local roughness that would otherwise disrupt printed traces; for wrapped rGO fibre electrodes, it prevents suspended contact regions and ensures intimate coupling between the active layer and the electrode. We contacted the MoS_2 fibre with conductive reduced graphene oxide (rGO) fibre electrodes, yielding MoS_2–rGO fibre PD (Error: Reference source not found a, b). The rGO fibres were helically wound around the MoS_2-coated PA core, forming a symmetric electrode configuration, which can be seen from the SEM image (Error: Reference source not found c). Error: Reference source not found d shows the photocurrent of the MoS_2–rGO fibre PD as a function of applied bias. Similar to the MoS_2–Ag fibre device, I_{ph} varies approximately linearly with V_b within the investigated range, confirming that the fibre geometry does not introduce additional non-linearities in the operating window. The device exhibits clear sensitivity across the visible range with a pronounced cut-off at wavelengths above ≈680 nm, consistent with the MoS_2–Ag fibre device. Under identical illumination and bias conditions (λ = 405 nm, P = 458 μW, V_b = 3 V), the MoS_2–rGO fibre PD exhibits a markedly reduced dark current compared to the MoS_2–Ag device. As shown in Error: Reference source not found f, the dark current was 29 nA while the photocurrent reaches ≈ 134 nA, nearly seven times higher than the 0.13 nA obtained for the MoS_2–Ag fibre PD, resulting in an increase in on/off ratio from 1.21 to 4.62. Error: Reference source not found f present the time-resolved photocurrent of the MoS_2–rGO fibre PD under periodic illumination at 3 V bias. The device displays stable and highly reproducible switching behaviour. The photocurrent of the

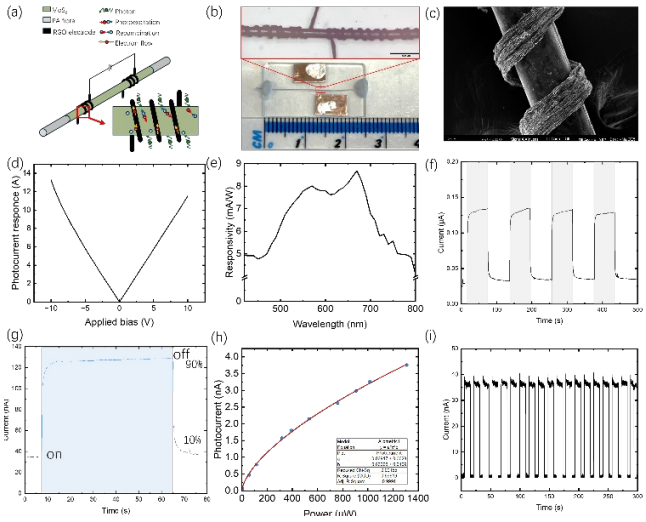

MoS_2–rGO fibre PD as a function of excitation power (Error: Reference source not found h) also follows a sub-linear trend, $I_{ph} = a \cdot P^b$, which is consistent with the improved responsivity and much shorter response times observed for the rGO-contacted devices.

IV. Conclusion

we have demonstrated all-fibre MoS_2 photodetectors that exploit a capillary-effect coating (CEC) process to realise conformal, continuous MoS_2 shells on polyamide fibres. The MoS_2–rGO fibre photodetectors show up to a seven-fold increase in photocurrent, a faster reposonse and improved responsivitycompared to the contact with metal electrodes.

Acknowledgments

We acknowledge support from the Centre for Processable Electronics, the HiApp 2D grant, the Chinese Scholarship Council.

References

[1] J. Zhou, L. Han, L. Chen, and Q. Zhang, Advanced Materials, vol. 37, no. 37, p. 2504006, Sep. 2025,
[2] A. Fakharuddin et al., Adv. Energy Mater., vol. 11, no. 34, p. 2101443, Sep. 2021

[3] Z. Zhang, Y. Wang, S. Jia, and C. Fan, Nature Photonics 2023 18:2, vol. 18, no. 2, pp. 114–126, Dec. 2023.
[4] K. Zhang et al., Nature Protocols 2024 19:5, vol. 19, no. 5, pp. 1557–1589, Mar. 2024

Resonance Raman spectroscopy as a tool to assess the scattering channels in van der Waals materials for near-IR applications

Leonetta Baldassarre[1,*]

[1]Department of Physics, Sapienza University of Rome
*Corresponding author: leonetta.baldassarre@uniroma1.it

***Abstract*—To explore electron-phonon interactions in van der Waals material we use a custom-built Raman setup with excitation at 1064 and 1550 nm, an energy seldom used in Raman spectroscopy. We demonstrate that it is possible to address the electron-phonon coupling in these material by studying their second-order two-phonon scattering processes.**

***Keywords*— spectroscopy, van der Waals materials**

I. Introduction

Among the vast class of two-dimensional materials, the semiconductor compounds, such as the transition metal dichalcogenides (TMDs) MX 2 with M= Mo, W and X = S, Se, Te, have attracted particular interest because of their potential applications in optoelectronic devices. The layered crystal structure, which leads to an extreme surface-to-volume ratio in the single layers, makes these materials some of the most promising candidates for the development of flexible and ultraflat optoelectronic devices. A deep understanding of the scattering channels, e.g., electron-phonon scattering, and of the related charge carrier transport properties is mandatory for the implementation of TMDs in any optoelectronic device.

Here we will discuss the possibilities opened up by performing resonance Raman spectroscopy with excitation in the infrared, in order to selectively probe the scattering processes of the low-energy carriers such as electrons in narrow-gap semiconductor and in Dirac materials like graphene.

II. Methods

The near-infrared (IR) radiation at 1550 nm is emitted by a continuous wave fiber laser, that at 1064 by a Nd:YAG laser. The setup can be used to acquire Raman/Photoluminescence spectra with both lasers just by interchanging the filters, which are placed on switchable mounts. The Raman/PL emission is collected in a back-scattering geometry. The filtered light is sent through a fiber to a Fourier-Transform interferometer (Bruker MultiRAM) and then detected by a single-pixel nitrogen-cooled germanium detector.

III. Results and Discussion

First we will present the results on $MoSe_2$ and $MoTe_2$ where first-order Raman modes remain off-resonant while second-order two-phonon scattering processes are enhanced as the laser energy matches the material's indirect infrared band gap

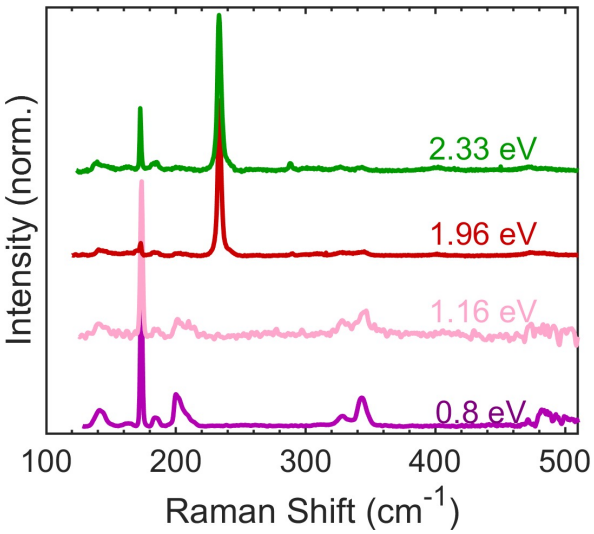

Fig. 1. Raman spectra of $MoTe_2$ measured with different excitation energies indicated in figure. It is possible to identify the emergence in the IR of several second order peaks.

[1], [2]. Supported by *ab-initio* calculations, we identify the microscopic scattering pathways and provide a new experimental framework for probing low-energy carrier dynamics in narrow-gap semiconductors something of paramount importance when modeling devices. Subsequently, I will discuss results on graphene where close to the Dirac point at K we find a giant increase of the intensity ratio between the double-resonant 2D and 2D' peaks[3]. By comparing to *ab-initio* calculations, we explain our experimental observation by an enhanced, momentum-dependent electron-phonon coupling between electrons and zone-boundary optical phonons. The modification of electron-phonon coupling is then studied as a function of dimensionality[4] and doping.

IV. Conclusion

We envision that the use of Raman spectroscopy with excitation energy down to 0.8 eV could pave the way to a deeper understanding of the scattering channels for low-energy carriers in semiconductors with bandgap energy in the infrared, as well as semimetals and topological insulators.

ACKNOWLEDGMENTS

This work was supported by the National Recovery and Resilience Plan (NRRP), Call for tender no. 1409 PRIN 2022 PNRR by Ministero dell' Universita' e della Ricerca (MUR), funded by the European Union - NextGenerationEU,

REFERENCES

[1] S. Sotgiu et al "Raman scattering with infrared excitation resonant with the $MoSe_2$ indirect band gap," *Physical Review B*, vol. 106, pp. 085204, 2022.

[2] S. Sotgiu et al "Raman spectroscopy at 1550 nm: Resonant enhancement of two-phonon scattering in $MoTe_2$ crystals," *Physical Review B*, vol. 113, pp. 085201, 2026.

[3] T. Venanzi et al "Probing Enhanced Electron-Phonon Coupling in Graphene by Infrared Resonance Raman Spectroscopy" *Physical Review Letters*, vol. 130, pp. 256901, 2023.

[4] L. Graziotto et al., "Infrared Resonance Raman of Bilayer Graphene: Signatures of Massive Fermions and Band Structure on the 2D Peak," *Nano Letters*, vol. 24, pp. 1867, 2024.

Antenna Theory and Design

Design and Optimization of a Multilayer Dielectric Radome for Ka-, Q-, and V-Band Applications

Olga Basile[1,*], Marco Simone[1], Santi C. Pavone[1], Gino Sorbello[1]

[1]Department of Electrical, Electronics, and Computer Engineering (DIEEI), University of Catania, Via Santa Sofia 64, 95123 Catania, Italy.

*Corresponding author: olga.basile@phd.unict.it

***Abstract*—This paper presents a multilayer radome for Ka-, Q-, and V-band operation. A longitudinally stratified model optimized via Particle Swarm Optimization maximizes transmission over multiple bands and incidence angles. The final 14-layer design, which considers all layers required by the manufacturing constraints, achieves a worst-case transmission loss below 0.4 dB.**

Keywords— multiband radome, multilayer, Ka/Q/V bands, Particle Swarm Optimization, transmission-line modeling.

I. Introduction

High-throughput satellite (HTS) systems are undergoing steady growth driven by the rising demand for broadband services. Current deployments primarily operate in Ka-band, exploiting frequency reuse techniques to increase system capacity. While the commercial adoption of Ka-band systems has been slower than initially expected, this band is now reaching maturity in terms of spectrum utilization and gateway scalability [1], [2], [3]. To support further capacity growth, future satellite systems are expected to exploit higher frequency bands [4]. In this context, Q- and V-band frequencies are widely regarded as key enablers for modern HTS systems.

Radomes play a critical role in this context, as they must simultaneously provide environmental protection and electromagnetic transparency across widely separated frequency bands. Achieving low reflection and low insertion loss over Ka/Q/V bands using a single radome structure is intrinsically challenging due to the strong frequency selectivity of multilayer interference effects [5], [6]. Commonly, the radome design is driven by the characteristics of the antenna system it is designed for Q/V ground antenna systems are typically parabolic reflectors, which provide high-gain radiation with a very narrow far field beamwidth, commonly under 5 degrees. Nonetheless, the radome is still required to guarantee adequate electromagnetic performance over a relatively wide angular range. Indeed, the transmitted field at the radome interface consists of a spatially extended, quasi-plane wavefront whose transverse extension is comparable to the antenna aperture, which can be about one meter or more [7]. When interacting with a curved radome surface, this extended wavefront inherently illuminates the radome over a wide range of local incidence angles, even under nominal boresight conditions. This effect constitutes the dominant contribution to the radome angular performance requirements, while pointing and tracking errors, or structural deformations due to thermal or wind loads, introduce secondary variations in the incident angle distribution. Moreover, the feed produces a set of side lobes which, if the radome has a limited angular range, may be reflected inside the radiating systems, degrading the performance by coupling back into the feed or interfering constructively or destructively with the main beam, causing beam distortion, beam squint, or increased side lobe levels. Therefore, Q/V band radomes are generally designed to exhibit stable transmission and polarization characteristics over a broad range of incidence angles, despite the intrinsically narrow beamwidth of the antenna system.

In this work, a multilayer dielectric radome enabling Fixed-Satellite Service (FSS) operation in the Ka-, Q-, and V-band frequency ranges is designed for satellite gateway and feeder-link applications, in accordance with the ITU Radio Regulations [8]. The radome is modeled as a stratified dielectric medium, and it is discussed in Sect. II. The requirement of a multi-band and wide-angle operation leads to a metaheuristic optimization-based approach in the design process, which combined the well-known transmission line model with an optimization algorithm to define the geometry of the radome. These two issues are discussed in Sections III, IV, together with the discussion on the optimized results. In this context, the Particle Swarm Optimization has been chosen as algorithm to define the thickness of the radome layers. This unified approach ensures consistency between design, predictive assessment, and future experimental validation.

II. Radome Architecture and Design Requirements

TABLE I
Operational frequency bands

Band	Frequency range (GHz)
Ka (DL)	19.7–20.2
Ka (UL)	29.5–30.0
Q	37.5–42.5
V (DL)	48.2–50.2
V (UL)	50.4–51.4

The proposed radome is a multilayer dielectric stack engineered to enable simultaneous operation over Ka-, Q-,

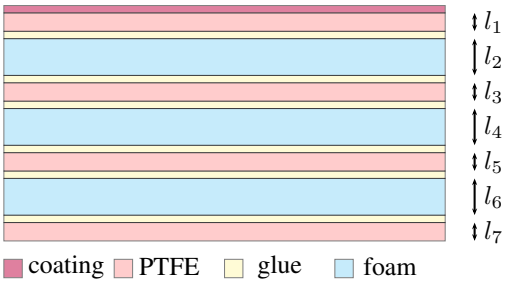

Fig. 1. Stack-up of the proposed radome configuration. Glue and coating thicknesses are fixed to 0.1 mm and 0.06 mm, respectively.

and V-band FSS frequency ranges defined in [8], which are summarized in Table I. The electromagnetic performance is quantified in terms of transmission coefficient over such bands for incidence angles $\theta_a = \{0°, 20°, 40°\}$, which are representative of practical illumination conditions in high-gain satellite applications, e.g., reflector and phased-array antennas [5], [6], [9].

Due to the high frequencies involved, the radome model includes the external (usually waterproof) painting and the glue layers [10] which hold the structure together, to accurately represent the as-manufactured radome, and consists of fourteen physical layers arranged as illustrated in Fig. 1. The electromagnetic behavior of the structure is mainly governed by seven internal layers composed of alternating ceramic-filled PTFE (Rogers RO3003) laminates and low-density foam slabs (ROHACELL® 31 A), whose thicknesses are the optimization variables, as summarized in Table II. These are modeled as frequency-dispersive media whose complex relative permittivity is defined by interpolating the dielectric properties available in [11], [12]. The remaining seven layers, corresponding to bonding adhesives and external paint coatings, are kept fixed throughout the optimization process with thicknesses respectively equal to 0.06 and 0.1 mm and dielectric properties assumed as in Table II. Manufacturing constraints define the optimization solution space. In particular, the thickness of the ceramic-filled PTFE skins is constrained between 0.127 mm and 1 mm, corresponding to the minimum and maximum commercially available laminate thicknesses, while the foam core layers are allowed to vary between 1 mm and 8 mm.

TABLE II
RADOME LAYER TYPES AND OPTIMIZATION STATUS

Layer	Material	ε_r / $\tan\delta$	Thick.
Coating	FEP	≈ 2.0 / $\sim 5\times10^{-3}$	Fix.
Glue	Bonding film	≈ 2.9 / $\sim 5\times10^{-2}$	Fix.
Skins	Rogers RO3003	≈ 3.0 / $(10^{-4} \div 10^{-3})$	Opt.
Foam	ROHACELL®31A	$1.05 \div 1.06$ / $(10^{-4} \div 10^{-3})$	Opt.

III. Electromagnetic Model

A multilayer dielectric radome can be modeled as a stack of N homogeneous dielectric slabs, each of l_i thickness and $n_i = \sqrt{\epsilon_{ri}\mu_{ri}}$ refractive index, as shown in Fig. 2. Under

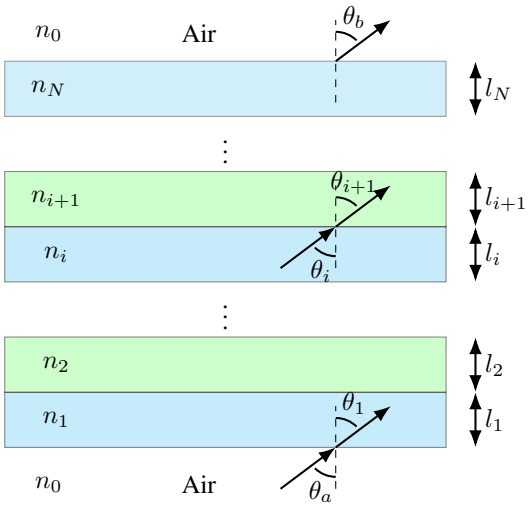

Fig. 2. Model of a multilayer radome.

plane-wave illumination hypothesis, TE and TM components propagate independently and incide with an angle θ_a on the radome. The longitudinal wavenumber in the i-th layer results

$$k_{z,i} = k_0\sqrt{\varepsilon_{r,i} - \varepsilon_{r,a}\sin^2\theta_a}, \qquad k_0 = \frac{2\pi f}{c_0}, \tag{1}$$

as dictated by Snell's law for stratified media [13], [14].

Each slab is equivalently represented by a transmission-line section with wave impedance $Z_i^{\mathrm{TE,TM}}$ and electrical length $k_{z,i}l_i$, leading to the transfer matrix

$$\mathbf{M}_i = \begin{bmatrix} \cos(k_{z,i}l_i) & jZ_i\sin(k_{z,i}l_i) \\ jZ_i^{-1}\sin(k_{z,i}l_i) & \cos(k_{z,i}l_i) \end{bmatrix}, \tag{2}$$

where material dielectric losses and dispersions are included through a complex permittivity $\varepsilon_{r,i}(f)$ [14].

The response of the radome is obtained by cascading the $\mathbf{M}_i$ matrices of the N layers $M^{(TE,TM)} = \prod_{i=1}^{M-1} M_i^{(TE,TM)}$, which provides the overall transmission coefficient [13].

IV. Optimization and Results

Due to the wide spectrally separated frequency bands and the inherently frequency-selective nature of multilayer interference phenomena, a numerical optimization strategy based on Particle Swarm Optimization (PSO) has been adopted to efficiently explore the highly non-convex solution space [15] with a population of 20 particles, to obtain the best transmission coefficient τ over all frequency ranges. The electromagnetic response of each candidate solution is evaluated using the transmission-line inspired formulation described in Section III, which allows a low-cost computation of τ over the full frequency, polarization, and angular domains with respect to a full-wave analysis. The optimization process is based on a fitness function, which is described as follows:

$$\mathrm{fit} = \frac{1}{\min\limits_{\theta_a,f,\mathrm{pol}} |\tau(\theta_a, f)|}, \tag{3}$$

where $\tau(\theta_a, f)$ represents the transmission coefficient calculated over the specified frequency bands, incidence angles, and polarizations.

TABLE III
OPTIMIZED THICKNESS VALUES OF THE RADOME DESIGN LAYERS

Layer	Thickness (mm)
l_1	0.127
l_2	1.161
l_3	0.309
l_4	1.071
l_5	0.248
l_6	1.316
l_7	0.127

The thickness values of the seven optimized layers are reported in Table III, resulting in an overall radome thickness of 4.819 mm. As illustrated in Fig. 3, the optimized multilayer radome achieves a stable and smoothly varying transmission response across the FSS Ka-, Q-, and V-band frequency ranges for both TE and TM polarizations and for all considered incidence angles. The transmission loss keeps lower than 0.43 dB, with a worst-case performance for TE polarization at 40° incidence. This behavior is expected and intrinsic to electrically thick multiband radomes. The multilayer stack architecture provides a good transparency over the target frequency ranges.

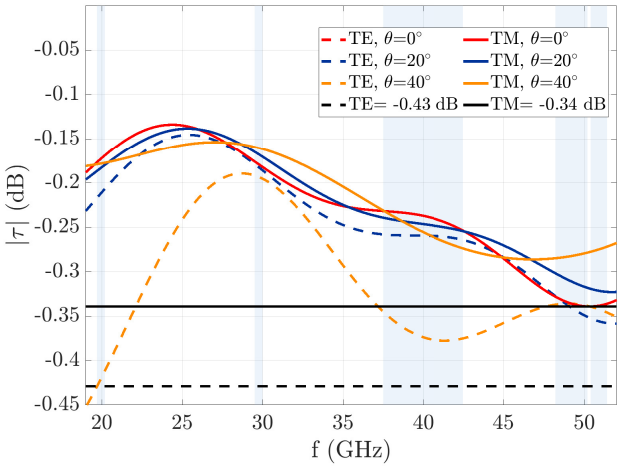

Fig. 3. Transmission coefficient $|\tau|$ of the optimized radome versus frequency, for TE and TM polarizations and different incidence angles. The shaded regions indicate the operational Ka-, Q-, and V-band frequency ranges. The black horizontal lines highlight the worst transmission level for both polarizations.

V. CONCLUSION

A systematic methodology for the design of multiband radomes has been presented. By combining a concise electromagnetic transmission-line model with Particle Swarm Optimization, a 14-layer radome operating over FSS Ka-, Q-, and V-band frequencies has been successfully designed. The proposed methodology effectively enforces wide-angle and multi-band transmission robustness, a key requirement for high-frequency satellite gateway radomes. Future work will focus on the fabrication of the optimized radome prototype and on its experimental characterization to validate the analytical predictions and assess performance under representative operating conditions.

VI. ACKNOLEDGMENT

This work was supported by the European Union under the Italian National Recovery and Resilience Plan (NRRP) of NextGenerationEU, partnership on “Telecommunications of the Future” (PE0000001- program “RESTART”); the authors acknowledge the ongoing collaboration between the University of Catania and Sicilsat Communications S.r.l. on multiband radome technologies for SatCom applications.

REFERENCES

[1] M. Aloisio, P. Angeletti, F. Coromina, and R. De Gaudenzi, “Technological challenges of future broadband telecommunication satellites in Q/V-band,” in *Proc. IEEE Int. Conf. Wireless Information Technology and Systems (ICWITS)*, Maui, HI, USA, 2012, pp. 1–4.

[2] M. Hasan and C. Bianchi, “Ka band enabling technologies for high throughput satellite (HTS) communications,” *Int. J. Satellite Commun. Netw.*, vol. 34, no. 4, pp. 483–501, 2016.

[3] COST 255, “Radiowave propagation modelling for new satcom services at Ku-band and above,” Final Report, ESA Publications Division, SP-1252, Mar. 2002.

[4] R. De Gaudenzi, P. Angeletti, D. Petrolati, and E. Re, “Future technologies for very high throughput satellite systems,” *Int. J. Satellite Commun. Netw.*, vol. 38, no. 2, pp. 141–161, 2020.

[5] L. Zhou *et al.*, “Design and characterization for dual-band and multiband A-sandwich composite radome walls,” *Compos. Sci. Technol.*, vol. 149, pp. 28 – 33, 2017.

[6] Y. Pei, A. Zeng, L. Zhou, R. Zhang, and K. Xu,, “Electromagnetic optimal design for dual-band radome wall with alternating layers of staggered composite and kagome lattice structure,” *Prog. Electromagn. Res.*, vol. 122, pp. 437–452, 2012.

[7] Calian, “Ka/Q/V-band gateway antennas,” Datasheet, 2024. [Online]. Available: https://sites.calian.com/app/uploads/sites/8/2024/06/calian-Ka_Q_V_band_gateway_antennas-final-WEB.pdf

[8] International Telecommunication Union (ITU), *Radio Regulations*, Article 5, No. 5.516B, Geneva, Switzerland, 2020. [Online]. Available: https://search.itu.int/history/HistoryDigitalCollectionDocLibrary/1.44.48.en.101.pdf

[9] Y. He, F. Yang, G. Han, and Y. Li, “High-throughput SatCom-on-the-move antennas: Technical overview and state-of-the-art,” *Digital Commun. Netw.*, vol. 10, no. 6, pp. 1760–1768, 2024.

[10] 3M Company, “3M™ Scotch-Weld™ Structural Adhesive Film AF 163-2 Technical Datasheet,” Aerospace and Aircraft Maintenance Dept., St. Paul, MN, USA, Nov. 2009. [Online].

[11] Evonik Resource Efficiency GmbH, “Dielectric properties of ROHACELL A, HF and WF,” Technical Information Report, Darmstadt, Germany, 2018. [Online].

[12] Rogers Corporation, RO3000® Series Circuit Materials: RO3003™, RO3006™, RO3010™, and RO3035™ High-Frequency Laminates, Datasheet, Chandler, AZ, USA, 2023.

[13] D. M. Pozar, “Microwave network analysis,” in *Microwave Engineering: Theory and Techniques*, 4th ed. Hoboken, NJ, USA: John Wiley & Sons, 2021, ch. 4, pp. 165–220.

[14] Orfanidis, S.J.: ‘Multilayer film applications’, in *Electromagnetic Waves and Antennas* (Rutgers Univ., New Brunswick, NJ, USA, 2002), ch. 8, pp. 303–361. [Online].

[15] J. Robinson and Y. Rahmat-Samii, “Particle swarm optimization in electromagnetics,” *IEEE Trans. Antennas Propag.*, vol. 52, no. 2, pp. 397–407, 2004.

868 MHz Yagi–Uda Antenna for Educational Purposes: Design and Measurement

Mauro da Silva Leme[1,*], J. A. B. Coelho[1], João Paulo Coelho[1]

[1]CeDRI, SusTEC, Instituto Politécnico de Bragança, Campus de Santa Apolónia, 5300-253 Bragança, Portugal
*Corresponding author: mauroleme@ipb.pt

***Abstract*—Antennas are fundamental in wireless systems. This paper describes the design, simulation, and fabrication of an 868 MHz Yagi–Uda antenna for educational laboratories. Featuring a handcrafted balun and PCB matching network, the project evaluates S-parameters and radiation patterns. Results align with simulations, offering a practical, affordable approach for hands-on learning.**

***Keywords*— Yagi–Uda antenna, radiation pattern, impedance matching, S-parameter, far-field.**

I. Introduction

Antennas are key devices in modern communication systems, with applications ranging from broadcast services to everyday technologies such as Wi-Fi, Bluetooth, and cellular networks. Their proper design and characterisation directly affect system performance, coverage area, and interference mitigation.

Several parameters are typically analysed to evaluate an antenna's behaviour, including its input reflection coefficient (S_{11}), impedance position on the Smith chart, and radiation pattern in two or three dimensions. These parameters provide a comprehensive view of how the antenna transmits and receives signals, its impedance matching within the desired frequency band, and how effectively it radiates energy [1].

Building and testing antennas are valuable tools for reinforcing theoretical knowledge in telecommunication classes. Such activities help students consolidate RF concepts and gain practical experience with instrumentation, potentially increasing engagement with the field.

One notable example is the Yagi–Uda antenna, originally developed by Shintaro Uda and later popularised by Hidetsugu Yagi, in the 1920s, this antenna remains a benchmark for achieving directive gain through a simple arrangement of parasitic elements [2]. Its enduring relevance lies in its balance between performance and ease of construction. In this work, the antenna was designed to operate at 868 MHz within the ISM band, combining mechanical simplicity with sufficient performance for laboratory demonstrations.

This paper presents the design, simulation, prototyping, and experimental characterisation of a low-cost Yagi–Uda antenna operating at 868 MHz in the ISM band [3]. This type of antenna was chosen due to its well-known properties and richer radiation pattern, providing valuable opportunities for both analysis and teaching compared to other types, such as dipoles or monopoles. The measurements obtained with a custom-built low-cost setup are compared against simulations to assess the behaviour of the antenna.

This paper is organised as follows: Section II reviews related work; Section III describes the antenna design and measurement methods; Section IV presents results and discussion; and Section V concludes the paper.

II. Related Work

Antenna characterisation requires analysing several parameters, including the radiation pattern, input impedance, and S-parameters, which together describe how efficiently electromagnetic energy is transmitted and received [1,4]. These quantities influence both the radiating performance and the system-level design of wireless devices. In academic environments, the experimental evaluation of such parameters helps students bridge theoretical electromagnetics and practical RF measurement techniques [5].

Among different antenna configurations, the Yagi–Uda antenna remains a popular choice for educational purposes due to its mechanical simplicity, well-defined directivity, and predictable behaviour [2]. Several works have reported Yagi–Uda implementations for different frequency ranges and materials, highlighting its suitability for teaching laboratories and antenna pattern behaviours [6]. Its geometry also allows a comparison between simulated and measured results, supporting a deeper understanding of radiation mechanisms.

In addition, baluns are essential components in antenna systems, as they suppress common-mode currents that can distort radiation characteristics and affect input impedance [7]. Different implementations have been explored in the literature, including ferrite-core, coaxial, and printed types, each aiming to achieve efficient current balance at the feed point. Among them, in-line coax choke baluns provide a simple and low-cost solution for suppressing common-mode currents using standard coaxial cable and lightweight supports. Furthermore, impedance matching is fundamental for maximising power transfer and minimising reflections [4]. Previous studies have shown that discrepancies between simulations and experimental measurements can emerge from environmental factors and fabrication tolerances [8,9]. Therefore, practical impedance matching techniques are usually required to mitigate these effects, such as LC networks and printed implementations.

Overall, although numerous studies have addressed individual aspects such as Yagi–Uda design, balun application,

impedance matching, and application in educational environments, few have considered their integration within a unified and low-cost experimental framework. The present work contributes in this direction by detailing the design, construction, and characterisation of a Yagi–Uda antenna optimised for academic use, providing a reproducible reference for teaching antenna measurement and analysis techniques.

III. Antenna Design and Methods

A. Design Considerations

The proposed design focuses on a six-element Yagi–Uda antenna optimised for educational use, balancing mechanical simplicity, electrical performance, and reproducibility with low-cost materials and tools. Although 433 MHz is also licence-free, antennas at this frequency require larger structures, while designs above 1 GHz demand tighter tolerances and precise alignment. Therefore, 868 MHz offers an ideal compromise between manageable dimensions and fabrication accuracy for didactic prototyping.

The array includes one reflector, one driven element, and four directors, a configuration that provides adequate gain and front-to-back ratio while maintaining mechanical simplicity. Increasing the number of directors could enhance directivity but would complicate construction, whereas reducing them would degrade performance. Thus, the selected layout achieves a balanced educational compromise between performance and simplicity.

The element lengths L were derived from the half-wavelength equation (1):

$$L \approx \frac{\lambda}{2} = \frac{c}{2f}, \tag{1}$$

where c is the speed of light and $f = 868$ MHz. End-effect corrections were then applied as recommended in the literature, using the following equation (2):

$$L_{\text{ref}} \approx 1.03\frac{\lambda}{2}, \quad L_{\text{driv}} \approx 0.98\frac{\lambda}{2}, \quad L_{\text{dir}} \approx 0.95\frac{\lambda}{2}. \tag{2}$$

The spacing between elements followed conventional Yagi-Uda design guidelines ($0.1\lambda \lesssim S \lesssim 0.25\lambda$) and was refined through simulation in CST Studio Suite[1] and MATLAB[2]. The mechanical layout was subsequently designed in SolidWorks[3], ensuring that the optimised dimensions were mechanically feasible [4].

Table I summarises the final element dimensions and spacings. The antenna was later fabricated using low-cost materials, as described in the next subsection.

B. Construction and Materials

Based on the optimised parameters defined in the previous subsection, the antenna was mechanically modelled in SolidWorks to ensure proper alignment of all elements along the boom and to verify the overall structural stability. The mechanical design also facilitated straightforward assembly using low-cost components and simple hand tools, making the prototype reproducible in an educational laboratory setting.

TABLE I: Element lengths and spacings for the Yagi-Uda antenna.

Element	Length (mm)	Position along boom (mm)
Reflector	166.41	-51.964
Driven	150.98	0.00
Director 1	143.85	30.104
Director 2	142.16	102.131
Director 3	140.48	166.814
Director 4	139.51	234.902

The supporting boom was manufactured by fused-deposition modelling (FDM) using polylactic acid (PLA). This material was selected for its low-cost, ease of printing, and relative permittivity ($\varepsilon_r \approx 2.7$–$2.9$), which makes it effectively transparent to RF radiation in this frequency range [10]. Consequently, the boom was not included in the electromagnetic simulation model. The printed boom provided sufficient rigidity to maintain element alignment while remaining lightweight and electrically neutral.

The radiating elements were fabricated from solid brass rods with a 3 mm diameter, chosen for their favourable combination of electrical conductivity, mechanical stiffness, and machinability compared with alternatives such as aluminium or copper tubing. Each rod was cut to the optimised length specified in Table I and press-fitted into the boom with positional accuracy better than 0.5 mm.

As shown in Fig. 1, the CAD model and fabricated prototype exhibit close correspondence between the simulated and constructed geometries.

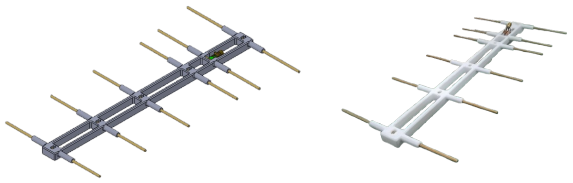

(a) 3D model (SolidWorks). (b) Fabricated prototype.

Fig. 1: Simulated design and fabricated prototype of the optimised Yagi–Uda antenna.

C. Balun for Common-Mode Current Suppression

Connecting a balanced antenna to an unbalanced coaxial line may excite common-mode currents on the feed's outer conductor, distorting the radiation pattern and input impedance [11]. To suppress these currents, an *air-wound coaxial choke balun* was inserted between the driven element and the feed.

The balun was built from a short RG-174 section wound on a 3D-printed PLA former, chosen for rigidity and low permittivity to avoid field perturbation. The required inductance for

[1]The free educational version of this software was used in the simulations.
[2]A campus version of this software is licensed to the Instituto Politécnico de Bragança.
[3]Educational version licensed to the Instituto Politécnico de Bragança.

common-mode suppression was estimated using the Nagaoka-corrected solenoid expression (3):

$$L_s = \frac{4\pi^2 N^2 r^2}{l} K, \tag{3}$$

where N is the number of turns, r the coil radius, l the length, and K Nagaoka's coefficient [12].

The fabricated balun used $N = 7$ turns, $r = 26$ mm, $l = 18.2$ mm, yielding a differential-mode loss of about -0.59 dB and common-mode suppression exceeding -47 dB at 868 MHz. Measurements with nanoVNA, a low-cost, open-source vector network analyzer, and nanoVNASaver[4] software confirmed effective isolation and negligible impact on the desired signal. The PLA support ensured low-cost, and suitability for educational builds.

D. Impedance Matching Network

Efficient power transfer between the transmission line and the antenna requires a proper impedance match, as mismatch losses reduce radiation efficiency and can distort the overall radiation pattern [13]. Initial characterisation of the antenna alone revealed an input impedance of approximately $29.7 + j8.2\ \Omega$ at 868 MHz, corresponding to $S_{11} \approx -11$ dB. Therefore, an impedance matching network was implemented to align the antenna input closer to the $50\ \Omega$ reference.

A compact LC matching circuit was designed on a small printed circuit board (PCB). Before component placement, the bare PCB was characterised to quantify its intrinsic parasitic effects, since at frequencies at 868 MHz, the copper traces and ground plane act as distributed reactive elements. Measurements performed with a nanoVNA showed a shunt impedance magnitude of approximately $|Z| \approx 21.5\ \Omega$, corresponding to an equivalent parasitic capacitance of about 8.5 pF. These parasitic contributions were incorporated into the network design through co-simulation in QucsStudio and SimNEC, using the measured Touchstone data of the bare PCB.

The LC network followed a simple topology consisting of a series capacitor and a shunt inductor, which was first optimised by simulation and then refined according to available commercial values. The selected component values were those closest to the calculated ones, as shown in Table II.

TABLE II: Final LC matching network component values.

Component	Calculated Value	Commercial Value Used
L (shunt to ground)	54.6 nH	56 nH
C (series with signal)	3.8 pF	3.9 pF

As shown in Figs. 2 and 3, the resulting improvement in impedance matching is observed. The Smith chart illustrates the trajectory of the impedance locus toward the 50 Ω centre, while the $|S_{11}|$ curve demonstrates the enhanced reflection coefficient. After the network integration, the measured response achieved $S_{11} \approx -21$ dB and VSWR ≈ 1.2 at 868 MHz, confirming the effectiveness of the matching design.

[4]nanoVNASaver is an open-source graphical interface for the nanoVNA

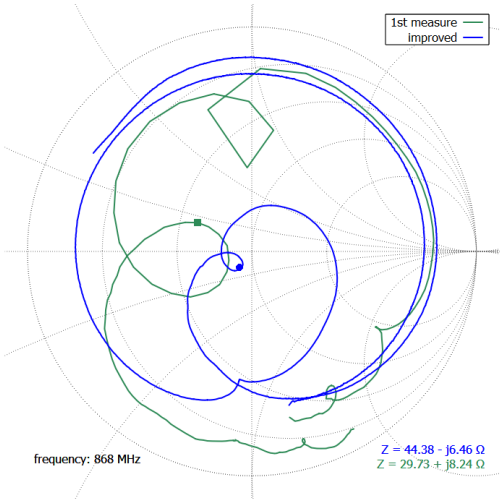

Fig. 2: Smith chart comparison of measured and improved matching at 868 MHz.

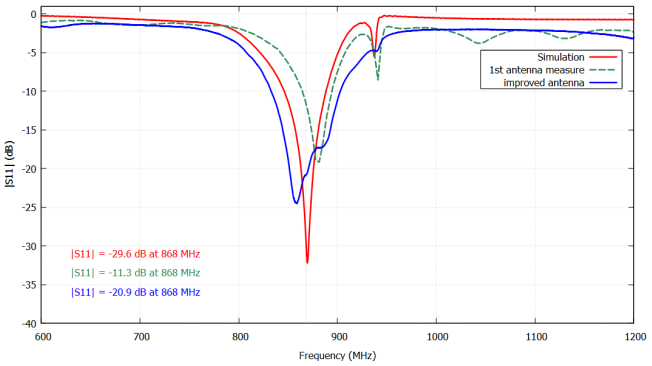

Fig. 3: Simulated and measured $|S_{11}|$ of the Yagi–Uda antenna before and after matching.

The implemented network significantly improved impedance matching while maintaining a compact and low-cost design, making it particularly suitable for educational antenna experiments and RF measurement training.

IV. Results and Discussion

The complete antenna system, including the air-choke balun and LC matching network, was evaluated at 868 MHz to verify the correspondence between simulated and measured results. All measurements were performed under outdoor far-field conditions, with the transmitting and receiving antennas spaced 2.5 m apart and mounted on non-conductive supports to minimise reflections.

Figure 4 presents the measured and simulated far-field radiation patterns in the azimuth plane. Both show a well-defined main lobe at 90° and consistent beamwidth, confirming correct alignment and balanced current distribution. The measured half-power beamwidth was 49°, close to the 47.7° in the simulation, and the front-to-back ratio reached

17 dB, validating the directional behaviour of the antenna. Minor deviations observed in the side lobes are attributed to environmental reflections and manufacturing tolerances.

The 3D comparison shown in Fig. 5 further confirms the antenna's directivity. The measured pattern retains the main-lobe orientation and low back radiation observed in the CST model, demonstrating that the implemented balun and matching network successfully preserved the expected current symmetry and impedance balance.

Overall, the measured results exhibit good agreement with simulations, confirming the effectiveness of the proposed low-cost design, demonstrating that students can design and characterise their own antennas using accessible tools. Future work will include bandwidth and gain measurements, as well as classroom implementation to assess antenna performance and educational impact.

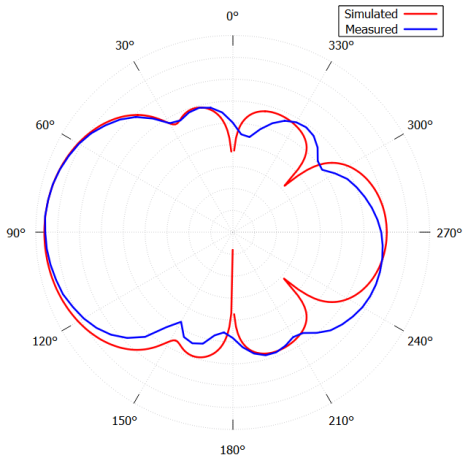

Fig. 4: Measured and simulated far-field radiation patterns at 868 MHz.

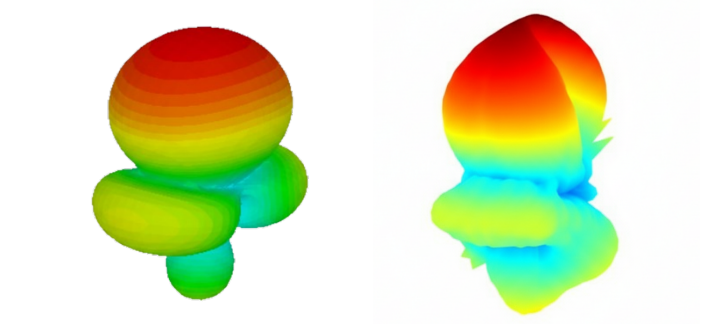

(a) Simulated 3D pattern. (b) Measured 3D pattern.

Fig. 5: Comparison between simulated and measured 3D radiation patterns of the optimised Yagi–Uda antenna.

Acknowledgments

This work was supported by FCT - Fundação para a Ciência e Tecnologia, I.P. by projects: CeDRI, UID/05757/2025 (DOI: 10.54499/UID/05757/2025) and UID/PRR/05757/2025 (DOI: 10.54499/UID/PRR/05757/2025); SusTEC, LA/P/0007/2020 (DOI: 10.54499/LA/ P/0007/2020).

References

[1] S. Z. Mohd Hamzah, N. F. A. Malek, F. T. Ahamad, S. Y. Mohamad, and M. H. Jamaluddin, "Reflection coefficient variation based on the configuration of integrated antenna and reflecting surface at 3.5 ghz," in *2023 IEEE International Symposium On Antennas And Propagation (ISAP)*, 2023, pp. 1–2.

[2] H. Yagi and S. Uda, "Projector of the sharpest beam of electric waves," *Proceedings of the Imperial Academy of Japan*, vol. 2, no. 2, pp. 49–52, 1926.

[3] ETSI, *ETSI EN 300 220-1 V2.4.1: Short Range Devices (SRD); Radio equipment to be used in the 25 MHz to 1 000 MHz frequency range with power levels up to 500 mW; Part 1: Technical characteristics and methods of measurement*, European Telecommunications Standards Institute (ETSI) Std., 2012, accessed: 2025-08-10. [Online]. Available: https://www.etsi.org/deliver/etsi_en/300200_300299/30022001/02.04.01_60/en_30022001v020401p.pdf

[4] C. A. Balanis, *Antenna Theory: Analysis and Design*, 3rd ed. Hoboken: John Wiley & Sons, 2005.

[5] S. Rachchompoo, N. Intarawiset, S. Akatimagool, and K. Chaiyawong, "Development of learning innovation of dtv antennas for telecommunication education," in *2020 7th International Conference on Technical Education (ICTechEd7)*, 2020, pp. 41–44.

[6] R. Reddy and R. Swaminathan, "Directivity improvement of 9-element yagi uda antenna by increasing director elements in comparison with 7-element yagi uda antenna," in *2022 3rd International Conference on Intelligent Engineering and Management (ICIEM)*, 2022, pp. 561–564.

[7] J. Sevick, *Transmission Line Transformers*, 4th ed. Noble Publishing, 2001.

[8] Y. P. Zhang, "Design and experiment on differentially-driven microstrip antennas," *IEEE Transactions on Antennas and Propagation*, vol. 55, no. 10, pp. 2701–2708, 2007.

[9] B. E. Fischer, I. J. LaHaie, M. D. Huang, M. H. A. J. Herben, A. C. F. Reniers, and P. F. M. Smulders, "Causes of discrepancies between measurements and em simulations of millimeter-wave antennas [measurements corner]," *IEEE Antennas and Propagation Magazine*, vol. 55, no. 6, pp. 139–149, 2013.

[10] G. Boussatour, P.-Y. Cresson, B. Genestie, N. Joly, and T. Lasri, "Dielectric characterization of polylactic acid substrate in the frequency band 0.5–67 ghz," *IEEE Microwave and Wireless Components Letters*, vol. 28, no. 5, pp. 374–376, 2018.

[11] F. Fiorelli *et al.*, "Effects of common-mode currents on antenna measurements," *IEEE Antennas and Propagation Magazine*, vol. 53, no. 5, pp. 186–194, 2011.

[12] R. Lundin, "A handbook formula for the inductance of a single-layer circular coil," *Proceedings of the IEEE*, vol. 73, no. 9, pp. 1428–1429, 1985.

[13] M. M. Hasan and M. Cheffena, "Adaptive antenna impedance matching using low-complexity shallow learning model," *IEEE Access*, vol. 11, pp. 74 101–74 111, 2023.

Electromagnetic Theory: Analytical, Computational and Numerical Methods

AES 2026 · Catania, Italy · ISSN 2491-2417

Leaky-Wave Analysis of Circularly Polarized Bessel-Beam Launchers based on Anisotropic Modulated Metasurfaces

Edoardo Negri[1,*], Federico Giusti[2], David González-Ovejero[3], Enrica Martini[2], Walter Fuscaldo[1]

[1]Istituto per la Microelettronica e i Microsistemi, Consiglio Nazionale delle Ricerche, Rome, Italy
[2]Department of Information Engineering and Mathematics, University of Siena, 53100 Siena
[3]University Rennes, CNRS, Institut d'Electronique et des Technologies du numeRique (IETR), UMR 6164, 35000 Rennes, France
*Corresponding author: edoardonegri@cnr.it

***Abstract*—This contribution deals with an original leaky-wave paradigm for characterizing circularly polarized Bessel-beam launchers based on anisotropic modulated metasurfaces. The proposed method is validated through a method of moments by achieving a remarkable agreement among full-wave and theoretical results.**

***Keywords*— Bessel beams, leaky waves, metasurfaces, near-field focusing.**

I. Introduction

Thanks to their remarkable limited-diffraction, self-healing, and focusing features, Bessel beams (BBs) have recently attracted much interest in different application contexts, such as high-data-rate near-field links and wireless power transfer [1]. Among different solutions able to generate a BB distribution, leaky-wave Bessel-beam launchers (BBLs) stand out for their compact, low-profile, and cost-effective architecture [1].

This contribution deals with leaky-wave wideband BBLs which are able to generate a BB profile over a wide frequency range. The working principle of such devices is based on the excitation of an inward cylindrical wave—which is required for the BB generation [2], [3]—through a leaky, periodic structure on top of a grounded dielectric slab (GDS) [1]. In this sense, the common architecture of wideband BBLs is based on a GDS with an annular metal strip grating on top [1]. Such a solution, however, presents a linearly polarized BB distribution and suffers the open-stopband (OSB) phenomenon which prevents the device to reach large nondiffractive-range values z_{ndr} (i.e., the maximum distance for which the BB profile preserves its intriguing, near-field properties) [4].

A solution able to provide a circularly polarized (CP) BB with an ultra-long nondiffractive range has been recently proposed [5] and it is based on a GDS with an anisotropic modulated metasurface on top (see Fig. 1). Such structure, however, lacks of a leaky-wave paradigm able to predict its radiating performance without restoring to complex full-wave method of moments (MoM). The aim of this contribution is to fill this gap by proposing a leaky-wave, CP, aperture-field distribution able to predict, through the Huygens–Fresnel radiation integral, the near-field profile of the considered BBL

Fig. 1. Pictorial representation of a circularly polarized Bessel-beam launcher and of its co-polarized, limited-diffraction, near-field distribution. The device is constituted by a grounded dielectric slab (orange region) with an anisotropic modulated metasurface on top (gray metallic patches in this figure).

(similarly to the computation, through the spectral domain, of the field generated by an aperture magnetic-current distribution in [2], [3], [6]). Theoretical results—retrieved through the model introduced in Sec. II—are compared with those coming from an established MoM full-wave approach (Sec. III). The remarkable agreement among these results corroborates the proposed method. Conclusions are finally drawn in Sec. IV.

II. Theoretical Framework

Although spiral-shaped anisotropic modulated metasurfaces (see, e.g., Fig. 1) are commonly used for achieving a CP far-field radiation pattern pointing at broadside, they are here exploited to obtain a focused near-field distribution. Such metasurfaces can be represented through the following penetrable impedance boundary condition (PIBC) [7]:

$$\begin{aligned} X_{\rho\rho}(\rho,\phi) &= \overline{X}\left[1+M\cos\left(\frac{2\pi}{d}\rho-\phi\right)\right] \\ X_{\rho\phi}(\rho,\phi) = X_{\phi\rho}(\rho,\phi) &= \overline{X}M\sin\left(\frac{2\pi}{d}\rho-\phi\right) \\ X_{\phi\phi}(\rho,\phi) &= \overline{X}\left[1-M\cos\left(\frac{2\pi}{d}\rho-\phi\right)\right] \end{aligned} \tag{1}$$

with d being the modulation period, M the modulation index, and $\overline{X}$ the average reactance. Interestingly, depending on the sign of ϕ and $X_{\rho\phi}$ in (1), it is possible to achieve a right- or left-hand CP [8].

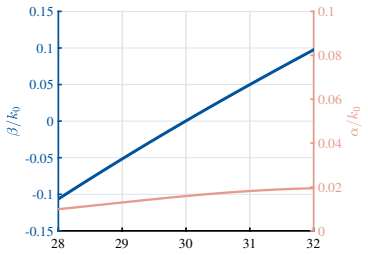

Fig. 2. Dispersion diagram showing the phase β and attenuation α constants of the leaky mode, normalized with respect to the free-space wavenumber k_0.

Based on the PIBC model, one can compute the dispersion curve of the leaky wavenumber $k_\rho = \beta - j\alpha$ [7], with β and α being the phase and attenuation (i.e., leakage) constants, respectively. Once β and α are known, under the assumption of an azimuthally symmetric, transverse-magnetic (TM) source (e.g., a coaxial feeder) and the dominance of the leaky-wave contribution on the radiating plane [1], the tangential aperture-field distribution reads:

$$\mathbf{E}_t(\rho) = E_0 H_1^{(2)}(k_\rho \rho)(\hat{\mathbf{x}} \pm j\hat{\mathbf{y}}) \tag{2}$$

with $H_1^{(2)}(\cdot)$ being the first-order Hankel function of the second kind, E_0 the electric field amplitude, and $(\hat{\mathbf{x}} \pm j\hat{\mathbf{y}})$ the right- or left-hand CP vector. At this point, the near-field distribution is achieved by computing the Huygens–Fresnel radiation integral of the sources on the aperture plane achieved by applying the equivalence principle on the electric-field profile in (2) (see, e.g., [1] for further details).

III. Results

To corroborate this approach, we consider here the same design parameters of [5], i.e., a substrate—with dielectric permittivity $\varepsilon_r = 3$ and height $h = 0.762\,\text{mm}$—topped with a metasurface described by $\overline{X} = -375\,\Omega$, $d = 8.8\,\text{mm}$, and $M = 0.48$. In this case study—which leads to the dispersion curves of the leaky wavenumber in Fig. 2—one can compare the co-polar component of the near-field distribution obtained through the radiation integral of the aperture-field profile in (2), with the results obtained by means of the MoM for homogenized PIBC proposed in [9]. In this context, as shown in Fig. 3, excellent agreement is observed between the results of the two approaches at the working frequency of $f_0 = 28.94\,\text{GHz}$. Minor discrepancies arise only in the vicinity of the launcher, attributable to the strong assumption in the theoretical model that the aperture field is solely composed of the leaky-wave contribution. A further corroboration of the results is found observing the BB nondiffractive behavior within the diamond-shaped region (white dashed lines in Fig. 3) and below the nondiffractive range (green dashed lines in Fig. 3) predicted by the leaky theory (see, e.g., [1] for further details).

IV. Conclusion

This paper proposed and corroborated, through full-wave results, an original leaky-wave approach for predicting the near-field distribution of circularly polarized Bessel-beam launchers based on anisotropic modulated metasurfaces. Further results and case studies will be discussed at the conference.

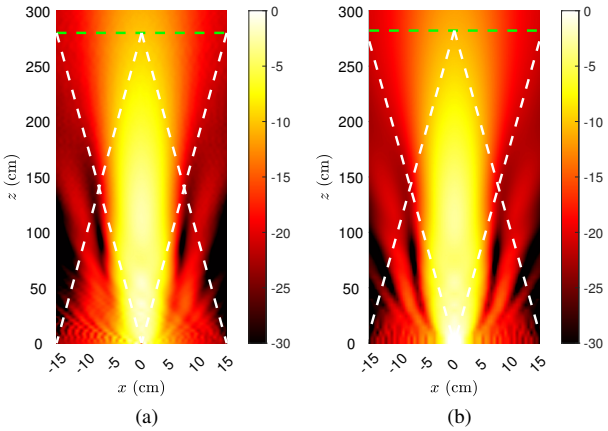

Fig. 3. Colormap, in dB, of the co-polarized electric-field distribution excited, at 28.94 GHz, by the considered Bessel-beam launcher with an aperture radius of 15 cm. The results, normalized with respect to their maximum, are computed through a (a) full-wave MoM approach and (b) the Huygens–Fresnel radiation integral of the aperture-field profile in (2). While white dashed lines indicate the diamond-shaped region where the Bessel beam is supposed to be generated, the green dashed lines represent its nondiffractive range.

Acknowledgment

E. N. and W.F acknowledge the project PRIN 2022 "SAFE" (Spiral and Focused Electromagnetic fields) 2022ESAC3K, Italian Ministry of University and Research (MUR), financed by the European Union, NextGeneration EU.

References

[1] E. Negri, J. Taillieu, W. Fuscaldo, M. Robin, X. Morvan, O. De Sagazan, P. Burghignoli, A. Galli, and D. González-Ovejero, "Design and experimental validation of an E-band wideband Bessel-beam launcher on quartz," *IEEE J. Microw.*, 2025, Early Access.

[2] M. Albani, S. C. Pavone, M. Casaletti, and M. Ettorre, "Generation of non-diffractive Bessel beams by inward cylindrical traveling wave aperture distributions," *Opt. Express*, vol. 22, no. 15, pp. 18 354–18 364, Jul. 2014.

[3] S. C. Pavone, M. Ettorre, and M. Albani, "Analysis and design of Bessel-beam launchers: Longitudinal polarization," *IEEE Trans. Antennas Propag.*, vol. 64, no. 6, pp. 2311–2318, Jun. 2016.

[4] E. Negri, F. Giusti, W. Fuscaldo, P. Burghignoli, E. Martini, and A. Galli, "Ultra-long-range bessel beams via leaky waves with mitigated open stopband," *Appl. Phys. Lett.*, vol. 126, no. 12, p. 121703, 03 2025.

[5] F. Giusti, E. Negri, D. González-Ovejero, W. Fuscaldo, and E. Martini, "Long non-diffractive-range Bessel-beam launcher with circular polarization," in *IEEE Int. Symp. Antennas Propag. (APS 2025)*, Ottawa, Canada, 2025, pp. 1–4.

[6] S. C. Pavone, M. Ettorre, M. Casaletti, and M. Albani, "Transverse circular-polarized Bessel beam generation by inward cylindrical aperture distribution," *Opt. Express*, vol. 24, no. 10, pp. 11 103–11 111, 2016.

[7] F. Giusti, S. Maci, and E. Martini, "Complete open-stopband suppression using sinusoidally modulated anisotropic metasurfaces," *IEEE Trans. Antennas Propag.*, vol. 71, no. 11, pp. 8537–8547, Nov. 2023.

[8] G. Minatti, F. Caminita, M. Casaletti, and S. Maci, "Spiral leaky-wave antennas based on modulated surface impedance," *IEEE Trans. Antennas Propag.*, vol. 59, no. 12, pp. 4436–4444, 2011.

[9] D. González-Ovejero and S. Maci, "Gaussian ring basis functions for the analysis of modulated metasurface antennas," *IEEE Trans. Antennas Propag.*, vol. 63, no. 9, pp. 3982–3993, Sep. 2015.

Improving the performance of Iterative Physical Optics algorithm with Div/Curl-conforming basic functions.

Michael Katsav[1],

[1]School of Electrical Engineering, Tel Aviv University, Tel Aviv 69978, Israel, katsav.michael@gmail.com

Abstract—This paper discusses various methods for discretization and testing the magnetic field integral equation (MFIE) used in the iterative physical optics (IPO) algorithm for solving the problem of induced currents on the inner walls of cavities. It is shown that the best results are achieved using Rao-Wilton-Glisson (RWG) functions for discretization and $\mathbf{n}\times$ Buffa-Christiansen (BC) functions for testing. It is also shown that using div/curl-conforming functions reduces the numerical complexity of the problem by almost four times compared to the standard method.

I. Introduction

The problem of electromagnetic scattering from open-ended large cavities is an important task in electromagnetic predictions of complex targets. Thus, the engine inlet and exhaust ducts may contribute very significantly to the backscattering of modern jet platforms. In the past, several alternative approaches have been developed for cavity analysis, they can be grouped into (1) exact methods, including integral methods (MoM), finite elements method and modal analysis. (ii) Hight frequency methods, including different ray/beam techniques (SBR, BSA), and the methods based on physical optics (PO) and iterative physical optics (IPO). In the current work, we concentrate on IPO method.

II. Iterative Physical Optics Algorithm.

The IPO algorithm is high frequency technique based on iterative solution of the MFIE [1] for induced currents on the cavity inner walls, where the PO currents are chosen as the first iteration. In IPO, the solution is obtained after several number of iterations, which is closely related to the number of expected internal reflections. In addition, IPO is much more numerically efficient than the full matrix solution of the integral equation because the grid density is coarser-usually three-four elements per wavelength, instead of the eight to ten elements used in discretization of integral equation. Its effectiveness has been widely discussed in literature. However, the main drawback of the IPO is that the process of updating of the induced currents requires the simultaneous discretization of the system of three equation (three component of electrical currents), then the overall complexity of the method is $O(9N^2)$, where N is a number of triangulation patches used to discretize the inner walls of a cavity. It should be noted that this complexity is due to method of IPO implementation used in [1]: namely, the authors in [1] assume that induced currents are constant on each triangular patch and are evaluated at centroid of each such patch.

III. Iterative Physical Optics Algorithm with Div/Curl-Conforming Basic Functions.

The induced current on the cavity inner walls is expanded as

$$\mathbf{J} = \sum_{n=1}^{N_e} I_n \mathbf{f}_n \tag{1}$$

where $\mathbf{f}_n$ is a basic function and N_e is number of triangular mesh edges.[1] In following we consider four different types of these functions: (i) RWG functions, these functions are related to div-conforming basic functions [2]. (ii) Rotated RWG: $\mathbf{n}\times$RWG. These functions are related to curl-conforming basic functions [2]. (iii) BC functions, they are related to div-conforming and quasi-curl conforming functions [3], [4]. (iv) And finally, rotated BC functions: $\mathbf{n}\times$BC, related to curl-conforming and quasi-div conforming functions [3], [4].

On the next step, the MFIE is converted into matrix equation via standard testing procedure, where either function from (i)-(iv) can be used as testing function. The numerical complexity of such a formulation is $O(N_e^2) \simeq O(9/4N^2)$, which is approximately four times smaller than in the formulation [1].

IV. Numerical Example.

The proposed numerical scheme for IPO was applied to analysis of backscattering from the annular open-ended cavity. A similar example was also considered in [1, Fig.6]. The proposed IPO scheme is verified through comparison with combined field integral equation (CFIE) formulation and for this goal we use in CST commercial code. The results are depicted on the Fig. 1. As can be seen from this figure, the least accurate results are obtained using RWG functions for both discretization and testing. Using $\mathbf{n}\times$RWG functions improves the results. Using the

[1]RWG basis functions are defined only on the interior edges of the mesh, while BC functions also include the boundary edges.

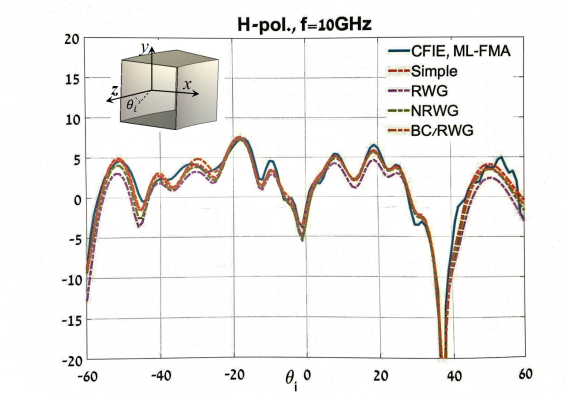

Fig. 1. Backscattered pattern of annular cavity at $f = 10$GHz. The solid blue color line represents CFIE solution, the red dotted line represents IPO result discretizied in accordance with [1] ('simple'); magenta dotted line represents IPO result discretizied and tested with RWG functions ('RWG'); green dotted line represents IPO result discretizied and tested with $\mathbf{n}\times$RWG functions ('NRWG'); and finally the dotted brown line represents IPO result discretizied with RWG and tested with $\mathbf{n}\times$BC ('BC/RWG').

numerical scheme described in [1] and $\mathbf{n}\times$BC/RWG yield results much closer to CFIE.

V. Conclusion

We investigated various discretization and testing strategies for the MFIE used in the IPO formulation with div/curl-conforming basis functions. It is shown that the best results are achieved using Rao-Wilton-Glisson (RWG) functions for discretization and $\mathbf{n}\times$ Buffa-Christiansen (BC) functions for testing. Using div/curl functions reduces the numerical complexity of the problem by almost a factor of four compared to the standard method [1].

References

[1] F. Obelleiro-Basteiro, J. Rodriguez, and R. Burkholder," An Iterative Physical Optics Approach for Analyzing the Electromagnetic Scattering by Large Open-Ended Cavities", IEEE Trans. Antennas Prop., Vol. 43, N. 4, 1995.

[2] W. Gibson, "The Method of Moments in Electromagnetics", Chapman Hall/CRC, 2008.

[3] F. Andriulli, K. Cools, H. Ba˘gci, F. Olyslager, A. Buffa, S. Christiansen, and E. Michielssen, "A Multiplicative Calderon Preconditioner for the Electric Field Integral Equation," IEEE Trans. Antennas Prop., vol. 56, N. 8, pp. 2398–2412, 2008.

[4] K. Cools, F. P. Andriulli, D. De Zutter, and E. Michielssen, "Accurate and Conforming Mixed Discretization of the MFIE," IEEE Antennas Wireless Prop. Letters., vol. 10, pp. 2398–2412, 2011.

Method of Moments for the Analysis of Arbitrarily Shaped Metasurfaces

Federico Giusti, Stefano Maci, Enrica Martini

Department of Information Engineering and Mathematics, University of Siena, 53100 Siena

*Corresponding author: federico.giusti2@unisi.it

***Abstract*—This paper presents a general framework for constructing entire-domain basis functions for the Method of Moments (MoM) analysis of metasurfaces (MTSs) composed of arbitrarily shaped metallic elements. The proposed basis functions are defined as linear combinations of Rao–Wilton–Glisson (RWG) functions and accurately reproduce the surface-current distributions associated with the propagating regime of the fundamental mode. As a result, the MoM formulation is reduced to only a few unknowns per element, leading to a significant decrease in computational complexity. The effectiveness of the approach is demonstrated through the dispersion analysis of a double-anchor patch printed on a grounded dielectric slab, with results showing excellent agreement with those obtained using the CST Eigenmode Solver. Basis functions derived for a reference element can be efficiently scaled and rotated to model all elements of a spatially modulated MTS.**

***Keywords*— Metasurfaces, dispersion analysis, method of moments, surface waves.**

I. Introduction

Metasurfaces (MTSs) provide a versatile platform for controlling electromagnetic fields and enable a wide range of devices, including anomalous refractors and reflectors, lenses, and surface-wave (SW)–based components and holograms [1], [2]. In the microwave regime, MTSs are commonly implemented using PCB technology, where the local electromagnetic response is controlled through gradual variations of electrically small printed elements. These variations are typically realized through in-plane scaling and rotation, which allow independent tuning of the diagonal and off-diagonal terms of the equivalent impedance tensor. This enables efficient design based on precomputed mappings between element geometry and equivalent impedance. Nevertheless, accurate performance assessment, including frequency behavior and sensitivity to tolerances, still requires full-wave analysis of the entire structure. For electrically large MTSs comprising tens of thousands of elements, this results in a computational burden that is often prohibitive for general-purpose solvers.

To address this issue, an efficient MoM-based approach was introduced in [3] for MTSs composed of elliptical patches, where a small set of entire-domain basis functions was used to represent the surface current. Owing to the subwavelength size of the unit cells, two basis functions per element were sufficient to accurately model the quasi-static current behavior, drastically reducing the number of unknowns compared to conventional Rao–Wilton–Glisson (RWG) discretizations. While this method offers notable computational advantages and closed-form spectral representations, the restriction to elliptical geometries limits the range of achievable equivalent impedances, motivating the need for more general element shapes.

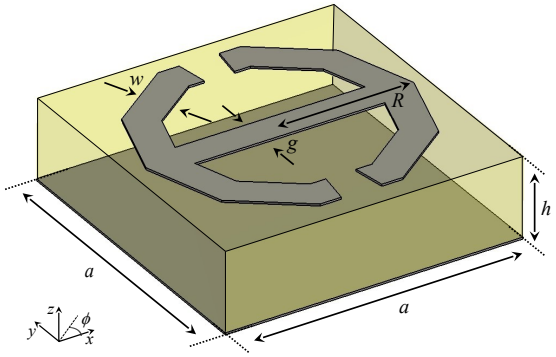

Fig. 1: Geometry of the unit cell of the double-anchor patch MTS.

In this work, we propose a general procedure for constructing generalized entire-domain basis functions for arbitrarily shaped metallic patches, enabling a computationally fast analysis of MTS-based devices for SW and leaky-wave manipulation. The approach follows the philosophy of characteristic or synthetic basis functions [4]–[6]. Here the entire-domain basis functions are expressed as linear combinations of Rao–Wilton–Glisson (RWG) basis functions. Since all elements can be obtained from a reference geometry through scaling and rotation, the basis functions computed once for the reference element can be efficiently adapted to all others without recomputation for the case of periodically and aperiodically modulated MTSs. The proposed basis functions are employed to characterize through a periodic spectral MoM the dispersion behavior of a MTS composed of a 2D periodic array of metallic double-anchor patches printed on a grounded dielectric slab. The dispersion analysis is validated against CST Eigenmode Solver (CST ES) results, showing excellent agreement.

II. Theoretical Formulation

Let us consider an infinite planar periodic MTS of general-shape metallic patches printed on a grounded dielectric slab and arranged on a square lattice with period a. Following

the procedure detailed in [7], [8], the MoM matrix can be compactly expressed in matrix form as

$$\left[\mathbf{Z}^{\mathrm{MoM}}\right] = [\mathbf{Q}]^H \left[\mathbf{Z}_{\mathrm{GF}}\right] [\mathbf{Q}] \tag{1}$$

where

$$[\mathbf{Z}_{\mathrm{GF}}] = \mathrm{diag}\left\{ Z_{\mathrm{GF}}^{\mathrm{TM}}(\mathbf{k}_q), Z_{\mathrm{GF}}^{\mathrm{TE}}(\mathbf{k}_q) \right\} \tag{2}$$

is a $2M \times 2M$ diagonal matrix (with M being the maximum index of Floquet harmonics) collecting the TM and TE spectral Green's-function components evaluated at the Floquet wavenumbers $\mathbf{k}_q$, and

$$[\mathbf{Q}] = \begin{bmatrix} \mathbf{Q}_1 & \mathbf{Q}_2 & \cdots & \mathbf{Q}_L \end{bmatrix} \tag{3}$$

is a $2(2M+1) \times L$ projection matrix. Here, L denotes the total number of unknown coefficients associated with the RWG basis expansion, equal to the number of internal edges in the mesh. Consequently, the RWG basis functions coefficients for the p-th entire-domain basis function are obtained from the eigenvalue problem defined by the MoM solution as the eigenvectors of the MoM matrix:

$$\mathbf{I}_p = \begin{bmatrix} I_{p1} & I_{p2} & \cdots & I_{pL} \end{bmatrix}^T. \tag{4}$$

For being able to accurately compute the dispersion analysis of a single cell, a set $\{\tilde{\mathbf{J}}_p(\mathbf{k})\}$ of basis function can be defined over P frequency samples. Consequently, the p-th entire-domain basis function is given by a linear combination of the spectral samples of all the RWG basis functions coefficients.

$$\tilde{\mathbf{J}}_p(\mathbf{k}) = \sum_{l=1}^{L} I_{pl} \mathbf{Q}_l \tag{5}$$

These P new spectral entire-domain basis functions are certainly problem matched [6], but to decide how many of them are strictly necessary a singular value decomposition is applied to the to the $L \times P$ matrix $[\mathbf{I}]$ with elements I_{pl} introduced in (5).

III. Numerical Results

The geometry of the analyzed unit cell is depicted in Fig. 1. The MTS consists of metallic double-anchor patches periodically arranged along the x- and y-directions on a grounded dielectric substrate of thickness $h = 0.762\,\mathrm{mm}$ and relative permittivity $\varepsilon_\mathrm{r} = 3$. The lattice is square with period $a = 1.5\,\mathrm{mm}$. The width of the central strip and the two anchors are $g = 0.155\,\mathrm{mm}$ and $w = 0.1705\,\mathrm{mm}$, respectively. Each patch is formed by discretizing a circular contour of radius $R = 0.675\,\mathrm{mm}$ into ten segments. Three entire-domain basis functions are considered after applying a singular value decomposition over 9 frequency samples from 9 to 33 GHz. The dispersion diagram of the unit cell under study is reported in Fig. 2, showing a perfect agreement with CST ES throughout its entire propagating regime.

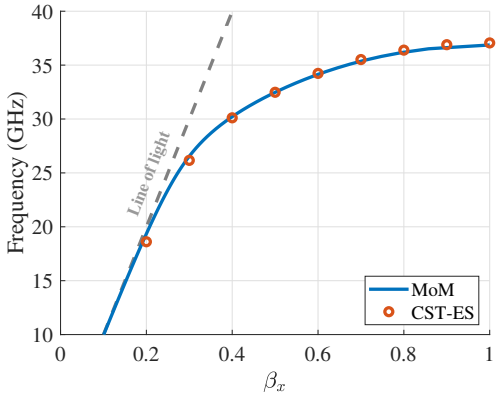

Fig. 2: Dispersion analysis of the double-anchor patch MTS shown in Fig. 1, computed using the proposed MoM (dashed lines) and validated with CST ES (solid lines).

IV. Conclusion

A generalized approach for defining entire-domain basis functions for the analysis of modulated metasurfaces with arbitrarily shaped metallic patches has been presented. The basis functions are derived from the eigenmodes of a reference unit cell and expressed as linear combinations of Rao–Wilton–Glisson functions, then reduced to its minimum number through a singular value decomposition. Their effectiveness is demonstrated through a spectral Method of Moments formulation for dispersion analysis, yielding a compact system matrix. Results for a periodic metasurface of double-anchor patches on a grounded dielectric slab show excellent agreement with CST Eigenmode Solver. Further applications to periodically modulated metasurfaces will be presented at the conference.

References

[1] C. L. Holloway, E. F. Kuester, J. A. Gordon, J. O'Hara, J. Booth, and D. R. Smith, "An overview of the theory and applications of metasurfaces: The two-dimensional equivalents of metamaterials," *IEEE Antennas and Propagation Magazine*, vol. 54, no. 2, pp. 10–35, 2012.

[2] S. B. Glybovski, S. A. Tretyakov, P. A. Belov, Y. S. Kivshar, and C. R. Simovski, "Metasurfaces: from microwaves to visible," *Physics Reports*, vol. 634, pp. 1–72, 2016.

[3] M. Mencagli, E. Martini, and S. Maci, "Surface wave dispersion for anisotropic metasurfaces constituted by elliptical patches," *IEEE Transactions on Antennas and Propagation*, vol. 63, no. 7, pp. 2992–3003, 2015.

[4] V. V. S. Prakash and R. Mittra, "Characteristic basis function method: A new technique for efficient solution of method of moments matrix equations," *Microwave and Optical Technology Letters*, vol. 36, no. 2, pp. 95–100, 2003.

[5] L. Matekovits, V. A. Laza, and G. Vecchi, "Analysis of large complex structures with the synthetic-functions approach," *IEEE Transactions on Antennas and Propagation*, vol. 55, no. 9, pp. 2509–2521, 2007.

[6] C. Aanandan, P. Debernardi, R. Orta, R. Tascone, and D. Trinchero, "Problem-matched basis functions for moment method analysis-an application to reflection gratings," *IEEE Transactions on Antennas and Propagation*, vol. 48, no. 1, pp. 35–40, 2000.

[7] S. Maci and A. Cucini, *FSS-Based EBG Surfaces*. John Wiley Sons, Ltd, 2006, ch. 13, pp. 351–376.

[8] F. Giusti, S. Maci, and E. Martini, "Generalized entire-domain basis functions for modulated metasurfaces analysis," in *2026 20th European Conference on Antennas and Propagation (EuCAP) - Accepted*, 2026, pp. 1–4.

Inverse Design by Alternating Projections of Physically Realizable Modulated Metasurface Antennas

Marco Faenzi[1,*], David González-Ovejero[2], Enrica Martini[1], Stefano Maci[1]

[1]Department of Information Engineering and Mathematics, University of Siena, Italy
[2]Univ Rennes, CNRS, IETR – UMR 6164, Rennes, France
*Corresponding author: marco.faenzi@unisi.it

***Abstract*—This paper introduces a physically sound inverse design technique for metasurface antennas using tensor surface reactance synthesis. Solving the EFIE cast into a MoM formulation and constraining a passive, reciprocal reactance tensor, an iterative Gerchberg-Papoulis inspired projection algorithm efficiently reconstructs aperture currents and surface impedance generating complex, directive radiation patterns.**

***Keywords*— metasurface antennas, inverse design, tensor impedance, alternating projections, EFIE.**

I. Introduction

Modulated metasurfaces (MTS) provide an efficient low-cost platform to manipulate wavefronts through subwavelength modulation of characteristic surface waves (SW) [1]–[4]. By appropriate design of the spatially varying equivalent tensor surface impedance, metasurface based antennas enable compact and low-profile implementations of beamforming, contoured and multibeam radiation, beam polarization control, or highly directive radiation [5]–[11].

MTS antennas analysis and synthesis are usually formulated using homogenized impedance boundary conditions (IBCs) representing the macroscopic electrical properties of the small texture; these relate average tangential electric and magnetic fields and embed an equivalent impedance tensor [12], [13]. Within this framework, the Electric Field Integral Equation (EFIE), solved via the Method of Moments (MoM) offers a robust and efficient model [14], [15]; in the present work Gaussian-ring sub-domain basis functions [14] are adopted for computational convenience.

While forward analysis (assessing radiation from known impedance boundary condition) is well established in literature, the inverse synthesis problem (defining IBCs from desired radiation properties) is still a challenge. Thus, desire is: from a prescribed radiation pattern, let's determine a finite-aperture impedance distribution generating the target far-field, additionally the latter must satisfy constraints of passivity and reciprocity. Existing approaches, including analytical Flat-Optics based methods, spectral-domain inversion, and optimization techniques [5], [6], [12], [13], [15]–[17], often require a tailored regularization or miss to explicitly enforce feasibility conditions of the synthesized impedance.

Alternating projection (AP) methods provide a robust and physically consistent framework [18]–[23] for addressing such constrained inverse problems. By iteratively enforcing spectral-domain field constraints and binding spatial-domain physical requirements, such projections lead to currents and impedance convergence toward self-consistent solutions compatible with the EFIE. In this context, the proposed EFIE-based alternating projection formulation retrieves finite-aperture current sets simultaneously with corresponding Hermitian tensor surface impedance, ensuring physical consistency.

II. Metasurface Homogenization

Let us consider a MTS aperture of finite extent S_a, characterized by radius a, lying in the plane $\hat{\boldsymbol{z}}=0$ and with outward normal unit vector $\hat{\boldsymbol{z}}=\hat{\boldsymbol{n}}$. For a metallic cladding with gently variable small texture features, one can assume the MTS is homogenizable, meaning the averaged tangential electric and magnetic fields are linked by an IBC of the kind

$$\mathbf{E}_t = \mathrm{j}\underline{\underline{\mathrm{X}}}_s \cdot \hat{\boldsymbol{n}} \times \left[\mathbf{H}_t^{0^+} - \mathbf{H}_t^{0^-}\right] = \mathrm{j}\underline{\underline{\mathrm{X}}}_s \cdot \mathbf{J} \tag{1}$$

where $\mathbf{J}(\boldsymbol{\rho})$ indicates the surface current distribution and $\underline{\underline{\mathrm{X}}}_s$ stands for tensor equivalent surface reactance of the MTS. Imposing Hermitianity on the reactance, (i.e., $\underline{\underline{\mathrm{X}}}_s^{\dagger}=\underline{\underline{\mathrm{X}}}_s$) ensures the physical realizability of the designed MTS by respecting passivity and reciprocity of the synthesized structure.

III. Metasurface Synthesis Process

The aperture synthesis is treated by considering the EFIE, where the surface current $\mathbf{J}$ is expanded via a set of basis functions (as mentioned, here the functions introduced in [14] are adopted) that are localized in the space domain with the corresponding expansion coefficients vector $\mathbf{j}$; the relevant radiated field can be expressed as

$$\mathbf{E}_t = \int_{S_a} \underline{\underline{\mathbf{G}}}_{EJ}(\boldsymbol{\rho},\boldsymbol{\rho}')\mathbf{J}(\boldsymbol{\rho}')dS' \tag{2}$$

where $\underline{\underline{\mathbf{G}}}_{EJ}$ is the dyadic Green's function of the homogeneous stacked medium.

A. Definition of the Analysis and Synthesis Operators

By expanding the quantities in (2) by the basis set and using Galerkin testing, (2) is discretised into a linear system expressed as

$$\mathbf{e} = \mathbf{L}_A \, \mathbf{j} \tag{3}$$

where the operator $\mathbf{L}_A$ represents the EFIE impedance matrix. Its inverse, the analysis operator $\mathbf{L}_A^{-1}$ (an admittance MoM matrix) leads to determine the surface currents distribution from a given excitation. Conversely if one expands the reactance on the same basis, from the surface currents set (or their expansion, in the discrete form of (2)) one can get the expansion of the surface tensor reactance as

$$\mathbf{x} = \mathbf{L}_s^{-1} \, \mathbf{j} \tag{4}$$

where the synthesis operator $\mathbf{L}_s^{-1}$ embeds constraints suited to enforce impedance solutions that are Hermitian, thus respect passivity and reciprocity.

B. The Alternating Projections Method

With reference to (2) we identify by $\tilde{\mathbf{J}}(\mathbf{k}_t)$ the Fourier transform of the MTS surface currents and the wish is to determine its distribution in the visible and evanescent range. Anyway, back propagation to the aperture of some custom target far-field, only identifies the surface currents spectrum located within the visible range, i.e, for $|\mathbf{k}_t| < k_0$, (being k_0 the free-space wavenumber). Instead, no spectral information is derived for the current distribution in the evanescent region.

Therefore, the alternating projections method should establish and algorithm whose solution progressively converge to a current set whose invisible spectrum complies with the finite-domain aperture, with a passive and reciprocal reactance; additionally the visible range should match the constraints $\tilde{\mathbf{J}}_{\text{ref}}$ imposed by the target far-field.

The alternating projections method relies on the definition of a spectral projection operator, named $\mathcal{P}_V$, the latter operates on the visible range $\mathcal{V}$ of $\tilde{\mathbf{J}}$ and transforms it into the projection $\tilde{\mathbf{J}}^{(+)}$ as follows

$$\tilde{\mathbf{J}}^{(+)}(\mathbf{k}_t) = \begin{cases} \tilde{\mathbf{J}}_{\text{ref}}(\mathbf{k}_t), & \text{if } \mathbf{k}_t \in \mathcal{V} \\ \tilde{\mathbf{J}}(\mathbf{k}_t), & \text{otherwise} \end{cases} \tag{5}$$

note that $\mathcal{P}_V$ leaves unaltered the invisible portion of the current spectrum. Such non-visible portion, typically showing a smooth envelope, assumes an important role in maintaining the current set bounded to the finite aperture in the physical space. Therefore, a key aspect concerns with the proper reconstruction of the non-visible part of the currents spectrum to ensure physical compliance, avoiding spatial spreading or impedance inconsistency (typically an over or under-modulated profile if too weak or too strong evanescent spectrum is added).

The alternating projections method offers instead a systematic process to reconstruct the missing spectral information without violating physical constraints. In this regard, the inverse synthesis solution configures itself as simultaneously compliant to the following constraint spaces: (i) the spectral sub-space whose visible portion matches the requirement $\tilde{\mathbf{J}}_{\text{ref}}$ and (ii) the physical space of boundary conditions limited to the aperture domain and described by an Hermitian impedance. In this regard, the AP method switches between enforcing spectral currents constraints and reconstruction of the surface impedance that matches the physical space constraints by the synthesis and analysis operators. Via successive projections the current set gradually approaches the intersection of the constraints sets (i) and (ii), while its convergence is measured by the decrease of a residual error: this is evaluated within the visible range of the currents set outcome of the analysis operator wrt the target $\tilde{\mathbf{J}}_{\text{ref}}$ at any iteration.

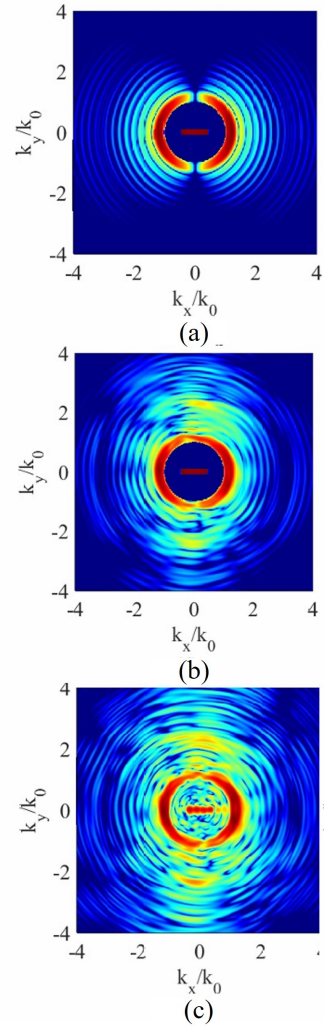

Fig. 1. Reconstruction of the currents spectrum performed by the AP algorithm for a flat-top antenna (only component x is represented). (a) Spectral projector $\mathcal{P}_V$ applied at the algorithm set up (at step 0 an homogeneous impedance surface wave spectrum complements the visible range information); (b) evolution of the non-visible spectrum content (operator $\mathcal{P}_V$ is applied to the current spectrum relevant to the impedance as outcome of the synthesis operator at step 4); and (c) final current spectrum of the flat-top antenna at the end of algorithm (step 5).

IV. Numerical Results

As an example the AP algorithm is applied to synthesize a flat-top right-handed polarized radiation pattern with an aperture of radius $4.5\lambda_0$ (with λ_0 the free-space wavelength at) at 24GHz implemented by a Rogers RO3003 substrate with $\varepsilon_r = 2.96$ and thickness $h = 1.02$mm. The aperture is discretised using Gaussian-rings basis functions [14] through which the current set is represented by the coefficients vector **j** and the surface impedance by **x** in (3), (4).

As represented in Fig.1 the non-visible range content progressively evolves as a consequence of the alternating enforcement of the visible range constraint in the spectral domain (note the visible range is simply constructed as a binary function) and compliance with physical realizability in the space domain. The corresponding far-field obtained at step 5 is represented in Fig.2; from the plot the quality of the obtained radiation properties clearly appears, with a noticeably low cross-polar component. Remarkably the synthesis takes only 5 steps to converge and less than 8 minutes on an Intel Core i9–11900K CPU with 128GB of RAM.

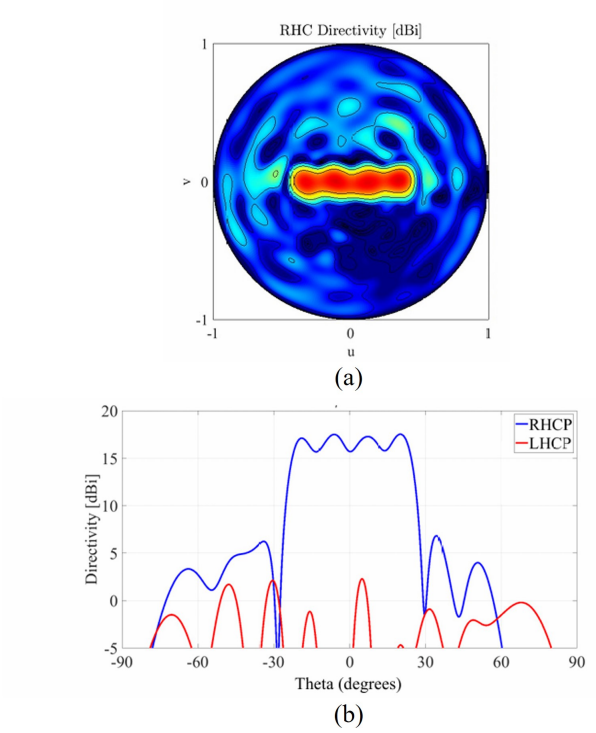

Fig. 2. Far-field pattern outcome of the AP algorithm for the flat-top antenna. (a) $u - v$ spectral map of the far-field at step 5 of the algorithm (only Rh component is shown), and (b) far-field cut along the k_y=0 cut.

V. Conclusion

In this work a method to synthesize modulated MTS aperture currents and their related boundary conditions that match prescribed radiation properties is presented. The method is structured by means of an iterative AP approach that is cast into an EFIE framework, whose solution automatically complies with spectral constraints (far-field shape compliance) and physical space constraints (limited spatial domain and realizability of the impedance). The presented method can be employed to synthesize a broad span of beams of contoured kind from relatively small apertures. The method has proven to be a powerful and efficient tool to obtain far-field patterns with high degree of fidelity with respect to the targets and very low cross polar components. The method allows for generalization to multi-source fed apertures, dual polarized or multi-beam operation. Extension to multi frequency or broadband application is currently under study.

References

[1] Grbic, A., Maci, S. (2022). EM metasurfaces [guest editorial]. IEEE Antennas and Propagation Magazine, 64(4), 16-22.

[2] Maci, S., Minatti, G., Casaletti, M., and Bosiljevac, M. (2012). Metasurfing: Addressing waves on impenetrable metasurfaces. IEEE Antennas and wireless propagation letters, 10, 1499-1502.

[3] Martini, E., Maci, S. (2022). Theory, analysis, and design of metasurfaces for smart radio environments. Proceedings of the IEEE, 110(9), 1227-1243.

[4] Martini, E., Maci, S. (2021). Modulated metasurfaces for microwave field manipulation: Models, applications, and design procedures. IEEE Journal of Microwaves, 2(1), 44-56.

[5] Minatti, G., Caminita, F., Martini, E., and Maci, S. (2016). Flat optics for leaky-waves on modulated metasurfaces: Adiabatic Floquet-wave analysis. IEEE Transactions on Antennas and Propagation, 64(9), 3896-3906.

[6] Minatti, G., Caminita, F., Martini, E., Sabbadini, M., and Maci, S. (2016). Synthesis of modulated-metasurface antennas with amplitude, phase, and polarization control. IEEE Transactions on antennas and propagation, 64(9), 3907-3919.

[7] González-Ovejero, D., Minatti, G., Chattopadhyay, G., and Maci, S. (2017). Multibeam by metasurface antennas. IEEE Transactions on Antennas and Propagation, 65(6), 2923-2930.

[8] Pereda, A. T., Caminita, F., Martini, E., Ederra, I., Iriarte, J. C., Gonzalo, R., and Maci, S. (2016). Dual circularly polarized broadside beam metasurface antenna. IEEE Transactions on Antennas and Propagation, 64(7), 2944-2953.

[9] Faenzi, M., Minatti, G., González-Ovejero, D., Caminita, F., Martini, E., Della Giovampaola, C., and Maci, S. (2019). Metasurface antennas: New models, applications and realizations. Scientific reports, 9(1), 10178.

[10] Pandi, S., Balanis, C. A., and Birtcher, C. R. (2015). Design of scalar impedance holographic metasurfaces for antenna beam formation with desired polarization. IEEE transactions on antennas and propagation, 63(7), 3016-3024.

[11] Faenzi, M., González-Ovejero, D., and Maci, S. (2021). Overlapped and sequential metasurface modulations for Bi-Chromatic beams generation. Applied Physics Letters, 118(18).

[12] Bleszynski, E. H., Bleszynski, M. K., and Jaroszewicz, T. (2002). Surface-integral equations for electromagnetic scattering from impenetrable and penetrable sheets. IEEE Antennas and Propagation Magazine, 35(6), 14-25.

[13] Kuester, E. F., Mohamed, M. A., Piket-May, M., and Holloway, C. L. (2003). Averaged transition conditions for electromagnetic fields at a metafilm. IEEE Transactions on Antennas and Propagation, 51(10), 2641-2651.

[14] Gonzalez-Ovejero, D., Maci, S. (2015). Gaussian ring basis functions for the analysis of modulated metasurface antennas. IEEE Transactions on Antennas and Propagation, 63(9), 3982-3993.

[15] M. Bodehou, C. Craeye, H. Bui-Van, and I. Huynen, "Fourier–bessel basis functions for the analysis of elliptical domain metasurface antennas," IEEE Antennas Wireless Propag. Lett., vol. 17, no. 4, pp. 675–678, 2018.

[16] Wen, Y., Qin, P. Y., Maci, S., and Guo, Y. J. (2023). Low-profile multibeam antenna based on modulated metasurface. IEEE Transactions on Antennas and Propagation, 71(8), 6568-6578.

[17] Bodehou, M., Craeye, C., Martini, E., and Huynen, I. (2018). A quasi-direct method for the surface impedance design of modulated metasurface antennas. IEEE Transactions on Antennas and Propagation, 67(1), 24-36.
[18] Zucchi, M., Vernì, F., Righero, M., and Vecchi, G. (2023). Current based automated design of realizable metasurface antennas with arbitrary pattern constraints. IEEE Transactions on Antennas and Propagation, 71(6), 4888-4902.
[19] Teodorani, L., Zucchi, M., and Vecchi, G. (2024). Generalized Deterministic Automated Design of Metasurface Antennas with 3D Feeding Structures. IEEE Transactions on Antennas and Propagation.
[20] Bregman, L. M. (1965). The method of successive projections for finding a common point of convex sets. In Soviet Math. Dokl. (Vol. 6, pp. 688-692).
[21] Poulton, G. T. (1986). Antenna power pattern synthesis using method of successive projections. Electronics Letters, 22(20), 1042-1043.
[22] Bucci, O. M., Franceschetti, G., Mazzarella, G., and Panariello, G. (1990, December). Intersection approach to array pattern synthesis. In IEE Proceedings H (Microwaves, Antennas and Propagation) (Vol. 137, No. 6, pp. 349-357). IEE.
[23] Quijano, J. L. A., Vecchi, G. (2009). Alternating adaptive projections in antenna synthesis. IEEE transactions on antennas and propagation, 58(3), 727-737.

Novel Materials, Metamaterials, Metasurfaces, FSS and EBG

A Wide-Angle Reconfigurable Metasurface Retroreflector with Enhanced Angular Stability

Xin Wei[1,2,3], Wei Zhou[1,2,3], Bin Zheng[1,2,3,*]

[1]State Key Laboratory of Extreme Photonics and Instrumentation, ZJU-Hangzhou Global Scientific and Technological Innovation Center, Zhejiang University, Hangzhou 310027, China

[2]The Electromagnetics Academy at Zhejiang University, College of Information Science and Electronic Engineering, Zhejiang University, Hangzhou 310027, China

[3]Zhejiang Key Lab. of Intelligent Electromagnetic Control and Advanced Electronic Integration, Jinhua Institute of Zhejiang University, Zhejiang University, Jinhua 321099, China

*Corresponding author: zhengbin@zju.edu.cn

***Abstract*— We propose a wide-angle reconfigurable metasurface retroreflector. By integrating varactor-loaded meta-atoms with cavity-enhanced angular stability, the metasurface enables large-angle retroreflection at a target frequency bands, suitable for adaptive radar and sensing applications.**

***Keywords*—reconfigurable metasurface retroreflector, angular stability.**

I. Introduction

Retroreflectors, which redirect incident electromagnetic (EM) waves back toward their source, play a vital role in numerous electromagnetic systems, including radar cross-section (RCS) manipulation, radio frequency identification, satellite communications, and wireless sensing, where reliable signal return is of paramount importance. Conventional retroreflective structures such as corner reflectors, cat's-eye reflectors, and Luneburg lenses[1–6] typically rely on bulky three-dimensional geometries, resulting in large profiles and limited compatibility with planar and integrated platforms. Planar retroreflection can be realized using Van Atta antenna arrays[7–11], which employ passive self-phasing mechanisms to reradiate incident waves toward their source. However, the complexity and loss of the feeding network increase rapidly with aperture size, and such arrays are generally constrained to retroreflection within a single incident plane, limiting their applicability in complex electromagnetic environments.

In recent years, metasurfaces have emerged as a powerful platform for low-profile and flexible electromagnetic wavefront manipulation[12-17]. Building on this capability, reconfigurable metasurfaces provide an effective approach for realizing compact and adaptable retroreflective devices[18-22]. By employing arrays of subwavelength meta-atoms with engineered impedance responses, metasurfaces enable precise control over the reflected wavefront while maintaining planar and compact form factors. When combined with active components, metasurfaces further allow dynamic reconfiguration of electromagnetic functionalities, making them particularly attractive for adaptive wireless systems.

Current reconfigurable metasurface designs often employ varactor diodes to provide continuous phase modulation with compact layouts. However, in dynamic communication environments, ensuring reliable wide-angle retroreflection remains a challenge due to spatial dispersion and mutual coupling that typically degrade performance under large-angle incidence.

To address these challenges, we propose a reconfigurable metasurface retroreflector with enhanced angular stability. The proposed design employs varactor diodes to provide continuous capacitance tuning to ensure accurate phase compensation required for retroreflection. Crucially, to suppress the spatial dispersion and mutual coupling that typically degrade large-angle performance in resonant metasurfaces, rows of metallic wall vias are introduced along the edges of each meta-atom. These metallic vias effectively isolate adjacent elements by suppressing parasitic coupling and multiple reflections, thereby transforming the meta-atoms into quasi-independent resonant cavities. As a result, the localized resonance behavior is preserved even at highly oblique incidence, ensuring a stable phase response and robust wide-angle retroreflection. Owing to its dynamic reconfigurability, angular robustness, and planar architecture, the proposed metasurface provides a promising solution for reliable signal return in dynamic wireless environments and shows strong potential for next-generation wireless system architectures and advanced radar platforms.

REFERENCES

[1] D.Y. Ao, Y.H. Li, C. Hu, et al., "Accurate Analysis of Target Characteristic in Bistatic SAR Images: A Dihedral Corner Reflectors Case," Sensors 18, 24 (2018).

[2] E. Moon, S.-W. Park, H. Chung, et al., "Truncated corner cubes with near-perfect retroreflection efficiency," Appl. Opt. 53, 7972–7978 (2014).

[3] P. Li, F. Tang, X. Z. Wang, et al., "High NA objective lens wavefront aberration measurement using a cat-eye retroreflector and Zernike polynomial," Opt. Express 29, 31812–31835 (2021).

[4] C. C. Chang, M. C. Su, Y. C. Yang, et al., "Design, Fabrication, and Characterization of Tunable Cat's Eye Retroreflector Arrays as Optical Identification Tags," J. Lightwave Technol. 32, 384–391 (2014).

[5] T. Zentgraf, Y. M. Liu, M. H. Mikkelsen, et al., "Plasmonic Luneburg and Eaton lenses," Nat. Nanotechnol. 6, 151–155 (2011).

[6] Y. Y. Fu, J. F. Li, Y. B. Xie, et al., "Compact acoustic retroreflector based on a mirrored Luneburg lens," Phys. Rev. Mater. 2, 105202 (2018).

[7] D. L. He, S. F. Li, L. J. Chen, et al., "A Wide-Angle and Ultrawideband Van Atta Array for Monostatic RCS Enhancement," IEEE Antennas Wireless Propag. Lett. 24, 68–72 (2025).

[8] X. F. Li, Y. L. Ban, Q. Sun, et al., "A Planar 2-D 8×8 Van Atta Retrodirective Array for RCS Enhancement in a Wide Angular Range," IEEE Trans. Antennas Propag. 70, 12364–12369 (2022).

[9] H. Shahi, N. Masoumi, M. Mohammad-Taheri, et al., "Dual-Mode Phase-Conjugating/Active Van Atta Array Design Based on Dual-Band Mixer/Reflection Amplifier," IEEE Trans. Microw. Theory Techn. 70, 3629–3639 (2022).

[10] X. F. Li, Y. L. Ban, Q. Sun, et al., "A Compact Dual-Band Van Atta Array Based on the Single-Port Single-Band/Dual-Band Antennas," IEEE Antennas Wireless Propag. Lett. 22, 888–892 (2023).

[11] X. F. Li, Y. L. Ban, Q. Sun, et al., "Compact Dual-Frequency 2-D Van Atta Array Using the Reconfigurable AMC Antenna," IEEE Antennas Wireless Propag. Lett. 22, 3162–3166 (2023).

[12] X. Wei, G. M. Wang, Y. W. Wang, et al., "Metasurface-based bandwidth and isolation enhancement for compact H-plane coupled antennas," J. Phys. D: Appl. Phys. 57, 135002 (2024).

[13] H. Lu, J. W. Zhao, B. Zheng, et al., "Eye accommodation-inspired neuro-metasurface focusing," Nat. Commun. 14, 3301 (2023).

[14] P. Zhu, H. Lu, H. R. Han, et al., "An Optically Transparent Transmissive Metasurface for User-Defined Broadband Electromagnetic Illusion Generation," Small Struct. e202500351 (2025).

[15] W. Zhou, S. Q. Zhu, Z. X. Zhang, et al., "Time-varying metasurface driven broadband radar jamming and deception," Opt. Express 32, 17911-17921 (2024).

[16] R. R. Zhu, D. Liu, H. Lu, et al., "High-Efficiency Pancharatnam–Berry Metasurface-Based Surface Plasma Coupler," Adv. Photonics Res. 5, 2300315 (2024).

[17] X. Y. Bai, S. R. Tan, S. Mikki, et al., "Information-theoretic Measures for Reconfigurable Metasurface-enabled Direct Digital Modulation Systems: An Electromagnetic Perspective," Prog. Electromagn. Res. 179, 1–18 (2024).

[18] Q. Z. Tan, B. Zheng, T. Cai, et al., "Broadband Spin‐Locked Metasurface Retroreflector," Adv. Sci. 9, 2201397 (2022).

[19] Y. X. Jia, J. F. Wang, J. Yang, et al., "Wideband planar retro-reflective metasurfaces for backscattering enhancement under oblique incidence," J. Phys. D: Appl. Phys. 51, 335103 (2018).

[20] Q. Yuan, Q. Ge, X. J. Zou, et al., "Scalable high-efficiency metasurface-refractive retro-reflector," PhotoniX 6, 14 (2025).

[21] C. J. Gao, T. J. Lai, L. Peng, et al., "Multifunctional Intelligent Reconfigurable Metasurface," ACS Appl. Mater. Interfaces 16, 55675–55683 (2024).

[22] W. Kang, S. J. Chen, Y. H. Li, et al., "Simultaneous Polarization Conversion and Retro-Reflection Based on Surface-Circuit Metasurfaces," IEEE Antennas Wireless Propag. Lett. 22, 2002–2006 (2023).

Performance Analysis of RIS-Assisted Secrecy Key Generation in Indoor Environments

Alessandro Santorsola[*1,2], Giovanni Magno[1], Vincenzo Petruzzelli[1], Sabino Roberto Caporusso[2], and Giovanna Calò[1]

[1]Department of Electrical and Information Engineering, Polytechnic University of Bari, Bari, Italy
[2]Cybersecurity Lab, BV TECH S.p.A., 20123 Milan, Italy
*Corresponding authors: a.santorsola1@phd.poliba.it, giovanna.calo@poliba.it

***Abstract*—We study RIS-assisted secrecy key generation in an indoor Wi-Fi (802.11ax) link by comparing single-threshold and multi-level quantization. By sweeping RIS aperture and target key length, we show that larger surfaces significantly reduce key mismatch, enabling reliable multi-bit extraction and improving an effective key-rate proxy accounting for reconciliation overhead. *Keywords*— Reconfigurable intelligent surface (RIS), Secrecy Key Generation (SKG), Physical Layer Security.**

I. Introduction

PHYSICAL-LAYER (PHY) Secrecy Key Generation (SKG) is a pivotal technology for securing 6G networks, as it extracts symmetric cryptographic keys from the inherent reciprocity and randomness of the wireless channel [5]. Despite its potential, the reliability of SKG in indoor environments is often compromised by limited spatial entropy and measurement noise. Recent studies, such as [2] and [3], have highlighted significant security challenges in indoor scenarios, particularly under *on-the-shoulder* eavesdropping attacks where the proximity of an adversary threatens the uniqueness of the legitimate channel. While standard Wi-Fi protocols provide a widespread platform for SKG, they lack native mechanisms to actively shape the propagation channel against such vulnerabilities [5]. Reconfigurable Intelligent Surfaces (RIS) have been proposed as a transformative solution to engineer the propagation environment and enhance Physical Layer Security (PLS) [4]. However, existing literature primarily focuses on secret key capacity or simple phase-randomization strategies. There is a lack of investigation into how the physical aperture of the RIS dictates the effectiveness of high-order quantization schemes in realistic, optimized links. In this work, we address this gap by analyzing a RIS-assisted indoor Wi-Fi 802.11ax link using a geometry-based stochastic channel model and a physically-consistent RIS model. We consider a phase-conjugated RIS configuration and compare single-threshold (1-bit) and multi-level quantization under a sweep of RIS size and target key length. We deliberately focus on a phase-conjugated RIS configuration, as the goal is to assess the suitability of SKG quantization schemes under links optimized according to conventional SNR-oriented criteria. The results demonstrate that increasing RIS aperture significantly improves key agreement, enabling reliable multi-level quantization.

II. System Model

a) Methodology and Layout: The system implements an IEEE 802.11ax PHY at $f_c = 2.4\,\text{GHz}$ ($B = 20\,\text{MHz}$, $N_{\text{FFT}} = 64$) in an indoor environment. In the analyzed scenario, Alice represents a Wi-Fi Access Point (AP) and Bob a Wi-Fi Station (STA). They are arbitrarily located at $(6, 4, 0.5)\,\text{m}$ and $(5, 0, 1.5)\,\text{m}$, respectively, both equipped with half-wave dipole antennas. A square RIS of $M_{\text{RIS}} = N^2$ elements with $\lambda/2$ spacing is wall-mounted at $(5, 5, 3.0)\,\text{m}$. The channel is characterized via the Quasi-Deterministic Radio Channel Generator (QuaDRiGa), following 3GPP TR 38.901 Indoor Line-of-Sight (LOS) specifications. According to the QRIS framework [1], each RIS unit-cell (UC) follows a microstrip patch radiation pattern, with a collective response defined by the diagonal matrix $\mathbf{\Phi} = \text{diag}(e^{j\phi_1}, \ldots, e^{j\phi_{M_{\text{RIS}}}})$, where $M_{\text{RIS}} = N^2$ is the number of elements, $\phi_m \in [-\pi, \pi)$ is the phase shift. Ideal reflection amplitude ($\alpha_m = 1$) is assumed to isolate the impact of phase optimization and aperture scaling. The composite channel is $\mathbf{h}_{tot} = \mathbf{h}_{\text{AB}}^{\text{dir}} + \mathbf{h}_{RB}\mathbf{\Phi}\mathbf{h}_{AR}$, where $\mathbf{h}_{AR}$ and $\mathbf{h}_{RB}$ are the Alice-RIS and RIS-Bob links. To maximize the Signal-to-Noise Ratio (SNR) at Bob location, we apply phase conjugation $\phi_m^{\text{opt}} = -\angle([\mathbf{h}_{RB}]_m \cdot [\mathbf{h}_{AR}]_m)$, adopting coherent phase alignment for RIS phase design. RIS hardware non-idealities and control losses are deferred to future investigations.

b) Signal Processing and Key Generation: We evaluate two links: (i) direct and (ii) RIS-assisted with optimized phases. The direct channel $\mathbf{h}_{\text{AB}}^{\text{dir}}$ and the RIS-assisted cascade $\mathbf{h}_{\text{RB}}\mathbf{\Phi}\mathbf{h}_{\text{AR}}$ are evaluated separately, each generating an independent raw key stream. For each received OFDM frame, key features $w(k)$ are computed from the received power spectrum. Measurement noise is emulated by adding independent Additive White Gaussian Noise (AWGN) realizations to the received signal prior to power computation. Keys of length $|K| \in \{64, 128, 256\}$ are generated via two quantization strategies. The *Single-Threshold* (ST) scheme maps each feature to one bit by comparison with its local mean computed over the considered OFDM subcarriers within the same frame [3]. The *Multi-Level* (ML) scheme partitions the spectrum into M_{SB} sub-bands, quantizing each into 2^q levels so that $|K| = M_{\text{SB}} \cdot q$ (e.g., $M_{\text{SB}} = 32, q = 4$ for $|K| = 128$)

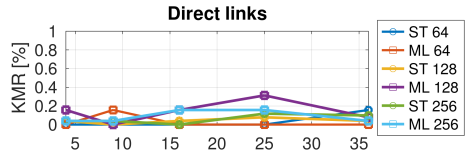

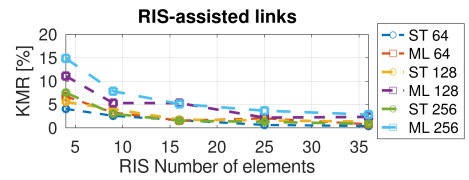

(a)

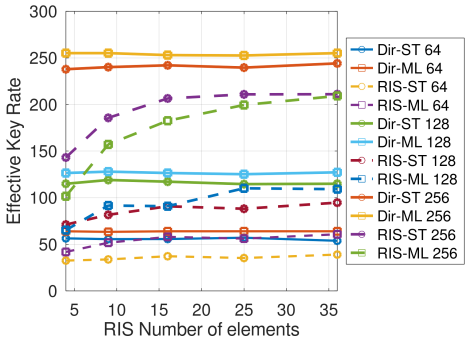

(b)

Fig. 1: Impact of RIS scaling and Quantization Strategy on SKG metrics: (a) Key Mismatch Rate (KMR) and (b) Effective Key Rate ($\tilde{R}$) for direct and RIS-assisted channels as a function of RIS number of elements.

[2]. Quantization thresholds are selected from feature quantiles and Gray coding is applied to reduce adjacent-level bit flips.

c) Evaluation Metrics: Performance is evaluated using two KPIs computed from Alice's and Bob's raw keys. The Key Mismatch Rate (KMR) is the normalized Hamming distance as $\mathrm{KMR} = \frac{1}{|K|}\sum_{i=1}^{|K|} |k_A(i) - k_B(i)|$. To compare quantization strategies, we adopt an effective key yield per extraction $\tilde{R}$ accounting for reconciliation overhead. The per-bit Shannon entropy of Alice raw key is expressed as $E = -p_1 \log_2 p_1 - (1-p_1)\log_2(1-p_1)$, where p_1 is the empirical probability of bit "1" estimated over the entire raw bitstream. Modeling key disagreement as a binary symmetric channel with crossover probability KMR yields the asymptotic upper bound $1-h_b(\mathrm{KMR})$ on reconciliation efficiency. Hence, $\tilde{R} = |K| \cdot E \cdot \big[1 - h_b(\mathrm{KMR})\big]$.

III. Results and Discussion

The RIS-assisted SKG framework is evaluated by sweeping the RIS aperture $M_{\mathrm{RIS}} = N^2$ and the target key length $|K| \in \{64, 128, 256\}$, comparing single-threshold (ST) and multi-level (ML) quantization. Fig. 1a reports the Key Mismatch Rate (KMR). The direct link (top panel) shows near-zero KMR for all $|K|$, as expected under ideal reciprocity and AWGN-only impairment. In the RIS-assisted link (bottom panel), ML exhibits higher mismatch than ST for small surfaces ($M_{\mathrm{RIS}} \leq 16$) due to its increased noise sensitivity; however, KMR rapidly decreases with M_{RIS} thanks to coherent combining and SNR gain. For $M_{\mathrm{RIS}} \geq 25$, KMR falls below 2% for both schemes even at $|K| = 256$, enabling reliable multi-bit extraction. Fig. 1b shows the effective key proxy $\tilde{R}$, accounting for reconciliation penalties through $1 - h_b(\mathrm{KMR})$. While the direct link is approximately constant versus M_{RIS}, the RIS-assisted link improves with aperture and approaches the baseline. When mismatch is sufficiently low, ML consistently achieves higher $\tilde{R}$ than ST due to its higher bit density, highlighting a trade-off between robustness (small M_{RIS}) and throughput (large M_{RIS}).

IV. Conclusions

This work investigated RIS-assisted secrecy key generation in an indoor Wi-Fi setup, focusing on the impact of RIS aperture on key extraction reliability and quantization strategy selection. Results showed that scaling the RIS size significantly reduces the Alice-Bob Key Mismatch Rate, especially for multi-level quantization, which is otherwise more sensitive to measurement noise (and, in practical systems, non-reciprocity effects). By adopting an effective key-rate proxy accounting for reconciliation overhead, we highlighted a clear trade-off: small surfaces favor robust single-threshold extraction, whereas larger RIS apertures enable efficient multi-bit key generation with improved throughput. Future work will address reconciliation-integrated SKG evaluations and adaptive RIS control policies jointly optimized for key generation performance, while progressively extending the model to more realistic RIS architectures.

References

[1] Ilya Burtakov et al. "QRIS: A QuaDRiGa-based simulation platform for reconfigurable intelligent surfaces". In: *IEEE Access* 11 (2023), pp. 90670–90682.

[2] Amitha Mayya et al. "A SKG Security Challenge: Indoor SKG Under an On-The-Shoulder Eavesdropping Attack". In: *GLOBECOM 2023 - 2023 IEEE Global Communications Conference*. 2023, pp. 3451–3456. DOI: 10.1109/GLOBECOM54140.2023.10437629.

[3] Alessandro Santorsola et al. "Effect of Antenna Radiation Pattern Variation on the Secrecy Key Generation in LoS Indoor Environment Under On-The-Shoulder Attack". In: *2025 19th European Conference on Antennas and Propagation (EuCAP)*. 2025, pp. 1–5. DOI: 10.23919/EuCAP63536.2025.10999850.

[4] Qingqing Wu and Rui Zhang. "Intelligent Reflecting Surface Enhanced Wireless Network via Joint Active and Passive Beamforming". In: *IEEE Transactions on Wireless Communications* 18.11 (2019), pp. 5394–5409. DOI: 10.1109/TWC.2019.2936025.

[5] Junqing Zhang et al. "Key Generation From Wireless Channels: A Review". In: *IEEE Communications Surveys Tutorials* 18.3 (2016), pp. 1897–1926. DOI: 10.1109/COMST.2016.2533612.

An Investigation of Aperiodic Array Design via Particle Swarm Optimization and Möbius-Transformed $N \times N$ Uniform Arrays

Waroth Kuhirun*

Electrical Engineering Department, Kasetsart University, Thailand

*Corresponding author: fengwrk@yahoo.com

Abstract—A conventional $N \times N$ uniform array is used as a prototype for performance improvement. This paper presents an investigation of aperiodic array design using particle swarm optimization for the mapping of Möbius transformation.

Keywords— aperiodic arrays, $N \times N$ uniform array, Möbius transformation, mapping, conformal mapping, Particle Swarm Optimization.

I. Introduction

Antenna arrays are of the paramount importance in wireless communication systems. Among arrays, periodic arrays generally have high sidelobe levels in comparison with aperiodic arrays. Although aperiodic arrays theoretically outperform periodic arrays; however, in practice, mutual effects can impact on the performance of arrays if the minimum spacing between adjacent antenna elements is not sufficiently large.

In this paper, $N \times N$ uniform array is used as a prototype for antenna performance improvement. This paper presents an investigation of aperiodic array design via particle swarm optimization. See subsection I-A for a brief discussion on particle swarm optimization. The evaluation of minimum spacing is computationally expensive for large arrays. To solve this problem, according to an interesting property, we will use a conformal mapping called Möbius transformation for generating feasible solutions. See subsection I-B for a brief discussion on conformal mapping and Möbius transformation.

A. Particle Swarm Optimization

Particle swarm optimization is an optimization technique. There are variations of particle swarm optimization. This paper follows real-number particle swarm optimization discussed in [2].

First of all initialize P_i^0 and $V_i^0, i = 1, \ldots, N_p$ where

$$P_i^0 = \begin{bmatrix} \alpha_{0,i} \\ \vdots \\ \alpha_{N_p-1,i} \end{bmatrix} \quad \text{and} \quad V_i^0 = \underline{0}_{N_p \times 1} = \begin{bmatrix} 0 \\ \vdots \\ 0 \end{bmatrix}$$

While the termination condition does not met,

$$V_i^t = \omega V_i^{t-1} + c_1 a_1 (P_{i,best}^{t-1} - P_i^{t-1}) + c_2 a_2 (G_{i,best}^{t-1} - P_i^{t-1})$$

$$P_i^t = P_i^{t-1} + V_i^t$$

Update $P_{best,i}, i = 1, \ldots, n$ and $G_{best,i}$ by maximizing the fitness function

$$fitness = f_{obj} + C f_{constraint}$$

where $f_{obj} \geq 0$ and $f_{constraint} \leq 0$ are the objective function and the constraint function, respectively and $C >> 1$ For more detailed discussion, see [2]

B. Conformal Mapping and Möbius Transformation

Consider an analytic function f that maps from z to w. If $f'(z)$ at $z = z_0$, the mapping f is said to be conformal at $z = z_0$ due to a property called "angle preserving". Moreover, if $f'(z) \neq 0$ throughout the domain, the mapping is called "conformal mapping". It should be mentioned that an analytic function f which is conformal at $z = z_0$ is also a conformal mapping in some neighborhood of z_0. For further detailed discussion, see [3], [4].

An interesting property of a conformal mapping f we can take advantage of is as follows:

$$|dw| = |f'(z)||dz| \tag{1}$$

This leads to

$$|\Delta w| \approx |f'(z)||\Delta z| \tag{2}$$

Among conformal mapping, Möbius transformation defined by

$$f(z) = \frac{az + b}{cz + d} \tag{3}$$

have a useful property called "local isometry". That is, Möbius transformation preserves intrinsic distances. It should be noted that $ad - bc \neq 0$. Otherwise, the transformation is not a conformal mapping. See [5] for further discussion on Möbius transformation.

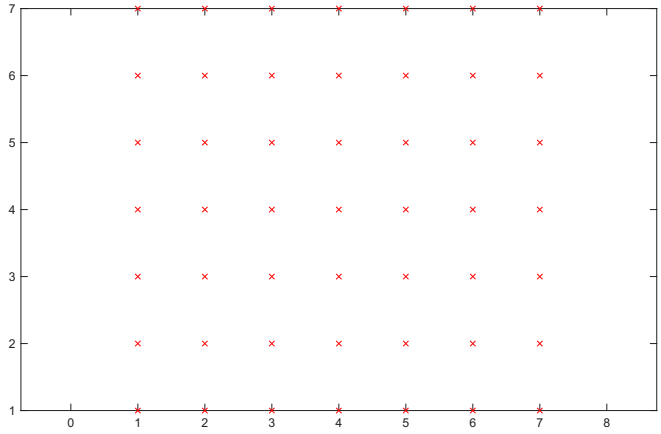

Fig. 1: A conventional $N \times N$ uniform array. Each individual antenna element is represented by "x".

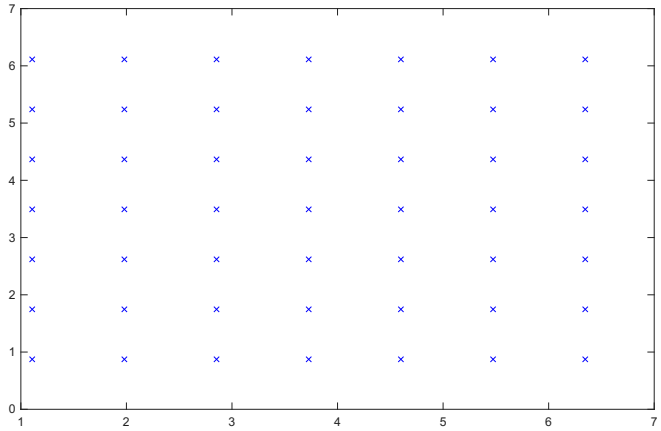

Fig. 2: An aperiodic array is optimized by particle swarm optimization and mapped by Möbius transformation. Each individual antenna element is represented by "x".

II. Simulation Methods

A. Fitness Function

The objective function used for optimization is chosen to be the directivity in dB. By setting $\beta_n = 0, n = 1, \ldots, N$ in Eq. A.18 in [1], we have:

$$D = \frac{\left(\sum_{n=1}^{N} I_n\right)^2}{\sum_{n=1}^{N} I_n^2 + 2\sum_{m=2}^{N}\sum_{n=1}^{m-1} I_n I_m \frac{sin(k(|\vec{r}_n - \vec{r}_m|)}{k(|\vec{r}_n - \vec{r}_m|)}} \tag{4}$$

where I_n and $\vec{r}_n$ are the relative current excitation and the position vector, respectively, of the n^{th} element and k is the wave number.
Next, we assume that the relative current excitations are

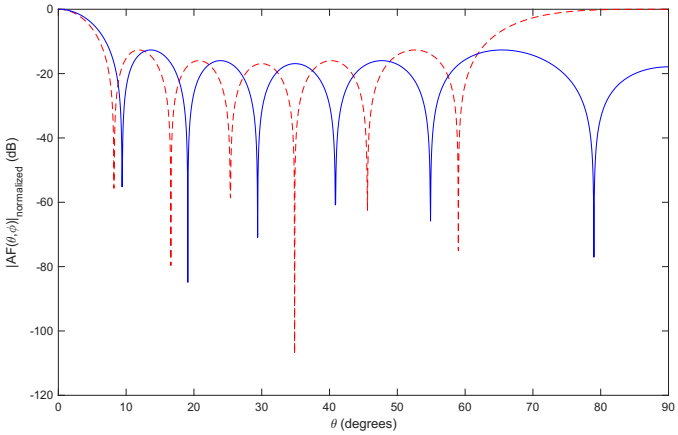

(a) $\phi = 0°$

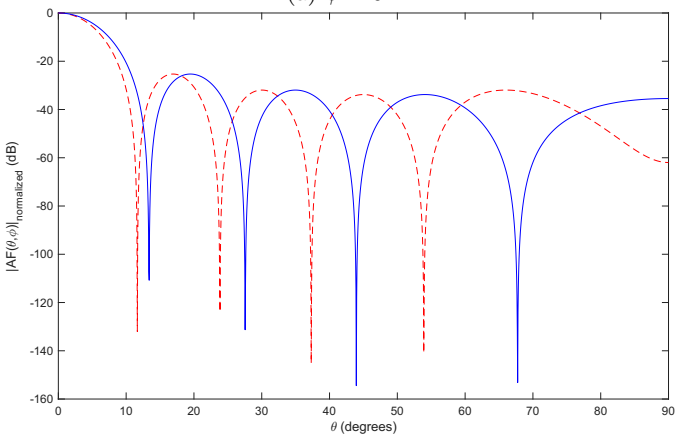

(b) $\phi = 45°$

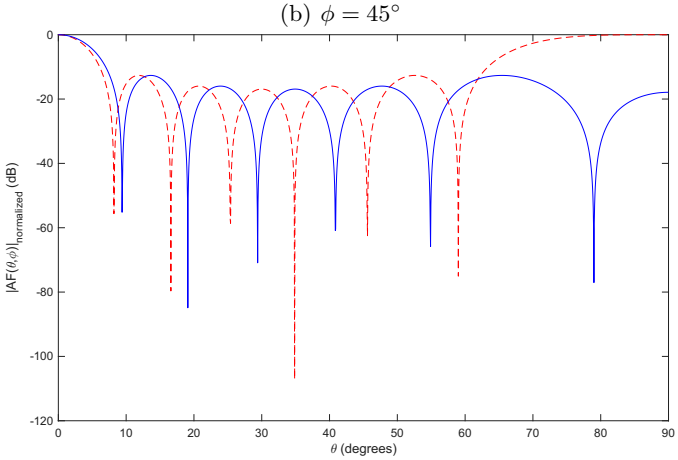

(c) $\phi = 90°$

Fig. 3: The magnitude of the array factor of an aperiodic array optimized using particle swarm optimization and mapped using Möbius transformation. The dashed lines represent the array factor pattern for a conventional $N \times N$ uniform array whereas the solid lines represent the aperiodic array designed via particle swarm optimization Möbius-transformed $N \times N$ uniform array.

uniform. That is, $I_n = 1, n = 1, \ldots, N$. This leads to

$$D = \frac{N^2}{N + 2\sum_{m=2}^{N}\sum_{n=1}^{m-1}\frac{sin(k(|\vec{r}_n - \vec{r}_m|)}{k(|\vec{r}_n - \vec{r}_m|)}} \tag{5}$$

The objective function f_{obj} is defined based on the directivity (in dB) as follows:

$$f_{obj} = 10log\left|\frac{N^2}{N + 2\sum_{m=2}^{N}\sum_{n=1}^{m-1}\frac{sin(k(|\vec{r}_n - \vec{r}_m|)}{k(|\vec{r}_n - \vec{r}_m|)}}\right| \tag{6}$$

The constraint function is chosen to be

$$f_{constraint} = min\left(\begin{array}{c}\epsilon - \frac{\sum_{n=1}^{N}(|f'(z_n)| - 1)^2}{N}, 0\end{array}\right) \tag{7}$$

where $\epsilon > 0$ is accepted tolerance. We select $\epsilon = 0.2$ and $C = 3000$. the fitness function is:

$$fitness = f_{obj} + 3000 f_{constraint} \tag{8}$$

B. Particle Swarm Optimization Setup

Our methodology is as follows

1) Create an $N \times N$ uniform array prototype.
2) Initialization is performed by creating N_p individual arrays by mapping the array prototype using a transformation f with randomized parameters. Let f be a Möbius transformation defined by Eq. 3, that is,
$$f(z) = \frac{az + b}{cz + d}$$
It should be noted that each individual array can be represented by the parameters of Möbius transformation.
3) Perform optimization using particle swarm optimization as follows:
   - Set $T = 10000, c_1 = 0.5, c_2 = 0.5, N_p = 200$ and $\omega = 0.5$
   - Initialize P_i^0 and $V_i^0, i = 1, \ldots, N_p$
     where
     $P_i^0 = \begin{bmatrix}a\\b\\c\\d\end{bmatrix}$ and $V_i^0 = \begin{bmatrix}0\\0\\0\\0\end{bmatrix}$
     $P_{best,i} = P_i^0, i = 1, \ldots, N_p$
     Update G_{best}
   - Perform iterations
     for $t = 1 : T$
     randomize a_1 and a_2
     $V_i^t = \omega V_i^{t-1} + c_1 a_1 (P_{i,best}^{t-1} - P_i^{t-1})$
     $+c_2 a_2 (G_{i,best}^{t-1} - P_i^{t-1})$
     $P_i^t = P_i^{t-1} + V_i^t$
     Update $P_{best,i}, i = 1, \ldots, N_p$
     Update G_{best}

C. Array Factor

This paper compare the array prototype with the aperiodic array optimized using particle swarm optimization and mapped by Möbius transformation. The array factor described by the following equation is used for comparison purpose. Assuming that the relative current excitations are uniform and in phase, this leads to

$$AF(\theta, \phi) = \sum_{n=1}^{N} exp(\jmath[k(x_n sin\,(\theta) cos\,(\phi) + y \sin\,(\theta) \sin\,(\phi))]) \tag{9}$$

where (x_n, y_n) is the coordinate of the n^{th} isotropic antenna element of the array.

III. Results and Discussion

The simulation results are as follows:

1) Fig. 2 shows an aperiodic array designed by particle swarm optimization and mapped by Möbius transformation; the antenna elements of which are located along the curve. Each individual antenna element is represented by "x". By optimizing using particle swarm optimization and mapping using Möbius transformation, by setting the minimum spacing between adjacent elements of the $N \times N$ array prototype to λ, a significant enhancement in directivity was observed, rising from 14.6095 dB to 22.1581 dB.
2) Fig.3 shows the comparison between the magnitude of the array factor pattern for $\phi = 0°, 45°$ and $90°$, respectively. These simulation results show that the proposed design using particle swarm optimization and mapping using Möbius transformation significantly improves the array factor performance.

Although the results of designing of an aperiodic array using particle swarm optimization and mapping Möbius transformation is significantly improved, the Möbius transformed $N \times N$ array still looks like a periodic array. This is attributed to the angle-preserving property of conformal mapping. Consequently, this shows a promising future research on aperiodic array design via particle swarm optimization and mapping beyond conformal mapping, in particular, Möbius transformation.

IV. Conclusion

This paper presents an investigation of aperiodic array design using particle swarm optimization and mapping via Möbius transformation. The optimization significantly improved the array factor performance. That is, a significant enhancement in directivity was observed, rising from 14.6095 dB to 22.1581 dB.

An interesting finding of this investigation is that the configuration of the array design via particle swarm

optimization and Möbius transformation remains similar to that of array prototype.

Future work will focus on further improving directivity as well as exploring other mapping techniques beyond Möbius transformation.

Acknowledgments

The author thanks Kasetsart University for financial support.

References

[1] W. Kuhirun, "A New Design Methodology for Modular Broadband Arrays based on Fractal Tilings," Ph.D. Thesis, Department of Electrical Engineering, The Pennsylvania State University, 2003.
[2] W. Kuhirun, W. Silabut, and P. Boonek, "Particle Swarm Optimisation for Antenna Element Design," in Swarm Intelligence, vol. 3,Y. Tan, Ed. London, UK: IET, pp. 369–402, 2018.
[3] Steven G. Krantz, Complex Variables A Physical Approach with Applications, 2nd ed. CRC Press, 2019.
[4] J. W. Brown and R. V. Churchill, Complex Variables and Applications, 8th ed. McGrawHill, 2009.
[5] T. Needham, Visual Complex Analysis, Reprinted with corrections Oxford University Press, 2000.

Advancements in Meta-Mirrors for High-Precision Optical Metrology

Mika Gaedtke[1,2], Sebastian Häfner[1,2], Celina Hellmich[1,2], Christian Kranhold[3], Stefanie Kroker[1,2,4,*], Steffen Sauer [1,2], Liam Shelling Neto[1,2], Thomas Siefke[3,5,6], Markus Walter[3]

[1]Institute of Semiconductor Technology, TU Braunschweig, Germany
[2]LENA Laboratory for Emerging Nanometrology, TU Braunschweig, Germany
[3]Institute of Applied Physics, Friedrich Schiller University Jena, Germany
[4]Physikalisch-technische Bundesanstalt, Braunschweig, Germany
[5]Fraunhofer Institute for Applied Optics and Precision Engineering IOF, Jena, Germany
[6]Ernst-Abbe-Hochschule Jena University of Applied Science, Jena, Germany
*Corresponding author: s.kroker@tu-braunschweig.de

***Abstract*— Meta-mirrors based on dielectric nanostructures offer a promising route to low-thermal-noise, high-reflectivity mirrors for next-generation laser stabilization and gravitational wave detection. We simulate the thermal noise of meta-mirrors and demonstrate that optical field tailoring enables co-optimization of reflectivity and noise performance, identifying robust low-noise parameter regimes across NIR and visible wavelengths.**

***Keywords*— metasurfaces, high-precision optical metrology, ultra-stable laser resonators, gravitational wave detection.**

I. Introduction

Ultra-stable lasers are a key enabling technology for the quantum revolution, supporting applications in quantum computing, precision metrology, timekeeping, and gravitational wave detection. They provide phase-stable optical fields essential for the precise interrogation of narrow atomic transitions and for maintaining the extreme interferometric sensitivity required in detectors such as advanced LIGO, Virgo, and KAGRA, as well as in future detectors, including the Einstein Telescope and LIGO Cosmic Explorer [1-4]. The phase stability of such light fields is fundamentally limited by the thermal noise of the resonator mirrors and their highly reflective coatings, typically amorphous or crystalline dielectric multilayer structures, achieving optical losses in the low single-digit ppm range. While amorphous coatings suffer from higher mechanical loss and thus large thermal noise, crystalline coatings feature lower mechanical loss but can exhibit photo-induced birefringence noise. Despite this, frequency instabilities as low as 2.5×10^{-17} have been achieved using advanced stabilization of crystalline coatings at cryogenic temperatures [7,6].

A promising alternative to conventional Bragg mirrors are meta-mirrors, which use dielectric nanostructured surfaces with sub-wavelength feature sizes. These mirrors can achieve extremely low optical and mechanical losses through tailored structuring of amorphous or crystalline materials, with mirror reflectivities corresponding to a finesse of 12,000 already demonstrated [8]. To qualify these meta-mirrors as an alternative to conventional mirrors in these applications, several challenges must be addressed. When it comes to the optical design, highest feasible reflectivity (i.e. lowest optical losses) needs to be ensured while ensuring lowest thermal noise. Currently, optical losses remain limited by line edge roughness (LER) and surface roughness of the nanostructures, both directly linked to the fabrication process [9]. In this contribution, we present a framework to study the link between optical performance and thermal noise in these systems and discuss the consequences for optical losses at application wavelengths in the near-infrared and the visible spectral range.

II. Methods

The thermal noise simulations are based on Levin's approach [10], which adapts the fluctuation-dissipation theorem [11] for application to functional optical surfaces [12,13]. In this framework, a virtual oscillating pressure is applied to the meta-mirror surface, introducing elastic energy into the material. Depending on the internal mechanical losses of the involved materials, this leads to dissipated power and, consequently, to thermal noise fluctuations. As demonstrated in previous work, the virtual pressure distribution is determined by Maxwell's stress tensor at the interfaces between the meta-mirror and its surroundings, and thus directly reflects the local optical field distribution within the structure. The spatial overlap between this elastically stored energy and the mechanical loss distribution of the constituent materials ultimately governs the overall noise performance.

This coupling between optical field distribution and thermal noise provides a powerful tool for understanding and mitigating noise in structured mirror systems. It also links noise performance to optical properties such as reflectivity and absorption losses, enabling co-optimization of both. We apply this framework to meta-mirrors composed of differently shaped meta-atoms and identify robust parameter regimes of high reflectivity for NIR and visible wavelengths.

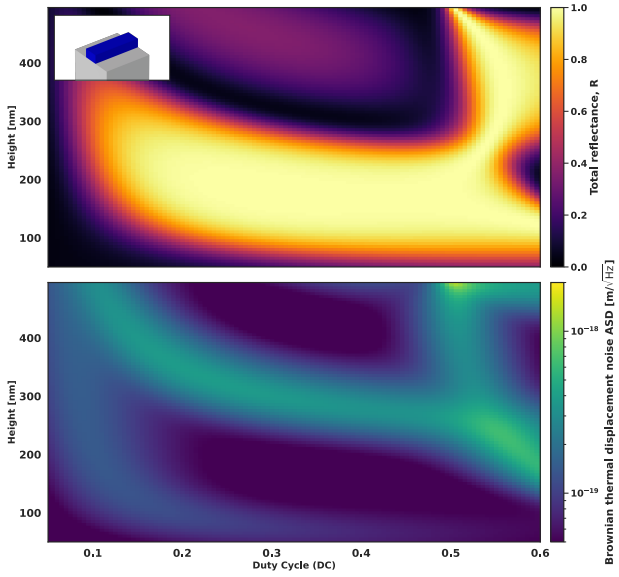

Fig. 1: Top: Dependence of the reflectance of a meta-mirror made of silicon on a fused silica substrate reflectance on the duty cycle and height of a 1D periodic structure as shown in the inset. Bottom: Thermal noise amplitude of the meta-mirror. For the simulations, a wavelength of 1550 nm, transverse-electric polarization, a beam radius of 500 µm, a temperature of 300 K, and a measurement frequency of 100 Hz have been used.

III. Results and Discussion

Fig. 1 shows the exemplary dependence of reflectance and thermal-noise amplitude on the duty cycle and height of the meta-atoms, obtained using COMSOL simulations. In the broad high-reflectivity region around a meta-atom height of approximately 200 nm, the thermal noise amplitude remains below 10^{-19} m/Hz$^{1/2}$ and varies little across the parameter range yielding near-unity reflectance. This robustness is beneficial for experimental realization, as fabrication-induced deviations from the design parameters will minimally affect noise performance. Interestingly, the thermal noise amplitude peaks for meta-atom parameters at which the reflectivity gradient is large. This can be attributed to a maximum in the light field amplitude at the meta-atom surface, leading to an increase in Maxwell's stress tensor. Therefore, to minimize thermal noise, these parameter regimes should be avoided.

IV. Conclusions

Our findings indicate that tailoring the optical field distribution in meta-mirrors is a viable and powerful tool for designing low-thermal-noise, high-performance mirror systems. Further studies linking different resonance mechanisms in meta-atoms to their geometry and thermal-noise amplitude are expected to reveal deeper physical insights into the interplay between structural design and noise performance, and may provide novel degrees of freedom for the co-optimization of reflectivity and thermal noise, ultimately pushing meta-mirror performance toward the fundamental limits required for next-generation laser stabilization and gravitational wave detection.

Acknowledgments

Funded by the European Union. Views and opinions expressed are however those of the author(s) only and do not necessarily reflect those of the European Union or European Research Council Executive Agency. Neither the European Union nor the granting authority can be held responsible for them. This work is supported by ERC grant (MightyMirrors, 101170022). S.K. and M.G. also acknowledge support by the Deutsche Forschungsgemeinschaft (DFG, German Research Foundation) under Germany's Excellence Strategy – EXC 2123/2 QuantumFrontiers – 390837967 and by the European Space Agency within the Open Space Innovation Platform (IDEA:I-2023-05251). S.K. and M.G, T.S., M.W. and C.K.. also acknowledge support by the German Federal Ministry of Education and Research (BMBF) under grant number 05A2023.

References

[1] The LIGO Scientific Collaboration, "Advanced LIGO", Class. Quantum Grav., vol. 32 1, 074001, 2015.
[2] F. Acernese *et al.,* "The Advanced Virgo detector", J. Phys. Conf. Ser., vol. 610, 012014, 2015.
[3] The KAGRA Collaboration, "Interferometer design of the KAGRA gravitational wave detector", Phys. Rev. D., vol. 88, 043007, 2013
[4] B. Sathyaprakash *et al.,* "Scientific objectives of Einstein Telescope", Classical and Quantum Gravity 29, 124013, 2012.
[5] D. Reitze et al., "Cosmic Explorer: The U.S. Contribution to Gravitational-Wave Astronomy beyond LIGO", arXiv:1907.04833, 2019.
[6] D. Kedar, J. Yu, E. Oelker, A. Staron, W. R. Milner, J. M. Robinson, T. Legero, F. Riehle, U. Sterr, and J. Ye "Frequency stability of cryogenic silicon cavities with semiconductor crystalline coatings", Optica, vol. 10, 4, pp. 464-470, 2023.
[7] D. Lee, Z.Z. Hu, B. Lewis, *et al, "*Frequency stability of 2.5×10−17 in a Si cavity with AlGaAs crystalline mirrors", Phys. Rev. Lett, vol. 136, pp. 033801, 2026.
[8] J. Dickmann, J. Dickmann, S. Sauer, J. Meyer, M. Gaedtke, T. Siefke, U. Brückner, J. Plentz, and S. Kroker, "Experimental realization of a 12,000-finesse laser cavity based on a low-noise microstructured mirror", Communications Physics, Vol. 6, 16, 2023.
[9] T. Siefke, M. Heusinger, C. B. Rojas Hurtado, J. Dickmann, U. Zeitner, A. Tünnermann, S. Kroker "Line-edge roughness as a challenge for high-performance wire grid polarizers in the far ultraviolet and beyond ", Optics Express, Vol. 26, 15, 2018.
[10] Y. Levin, "Internal thermal noise in the LIGO test masses: A direct approach," Physical Review D - Particles, Fields, Gravitation and Cosmology 57(2), pp. 659 – 663, 1998.
[11] H. B. Callen and T. A. Welton, "Irreversibility and generalized noise," Physical Review 83(1), pp. 34 – 40, 1951.
[12] S. Kroker, J. Dickmann, C. B.Rojas Hurtado, D. Heinert, R. Nawrodt, Y. Levin, and S.P. Vyatchanin, "Brownian thermal noise in functional optical surfaces," Phys. Rev. D 96, 022002, 2017.

[13] J. Dickmann, J., Rojas Hurtado, C., Nawrodt, R., and Kroker, S., “Influence of polarization and material on Brownian thermal noise of binary grating reflectors,” Physics Letters A 382(33), 2275–2281 (2018).

Terahertz, Nanophotonics and Quantum Optics

Tunable Subterahertz Reflectarrays based on Novel Highly Anisotropic Liquid Crystals

Sergei A. Kuznetsov[1,*], Valeri I. Lapanik[1], and Uładzimir I. Kislyi[1]

[1]Maramako Ltd, Cyprus

*Corresponding author: mr.s.kuznetsov@gmail.com

***Abstract*— We report on unique nematic liquid crystal (LC) compositions based on quaterphenyl and quinquiphenyl substances and distinguished by high dielectric anisotropy and low dielectric losses at subTHz frequencies. Practical examples of reflective LC-based metamaterial structures with high phase and amplitude tunability promising for 6G communications and subTHz imaging applications are presented.**

***Keywords*— nematic liquid crystals, reconfigurable metasurfaces, high impedance surfaces.**

I. Introduction

The last decade demonstrates a gradual progress in terahertz (THz) sciences and studies of THz-related phenomena, expanding topics for fundamental and applied research, as well as opening up new possibilities in optoelectronic technologies [1]. From a practical standpoint, the low-frequency edge of the THz spectrum, where attenuation in atmosphere and dielectric media is not as strong as at higher frequencies, is of most interest. In particular, the subrange of 0.1-0.3 THz is considered as the key operating domain for sixth-generation (6G) wireless communication systems [2]. This subrange also favorably combines acceptable values of spatial resolution (~ 1 mm) and penetrating power when visualizing optically opaque objects that makes it promising for security scanners and nondestructive testing systems in industry. SubTHz imagers are especially attractive when implemented by means of a cost-effective single-pixel imaging technology, wherein object visualization is performed by comparing its integral illumination, registered by a single-pixel detector, with a set of amplitude 2D patterns (masks) that spatially modulate the wave beam [3].

Both 6G and subTHz imaging technologies necessitate employing electronically reconfigurable planar quasi-optical devices for dynamic and spatial control of the amplitude, phase and polarization of the radiation beams. Liquid crystals (LCs) represent an effective and promising approach to such manipulations [4], in particular due to possibility of using mature and cost-efficient fabrication platform of LC displays. When integrated with metamaterial resonators or metasurfaces, LCs allow one to overcome an obstacle of a relatively large length λ of subTHz waves with respect to the LC layer thickness h_{LC} relevant for achieving an acceptable response speed.

In this contribution, we report on progress in the development of novel LC compositions characterized by high dielectric anisotropy and low dielectric losses at subTHz frequencies. We further demonstrate experimental prototypes of planar subTHz LC devices implemented in configurations of reflectarrays operating both in phase and amplitude regimes, including spatially controlled modulation. This work continues our research line previously reported in [5, 6].

II. Selected Results

Among the classes of LC compounds most promissory for microwave and subTHz applications, we may distinguish the nematic LC compositions based on polycyclic LC substances, in particular, derivatives of n-quaterphenyl

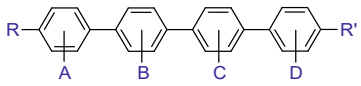

and n-quinquiphenyl

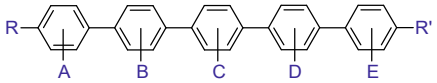

with different terminal (R, R') and lateral (A, B, C, D, E) substituents: R, R' = alkyl, F, NCS; A, B, C, D, E = Cl, CH3 [7]. As compared to 2- and 3-ring substances, 4- and 5-ring LC compounds are characterized by higher optical anisotropy, while the introduction of lateral substituents into the ring molecules enables to decrease their melting point and improve miscibility.

We developed new approaches to the synthesis of liquid-crystalline laterally substituted polyaromatic derivatives of n-quaterphenyl and n-quinquiphenyl, which involve condensation methods to form substituted cyclic fragments [8, 9]. These methods are distinguished by implementation, simplicity and availability of the initial reagents. The developed technology allows us to synthesize new polyaromatic LC compounds with high optical anisotropy ($\Delta n \geq 0.4$, where Δn is the refractive index difference between ordinary and extraordinary axes), as well as high chemical and photochemical stability. The melting point of most synthesized substances does not exceed +(80÷90)°C (for the best n-quaterphenyl compound it is even

below +65°C, thereby representing the best result ever achieved in the world), while their temperature of transition to the isotropic state is less than 210°C. Synthesized LC compounds have rod-shaped molecules and are characterized by good solubility in most organic solvents and good miscibility with all known low-viscosity classes of LC compounds.

Based on the synthesized LC compounds, we experimentally optimized and produced a set of LC compositions applicable to tunable high-performance subTHz metamateral structures. These compositions are highlighted by low dielectric losses ($\tan\delta < 0.01$), high dielectric anisotropy ($\varepsilon'_{\parallel} - \varepsilon'_{\perp} > 1$), and low dispersion in comparison with similar products of alternative developers.

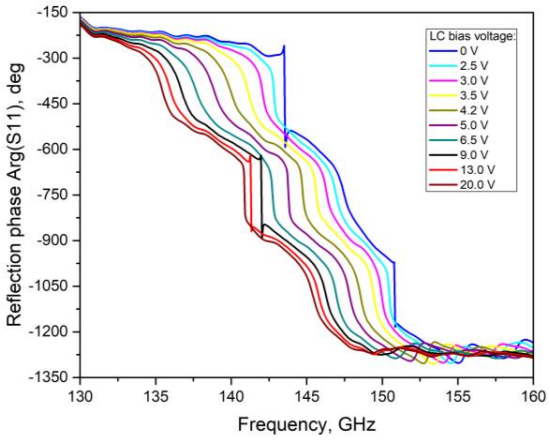

Fig. 1 Experimental spectra of the reflection phase at different bias voltages applied to LC pixels of the reflectarray. Normalization to a metallic mirror.

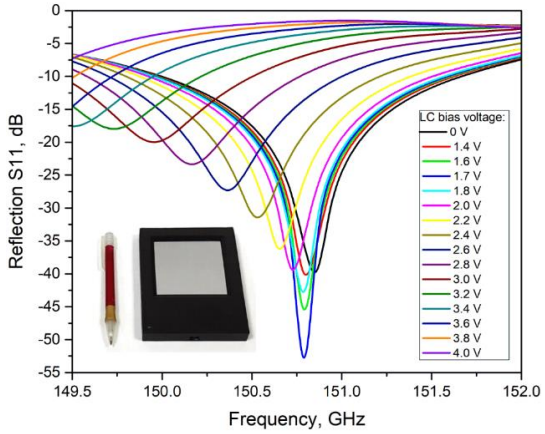

Fig. 2 Experimental spectra of the reflection amplitude at different bias voltages in vicinity of the deepest absorption resonance. Normalization to the metallic mirror. Photograph of the fabricated device is shown in the inset.

Figures 1 and 2 exemplify spectral characteristics for one of the developed experimental prototypes. The device operates in reflection and has a configuration of a multi-resonant high-impedance metasurface optimized for the band of 0.13–0.15 THz. Exploiting the LC layer as thin as $h_{LC} \approx 0.017 - 0.020\ \lambda$, the prototype has an optical aperture of 70×70 mm and 75×64 operating pixels realized in a passive LC matrix format with crossbar electronic control. The regimes of both phase and amplitude deep modulation are shown on the same device, demonstrating the ability to tune the pixel's reflection phase and amplitude up to 630 degrees (Fig. 1) and 52 dB (Fig. 2), respectively. It is worth highlighting the importance of using multiple resonances in the metastructure design to widen its phase alteration range versus single-resonance structures.

III. Conclusion

Due to high dielectric anisotropy and low dielectric losses, the nematic LC compositions based on quaterphenyl and quinquiphenyl derivatives developed in our team are estimated to have high prospects for applications in various optoelectronic devices: from microwave to infrared spectral regions.

Our presentation will provide more details on the advances in LC technology from Maramako Ltd [10] and the progress overlook in the implementation of LC-based metamaterial-inspired reflectarrays for subTHz wavefront manipulation will be discussed.

References

[1] A. Leitenstorfer, A. S. Moskalenko, T. Kampfrath et al., "The 2023 terahertz science and technology roadmap," J. Phys. D: Appl. Phys., vol. 56, No. 22, 223001, 2023.

[2] T. S. Rappaport, Y. Xing, O. Kanhere et al., "Wireless Communications and Applications Above 100 GHz: Opportunities and Challenges for 6G and Beyond," IEEE Access, vol. 7, pp. 78729–78757, 2019.

[3] L. Zanotto, R. Piccoli, J. Dong, et al., "Single-pixel terahertz imaging: a review," Opto-Electron. Adv., vol. 3, No. 9, 200012, 2020.

[4] H. Yu, H. Wang, Q. Wang, et al., "Liquid Crystal-Tuned Planar Optics in Terahertz Range," Appl. Sci., vol. 13, No. 3, 1428, 2023.

[5] V. Lapanik, S. Kuznetsov, J. A. Marcotegui, "Tunable quasioptical notch filter based on liquid-crystal-metastructure for the millimeter-wave range," Digest Tech. Papers - SID Int. Symp., vol. 52, No. S2, p. 579, 2021.

[6] D. Pérez-Quintana, E. Aguirre, E. Olariaga, et al., "Reconfigurable Millimeter-Wave Reflectarray based on Low Loss Liquid Crystals," IEEE Trans. Antennas Propag., vol. 72, No. 1, pp. 531–541, 2024.

[7] V. Lapanik, G. M. Sasnouski, S. Timofeev, et al. "New highly anisotropic liquid crystal materials for high-frequency applications," Liq. Cryst., vol. 45, No. 8, pp. 1242–1249, 2018.

[8] G. Sasnouski, V. Lapanik, R. Dabrowski, J. Dziaduszek, "Synthesis of new LC compounds with high optical anisotropy: pentaphenyl derivatives lateral substituted," Phase Transit., vol. 85, No. 4, pp. 309–313, 2012.

[9] G. Sasnouski, V. Lapanik, V. Bezborodov, et al., "Synthesis of fluoro substituted quaterphenyl liquid crystals," Phase Transit., vol. 87. No. 8, pp. 783–789, 2014.

[10] Maramako Limited, Cyprus, website: https://maramako.com

Temporal Dispersion Effects in Optical Spectra of Exciton-Plasmon Systems at Strong Coupling

Gabriele Williams, Sancenia Johnson, Tigran V. Shahbazyan

Department of Physics, Jackson State University, Jackson, MS 39217 USA
*Corresponding author: shahbazyan@jsums.edu

***Abstract*— We show that temporal dispersion of the metal dielectric function significantly modifies the shape of scattering spectra of quantum emitters strongly coupled to surface plasmons by shifting spectral weight towards lower energy polaritonic band.**

***Keywords*— surface plasmon, strong coupling, excitons**

I. Introduction

The shape of scattering spectra of quantum emitters (QE) resonantly coupled to localized surface plasmons (LSP) in metal nanoparticles (NP) as the system transitions to the strong coupling regime has been an actively debated topic [1,2]. In general, the scattering spectrum of a hybrid system characterized by broad spectral band should be enhanced on the higher frequency side due to faster radiation rate of the upper-energy states, implying that, in the strong coupling regime, the spectral band associated with the upper-energy polaritonic state should be relatively enhanced. Such a spectral profile is consistent with the classical model of two coupled Lorentzian oscillators, in which one of the oscillators (LSP) couples much stronger to the electromagnetic (EM) field due to its much greater optical dipole moment as compared to the QE one [3]. However, recent experiments for excitons resonantly coupled to LSP in metal-dielectric structures [1,2] reveal the opposite asymmetry pattern characterized by enhancement of the lower polaritonic band. In this paper, we demonstrate that non-Lorentzian effects originating from the material optical dispersion and losses strongly affect the optical spectra of hybrid QE-LSP systems and, in the strong coupling regime, result in a pronounced shift of the spectral weight towards the lower-energy polaritonic band, consistent with the experiment.

II. Methods

We consider a hybrid system of QE located near metal NP in the external EM field $\boldsymbol{E}_0 e^{-i\omega t}$ characterized by complex metal dielectric function $\varepsilon(\omega) = \varepsilon'(\omega) + i\varepsilon''(\omega)$ and QE excitation frequency ω_e tuned to resonance with the LSP frequency ω_n. Using the LSP Green function for NP of arbitrary shape [4], we set up non-Lorentzian semiclassical Maxwell-Bloch equations which include the full complex dielectric function of the metal rather than using Lorentzian approximation for the LSP resonance:

$$\Omega_n \rho_n = g\rho_e + \boldsymbol{\mu}_n \cdot \boldsymbol{E}_0$$

$$\Omega_e \rho_e = g\rho_n + \boldsymbol{\mu}_e \cdot \boldsymbol{E}_0$$

where ρ_e and ρ_n are, respectively, the QE and LSP polarizations, which determine their induced dipole moments as $\boldsymbol{p}_e(\omega) = \boldsymbol{\mu}_e \rho_e$ and $\boldsymbol{p}_n(\omega) = \boldsymbol{\mu}_n(\omega)\rho_n$, and g is QE-LSP coupling. Here, $\Omega_e = \omega_e - \omega - i\gamma_e/2$ is QE detuning, where γ_e is the QE decay rate, $\Omega_n = [\varepsilon'(\omega_n) - \varepsilon(\omega)]/\varepsilon_n'$, with $\varepsilon_n' = \partial\varepsilon'(\omega_n)/\partial\omega_n$, is non-Lorentzian LSP detuning, and $\boldsymbol{\mu}_e$ and $\boldsymbol{\mu}_n(\omega)$ are the corresponding optical dipole moments. The latter is defined as $\boldsymbol{\mu}_n(\omega) = (1 / 4\pi) \int dV [\varepsilon(\omega) - 1]\boldsymbol{E}_n(\boldsymbol{r})$, where $\boldsymbol{E}_n(\boldsymbol{r})$ is electric field of the LSP mode. The full system induced dipole moment $\boldsymbol{p}(\omega) = \boldsymbol{p}_e(\omega) + \boldsymbol{p}_n(\omega)$ determines the system scattering spectrum near the LSP resonance.

III. Results and Discussion

In Fig. 1 we show the scattering spectra for a QE near an Au NP at two different LSP frequencies calculated using the non-Lorentzian model (left panel) compared to Lorentzian model of coupled oscillators (right panel). As the QE-LSP coupling g increases relative to LSP decay rate γ_n, the system undergoes the transition to strong coupling regime signaled by the emergence of Rabi splitting between the polaritonic bands. The scattering spectra calculated using the non-Lorentzian model (left panel) exhibit pronounced enhancement of the lower energy polaritonic band [5], consistent with the experiment [1,2]. In contrast, for scattering spectra calculated in the Lorentzian approximation shown in Fig. 2, the upper energy polaritonic band is relatively enhanced, as predicted by the coupled oscillators model. This reversal of spectral asymmetry is traced to the effect temporal dispersion of the metal dielectric function on the LSP optical dipole moment which results in a suppression of the LSP radiation efficiency for higher energies.

Acknowledgments

This work was supported in part by the US National Science Foundation grants DMR- 2302088, DMR-2301350, and NSF-PREM-2423854.

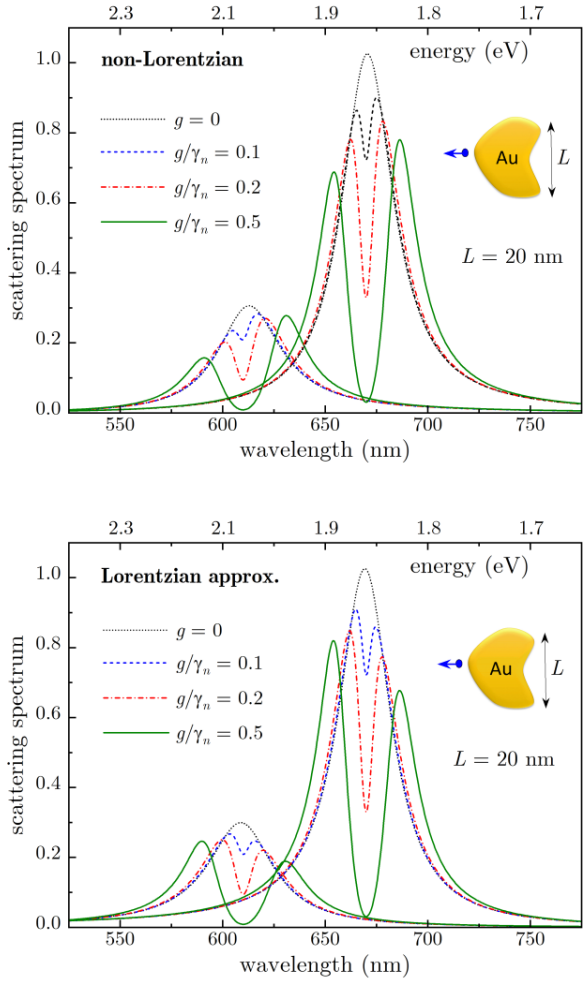

Fig. 1. Scattering spectra for a QE coupled to LSP in Au NP calculated using non-Lorentzian model (upper panel) and its Lorentzian approximation (lower panel) exhibit inversion of spectral asymmetry caused by temporal dispersion of the metal dielectric function.

REFERENCES

[1] H. Leng, B. Szychowski, M.-C. Daniel, and M. Pelton, "Strong coupling and induced transparency at room temperature with single quantum dots and gap plasmons," Nat. Commun. 9, 4012 (2018).

[2] M. Wersäll, B. Munkhbat, D. G. Baranov, F. Herrera, J. Cao, T. J. Antosiewicz, and T. Shegai, "Correlative Dark-Field and Photoluminescence Spectroscopy of Individual Plasmon–Molecule Hybrid Nanostructures in a Strong Coupling Regime," ACS Photon. 6, 2570–2576 (2019).

[3] K.-D. Park, M. A. May, H. Leng, J. Wang, J. A. Kropp, T. Gougousi, M. Pelton, and M. B. Raschke, Sci. Adv. 5, eaav5931 (2019).

[4] T. V. Shahbazyan, "Universal optical polarizability for plasmonic nanostructures", Phys. Rev. A 107, L061503, (2023).

[5] T. V. Shahbazyan, "A Non-Lorentzian Model for Strong Exciton–Plasmon Coupling," J. Phys. Chem C. 129, 19, 9026–9034 (2025).

Ultra-small and ultra-efficient source of photon pairs

Stanislas Pasternak[1,2,*], Alfredo De Rossi[2], Sylvain Combrie[2]

[1]Centre de Nanosciences et de Nanotechnologies, CNRS, Université Paris Saclay, Palaiseau, France
[2]Thales Research and Technology, Campus Polytechnique, 1 avenue Augustin Fresnel, 91767 Palaiseau, France
*Corresponding author: stanislas.pasternak@universite-paris-saclay.fr

***Abstract*—We demonstrate efficient single photon generation using a InGaP photonic cristal cavities by taking advantage of the intrinsic small volume of the cavities. We measure generation rate of around 1MHz with high CAR of 250 for pump power in cavity of 4µW.**

***Keywords*— photonic crystals, single photon pair sources, quantum optics.**

I. Introduction

The development of quantum technologies for computing and communication require manipulation of entangled state of light. One way of generating those states is through parametric down-conversion, nonlinear optical process. Since these sources are probabilistic, achieving a high generation rate is essential. Several technologies are competing for the optimization of those sources using second order and third order non linearity in ring resonator with high Q factor ($Q > 10^6$ [1]). However the dimension of those sources are limited by the bending losses.

II. Methods

Photonic crystal (PhC) allow for very strong light confinement which mean we can take advantage of the dependence of the inverse of the volume of the cavity for the pair generation formula (Ref[4]):

$$R \propto n_2^2 \frac{Q^3}{V_\chi^2} P^2 \tag{1}$$

where n_2 denotes the Kerr non linear index, Q the quality factor, V_χ^2 the effective mode volume, and P the pump power in the cavity. The total length of one source is around 40 µm. Our source are made in InGaP which has a very strong n_2 coefficient and its large bandgap prevent two-photon absorption at telecom wavelength .

III. Results and Discussion

We use the first three cavity modes, which are separated by a free spectral range (FSR) of approximately 1 GHz and exhibit quality factors on the order of 10^5 (Fig.1). This detuning is then compensated by unequal thermal tuning of the different mode by optical pumping of the seconde mode. We achieve an internal photon-pair generation rate of 20 MHz with a pump power of approximately 4 µW. At this generation rate the coincidental-to-accidental ratio (CAR) approaches the theoretical multi-photon limit. A maximum CAR of 250 is obtained for an internal generation rate of 1 MHz with an in-cavity pump power of approximately 2 µW.

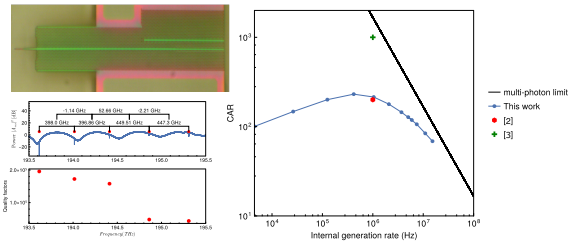

Fig. 1. **Photonics crystal source photon pairs generation**.(a) Photonic crystal cavity and waveguide. (b) OCT measurement of the resonance, the free spectral range (FSR) between the resonances and Q factor for each resonance. (c) Estimated pair generation inside the chip and CAR for different regimes of operation of the source. Other recent work are reported for comparison. (Ref[2] : AlGaAs ring resonator, Ref[3] : SiN ring resonator)

References

[1] Li, B., Yuan, Z., Williams, J. et al. “Down-converted photon pairs in a high-Q silicon nitride microresonator,” *Nature* 639, 922–927 (2025).
[2] Yiming Pang, Joshua E. Castro1, et al., “Versatile Chip-Scale Platform for High-Rate Entanglement Generation Using an AlGaAs Microresonator Array,” *PRX Quantum*, 6, 010338 – Published 3 March, 2025
[3] Rahmouni, A., Wang, R., Li, J. et al. “Entangled photon pair generation in an integrated SiC platform,” L*Light Sci Appl* 13, 110 (2024).
[4] Alexandre Chopin, Inès Ghorbel, Sylvain Combrié, Gabriel Marty, Fabrice Raineri, and Alfredo De Rossi “Time-correlated photons from an In0.5Ga0.5P photonic crystal cavity on a silicon chip,” L*Phys. Rev. Research* 13, 110 (2024).

Optics, Photonics and Nanophotonics

Bridging Simulation and Measurement: Complex Permittivity Estimate with Neural Network Based on Calibrated Data

Francesco Ferretti[1,*], Emidio Di Giampaolo[1], Alessandro Di Carlofelice[1]

[1]Department of Industrial and Information Engineering & Economics University of L'Aquila – Italy
*Corresponding author: francesco.ferretti@graduate.univaq.it

***Abstract*—Artificial neural networks have the potential to treat complex inverse problems as estimating permittivity and the components of a solution. We propose a neural network approach utilizing calibrated scattering parameters to align simulated training data with real experimental measurements. This strategy ensures precise dielectric estimation when real-world data are used.**

***Keywords*— complex permittivity estimation, machine learning, open-ended coaxial probe, inverse problems, calibration.**

I. Introduction

The electromagnetic characterization of materials is of paramount importance across various scientific and industrial fields. To cite a few examples in the medical field, measuring the permittivity of biological tissues is useful for disease diagnosis: a tumor mass exhibits a different permittivity compared to healthy tissue, enabling the detection of abnormalities [1], or the diagnostic application of permittivity measurements of blood [2], which depends from the concentrations of its components. Dielectric spectroscopy plays a role in bio-process engineering for real-time monitoring of microbial growth. Industrial processes such as crystallization have support from the dielectric characterization of aqueous chemical systems as ternary and quaternary salt solutions for monitoring the phase equilibria [3].

The use of permittivity for diagnostic or chemical monitoring is a complex inverse problem which is still open. In fact, permittivity is a macroscopic indicator that is unable to distinguish among the different components of a complex system (e.g. blood, multi-component solution) so a given value of permittivity may correspond to different concentrations of components. Recently, many authors proposed the use of multi-resonant microwave sensors (e.g. based on split ring resonator or similar) for dielectric spectroscopy of aqueous multi-component systems, nevertheless the inversion for retrieving concentrations of components from measured data is typically cumbersome. To overcome the difficulties of inversion some authors [4] strengthens the role of resonators by using a neural network.

Artificial Neural Networks (ANNs) are extensively employed due to their proven capability to approximate high-dimensional nonlinear input–output mappings in complex dynamical systems with arbitrary accuracy, a property theoretically established by the Universal Approximation Theorem [5]. So that an ANN can be a good method for solving the considered inverse problem if adequately trained with appropriate techniques. Several attempts have been made to develop an ANN capable of mapping the scattering parameters measured with an Open-Ended Coaxial Probe (OECP) directly to the complex permittivity of the material under test (MUT). The authors in [6] proposed a deep neural network designed to extract the constitutive parameters of the Debye model directly from the measured scattering parameters. Furthermore, the integration of ANNs with monopole probes has been investigated in [7] as a potential substitute for the OECP, although that study is limited to simulated data and to a narrow range of permittivity.

In this context, the present work shows a twofold advancement of the state of the art: demonstrating that a simple not resonant OECP is adequate for multi-component analysis of aqueous solutions and proposing an ANN trained on synthetic calibrated data that effectively bridges the gap between simulated training data and real-world measurements. This approach holds strategic importance for future developments, as it enables the use of synthetic data alone to train networks for any given task dealing with permittivity measurements. By aligning simulated and real-world distributions through calibration, the need for costly and time-consuming real-world data collection is bypassed, establishing a unified domain where virtual training translates seamlessly to physical systems.

The paper is organized as follows: Section II provides a brief description of the used methods, Section III shows the results obtained with synthetic data and the effectiveness of the ANN in comparison with analytical methods using also experimental measurements.

II. Methods

A. Numerical model of the probe

A numerical model of a real, home made, OECP based on the semi-rigid coaxial cable UT-141 was implemented in CST Studio Suite [8]. An ISO 3819 low-form borosilicate glass (Pyrex) beaker is positioned beneath the probe. The beaker is filled with the MUT to a height of 4 cm and probe is immersed

in the material to a depth of 1 cm. The simulated model employs a coaxial cable with a length shorter than the actual one in order to reduce the computational load. This discrepancy is immaterial since we resort to a calibration procedure for both real and numerical model probes, effectively de-embedding the coaxial line and making the inversion independent of the probe's physical length.

A congruent electromagnetic model has been developed for the MUT, in particular a solution made of distilled water with sodium chloride ($NaCl$) and sucrose ($C_{12}H_{22}O_{11}$) dissolved in various concentrations. The complex permittivity of that solution was determined using the analytical formulations reported in [9].

B. Analytical calibration and inversion model

We overcome the gap between simulated training data and real-world measurements by resorting to a calibration procedure that is used in measurements of permittivity with OECP [10]. The three-steps calibration procedure employs a known liquid (e.g. physiological water), in-air open load, and a short circuit is applied to both systems, i.e. real and numerical. It permits to de-embed data (i.e. reflection coefficients) from the specific probes and systematic errors. Using companion equations the complex permittivity is obtained with an analytical inversion procedure. That procedure is applied to both physically measured and simulated quantities allowing us to have an assessment, by results comparison, of the realized network.

C. Architecture of ANN

Since we are interested in estimating many different parameters (i.e. the real and the imaginary parts of permittivity and concentrations of sodium chloride and sucrose), we develop three fully connected networks working in parallel. Each network is trained with a set of data taken from 625 simulations (different concentration of solutes): 80% training set, 10% test set and 10% validation set. As input for the network we provide real and imaginary part of calibrated S-parameter at 100 MHz, 7.55 GHz and 15 GHz.

III. Results and Discussion

The developed ANNs yield highly consistent results on the simulated testing set and gives results in good agreement with analytical formula. Its estimate has a Mean Square Error (MSE) of 0.68 and 0.033 for real and imaginary part of permittivity, respectively, while the corresponding MSE for the analytical formula are 0.22 and 0.058. Table I reports a comparison between analytical formula [10] and ANN estimate in case of measured data. The measurements were performed on a reference material for which the permittivity is well known: distilled water at different temperatures. The agreement between the two techniques is noticeable. A test based on numerical dataset has been done for evaluating the effectiveness of the network to predict the concentration (mol/L) of solutes of the aqueous solution with $NaCl$ and $C_{12}H_{22}O_{11}$. The obtained results are satisfying: the total MSE on test set predicting NaCl is $1.5 \cdot 10^{-7}$ meanwhile the Maximum Absolute Error (MAE) is $3.0 \cdot 10^{-4}$. The MSE for the predicting sucrose is $1.1 \cdot 10^{-5}$ meanwhile the MAE is $2.7 \cdot 10^{-3}$.

This study demonstrates that a network trained on calibrated synthetic data is capable of accurately predicting the complex permittivity from experimental measurements together with the concentration of the components of a solution. This finding is of fundamental importance as it establishes a framework for realistic AI applications that bypass the need for extensive experimental datasets, effectively bridging the gap between simulated environments and real-world data. Numerical results have been corroborated by a limited number of real measurements. An extensive campaign of measurements is planned to fully validate the work.

TABLE I
Comparison of permittivity estimate from measured data using different models: Stogryn, formula [10] and ANN.

Temperature	Stogryn [11]	Formula [10]	ANN
20.6 °C	$79.66 - j4.28$	$77.25 - j4.14$	$76.77 - j3.88$
21.7 °C	$79.29 - j4.13$	$76.74 - j3.23$	$76.57 - j2.95$
31.5 °C	$75.98 - j3.09$	$74.19 - j3.22$	$74.01 - j2.98$
38.8 °C	$73.62 - j2.57$	$70.65 - j2.59$	$70.66 - j2.39$

References

[1] Lazebnik M, et al., A large-scale study of the ultrawideband microwave dielectric properties of normal, benign and malignant breast tissues obtained from cancer surgeries. Phys Med Biol. 2007 Oct 21;52(20):6093-115.

[2] F Jaspard and M Nadi and A Rouane, Dielectric properties of blood: an investigation of haematocrit dependence. Physiological Measurement, 2003, 24, 1, pp. 137.

[3] Ralf Dohrn, Gerd Brunner, Phase equilibria in ternary and quaternary systems of hydrogen, water and hydrocarbons at elevated temperatures and pressures., Fluid Phase Equilibria, Volume 29, 1986, Pages 535-544, ISSN 0378-3812

[4] P. Casacuberta, P. Vélez, F. Paredes and F. Martín, "Artificial Intelligence Assisted Measurement of Glucose, Sodium, and Potassium Concentrations in Diluted Aqueous Solutions Using Microwaves," in IEEE Sensors Letters, vol. 9, no. 8, pp. 1-4, Aug. 2025

[5] Kurt Hornik, Approximation capabilities of multilayer feedforward networks, Neural Networks, Volume 4, Issue 2, 1991, Pages 251-257, ISSN 0893-6080.

[6] Aydinalp, Cemanur & Joof, Sulayman & Akıncı, M. & Akduman, Ibrahim & Yilmaz, Tuba. (2021). Microwave Dielectric Property Retrieval From Open-Ended Coaxial Probe Response With Deep Learning. IEEE Access, vol. 10, pp. 1216-1227, 2022.

[7] A. Hasan and A. F. Peterson, "Measurement of Complex Permittivity using Artificial Neural Networks," in IEEE Antennas and Propagation Magazine, vol. 53, no. 1, pp. 200-203, Feb. 2011

[8] CST Studio Suite, version 2025, Dassault Systèmes, Darmstadt, Germany. [Online]. Available: https://www.3ds.com/products-services/simulia/products/cst-studio-suite/

[9] Bakam Nguenouho OS, Chevalier A, Potelon B, Benedicto J, Quendo C. Dielectric characterization and modelling of aqueous solutions involving sodium chloride and sucrose and application to the design of a bi-parameter RF-sensor. Sci Rep. 2022 May 3;12(1):7209.

[10] K. F. Staebell and D. Misra, "An experimental technique for in vivo permittivity measurement of materials at microwave frequencies," in IEEE Transactions on Microwave Theory and Techniques, vol. 38, no. 3, pp. 337-339, March 1990.

[11] A. Stogryn, "Equations for Calculating the Dielectric Constant of Saline Water (Correspondence)," in IEEE Transactions on Microwave Theory and Techniques, vol. 19, no. 8, pp. 733-736, Aug. 1971

Investigation of Co-Directional Coupling in Mid-Infrared Fiber Gratings Fabricated by the Pull-and-Heat Technique

Francesco Anelli[1], Antonella Maria Loconsole[1], Federico Moscatelli[1], Francesco Prudenzano[1,*]

[1]Department of Electrical and Information Engineering, Polytechnic University of Bari, Italy
*Corresponding author: francesco.prudenzano@poliba.it

***Abstract*— This work illustrates the design and fabrication of mid-infrared fiber gratings based on co-directional mode coupling in ZBLAN optical fibers. Due to their low attenuation and wide transparency window extending into the mid-infrared region, ZBLAN fibers are well suited for photonic and sensing applications beyond the silica limit. Electromagnetic simulations were used to support the design. The grating was fabricated using a controlled pull-and-heat tapering process by means of a Vytran GPX-2400 glass processing system. This equipment enables precise adjustment of heating power, pulling speed, and elongation length, this allowing accurate control of the taper waist diameter and transition regions. Special attention was given to maintaining mechanical integrity and minimizing surface defects during processing, which is particularly important for soft-glass fibers such as ZBLAN. The resulting tapered structures exhibited good reproducibility. These results confirm the suitability of the pull-and-heat technique for fabricating mid-infrared tapered gratings in ZBLAN fibers and demonstrate their potential for mid-infrared photonic and sensing applications.**

***Keywords*— ZBLAN fiber, mid-infrared, fiber gratings, tapered optical fibers, pull-and-heat technique, co-directional mode coupling, coupled local mode theory, mode coupling, soft-glass fibers**

I. Introduction

In recent years, increasing attention has been directed toward the mid-infrared (mid-IR) spectral region, typically defined from the wavelength $\lambda = 2\ \mu m$ to $\lambda = 5\ \mu m$ and beyond. This wavelength range is of particular interest because many molecular absorption fingerprints lie in the mid-IR, this paving the way for novel applications in environmental monitoring, biomedical diagnostics, chemical sensing, and industrial process control [1]. The widely adopted silica optical fibers exhibit strong absorption beyond approximately $\lambda = 2.4\ \mu m$, which limits their use in this spectral domain [2]. Consequently, alternative glass materials have been explored to extend fiber-based technologies into the mid-IR region [3], [4].

Among the materials compatible with mid-IR wavelengths, ZBLAN fluoride glass fibers have emerged as a promising platform [5]. ZBLAN, composed primarily of ZrF_4-BaF_2-LaF_3-AlF_3-NaF, offers broad transparency extending into the mid-IR range up to approximately to $\lambda = 4.5\ \mu m$ [6], [7]. This makes this glass attractive for mid-IR laser delivering and sensing applications [8]. Nevertheless, fluoride is a soft-glass material with lower mechanical strength than silica, requiring careful handling and accurately optimized fabrication techniques [9], [10], [11].

Fiber gratings are highly versatile and widely used components in various optical fiber systems. They enable, depending on the grating length and coupling mechanism, i) wavelength-selective filtering or ii) operation as reflective elements [12]. Co-directional coupling can be obtained via long-period gratings and typically results in transmission-based spectral features [13]. On the contrary, counter-directional coupling, generally obtained via Bragg gratings, leads to reflective behavior, allowing the grating to function as a wavelength-selective mirror [14]. These spectra can be highly sensitive to variations in geometry, refractive index, and environmental conditions.

Recently, the fabrication of long-period gratings in soft-glass fibers such as ZBLAN has been achieved via femto-second laser, corrugated structures inducing strain on the fiber and pull-and-heat technique [15], [16], [17], [18]. The latter technique is based on several micro-tapers, fabricated by locally heating the fiber while applying controlled longitudinal tension.

In this work, co-directional mode coupling in tapered ZBLAN fiber gratings, fabricated using a commercial glass processing system, is investigated. The numerical analysis and fabrication process are reported, highlighting the potential of tapered fluoride fibers for mid-IR photonic and sensing applications.

II. Electromagnetic Design

A single-mode ZBLAN fiber from Le Verre Fluoré is considered. It is characterized by core diameter $d_1 = 6.5\ \mu m$, cladding diameter $d_2 = 125\ \mu m$ and numerical aperture $NA = 0.23$. Due to diameter variations introduced during the fabrication process, the modal field profiles and propagation constants vary along the longitudinal direction. For a preliminary electromagnetic design of the grating, the well-known phase-matching condition for co-directional coupling

can be adopted [19]:

$$\Delta\beta_{co-cl_i} = \frac{2\pi}{\Lambda} \quad (1)$$

where $\Delta\beta_{co-cl_i}$ represents the propagation constant difference between the fundamental core mode LP_{01} and the co-propagating cladding modes, usually of the same symmetry, LP_{0i} with $i > 2$; Λ is the grating period. Electromagnetic modal analysis were performed to determine the phase-matching conditions for the $LP_{01} - LP_{02}$ and $LP_{01} - LP_{03}$ mode couplings. In the simulations, material dispersion was included by accounting for the wavelength dependence of both core and cladding refractive indices [6]. Additionally, an air domain and a perfectly matched layer were employed to ensure accurate estimation of the cladding mode propagation constants. Since tapering reduces the fiber diameter, a smaller cladding (and consequently core) diameter have been considered to estimate the resonant wavelengths. Specifically, the selected diameter should correspond to the effective diameter of the taper region where modal coupling is strongest. Indeed, according to coupled local-mode theory, sections of the grating exhibiting steeper diameter variations produce stronger mode coupling, whereas regions with nearly constant diameter contribute negligibly to coupling [20]. In this work, a reduced cladding diameter $d_2 = 105\ \mu$m is analysed.

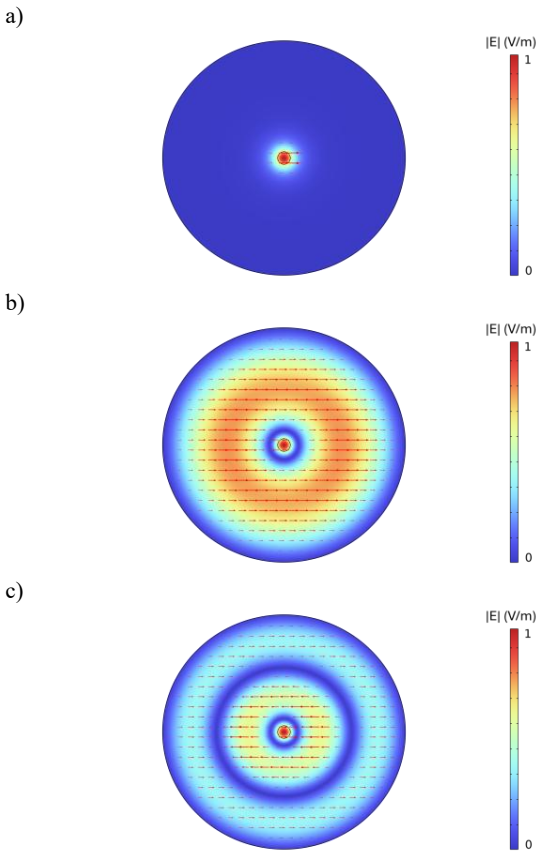

Fig. 1 Simulated electric field norm $|E|$ for the x-polarization of the a) LP_{01}, b) LP_{02}, c) LP_{03} modes, at the wavelength $\lambda = 3100\ nm$ for a cladding diameter $d_2 = 105\ \mu m$.

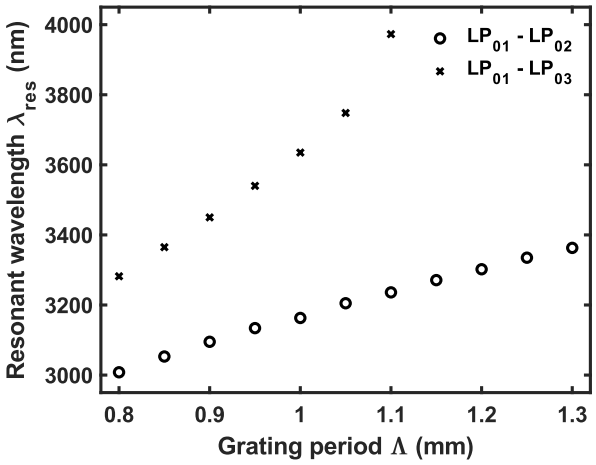

Fig. 2 Calculated resonant wavelength λ_{res} due to the $LP_{01} - LP_{02}$ (circle markers) and due to the $LP_{01} - LP_{03}$ (cross markers) couplings for different value of the grating period Λ for a cladding diameter $d_2 = 105\ \mu m$.

Figure 1 shows the electric field magnitude $|E|$ of the fundamental mode LP_{01} and the first two higher-order modes with the same azimuthal symmetry, i.e. LP_{02} and LP_{03}.

Figure 2 reports the calculated resonant wavelength λ_{res} due to the $LP_{01} - LP_{02}$ (circle markers) and due to the $LP_{01} - LP_{03}$ (cross markers) coupling for different value of the grating period Λ. As expected, both resonances experience a redshift for increasing values of the grating period. The larger effective index difference for $LP_{01} - LP_{03}$ explains the higher resonant wavelength.

III. Fabrication

The tapering process was carried out using a Vytran GPX-2400 glass processing system, which provides precise control of heating power, pulling velocity, and elongation length during the pull-and-heat procedure. Such control is particularly important for soft-glass fibers like ZBLAN, where temperature stability is critical to prevent crystallization, surface defects, or structural degradation [21]. The fabrication parameters were carefully optimized to obtain reproducible taper geometries with well-defined waist regions and smooth transition sections.

As a result of the fabrication process, the fiber diameter varies continuously along the propagation direction, as shown in Figure 3.

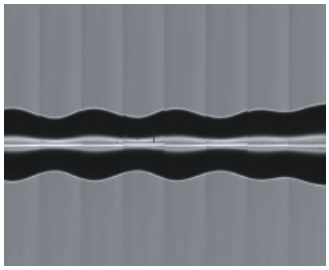

Fig. 3 Longitudinal profile of a section of one of the fabricated long-period gratings on ZBLAN optical fiber; each picture of the montage extends for a longitudinal length $L = 800\ \mu m$.

This controlled geometric modulation directly influences the modal properties of the structure and enables the tailoring of co-directional coupling in the mid-IR range. The spectral response of the device is therefore strongly governed by the local fiber diameter and taper length, highlighting the importance of precise fabrication control for reliable mid-IR photonic components. The characterization of the fabricated long-period grating will be carried out with a broadband setup operating in the mid-IR spectral range.

IV. Conclusion

In this work, co-directional mode coupling in tapered ZBLAN fiber gratings operating in the mid-IR region has been investigated. The device was fabricated using a controlled pull-and-heat technique implemented with a Vytran GPX-2400 glass processing system, enabling precise adjustment of the taper geometry and reproducible fabrication of soft-glass fiber structures. The longitudinal variation of the fiber diameter plays a key role in defining the modal properties and phase-matching conditions responsible for the observed spectral features. The results demonstrate the feasibility of realizing tapered gratings in ZBLAN fibers for mid-IR photonic applications.

Acknowledgments

The authors would like to thank the company Le Verre Fluoré, Bruz, France for the optical fibers employed in the experiment.

References

[1] C. Feng *et al.*, 'Detection of NH3 impurities in H2 environment exploiting quartz-enhanced photoacoustic spectroscopy with an optimized spectrophone', *Sensors and Actuators B: Chemical*, vol. 432, p. 137488, Jun. 2025, doi: 10.1016/j.snb.2025.137488.

[2] F. Prudenzano *et al.*, 'Optimization and Characterization of Rare-Earth-Doped Photonic-Crystal-Fiber Amplifier Using Genetic Algorithm', *J. Lightwave Technol.*, vol. 25, no. 8, pp. 2135–2142, Aug. 2007, doi: 10.1109/JLT.2007.901331.

[3] G. Tao *et al.*, 'Infrared fibers', *Adv. Opt. Photon.*, vol. 7, no. 2, p. 379, Jun. 2015, doi: 10.1364/AOP.7.000379.

[4] F. Anelli, A. M. Loconsole, and F. Prudenzano, 'Mid-infrared optical fiber Devices: Challenges, advances and applications', *Optical Materials*, vol. 167, p. 117294, Oct. 2025, doi: 10.1016/j.optmat.2025.117294.

[5] K. Grebnev, B. Perminov, T. T. Fernandez, A. Fuerbach, and M. Chernysheva, 'Fluoride and chalcogenide glass fiber components for mid-infrared lasers and amplifiers: Breakthroughs, challenges, and future perspective', *APL Photonics*, vol. 9, no. 11, p. 110901, Nov. 2024, doi: 10.1063/5.0225887.

[6] F. Anelli, S. Venck, S. Cozic, and F. Prudenzano, 'S-Tapered Fluoride Optical Fiber for Refractive Index Sensing in the Mid-Infrared', *J. Lightwave Technol.*, vol. 43, no. 12, pp. 5982–5988, Jun. 2025, doi: 10.1109/JLT.2025.3552855.

[7] I. Cozmuta *et al.*, 'In-space manufacturing facts and myths: lessons learned from ZBLAN optical fiber space manufacturing', *Acta Astronautica*, vol. 236, pp. 311–323, Nov. 2025, doi: 10.1016/j.actaastro.2025.06.030.

[8] A. M. Loconsole, V. V. Francione, F. Anelli, S. Taccheo, and F. Prudenzano, 'Mid-IR Amplification Based on a Pr^{3+}: InF_3 Optical Fiber in the Range 3.8 - 4.2 μm', *J. Lightwave Technol.*, vol. 43, no. 11, pp. 5451–5458, Jun. 2025, doi: 10.1109/JLT.2025.3547482.

[9] T. An *et al.*, 'Mid-Infrared Adaptive Fiber Micro-Lenses for Inline Beam Shaping', *J. Lightwave Technol.*, vol. 43, no. 6, pp. 2811–2818, Mar. 2025, doi: 10.1109/JLT.2024.3493892.

[10] E. Galdo *et al.*, 'ZBLAN glass 3D printing: the first steps', *Opt. Mater. Express*, vol. 15, no. 6, p. 1189, Jun. 2025, doi: 10.1364/OME.562288.

[11] F. Anelli, A. Annunziato, J. Letourneur, S. Cozic, and F. Prudenzano, 'Mid-infrared fused fiber optics: a fluoride coupler for 5000 nm applications', *J. Phys. Photonics*, vol. 7, no. 4, p. 045010, Oct. 2025, doi: 10.1088/2515-7647/adffd1.

[12] T. Erdogan, 'Fiber grating spectra', *J. Lightwave Technol.*, vol. 15, no. 8, pp. 1277–1294, Aug. 1997, doi: 10.1109/50.618322.

[13] T. Erdogan, 'Cladding-mode resonances in short- and long-period fiber grating filters', *J. Opt. Soc. Am. A*, vol. 14, no. 8, p. 1760, Aug. 1997, doi: 10.1364/JOSAA.14.001760.

[14] A. Annunziato, M. Godfrey, F. Anelli, J. Dulieu-Barton, C. Holmes, and F. Prudenzano, 'Flexible Photonic Sensors: Investigation of an Approach Based on Ratiometric Power in Few-Mode Waveguides for Bending Measurement', *IEEE Access*, vol. 12, pp. 29166–29174, 2024, doi: 10.1109/ACCESS.2024.3368885.

[15] L. She *et al.*, 'Mid-infrared fluoroindate glass long-period fiber grating by femtosecond laser inscription', *Infrared Physics & Technology*, vol. 116, p. 103808, Aug. 2021, doi: 10.1016/j.infrared.2021.103808.

[16] M. Heck, S. Nolte, A. Tünnermann, R. Vallée, and M. Bernier, 'Femtosecond-written long-period gratings in fluoride fibers', *Opt. Lett.*, vol. 43, no. 9, p. 1994, May 2018, doi: 10.1364/OL.43.001994.

[17] H. Lu, R. Adams, M. Saad, P. Orsini, R. Burga, and L. R. Chen, 'Mechanically induced long period gratings in ZBLAN fibers', in *2011 ICO International Conference on Information Photonics*, Ottawa, ON, Canada: IEEE, May 2011, pp. 1–2. doi: 10.1109/ICO-IP.2011.5953784.

[18] A. Theodosiou, Y. Baravets, and P. Peterka, 'Long period grating in ZBLAN fiber using the *pull-and-heat* method', *Opt. Lett.*, vol. 50, no. 18, p. 5678, Sep. 2025, doi: 10.1364/OL.571074.

[19] R. Y. N. Wong, E. Chehura, S. E. Staines, S. W. James, and R. P. Tatam, 'Fabrication of fiber optic long period gratings operating at the phase matching turning point using an ultraviolet laser', *Appl. Opt.*, vol. 53, no. 21, p. 4669, Jul. 2014, doi: 10.1364/AO.53.004669.

[20] Long Jin, Wei Jin, Jian Ju, and Yiping Wang, 'Coupled Local-Mode Theory for Strongly Modulated Long Period Gratings', *J. Lightwave Technol.*, vol. 28, no. 12, pp. 1745–1751, Jun. 2010, doi: 10.1109/JLT.2010.2049252.

[21] F. Anelli *et al.*, 'Mid-infrared interferometry with non-adiabatic tapered ZBLAN optical fiber', *Opt. Express*, vol. 32, no. 11, p. 18944, May 2024, doi: 10.1364/OE.521239.

Convex Optimization for Deep-Null Synthesis in SKA-Low Station Beamforming

G. Caruso[1,*], G. M. Battaglia[1], P. Bolli[2], M. G. Labate [3], A. F. Morabito[1]

[1]Università degli Studi Mediterranea di Reggio Calabria, Italy
[2]INAF - National Institute of Astrophysics, Arcetri Astrophysical Observatory, Italy
[3]INAF - National Institute of Astrophysics, Catania Astrophysical Observatory, Italy
*Corresponding author: g.caruso@unirc.it

***Abstract*—This contribution presents an initial investigation into the feasibility of generating deep nulls (DNs) within the receiving patterns of individual SKA-Low stations. The proposed approach employs a convex programming (CP)-based antenna synthesis algorithm tailored for pencil beam design. In addition to producing DNs, the method aims to achieve an overall reduction in sidelobe level, thereby enhancing the station's robustness against external interference. The study takes into account the real station layout, known as the Perturbed Vogel configuration, and includes the mutual coupling effects among array elements in a dense configuration case (75 MHz), thereby demonstrating the practical applicability of the proposed methodology under realistic conditions.**

***Keywords*— Array, Sparse array, Antenna Synthesis, Radio Astronomy, Radio telescope**

I. Introduction

The increasing need to investigate astrophysical phenomena such as fast radio bursts, gravitational waves, and the epoch of re-ionization has driven the development of advanced tools for cosmic signal analysis [1]. Within this context, the Square Kilometre Array (SKA) project was conceived. SKA-Obervatory will comprise two radio telescopes, SKA-Low and SKA-Mid, each dedicated to a specific frequency band of interest [2]. SKA-Low, under construction in the Murchison Shire (Australia), will provide unprecedented performance in terms of sensitivity, resolution, and survey speed within the 50–350 MHz frequency range. To achieve these objectives, the complete system will consist of 512 circular stations, each approximately 40 m in diameter and containing 256 antennas [3]. The preliminary design phase has been completed, and construction has commenced, with the deployments of stations equipped with SKALA 4.1 antennas [4], i.e., dual-polarized log-periodic element arranged according to the Perturbed Vogel (PV) configuration. This layout, derived from the randomization of a sunflower-like distribution [5]–[7], is illustrated in Fig. 1. The PV configuration mitigates the mutual coupling effects that previously caused 125 MHz scan blindness [7]; however, it also results in an increase in station sidelobes. Since the reception of cosmic signals from spatial regions outside the main beam introduces additional noise into the data [8], this issue must be addressed carefully. This is also particularly relevant given the increasing number of interfering radio signals (e.g., satellite constellations). To mitigate such effects,

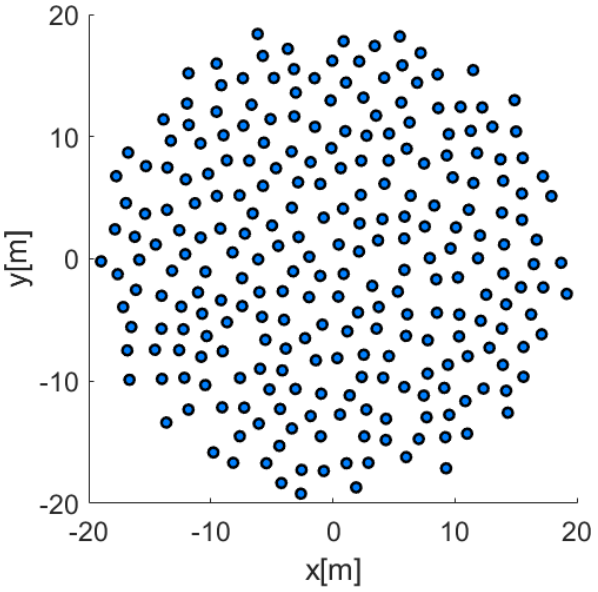

Fig. 1: Perturbed Vogel Layout.

a CP-based beamforming network (BFN) weight optimization framework has been developed and applied to an SKA-Low station under realistic condition [9], [10].
The presence of very strong sources radiating from regions of the sky outside the main beam may necessitates the generation of DNs in the receiving pattern to effectively isolate unwanted sources [13]. This work explores the extension of the methodology proposed in [9] and [10] to achieve a uniform sidelobe level distribution incorporating specific DNs within it.

II. Methods

The proposed methodology is based on the CP optimization of BFN weights to generate a properly shaped pencil beam in the SKA-Low station receiving patterns.
In order to achieve this objective, the mask-constrained power synthesis method described in [9] and [10], further supported by the array synthesis frameworks in [11] and [12], has been extended to the present study scenario, and a frequency, of 75 MHz, corresponding to the station's dense configuration regime (where element coupling effects are significant)

[11], has been chosen as an example of applicability of the proposed methodology.
The problem is described as follows:

Find $(\omega_1, ..., \omega_{256})$ *such that*

$$\max \ \Re\{E_{TOT}(\Omega_T)\} \tag{1}$$

subject to:

$$\Im\{E_{TOT}(\Omega_T)\} = 0 \tag{2}$$

$$|E_{TOT}(\phi,\theta)|^2 \leq UB(\phi,\theta), \ \forall(\phi,\theta) \in \Omega \tag{3}$$

where:

- $(\omega_1, ..., \omega_{256})$ represents the optimized weights set;
- Ω_T defines the target direction in the (ϕ, θ) plane;
- Ω is the region outside the target direction in the (ϕ, θ) plane;
- UB indicates the properly chosen upper bound defining the mask.

This optimization problem, which maximizes the square amplitude of the field in the target direction [14], is convex [15] in the form in which it is expressed; therefore, if a solution exists, it represents the best possible one [16], [17].
It is worth emphasizing that the proposed technique offers two key advantages: the capability to precisely shape the radiation pattern according to specific requirements, providing a high degree of control; and the applicability of the framework to realistic scenarios, where mutual coupling among elements is accounted for through the embedded element patterns (EEPs) of the station.

III. Results and Discussion

A preliminary analysis was carried out considering the station pattern generated using a set of constant and unitary weights. This configuration is referred to as the initial scenario. The embedded element pattern of each SKALA 4.1 antenna was simulated in FEKO , and, during data pre-processing, the EEP phases were adjusted to conform to the station geometry [18], considering the antenna itself as the origin of the reference system. Subsequently, the co-polar field component was extracted and employed for the CP optimization process [19]. The receiving pattern corresponding to the initial scenario, see Fig. 2(a), exhibits a circularly symmetric main beam, while the presence of secondary lobes defines an initial sidelobe level (SLL) of 16.8 dB.
The constraint in (3) enables complete control over the imposed mask. This property is exploited, as shown in Fig. 3, to obtain a receiving pattern in which the region Ω is subject to a uniform constraint equal to -3 dB relative to the first sidelobe level. Four DNs are positioned at an elevation of 45°, with azimuthal locations at ϕ =0°, 90°, 180°, and 270°. Each null spans 15° in both azimuth and elevation, reaching a minimum of –10 dB. The positions of these DNs were selected to emulate interfering sources acting within those specific spatial regions. Both the spatial configuration and the mask values are arbitrary and can be adjusted according to the characteristics or requirements of the interfering sources.
The resulting optimized pattern is shown in Fig. 2(b) and in Fig. 4. Energy redistribution within the (ϕ, θ) plane leads to an SLL increase of 7.9 dB compared to the initial scenario, while the DNs successfully achieve the targeted –10 dB level. The main lobe amplitude increases from 45.28 dB to 50.18 dB, with no significant change in half-power beamwidth.
This energy redistribution causes the secondary lobes to rise until they become tangent to the imposed mask across the entire pattern (Fig. 2). Consequently, the directivity in the optimized case slightly decreases compared to the uniform and unitary excitation case, with a reduction of approximately 1.5 dBi. Nonetheless, all sidelobes remain below the imposed mask, maintaining a clear separation from the main lobe peak. These results demonstrate the practical applicability of the CP-based optimization framework for effective deep-null formation in SKA-Low station beam synthesis.

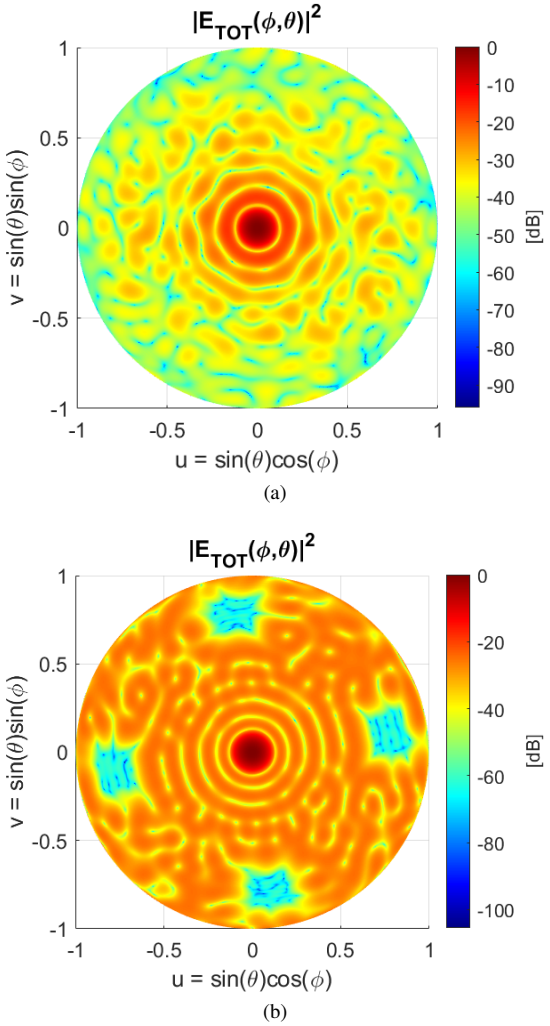

Fig. 2: Synthesized receiving station pattern (normalized to the maximum) in the (u,v) plane generated by: (a) uniform and unitary weights, and (b) the optimized weight set.

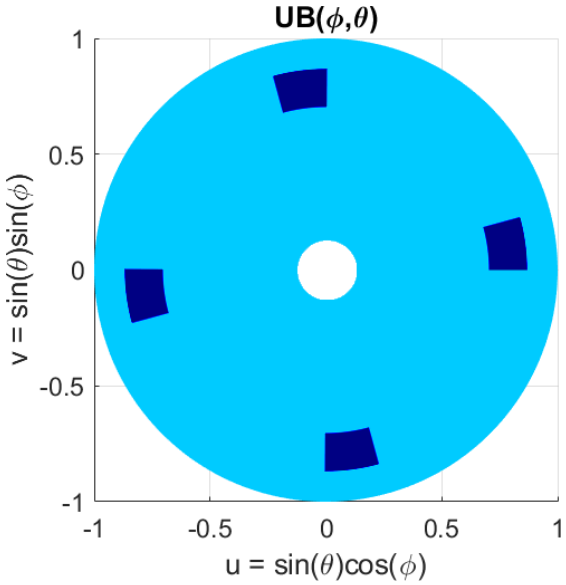

Fig. 3: Adopted mask (Upper Bound) in the (u,v) plane, where the dark blue rectangles represent the DNs at -10 dB.

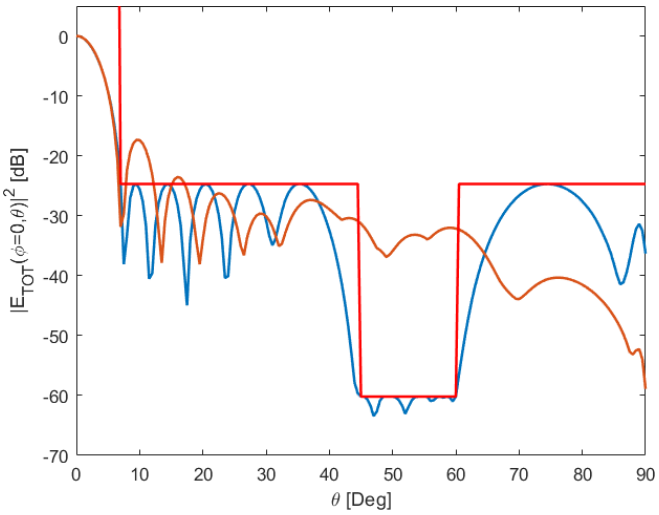

Fig. 4: Superposition of synthetized receiving pattern in the (ϕ, θ) plane generated by: uniform and unitary weight set (orange curve), the optimized weight set (blue curve) and imposed mask (red line) in $\phi = 0$.

IV. Conclusion

The application of the proposed methodology demonstrates the ability to generate deep nulls (DNs) at desired angular positions and desired level while simultaneously achieving a significant increase in sidelobe level (SLL) control within a realistic SKA-Low station scenario. The minor reduction in directivity, resulting from the redistribution of power within the receiving pattern, represents an acceptable trade-off considering the substantial improvement in SLL performance and the absence of any notable variation in half-power beamwidth.

Future work will focus on extending this study to the other operational frequency bands of the SKA-Low station. Additional investigations will explore the use of alternative DN shapes, as well as constraints on the dynamic range of the excitation weights, to further enhance robustness and adaptability of the beam synthesis process under realistic operating conditions.

Acknowledgments

The authors gratefully acknowledge ICRAR-Curtin, Australia, where the EEPs dataset used in this study was computed.

This work was funded in part by the Next Generation EUItalian NRRP, Mission 4, Component 2, Investment 1.5, call for the creation and strengthening of 'Innovation Ecosystems', building 'Territorial R&D Leaders' (Directorial Decree n. 2021/3277) - project Tech4You - Technologies for climate change adaptation and quality of life improvement, n. ECS0000009, and in part by the European Union under the Italian National Recovery and Resilience Plan (NRRP) of NextGenerationEU, partnership on "Telecommunications of the Future" (PE00000001 - program "RESTART").

References

[1] R. Braun, T. L. Bourke, J. A. Green, E. Keane, and J. Wagg, Advancing Astrophysics with the Square Kilometre Array, in *Advancing Astrophysics with the Square Kilometre Array*, vol. 215, p. 174, 2015, Sissa Medialab.

[2] M. G. Labate, J. Wagg, B. Alachkar, S. Breen, G. Swart, and A. van Es, The most sensitive radio telescope to deliver unprecedented and global open science: The Square Kilometer Array (50 MHz–15.3 GHz), in *Proc. 15th European Conf. on Antennas and Propagation (EUCAP)*, 2021, pp. 1–5, IEEE.

[3] M. G. Labate, P. Dewdney, R. Braun, M. Waterson, and J. Wagg, The SKA Low-Frequency Telescope: Performance Parameters and Constraints on the Array Configuration, in *Proc. 2017 11th European Conf. on Antennas and Propagation (EUCAP)*, pp. 2259–2263, 2017.

[4] P. Bolli, L. Mezzadrelli, J. Monari, F. Perini, A. Tibaldi, G. Virone, M. Bercigli, L. Ciorba, P. Di Ninni, M. G. Labate, V. G. Loi, A. Mattana, F. Paonessa, S. Rusticelli, and M. Schiaffino, Test-Driven Design of an Active Dual-Polarized Log-Periodic Antenna for the Square Kilometre Array, *IEEE Open Journal of Antennas and Propagation*, vol. 1, pp. 253–263, 2020.

[5] P. Bolli, D. B. Davidson, R. Braun, P. Di Ninni, and D. Ung, Evaluating an Alternate Layout for the SKA-Low Aperture Array Stations Using Computational Electromagnetic Simulations, in *Proc. 2022 Int. Conf. on Electromagnetics in Advanced Applications (ICEAA)*, pp. 200–205, 2022.

[6] D. B. Davidson, R. B. Wyath, and D. Ung, Evaluation of Alternative SKA-Low Station Layouts, in *Proc. XXXVth General Assembly and Scientific Symposium of the International Union of Radio Science (URSI GASS)*, Sapporo, Japan, 19–26 August 2023, pp. 1–4.

[7] D. Anstey, J. Cumner, Q. Gueuning, O. O'Hara, E. De Lera Acedo, and A. Brown, Mitigating Zenith Blindness from Mutual Coupling in a Sunflower Phased Array, in *Proc. 18th European Conf. on Antennas and Propagation (EuCAP)*, Glasgow, UK, 17–22 March 2024, pp. 1–5.

[8] B. Mort, F. Dulwich, N. Razavi-Ghods, E. de Lera Acedo, and K. Grainge, Analysing the Impact of Far-Out Side-Lobes on the Imaging Performance of the SKA-LOW Telescope, *Monthly Notices of the Royal Astronomical Society*, pp. stw2814, 2016, Oxford University Press.

[9] G. M. Battaglia, G. Caruso, P. Bolli, R. Palmeri, and A. F. Morabito, Square Kilometre Array Enhancement: A Convex Programming Approach to Optimize SKA-Low Stations in the Case of Perturbed Vogel Layout, *Sensors*, vol. 25, no. 16, p. 5039, 2025, MDPI.

[10] G. M. Battaglia, G. Caruso, P. Bolli, M. G. Labate, R. Palmeri, and A. F. Morabito, Low-Frequency Square Kilometer Array Pattern Optimization via Convex Programming, *Applied Sciences*, vol. 15, no. 11, p. 5929, 2025, MDPI.

[11] G. M. Battaglia, T. Isernia, R. Palmeri, M. A. Maisto, R. Solimene, and A. F. Morabito, Near-Field Synthesis of 1-D Shaped Patterns Through Spectral Factorization and Minimally-Redundant Array-Like Representations, in *IEEE Transactions on Antennas and Propagation*, vol. 73, no. 5, pp. 2713–2724, May 2025, doi:10.1109/TAP.2024.3525137.

[12] G. M. Battaglia, T. Isernia, R. Palmeri, and A. F. Morabito, Four-beams-reconfigurable circular-ring array antennas for monopulse radar applications, in *Radio Science*, vol. 58, no. 9, pp. 1–14, Sept. 2023, doi:10.1029/2023RS007776.

[13] G. Peng, L. Jiang, X. Tao, Y. Zhang, and R. Cao, A Real-Time Adaptive Station Beamforming Strategy for Next Generation Phased Array Radio Telescopes, *Sensors (Basel, Switzerland)*, vol. 24, no. 14, p. 4723, 2024.

[14] T. Isernia and G. Panariello, Optimal Focusing of Scalar Fields Subject to Arbitrary Upper Bounds, *Electronics Letters*, vol. 34, no. 2, pp. 162–164, 1998, IET Digital Library.

[15] S. Boyd and L. Vandenberghe, *Convex Optimization*, Cambridge University Press, 2003.

[16] G. M. Battaglia, A. F. Morabito, G. Sorbello, and T. Isernia, Mask-constrained power synthesis of large and arbitrary arraysas a few-samples global optimization, *Progress In Electromagnetics Research C*, vol. 98, pp. 69-81, 2020, doi:10.2528/PIERC19082904.

[17] G. M. Battaglia, G. G. Bellizzi, A. F. Morabito, G. Sorbello, and T. Isernia, A general effective approach to the synthesis of shaped beams for arbitrary fixed-geometry arrays, *Journal of Electromagnetic Waves and Applications*, vol. 33, no. 18, pp. 2404-2422, 2019.

[18] C. A. Balanis, *Antenna Theory: Analysis and Design*, John Wiley & Sons Inc., 2016.

[19] A. Ludwig, The Definition of Cross Polarization, *IEEE Transactions on Antennas and Propagation*, vol. 21, no. 1, pp. 116–119, 1973. doi: 10.1109/TAP.1973.1140406

Scalar Potentials of Solutions to the Vibrotransport Maxwell's Equations

Lyudmila Alexeyeva[1], Ilmira Kanymgaziyeva[1,2,*]

[1]Institute of Mechanics and Engineering named after U.A. Dzholdasbekov, Almaty, Kazakhstan
[2]Department of Radio Engineering, Electronics and Telecommunications, L.N. Gumilyov Eurasian National University, Astana, Kazakhstan
*Corresponding author: : kanymgazy1@gmail.com

***Abstract*—Provide a concise summary of your work in This work uses vibrotransport solutions of Maxwell's equations to research the electromagnetic fields of electromagnetic wave emitters of various wavelengths (frequencies) located on moving platforms. Vibrotransport solutions of these equations are constructed using scalar potentials, which are vibrotransport solutions of the wave equation.**

***Keywords*– Makh number; Maxwell's equations; Fourier transform; Vibroransport solutions.**

I. Introduction

This article examines the system of Maxwell's equations that describes electromagnetic fields and currents in continuous media. Using the Fourier transform of generalized functions, fundamental and generalized solutions of Maxwell's vibration transport equations for moving alternating currents at sublight velocities of their carriers are obtained. Analytical formulas are obtained for calculating the electromagnetic field strengths both in image space and their originals. Unlike transport solutions of these equations [1]-3, here the wave frequency (length) of the emitter of EM waves is taken into account, and not just the speed of its movement.

II. Methods

The system of Maxwell's equations is considered [1]:

$$\begin{gathered} \mathrm{rot}\mathbf{E}(\mathbf{x},t)+\mu\frac{\partial \mathbf{H}(\mathbf{x},t)}{\partial t}=0, \\ \mathrm{rot}\mathbf{H}(\mathbf{x},t)-\varepsilon\frac{\partial \mathbf{E}(\mathbf{x},t)}{\partial t}=\mathbf{j}^e(\mathbf{x},t), \\ \mu\mathrm{div}\mathbf{H}(\mathbf{x},t)=0,\quad \varepsilon\mathrm{div}\mathbf{E}(\mathbf{x},t)=p^e. \end{gathered} \tag{1}$$

Here p^e is the volumetric charge density.

Solutions (1) are constructed when the right-hand side has the form:

$$\mathbf{j}^e(\mathbf{x},t)=\mathbf{J}^e(x_1,x_2,x_3-Vt)e^{i\omega t} \tag{2}$$

Here $\mathbf{j}^e(\mathbf{x},t)$ describes an emitter of EM waves of frequency w, which moves at a constant speed V in the direction of the x_3 axis.

The Fourier transform of basis functions $\bar{f}_0(\mathbf{k}), \bar{f}_1(\mathbf{k})$ in image space is equal to:

$$\bar{f}_0(\mathbf{k})=\frac{1}{k_1^2+k_2^2+m^2k_3^2-2Mwk_3-w^2}, \tag{3}$$

$$\bar{f}_1(\mathbf{k})=\frac{\bar{f}_0(\mathbf{k})}{k_3V+\omega}=\frac{\bar{f}_0(\mathbf{k})}{Mc\left(k_3+\frac{w}{M}\right)}. \tag{4}$$

It is required to find the electric $\mathbf{E}(\mathbf{x},t)$ and magnetic $\mathbf{H}(\mathbf{x},t)$ strengths EM fields at sublight speeds: $V<c$.

To solve the problem, a moving coordinate system was introduced $(\mathbf{x},z)$: x=(x_1,x_2), $z=x_3-Vt$ and Makh number $M=Vc^{-1}$, $c=(\sqrt{\varepsilon\mu})^{-1}$ is the light speed in EM medium. The subluminal case is considered: $M<1$.

The solution is constructed in a moving coordinate system using the Fourier transform $\mathbf{E}(\mathbf{x},t)$, $\mathbf{H}(\mathbf{x},t)$ of generalized functions. When constructing Fourier transforms, computer software Mathcad-15 for symbolic calculus was used.

The original solutions were constructed using scalar potentials:

$$f_0(x,z)=\frac{\exp(-iwm^{-2}Mz)}{4\pi\sqrt{z^2+m^2r^2}}\exp\left(\frac{iw}{m^2}\sqrt{z^2+m^2r^2}\right), \tag{5}$$

$$f_1(x,z)=\frac{i}{2Mc}sgn(z)\exp(iwz/M)\delta(x)*_z f_0(x,z). \tag{6}$$

Here $r^2=\sqrt{x_1^2+x_2^2}$, $w=\omega c^{-1}$, m=$\sqrt{1-M^2}$, sign $*_z$ means convolution along z.

Figures 1 and 2 show the actual part of the functions $Re(\Psi_0(x,z))=f_0(x,z)\exp(i\omega t)$ and $Re(\Psi_1(x,z))=f_1(x,z)\exp(i\omega t)$.

III. Results and Discussion

It is clear from the figures that the amplitudes of electromagnetic waves differ at the same Makh numbers and oscillation frequencies. In the second figure, the oscillation frequencies of electromagnetic waves have been changed.

To construct the originals, scalar potentials were used, which are vibrotransport solutions of the classical wave equation.

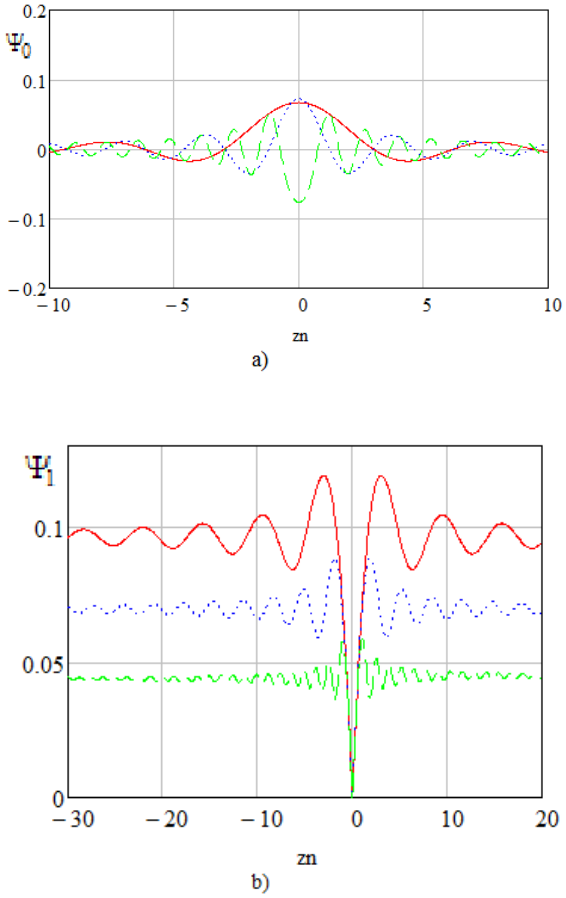

Fig. 1. Graph of basis functions a) $Re(\Psi_1(x,z))$ and b) $Re(\Psi_1(x,z))$ versus Makh numbers and frequencies. $x = (1,0); z = zn; M = 10^{-4}, 10^{-3}, 10^{-2}; \omega = 1, 2, 5.$

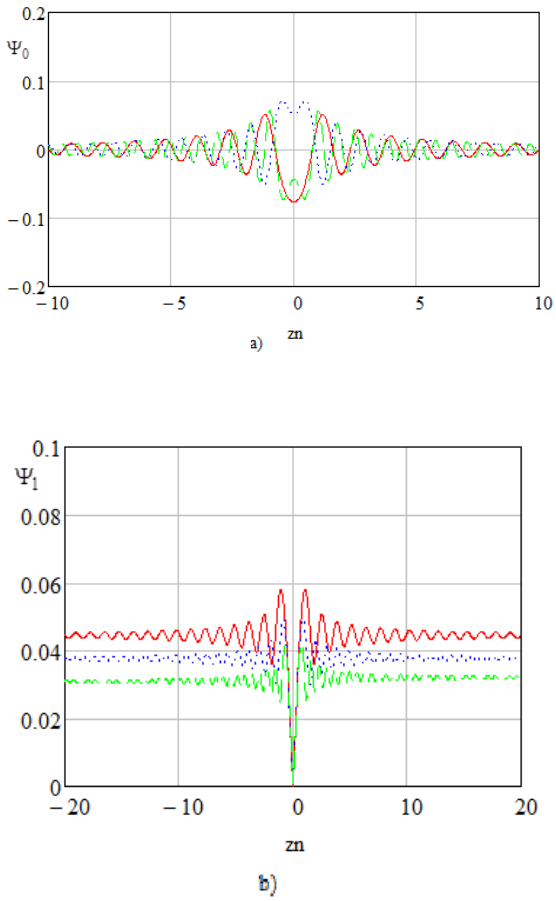

Fig. 2. Graph of basis functions a) $Re(\Psi_1(x,z))$ and b) $Re(\Psi_1(x,z))$ versus Makh numbers and frequencies. $x = (1,0); z = zn; M = 10^{-4}, 10^{-3}, 10^{-2}; \omega = 5, 7, 10.$

IV. Conclusion

A computer implementation of the constructed solutions was carried out, which shows the influence of vibration frequency and movement speed on the wave characteristics of the EM field. The constructed solutions can be used in calculations of electromagnetic wave processes in the range of sub-light velocities of EM wave radiation sources.

Acknowledgments

The work was carried out with the financial support of the Science Committee of the Ministry of Science and Higher Education of the Republic of Kazakhstan (Grant AP23488145, 2024–2026).

References

[1] L. A. Alexeyeva and I. A. Kanymgazieva, 'Maxwell's Transport Equtions, Their Fundamental and Generalized Solutions at Constant Speed of Moving Emitters," *Technical Physics*, vol. 69, Issue 4. pp. 507-515, 2024.

[2] L. A. Alexeyeva and I. A. Kanymgazieva, 'Fundamental and Regular Transport Solutions of Maxwell's Equations and Their Properties at Superluminal Speeds: Shock Electromagnetic Waves." *Technical Physics*, vol. 69, Issue 11. pp. 1635-1642, 2024.

[3] L. A. Alexeyeva and I. A. Kanymgazieva, 'Fundamental and Generalized Solutions of Maxwell's Equations at Moving Emitters of Electromagnetic Waves," *Photonics and Electromagnetics Research Symposium-Spring. IEEE Xplore*, 2025.

Antennas, Metasurfaces and Electromagnetic Devices

Photonic space-time metamaterials: mimicking isotropic-to-anisotropic time interfaces

Andrew M. Naylor[1] and Victor Pacheco-Peña[1*]

[1]School of Mathematics, Statistics and Physics, Newcastle University, Newcastle Upon Tyne, NE1 7RU, UK

*Corresponding author: victor.pachecopena@gmail.com

***Abstract*— Time interfaces are an example of how four-dimensional media can be used to enable full wave manipulation. Here, we show how spacetime media can be used to mimic isotropic-to-anisotropic time interfaces. Theoretical analysis accompanied by numerical results will be presented at the conference.**

***Keywords*— metamaterials, spacetime, time interfaces, effective medium.**

I. Introduction

Progress in metamaterials research and innovation have enabled the exploration of interesting physical phenomena, giving rise to the improvement of groundbreaking technologies including metatronics[1-3], sensing[4-6] and antennas[7-9], to name a few[10-17]. Manipulating wave propagation in space is central in this context[18]. Time-varying media have recently experienced growing interest, as they can allow the manipulation of waves in both space and time (*x,y,z,t*)[19-22]. An example of a mechanism that can enable wave manipulation in four dimensions is the time interface.

Photonic time interfaces [23] are the result of rapid changes of the optical properties of a material [i.e. the permittivity (ε) and/or permeability (μ)] where a wave propagates between an initial and a final value. As a result, a transmitted forward wave (FW) and a reflected backwards wave (BW) are generated, like those that occur due to a spatial interface[24]. The application space of photonic time interfaces is vast [25-40], with experimental demonstrations also being reported by the scientific community [41-43]. Time interfaces have been explored in multiple scenarios such as microwaves[42,44], water waves[45] and optics[41,46], demonstrating their applicability across different technologies.

Recent studies on isotropic-to-anisotropic photonic interfaces have also revealed interesting phenomena [47-50]. In this context, it has been shown that when the permittivity of the medium is rapidly changed from isotropic to a tensor in time, the direction of the Poynting vector is modified[49,50].

Here we discuss our recent and ongoing efforts to explore the possibility of emulating isotropic-to-anisotropic time interfaces using isotropic space-time modulations. This is done by applying time interfaces to discrete spatial regions in order to induce spatially subwavelength multilayers. A full theoretical/numerical analysis will be presented during the conference[51].

II. Discussion

First, let us consider the case shown in Figure 1a where a *p*-polarized monochromatic signal exists in an unbounded isotropic medium. The permittivity of this medium is ε_{r1} for $t < t_0$. While propagation angle does not necessarily have a meaning in an unbounded medium, here, we will consider that, on the *xz* plane, the incidence angle is θ_1, with the wavenumber $\boldsymbol{k}$ parallel to the Poynting vector $\boldsymbol{S}$, such that $\theta_1 = \theta_{1\boldsymbol{k}} = \theta_{1\boldsymbol{S}}$. An isotropic-to-anisotropic time interface is then applied to the whole medium, resulting in the case shown in Figure 1b. As explained in [49], the direction of the Poynting vector is changed for $t > t_0$, such that, $\theta_1 = \theta_{2\boldsymbol{k}} \neq \theta_{2\boldsymbol{S}}$.

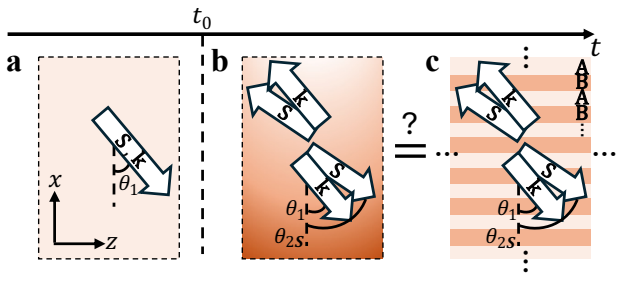

Fig. 1 Schematic of **a.** an incident signal propagating within an isotropic (ε_{r1}) unbounded medium at an angle, θ_1 for $t < t_0$. **b.** Resulting signals for $t > t_0$ (after the permittivity is rapidly changed to a tensor $\overline{\overline{\varepsilon_{r2}}}$). The direction of $\boldsymbol{k}$ and $\boldsymbol{S}$ are no longer parallel, $\theta_1 = \theta_{2\boldsymbol{k}} \neq \theta_{2\boldsymbol{S}}$. **c.** Resulting signals for $t > t_0$ when multiple isotropic spatially subwavelength layers are induced in time with layers A and B defined as $\varepsilon_{rA} = \varepsilon_{r1}$ and $\varepsilon_{rB} \neq \varepsilon_{r1}$, respectively.

To mimic this behavior (i.e., to mimic *temporal aiming*), here we propose the scenario shown in Figure 1c. In this case, at $t = t_0$, multiple isotropic-to-isotropic time interfaces are applied to different spatial regions, resulting in a spatially subwavelength multilayer structure being induced in time.

The spacetime structure shown in Figure 1c has previously been studied at normal incidence[28] where it was demonstrated that the structure has an effective relative permittivity dependent on the direction of the incident signal, such that, $\varepsilon_{reff,x} \neq \varepsilon_{reff,z}$. If we now consider a signal at oblique incidence, can a space-time structure, such as the one shown in Figure 1c, be described by an effective anisotropic tensor? If this is the case, can it be used to mimic the behavior that occurs at isotropic-to-anisotropic time interfaces? In the conference it will be shown that, indeed, this is the case. Multiple space-time configurations will be presented including horizontal and vertical layers created in time via time interfaces, as well as the effect of the spatial filling fraction on the direction of the Poynting vector. All the results will be supported by numerical simulations.

III. Conclusion

In summary, we have discussed a technique to emulate photonic temporal anisotropy through a space-time configuration. The proposed framework uses multiple isotropic-to-isotropic time interfaces to create, at the same time, discrete spatially subwavelength layers. During the conference, we will present a full theoretical and numerical analysis, detailing multiple space-time configurations, including horizontally aligned spatial layers and vertically aligned spatial layers.

Acknowledgments

This work was supported by the Leverhulme Trust under the Leverhulme Trust Research Project Grant scheme (No. RPG-2023-024).

References

[1] Y. Li, I. Liberal, C. Della Giovampaola, and N. Engheta, "Waveguide metatronics: Lumped circuitry based on structural dispersion," *Science Advances*, vol. 2, 2016.

[2] R. G. MacDonald, A. Yakovlev, and V. Pacheco-Peña, "Solving partial differential equations with waveguide-based metatronic networks," *Advanced Photonics Nexus*, vol. 3, 2024.

[3] M. Miscuglio *et al.*, "Approximate analog computing with metatronic circuits," *Communications Physics*, vol. 4, 2021.

[4] V. Pacheco-Peña, M. Beruete, P. Rodríguez-Ulibarri, and N. Engheta, "On the performance of an ENZ-based sensor using transmission line theory and effective medium approach," *New Journal of Physics*, vol. 21, p. 043056, 2019.

[5] M. Huang, J. Yang, and A. Petrin, "Microwave sensor using metamaterials," *Wave propagation*, vol. 13, p. 36, 2011.

[6] H. de Souza Oliveira *et al.*, "Mechanical metamaterial sensors: from design to applications," *Journal of Physics D: Applied Physics*, vol. 58, p. 133002, 2025.

[7] V. Pacheco-Peña *et al.*, "Mechanical 144 GHz beam steering with all-metallic epsilon-near-zero lens antenna," *Applied Physics Letters*, vol. 105, 2014.

[8] G. Minatti *et al.*, "Modulated Metasurface Antennas for Space: Synthesis, Analysis and Realizations," *IEEE Transactions on Antennas and Propagation*, vol. 63, pp. 1288–1300, 2015.

[9] B. A. F. Esmail, S. Koziel, L. Golunski, H. B. A. Majid, and R. K. Barik, "Overview of Metamaterials-Integrated Antennas for Beam Manipulation Applications: The Two Decades of Progress," *IEEE Access*, vol. 10, pp. 67096–67116, 2022.

[10] S. Hrabar, J. Bartolic, and Z. Sipus, "Waveguide miniaturization using uniaxial negative permeability metamaterial," *IEEE Transactions on Antennas and Propagation*, vol. 53, pp. 110–119, 2005.

[11] T. Nakanishi, T. Otani, Y. Tamayama, and M. Kitano, "Storage of electromagnetic waves in a metamaterial that mimics electromagnetically induced transparency," *Physical Review B*, vol. 87, p. 161110, 2013.

[12] R. Maas, J. Parsons, N. Engheta, and A. Polman, "Experimental realization of an epsilon-near-zero metamaterial at visible wavelengths," *Nature Photonics*, vol. 7, pp. 907–912, 2013.

[13] E. Almeida, O. Bitton, and Y. Prior, "Nonlinear metamaterials for holography," *Nature Communications*, vol. 7, p. 12533, 2016.

[14] M. Koivurova, T. Hakala, J. Turunen, A. T. Friberg, M. Ornigotti, and H. Caglayan, "Metamaterials designed for enhanced ENZ properties," *New Journal of Physics*, vol. 22, p. 093054, 2020.

[15] F. Zangeneh-Nejad, D. L. Sounas, A. Alù, and R. Fleury, "Analogue computing with metamaterials," *Nature Reviews Materials*, vol. 6, pp. 207–225, 2020.

[16] C. Johnson-Richards, A. Yakovlev, and V. Pacheco-Peña, "Topological Valley Photonic Waveguides: Scattering matrix evaluation for linear computing," *arXiv preprint arXiv:2412.02388*, 2024.

[17] W. Rogers, C. Johnson-Richards, A. Yakovlev, and V. Pacheco-Peña, "Perfect splitting in rectangular-waveguide junctions for analog computing," *Physical Review Applied*, vol. 21, p. 054054, 2024.

[18] N. Engheta and R. W. Ziolkowski, *Metamaterials*. Wiley, 2006.

[19] E. Galiffi *et al.*, "Photonics of time-varying media," *Advanced Photonics*, vol. 4, 2022.

[20] N. Engheta, "Metamaterials with high degrees of freedom: space, time, and more," *Nanophotonics*, vol. 10, pp. 639–642, 2020.

[21] C. Caloz and Z.-L. Deck-Leger, "Spacetime Metamaterials—Part I: General Concepts," *IEEE Transactions on Antennas and Propagation*, vol. 68, pp. 1569–1582, 2020.

[22] C. Caloz and Z.-L. Deck-Leger, "Spacetime Metamaterials—Part II: Theory and Applications," *IEEE Transactions on Antennas and Propagation*, vol. 68, pp. 1583–1598, 2020.

[23] F. R. Morgenthaler, "Velocity Modulation of Electromagnetic Waves," *IEEE Transactions on Microwave Theory and Techniques*, vol. 6, pp. 167–172, 1958.

[24] D. M. . Pozar, *Microwave engineering*. John Wiley & Sons Incorporated, 2013.

[25] D. Ramaccia, A. Alù, A. Toscano, and F. Bilotti, "Temporal multilayer structures for designing higher-order transfer functions using time-varying metamaterials," *Applied Physics Letters*, vol. 118, 2021.

[26] G. Castaldi, V. Pacheco-Peña, M. Moccia, N. Engheta, and V. Galdi, "Exploiting space-time duality in the synthesis of impedance transformers via temporal metamaterials," *Nanophotonics*, vol. 10, pp. 3687–3699, 2021.

[27] V. Pacheco-Peña and N. Engheta, "Effective medium concept in temporal metamaterials," *Nanophotonics*, vol. 9, pp. 379–391, 2020.

[28] V. Pacheco-Peña and N. Engheta, "Merging Effective Medium Concepts of Spatial and Temporal Media: Opening new avenues for manipulating wave-matter interaction in 4D," *IEEE Antennas and Propagation Magazine*, vol. 65, pp. 39–49, 2023.

[29] P. A. Huidobro, M. G. Silveirinha, E. Galiffi, and J. B. Pendry, "Homogenization Theory of Space-Time Metamaterials," *Physical Review Applied*, vol. 16, p. 014044, 2021.

[30] J. T. Mendonça, A. M. Martins, and A. Guerreiro, "Temporal beam splitter and temporal interference," *Physical Review A*, vol. 68, p. 043801, 2003.

[31] I. Liberal, J. E. Vázquez-Lozano, and V. Pacheco-Peña, "Quantum Antireflection Temporal Coatings: Quantum State Frequency Shifting and Inhibited Thermal Noise Amplification," *Laser & Photonics Reviews*, vol. 17, 2023.

[32] J. E. Vázquez-Lozano and I. Liberal, "Shaping the quantum vacuum with anisotropic temporal boundaries," *Nanophotonics*, vol. 12, pp. 539–548, 2023.
[33] J. E. Sustaeta-Osuna, F. J. García-Vidal, and P. A. Huidobro, "Quantum Theory of Photon Pair Creation in Photonic Time Crystals," *ACS Photonics*, vol. 12, pp. 1873–1880, 2025.
[34] V. Pacheco-Peña, M. Fink, and N. Engheta, "Temporal chirp, temporal lensing, and temporal routing via space-time interfaces," *Physical Review B*, vol. 111, p. L100306, 2025.
[35] V. Pacheco-Peña and N. Engheta, "Antireflection temporal coatings," *Optica*, vol. 7, p. 323, 2020.
[36] S. Yin and A. Alù, "Efficient Phase Conjugation in a Space-Time Leaky Waveguide," *ACS Photonics*, vol. 9, pp. 979–984, 2022.
[37] C. Rizza, G. Castaldi, and V. Galdi, "Short-Pulsed Metamaterials," *Physical Review Letters*, vol. 128, p. 257402, 2022.
[38] M. Antyufeyeva and V. Pacheco-Peña, "Emulating time refraction at photonic time interfaces via smooth temporal transitions," *Physical Review Applied*, vol. 24, p. 034004, 2025.
[39] A. Shlivinski and Y. Hadad, "Universal transient radiation dynamics by abrupt and soft temporal transitions in optical waveguides," *Nanophotonics*, vol. 14, pp. 785–793, 2025.
[40] M. J. Mencagli, D. L. Sounas, M. Fink, and N. Engheta, "Static-to-dynamic field conversion with time-varying media," *Physical Review B*, vol. 105, p. 144301, 2022.
[41] R. Tirole *et al.*, "Double-slit time diffraction at optical frequencies," *Nature Physics*, vol. 19, pp. 999–1002, 2023.
[42] H. Moussa, G. Xu, S. Yin, E. Galiffi, Y. Ra'di, and A. Alù, "Observation of temporal reflection and broadband frequency translation at photonic time interfaces," *Nature Physics*, vol. 19, pp. 863–868, 2023.
[43] J. Bohn, T. S. Luk, S. Horsley, and E. Hendry, "Spatiotemporal refraction of light in an epsilon-near-zero indium tin oxide layer: frequency shifting effects arising from interfaces," *Optica*, vol. 8, p. 1532, 2021.
[44] T. R. Jones, A. V. Kildishev, M. Segev, and D. Peroulis, "Time-reflection of microwaves by a fast optically-controlled time-boundary," *Nature Communications*, vol. 15, p. 6786, 2024.
[45] M. Koukouraki, P. Petitjeans, A. Maurel, and V. Pagneux, "Characterization of temporal aiming for water waves with an anisotropic metabathymetry," *Physical Review B*, vol. 112, p. 214301, 2025.
[46] E. Galiffi, A. C. Harwood, S. Vezzoli, R. Tirole, A. Alù, and R. Sapienza, "Optical coherent perfect absorption and amplification in a time-varying medium," *Nature Photonics*, 2026.
[47] G. Ptitcyn, D. M. Solís, M. S. Mirmoosa, and N. Engheta, "Temporal interface in dispersive hyperbolic media," *Nanophotonics*, 2025.
[48] G. Ptitcyn and N. Engheta, "Temporal twistronics," *arXiv preprint arXiv:2403.10477*, 2024.
[49] V. Pacheco-Peña and N. Engheta, "Temporal aiming," *Light: Science and Applications*, vol. 9, 2020.
[50] V. Pacheco-Peña and N. Engheta, "Temporal equivalent of the Brewster angle," *Physical Review B*, vol. 104, 2021.
[51] A. M. Naylor and V. Pacheco-Peña, "Anisotropic photonic time interfaces via isotropic spacetime modulations," *in preparation*, 2026.

Calculating the solution of partial differential equations using photonics analog processors

Ross G. MacDonald[1], Victor Pacheco-Peña[1,*]

[1]School of Mathematics, Statistics and Physics, Newcastle University, Newcastle Upon Tyne, NE1 7RU, United Kingdom

*Corresponding author: victor.pachecopena@gmail.com

***Abstract*— Grid-like networks of dielectric waveguides are used to emulate a finite-difference representation of the Helmholtz equation. For this, simple wave splitters and Bragg gratings are implemented within the network. A full theoretical analysis of the proposed structure will be presented including a discussion regarding the impact of non-ideal components. Numerical results of the proposed structure will also be presented demonstrating the capability of solving Dirichlet boundary value problems.**

***Keywords*— analog computing, optical computing**

I. Introduction

The ability to produce fast, accurate and energy efficient solutions to partial differential equations (PDE) is important if many fields within science and engineering [1-3]. Using hardware-based structures, it is known that solutions to PDEs may be calculated by implementing analog networks of electrical lumped elements designed to mimic the behavior of a finite difference mesh [4, 5].

In the realm of computing, continued scaling of traditional semiconductor-based digital technology has become increasingly challenging as devices approach atomic scales [6-8]. This has led some research to investigate alternative computing paradigms as a way of circumventing these challenges. One such paradigm is photonic analog computing [9, 10] which harnesses the potential advantages of light [11-14]. This has become increasingly interesting as advances in technologies such as metamaterials and metasurfaces [9, 10, 15, 16], among others [17-24], enable arbitrary control over light propagation in both space and time [25-31]. Analog processors have been proposed and demonstrated to perform operations such as differentiation (spatial [17, 18, 21, 32, 33] and temporal [19, 22-24]), vector-matrix multiplication [34] and PDE solving [11, 35-37], to name a few.

Within the context of PDE solving, methods of emulating finite different mesh behavior have also been proposed at higher frequencies. For instance, by exploiting photonic integrated circuits [11, 35] and epsilon-near-zero media [36] in the optical regime to solve the Poison equation or metatronic circuit [37] in the microwave regime. In this study, we propose and discuss a method of calculating solutions to the Helmholtz equation at telecommunications wavelengths ($\lambda = 1.55\ \mu m$). This is done by using arrays of simple dielectric wave splitters and Bragg gratings [38]. During the conference, the design process of the PDE solving network will be described in detail and a complete theoretical analysis of the structure will be presented. Numerical simulation results of these structures solving Dirichlet boundary value problems will also be presented, demonstrating the validity of the calculated solutions.

II. Methods

In line with the approaches outlined in the introduction [35-37], the proposed PDE solving network is designed to emulate the performance of a numerical finite difference mesh [35-37]. To enable this operation, two components are designed. The first is a dielectric wave splitter which controls the scattering of signals throughout the network. Specifically, we design this splitter to divide an incident signal equally amongst four connected waveguides [39-41] as a fundamental requirement of the PDE solving technique [37, 38]. When considering the analogy with the finite difference method, these wave splitters (hereby referred to as junctions) also serve as the sampling points from which the PDE solution is extracted. The second component is a semi-reflective mirror, implemented via a Bragg grating. These gratings are placed between junctions to control the coupling between them, enabling an at will control of the parameters of the PDE to be solved. To form the network, the wave splitters and Bragg gratings are connected in a grid-like array which resembles a regular quadrilateral mesh

The unit cell of this network is presented in Fig. 1a. As it can be seen, the wave splitters are formed by connecting four dielectric waveguides to a hollowed dielectric cylinder with an inner and outer radius r_i and r_o, respectively. They are optimized to achieve equal power splitting towards each connected waveguide by minimizing the following objective function:

$$obj^2 = \sum_{a\in A} (|S_{a1}| - x)^2 \quad (1a)$$

$$x = (|S_{11}| + |S_{21}| + |S_{31}| + |S_{41}|)/4 \quad (1b)$$

where S_{ab} is the scattering coefficient between ports a and b and $A = \{1,2,3,4\}$ is the set containing the 4 input ports. As the splitter is rotationally symmetric, minimizing Eq. 1a for an incoming signal from port 1 enforces equal splitting for an

incoming signal from all ports. Numerical simulation results showing the objective function value of the optimized wave splitter are presented in Fig. 1b. As it can be seen, the function is minimized at $\lambda \approx 1.55\ \mu m$ as intended.

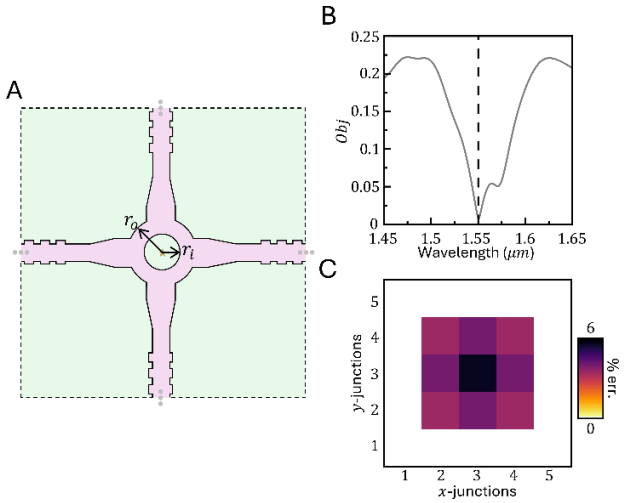

Fig. 1 Design of the proposed PDE-solving structure. **a**. Schematic representation of the unit cell. **b**. Numerical simulation results for the objective function (Eq. 1) of the optimized splitter. **c**. Numerical simulation results showing the percentage error of a PDE network solution when designed to solve a PDE with $h^2k^2 = -0.1944 - 0.1652i$.

III. Results and Discussion

To assess the performance of this PDE solving technique, numerical simulations of a 5×5 network are conducted using CST Studio Suite®. In this example, the network is designed to solve the standard five-point central difference representation of the Helmholtz equation $\nabla^2 H + k^2 H = 0$, when $h^2k^2 = -0.1944 - 0.1652i$. i.e. $\nabla^2 H|_{i,j} = (H_{i+1,j} + H_{i-1,j} + H_{i,j-1} + H_{i,j+1} - 4H_{i,j})/h^2$ where i,j are the sampling points of the solution h is the separation between adjacent points and k is the wavenumber. By applying external input signals to the outermost junctions of the waveguide network $H = 1$ (arb. units) Dirichlet boundary values are enforced. The PDE solution is extracted from the magnetic field distribution sampled at the center of the junctions. Fig. 1c shows the percentage error between the numerically calculated PDE solution produced using the PDE solving network, and an ideal solution using the finite difference method. As it can be seen, for this example there is a maximum error of ~6% between the two solutions, indicating the network can produce a valid approximate PDE solution. During the conference, the method of controlling the PDE to be solved will be discussed in detail. This is done when considering the relatively simple splitting geometry presented in Fig. 1a, with non-ideal behavior. It will be shown how this non-ideal performance may be included into the mapping between the reflection and transmission coefficients of the Bragg grating and the PDE parameters, allowing for approximate PDE solutions to be calculated using non-ideal wave-splitters.

IV. Conclusion

To summarize, an analog network of dielectric waveguides with wave splitters and Bragg gratings have been presented. This system is exploited to produce solutions to the Helmholtz equation at $\lambda = 1.55\ \mu m$. Numerical simulation results of this PDE-solving network indicate a good agreement with analytical PDE solutions demonstrating the potential for simple optical structures to produce accurate PDE solutions.

Acknowledgments

This work was supported by the Leverhulme Trust under the Leverhulme Trust Research Project Grant scheme (No. RPG-2023-024).

References

[1] C. Grossmann, H.-G. Roos, and M. Stynes, *Numerical Treatment of Partial Differential Equations*. Berlin, Heidelberg: Springer Berlin Heidelberg, 2007.
[2] I. H. Herron and M. R. Foster, *Partial Differential Equations in Fluid Dynamics*. Cambridge University Press, 2008.
[3] K. Nandakumaran, A and S. Datti, P, "Heat Equation," in *Partial Differential Equations*, Cambridge University Press, 2020, pp. 216–251.
[4] Y. D. Save, H. Narayanan, and S. B. Patkar, "Solution of Partial Differential Equations by electrical analogy," *J. Comput. Sci.*, vol. 2, no. 1, pp. 18–30, Mar. 2011.
[5] G. Kron, "Electric circuit models of partial differential equations," *Electrical Engineering*, vol. 67, no. 7, pp. 672–684, Jul. 1948.
[6] J. M. Shalf and R. Leland, "Computing beyond Moore's Law," *Computer (Long Beach. Calif).*, vol. 48, no. 12, pp. 14–23, Dec. 2015.
[7] J. Shalf, "The future of computing beyond Moore's Law," *Philosophical Transactions of the Royal Society A: Mathematical, Physical and Engineering Sciences*, vol. 378, no. 2166, p. 20190061, Mar. 2020.
[8] R. S. Williams, "What's Next? [The end of Moore's law]," *Comput. Sci. Eng.*, vol. 19, no. 2, pp. 7–13, Mar. 2017.
[9] F. Zangeneh-Nejad, D. L. Sounas, A. Alù, and R. Fleury, "Analogue computing with metamaterials," *Nat. Rev. Mater.*, vol. 6, no. 3, pp. 207–225, Oct. 2020.
[10] A. Silva, F. Monticone, G. Castaldi, V. Galdi, A. Alù, and N. Engheta, "Performing Mathematical Operations with Metamaterials," *Science (1979).*, vol. 343, no. 6167, pp. 160–163, Jan. 2014.
[11] J. Anderson *et al.*, "Virtualizing a Post-Moore's Law Analog Mesh Processor: The Case of a Photonic PDE Accelerator," *ACM Transactions on Embedded Computing Systems*, vol. 22, no. 2, pp. 1–26, Mar. 2023.
[12] A. Momeni, K. Rouhi, and R. Fleury, "Switchable and simultaneous spatiotemporal analog computing with computational graphene-based multilayers," *Carbon N. Y.*, vol. 186, pp. 599–611, Jan. 2022.
[13] H. Rajabalipanah, A. Momeni, M. Rahmanzadeh, A. Abdolali, and R. Fleury, "Parallel wave-based analog computing using metagratings," *Nanophotonics*, vol. 11, no. 8, pp. 1561–1571, May 2022.
[14] H. Ouyang, Z. Zhao, Z. Tao, J. You, X. Cheng, and T. Jiang, "Parallel edge extraction operators on chip speed up photonic convolutional neural networks," *Opt. Lett.*, vol. 49, no. 4, p. 838, Feb. 2024.
[15] H. Li *et al.*, "Performing calculus with epsilon-near-zero metamaterials," *Sci. Adv.*, vol. 8, no. 30, 2022.
[16] K. Cheng, Y. Fan, W. Zhang, Y. Gong, S. Fei, and H. Li, "Optical Realization of Wave-Based Analog Computing with Metamaterials," *Applied Sciences*, vol. 11, no. 1, p. 141, Dec. 2020.
[17] T. Zhu *et al.*, "Plasmonic computing of spatial differentiation," *Nat. Commun.*, vol. 8, no. 1, p. 15391, Aug. 2017.
[18] J. Zhang, Q. Ying, and Z. Ruan, "Time response of plasmonic spatial differentiators," *Opt. Lett.*, vol. 44, no. 18, p. 4511, Sep. 2019.
[19] J. Sol, D. R. Smith, and P. del Hougne, "Meta-programmable analog differentiator," *Nat. Commun.*, vol. 13, no. 1, p. 1713, Mar. 2022.
[20] J. Azana, R. Slavik, Y. Park, and M. Kulishov, "Ultrafast All-Optical Differentiators Based on Fiber Gratings," in *2007 9th International Conference on Transparent Optical Networks*, IEEE, Jul. 2007, pp. 101–104.

[21] Z. Dong, J. Si, X. Yu, and X. Deng, "Optical spatial differentiator based on subwavelength high-contrast gratings," *Appl. Phys. Lett.*, vol. 112, no. 18, Apr. 2018.
[22] J. Dong, A. Zheng, D. Gao, L. Lei, D. Huang, and X. Zhang, "Compact, flexible and versatile photonic differentiator using silicon Mach-Zehnder interferometers," *Opt. Express*, vol. 21, no. 6, p. 7014, Mar. 2013.
[23] T. Knightley, A. Yakovlev, and V. Pacheco-Peña, "Neural Network Design of Multilayer Metamaterial for Temporal Differentiation," *Adv. Opt. Mater.*, vol. 11, no. 5, p. 2202351, Mar. 2023.
[24] R. G. MacDonald, A. Yakovlev, and V. Pacheco-Peña, "Time derivatives via interconnected waveguides," *Sci. Rep.*, vol. 13, no. 1, p. 13126, Aug. 2023.
[25] V. Pacheco-Peña and N. Engheta, "Temporal equivalent of the Brewster angle," *Phys. Rev. B*, vol. 104, no. 21, p. 214308, Dec. 2021.
[26] V. Pacheco-Peña and N. Engheta, "Effective medium concept in temporal metamaterials," *Nanophotonics*, vol. 9, no. 2, pp. 379–391, Feb. 2020.
[27] A. Akbarzadeh, N. Chamanara, and C. Caloz, "Inverse prism based on temporal discontinuity and spatial dispersion," *Opt. Lett.*, vol. 43, no. 14, p. 3297, Jul. 2018.
[28] V. Pacheco-Peña, Y. Kiasat, D. M. Solís, B. Edwards, and N. Engheta, "Holding and amplifying electromagnetic waves with temporal non-foster metastructures," *Nat. Commun.*, vol. 16, no. 1, p. 2757, Mar. 2025.
[29] V. Pacheco-Peña and N. Engheta, "Temporal aiming," *Light Sci. Appl.*, vol. 9, no. 1, p. 129, Dec. 2020.
[30] L. Stefanini, S. Yin, D. Ramaccia, A. Alù, A. Toscano, and F. Bilotti, "Temporal interfaces by instantaneously varying boundary conditions," *Phys. Rev. B*, vol. 106, no. 9, p. 094312, Sep. 2022.
[31] M. Antyufeyeva and V. Pacheco-Peña, "Emulating time refraction at photonic time interfaces via smooth temporal transitions," *Phys. Rev. Appl.*, vol. 24, no. 3, p. 034004, Sep. 2025.
[32] Y. Hwang, T. J. Davis, J. Lin, and X.-C. Yuan, "Plasmonic circuit for second-order spatial differentiation at the subwavelength scale," *Opt. Express*, vol. 26, no. 6, p. 7368, Mar. 2018.
[33] E. A. Bezus, L. L. Doskolovich, D. A. Bykov, and V. A. Soifer, "Spatial integration and differentiation of optical beams in a slab waveguide by a dielectric ridge supporting high-Q resonances," *Opt. Express*, vol. 26, no. 19, p. 25156, Sep. 2018.
[34] V. Nikkhah, A. Pirmoradi, F. Ashtiani, B. Edwards, F. Aflatouni, and N. Engheta, "Inverse-designed low-index-contrast structures on a silicon photonics platform for vector–matrix multiplication," *Nat. Photonics*, vol. 18, no. 5, pp. 501–508, May 2024.
[35] S. Sun *et al.*, "Induced homomorphism: Kirchhoff's law in photonics," *Nanophotonics*, vol. 10, no. 6, pp. 1711–1721, Apr. 2021.
[36] M. Miscuglio *et al.*, "Approximate analog computing with metatronic circuits," *Commun. Phys.*, vol. 4, no. 1, p. 196, Aug. 2021.
[37] R. G. MacDonald, A. Yakovlev, and V. Pacheco-Peña, "Solving partial differential equations with waveguide-based metatronic networks," *Advanced Photonics Nexus*, vol. 3, no. 05, p. 056007, Oct. 2024.
[38] R. G. Macdonald and V. Pacheco-Peña, *In Prep*.
[39] A. Yakovlev and V. Pacheco-Peña, "Enabling High-Speed Computing with Electromagnetic Pulse Switching," *Adv. Mater. Technol.*, vol. 5, no. 12, p. 2000796, Dec. 2020.
[40] V. Pacheco-Peña and A. Yakovlev, "Computing with Square Electromagnetic Pulses," in *Handbook of Unconventional Computing,* 1st ed., A. Adamatzky, Ed., London: World Scientific, 2021, pp. 465–492.
[41] R. G. MacDonald, A. Yakovlev, and V. Pacheco-Peña, "Amplitude-Controlled Electromagnetic Pulse Switching Using Waveguide Junctions for High-Speed Computing Processes," *Advanced Intelligent Systems*, vol. 4, no. 12, p. 2200137, Dec. 2022.

Plasmonic Nanoantenna Architectures for Solar-Driven Hydrogen Production and Biomass Upgrading

T. L. Bui[1], L. Mascaretti,[1,2] R. Yalavarthi[1],H. Kmentova,[1] A. Naldoni,[4]and S. Kment[1,3*]

[1]Czech Advanced Technology and Research Institute, Regional Centre of Advanced Technologies and Materials, Palacký University Olomouc, Czech Republic
[2]Faculty of Nuclear Sciences and Physical Engineering, Czech Technical University in Prague, Czech Republic
[3]CEET, Nanotechnology Centre, VŠB-Technical University of Ostrava, Czech Republic
[4]Department of Chemistry and NIS Centre, University of Turin, Italy
*Corresponding author: stepan.kment@upol.cz

***Abstract* — Periodic plasmonic nanoantenna architectures enable efficient solar-driven chemical transformations by coupling broadband light harvesting with non-equilibrium catalytic activation. Scalable nanoantenna–reactor systems based on earth-abundant and plasmonic materials are presented for photoelectrochemical water splitting, low-temperature ammonia decomposition, and selective biomass upgrading, highlighting the role of plasmon-induced hot carriers and photothermal effects in sustainable solar-to-fuel conversion.**

***Keywords* — plasmonic nanoantennas, solar fuels, ammonia cracking, photoelectrochemistry, biomass valorization.**

I. Introduction

The efficient conversion of solar energy into chemical fuels and value-added chemicals remains a central challenge in the transition toward sustainable energy systems. Plasmonic nanostructures provide a powerful route to overcome kinetic and thermodynamic limitations by concentrating electromagnetic fields, generating hot charge carriers, and inducing localized photothermal heating at catalytic interfaces. In contrast to conventional semiconductor photocatalysts, plasmonic nanoantennas enable non-equilibrium reaction pathways that are inaccessible under purely thermal or electrochemical conditions.

While gold-based plasmonic architectures have demonstrated outstanding optical performance, their high cost and limited scalability hinder widespread application. Consequently, there is growing interest in earth-abundant metals, plasmonic nitrides, and nanoengineered oxide scaffolds that retain strong light–matter interaction while enabling scalable fabrication. Periodic nanoantenna arrays further enhance plasmonic performance by supporting collective resonances and hybrid photonic–plasmonic modes, offering precise control over absorption across the ultraviolet, visible, and near-infrared spectral ranges.

This contribution presents complementary plasmonic nanoantenna–reactor platforms designed for three key solar-driven transformations: photoelectrochemical water splitting, low-temperature ammonia decomposition for hydrogen production, and selective biomass upgrading. Together, these examples illustrate how rational nanoantenna design enables efficient solar-to-chemical energy conversion across diverse reaction classes.

II. Results and Discussion

A. Photoelectrochemical Water Splitting on Ni Nanoantenna Arrays:

Nickel nanopillar arrays integrated with CdS thin films exhibit a pronounced enhancement in photoelectrochemical performance compared to planar Ni/CdS systems. By tuning the nanopillar pitch and diameter, broadband optical absorption extending from the ultraviolet to the near-infrared is achieved. This enhanced absorption results from the coexistence of photonic modes in the UV region and hybrid cavity–plasmonic modes in the visible and NIR ranges.

The increased photocurrent arises from efficient coupling between the nanoantenna array, the semiconductor absorber, and the electrolyte, facilitating energy transfer and hot-carrier injection. Notably, the performance of the Ni-based nanoantenna arrays approaches that of previously reported gold nanoantenna systems, while relying on earth-abundant materials and scalable fabrication routes. These results demonstrate that carefully engineered non-noble metal plasmonic architectures can serve as viable platforms for low-cost photoelectrochemical solar energy conversion.

B. Plasmon-Driven Low-Temperature Ammonia Decomposition:

Ammonia is an attractive hydrogen carrier due to its high volumetric energy density and established storage and transport infrastructure, yet its decomposition traditionally requires high temperatures. A plasmon-driven antenna–reactor system based

on sharp-tip AAO nanospikes enables ammonia cracking at near-room temperature under visible-light illumination. The system consists of an AAO nanoantenna array coated with a plasmonic metal film and decorated with Cu nanoparticles acting as catalytic reaction sites.

Under 1 sun illumination at 35 °C, the optimized AAO@Au@Cu architecture achieves a hydrogen evolution rate of 227 $\mu mol\ h^{-1}\ gCu^{-1}$, with maximum activity observed at 565 nm, corresponding to the dominant surface plasmon resonance mode. Spectroscopic and theoretical analysis reveals a multi-step ammonia decomposition pathway involving NH_2NH_2 and NH–NH intermediates, indicating that plasmon-induced non-thermal hot carriers play a decisive role in lowering kinetic barriers. The replacement of gold with plasmonic titanium nitride further demonstrates the scalability and economic viability of this approach.

C. Plasmonic Biomass Upgrading:

The antenna–reactor concept is extended to biomass valorization through the selective oxidation of 5-hydroxymethylfurfural to 2,5-furandicarboxylic acid under base-free conditions. Plasmonic TiN nanocubes coupled with bimetallic RuPt nanoparticles enable complete HMF conversion with high FDCA selectivity. The enhanced reactivity originates from synergistic photothermal heating and hot-electron-mediated activation of molecular oxygen, as confirmed by kinetic isotope effects and density functional theory calculations. This approach highlights the versatility of plasmonic nanoarchitectures in enabling selective chemical transformations beyond hydrogen production.

III. Conclusion

Scalable plasmonic nanoantenna–reactor architectures based on nickel nanopillars, anodized alumina nanospikes, and plasmonic nitrides provide a unified strategy for solar-driven water splitting, low-temperature ammonia decomposition, and selective biomass upgrading. By exploiting plasmon-induced non-equilibrium effects, these systems unlock reaction pathways inaccessible under conventional thermal or electrochemical conditions, offering promising routes toward sustainable hydrogen production and next-generation solar-to-fuel technologies.

Acknowledgments

The authors acknowledge the financial support of the European Union under the REFRESH – Research Excellence For Region Sustainability and High-tech Industries project number CZ.10.03.01/00/22_003/0000048 via the Operational Programme Just Transition. The study was further supported by the project TECHSCALE (CZ.02.01.01/00/22_008/0004587) via the Operational Programme Johannes Amos Comenius.

References

[1] Yalavarthi, R. et al. “Enhancing Photoelectrochemical Energy Storage by Large-Area CdS-Coated Nickel Nanoantenna Arrays.” ACS Appl. Energy Mater. 4, 11367–11376, 2021.

[2] Mascaretti, L. et al. “Plasmonic titanium nitride nanomaterials prepared by physical vapor deposition methods.” Nanotechnology 34, 502003, 2023.

[3] Bui, T. L.et al., “Non Thermal-Driven Photocatalytic Ammonia Decomposition at Near-Room Temperature on a Plasmonic Nanocone Array.” Adv. Funct. Mater. e05216, 2025.

[4] Kaur, M. et al. “Near-infrared plasmonic activation of molecular oxygen for selective oxidation of biomass derivatives”, Nat. Catal., 8, 1370–1381, 2025.

.

Phase-Transparent Frequency Selective Metasurface Design via Kolmogorov–Arnold Network Based Generative Modeling

Wei DU[1,2], Jiwei ZHAO[1,2,3], Bin ZHENG[1,2,3],

[1]State Key Laboratory of Extreme Photonics and Instrumentation,
ZJU-Hangzhou Global Scientific and Technological Innovation Center, Zhejiang University, Hangzhou 310027, China
[2]International Joint Innovation Center, The Electromagnetics Academy at Zhejiang University,
Zhejiang University, Haining 314400, China
[3]Zhejiang Key Laboratory of Intelligent Electromagnetic Control and Advanced Electronic Integration,
Jinhua Institute of Zhejiang University, Zhejiang University, Jinhua 321099, China
*Corresponding author: zhengbin@zju.edu.cn

***Abstract*—A phase-transparent frequency selective metasurface is designed using a Kolmogorov–Arnold network based generative model. The approach enables target-driven bandwidth control while maintaining near-zero insertion phase delay. Two prototypes demonstrate broadband transmission, angular stability, and strong agreement between simulation and measurement.**

***Keywords*— frequency selective surface, phase transparency, Kolmogorov–Arnold Network, generative design.**

I. Introduction

Frequency-selective surfaces (FSSs) consist of single- or multilayer periodic metallic patterns printed on dielectric substrates and are widely used in wireless communication and radar systems [1], [2], [3], [4], as well as electromagnetic manipulation applications [5], [6]. They enable transmission within a designated frequency band while suppressing out-of-band signals.

Existing studies primarily focus on amplitude characteristics, including transmission bandwidth, out-of-band suppression, and selectivity [7], [8], [9], [10], [11]. However, the transmission phase of conventional FSSs is often nonuniform and difficult to control within the passband, which may distort wavefronts and degrade performance in phase-sensitive systems.

To address this issue, phase-transparent frequency selective metasurfaces (PTFSs) have been proposed [12]. Phase transparency is evaluated by the insertion phase delay (IPD), defined as the phase difference between the FSS and an equivalent free-space layer of the same thickness. When the IPD approaches $0°$, the metasurface introduces negligible additional phase shift, preserving the incident wave's propagation characteristics—an essential requirement in radar and communication systems.

Achieving simultaneous frequency selectivity and prescribed phase transparency remains challenging. Conventional design relies on parameter sweeping and empirical optimization, which become inefficient under multiple frequency and bandwidth constraints. Generative modeling techniques have recently shown strong capability in inverse design [13], [14] and have attracted growing interest in electromagnetic and metasurface applications [15], [16], offering a data-driven route to accelerate synthesis.

However, many neural-network-based approaches do not explicitly capture the intrinsic physical correlations between structural parameters and electromagnetic responses. The Kolmogorov–Arnold Network (KAN), with learnable activation functions, enhances nonlinear representation and interpretability [17], [18], [19], providing a mechanism to model hidden physical relationships.

In this work, a KAN-based conditional variational autoencoder [20] (KAE) is developed for inverse design of phase-transparent FSSs. The proposed framework enables efficient synthesis under predefined spectral and phase constraints, offering a scalable solution for phase-sensitive metasurface systems.

II. Methods

A. Insertion Phase Delay

The insertion phase delay (IPD) is defined as the difference between the transmission phase of the metasurface and that of an air slab with identical thickness:

$$IPD = \phi_{PTFS}(f) - \phi_{air}(f) \tag{1}$$

where

$$\phi_{air}(f) = k_0 h, \quad k_0 = \frac{2\pi}{\lambda} \tag{2}$$

Phase transparency is achieved when:

$$IPD \approx 0° \tag{3}$$

Under this condition, the metasurface introduces negligible additional phase shift relative to free space.

B. KAN-Based Generative Design

A conditional variational autoencoder (CVAE) integrated with Kolmogorov–Arnold Networks is employed for inverse design. Compared with conventional multilayer perceptrons, KAN utilizes learnable spline-based activation functions to improve nonlinear representation.

The training objective is:

$$Loss = MSE + \tau L_{KL} \tag{4}$$

where L_{KL} constrains the latent distribution.

C. Spectral Prediction

To avoid phase discontinuity, transmission phase is represented by its real and imaginary components. An inverse discrete Fourier transform (IDFT) layer reduces output dimensionality and stabilizes training. This framework enables direct synthesis of metasurfaces satisfying predefined bandwidth and phase constraints.

REFERENCES

[1] S. Sun, Y. Gou, T. J. Cui, *et al.*, "High-security nondeterministic encryption communication based on spin-space-frequency multiplexing metasurface," *PhotoniX*, vol. 5, p. 38, 2024.

[2] Q. Ma and T. J. Cui, "Information metamaterials: Bridging the physical world and digital world," *PhotoniX*, vol. 1, p. 1, 2020.

[3] W. Zhou, S. Zhu, Z. Zhang, *et al.*, "Time-varying metasurface driven broadband radar jamming and deceptions," *Optics Express*, vol. 32, pp. 17911–17921, 2024.

[4] A. M. Hegazy, M. Alizadeh, A. Samir, *et al.*, "Remote material characterization with complex baseband FMCW radar sensors," *Progress In Electromagnetics Research*, vol. 177, pp. 107–126, 2023.

[5] H. Lu, J. Zhao, B. Zheng, *et al.*, "Eye accommodation-inspired neuro-metasurface focusing," *Nature Communications*, vol. 14, p. 3301, 2023.

[6] K. Xue, H. Wei, C. Zhang, *et al.*, "Transmissive reconfigurable metasurface enabling independent control of active and passive modules through weak coupling," *Photonics Research*, vol. 12, p. 1449, 2024.

[7] W. Y. Yong and A. A. Glazunov, "Miniaturization of a fully metallic bandpass frequency selective surface for millimeter-wave band applications," *IEEE Trans. Electromagn. Compat.*, vol. 65, pp. 1072–1080, 2023.

[8] J. Ge, T. Hong, J. Tang, *et al.*, "Miniaturized FSS with ultrawide out-of-band suppression based on parallel-plate capacitor," *IEEE Antennas Wireless Propag. Lett.*, vol. 23, pp. 3892–3896, 2024.

[9] T. Hong, S. Guo, W. Jiang, *et al.*, "Highly selective frequency selective surface with ultrawideband rejection," *IEEE Trans. Antennas Propag.*, vol. 70, pp. 3459–3468, 2022.

[10] Z. Zhou, Z. Wei, J. Ren, *et al.*, "Representation learning-driven fully automated framework for the inverse design of frequency-selective surfaces," *IEEE Trans. Microw. Theory Techn.*, vol. 71, pp. 2409–2421, 2023.

[11] D. Wang, X. Cui, D. Liu, *et al.*, "Multi-characteristic integrated ultra-wideband frequency selective rasorber," *Progress In Electromagnetics Research*, vol. 179, pp. 49–59, 2024.

[12] X. J. Hu, Z. Shen, and D. L. Wu, "Bandpass frequency-selective surface with stable transmission amplitude and insertion phase delay," *IEEE Trans. Antennas Propag.*, vol. 73, pp. 5384–5392, 2025.

[13] I. Goodfellow *et al.*, "Generative adversarial networks," *Commun. ACM*, vol. 63, pp. 139–144, 2020.

[14] J. Jumper, R. Evans, A. Pritzel, *et al.*, "Highly accurate protein structure prediction with AlphaFold," *Nature*, vol. 596, pp. 583–589, 2021.

[15] Z. Gu, D. Li, Y. Wu, *et al.*, "A solution to the dilemma for FSS inverse design using generative models," *IEEE Trans. Antennas Propag.*, vol. 71, pp. 5100–5109, 2023.

[16] P. Naseri and S. V. Hum, "A generative machine learning-based approach for inverse design of multilayer metasurfaces," *IEEE Trans. Antennas Propag.*, vol. 69, pp. 5725–5739, 2021.

[17] Z. Liu, Y. Wang, S. Vaidya, *et al.*, "KAN: Kolmogorov-Arnold networks," *arXiv preprint arXiv:2404.19756*, 2024.

[18] Z. Liu, P. Ma, Y. Wang, *et al.*, "KAN 2.0: Kolmogorov-Arnold networks meet science," *arXiv preprint arXiv:2408.10205*, 2024.

[19] A. A. Howard, B. Jacob, S. H. Murphy, *et al.*, "Finite basis Kolmogorov-Arnold networks: Domain decomposition for data-driven and physics-informed problems," *arXiv preprint arXiv:2406.19662*, 2024.

[20] D. P. Kingma, D. J. Rezende, S. Mohamed, and M. Welling, "Semi-supervised learning with deep generative models," in *Advances in Neural Information Processing Systems*, pp. 3581–3589, 2014.

Antennas, Microwave Systems and Electromagnetic Structures

Probabilistic Risk Mapping for Low-Altitude UAV Communications: An Empirical Tail Approach to Multipath and Interference Modeling

Hang ZHOU *, Zeyu LONG, Yalong QIN

Sino-European Institute of Aviation Engineering, Civil Aviation University of China, China
*Corresponding author: h-zhou@cauc.edu.cn

***Abstract*— An empirical tail-probability-based risk mapping method is proposed for low-altitude UAV communications, integrating deterministic propagation and stochastic modeling. Experiments show over 0.93 risk consistency and 30 times faster computation than baselines, with high-risk zones near dense urban structures, supporting optimized NLOS flight path planning.**

***Keywords*— UAV communication, risk mapping, empirical tail probability**

I. Introduction

The integration of Unmanned Aerial Vehicles (UAVs) into low-altitude airspace introduces significant challenges for wireless communication reliability.[1] Unlike terrestrial networks, UAV-to-Ground links are highly susceptible to heterogeneous interference sources. These include environmental occlusion caused by buildings (inducing shadowing and multipath scattering), meteorological attenuation from precipitation and fog, and electromagnetic interference (EMI) from anthropogenic sources. Traditional statistical methods, which often rely on mean-based metrics, fail to adequately capture rare but catastrophic communication failures characterized by the distribution tails. To address this, we propose a communication risk mapping methodology based on empirical tail probability.[2] This paper integrates electromagnetic simulations with statistical risk quantification to identify and map extreme interference scenarios.

II. System Model and Propagation Environment

1. Simulation Scenario: A 12 km × 13 km urban area in Shenzhen (Fig. 1) is modeled using WINPROP software, adhering to ITU-R propagation standards to ensure physical fidelity. The environment accounts for complex urban geometries essential for analyzing diffraction and scattering effects [3].

We model three distinct interference factors affecting the Signal-to-Interference-plus-Noise Ratio (SINR):

1) Environmental Occlusion (Shadowing / Multipath): The occlusion coefficient $V(x,y,z)$ is calculated based on Line-of-Sight (LOS) availability and sector blockage. High values correspond to deep shadowing regions caused by buildings and terrain, where diffraction and scattering dominate the propagation mechanism.

2) Meteorological Attenuation: The total atmospheric attenuation $L_A(x,y,z)$ is defined as the sum of rain attenuation L_R and fog attenuation L_C, where L_R is derived from rainfall rate (mm/h) and L_C from visibility (km).

3) Electromagnetic Interference (EMI): EMI is quantified by the interference power increment $\Delta P_r(x,y,z)$, representing the degradation in received power due to ground-based interference sources.

Fig. 1 Simulation scenario

2. Empirical Tail Risk Methodology: To normalize the heterogeneous scales of the interference factors, we apply Min-Max normalization. The core contribution of this work is the risk quantification based on the distribution's tail.

We estimate the empirical cumulative distribution function (ECDF) of three interference indicators, denoted as $\hat{F}(x)$, using Bootstrap resampling to ensure statistical robustness against limited sample sizes.

The risk value r_i for a given interference indicator x_i is derived using a negative log-likelihood transformation to emphasize low-probability extreme events:

$$r_i = -\ln(1-\hat{F}(x_i))$$

This transformation maps the probability of rare events (the tail) to higher risk values.

Risks are classified into four levels based on quantile thresholds: Common (<50%), Occasional (50%-90%), Rare (90%-99%), and Extreme (>99%).

III. Results and Discussion

The proposed method was validated against Isolation Forest (iForest) and One-Class Support Vector Machine (OCSVM) at altitudes of 10 m, 50 m, 100 m, and 200 m. The method maintains a risk consistency rate >0.93 across all scenarios, outperforming the baselines. The execution time ranges from 0.05 s to 0.12 s, which is approximately 30 times faster than the machine learning baselines. High-risk zones are concentrated around high-density urban structures, particularly below 50 m, confirming the significant impact of building shadowing and multipath fading in the urban canopy. Electromagnetic risks are sparse, covering <1% of the airspace, which suggests that EMI is a localized rather than systemic threat.

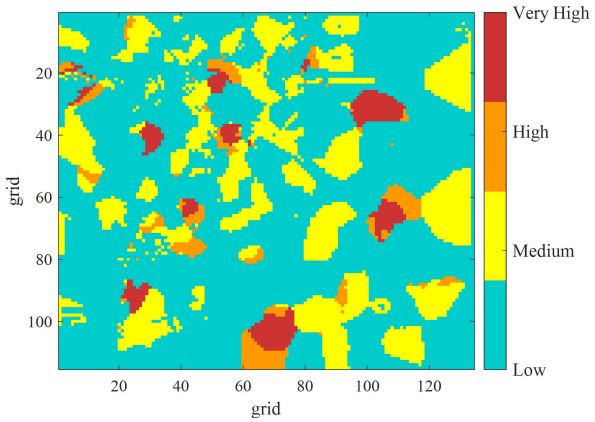

Fig. 2 Risk map under electromagnetic environment

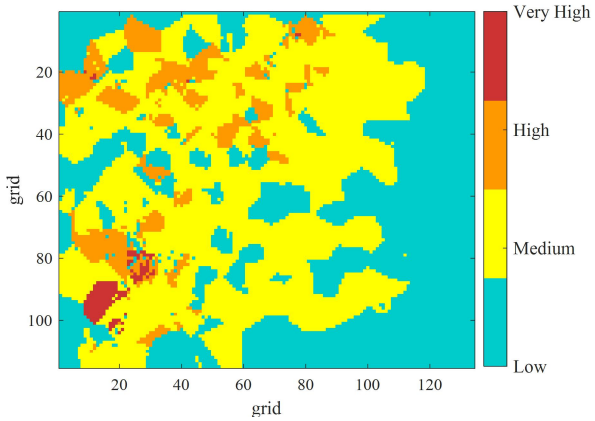

Fig. 3 Risk map under environmental occlusion

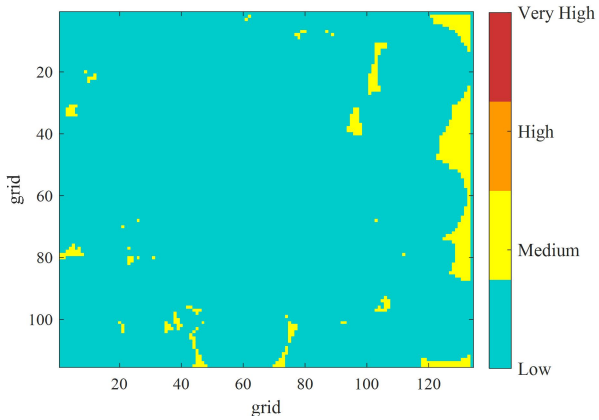

Fig. 4 Risk map under meteorological conditions

Table 1 Comparison of risk consistency rate among different methods coefficients in various scenarios

Scenarios		Proposed method vs OCSVM	Proposed method vs iForest	Proposed method vs iForest
Environmental occlusion /m	100	0.9958	1.0000	0.9958
	50	0.9839	1.0000	0.9839
	10	0.8015	1.0000	0.8015
Meteorological conditions /(mm·h-1)	10	0.9996	0.9821	0.9825
	25	0.9786	0.9657	0.9452
	50	0.9322	0.9768	0.9179
Electromagnetic environment/dBm	45	0.9852	0.9987	0.9845
	46	0.9785	0.9993	0.9779
	48	0.9844	0.9995	0.9839

Table 2 Comparison of computation times among different methods

Scenarios		Proposed method	iForest	OCSVM
Environmental occlusion /m	100	0.0871	1.8206	2.5926
	50	0.1054	1.5100	2.7309
	10	0.0858	1.9328	2.6879
Meteorological conditions /(mm·h-1)	10	0.1163	3.3541	3.2888
	25	0.1137	3.0617	3.8347
	50	0.1041	3.5761	3.4301
Electromagnetic environment/dBm	45	0.0537	1.5355	1.6260
	46	0.0496	1.9263	1.5909
	48	0.0503	2.0913	1.6580

IV. Conclusion

This paper presented an empirical tail probability approach for generating UAV communication risk maps. By accurately modeling propagation losses and quantifying tail events, the method effectively identifies high-risk zones caused by environmental occlusion and EMI. The approach offers a computationally efficient alternative to complex machine learning models, making it suitable for real-time flight planning. Future work will incorporate real-world measurement data to validate the multipath coupling effects.

Acknowledgments

This work was supported by the National Natural Science Foundation of China under Grant 62201577.

References

[1] Y. Zeng, R. Zhang, and T. J. Lim, "Wireless communications with unmanned aerial vehicles: Opportunities and challenges," IEEE Communications Magazine, vol. 54, no. 5, pp. 36-42, 2016.

[2] Z. Li et al., "ECOD: Unsupervised outlier detection using empirical cumulative distribution functions," IEEE Transactions on Knowledge and Data Engineering, vol. 35, no. 12, pp. 12181-12193, 2022.

[3] ITU-R, "Propagation data and prediction methods required for the design of terrestrial line-of-sight systems," Recommendation ITU-R P.530-19, 2025.

[4] E. Ancel et al., "Real-time risk assessment framework for unmanned aircraft system traffic management," in Proc. 17th AIAA Aviation Technology Integration and Operations Conference, 2017, p. 3273.

Ni-Co-Zn Composite Loaded Patch Antenna for MICS Band Biomedical Communications

Poonam Lathiya[1, *], Jing Wang[2]

[1]Department of Electrical Engineering and Computer Science, IISER Bhopal, India
[2]Department of Electrical Engineering, University of South Florida, USA
*Corresponding author: poonam@iiserb.ac.in

Abstract— Microwave properties of Ni–Co–Zn/epoxy magneto-dielectric composites were studied for MICS band applications. Two patch antennas using Rogers (dielectric – control) and Ni–Co–Zn/epoxy substrates, were designed and analyzed through electromagnetic simulations, and the measured results were compared. An improved bandwidth and a smaller size of antenna were achieved.

***Keywords*— Antenna, MICS Band, Ferrite Composite, Dynamic Magnetic Property.**

I. Introduction

The increasing demand for implantable biomedical devices has driven the need for compact and reliable wireless communication systems operating in the Medical Implant Communication Service (MICS) band (402–405 MHz) [1]. MICS band is well-suited for in-body communications due to its low interference, favorable tissue penetration, and regulatory approval for medical applications [2]. However, antenna miniaturization at MICS-band frequencies remains a major challenge because of the low frequencies and impedance mismatch between the surrounding and the implantable platforms [3, 4].

Microstrip patch antennas are attractive for biomedical applications due to their low profile, planar structure, and ease of integration with the body. The conventional dielectric substrates that are used in current implants lead to relatively large antenna dimensions at sub-GHz frequencies (MICS band) [5]. To overcome this limitation, magneto-dielectric substrates based on Ni–Co–Zn ferrite composites offer an effective solution by simultaneously enhancing permeability and permittivity, enabling significant antenna size reduction [6-8].

Here, the performance and miniaturization capabilities of a magneto-dielectric microstrip patch antenna (Ni-Co-Zn composite) compared to the dielectric antenna have been studied for the 401-406 MHz frequency range. The tailored properties of the composite substrate are used to achieve better bandwidth and compact size while maintaining good return loss, and radiation performance, demonstrating the suitability of magnetic composite loading for miniaturized implantable antenna applications [5].

II. Methods

Initially, Ni-Co-Zn ferrite powders were prepared in bulk quantity via a top-down approach. For the preparation of ferrite/epoxy composites, doped ferrite powders were used in epoxy matrix (MED-302-3M). Different volume percentages of ferrite powder in epoxy matrix were investigated to study the optimum magnetic and dielectric properties of the ferrite composites [5]. The Ferrite/epoxy composite was formed by the compression molding technique. Subsequently, the microstrip patch antenna was fabricated using the magnetic composite with a measured permittivity of 4.4, permeability of 2.4, magnetic loss tangent of 0.03 and dielectric loss tangents of 0.006. A dielectric substrate (dielectric core of a Rogers RO3010 commercial laminate with a permittivity of 10.2 and loss tangent of 0.003) based antenna was also designed for the comparison [5]. The resonance frequency of the rectangular microstrip patch antenna is calculated by following equation 1[9, 10].

$$f_r = \frac{c}{2L\sqrt{\epsilon_{eff}\mu_{eff}}} \qquad (1)$$

Where c is the speed of light, L is the length of patch, ε_{eff} denotes the effective permittivity, f_r the resonance frequency, and μ_{eff} denotes effective permeability.

Over the UHF frequency range, permittivity is considered nondispersive. Hence, it can be calculated using Schneider's equation 2

$$\epsilon_{eff} = 0.5[(\epsilon_r + 1) + \frac{(\epsilon_r - 1)}{(1+10\frac{h}{w})^{\frac{1}{2}}}] \qquad (2)$$

μ_{eff} can be calculated using the formula given by Pucel and Masse (equation 3)

$$\mu_{eff} \approx \mu_r(\frac{C}{C-D})^2 \qquad (3)$$

The patch width of the antenna for a good radiation efficiency is given by equation 4

$$w = \frac{c}{2f_r\sqrt{\frac{(\epsilon_{eff}+1)(\mu_{eff}+1)}{2}}} \quad (4)$$

The effective patch length is given by the following equation 5

$$L_{eff} = \frac{1}{2f_r\sqrt{\mu_{eff}\varepsilon_{eff}}\sqrt{\mu_0\varepsilon_0}} \quad (5)$$

III. Results and Discussion

All dimensions of patch antennas for both dielectric and magnetic composite substrates were calculated using the aforementioned antenna equations. The dimensions of the patch antenna were optimized during the design to achieve the desired resonance frequency in the MICS band [5]. Figure 1 depicts the micrograph of the prototype dielectric antenna and the magnetic composite patch antenna. Table 1 shows the dimensions of patch antennas for both dielectric and magnetic substrates.

Antenna performance is compared using figures of merit such as bandwidth, return loss, gain, and patch size. Table 2 presents the microwave properties of both substrates used.

Table 1 Patch antenna design parameters for devices over different substrates

Substrate	Patch Length (mm)	Patch Width (mm)	Substrate Height (mm)
Rogers (RO3010)	111	135	1.27
NiCoZn/Epoxy	112	115	2

Table 2 Antenna substrate properties

Substrate Properties	Permittivity (ε)	Dielectric Loss Tangent ($\tan\delta_\varepsilon$)	Permeability (μ)	Magnetic Loss Tangent ($\tan\delta_\mu$)
Rogers (RO3010)	10.2	0.003	1	0
NiCoZn/Epoxy	4.4	0.006	2.4	0.03

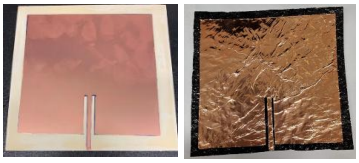

Figure 1: Micrograph of the magnetic patch antenna using (Left): Dilectric substrate, (Right): Ni-Co-Zn/Epoxy as the substrate.

Return loss and radiation pattern of the patch antenna fabricated over a Rogers RO3010 dielectric substrate were measured using a 50 MHz-6 GHz VNA and an anechoic antenna test chamber, respectively. Simulated and measured return loss for the dielectric substrate patch antenna are shown in Figure 2.

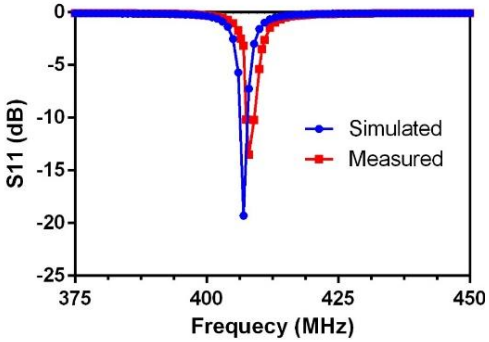

Figure 2: Simulated and measured return loss of custom-designed dielectric substrate patch antenna.

The small frequency shift can be ascribed to the effects of the SMA connectors and to the geometrical discrepancy between the HFSS simulated design and the actual device due to fabrication tolerances. Also. the difference in measured and simulated return loss values can be attributed to the glue used while attaching copper foil to the substrate, which in turn reduces the return loss.

Measured return losses for dielectric substrate (Rogers RO3010) and magnetic composite substrate (ferrite loading 47 vol %) patch antennas are shown in Figure 3. The miniaturization factor of the substrate is calculated by the equation: $\eta = \sqrt{\varepsilon \times \mu}$. For the dielectric substrate, η is 3.2; while for the magnetic composite substrate, η is 3.24. Also, both antennas are designed for the same frequency, so that a direct comparison can be made between the antenna performances. As seen in Figure 3, the magnetic composite antenna presents 7.5 times higher bandwidth compared to the dielectric substrate antenna fabricated on Rogers RO3010 substrate.

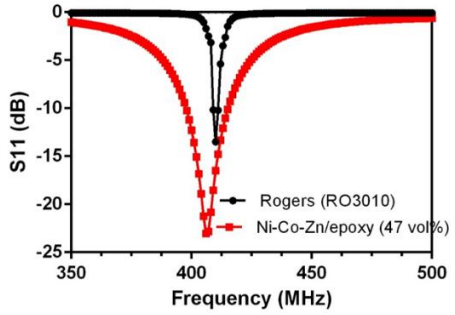

Figure 3:Measured return loss for dielectric substrate (RO3010) and magnetic composite substrate (Ni-Co-Zn/Epoxy) patch antennas.

Measured return loss is also higher for the magnetic composite substrate patch antenna. The antenna designed on the magnetic substrate offers the smaller antenna patch size as compared to that of the dielectric substrate patch antenna. The magnetic composite patch antenna is 17. 5% smaller in size than the dielectric substrate patch antenna. Higher antenna gain can

be achieved by reducing substrate losses. All the performance parameters are presented in Table 3.

Table 3 Measured parameters of dielectric substrate and magnetic composite patch antennas.

Antenna (Measured)	Resonance Frequency (MHz)	Return Loss (dB)	Gain (dBi)	Bandwidth (MHz)	Area (cm^2)
Dielectric (RO3010)	406	-13.65	4.32	2.1	149
Magnetic Composite (47 vol %)	405.5	-23.09	1.59	15	127

IV. Conclusion

A comparison was made between the performance of an antenna designed and fabricated on a commercial dielectric substrate (Rogers RO3010) and on a magnetic composite (Ni-Co-Zn/epoxy, 47 vol% ferrite loading) substrate, using HFSS 3D EM simulations and measurement results. We have demonstrated magnetic-dielectric substrates are better than dielectric-only substrates for increasing bandwidth and reducing patch antenna size. Based on the microwave properties and performance of the prototype antenna, Ni-Co-Zn/epoxy-based magnetic substrate has great promise as a suitable candidate for biomedical implants, RFID and MICS band applications.

Acknowledgments

This work was supported by the University of South Florida, Tampa, Florida, USA and the Indian Institute of Science and Education Research Bhopal, India.

References

[1] K. Han *et al.*, "Magneto-dielectric nanocomposite for antenna miniaturization and SAR reduction," vol. 15, pp. 72-75, 2015.

[2] A. K. Skrivervik, J.-F. Zurcher, O. Staub, J. J. I. A. Mosig, and p. Magazine, "PCS antenna design: The challenge of miniaturization," vol. 43, no. 4, pp. 12-27, 2002.

[3] E. Y. Chow, M. M. Morris, and P. P. J. I. M. M. Irazoqui, "Implantable RF medical devices: The benefits of high-speed communication and much greater communication distances in biomedical applications," vol. 14, no. 4, pp. 64-73, 2013.

[4] E. Le Guen, A.-C. Tarot, and J.-L. Mattei, "Half-massive ceramics for antenna downsizing: improvement of a smart magneto-dielectric material with matching permeability and permittivity, and with enhanced low-loss frequency range," in *2015 9th European Conference on Antennas and Propagation (EuCAP)*, 2015, pp. 1-5: IEEE.

[5] P. Lathiya, "Soft Magnetic Composite Substrates for RF/Microwave Applications," University of South Florida, 2022.

[6] L. Kong, Z. Li, G. Lin, and Y. J. I. T. o. M. Gan, "Ni-Zn ferrites composites with almost equal values of permeability and permittivity for low-frequency antenna design," vol. 43, no. 1, pp. 6-10, 2006.

[7] A. Paduraru, M. Feder, O. J. J. o. o. Caltun, and a. materials, "Magnetic properties of some perminvar ferrites," vol. 5, no. 4, pp. 945-950, 2003.

[8] F. Xie, Y. Chen, M. Bai, and P. J. C. I. Wang, "Co-substituted LiZnTiBi ferrite with equivalent permeability and permittivity for high-frequency miniaturized antenna application," vol. 45, no. 14, pp. 17915-17919, 2019.

[9] T. J. J. o. C. S. AlSharabati and Systems, "Microstrip patch antenna miniaturization using magneto-dielectric substrates for electromagnetic energy harvesting," vol. 17, no. 2, pp. 116-123, 2021.

[10] Z. Luan, L. Liu, W.-H. Zong, Z. Jin, and S. J. P. I. E. R. L. Li, "Design of an implantable antenna operating at ISM band using magneto-dielectric material," vol. 82, pp. 65-72, 2019.

Flexible metasurface integrated planar rigid antenna for circular polarization in K band

Garima Joshi[1,*] and R. Vijaya[1,2]
[1]Centre for Lasers and Photonics, Indian Institute of Technology Kanpur, Kanpur-208016, India
[2]Department of Physics, Indian Institute of Technology Kanpur, Kanpur-208016, India
*Corresponding author: garimaj@iitk.ac.in

***Abstract*— A flexible and lightweight metasurface integrated with a rigid planar antenna in Fabry- Perot arrangement changes the polarization state of radiation and enhances the gain and bandwidth of the antenna. Linear to circular polarization conversion over 18.6 to 21.3 GHz and a gain improvement of 2.7 dB is obtained.**

***Keywords*— metasurface, microstrip patch antenna, polarization conversion, gain improvement**

I. Introduction

Circularly polarized (CP) antennas are widely used in satellite communication, radar, microwave imaging, and modern wireless systems because they reduce the polarization mismatch loss and perform better under multipath conditions [1,2]. CP antennas are important in K-band systems, where stable polarization and high gain are required for reliable long-distance links. Achieving wideband CP operation with high gain at high frequencies remains a challenge, especially with lightweight, flexible and conformal antenna systems [3]. Metasurfaces (MS) are surfaces containing patterns of subwavelength size, period and thickness and are effective in controlling the characteristics of electromagnetic waves. They can be used with antennas to modify their radiation pattern and achieve more desirable features such as certain polarization states. Flexible metasurfaces are more attractive due to their lightweight nature, mechanical bendability, and conformal capability, making them suitable for space-grade and wearable communication systems. Rigid metasurfaces integrated with microstrip patch antennas (MPA) are extensively studied [3,4]. However, integrating metasurfaces on flexible substrate with rigid MPA, while offering variable polarization properties and high gain remains unexplored.

To address this gap, our work demonstrates a polarization converting MS made of polyethylene terephthalate (PET) integrated with an MPA to form a compact Fabry- Perot (FP) cavity. This integration converts the linearly polarized (LP) radiation of the MPA into CP, while the cavity configuration enhances the reflection coefficient, impedance bandwidth and gain. The combined flexible-rigid antenna system is a low-profile lightweight CP-MPA suitable for satellite communication and sensing applications in K band [3,4].

II. Design Of Flexible Metasurface integrated MPA

A. Flexible metasurface as a polarization converter

Figure 1 (a) shows the schematic of the unit cell of the pattern on the MS. It is a split-ring resonator. The annular ring contains a slot at an angle of $\alpha = 45^o$. Commercially available flexible PET sheet with a thickness of 0.125 mm and relative permittivity (ϵ_r) of 3.2 at a frequency of 10 GHz is considered as the substrate. The annular ring is of conductive silver ink (conductivity of 2.22 x 10^6 S/m) and the thickness of silver ink on the PET film is 3 µm.

The split-ring resonator is especially useful as it provides built-in anisotropy and strong coupling to the incident radiation to obtain the required polarization conversion characteristics. Our design of the MS is studied for polarization conversion characteristics for the broad range of 1-40 GHz [5]. It provides multiband and multiple type LP to cross LP/ CP /EP conversion in sub bands between 4-40 GHz. The detailed analysis of its S-parameters and polarization conversion characteristics has been carried out to confirm its utility as a reconfigurable MS [5]. Among the multiple types of conversion possible in multiple bands with this MS, LP to CP conversion is achieved in K band in both reflection and transmission geometry. This advantage was utilized in the present work to achieve polarization conversion of the radiation of an MPA, using the MS in reflection geometry and integrating the two together in a Fabry-Perot design.

B. Stand-alone K-band MPA

Figure 1 (b) shows the schematic of stand-alone MPA. This is a conventional design and is made with a rigid dielectric substrate backed by a metallic ground plane. The length (L_g), width (W_g) and thickness of the substrate are 50.00 mm, 50.00 mm and 0.79 mm respectively. The ground plane is of copper with comparable length and width, and a thickness of 0.35 mm. The rectangular patch has the length and width of W x L = 8 mm x 9.5 mm.

C. *Integration of flexible metasurface with rigid MPA*

The flexible MS is used as partially reflecting surface for the MPA and is mounted above the MPA. The substrate-superstrate configuration constitutes a Fabry- Perot cavity. The metasurface with 6 X 5 array of unit cell is loaded on the MPA at a distance (d) of 5 mm (0.33 λ_0), where λ_0 is the resonant wavelength (considered 20 GHz). The inset-fed MPA (Fig. 1(b)) is selected as the feeding for the Fabry-Perot cavity antenna. The patterned side of the MS faces the MPA in the integrated system.

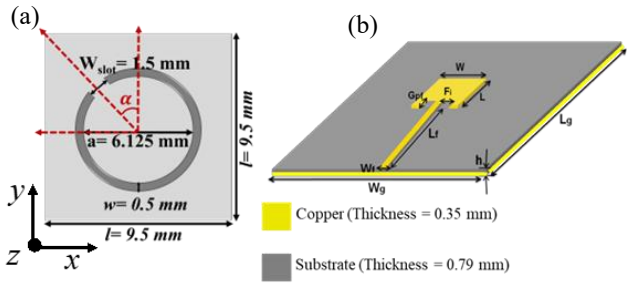

Figure 1. (a) Schematic of the unit cell of the metasurface. (b) Schematic of stand-alone MPA.

III. Results and Discussion

A. *Simulated results of MPA and integrated CP-MPA*

The S-parameters are calculated using the CST Microwave Studio Suite. Figure 2 (a) has the simulated reflection coefficient (S_{11}) of the stand-alone MPA (dash blue line) and of the metasurface integrated MPA (solid blue line) in the frequency range from 14 GHz to 26 GHz. The MPA resonates at 19.66 GHz with S_{11} = −17 dB and has a −10 dB bandwidth of 3.35% (19.40 GHz to 20.06 GHz). After loading the metasurface on the MPA, the reflection coefficient of FP-MPA is −25.01 dB at 19.67 GHz, shown with blue solid line in Fig. 2 (a). The reflection coefficient improves by nearly 8 dB after loading the metasurface as superstrate on MPA. The MS integrated MPA has an impedance bandwidth of nearly 3.2 GHz, ranging from 18.51 GHz to 21.70 GHz as shown using pink shaded region in Fig. 2 (a). The significant improvement of nearly 2.56 GHz in antenna bandwidth is attained through Fabry-Perot cavity configuration.

The integrated MS- MPA configuration is studied further for polarization conversion of MPA. Figure 2 (b) shows the simulated axial ratio of MPA (red dash line) and MS integrated MPA (red solid line). MPA shows a very high axial ratio implying LP as the polarization state of its radiation. When the MS is present as a partially reflecting surface at the appropriate distance from the MPA, the axial ratio is changed drastically (Fig. 2(b)). Its value is below -3 dB from 18.61 GHz to 21.36 GHz. This is the range of LP to CP conversion. This indicates that the integrated MS-MPA has a polarization conversion bandwidth of 2.75 GHz, which is highly useful in SatCom and remote sensing applications [3].

Figures 2(c) and (d) depict the simulated radiation patterns of MPA and MS-MPA in E- and H-planes respectively at the frequency of 19.60 GHz. In order to analyse the polarization behaviour of MPA and MS-MPA, the radiation pattern is shown for the two polarizations of right-handed circular polarization (RHCP) and left-handed circular polarization (LHCP). The radiation patterns clearly show that the MS-MPA offers LP to CP conversion and is RHCP dominant. The gain is dominant at bore side (0^0) for RHCP case after loading MS on MPA. Radiation pattern of LHCP is less than −20 dBi in both the planes. The gain of MS-MPA (at 19.60 GHz) is 7.83 dBi in E-plane and 7.85 dBi in H-plane. Gain enhancement is nearly 2.72 dB in E- plane and 1.87 dB in H- plane after integrating the MS with MPA.

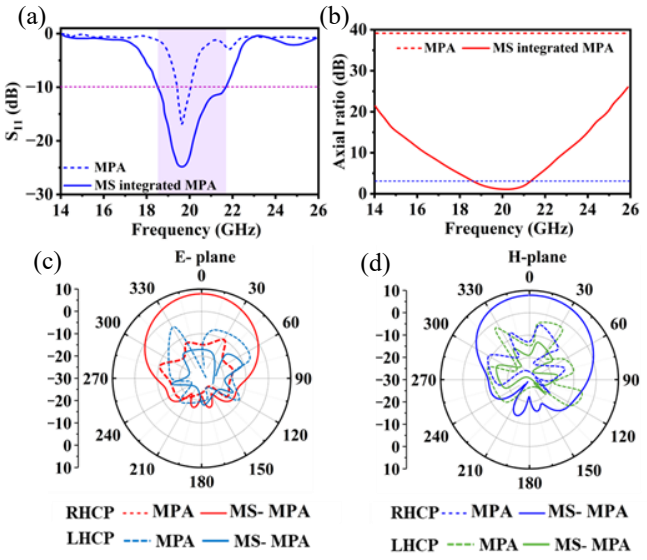

Figure 2. Simulated (a) reflection coefficient, (b) axial ratio, and radiation patterns in (c) E- plane and (d) in H- plane of MPA and MS integrated MPA.

B. *Experimental work*

The metasurface is printed using a semi-automatic screen printer (Duratech, Easiprint M-series). Figure 3 (a) shows the photograph of the MS. Its overall thickness is very less and it can be folded as shown in Fig. 3 (a). The overall printed area of the MS is 30 cm x 30 cm and contains an array of 32 x 32 unit cells. It was characterized both through simulation and with standard measurements in anechoic chamber for its polarization conversion properties. Fig. 3 (b) shows the measured co- and cross-polarized reflection coefficient of MS when an x-polarized wave is incident. It provides LP to CP conversion at 20.47 GHz in reflection geometry with a conversion bandwidth of 3.80 GHz with an axial ratio of 0.13 dB in this band.

The photographs of integrated MS-MPA are shown in Fig. 3(c) as the tilted view. Figure 3 (d) shows the measured reflection coefficient of MPA and MS integrated MPA. The measured S_{11} of MPA is -16.27 dB at 19.59 GHz and of integrated MPA is -24.87 dB at 19.61 GHz. Measured -10 dB bandwidth is 3.18 GHz of integrated MPA. Fig. 3(d) matches quite well with Fig.

2(a) both in the trend and in the values. Overall, measured results show quite good agreement with simulated results and slight dispensaries may occur because of fabrication tolerance and misalignment.

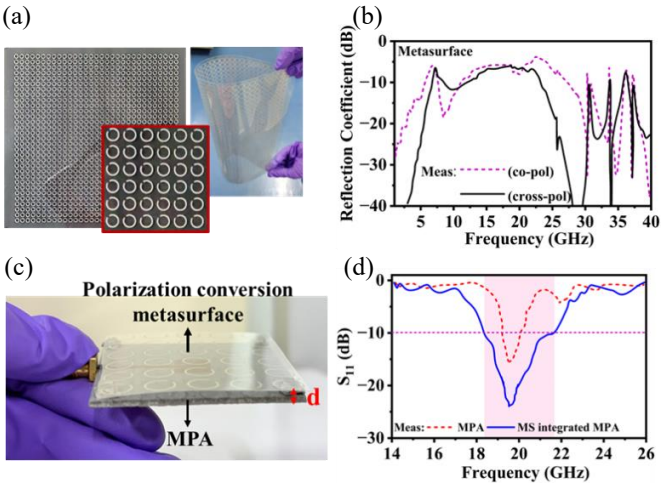

Figure 3. (a) Photograph of the metasurface, with zoomed image in inset. The bending capability of the metasurface is shown through folding. (b) Measured reflection coefficient of co- and cross- polarized waves when linearly polarized wave is incident on the metasurface. (c) Photograph of the MS integrated MPA (tilted view). (d) Measured reflection coefficient of MPA and MS integrated MPA.

IV. Conclusion

A flexible PET-based metasurface is designed for polarization conversion from LP to CP and then integrated with MPA in a Fabry-Perot configuration. The metasurface is useful to convert the LP radiation from the antenna into CP state in the K-band and to improve the overall antenna performance. It enhances the impedance bandwidth and the gain of MPA. After integrating the metasurface, the reflection coefficient is improved from –17 dB to –25 dB at a frequency of 20 GHz, and the impedance bandwidth is increased from 3.35% to 16.21% in the simulations. The MS integrated MPA also achieved a wide circular polarization (LP to RHCP) bandwidth of 2.75 GHz from 18.61 and 21.36 GHz. The gain also increased by 2.72 dB in the E-plane and 1.87 dB in the H-plane at 19.60 GHz with integrated MPA in the simulation studies. The MS is fabricated on a PET sheet and its polarization properties are measured. The MPA is made using photolithography and integrated with the MS. The close agreement between the measured and simulated results highlights the practical utility and reliability of the proposed integrated MPA. Measurements of the radiation patterns are in progress. Overall, the work shows that using an ultra- thin and flexible metasurface as superstrate is an effective way to enhance the bandwidth and gain of antennas. In addition, the individual polarization conversion characteristic of metasurface can be utilized to convert linear MPA to circularly polarized MPA making it promising for K-band satellite communication and sensing applications. The integrated configuration can be explored for beam steering of the antenna radiation by rotating the metasurface in its own plane to control the radiated beam direction at 20 GHz.

Acknowledgments

The authors acknowledge the fabrication facility at NCFlexE and photolithography lab in EE department at IIT Kanpur. ISRO- SAC, Ahmedabad for providing measurement facilities. The work was sponsored by ISRO, India (project ID 0414).

References

[1] Balanis, C.A. “Antenna Theory: Analysis and Design”. 3rd Edition, John Wiley & Sons, Hoboke, 2005.

[2] Sahal, M. and Tiwari, V.N., “Review of circular polarization techniques for design of microstrip patch antenna. In Proceedings of ICRCWIP-2016, pp. 663-669, 2016 Springer India.

[3] Undrasi, A. and Khairnar, V.V., “A compact dual-band linear-to-circular polarization converter for X-band and Ku-band applications”. Opt. Commun., vol. 570, pp. 130890, 2024.

[4] Wei, J., Liao, S., Xue, Q. and Che, W.,“Wideband circularly polarized phased array antenna for K/Ka-band satellite communication using ME-dipole elements”. IEEE Antennas Wirel. Propag. Lett., 23(8), pp.2496-2500, 2024.

[5] Joshi, G., Bhattacharya, A., Priyanshu and Vijaya, R., “Mechanically Reconfigurable Single-layer Metasurface for Continuously Tunable Polarization Conversion and Frequency Filtering in C- Ka band for Reflection and Transmission”, 2026 (submitted).

Advanced Dielectric Transmit-array Antennas for RF and Microwave Applications

Álvaro F. Vaquero[1,*], Marcos R. Pino[1]

[1]Department of Electrical Engineering, University of Oviedo, Spain
*Corresponding author: fernandezvalvaro@uniovi.es

***Abstract*—This work presents an studio of dielectric transmit-array based on advanced unit cell geometries enabled by novel manufacturing processes. Different dielectric topologies and periodic surfaces are analyzed to assess their impact on antenna performance. The results highlight the potential of these unit cells for improved RF and microwace transmit-array performance.**

***Keywords*— Additive manufacturing, dielectric transmit-array, lenses, ink deposition.**

I. Introduction

Transmit-array antennas are based on periodic structures composed of unit cells that, when illuminated by a primary feed (typically a horn antenna), induce a specific phase shift on the incident field. By controlling the phase response of each unit cell, it is possible to modify the tangential field over the transmit-array surface and, consequently, to control the radiation pattern.

Unit cells are commonly based on resonant structures, such as dipole, patch, or other resonant geometries. Although excellent single-layer configurations exits, particularly those based on Huygens-type resonators [1], most unit cells require multilayer structures to achieve at least a full 2π phase cycle [2]. As typical for resonant periodic structures, the achievable bandwidth is inherently limited.

More recently, driven by advances in additive manufacturing, purely dielectric unit cells have gained increasing attention. Unlike conventional resonant topologies, these cells do not rely on resonance phenomena but instead control the effective dielectric constant of the medium to impose the desired phase shift on the incident field. These solutions emulate the behavior of conventional dielectric lenses using planar structures. To this end, the planar surface is discretized into unit cells, and by changing the electromagnetic response of the material, the phase response of the incident field can be controlled. Since the phase shift is purely determined by the material composing the unit cell, such unit cells exhibit improved bandwidth performance, at the expense of increased losses. Several topologies have been proposed, with dielectric prisms featuring perforated geometries being among the most commonly employed, as well as dielectric piles in which the height is changed to control the phase shift. [3], [4].

This work presents a comparative study of different unit-cell configurations, primarily based on purely dielectric structures. Although all configurations operate under the same physical principle, the geometry of the unit cell can be exploited to improve the overall antenna performance. In addition, preliminary results are presented for hybrid unit cells based on dielectric substrates incorporating metallized regions realized through conductive ink deposition.

II. Results

Different unit-cell geometries will be presented and analyzed, showing how they can be exploited using regular or triangular lattices to achieve enhanced bandwidth or shaped radiation patterns. Different fabrication approaches for transmit-array antennas will also be discussed, highlighting their main advantages and limitations, as well as potential manufacturing methods.

III. Conclusion

This work presents several dielectric unit cells topologies together with fabrication processes based on additive manufacturing, as well as emerging techniques such as conductive ink deposition. The reported results demonstrate the potential of advanced fabrication technologies to improve the performance of transmit-array antennas for RF and microwave applications.

Acknowledgments

This work was supported in part by Grant PID2023-146246OB-C32 (ANT4IT) funded by Spanish Government through MCIU /AEI /10.13039/501100011033 / FEDER, UE (Ministerio de Ciencia, Innovación y Universidades, Agencia Estatal de Investigación y Fondo Europeo de Desarrollo Regional de la Unión Europea); and in part by the Government of Asturias-Sekuens/FEDER under grant IDE-2024-000693.

References

[1] C. Pfeiffer and A. Grbic, "Metamaterial Huygens' surfaces: Tailoring wave fronts with reflectionless sheets," *Phys. Rev. Lett.*, vol. 110, Art. no. 197401, May 2013.

[2] A. H. Abdelrahman, A. Z. Elsherbeni, and F. Yang, "Transmission phase limit of multilayer frequency-selective surfaces for transmitarray designs," *IEEE Trans. Antennas Propag.*, vol. 62, no. 2, pp. 690–697, Feb. 2014.

[3] Á. F. Vaquero, M. R. Pino, M. Arrebola, S. A. Matos, J. R. Costa, and C. A. Fernandes, "Bessel beam generation using dielectric planar lenses at millimeter frequencies," *IEEE Access*, vol. 8, pp. 216185–216196, 2020.

[4] J. Lai, X. Lv, and Y. Yang, "A 3-D printed 140 GHz multifocal dielectric transmitarray antenna for 2-D mechanical beam scanning," *IEEE Antennas Wireless Propag. Lett.*, vol. 23, no. 4, pp. 1366–1370, Apr. 2024.

A Comparison of Dirichlet-Impulse Frequency Diverse Array and Phased Array Radars

A. Hizal[1,*], R. Cetiner[1], H. Yildiz[2]

[1]Rehis, Aselsan Inc., Ankara, Türkiye
[2]Dept. of E & E Engineering, Baskent University, Ankara,Türkiye
* hizal@metu.edu.tr

***Abstract*—Frequency diverse array (FDA) radar employing Dirichlet-kernel-waveform is compared with conventional phased array radar in terms of performance and signal-to-noise ratio (SNR). The proposed FDA achieves comparable SNR while preserving range–angle–time coupling. A planar radiating aperture is also developed to realise the FDA and enable electronic Gaussian-beam steering.**

***Keywords*— frequency diverse array, phased array, radar**

I. Introduction

A frequency diverse array (FDA) radar [1], owing to the range-angle-time coupling, is preferable in search and track applications compared to a phased array radar (PA) for better clutter and jamming performance. However, the SNR of the conventional FDA radar, in a radar equation, is less than that of PA by about the number of elements of the array due to the energy radiated in a pulse width τ being spent in continuous scanning of the angular space. A recent concept of beam-focusing type coherent FDA radar, using multiple matched filters (MFs), is proposed to increase the SNR to match that of a PA [7], [8]. Here, like in [8], we also use multiple MFs , but with a non-rectangular pulse waveform (WF) having a spiky shape, the FDA$^{(ds)}$-WF, where (ds) is not a numerical value, but it denotes the order ds of the FDA$^{(ds)}$-WF. The FDA$^{(ds)}$-WF for $ds = 2$ is the same as the Dirichlet kernel. We will call the associated radar the Dirichlet-impulse FDA$^{(ds)}$ radar. This idea, illustrated in Fig. 1, was previously introduced as a discrete-scanning FDA radar [3]. We radiate the energy only along an angular direction ϑ by the timing of the transmission (TX) using the FDA feature. The signal processing (SP) phase, $kd\,sin\vartheta_o$, $|sin\vartheta_o| \lessgtr 1$, positions the WF for a ϑ at a specified time t_o in τ. Here, we give the theory of FDA$^{(ds)}$ and compare its SNR with that of PA, at the MF output, for the same input energy. The FDA$^{(ds)}$ has a shorter effective pulse width $\tau_e^{(ds)}$, (22), than τ of PA. If the peak power of FDA$^{(ds)}$-WF V_{oF}^2 is $\tau/\tau_e^{(ds)}$ times more than V_{oP}^2 of PA-WF, The input energy of both radars is the same, yielding the same SNR, at the output of MF. In a pulse-burst type TX, The duty cycle ratio is $d_{cFDA^{(ds)}}/d_{cPA} \leq 1$. The peak input signal power ratio is $\varrho_W = V_{oF}^2/V_{oP}^2 = \tau/\tau_e^{(ds)} > 1$. The peak voltages are V_{oF} and V_{oP} . For the same input energy (1μJ), we have $V_{oF} = 1/(N\,\tau_e^{(ds)})^{½}$ and $V_{oP} = 1/(N\tau)^{½}$, where $\tau_e^{(ds)}$and τ are in μs, and V_{oF} and V_{oP} are in Volts.

Moreover, the FDA$^{(ds)}$, described in Fig. 2b, can be realised as a radiating aperture (RAP) having an electronically steerable, Gaussian beam (GB). The method, depicted in Fig. 12, Sec.V, is based on the electromagnetic field equivalence principle (FEP) [14]. A FDA$^{(ds)}$-WF radiating point source (PS) illuminates a paraboloidal reflector (PaR), where the PS and PaR are virtual sources (VSs). The reactive near-field (NF) of PaR over RAP is used to synthesise the excitation coefficients (ECs) of the microstrip patch (μsP) elements on RAP. The far-field (FF) of a large RAP with a high number of μsPs is almost identical to that of the PaR, which is a high gain GB with FDA$^{(ds)}$ properties.

II. Theory

The conceptual circuit diagrams given in Fig. 2 form the basis for the theory and the SP for PA and FDA$^{(ds)}$ radars..

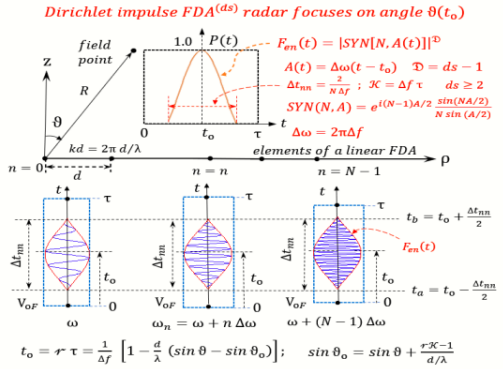

Fig. 1 Dirichlet-kernel FDA-WF; $e^{i\omega_n t}$; $\omega_n = \omega + n\,\Delta\omega$

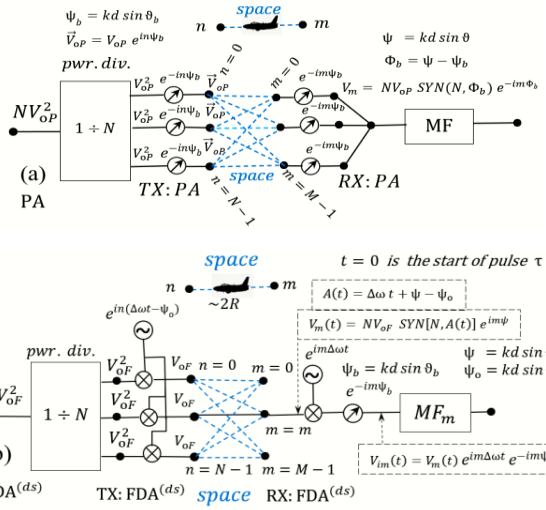

Fig. 2 Base-band circuits of (a) PA and (b) FDA$^{(ds)}$ radars

(i) For PA, $\Phi_b = \psi - \psi_b,\ \psi = kd\sin\vartheta,\ \psi_b = kd\sin\vartheta_b$

$$V_m(t) = N\,V_{oP}\,P(t)\,SYN(N,\Phi_b)\,e^{im\Phi_b} \quad (1)$$

$$MF_{om}(t) = \int_0^{\tau} V_m(t')\,h_m(t-t')\,dt' \quad (2)$$

$$h_m(t) = N\,V_{oP}\,P(\tau - t)\,SYN(N,-\Phi_b) \quad (3)$$

Since, the m RX channels, and the associated $h_m(t)$ are independent with respect to m, we sum over m and obtain

$$MF_{oPA}(t) = (N\,V_{oP})^2\,M\,\mathcal{S}_{NM}(\Phi_b)\int_0^{\tau} P(t')\,P(t_u)\,dt' \quad (4)$$

$$\mathcal{S}_{NM}(\Phi_b) = SYN(N,\Phi_b)\cdot SYN(M,\Phi_b);\quad t_u = \tau - t + t' \quad (5)$$

$$MF_{oPA}(\tau) = N^2\,M\,V_o^2\,\tau \quad (6)$$

$$\mathcal{E}_{N\,PA} = N\,V_o^2\,\tau \quad (7)$$

is the input energy. Defining array gains by $G_{TX} = N$, and $G_{RX} = M$, and $G_A^2 = G_{TX}\cdot G_{RX}$, The radar equation at $\mathrm{MF_o}$ is

$$SNR_{PA}^{MF_o} = \frac{2\,\mathcal{E}_{N\,PA}}{\mathcal{N}_o}\,G_A^2\,\Upsilon \quad (8)$$

$$\mathcal{N}_o = \kappa\,T_s\ \text{(noise-PSD)}\ \&\ \Upsilon = \frac{\lambda^2\,\bar{\sigma}}{(4\pi)^3\,R^4};\quad \bar{\sigma} = RCS \quad (9)$$

In Fig. 3, we display an example of $MF_{oPA}(t)$ for PA radar.

(ii) For FDA$^{(ds)}$, Fig. 2b. For the m^{th} RX channel

$$V_{im}(t) = P(t)\,N\,V_{oF}\,SYN[N,A(t)]\,e^{im\Phi_b}\,e^{im\,\Delta\omega\,t} \quad (10)$$

$$A(t) = \Delta\omega\,t + \Phi_o = \Delta\omega\,(t - t_o);\ \text{(Fig. 4)} \quad (11)$$

$$\Phi_o = \psi - \psi_o\ ;\ \psi_o = kd\sin\vartheta_o \quad (12)$$

From the convolution integral of MF, it can be shown that

$$MF_{om\,FDA^{(ds)}}(t) = (N\,V_{oF})^2\,e^{imU(t)}\tau_e^{(ds)}(t) \quad (13)$$

$$U(t) = -\Delta\omega(\tau - t) + \Phi_b \quad (14)$$

$$\tau_e^{(ds)}(t) = \int_0^{\tau} P(t')\,SYN[N,A(t')]\,P(t_u)\,SYN[N,-A(t_u)]\,dt' \quad (15)$$

Summing over m independent RX channel outputs, we get

$$MF_{o\,FDA^{(ds)}}(t) = \sum_{m=0}^{M-1} MF_{om\,FDA^{(ds)}}(t)\cdot\tau_e^{(ds)}(t) \quad (16)$$

$P(t)$, $F_{en}(t)$ and $\{t_a,\ t_b\}$ are defined as follows (Fig. 4)

For $ds = 0$ $\quad P(t) = F_{en}(t) = 1\ for\ 0 \le t \le \tau\,;\ else\ 0$ (17)

For $ds = 1$: $\quad P(t) = F_{en}(t) = 1\ for\ t_a \le t \le t_b;\ else\ 0$ (18)

For $ds \ge 2$: $\quad P(t) = F_{en}(t) = |SYN[N,\Delta\omega(t-t_o)]|^{ds-1}$

$$for\ t_a \le t \le t_b;\ else\ 0 \quad (19)$$

For $ds = 0$ $\quad t_a = 0;\quad t_b = \tau$ (20)

For $ds \ge 1$ $\quad t_a = t_o - \Delta t_{nn}/2\,;\quad t_b = t_o + \Delta t_{nn}/2$ (21)

For $t = \tau$ & $\psi = \psi_b$ and $\Phi_b = 0$

$$\tau_e^{(ds)} = \tau_e^{(ds)}(\tau) = \int_{t_a}^{t_b} |\,P(t')\,SYN[N,A(t')]\,|^2\,dt' \quad (22)$$

$$(16)\rightarrow \quad MF_{o\,FDA^{(ds)}}(\tau) = (N\,V_{oF})^2\,M\,\tau_e^{(ds)} \quad (23)$$

$$\mathcal{E}_{A\,FDA^{(ds)}} = MF_{o\,FDA^{(ds)}}(\tau) = (N\,V_{oF})^2\,M\,\tau_e^{(ds)} \quad (24)$$

From these equations, we can write

$$SNR_{FDA^{(ds)}}^{MF_o} = \frac{2\,\mathcal{E}_{A\,FDA^{(ds)}}}{\mathcal{N}_o}\,G_A^2\,\Upsilon \quad (25)$$

Thus, $\quad SNR_{r\,FDA^{(ds)}}^{MF_o} = \dfrac{\mathcal{E}_{A\,FDA^{(ds)}}}{\mathcal{E}_{A\,PA}} = \dfrac{V_{oF}^2}{V_{oP}^2}\,\dfrac{\tau_e^{(ds)}}{\tau}$ (26)

For the equal input energy i.e. $\mathcal{E}_{N\,FDA^{(ds)}} = \mathcal{E}_{N\,PA}$ (27)

we have $\quad V_{oF}^2\,\tau_e^{(ds)} = V_{oP}^2\,\tau$ (28)

The WF peak-power ratio $= \varrho_W = \dfrac{V_{oF}^2}{V_{oP}^2} = \dfrac{\tau}{\tau_e^{(ds)}} > 1$ (29)

An example of ϱ_W is given in Fig. 5.

The SP gain $G_{pro\,MF}$ of the FDA$^{(ds)}$ MF , the time-bandwidth product of the MF, can be calculated from the ratio

$$G_{pro\,MF} = SNR_{FDA^{(ds)}}^{MF_o} \,/\, SNR_{FDA^{(ds)}}^{MF_{in}} \quad (30)$$

where $\quad SNR_{FDA^{(ds)}}^{MF_o} = \dfrac{2\,\mathcal{E}_{A\,FDA^{(ds)}}}{\mathcal{N}_o}\Upsilon$ (31)

$$SNR_{FDA^{(ds)}}^{MF_{in}} = \frac{(N\,V_{oF})^2 M}{\frac{\mathcal{N}_o}{2}B_{e\,FDA}^{(ds)}}\Upsilon \quad (32)$$

Thus, $\quad G_{pro\,MF} = \tau_e^{(ds)}B_{e\,FDA}^{(ds)}$ (33)

The bandwidth is expressed by $B_{e\,FDA}^{(ds)} = \dfrac{\tau_e^{(ds)}}{max_\omega\{|\tilde{S}(\omega)|^2\}}$ (34)

$$\tilde{S}(\omega) = \int_{t_a}^{t_b} F_{en}(t)\,SYN[N,\Delta\omega(t-t_o)]e^{-i\omega t}\,dt \quad (35)$$

III. Numerical Simulations

The numerical simulations, obtained using a MATLAB code, based on the theory given in Section II, are presented and discussed in this section. $\mathbb{D} = \{rad, data, ds\}$ identifies the input data.The values $rad = 1$, and $rad = 2$ indicate the PA, and FDA$^{(ds)}$ radars. $\mathbb{D}$ refers to the set $\{M,N,\Delta f,\tau,\varkappa,ds,\vartheta\}$ which determine $t_o = \varkappa\,\tau$, $sin\,\vartheta_o$, $\mathcal{K}$ and Δt_{nn} (Figs. 1 and 4). The case of $ds = 2$ is the Dirichlet-impulse radar (17)–(22).

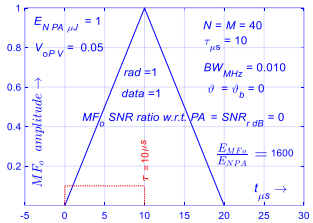

Fig. 3 $MF_{oPA}(t)$ for a PA for $N = M = 40$, $\tau_{\mu s} = 10$

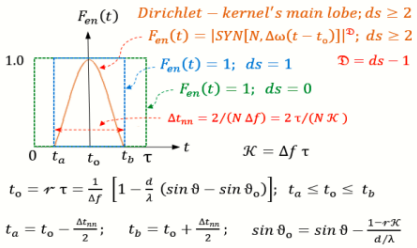

Fig. 4 The definition of the WF function $F_{en}(t)$

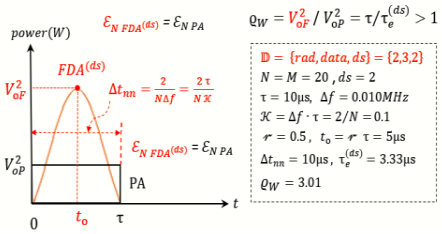

Fig. 5 The peak powers of PA-WF and FDA$^{(ds)}$-WF for $\Delta t_{nn} = \tau$

The plots for two $\mathbb{D}$ sets are displayed in Figs. 6 and 7. The FDA$^{(ds)}$ parameters, in detail, are given in Table 1. We observed that $\Delta t_{nn}^{\mathrm{MF_o}} \cong \Delta t_{nn}^{TX}$. In these graphs, notice the low sidelobes. Also, $\Delta t_{nn} = \tau$ for $\mathcal{K} = \Delta f\, \tau = 2/N$ to reduce $\varrho_W = V_{oF}^2/V_{oP}^2$. A FDA$^{(ds)}$radar with a power ratio $\varrho_W > 3$ may not be feasible from the TX-hardware point of view.

The MF output ($\mathrm{MF_o}$) peak occurs at $t = \tau$ ($t = 0$ is the start time of the TX pulse of duration τ). In a search, after sliding the SP delay by $2R/c$, a time peak associated with a target is detected (Figs. 6-9). The observation time at the radar's position is $\tilde{t} = 0$, and the $\mathrm{MF_o}$ peaks at time $\tilde{t} = 2R/c + \tau$. Then, we determine the range R. Also, notice that the FDA$^{(ds)}$-WF peak response, preceding the $\mathrm{MF_o}$, is at $\tilde{t} = 2R/c + t_o$. Since, a priori, we have chosen $t_o = \curlyvee\, \tau$, the WF peaking time in τ, with its steering SP phase $sin\, \vartheta_o$, We can retrieve ϑ from $sin\, \vartheta = sin\, \vartheta_o - (\curlyvee\, \mathcal{K} - 1)/(d/\lambda)$.

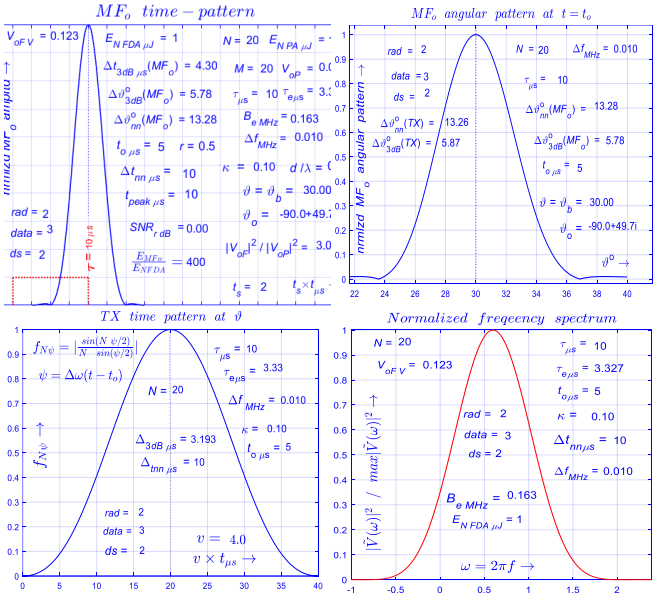

Fig. 6 $\mathbb{D} = \{2,3,2\}$ FDA$^{(ds)}$ time, angle and spectrum patterns

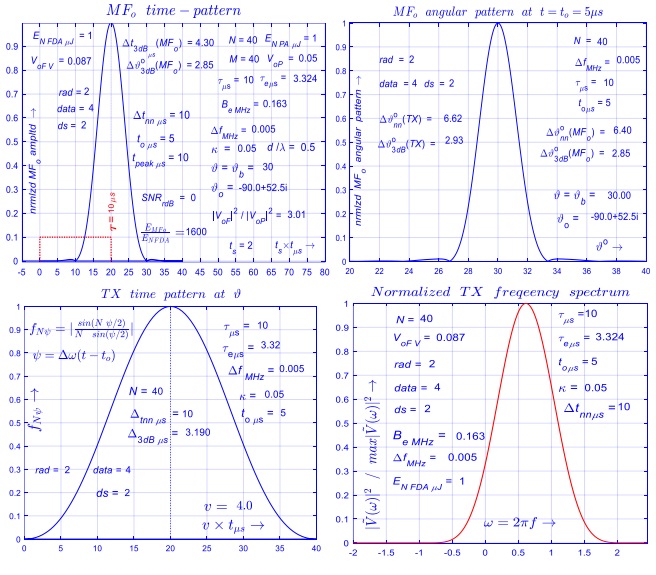

Fig. 7 $\mathbb{D} = \{2,4,2\}$ FDA$^{(ds)}$ time, angle and spectrum patterns

TABLE I
PATTERN PARAMETERS OF THE FDA$^{(ds)}$ FOR $\mathbb{D} = \{2, data, ds\}$

$\varrho_W = V_{oF}^2/V_{oP}^2$, $SNR_r = SNR_{FDA^{(ds)}}^{MF_o}/SNR_{PA}^{MF_o} = \varrho_W\, \tau_e^{(ds)}/\tau$, Also, $\Delta t_{nn}^{MF_o} \cong \Delta t_{nn}^{TX}$
rad = 2, $M = N$, $\curlyvee = 0.5$, $t_o = \curlyvee\, \tau$, $\mathcal{K} = \tau \Delta f$, $\vartheta_b = \vartheta$

data	ds	N	τ	Δf	$\mathcal{K}$	ϑ, ϑ_o	MF_o $\tau_e^{(ds)}$	TX $B_e^{(ds)}$	ϱ_W	SNR_r	TX Δt_{nn}	TX Δt_{3dB}	TX $\Delta\vartheta_{3dB}$	TX $\Delta\vartheta_{nn}$	MF_o Δt_{3dB}	MF_o $\Delta\vartheta_{3dB}$	MF_o $\Delta\vartheta_{nn}$
#	#	#	μs	MHz	#	deg	μs	MHz	#	dB	μs	μs	deg	deg	μs	deg	deg
1	0	20	40	0.010	0.4	30,−90 +i25.4	4.89	0.158	1.00	-9.3	10.0	4.43	5.87	13.26	4.50	8.15	13.60
1	1	20	40	0.010	0.4	"	4.52	0.130	8.85	0.0	10	4.43	5.87	13.26	4.70	7.68	13.30
1	2	20	40	0.010	0.4	"	3.33	0.163	12.0	0.0	10	3.19	5.87	13.26	4.30	5.75	13.00
2	0	20	20	0.020	0.4	40, 73.2	2.45	0.317	1.00	-9.3	5.0	2.22	5.87	13.26	2.30	9.35	15.80
2	1	20	20	0.020	0.4	"	2.26	0.260	8.85	0.0	5.0	2.22	5.87	13.26	2.30	8.75	15.70
2	2	20	20	0.020	0.4	"	1.66	0.326	12.0	0.0	5.0	1.59	5.87	13.26	2.10	6.65	15.00
3	0	20	10	0.010	0.1	30, −90 + i49.7	4.52	0.130	2.00	-3.45	10.0	4.43	5.87	13.26	4.70	5.78	13.28
3	1	20	10	0.010	0.1	"	4.52	0.130	2.21	0.0	10.0	4.43	5.87	13.26	4.70	7.65	13.50
3	2	20	10	0.010	0.1	"	3.33	0.163	3.01	0.0	10.0	3.19	5.87	13.26	4.30	5.75	13.28
4	0	40	10	0.005	0.05	30, −90 + i52.5	4.51	0.130	1.00	-3.45	10.0	4.43	2.93	6.62	4.70	3.75	6.70
4	1	40	10	0.005	0.05	"	4.51	0.130	2.21	0.0	10	4.43	2.93	6.62	4.70	3.75	6.70
4	2	40	10	0.005	0.05	"	3.32	0.163	3.01	0.0	10	3.19	2.93	6.62	4.30	2.85	6.40

$$t_o = \frac{1}{\Delta f}\left[1 - \frac{d}{\lambda}(sin\, \vartheta - sin\, \vartheta_o)\right] \tag{36}$$

It can be used for the verification of peaking retarded time.

The average power for PA in τ, The fast time of PA is $\bar{P}_{PA} = V_{oP}^2$. The fast time of FDA$^{(ds)}$ is Δt_{nn}. So,

$$\bar{P}_{\Delta t_{nn}}^{FDA^{(ds)}} = V_{oF}^2\, \tau_e^{(ds)}/\Delta t_{nn} = \frac{\mathcal{K}\, N}{2} V_{oF}^2\, \frac{\tau_e^{(ds)}}{\tau} \tag{37}$$

In the slow time T_p (the pulse period PRI) $\bar{P}_{T_p}^{PA} = V_{oP}^2\, \tau/T_p$ and $\bar{P}_{T_p}^{FDA^{(ds)}} = V_{oF}^2\, \tau_e^{(ds)}/T_p$. Also, the duty cycles are expressed by $d_{cPA} = \tau/T_p$ and $d_{cFDA^{(ds)}} = \Delta t_{nn}/T_p$. We form the $\bar{P}$-ratios:

Fast time $\bar{P}$-ratio $$\frac{\bar{P}_{\Delta t_{nn}}^{FDA^{(ds)}}}{\bar{P}_{\tau}^{PA}} = \frac{\mathcal{K}\, N}{2}\frac{V_{oF}^2}{V_{oP}^2}\frac{\tau_e^{(ds)}}{\tau} \tag{38}$$

Slow time $\bar{P}$-ratio $$\frac{\bar{P}_{T_p}^{FDA^{(ds)}}}{\bar{P}_{T_p}^{PA}} = \frac{V_{oF}^2}{V_{oP}^2}\frac{\tau_e^{(ds)}}{\tau} \tag{39}$$

Duty-cycle-ratio $$\frac{d_{cFDA^{(ds)}}}{d_{cPA}} = \Delta t_{nn}/\tau = \frac{2}{\mathcal{K}\, N} \le 1 \tag{40}$$

For $\mathcal{K} = 2/N$, $\Delta t_{nn} = \tau$, $$d_{cFDA^{(ds)}} = d_{c\,PA} \tag{41}$$

and $$\bar{P}_{\Delta t_{nn}}^{FDA^{(ds)}}/\bar{P}_{\tau}^{PA} = \bar{P}_{T_p}^{FDA^{(ds)}}/\bar{P}_{T_p}^{PA} = \frac{V_{oF}^2}{V_{oP}^2}\frac{\tau_e^{(ds)}}{\tau} \tag{42}$$

For $$V_{oF}^2\, \tau_e^{(ds)} = V_{oP}^2\, \tau, \quad \bar{P}_{T_p}^{FDA^{(ds)}}/\bar{P}_{T_p}^{PA} = 1 \tag{43}$$

The angular focusing (or beam steering) corresponds to positioning the time response in a preselected position in τ via $\curlyvee$ in $t_o = \curlyvee\, \tau$ and $sin\, \vartheta_o$. If there is a target at ϑ within the beamwidth $\Delta\vartheta_{3dB}^{TX}(\vartheta)$, then for a selected $\curlyvee$, we calculate $sin\, \vartheta_o$, and position the peak of the response at t_o. Let us determine the three positions of a target for ϑ and t_o. The positions ϑ and $\vartheta_\pm = \vartheta \pm \Delta\vartheta_{3dB}^{TX}(\vartheta)$ have time positions

$$t_o = \frac{1}{\Delta f}\left[1 - \frac{d}{\lambda}(sin\, \vartheta - sin\, \vartheta_o)\right]; \quad \curlyvee = t_o/\tau \tag{44}$$

and $$t_{o\pm} = \frac{1}{\Delta f}\left[1 - \frac{d}{\lambda}(sin\, \vartheta_\pm - sin\, \vartheta_{o\pm})\right]; \quad \curlyvee_\pm = t_{o\pm}/\tau \tag{45}$$

For $\mathbb{D} = \{2,3,2\}$, $N = 20$, $\Delta f = 0.01MHz$, $\tau = 10\mu s$, $d/\lambda = 0.5$, $\mathcal{K} = 2/N = 0.1$, $\Delta t_{nn} = 10\mu s$, $\vartheta = 30^o$, $\Delta\vartheta_{3dB}^{TX} = 5.87^o$. The ratios $\curlyvee$, $\curlyvee_\pm$ are chosen. We have, $\mathcal{K} = 2/N$ and $\Delta t_{nn} = \tau$. Then, $\vartheta = 30^o$, $\vartheta_+ = 35.87^o$ and $\vartheta_- = 24.13^o$. The output parameters for these angles are given in Table 2, while the associated patterns are displayed in Figs. 8, 9, and 10.

It is seen that when a target is within an angular beamwidth, in steering the FDA$^{(ds)}$ patterns, they can be observed with some losses conventionally called the beam

shape loss. Also, notice that the MF-output-angular patterns and the associated parameters are affected by the time-position of the ttime-pattern peaks So, the FDA$^{(ds)}$ radar should scan the angular space by aligning the time peak such that $t_o = \tau/2$ with $\mathcal{K} = 2/N$ and $\Delta t_{nn} = \tau$, which is a choice for the minimum value of ϱ_W.

If multiple targets are simultaneously present within the TX beamwidth $\vartheta \pm \Delta\vartheta_{3dB}^{TX}$ and fall into the same range cell, their separation is possible only through their Doppler shifts, provided that they are distinct. Otherwise, their mean *RCS* values will add up, causing an increase in *SNR*. However, normally, the radar echo will be perceived as a single target.

The FDA$^{(ds)}$ radar can be focused[1],[2] at a range R_o as illustrated in Fig. 11. For this purpose, we apply a phase to the elements of FDA$^{(ds)}$ via $e^{in\Delta\omega R_o/c}$. This makes the FDA$^{(ds)}$ radar to focus at R_o at a SP time $\tilde{t}_{SP} = t_o$. Range focusing can be used to suppress range-ambiguous and folded clutter, as well as main-lobe jamming interference [4],[5],[6],[7], and [8].

The peak power sustains for a short duration in the vicinity of t_o, and drops to $V_{oF}^2/2$ at $t_o \pm \Delta t_{3db}/2$. Thus, although $V_{oF}^2 > V_{oP}^2$, solid-state linear power amplifiers for the T/R modules of the array elements can still be feasible.

IV. Microwave Breakdown (MB)

The FDA$^{(ds)}$-WF increases the peak power compared to PA. If the radar is implemented on a RAP with T/R modules, it can meet the peak power requirements using the state-of-the-art solid-state power amplifiers. The MB issue in an FDA$^{(ds)}$ radar requires investigation. It has been found that the MB power P_{bd} is proportional to τ and $f_p = 1/T_p$, [11], [12].

$$P_{bd} \propto \eta_{bd}(\tau, f_p) \cong \tau^{-1/3} f_p^{-1/8} \qquad (46)$$

As $\{\tau\downarrow \& f_p\downarrow\}$ have$P_{bd}\uparrow$. Let $\varrho_W \in [2,\ 10]$. We require $V_{oF} < V_{bd}$, where V_{bd} is the MB voltage of the TX system. Also, it is required that $\tau_e^{(ds)} \geq \delta t_{bd}$, where δt_{bd} is the minimum sustaining duration of V_{bd}. In an MB experiment [11], [12] performed at X-band, with $\lambda = 3.3cm$, $\lambda_g/2 = 2.24cm$, a rectangular waveguide (RW) half a guided-wavelength long, $a = 22.86mm$ wide, $d = 0.0965mm$ deep (gap), filled with dry air having a pressure of $760mmHg$ was used. In the MB experiment, the parameters $\tau = 1\mu s$ and $f_p = 0.5kHz$ were used. The resulting values are $\eta_{bd}(1,\ 0.5) = 1.091$ and $P_{bd}(\tau, f_p) = 125kW$. For an FDA$^{(ds)}$ radar, the parameters, $\tau_e^{(ds)} = 3.3\mu s$, $f_p = 10kHz$ and $\eta_{bd}(3.3{,}10) = 0.504$, amounts to $P_{bd}(3.3{,}10) = P_{bd}(1,\ 0.5)\cdot\eta_{bd}(3.3,\ 10)/\eta_{bd}(1,\ 0.5) = 58kW$. We have $E_{bd\,rms} = P_{bd}^{½}\,(0.00133\ a\cdot d\cdot\lambda/\lambda_g\ )^{-½} = 192\ V/mm$ as the MB field strength in a RW [12]. Also, the high-peak-power constraint is mitigated by coherent integration within a pulse-burst and noncoherent integration across multiple bursts.

V. Electronically Steerable PA-FDA$^{(ds)}$ Radar

The concept of FDA$^{(ds)}$ radar shown in Fig. 2b, can also be realised by synthesising a planar RAP by finding the EC of the µsP elements on RAP, such that the FF of RAP acquires almost the same FDA$^{(ds)}$-WF as described in sections II and III. For this purpose, we may use the concept proposed in [13].

TABLE II
Parameters of The Three Positions of a Target in a Beamwidth

ϑ deg	t_o µs	τ	τ_e µs	B_e MHz	t_a t_b µs	$\varrho_W = \frac{V_{oF}^2}{V_{oP}^2}$	Δt_{3dB}^{TX} µs	Δt_{nn}^{TX} µs	$\Delta\vartheta_{3dB}^{TX}$ deg	$\Delta\vartheta_{nn}^{TX}$ deg	$\Delta t_{3dB}^{MF_o}$ µs	$\Delta t_{nn}^{MF_o}$ µs	$\Delta\vartheta_{3dB}^{MF_o}$ deg	$\Delta\vartheta_{nn}^{MF_o}$ deg
ϑ_+ 35.87°	0.703	0.0703	2.34	0.27	0 5.703	4.28	3.19	10	6.27	14.18	2.90	10	5.77	14.00
ϑ 30°	t_o 5	τ 0.5	τ_e 3.33	B_e 0.16	0 10	3.01	3.19	10	5.87	13.26	4.30	10	5.78	13.28
ϑ_- 24.13°	t_{o-} 8.3	τ_- 0.83	τ_{e-} 3.01	B_{e-} 0.21	3.3 10	3.32	3.19	10	5.57	12.58	3.70	10	5.23	12.70

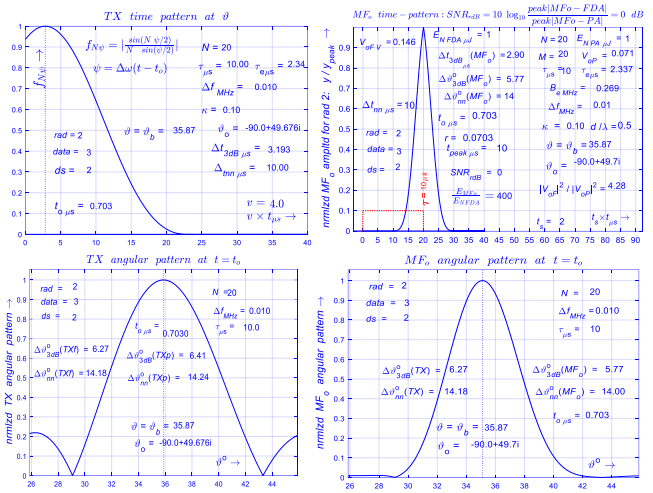

Fig. 8 FDA$^{(ds)}$ $\{t, \vartheta\}$ patterns in a beamwidth for $\vartheta_+ = 35.87°$

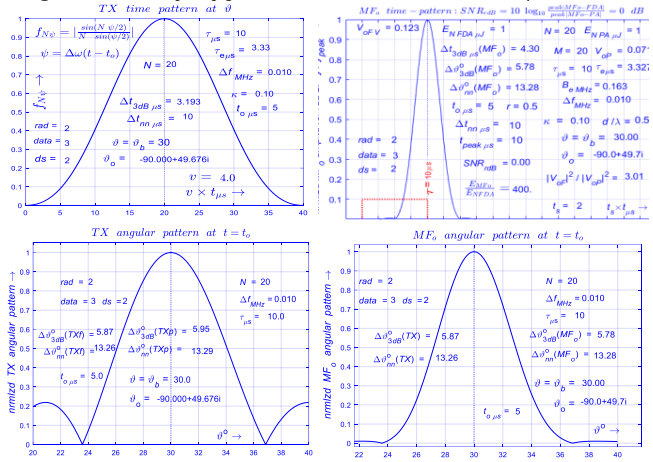

Fig. 9 FDA$^{(ds)}$ $\{t, \vartheta\}$ patterns in a beamwidth for $\vartheta = 30°$

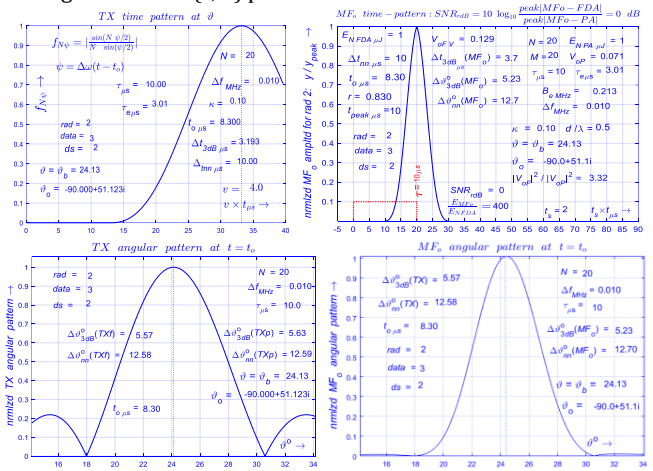

Fig. 10 FDA$^{(ds)}$ $\{t, \vartheta\}$ patterns in a beamwidth for $\vartheta_- = 24.13°$

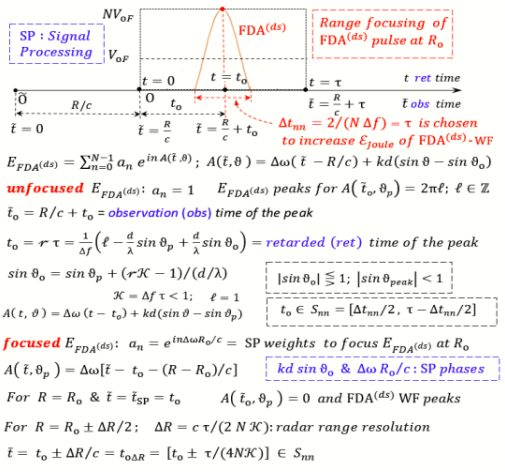

Fig. 11 Range focusing at R_o in an FDA$^{(ds)}$ radar

The method of RAP is described geometrically in Fig. 12. The VS consists of a PaR fed by a PS-FDA$^{(ds)}$ radiator at the focal point. The VS illuminates the surface of RAP within its reactive NF. According to FEP [14], If the size of the RAP, and the number of subapertures (SAP) are sufficiently high, the FF of the RAP is a high-fidelity reproduction of the FF of the PaR.

The chosen PS feed of PaR is a y-polarized FDA source whose electric field for the n^{th} FDA element at S_1 is expressed by [15].

$$\vec{E}_{nP_1} = \mathcal{F}(\vartheta_1)\hat{u}(\varphi)\frac{P(t)}{r_1}\, e^{i\omega_n[t+n\,(d/c)\,sin\vartheta_1]}\, e^{-inkdsin\vartheta_o} \quad (47)$$

$$\mathcal{F}(\vartheta_1) = cos\vartheta_1;\ \vartheta_1 \in [0,\vartheta_m];\ \ \hat{u}(\varphi) = sin\,\varphi\ \hat{\vartheta} + cos\,\varphi\ \hat{\varphi} \quad (48)$$

$t = \tilde{t} - r_1/c$ is the retarded time while $\tilde{t}$ is the observation time at P_1. The fields $\vec{E}_{nP_1}$ satisfy Maxwell's equations owing to the FF approximation $\nabla_n \approx jk_n\hat{r}$, where $k_n = \omega_n/c$. Using physical optics (Huygens' principle) [16], we can show that

$$\vec{E}_{nP_2} = \frac{i}{\lambda}\iint_S \frac{P(t)\ \mathcal{F}(\vartheta_1)}{r_2}\, e^{i\omega t}\, e^{inA(t,\vartheta_1)}\ \vec{S}_{12}\,\frac{ds_1}{r_1} \quad (49)$$

$$A(t,\vartheta_1) = \Delta\omega\, t + \Phi_1\ ;\quad \vec{S}_{12} = \hat{r}_2 \times [\hat{n}_1 \times \hat{u}(\varphi)] \quad (50)$$

$$t = \tilde{t} - r/c;\ r = r_1 + r_2 \ \text{ and } \ \Phi_1 = kd\,(sin\vartheta_1 - sin\vartheta_o) \quad (51)$$

In the FF of PaR $r_2 \gg r_1$ and $r \cong R$. For a high-gain GB of PaR, $\vec{E}_{nP_1}$ should peak at $\vartheta_1 = 0$ and $t = t_o = r\,\tau$, which yields $sin\,\vartheta_o = (r\mathcal{K} - 1)/(d/\lambda)$. Summing $\vec{E}_{nP_2}$ over n, We can express the reflected field at P_2 as

$$\vec{E}_{P_2} = \frac{i}{\lambda}\iint_S \frac{P(t)\ \mathcal{F}(\vartheta_1)}{r_2}\, e^{i\omega t}\ \frac{sin\,(N\,A/2)}{sin(A/2)}\ \vec{S}_{12}\,\frac{ds_1}{r_1} \quad (52)$$

$$A = \Delta\omega\,(t - t_o) + kd\ sin\vartheta_1 \quad (53)$$

Equation (52) shows that the incident field on PaR has the properties of FDA$^{(ds)}$. When focusing at range R_o as in Fig. 11, by $\Lambda_o = e^{in\Delta\omega R_o/c}$, (53) becomes $A = \Delta\omega\,(t_{SP} - t_o) + kd\ sin\vartheta_1$. where $t_{SP} = \tilde{t} - \Delta R/c;\ \Delta R = r - R_o$. The time t_{SP} is the retarded time obtained by SP via the time shift R_o/c in Λ_o. The field $\vec{E}_{nP_2}$ peaks for $t_{SP} = t_o$, which yields $\tilde{t} = t_o + \Delta R/c = t_{o\Delta R} = r_{\Delta R}\,\tau$; $r_{\Delta R} = r + \Delta r;\ \Delta r = \Delta R/(c\,\tau)$. Thus, for $\Delta R \neq 0$, the patterns of PS are shifted in time and angle, as shown in Figs. 14 and 15. The angles $\vartheta_1 < 0$ are for the $-(x,y)z$ plane (Fig. 12). As PaR reflects all the incident fields for $\vartheta_1 \lessgtr 0$, The FF of PaR is proportional to $\tau_e^{(ds)/2}$ (22) with $t_a = 0$ and $t_b = \tau$, for the time WFs corresponding to $|\vartheta_1| < |\vartheta_m|$ in Figs. 14 and 15. It is found that due to the reflection from PaR, The resultant pattern is not much affected by the intra-pulse scanning. Thus, from (52), we can conclude that the FF of PaR possesses all the characteristics of FDA$^{(ds)}$.

In the method of RAP [13], we synthesise a PA antenna with the replacement of SAPs by μsP elements. The EC of the SAP antennas are found by evaluating the NF of PaR on a square RAP tilted by an angle β with respect to PaR. The geometry of PaR and RAP is shown in Fig. 12. In the RAP-FF , the retarded time of a SAP is $t \cong \tilde{t} - R_a/c$ (Fig. 12). It is inferred from the FEP [14] that the FF of RAP is expected to be a high-fidelity reproduction of the FF of PaR. The method of calculating the FF of RAP is given in [13]. Hence, the RAP-FF possesses the properties of an FDA$^{(ds)}$-PaR within the accuracy of the FEP's implementation. The RAP-FF Patterns are displayed in Fig. 13. The isosceles triangular lattice is used to suppress the grating lobes. The final retarded time becomes $t \cong \tilde{t} - R/c$. Notice that the input energy is that captured by RAP.

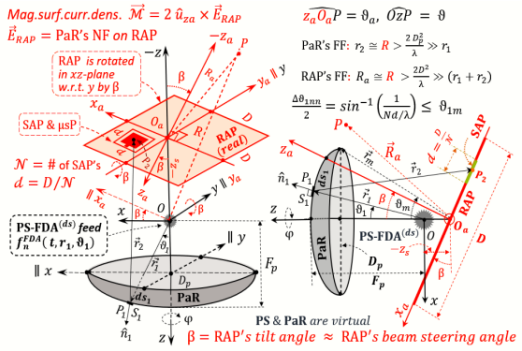

Fig. 12 Realisation of the FDA$^{(ds)}$ radar by the RAP-method

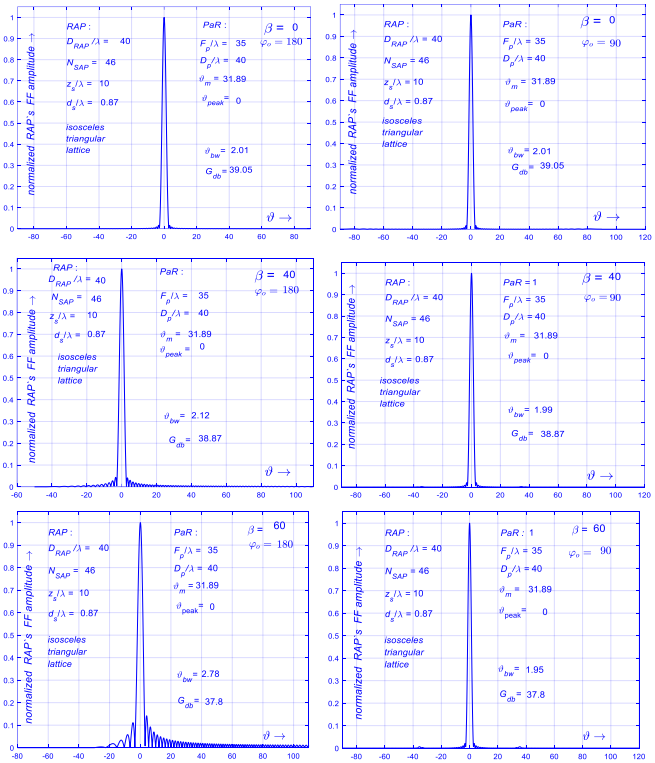

Fig. 13 FF patterns of RAP at t_o for $r = 0.5$ and β ∈ {0,40 60}

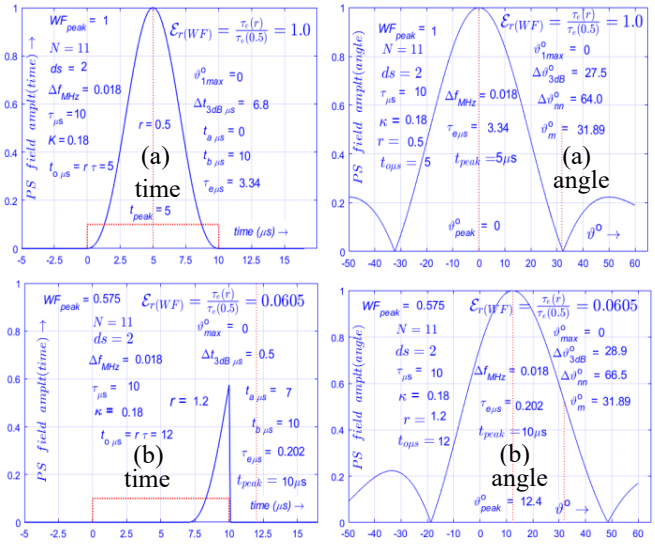

Fig. 14 Time and angle patterns of PS: (a) $\varkappa = 0.5$, (b) $\varkappa = 1.2$

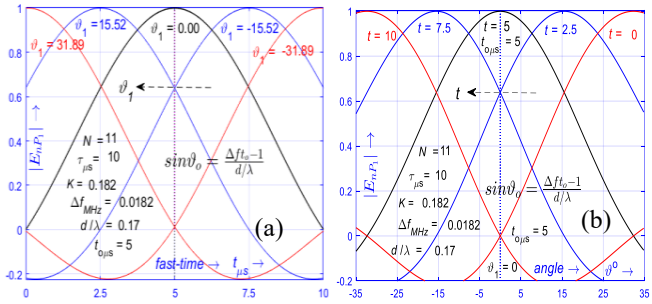

Fig. 15 Parametric time (a) and angle (b) patterns of PS for $\varkappa = 0.5$

VI. Conclusion

In this work, a focusing FDA$^{(ds)}$ is developed to concentrate the radiated energy at a desired angle and range, thereby achieving a high *SNR*, at the expense of continuous scanning.

The theory and numerical simulations indicated that the FDA$^{(ds)}$ radar has an *SNR* performance equivalent to that of PA radars [7], [8], and [10]. Moreover, FDA$^{(ds)}$ radar has range focusing and angle-time coupling advantages [6],[7], and [8].

A spiky (ds ≥ 2) FDA$^{(ds)}$-WF has further advantages for reducing volume clutter, such as rain clutter. Also, if a high range resolution is required, intrapulse phase coding can be used for pulse compression with a smaller number of chips. Moreover, the time side lobes after the pulse compression will be smaller owing to the spiky FDA$^{(ds)}$-WF.

The range-ambiguous and range-folded-over clutter can be suppressed by range focusing of an FDA$^{(ds)}$ radar (Fig. 11). The FDA$^{(ds)}$-WF is almost invariant in form. The range dependence introduces only a time shift, while the TX pulse of duration τ acts as a finite observation window. Therefore, in range focusing, different ranges correspond to observing different portions (main lobe or sidelobes) of the same WF. This selective sampling in fast time constitutes the range–time coupling.

DRFM in an ECM may not work if the range and angle of a target can be correctly estimated before the DRFM takes over [9]. Moreover, the angle focusing, characterised by low sidelobes in both the time and angle domains, provides enhanced robustness to clutter and jamming. Unwanted target angles can be displaced beyond the pulse duration τ by leveraging the time-shift phase term $sin\vartheta_o$, thereby enabling a time-filtering effect, [4], [5], and [8]. An FDA$^{(ds)}$ radar is advantageous for special applications, such as imaging, provided that the high peak-power requirements and the use of linear power amplifiers in the T/R modules of a PA-FDA$^{(ds)}$ are acceptable.

An electronically steerable, high-gain GB FDA$^{(ds)}$ can be realised by synthesising a planar radiating PA, using the method of RAP [13], while retaining the inherent characteristics of a FDA$^{(ds)}$ such as the range-focusing. Moreover, the *SNR* performance of the resulting RAP type PA-FDA$^{(ds)}$ radar is the same as that of an equivalent PA pulsed radar.

Acknowledgment

Rehis of Aselsan supported this work. The authors thank Aselsan and Rehis for the motivation and the support provided.

References

[1] Antonik, P., Wicks, M.C., Griffiths, H.D., and Baker, C.J.: “Frequency Diverse Array of radars”, IEEE Radar Conf. USA, pp.215-217, 2006.

[2] Secmen, M., Demir, S., Hizal, A., Eker, A.T.: “Frequency diverse array antenna with a periodic time modulated pattern in range and angle”. IEEE Radar Conf., USA, pp. 427-430,2007.

[3] Cetiner, R., and Hizal, A., "Discrete Scanning Low Energy-Time Product Linear Frequency Diverse Array Radar," 2019 International Radar Conference (RADAR), Toulon, France, pp. 1-6, 2019.

[4] Wang, W-Q, “Overview of frequency diverse array in radar and navigation applications”, IET Radar Sonar Navig., Vol. 10, Iss. 6, pp. 1001–1012, 2016.

[5] Basit, A., Khan, W., Khan, S., Qureshi, I. M., ‘Development of frequency diverse array radar technology: a review’, IET Radar Sonar Navig., Vol. 12, pp165-175, 2018.

[6] W. Jia, A. Jakobsson, and W.-Q. Wang, "Coherent FDA Receiver and Joint Range–Space–Time Processing," in IEEE Transactions on Antennas and Propagation, vol. 72, no. 1, pp. 745-755, Jan. 2024.

[7] Y. Sun, W. -Q. Wang, M. S. Greco, and F. Gini, "Subspace-Based Range-Angle Tracking for Coherent FDA Radar," ICASSP 2025 - 2025 IEEE International Conference on Acoustics, Speech and Signal Processing (ICASSP), Hyderabad, India, pp. 1-5, 2025.

[8] Y. Sun, M. -J. Jia, W. -Q., Wang, M. S., Greco, F., Gini, and S. Zhang, "Coherent FDA Radar: Transmitter and Receiver Design and Analysis," in IEEE Transactions on Aerospace and Electronic Systems, vol. 61, no. 4, pp. 9154-9170, Aug. 2025.

[9] Wan, P., Weng, Y., Xu, J.and Lio, G., “Range gate pull-off main lobe jamming suppression approach with FDA-MIMO radar: Theoretical Formalism”, Remote Sensing pp. Vol. 14, 1499, pp.1-16, 2022.

[10] Feng, Y.P.F., Kim, S.C., He, Z., Chen, F., L.Chen, and Muhaidat, S., ”Joint PA and FDA Beamforming for radar-communication systems” Journal of Com. and Networks, Vol. 26, No. 5, Oct. pp.554,56,2024.

[11] Ragan G.L., ed. “Microwave transmission circuits”, MIT Radiation Laboratory S. 9, USA, pp.227,242, 1964.

[12] Gilden M., Gould L.,” Handbook on high power capabilities of waveguide systems”, eqn. 14, p.41, Microwave Associates Inc., 1964.

[13] Hizal, A., Cetiner, R., Koc, S., and Yildiz H., "Steerable collimated vortex wave beam generation by a planar radiating aperture as a phased array excited by multi-parameter virtual antenna systems," 19th Euro Con. on Antennas and Propagation (EuCAP), Stockholm, pp. 1-4, 2025.

[14] Rengarajan, S.R. and Rahmat-Samii, Y., "The field equivalence principle: illustration of the establishment of the non-intuitive null fields," IEEE Antenna and Propagation Magazine, vol. 42, no. 4, pp. 122-128, Aug. 2000,

[15] Rahmat-Samii, Y. and Lee,S-W., “Directivity of planar array feeds for satellite reflector applications”, IEEE TAP, vol.31, no.3, pp.463-470,1983.

[16] Clark, R.H. and Brown, J., “Diffraction Theory & Antennas”, John Wiley, 1980.

A 2-D Leaky-Wave Antenna Array for joint sensing, communication and wireless power transfer

Alejandro Gil-Martínez*, Antonio Skarmeta[1], José Luis Gómez Tornero[2]

[1]Departmento de Ingeniería de la Información y las Comunicaciones, Universidad de Murcia, 30100, Murcia, Spain.

[2]Departamento de Tecnología de la Información y las Comunicaciones, Universidad Politécnica de Cartagena, 30202, Cartagena, Spain.

*Corresponding author: alejandrorafael.gil@um.es

***Abstract*— This paper presents a compact two-dimensional (2-D) multibeam leaky-wave antenna (LWA) array conceived as a front-end for integrated sensing and communication (ISAC) and wireless power transfer (WPT) applications. The proposed architecture combines a four-element half-width microstrip leaky-wave antenna (HWM-LWA) array with a low-complexity 4×4 Butler matrix beamforming network, achieving a 2-D scanning over a wide field of view (FoV) with a simple and low-profile planar structure. The antenna operates in the 5 GHz ISM band and provides multi-beam coverage in both elevation and azimuth planes by exploiting the intrinsic frequency dispersion of LWAs together with analog beamforming. Simulation results demonstrate the synthesis of multiple directive beams covering up to 160° × 90° FoV with realized gains above 11.8 dBi, enabling spatial multiplexing for simultaneous communication links, environmental sensing, and directional wireless power delivery. Owing to its compactness, low cost, and passive beam-steering capability, the proposed 2-D multibeam LWA array constitutes a promising candidate for energy-aware ISAC nodes, access points, and smart surfaces in future 5G-Advanced and 6G networks.**

***Keywords*— Localization, Leaky-Wave Antennas, Integrated Sensing and Communication, Wireless Power Transfer.**

I. Introduction

The convergence of wireless communication, environmental sensing, and energy delivery is emerging as a key paradigm for future 5G-Advanced and 6G networks [1]-[3]. Beyond high data-rate connectivity, next-generation wireless systems are expected to natively support localization, radar-like sensing, and energy-aware operation for massive Internet-of-Things (IoT) deployments, autonomous systems, and smart environments [4]. This vision has motivated the rapid development of integrated sensing and communication (ISAC) architectures [5], where a single radio front-end is jointly exploited for data transmission and situational awareness. In parallel, wireless power transfer (WPT) and radio-frequency (RF) energy harvesting are gaining attention as enabling technologies to prolong the lifetime of low-power devices and sensors [6], especially in dense and infrastructure-assisted scenarios.

A central challenge in ISAC and WPT systems lies in the design of antenna front-ends capable of providing high spatial selectivity, wide angular coverage, and multi-beam operation with low hardware complexity and energy consumption. Conventional digital or hybrid phased arrays offer flexible beam steering and beamforming capabilities, but their cost, power consumption, and calibration complexity may limit scalability in dense access points, smart surfaces, and low-cost sensing nodes. As a result, analog and passive multi-beam solutions based on beamforming networks (BFNs) have recently attracted significant interest as energy-efficient alternatives for multi-directional transmission and reception.

Among the different BFN-based solutions, Butler matrices provide a particularly attractive trade-off between complexity, footprint, and beamforming capability, enabling the synthesis of multiple fixed phase gradients with simple planar microwave circuits. When combined with frequency-dispersive radiating structures, such as leaky-wave antennas (LWAs), Butler-matrix-fed arrays can achieve two-dimensional (2-D) beam steering by jointly exploiting phase and frequency scanning, without requiring active phase shifters or large-scale RF chains. In this context, half-width microstrip leaky-wave antennas (HWM-LWAs) have been shown to offer low-profile, low-cost, and highly dispersive radiation characteristics, making them suitable candidates for wide field-of-view (FoV) coverage using narrowband industrial, scientific and medical (ISM) frequency allocations.

From the perspective of ISAC, multi-beam and multi-directional radiation patterns enable simultaneous illumination of different spatial sectors, which is beneficial for multi-user communications, spatial sensing, and direction-of-arrival/departure estimation. From the WPT standpoint, directive and steerable beams allow energy focusing toward selected devices or regions of interest, increasing the RF power transfer efficiency and enabling spatially selective energy delivery. Therefore, a compact 2-D multibeam antenna front-end capable of providing joint frequency–beam-switching scanning constitutes a promising hardware enabler for the joint

realization of communication, sensing, and wireless power transfer functionalities within a unified RF platform.

In this paper, we propose a compact 2-D multibeam antenna architecture based on a four-element HWM-LWA array fed by a 4×4 Butler matrix beamforming network. Operating in the 5 GHz ISM band, the proposed structure enables passive 2-D beam scanning over a wide FoV by combining the intrinsic frequency dispersion of LWAs with multi-port analog beamforming. The resulting antenna front-end can synthesize multiple directive beams covering both azimuth and elevation planes, enabling spatial multiplexing for ISAC links while simultaneously supporting directional RF power delivery for low-power devices. The proposed design is conceived as an early-stage proof-of-concept for ISAC-WPT front-ends, highlighting the potential of frequency–beam switching multibeam LWA arrays as low-complexity alternatives to conventional phased arrays in future energy-aware wireless networks.

II. Antenna Design and Results

The proposed antenna front-end is conceived as a compact two-dimensional (2-D) multibeam antenna enabling joint frequency–port-switching beam scanning for integrated sensing and communication (ISAC) and wireless power transfer (WPT) applications. The overall architecture, depicted in Fig. 1, consists of a four-element half-width microstrip leaky-wave antenna (HWM-LWA) array fed by a low-complexity 4×4 Butler matrix beamforming network (BFN). This configuration enables the synthesis of multiple directive beams in both elevation and azimuth planes by combining the intrinsic frequency dispersion of the leaky-wave radiators with the fixed phase gradients provided by the Butler matrix when it is fed by all the different ports.

Each HWM-LWA element operates as a one-dimensional frequency-scanned radiator, producing directive beams whose pointing angle varies with frequency along one principal plane YZ. By arranging four identical HWM-LWA elements in a linear array and exciting them through the Butler matrix, an additional phase-controlled beam steering is introduced in the orthogonal plane XZ. This hybrid frequency–beam-switching beamforming mechanism enables 2-D beam scanning without the need for active phase shifters or complex RF front-ends, making the proposed structure particularly attractive for low-cost and energy-efficient ISAC and WPT nodes.

The beamforming network topology is based on a conventional 4×4 Butler matrix, whose functional block diagram is shown in Fig. 2. The network is composed of quadrature hybrid couplers, crossover sections, and fixed phase shifters, arranged to provide predefined progressive phase distributions at the output ports depending on the selected input port. By sequentially exciting the different input ports of the Butler matrix, multiple orthogonal phase gradients are obtained across the four antenna elements, resulting in the generation of multiple simultaneous beam directions in the azimuth plane. This multi-port excitation scheme enables the synthesis of a

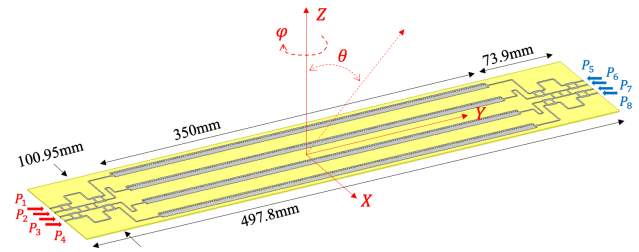

Fig. 1 Proposed leaky-wave antenna array geometry for 2-D ISAC+WPT coverage.

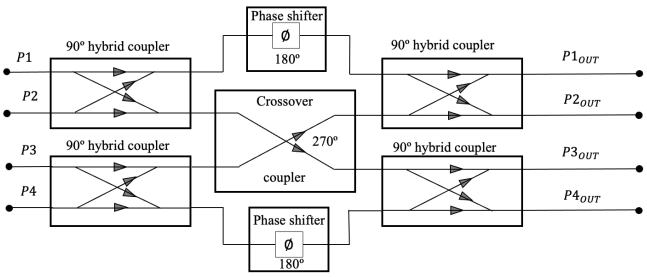

Fig. 2. Designed 4x4 Butler matrix block diagram.

discrete set of directive beams with low mutual coupling and well-defined angular separation, which is well suited for multi-user communication, spatial sensing, and directional energy delivery.

The HWM-LWA elements are designed to operate in the 5 GHz ISM band and to exhibit a controlled frequency dispersion of the dominant leaky mode. This dispersion is exploited to achieve continuous beam scanning in the elevation plane as the operating frequency is varied within the available band. By properly selecting the substrate parameters and the geometrical dimensions of the half-width microstrip structure, the simulated dispersion characteristics provide wide angular coverage within the targeted frequency range. This frequency-scanning capability complements the phase-controlled steering introduced by the Butler matrix, enabling 2-D coverage of the radiated field using only passive microwave components.

From an ISAC perspective, the proposed architecture allows simultaneous illumination of multiple spatial sectors, enabling parallel communication links and angular diversity for sensing and localization. From a WPT standpoint, the generation of multiple directive beams enables spatially selective RF power delivery, which can be exploited to focus energy toward specific devices or regions of interest while maintaining communication and sensing functionality.

The resulting 2-D multibeam radiation characteristics obtained from full-wave simulations are illustrated in Fig. 3, where the synthesized beams jointly cover a wide field of view in both elevation and azimuth planes. These simulated radiation patterns confirm the feasibility of the proposed frequency–beam-switching multibeam LWA architecture as a low-complexity front-end for joint sensing, communication, and wireless power transfer, and motivate further investigation toward system-level integration in future ISAC-WPT platforms.

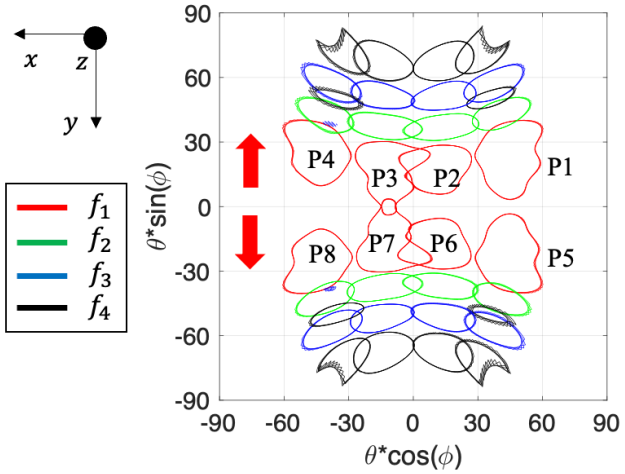

Fig. 3. UV 2-D simulated radiation patterns.

III. Conclusion

This paper has presented a simulation-based study of a compact two-dimensional multibeam leaky-wave antenna array combining a four-element half-width microstrip LWA with a 4×4 Butler matrix beamforming network for joint sensing, communication, and wireless power transfer applications. By exploiting the inherent frequency dispersion of leaky-wave antennas together with passive phase beamforming, the proposed architecture enables wide field-of-view 2-D beam scanning with low hardware complexity and fully planar implementation. The simulated radiation characteristics demonstrate the capability to synthesize multiple directive beams covering both azimuth and elevation planes, supporting spatial multiplexing for ISAC links as well as directional RF energy delivery for low-power devices. These results highlight the potential of frequency–beam-switching multibeam LWA arrays as low-cost and energy-efficient front-ends for future 5G-Advanced and 6G ISAC-WPT platforms, motivating further system-level investigations and experimental validation in future work.

Acknowledgments

A. Gil-Martınez and A. Skarmeta are with the Department of Information and Communication Engineering, Universidad de Murcia, 30100, Spain.

References

[1] W. Chen et al., ”5G-Advanced Toward 6G: Past, Present, and Future,” in *IEEE Journal on Selected Areas in Communications*, vol. 41, no. 6, pp. 1592-1619, June 2023.

[2] W. Saad, M. Bennis and M. Chen, "A vision of 6G wireless systems: Applications, trends, technologies, and open research problems," in *IEEE Network*, vol. 34, no. 3, pp. 134-142, May/June 2020.

[3] T. Jiang et al., “3GPP standardized 5G channel model for IIoT scenarios: A survey,” *IEEE Internet of Things Journal*, vol. 8, no. 11, pp. 8799–8815, 2021.

[4] Y. Cui, F. Liu, X. Jing, and J. Mu, “Integrating sensing and communications for ubiquitous IoT: Applications, trends, and challenges,” *IEEE Netw.*, vol. 35, no. 5, pp. 158–167, Sep./Oct. 2021.

[5] H. Wymeersch et al., “Integration of communication and sensing in 6G: a joint industrial and academic perspective,” in 2021 *IEEE 32nd Annual International Symposium on Personal, Indoor and Mobile Radio Communications (PIMRC),* 2021, pp. 1–7.

[6] Y. Liu, M. Gidlund, H. Wang and G. P. Hancke, "Autonomous networked wireless power transfer for the Internet of Batteryless Things: Future Vision and research opportunities," in *IEEE Wireless Communications*, vol. 32, no. 6, pp. 165-172, Dec. 2025.

Wideband Design of a Breakdown-Safe WR–15 Multilayer Vacuum Window

Olga Basile[1,*], Marco Simone[1], Santi C. Pavone[1], Gino Sorbello[1]

[1]Department of Electrical, Electronics, and Computer Engineering (DIEEI), University of Catania, Via Santa Sofia 64, 95123 Catania, Italy.

*Corresponding author: olga.basile@phd.unict.it

***Abstract*—This paper presents the design of a wideband waveguide vacuum window based on a transfer-matrix formulation. A three-layer dielectric stack for a WR-15 waveguide is synthesized via Particle Swarm Optimization to minimize reflections while imposing a power-handling constraint via a stress coefficient χ, enabling estimation of the breakdown-safe input power.**

***Keywords*— Waveguide vacuum window, multilayer dielectric, wideband design, power handling, particle swarm optimization.**

I. Introduction

Waveguide vacuum windows (WVW) are critical components in microwave tubes when RF power must be transmitted across a vacuum barrier [1]. They are required to exhibit very low insertion loss over the entire operating bandwidth of the waveguide while ensuring adequate mechanical robustness [2]. Examples of WVW application are electron cyclotron resonance heating [3] or electron-positron colliders power sources [4]. Vacuum windows are also employed in cryogenic receiving chains, as in radio astronomy receiving systems [5], [6]. The output window is particularly critical, as it is subjected to combined electrical, thermal, and mechanical stresses. On the vacuum side, multipactor phenomena may occur, leading to electron bombardment, localized heating, RF noise generation, and degradation of the electromagnetic matching. To mitigate these effects, anti-multipactor coatings such as titanium nitride (TiN) are commonly employed [7], [8], [9]. In addition, dielectric losses within the window material can produce significant heating, especially at high power levels, with losses typically increasing as a function of temperature. From a mechanical standpoint, the window must withstand the pressure differential between the vacuum region and the external environment, particularly when the external waveguide is pressurized. Several dielectric materials are adopted for high-power microwave windows, including alumina [8], beryllium oxide [10], and chemical-vapour-deposited (CVD) diamond [11], selected according to their dielectric properties, thermal conductivity, and mechanical strength. The simplest configuration consists of an inductive iris supporting a circular capacitive dielectric disk [12]. Although bandwidth enhancement can be achieved by shaping the aperture (e.g., elliptical geometries), the achievable matching remains inherently narrowband. A second canonical configuration consists of a uniform dielectric slab with relative permittivity ϵ_r inserted into the waveguide. Assuming single-mode propagation and no excitation of higher-order modes, the cut-off frequency in the dielectric-filled section is reduced by a factor $\sqrt{\epsilon_r}$ with respect to the empty waveguide. The impedance discontinuity at the dielectric interfaces produces a non-negligible reflection, which can be evaluated using the modal wave impedance formulation. Even in the case of a half-wavelength thick slab, the achievable fractional bandwidth is typically limited to approximately 10–15% and decreases with increasing ϵ_r [13]. The bandwidth enhancement can be achieved through the use of properly designed multilayer dielectric stacks [14]. In this work, a multilayer vacuum window is designed by means of numerical optimization to maximize performance over the target frequency band. The WVW dielectric profile is designed for a WR–15 rectangular waveguide (50–75 GHz), targeting the widest possible impedance matching bandwidth within the 55–75 GHz range. The structure consists of alternating Quartz and Zirconium dioxide (ZrO_2) dielectric layers, whose thicknesses are treated as optimization variables. Any low thickness layer, if present, is implicited in the proposed electromagnetic model, such as the TiN coating, which is typically below 1 μm (often in the range of 5–10 nm) [9], i.e., much smaller than the electromagnetic skin depth. Therefore, despite its finite conductivity, its effect can be neglected and it can be omitted from the multilayer model. From an electromagnetic standpoint, the multilayer window can be modeled as a cascade of dielectric-filled waveguide sections, each characterized by its modal propagation constant and wave impedance [14]. This can be studied in terms of transmission-matrix formulation, as discussed in Sect. II-A, which provides a framework for the optimization described in the following sections III, IV.

II. Theoretical Background

A. Electromagnetic propagation

Let us consider a rectangular waveguide of broad-wall dimension a operating in the dominant TE_{10} mode (Fig. 1). The longitudinal wavenumber in a homogeneous medium with relative permittivity ε_r (assuming $\mu_r \simeq 1$) is

$$\beta = \sqrt{k_0^2 \varepsilon_r - \left(\frac{\pi}{a}\right)^2}, \qquad k_0 = \frac{\omega}{c_0}, \tag{1}$$

and the corresponding modal impedance for TE modes [15] is

$$Z_{TE} = \frac{\omega\mu_0}{\beta} = \frac{Z_0\sqrt{\mu_r/\epsilon_r}}{\sqrt{1-\left(\frac{f_c}{f}\right)^2}} \tag{2}$$

where Z_0 denotes the free space impedance.

A dielectric section of thickness l_i can therefore be modeled as a transmission-line segment characterized by the propagation constant β_i and the impedance Z_i, with ABCD matrix

$$\mathbf{M}_i = \begin{bmatrix} \cos(\beta_i l_i) & jZ_i \sin(\beta_i l_i) \\ j\dfrac{\sin(\beta_i l_i)}{Z_i} & \cos(\beta_i l_i) \end{bmatrix}. \tag{3}$$

For a multilayer window composed of M dielectric slabs, the overall response is obtained by cascading the individual matrices,

$$\mathbf{M} = \prod_{i=1}^{M} \mathbf{M}_i = \begin{bmatrix} A & B \\ C & D \end{bmatrix}, \tag{4}$$

from which the reflection Γ and transmission τ coefficients are derived [1], [16].

B. Power handling and Breakdown

The dielectric breakdown field E_{bd} is the maximum electric field which an insulating material (dielectric) can withstand before it becomes electrically conductive, i.e. the electric field strength above which an electrical discharge occurs in a material with (traditionally) insulating properties. When the applied electric field exceeds the breakdown threshold ($E > E_{bd}$), charge carriers gain sufficient energy to ionize the medium, initiating an electron avalanche that leads to dielectric breakdown and macroscopic conduction [17]. For air at 1 atm and 20°C, the breakdown field is approximately $E_{bd} \approx 3 \times 10^6$ V/m. In the microwave regime, the breakdown threshold depends not only on frequency, but also on pressure (Paschen-like behavior in gases) and surface conditions [18]. Although E_{bd} is an intrinsic material property independent of the electromagnetic structure, waveguide operation introduces practical limitations. Indeed, local field enhancement due to geometrical discontinuities may cause premature breakdown, gas pressurization increases the threshold, and the power–field relation depends on the modal impedance Z_{TE}, hence on frequency. Under the assumption of a rectangular waveguide operating in its fundamental TE_{10} mode, the maximum power is related to the dielectric strength as

$$P_{\max} = \frac{ab}{4Z_{TE}}|E_{bd}|^2 \tag{5}$$

where a and b are the waveguide transverse dimensions. Therefore, the dielectric strength E_{bd} ultimately limits the power handling capability of the waveguide.

In practical operation, contaminants such as dust, humidity, or metallic surface irregularities may induce local charge accumulation and trigger breakdown below the theoretical threshold. For this reason, a safety factor (SF) is commonly introduced, and the maximum operating field is typically limited to $E_{\max} \approx (0.3 \div 0.5)\, E_{bd}$.

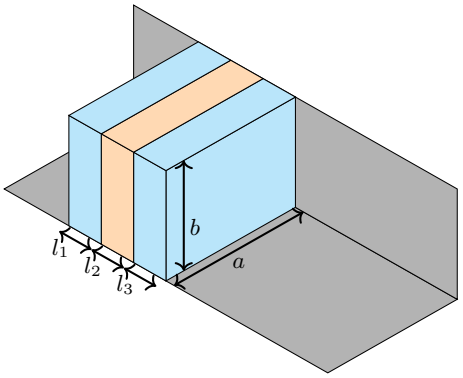

Fig. 1: Waveguide Vacuum Window geometry: multilayer stack of Quartz (cyan) and Zirconium dioxide (orange) (two metallic walls are neglected for a sake of clarity).

III. Design Constraints and Optimization

A. Power Handling Constraint

In high–power WVW operation, the maximum admissible input power is limited by dielectric breakdown. Although the reflection coefficient of a properly designed window is small, any residual reflected wave generates a standing–wave pattern in the input hollow waveguide section. The resulting field maxima may locally exceed the breakdown threshold even when the average transmitted power is below the theoretical limit. It is therefore necessary to evaluate the relationship between the input power and the electric field amplitude in the first hollow waveguide section.

For TE modes, the input power is related to the electric field magnitude as $P \propto |E|^2$, similarly to Eq. (5). Consequently, the power handling is linked to the peak electric field $|E_{\max}|$.

To quantify the electrical stress, a normalized field coefficient is introduced:

$$\chi = \frac{|E_{\max}|}{SF \cdot E_{bd}} \tag{6}$$

where SF is the safety factor. By exciting the structure with $P_{inc} = 1$ W, a reference value χ_{1W} is obtained. The maximum allowed power is given by

$$P_{\max} = \frac{1\ \mathrm{W}}{\chi_{1W}^2} \tag{7}$$

Breakdown may occur in any of the materials forming the WVW, as well as in the surrounding air or vacuum environments. The limiting material is the one exhibiting the highest χ, which is typically the air section upstream the WVW.

B. Waveguide Vacuum Window Architecture and Parameters

The proposed WVW consists of a three–layer dielectric stack inserted inside a WR-15 rectangular waveguide, as

schematically shown in Fig. 1. The electromagnetic parameters of the adopted dielectric materials, a central Zirconium dioxide [19] core sandwiched by two Quartz [20] slabs, are summarized in Table I.

TABLE I: Material parameters

Material	ε_r	$\tan\delta$
Quartz	3.7	2×10^{-4}
Zirconium dioxide	29	1×10^{-4}

C. Optimization Strategy

The WVW has been designed through a numerical optimization routine based on Particle Swarm Optimization [21], where the different dielectric layers are modeled as described in Sect. II-A. The process aims to minimize the reflection in the target frequency band by tuning the layer thickness l_1, l_2, l_3 (Fig. 1). In addition, the power handling is taken into account by considering the field intensity over the whole guiding structure. The WVW thicknesses are synthesized through a physics–driven procedure, structured into the following steps:

1) Definition of geometric and material parameters: ε_r, $\tan\delta$, E_{bd};
2) Solution of the electromagnetic problem under unit–power excitation ($P_{inc} = 1$ W);
3) Evaluation of the peak electric field $E_{\max}$ in each region;
4) Evaluation of the maximum electrical stress $\chi_m = \max(\chi_{1W})$;
5) Scaling of the admissible input power $P_{\max}$ via Eq. (7).

The design simultaneously minimized reflection $|\Gamma| = |S_{11}|$ while keeping the maximum power handling which maintains the field intensity under a desired SF, which has been chosen equal to 0.4. These requirements are coupled since the reflected wave increases the standing–wave ratio and therefore the peak field amplitude. The adopted objective function is

$$F = \frac{\chi_m}{1 - |\Gamma_{\max}|^2} \tag{8}$$

which penalizes both high electric stress and poor impedance matching.

IV. Results and Validation

This section reports the performance of the optimized three-layer Quartz–Zirconium dioxide–Quartz WVW implemented in a WR–15. The optimized thicknesses of the dielectric layers are listed in Table II, for a total equal to 2.078 mm.

TABLE II: Optimized parameters for the WVW

Parameter	Value (mm)
l_1	0.618
l_2	0.843
l_3	0.617

The performance is evaluated over the 55–75 GHz frequency range and compared with a conventional quarter-wave reference design ($\lambda/4-\lambda/2-\lambda/4$) with respect to the central frequency $f = 62.5$ GHz. Figure 2 shows the computed reflection coefficient Γ of the optimized multilayer window (solid line) and of the classical quarter-wave design (dashed line). The optimized solution exhibits a broadband matching behavior with multiple reflection minima. The frequency interval $|\Gamma| \leq -20$ dB is significantly enlarged compared to the conventional design, which provides a narrower matching region. The electric-field magnitude $|E|$ along the propagation in the WVW is reported in Fig. 3. The dashed horizontal line represents the field threshold $E_{\text{lim}} = SF \cdot E_{bd}$ in vacuum WG, which is reached by feeding the wavegude with a input power equal to $P_{inc} = 3885.361\ W$, evaluated via Eq. (7).

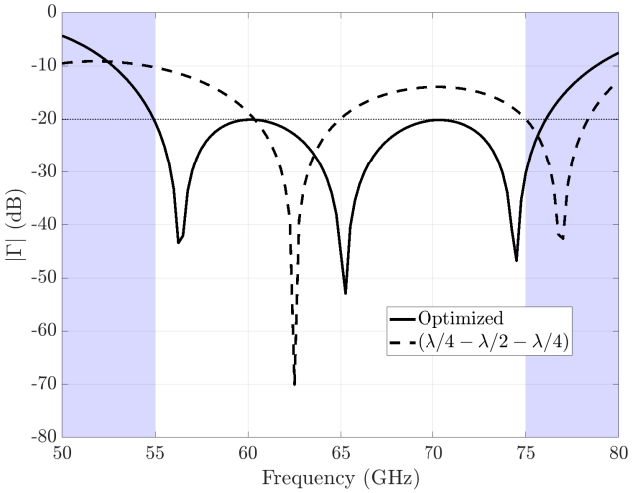

Fig. 2: Reflection coefficient of the optimized WVW (solid line) and of a theoretical $\lambda/4 - \lambda/2 - \lambda/4$ profile (dashed).

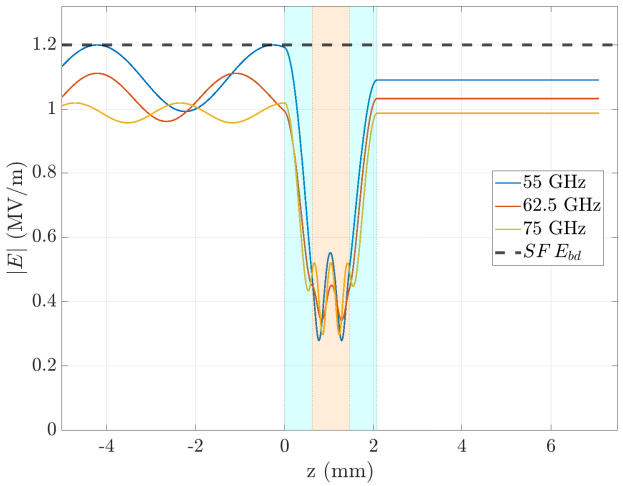

Fig. 3: Electric field amplitude along the waveguide. The WVW section is highlighted in cyan (Quartz) and orange (Zirconium dioxide).

V. Conclusion

A synthesis-driven design procedure for wideband rectangular-waveguide vacuum windows has been presented, based on a transfer-matrix model coupled with Particle Swarm Optimization. Broadband matching is obtained by optimizing the reflection coefficient over the target frequency band, while high-power operation is addressed through a field stress coefficient χ.

The proposed χ-based evaluation enables a direct and quantitative estimation of the breakdown-safe input power, $P_{\max}$, for a given safety factor SF. As a result, the method provides a practical framework to simultaneously achieve wide operational bandwidth and controlled electric-field stress, supporting reliable WVW design under power and matching constraints.

Acknowledgments

This work was supported by the European Union under the Italian National Recovery and Resilience Plan (NRRP) of NextGenerationEU, partnership on "Telecommunications of the Future" (PE0000001- program "RESTART"); the authors acknowledge the ongoing collaboration between the University of Catania and Sicilsat Communications S.r.l.

References

[1] M. E. Hill, R. S. Callin, and D. H. Whittum, "High-power vacuum window in WR10," *IEEE Trans. Microw. Theory Techn.*, vol. 49, no. 5, pp. 994–995, 2001.

[2] A. Kumar and V. Kesari, "Ultra-wideband TE_{01}-mode dielectric window assisted with ring-based meta-surface," *J. Electromagn. Waves Appl.*, vol. 36, no. 17, pp. 2463–2472, 2022.

[3] T. Saito, Y. Kiwamoto, T. Kariya, and S. Miyoshi, "High-power microwave vacuum window of fused quartz in circular waveguide," *Rev. Sci. Instrum.*, vol. 56, no. 5, pp. 764–765, 1985.

[4] S. C. Wang, Z. S. Zhou, Z. J. Lu, *et al.*, "Development of RF windows for 650 MHz multibeam klystron," *Nucl. Sci. Tech.*, vol. 34, no. 9, p. 136, 2023.

[5] G. Valente, T. Pisanu, P. Bolli, *et al.*, "The dual-band LP feed system for the Sardinia radio telescope prime focus," in *Proc. SPIE Mill., Submill., and Far-Infrared Detec. and Instrum. for Astronomy V*, 2010.

[6] A. Navarrini, L. Olmi, R. Nesti, *et al.*, "Feasibility study of a W-band multibeam heterodyne receiver for the Gregorian focus of the Sardinia radio telescope," *IEEE Access*, vol. 10, pp. 26369–26403, 2022.

[7] S. Michizono, A. Kinbara, Y. Saito, *et al.*, "TiN film coatings on alumina radio frequency windows," *J. Vac. Sci. Technol. A*, vol. 10, no. 4, pp. 1180–1184, 1992.

[8] S. U. Thielk, R. Agustsson, P. Carriere, *et al.*, "Evaluation of low-loss alumina material for high-power RF windows," *J. Phys. Conf. Ser.*, vol. 2687, p. 082044, 2024.

[9] W. Kaabi, H. Jenhani, A. Variola, *et al.*, "Titanium nitride coating as a multipactor suppressor on RF coupler ceramic windows," in *Proc. Particle Accelerator Conf. (PAC)*, 2009.

[10] G. Liu, Y. Wang, W. Wang, *et al.*, "Design and measurement of a broadband beryllium oxide window with high power handling capability," *IEEE Trans. Electron Devices*, vol. 68, no. 9, pp. 4711–4716, 2021.

[11] G. Guo, G. Zhang, C. Guo, *et al.*, "Investigation and Batch Fabrication of G-Band Broad Band and Low Loss Monocrystalline Diamond Window for Vacuum Electron Devices," *IEEE Electron Device Lett.*,vol. 45, no. 10, pp. 1981–1984, 2024.

[12] A. S. Gilmour, *Klystrons, Traveling Wave Tubes, Magnetrons, Crossed-Field Amplifiers, and Gyrotrons*. Boston, MA, USA: Artech House, 2011.

[13] A. Staprans, E. W. McCune, and J. A. Ruetz, "High-power linear-beam tubes," *Proc. IEEE*, vol. 61, no. 3, pp. 299–330, 1973.

[14] M.-C. Lin, "A multilayer waveguide window for wide-bandwidth millimeter wave tubes," *Int. J. Infrared Millim. Waves*, vol. 28, no. 5, pp. 355–362, 2007.

[15] S. J. Orfanidis, "Waveguides," in *Electromagnetic Waves and Antennas*. New Brunswick, NJ, USA: Rutgers Univ., 2002, ch. 9, pp. 362–408.

[16] O. Basile, M. Simone, S.C. Pavone, and G. Sorbello "Multi-band Radome Design for Satellite Communication based on Particle Swarm Optimization" accepted in *IET Microwaves, Antennas & Propagation*.

[17] X. Li, J. Wang, Y. Wan, *et al.*, "Meta-Surface-Assisted High-Power Broadband Rectangular TE_{10} Mode Window for Vacuum Electronic Devices," *IEEE Trans. Microw. Theory Techn.*, vol. 73, no. 8, 2025.

[18] J. M. Meek and J. D. Craggs, *Electrical Breakdown of Gases*. New York, NY, USA: Wiley, 1978.

[19] Precision Ceramics, Zirconia (ZrO2)–CeramaZirc™, Material Datasheet, available at https://precision-ceramics.com/wp-content/uploads/Zirconia-Combined-Technical-Data-Sheet.pdf

[20] Saint-Gobain, Quartz, Material datasheet, available at https://www.advanced-ceramic-composites.saint-gobain.com/fr/files/1956/view

[21] J. Robinson and Y. Rahmat-Samii, "Particle swarm optimization in electromagnetics," *IEEE Trans. Antennas Propag.*, vol. 52, no. 2, pp. 397–407, 2004.

Control of Mode Propagation and End-Fire Radiation in Rectangular Waveguides with Metasurface Boundaries

Zisis Foufas[1], Thomas Koschny[2], Odysseas Tsilipakos[1,*]

[1]Theoretical and Physical Chemistry Institute, National Hellenic Research Foundation, Athens GR-11635, Greece

[2]Ames Laboratory—U.S. DOE and Department of Physics and Astronomy, Iowa State University, Ames, Iowa 50011, USA

*Corresponding author: otsilipakos@eie.gr

***Abstract*—We study rectangular waveguides formed by metasurface boundaries made of cut-wire meta-atoms. We find novel opportunities for controlling the mode profile and propagation constant. As an example, we design a waveguide mode converter with gradient walls that shapes the mode profile along propagation from concave, to flat, to convex. Moreover, we demonstrate that an asymmetric mode profile within the waveguide can lead to off-axis radiation from the open waveguide end. We show an example of beam tilting by 12 degrees.**

***Keywords*— Metasurface waveguide boundaries, cut-wire meta-atom, dispersion engineering, mode profile engineering, microwaves.**

I. Introduction

Metasurfaces can be used as waveguide boundaries in order to enable exotic phenomena [1], [2], [3]. We have recently showcased in [4] various exciting possibilities in controlling mode propagation with waveguides comprising electrically- and magnetically-polarizable, dispersive metasurface boundaries. Physically, this is because compared to conventional waveguide boundaries, a general metasurface can provide great versatility in the reflection phase supplied by the boundary and control its dispersion.

Here, we focus on rectangular microwave waveguides and study an implementation based on cut-wire (dogbone) meta-atoms on a standard metal-backed board with $\varepsilon_r = 3.6$ and $\tan\delta = 10^{-2}$ [Fig. 1(a)]. Depending on the cut-wire length L, the dispersion of the fundamental mode (TE_{10}-like, symmetric along x) can be controlled at will. For instance, for an operating frequency of 7 GHz, the three different lengths in Fig. 1(b) lead to a phase advance, $\Delta\phi_z$, of ~ 29, 30.5, and 37.5 degrees, respectively, corresponding to an effective index of 0.86, 0.91, and 1.11. Values of n_{eff} over unity signify a transition to coupled surface states with an exponential decay away from the boundary [4].

II. Control of Mode Profile by Gradient Metasurface Boundaries

Using the aforementioned design principle, we construct a waveguide mode converter which can effectively shape the mode profile along propagation, in this case from concave to flat, to convex, and back again [Fig. 1(c)]. That is, the converter comprises "ramp-up", "constant", and "ramp-down" sections. The proposed metasurface boundary is composed of two identical rows of unit cells [Fig. 1(a)]. The cut-wire length L, which is the main design parameter to control the resonant frequency of the meta-atom, is varied in the waveguide converter every three consecutive cells, thus leading to a piecewise constant approximation of the desired spatial profile with subwavelength segments that are $3a_z$ long. We start from an effective index value that is close to that of a standard metallic waveguide with PEC boundaries and then gradually increase this value to reach unity ("plane wave" with final extent [4]) and surpass it, crossing into the regime of coupled surface states with an exponential decay away from the boundaries. The second part of the structure is mirrored so as to restore the initial wavefront profile. The resulting behavior is verified through full-wave simulations. Specifically, in Fig. 1(c),(d) it is shown how the TE_{10} mode transitions from a sinusoidal concave profile into a flat profile and then a convex one. The configuration of the metasurface boundaries is described in Table I. It respects practical fabrication limitations and achieves mode conversion with negligible reflection ($S_{11} = 0.014$). The absorption is $\sim 55\%$ since the component operates near the resonance frequency of the cut wire meta-atoms, but it can be reduced to $< 10\%$ with high-frequency specialty materials with lower loss tangent.

TABLE I
Configuration of Metasurface Boundaries for Waveguide Mode Converter

Cut-wire length (mm)					
L_1	0.60	L_5	7.09	L_9	7.48
L_2	3.00	L_6	7.29	L_{10}	7.51
L_3	5.50	L_7	7.38	L_{11}	7.53
L_4	6.40	L_8	7.44	L_{12}	7.56

III. Control of End-Fire Radiation

We can also achieve asymmetric mode profiles by using only one metasurface boundary. For instance, this can be

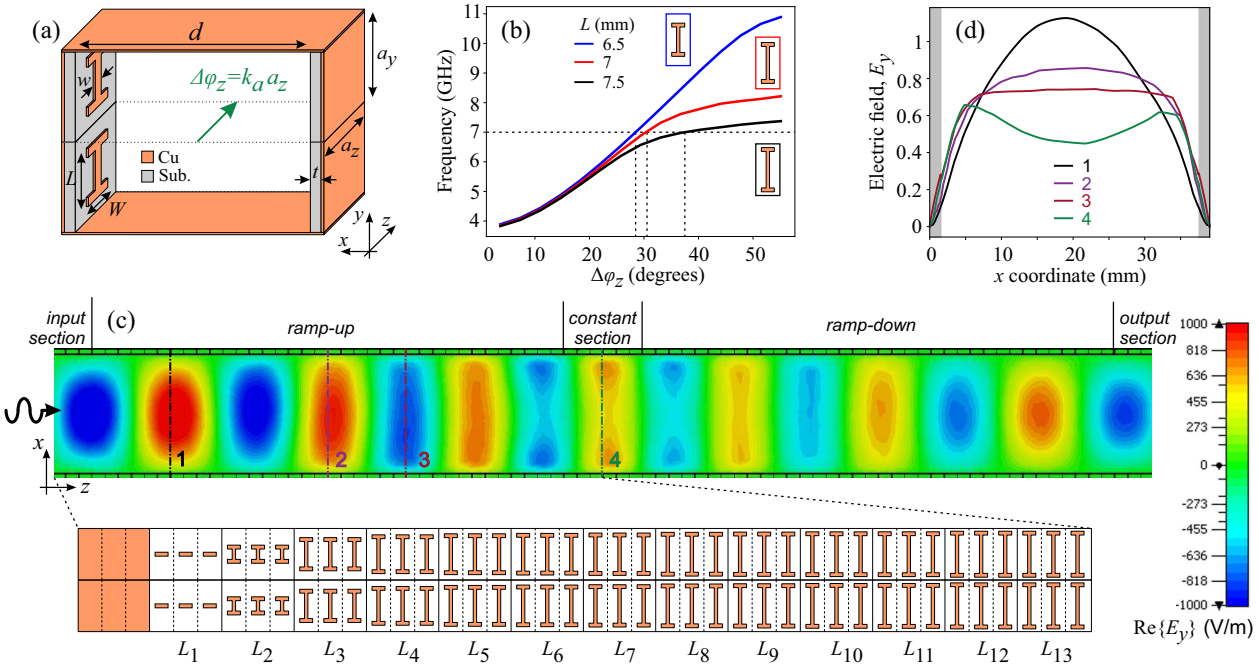

Fig. 1. (a) Periodic waveguide based on cut-wire metasurface boundaries. The geometrical parameters are: $w = 0.6$ mm, $W = 2$ mm, $a_z = 4$ mm, $a_y = 8$ mm, $t = 1.524$ mm, $d = 36$ mm, and the metallization thickness is 35 μm; L is a design parameter. (b) Design process of gradient metasurface boundaries: Dispersion of TE_{10} for different cut-wire lengths. (c) Evolution of mode profile (E_y component) in a waveguide with gradient walls. The field distribution is plotted on the cut-plane $y = a_y/2$. (d) Line plots at different positions along propagation marked in panel (c).

used to tilt the end-fire radiation out of an open waveguide end [5]. More specifically, forcing the propagating mode to become confined to one side of the waveguide leads to a tilted end-fire radiation from the open waveguide end [Fig. 2]. In this case, the adopted distance between waveguide boundaries is $d = 30$ mm; other geometric parameters are as in Fig. 1. In the shown example, the output angle is 12 degrees, as specified with a far field transformation. The configuration of the metasurface boundary (right one) is described in Table II. Again, reflections are quite benign ($S_{11} = 0.155$ corresponding to a reflection of 2.4%) and absorption amounts to 30%.

TABLE II
CONFIGURATION OF METASURFACE BOUNDARY FOR END-FIRE RADIATION EXAMPLE.

Cut-wire length (mm)			
L_1	0.60	L_5	7.42
L_2	5.50	L_6	7.48
L_3	6.92	L_7	7.53
L_4	7.30	L_8	7.57

IV. CONCLUSION

We have presented a rectangular waveguide with metasurface boundaries that can shape the mode profile and propagation constant of the supported modes. We have exploited this versatility to design a waveguide mode converter and a beam steering component.

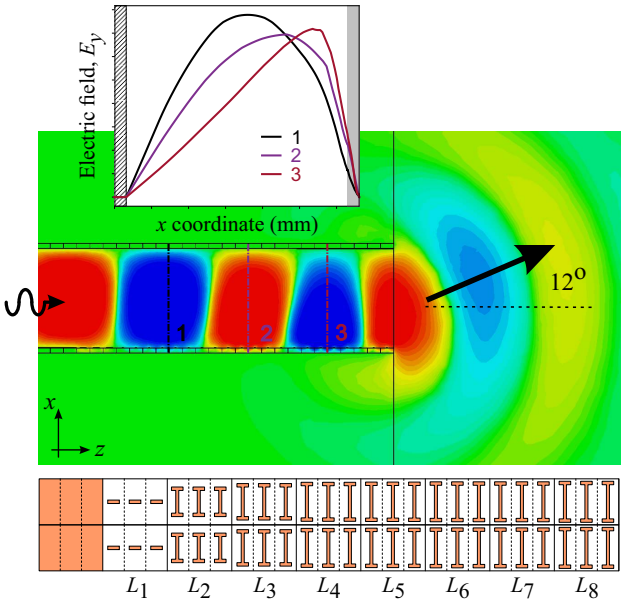

Fig. 2. Tilting of end-fire radiation by an asymmetric gradient boundary. Distribution of E_y component (real part) plotted on the cut-plane $y = a_y/2$. Top inset: Line plots at different positions along propagation indicating that the mode profile becomes highly asymmetric. Bottom inset: Configuration of the right metasurface wall.

ACKNOWLEDGMENTS

Work at Ames National Laboratory was supported by the U.S. Department of Energy (DOE), Basic Energy Sciences,

Division of Materials Sciences and Engineering, under Contract No. DE-AC02-07CH11358.

REFERENCES

[1] A. Ohadi and G. V. Eleftheriades, "Fixed-frequency beam-steering using slotted waveguide with tunable impedance walls," *IEEE Open Journal of Antennas and Propagation*, vol. 2, pp. 978–990, 2021.

[2] G. Valerio, Z. Sipus, A. Grbic, and O. Quevedo-Teruel, "Accurate equivalent-circuit descriptions of thin glide-symmetric corrugated metasurfaces," *IEEE Transactions on Antennas and Propagation*, vol. 65, no. 5, pp. 2695–2700, May 2017.

[3] Z. Li, M.-H. Kim, C. Wang, Z. Han, S. Shrestha, A. C. Overvig, M. Lu, A. Stein, A. M. Agarwal, M. Lončar, and N. Yu, "Controlling propagation and coupling of waveguide modes using phase-gradient metasurfaces," *Nature Nanotechnology*, vol. 12, no. 7, pp. 675–683, Apr. 2017.

[4] O. Tsilipakos and T. Koschny, "Shaping the profile and dispersion of waves guided between spatiotemporally dispersive, electrically and magnetically conductive metasurface boundaries," *IEEE Transactions on Antennas and Propagation*, vol. 72, no. 8, pp. 6472–6480, 2024.

[5] ——, "Controlling the mode profile, dispersion, and end-fire radiation in parallel-plate waveguides with metasurface boundaries," in *2025 Nineteenth International Congress on Artificial Materials for Novel Wave Phenomena (Metamaterials)*, 2025, pp. X–336–X–338.

A Preliminary Study on Multipath-Based Techniques for Radar Imaging

A. Cuccaro [1], A. Dell'Aversano [1], L. Di Donato [2], S. Solimene [1]
[1]Department of Engineering, University of Campania L Vanvitelli, Italy
[2]Department of Electrical, Electronics and Computer Engineering, University of Catania, Italy
*Corresponding author: angela.dellaversano@unicampania.it

***Abstract*—This paper presents a simple backpropagation-based radar imaging method that exploits single- and double-bounce wall reflections to estimate wall position and improve imaging in multipath indoor environments. By modeling propagators to separate LoS and NLoS components, it enables joint wall localization and imaging with low computational cost and strong robustness.**

***Keywords*— Radar Imaging, Multipath Exploitation, Back-propagation.**

I. Introduction

Radar and microwave imaging play a key role in modern and future wireless systems, supporting applications such as occupancy monitoring, density estimation, automotive radar, and emerging Integrated Sensing and Communication (ISAC). In many practical scenarios—particularly indoor and automotive environments—the propagation medium is characterized by strong multipath, clutter, and shadowing effects. These phenomena deteriorate imaging quality, target discrimination, and reduce localization accuracy, especially when communication and sensing functionalities must coexist within shared spectral and hardware resources [1], [2].

Existing multipath-aware radar imaging techniques can be broadly classified into two categories. The first aims at suppressing multipath contributions, treating them as unwanted distortions of the line-of-sight response [3], [4]. The second class instead exploits multipath propagation, modeling reflections as virtual transmitters or receivers to enhance angular resolution, enable non-line-of-sight imaging, and improve target observability in occluded regions [5], [6], [7] or in presence of reflecting surfaces [8]. However, many exploitation-based approaches rely on prior knowledge of the environment (e.g., wall geometry or Green's functions), resulting in high computational complexity and limited robustness in dynamic or partially unknown scenarios [9], [10], [11]

These limitations motivate the development of imaging strategies capable of handling multi-path without requiring detailed a priori information on the environment.

II. Methods

A. Forward modelling

The 2D forward scattering model for a multistatic linear array is considered. The array, composed of (M) elements placed along the (x)-axis, probes a rectangular region of interest (RoI) located between two infinite walls at $(x = \pm a)$. Wave propagation is modeled in the frequency domain using the 2D free-space Green's function. To account for wall reflections, a mirror-image approach is introduced: each physical sensor is associated with virtual sensor obtained through reflections across the two walls. This allows multipath propagation to be interpreted as line-of-sight (LoS) propagation from virtual transmitter/receiver positions.

Propagation paths are classified through TX/RX label pairs, (ℓ_t, ℓ_r), representing direct paths, single- and double-bounce reflections (on transmit or receive) on the same wall, see Fig 1. Cross-wall double reflections are neglected. Under the Born single-scattering approximation, the total scattered field is expressed as the superposition of seven path contributions, each modeled as an integral over the RoI of the target reflectivity multiplied by a path-dependent propagator and amplitude terms, i.e.

$$E^s(\mathbf{s}_m, f) \simeq \sum_{p(\ell_t,\ell_r)=1}^{7} \int_\Omega \rho(\mathbf{r})\, A_p(f; \mathbf{s}_m, \mathbf{r}) \mathcal{G}_p\big(k; \mathbf{r}, \mathbf{s}_m\big)\, d\mathbf{r}, \tag{1}$$

where the summation idex corresponds to the path combination. The amplitude factor $\rho(\mathbf{r})$ takes the reflectivity of the target, while the $A_p(f; s_m, \mathbf{r})$ takes into account the wall Fresnel coefficients, antenna patterns and incidence angles, as well as possibly non idealities introduced in the scattering process.

B. Inverse Modeling and Image Indicator

The first step of the proposed method is the estimation of the wall abscissa. To cope with this goal, we consider the standard back-propagation operator, i.e.

$$I_p(\mathbf{r}) = \sum_{m=1}^{M} \int_B \overline{\mathcal{G}_p\big(k; \mathbf{r}, \mathbf{s}_m\big)}\, E^s(\mathbf{s}_m, f) df \tag{2}$$

as applied to the direct path, let say $I_0(\mathbf{r})$, and the backpropagation of the double bounce reflection path, let say $I_5(\mathbf{r})$ and $I_6(\mathbf{r})$ obtained using the virtual array as parametrized by the wall abscissa.

We start by selecting the brightest pixels in the RoI Ω for each reconstructions by means of a percentile threshold and then defining a binary masks. We then quantify overlapping

using standard set–similarity indices. In particular, we use the intersection over union Jaccard index and Dice index, i.e.,

$$J(a) = \frac{\sum_\Omega |I_0^T \cap I_5^T \cap I_6^T|}{\sum_\Omega |I_0^T \cup I_5^T \cup I_6^T|}, \tag{3}$$

$$D(a) = \frac{2\sum_\Omega |I_0^T \cap I_5^T \cap I_6^T|}{\sum_\Omega |I_0^T| + \sum_\Omega |I_5^T| + \sum_\Omega |I_6^T|}, \tag{4}$$

where the upper script T represents a thresholding of the backpropagation maps followed by a binary map conversion. Finally, the wall abscissa is obtained as the maximum value of an objective function which is given by the weighted sum of the two similarity index, i.e.,

$$\hat{a} = \arg\,\min_a\{(\eta-1)D(a) - \eta J(a)\}. \tag{5}$$

It is to be noted that in the case of symmetric walls, only I_0 and I_5 or I_0 and I_6 can be exploited. On the other side, for asymmetric walls I_0 and I_5 is processed to estimate the rightmost wall and I_0 and I_6 the leftmost one.

Once the wall abscissa has been determined according to the above procedure, image formation can be obtained by summing incoherently or coherently the single backpropagation contribution related to the different paths. In this case, we use a coherent weighted sum to define the image indicator. In practice, the amplitude of coherent sum of the different backpropagation NLoS paths is multiplied by the amplitude of the LoS backpropagation. The weighted sum avoids partial or total destructive interference between the complex I_p maps, and amplitude mismatch compensation between the different paths. On the other hand, the multiplication by $|I_0|$ is introduced to avoid (or at least to mitigate) as much as possible artifacts due to non-uniform k-space coverage and improve resolution by reducing the level of side-lobes and possible pseudo-gratings. The proposed indicator reads as

$$\Lambda(\mathbf{r}) = |I_0(\mathbf{r})| \cdot |\sum_{p=1}^{\text{NLoS paths}} u_p v_p I_p(\mathbf{r})|. \tag{6}$$

wherein u_p and v_p are two weighting used to mitigate the drawbacks of the backpropagation coherent sum mentioned above.

III. Results and Discussion

More theoretical details and results against both data model and numerical full-wave simulation will be shown at the conference to corroborate the effectiveness of the proposed method.

Acknowledgments

This work was supported in part by the European Union through the Italian National Recovery and Resilience Plan (NRRP) of NextGenerationEU, Partnership on "Telecommunications of the Future" (Program "RESTART") under Grant PE0000001.

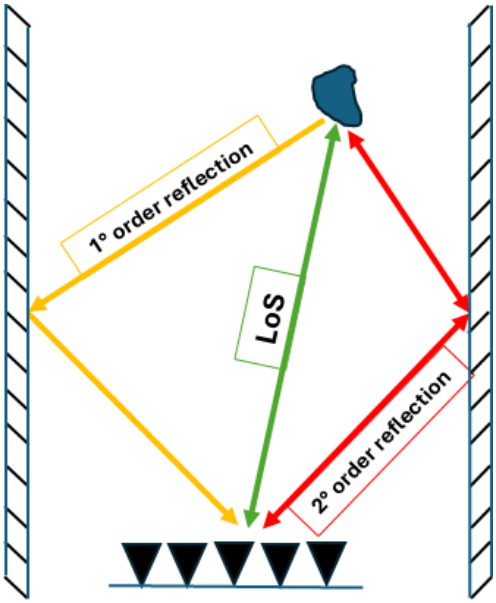

Fig. 1. Geometry of the considered wall indoor multipath affected scenario. The arrows' direction indicate allowed propagation paths, i.e. one-way two-way. The red and yellow paths must be duplicated symmetrically for both walls.

References

[1] D. Zhang, Y. Cui, X. Cao, N. Su, Y. Gong, F. Liu, W. Yuan, X. Jing, J. A. Zhang, J. Xu *et al.*, "Integrated sensing and communications over the years: An evolution perspective," *IEEE Communications Surveys & Tutorials*, 2026.

[2] A. Liu, Z. Huang, M. Li, Y. Wan, W. Li, T. X. Han, C. Liu, R. Du, D. K. P. Tan, J. Lu *et al.*, "A survey on fundamental limits of integrated sensing and communication," *IEEE Communications Surveys & Tutorials*, vol. 24, no. 2, pp. 994–1034, 2022.

[3] R. Feng, E. De Greef, M. Rykunov, S. Pollin, A. Bourdoux, and H. Sahli, "Multipath ghost recognition and joint target tracking with wall estimation for indoor mimo radar," *IEEE Transactions on Radar Systems*, vol. 2, pp. 154–164, 2024.

[4] J.-K. Park, J.-H. Park, and K.-T. Kim, "Multipath signal mitigation for indoor localization based on mimo fmcw radar system," *IEEE internet of things journal*, vol. 11, no. 2, pp. 2618–2629, 2023.

[5] R. Solimene and A. Cuccaro, "Back-propagation imaging by exploiting multipath from point scatterers," *Inverse Problems*, vol. 33, no. 10, p. 105010, 2017.

[6] Y. Lin, X. Qiu, Y. Luo, and C. Ding, "Multipath exploitation: Non-line-of-sight target relocation in array-insar 3-d imaging," *IEEE Transactions on Geoscience and Remote Sensing*, vol. 62, pp. 1–14, 2024.

[7] J. Chen, Y. Zhang, H. Li, P. Wu, S. Guo, and G. Cui, "Ultrawideband tomographic imaging in multipath-rich environment," *IEEE Geoscience and Remote Sensing Letters*, vol. 19, pp. 1–5, 2021.

[8] M. A. Maisto, R. Dima, L. Di Donato, A. Dell'Aversano, R. Solimene, and A. Cuccaro, "Linear one-dimensional inverse profiling: the role of a perfect reflecting plane in the background," *Journal of the Optical Society of America A*, vol. 42, no. 8, pp. 1191–1205, 2025.

[9] G. Gennarelli and F. Soldovieri, "A linear inverse scattering algorithm for radar imaging in multipath environments," *IEEE Geoscience and Remote Sensing Letters*, vol. 10, no. 5, pp. 1085–1089, 2013.

[10] H. Suenobu, S. Kidera, T. Nakanishi, R. Kobayashi, Y. Nishioka, and Y. Inasawa, "Multipath exploitation-based linearized inverse scattering method for non-line-of-sight indoor imaging of pec objects," *IEEE Journal of Selected Topics in Applied Earth Observations and Remote Sensing*, vol. 18, pp. 6694–6709, 2025.

[11] Q. Tang, J. Li, L. Wang, Y. Jia, and G. Cui, "Multipath imaging for nlos targets behind an l-shaped corner with single-channel uwb radar," *IEEE Sensors Journal*, vol. 22, no. 2, pp. 1531–1540, 2021.

Time-Modulated Metasurface-Based Corner Reflector for Radar Target Feature Manipulation

Haoran Han[1,2,3], Jiwei Zhao[1,2,3], Huan Lu[1,2,3], Peixuan Zhu[1,2,3], Rongrong Zhu[4], Bin Zheng[1,2,3*]

[1]Interdisciplinary Center for Quantum Information, State Key Laboratory of Modern Optical Instrumentation, ZJU-Hangzhou Global Scientific and Technological Innovation Center, Zhejiang University, Hangzhou 310027, China
[2]International Joint Innovation Center, Key Lab. of Advanced Micro/Nano Electronic Devices & Smart Systems of Zhejiang, The Electromagnetics Academy at Zhejiang University, Zhejiang University, Haining 314400, China
[3]Jinhua Institute of Zhejiang University, Zhejiang University, Jinhua 321099, China
[4]School of Information and Electrical Engineering, Hangzhou City University, Zhejiang 310015, China
*Corresponding author: zhengbin@zju.edu.cn

***Abstract*— To overcome angular and polarization sensitivity in radar countermeasures, this paper combines time-modulated metasurfaces with corner reflectors. This approach generates Doppler frequency components across wide angles. By applying fast and slow-time modulations, the system creates effective interference strips in SAR imaging, demonstrating significant value for passive electronic countermeasures.**

***Keywords*— time-modulated metasurface, Synthetic Aperture Radar jamming, passive electronic countermeasures.**

I. Introduction

With the evolution of radar sensing toward multi-dimensional intelligence and cross-domain coordination, the on-demand manipulation of electromagnetic responses has become a critical imperative. However, current countermeasures face significant limitations. Active jamming, while proactive, relies heavily on real-time reconnaissance and substantial computational resources, carrying inherent risks of self-exposure and high costs that restrict deployment on expendable platforms[1-3]. Conversely, passive jamming offers covertness but is constrained by static physical structures. Its inability to adapt to varying radar waveforms or observation geometries fails to meet the requirements of dynamic electronic warfare[4,5]. Consequently, there is an urgent need to explore a novel, flexibly reconfigurable approach to overcome these dual bottlenecks.

Electromagnetic metamaterials consist of a series of periodically arranged sub-wavelength units, which can generate electromagnetic properties that cannot be formed by natural materials. Due to the unique electromagnetic wave modulation capability of electromagnetic metamaterials, they have been widely concerned and researched by many scholars. Therefore, electromagnetic metamaterials have been widely designed and applied in many aspects, such as target stealth, electromagnetic shielding, beam modulation and so on[6-11]. As a hotspot of electromagnetic metamaterials research, active electromagnetic metasurface have attracted extensive research due to their reconfigurable ability to realize real-time electromagnetic wave manipulation under external excitation[12].

Time-modulated metasurfaces (TMMs) have emerged as a promising solution, introducing temporal coding to generate frequency harmonics and manipulate spectral characteristics[13,14]. While TMMs have been extensively studied in wireless communications, their potential in radar countermeasures remains underexplored. A critical limitation is that planar metasurfaces often suffer from performance degradation under oblique incidence, limiting their angular stability[15,16]. In contrast, corner reflectors are the standard for passive jamming due to their strong, wide-angle backscattering, yet they lack the capability for real-time modulation. Thus, the integration of TMMs with CRs presents a unique opportunity to combine spectral reconfigurability with angular robustness.

In brief, the combination of time-modulated metasurface s and corner reflectors plays an extremely important role in the development of radar electronic countermeasures. In this paper, based on the flexibility of temporal metasurface modulation and the scattering characteristics of a corner reflector, a time-modulated corner reflector is proposed, which is able to manipulate the spectral distribution of the backward reflected wave by real-time modulation of the incident wave through the metasurface attached to the corner reflector; And the wide-angle domain stability of the corner reflector improves the scattering function of the time-modulated metasurface. Based on this time-modulated angular reflector, this paper gives five time-modulation modes in detail and gives the SAR image after the interference, which realizes different target feature

transformation functions.

II. System Design and Working Principle

The time-modulated corner reflector comprises an active reconfigurable metasurface integrated onto the facets of a trihedral corner reflector and controlled by an FPGA circuit, where unit cells embedded with PIN diodes are toggled between conductive and cutoff states via feeder lines.

These states, driven by high ("1") and low ("0") control signals respectively, correspond to a reflection phase difference of 180°, thereby realizing 1-bit phase quantization. By applying specific time-domain control sequences to the PIN diodes to modulate the reflection coefficient $\Gamma(t)$, the system induces Doppler shifts and harmonic generation within the reflected spectrum; consequently, the pulse compression of these modulated echoes leads to specific, controllable transformations of the target's image features in the synthetic aperture radar (SAR) domain.

III. Temporal Modulation Strategies and SAR Signature Synthesis

The core contribution of this work is the design of five distinct temporal modulation modes to orchestrate versatile radar target feature transformations.

Mode 1 employs uniform fast-time square-wave modulation within each pulse duration, generating symmetric harmonic sidebands that manifest as paired ghost targets along the range direction.

Mode 2 utilizes slow-time periodic intermittent modulation by alternating between static and modulated pulse blocks, which creates discrete interference strips along the azimuth direction via a periodic weighting of the synthetic aperture.

Mode 3 introduces fast-time uniform sequence coding, applying complex binary sequences to every pulse to synthesize sophisticated deceptive signatures or smearing effects in the range profile.

Mode 4 extends this to the slow-time domain through periodic intermittent sequence coding, modulating the target's Doppler history to produce high-density, multi-dimensional false targets that disperse interference energy across both range and azimuth.

Mode 5 implements stochastic modulation using random bit streams to destroy phase coherence, effectively diffusing the focused energy of the target into a noise-like floor to achieve target feature suppression.

IV. Conclusion

This work validates a phase-reconfigurable time-modulated corner reflector capable of flexible SAR jamming. By switching between the five proposed modulation modes, the system can adaptively transition between generating deceptive ghost targets (Modes 1-4) and suppressing target features via noise-like jamming (Mode 5). This approach offers a promising direction for wide-angle, low-cost, and passive electronic countermeasures.

References

[1] Talati S, EtezadiFar P. Electronic attack on radar systems using noise interference[J]. Majlesi Journal of Mechatronic Systems, 2021, 10(3): 7-11.

[2] Ning W, Haibing F, Danyang L I, et al. Smart Jamming Method for SAR Multiple Areas Based on Noise Convolutional Modulation[J]. Modern Defense Technology, 2024, 52(4): 117.

[3] Feng D, Xu L, Pan X, et al. Jamming wideband radar using interrupted-sampling repeater[J]. IEEE Transactions on Aerospace and Electronic Systems, 2017, 53(3): 1341-1354.

[4] Lin G A N, Jianbing L I, Kunlong Y, et al. Research on the motion and scattering characteristics of intermittent long chaff[J]. CHINESE JOURNAL OF RADIO SCIENCE, 2023, 38(1): 114-122.

[5] Kim S H, Lee S Y, Zhang Y, et al. Carbon-based radar absorbing materials toward stealth technologies[J]. Advanced Science, 2023, 10(32): 2303104.

[6] Chen H, Wu B I, Zhang B, et al. Electromagnetic wave interactions with a metamaterial cloak[J]. Physical Review Letters, 2007, 99(6): 063903.

[7] T. J. Cui, M. Q. Qi, X. Wan, J. Zhao, Q. Cheng. Coding metamaterials, digital metamaterials and programmable metamaterials. Light: Science & Applications 3, e218, 2014.

[8] Bai L, Liu Y K, Xu L, et al. A smart metasurface for electromagnetic manipulation based on speech recognition[J]. Engineering, 2023, 22: 185-190.

[9] Y. Zou, X. Kong et al. A slot antenna array with reconfigurable RCS using liquid absorber. IEEE Transactions on Antennas and Propagation 70, 6095–6100, 2022.

[10] Yu H, Cao X, Gao J, et al. Design of a wideband and reconfigurable polarization converter using a manipulable metasurface[J]. Optical Materials Express, 2018, 8(11): 3373-3381.

[11] H. Li, K. Luo, D. P. Tsai, Y. Li, L. Dou et al. Broadband, wide-angle, and versatile metasurface illusions with inverse synthetic aperture radar imaging. Advanced Science 12, 2416172, 2025.

[12] Wu Z, Grbic A. Serrodyne frequency translation using time-modulated metasurfaces[J]. IEEE Transactions on Antennas and Propagation, 2019, 68(3): 1599-1606.

[13] Zhang X G, Sun Y L, Yu Q, et al. Smart Doppler cloak operating in broad band and full polarizations[J]. Advanced Materials, 2021, 33(17): 2007966.

[14] W. Zhou, S. Zhu, Z. Zhang, R. Zhu, B. Chen, J. Zhao, B. Zheng. Time-varying metasurface driven broadband radar jamming and deceptions. Optics Express 32, 17911–17921, 2024.

[15] S. Yu, D. Guan, H. Xu, Z. Yang, Z. Liu, Y. Liu. A dual-metasurface based imaging radar deception jammer with angular adaptability and scattering enhancement. IEEE Transactions on Antennas and Propagation 72, 5261–5272, 2024.

[16] Y. Chen, J. Liao, H. Zhu, J. Luo, X. Ma, C. Huang, X. Luo. Broadband spatio-temporal modulated metasurface for multifunctional radar camouflage. Laser & Photonics Reviews, e01607, 2025.

A Wideband Fast-response Energy Selective Surface

Jinghao Lv[1,2,3] , Jiwei Zhao[1,2,3], Haoran Han[1,2,3], Huan Lu[1,2,3] and Bin Zheng[1,2,3,*]

[1]The username can contain only lower-case alphanumeric characters, underscores, and hyphens, and must begin and end with an alphanumeric character.
[2]International Joint Innovation Center, Key Lab. of Advanced Micro/Nano Electronic Devices & Smart Systems of Zhejiang, The Electromagnetics Academy at Zhejiang University, Zhejiang University, Haining 314400, China.
[3]Jinhua Institute of Zhejiang University, Zhejiang University, Jinhua 321099, China.
*Corresponding author: zhengbin@zju.edu.cn

***Abstract*— This paper introduces a wideband energy-selective surface (ESS) based on diode-integrated metasurface units in a grid topology. It enables adaptive, power-dependent shielding from 1.68 to 5.97 GHz, ensuring low-power signal transmission while reflecting high-power microwaves with a fast response for effective electromagnetic protection.**

***Keywords*— metasurfaces, energy selective, adaptive response.**

I. Introduction

The rapid development of electronic technology has resulted in the miniaturization, multi-functionality, and low power consumption of electronic devices, but it has also made high-precision integrated circuits more vulnerable. When a part of a system encounters an external electromagnetic pulse (EMP), especially a high-power microwave (HPM) attack, it can lead to severe damage to the device's functionality and even cause cascading failures, ultimately disabling the entire system[1-3]. Therefore, in recent years, electromagnetic protection technology has gained significant attention and been researched globally[4,5].

Current protective measures against strong electromagnetic threats primarily rely on traditional "back-channel" techniques such as filtering, shielding, and grounding. While these methods are relatively easier to implement at the circuit design level, they often significantly increase system complexity and design difficulty. As for the "front-channel" through which electromagnetic energy directly intrudes, existing technologies commonly employ solutions such as adding high-power limiters[6-9] or attenuators at the front end. Although such solutions can provide some attenuation of strong currents, they often cause severe distortion of normal signals, affecting communication quality. If frequency selective surfaces (FSS) or bandpass filters are used for out-of-band isolation[11-15], their fixed operating frequency bands and lack of adaptive capability make them ineffective against strong electromagnetic pulse threats within the passband, revealing clear protective limitations.

In 2009, Liu's team from the National University of Defense Technology proposed the concept of an energy-selective surface (ESS) to address the limitations of traditional protection methods[16-20]. An ESS utilizes nonlinear devices to respond to electromagnetic fields at different power levels, providing adaptive protection against both high- and low-power electromagneticwaves.It exhibits a passband for low-energy signals and a stopband for high-energy signals within specific frequency bands.Based on the principles of frequency-selective surfaces,an ESS not only provides effective shielding from high-power electromagnetic waves but also filters out out-of-band noise,offering dual protection in both the energy and frequency domains.

However, existing ESS technologies still exhibit notable limitations, primarily characterized by narrow transmission bandwidth and slow response times, making it difficult to meet the demand of modern electronic devices for wideband composite and rapid-response protection[21-25]. Specifically, conventional ESS designs typically achieve low insertion loss only within relatively narrow frequency bands in the transmission state, which significantly falls short of the requirements of modern multi-band and broadband communication systems. Additionally, traditional ESS designs mostly rely on GaAs PIN diodes, whose response times are generally on the order of microseconds. These technical bottlenecks severely restrict the practical engineering application and widespread adoption of ESS.

Therefore, this paper proposes a wideband fast-response protective energy-selective surface to address the limitations of existing technologies. The proposed ESS consists of a dielectric layer and multiple metasurface units attached to its surface. Each metasurface unit includes a substrate dielectric board with a metallic circuit pattern printed on its upper surface. The metallic structure adopts a grid-like configuration interconnected by multiple GaN Schottky diodes. The switching states of the diodes enable adaptive protection against incident electromagnetic waves, allowing transmission under low-power conditions while blocking high-power signals. Based on the Jerusalem cross structure, an additional small metallic strip is incorporated between the cross arms. This modification increases the number of diodes connecting

adjacent cross structures from one to two. The series diode configuration effectively reduces the equivalent capacitance without changing the diode type, thereby enhancing the transmission bandwidth of the structure. The fast-response characteristics of the GaN Schottky diodes enable the ESS to effectively counteract most electromagnetic pulse threats. It integrates wideband transmission, broadband high-efficiency protection, and rapid response capabilities. The ESS exhibits energy selectivity within the frequency range of 1.68 GHz to 5.97 GHz, permitting low-power signal transmission while reflecting or blocking high-power electromagnetic energy, with a response time of less than 10 nanoseconds. This design enables adaptive electromagnetic protection across multiple frequency bands.

REFERENCES

[1] Giri, D.; Tesche, F. Classification of intentional electromagnetic environments (IEME). IEEE Trans. Electromagn. Compat. 2004,46, 322 –328.

[2] Baum, C.E. Reminiscences of high-power electromagnetics. IEEE Trans. Electromagn. Compat. 2007, 49, 211–218.

[3] Lin, J.C. Weaponizing the microwave auditory effect and the Havana Syndrome. URSI Radio Sci. Bull. 2021, 2021, 36–38.

[4] Arnesen, O.H.; Hoad, R. Overview of the European project 'HIPOW'. IEEE Electromagn. Compat. Mag. 2014, 3, 64–67.

[5] Feng, H.; Wu, X.; Li, Y. Review of the U.S. Congress' Commission to Assess the Threat to the United States from Electromagnetic Pulse Attack and Its Reports. Equip. Environ. Eng. 2020, 17, 132–137.

[6] Zhao, R.; Kang, X.; Zheng, Y.; Wu, H.; Wei, N.; Deng, S.; Wei, K.; Liu, X. High-power microwave limiters using recess-free AlGaN/GaN Schottky barrier diodes. IEEE Microw. Wirel. Technol. Lett. 2022, 33, 208 – 211.

[7] Chen, D.; Xu, L.; Zhang, B.; Ma, H. Research on the effect of high power microwave on low noise amplifier and limiter based on the injection method. J. Electromagn. Anal. Appl. 2010, 2010, 1393.

[8] Miligy, A.F.; Elfeky, A.H.; Kheirallah, H.N.; Rizk, M.R.; Madany, Y.M. Study of Miniaturized SIW and RWG Limiters for S-Band Receiver Protector Radar and Communication Applications. Prog. Electromagn. Res. 2023, 132, 171 – 185.

[9] Salehi, M.; Behdad, N. A second-order dual X-/Ka-band frequency selective surface. IEEE Microw. Wirel. Components Lett. 2008,18, 785–787.

[10] Tao, K.; Li, B.; Tang, Y.; Wu, Q. Multi-layer tri-band frequency selective surface using stepped-and uniform-impedance resonators.Electron. Lett. 2016, 52, 583 – 585.

[11] Wang, Y.; Xu, X.; Dai, Z.; Hua, Z.; Lin, C.; Hou, Y.; Zhang, Q.; Wang, P.; Tan, Y. Frequency-swept feedback interferometry for noncooperative-target ranging with a stand-off distance of several hundred meters. PhotoniX 2022, 3, 21.

[12] Wang, D.; Cui, X.; Liu, D.; Zou, X.; Wang, G.; Zheng, B.; Cai, T. Multi-Characteristic Integrated Ultra-Wideband Frequency Selective Rasorber. Prog. Electromagn. Res. 2024, 179, 49 – 59.

[13] Tian, J.; Cao, W. Reconfigurable flexible metasurfaces: From fundamentals towards biomedical applications. PhotoniX 2024, 5, 2.

[14] Yang, C.; Huang, J.; Liu, P. A new method of electromagnetic protection based on energy selective surface. J. Hebei Univ. Sci.Technol. 2011, 32, 81 – 84.[58]

[15] Yang, C.; Huang, J.; Liu, P. Protection and simulation of energy selective surface based on voltage conductive structure. Chin. J.Ship Res. 2012, 7, 98 – 103.

[16] Yang, C.; Liu, P.; Liu, J.; Zhou, D.; Li, G. Transient response of energy selective surface. High Power Laser Part. Beams 2013,25, 1045 – 1049.

[17] Hu, N.; Wang, K.; Zhang, J.; Zha, S.; Wu, Z.; Liu, C.; Liu, P. Design of ultrawideband energy-selective surface for high-power microwave protection. IEEE Antennas Wirel. Propag. Lett. 2019, 18, 669 – 673.

[18] Wu, H.; Hu, J.; Zhong, L.; Lin, J. Field-path collaborative simulation and experimental study of electromagnetic energy selective surfaces. High Power Laser Part. Beams 2017, 29, 105 – 109.

[19] Hu, N.; Zhao, Y.; Zhang, J.; Liu, P.; Xu, H.; Costa, F. High-performance energy selective surface based on equivalent circuit design approach. IEEE Trans. Antennas Propag. 2021, 70, 4526 – 4538.

[20] Liu, P.; Hu, N. Theory and application of energy selective electromagnetic protection method. Chin. J. Radio Sci. 2024.

[21] Hu, Y.; Shi, G.; Chen, Y.; Wei, F.; Liao, Y. Design and Simulation of An X-band bandpass energy selection surface. In Proceedings of nthe 2020 6th Global Electromagnetic Compatibility Conference (GEMCCON), Xi'an, China, 20 – 23 October 2020 ; IEEE: Piscataway,NJ, USA, 2020; pp. 1 – 3.

[22] Yi, B.; Dong, Y.; Yang, C.; Liu, P.; Li, Y. Design and simulation of an improved energy selective surface. Prog. Electromagn. Res.2015, 60, 57 – 66.

[23] Liu, X.; Tang, S.; Ren, J. A Ku Band Broadband Energy Selective Surface Design. In Proceedings of the 2023 IEEE 6th Information Technology, Networking, Electronic and Automation Control Conference (ITNEC), Chongqing, China, 24 – 26 February 2023; IEEE: Piscataway, NJ, USA, 2023; Volume 6, pp. 373 – 377.

[24] Jiang, H.; Deng, B.; Xu, Y.; Tian, T.; Liu, P. Ultra-Wideband Energy-Selective Structure Based on Spoof Surface Plasmon Polariton. IEEE Antennas Wirel. Propag. Lett. 2024, 24, 537 – 541.

[25] Li, C.; Zhang, T.; Bao, H.; Ding, D. Design of a Broadband Energy Selective Surface with Ultra-High Shielding Efficiency. IEEE Antennas Wirel. Propag. Lett. 2024, 23, 4303 – 4307.

Diffraction Contribution by a Junction of Chiral Layers with PEC Backing

Giovanni Riccio[1,*], Flaminio Ferrara[2], Gianluca Gennarelli[3], Rocco Guerriero[2], Francesco Chiadini[2]

[1]D.I.E.M., University of Salerno, Italy
[2]D.I.In., University of Salerno, Italy
[3]I.R.E.A.-C.N.R., Naples, Italy
*Corresponding author: griccio@unisa.it

***Abstract*— The plane wave diffraction by the discontinuity of a PEC-backed planar junction formed by two uniaxial anisotropic chiral half-layers is addressed. A heuristic approach is applied to evaluate this contribution in the framework of the uniform geometrical theory of diffraction.**

***Keywords*— chiral material, planar junction, diffraction, asymptotic solution.**

I. Introduction

The use of heuristic approaches in the framework of the Uniform Geometrical Theory of Diffraction (UTD) [1] allows one to obtain approximate high-frequency solutions to diffraction problems. Such solutions account for requirements to be satisfied in accordance with the physical phenomenon under observation, but their formulation is not based on a rigorous mathematical justification. Moreover, they are manageable and easy to be applied.

Burnside and Burgener proposed [2] a well-known heuristic method to compute the diffraction contribution by a dielectric half-screen. The idea presented in [2] was recently customized by the authors to evaluate the diffracted field by uniaxial anisotropic chiral half-screens [3]. These last are penetrable structures characterized by constitutive relations involving permittivity and permeability diagonal matrices. The electromagnetic coupling is given by the chirality parameter κ.

The Uniform Asymptotic Physical Optics (UAPO) approach was applied in [4] to compute the plane wave diffraction by a non-penetrable truncated structure consisting of a uniaxial anisotropic chiral half-sheet with perfect electrical conductor (PEC) backing. A two-dimensional propagation scenario was considered.

Continuing their research activity, the authors propose a heuristic UTD solution for the plane wave diffraction by the discontinuity of a PEC-backed planar junction formed by two uniaxial anisotropic chiral half-sheets (see Fig. 1). The incidence direction is arbitrary and determines the angle β' with the common edge.

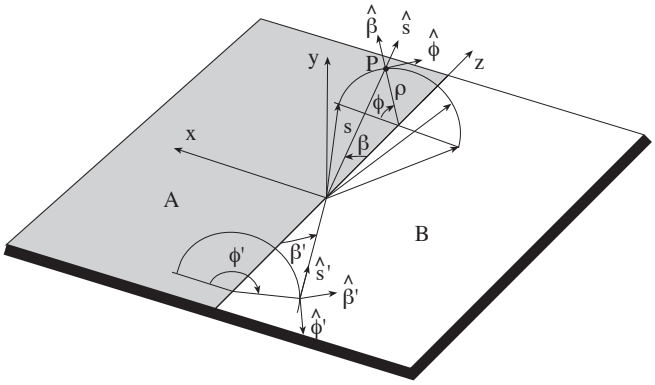

Fig. 1 Planar junction formed by two PEC-backed chiral layers.

II. Heuristic UTD Solution

According to [1], the components of the diffracted field associated to the edge-fixed plane of diffraction (it contains $\hat{z}$ and the diffraction unit vector $\hat{s}$ in Fig. 1) can be coupled to the incident field components that are parallel and orthogonal to the edge-fixed plane of incidence (it contains $\hat{z}$ and the incidence unit vector $\hat{s}'$ in Fig. 1) by means of the diffraction matrix $\underline{\underline{D}}$:

$$\begin{pmatrix} E_\beta^d \\ E_\phi^d \end{pmatrix} = \underline{\underline{D}} \begin{pmatrix} E_{\beta'}^i \\ E_{\phi'}^i \end{pmatrix} \frac{\exp(-jk_0 s)}{\sqrt{s}} \qquad (1)$$

where k_0 is the free-space propagation constant and s is the distance between the observation point P and the diffraction point on the discontinuity. Since P is on the Keller's cone, the angles β', ϕ', and ϕ (Fig. 1) define the incidence direction (β',ϕ') and the diffraction direction $(\beta=\beta',\phi)$. Moreover, if $F(\cdot)$ denotes the UTD transition function, the function

$$D(\phi+\phi',\beta') = \frac{-\exp(-j\pi/4)}{2\sqrt{2\pi k_0}} \frac{F\left(2k_0 s \sin^2\beta' \cos^2\left(\frac{\phi+\phi'}{2}\right)\right)}{\sin\beta' \cos\left(\frac{\phi+\phi'}{2}\right)} \quad (2)$$

is given in $\underline{\underline{D}}$ to compensate the jump of the electric field at the reflection boundary [1]-[3].

The idea proposed in [2], [3] is then adapted to the here considered problem, thus obtaining

$$\underline{\underline{D}} = \left[\underline{\underline{R}}'_A - \underline{\underline{R}}'_B\right] D(\phi+\phi',\beta') \quad (3)$$

where

$$\underline{\underline{R}}'_{A,B} = \begin{pmatrix} \cos\alpha & \sin\alpha \\ -\sin\alpha & \cos\alpha \end{pmatrix} \underline{\underline{R}}_{A,B} \begin{pmatrix} \cos\alpha & \sin\alpha \\ -\sin\alpha & \cos\alpha \end{pmatrix} \quad (4)$$

with

$$\cos\alpha = \frac{\cos\beta' \sin\phi'}{\sqrt{1-\sin^2\beta' \sin^2\phi'}} \quad (5)$$

The reflection matrices $\underline{\underline{R}}_{A,B}$ are associated to the half-layer A ($x>0, y=0$) and B ($x<0, y=0$), respectively, and couple the parallel and perpendicular components of the reflected electric field to the counterparts of the incident electric field. These matrices are determined by taking into account that two eigenwaves with different refraction angles propagate into the chiral medium when an incident plane wave impacts the external surface (Fig. 2) [5], [6].

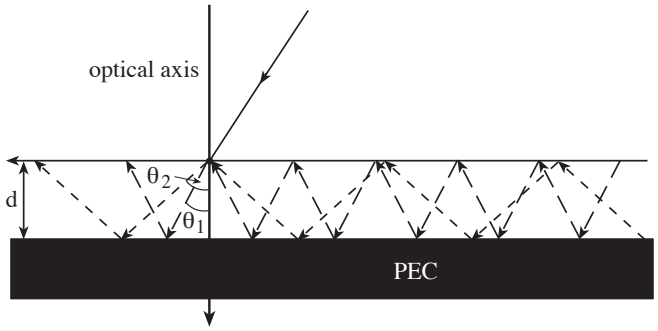

Fig. 2 Eigenwaves propagate in the PEC-backed chiral layer.

III. Numerical Results

According to [3]-[6], the considered chiral layers *A* and *B* are characterized by the following parameters: thickness $d_{A,B} = 0.05\lambda_0$ (λ_0 is the free-space wavelength), relative permeability associated to the optical axis direction (*n*) and the transverse axes (*t*) $\mu_{t_{A,B}} = \mu_{n_{A,B}} = \mu_0$, relative permittivity $\varepsilon_{t_A} = 3\varepsilon_0$, $\varepsilon_{n_A} = 4\varepsilon_0$, $\varepsilon_{t_B} = 15\varepsilon_0$, $\varepsilon_{n_B} = 20\varepsilon_0$ (the free-space parameters are denoted by the index "0"), and chirality parameter $\kappa_A = 1.5$, $\kappa_B = 0.5$ describing the electromagnetic coupling.

Figure 3 is relevant to a circular observation path with radius $\rho = 6\lambda_0$ and is reported to demonstrate the efficacy of the proposed heuristic UTD solution to compensate the jump of the Geometrical Optics (GO) field when crossing the reflection shadow boundary at $\phi = 110°$.

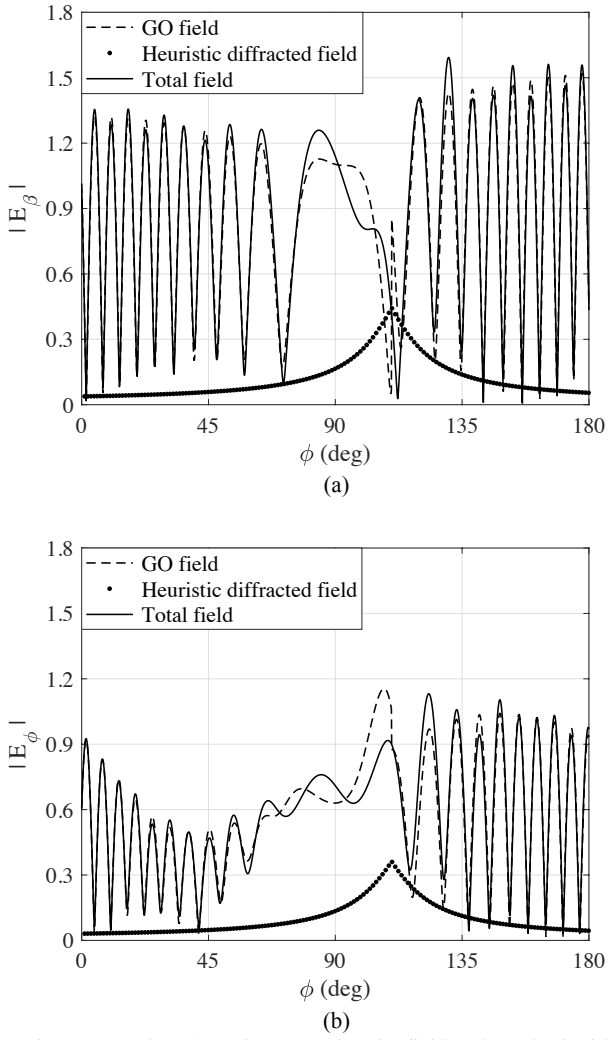

Fig. 3 Co-polar (a) and cross-polar (b) fields when the incidence direction is $\beta' = 60°, \phi' = 70°$ and $E^i_{\beta'} = 1, E^i_{\phi'} = 0$.

IV. Conclusion

The diffraction contribution due to the discontinuity of a PEC-backed planar junction formed by two uniaxial anisotropic chiral half-layers has been determined by means of a heuristic UTD approach able to balance the jump of the GO field.

REFERENCES

[1] R.G. Kouyoumjian and P.H. Pathak, "A uniform geometrical theory of diffraction for an edge in a perfectly conducting surface," Proceedings of IEEE, vol. 62, pp. 1448-1461, 1974.

[2] W.D. Burnside and K.W. Burgener, "High frequency scattering by a thin lossless dielectric slab," IEEE Transactions on Antennas and Propagation, vol. 31, pp. 104-110, 1983.

[3] G.Riccio, G.Gennarelli, F.Ferrara, R.Guerriero, and F.Chiadini, "Heuristic UTD Solutions for Plane Wave Diffraction by Uniaxial Chiral Half-Sheets," International Journal of Microwave and Optical Technology, vol. 19, pp. 325-333, 2024.

[4] G.Riccio, F.Ferrara, G.Gennarelli, R.Guerriero, and F.Chiadini, "UAPO Diffracted Field by a PEC-Backed Chiral Half-Sheet," Proceedings of International Conference on Metamaterials, Photonic Crystals and Plasmonics, META 2025, Malaga, Spain, pp. 1687-1688, 2025.

[5] J.F. Dong and J. Li, "The reflection and transmission of electromagnetic waves by a uniaxial chiral slab," Progress in Electromagnetic Research, vol. 127, pp. 389-404, 2012.

[6] G.Riccio, F.Ferrara, G.Gennarelli, R.Guerriero, and F.Chiadini, "Reflection, Transmission and Diffraction by Lossless Anisotropic Chiral Sheets," IEEE Transactions on Antennas and Propagation, vol. 72, pp. 8719-8727, 2024.

Photonics, Plasmonics and Optical Devices

Effect of asymmetry and disorder on spontaneous emission in resonant gratings supporting quasi-bound states in the continuum

Victor Kalt[1,*], Emmanuel Centeno[2], Rafik Smaali[2], Antoine Moreau[2]

[1]Université de Lyon, Laboratoire Hubert Curien, UMR 5516, Université Jean Monnet, Saint-Etienne, France
[2]Université Clermont Auvergne, Clermont Auvergne INP, CNRS, Institut Pascal, Clermont-Ferrand, France
*Corresponding author: victor.kalt@univ-st-etienne.fr

***Abstract*—We study the effect of controlled asymmetry and structural disorder on the light emission in the normal direction of a dipole source in a resonant grating supporting a bound state in the continuum (BIC) or a quasi-BIC (QBIC). Both regular and dimer gratings are compared.**

***Keywords*— Bound state in the continuum, resonant grating, photoluminescence, structural disorder.**

I. Introduction

Enhancing and controlling the spontaneous emission of quantum emitters is a major topic in photonics [1]. Potential applications range from lighting to imaging and communications technologies. Devices such as resonant gratings, photonic crystals and metasurfaces have been designed to achieve high and controlled emission rates. The efficiency of such structures is characterized by the radiative enhancement (RE), which represents the total enhancement of detectable photon emission compared to free space. It is defined as the product of the normalized decay rate and the light extraction efficiency (LEE). Symmetry-protected BICs supported by periodic grating structures have been proposed as an efficient solution to increase light emission in off-normal directions [2], [3]. Breaking the symmetry of the structure leads to the transformation of the BIC into a QBIC [5], [6]. In this work, we study the effect of symmetry breaking on the redirection of this emission at the Γ point through numerical simulations of dimer gratings with controlled asymmetry or through the introduction of structural disorder [7].

II. Methods

A resonant grating of period $D = 420$ nm is built from TiO_2 ribbons of height $h = 150$ nm and width $w = D/2$ covered by a 200 nm TEOS protective layer. This structure is referred to as the regular grating. We study the effect of two kinds of perturbations in this structure by considering the dimer grating of period $2D$ shown in Fig. 1. It is characterized by width variations $w \pm \Delta w$ and gap variations $L \pm \Delta L$, respectively characterized by parameters $\alpha = \Delta w/w$ and $\beta = \Delta L/L$. A dipole emitter at a wavelength $\lambda = 681.5$ nm is placed between the two ribbons.

The quasi-normal mode (QNM) method [4] is used to numerically study the radiative efficiency (RE) of this single emitter embedded inside the periodic structure. The modes are computed using the finite-element method implemented in COMSOL Multiphysics.

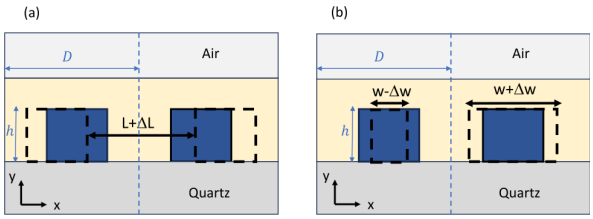

Fig. 1. Schematic of a dimer grating made of two TiO_2 ribbons embedded in a TEOS layer. (a) and (b) are respectively modified gap $L \pm \Delta L$ and widths $w \pm \Delta w$ dimer gratings.

Structural disorder is then introduced to model fabrication imperfections. It is implemented by adding independent random perturbations to the position and width of the dimer grating elements in a supercell of width 6D (representing three dimer grating elements).

III. Results and Discussion

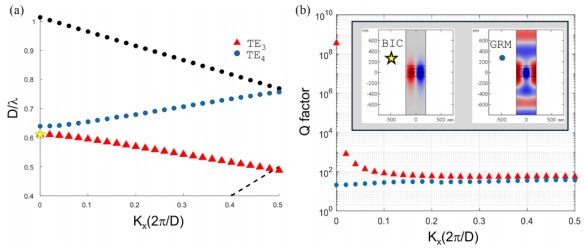

Fig. 2. (a) Dispersion relation of the regular grating. (b) Quality factor as a function of the transverse wave vector. The inset shows the out-of-plane electric field maps of the BIC and grating resonant mode (GRM) calculated at the Γ point.

At the Γ point, the TE_3 mode of the regular grating structure ($\alpha = \beta = 0$) harbors a BIC, as demonstrated by the quality factor and the electric field map shown in Fig. 2b. The infinite Q-factor leads to a null radiative enhancement as the emitted light is confined inside the structure (resulting in

a zero LEE). This cancels the increase in the dipole emission rate through the Purcell effect. If the structure's symmetry is broken by introducing α or β perturbations, the BIC becomes a QBIC that radiates at the Γ point: the high Q-factor of the QBIC results in a non-zero LEE and a high Purcell factor. RE values shown in Fig. 3 demonstrate that the enhancement pattern is nearly isotropic in the (α, β) plane for medium perturbations.

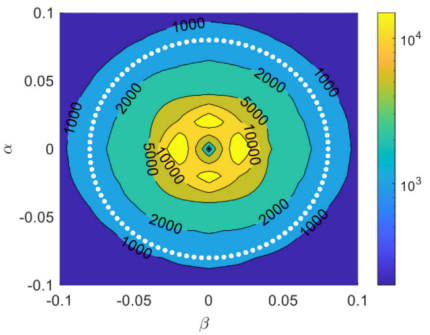

Fig. 3. Maximum of the radiative enhancement coefficient at the Γ-point as a function of α and β.

We now focus on a feasible dimer structure with a gap asymmetry of $\beta = 0.08$ (a ± 16.8 nm variation of the gap) and compare in Fig. 4 the directive RE of this dimer structure to the one of the regular grating. Values up to 1600 are obtained in the normal direction with the dimer grating.

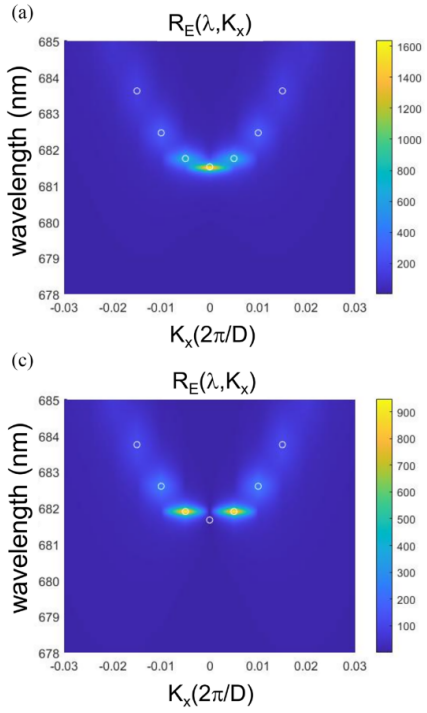

Fig. 4. Directive radiative enhancement coefficient $RE(\lambda, k_x)$ (a) for the dimer structure ($\alpha = 0$, $\beta = 0.08$), (b) for the regular grating.

Asymmetry can also be introduced in the system during manufacturing from fabrication imperfection or structural disorder. BICs have been shown to be sensitive to this kind of perturbation [8]. The directive radiative enhancement of the dimer structure and the regular grating perturbed by a $\delta = 1.2\%$ structural disorder is shown in Fig. 5. We clearly see that new radiation channels have been opened by the presence of disorder, leading to lower RE values and an emission on a broader range of frequencies. In the case of the regular grating, disorder breaks the symmetry, transforming the BIC into a QBIC and allowing radiation at the Γ point with a highly irregular RE spectrum, indicative of mode hybridization and constructive interference among multiple leaky modes. The radiative efficiency of the structure is affected differently by perturbations in the width or position of the grating elements. Structural disorder in the ribbon's width causes a splitting of the resonant frequencies of the QBIC, leading to multiple radiative channels in the normal direction. Disorder in the position of the ribbons only affects the RE, with no effect on the QBIC frequency. The total emission at the Γ point (obtained by integrating the RE over all wavelengths) is higher for the dimer structure, highlighting that it is more robust to structural disorder (for $\delta < 10\%$).

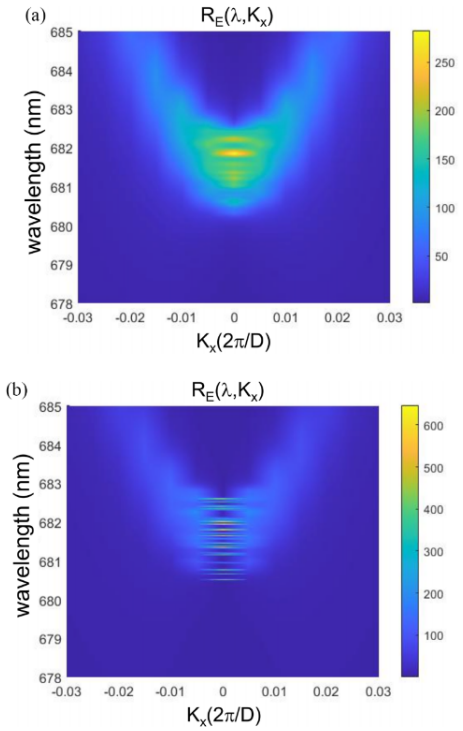

Fig. 5. Average $RE(\lambda, k_x)$: (a) for the randomly perturbed dimer structure, (b) for the randomly perturbed regular grating.

IV. Conclusion

We engineered a dimer grating to increase the light emission of a dipole source in the normal direction through the transformation of a BIC into a QBIC and numerically studied

the effect of controlled asymmetry and structural disorder. Numerical simulations showed that a dimer structure is more efficient than a regular grating for structural disorder lower than 10%. Dimensional disorder emmerges as the key parameter controlling the QBIC frequency.

ACKNOWLEDGMENTS

The authors thank the French "Agence Nationale de la Recherche" in the framework of the COULEURS project (ANR-22-CE39-0013).

REFERENCES

[1] A. Vaskin, R. Kolkowski, A. F. Koenderink, and I. Staude, "Light-emitting metasurfaces", '*Nanophotonics* Vol. 8, 1151 (2019)

[2] S. Farazi and S. Tadigadapa. "Coherent light-emitting metasurfaces based on bound states in the continuum" *Nanophotonics*, vol. 13, no. 16, 2024, pp. 2915-2924

[3] L. Liu, R. Wang, Y. Sun, Y. Jin and A. Wu. "Fluorescence enhancement of PbS colloidal quantum dots from silicon metasurfaces sustaining bound states in the continuum" *Nanophotonics*, vol. 12, no. 15, 2023, pp. 3159-3164.

[4] C. Sauvan, J.-P. Hugonin, I. S. Maksymov, and P. Lalanne, "Theory of the spontaneous optical emission of nanosize photonic and plasmon resonators", *Physical Review Letters* Vol. 110 (2013).

[5] S. You, H. He, Y. Zhang, H. Duan, L. Wang, Y. Wang, S. Luo and C. Zhou. "Resonance wavelength stabilization of quasi-bound states in the continuum constructed by symmetry breaking and area compensation" *Nano Letters*, vol. 24, no. 48, 2024.

[6] M. A. Vincenti, L. Carletti, D. De Ceglia, D. Rocco, H. Weigand, G. Saerens, V. Falcone, R. Grange, H. Barati Sedeh, W. Li, N. M. Litchinitser and M. Scalora. "From high-to low-contrast: the role of asymmetries in dielectric gratings supporting bound states in the continuum" *Optics Express*, vol. 32, no. 18, 2024.

[7] E. Centeno, V. Kalt, R. Smaali and A. Moreau. "Disorder-induced effects on spontaneous emission from quasi-bound states in the continuum in regular and dimer gratings" *Physical Review B*, vol. 112, no. 13, 2025.

[8] E. Maslova, M. Rybin, A. Bogdanov, and Z. Sadrieva. "Bound states in the continuum in periodic structures with structural disorder" *Nanophotonics*, vol. 10, no. 17, 2021, pp. 4313-4321.

Defect-Engineered ZnO/Ag Nano-heterostructures for Energy-Related Applications

Roman Redko[1,2,3,4*], Grigorii Milenin[1], Vitaliy Shvalagin[5], Svitlana Redko[1], Yelizaveta Savchuk[1]

[1]V. Lashkaryov Institute of Semiconductor Physics of the National Academy of Sciences of Ukraine, Ukraine
[2]Department of Mathematics, Kyiv School of Economics, Ukraine
[3]Department of General Physics and Modeling of Physical Processes, National Technical University of Ukraine "Igor Sikorsky Kyiv Polytechnic Institute", Ukraine
[4]State University of Information and Communication Technologies, Ukraine
*Corresponding author: redko.rom@gmail.com

***Abstract*— Defect engineered ZnO/Ag nanocomposites demonstrate magnetically tunable plasmonic properties relevant to useful applications. Defect induced ferromagnetism in ZnO nanoparticles enables controllable and long-lived blue shifts of localized surface plasmon resonance. These effects provide new routes for plasmon enhanced photovoltaics photocatalysis and multifunctional sensing technologies**

***Keywords*— nanostructures, ZnO/Ag, plasmon properties, blue shift, magnetic field.**

I. Introduction

Nanophotonics plays a key role in the development of advanced energy-related technologies, including photovoltaics, photocatalysis, and sensor systems for energy and environmental monitoring [1]. Among functional nanomaterials, zinc oxide (ZnO) occupies a special position due to its wide band gap, high exciton binding energy, chemical stability, and exceptional flexibility of defect engineering. The possibility to control intrinsic defects makes ZnO a versatile platform for tailoring optical, electronic, magnetic, and plasmonic properties without introducing extrinsic dopants, which is critically important for both fundamental studies and practical energy applications [2].

In recent years, hybrid nanostructures combining ZnO with plasmonic metals such as silver (Ag) have attracted considerable attention. ZnO/Ag nanocomposites exhibit pronounced localized surface plasmon resonance (LSPR), enabling strong light–matter interaction, enhanced optical absorption, and improved energy conversion efficiency. These features are particularly relevant for plasmonically enhanced solar cells, photocatalytic systems, and optical sensors operating in different environments.

II. Defect-Induced Ferromagnetism in ZnO Nanoparticles

An important and nontrivial property of ZnO nanostructures is the emergence of defect-induced ferromagnetism, often referred to as d^0 ferromagnetism [3]. This phenomenon arises due to intrinsic point defects such as oxygen vacancies, zinc vacancies, interstitial atoms, and complex defect states, which act as sources of localized magnetic moments [4]. Unlike conventional ferromagnetism, this magnetic ordering occurs in the absence of partially filled *d*- or *f*-shells and is therefore of high fundamental interest.

Experimental and theoretical studies indicate that the surface region of ZnO nanoparticles plays a dominant role in this behavior. Due to a high density of dangling bonds and defects, ZnO nanoparticles may possess a nonzero magnetic moment even without external magnetic impurities [5]. As a result, ensembles of ZnO nanoparticles can exhibit ferromagnetic-like behavior at room temperature, which can be manipulated by external magnetic fields.

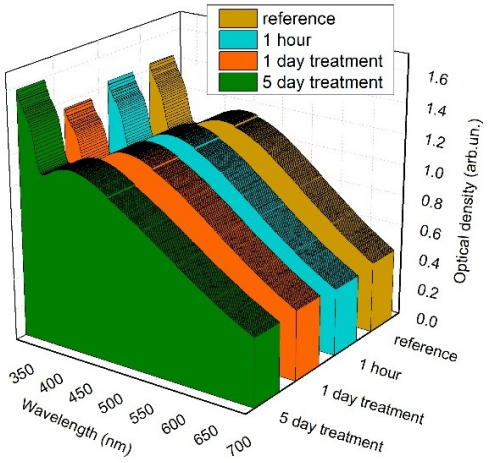

Fig. 1 Blue shift of LSPR peak of ZnO/Ag nanocomposites due to magnetic field pre-treatment.

This defect-induced magnetism provides an additional

degree of freedom for controlling the optical and plasmonic properties of ZnO-based nanostructures, opening new opportunities for multifunctional nanophotonic systems.

III. Magnetic-field influent on plasmonic properties in ZnO/Ag nanocomposites

Colloidal solutions of ZnO nanoparticles serve as effective precursors for the fabrication of ZnO/Ag core–shell (5 nm-12 nm) and heterostructured nanocomposites via photocatalytic reduction of silver ions under ultraviolet irradiation. Such nanocomposites exhibit a pronounced LSPR band in the visible spectral range (typically 400–460 nm), which is highly sensitive to particle size, shape, dielectric environment, and interfacial properties. A key finding demonstrated in the analyzed studies [6] is that weak magnetic-field pre-treatment of ZnO nanoparticle solutions (on the order of tens of millitesla) leads to a measurable shift of the LSPR peak position in subsequently formed ZnO/Ag nanocomposites. This effect is unexpected for a nominally paramagnetic material such as undoped ZnO and strongly suggests the involvement of defect-induced ferromagnetism.

The observed LSPR blue shift (Fig. 1) depends on the duration of magnetic-field exposure: 5 days of magnetic field pre-treatment result in 40 nm displacement (from 450 to 410 nm). Moreover, a pronounced “memory effect” has been identified: the modified plasmonic response persists for up to 30 days after magnetic-field treatment and gradually relaxes toward the reference state due to thermal disordering of the magnetized nanoparticle ensemble [6].

IV. Physical mechanisms and optical modeling

The magnetic-field-induced modification of LSPR in ZnO/Ag nanocomposites can be explained by changes in the optical properties of ZnO nanoparticles caused by magnetization. In particular, magnetization of the defect-rich near-surface region of ZnO nanoparticles may lead to variations in the local refractive index and/or subtle changes in nanoparticle geometry. Both factors directly affect the resonance conditions for localized surface plasmons in the Ag shell.

Numerical modeling of optical absorption spectra using core/shell modeling confirms the principal possibility of LSPR peak shifting due to changes in the refractive index of the ZnO core [7]. Simulations demonstrate that even relatively small variations in the dielectric function of ZnO can result in noticeable spectral shifts of the plasmon resonance. For more accurate quantitative agreement with experiment, advanced models involving a three-layer structure (paramagnetic ZnO core / ferromagnetic-like surface layer / Ag shell) are required.

V. Relevance for energy applications

The ability to control plasmonic properties through defect engineering and external magnetic fields is highly promising for energy-related nanophotonic applications. In plasmonically enhanced photovoltaic devices, controlled LSPR tuning enables optimization of light absorption and near-field enhancement, leading to improved solar energy conversion efficiency. In photocatalysis, magneto-plasmonic ZnO/Ag nanostructures may enhance reaction rates by increasing local electromagnetic fields and promoting charge separation.

Furthermore, the demonstrated sensitivity of LSPR to defect-induced magnetization provides a foundation for multifunctional sensor systems capable of responding simultaneously to optical, magnetic, and chemical stimuli. Such systems are of particular interest for energy infrastructure monitoring, environmental control, and smart energy technologies.

VI. Conclusion

The analyzed results demonstrate that defect-engineered ZnO/Ag nanocomposites represent a useful platform for nanophotonics in energy applications. Defect-induced ferromagnetism in ZnO nanoparticles enables magnetic-field influent on plasmonic properties, including tunable and long-lived shifts of the LSPR peak. The combination of experimental observations and optical modeling reveals the key role of defects and near-surface effects in governing light–matter interaction at the nanoscale.

These findings open new pathways for the design of adaptive, multifunctional nanophotonic materials for next-generation energy conversion, sensing, and monitoring technologies.

Acknowledgments

This work was sponsored by the NATO SPS project G6197 “Plasmonically Enhanced Perovskite Thin-Film Solar Cells”, the National Academy of Sciences of Ukraine (Projects #0125U000799, 0125U000995)

References

[1] K. Anggraeni, M. Riswan, P. D. Jayanti, et al. “Microstructure, magnetic, and surface plasmon resonance studies of green-synthesized ferrite nanoparticles for biosensor applications,” Journal of Magnetism and Magnetic Materials, vol. 614, p. 172727, 2025.

[2] S.S. Abdullaev, Y. Fahad Breesam, A.A.H. AlZubaidi, et al. ”ZnO@$ZnCo_2O_4$ core-shell: A novel high electrocatalytic nanostructure to replace platinum as the counter electrode in dye-sensitized solar cells,” Materials Science in Semiconductor Processing, vol. 165, p. 107709, 2023.

[3] S. B. Singh, Y.-F. Wang, Y.-C. Shao, et al. “Observation of the origin of d0 magnetism in ZnO nanostructures using X-ray-based microscopic and spectroscopic techniques,” Nanoscale, vol. 6, pp. 9166-9176, 2014

[4] X. Yin, Y. Wang. R. Jacobs et al. “Massive Vacancy Concentration Yields Strong Room-Temperature Ferromagnetism in Two-Dimensional ZnO,” Nano Lett., vol. 19, pp. 7085–7092, 2019.

[5] Guglieri, C.; Laguna-Marco, M. A.; García, et al. “XMCD Proof of Ferromagnetic Behavior in ZnO Nanoparticles,” The Journal of Physical Chemistry C 2012, vol. 116, pp. 6608-6614.

[6] R. Redko, V. Shvalagin, G. Milenin, et al. “Identification of the Mechanisms of a Localized Surface Plasmon Resonance Peak Blue Shift in Magnetic Field Pretreated ZnO/Ag Nanocomposites,” ACS Omega, vol. 10, pp. 37154-37161, 2025.

[7] R. Redko, G. Milenin, V. Shvalagin, O. Kapush, A. Fedorenko, “Shift of LSPR Peak of ZnO/Ag Nanocomposites due to Zinc Oxide Refractive Index Modification after Magnetic Field Pre-Treatment,” Proceedings of the 2025 IEEE 15th International Conference "Nanomaterials: Applications and Properties", pp. NMP01-1-NMP01-4, 2025.

Metasurfaces for Light Harvesting in Perovskite Solar Cells

Sergii Mamykin[1,*], Iryna Mamontova[1], Roman Redko[1], Olena Shtykalo[1], Tetiana Lunko[1], Igor Dmytruk[2], Oleg Yeshchenko[2], Olexander Fedotov[2], Nataliya Berezovska[2], Anatoliy Pinchuk[3]

[1]V. Lashkaryov Institute of Semiconductor Physics, National Academy of Sciences of Ukraine, Kyiv, Ukraine
[2]Taras Shevchenko National University of Kyiv, Kyiv, Ukraine
[3]Department of Physics and Energy Sciences, University of Colorado at Colorado Springs, USA
*Corresponding author: mamykin@isp.kiev.ua

***Abstract*- We propose a plasmonic metasurface design integrating Au/SiO_2 core-shell nanoparticles to enhance absorption in thin-film perovskite solar cells. FDTD simulations demonstrate significant efficiency improvements in the near-infrared region driven by hybrid plasmon-gap modes. This architecture offers a pathway to stable, high-performance photovoltaics with reduced active layer thickness.**

***Keywords*- plasmonic metasurfaces, perovskite solar cells, core-shell nanoparticles, FDTD simulation, light harvesting, gap modes.**

I. Introduction

Perovskite thin films have emerged as highly promising materials for next-generation photovoltaic technologies due to their excellent optoelectronic properties and low-cost solution-based fabrication. However, widespread commercialization is currently hindered by two critical challenges: the instability of perovskite materials under real-world environmental conditions (moisture, oxygen, UV radiation) and the toxicity associated with lead (Pb) in the most efficient formulations [1]. Reducing the thickness of the perovskite absorber layer can mitigate lead content and potentially improve stability, but this comes at the cost of reduced light absorption, particularly in the near-infrared (NIR) spectral range where perovskite films are optically thin.

To address this trade-off, we propose the integration of plasmonic metasurfaces-specifically, monolayers of gold-silica (Au/SiO_2) core-shell nanoparticles (NPs)-into the solar cell architecture [2]. Plasmonic nanostructures can confine and scatter light at the subwavelength scale, exciting localized surface plasmon resonances (LSPR). When placed in close proximity to a metal back-contact, these NPs can support hybrid "gap modes" that strongly localize the electromagnetic field within the photoactive layer [3]. This study presents a design for a plasmonic perovskite solar cell (PPSC) that leverages these modes to enhance power conversion efficiency (PCE) while allowing for thinner, more environmentally friendly active layers.

II. Methods

2.1. Solar Cell Design and Fabrication

We investigated a multilayer solar cell structure comprising: Glass / ITO / Hole Transport Layer (HTL) / Perovskite / Electron Transport Layer (ETL) / Back Contact.

Substrate: Fluorine-doped tin oxide (FTO) or Indium tin oxide (ITO) coated glass.

HTL: PEDOT:PSS (poly(3,4-ethylenedioxythiophene) polystyrene sulfonate), chosen for its stability and conductivity, with a thickness of 50–100 nm. Other variations included nickel oxide (NiOx) and copper sulfide (CuS).

Absorber: Cesium-lead-iodide ($CsPbI_3$) perovskite layer, with thickness varied between 100 and 300 nm to study the effect of thinning.

Plasmonic Metasurface: A monolayer of Au/SiO_2 core-shell NPs embedded at the interface between the perovskite and the ETL. The core diameter was varied (40–100 nm) with a thin silica shell (2–5 nm) to prevent non-radiative quenching and chemical reaction with the perovskite.

ETL: Zinc oxide (ZnO) or Titanium dioxide (TiO_2) with a thickness of 15–50 nm.

Back Contact: A continuous film of Aluminum (Al) or Gold (Au) (100 nm), serving as both an electrode and a mirror to form the plasmonic cavity.

2.2. Numerical Modeling

The optical properties and electromagnetic near-field distributions were simulated using the Finite-Difference Time-Domain (FDTD) method [5]. The simulation domain employed periodic boundary conditions in the x- and y-directions to model an infinite array of NPs, and perfectly matched layers (PML) in the z-direction. We calculated the absorption cross-sections, electric field enhancement distributions ($|E|^2/|E_0|^2$), and total absorption efficiency of the device. Key parameters for optimization included the NP core

size, shell thickness, inter-particle distance (D), and the thickness of the spacing layers.

2.3. Characterization Techniques

Experimental validation involved structural and optical characterization. The morphology of the deposited layers and NP distribution was analyzed using Scanning Electron Microscopy (SEM) and Atomic Force Microscopy (AFM). The optical constants (n, k) of the individual layers, necessary for accurate FDTD modeling, were determined using a multi-angle spectroscopic ellipsometer (SE-2000, Semilab) [4].

III. Results and Discussion

3.1. Absorption Enhancement via Gap Modes

FDTD simulations revealed that the reference cell (without NPs) exhibits typical Fabry-Pérot interference fringes due to the thin-film structure. Upon introducing the Au/SiO_2 metasurface, a pronounced enhancement in light absorption was observed across the entire visible spectrum, extending significantly into the NIR up to 1200 nm.

Specifically, a distinct and intense absorption peak was identified around **960 nm**. Analysis of the electric field distribution indicates that this peak corresponds to the excitation of a **plasmonic gap mode** - a hybrid resonance formed by the coupling between the LSPR of the Au core and the image charges in the Al back-contact [3]. This mode effectively traps long-wavelength photons that would otherwise pass through the thin perovskite layer unabsorbed.

3.2. Tuning the Resonance

We investigated the dependence of the absorption spectra on the inter-particle distance (D) within the monolayer.

Effect of Spacing: Decreasing D resulted in a blue shift of the collective plasmon mode (from the NIR towards the visible), while the spectral position of other interference-related bands remained largely unchanged. This tunability allows us to align the plasmonic resonance with the absorption edge of the perovskite material, maximizing the generation of charge carriers.

Field Localization: Strong "hot spots" with electric field enhancement factors exceeding 10^2 were observed in the gaps between the NPs and the Al film. This intense near-field enhancement is crucial for boosting the excitation rate of electron-hole pairs in the adjacent perovskite material.

3.3. Role of Perovskite Quantum Dots

In addition to the thin-film approach, we explored the potential of metal halide perovskite quantum dots (QDs) and clusters [4]. These nanomaterials offer size-tunable bandgaps and high photoluminescence quantum yields. Integrating QDs into the "ink" for spin-coating allows for scalable fabrication of large-area devices. Our preliminary DFT calculations of icosahedral perovskite clusters suggest they maintain structural stability, making them viable candidates for inclusion in the plasmonic matrix to further broaden the absorption spectrum.

IV. Conclusion

We have demonstrated that integrating a plasmonic metasurface based on Au/SiO_2 core-shell nanoparticles is an effective strategy to enhance the light-harvesting performance of thin-film perovskite solar cells. The formation of plasmonic gap modes provides a mechanism to significantly increase absorption in the NIR region, addressing a key limitation of thin-film photovoltaics. This design not only improves efficiency but also supports the use of thinner active layers, thereby reducing toxic lead consumption and potentially enhancing device lifetime.

Acknowledgments

This work was supported by the NATO Science for Peace and Security (SPS) Programme under project G6197 “Plasmonically Enhanced Perovskite Thin-Film Solar Cells”, the National Academy of Sciences of Ukraine within the framework of the project #0125U000799 "New physical principles and technologies for the development of the element base of modern infrared photoelectronics", the National Research Foundation of Ukraine, project 2025.06/0077 “Technologies for forming passivating coatings for IR photodetectors to increase their detection capability and reliability”.

References

[1] Y. Rong, Y. Hu, A. Mei, H. Tan, M. I. Saidaminov, S. I. Seok, M. D. McGehee, E. H. Sargent, and H. Han, "Challenges for commercializing perovskite solar cells," *Science*, vol. 361, no. 6408, 8235, 2018.

[2] S. Carretero-Palacios, A. Jiménez-Solano, and H. Míguez, "Plasmonic nanoparticles as light-harvesting enhancers in perovskite solar cells: a user’s guide," *ACS Energy Letters*, vol. 1, no. 1, pp. 323-331, 2016.

[3] O. A. Yeshchenko, V. V. Kozachenko, A. P. Naumenko, N. I. Berezovska, N. V. Kutsevol, V. A. Chumachenko, M. Haftel, and A. O. Pinchuk, "Gold nanoparticle plasmon resonance in near-field coupled Au NPs layer/Al film nanostructure: dependence on metal film thickness," *Photonics and Nanostructures-Fundamentals and Applications*, vol. 29, pp. 1-7, 2018.

[4] L. Hu, Q. Zhao, S. Huang, J. Zheng, X. Guan, R. Patterson, J. Kim, L. Shi, C. Lin, and Q. Lei, "Flexible and efficient perovskite quantum dot solar cells via hybrid interfacial architecture," *Nature Communications*, vol. 12, no. 1, p. 466, 2021.

[5] J. Zhao et al., "Methods for describing the electromagnetic properties of silver and gold nanoparticles," *Accounts of Chemical Research*, vol. 41, no. 12, pp. 1710-1720, 2008.

Numerical Design of Field-of-View-Efficient Silicon Optical Phased Arrays

Henna Farheen[1,*], Andreas Strauch[1], J. Christoph Scheytt[2], Viktor Myroshnychenko[1], and Jens Förstner[1]

[1]Paderborn University, Theoretical Electrical Engineering, Warburger Str. 100, 33098 Paderborn, Germany
[2]Paderborn University, System and Circuit Technology, Fuerstenallee 11, 33102 Paderborn, Germany
*Corresponding author: henna18@mail.uni-paderborn.de

***Abstract*—We numerically demonstrate a large-scale two-dimensional silicon optical phased array (OPA) using circular-grating nanoantennas with balanced power and phase. At 1.55 µm, optimized antennas achieve 90% upward radiation efficiency, with 6.8% of optical power within the field-of-view, enabling complex holography for LiDAR, optical trapping, optogenetics, and augmented-reality displays.**

***Keywords*—optical phased array, nanoantenna, field-of-view.**

I. Introduction

Phased arrays are composed of transmitting or receiving antennas whose individually controlled amplitude and phase enable precise steering and shaping of radiation patterns through constructive and destructive interference. In the optical regime, silicon photonics has emerged as a promising platform for implementing such systems, offering scalability and dense integration of optical components. These capabilities have driven significant progress in integrated OPAs, where the number of antenna elements and their spacing govern critical characteristics such as angular resolution, beamwidth, grating-lobe spacing, and radiated power. While increasing the antenna count improves resolution, the resulting inter-element spacing often exceeds the optical wavelength, giving rise to undesired grating lobes that restrict the field-of-view (FOV) and limit grating-lobe-free beam steering [1], [2].

II. Results and Discussion

We optimize the radiation performance of two antenna designs for use in a 2D OPA. Each OPA unit cell comprises three main components: a directional coupler, a phase shifter, and a low-loss dielectric antenna, as shown in Fig. 1. The design specifications of the directional coupler and phase shifter are incorporated as footprint constraints during the antenna optimization process, ensuring compatibility with the compact 9 µm × 9 µm unit-cell area of the reference design reported in Ref. [3].

To this end, full-wave simulations combined with a hybrid particle-swarm and trust-region optimization are employed to maximize the optical power radiated into the array's FOV. The FOV, defined as the grating-lobe-free angular region along the θ_x and θ_y directions and can be expressed as

$$| \Delta\text{FOV} | < \sin^{-1}\left(\frac{\lambda_\text{n}}{2\text{d}}\right),$$

where $\text{d} = 9\,\mu\text{m}$ and λ_n is the wavelength in the propagation medium. This configuration yields an approximate FOV of $6.8^\circ \times 6.8^\circ$. The resulting radiation pattern contains multiple propagating interference orders, with the total number determined by the largest integer m satisfying $| \ m\lambda_n/d \ | < 2$, resulting in 16 orders along each direction for this case.

Figures 2a and 2c illustrate the schematics of the two optimized antenna designs, which share an identical fundamental geometry. The second design incorporates a silicon Bragg reflector, as shown in Fig. 2c. The reflector consists of mirrors with a thickness of $\lambda_{Si}/4$, separated by a gap of $\lambda_{SiO_2}/4$. These added layers enhance the antenna's upward radiation efficiency, a behavior that is also evident in the near-field distribution in Fig. 2d, where the Bragg-reflector-assisted antenna exhibits stronger upward emission than the first design shown in Fig. 2b.

To assess the impact of increased in-FOV power, we simulated the far-field patterns of a 64×64 phased array using the radiation characteristics of the individual antennas. The Gerchberg–Saxton algorithm was employed to synthesize the UPB (Paderborn University) logo. As shown in Fig. 3, the Bragg reflector antenna (Fig. 3b) exhibits stronger radiation at the zenith, indicated by the brighter red region compared to the other antenna. The target UPB logo used is displayed at the center.

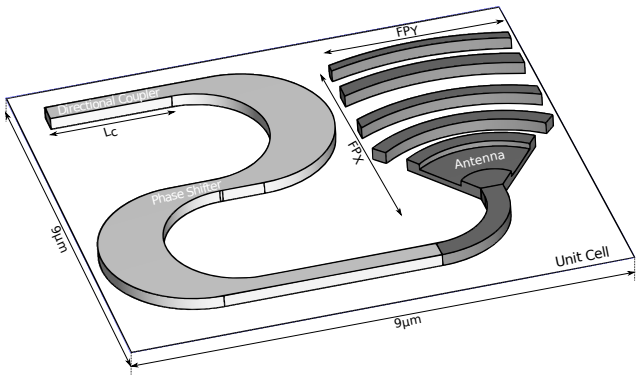

Fig. 1. Schematic of the 9 µm × 9 µm unit cell showing the directional coupler, phase shifter, and dielectric antenna. FPx and FPy denote the antenna footprint along the x- and y- directions, respectively. The dark grey area indicates the region optimized in this work.

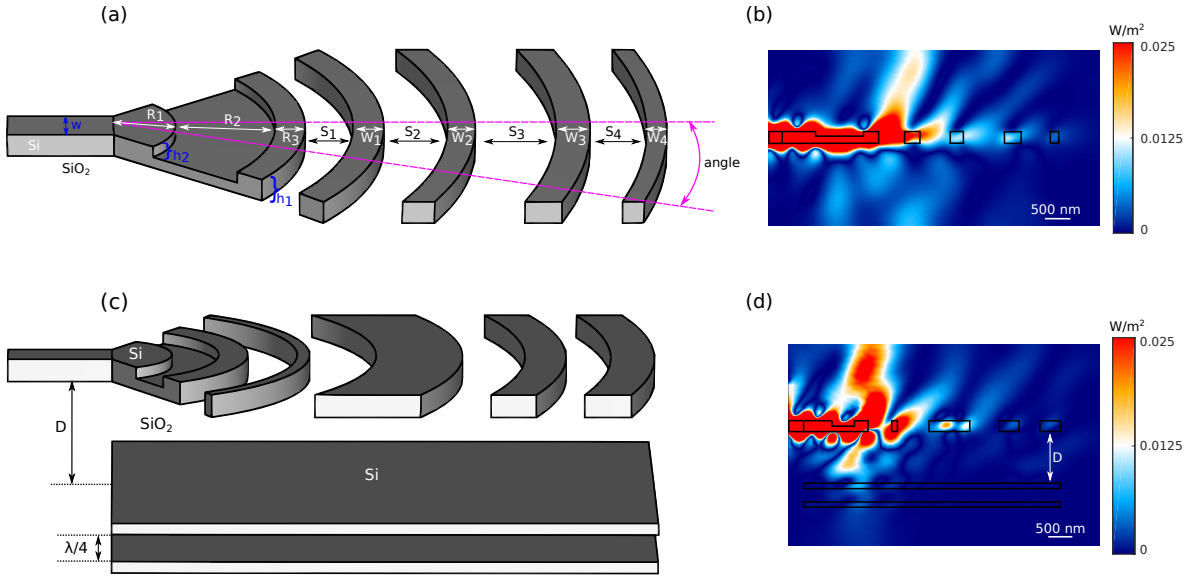

Fig. 2. (a,c) Schematics of the two optimized dielectric antennas showing the parameters used in the hybrid optimization. (b,d) Simulated near-field power-flow distributions of the optimized antennas in the xz-plane at $y = 0$.

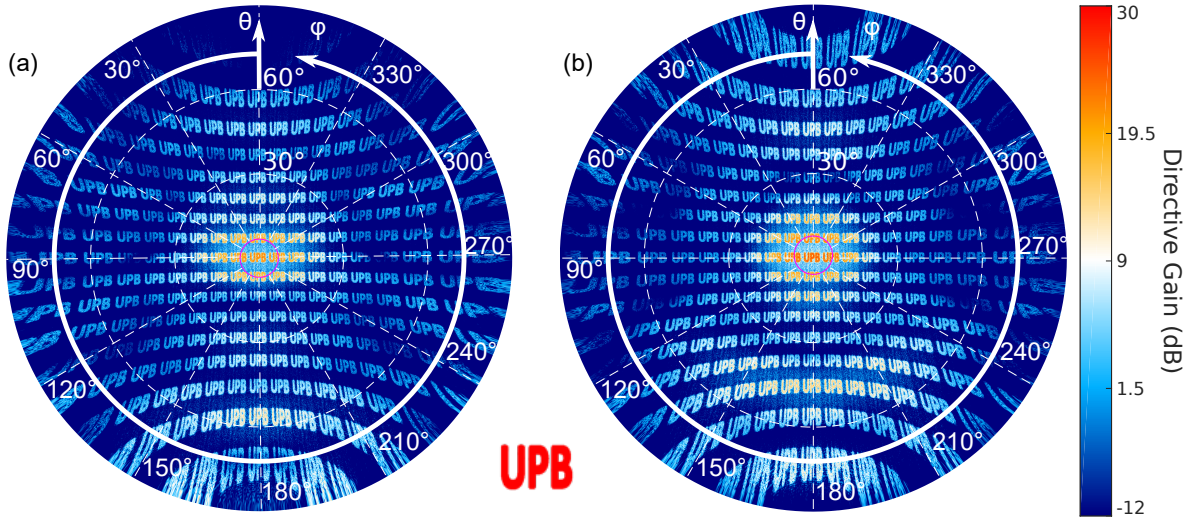

Fig. 3. Simulated far-field radiation patterns of a 64×64 phased array using antennas (a) without and (b) with a Bragg reflector to project the UPB logo at 1.55 µm. The original logo is shown at the center, and the FOV is marked by the pink circle.

III. Conclusion

The dielectric nanoantennas presented in this work are optimized to enhance power delivery into a $6.8° \times 6.8°$ FOV at 1.55 µm. The first design achieves 51% upward efficiency with 3.2% of power in the FOV, while a Bragg-reflector-assisted design reaches ∼90% efficiency and 6.8% in-FOV power, a tenfold improvement over the reference antenna. Phase control across the 2D array enables beam steering and beamforming, with strong potential for LiDAR and other OPA applications.

Acknowledgments

The work was funded by the Ministry of Culture and Science of the state of North Rhine-Westphalia via the PhoQC project. Additionally, the authors gratefully acknowledge the computing time support provided by the Paderborn Center for Parallel Computing (PC^2).

References

[1] H. Farheen, A. Strauch, J. C. Scheytt, V. Myroshnychenko, and J. Förstner, "Optimized, highly efficient silicon antennas for optical phased arrays," *Photonics and Nanostructures-Fundamentals and Applications*, vol. 58, p. 101207, 2024.

[2] H. Farheen, S. Joshi, J. C. Scheytt, V. Myroshnychenko, and J. Förstner, "An efficient compact blazed grating antenna for optical phased arrays," *Journal of Physics: Photonics*, vol. 6, no. 4, p. 045010, 2024.

[3] J. Sun, E. Timurdogan, A. Yaacobi, Z. Su, E. S. Hosseini, D. B. Cole, and M. R. Watts, "Large-scale silicon photonic circuits for optical phased arrays," *IEEE Journal of Selected Topics in Quantum Electronics*, vol. 20, no. 4, pp. 264–278, 2013.

Investigation on Q-switching pulsed lasing in Mid-IR via Semiconductor Saturable-Absorber Mirrors

Antonella M. Loconsole[1], Francesco Anelli, Federico Moscatelli, Francesco Prudenzano[1,*]

[1]Department of Electrical and Information Engineering, Politecnico di Bari, Bari, Italy
*Corresponding author: francesco.prudenzano@poliba.it

***Abstract*— The dynamics of a mid-infrared passively Q-switching pulsed erbium-doped ZBLAN fiber laser, emitting at 3.44 µm, has been investigated via a Finite-Difference Time Domain homemade code. It has been designed by considering actual components as available on market Semiconductor Saturable Absorber Mirror (SESAM) and fluoride fibers. Preliminary results predict average signal power higher than P_s = 0.9 W, pulse duration shorter than τ = 230 ns and repetition rate higher than f = 70 kHz, paving the way for further optimization. The aim of the work is to provide an optimized design promising higher performance with respect to the state-of-the-art fabricated laser cavities.**

***Keywords*— fiber laser, Q-switching, semiconductor saturable-absorber mirror, ZBLAN fiber.**

I. Introduction

The mid-infrared (Mid-IR) spectral region, specifically beyond 3 µm, has gained significant interest due to its overlap with the fundamental absorption bands of various hydrocarbons environmental gases and biomolecules [1-4]. To obtain emissions in this region, rare-earth doped fluoride and chalcogenide glass fibers can be employed as active medium for the laser cavity [5-10]. In particular, erbium-doped fluoride ZBLAN fibers have provided efficient lasing on the ${}^4F_{9/2} \rightarrow {}^4I_{9/2}$ transition at $\lambda_s = 3.44\,\mu m$, achieving total slope efficiency better than $\eta = 27\%$ when employing dual-pumping solutions at $\lambda_{p1} = 976\,nm$ and $\lambda_{p2} = 1973\,nm$, with the aim of overcoming the bottleneck of the lower laser level [10-13]. During the last years pulsed lasing has been obtained by considering gain-switching, active Q-switching or mode-locking [11,14]. However, stable passive Q-switching pulsed operation, with performance comparable to the other solutions exhibits a renewed potential due to the development of novel Semiconductor Saturable Absorber Mirrors (SESAMs) working beyond 3 μm. In [15] a Q-switching pulsed laser at $\lambda_s = 3.46\,\mu m$ has been demonstrated, employing a SESAM working at 3 μm, without the help of a model. In particular, even by employing a non-optimized SESAM, pulses with 2 μs-width, repetition rate around $f = 58\,kHz$ efficiency η = 2.7 % have been obtained.

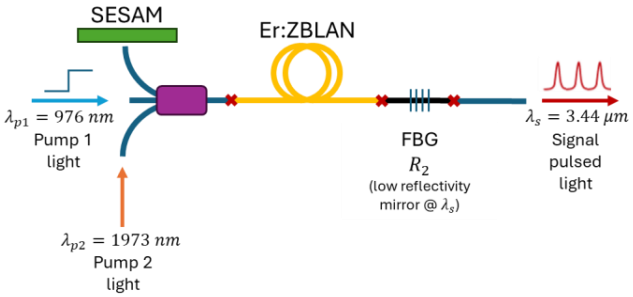

Fig. 1 SESAM-based Q-switching fiber laser scheme.

This work explores the dynamics of a passively Q-switched system based on an erbium-doped ZBLAN fiber working at $\lambda_s = 3.44\,\mu m$, when pumped at $\lambda_{p1} = 976\,nm$ and $\lambda_{p2} = 1973\,nm$ by using a commercial SESAM optimized at 3.5 μm. A comprehensive investigation on pulse stability and energy extraction is illustrated.

II. Q-switching laser design

The system is based on a 7-level energy diagram for Er^{3+}, in order to consider second order phenomena such as cross-relaxation (CR) and up-conversion (UP), as reported in literature [7,8,10].

Fig. 1 shows the scheme of the designed fiber laser. It is based on a step-index 2-D shaped double-cladding ZBLAN fiber doped with $N_{Er} = 1\,mol.\%$, by Le Verre Fluoré. The geometrical parameters of the fiber are:

- Core diameter $d_{co} = 16.5\,\mu m$;
- First cladding diameter $d_{cl1} = 260\,\mu m$, truncated at $d = 240\,\mu m$;
- Second cladding diameter $d_{cl2} = 290\,\mu m$;
- Numerical aperture $NA_1 = 0.125$;
- Numerical aperture $NA_2 = 0.3$.

The fiber is monomodal at signal wavelength $\lambda_s = 3.44\,\mu m$. A dual-pumping solution has been considered. The first pump at $\lambda_{p1} = 976\,nm$ is injected into the inner cladding, while the second pump at $\lambda_{p2} = 1976\,nm$ is injected into the core. The fiber has been investigated via a Finite Element Method (FEM) software, in order to calculate the first and the second pump and the signal overlap coefficients $\Gamma_{p1} = 0.009$, $\Gamma_{p2} = 0.8$, and

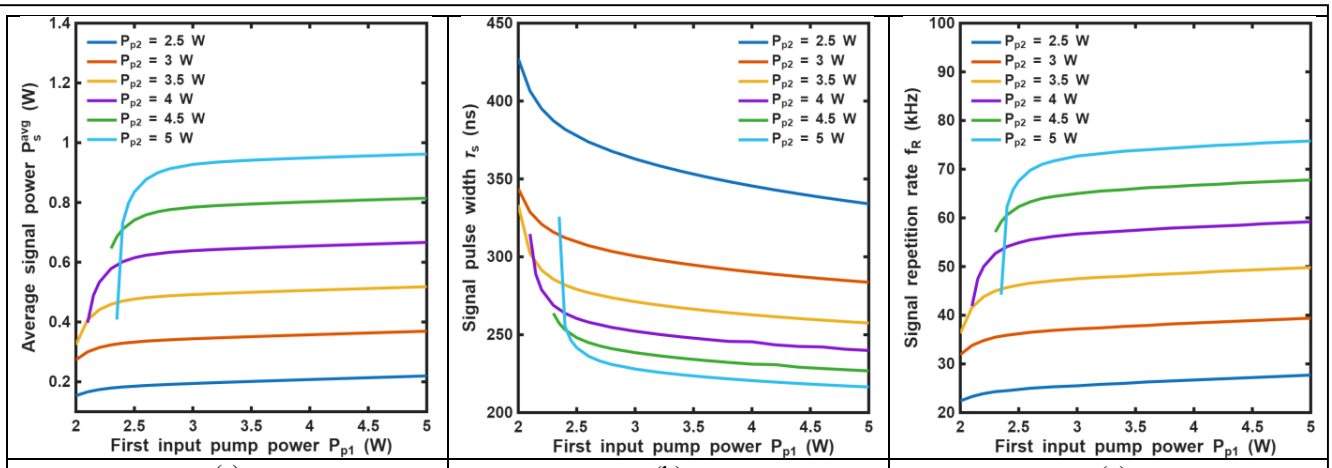

Fig. 2 (a) Average signal power P_s^{avg}, (b) signal pulse width τ_s and (c) signal repetition rate f as a function of the first input pump power P_{p1}, for different values of the second input pump power P_{p2}, fiber length $L = 1.5\ m$ and output mirror reflectivity $R_2 = 75\%$.

$\Gamma_s = 0.69$ respectively. These values are the same also reported in []. Experimental spectroscopical parameters have been taken from literature. The chosen SESAM is the SAM-3500-38-7ps-c/e by Crystrong Photonics Technology Co.

The design is carried out via a home-made solver code, solving rate equations and power propagation equations using Finite-Difference Time-Domain (FDTD) method, considering a time grid with step $\Delta t = 1\ ns$ and a space grid with step $\Delta z = 10\ mm$. The simulation time window is $\Delta T = 10\ ms$, longer than the biggest lifetime $\tau_2 = 9.8\ ms$ of level ${}^4I_{13/2}$ of erbium ions. The code has been validated by considering an experimental continuous wave (CW) scenario from literature, obtaining good agreement in terms of slope efficiency and input pump threshold for the limit case of a SESAM working as a simple mirror with reflectivity $R_1 = 95\%$ [16]. The CW simulations have shown that the system reaches the steady-state condition after $t = 3.5\ ms$.

Several simulations have been carried out, by varying the input pump power for first and second pump, for fiber length $L = 1.5\ m$ and output mirror reflectivity $R_2 = 75\%$.

Fig. 2(a) reports the average signal power P_s^{avg} as a function of the first input pump power P_{p1}, for different values of the second input pump power P_{p2}. For values less than $P_{p2} = 2\ W$, no stable pulses were observed in the range $P_{p1} = 2\ W \div 5\ W$. As the first input pump power P_{p1}, the average signal power P_s^{avg} slightly increases, while the first input pump power threshold P_{p1}^{th} increases with the second input pump power P_{p2}.

Fig. 2(b) reports the signal pulse width τ_s as a function of the first input pump power P_{p1}, for different values of the second input pump power P_{p2}. For increasing both P_{p1} and P_{p2} the signal pulse width τ_s always decreases, reaching $\tau_s = 219\ ns$ for $P_{p1} = P_{p2} = 5\ W$.

Fig. 2(c) reports the signal repetition rate f as a function of the first input pump power P_{p1}, for different values of the second input pump power P_{p2}. As for the average signal power P_s^{avg}, also the repetition rate f slightly increases with the first input pump power P_{p1}, while it rapidly increases with the second input pump power P_{p2}. From these results, it is possible to obtain the signal pulse energy E_s and signal peak power P_s^{peak}, reaching $E_s = 12.7\ \mu J$ and $P_s^{peak} = 58\ W$ for $P_{p1} = P_{p2} = 5\ W$.

To evaluate the second input pump power threshold P_{p2}^{th}, Fig. 3 reports the average signal power P_s^{avg} as a function of the first input pump power P_{p2}, for first input pump power $P_{p1} = 4\ W$, fiber length $L = 1.5\ m$, and output mirror reflectivity $R_2 = 75\%$. The average signal power P_s^{avg} shows a linear behavior with second input pump power threshold $P_{p2}^{th} = 1.75\ W$ and slope efficiency $\eta_2 = 20.2\%$. It is worthwhile noting that stable pulsing regime is achieved only for $P_{p2} > 2.25\ W$.

Fig. 4 depicts the output signal power P_s as function of the time t, for first and second input pump power $P_{p1} = P_{p2} = 4\ W$, fiber length $L = 1.5\ m$, and output mirror reflectivity $R_2 = 75\%$. The pulsed regime is obtained after $t = 0.8\ ms$, while constant pulses are achieved after $t = 3\ ms$.

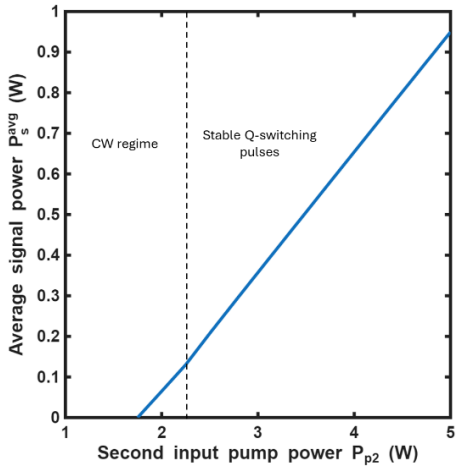

Fig. 3 Average signal power P_s^{avg} as a function of the second input pump power P_{p2}, for first input pump power $P_{p1} = 4\ W$, fiber length $L = 1.5\ m$ and output mirror reflectivity $R_2 = 75\%$.

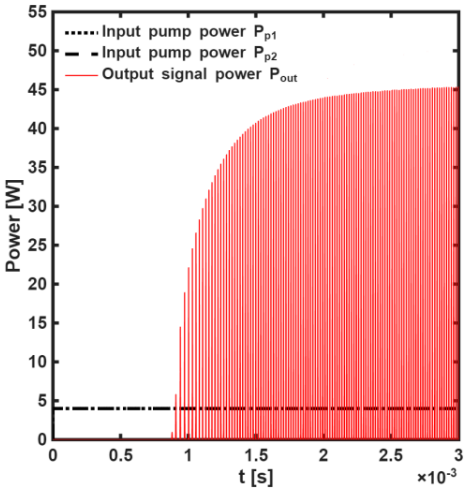

Fig. 4 Output signal power P_s as a function of the time t, for first input pump power $P_{p1} = 4\ W$, second input pump power $P_{p2} = 4\ W$, fiber length $L = 1.5\ m$ and output mirror reflectivity $R_2 = 75\%$.

III. Conclusion

In this work, a passive Q-switching pulsed laser based on a ZBLAN erbium-doped fiber has been investigated for emission at $\lambda_s = 3.44\ \mu m$ considering a dual-pumping scheme at $\lambda_{p1} = 976\ nm$ and $\lambda_{p2} = 1973\ nm$. Preliminary results have showed average signal power higher than $P_s^{avg} = 0.9\ W$ with maximum slope efficiency respect to the second pump power $\eta_2 = 20.2\ \%$, signal pulse width shorter than $\tau_s = 230\ ns$, and signal repetition rate higher than $f = 70\ kHz$. These results can be considered a good starting point for further optimization by considering that the state of the art of fabricated lasers reported in literature exhibited a maximum slope efficiency with respect to the second pump power $\eta_2 = 2.7\ \%$ by employing a SESAM not properly optimized at $\lambda_s = 3.44\ \mu m$.

Acknowledgments

This work was supported in part by Telecommunications of the Future (PE00000001 "RESTART") under Grant CUP: D93C22000910001, STRUCTURAL PROJECT Antennas & Devices foR mixing, dEtection And Manipulation of mmWaves; in part by MIUR PRIN 2022, NRPP – DD n. 1181 del 27-07-2023 VEGETATION under Grant P2022ZF9P2 and Grant I53D23005710 001; in part by H2020-ICT-37-2020 – PASSEPARTOUT under Grant 101016956; in part by ASI 2024-68-I.0 "Origami Reconfigurable Beam-steering Antennas with METAsurfaces for Communication on Small Satellites - ORBIT-META" under Grant CUP: F93C24000550001; in part by ASI 687/2022 - MUR 341 15/03/22 "SPACE IT UP" under Grant CUP: D53C24000570006; and in part by HORIZON-TMA-MSCA-SE HORIZON TMA MSCA Staff Exchanges through "Cr4+:YAG/Polymer nanocomposite as alternative materials for Q-switched lasers: properties, modeling, and applications - ALTER-Q" under Grant 101182995.

References

[1] X. Li, X. Huang, X. Hu, X. Guo, Y. Han, "Recent progress on mid-infrared pulsed fiber lasers and the applications", *Opt. Laser Technol*., vol. 158, Part B, 2023.

[2] A. E. Klingbeil, J. B. Jeffries, R. K. Hanson, "Temperature-dependent mid-IR absorption spectra of gaseous hydrocarbons," *J. Quant. Spectrosc. Radiat. Transf.*, vol. 107, vol. 3, pp. 407-420, Oct. 2007.

[3] A. Annunziato, F. Anelli, P. Le Pays Du Teilleul, S. Cozic, S. Poulain, and F. Prudenzano, "Fused optical fiber combiner based on indium fluoride glass: perspectives for mid-IR applications", *Opt. Express*, vol. 30.

[4] L. Zhang, F. Guan, L. Zhang, Y. Jiang, "Next generation mid-infrared fiber: fluoroindate glass fiber," *Opt. Mater. Express*, vol. 12, pp. 1683-1707, 2022.

[5] F. Anelli, A. Annunziato, A. M. Loconsole, V. Portosi, S. Cozic, P. Le Pays du Teilleul, S. Venck, S. Poulin, F. Prudenzano, "Low-Loss Fluoride Optical Fiber Coupler for Mid-Infrared Applications," *J. Light. Technol*, vol. 42, no. 7, pp. 2457-2463, Apr. 2024.

[6] J. J. Nunes, Ł. Sojka, R. W. Crane, D. Furniss, Z. Q. Tang, D. Mabwa, B. Xiao, T. M. Benson, M. Farries, N. Kalfagiannis, E. Barney, S. Phang, A. B. Seddon, and S. Sujecki, "Room temperature mid-infrared fiber lasing beyond 5 µm in chalcogenide glass small-core step index fiber," in *Opt. Lett.*, vol. 46, pp. 3504-3507, 19 Jul. 2021.

[7] A. M. Loconsole, M. C. Falconi, V. Portosi, F. Prudenzano, "Numerical Design of a Gain-Switched Pulsed Laser at 3.92 µm Wavelength Based on a Ho3+-Doped Fluoroindate Fiber," *J. Lightw. Technol.*, vol.39, no. 10, pp. 3276-3283, May 2021.

[8] A. M. Loconsole, V. V. Francione, A. Annunziato, F. Anelli and F. Prudenzano, "Design of a High-Performance Mid-IR Fiber Laser Based on Pr3+-Doped Fluoroindate Glass," *J. Light. Technol*., vol. 42, no. 7, pp. 2488-2493, Apr. 2024.

[9] V. Fortin, F. Maes, M. Bernier, S. Toubou Bah, M. D'Auteuil, R. Vallée, "Watt-level erbium-doped all-fiber laser at 3.44 µm," *Opt. Lett.*, vol. 41, pp. 559-562, 2016.

[10] O. Henderson-Sapir, A. Malouf, N. Bawden, J. Munch, S. D. Jackson, D. J. Ottaway, "Recent Advances in 3.5 µm Erbium-Doped Mid-Infrared Fiber Lasers," *IEEE J. Sel. Top Quantum Electron*., vol. 23, no. 3, pp. 6-14, May 2017, Art no. 0900509.

[11] O. Henderson-Sapir, N. Bawden, A. Theodosiou, Matthew R. Majewski, *et al.,* "Mode-Locked and Tunable 3.5 µm Fiber Laser Using an Acousto-Optic Modulator," in *J. Light. Technol,* vol. 41, no. 2, pp. 716-725, 15 Jan. 2023.

[12] F. Maes, V. Fortin, M. Bernier, R. Vallée, "Quenching of 3.4 µm Dual-Wavelength Pumped Erbium Doped Fiber Lasers", *IEEE Journal of Quantum Electronics*, vol. 53, no. 2, Apr. 2017.

[13] M. C. Falconi, A. M. Loconsole, A. Annunziato, S. Cozic, S. Poulain and F. Prudenzano, "Design of a Broadband Erbium-Doped Fluoroindate Fiber Laser Emitting Up to 3.91 µm," *J. Lightw. Technol*., vol. 41, no. 18, pp. 6065-6072, Sep. 2023.

[14] L. Sójka, L. Pajewski, S. Lamrini, M. Farries, T.M. Benson, A. B. Seddon, S. Sujecki, "High Peak Power Q-switched Er:ZBLAN Fiber Laser," *J. Lightw. Technol.*, vol. 39, no. 20, Oct. 2021.

[15] Z. Fang, C. Zhang, J. Liu, Y. Chen, D. Fan, "3.46 µm Q-switched Er3+:ZBLAN fiber laser based on a semiconductor saturable absorber mirror", *Optics & Laser Technology*, vol. 141, 2021.

[16] O. Henderson-Sapir, S. D. Jackson, D. J. Ottaway, "Versatile and widely tunable mid-infrared erbium doped ZBLAN fiber laser", *Optics Letters*, vol. 41, no. 7, Apr. 2016.

Plasmonic switches based on the composite gold–vanadium dioxide material platform

Rostislav Řepa[1], Jiří Kabát[1], Jiří Liška[1], Tomáš Šikola[1], and Vlastimil Křápek[1,*],

[1]Brno University of Technology, Brno, Czechia

*Corresponding author: krapek@vutbr.cz

***Abstract*—We introduce reconfigurable plasmonic devices (plasmonic switches) based on a composite material platform that combines gold and vanadium dioxide. Our approach represents both quantitative and qualitative advancement of traditional plasmonic switches based on vanadium dioxide. As a case study, we present switching between a bowtie and a diabolo plasmonic antenna. *Keywords*— plasmonic switch, bowtie, diabolo, hot spot, field enhancement, vanadium dioxide, active plasmonics.**

I. Introduction

Plasmonic antennas (PAs) are metallic nanostructures that exploit localized surface plasmons (LSP) to control light at the nanoscale, including subwavelength confinement and enhancement [1]. They offer numerous functionalities that find applications, e.g, in enhanced spectroscopy, enhanced light-matter interaction, energy harvesting, or sensing [2], [3], [4]. PAs are traditionally composed of conventional metals, with gold being a common option due to its high electrical conductivity and chemical stability. However, the functionality of such PAs is fixed after their fabrication. Driven by the desire for reconfigurable and tunable PAs, exploitation of phase-change materials (PCMs) is being considered.

Vanadium dioxide (VO_2) belongs to one of the most popular PCMs for plasmonic applications. It exhibits a metal-insulator transition (MIT) with a convenient transition temperature around 68 °C. which can be triggered by thermal, electrical, mechanical, or optical stimuli [5]. During the MIT, the material exhibits significant changes in electrical conductivity (five orders of magnitude within a picosecond timescale) and optical properties (especially in the infrared region) [5]. All these properties make VO_2 highly attractive for cutting-edge applications, including optical switching [6] or active optical metamaterials [7]. However, VO_2 also possesses some unfavourable properties, such as low optical conductivity even in the metallic phase and low Q factor of plasmon resonances [8], as well as restricted functionality, often limited to ON/OFF switching [9], and challenging lithographic nanofabrication VO_2 [10].

To overcome these limitations, we propose to combine VO_2 as the active element and a conventional metal as a good conductor into composite plasmonic antennas. Motivated by our recent development of high-quality self-assembled single-crystalline nanoparticles [8], [11], we consider a planar arrangement of the materials, which further reduces the amount of VO_2 to a necessary minimum and also increases the design flexibility by allowing for a local change of the conductivity. The feasibility of this approach is manifested using a case study of switching between the bowtie PA, which supports the electric hot spot, and the diabolo PA, which supports the magnetic hot spot.

II. Methods

Theoretical modeling was performed using a formalism of classical electrodynamics with the numerical solution performed using the finite element method (software package Comsol Multiphysics). The geometry of the modeled PAs was set as follows: the length $L = 500$ nm, the width $W = 300$ nm, the length and the width of the bridge $B_L = 40$ nm and $B_W = 40$ nm, respectively, the thickness $T = 30$ nm.

III. Results and Discussion

Bowtie and diabolo PAs produce electric and magnetic hot spots, i.e., strongly confined and enhanced electric or magnetic fields, respectively. They find numerous applications, e.g., in plasmon-enhanced spectroscopy [2], [3] or enhanced light-matter coupling [4].

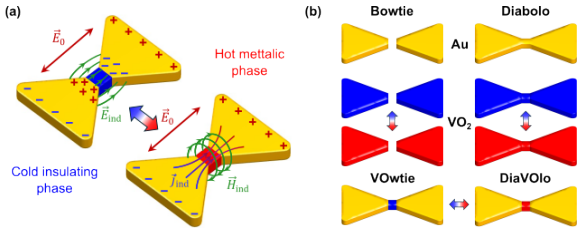

Fig. 1. (a) Bowtie and diabolo antennas with schemes of their operation and formation of hot spots. Red arrows indicated the polarization of the light used for the excitation. The symbols + and − indicate areas of the charge concentration. The field lines showing a formation of hot spots are also indicated. (b) Bowtie (left) and diabolo (right) antennas involved in our study: gold (first row), vanadium dioxide (second and third row), and composite (fourth row). The color of individual PA parts indicates their material composition: gold (yellow), metallic VO_2 (red), and insulating VO_2 (blue).

The bowtie and diabolo PAs are schematically shown in Fig. 1(a). They consist of two metallic wings with a triangular shape, with the proximal vertices either separated by an insulating gap (bowtie) or connected with a conducting bridge (diabolo). When excited with a plane wave polarized parallel

to the long axis of the PA [as indicated by red arrows in Fig. 1(a)], the LSP resonances result in the formation of hot spots, as indicated in Fig. 1(a). In the case of the bowtie PA, the charge is concentrated on the sides of the insulating gap, resulting in the electric hot spot. In the case of the diabolo PA, the current is funnelled through the conducting bridge, resulting in the magnetic hot spot. The properties of the bowtie and diabolo PAs, their LSP resonances, and hot spots have been thoroughly studied [12].

In our study, we compare 8 bowtie and diabolo PAs: homogeneous PAs fabricated from gold, homogeneous PAs fabricated from metallic VO_2, homogeneous structures fabricated from insulating VO_2 (they do not support LSP and lack the functionality of PAs), and the composite PAs with gold wings and VO_2 bridge. The composite PAs are labeled as VOwtie(an analogue of the bowtie) when the VO_2 bridge is insulating, and as diaVOlo (an analogue of the diabolo) when the VO_2 bridge is metallic. We focus on the electric and magnetic field distribution corresponding to the hot spot. To this end, we calculate the spectral dependences of the scattering and absorption cross sections (not shown), from which we determine the spectral position of the LSP resonance, which corresponds to the formation of the hot spot, and for the corresponding frequency, we calculate the total field produced by the PA. Finally, we normalize the total field with respect to the field of the plane wave utilized as the excitation.

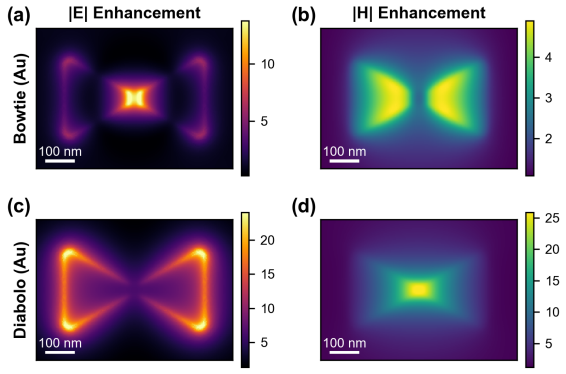

Fig. 2. Normalized electromagnetic field produced by the gold bowtie and diabolo PAs: planar cross sections at the height of 10 nm above the upper surface of PAs. (a,b) The electric (a) and the magnetic (b) field of the bowtie PA. (c,d) The electric (c) and the magnetic (d) field of the diabolo PA.

As a reference, we inspect the fields of the homogeneous gold bowtie and diabolo PAs. The fields are shown in Fig. 2. They clearly manifest the expected formation of hot spots. The electric field of the bowtie is localized at the gap and strongly enhanced (14×), while the magnetic field of the bowtie is delocalized and weaker. On the other hand, the magnetic field of the diabolo is localized around the bridge and strongly enhanced (24×), while the electric field is weak in that region (although it reaches fairly high numbers at the sides of the diabolo).

The fields of the composite PAs, the VOwtie and the diaVOlo, shown in Fig. 3, are clearly distinct. Both the electric and magnetic fields are confined and enhanced at the central part of both PAs, resulting in the formation of mixed electric-magnetic hot spots. This observation is attributed to the nature of the VO_2 bridge, which is not a perfect insulator in the case of the VOwtie, and is rather a bad conductor (with the conductivity significantly lower than gold) in the case of the diaVOlo. The unique properties of the composite PAs predestinate them for specific application fields, distinct from gold bowtie and diabolo PAs.

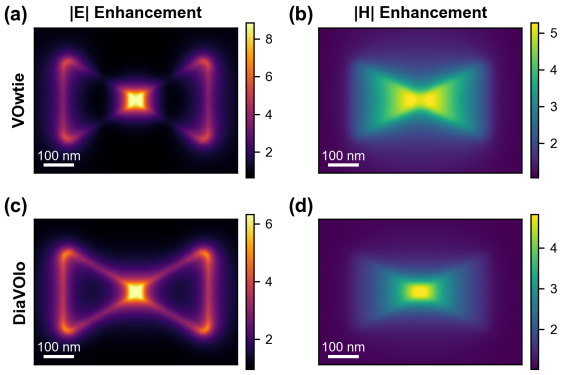

Fig. 3. Normalized electromagnetic field produced by the composite VOwtie and diaVOlo PAs: planar cross sections at the height of 10 nm above the upper surface of PAs. (a,b) The electric (a) and the magnetic (b) field of the VOwtie PA. (c,d) The electric (c) and the magnetic (d) field of the diaVOlo PA.

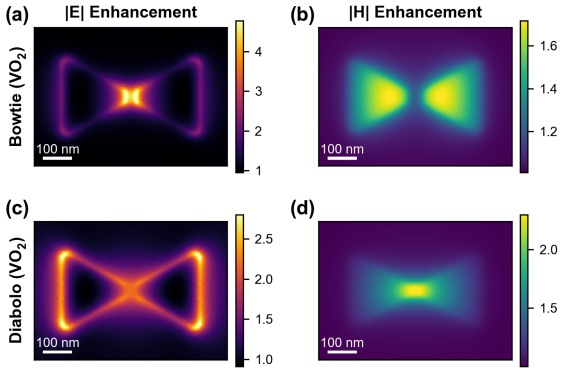

Fig. 4. Normalized electromagnetic field produced by the metallic VO_2 bowtie and diabolo PAs: planar cross sections at the height of 10 nm above the upper surface of PAs. (a,b) The electric (a) and the magnetic (b) field of the bowtie PA. (c,d) The electric (c) and the magnetic (d) field of the diabolo PA.

In Fig. 4, we show for completeness the fields of the homogeneous PAs of metallic VO_2. The field distribution is rather similar to that of the gold PAs (shown in Fig. 2), although the magnitudes of the field are significantly lower, reflecting high optical losses of the metallic VO_2.

In the conference presentation, we will further discuss other aspects of the switching: the spectral shift of the plasmon

resonances and the change in the absorption and scattering cross sections and their ratio, the so-called scattering-absorption ratio (SAR). We will demonstrate that the switching of SAR is particularly attractive for applications in broadband antireflection coating or fast control of the solar intensity for photovoltaic cells.

IV. Conclusion

We have presented the composite material platform for plasmonic switches based on the planar arrangement of gold and vanadium dioxide. We have shown that the composite PAs offer a significant improvement over homogeneous VO_2 PAs in terms of the magnitude of the electric and magnetic fields at the hot spots, but also qualitatively distinct functionality consisting in the formation of mixed electric-magnetic hot spots.

Acknowledgments

We acknowledge support from the Ministry of Education, Youth, and Sports of the Czech Republic, projects No. CZ.02.01.01/00/22_008/0004572 (QM4ST) and LM2023051 (CzechNanoLab). RŘ was supported by Brno University of Technology (project No. CEITEC VUT-J-25-8860).

References

[1] L. Novotny and B. Hecht, "Principles of Nano-Optics," Cambridge University Press, 2012.
[2] A. Kinkhabwala et al., "Large single-molecule fluorescence enhancements produced by a bowtie nanoantenna," *Nature Photonics*, vol. 3, pp. 654–657, 2009.
[3] L. Tesi et al., "Plasmonic Metasurface Resonators to Enhance Terahertz Magnetic Fields for High-Frequency Electron Paramagnetic Resonance," *Small Methods*, vol. 5, p. 2100376, 2021.
[4] O. Bitton et al., "Vacuum Rabi splitting of a dark plasmonic cavity mode revealed by fast electrons," *Nature Communications*, vol. 11, p. 487, 2020.
[5] K. Liu et al., "Recent progresses on physics and applications of vanadium dioxide," *Materials Today*, vol. 21, pp. 875–896, 2018.
[6] L. Long et al., "Enhanced Infrared Emission by Thermally Switching the Excitation of Magnetic Polariton with Scalable Microstructured VO2 Metasurfaces," *ACS Photonics*, vol. 7, pp. 2219–2227, 2020.
[7] P. Kepič et al., "Optically Tunable Mie Resonance VO2 Nanoantennas for Metasurfaces in the Visible," *ACS Photonics*, vol. 8, pp. 1048–1057, 2021.
[8] J. Kabát et al., "," *arXiv*, , 2026.
[9] S. Cueff et al., "VO2 nanophotonics," *APL Photonics*, vol. 5, p. 110901, 2020.
[10] J. Krpenský et al., "Analytical electron microscopy analysis of insulating and metallic phases in nanostructured vanadium dioxide," *Nanoscale Advances*, vol. 6, pp. 3338–3346, 2024.
[11] M. Horák et al., "Tuning of Localized Surface Plasmons in Vanadium Dioxide Nanoparticles via Size and Insulator-Metal Transition," *arXiv*, 2602.00673, 2026.
[12] V. Křápek et al., "Independent engineering of individual plasmon modes in plasmonic dimers with conductive and capacitive coupling," *Nanophotonics*, vol. 9, pp. 623–632, 2020.

Lithium-Niobate-Enabled Tuning of Optical Absorbance in Single- and Double-Layer Metallic Circular-Hole Arrays

H. Alhesseny[(1)], C. Johnson-Richards[(1)], R. G. MacDonald[(1)], N. Healy[(1)], T. Hallam[(1)], and V. Pacheco-Peña [(1),*]
(1) School of Mathematics, Statistics and Physics, Newcastle University, Newcastle Upon Tyne, NE1 7RU, UK.
e-mail: victor.pachecopena@gmail.com

***Abstract*— We present the design and study of a tunable structure based on extraordinary optical transmission (EOT) at telecommunication wavelengths (1550 nm). The design consists of a perforated metallic structure on a Lithium Niobate ($LiNbO_3$) layer. A single-metal layer design is compared with a double-layer $Ag/SiO_2/Ag$ configuration. Higher absorbance and improved Q-factor is observed for the double-layer configuration. The tunable properties of the structure are studied by applying a DC voltage, which may open opportunities for sensing application.**

***Keywords*— metamaterials, lithium niobate, extraordinary optical transmission.**

I. Introduction

Since it was first reported, extraordinary optical transmission (EOT) [1,2] has been intensively explored, studied and implemented in applications including sensing [3] and lenses [4-6], as examples. Additionally, recent scientific progress has also placed an emphasis into tunable structures as a mechanism to enable flexible designs with adjustable resonances once the structures have been fabricated [7,8]. Indeed, while it is a concept in the frequency domain, tunability is becoming more relevant as a mechanism to enable the control of waves in space [9,10] and time [11-15]. Different approaches have been proposed to enable tunability in subwavelength periodic/aperiodic structures including tunable resonances using semiconductors [16,17], phase-change materials [18], and graphene [19,20]. Electro-optic tuning using Lithium Niobate ($LiNbO_3$) has also become interesting because of its strong second-order nonlinearity and low loss at telecom wavelengths [21-23].

Motivated by the interesting features of tunable structures and EOT in subwavelength periodic hole arrays, here we present our recent and ongoing efforts in this field. Specifically, we show two designs: (I) a single Silver (Ag) layer with subwavelength periodic holes and (II) a perforated Ag/Silicon Dioxide (SiO_2)/Ag stack (called double-layer in this work). Both designs are placed on a ($LiNbO_3$) layer to enable tuning of the EOT resonance under an applied voltage.

Preliminary results show an improvement of absorption (up to approximately 3×) and enhanced Q-factor for the double-layer structure when compared to the single layer. In addition to these features, a detailed discussion in terms of tunability, transmittance spectra and tuning sensitivity will be presented. Further structures that involve variation to the single and two-layer configurations will also be discussed during the conference.

II. Results and Discussions

To begin with, the schematic representations of the two structures under study are shown as insets in Fig. 1a. Here case I and II represent the single and double layers, respectively. The period of case I and II is $a = 930$ nm and $a = 992$ nm, respectively. These values were selected to target operation at a wavelength of 1550 nm. The baseline stack consists of five fixed layers arranged from bottom to top: Silicon (Si), SiO_2, $LiNbO_3$ -x-cut, Chromium (Cr), and Ag, with thicknesses of 4 μm, 500 nm, 300 nm, 10 nm, and 100 nm, respectively. The holes within the Ag and Cr layers have a diameter $d = 0.5a$. For case II, the added SiO_2 layer has a thickness of 300 nm.

The structures are simulated using CST Studio Suite® with periodic boundary conditions on the x and y planes. The Ag and Cr optical properties follow the Johnson and Christy model [24,25], and $LiNbO_3$ is modeled as a uniaxial anisotropic material following [26].

With this configuration the absorption spectra for cases I and II are shown in Fig. 1a as black and red lines, respectively. As observed, the introduction of the SiO_2 spacer together with the additional Ag layer results in a pronounced increase in the peak absorption, from 0.2 to 0.66, which is consistent with previously reported metal–insulator–metal (MIM) resonant structures [27]. At the same time, the resonance Q-factor improves from ≈20 to ≈104.

Using case II, we evaluated the electrical tunability by applying a voltage from −50 V to +50 V across a unit cell along the x-direction and the results are shown in Fig. 1b. A shift of

the resonance is observed, with a tuning sensitivity of ($\frac{\Delta f}{\Delta V}$ ~1.9 GHz/V).

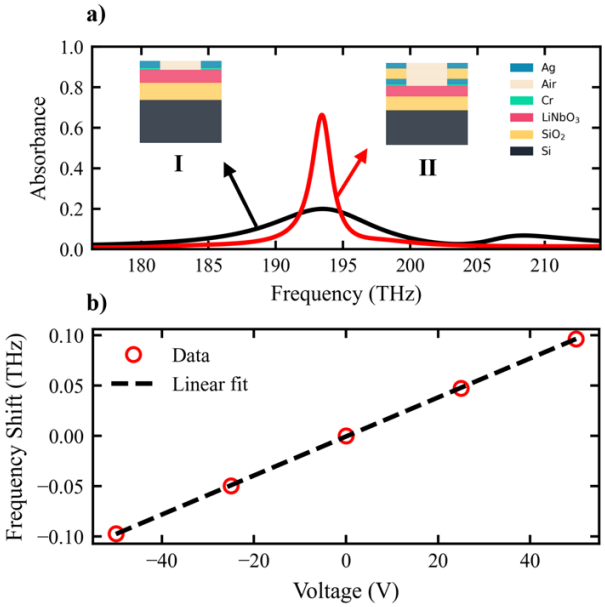

Fig. 1 (a) Schematics and absorbance spectra of the single-layer Ag and the double-layer $Ag/SiO_2/Ag$ structure. The stack comprises $Ag/Cr/LiNbO_3$ on a SiO_2/Si stack. (b) Resonance frequency shift as a function of the applied voltage bias (-50 V to $+50$ V).

III. Conclusion

In this work, we investigated an electrically tunable EOT resonance in a periodic structure operating at 1550 nm using two configurations: a single-layer and a double-layer stack. The stacked design yields an increase in Q-factor and absorbance. Further details, including the EOT transmittance and the tunability of single-layer as well as additional structural configurations will be discussed during the conference.

Acknowledgments

This work was supported by the Leverhulme Trust under the Leverhulme Trust Research Project Grant scheme (RPG-2023-024).

References

[1] T. W. Ebbesen, H. J. Lezec, H. F. Ghaemi, T. Thio, and P. A. Wolff, 'Extraordinary optical transmission through sub-wavelength hole arrays', *Nature*, vol. 391, no. 6668, pp. 667–669, Feb. 1998.

[2] M. Beruete, P. Rodriguez-Ulibarri, V. Pacheco-Peña, M. Navarro-Cía, and A. E. Serebryannikov, 'Frozen mode from hybridized extraordinary transmission and Fabry-Perot resonances', *Phys. Rev. B*, vol. 87, no. 20, p. 205128, May 2013.

[3] I. Jáuregui-López, P. Rodriguez-Ulibarri, S. A. Kuznetsov, N. A. Nikolaev, and M. Beruete, 'THz Sensing With Anomalous Extraordinary Optical Transmission Hole Arrays', *Sensors*, vol. 18, no. 11, p. 3848, Nov. 2018.

[4] V. Pacheco-Peña, B. Orazbayev, V. Torres, M. Beruete, and M. Navarro-Cía, 'Ultra-compact planoconcave zoned metallic lens based on the fishnet metamaterial', *Appl. Phys. Lett.*, vol. 103, no. 18, p. 183507, Oct. 2013.

[5] V. Pacheco-Pena, M. Navarro-Cia, B. Orazbayev, I. V. Minin, O. V. Minin, and M. Beruete, 'Zoned Fishnet Lens Antenna With Reference Phase for Side-Lobe Reduction', *IEEE Trans. Antennas Propag.*, vol. 63, no. 8, pp. 3710–3714, Aug. 2015.

[6] B. Orazbayev, M. Beruete, V. Pacheco-Peña, G. Crespo, J. Teniente, and M. Navarro-Cía, 'Soret Fishnet Metalens Antenna', *Sci. Rep.*, vol. 5, no. 1, p. 9988, May 2015.

[7] A. Pitilakis *et al.*, 'A Multi-Functional Reconfigurable Metasurface: Electromagnetic Design Accounting for Fabrication Aspects', *IEEE Trans. Antennas Propag.*, vol. 69, no. 3, pp. 1440–1454, Mar. 2021.

[8] C. Huang, C. Zhang, J. Yang, B. Sun, B. Zhao, and X. Luo, 'Reconfigurable Metasurface for Multifunctional Control of Electromagnetic Waves', *Adv. Opt. Mater.*, vol. 5, no. 22, p. 1700485, Nov. 2017.

[9] R. G. MacDonald, A. Yakovlev, and V. Pacheco-Peña, 'Amplitude-Controlled Electromagnetic Pulse Switching Using Waveguide Junctions for High-Speed Computing Processes', *Adv. Intell. Syst.*, vol. 4, no. 12, p. 2200137, Dec. 2022.

[10] R. Glyn MacDonald, A. Yakovlev, and V. Pacheco-Peña, 'Time derivatives via interconnected waveguides', *Sci. Rep.*, vol. 13, no. 1, p. 13126, Aug. 2023.

[11] V. Pacheco-Peña and N. Engheta, 'Temporal aiming', *Light Sci. Appl.*, vol. 9, no. 1, p. 129, Jul. 2020.

[12] V. Pacheco-Peña and N. Engheta, 'Merging Effective Medium Concepts of Spatial and Temporal Media: Opening new avenues for manipulating wave-matter interaction in 4D', *IEEE Antennas Propag. Mag.*, vol. 65, no. 4, pp. 39–49, Aug. 2023.

[13] L. Stefanini *et al.*, 'Theory and Experimental Observation of Scattering by a Space-Time Corner', *Phys. Rev. Lett.*, vol. 135, no. 11, p. 113802, Sep. 2025.

[14] V. Pacheco-Peña and N. Engheta, 'Antireflection temporal coatings', *Optica*, vol. 7, no. 4, p. 323, Apr. 2020.

[15] M. Antyufeyeva and V. Pacheco-Peña, 'Emulating time refraction at photonic time interfaces via smooth temporal transitions', *Phys. Rev. Appl.*, vol. 24, no. 3, p. 034004, Sep. 2025.

[16] E. A. Shaner, J. G. Cederberg, and D. Wasserman, 'Electrically tunable extraordinary optical transmission gratings', *Appl. Phys. Lett.*, vol. 91, no. 18, p. 181110, Oct. 2007.

[17] H.-T. Chen *et al.*, 'Electronic control of extraordinary terahertz transmission through subwavelength metal hole arrays', *Opt. Express*, vol. 16, no. 11, p. 7641, May 2008.

[18] E. Humphreys, J. Bertolotti, C. R. De Galarreta, N. Casquero, J. Siegel, and C. D. Wright, 'Filtering and Modulation from the Infrared to the Terahertz using Phase-Change Extraordinary Optical Transmission Metasurfaces', *Phys. Status Solidi RRL – Rapid Res. Lett.*, vol. 17, no. 8, p. 2200474, Aug. 2023.

[19] Z. Gao *et al.*, 'Tunable Extraordinary Optical Transmission with Graphene in Terahertz', *ACS Omega*, vol. 6, no. 44, pp. 29746–29751, Nov. 2021.

[20] S. Kim, M. S. Jang, V. W. Brar, Y. Tolstova, K. W. Mauser, and H. A. Atwater, 'Electronically tunable extraordinary optical transmission in graphene plasmonic ribbons coupled to subwavelength metallic slit arrays', *Nat. Commun.*, vol. 7, no. 1, p. 12323, Aug. 2016.

[21] B. Gao, M. Ren, W. Wu, W. Cai, and J. Xu, 'Electro-optic lithium niobate metasurfaces', *Sci. China Phys. Mech. Astron.*, vol. 64, no. 4, p. 240362, Apr. 2021.

[22] C.-C. Shih and A. Yariv, 'A theoretical model of the linear electro-optic effect', *J. Phys. C Solid State Phys.*, vol. 15, no. 4, pp. 825–846, Feb. 1982.

[23] Z. Chen, N. Mazurski, J. Engelberg, and U. Levy, 'Tunable Transmissive Metasurface Based on Thin-Film Lithium Niobate', *ACS Photonics*, vol. 12, no. 2, pp. 1174–1183, Feb. 2025.

[24] P. B. Johnson and R. W. Christy, 'Optical Constants of the Noble Metals', *Phys. Rev. B*, vol. 6, no. 12, pp. 4370–4379, Dec. 1972.

[25] P. Johnson and R. Christy, 'Optical constants of transition metals: Ti, V, Cr, Mn, Fe, Co, Ni, and Pd', *Phys. Rev. B*, vol. 9, no. 12, pp. 5056–5070, Jun. 1974.

[26] A. Weiss *et al.*, 'Tunable Metasurface Using Thin-Film Lithium Niobate in the Telecom Regime', *ACS Photonics*, vol. 9, no. 2, pp. 605–612, Feb. 2022.

[27] G. Wu, W. Xiao, Z. Wang, Y. Zhang, and C. Huang, 'Transparent absorber composed of two stacked ultrathin metal films perforated with small holes', *Opt. Express*, vol. 30, no. 13, p. 22922, Jun. 2022.

Triple-doping in optical plasmonic glass nanocomposites

Katarzyna Klepacka[1]*, Piotr Piotrowski[1,2]*, Rafał Nowaczyński[1], Barbara H. Surma[1], Dorota A. Pawlak[1,2]

[1]Centre of Excellence ENSEMBLE3 sp. z o.o, Wolczynska 133, Warsaw, Poland
[2]Faculty of Chemistry, University of Warsaw, Pasteura 1, Warsaw, Poland
*Corresponding author: katarzyna.klepacka@ensemble3.eu, piotr.piotrowski@ensemble3.eu

***Abstract* – In this work we present a triple-doped material that combines excitonic and plasmonic properties in one matrix. Localized surface plasmon resonance enhances light–matter interaction, enabling tunable luminescence and multifunctional applications in photonics, sensing, and plasmonic devices.**

***Keywords* – plasmon, quantum dots, glass nanocomposite, enhanced luminescence**

I. Introduction

Materials used in photonics and optoelectronics are usually doped with a single active component. Each material is chosen because of its specific optical properties. Rare-earth ions are used in lasers, optical amplifiers, and sensors because they have rich emission spectra. This allows them to generate and amplify light over a wide range of wavelengths.[1] Quantum dots have high photostability and strong luminescence. Because of this, they are used in broadband optical amplifiers, LCD backlighting, high-power LEDs, and luminescent solar concentrators that improve solar cell efficiency.[2,3,4] Plasmonic nanoparticles find application in emission enhancement, in photodetectors, plasmonic structures, photonic devices, and sensors. They are especially useful where strong localization and amplification of the electromagnetic field are needed.[5,6]

II. Methods

In this work, we combine these three types of materials in one system. Each of them is based on a different optical mechanism: lanthanide emission, excitonic emission, and plasmonic effects. They are embedded in a sodium borophosphate glass matrix ($Na_5B_2P_3O_{13}$, NBP). The material was prepared using the Nanoparticle Direct Doping (NPDD) method. This method allows direct introduction of plasmonic nanoparticles or quantum dots into the glass. It reduces processing time and improves the quality and uniformity of the material.

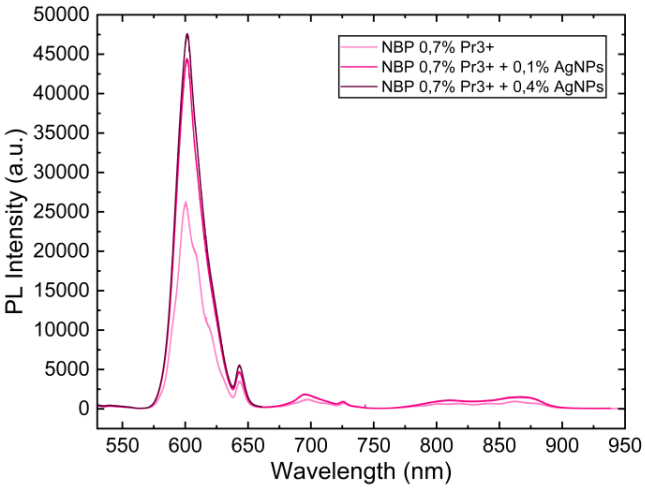

Fig. 1 Enhancement of luminescence in praseodymium-doped plasmonic glasses.

III. Results and Discussion

This type of doping is beneficial because one of the key effects in the material is localized surface plasmon resonance (LSPR), which enhances the local electromagnetic field in the vicinity of the plasmonic nanoparticles. LSPR occurs when incident light of a suitable wavelength interacts with the nanoparticles and induces collective oscillations of their conduction electrons. As a result, rare-earth ions and quantum dots located near the plasmonic particles experience a strongly enhanced local electromagnetic field compared with the incident field (Fig.1). This effect enhances the efficiency of optical processes in the system, such as luminescence and Raman scattering. [2,5,7]

IV. Conclusion

The obtained material can act as a multifunctional photonic platform. It shows tunable luminescence and stronger light – matter interaction. It may be used in nanophotonics, plasmonics, optical sensing, and spectrally engineered photonic devices. This hybrid glass is a promising material for compact systems that combine rare-earth ions, quantum dots, and plasmonic effects in advanced electromagnetic and photonic applications.

ACKNOWLEDGMENTS

We are grateful for the „Centre of ExcelleNce for nanophotonicS, advancEd Materials and novel crystal growth-Based technoLogiEs - ENSEMBLE3" project which is carried out within the 2.1 International Research Agendas programme of the Foundation for Polish Science co-financed by the European Union under the European Funds for Smart Economy 2021-2027 (FENG) and the European Union Horizon 2020 research and innovation program Teaming for Excellence (GA. No. 857543) for supporting this work. The publication was created as part of the project of the Minister of Science and Higher Education "Support for the activities of Centers of Excellence established in Poland under the Horizon 2020 program" under contract No. MEiN/2023/DIR/3797.

REFERENCES

[1] K. Maheshwari, Ravita *et al.*, "Spectroscopic studies of Pr3+ doped red-emitting BaO–ZnO– Li2O–P2O5 glasses for luminescent devices applications" Optical Materials, vol. 140, 113910, 2023.

[2] R. Nowaczynski, M. Gajc *et al.*, "Manufacturing of Volumetric Glass–Based Composites with Single- and Double-QD Doping" Part. Part. Syst. Charact., vol. 36, 1800124, 2019.

[3] B. Xu, H. Chen, T. Zhang *et al.*, "High quality quarternary-alloyed ZnCdSSe/ZnS quantum dots with single photoluminescence decay channel and high devise stability", J.Lumin., Vol. 240, 118463, 2021.

[4] J. E. Gan, H. S. Chen, "Photostable Quantum Dots for Energy-Efficient Color Conversion: Mapping Irradiance-Driven Degradation Pathways and Facet-Protected Structure." Adv. Optical Mater., vol. 13, no. 33 e01787, 2025.

[5] P. Piotrowski, Buza, M., Nowaczyński, R. *et al.* „Ultrafast photoluminescence and multiscale light amplification in nanoplasmonic cavity glass." Nat Commun, vol. 15, 3309, 2024.

[6] F. Ligmajer, M. Horák *et al.*, "Silver Amalgam Nanoparticles and Microparticles: A Novel Plasmonic Platform for Spectroelectrochemistry" J. Phys. Chem. C, vol. *123* (27), 16957-16964, 2019.

[7] K. Szlachetko, P. Piotrowski *et al.* "Selective surface-enhanced Raman scattering in a bulk nanoplasmonic Bi_2O_3-Ag eutectic composite" *Nanophotonics*, vol. 9, no. 14, 2020, pp. 4307-4314.

Electromagnetic Sensing and Materials Characterization

Giant Magnetoimpedance effect at GHz frequencies in amorphous microwires

Arcady Zhukov[1,2,3] Mihail Ipatov[4], Paula Corte-Leon[1,2,3,5], Juan Maria Blanco[1] and Valentina Zhukova[2,5*],

[1]Dept. Appl. Phys., Faculty of Engineering, Gipuzkoa, University of the Basque Country, EHU, 20018 Donostia-San Sebastian, Spain.
[2]EHU Quantum Center, University of the Basque Country, EHU, 20018 Donostia-San Sebastian, Spain.
[3]IKERBASQUE, Basque Foundation for Science, 48011 Bilbao, Spain.
[4]General Magnetic Measurement Service of Advanced Research Facilities (SGIker), University of the Basque Country, UPV/EHU, Donostia-San Sebastián, Spain.
[5]Dept. Polym. Adv. Mater., University of the Basque Country, EHU, 20018 Donostia-San Sebastian, Spain
[4]Dept. Mater. Science & Metallurgy, Univ. Cambridge, Cambridge CB3 0FS, UK
*Corresponding author: valentina.zhukova@ehu.eus

***Abstract*—We studied Giant magnetoimpedance (GMI) effect and magnetic properties of various Co-rich amorphous microwires. We measured magnetic field dependences of the GMI ratio up to GHz frequency range and observed quite high GMI ratio in studied microwires even at GHz frequencies. We observed different values of the magnetic anisotropy field obtained from the hysteresis loops and the GMI curves. Observed dependences can be explained considering different magnetic anisotropy in the surface layers and in the inner part of metallic nucleus and skin depth effect. Features of high frequency GMI effect have been analyzed using FMR-like approximation.**

***Keywords*—Giant magnetoimpedance effect, magnetic microwires, magnetic anisotropy, skin depth.**

I. Introduction

Studies of Giant magnetoimpedance, GMI, of soft magnetic materials have attracted considerable attention owing to extremely high sensitivity of the GMI effect to low magnetic field. From the viewpoint of technological applications main interest in GMI effect is related to creation of magnetic sensors for weak magnetic field detection applications [1,2].

Among soft magnetic materials thin ferromagnetic amorphous microwires (typically of 1-30 μm in diameter) are considered as the most promising materials owing to outstanding soft magnetic properties, highest GMI effect and reduced diameters suitable for microsensor applications [3]. Comparison of various magnetic field sensors shows that magnetic sensors using GMI effect of amorphous microwires present a number of advantages such as cheap technology, excellent performance (magnetic field resolution,) and low sensor dimensions [2].

Recently major attention is paid to the studies of high frequencies (GHz range) GMI owing to the development of thinner magnetically soft materials as well as recent tendency in miniaturization of magnetic field sensors [3].It is predicted that the diameter reduction must be associated with the increasing of the optimal GMI frequency range: a tradeoff between dimension and frequency is required in order to obtain a maximum GMI effect [3].

The thinnest soft magnetic microwires can be produced by so-called Tailor-Ulitovsky method allowing fabrication of glass-coated microwires with metallic nucleus diameter, d, from 0.05 to 80 μm and total diameter, D, from 5 to 100 μm.

We present our last results on the GMI effect of thin amorphous magnetically soft Co-rich microwires suitable for creation of microsensors based on high frequency GMI effect.

II. Methods

We studied glass-coated amorphous microwires with metallic nucleus diameters, d, of about 10-12 μm and a total diameter, D, of about 15 μm manufactured by the aforementioned Taylor-Ulitovsky method [3]. We measured magnetoimpedance effect in Co- rich microwires at frequencies up to 4 GHz. We used specially designed micro-strip sample holder placed inside a sufficiently long solenoid that creates a homogeneous magnetic field, H. The sample impedance, Z, was measured using vector network analyzer from reflection coefficient S_{11}. The GMI effect is expressed in terms of the GMI ratio, $\Delta Z/Z$, given as:

$$\Delta Z/Z = [Z(H) - Z(H_{max})] / Z(Hmax), \quad (1)$$

where H_{max} is the maximum applied field.

Hysteresis loops have been determined by flux-metric method, as described elsewhere [3].

III. Results and Discussion

Experimentally measured Z(H) dependencies measured in $Co_{67.7}Fe_{4.3}Ni_{1.6}Si_{11.2}B_{12.3}Mo_{1.3}C_{1.6}$ microwire (d ≈10μm, D=13.8 μm) present considerable influence of magnetic field on sample impedance up at GHz frequency (see Fig.1). Additionally, the magnetic field of maximum shifts to the higher field region with increasing of the frequency, f. But at GHz frequencies the magnetic fields corresponding to the impedance maximum, H_m,

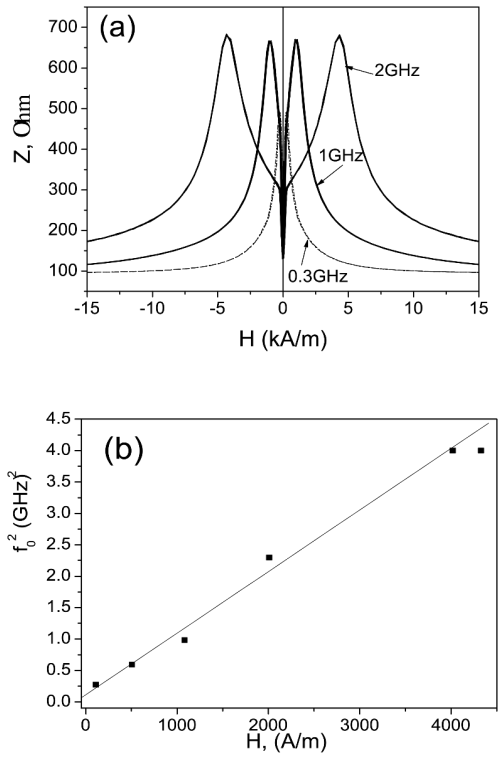

Fig.1. *Z(H)* dependence of $Co_{67.7}Fe_{4.3}Ni_{1.6}Si_{11.2}B_{12.3}Mo_{1.3}C_{1.6}$ microwires (d=10 μm, D=13.8 μm) measured at different frequencies (a) and $f_0^2(H)$ dependence for the same microwire (b).

are much higher than the magnetic anisotropy field (see Fig.2). Therefore we must assume that studied samples are magnetically saturated when exhibit an impedance maximum at GHz frequency range.

For interpretation of this behavior we paid attention on the fundamental link between ferromagnetic resonance, FMR and GMI [2]. Previously, we already get quite reasonable Ms values for lower frequencies considering this similarity[4]. Thus the saturation magnetization can be estimated from this approach using the equation:

$$Ms = 0.805x10^{-9}\, df_0^2/dH \qquad (2)$$

where f_0 is the resonant frequency, H is the applied magnetic field, M_s is the saturation magnetization. For studied samples and for GHz range we obtained linear fit of the square of the

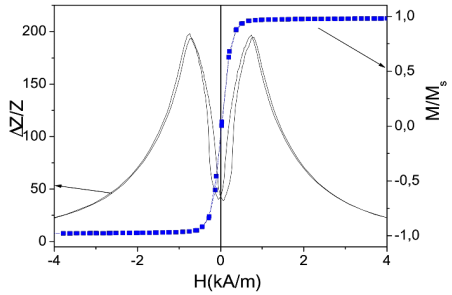

Fig.2. Hysteresis loop and ΔZ/Z(H) dependence of $Co_{77.3}Fe_{3.6}Ni_{0.2}Si_{10.5}B_{13.4}Mo_{0.9}$ microwires with d=11.4 μm, D=14 μm measured at 1 GHz

resonance frequency, f_0, on applied field. Some deviation can be appreciated in low-field region (Fig. 1b). The origin of this deviation is unclear and can be related with low field magnetization process.

IV. Conclusion

Concluding, studies of magnetic properties and GMI effect of amorphous Co-Fe rich microwires reveals that they present considerable GMI effect at GHz frequencies. We discussed observed experimental dependences considering both different magnetic structure, saturation magnetization and magnetic anisotropy in the bulk and near the surface and close analogy between giant magnetoimpedance and ferromagnetic resonance. Features of high frequency GMI effect can be described using FMR-like approximation.

Acknowledgments

The authors are thankful for the technical and human support provided by SGIker of UPV/EHU (Medidas Magnéticas Gipuzkoa) and European funding (ERDF and ESF). This research was funded by the Spanish MICIN, under PID2022-141373NB-I00 project, by EU "HARMONY" (Horizon Europe) project and by the Government of the Basque Country, under Elkartek (MOSINCO and ATLANTIS) projects and by under the scheme of "Ayuda a Grupos Consolidados" (Ref.: IT1670-22).

References

[1] L.V. Panina and K.Mohri, K. "Magneto-impedance effect in amorphous wires", Appl Phys Lett. Vol. 65, pp. 1189-1191, 1994

[2] D. Ménard, M. Britel, P. Ciureanu, and A. Yelon, "Equivalent Magnetic p.Noise Limit of Low-Cost GMI Magnetometer,",J. Appl. Phys., vol.84 p2805–2814, (1998).

[3] A. Zhukov, P. Corte-Leon, L. Gonzalez-Legarreta, M. Ipatov, J.M. Blanco, A. Gonzalez, V. Zhukova, "Advanced functional magnetic microwires for technological applications, "J. Phys. D: Appl. Phys. vol. 55, p. 253003, 2022, doi: 10.1088/1361-6463/ac4fd7

Numerical Simulation of a Low-Frequency Electromagnetic Induction Sensor for Non-Contact Soil Electrical Conductivity Measurement

Nahal Akbari[1], Mohammad Asefi[2,1], Greg E. Bridges[1], Behzad Kordi[1*]

[1]Department of Electrical & Computer Engineering, University of Manitoba, Winnipeg, MB, Canada
[2]TerraWave Radar Solutions, Winnipeg, MB, Canada
*Corresponding author: behzad.kordi@umanitoba.ca

***Abstract*—This paper presents a numerical model for a low-frequency electromagnetic induction sensor for non-contact soil conductivity measurement. A 3D finite element model is developed to solve the quasi-magnetostatic problem and evaluate the magnetic fields and induced currents. The effects of soil conductivity and frequency on the responses are analyzed.**

***Keywords*— electromagnetic induction, soil electrical conductivity, low-frequency sensing, eddy currents.**

I. Introduction

Measuring soil electrical conductivity provides valuable information in a broad range of applications, from environmental and agricultural monitoring [1] to the design of grounding electrodes in electric power systems [2]. Traditional contact-based methods require electrodes inserted into the soil, which can be slow, intrusive, and sensitive to surface conditions [3]. Electromagnetic induction (EMI) sensing is widely used for non-contact soil conductivity measurements [4]. A lightweight, contactless, air-coupled system of coils that operates above the ground would allow faster and more practical field measurements. In EMI systems, a transmitter coil generates a time-varying magnetic field that induces currents in the ground. These currents create a secondary magnetic field that is detected by a receiver coil. Several commercial and research systems exist that operate in the low kilohertz range to measure shallow subsurface conductivity. However, the electromagnetic response of such systems strongly depends on coil geometry, operating frequency, and soil properties, and these effects must be clearly understood before building a practical sensor [5]. Previous studies have shown that the measured signal depends on coil spacing, coil orientation, sensor height, and soil conductivity [6]. Some limited numerical modeling studies have been conducted to study these effects when analytical solutions are not sufficient [7].

In this work, a three-dimensional, numerical simulation model of a low-frequency EMI sensing system is developed that employs finite element method (FEM) to solve a quasi-magnetostatic formulation of the problem. Low-frequency operation is selected because it increases magnetic field penetration depth and keeps the system in the quasi-static regime, where the response is mainly controlled by soil conductivity rather than wave propagation effects. The system consists of a transmitter and receiver coil placed above the soil surface. The computational domain includes an infinite element boundary to simulate an open space and avoid artificial reflections or field distortion at the outer boundaries. This allows the magnetic field to decay naturally, representing realistic free-space conditions. The model calculates the magnetic field distribution in the air and in the soil, the induced current density in the soil, the induced current in the receiver coil, the power supplied to the transmitter, and the power loss in the soil. The effects of soil conductivity and operating frequency on the amplitude and phase of the receiver signal are analyzed. The ultimate goal of this research is to provide a clear numerical framework for understanding conductivity-dependent sensor behavior and supporting future sensor design.

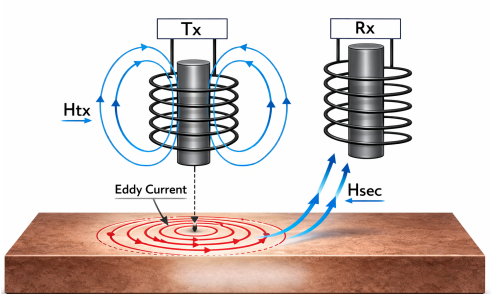

Fig. 1. Conceptual illustration of the electromagnetic induction (EMI) sensing principle showing the transmitter and receiver coils above soil. The transmitter coil induces eddy currents in the soil, which in turn generate a secondary magnetic field that induces a current in the receiver coils.

II. Formulation of the Problem

The operating principle of the proposed electromagnetic induction (EMI) sensor is illustrated in Fig. 1. A transmitter coil placed above the ground is excited by a time-harmonic current, generating a primary magnetic field $\mathbf{H}_{\mathrm{tx}}$. This magnetic field penetrates into the subsurface. When the soil has finite electrical conductivity ($\sigma > 0$), circulating eddy currents are induced within the ground. These induced currents generate a secondary magnetic field $\mathbf{H}_{\mathrm{sec}}$, which combines with the primary field. The receiver coil measures the total

magnetic response, which depends on soil conductivity, operating frequency, and coil configuration.

To describe this behavior mathematically, the system is modeled in the frequency domain under quasi-static conditions. The electromagnetic field formulation is based on Maxwell's equations expressed in a quasi-static regime in terms of the magnetic vector potential in a magnetically-homogeneous medium. The resulting Helmholtz equations is given by

$$\nabla^2 \mathbf{A} - j\omega\mu_r\mu_0\sigma\mathbf{A} = -\mu_r\mu_0\,\mathbf{J}_e \tag{1}$$

where $\mathbf{A}$ is the magnetic vector potential, ω is the radial frequency, μ_r is the relative permeability of the medium, $\mu_0 = 4\pi \times 10^{-7}$ H/m is the free space permeability, and σ is the electrical conductivity. In this equation, $\mathbf{J}_e$ is the external current density that is zero everywhere other than the transmitter coil. One can determine the magnetic field intensity $\mathbf{H}$ and the electric field intensity $\mathbf{E}$ using

$$\mathbf{H} = \frac{1}{\mu_r\mu_0}\nabla \times \mathbf{A} \quad \text{and} \quad \mathbf{E} = -j\omega\mathbf{A}. \tag{2}$$

The induced conduction current density is determined by

$$\mathbf{J} = \sigma\mathbf{E}. \tag{3}$$

To solve (1), a three-dimensional model of the schematic shown in Fig. 2 in developed in a commercial finite element software (COMSOL™ Multiphysics). In the model, each coil is represented as a hollow cylinder made of copper with a radius of a, height of h, and a thickness of t. The coils are at a height d above the ground and separated by a distance r.

III. Results and Discussion

To verify the accuracy of the model, a transmitter coil with the dimensions of $h = 60\,\text{cm}$, $a = 10\,\text{cm}$, and $t = 5\,\text{mm}$ carrying a current of $I_{\text{Tx}} = 1\,\text{A}$ is simulated. A magnetic field of $\mathbf{H} = 1.58\,\hat{\mathbf{z}}\,\text{A/m}$ is calculated at the centre of the coil. Theoretically, an approximation of the magnetic field at the centre of an N-turn solenoid of height h and carrying a current of I is given by

$$\mathbf{H} = \frac{NI}{h}\,\hat{\mathbf{z}}. \tag{4}$$

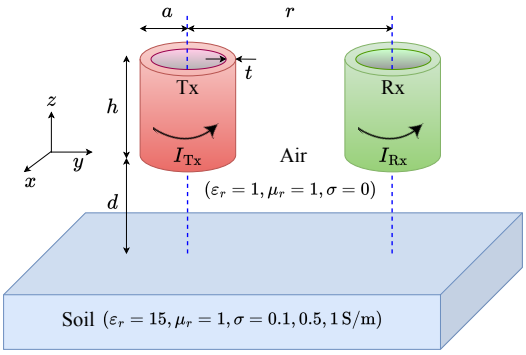

Fig. 2. Topology of the transmitter and receiver coils located above a lossy ground.

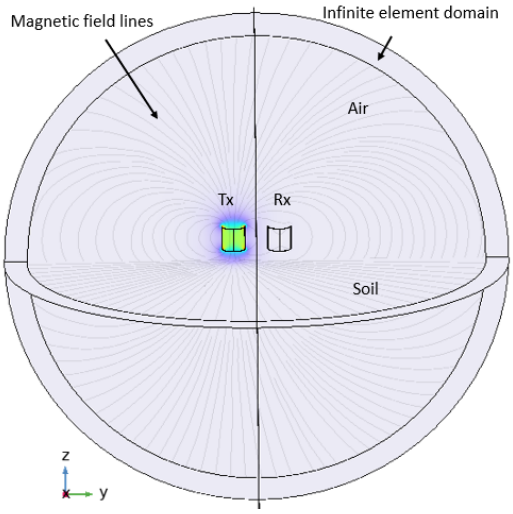

Fig. 3. Simulated magnetic flux density magnitude at $f = 20\,\text{kHz}$, showing magnetic field distribution and penetration into the soil.

Using this equation, a value of 1.66 A/m is calculated which is very close to the simulation result.

Next, two coils are simulated, assuming $h = 20\,\text{cm}$, $a = 10\,\text{cm}$, $t = 5\,\text{mm}$, $d = 10\,\text{cm}$, $r = 40\,\text{cm}$, and $I_{\text{Tx}} = 1\,\text{A}$. The transmitter coil creates a primary magnetic field that spreads outward and goes into the soil. The field is strongest near the transmitter and becomes weaker with distance. The infinite element domain allows the magnetic field to fade naturally at the outer edges of the model, so the model represents an open-space without artificial reflections. Figure 3 shows the distribution of the magnetic field in air and soil. We can also calculate the induced current in the receiver coil I_{Rx} and the eddy currents induced in the ground, as well as the voltages of the transmitter and receiver coils.

Figure 4.a shows the density of the eddy current (A/m^2) induced in the soil at $f = 20\,\text{kHz}$. Circular eddy currents are formed under the transmitter coil because of the time-varying magnetic field. The highest current density appears directly below the transmitter, where the magnetic field change is greatest. The current becomes weaker as we move away from the center. This confirms that the induced currents are caused by electromagnetic induction.

Figure 4.b shows a cross sectional view of the eddy currents on the yz plane inside the soil domain. The induced current density distribution clearly shows that the eddy currents are concentrated near the soil surface and directly beneath the transmitter coil. The extracted maximum current density values for different excitation frequencies are summarized in Table I. As the excitation frequency increases, the maximum induced eddy current density increases proportional to the frequency, consistent with reduced skin depth at higher frequency.

To study the effect of frequency further, a frequency sweep was performed while keeping the transmitter current and

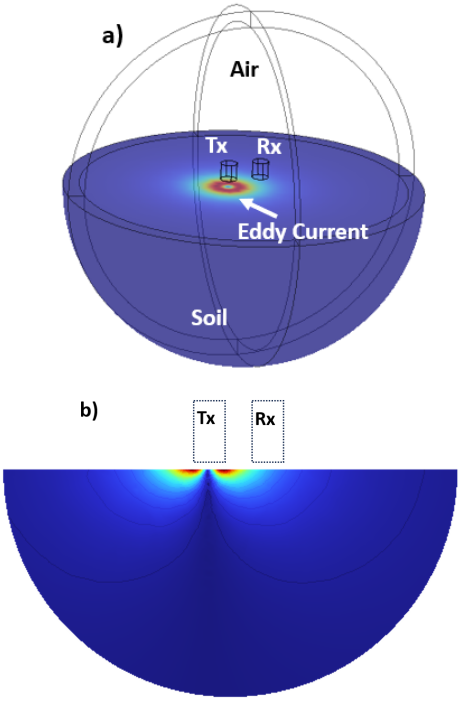

Fig. 4. (a) Induced current density distribution in the soil at 20 kHz showing circular eddy currents beneath the transmitter coil. (b) Current density magnitude on the yz plane, illustrating the concentration of eddy currents near the surface and directly below the transmitter coil.

TABLE I
MAXIMUM INDUCED EDDY CURRENT DENSITY VERSUS FREQUENCY.

f (kHz)	Maximum eddy current density (μA/m^2)
5	105
10	210
20	448

soil conductivity fixed ($I_{\mathrm{Tx}} = 1\,\mathrm{A}$ and $\sigma = 0.1\,\mathrm{S/m}$). The simulated induced current in the receiver coil I_{Rx}, the voltage required by the transmitter coil V_{Tx}, the total real power supplied to the transmitter coil P_{Tx}, and the total power loss in the soil P_{Soil} are summarized in Table II. The results shown in this table confirm that the transmitter voltage increases almost linearly with frequency, which is expected for an inductive behavior ($V_{\mathrm{Tx}} \propto f$). The soil power loss increases proportional to the square of the frequency ($P_{\mathrm{Soil}} \propto f^2$), which is well know for eddy current losses. In contrast, the receiver current magnitude I_{Rx} remains nearly constant over the tested frequency range. This indicates that the induced current in the receiver coil is primarily by direct coupling from the transmitter coil ($\mathbf{H}_{\mathrm{sec}} \ll \mathbf{H}_{\mathrm{tx}}$). One of the challenges of a sensing system for the measurement of soil electrical conductivity is to detect the change of the receiver current due to the eddy current induced in the soil.

To analyze the effect of soil conductivity, the total induced eddy current I_{eddy} and the the total loss in the soil P_{Soil}. The results are shown in Table III. As conductivity increases, the total eddy current in the soil increases proportionally, indicating stronger eddy current formation beneath the transmitter. The total volumetric loss in the soil also increases linearly with soil conductivity. These results confirm that increasing soil conductivity strengthens both the local induced currents and the overall energy absorption in the soil.

TABLE II
FREQUENCY SWEEP RESULTS ($I_{\mathrm{Tx}} = 1\,A, \sigma = 0.1$ S/M).

f (kHz)	I_{Rx} (mA)	V_{Tx} (mV)	P_{Tx} (μW)	P_{Soil} (nW)
5	10.513	$3.8 \angle 89.1°$	30	3
10	10.509	$7.6 \angle 89.4°$	38	12
20	10.507	$15.1 \angle 89.7°$	42	46

TABLE III
INDUCED EDDY CURRENT AND SOIL LOSS AT $f = 20$ KHZ.

σ (S/m)	I_{eddy} (μA)	P_{Soil} (nW)
0.1	114	46
0.5	566	231
1	1126	460

IV. CONCLUSION

A 3D frequency-domain numerical model of a low-frequency electromagnetic induction (EMI) sensor was developed to investigate non-contact soil conductivity measurement. Parametric studies were conducted, including frequency sweep and soil conductivity variation. The results show that (i) the induced eddy current and power loss in the soil increase with frequency linearly and quadratically, respectively, and (ii) increasing the soil conductivity results in a linear increase in both the eddy current and power loss, which are both consistent with the well-known facts about eddy current. The presented model provides a validated framework for developing air-coupled soil sensing systems.

REFERENCES

[1] P. A. Petsetidi, G. Kargas, and K. Sotirakoglou, "Investigation of topsoil salinity and soil texture using the em38-mk2 and the wet-2 sensors in greece," *AgriEngineering*, vol. 7, p. 347, 2025.
[2] B. Salarieh, H. J. De Silva, and B. Kordi, "Electromagnetic transient modeling of grounding electrodes buried in frequency dependent soil with variable water content," *Electric Power Systems Research*, vol. 189, p. 106595, 2020.
[3] Y. Yao, J. Fan, and J. Li, "A review of advanced soil moisture monitoring techniques for slope stability assessment," *Water*, vol. 17, p. 390, 2025.
[4] L. Wolf and A. Flores Orozco, "Design, development and application of a modular electromagnetic induction (EMI) sensor for near-surface geophysical surveys," *Sensors*, vol. 24, p. 4159, 2024.
[5] G. Wilson, J. Conrad, J. Anderson, A. Swidinsky, and J. Shragge, "Developing a low-cost frequency-domain electromagnetic induction instrument," *Geoscientific Instrumentation, Methods and Data Systems*, vol. 11, pp. 251–263, 2022.
[6] C. Finco, A. Wang, F. Rejiba, C. Schamper, and L. H. C. Fraga, "Calibration of near-surface multi-frequency electromagnetic induction data," *Geophysical Prospecting*, vol. 69, no. 8, pp. 1747–1764, 2021.
[7] P. E. Ratshiedana, M. A. M. Abd Elbasit, J. G. Chirima, G. Liu, E. Adam, and E. B. Economon, "Determination of soil electrical conductivity and moisture on different soil layers using electromagnetic techniques in irrigated arid environments in South Africa," *Water*, vol. 15, p. 1911, 2023.

Contactless Determination of Martensitic Phase in Austenitic Steels

Tatiana Damatopoulou, Athanasios Markoulis, Nikolaos Tsouvalis and Evangelos Hristoforou

[1]Laboratory of Electronic Sensors, National TU of Athens, Zografou Campus, Athens 15780, Greece, hristoforou@ece.ntua.gr
[2]School of Naval & Mechanical Engineering, National TU of Athens, Zografou Campus, Athens 15780, Greece,

In this paper we report results on the detection of martensitic phase in the SS316 austenitic steel grade during stress – strain and non-monotonic stress tests. Although the austenitic steels do not exhibit magnetic properties, the accumulated stresses due to their stress or fatigue result in martensitic phase transformation. The development and increase of the martensitic phase is the indication of the austenitic steel failure process, that has been studied in this work. During stress and fatigue, the three magnetic field components on the surface of the steel dogbone were monitored using AMR sensors with sensitivity and dynamic range of 100 nTHz$^{-1/2}$ and $\pm$10 mT respectively, allowing for the indirect observation of the martensitic phase development on the surface of the austenitic steel dogbone. This response appeared to be monotonic up to the ultimate tensile stress (UTS) point in the stress – strain measurement. Furthermore, the non-monotonic low-frequency cyclic stress resulted in a periodic stress effective field effect at least 18,000 cycles before the steel failure, allowing for time to perform emergency actions in corresponding engineering applicatins.

***Index Terms*—Austenitic steels, martensitic phase, magnetic memory method, fatigue tests, anisotropic magnetoresistance (TMR)**

Author Index

Gregory Abadias **165**
Ali Abbas **125**
Renat Abdullin **321**
Eslam Abubakr **66**
Giuseppe Addamo **237**
Badri Aekbote **79**
Andrei Afanasev **178**
Morteza Afshar **73**
Nada Aghad **125**
Javier Aizpurua **76, 98**
Nahal Akbari **475**
Alessandro Alabastri **73, 190**
Matteo Albani **256**
Ivano Alessandri **232**
Lyudmila Alexeyeva **404**
Astrid Algaba-Brazalez **316**
Hanan Alhesseny **468**
Malik Almunif **53**
Hatice Altug **248, 290**
Andrea Alu **52, 235**
Andrea Alù **77**
Yuri Álvarez-López **203**
Guillermo Alvarez-Narciandi **197, 199**
Francesco Anelli **397, 462**
Federica Anfuso **303**
Costantino De Angelis **153, 180, 232, 247, 250, 285, 288**
Simon Anglhuber **348**
Jaume Anguera **176**
Manuel Arrebola **262, 263**
Guillermo Arregui **350**
Samel Arslanagić **268**
Viktar Asadchy **60, 259**
Mohammad Asefi **475**
Mohammad Asgari **60**
Rizwan Asif **277**
Luca Assogna **140**
Fatih Bilge Atar **337**
Lorenzo Audibert **212**
Oscar Avalos-Ovando **94**
David Ayuso **70**
Jose Azana **148**
Amirhossein Babaee **271**
David Babonneau **165**
Paolo Baccarelli **158**
Alberto Bacci **92**
Artem Bakulin **352**
Leonetta Baldassarre **57, 355**
Pietro Baldin **288**
Maria Vanessa Balois-Oguchi **161**
Kingshuk Bandopadhyay **125**
Francesco Banfi **283**
Ole Bang **247**
Mirko Barbuto **229**
W. Bardyszewski **151**
Witold Bardyszewski **156**
Matteo Barelli **57**
B. K. Barman **186**
Michal Baronowski **172**
Olga Basile **358, 436**
Giada Maria Battaglia **321, 400**
Jérémie Béal **165**
A. Belardini **71**
Alessandro Belardini **116**
Leonid Y. Beliaev **232**
Joel Bellessa **218**
Jean-Michel Benoit **218**
Jamal Berakdar **185**
Nataliya Berezovska **458**
Aurélie Bertaux **173**
Miguel Beruete **127**
François Bessueille **218**
Lucas Besteiro **94**
Sylvain Betoule **70**
Filiberto Bilotti **158, 229**
Wilfried Blanc **333**
Valérie Blanchet **70**
Juan Maria Blanco **473**
D. Bobylev **151**
Nadia Giovanna Boetti **333, 344**
Pietro Bolli **400**
Alexandra Boltasseva **54**
N. Borriello **71**
Alexandre Bouhelier **173**
Alain Alain Braud **344**
Greg Bridges **475**
Felix Brikh **248, 290**
Pietro Brugnolo **268**

Author Index (cont.)

Simona Bruni **300**
Thanh-Lam Bui **413**
Paolo Burghignoli **158, 189**
Andrei Bylinkin **216**
Flaviana Calignano **237**
Giovanna Calò **115, 337**
Giovanna Calo **379**
Gabriele Calusi **350**
Sophie Camelio **165**
Marta Arias Campo **300**
Patrice Camy **344**
Angela Capocefalo **99**
Sabino Roberto Caporusso **379**
Luca Carletti **250, 285**
Alessandro Di Carlofelice **395**
Giuseppe Caruso **400**
Massimiliano Casaletti **297, 300**
Giuseppe Castaldi **274**
Alessandro Casto **283**
Nelson Castro **280**
Domenico de Ceglia **232**
Luigi Celona **329**
Emmanuel Centeno **179, 453**
Ramazan Cetiner **427**
Dimitrios Chatzidimitriou **167**
Mayeul Chavanne **212**
Zhi Ning Chen **37**
Fujia Chen **138**
Hongsheng Chen **138**
Maria Chernysheva **341**
Francesco Chiadini **449**
Thomas Christopoulos **81**
Maria Rita Cicconi **333**
Alfonso C. Cino **232**
Alasdair Clark **79**
João Alexandre Batista Coelho **361**
João Paulo Coelho **361**
Camilla Coletti **216**
Sylvain Combrie **393**
Alessandra Contestabile **274**
Brian Corbett **337**
Andrea Cordaro **219**
Paula Corte-Leon **473**
Christophe Couteau **147, 165**
Joel D. Cox **163**
Cristophe Craeye **304**
Lorenzo Crocco **51**
Benjamin Crockett **148**
Giulia Crotti **246, 288**
Marius Crouzier **115**
Aurélien Crut **101, 283**
Antonio Cuccaro **443**
Francisco Cuesta **60**
Alberto G. Curto **68**
Antonella D'Orazio **115**
Alicja Dabrowska **335**
Béatrice Dagens **115**
Tatiana Damatopoulou **478**
Mauro David **335**
Piero Decleva **70**
Cyril Decroze **282**
Kaveh Delfanazari **131**
Angela Dell'Aversano **443**
Florian Dell'Ova **173**
Dominique Descamps **70**
Miguel Beruete Diaz **294**
Emidio DiGiampaolo **395**
Igor Dmytruk **458**
Loreto Di Donato **329, 443**
Hatou Yvelin Donkeng **92**
D. Dovzhenko **151**
Wei Du **415**
Erik Dujardin **173**
Mehmet Atif Durmus **142**
Heike Ebendorff-Heidepriem **338**
Parastoo Ebrahimi **65**
Manfred Eich **65**
Ramy ElGanainy **122**
Shaimaa Elseddiq Abuelsaud Ali Elghetany **329**
Ruggero Emmanuele **94**
K. Łempicka-Mirek **151**
Jose A. Encinar **263**
Mikel Aldea Esnaola **294**
Ruben Esteban **98**
Mauro Ettorre **45**
Aleksei Ezerskii **290**
Marco Faenzi **372**
Andrea Di Falco **43**

Author Index (cont.)

Virginia Falcone **254**
Tongmiao Fan **110**
Henna Farheen **460**
Maria Josè Lo Faro **193**
Matteo Fasano **283**
Natalia Del Fatti **101, 283**
Barbara Fazio **193**
Letizia Fede **70**
Alessandro Fedeli **214, 331**
Gabriele Federico **308**
G. Fedorov **132**
Olexander Fedotov **458**
Dou Feng **77**
Toney Fernandez **338**
Giulio Ferrando **57**
Carino Ferrante **140**
Flaminio Ferrara **449**
Catarina Ferreira **163**
Marcello Ferrera **274**
Stefano Ferretti **99**
Francesco Ferretti **395**
Francesca Filograno **115**
Andrea Fiore **350**
Marian Florescu **149**
Paolo Fornasiero **73**
Jens Forssén **316**
M. Forster **151**
Jens Förstner **460**
Stiven Forti **216**
Antonino Foti **57**
Zisis Foufas **440**
Erica Fragomeni **57**
Paolo Franceschini **232, 247, 250**
Gérard Colas des Francs **173**
Lars Franke **85**
Jesse Frantz **180**
Kristina Frizyuk **253**
Thomas Fromentèze **282**
Peng Fu **63**
Walter Fuscaldo **189, 366**
Matteo Gabardi **277**
Pavel Gajdoš **170**
Vincenzo Galdi **274**
Maurilio Galletta **193**
Alessandro Galli **189**
Marco Gandolfi **153, 180, 277**
Hanyu Gao **79**
Bruno Garavelli **277**
Alicia Elena Torres García **294**
Maria Garcia-Fernandez **197, 199**
Kasper van Gasse **112**
Caroline Gauchotte-Lindsay **79**
Sylwester Gawinkowski **75**
Li Ge **103, 122**
Gianluca Gennarelli **449**
I. Georgakilas **151**
Davy Gerard **111**
Davy Gérard **165**
Yaroslav A. Gerasimenko **348**
Lim Geunweon **148**
Neda Ghofraniha **99**
Claudio Giannetti **277**
Alejandro Gil-Martínez **310, 433**
Maria Caterina Giordano **57**
Tommaso Giovannini **91**
Federico Giusti **256, 366, 370**
Nikita Glebov **290**
Heedong Goh **77**
Jose Luis Gomez-Tornero **316**
P. André Gonçalves **96**
David Gonzalez-Ovejero **293, 366**
Camilla Gonzini **350**
Majid Goodarzi **148**
Maxim Gorkunov **80**
Alexander Govorov **94**
Gabriele Gradoni **205, 267**
Nicoletta Granchi **350**
Rachel Grange **254**
Thomas Grant **89**
Anthony Grbic **53, 271**
Kirill Grebnev **341**
Jorik van de Groep **142**
Imke Gronwald **348**
Nicolas Gros **173**
Changzhi Gu **63**
Davide Guarnera **92**
Massimiliano Guasoni **287**
Pietro Gucciardi **57**

Author Index (cont.)

Pietro G. Gucciardi **59**
Rocco Guerriero **449**
Alexa Guglielmelli **119**
John Guillamon **192**
Jan de Haan **112**
Houssem Haddar **212**
Emebet Hadgu **282**
Nikolas Hadjiantoni **77**
Tuomas Haggren **110**
Toby Hallam **468**
Haoran Han **265, 445, 447**
Stephen Hanham **77**
Hayk Harutyunyan **97**
Noel Healy **468**
Melissa Hedir **122**
Frank Hegmann **347**
Matthias Heinrich **145**
Ori Henderson-Sapir **338**
D. Hernandez-Pinilla **186**
Ortwin Hess **46**
Rainer Hillenbrand **76, 216**
Altunkan Hizal **427**
Michal Horák **170**
Evangelos Hristoforou **478**
Yitian Huang **265**
Min Huang **265**
Rupert Huber **348**
Markus A. Huber **348**
Jakob Hüpfl **89**
Simone Iadanza **337**
Maria Antonia Iatì **59**
Maryam Iftikhar **331**
Eva Rajo Iglesias **280**
Hiroshi Imada **102**
Miyabi Imai-Imada **195**
Francesca Intonti **350**
Mihail Ipatov **133, 473**
Alessia Irrera **193**
Tommaso Isernia **321**
Amiel Ishaaya **344**
Rasmus E. Jacobsen **268**
Chennupati Jagadish **110**
Venkatesan Jambunathan **344**
Davide Janner **344**
Line Jelver **163**
Kaiwen Ji **122**
Sancenia Johnson **391**
Christian Johnson-Richards **468**
Magnus Jonsson **88**
Garima Joshi **423**
Jiří Kabát **465**
M. Kafesaki **132**
Maria Kafesaki **259**
Sota Kagami **107**
Kotaro Kajikawa **161**
G. Kakarantzas **132**
Victor Kalt **179, 453**
Ladislav Kalvoda **73**
Tetsuo Kan **66**
Ilmira Kanymgaziyeva **404**
P. Kapuscinski **151**
Ioannis Katsantonis **259**
Michael Katsav **368**
Georgy A. Kazakov **112**
M. Kedziora **151**
Ahsan Ullah Khan **303**
Kedar Khare **323**
Amine Khitous **173**
Ioannis Kiorpelidis **145**
Uładzimir Kislyi **389**
Yuri Kivshar **248**
Steffen Klingel **85**
Stepan Kment **73, 413**
Hana kmentova **413**
Snezana Lazic Knezevic **223**
P. Kokhanchik **151**
Karol Kolataj **221**
Behzad Kordi **475**
Thomas Koschny **440**
Tsampikos Kottos **192**
Imene Kouicem **116**
A. D. Koulouklidis **132**
Anastasios D. Koulouklidis **348**
Jan Krajczewski **117**
Vlastimil Křápek **170, 465**
Alexey Krasavin **108**
Thomas Krauss **47**
Emmanouil Kriezis **81**

Author Index (cont.)

Artemijs Krimovs **68**
Stefanie Kroker **385**
M. Krol **151**
Andrzej Kudelski **135**
Waroth Kuhirun **381**
P. Kula **151**
Yuiichi Kurashima **107**
P. Kuzhir **132**
Sergei Kuznetsov **389**
Maria Grazia Labate **400**
P. G. Lagoudakis **151**
Adam Lamecki **172**
David Lancaster **338**
Valeri Lapanik **389**
Samuel Lara-Avila **216**
Fernando Las-Heras **197, 203**
Noelle Lascoux **101**
Poonam Lathiya **420**
Andrei Laurynenka **247**
Jaime Laviada **197, 203**
Andrei V. Lavrinenko **232**
Hac Huong Thu Le **107**
G. Leahu **71**
Grigore Leahu **116**
Mauro da Silva Leme **361**
Bernhard Lendl **335**
Giuseppe Leo **39**
Iker Herrero Leon **76**
Unai Arregui Leon **250, 285**
Antonio Leonardi **193**
Giovanni Leone **320**
Wiktor Lewandowski **220**
Huanan Li **123**
Ruichen Li **265**
Longren Li **352**
Carlo Liberale **121**
Zin Lin **192**
Leopold Lindenbauer **335**
I. Liontos **132**
Silvia Liprandi **277**
H. Lipsanen **132**
Jiří Liška **465**
Natalia M. Litchinitser **180**
Andrea Locatelli **92**
Antonella Maria Loconsole **397, 462**
Matteo Lodde **350**
Pavel Loiko **344**
Zeyu Long **418**
Michela Longhi **302**
Joris Lousteau **333, 344**
Zhuorui Lu **333**
Huan Lu **445, 447**
Tetiana Lunko **458**
Haiyao Luo **138**
Jinghao Lv **447**
Yanhe Lyu **37**
Xuedan Ma **94**
Jinyong Ma **110**
Kevin MacDonald **89**
Ross Glyn MacDonald **226, 410, 468**
Stefano Maci **44, 256, 280, 293, 370, 372**
Mikhail Madji **158**
Giovanni Magno **115, 379**
R. F. Mahrt **151**
Paolo Maioli **283**
Yann Mairesse **70**
Maria Antonia Maisto **319, 324**
Maria A. Maisto **329**
Margherita Maiuri **288**
Sergey Makarov **290**
Konstantinos G. Makris **145**
Konstantinos Makris **183**
G. Malpuech **151**
Radu Malureanu **232, 247**
Karen Mamian **112**
Alena Mamonova **80**
Iryna Mamontova **458**
Sergii Mamykin **458**
Onofrio M. Maragò **59**
Nicola Maraviglia **337**
Bouchez Marceau **293**
Sylvie Marguet **101**
Andrea Marini **140**
Athanasios Markoulis **478**
Krzysztof Markus **125**
Léo Martin **173**
Rubén Pedreño Martínez **238**
Daniel Martinez-de-Rioja **263**

Author Index (cont.)

Eduardo Martinez-de-Rioja **263**
Enrica Martini **36, 256, 366, 370, 372**
Alex Ramiro Masaquiza-Caiza **201**
Luca Mascaretti **73, 413**
Antonio David Hernández Mateos **313**
Andrzej Materna **125**
N. Matthaiakakis **132**
Giorgio Sebastiano Mauro **92**
R. Mazur **151**
Alexander Meek **149**
Mario Junior Mencagli **275**
Davide Mencarelli **302**
Evgenii Menshikov **232**
Moritz Merklein **150**
Aleksandra Michałowska **117**
Sanja Đurđić Mijina **223**
Grigorii Milenin **456**
Song Young Min **114**
Seokhwan Min **129**
R. Mirek **151**
Xenofon Mitsalas **280**
Ershad Mohammadi **142**
Francesco Buatier de Mongeot **57**
Davide Monopoli **337**
Luis Montano-Priede **98**
Alessio Monti **158, 229**
Andrea Francesco Morabito **321, 400**
P. Morawiak **151**
Antoine Moreau **179, 453**
Federico Moscatelli **397, 462**
Mohamed Mostafa **259**
Taisei Motomura **107**
Vincenzo Mottola **210**
Michal Mrozowski **172**
Giacomo Muntoni **242**
P. Mustonen **132**
M. Muszynski **151**
Viktor Myroshnychenko **460**
Tadaaki Nagao **186**
Pooja Uday Naik **287**
Alberto Naldoni **73, 413**
Ouassila Narsis-Labbani **173**
Miguel Navarro-Cía **77**
Andrew Naylor **407**
Edoardo Negri **189, 366**
Svenja Nerreter **348**
Luca Neubacher **89**
D. Thien Ngo **186**
Christophe Nicolle **173**
Maxim Nikitin **247**
Teruya Noguchi **66**
Simone Normani **344**
Georgios Nousios **81**
Libor Nozka **117**
Liam O'Faolain **337**
Maria Vanessa Oguchi **187**
P. Oliwa **151**
Przemysław Oliwa **156**
Mohammad Omki **214**
Andrés Ordóñez **70**
Daniel Osborne **79**
I. Appiah Oto **132**
E. Oton **151**
David Ottaway **338**
Daigo Oue **90**
David Gonzalez Ovejero **372**
Victor Pacheco-Peña **226, 272, 407, 410, 468**
Robert Pal **68**
Giovanna Palermo **119**
Roberta Palmeri **92, 321**
Chenxinyu Pan **108**
Clément Panais **101**
Fabio Paonessa **237**
Junhyung Park **129**
Olesiya Pashina **288**
Olesia Pashina **290**
Stanislas Pasternak **393**
José Antonio López Pastor **313**
Santi Concetto Pavone **92, 303, 358, 436**
Dorota Pawlak **125**
Asier Marzo Pérez **294**
Jesus Perez-Valero **310**
Anthony Perri **79**
Raphaël Pestourie **282**
Martin Petek **304**
Stéphane Petit **70**
E. Petronijevic **71**
Emilija Petronijevic **116**

Author Index (cont.)

Alexander Yu. Petrov **65**
Mihail Petrov **288, 290**
Vincenzo Petruzzelli **379**
William Peveler **79**
Oscar Antonio Peverini **237**
Maurice Pfeiffer **65**
W. Piecek **151**
Luca Pierantoni **302**
Rocco Pierri **320**
B. Pietka **151**
Franck Pigeonneau **333**
Ravel Carlos de Miranda Pimenta **297**
Anatoliy Pinchuk **458**
Marcos R. Pino **262, 426**
Antonio Pino **263**
Piotr Piotrowski **125**
Gianpaolo Piscitelli **210**
Giovanni Piscopo **115**
Alexandros Pitilakis **167**
Jérôme Plain **165**
Eva A. A. Pogna **348**
Bernard Pons **70**
Baptiste Poursat **79**
Mario Del Prete **319**
Francesco Priolo **193**
Eleni Prountzou **254**
Francesco Prudenzano **397, 462**
Natale Pruiti **337**
Patryk Pyrcz **75**
Yalong Qin **418**
Xianghui Qiu **60**
Xiwen Qiu **110**
Marco Rahm **85**
Debobrata Rajak **70**
Eva Rajo-Iglesias **40**
Georg Ramer **335**
Andrea Randazzo **214, 331**
David Cañete Rebenaque **238**
Roman Redko **456, 458**
Svitlana Redko **456**
Yudong Ren **138**
Rostislav Řepa **170, 465**
Hamid Reza-Darabian **125**
Shadi Rezaei **59**
Giovanni Riccio **449**
Ivan Richter **73**
Carlo Rizza **274**
Isabel Pascual Robledo **76**
Davide Rocco **250, 285**
David Orlando Rodriguez-Duarte **201**
Damián E. Rodríguez-Trujillo **127**
Yolanda Rodriguez-Vaqueiro **263**
Philippe Roelli **76, 216**
Silvia Romano **136**
Charles Roques-Carmes **112**
Alfredo De Rossi **393**
Stefan Rotter **89**
Connor Rowe **148**
Katarzyna Sadecka **125**
Wouter Saeys **277**
Rosalba Saija **59**
Shiro Saito **66**
Nunzio Salerno **92**
Ermelinda Salvaggio **165**
Davide Santagata **205, 324**
Alessandro Santorsola **379**
Julien Sarrazin **310**
Yutaro Sato **161**
Yelizaveta Savchuk **456**
Lorenzo Scalcinati **237**
Michael Scalora **153, 248, 274**
U. Scherf **151**
J. Christoph Scheytt **460**
Rudolf Schick **79**
Olav Thorbjørn Sandberg Schiess **247**
Andrea Schirato **73, 246, 288**
Thorsten Schumm **112**
Martha Segura **344**
Kaushik Sengupta **177**
I. Septembre **151**
Olga Sergaeva **250, 288**
Rebecca Setford **79**
Guy Shafriri **344**
Tigran Shahbazyan **391**
Vladimir M. Shalaev **41**
Naveen Shetty **216**
Jonghwa Shin **129**
Olena Shtykalo **458**

Author Index (cont.)

Vitaliy Shvalagin **456**
C. Sibilia **71**
Concita Sibilia **116**
Helgi Sigurdsson **156**
Tomáš Šikola **170, 465**
Vyacheslav M. Silkin **216**
Mário Silveirinha **90**
Matteo Silvestri **140**
Marco Simone **358, 436**
Ivan Sinev **248, 290**
Chad Siperley **79**
Zvonimir Šipuš **306**
Tom T. C. Sistermans **68**
Georgios A. Siviloglou **145**
Antonio Skarmeta **310, 433**
Claudia Skubisz **71, 116**
Rafik Smaali **179, 453**
Bart Smolders **308**
Igor Smolyaninov **182**
Raffaele Solimene **205, 319, 324, 329, 443**
Marin Soljacic **55**
Dmitry Solnyshkov **151**
Qinghua Song **105**
Gino Sorbello **92, 303, 329, 358, 436**
Marc Sorel **337**
Simone Sotgiu **57**
Dimitrios Sounas **275**
Chris Sparling **70**
Justin Sperling **79**
Ulrich Starke **216**
T. Stoferle **151**
Giuseppe Strangi **119**
Andreas Strauch **460**
Andrey Sukhorukov **110**
Hao Sun **148**
Hironori Suzuki **66**
Clementine Symonds **218**
Alexander Szameit **145**
J. Szczytko **151**
Jacek Szczytko **156**
Aleksandra Szymańska **117**
Junichi Takahara **93**
Akifumi Takamizawa **107**
Osamu Takayama **232, 247**
Ryohei Takei **107**
Antonello Tamburrino **210**
Hark Hoe Tan **110**
Takasumi Tanabe **87**
Alfonso Tanga **277**
Pilar Castillo Tapia **308**
Fabiano Tarulli **283**
P. Tassan **151**
Davide Tedeschi **140**
Jorge Teniente **127**
A. Theodosi **132**
Antreas Theodosiou **334**
Denis Tihon **304**
Ivan Toftul **248**
Andrea Tognazzi **232, 234, 247, 250**
Monika Tomczyk **125**
Dubravko Tomić **306**
Limin Tong **108**
Pavel Tonkaev **248**
José Luis Gómez Tornero **238, 313, 433**
Alicia E. Torres-García **127**
Giuseppe Torrisi **92**
Felice Torrisi **352**
Alessandro Toscano **158, 229, 302**
Sergei Tretyakov **60**
Damián Ernesto Rodríguez Trujillo **294**
Odysseas Tsilipakos **81, 132, 167, 440**
Nikolaos Tsouvalis **478**
Stelios Tzortzakis **132**
Chidinma Uche **282**
Kosei Ueno **159**
Ashray Ugle **300**
Sergio Ulloa **94**
D. Urbonas **151**
Guido Valerio **300, 310**
Giuseppe Della Valle **246, 250, 285, 288**
Jorge Teniente Vallinas **294**
Alvaro F. Vaquero **262, 426**
Jorge Alberto Tobon Vasquez **304**
René P. J. van Veldhoven **350**
Stefano Vellucci **229**
Alessandro Veltri **59**
Tommaso Venanzi **57**
Stella Ventucci **189**

Author Index (cont.)

Pablo Antonio Martínez Vicente **316**
Alejandro del Hoyo Vijande **203**
R. Vijaya **423**
Maria Antonietta Vincenti **153, 180, 248, 274**
Luca Vincetti **342**
Francesca Vipiana **50, 201, 304**
Leonardo Viti **348**
Miriam S. Vitiello **348**
Margherita Vittucci **283**
Frank Vollmer **217**
Giovanni Volpicelli **320**
Artem Vorobev **337**
R. Li Voti **71**
Roberto Li Voti **116**
Muhammad Salman Wahidi **65**
Finlay Walton **79**
Xuchen Wang **60**
Wei Wang **94**
Pan Wang **108**
Cheng-Zhen Wang **192**
Tong Wang **352**
K. Watanabe **186**
Xin Wei **377**
Maximilian Weimar **89**
Gary Wiederrecht **94**
Gabriele Williams **391**
Liam Wilson **79**
Xinyan Wu **65**
Bei Wu **138**
Shuwei Wu **352**
Dan-Xia Xu **48**
Alejandro Yacomotti **122**
Rositsa Yakimova **216**
Alex Yakovlev **226**
Rambabu Yalavarthi **413**
Jiaruo Yan **259**
Ao Yan **352**
Yihao Yang **138**
Oleh Yermakov **64**
Oleg Yeshchenko **458**
Hayrullah Yildiz **427**
Gang Yu **267**
Shuai Yuan **60**
Okan Yurduseven **199**
Nerea Zabala **98**
A. Zakharov **216**
Giorgio Zambito **57**
Mario Zannoni **237**
Mark Justine Zapanta **277**
Mario Zapata-Herrera **98**
Anatoly Zayats **108**
Li Zhang **138**
Lu Zhang **138**
Rui Zhao **138**
Jiwei Zhao **265, 415, 445, 447**
Nikolay Zheludev **89**
Junsheng Zheng **108**
Bin Zheng **265, 377, 415, 445, 447**
Qi Zhong **122**
Huanli Zhou **89**
Wei Zhou **377**
Hang Zhou **418**
Xinyi Zhu **148**
Peixuan Zhu **445**
Rongrong Zhu **445**
Arcady Zhukov **133, 473**
Valentina Zhukova **133, 473**
Martin Zizlsperger **348**
Dimitrios Zografopoulos **81**

Session Index

Plenary Presentations	**35**
Keynote Presentations	**42**
Recent Advances in Nanophotonics and Metamaterials	**56**
Computational Electromagnetics for Radiating Structures and Complex Media	**155**
Electromagnetic Inverse Scattering Problems for Imaging, Sensing and Communications	**196**
Light Engineering at the Nano-Scale: Insights from Plasmonics and Metamaterials	**215**
Metasurface modeling from Microwave to Optics	**225**
Advanced Techniques for Antennas, RF, and MW Components Fabrication	**236**
Nonlinear metasurface and flat-optics	**245**
Recent Advancements in Metamaterials and Metasurfaces for Scattering and Wave Engineering	**255**
Time-modulated Electromagnetic Systems	**270**
Nano-objects and metasurfaces for opto-thermo-mechanical management	**276**
Young Researchers in Antennas and Metasurfaces	**292**
Advanced antenna designs for Joint Communication and Sensing, Localization and Radiative Wireless Power Transfer	**309**
Inverse problems for synthesis, design and characterization of electromagnetic devices	**318**
From UV to Mid-IR: A Broad Spectrum for Innovative Applications	**332**
Nanomaterials and Complex Media for Sensing and Optoelectronic Devices	**346**
Antenna Theory and Design	**357**
Electromagnetic Theory: Analytical, Computational and Numerical Methods	**365**
Novel Materials, Metamaterials, Metasurfaces, FSS and EBG	**376**
Terahertz, Nanophotonics and Quantum Optics	**388**
Optics, Photonics and Nanophotonics	**394**
Antennas, Metasurfaces and Electromagnetic Devices	**406**
Antennas, Microwave Systems and Electromagnetic Structures	**417**
Photonics, Plasmonics and Optical Devices	**452**
Electromagnetic Sensing and Materials Characterization	**472**

Country Index

Algeria **116**

Australia **110, 150, 248, 338**

Austria **89, 112, 335**

Belgium **68, 112, 277, 304**

Canada **48, 148, 347, 475**

China **60, 63, 105, 108, 110, 123, 138, 265, 290, 377, 415, 418, 445, 447**

Croatia **306**

Cyprus **334, 389**

Czech Republic **73, 117, 170, 413, 465**

Denmark **96, 163, 232, 247, 268**

Finland **60, 132, 259**

France **39, 70, 81, 101, 111, 115, 122, 147, 151, 165, 173, 179, 212, 218, 282, 283, 293, 297, 300, 310, 333, 344, 366, 372, 393, 453**

Germany **64, 65, 70, 85, 145, 151, 185, 216, 253, 300, 333, 341, 348, 385, 460**

Greece **81, 132, 145, 167, 183, 259, 440, 478**

Hungary **70**

India **323, 420, 423**

Ireland **46, 337**

Israel **344, 368**

Italy **36, 44, 50, 51, 57, 59, 70, 71, 73, 91, 92, 99, 115, 116, 119, 136, 140, 153, 158, 180, 189, 193, 201, 205, 210, 214, 216, 229, 232, 234, 237, 242, 246, 247, 248, 250, 256, 274, 277, 280, 283, 285, 288, 293, 302, 303, 304, 319, 320, 321, 324, 329, 331, 333, 337, 342, 344, 348, 350, 352, 355, 358, 366, 370, 372, 379, 395, 397, 400, 413, 436, 443, 449, 462**

Japan **66, 87, 90, 93, 102, 107, 159, 161, 186, 187, 195**

Kazakhstan **404**

Korea **77, 114, 129**

Poland **75, 117, 125, 135, 151, 156, 172, 220**

Portugal **90, 361**

Russia **80, 288, 290**

Saudi Arabia **121**

Singapore **37**

Spain **40, 76, 94, 98, 127, 133, 176, 197, 199, 203, 216, 223, 238, 262, 263, 280, 294, 310, 313, 316, 344, 426, 433, 473**

Sweden **88, 216, 268, 316**

Switzerland **151, 221, 248, 254, 290, 337**

Thailand **381**

The Netherlands **142, 308, 350**

Türkiye **427**

Ukraine **456, 458**

United Kingdom **43, 47, 68, 70, 77, 79, 89, 108, 131, 149, 151, 199, 205, 217, 226, 267, 272, 274, 287, 337, 352, 407, 410, 468, 473**

USA **41, 45, 52, 53, 54, 55, 73, 77, 79, 94, 97, 103, 122, 177, 178, 180, 182, 190, 192, 219, 235, 248, 271, 275, 282, 391, 440, 458**